

PROCEEDINGS OF THE 59TH ASNR ANNUAL MEETING

Electronic Educational Exhibits

1283

"Complex" Chiari: What the neurosurgeon needs to know

M Papachristou¹, R Ward², V Agarwal², B Branstetter²

¹Unaffiliated, Pittsburgh, PA, ²University of Pittsburgh, Pittsburgh, PA

Purpose

PRESENTATION OUTLINE: I. COMPLEX CHIARI A. Definition B. Overview of clinical presentation and imaging features II. CNS ELEMENTS A. Chiari I Malformation B. Chiari 1.5 C. Cervicomedullary Kink D. Syringomyelia III. SKULL BASE/CVJ ABNORMALITIES A. Central pillar variants: i. Short Clivus ii. retroflexed dens B. Platybasia with basilar invagination: Group I and II basilar invagination C. Biomechanics of the craniovertebral junction and clivo-dental pivot IV. MASS EFFECT AND NEURAXIAL DEFORMATION STRESS A. Causes of ventral brainstem compression i. Posterior fossa mass effect ii. Bony fulcrum formed by CVJ variants and CC kyphosis B. Neuraxial Deformation Stress i. Ventral longitudinal compression ii. Stretch-induced myelopathy V. METRICS: A. Tonsillar descent caudal to McRae's line B. Odontoid violation of Chamberlain's line C. NDS metrics i. Clivo-axial angle ii. Grabb's line (pB-C2) VI. TREATMENT IMPLICATIONS: Surgical triage algorithms per Brockmeyer and Henderson VII. SUMMARY

Materials and Methods

OBJECTIVES: 1. To review the pathophysiology and radiographic features of "Complex" Chiari 2. To learn measurement methods of CXA and pB-C2 and integrate them into clinical reports 3. To gain awareness of algorithms used by neurosurgeons to plan appropriate surgical strategy.

Results

n/a

Conclusions

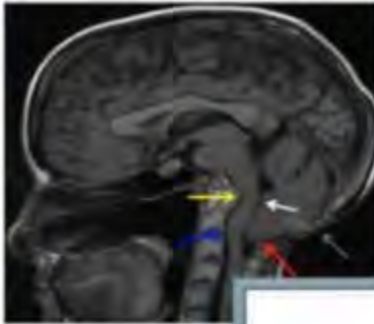
Chiari I Malformation (CMI) accompanied by additional radiographic findings is often referred to as "Complex" Chiari (CC). Relevant abnormalities may be grouped into deformities of the craniovertebral junction (CVJ) and central nervous system components. Because these abnormalities contribute to the overall disease process, such patients often require different surgical procedures to achieve symptom relief. Recently, the neurosurgical community has increasingly recognized the importance of neuraxial deformation stress (NDS) in the pathogenesis of cervicomedullary syndrome. Mechanisms of NDS may be subdivided into ventral brainstem compression (VBSC) and stretch-induced myelopathy (SIM). The risk of VBSC and SIM associated with CVJ variants is subsumed into certain radiographic metrics: clivo-axial angle and pB-C2. Familiarity with the imaging findings and relevant metrics of Complex Chiari can improve radiologists' relevance to our neurosurgical colleagues and the patients we both serve.

"Complex" Chiari: Features

Failed posterior fossa decompression (gray arrow)

Caudal descent of the Cerebellar tonsils (red arrow) and obex (white arrow): Chiari I?

Cervicomedullary kink (blue arrow) and basilar deformity (yellow arrow)

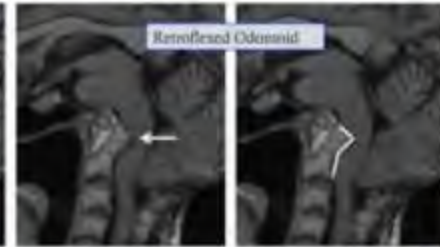


"Complex" Chiari: Central Pillar Features

Basoccipital hypoplasia and Platybasia



Retroflexed Odontoid



"Complex" Chiari: Classic Metrics

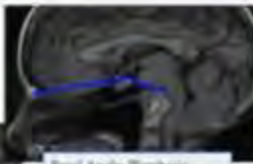


Cerebellar tonsil and obex caudal to (estimated) Chamberlain's line^a

Demarcates Chamberlain's Line^a
Type II Basilar Invagination



Basilar Angle: Platybasia



^aMeasured using the posterior border of the

"Complex" Chiari: NDS Metrics

Abnormal CXA (<135°)

Abnormal pB-C2 (>9mm)

Normal BAI (<12mm)^b



"Don't Forget" the PET: The Utility of FDG Brain PET Imaging in Neurodegenerative Disease

A Rizvi¹, J Young¹, D Johnson²

¹Mayo Clinic, Rochester, MN, ²Mayo Clinic, ROCHESTER, MN

Purpose

Summary of Planned Presentation We will discuss the role of F-18 fluorodeoxyglucose (FDG) brain PET imaging in the evaluation of various neurodegenerative processes. We will give an overview of the relevant anatomy, as it pertains to FDG brain PET evaluation of neurodegenerative disease. Using cases from our institution, we will discuss several examples of both common and rare neurodegenerative processes and their imaging appearance on FDG brain PET, highlighting the differences in uptake patterns among the different pathologies. Examples of the disease processes we plan to discuss are: Alzheimer's disease, behavioral variant frontotemporal dementia (FTD), dementia with Lewy bodies, corticobasal syndrome, progressive supranuclear palsy, various subtypes of primary progressive aphasia (PPA), and normal pressure hydrocephalus. We will conclude by summarizing the role of FDG brain PET in the evaluation of neurodegenerative disease and how recognizing patterns of differential metabolism can guide the clinician in their diagnosis. **Educational Objectives** • Understand the role of FDG brain PET imaging in the evaluation of neurodegenerative disease. • Recognize the relevant anatomy in FDG brain PET imaging. • Identify the characteristic patterns of differential metabolism associated with each of the neurodegenerative processes discussed.

Materials and Methods

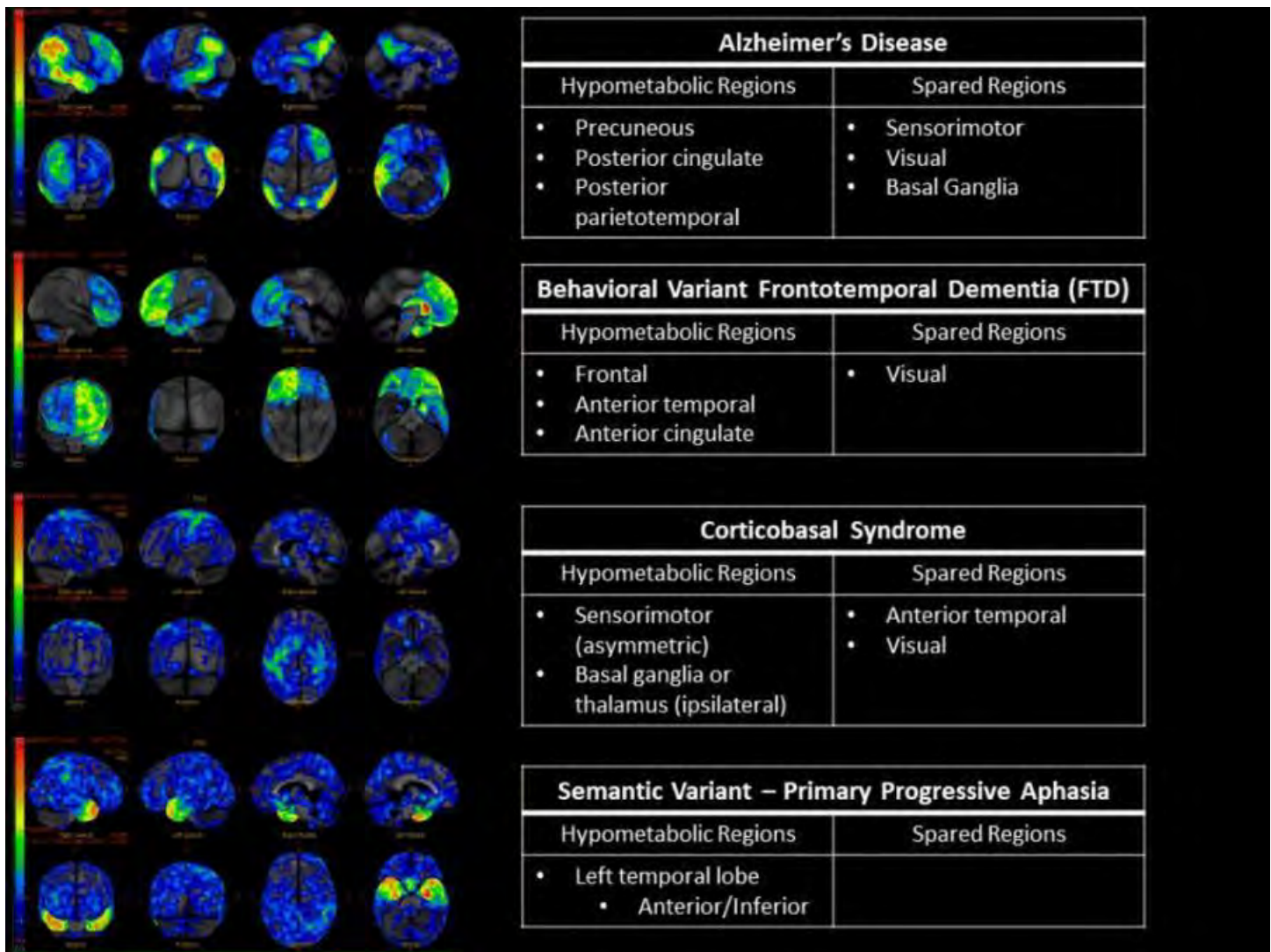
• Understand the role of FDG brain PET imaging in the evaluation of neurodegenerative disease. • Recognize the relevant anatomy in FDG brain PET imaging. • Identify the characteristic patterns of differential metabolism associated with each of the neurodegenerative processes discussed.

Results

n/a

Conclusions

n/a



(Filename: TCT_660_ASNRAbstractFigure3.jpg)

121

"The Sights, Sounds, and Smells of the Reading Room: An Overview of the Cranial Nerves"

N Sakla¹, K Brock¹, G Singh¹, R Gattu¹, A True¹, A Vaysberg¹, J Matthews¹

¹Newark Beth Israel Medical Center, Newark, NJ

Purpose

Summary: The presentation will provide an overview of the cranial nerves through the use of created pictorials, diagrams, and color coded text. CT and MRI localization of each cranial nerve, function, type of cranial nerve (i.e. extension of the brain vs. true cranial nerve), motor vs sensory function will be provided for each nerve. Additionally, the labeled intracranial course and associated cranial nerve nuclei will be shown on CT/MRI imaging and/or on created diagrams. Note that all pictorial diagrams of cranial nerve course, lesion location, cranial nerve nuclei and associated flowcharts have been created by the author and team. A section of "facts and associated clinical implications" will include labeled CT/MRI images of associated pathologies for each cranial nerve where applicable. The presentation will conclude with a summary of the most notable cranial nerve functions and facts as well as a review of the ideal MRI sequences used for cranial nerve evaluation. Educational Objectives: • Recognize the nuclei, intracranial course and function of the cranial nerves seen on CT/MRI. • Differentiate between extensions of the brain versus true cranial nerves. • Understand the clinical implications of cranial nerve location and various disease processes. • Differentiate between cranial nerves that are easily versus poorly identified on CT/MRI. • Differentiate between motor and/or sensory cranial nerves. • Develop a systematic approach for lesion (e.g. bleed, infarct, intracranial mass) location based on associated clinical findings and remaining neural function.

Materials and Methods

The purpose of this presentation is to provide radiology residents, particularly 1st and 2nd year residents, with a clear framework of the cranial nerves with respect to function, MRI localization, intracranial course, and associated pathologies when any component of a

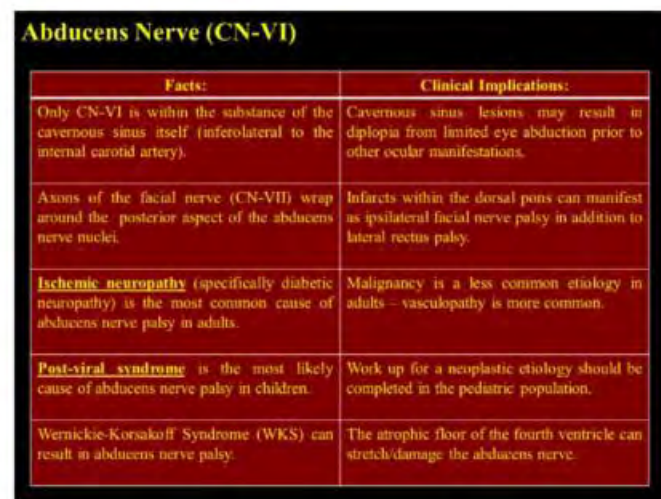
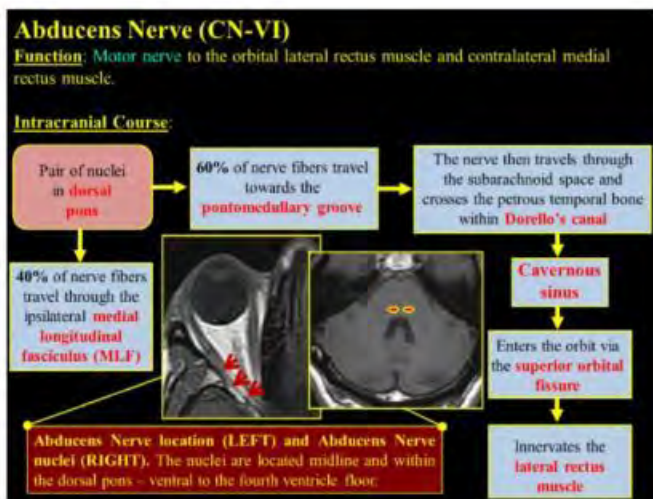
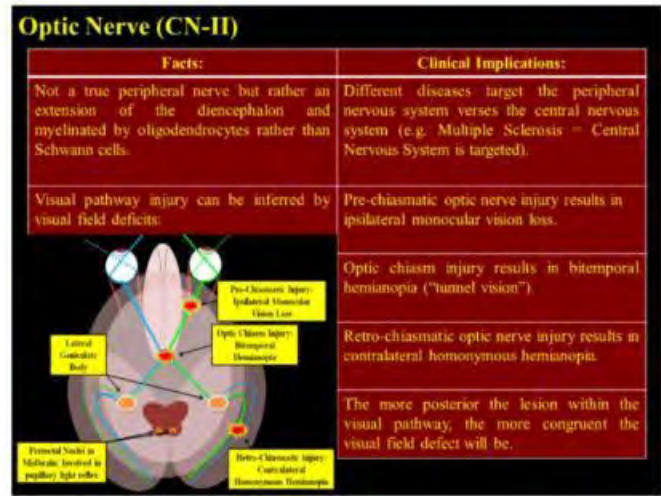
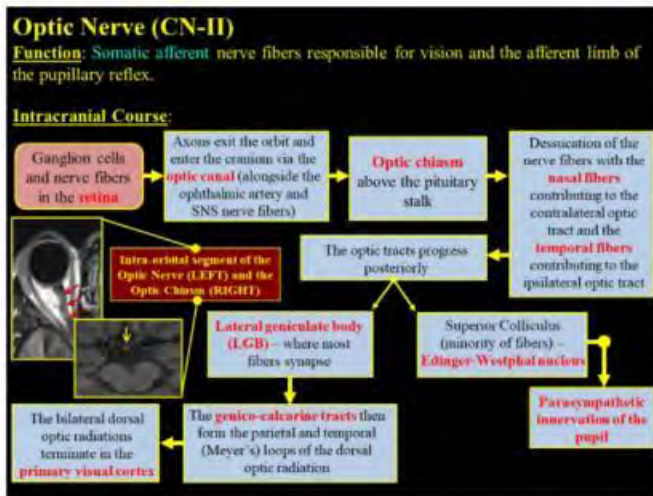
nerve is damaged. The presentation will enable residents to learn and understand why pathology arises from cranial nerve injury via an improved understanding of their course and function with an in depth pictorial review (i.e. MRI, pictorials, and flowcharts).

Results

N/A

Conclusions

N/A



(Filename: TCT_121_CranialNervesSample.jpg)

175

"To Remember, the Brain Must Actively Forget": Imaging of the Hippocampus

A Agarwal¹, B Srivastava¹, C Ball¹

¹UT Southwestern Medical Center, Dallas, TX

Purpose

(1) To discuss the MR imaging and functional anatomy of the hippocampus (2) To illustrate the wide range of hippocampal pathologies including neurodegenerative, inflammatory, epileptic and neoplastic conditions (3) Post-treatment changes in the hippocampus

Materials and Methods

This exhibit covers three sections: normal hippocampal anatomy, MR imaging techniques and lesions affecting the hippocampus. Recent advancements in Epilepsy treatment and post-treatment imaging changes are also discussed.

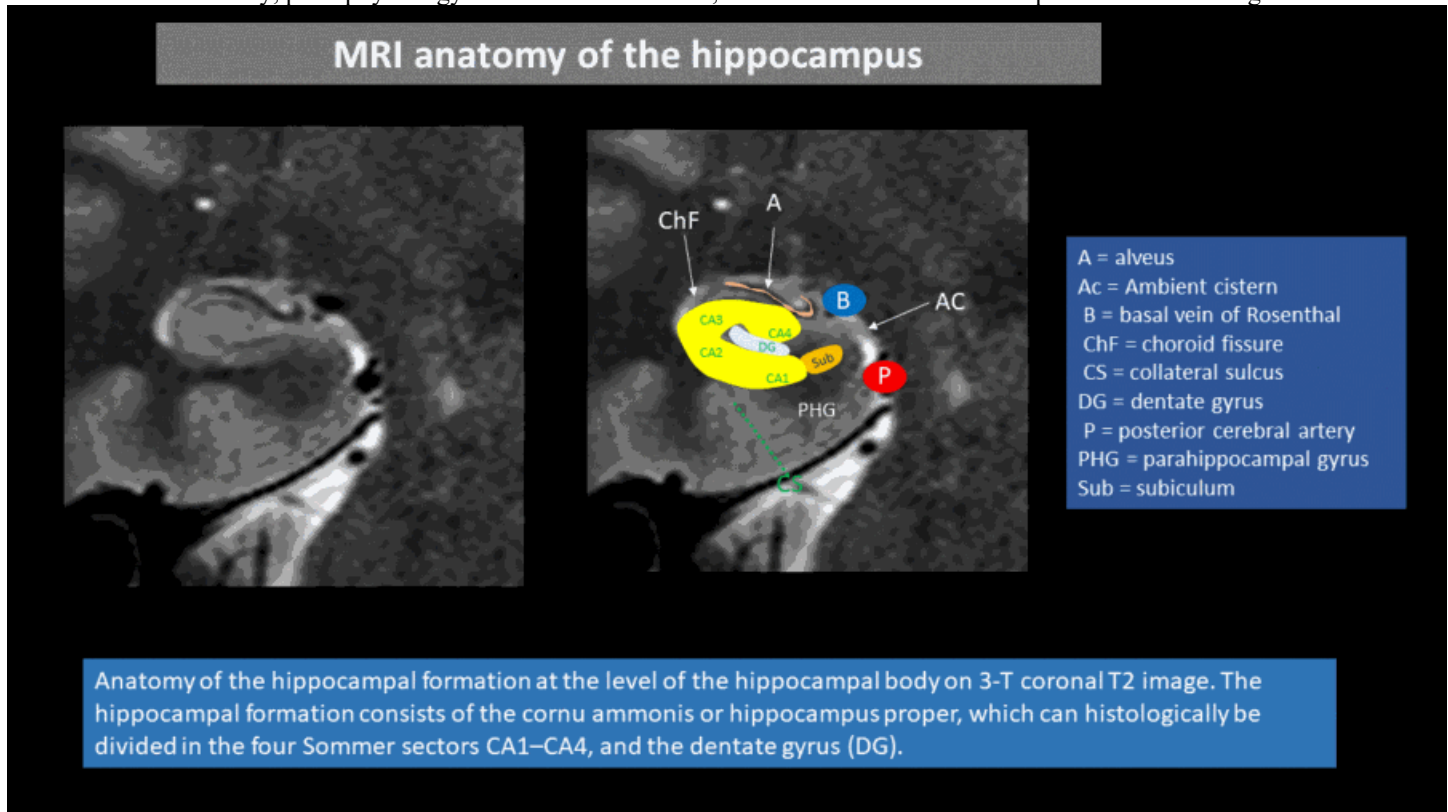
Results

(A) Imaging and functional anatomy of the hippocampus (B) Imaging protocol (focus on dementia and epilepsy) (C) Pathological conditions: • Congenital anomalies • Neurodegenerative disease (Dementia and epilepsy) • Infective and auto-immune inflammatory

conditions • Neoplasms • Vascular disease (D) Recent advancements in treatment of mesial temporal sclerosis and post treatment changes in hippocampus (C) Conclusion

Conclusions

Hippocampus has a complex anatomy and wide range of abnormalities, primarily epilepsy and dementia. This exhibit provides an overview of the anatomy, pathophysiology of the common lesions, treatment advancements and post-treatment changes.



(Filename: TCT_175_Anatomy.gif)

1080

3D Cinematic Volume Rendering Technique of Traumatic Spine Injuries – A Powerful Tool for Radiology Education

M Breen¹, O Jawhar², e lustrin³, M Young⁴

¹NYU, New York, NY, ²NYU, Mineola, NY, ³NYU Langone Health, great neck, NY, ⁴NYU School of Medicine, New York, NY

Purpose

Spine trauma represents a common indication for imaging in the Emergency Department. Multi-detector CT imaging, with its advantage of multi-planar reconstructions and fast image acquisition, is the modality of choice in the initial assessment of the polytrauma patient in the ED setting. While most stable spinal fractures are adequately evaluated on 2D multi-planar images, more complex, potentially unstable fracture patterns can be more fully highlighted on 3D reconstructions. Compared to conventional volume rendering techniques, Cinematic rendering uses a more complex illumination model to create a more photo-realistic representation of the fracture patterns.

Materials and Methods

The purpose of this exhibit is to demonstrate the educational utility of 3D Cinematically rendered images in understanding complex spinal column injuries. Unstable or potentially unstable injuries according to the AO Spine Trauma classification system will be shown in a case-based review.

Results

3D volumetric Cinematic rendering was performed using Siemens syngo.via postprocessing software to produce representative images of unstable spine trauma. Input data consisted of multidetector CT images of ED trauma cases identified by report search within NYU hospitals database. Input data was assessed for quality (favorable signal-to-noise ratio, lack of obscuring artifact, satisfactory bone density) and for the presence of representative, visually striking traumatic pathology. Images were rendered by residents trained in use of the syngo.via software.

Conclusions

Sample representative images are provided.



(Filename: TCT_1080_unstablespine300dpifinal_bfz4uDbX.jpg)

1245

A Case Based Review on Cerebral Arteriovenous Malformation and Cerebral Dural Venous Fistula

J Bregni¹, G Torres Flores¹, J Cook², B Martin³

¹University of South Alabama, Mobile, AL, ²University of South Alabama, Daphne, AL, ³USA Health University Hospital, Mobile, AL

Purpose

Brain arteriovenous malformations (AVM) are rare congenital pathological high flow vascular shunts that occur in approximately 0.1 percent of the population. The clinical manifestations range from being asymptomatic to seizures and intracranial hemorrhage. Brain AVM are classified utilizing the Spetzler-Martin grading system based on size, location and venous drainage. This scale is used to help guide treatment options and correlates with operative outcome. Cerebral dural arteriovenous fistulas (DAVF) are pathological anastomoses between meningeal arteries and dural venous sinuses and/or cortical veins. They account for 10-15% of all intracranial vascular pathologies. The cause of DAVF is usually unknown, however it is thought to arise from previous sinus thrombosis and may be associated with prior trauma. Clinical manifestations are highly variable depending on location and arterial/venous supply and drainage. The most widely used and simplest classification system is the Borden-Shucart, however other tools have been developed including the Cognard system. The Borden-Shucart and Cognard classification systems stratify risk and aids in management decision making by predicting hemorrhagic and non-hemorrhagic events. The gold standard to diagnose AVM and DAVF is digital subtraction angiography, however they can be diagnosed by Computed Tomography Angiography (CTA) and MRI/MRA. In this education exhibit we will present a series of cases from our institution that demonstrate the characteristic imaging findings of AVM and DAVF. Additionally, we will discuss the classification systems and management options for AVM and DAVF.

Materials and Methods

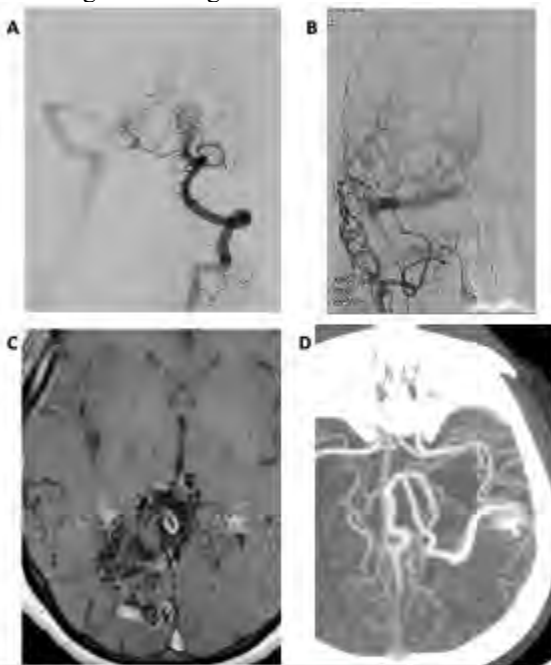
Describe the clinical presentations and imaging findings of brain arteriovenous malformation (AVM) and cerebral dural arteriovenous fistula (DAVF). Review classification systems of AVM and DAVF. Review treatment options of AVM and DAVF.

Results

Institutional review of 4 cases of cerebral arteriovenous malformation and cerebral dural arteriovenous fistula and their respective classifications. Review of current literature to identify the epidemiology, pathophysiology, classification and management associated with these entities.

Conclusions

Cerebral arteriovenous malformation and cerebral dural arteriovenous fistula have typical imaging characteristics and classifications systems that correlate with outcome and aid in risk stratification and management. It is important to correctly apply these classification systems to guide management and treatment.



A: Digital subtraction angiography (DSA) of a Cognard type IIa DAVF supplied by the right anterior inferior cerebellar artery and the superior cerebellar artery draining into the transverse sinus.
B: DSA of a Cognard type IIa DAVF between the distal right occipital artery and the right transverse sinus. There is reflux noted into the cortical veins as well as into the left transverse sinus.
C: Axial CT image of a right occipital AVM Spetzler-Martin Grade 4 (given by size, location and 2 for deep draining veins) with 2 prominent draining veins into the straight sinus and the superior sagittal sinus.
D: Axial CT image of a left parietal Spetzler-Martin II AVM (given by location and size) associated with intraparenchymal hemorrhage (crosshair). Lesion was successfully embolized.

(Filename: TCT_1245_Picture1.jpg)

1402

A Compartment Based Approach for the Imaging Evaluation of Facial Nerve Palsy

Purpose

Facial nerve palsy may be acute or insidious in onset and either central or peripheral in nature, depending on the site of involvement. The clinical history and examination findings influence the choice of imaging modality and aid in predicting the site of a lesion. CT and MR imaging are complementary in the evaluation of multiple entities that may cause facial nerve palsy.

Materials and Methods

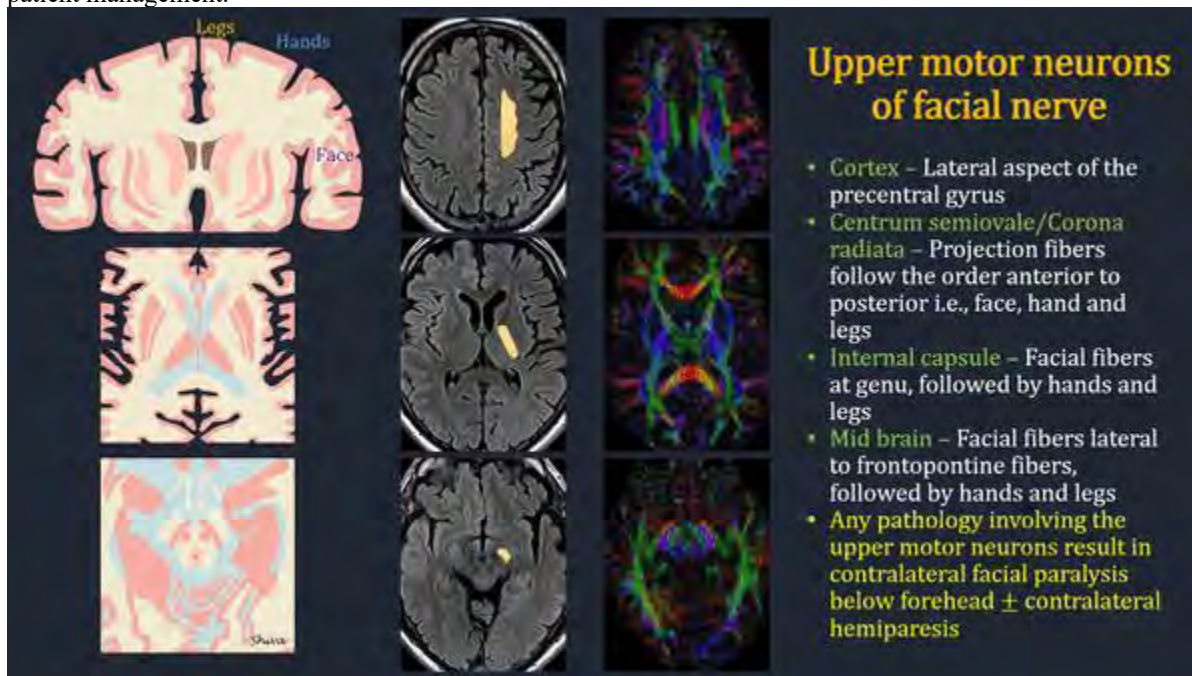
This educational exhibit aims to, 1. To describe the imaging anatomy and salient clinical features that point to the location of a lesion affecting the facial nerve. 2. To describe imaging protocols for the evaluation of the facial nerve. 3. To illustrate imaging findings in common and infrequent entities resulting in facial nerve palsy based on a compartment approach.

Results

The imaging findings of pathologies causing central and peripheral facial palsy will be depicted in a case based format using a compartmental approach. The central causes of facial palsy include: acute infarction, demyelination, pontine tumors, and vascular or hemorrhagic lesions affecting the facial colliculus. The intrinsic and extrinsic facial nerve pathologies resulting in peripheral facial palsy include infectious, inflammatory and neoplastic lesions.

Conclusions

It is important to understand the anatomy of the facial nerve and to recognize the differences in clinical presentation of patients with facial nerve palsy, in order to protocol and obtain the best imaging test to make a diagnosis. Herein, we describe the imaging findings of common and infrequent lesions involving the facial nerve, in a compartment based approach and we discuss their implications on patient management.



(Filename: TCT_1402_Facialpalsy.gif)

1195

A Focused Case Based Review of Blunt Traumatic Vascular Injury of the Head and Neck

Purpose

Trauma encounters account for more than 50 million emergency department visits each year. More than 5 million of these ED visits are related to head and neck injuries. Blunt cerebrovascular injury (BCVI) accounts for 1-2% of all in hospital trauma patients and carries a mortality of 17-38% in carotid injury and 8-18% in vertebral artery injury. The Expanded Denver criteria is currently the tool of choice to screen for blunt cerebrovascular injury. The Denver protocol was originally created by Biffel et al., who also developed the grading system for the classification of blunt cerebrovascular injury. The Biffel scale is graded from I-V in ascending order of severity. Treatment options for BCVI range from observation to surgical intervention. Biffel scale helps guide treatment, management, and follow up. In our educational exhibit, we will present a series of cases from our institution, a level one trauma center, that demonstrate the

characteristic imaging findings of each grade of the Biffel scale and their management options as well as selected cases of post-traumatic carotid-cavernous fistulas.

Materials and Methods

Describe the presentation of blunt cerebrovascular injury. Review the indications for CT angiography of the head and neck in the setting of trauma. Review the imaging findings and grading system of blunt cerebrovascular injury. Describe treatment and follow up options of blunt cerebrovascular injury.

Results

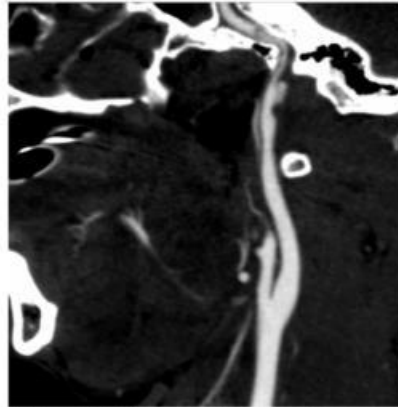
We performed an institutional review of all CTAs performed in the trauma setting. We identified 5 cases exemplifying grade I-V blunt cerebrovascular injury using the Biffel or Denver Scale.

Conclusions

Blunt cerebrovascular injuries have variable imaging characteristics and findings which can have immense clinical and prognostic implications. It is important to be aware of the indications for CTA and identify imaging findings as to not delay diagnosis and treatment.



Irregularity of the right ICA as it enters the carotid canal represents grade 1 blunt cerebrovascular injury.



Cervical phase reformatted CTA shows right internal carotid artery dissection and pseudoaneurysm measuring 5 x 3 mm, representing a grade 3 injury. Distal to the pseudoaneurysm, there is severe stenosis of the internal carotid artery and dissection over a segment of about 1.5 cm in its petrous segment. This represents grade IV BCVI.



8 mm dissection flap in the left vertebral artery at the left transverse foramen of C4, consistent with grade 2 injury.



There is left common carotid artery is non-specified. There is post-traumatic occlusion of the left common carotid artery from its origin to the carotid bifurcation. Grade 4 BCVI of the proximal left common carotid artery with recanalization at the bifurcation.

(Filename: TCT_1195_BCVEE.jpg)

795

A Pictorial Review: Post-septal Orbital Fat lesions

Q Kuse¹, R Assadsangabi², A Ozturk³, V Ivanovic⁴, J CHANG³, M Bobinski³, O Raslan³

¹University of California, Davis, Sacramento, CA, ²University of California Davis, Sacramento, CA, ³UC Davis, Sacramento, CA, ⁴UC Davis Medical Center, Sacramento, CA

Purpose

Focused pictorial review highlighting the image finding and differential diagnostic considerations of the post septal orbital fat lesions, and the impact of radiographic findings in clinical decision making and patient management.

Materials and Methods

Provide a comprehensive review of lesions affecting the orbital fat.

Results

We retrospectively evaluated orbital cases in our PACS system for lesions involving the orbital fat.

Conclusions

Increased orbital fat volume: Graves ophthalmopathy (GO), Cushing disease/syndrome, and obesity can increase orbital fat volume resulting in proptosis (1). Expansion of the extraocular muscles (EOM) is a well-known imaging finding in GO; however, some affected orbits show increased orbital fat volume without EOM involvement. This subset is associated with more proptosis and longer GO duration and suggests different phenotypes of GO2. Decreased orbital fat volume: Fat atrophy can be seen with senile changes, localized scleroderma, Parry–Romberg syndrome, lipodystrophy, Cockayne's dystrophy and post orbital irradiation, resulting in non-traumatic enophthalmos(3). Traumatic lesions: Finding of large volume orbital fat hematoma and/or air may result in compartment syndrome, optic neuropathy and blindness necessitating emergent surgical intervention. Nonemergent operative indication include hypoglobus or enophthalmos > 2 mm(4). Inflammatory/infectious lesions: Orbital cellulitis requires hospitalization and parenteral antibiotics and possibly abscess drainage surgically. Idiopathic orbital inflammation, granulomatosis with polyangiitis (Wegener), sarcoidosis, and IgG4-related disease can involve the orbital fat(5). Neoplastic lesions: Tumors of the orbital fat include ocular Melanoma, lymphoproliferative lesions (lymphoma), and metastasis. Vascular lesions: Infantile hemangioma is a self-involuting intensely enhancing extraconal lesions that may involve the orbital fat. Cavernous Malformations are well circumscribed, homogeneously hyperattenuating, lateral intraconal lesions in adults, which accumulate contrast on delayed dynamic imaging and may contain calcified phleboliths. Orbital varices are intensely enhancing orbital mass that distends with increased venous pressure. Venous lymphatic malformations show multiple fluid-fluid levels. Arteriovenous malformations, fistulas, and aneurysms have similar angiographic features to the intracranial lesions.



Figure 1

Fig 1. 55-year-old female drug abuser presenting with small bowel obstruction showing loss of the orbital fat volume with subsequent enophthalmos.



Figure 2a

Fig 2. 41-year-old female patient. Showing infiltrative intra and extraconal enhancing lesions involving the orbital fat and extraocular muscles of the left more than right orbit (a). The patient also had subglottic stenosis and paranasal sinus disease (not shown), together with the low T2 signal findings (b) are consistent with granulomatosis with polyangiitis (Wagner).

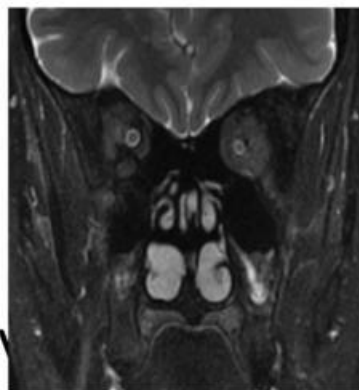


Figure 2b

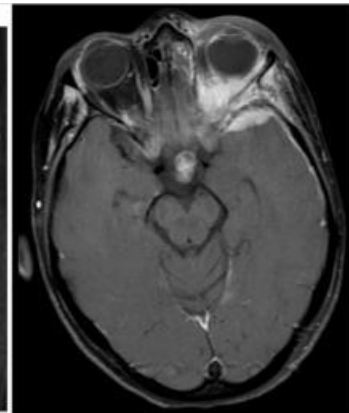


Fig 3. 29-Year-old female patient metastatic adenoid cystic carcinoma of the lungs showing diffuse infiltrative enhancing intra and extraconal mass with infiltration of the orbital fat and intracranial dural extension. There is subsequent enophthalmos instead of the typical exophthalmos secondary to prior maxillectomy and collapse of orbital floor.

(Filename: TCT_795_Figures_QK.jpg)

905

A Pictorial Review: Understanding Congenital Craniospinal Axis Anomalies with Fetal Neuroimaging

G Biddle¹, A Ozturk¹, K Gwal¹, O Raslan¹, R Assadsangabi¹, V Ivanovic¹, M Bobinski¹, J CHANG¹

¹UC Davis Medical Center, Sacramento, CA

Purpose

Describe and highlight the imaging findings and diagnostic key points of congenital brain and spinal abnormalities in the antenatal period with fetal Magnetic Resonance Imaging (MRI).

Materials and Methods

Describe and review neuroimaging findings on fetal MRI.

Results

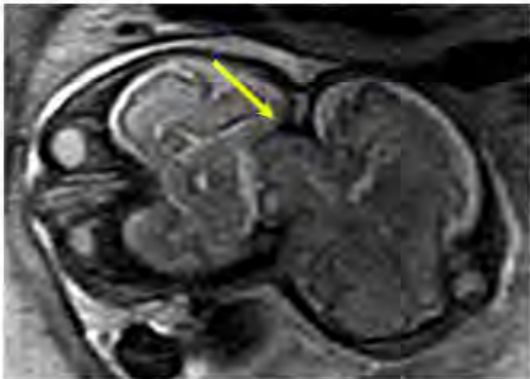
We retrospectively evaluated all fetal MRI studies from our PACS system with congenital brain and spine abnormalities for this pictorial essay.

Conclusions

Posterior Fossa Anomalies MRI of the posterior fossa is performed to evaluate the cerebellum for hypoplasia, dysplasia, hemorrhage, Chiari malformations, and Dandy Walker malformations. Findings vary from abnormal size of the cerebellum, inferior displacement of the cerebellar tonsils through the foramen magnum with a small posterior fossa, and hydrocephalus. Corpus Callosum Anomalies The spectrum of corpus callosal anomalies includes hypoplasia, hypogenesis/partial agenesis, dysgenesis, and complete agenesis. Mild ventriculomegaly is often the first clue for diagnosis of an abnormal corpus callosal complex [1]. Ventriculomegaly Enlargement of the lateral ventricles measuring >10 mm at the level of the atrium is the basis for fetal ventriculomegaly, and fetal MRI can help determine the underlying cause, such as infections or malformations [2]. Middle Interhemispheric Variant holoprosencephaly (MIH) MIH is a subtype of holoprosencephaly (syntelencephaly), in which an abnormal midline connection of the posterior frontal and parietal lobes is present but there is interhemispheric separation of the basal forebrain, anterior frontal lobes, and occipital regions [3]. Craniopagus Craniopagus conjoined twins are fused at the cranial level, and can be classified into complete or partial craniopagus. Complete includes deep fusion with sharing of brain parenchyma and/or vasculature. Partial has a more superficial fusion with shared cranium including the calvarium, dura, and/or skin [4]. Spinal dysraphism Neural tube defects develop early in gestation, and include myelomeningocele, meningocele, and spina bifida. Imaging findings include incomplete fusion or absence of the posterior spinal elements possibly with herniation of CSF and neural elements through the bony defect [5]. Conclusion Fetal MRI plays an important role in the evaluation of congenital brain and spinal abnormalities in the antenatal period. Diagnosis of these congenital abnormalities in a timely manner has significant impact on prenatal counseling, fetal treatment planning, delivery planning, and perinatal care.



- Middle Interhemispheric variant of holoprosencephaly
 - Vertically oriented sylvian fissures which extend towards the midline and superiorly at the vertex
 - No septum pellucidum with contiguous dysmorphic dorsal aspects of the lateral ventricles



- Craniopagus
 - Conjoined twins connected at the occipital region of one and the parietal region of another, with parietal lobe herniating through the defect
 - Flow void on fetal MRI diagnosed the abnormal fistulous connection of the transverse sinus of one twin with the other's sagittal sinus (arrow)

(Filename: TCT_905_fetal_asnr.jpg)

464

A RAPID Checklist: Understanding Pitfalls and Artifacts in Stroke

J Bregni¹, M Castillo²

¹University of South Alabama, Mobile, AL, ²Radiology, Chapel Hill, NC

Purpose

Objectives: 1. Understand the basic principles of acquisition of RAPID. 2. Propose a checklist for reading an automated CT perfusion (CTP) scan using RAPID. 3. Understand the main pitfalls of RAPID. Summary: Automated CTP helps identify patients who benefit from treatment. RAPID is the most widely used automated perfusion software defining core infarct with a relative cerebral blood volume (rCBV) <30% and penumbra as a time-to-peak concentration (Tmax) >6 seconds (s). Acquisition starts with 40mL contrast injection followed by scanning 8cm of brain for 60 to 70-s. Scan cycles every 1-3s obtaining arterial, parenchymal and venous phases of contrast. RAPID measures the attenuation curve automatically by selecting an Arterial Input Function (AIF) and a Venous Outflow Function (VOF). After correcting for motion and timing, circular deconvolution is used to calculate rCBV, mean transit time, Tmax and cerebral blood flow. Artifacts can be related to technic and calculations. Motion, poor and delayed contrast bolus, truncated curves and incorrect placement of AIF and VOF are related to technic. Over- and underestimation of core infarct and penumbra, bilateral disease and acute on chronic infarcts are related to calculations. These artifacts will be reviewed, explained, and illustrated so that the user can understand and avoid them. RAPID checklist 1. Evaluate for motion in the post injection images. 2. Arterial curve normally spikes earlier, venous curve peaks later. There is no return to baseline due to recirculation of contrast. Curves should not be truncated. 3. Check locations of AIF and VOF. AIF should be on the anterior cerebral artery or contralateral and normal middle cerebral artery.

VOF should be on the straight or distal superior sagittal sinus. Normal looking curves imply adequate AIF and VOF placement. 4. Determine presence of core and/or penumbra. A benefit from treatment is likely if these criteria are met: ratio of penumbra:core >1.8, core volume <70 mL, and severely delayed volume (Tmax > 1s) less than 100 mL. 5. Review CTA and non-contrast images. Compare affected area and recognize occluded vessel. CTP of the posterior fossa has limited value as volume calculations are affected by skull base and orbit artifacts and its perfusion thresholds have not been established.

Materials and Methods

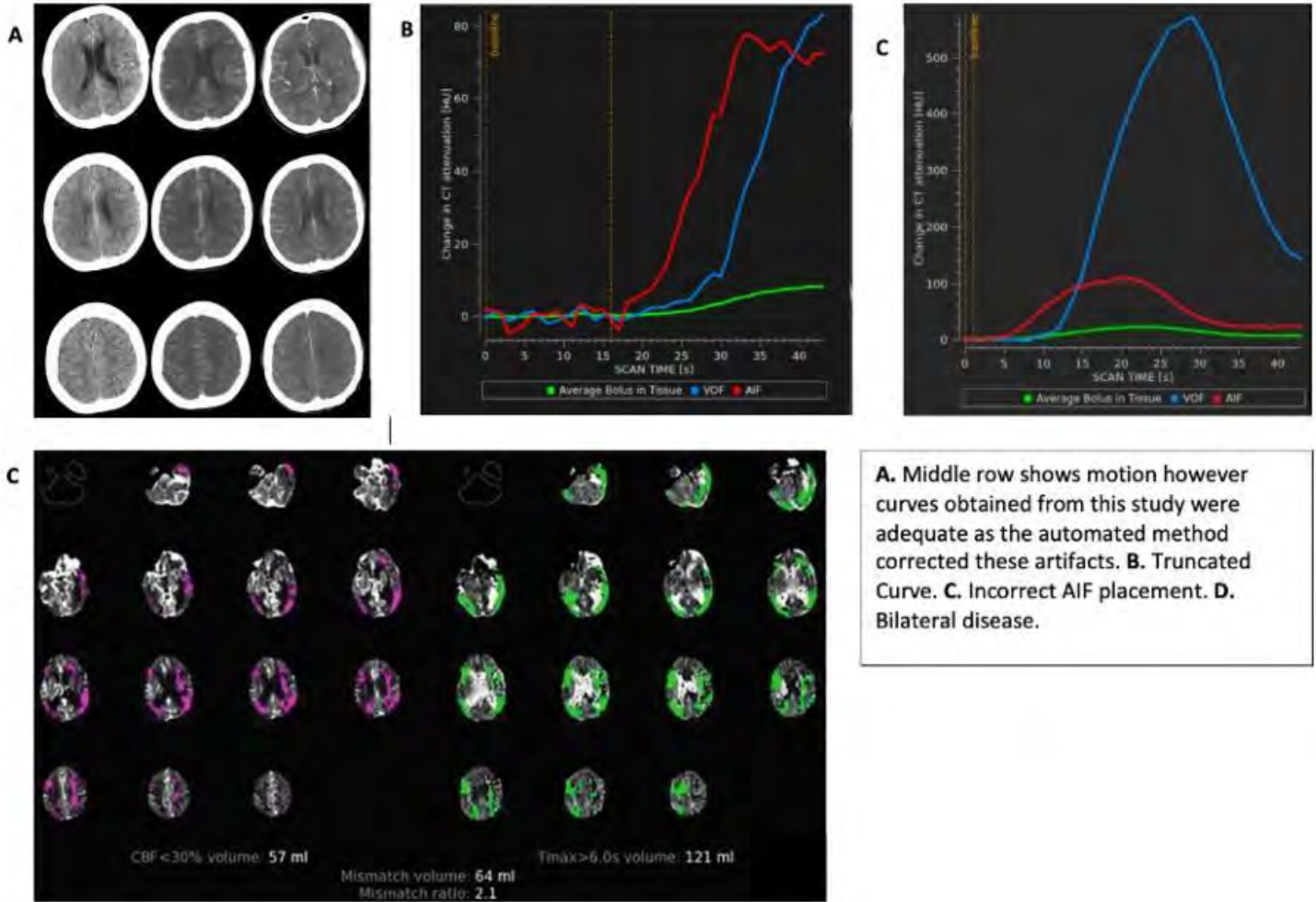
N/A

Results

N/A

Conclusions

It is encouraged to follow a checklist when interpreting CTP examinations to identify flaws that may influence medical decisions for treatment of acute ischemic stroke.



(Filename: TCT_464_Picture1.jpg)

589

A Review of Amyloid Goiter and Fat-containing Masses of the Thyroid

C McNulty¹, C Ju², N Pham¹

¹UCLA, Los Angeles, CA, ²UCLA, Los angeles, CA

Purpose

Fat-containing thyroid masses are rare given the lack of adipose tissue in normal thyroid glands. In this educational exhibit, the distinct imaging spectrum of amyloid goiter and other fat-containing masses will be examined. 1.To review the etiology, histology, and pathophysiology of amyloid deposition in the thyroid gland. 2.To review imaging patterns of amyloid goiters. 3.To review the differential diagnosis and imaging findings of other thyroid fat-containing masses.

Materials and Methods

The purpose of this educational exhibit is to review the imaging patterns, histology, and pathophysiology of amyloid goiter and distinguish it from other fat-containing lesions. Thyroid gland involvement in amyloidosis is common, occurring in approximately

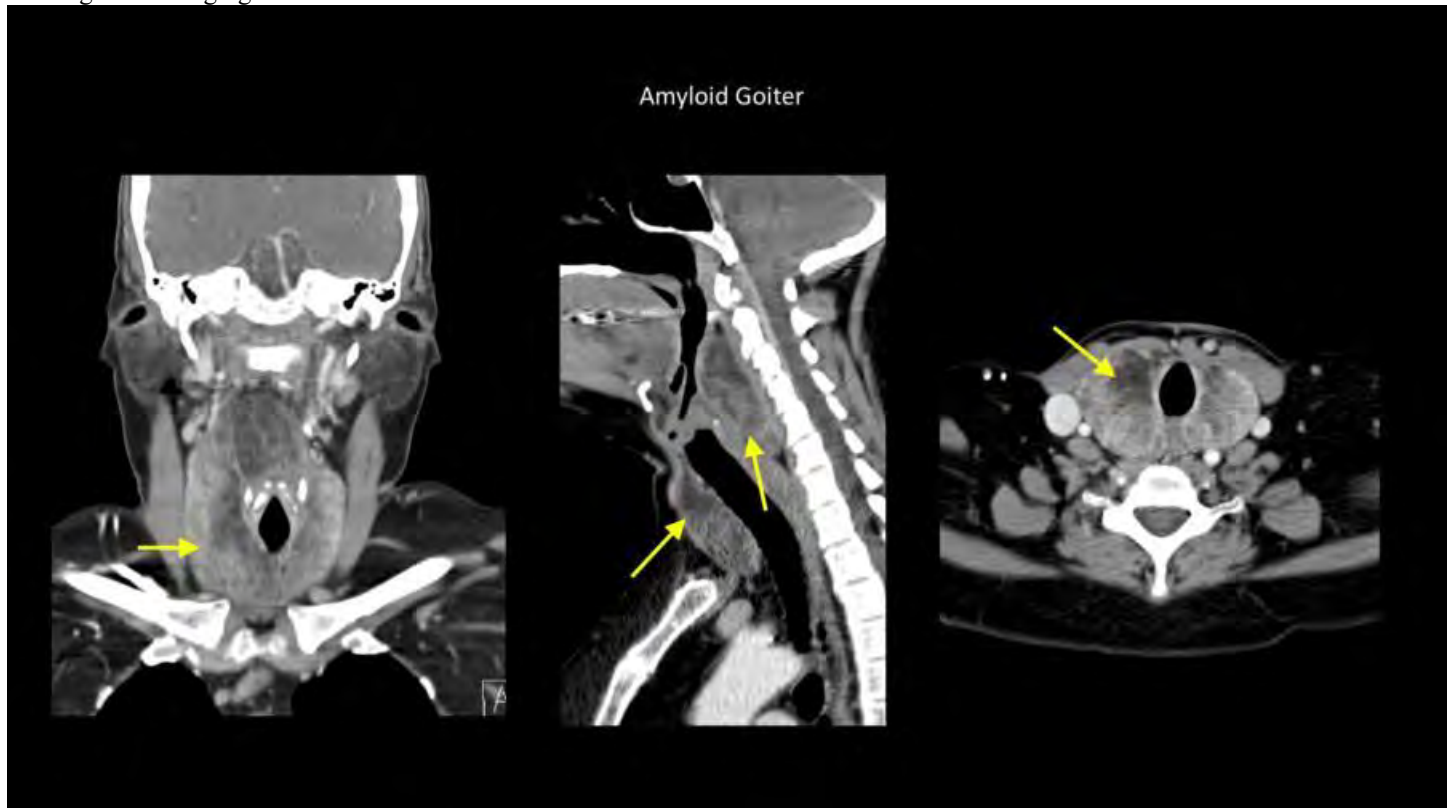
80% of patients with secondary amyloidosis. The development of amyloid goiter, however, is an exceedingly rare phenomenon. Amyloid deposits can occur in the setting of primary or secondary amyloidosis, involving AL amyloid and AA amyloid respectively. It has been hypothesized that amyloid deposition causes tissue hypoxia and progressive capillary and thyroid follicle destruction resulting in metaplasia of stromal fibroblasts to adipose cells. Histologic confirmation of amyloid can be made using polarized-light microscopy and Congo Red dye. The orientation of the dye molecules on amyloid fibrils produces two refractive indices under polarized light and creates the characteristic apple-green birefringence. MR and CT characteristics vary depending on the extent of adiposity and calcification, but the enlarged thyroid often appears heterogenous with fat-attenuating components. Ultrasound may reveal a heterogenous gland with hypoechoic, complex foci representing amyloid deposition. Additional fat-containing lesions of the thyroid gland include thyrolipomatosis, thyrolipoma, lymphocytic thyroiditis, and neoplasms such as liposarcoma or parathyroid lipoma.

Results

A single institutional retrospective review was performed to identify cases of fat-containing masses of the thyroid gland. Subsequently, a comprehensive literature review was performed to elucidate pertinent background, histologic and imaging findings of fat-containing thyroid masses.

Conclusions

Fatty infiltration of the thyroid is rare, but its presence alludes to specific disease entities. One such process is an amyloid goiter, which is a rare derivation of systemic amyloidosis and can be reliably distinguished from other fat-containing lesions on the basis of histologic and imaging characteristics.



(Filename: TCT_589_AmyloidGoiter.jpg)

564

A Review of Bitemporal Hemianopia and Pseudo-hemianopia

C Ju¹, N Pham¹

¹UCLA, Los Angeles, CA

Purpose

Bitemporal hemianopia is a visual field defect with a broad differential diagnosis. Causes of bitemporal pseudo-hemianopia secondary to tilted disc syndrome (TDS) or staphylomas are less frequently discussed but are important considerations in patients with temporal visual field defects. 1. To review the etiologies of bitemporal hemianopia and bitemporal pseudo-hemianopia. 2. To review imaging findings for bitemporal hemianopia and bitemporal pseudo-hemianopia, including tilted disc syndrome and staphylomas.

Materials and Methods

Bitemporal hemianopia presents when the optic chiasm, containing decussating nasal fibers from the retina, is altered by sellar, suprasellar, or chiasmal lesions. Tumors such as pituitary adenomas, meningiomas, or craniopharyngiomas can exert mass effect on

the optic chiasm and interrupt afferent optic nerve signal from the nasal retinal fibers, thereby producing a temporal visual field defect. Inflammatory conditions including granulomatous or lymphocytic hypophysitis can cause similar mass effect via enlargement of the pituitary stalk. Conditions that mimic chiasmal compression are termed bitemporal pseudo-hemianopia and include tilted disc syndrome and staphylomas. TDS is a congenital condition resulting in nasal ectasia of the ocular globe. Staphylomas are degenerative outpouchings of the globe secondary to congenital weakness of scleral tissue. MRI of the orbits in TDS demonstrate posterior nasal wall thinning of the orbits and oblique insertion of the optic nerves, with a wider insertion angle in the temporal quadrant. TDS may be associated with inferior staphylomas, best represented by increased anterior-posterior orbital diameter on imaging.

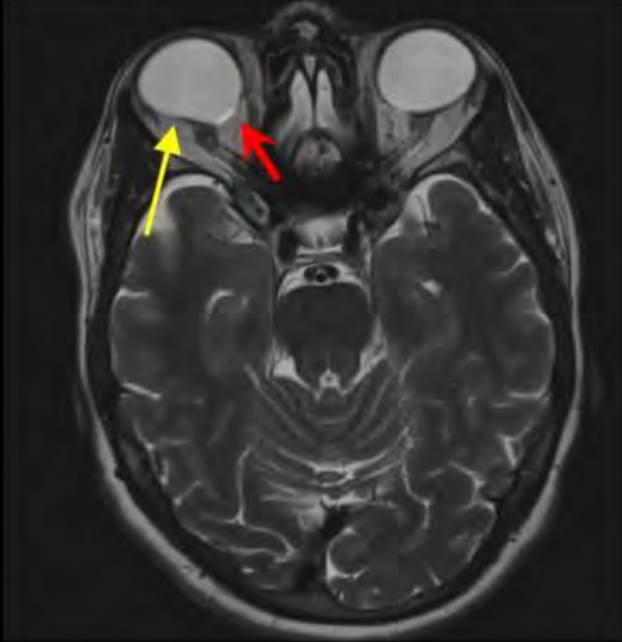
Results

A single institutional retrospective review was performed to identify cases of TDS, staphylomas, sellar, suprasellar, and chiasmal masses. A comprehensive literature review was performed to elucidate pertinent incidence rates, demographics, histologic and imaging findings.

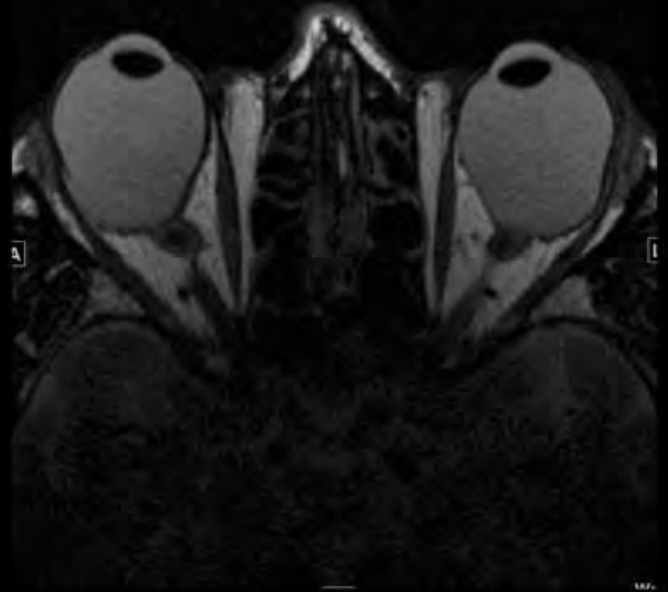
Conclusions

Tilted disc syndrome is a rare congenital malformation affecting approximately 2% of the general population. MRI is often performed to rule out chiasmatic lesions in patients with temporal visual field defects, thus anticipating etiologies of bitemporal pseudohemianopia are imperative when intracranial lesions are absent. Other differential considerations for TDS may include congenital anomalies such as optic nerve hypoplasia or peripapillary staphyloma.

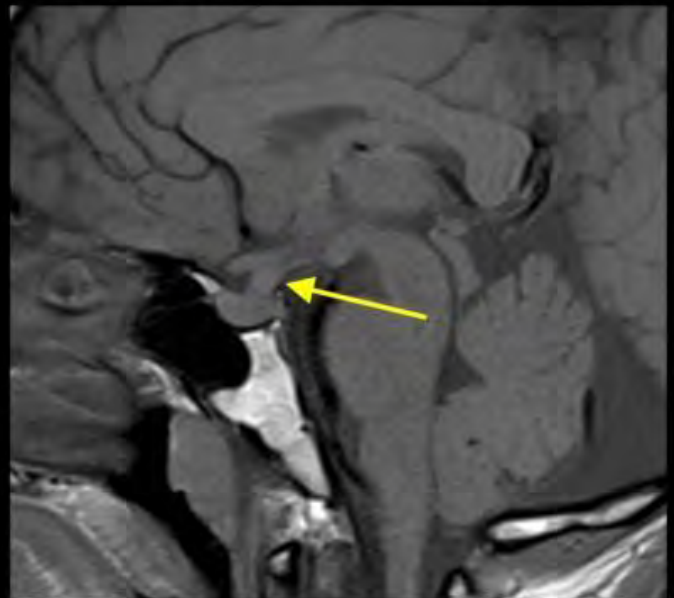
Tilted Disc Syndrome



Staphyloma



Pituitary Macroadenoma



Lymphocytic hypophysitis

(Filename: TCT_564_TDS.jpg)

404

A Single-Center Case Series of MRI-Guided Laser Interstitial Thermal Therapy (LITT) for Intracranial Tumors: A Tutorial on Normal and Abnormal Postoperative Imaging

A Sidor¹, A Weekley¹, Y Bechlibnyk¹, R Murtagh¹
¹University of South Florida, Tampa, FL

Purpose
N/A

Materials and Methods

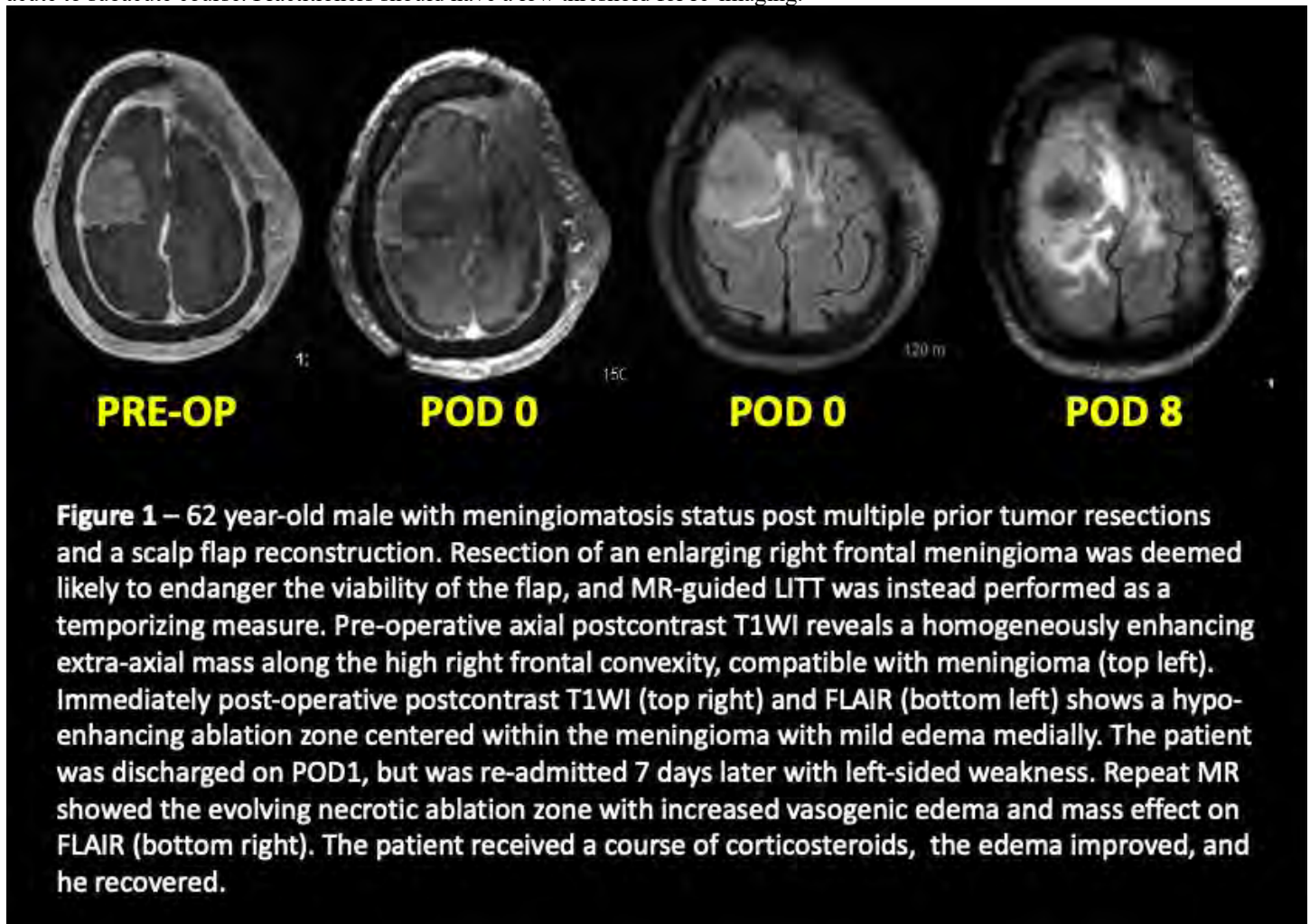
LITT is a minimally invasive percutaneous photothermal ablation technique for intracranial tumors, epileptogenic foci, and radiation necrosis which has demonstrated similar efficacy to surgical resection [1]. It is a relatively new option that allows treatment of previously inaccessible lesions and boasts decreased complication rates and hospital stay [2]. Its use has been rather limited until recent advances in laser technology and MR thermometry, which allows intraoperative visualization of the developing ablation zone while monitoring effects on neighboring non-target structures. In this study, we present our experience with a small cohort of patients who underwent LITT. Additionally, we seek to provide a summary of expected and abnormal imaging finds during and after treatment.

Results

Retrospective chart review was performed to collect patient, operative, imaging, hospital course, and complication data. Each patient was brought to the MRI suite and general anesthesia was induced. Preoperative anti-epileptics and corticosteroids were administered. 1 to 3 Visualase 15W 980-nm laser catheters were placed into the target lesion using sterile stereotactic technique. Intraoperative MRI was used for catheter positioning and real-time thermography. After the procedure, patients were admitted for observation and follow-up imaging.

Conclusions

A total of 3 patients underwent LITT over 15 months. 2/3 (66%) were male and the median age was 62. Diagnoses included epileptogenic ganglioglioma, meningiomatosis, and recurrent glioblastoma multiforme. Tumors were located in the mesial temporal, superior frontal, and parietooccipital lobes. Mean tumor size was 3.0 cm by greatest dimension. Mean length of stay was 1.3 days. 1 patient developed symptomatic edema requiring readmission but subsequently recovered after a course of corticosteroids (Fig. 1). No other complications were identified. LITT is a minimally invasive alternative to surgery that is both safe and effective. Normal post-operative findings include a round ablation zone that is hypodense on non-contrast CT and hypointense on T1WI, and also commonly demonstrates thin peripheral enhancement. Early imaging can show mild blood products within the ablation zone, and mild vasogenic edema is expected in neighboring parenchyma. Significant edema with mass effect is a known etiology of neurological deficit in the acute to subacute course. Practitioners should have a low threshold for re-imaging.



(Filename: TCT_404_Fig1.jpg)

Acute Global Encephalopathies: Imaging patterns of Hypoxic, Metabolic, and Toxic Encephalopathies

E Velez¹, P Joyce², G Hoang³, J Acharya³, S Ponrartana⁴, L Lai³, A Rajamohan⁵

¹USC Keck School of Medicine, Los Angeles, CA, ²LAC+USC Medical Center, Glendale, CA, ³Keck School of Medicine of USC, Los Angeles, CA, ⁴Children's Hospital Los Angeles, Los Angeles, CA, ⁵University of Southern California, Los Angeles, CA

Purpose

1) To review the imaging findings of hypoxic, metabolic, and toxic encephalopathies. 2) To create a diagnostic decision tree to aid in the diagnosis of acute global encephalopathies.

Materials and Methods

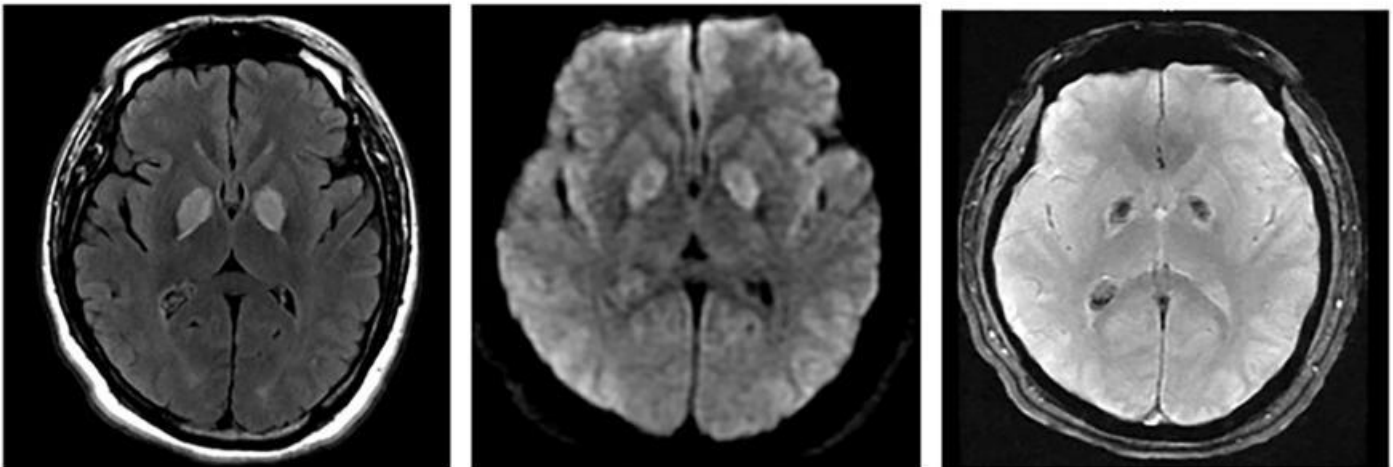
Acute global encephalopathies encompass a wide array of pathologies and are one of the most diagnostically challenging issues in neuroimaging. Patients often present with nonspecific global cerebral dysfunction and imaging can play a critical role in the diagnosis, ensuring effective management and possibly preventing permanent structural damage. The purpose of this educational exhibit is to provide a comprehensive review of acute global encephalopathies, including their imaging features and clinical manifestations.

Results

We will individually review various acute global encephalopathies (hypoxic, metabolic, toxic) in a systematic approach based on distribution of findings: 1) Basal ganglia/thalami involvement (carbon monoxide poisoning, methanol poisoning, Wernicke encephalopathy, Leigh syndrome, uremic encephalopathy, diabetic striatopathy), 2) Cortical involvement (hypoglycemic encephalopathy, hyperammonemic/hepatic encephalopathy, hypoxic-ischemic encephalopathy), 3) Periventricular white matter (methotrexate/antineoplastic drugs, immunosuppressive drugs, antimicrobial agents, heroin toxic leukoencephalopathy), 4) Corpus callosum involvement (cytotoxic lesions of the corpus callosum, Marchiafava-Bignami disease), 5) Dentate nuclei involvement (metronidazole-induced encephalopathy).

Conclusions

This educational exhibit will provide a comprehensive review of acute global encephalopathies. In addition, we will provide a diagnostic decision tree for acute global encephalopathies based on the constellation of imaging findings. After reviewing the exhibit, we expect viewers will have a better understanding of the global encephalopathies and hope this will serve as a useful resource for radiologists in practice when reviewing cases of suspected acute global encephalopathy.



Carbon monoxide poisoning. Left-to-right: axial T2 FLAIR, axial DWI, axial SWI of the brain demonstrate symmetric T2 FLAIR hyperintense signal and diffusion restriction of the globus pallidi with susceptibility artifact on SWI sequences consistent with microhemorrhages.

(Filename: TCT_1548_COpoisoning.jpg)

903

Acute Traumatic Venous Injuries: Imaging and Challenges

E Supsupin¹, M Fabrega¹

¹University of Texas Health Science Center McGovern Medical School Houston Texas, Houston, TX

Purpose

Acute dural venous sinus injuries (DVSI) and dural venous sinus thrombosis (DVST) are increasingly detected following cranial imaging in the setting of trauma. Early imaging-based diagnosis is of paramount importance in addressing the potentially treatable complications of these conditions, which may improve outcomes. OBJECTIVES: 1. Review the angiographic anatomy of the major dural venous sinuses 2. Describe the anatomic basis and proposed pathophysiology of acute traumatic injuries to the dural venous sinuses 3. Illustrate the role of imaging in the rapid diagnosis of acute traumatic DVSI and DVST 4. Describe the radiologic signs of

DVST 5. Discuss the management approach to acute traumatic DVST 6. Describe the challenges posed by acute DVST in the management of traumatic brain injuries

Materials and Methods

This presentation aims to raise awareness, a call to include DVST in the diagnostic checklist when evaluating patients with traumatic head injuries. Early diagnosis by imaging is of paramount importance in recognizing and addressing the potentially treatable complications of DVST.

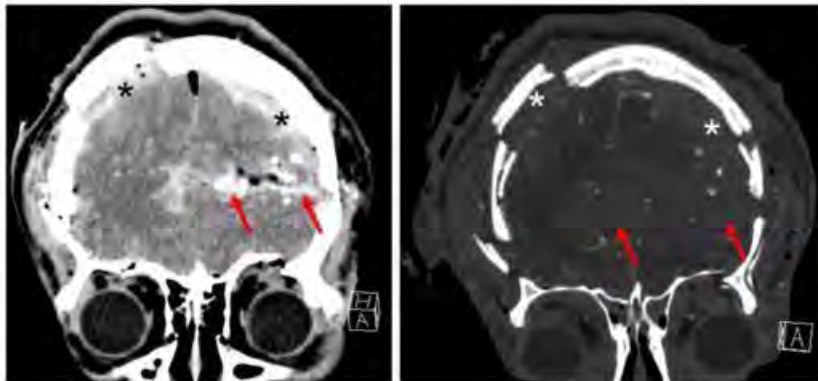
Results

APPROACH/METHODS: A review of the angiographic anatomy of the major dural venous sinuses frequently involved in closed and penetrating head trauma is undertaken. The proposed pathophysiology pertaining to DVST is discussed. Cases illustrating the role of imaging in the diagnosis of DVST are provided, including a description of important radiologic signs. The management approach and challenges posed by acute traumatic DVST are addressed.

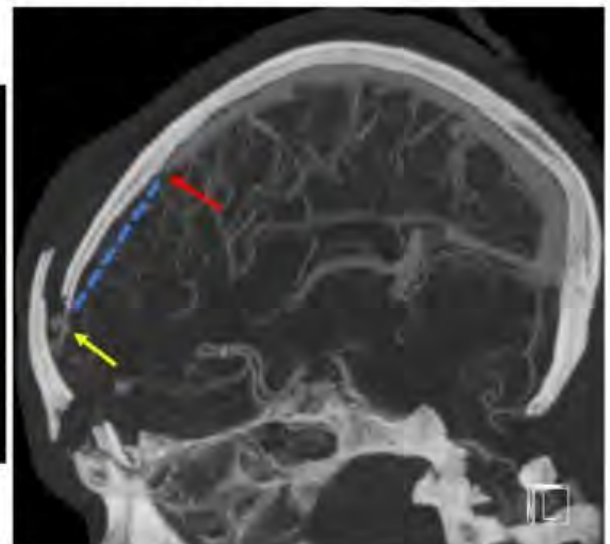
Conclusions

Acute DVST can be serious and potentially fatal. This is associated with depressed skull fractures and intracerebral hematomas that compress the sinus wall, altering blood flow until thrombosis. The risk is highest when a fracture extends to the dural sinus or jugular bulb. Early diagnosis based on imaging is crucial in preventing grave consequences of venous hypertension. Imaging not only plays an important role in early diagnosis, but may also help improve patient outcomes. There is no consensus as to the imaging and management of acute post-traumatic DVST. The latter can pose challenges in the management of traumatic brain injuries, particularly as they often coexist with cerebral contusions, parenchymal hemorrhages, and subdural and epidural hematomas.

Superior sagittal sinus injury from gunshot



Comminuted, displaced fractures of the bilateral calvarium with hemorrhagic parenchymal changes (red arrows) along the path of the projectile and epidural hematomas* at the bilateral convexities



CT venogram showing lack of filling of the anterior segment of the superior sagittal sinus (SSS) [dashed line] with abrupt change in caliber (red arrow) at the anterior aspect of its opacified posterior segment

Irregular contrast-filled structure anteriorly (yellow arrow) is part of the injured anterior segment of the SSS.

(Filename: TCT_903_VenousInjuryGSW.jpg)

794

Adult Hypoxic-Ischemic Brain Injury (HIBI): Overview of Imaging Characteristics, Role of Imaging and Role of State-of-the-Art Imaging Techniques for Neuroprognostication

K Terashima¹, R Rabei¹, E Calabrese¹, J Shih¹, E Amorim¹, J Talbott¹, S Gandhi¹

¹University of California San Francisco, San Francisco, CA

Purpose

1. Review the epidemiology and various causes of adult HIBI 2. Review the imaging characteristics of HIBI on CT and MRI observed in the post-cardiac arrest setting, which is the most common cause of HIBI 3. Review HIBI patterns described in more specific scenarios such as substance abuse, carbon monoxide poisoning, and delayed post hypoxic leukoencephalopathy 4. Review the current role of imaging in neuroprognostication of comatose patients secondary to HIBI 5. Review the literature describing potential applications of advanced imaging techniques such as quantitative diffusion weighted imaging (including summarize our experience thus far), diffusion tensor imaging, and functional MRI

Materials and Methods

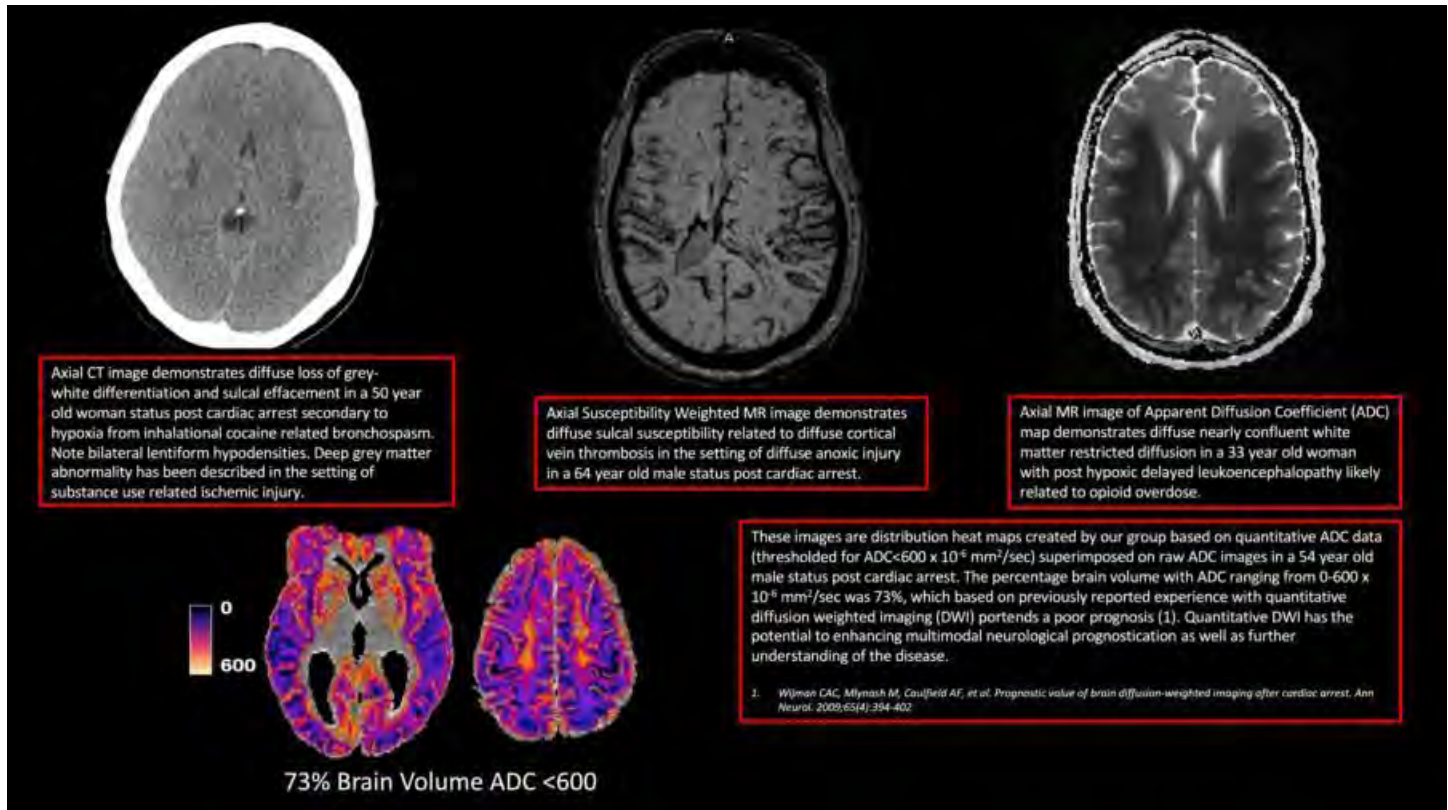
Hypoxic-ischemic brain injury carries significant morbidity and mortality, withdrawal of life-sustaining therapies being a frequent proximate cause of the latter. The purpose of this exhibit is to increase awareness, particularly amongst trainees and radiologists that infrequently encounter patients with HIBI, of what is known about the imaging appearance of HIBI and the role of imaging in enabling earlier and more accurate assessment of disease burden for neuroprognostication. This knowledge can support the referring clinician and families who often face the moral and ethical dilemma related to withdrawal of life-sustaining therapies for many of these patients.

Results

N/A

Conclusions

N/A



(Filename: TCT_794_Shital_ASNRHIBI_EA-new.jpg)

393

Advanced Imaging in Common Neurodegenerative Disorders

M Depuydt¹, M Aftab²

¹Michigan State University College of Osteopathic Medicine, Holly, MI, ²Ascension Genesys, Grand Blanc, MI

Purpose

Advanced imaging plays a significant role in diagnosis and differentiation of neurodegenerative disorders such as Alzheimer's Disease, Parkinson's Disease, Normal Pressure Hydrocephalus, and Progressive Supranuclear Palsy. Common imaging techniques include structural MRI, PET scan, DaTscan, and cisternography. Objectives Understand the role of various imaging techniques and the diagnosis of common dementias. Identify the imaging findings of the neurodegenerative disorders on MR, CT and NM. Recognize the characteristic and classic features of each entity on advanced imaging.

Materials and Methods

The purpose of this project is to compare the various techniques and how they are used to aid in diagnosis of diseases.

Results

N/A

Conclusions

Alzheimer's Disease is a neurodegenerative disease characterized by impairment in short term memory. Structural MRI shows atrophy of medial temporal structures. FDG PET allows visualization of symmetric hypometabolism in the bilateral temporoparietal regions of the brain. 18F-Florbetapir is the most common biomarker for amyloid imaging. Tracer retention is higher in patients with AD than healthy controls in frontal, cingulate, parietal, and lateral temporal cortices. Parkinson's Disease is caused by depletion of dopamine in

the substantia nigra. The DaTscan is used for the diagnosis of PD. 123I-Ioflupane is a SPECT radioligand with high affinity for the dopamine transporter. This radioligand is used to assess the loss of dopaminergic neurons in the striatum. The swallow-tail appearance of a healthy nigrosome can be imaged using 3T MRI. A loss of this normal sign is indicative of PD. Normal Pressure Hydrocephalus is a communicating hydrocephalus characterized by gait disturbance, mental deterioration, and urinary incontinence associated with ventriculomegaly with normal CSF pressure. MRI findings diagnostic of NPH include ventricular enlargement disproportionate to cerebral atrophy and ballooning of frontal horns. Radionuclide cisternography show CSF dynamics dysfunction. A positive result shows ventricular reflux and convexity block. Progressive Supranuclear Palsy is the second most common neurodegenerative form of parkinsonism. Two common features on structural MRI include the hummingbird sign and morning glory sign. The hummingbird sign is a visualization of atrophy of the rostral tegmentum on midsagittal view of midbrain. The morning glory sign is seen on axial view and is due to midbrain atrophy with concavity on the lateral margin of the midbrain tegmentum.

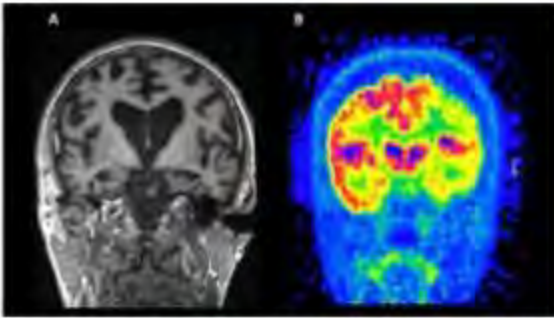


Figure 1. Structural MRI (left) and FDG PET (right) in AD.

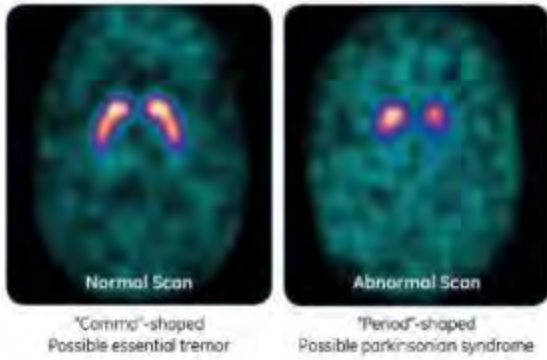


Figure 2. DaTscan in PD.

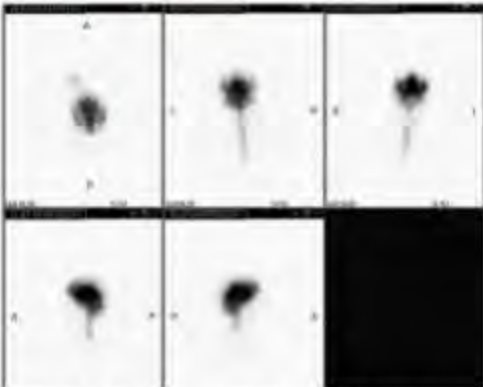


Figure 3. Radionuclide cisternography in NPH.

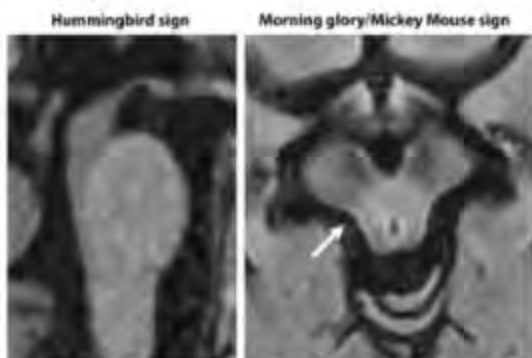


Figure 4. Hummingbird sign (left) and Morning glory sign (right) in PSP.

(Filename: TCT_393_ImagesASNR.jpg)

Aggressive-appearing calvarial lesions – they’re not all bad! Evaluation and review of benign entities with “aggressive” imaging features.

J Junn¹, M Schecht², L Eisenmenger³

¹Mount Sinai Hospital Icahn School of Medicine, NYC, NY, ²Mount Sinai Hospital, NYC, NY, ³University of Wisconsin - Madison, Middleton, WI

Purpose

Illustrate spectrum of imaging appearance of "aggressive" osseous features Expand radiologists' understanding and recognition of benign calvarial entities with aggressive features.

Materials and Methods

In this exhibit, we want to educate radiologists about benign calvarial entities with "aggressive" imaging features. We intend to highlight "aggressive" features seen in benign calvarial lesions to widen the interpreting radiologists' depth of knowledge.

Results

Calvarial lesions can be evaluated with CT or MRI. Often these findings are incidental with some presenting with symptoms such as pain or as a palpable mass. Evaluation of lytic and sclerotic calvarial lesions can be challenging, especially when these lesions have "aggressive" radiologic findings including reduced diffusion, poor margination, wide-zone of transition, destruction of the bone, or accompanied soft tissue. However, not all lesions with these findings are malignant lesions. In this exhibit, we will focus on both lytic and sclerotic lesions that the interpreting radiologists need to know to by highlighting salient imaging features associated with these entities. Discussed disease processes will include entities such as intraosseous meningioma, ossifying fibroma, Paget disease, brown tumor, solitary plasmacytoma, periosteal desmoid, and osteomyelitis.

Conclusions

Through this exhibit, the viewers should have a better understanding for benign osseous lesions with aggressive features and be able to apply their salient imaging findings to narrow the diagnosis.

413

AI for the Neuroradiology Neophyte: Pitfalls and Pragmatic Considerations When Just Starting Out

E Wannamaker¹, O Wu², C Filippi³, A Thaker¹, J Tanabe¹

¹University of Colorado Anschutz Medical Campus, Aurora, CO, ²Massachusetts General Hospital, Charlestown, MA, ³Tufts University Medical Center, Boston, MA

Purpose

N/A

Materials and Methods

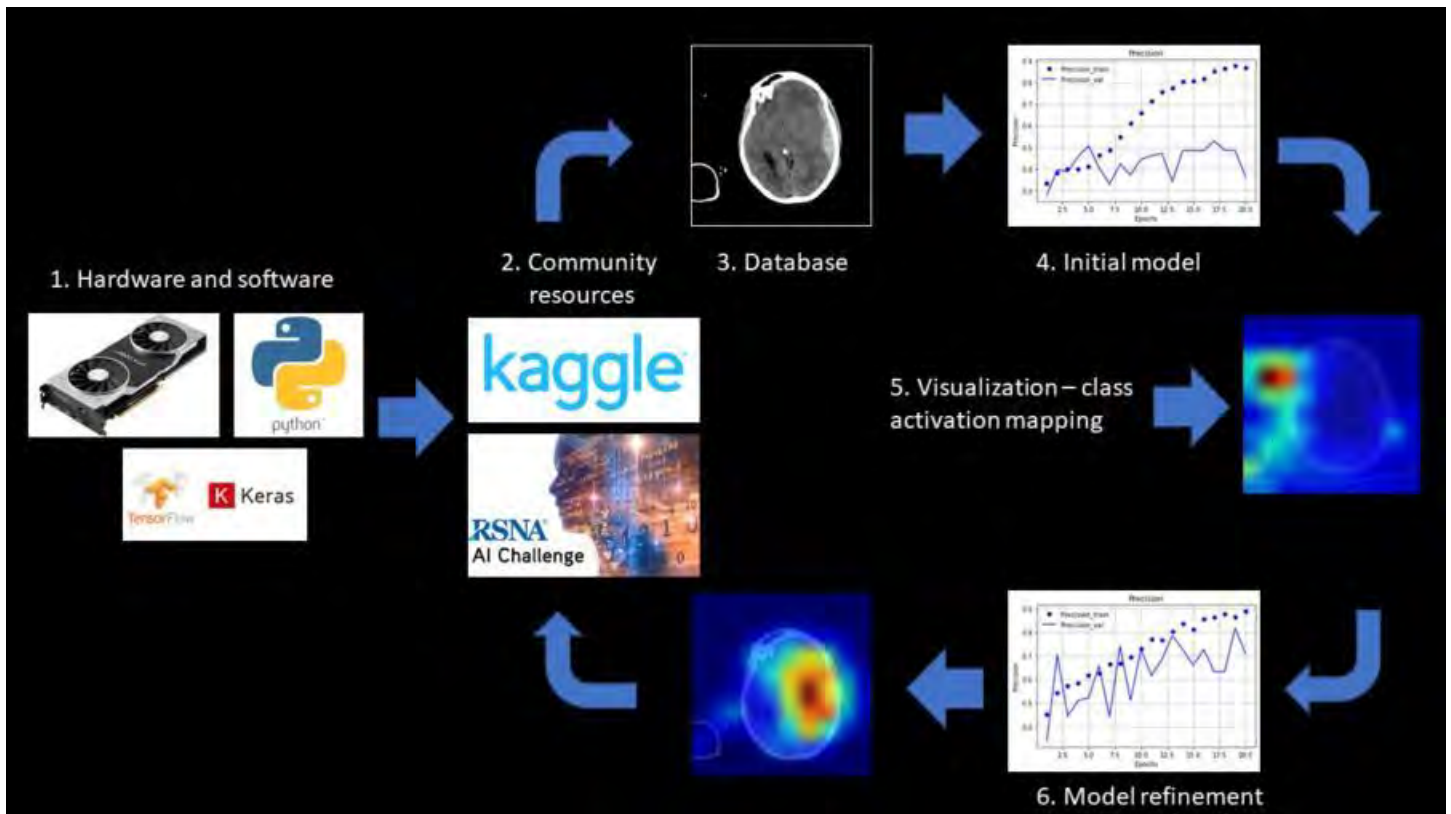
While there is a rapidly growing body of literature on application of artificial intelligence (AI) methods in neuroradiology, the learning curve is a steep one. The initial challenges can overwhelm even the most motivated clinician-scientist. This educational exhibit offers a pragmatic approach to getting started with a neuroradiology AI project, while avoiding common pitfalls, utilizing automated CT hemorrhage detection as an example project.

Results

Provide a framework for developing an AI project from a starting point of zero or limited AI research experience using a CT hemorrhage classification project as an example. Topics include: 1. Importance of mentorship: informal or organized such as through the ASNR/ASFNR AI workshop. 2. Summarize basic concepts and vocabulary needed to begin an AI project. 3. Understand minimum and optimum hardware requirements. 4. Describe strategies for gaining fluency with Python and essential AI software packages. 5. Gain an understanding of strategies for obtaining or creating a project database. Avoid common pitfalls. 6. Outline the steps for creating or adapting a basic binary classification model. 7. Describe methods for model optimization. 8. Address common idiosyncrasies of diagnostic imaging data. 9. Introduce methods to explain model behavior with focus on heat maps.

Conclusions

Clinician-scientist neuroradiologists have a unique and important role in the development of AI technology. A pragmatic road map for overcoming the steep learning curve for entry into this field of research can help expedite the process and empower more radiologists to get involved.



(Filename: TCT_413_AI_ED_Figure_v2.jpg)

1595

All That Bright in Brain on Diffusion-Weighted Imaging (DWI) is Not Stroke: A Case Based Review

R Patel¹, S Khanpara¹, A Aein¹, Y Cai¹, R Samant¹

¹The University of Texas Health Science Center at Houston, Houston, TX

Purpose

Diffusion-weighted imaging (DWI) is most commonly used sequence in diagnosis of acute stroke/cerebral infarction, but it can be used as a very important tool for diagnosing of various neurological disorders include infectious, toxic/metabolic, neoplastic, traumatic and demyelinating processes along with correlating clinical presentations. After reviewing this presentation, reviewer will be able to understand physics of diffusion weighted imaging (DWI) sequence and its application in diagnosing non-stroke etiologies.

Materials and Methods

1. To describe and illustrate physics of diffusion weighted imaging (DWI) sequence. 2. To illustrate various categories of neurological disorders demonstrate restricted diffusion on DWI in a case based format. 3. To illustrate characteristics of neurological disorders on conventional MRI sequences and most importantly understand how DWI can aid in the diagnostic challenge.

Results

We performed a HIPAA-compliant retrospective review of our institution's radiology databases, for illustrative cases of restricted diffusion on DWI with multiparametric imaging analysis. Additionally, a review of the current medical literature was performed.

Conclusions

Diffusion-weighted imaging (DWI) is most commonly used sequence for diagnosis of acute cerebral infarction, but there are several other diseases of the brain that demonstrate restricted diffusion which radiologists must be familiar with that include infectious, toxic/metabolic, neoplastic, traumatic and demyelinating processes. This exhibit will focus on how DWI and typical clinical presentation can be used to narrow the differential in cases.

1564

All you need to know about Pediatric Cervical Spine Injury: birth related injury, accidental and non-accidental trauma and beyond

M Gurvildirim¹, L Bonacorsi¹, J Machnitz¹, J Son¹, A Tekes-Brady²

¹Johns Hopkins Hospital, Baltimore, MD, ²N/A, N/A

Purpose

1. The majority of pediatric cervical spine injuries occur between the skull base and the C4 vertebra, given the different biomechanics of pediatric cervical spine compared to adults. 2. Fatal spine injuries most commonly involve the cervical spine and imaging plays a critical role.

Materials and Methods

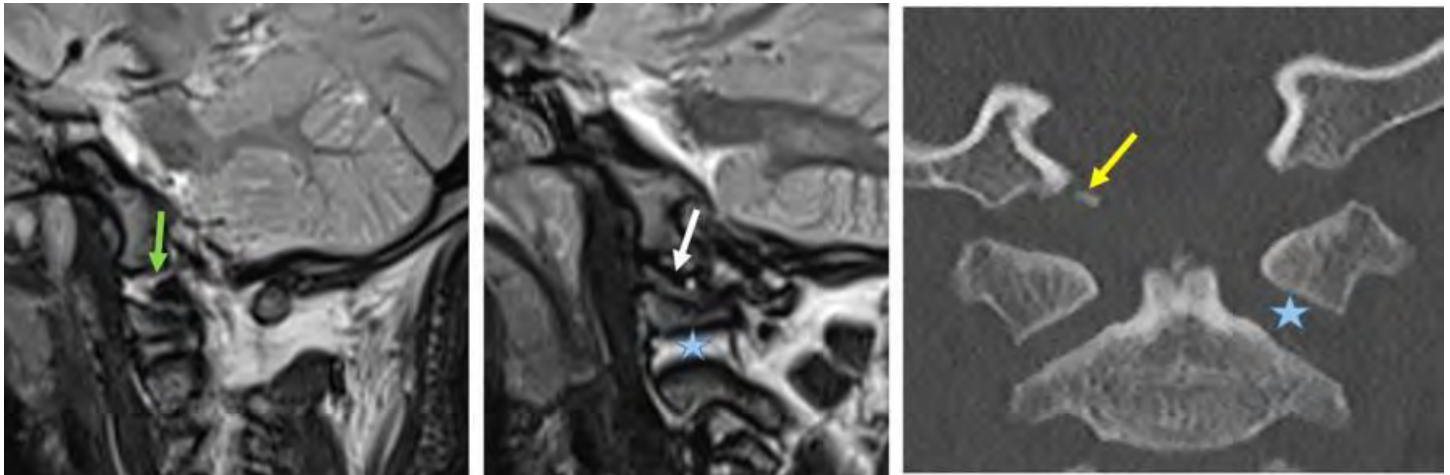
In this education exhibit, we will review embryology, anatomy and anatomical variants of the pediatric cervical spine. Imaging recommendations for different clinical scenarios will be presented following ACR and PECARN.

Results

Case based review of birth related trauma, accidental injury and non-accidental trauma focusing on soft tissue, ligamentous and bone injuries in relation to common mechanisms of injury.

Conclusions

1. Review of embryology, normal anatomy and anatomical variants of the cervical spine in different age groups 2. Neuroimaging findings of birth related, accidental and non-accidental traumatic injury on radiographs, US, CT or MR imaging with comparison to normal controls.



(Filename: TCT_1564_Figure4300dpi.jpg)

1244

All You Need to Know About the “Wandering” Nerve: A Neuroradiological Review of the Anatomy, Pathology and Imaging Techniques of the Vagus Nerve, and Future Directions

H Rajebi¹, W Mehan¹, K Buch¹

¹Massachusetts General Hospital, Boston, MA

Purpose

The long course of the vagus nerve with complex intracranial, skull base and neck anatomy yield to abnormal imaging findings in the context of multiple underlying pathologies. It is essential that neuroradiologists become familiar with the normal anatomy, newer available imaging methods and numerous neuropathies for early and precise diagnosis.

Materials and Methods

The vagus nerve is the longest cranial nerve, traveling from its nuclei in the brainstem, through the neck, chest and upper abdomen. The knowledge about this path is crucial for the neuroradiologist to understand the associated underlying pathologies. In this exhibit, we aim to review the normal anatomy, available novel imaging techniques and radiologic features of various conditions involving the vagus nerve.

Results

After a detailed review of the relevant anatomy of the vagus nerve and its branches, a comprehensive institutional case-based review of the primary and secondary pathologies involving the tenth cranial nerve will be illustrated. Diagnostic hints and pitfalls will be presented in each case. CT and MR imaging techniques will be discussed for evaluating the course of the vagus nerve.

Conclusions

Cases in multiple locations and within different categories through the course of the nerve including but not limited to; supranuclear lesions, brainstem (demyelinating/inflammatory, vascular, neoplasms, syringobulbia, Avellis syndrome), jugular foramen (primary or secondary neoplasms, skull base fracture, Vernet syndrome), neck (primary neoplasm, mononeuritis, inflammatory/tumoral infiltration) will be shown. Different MR sequences, distinct imaging features and pertinent negative findings of each entity will be explained. A brief demographic feature of each condition, clinical presentation and predisposing risk factors will also be reviewed.

Jugular Foramen Schwannoma



Heterogeneously enhancing mass with increased T2 signal & calcifications (rarely seen) appears to arise from the left jugular foramen & produces mass effect on the brainstem & effacement of the fourth ventricle.

(Filename: TCT_1244_ASNRVagusNerve.JPG)

578

Amide proton transfer, diffusion and perfusion weighted imaging of high grade gliomas

S Turk¹, T Moritani², J Kim³

¹University of Michigan, Ann arbor, MI, ²N/A, N/A, ³University of Michigan, Ann Arbor, MI

Purpose

After viewing this exhibit, the reader will be familiar with the complementary roles of perfusion, diffusion and APTw imaging in evaluating high grade gliomas: their imaging features, assessment of treatment effects/response and other pearls and pitfalls.

Materials and Methods

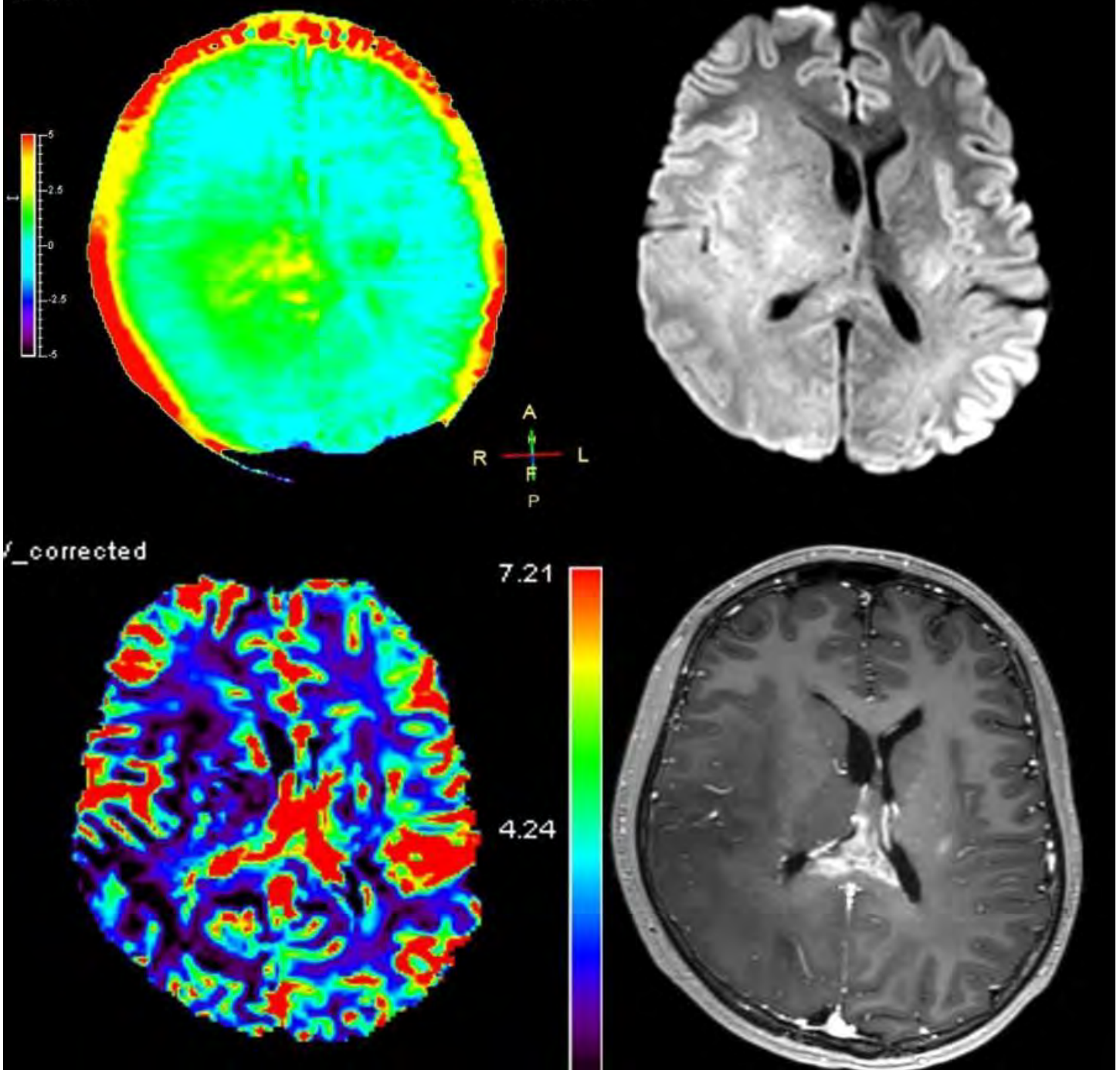
- Highlight the role of amide proton transfer weighted (APTw) imaging and the use of diffusion and perfusion parameters in high grade gliomas.
- Discuss the potential of using APTw imaging in assessing treatment response and discrimination of true tumor progression from pseudoprogression.
- Discuss the pearls and pitfalls in interpreting APTw, diffusion and perfusion weighted imaging.

Results

Overview of imaging characteristics of high grade glial tumors with emphasis on perfusion (DSC, DCE, ASL), diffusion and APTw imaging. Demonstrate cases of tumor progression versus treatment effects and genetic mutation correlation with diffusion and APT parameters.

Conclusions

Advanced MRI techniques add value to conventional imaging sequences in the assessment of high grade glial tumors. Tumor grade prediction, treatment response assessment, differentiation of true tumor progression from pseudoprogression, and genetic mutation prediction are discussed based on the combination of perfusion, diffusion and APTw imaging. Necrosis, hemorrhage, calcification and extracellular matrix can affect the signal intensity in APT, perfusion and diffusion weighted imaging differently. Pitfalls and accuracy of each advanced imaging methods differs but complement each other when used together.



(Filename: TCT_578_hgg.jpg)

584

Amide proton transfer, perfusion and diffusion weighted imaging of pediatric brain tumors with pathological correlation

S Turk¹, T Moritani², J Kim³, M Ibrahim⁴

¹University of Michigan, Ann arbor, MI, ²N/A, N/A, ³University of Michigan, Ann Arbor, MI, ⁴University of Michigan Health System, Ann Arbor, MI

Purpose

After viewing this exhibit, the reader will be familiar with the complementary roles of perfusion and diffusion-weighted imaging and APT maps in pediatric brain tumors, their imaging features, assessment of treatment effects and the pearls and pitfalls to make accurate discrimination.

Materials and Methods

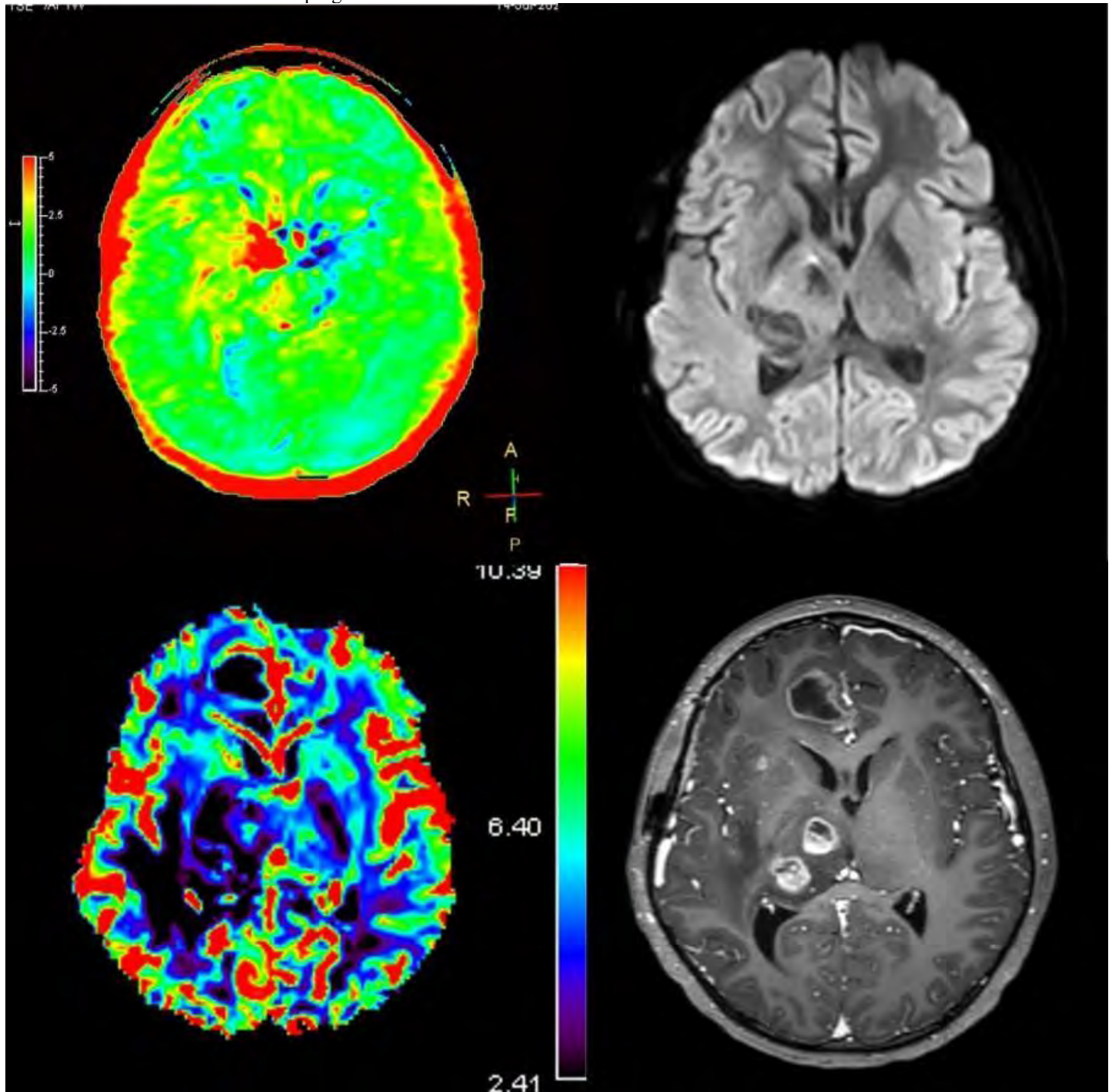
- Highlight the role of amide proton transfer weighted (APT_w) imaging and the use of diffusion and perfusion imaging in pediatric brain tumors, with pathological correlation.
- Discuss pearls and pitfalls in interpreting APT_w, diffusion and perfusion weighted imaging in pediatric brain tumors.

Results

- Overview of imaging characteristics of supratentorial and infratentorial pediatric brain tumors (pilocytic astrocytoma, other low and high grade glial tumors, ependymoma, medulloblastoma, choroid plexus papilloma, embryonal tumors) with emphasis on perfusion (DSC, DCE, ASL), diffusion and APT_w imaging.

Conclusions

Advanced MRI techniques add value to conventional imaging sequences in classification of tumors, prediction of tumor grade, differentiation of true tumor progression and pseudoprogession, treatment response assessment, and even for predicting genetic mutations. There are pitfalls and differing accuracy for each method. Necrosis, hemorrhage, calcification and extracellular matrix can affect APT_w, perfusion and diffusion imaging differently. However, these advanced MRI techniques complement each other when used together. Perfusion, diffusion and APT_w maps are useful in detection of recurrent tumors, and potentially useful in differentiation of treatment effects from true tumor progression.



1193

An Eye for Eyes: Pediatric Ophthalmologic Pathology on MRI

J Morris¹, S Chiu¹, E Negron-Rubio¹, S Schaffner¹, T Rahim¹, M Bajaj¹

¹*Medical College of Georgia at Augusta University, Augusta, GA*

Purpose

The globe and orbit are complex histologic and anatomic structures composed of numerous tissue types allowing for a broad array of pathologies to arise in a confined space. The learner should come away from this presentation with a deeper understanding of the MR appearance of the globe and orbit and how various infectious, inflammatory, neoplastic, and congenital processes may appear. The learner should also identify how to approach the diagnosis and differentiation of ophthalmologic processes, with a specific emphasis on the pediatric patient, and the clinical importance of these findings.

Materials and Methods

Magnetic resonance imaging (MRI) is a powerful tool for evaluation of the globe and orbit. MRI provides detailed information on a wide array of pathology from congenital to vascular to malignant using multiple sequences, including diffusion weighted imaging and spectroscopy. With the addition of gadolinium contrast, further information can be gathered about the properties and composition of orbital lesions. With this myriad of information, it is crucial for the radiologist to be familiar with important MRI sequences and the common appearances of abnormalities when using MRI. The goal of our presentation is to provide an overview of orbital MRI and the imaging features of selected pathologies.

Results

n/a

Conclusions

A broad range of pediatric ophthalmologic pathology will be presented with focused discussion on their characteristic MR findings. These topics include infectious, inflammatory, neoplastic, congenital, and other processes, as outlined below. Infectious: Orbital cellulitis, orbital subperiosteal abscess, frontal epidural abscess with superior ophthalmic vein thrombosis Inflammatory: Optic neuritis (MS, NMO, etc.), chiasmatic neuritis, orbital inflammation Neoplastic: Oculomotor schwannoma, orbital hemangioma, NF1 optic glioma, optic chiasm astrocytoma, optic nerve metastasis Congenital: Absent abducens, atrophic medial rectus, Duane retraction syndrome, Morning Glory optic disc, orbital encephalocele, orbital dermoid, PHACE hemangioma, persistent hyperplastic primary vitreous, septo-optic dysplasia Other: retinal hemorrhage, retinal detachment, idiopathic intracranial hypertension

729

An Imaging Review of Cranial Surgical Approaches and Spectrum of Pathologies Tackled

A Kulkarni¹, A Kumar¹, A Chen¹

¹*University of Massachusetts, Worcester, MA*

Purpose

There are different types of craniotomies performed to gain surgical access for treating intracranial pathologies depending on their anatomic location. It is helpful to have basic knowledge of these varying surgical approaches and to understand group of common pathologies that are being addressed by these surgical methods.

Materials and Methods

To review types of cranial vault surgeries. To describe imaging appearance of different types of pathologies associated with individual surgical approach.

Results

Retrospective analysis of our imaging database was performed to identify patients undergoing CT and or MRI imaging after major neurosurgery over period of last five years. Cases were grouped together based on the surgical approach such as burr holes, types of craniotomies, craniectomies and cranioplasty. Imaging spectrum of pathologies addressed by these surgical methods were identified and described.

Conclusions

Our educational exhibit aims to review imaging appearances of common neurosurgical techniques such as burr holes, types of craniotomies, craniectomy and cranioplasty. We also review the imaging spectrum of pathologies addressed by them. We try to understand neurosurgeons point of view in choosing one technique over other. It is important to be aware of these common surgical approaches, pathologic spectrum addressed by these techniques and their common complications in order to be more helpful as a radiologist in pre-surgical planning and contributing successfully to patient care.

562

Anatomic Variants, Malformations, and Acquired Venous Intracranial Abnormalities in Children

F Koudoro¹, I Saramago², C Zamora³, M Castillo⁴

¹*The University of North Carolina at Chapel Hill, Chapel Hill, NC*, ²*N/A, N/A*, ³*UNC Department of Radiology, Chapel Hill, NC*, ⁴*Radiology, Chapel Hill, NC*

Purpose

Review embryology and anatomy of the intracranial venous system Review pediatric intracranial venous anatomy, its normal and pathologic variants with their corresponding imaging characteristics

Materials and Methods

There is a wide spectrum of entities that can affect the intracranial venous structures in children, ranging from anatomic variants to congenital/acquired lesions. This exhibit summarizes the normal venous anatomy and its variants as well as imaging findings associated with related lesions.

Results

We searched our teaching files over the past 10 years for cases of pediatric patients aged 0-18 years old who presented with venous anomalies/lesions.

Conclusions

The intracranial venous system is divided into the cerebral veins (composed of superficial and deep systems) and the dural sinuses. The complexity of the intracranial venous system predisposes it to wide variations that include aberrant vessels and/or unusual drainage patterns. Veins may also be affected in a large number of pathologies which can be syndromic or occur in isolation which includes: infection (thrombophlebitis), trauma (bridging vein thrombosis/rupture in abusive head trauma), ischemic (venous infarction), congenital and/or malformations (atretic parietal cephalocele, venous varix, sinus pericranii, Vein of Galen malformation, and dural arteriovenous fistulae with venous aneurysms and arterialized veins, amongst others. Cerebrofacial venous metamerism harbor facial venous malformations, developmental venous anomalies, venous angiomas, cavernous malformations, and dural sinus malformations. Abnormal venous drainage can also be a sign of adjacent cortical architecture abnormalities such as dysplasia and schizencephaly. Conclusion Here we present a review of anatomic variants, malformations, and acquired venous pathologies in children. Knowledge of the clinical presentation and venous anatomy in conjunction with the imaging appearance are essential for an accurate interpretation and for identification of potential syndromic associations.

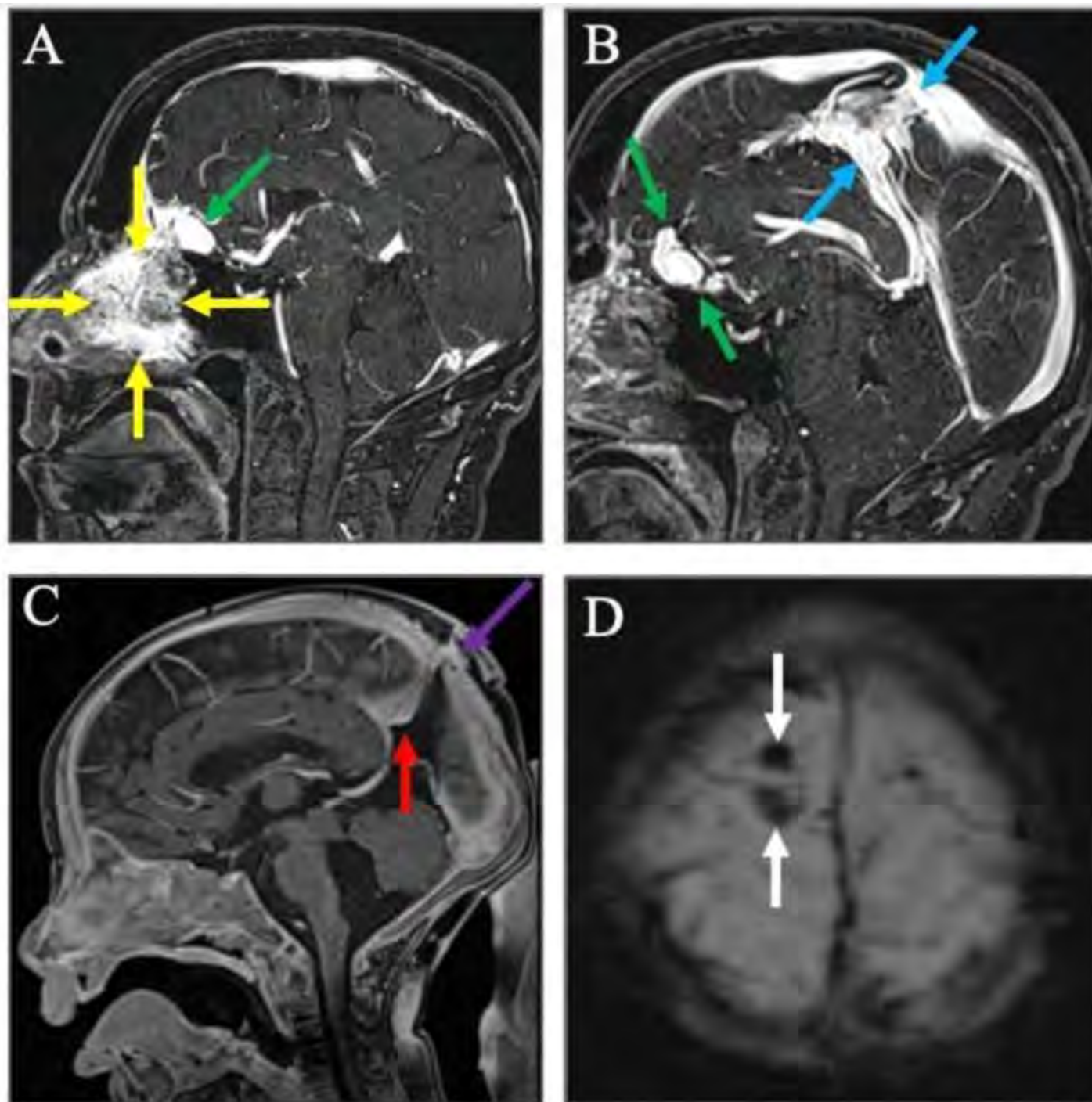


Figure Legend: Examples of select venous pathologies. (A, B) Sagittal postcontrast T1 shows an avidly enhancing venous vascular malformation involving the nasal cavity (yellow arrows), anterior skull base (green arrows), sagittal sinus and deep cerebral veins (light blue arrows) in a patient with cerebrofacial venous metamerism syndrome. (C) Sagittal post contrast T1 shows a persistent falcine sinus (red arrow) in a patient with an atretic parietal cephalocele (purple arrow). (D) Axial SWI shows injury to bridging veins (“tadpole” sign) (white arrows) in the right frontal lobe in the setting of abusive head trauma.

(Filename: TCT_562_ASNR.jpg)

Aneurysmal Dissections in the Posterior Circulation

A Saini¹, S Srour², J Loeb³, J Asmar⁴

¹Department of Radiology, St. Luke's Hospital of Kansas City, Kansas City, MO, ²St. Luke's Hospital of Kansas City, Kansas City, MO, ³Saint Luke's Hospital of Kansas City, Kansas City, MO, ⁴University of Missouri Kansas City, KANSAS CITY, MO

Purpose

The purpose of this educational exhibit is to review aneurysmal dissecting aneurysms of the posterior circulation. This will be accomplished by the following: -Provide an overview of aneurysmal dissections including their epidemiology, clinical presentation, diagnosis and management. -Categorize aneurysmal dissections based upon their location: Vertebral artery, Vertebral-PICA complex and other posterior circulation arteries. -Review endovascular interventions and techniques for the treatment of aneurysmal dissections, including unruptured versus ruptured dissecting aneurysms. -Discuss the various treatment options for unruptured aneurysmal dissections with or without infarction, which includes observation, antiplatelet therapy, or vessel sacrifice. Additionally review the advantages/disadvantages of each. -Discuss the various treatment options for ruptured dissecting aneurysms including flow diverting stents including the Pipeline Flex embolization device, arterial sacrifice with coil embolization, and glue or onyx embolization. Additionally review the advantages/disadvantages of each. -Briefly highlight emerging/future treatment options. - Provide a case based review of aneurysmal dissections treated with minimally invasive interventions at our institution. Pre- and post-treatment images will be provided. Patient outcomes discussed.

Materials and Methods

To inform general radiologists and neuroradiologists on conservative management and endovascular interventions for treating aneurysmal dissections of the posterior circulation.

Results

N/A

Conclusions

N/A



Figure 1. Patient developed severe vertigo while on vacation. Cerebellar infarct on CT. No acute hemorrhage. Angiogram shows dissecting aneurysm of the left PICA.

(Filename: TCT_855_Figure1and2.jpg)

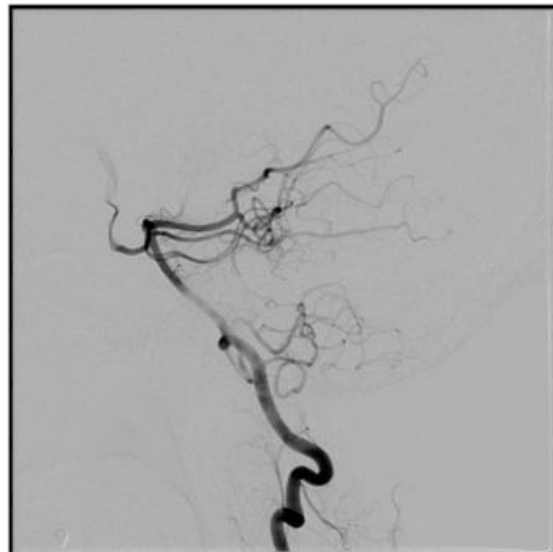


Figure 2. Angiogram after 8 months of antiplatelet therapy demonstrates resolving AD.

1075

AO Spine Injury Classification Systems Made Easy

K Hsieh¹, K RAGHURAM², S Owji³

¹University of Texas Medical Branch, Galveston, TX, ²N/A, N/A, ³University of Texas Medical Branch, Houston, TX

Purpose

Spine trauma requires accurate and efficient diagnosis for effective management. A number of classification schemes have been proposed, and the AO Spine classification systems is the newest, most user-friendly, and most widely used by the surgical community. The thoracolumbar classification (TLICS) was proposed in 2013 followed by the subaxial cervical spine injury classification system (SLIC), and the newest is the upper cervical classification system. A number of studies have proven the AO Spine classification systems to be reliable and reproducible. The objective of this exhibit will be to review the AO Spine classification systems with graphics, cases, and Powerscribe360 macros of Common Data Elements (CDE).

Materials and Methods

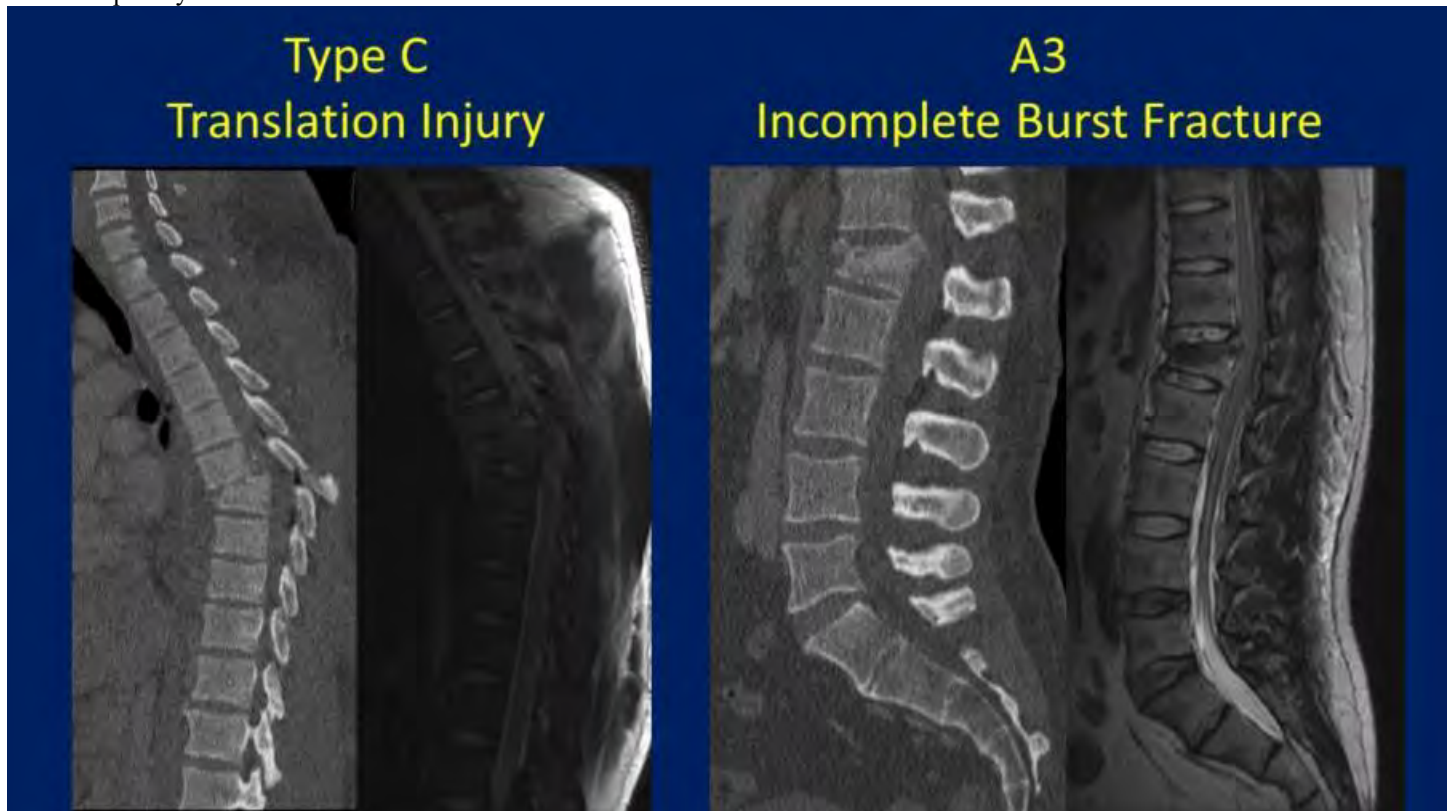
The AO Spine classification system considers three criteria: fracture morphology, the presence of specific clinical modifiers, and the neurological status. Data for the first two of these criteria come from the radiological evaluation. The ASNR-ACR-RSNA Common Data Elements (CDE) Neuroradiology Workgroup has come up with macros to aid in reporting spine trauma. After reviewing this exhibit, one should have the knowledge and tools to accurately and efficiently report spine trauma injury in the language of the multidisciplinary team.

Results

Fracture morphology is classified into three primary groups by severity. Type C translation or displacement of the vertebral body is the most severe. Type B are fractures with failure of the anterior or posterior tension band, and Type A are compression or burst fractures. For example, Type A injuries are further subdivided depending upon involvement of the posterior vertebral body wall (Burst Types A3 and A4) and endplates (One endplate Type A1 and both endplates Type A2). The algorithm goes from most severe to least severe to determine the morphologic classification. Clinical modifiers include indeterminate injury to the tension band and patient-specific comorbidities, which might argue either for or against surgery such as ankylosing spondylitis. The CDE macros include Pick Lists of all the fracture morphologic classifications and clinical modifiers for easy reference and documentation in reports.

Conclusions

Understanding the AO Spine Classification Systems is important for the radiologist as it is emerging as the most widely used by the surgical community. The AO Spine CDE macros are helpful tools to aid in reporting spine trauma in the language of the multidisciplinary team.



(Filename: TCT_1075_aospine.jpg)

1492

AO Thoracolumbar Spine Injury Classification System: A Pictorial Review

R Cua¹, C Lee¹, A Rajamohan¹, J Go¹, P Kim¹, J Acharya¹

¹Keck School of Medicine of USC, Los Angeles, CA

Purpose

Thoracolumbar spine injuries remain exceedingly common with numerous classification schemes having been proposed throughout the years to guide clinical management and prognosis. Injuries to the thoracolumbar spine are usually the result of high energy blunt trauma with two thirds of fractures due to motor vehicle injuries and falls from height with the remaining third secondary to sports injuries and violence. Classification systems aim to facilitate communication and aid in the comparison of similar fractures to help guide treatment. Previously proposed schemes have used determinants such as inferred mechanism of injury, bony morphology, anatomic determinates of fracture stability, and neurological status. Recently, the AOSpine Knowledge Forum has proposed a comprehensive modified classification system which simplifies fracture classification to include morphology of the fracture, neurological status, and description of relevant patient-specific modifiers. Although the AO Thoracolumbar Spine Injury Classification System aims to provide a comprehensive yet simple classification system to facilitate intra and interobserver reliability, new trainees may have limited knowledge and experience with application of the classification system, particularly in centers with limited trauma exposure. AOSpine subdivides the spine into 4 regions: upper cervical, subaxial cervical spine, thoracolumbar spine, and the sacral spine. Our presentation will focus on fractures in the thoracolumbar spine. Fractures are classified into A, B, and C types with further sub-classification and use of clinical modifiers as necessary. Educational Objectives: 1. To illustrate the historical context regarding radiologic classification of thoracolumbar spine injuries 2. To describe and apply the AO Thoracolumbar Spine Injury Classification System 3. To provide imaging examples of each morphologic pattern and grade for the various injury patterns

Materials and Methods

N/A

Results

N/A

Conclusions

N/A



Figure 1. Translocation injury of the thoracic spine at the T8-T9 level (C)



Figure 2. Fracture of the T12 vertebral body extending through the anterior and posterior cortices as well as the superior and inferior end plates (A4)



Figure 3. Fracture of the T9 vertebral body extending through the posterior elements with focal disruption of the ligamentum flavum (B1)



Figure 4. Fracture of the T6 vertebral body involving the anterior cortex and superior and inferior end plates (A3)

(Filename: TCT_1492_Presentation2.gif)

470

AOSpine Classification of Thoracolumbar Injuries Demystified

A Wang¹, E RODRIGUEZ², J Lally³, A Singh⁴

¹University of Texas Health Science Center San Antonio, San Antonio, TX, ²UNIVERSITY OF TX HEALTH SAN ANTONIO, SAN ANTONIO, TX, ³UT Health San Antonio, San Antonio, TX, ⁴N/A, N/A

Purpose

The AOSpine classification of thoracolumbar spine injuries helps communicate the morphology of a fracture to the surgeon. This reduces the variability in reporting complex spinal fractures. Using cases of spinal injuries from our level 1 trauma center, a methodical, stepwise approach is presented to learn how to classify thoracolumbar fractures. The AOSpine classification system can

organize various types of complex fractures into 3 types - compression, distraction, or translation injuries. The mechanisms of each injury, such as flexion, extension, rotation, axial loading, is important to know in order to find associated fractures or ligamentous disruptions. Each subtype in the AOSpine classification will include a mechanism that resulted in the injury as well as a description of the components of the injury. The objectives of the exhibit are: - Learn a stepwise practical approach for using the AOSpine classification for thoracolumbar spine injuries - Learn the various types of thoracolumbar fractures using the AOSpine classification - Learn the mechanisms of traumatic injuries that contribute to the different classifications of fracture types

Materials and Methods

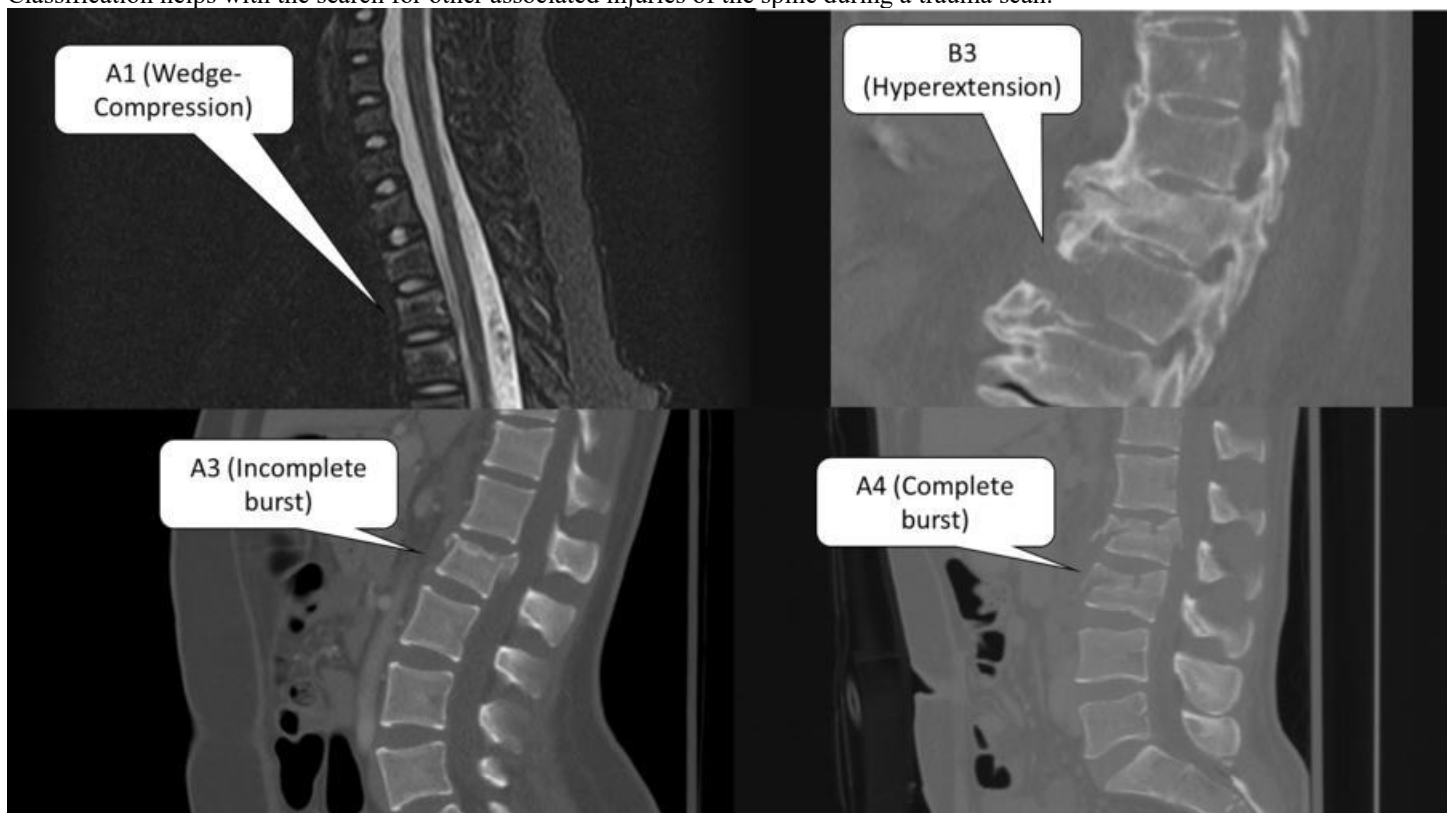
To present a stepwise approach to learn the types, how to classify, and mechanism of thoracolumbar spine injuries using the AOSpine Classification system.

Results

Multiple high-quality images of thoracolumbar spine fractures were collected from our institution. The AOSpine classification system and other peer-reviewed articles were used to create an educational multi-slide PowerPoint presentation.

Conclusions

An international standard for reporting thoracolumbar spine injuries is not currently in use. We have adopted the AOSpine Classification for thoracolumbar spinal injuries at our institution to improve communication of fractures with the surgeon. A concise, step wise approach to characterizing and categorizing various types of spinal injuries is a practical way to learn how the AOSpine Classification can be utilized in radiology reporting. The benefits of a standardized system includes reducing variability in reports and increasing reliability amongst radiologists and clinicians. In addition, learning the mechanism of injuries associated with the AOSpine Classification helps with the search for other associated injuries of the spine during a trauma scan.



(Filename: TCT_470_Untitled1.jpg)

1184

Applications of Dual Energy Computed Tomography (DECT) in Neuroradiology

M Aslam¹, C Pedersen¹, O Teytelboym²

¹Mercy Catholic Medical Center, Darby, PA, ²Mercy catholic medical center, darby, PA

Purpose

This exhibit provides pictorial based review of DECT in Neuroimaging including application of bone subtraction, hard plaque removal, monoenergetic low keV, Iodine overlay map and virtual non contrast automated reformats. Understanding applications of automated DECT reformats, impact on radiation and awareness of artifacts is essential for neuroradiology practice. Our educational objectives are: -To review basic physics of DECT, artifacts and impact on patient radiation doses. -Illustrate and review applications of different automated reformats of DECT in Neuroimaging.

Materials and Methods

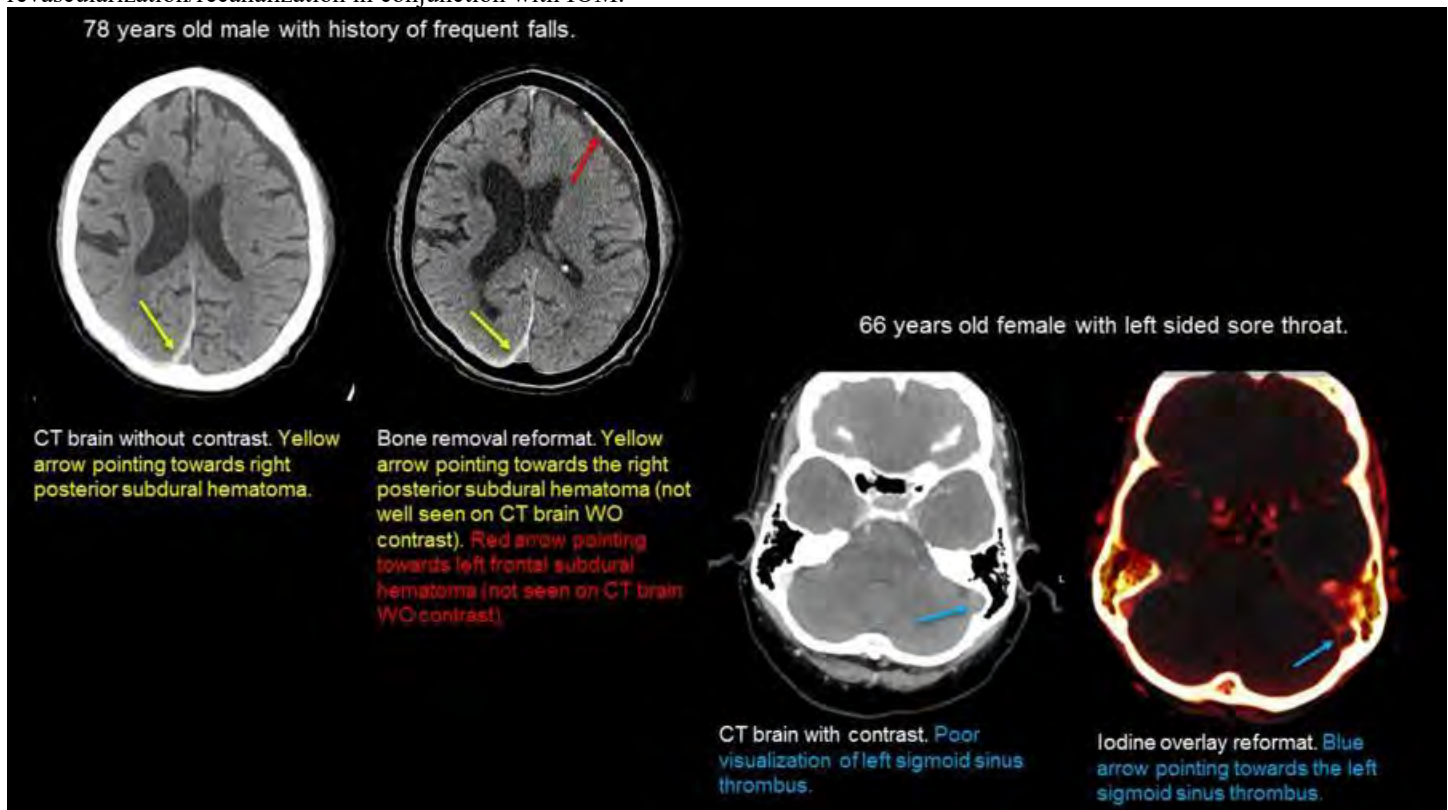
Dual Energy CT (DECT) is a Computed Tomography technique that uses 2 different energy spectra for image acquisition and data processing, as tissues have different attenuations at different energy voltages. Recent advances and automated processing in DECT has a substantial impact in neuroradiology and substantially expanded DECT potential for tissue characterization and differentiation.

Results

A review of published literature on clinical use of Dual Energy CT in neuroimaging was performed and key articles were identified. Protocols and clinical use of Dual Energy CT were obtained based on publications and the author's own experience.

Conclusions

-Bone subtraction reformat (BSR): detection of extra axial hemorrhages and skull lesions, CT angiography/venography, detection of aneurysms at skull base, and visualization of intracavernous part of internal carotid arteries. -Hard plaque removal reformat (HPRR) for evaluation of vascular stenosis in moderate to heavily calcified blood vessels. -Iodine overlay maps (IOM) and monoenergetic low KeV reformats for evaluation of enhancement or scans degraded by poor contrast opacification. -Virtual non contrast reformat (VNC) as replacement for non-enhanced CT, radiation dose reduction, and evaluation of blood brain barrier after intra arterial revascularization/recanalization in conjunction with IOM.



(Filename: TCT_1184_DECTfinal.jpg)

568

Approach Considerations in the Diagnosis of Delayed Presenting Subarachnoid Hemorrhage

A Ahmed¹, A Aly², M Ali¹, E Pedersen¹

¹Creighton university, Omaha, NE, ²Creighton University Medical Center, Omaha, NE

Purpose

Learning objectives: • Review the clinical presentation of subarachnoid hemorrhage. • Explain the chronological changes of the blood products in the subarachnoid space and its relation to their imaging properties. • Discuss the role of different diagnostic modalities in delayed presentation of subarachnoid hemorrhage. Background: Subarachnoid hemorrhage (SAH) is a life-threatening condition that should be ruled out in any patient with acute severe onset of headache. Computed tomography (CT) is highly sensitive in the detection of subarachnoid hemorrhage in the first 6 hours from onset of symptoms. The sensitivity of CT drops rapidly as time progresses from the onset of symptoms. Adopting algorithm for approaching delayed presentation of subarachnoid hemorrhage is very important for proper handling of this critical situation. Findings: Non contrast head CT is the gold standard in the diagnosis of subarachnoid hemorrhage with significantly dropping sensitivity in patients presenting after 6 hours from onset of symptoms. CT/lumbar puncture approach is the traditional recommendation for delayed presenting subarachnoid hemorrhage. Lumbar puncture is a minimally invasive procedure that allows detection of xanthochromia. Xanthochromia remains positive in 75% of patients with subarachnoid hemorrhage for 3 weeks. CT angiography (CTA) is highly sensitive in the detection, localization and characterization of cerebral

aneurysms more than 3 mm in size. It also has the additional benefit of excluding other serious causes of intracranial bleed as arteriovenous malformations. MRI has considerably higher accuracy in the detection of late presenting subarachnoid hemorrhage. Fluid attenuation inversion recovery (FLAIR) sequence is 89-100% sensitive in patients presenting 4-15 days from ictus with sensitivity dropping to 30% after 30 days. Gradient echo (GE) T2* weighted sequence and susceptibility weighted imaging allows better detection of more delayed SAH. Double inversion recovery (DIR) was found to be more sensitive in detection of subarachnoid hemorrhage when compared to other sequences. MRA has the added value of detecting aneurysms. Conclusion and teaching points: Diagnosis of late presenting subarachnoid hemorrhage is challenging. Different diagnostic approaches have varying benefits, risks and costs and should be tailored specifically according to the clinical situation.

Materials and Methods

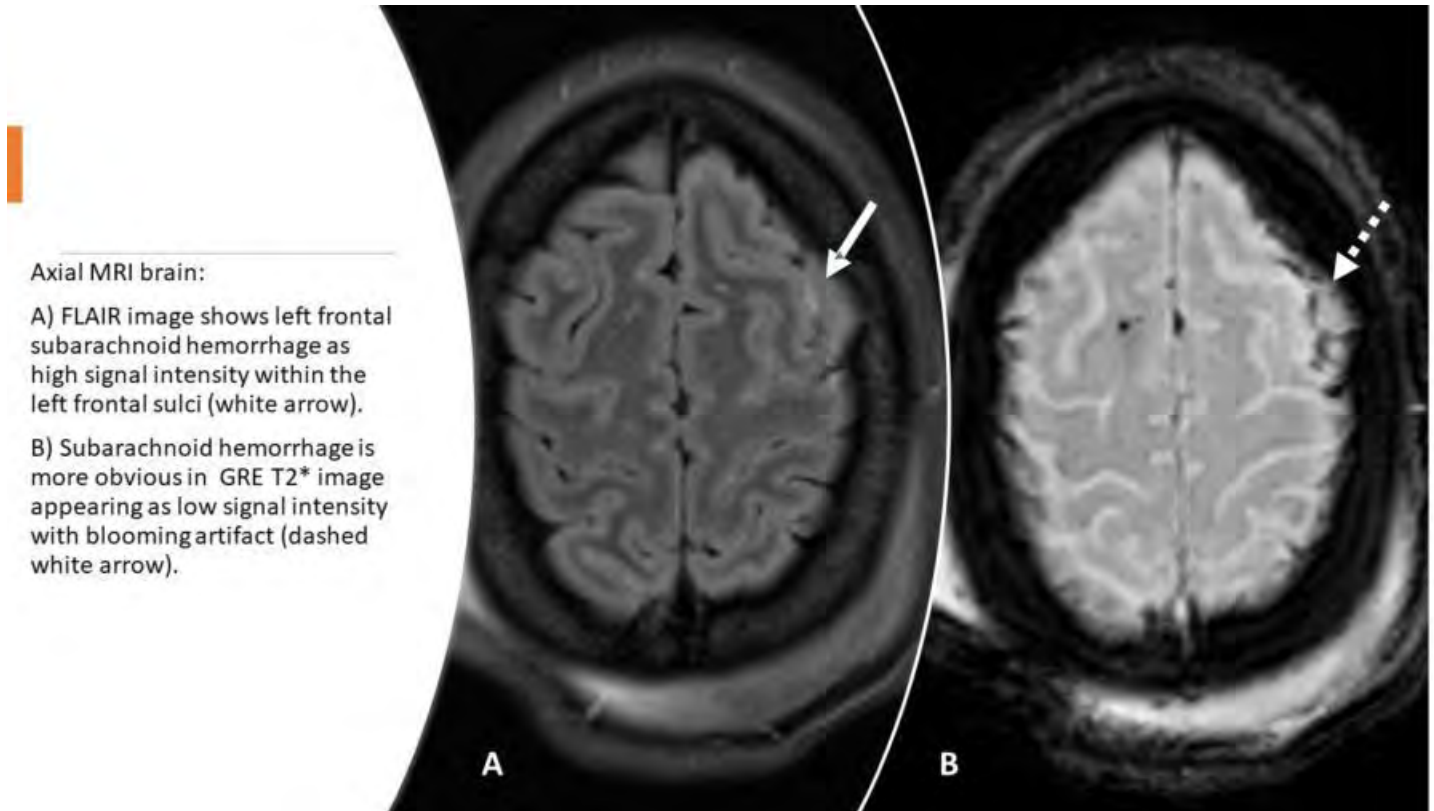
N/A

Results

N/A

Conclusions

N/A



(Filename: TCT_568_FigureAbstarct.jpg)

317

Arterial Spin Labeling Perfusion for Neuroradiologists: The Essentials

T Marini¹, D Mistry¹, S Jetty¹, H Wang¹, E Lin¹, J Almast¹, S ELLIKA²

¹University of Rochester, Rochester, NY, ²University of Rochester, Rochester NY

Purpose

Arterial spin labeling (ASL) is a non-invasive, contrast-free, magnetic resonance imaging (MRI) imaging technique that allows estimation of cerebral blood flow. In this review we provide a practical overview of the clinical applications of ASL in neuroradiology including potential pitfalls. The physics of ASL is complicated and involves magnetically labeling the body's endogenous water. This magnetically labeled water can be measured to determine cerebral perfusion. Three main categories of ASL pulse sequences are available: continuous ASL (CASL), pseudocontinuous ASL (pCASL) and pulsed ASL (PASL), each with its own strengths and limitations to be described in the presentation. There are many clinical applications of ASL in neuroradiology (adult & pediatric) including cerebrovascular disease, migraine, stroke, hypoxic ischemic injury, epilepsy, brain tumors, dementia, vascular malformations & head & neck vascular tumors. In cases of brain tumors, ASL may help in predicting tumor grade, preoperative planning of stereotactic biopsy site and differentiation of recurrent tumor from radiation necrosis. In neonates with HIE, combination of Lac/NAA and ASL has been shown to be the best predictor of outcome. In brain arteriovenous malformations and dural arteriovenous fistulas, ASL is accurate in determining arteriovenous shunting, measuring shunt reduction after embolization and

confirming obliteration of the AVM after stereotactic radiosurgery. ASL can be combined with acetazolamide challenge to assess cerebrovascular reserve in patients with moya moya vasculopathy, thus guiding therapeutic or preventative intervention. The classic pattern of dementia syndromes on ASL perfusion mimics those on PET examinations. Finally, in epilepsy imaging, ASL perfusion imaging can allow elucidation of the epileptic focus.

Materials and Methods

ASL cerebral perfusion is a useful imaging technique to investigate cerebral perfusion in a wide variety of pathologies. The neuroradiologist should be familiar with the applications of ASL along with its pitfalls to best answer the ordering provider's clinical question and offer the best patient care.

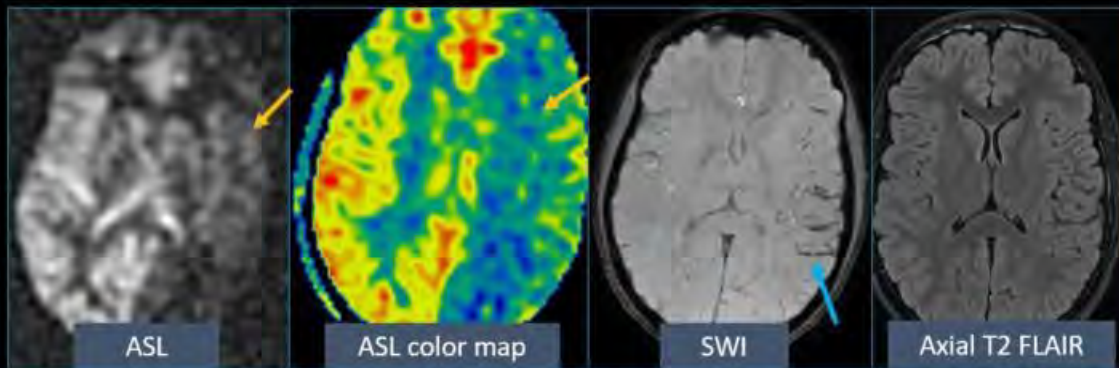
Results

N/a

Conclusions

N/A

ASL Perfusion Imaging: Hemiplegic Migraine



15 year old presenting with severe headache. ASL map demonstrates **markedly decreased perfusion in the left cerebral hemisphere**, with **increased deoxyhemoglobin /congestion in the left cortical veins on SWI**, and normal appearance of the brain on T2 FLAIR. Imaging findings are consistent with hemiplegic migraine.

(Filename: TCT_317_Hemiplegicmigraine2.JPG)

1084

Assessment of Cerebrovascular Reserve in the Setting of Moyamoya Disease Using Arterial Spin Labeling and Acetazolamide Challenge

E McConnell¹, T Marini², S ELLIKA³, H Wang⁴

¹University of Rochester Medical Center, rochester, NY, ²University of Rochester, East Syracuse, NY, ³UNIVERSITY OF ROCHESTER MEDICAL CENTER, ROCHESTER, NY, ⁴UNIVERSITY OF ROCHESTER MEDICAL CENTER, Rochester, NY

Purpose

Arterial spin labeling (ASL) is a safe, non-invasive, contrast free magnetic resonance imaging (MRI) technique that can be used to assess cerebral blood flow (CBF). In this educational poster we will briefly review the advantages and disadvantages of arterial spin labeling (ASL) compared to previously established modalities of cerebral perfusion imaging, summarize the materials and methods required for ASL and provide clinical case examples in which application of ASL combined with acetazolamide challenge were used safely to improve patient outcomes in the setting of Moyamoya disease. ASL takes advantage of the directionality of arterial blood flow by labeling the patient's own endogenous water within the neck via a radio frequency pulse and imaging the brain after a post labeling delay (PLD). This allows for repeatable intra and intersession estimation of CBF to better assess post-interventional outcomes in cerebrovascular dysfunction. One example of the utility of ASL that will be presented is its use in evaluating the efficacy of encephaloduroarteriosynangiosis (EDAS) bypass surgery in patients with Moyamoya disease. Patients found to have vascular steal may require bypass surgery. We have implemented a technique on a clinical 3T MRI scanner using a commercially available ASL pulse

sequence combined with subtraction to generate an augmentation map and reverse subtraction to generate a steal map. The entire study can be completed in only 20 minutes in a routine clinical setting.

Materials and Methods

To elucidate and disseminate a safe, non-invasive, contrast free MRI technique that can be done in a routine clinical setting for selecting patients and for assessing the efficacy of current therapeutic interventions in patients with Moyamoya disease.

Results

N/A

Conclusions

ASL combined with acetazolamide challenge is a useful MRI technique for selecting patients and for assessing the efficacy of current therapeutic interventions (e.g. EDAS) as well as future potential interventions in patients with Moyamoya disease. As such neuroradiologists should be aware of the abilities and limitations of the ASL-acetazolamide technique to better provide patient care. The technique we present can be easily implemented on a 3T MRI scanner in a routine clinical setting.

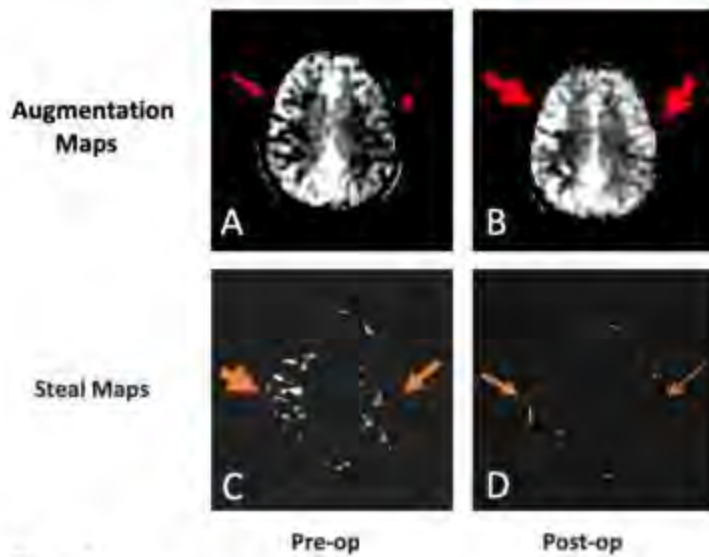


Figure 1. Cerebrovascular reserve assessment pre and post left sided EDAS bypass in 47-year-old female patient with recurrent left hemispheric strokes found to have bilateral Moyamoya disease. Images A and B represent augmentation maps which were obtained by subtracting baseline CBF from CBF collected 10 minutes after administration of IV acetazolamide in a patient with bilateral Moyamoya disease pre (A) and post (B) EDAS bypass surgery. B shows improved augmentation of left greater than right sided CBF compared to A as indicated by the red arrows. Images C and D represent steal maps obtained by subtracting CBF collected 10 minutes after administration of IV acetazolamide from baseline CBF from the same patient in A and B, pre (C) and post (D) EDAS bypass surgery as indicated by the orange arrows. D shows diminished bilateral vascular steal phenomenon. The patient was symptom free after EDAS.

Atlantoaxial Rotatory Subluxation: What a Radiologist Needs to Know

M Krycia¹, F Memon²

¹Henry Ford Hospital, Detroit, MI, ²Yale University, New Haven, CT

Purpose

Key concepts of anatomy, types, and etiologies of atlantoaxial rotatory subluxation are discussed. Objectives: 1. To discuss anatomy as it pertains to atlantoaxial rotatory subluxation. 2. Discuss normal and abnormal radiologic appearance of relevant joints, intervals and ligaments. 3. Discuss subtypes of atlantoaxial rotatory subluxation and key intervals, measurements and angles a radiologist needs to report. 4. Discuss etiologies of atlantoaxial rotatory subluxation and demonstrate a variety of interesting, unique and rare cases.

Materials and Methods

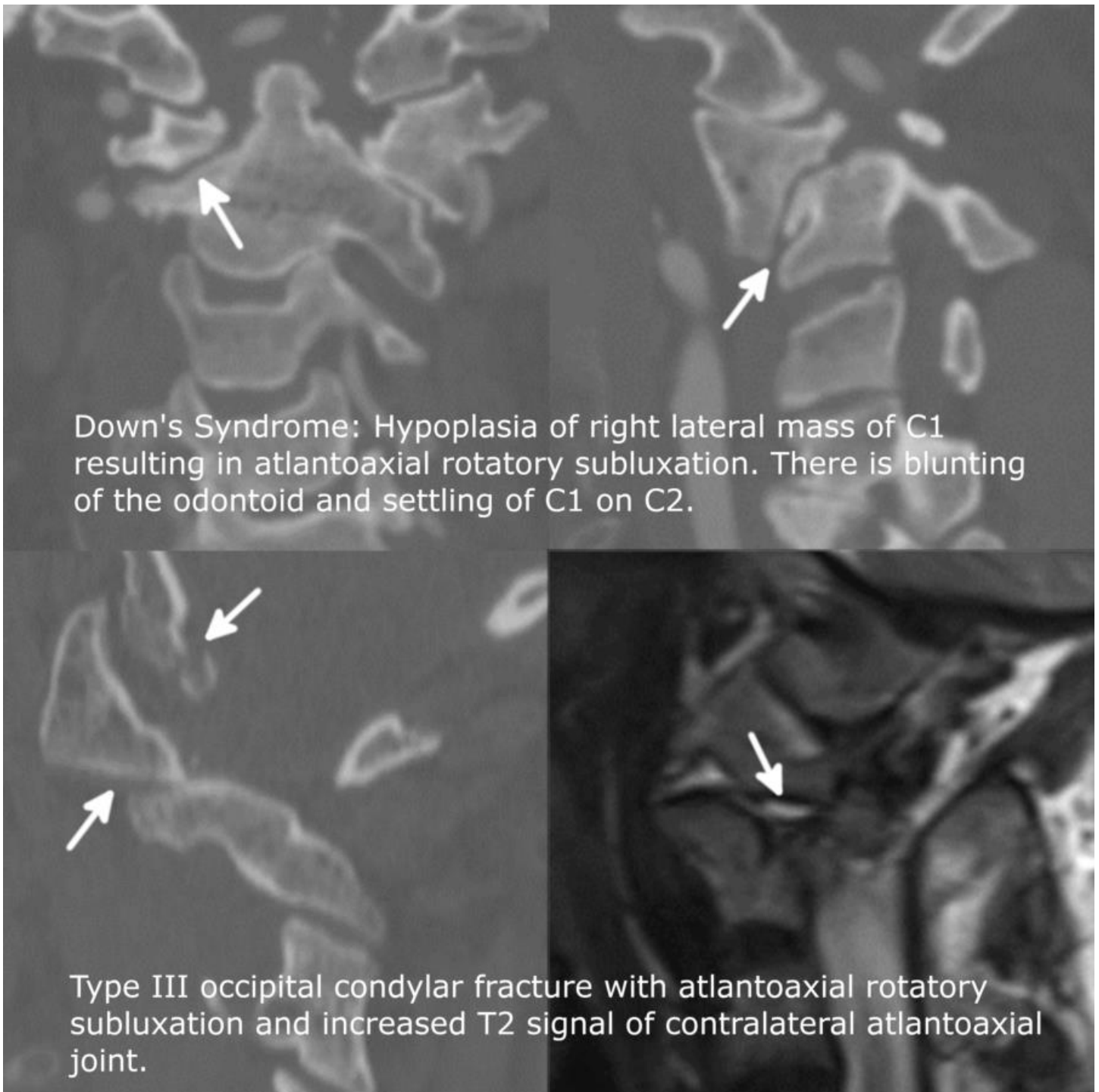
To provide knowledge essential to an interpreting radiologist as it pertains to relevant anatomy, subtypes, and etiologies of atlantoaxial rotatory subluxation.

Results

The Yale University Hospital archives were searched and all cases of atlantoaxial rotatory subluxation from the last 20 years were retrieved. The reports were searched and all positive cases were reviewed. A variety of cases to include common, interesting, unique and rare etiologies were selected. Key observations were made and will be reported. Existing text and literature was studied and built upon.

Conclusions

Currently, there is significant variation in the way findings are reported by radiologists in regard to cases of atlantoaxial rotatory subluxation. This aims to highlight key findings and measurements that should be reported in suspected cases of atlantoaxial rotatory subluxation in order to standardize reporting. Utilizing a systematic approach to cases or suspected cases of atlantoaxial rotatory subluxation makes reporting easy and efficient.



Down's Syndrome: Hypoplasia of right lateral mass of C1 resulting in atlantoaxial rotatory subluxation. There is blunting of the odontoid and settling of C1 on C2.

Type III occipital condylar fracture with atlantoaxial rotatory subluxation and increased T2 signal of contralateral atlantoaxial joint.

(Filename: TCT_333_AARS.gif)

1323

Autoimmune Encephalitis and Cerebellitis

T Lu¹, J Martin¹, A Rajamohan², J Acharya³, M Shiroishi⁴, A Lerner¹

¹USC Keck School of Medicine, Los Angeles, CA, ²University of Southern California, Los Angeles, CA, ³Keck School of Medicine of USC, Los Angeles, CA, ⁴KECK SCHOOL OF MEDICINE, USC, Los Angeles, CA

Purpose

Frequently overlooked and misdiagnosed as one of the more well-known causes of encephalitis, autoimmune encephalitis represent a group of inflammatory neurological disorders that have recently been getting more attention in the scientific community. The patients can present with nonspecific symptoms such as seizures, behavioral changes, movement disorders, and cognitive decline.

Autoimmune encephalitis was initially described as limbic encephalitis in the 1960s and had a strong association with neoplastic processes. As the research on autoimmune encephalitis has progressed, this disease entity is currently categorized based on auto-antibodies against either intracellular or auto-antibodies cellular surface antigens. Recently published studies have shown that prevalence of autoimmune encephalitis approaches the prevalence of infectious encephalitis. Paraneoplastic cerebellar degeneration is a similar autoimmune disorder involving the cerebellum which is much less common. ADEM and acute cerebellitis are related disorders which usually present as complications of viral infection. Additionally, although both these diagnoses are more frequently reported in pediatric populations, they have a surprising prevalence in the adult population. Given the overlapping clinical presentation and imaging features of this diverse group of autoimmune disorders of the brain it is important for radiologists to be familiar with these disease entities and consider them in imaging differential diagnosis.

Materials and Methods

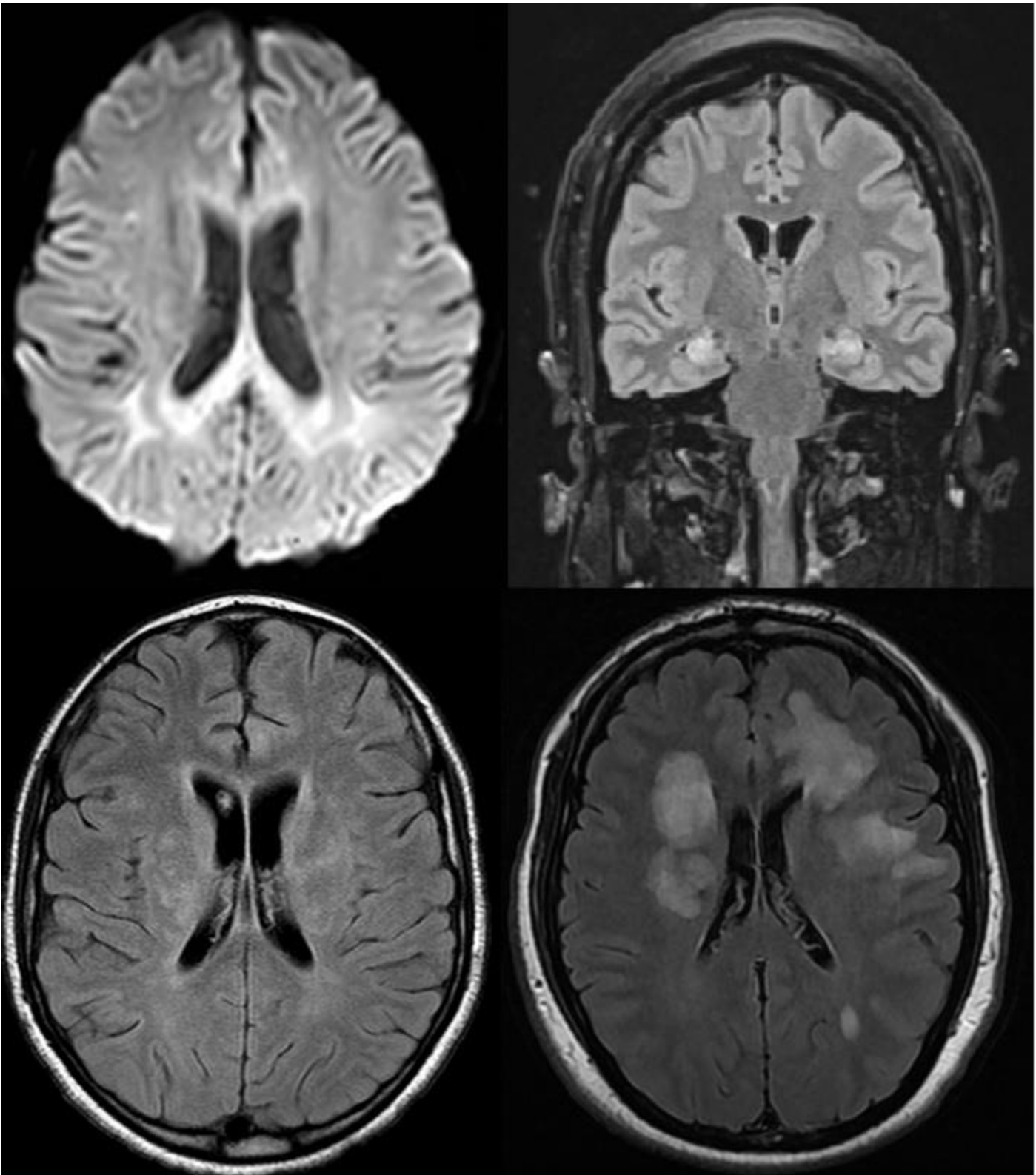
This exhibit seeks to educate the radiologist regarding the most recent advances in understanding this disorder including: • The pathophysiology of autoimmune encephalitis and cerebellitis • Imaging features of these disorders. • Differentiation from other disorders such as neoplasms, infectious disease, and toxic metabolic disorders.

Results

N/A

Conclusions

Autoimmune encephalitis and acute cerebellitis are more common than previously thought. While these disorders are ultimately diagnosed via laboratory results, the nonspecific presentation of the symptoms often delays the correct diagnosis by the clinician. By properly recognizing the imaging findings and including of the diagnosis in the differential, the radiologist can contribute to not only earlier diagnosis but also allow earlier treatment which will result in improved patient outcome.



(Filename: TCT_1323_Autoimmuneencephalitisandcerebellitis.jpg)

1192

Balo's Concentric Sclerosis (BCS): Classic Appearance and Differential Considerations

H Ahn¹, J Seaman¹, M Grant¹, B Boldt¹

¹Madigan Army Medical Center, Tacoma, WA

Purpose

1. Identify which patient population has the highest prevalence of Balo's concentric sclerosis (BCS); and be aware of possible clinical presentations and available treatment options. 2. Describe the classic imaging features of BCS. 3. List imaging differential considerations of BCS and describe some of their differentiating characteristics.

Materials and Methods

The purpose of this educational exhibit is to review both the common and less common presentations/appearances of Balo's concentric sclerosis. Following this, we will provide a pictorial review of various ring-enhancing lesions of the brain that should be differential considerations. A summary table will be provided.

Results

- Helical CT images of the brain/head were acquired without contrast. Multiplanar reformats were then created from source images. - MRI images of the brain were acquired on a 3.0 Tesla scanner before and after administration of intravenous Gadavist agent. - MRI images of the cervical and thoracic spines were acquired on a 3.0 Tesla scanner before and after administration of intravenous Gadavist agent.

Conclusions

1. Balo's concentric sclerosis subtype of multiple sclerosis usually presents with acute/subacute onset of symptoms and rapid clinical deterioration; however, there are also self-limiting monophasic and relapsing-remitting courses. 2. Treatment includes corticosteroids for active inflammation and immunomodulatory therapy for more aggressive disease processes. 3. There are many differential considerations for rim-enhancing lesions on brain MRI to include demyelinating, inflammatory, infectious, and neoplastic processes. 4. Our patient's follow-up MRI demonstrated worsening white matter lesions despite completion of a high dose steroid regimen; yet patient's neurologic symptoms (weakness and discoordination of the left hemi-body) slightly improved and remained stable during this period. Is there a correlation between imaging findings and clinical presentation?

	Distinguishing features	NECT	T1WI	T2WI / FLAIR	T1WI + C	DWI / ADC
Relapsing MS	No concentric rings	<u>Hypodense</u>	<u>Hypo-/isointense</u> lesions (black holes); may see <u>hyperintense</u> lesions with advanced disease	<u>Hyperintense</u> white matter lesions (juxtacortical, periventricular, pericallosal)	May see incomplete peripheral enhancement (open ring sign) of active lesions	May see restricted diffusion of active lesions
ADEM	Viral prodrome; more common in children; gray matter often involved; lesions tend to be larger, more edematous, and often symmetric	<u>Hypodense</u>	<u>Hypointense</u>	<u>Hyperintense</u> lesions are usually subcortical and may involve thalami and brainstem	May see punctate or incomplete peripheral enhancement (open ring sign) at the leading point of inflammation	May see restricted diffusion peripherally
Leukoencephalopathy (i.e. levetamisole-induced)	Positive medication reconciliation	Normal or may see <u>hypodense</u> white matter lesions	<u>Hypointense</u>	Multifocal <u>hyperintense</u> lesions without edema or mass effect	May see incomplete peripheral enhancement	May see patchy restricted diffusion
Subacute subcortical infarction	Vascular territory involvement	<u>Hypodense</u> ; may see <u>hyperdensity</u> if there is hemorrhagic component	<u>Hypointense</u> ; may see <u>hyperintense</u> signal with hemorrhagic component	<u>Hyperintense</u>	May see curvilinear enhancement of meninges/gyri	Restricted diffusion
Cerebral abscess	Infectious symptoms; no concentric rings	<u>Hypodense</u> lesion with <u>hypodense</u> white matter edema	<u>Hypointense</u>	Pus is <u>hyperintense</u>	Thin peripheral enhancement of abscess cavity	Restricted diffusion of pus within abscess cavity
CNS tumors (i.e. high grade glioma)	Usually occur in older patients	May see irregular <u>hypodense</u> areas of necrosis and irregular thick <u>iso-/hyperdense</u> margins	<u>Hypo-/isointense</u> mass	<u>Hyperintense</u> lesion with mass effect; may see flow voids	Variable but usually peripheral and irregular with nodular components	May see restricted diffusion of solid enhancing components

(Filename: TCT_1192_BCSDDx.JPG)

278

Beyond Time of Flight MRA: Review of Flow Imaging Techniques

K Capel¹, G Roberts¹, A Kuner¹, J Manunga², W CHANG³, O Wieben¹, K Johnson¹, L Eisenmenger¹

¹University of Wisconsin, Madison, WI, ²Minneapolis Heart Institute, Chaska, MN, ³Allegheny Health Network, Pittsburgh, PA

Purpose

- Describe TOF and advanced flow imaging techniques and their applications
- Outline pros and cons of non-contrast and contrast enhanced (CE) MRA techniques
- Explain principles of phase contrast MRA including velocity encoding (VENC) gradients, velocity quantification, and VENC optimization
- Illustrate 4D flow applications for evaluating aneurysms, vascular malformations, and neurodegenerative diseases
- Review variations and optimization of ASL

Materials and Methods

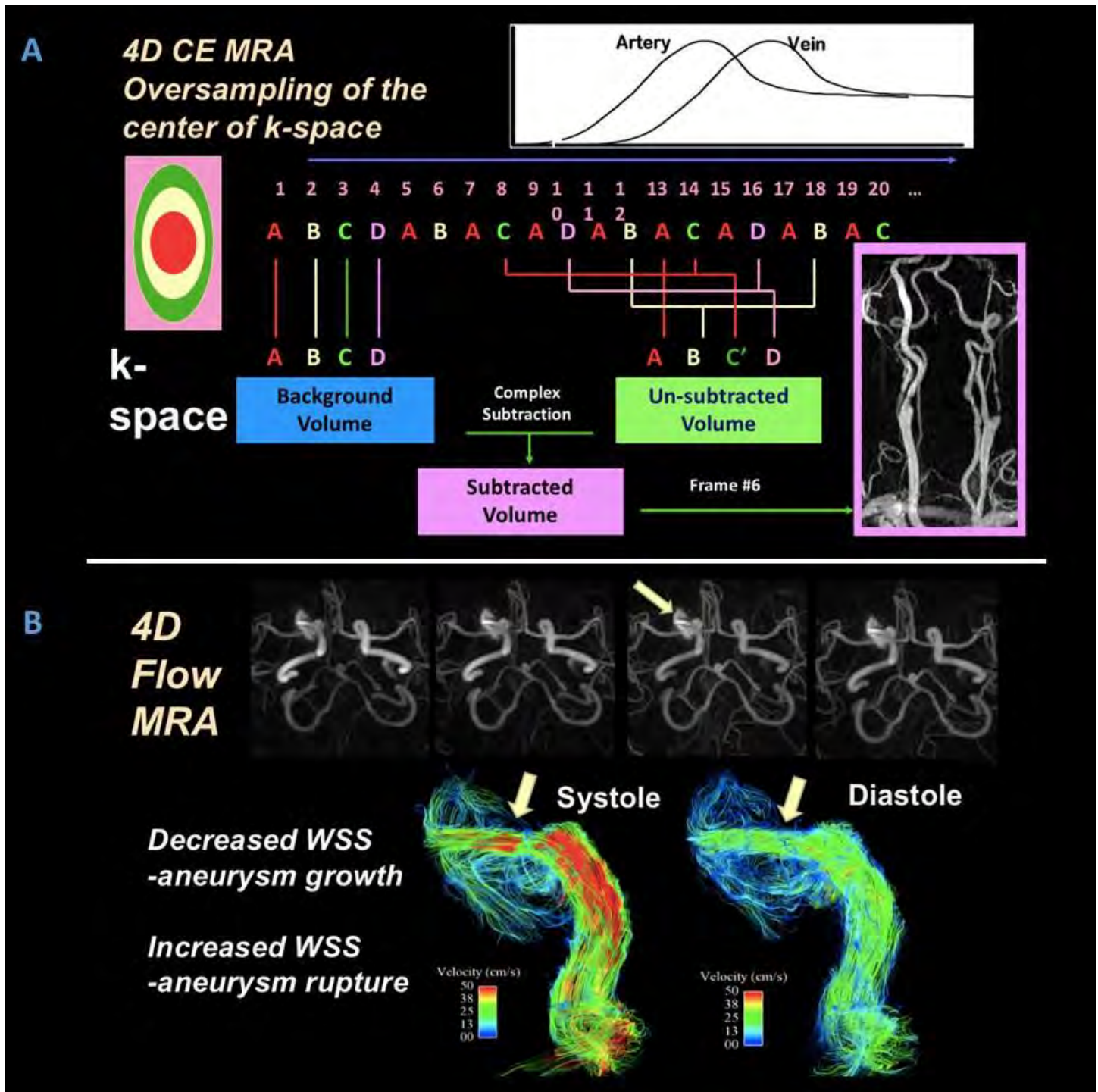
Magnetic resonance angiography (MRA) is essential for vasculature evaluation with applications in anatomic mapping, atherosclerotic disease, stroke, aneurysm, vascular malformations, and vascular dysfunction in neurodegenerative diseases. Time of Flight (TOF) MRA is a mainstay in the clinical setting, but there are many new and important techniques in flow imaging. The purpose of this exhibit is to highlight appropriate applications, advantages, and pitfalls for both traditional MRA techniques (TOF) as well as more advanced non-contrast and contrast-enhanced (CE) MRA techniques.

Results

After reviewing general principles of flow imaging acquisition, we will outline MRI parameter manipulation for advanced imaging techniques both with and without contrast agents. We will discuss TOF (both 2D and 3D), phase contrast (2D and 4D flow), time-resolved CE imaging (TRICKS, TWIST), and non-contrast arterial spin labeling (ASL) MRA as well as advanced reconstruction techniques such as 7D Highly Constrained Projection Reconstruction (HYPR)Flow.

Conclusions

TOF imaging is a workhorse for neuroradiology applications. Most 4D CE methods rely on rapid imaging during first passage of the contrast bolus with oversampling the center of k-space (Image A), providing multiple images of passage of contrast through the vascular system. Continuous and pseudo-continuous (PC) ASL are non-contrast dynamic MRA techniques which can provide time of arrival maps. Phase contrast 4D flow MRA can quantify blood flow velocities, pulsatility, wall shear stress (WSS), and pulse wave velocity (Image B). Methodological improvements in flow imaging have led to better image quality and more accurate flow quantification for clinical applications including stroke, atherosclerosis, vascular malformations, and neurodegenerative diseases. Understanding the underlying concepts, advantages, and challenges for each type of flow imaging is necessary for neuroradiologists to make appropriate diagnoses that will impact clinical care.



(Filename: TCT_278_FlowKC1110.jpg)

1403

Biryani Sign: A Novel Sign for the Diagnosis of Multinodular and Vacuolating Neuronal Tumor

M Siddiqi¹, K Faiz², F Salehi³, M Khan³

¹McMaster University, Mississauga, Ontario, ²McMaster university, Hamilton, Ontario, ³McMaster University, Hamilton, Ontario

Purpose

Multinodular and vacuolating neuronal tumor (MVNT) is a new entity included in the 2016 World Health Organization classification of CNS tumors (1). MVNTs demonstrate a unique cytoarchitectural and radiological pattern, and are considered to be benign "leave alone" lesions. In the largest published series, MVNTs appear as a cluster of variably sized nodular subcortical lesions following the gyral contour on MRI (2). As MVNTs have not been extensively reported in the radiological literature, knowledge of imaging features

which are unique to this lesion will help the radiologist to be confident when making this diagnosis. Educational Goals/Objectives To introduce the biryani sign - a novel sign for multinodular and vacuolating neuronal tumor.

Materials and Methods

We propose a novel sign seen in all cases of MVNTs to date at our institution as well as within the images of MVNT provided in the literature which demonstrate satellite lesions adjacent to the dominant cluster of nodules within the subcortical white matter. These satellite foci are noncontiguous with the primary cluster and demonstrate an intervening bridge of normal brain parenchyma. The dominant cluster of nodule has the appearance of a mound of rice with satellite lesions representative of fallen grains of rice scattered around the main heap of rice. The appearance is particularly reminiscent of the popular South Asian dish called Biryani, wherein scattered grains of white rice appear more conspicuous on a background of saffron stained rice.

Results

N/A

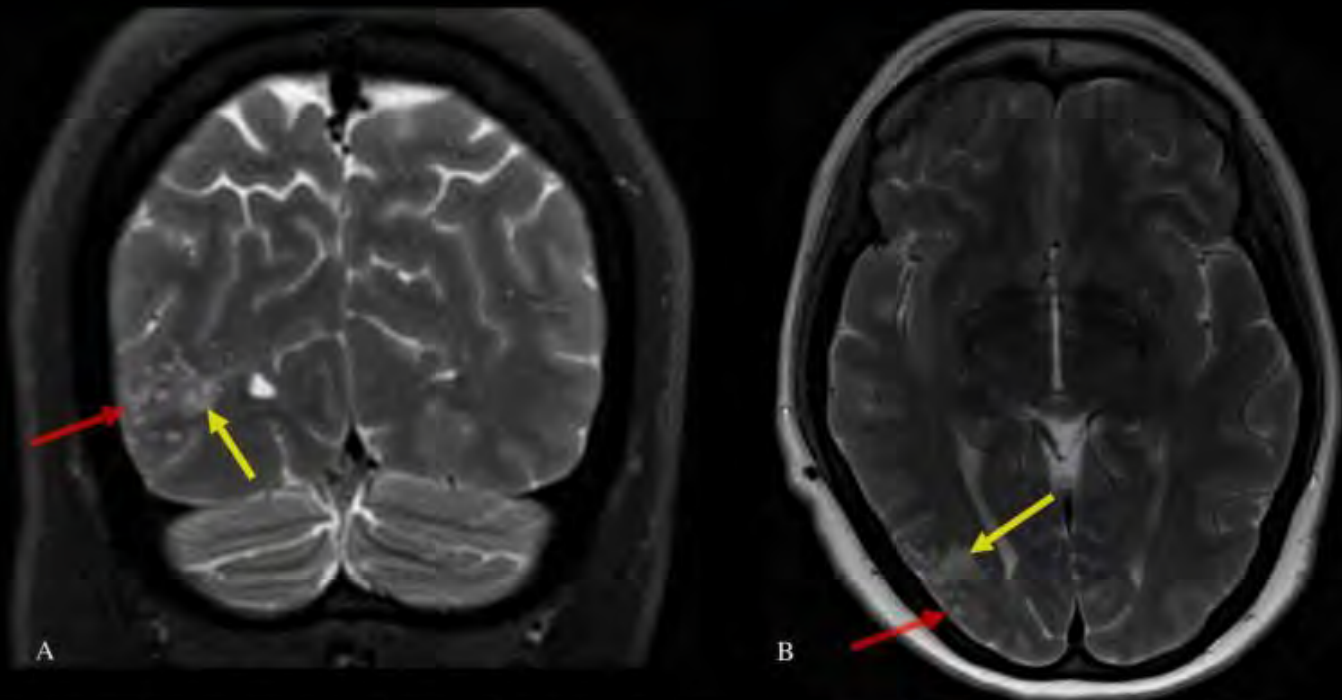
Conclusions

N/A

The “Biryani” sign of MVNT



Image demonstrates the main heap of biryani representative of the dominant lesion (yellow circle) with adjacent fallen away grains of rice similar to satellite lesions (red arrows) which are specific for multinodular vacuolated neuronal tumor (MVNT).



Coronal (Image A) and axial (Image B) T2 weighted images demonstrate a dominant T2 hyperintense subcortical lesion (yellow arrows) with adjacent smaller satellite nodules (red arrows) similar to grains of rice in a biryani.

(Filename: TCT_1403_ASNR2021BiryansignMVNT.jpg)

798

Bone MRI: Techniques and Applications

M Ho¹, S Bambach²

¹Nationwide Children's Hospital, Dublin, OH, ²Nationwide Children's Hospital, Columbus, OH

Purpose

1. Introduce spectrum of bone MRI techniques, sequence options, pitfalls and artifacts. 2. Present multiple clinical cases of bone MRI to demonstrate utility in pediatric neuroimaging, with conventional CT comparisons when available. 3. Discuss postprocessing advances including synthetic CT image generation, 3D visualization and printing, and virtual surgical planning.

Materials and Methods

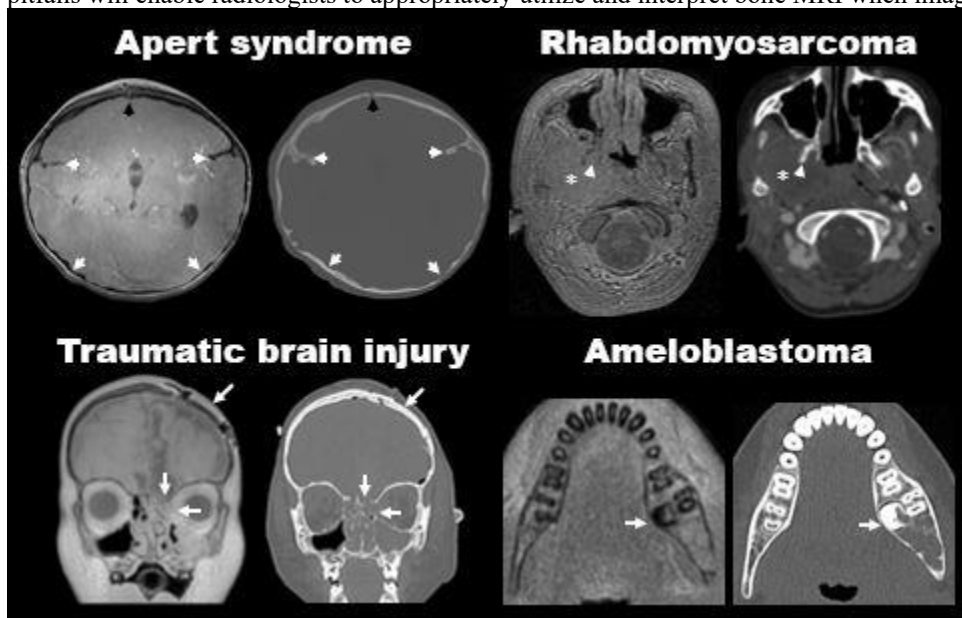
To educate neuroradiologists about bone MRI techniques, interpretive pearls and pitfalls, current applications, and future advances in pediatric neuroimaging.

Results

Bone MRI refers to a family of rapid, high-resolution, quiet, and artifact-resistant sequences that enable visualization of cortical bone without the use of ionizing radiation. We will begin by discussing the spectrum of techniques including gradient-echo, ultrashort-echo, and zero echo-time MRI. Sequence options to be presented and discussed include flip angle selection, off-resonance acquisition, prescan normalize, off-center field-of-view, gradient modulation, adaptive combine, multiecho acquisition, and fat suppression. Technical pitfalls and major artifacts including motion, susceptibility, and tissue interfaces will be demonstrated. Subsequently, we will present selected teaching cases from our repository of over 200 patients. Key teaching examples will include plagiocephaly, single-suture and multisuture craniosynostosis, sinonasal and skull base malformations, head & neck tumors, chronic sinusitis, accidental and nonaccidental trauma, cerebrospinal fluid derangements, postoperative evaluation and complications. We will discuss clinical validation through the use of diagnostic MRI-CT comparison, 3D visualization and virtual surgical planning, and conventional processing and deep learning techniques for synthetic CT image generation.

Conclusions

Bone MRI techniques show promise as an alternative to CT for rapid brain screening or "one-stop-shop" neuroimaging, particularly in the pediatric population for whom ionizing radiation exposure must be minimized. Understanding of technical concepts and potential pitfalls will enable radiologists to appropriately utilize and interpret bone MRI when imaging the pediatric head, neck, and spine.



(Filename: TCT_798_ZTEcases.JPG)

506

Brain Imaging Findings in COVID-19: Our Experience From a Tertiary Center in the Largest Populated City of South India

JJOSE¹, K KALENAHALLI¹, A Chakkappan¹, S E¹
¹SAGAR HOSPITALS, BENGALURU, KARNATAKA

Purpose

Coronavirus disease 2019 (COVID-19) is a serious ongoing public health crisis around the globe and can have neurological manifestations. We have evaluated various MRI and CT imaging findings of brain in patients of COVID-19 infection with neurological manifestations at our institution from June 20 to October 2020.

Materials and Methods

To evaluate various MR and CT imaging findings of brain in patients with COVID-19 infection having neurological manifestations at our institution from June to October 2020.

Results

1199 Covid RT-PCR positive patients were treated at Sagar Hospitals, Bengaluru from June 1st, 2020 to October 30, 2020. Of these

25 patients had neurological manifestations and underwent CT and MRI imaging of brain. We have done a retrospective observational case study of these 25 cases with neurological manifestations. Clinical and imaging data were reviewed.

Conclusions

RESULTS: MR imaging findings of brain included acute infarcts, parenchymal hemorrhage, microhemorrhage and other imaging features like T2/ FLAIR white matter signal abnormalities. The most frequent diagnoses made on brain CT and MR imaging in patients with COVID-19 were acute and subacute infarcts. One patient had findings of meningoencephalitis proved to be viral meningoencephalitis in CSF analysis. Our study observations are mostly in concurrence with the limited literature available on this topic. **CONCLUSION:** Neurological manifestations in Covid-19 infection is not uncommon. Imaging will usually reveal some findings in these patients, most common being ischemic changes.

1025

Brain Metabolite Clearance: Glymphatic System and IPAD Pathway Hypothesis

A Peret¹, A Kuner², J Yu¹, W CHANG³, G Roberts¹, M Jen⁴, K Johnson⁵, L Eisenmenger², C STROTHER⁶

¹University of Wisconsin - Madison, Madison, WI, ²University of Wisconsin - Madison, Middleton, WI, ³Allegheny Health Network, Pittsburgh, PA, ⁴University of Wisconsin, Madison, WI, ⁵University of Madison - Wisconsin, Madison, WI, ⁶UW Madison, MADISON, WI

Purpose

Learning objectives: - Review the theories of brain metabolite clearance. - Present the supporting research for the glymphatic system and IPAD pathway. - Discuss the relationship of altered metabolite clearance to neurodegenerative conditions and imaging techniques that can be used to study this in vivo.

Materials and Methods

The central nervous system is unique in lacking a traditional lymphatic system. Thereby it must use alternative pathways for the clearance of metabolite waste products. Dysfunction in the metabolite clearance is closely related to neurodegenerative diseases, although the exact mechanisms are still unknown. The purpose of this exhibit is to present the theorized mechanisms of metabolite clearance, studies supporting these mechanisms, and imaging methods that might be used to study these systems in vivo.

Results

We will present the theories and studies supporting the existence of two main drainage routes: the glymphatic system and the intramural periarterial (IPAD) pathway. They both follow the vascular channels and are sometimes regrouped under the term "paravascular clearance." We will also present innovative MRI sequences that can be used to directly study the potential vascular mechanisms that may be involved including 4D flow MRI, Blood Oxygenation Level Dependent (BOLD), Arterial Spin Labelling (ASL), Displacement Encoding with Stimulated Echoes (DENSE), and Diffusion Tensor Imaging (DTI).

Conclusions

The glymphatic system represents a brain-wide network involving the circulation of cerebrospinal fluid (CSF) in the perivascular space, depending on astroglial aquaporin-4 (AQP4) water transport (Fig. 1), whereas the IPAD pathway refers to a drainage route along the basement membrane in the cerebral blood vessels' walls. The driving force responsible for the paravascular clearance pathway remains unidentified. The cardiac cycle-related blood flow is considered by some a major driving force of paravascular clearance; however, recent data claim arterial pulsations are too weak to drive clearance of waste products. Another mechanism is vasomotion, a low-frequency oscillation in vasodilation of arterioles, relatively independent of the cardiac cycle and likely regulated by vascular smooth muscle cells. Advanced magnetic resonance imaging (MRI) techniques are of paramount interest in assessing metabolite clearance. As this area of research progresses, it will be essential for the neuroradiologist to understand the concept of brain metabolite clearance and the potential implications.

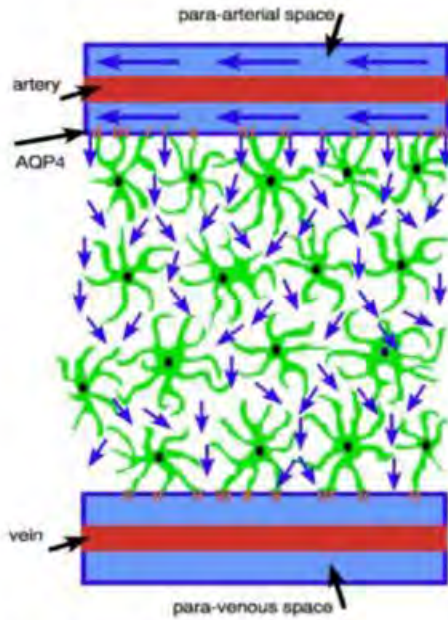


Fig. 1 – The glymphatic system is a waste clearance system of the cerebrospinal fluid (CSF) through the perivascular and interstitial spaces. Numerous interactions between the vascular system and the brain tissue have been described, implying hemodynamics of large vessels, direct interactions between the microvasculature and brain tissue, and drainage from CSF and veins. Decoupling of this system has been implicated in altered clearance of brain metabolites and neurodegenerative diseases pathology.

(Filename: TCT_1025_Abstract1-Figure1.jpg)

1109

Breaking the Rules: Atypical Imaging Appearances of Parathyroid Disease

S Kumar¹, M Czaplicki¹, K Mathew¹, K Sargar¹, A Moreno De Luca¹, T Ly¹, G Mongelluzzo¹, P Manickam²
¹Geisinger Medical Center Radiology, Danville, PA, ²Geisinger, Danville, PA

Purpose

Primary hyperparathyroidism is caused by inappropriate secretion of parathyroid hormone resulting in dysregulation of calcium metabolism. Although most commonly occurring in the setting of a hormone-secreting parathyroid adenoma (up to 88%), double adenomas, multigland hyperplasia, and parathyroid adenocarcinoma are less common causes. The goal of imaging is to localize abnormal parathyroid tissue, in hopes of rendering a cure through minimally invasive parathyroidectomy. Accurate localization can lead to a precise surgical excision, reducing the risk of postoperative hypoparathyroidism and potentially reducing operative time. Reoperation has added risks, mainly of recurrent laryngeal nerve injury. 4D CT offers more precise localization than alternative modalities such as ultrasound and nuclear medicine Tc-99m sestamibi SPECT3 and at many institutions, including the authors', has become the first-line modality in the evaluation of these patients. Although the typical findings of parathyroid adenoma on 4D CT are well-described, the classic pattern of a hypoattenuating nodule with arterial-phase enhancement and delayed-phase washout is only observed 20% of the time⁴. Atypical imaging findings include cystic change, calcification, and fat deposition. With modern techniques, patients are being increasingly diagnosed preoperatively with multigland disease. In a busy practice with a high volume of 4D CTs, it is not uncommon to encounter lesions that do not "follow the rules" typically expected in a parathyroid adenoma. Failing to recognize alternative imaging appearances of parathyroid lesions may lead to delayed treatment or reoperation. Objectives: To understand classic 4D CT imaging characteristics of parathyroid disease. To illustrate atypical imaging appearances of pathology-proven parathyroid adenomas that may lead to difficulty in interpretation.

Materials and Methods

NA

Results

Classic imaging characteristics of parathyroid adenomas will be reviewed. Subsequently, multiple pathology-proven cases of parathyroid lesions which deviate from the classic imaging appearance will be presented.

Conclusions

Understanding the expected imaging characteristics of the parathyroid adenoma, as well as atypical appearances, can empower a radiologist to more effectively and confidently identify these culprit lesions, reducing patient morbidity and improving quality of life.



(Filename: TCT_1109_All_pt.JPG)

1058

Can You See It Now? - Checklists and Reformats in Emergency Head CT

M Oad¹, W Lee¹, S Patel², D Hodges³, S Lev¹

¹Nassau University Medical Center, East Meadow, NY, ²Nassau University medical center, East Meadow, NY, ³American University of the Caribbean School of Medicine, East Meadow, NY

Purpose

n/a

Materials and Methods

1. To develop a systematic checklist and schematic diagram approach for emergency head CT evaluation. 2. To demonstrate examples of perceptual pitfalls and show how reformatted images can help mitigate errors.

Results

Our simplified approach begins with clinical history and scout. An overview focuses on symmetry and assessment of basilar cisterns for effacement. We use a "bottom-up" and "in-out" survey and organize content according to alternating positive (parenchyma and bone) and negative CSF spaces. We emphasize key axial levels, highlighting essential anatomy and pathology, noting morphology, pattern and density attributes. Specific indications, such as stroke and trauma, are addressed. Intracranial vascular systems, both arterial and venous, are evaluated. The skull base (anterior, middle and posterior cranial fossa), maxillofacial structures (orbits and paranasal sinuses) and craniovertebral junction (CVJ) are then reviewed.

Conclusions

The scout can reveal abnormal air, fractures, and extrinsic devices. Do not neglect the CVJ. Ventricular asymmetry can identify subtle parenchymal or extra-axial lesions, such as isodense SDH. Evaluation of grey-white matter interface is helpful to assess for vasogenic or cytotoxic edema. Consideration of relative ventricular and sulcal proportions can suggest hydrocephalus. Six key anatomic levels are pons, midbrain, quadrigeminal cistern, basal ganglia, lateral ventricles and centrum semiovale. Skull base review includes neural and vascular channels, petrous apex and sella. Calvarial fractures must be distinguished from sutures and vascular variants. Assess vessels for aneurysms and thromboses. Look at the orbits and paranasal sinuses in tandem and note associated intracranial pathology. Coronal and sagittal reformats, over axial images alone, should be routine. They are integral not only for maxillofacial structures, but in assessing indeterminate neuroimaging findings, artifacts, and radiological blind spots. Reformats can better elucidate tentorial, interhemispheric fissure and convexity subdural hemorrhage, subarachnoid hemorrhage and inferior frontal and temporal contusions.

They can further assist with identifying herniations in the trauma setting. Using a head CT checklist can help the on-call radiologist avoid blind spots and other pitfalls, and provide a structured approach to image assessment. Our schematic approach can be incorporated into the clinical environment as educational reference charts at each workstation.

Can You See it Now? The Value of Checklists and Reformats in Emergency Head CT

Clinical History	Why?	Alerts	
Scout	<ul style="list-style-type: none"> Fracture Air Extrinsic devices Crani 		
Overview	<ul style="list-style-type: none"> Symmetry 4th ventricle 3rd ventricle Lateral ventricles Unrimmed sulcal indentations Gray white matter interface Basilar cisterns 	Alerts S stroke T trauma NT-H Non-traumatic hemorrhage	Positive Spaces G tubex P Pons C Cerebellum O Occipital Occ Occipital
Levels	Alerts S stroke T trauma NT-H Non-traumatic hemorrhage	Positive Spaces G tubex P Pons C Cerebellum O Occipital Occ Occipital	Negative Spaces C cisterns V ventricles P Pons C Cerebellum O Occipital Occ Occipital Occ Occipital Occ Occipital Occ Occipital
Quadrigeminal Plate	<ul style="list-style-type: none"> ✓ Placement of QP cistern indicates impending herniation 	Positive Spaces G tubex P Pons C Cerebellum O Occipital Occ Occipital	Negative Spaces C cisterns V ventricles P Pons C Cerebellum O Occipital Occ Occipital Occ Occipital Occ Occipital
Rosal Ganglia	<ul style="list-style-type: none"> ✓ Insular ribbon sign ✓ Vanishing basal ganglia sign ✓ Dense MCA sign ✓ Thalami (venous infarct) ✓ Hypertensive ✓ Subarachnoid (intraventricular) 	Positive Spaces G tubex P Pons C Cerebellum O Occipital Occ Occipital	Negative Spaces C cisterns V ventricles P Pons C Cerebellum O Occipital Occ Occipital Occ Occipital Occ Occipital
Lateral Ventricles	<ul style="list-style-type: none"> ✓ Ventricular compression ✓ Window for extraaxial bleeds ✓ Evaluate GW interface 	Positive Spaces G tubex P Pons C Cerebellum O Occipital Occ Occipital	Negative Spaces C cisterns V ventricles P Pons C Cerebellum O Occipital Occ Occipital Occ Occipital Occ Occipital
Centrum Semiovale	<ul style="list-style-type: none"> ✓ Window for extraaxial bleeds ✓ Evaluate GW interface 	Positive Spaces G tubex P Pons C Cerebellum O Occipital Occ Occipital	Negative Spaces C cisterns V ventricles P Pons C Cerebellum O Occipital Occ Occipital Occ Occipital Occ Occipital

(Filename: TCT_1058_Capture11.JPG)

1094

Carotid Space Anatomy and Pathology

A Rehman¹, D Drumsta¹

¹University at Buffalo, Buffalo, NY

Purpose

The carotid space anatomy is complex and unique. Although it is a confined space, it has extensive pathology of which four different disease processes will be discussed. An understanding of this space can help radiologists narrow down a differential and make an accurate diagnosis. This presentation will go over the anatomy, borders and contents of the carotid space.

Materials and Methods

The purpose of this abstract is to review the anatomy of the carotid space and build a differential diagnosis based on the contents. It will review some pathologies of the space including a common carotid artery and internal jugular vein fistula, glomus vagale tumor, Lemierre's syndrome and a parathyroid adenoma. The imaging features and lesion characteristics of each will be described across multiple imaging modalities.

Results

Comprehensive analysis of numerous patient's CT head and neck imaging and Cerner health system EMR for carotid pathology was performed and collected through a single tertiary care center, Erie County Medical Center. Radiopedia and StatDx for imaging sources of the carotid space anatomy were also used.

Conclusions

Arteriovenous fistulas between the common carotid artery and internal jugular vein are usually a rare complication of trauma or medical intervention such as catheterization. When suspected duplex scanning and angiography is recommended. Glomus vagale tumors are paragangliomas that occur along CNX presenting as a mass behind the carotid artery. Important landmarks it displaces include the internal and external carotid arteries anteriorly and the internal jugular vein posteriorly. May be seen on ultrasound as a heterogeneous hypoechoic lesion; however, MRI is preferred. Lemierre's syndrome is thrombophlebitis of the internal jugular vein typically in the setting of an oropharyngeal infection with metastatic sepsis. Usually IJ vein thrombophlebitis is the first clue. Contrast enhanced CT imaging is the gold standard which demonstrates intraluminal filling defects and sites of septic emboli. Parathyroid adenomas are benign tumors and the most common cause of primary hyperparathyroidism. Ultrasound is most commonly used and these tend to be oval and homogeneously hypoechoic with internal vascularity. It is also crucial to note that the visceral and perivertebral spaces border the carotid space all which lie within the superficial layer of the deep cervical fascia. Understanding the contents and the borders will allow one to make a better diagnosis.



Figure 1. CCA-IJ Fistula



Figure 2. Glomus Vagale Tumor

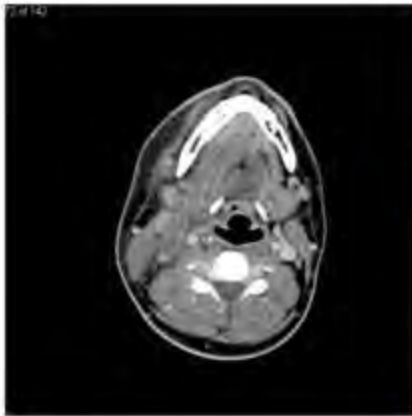


Figure 3. Lemierre's Syndrome

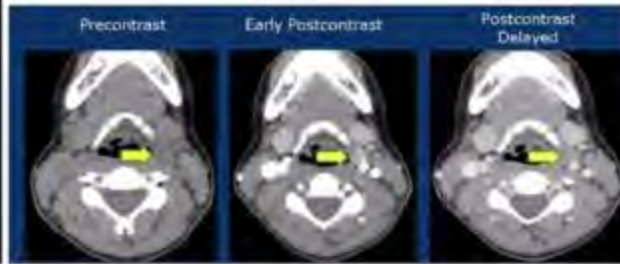


Figure 4. Parathyroid Adenoma

Cerebral Vascular Malformations: A Multimodality Imaging Approach and Review

M Ayoub¹, C Dixon²

¹Rush Univeristy Medical Center, Chicago, IL, ²Rush University Medical Center, Chicago, IL

Purpose

N/A

Materials and Methods

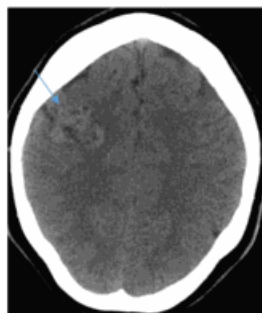
- Briefly review intracranial vasculature including superficial and deep venous drainage patterns. - Familiarize the reader with the various types of cerebral vascular malformations and their classification schemes. - Discuss preoperative and postoperative imaging findings of utilizing CT, MRI, and conventional angiography, - Highlight pertinent imaging findings of each entity that clinicians/surgeons want to know prior to scheduled operative management.

Results

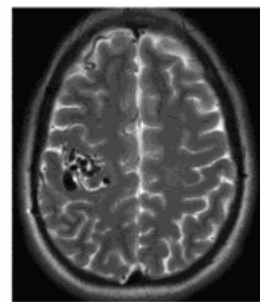
We will review the imaging characteristics of vascular malformations by grouping them into high flow, low flow, and mixed malformations. High flow malformations will include arteriovenous malformations (AVM), arteriovenous fistulas (AVF), and vein of Galen aneurysm malformations. Low flow malformations will include developmental venous anomalies, capillary telangiectasia, and sinus pericranii. Finally, mixed vascular malformations will include cavernous malformations.

Conclusions

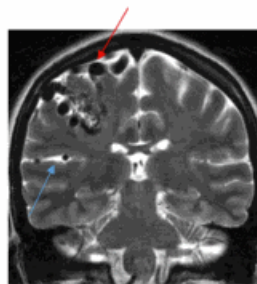
Although vascular malformations can be seen as an incidental finding on brain imaging, symptomatic patients typically present with seizures, headaches, or focal neurological deficits. Spontaneous intracranial hemorrhage in a child or a young adult is highly suspicious for a vascular malformation, particularly an AVM or a cavernous malformation. Initial workup is typically with noncontrast CT head to assess for intracranial hemorrhage or MRI brain to assess for a structural abnormality when symptoms are nonspecific. Dedicated vascular imaging is invariably performed, particularly in the setting of high or mixed flow vascular malformations. This is necessary to evaluate the location, morphology, internal architecture, supply/drainage, presence of aneurysms or stenosis, etc. Conventional angiography is performed when there is a high clinical suspicion for a vascular malformation but one is not visualized on CT or MRI angiography or for endovascular intervention/preoperative planning. In conclusion, cross sectional vascular imaging is an indispensable tool for identifying vascular malformations and providing the necessary information for treatment planning and follow up. A good knowledge of arterial and venous anatomy is important for accurate description of vascular malformations.



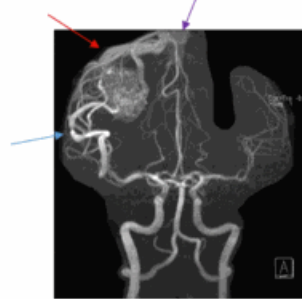
Noncontrast CT showing subtle tangle of hyperdense vessels in the right frontal lobe



MRI (T2) showing arteriovenous malformation centered in the right precentral gyrus



MRI (T2 coronal) showing arteriovenous malformation with prominent right middle cerebral artery (blue arrow) and large draining vein (red arrow)



MRA showing arterial supply from the right middle cerebral artery (blue arrow) and a large draining vein (red arrow) emptying into the superior sagittal sinus (purple arrow)

(Filename: TCT_475_Slide1.GIF)

Chemical Exchange Saturation Transfer (CEST) Imaging: An Introduction and Clinical Application Overview

D Hampton¹, H Kim¹, P Sun¹, R Hu¹

¹Emory University, Atlanta, GA

Purpose

Although exogenous administration of gadolinium-based contrast material has played the dominant clinical role since the introduction of MRI to patient care in the 1970s, there is an urgent need for novel contrast agents in light of recent concerns of gadolinium deposition and potential benefits of non-invasive assessment of tissue biochemistry. Chemical exchange saturation transfer (CEST) is an active and growing area of investigation that shows promise as an alternative method of gathering clinically relevant information about both the physiologic environment of imaged tissue and the concentration of various molecules that are not traditionally considered contrast agents. The objectives of this exhibit are to summarize the basic principles of CEST imaging, survey methods that are closest to clinical translation, and discuss challenges facing further implementation of this advanced imaging technique.

Materials and Methods

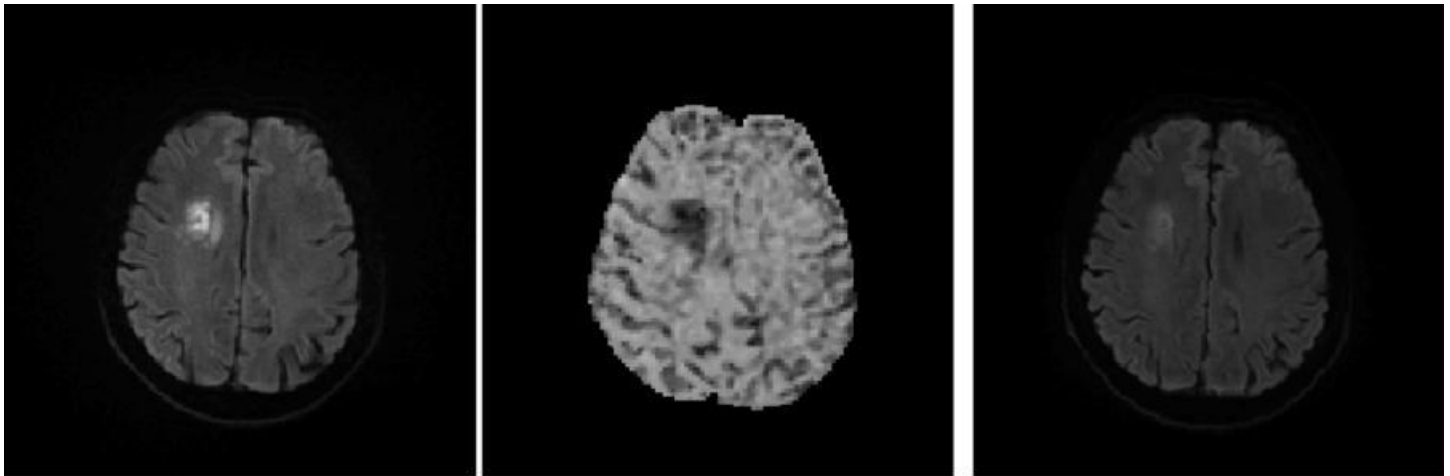
N/A

Results

We describe the basic MR physics and chemical principles involved with generating CEST contrast. Furthermore, we review the current state of research and potential clinical applications of glucose CEST, amide proton transfer for pH imaging, and glutamine CEST. Limitations inherent to CEST imaging including SAR, B0 inhomogeneities, and the challenges of reproducibility across different scanners are described. Current work in CEST sequence development at our institution is also presented, including preliminary imaging data from one stroke patient at admission and at one-week follow-up. We used a pulsed CEST MRI protocol, with a train of inversion pulses of 15 ms interleaved by an inter-pulsed delay of 15 ms (TS/TR=3000ms/3320 ms, time=5 min 40 s). The Z-spectrum was obtained from -5 to 5 ppm with intervals of 0.1 ppm. We have an in-plane matrix of 96 by 96, 3 slices (5 mm/slice, FOV=220x220 mm). We corrected field inhomogeneity following the water saturation reference (WASRR) approach and performed pH-specific R1w and magnetization transfer (MT)-normalized APT analysis. The representative images show acute DWI, pH-specific image and follow-up DWI. There was little mismatch between diffusion and pH during the first scan, and little expansion of DWI lesion was observed.

Conclusions

CEST imaging is an exciting advanced MRI technique that enables in-vivo assessment of tissue biochemistry and has great potential for clinical translation. An understanding of the principles, applications, and limitations of the technique will serve the radiologist well.



DWI

pHw

1wk DWI

(Filename: TCT_656_stroke_DWI_PH.jpg)

583

Chew on This: Odontogenic and Non-Odontogenic Jaw Lesions

R Ismail¹, M Bashir², P Cohen³, R Hegde⁴, A Megahed⁵, A Saeed Bamashmos⁶, G Muro⁷

¹Yale New Haven Health, Bridgeport, CT, ²Loyola University Medical Center, Maywood, IL, ³Bridgeport Hospital, Bridgeport, CT, ⁴Bridgeport Hospital Yale New Haven Health system, Bridgeport, CT, ⁵Yale New Haven Health, Bridgeport Hospital, Bridgeport, CT, ⁶Yale New Haven Health Bridgeport Hospital, Bridgeport, CT, ⁷Yale New Haven Health-Bridgeport Hospital, Bridgeport, CT

Purpose

Odontogenic and Nonodontogenic Jaw lesions include common benign cystic lesions as periapical (radicular) cysts, follicular (dentigerous) cysts, and odontogenic keratocysts. Benign solid tumors represent a broad spectrum of lesions such as ameloblastomas, odontomas, ossifying fibromas, and periapical cemental dysplasia. Malignant tumors include squamous cell carcinomas, osteosarcomas, and metastatic tumors. The main objectives of this educational exhibit is to describe the epidemiologic, anatomic and imaging characteristics of the most common Odontogenic and Nonodontogenic Jaw lesions, to emphasize the aspects that aid in the differential diagnosis, and to present illustrative examples of these lesions with pathological correlation.

Materials and Methods

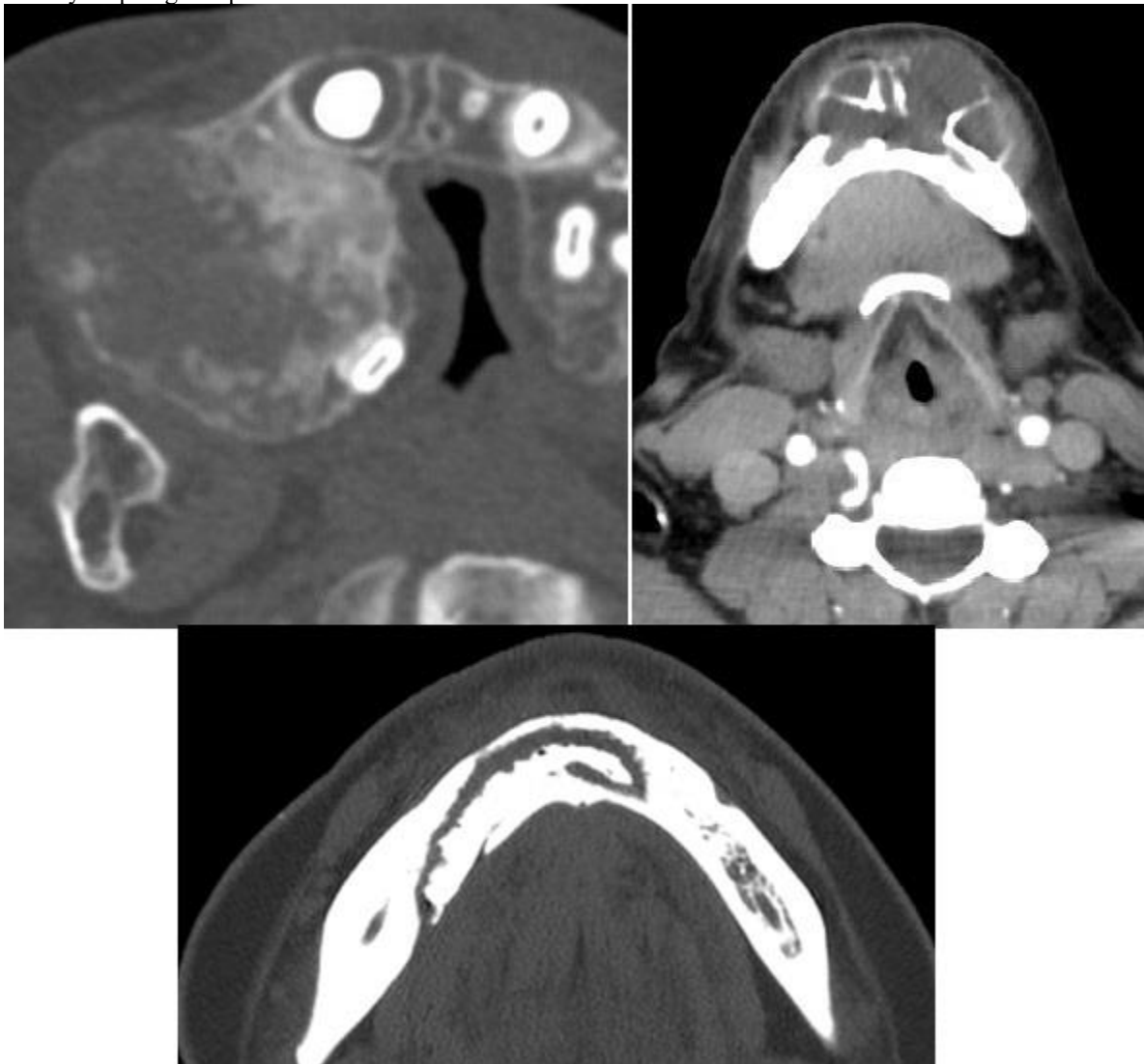
Discuss the differential diagnosis for various Odontogenic and Nonodontogenic Jaw lesions based on their demographic characteristics, location, and morphologic features. Describe the clinical and imaging features of various Odontogenic and Nonodontogenic Jaw lesions. Identify key imaging and pathological features of various Jaw lesions.

Results

Retrospective review of multiple odontogenic and Nonodontogenic Jaw tumors from Loyola University Medical Center and Bridgeport Hospital/Yale New Haven Health with pathological correlation. Cases included: - Odontogenic myxoma left maxilla - Ossifying fibroma right maxilla - Cementoblastoma of left mandible - Dentigerous cyst of left mandible - SCC of the right mandible - Chondroblastic osteosarcoma of the right maxilla - Osteonecrosis of the Jaw - Ameloblastoma of left mandible. - Odontogenic keratocyst of right maxilla - Fibrous Dysplasia of right maxilla

Conclusions

Majority of Jaw lesions have similar imaging appearances but wide range of pathologic features. Although imaging will not always provide a specific diagnosis, and biopsy is warranted for definite diagnosis. Consideration of patient age, location, cystic or solid appearance, border contour, and effect of the lesion on adjacent structures are all helpful in narrowing the differential diagnosis, and thereby help to guide patient treatment.



(Filename: TCT_583_jawlesions.jpg)

Child Abuse Litigation: How long before skull fractures heal in children < 3 years old?

N Kadom¹, Z Lasiecka¹, J Chern², M Pitot³, B Chern²

¹Emory University, Atlanta, GA, ²Children's Healthcare of Atlanta, ATLANTA, GA, ³LewisGale Hospital Montgomery, Blacksburg, VA

Purpose

When cases of non-accidental trauma in children age ≤3 years are brought to court, defense experts often claim that skull fractures detected on imaging studies are sequelae of "birth trauma". There is lack of scientific evidence informing the healing time for skull fractures in this age group, which could aid in debunking claims that certain skull fractures are birth injuries.

Materials and Methods

Literature review and single institution cohort review to determine skull fracture healing time in newborns (0-30 days old), infants (1-12 months old), and toddlers (1-3 years old).

Results

The study was IRB approved and HIPAA compliant. A focused literature review was conducted using the search terms (and MESH terms): skull fracture, healing, pediatric, imaging. A retrospective radiology information system search was conducted for radiographs and CTs with findings for skull fracture in children ≤ 3 years old; all patients with follow-up imaging within 18- days were included, any patients who underwent neurosurgery were excluded. We recorded patient age, gender, trauma mechanism, imaging modality, and time between imaging studies. The initial imaging at time of injury was reviewed to document the location and severity of the fracture, and the follow up imaging was reviewed and the stages of healing was stratified (i.e. healed, partially healed, not healed). Descriptive statistics (mean, shortest and longest healing time) were generated using a spread sheet (Microsoft® Excel, Microsoft Corporation, Albuquerque, NM).

Conclusions

We found 4 publications that included comments regarding healing time of skull fractures; but only 3 pertained to pediatric populations and 2 of these were educational reviews. One study in 4 adult postmortem skull fractures included 3 skull fractures that had radiographs and/or CT imaging which were associated with estimates of timing of healing [Cappella 2019]. Another study of 316 pediatric skull fractures undergoing imaging failed to document the timing of healing but presented one case of skull fracture healing within 3 months in a 9-month old [Zulfiqar 2017]. A total of 243 patients were reviewed. Our institutional assessment found that skull fractures heal as early as 57 days (1-12 months of age) and 136 days (1-3 years of age). The analysis is ongoing. Our data informs important time-points that can help in the medicolegal setting when defense experts claim that skull fractures are the result of injuries in the past, such as birth trauma.

Table 1: Results from literature review and single institution imaging analysis.

Imaging Feature [Conventional Radiograph = CR]	Cappella 2019	Zulfiqar 2017	Slovic 2008	Adamsbaum 2014	Single Institution Cohort Study
Population	Adult	Pediatric	Pediatric	Pediatric	Pediatric
#Fractures assessed	3	316	Review article	Review article	243
No imaging signs of healing features (CR/CT)	n/a	n/a	n/a	n/a	Up to 37 days
Healed bone (CT)	n/a	3 months in a 9-month old (n=1)	3-6 months	A few months without periosteal thickening	0-30 day olds: analysis pending 1-12 months old: 57 days 1-3 years old: 136 days

(Filename: TCT_980_Table1300DPI.jpg)

1032

Circuit Court: Exploring the Unanswered Ethical and Medicolegal Questions of AI in Radiology

D Martin¹

¹Vanderbilt University Medical Center, Nashville, TN

Purpose

There is no denying the increasing role that AI is playing in the field of medicine, and perhaps no specialty more than radiology. While radiologists are becoming more familiar with the theory and application of AI in imaging, there remains a large amount of

misunderstanding of how AI will ultimately fit into everyday practice. We currently do not have a full understanding of how AI experiences the world, though it is certainly different than humans do. This lack of understanding will likely prevent the public and physician community from developing full trust in the technology, especially when lives may be at stake. Understanding the potential sources of error and how to deal with them from an ethical and legal perspective is crucial to predicting how AI will be adopted in the field of radiology.

Materials and Methods

While AI presents a powerful tool for clinical radiologists, there are several ethical and medicolegal issues regarding how it will impact patient care. What role AI should play in the management of patients and who should be accountable for the errors that may arise from its use are questions that do not yet have clear answers. This presentation's goal is to explore the ethical and legal questions surrounding the evolving role of AI in patient care and presenting how such legal issues have been addressed in non-medical situations.

Results

Medical reviews of machine learning in the clinical setting are discussed to demonstrate the current and potential future roles of AI in radiology. As the widespread adoption of AI within the clinical setting remains hypothetical at this point, analogous examples of how the law has dealt with AI induced injury is used as a precedent.

Conclusions

As a new technology that is currently restricted in the clinical setting, many of the potential consequences of AI's use in the clinical care of patients are unknown. While some legal precedent exists regarding the liability of deep learning algorithms involved in human interaction/decision making, there are not enough examples to constitute a definitive legislative body. Most precedent involves direct harm from AI controlling vehicles, though medical imaging presents the possibility subtle types of injuries, such as a missed or misinterpreted findings. Based on the criteria for proving malpractice by a physician, it does not seem that it is possible for an algorithm to commit such an act and traditional concepts such as "duty" and "maleficence" may need to be revised before they can be applied to algorithms.

561

Clinical Fast Diffusion Kurtosis Imaging in the Evaluation of CNS masses

P Felix¹, R Hu², J Allen³, H Kim³, P Sun²

¹Emory University Hospital, Atlanta, GA, ²Emory University School of Medicine, Atlanta, GA, ³Emory University, Atlanta, GA

Purpose

- Review the concept of Diffusion Kurtosis Imaging (DKI) and the advantage of including it in MRI protocols for intracranial mass characterization. - Describe our institution's clinical experience using a fast DKI sequence as part of a routine brain MRI protocol in the evaluation of CNS masses.

Materials and Methods

DKI is an advanced diffusion technique that has been recently studied in the assessment of brain tumors. We reviewed the most recent literature and demonstrate the clinical feasibility and use of a fast DKI sequence in the evaluation of neoplastic and non-neoplastic intracranial masses.

Results

At our institution, a fast DKI sequence (1 B0, 3 B1000, and 18 B2000 gradient directions, 3.2 min acquisition time) was implemented in routine brain MRI protocols on a 3T clinical MRI (Magnetom Trio, Siemens) with automated post-processing and sending of mean kurtosis (MK) and mean diffusivity (MD) maps to the clinical PACS. We present case examples of various intracranial masses with conventional and fast DKI imaging and highlight useful diagnostic features of DKI in the context of current literature.

Conclusions

137 patients undergoing brain MRI including fast DKI between August 2020–October 2020 were reviewed with IRB approval; 14 patients were found to have space occupying lesions on imaging, including 8 gliomas, 2 metastases, 2 meningiomas, 1 primary CNS lymphoma (PCNSL) and 1 case of intracranial toxoplasmosis. All gliomas were histologically proven WHO grade IV glioblastomas (GBM); 4 had well defined solid enhancing components, 2 only scant enhancement and 2 were imaged after gross total resection of the enhancing region. The enhancing rim of the PCNSL had higher MK than the enhancing portion of GBMs (Figure 1, 1.16 vs 0.81). A case of toxoplasmosis had the highest MK of intracranial masses (2.27). The imaging and kurtosis metrics of these and other intracranial masses from the literature are reviewed. In this education exhibit, we review the applications of DKI in evaluating brain tumors and show its implementation in our clinical practice. Using our fast, clinically feasible DKI sequence, automated on-line MK and MD maps were successfully derived and useful in evaluating intracranial masses. Our preliminary results support those of previous studies, with higher MK values in lymphomas compared to gliomas. We also show case examples of other neoplastic and non-neoplastic intracranial masses, including metastases, meningiomas, and toxoplasmosis.

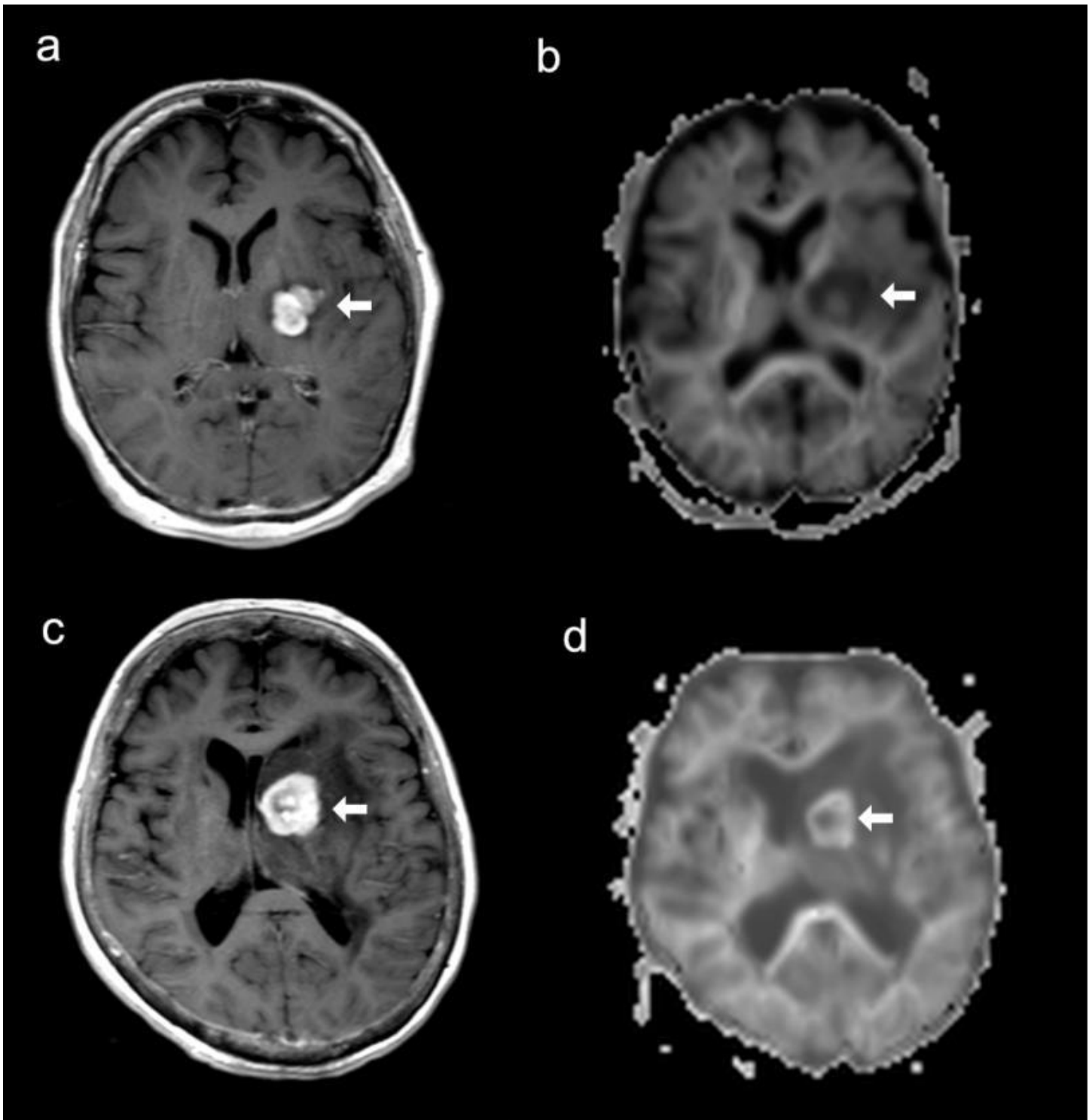


Figure 1. The solid enhancing rim of a left basal ganglia GBM (a) demonstrating low MK (b), while that of a similar appearing PCNSL (c) demonstrating high MK (d).

(Filename: TCT_561_DKIfigure.jpg)

1335

Clinical Utilities of 3 Dimensional Pseudo Continuous Arterial Spin Labelling (PC ASL) Perfusion in Routine Neuroimaging

P BAISHYA¹, S M², K Kulanthaivelu³

¹NATIONAL INSTITUTE OF MENTAL HEALTH AND NEUROSCIENCES (NIMHANS), BENGALURU, INDIA, BENGALURU, India, ²National Institute of Mental Health and Neurosciences (NIMHANS), Bengaluru, India, Bengaluru, Karnataka, ³National Institute of Mental Health and Neurosciences (NIMHANS), Bengaluru, Karnataka

Purpose

Arterial spin Labelling (ASL) is a promising non-invasive tool for perfusion assessment. Through this educational exhibit, we aim to demonstrate the versatility of 3D Pseudo continuous (PC) ASL and explore additional information it can provide when incorporated into routine neuroimaging. Learning objectives: 1. 3D PCASL helps in estimation of micro-vascular density and neo-angiogenesis in brain tumors. 2. 3D PC ASL could localize seizure onset zone with explicit illustration of the post-ictal perfusion defects. 3. 3D PCASL can detect perfusion changes in neurodegenerative disorders when standard structural MR imaging may remain inconclusive. 3. Arterial transit time (ATT) information derived from multi-delay ASL may help in prognosticating outcome and risk stratification in patients of cerebrovascular diseases.

Materials and Methods

Through this educational exhibit, we illustrate the utility of 3D PCASL in various neurological, neurosurgical, neurovascular and neurodegenerative conditions.

Results

3D PCASL was incorporated into routine neuroimaging protocol of various central nervous system pathologies. Imaging was done on a 3T MR scanner. Number of cases included were 95, out of which 30 were brain tumors, 12 cases were of seizure disorder, 8 cases of neurodegeneration, 5 cases of head trauma, 25 cases of neuro infection, 5 cases of demyelination and 10 cases of neurovascular diseases. Multi-delay 3D PC-ASL was done in cases of arteriovenous Malformation (AVM) and dural arteriovenous fistula (DAVF). In cases of brain tumors, ASL-PET- DSC perfusion correlation was done.

Conclusions

PC ASL shows perfusion abnormalities in various CNS pathologies. It showed excellent correlation with DSC perfusion and 11 C Methionine/ Fluorodeoxyglucose (FDG) positron emission tomography (PET) studies in cases of brain tumors. It can fairly detect seizure onset zone and postictal perfusion changes, specially in those cases in which structural MRI remains normal. It can detect perfusion changes in neurodegenerative conditions, hence valuable in cases in which structural MRI is inconclusive. Multi-delay PCASL could detect the extent of AV shunting in AVF/ AVM, perfusion abnormalities in adjacent brain parenchyma. PC ASL provides complementary diagnostic information via quantitative Cerebral Blood Flow (CBF) estimation and complements structural information of standard MR imaging. Through this educational exhibit, we propose 3D PCASL as a promising tool that can be incorporated into routine neuroimaging.

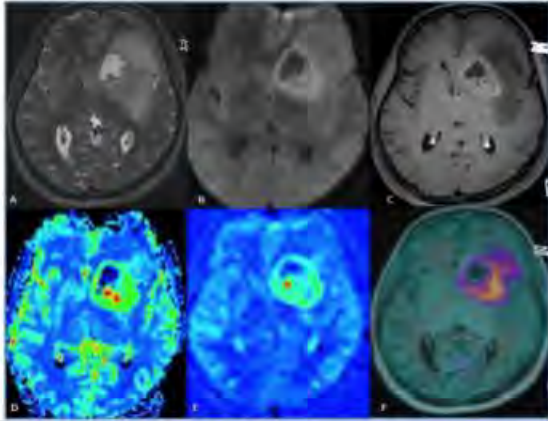


FIG1: Case of anaplastic astrocytoma. Axial T2W (A) images shows a heterogeneous mass lesion in the left frontal lobe and insular region. DWI (B) shows diffusion restriction along the periphery and posterior aspect of the lesion. Axial T1 W post contrast image (C) shows peripheral and nodular areas of enhancement. DSC perfusion (D) and 3D PCASL image (E) shows increased perfusion in these enhancing areas. C11 methionine PET image (F) shows tracer uptake along the periphery and posterior part of the lesion

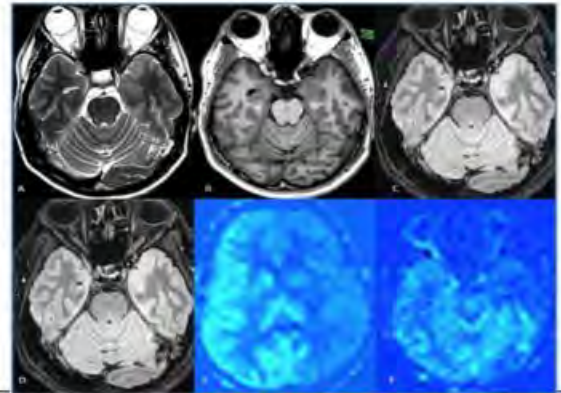
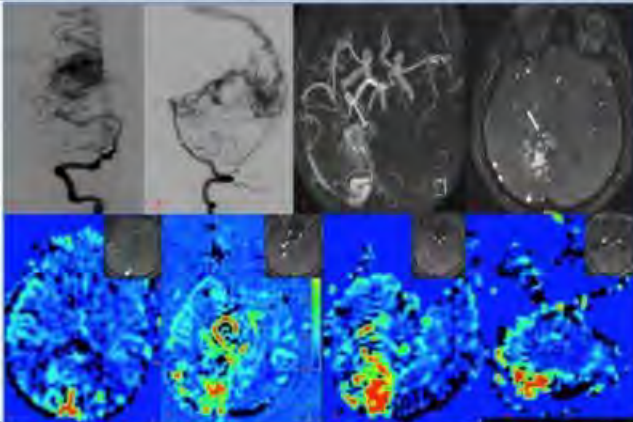


FIG 2: Case of temporal lobe epilepsy. Axial T2W (A), T1W (B) and FLAIR (C, D) images show bulky left medial temporal lobe, amygdala along with thickening of the cortex, blurring of grey- white differentiation in left antero basal and medial temporal lobe- suggestive of focal cortical dysplasia. 3D PCASL images (E,F) shows hypoperfusion in left cerebral hemisphere suggesting post ictal hypoperfusion.



Case of right parieto-occipital AVM. FIG 3: DSA images (A,B) shows arterial feeders from right PCA and cortical branches of right MCA, moderate size nidus with early venous drainage to the superior, inferior sagittal & right transverse sinus. Time of flight (TOF) images (C,D) shows the arterial feeders, draining venous sinuses with congestion in the right temporo-parieto-occipital region. Multi-delay PCASL images (E,F,G,H) along with insets reveals arterIALIZED flow in the draining venous sinuses along with increased perinidal perfusion (image F,G).

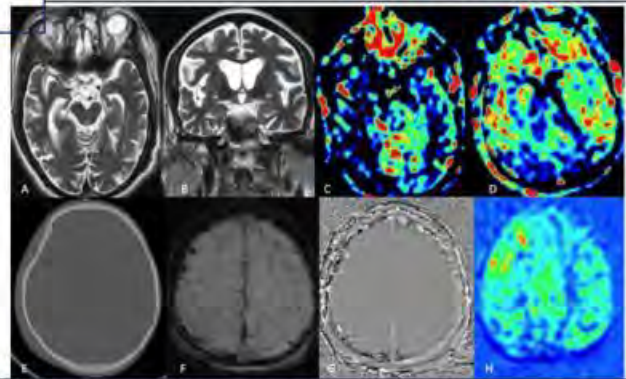


Fig4: 1st row shows images of a case of posterior cortical variant of Alzheimer's disease. Axial (A), coronal (B) T2W images shows predominant atrophy of bilateral medial temporal lobes & hippocampi. PCASL images (C,D) shows hypoperfusion of bilateral posterior parietal regions and bilateral temporal lobes. 2nd row shows images of a case of Head Injury. Bone algorithm CT image (E) shows comminuted fracture in frontal bone. Susceptibility Weighted image (F) and phase map (G) shows hemorrhagic contusions in right frontal lobe. PCASL Image (H) shows hyper perfusion of this region suggestive of trauma induced perfusion changes

(Filename: TCT_1335_Untitled3400.jpg)

1314

Clinical Utility of Arterial spin labeling and Vessel wall imaging in the evaluation of Pediatric stroke and stroke mimics.

S Narayanan¹, S Subramanian²

¹Children's hospital of Pittsburgh of UPMC, Pittsburgh, PA, ²UPMC Children's Hospital of Pittsburgh, Pittsburgh, PA

Purpose

Summary: The incidence of pediatric stroke is estimated to be about 4.6–6.4 per 100,000 children, based on US population studies. Pediatric stroke is unique with its varied etiologies and diagnostic challenges. Moreover, in the emergent setting, it is important to distinguish pediatric stroke from stroke mimics, which are commonly encountered. In practice, these can be clinical or radiological mimics. In our institution we use arterial spin labeling (ASL) as a part of our rapid stroke protocol and vessel wall imaging (VWI) as an advanced imaging tool, when indicated. ASL is a non-invasive novel technique of evaluating cerebral perfusion, utilizing arterial blood water as an endogenous tracer, providing complementary physiologic information, expanding its application. Intracranial VWI has a novel role in evaluation of unique etiologies such as focal arteriopathy. In this abstract we will discuss the role of ASL and VWI in evaluating stroke and stroke mimics. We will do this via illustrative cases including examples of arterial ischemic stroke, DWI negative stroke, Moya-Moya, focal arteriopathy, cerebral arteriopathy related to ACTA2 mutation etc and common stroke mimics such as migraine with aura, infection etc. We will discuss the pearls and pitfalls of these sequences as well. Educational objectives: Describing the utility of ASL in stroke and stroke mimics. Understanding pearls and pitfalls of ASL imaging Understanding Vessel wall imaging- sequences, its role in pediatric stroke and limitations.

Materials and Methods

Understanding the role of ASL and VWI in evaluating stroke and stroke mimics.

Results

N/A

Conclusions
N/A

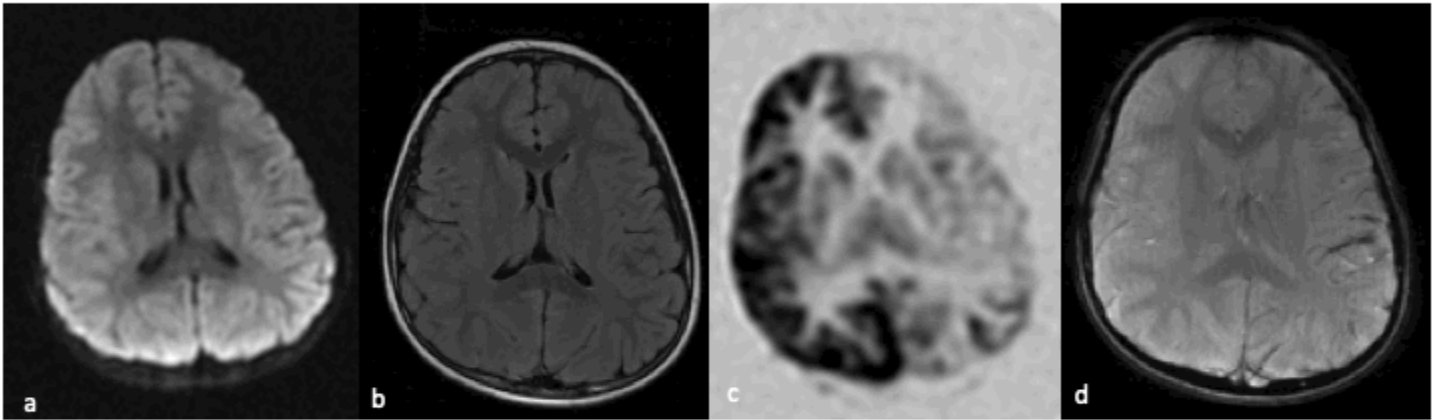


Figure 1: STROKE MIMIC : migraine with aura. Clinical history-15 year old with right hemiplegia and headaches. Imaging-rapid stroke protocol MRI showing a) DWI- no restricted diffusion b) axial T2 flair – no abnormal signal alteration c) ASL with hypoperfusion pattern involving the left cerebral hemisphere and d) SWI - prominent hypointense signals of the venous vasculature within areas of impaired perfusion.

(Filename: TCT_1314_ASNR2021.gif)

190

Clinical-Radiologic Presentations in NeuroCOVID-19

F Assunção¹, E Agapito Valadares¹, L Martins¹, L Freitas¹, B Nóbrega¹, L Scopetta¹, T Scopetta¹
¹Hospital São Camilo, São Paulo, SP

Purpose

The clinical syndrome caused by SARS-CoV-2 is called COVID-19. Commonly the symptoms of the disease are similar to common flu. However, neurological manifestations and symptoms associated with COVID-19, also called NeuroCovid-19, are being more and more related to the virus infection. NeuroCovid-19 manifestations may be explained by a direct and an indirect mechanism of the virus infection. Some studies are showing that the virus SARS-CoV-2 can enter the central nervous system, leading for example to neurodegeneration, neuroinflammation and demyelination processes. Another form of neurological compromise could be secondary to other systemic abnormalities caused during the virus infection like systemic inflammation, coagulation disorders and vascular injury. This study aims to describe numerous clinical and radiological neurological presentations in patients with COVID-19 disease seen at our hospital since the beginning of the pandemic.

Materials and Methods

The purpose of the study is to show the different NeuroCovid-19 manifestations to the physicians and radiologists. We have to be aware about the different forms of presentation of this new entity, specially in the nervous system, considering the risk of irreversible damage.

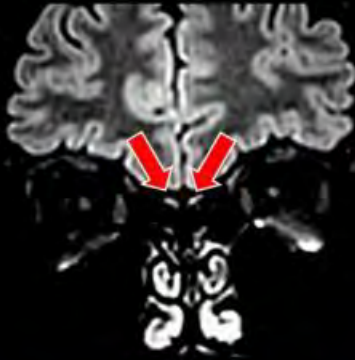
Results

We searched in our database for the patients with the diagnosis of COVID-19 and whom presented with neurological clinical-radiological manifestations.

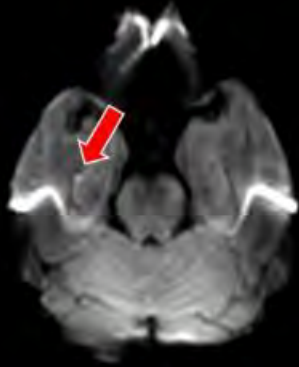
Conclusions

We found cases of acute disseminated encephalomyelitis, transient global amnesia, olfactory neuropathy in patients with hyposmia, olfactory cleft obliteration by soft tissue, reversible cerebral vasoconstriction syndrome, cerebral venous thrombosis, ischemic stroke (due to internal carotid artery dissection, thrombotic microangiopathy or thromboembolic phenomenon), catastrophic cerebral hemorrhages and diffuse ischemic hypoxic damage and more. The clinical-radiologic presentations in patients with NeuroCovid-19 were quite varied so it's of fundamental importance that the neuroradiologist/radiologist is aware of these presentations to improve the management of these patients.

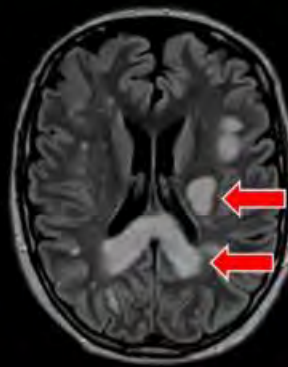
Clinical-Radiologic Presentations in NeuroCOVID-19



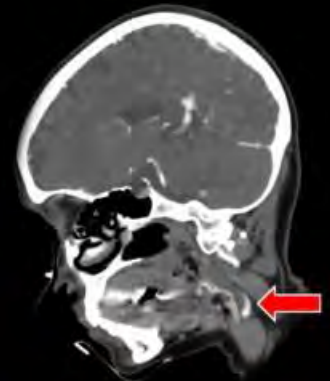
Olfactory
Neuropathy



Transient Global
amnesia



Acute Disseminated
Encephalomyelitis



Ischemic Stroke
due Internal
carotid artery
dissection

(Filename: TCT_190_neurocovid.jpg)

1230

CLOSE-ing the gap in identifying sinus anatomical variants in pre-operative reporting for sinus surgery

A Wong¹, J Kavanaugh²

¹Dalhousie University, Saint John, New Brunswick, Canada, ²Saint John Regional Hospital, Quispamsis, NB

Purpose

Chronic rhinosinusitis affects approximately 5% of the population in Canada and is associated with significant negative impact on quality of life, disability, and decreased productivity. While endoscopic sinus surgery is typically a very successful treatment, anatomical abnormalities of the paranasal sinuses and skull base have been associated with increased risk of surgical complications. The CLOSE checklist (Cribriform Plate, Lamina Papyracea, Onodi Cell, Sphenoid Sinus, Ethmoid Artery) lists 5 key anatomical abnormalities critical for identification on preoperative CT before sinus surgery. In this exhibit, the major goals are to help readers become familiar with the CLOSE checklist, and be able to use it as a guide in recognizing anatomical variants in the paranasal sinuses on preoperative CT. Accurate and consistent identification of the 5 key anatomical abnormalities listed in the checklist will help the radiologist make comprehensive reports, and contribute to safer endoscopic sinus surgeries for patients. Learning Objectives: 1) Review normal anatomy of sinus computed tomography (CT). 2) Educate the reader on the anatomical landmarks and normal variants seen on pre-operative sinus CTs which put the patient at increased risk for potential surgical complications. 3) Present the CLOSE checklist as a helpful guide to recall and describe these anatomical landmarks, thereby reducing the risk of surgical complications.

Materials and Methods

N/A

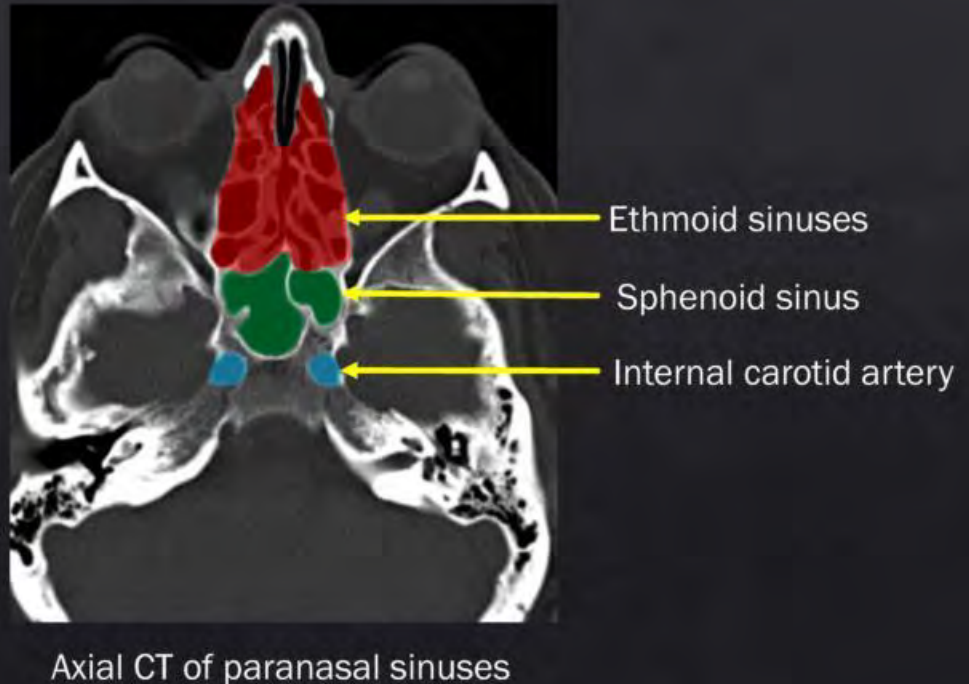
Results

N/A

Conclusions

N/A

Normal sinus anatomy (cont'd)



(Filename: TCT_1230_CLOSEproject_Page_3.jpg)

1180

CNS Infections: From A to Z

D Vu¹, I Boyack¹, E Stein¹

¹Maimonides Medical Center, Brooklyn, NY

Purpose

Educational Objectives: CNS infections can have nonspecific imaging characteristics. The purpose of this educational exhibit is to review the key differentiating image findings for some of the most commonly encountered CNS infections and review a few rare CNS infections. Using the patient's history and clinical presentation can further narrow the differential diagnosis. Summary: The cases will be presented in a quiz format. Each case will start with a multiple-choice question followed by informational slides about each CNS infection. The key differential diagnostic information across multiple modalities will be discussed for each case. The list of cases includes: 1. Acute Flaccid Myelitis 2. COVID-19-associated Acute Necrotizing Hemorrhagic Encephalopathy 3. Cryptococcal Meningitis 4. HSV Encephalitis 5. Lyme Disease 6. Neurocysticercosis 7. Progressive Multifocal Leukoencephalopathy (PML) 8. Subdural Empyema 9. Toxoplasmosis 10. Ventriculitis 11. Zika Virus

Materials and Methods

N/A

Results

N/A

Conclusions

N/A

1217

CNS Systemic Lupus Erythematosus: Pathophysiologies, Imaging Findings and Complications

Y Ota¹, A Baba², R Kurokawa³, A Capizzano¹, T Moritani¹

¹University of Michigan, Ann Arbor, MI, ²The Jikei University of Medicine, Minato, Tokyo, ³Graduate School of Medicine, The University of Tokyo, Tokyo, Japan

Purpose

We reviewed pathophysiologies, clinical manifestations and imaging findings of CNS systematic lupus erythematosus and its complication. Objectives: 1. Pathophysiology 2. Antibodies associated with SLE 3. Clinical manifestations 4. Imaging features based on different pathophysiologies

Materials and Methods

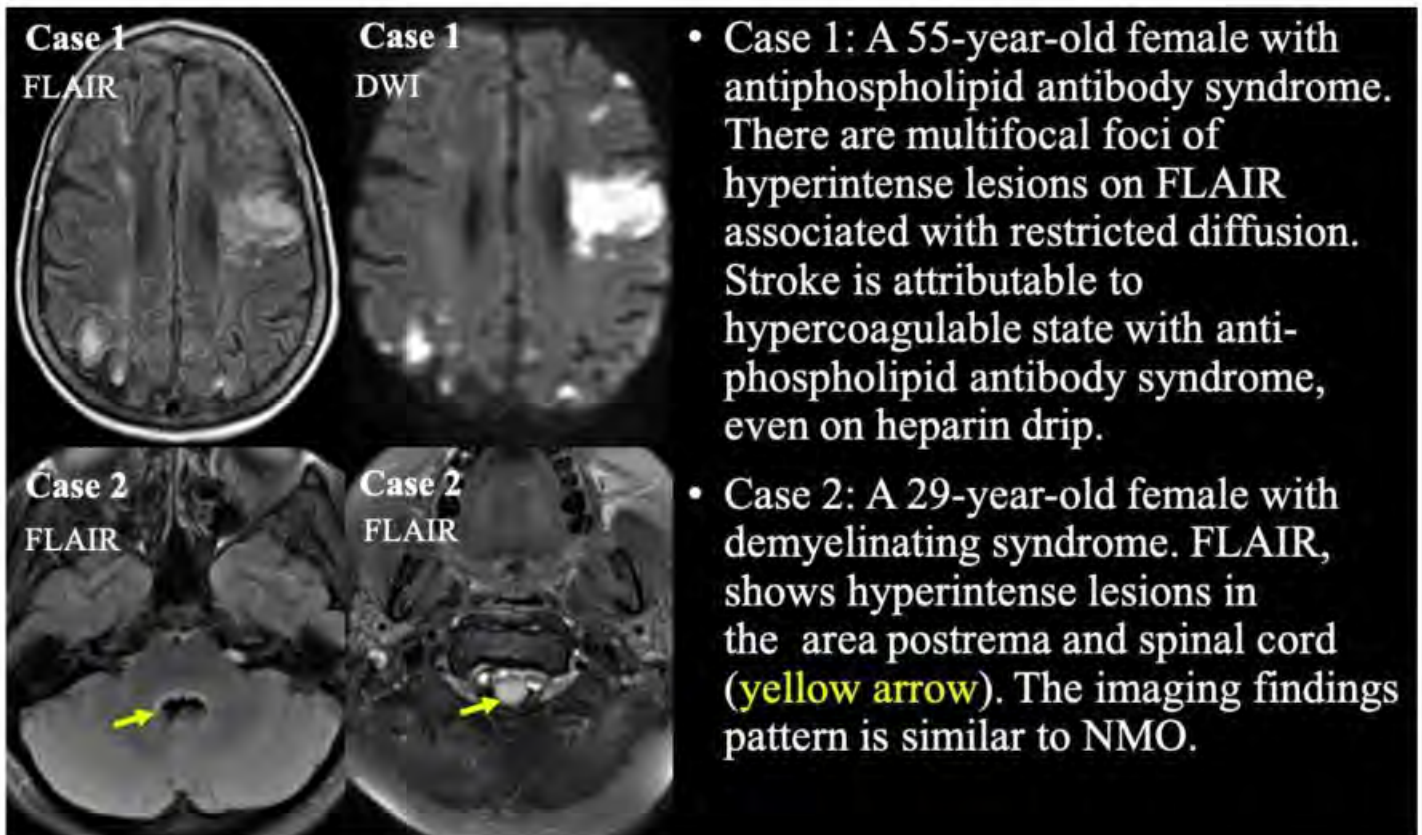
After reviewing this poster, readers will be able to: 1. Understand pathophysiology, pathological basis of neuroinflammation and relevant antibodies, and clinical manifestations of SLE 2. Recognize imaging features based on different pathophysiology 3. Identify complications and treatments

Results

1. Pathophysiology - Vasculopathy - Vasculitis - Demyelinating syndrome - Encephalitis/Autoimmune mediated encephalitis - Antiphospholipid antibody syndrome 2. Antibodies associated with SLE 3. Clinical manifestations - Neurological symptoms - Major and minor neuropsychiatric symptoms 4. Imaging features based on different pathophysiologies - Vasculopathy/vasculitis: mainly small vessel affected, signal intensity alterations in deep and subcortical white matter and basal ganglia - Demyelinating syndrome, and similar distribution pattern or coexistence with NMO spectrum disorders, multiple sclerosis, ADEM and Sjogren's syndrome - Autoimmune mediated encephalitis: NMDA receptor antigens, signal intensity alterations in cortex, basal ganglia, and thalamus 5. Complications and mimics (Stroke, Libman-Sachs endocarditis, PRES, PML, primary central nervous system lymphomas, demyelinating diseases) 6. Management and treatment

Conclusions

We reviewed pathophysiologies, clinical manifestations and imaging findings of CNS systematic lupus erythematosus and its complication.



(Filename: TCT_1217_SLE.jpg)

1279

Colloid Cyst Imaging Features and Approach to Management

W Witwit¹, G Pappas¹

¹St. Joseph Mercy Oakland, Pontiac, MI

Purpose

- Identify the imaging features of colloid cyst. - Underline symptoms, potential complications, treatment, and approach to management. - Highlight the colloid cyst risk score as a validated method to stratify complications risk and support management.

Materials and Methods

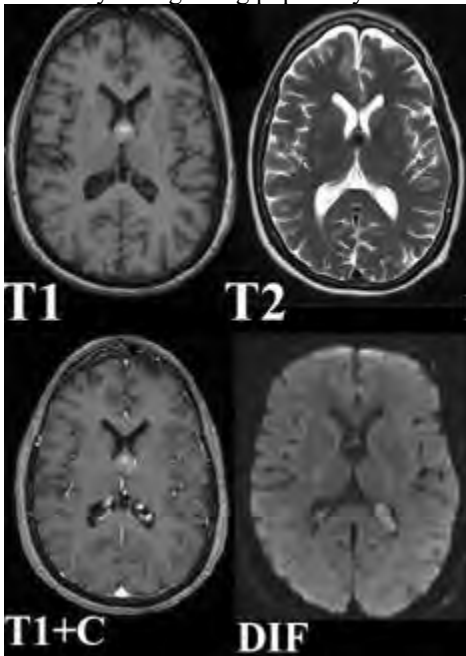
- Identifying the typical imaging features of colloid cysts for early and accurate diagnosis and hence facilitating clinical management. - Avoid the potential devastating complications of colloid cysts, including sudden death.

Results

- A case report of a patient presented to the emergency department with headache. - Review of several articles and recent literature. - Case description: A 73 years old female with a history of colloid cyst presented to the emergency room with acute onset diffuse headache for the last two days. Neurological examination was not significant. Head CT showed interval enlargement of the colloid cyst which appears hyperdense in relation to the brain tissue. MRI confirmed the colloid cyst and evolving hydrocephalus could not be ruled out. The patient was managed according to colloid cyst risk score.

Conclusions

- Colloid cysts are rare benign lesions that appear on the roof of the third ventricle. They are often asymptomatic but may present with headaches, coma, or sudden death. - IMAGING FEATURES: On unenhanced CT-head, most colloid cysts demonstrate high density due to high protein content. On T1-weighted sequences, the central portion of the uncomplicated cyst is of increased signal intensity relative to brain, whereas the periphery is isointense. On T2-weighted sequences, the center is markedly hypointense due to hemosiderin content, while the periphery is isointense. The presence of protein and hemosiderin complicates the evaluation for acute hemorrhage in symptomatic patients. - Colloid Cyst Risk Score (CCRS) is a validated method to support management. CCRS records one point to each of the following: Age<65, headache, Axial diameter >7 mm, risk zone of 3rd ventricle, and FLAIR hyperintensity on MRI. CCRS 0-2 represented low-risk group. CCRS 3 was considered intermediate risk where observation can be reasonable. While CCRS 4-5 represented the high risk group where surgical intervention should be considered. - Endoscopic approach for excision of colloid cysts is gaining popularity.



(Filename: TCT_1279_colloidfig.jpg)

1007

Complicated Migraines: More at Stake than Just a Headache

J Mangere¹, K Hsu²

¹Albert Einstein College of Medicine, Bronx, NY, ²Montefiore Medical Center, Bronx, NY

Purpose

Migraines are the most common neurological disorders in adults, with the World Health Organization estimating between 12-15% of the global population being affected. Pathophysiology of migraine is thought to involve transient changes to cerebral blood flow leading to unilateral moderate to severe headache with reversible focal neurologic symptoms, however treatment strategies remain a challenge and research into changes detectable on neuroimaging is ongoing.

Materials and Methods

Literature review and pertinent case examples will be presented. Learning objectives of this educational poster is to describe the clinical aspects, imaging findings, and existing research of complicated migraines with a focus on advanced neuroimaging.

Results

Outline of topics to be covered: 1) Clinical differentiation of type of headaches. 2) Evidence for imaging of headaches and appropriateness. 3) Clinical manifestations of complicated migraine, pediatric and adult. 4) Current pathophysiology and treatment strategies for migraine 5) Imaging findings in migraines and research basis a. T2/FLAIR hyperintensities b. Susceptibility Weighted Imaging (SWI) c. Perfusion Arterial Spin Labelling (ASL)/Dynamic Susceptibility Contrast (DSC) d. fMRI, resting state fMRI e. Diffusion Tensor Imaging (DTI) 6) Migraine mimics and their imaging findings

Conclusions

White matter hyperintense lesions on brain MRI appear to be associated with poorer migraine prognosis and older age.

1425

Complications of Spinal Trauma: The Acute, Subacute and Chronic manifestations.

L Nash¹, A Herwadkar²

¹Salford Royal NHS Foundation Trust, Northern Care Alliance, Greater Manchester Neurosciences Centre, Greater Manchester, United Kingdom, ²Salford Royal NHS Foundation Trust, Northern Care Alliance, Greater Manchester Neurosciences Centre, Greater Manchester, United Kingdom

Purpose

N/A

Materials and Methods

Spinal trauma is a common presentation to emergency departments across the world. The acquired injuries can be extremely disabling, if not fatal, especially in patients who have focal neurological defects at presentation. Effective treatment of the various injuries can assist in long term prevention of significant morbidity (particularly in patients with initial preservation of neurological function). Radiologists play a key role in identifying post traumatic sequelae in the acute, subacute and chronic stages in order to assist in preserving both life and quality of life.

Results

We present a variety of cases of spinal trauma that presented to our tertiary centre over a period of fifteen years. We have grouped the traumatic injuries into acute, subacute and chronic to enable the viewer to appreciate the types of abnormality that may present at different timeframes after initial injury.

Conclusions

Acute complications are present on the initial imaging following traumatic injury. These can be widespread and may involve the bony spinal column (e.g. fractures, dislocations); disruption of intervertebral disc (e.g. protrusion causing cord compromise); ligamentous injury (eg. posterior ligamentous band disruption); spinal cord injury (e.g. contusion, transection); nerve root injury (e.g. avulsion); haemorrhage (e.g. epidural, cord haematoma) and vascular injury (e.g. vertebral artery dissection). Subacute complications typically present 4-6 weeks after initial event and include: Infections (e.g.osteomyelitis, discitis) which may be related to either mechanism of injury or therapeutic instrumentation; early complications of instrumentation (e.g. post-operative haemorrhage, loosening of metalwork) and cord abnormalities (e.g. oedema, subacute progressive ascending myelopathy, early syrinx). Chronic complications present months to years after initial injury. These can be subdivided into those that were managed conservatively (e.g. kyphotic deformity in previously stable fractures), and those that had surgical instrumentation (e.g loosening of metalwork, arachnoiditis, meningitis, Charcot spinal arthropathy, syringomyelia). Spine trauma has significant associated morbidity and mortality rates. The possible injuries are vast. We have illustrated specific imaging findings associated with these injuries, not only at time of presentation, but on any subsequent spinal imaging in order to assist in improving patient outcomes.

297

Connecting the Dots: Radiologic Diagnosis and Endovascular Treatment of Carotid-Cavernous Fistulas

D Skelton¹, K Patel², J Buckley³, N Akhtar⁴, J Halpin⁴

¹University of Missouri - Kansas City, Kansas City, MO, ²N/A, N/A, ³University of Missouri at Kansas City, Kansas City, MO, ⁴St. Luke's Hospital, Kansas City, MO

Purpose

Teaching Points: Carotid-cavernous fistulas (CCFs) are a type of arteriovenous shunt in which there is an abnormal connection between the carotid circulation and the cavernous venous sinus. CCFs may develop spontaneously or secondarily after trauma or other predisposing conditions and commonly present with changes to the eye (exophthalmos, chemosis, proptosis), vision, or pulsatile tinnitus. Though catheter-based angiography is the gold standard for diagnosis and facilitates endovascular treatment, most CCFs are initially diagnosed by CT or MR. Diagnostic radiologists should be familiar with the diagnostic features of CCFs – including secondary sequela and treatment considerations – as well as post-treatment appearance and potential complications. Table of Contents: A. Introduction to carotid-cavernous fistulas (CCFs) B. Clinical presentation, etiology, classification C. Diagnostic imaging of CCFs: CT, MR, angiography D. Endovascular treatment of CCFs E. Post-treatment diagnostic imaging and potential complications

Materials and Methods

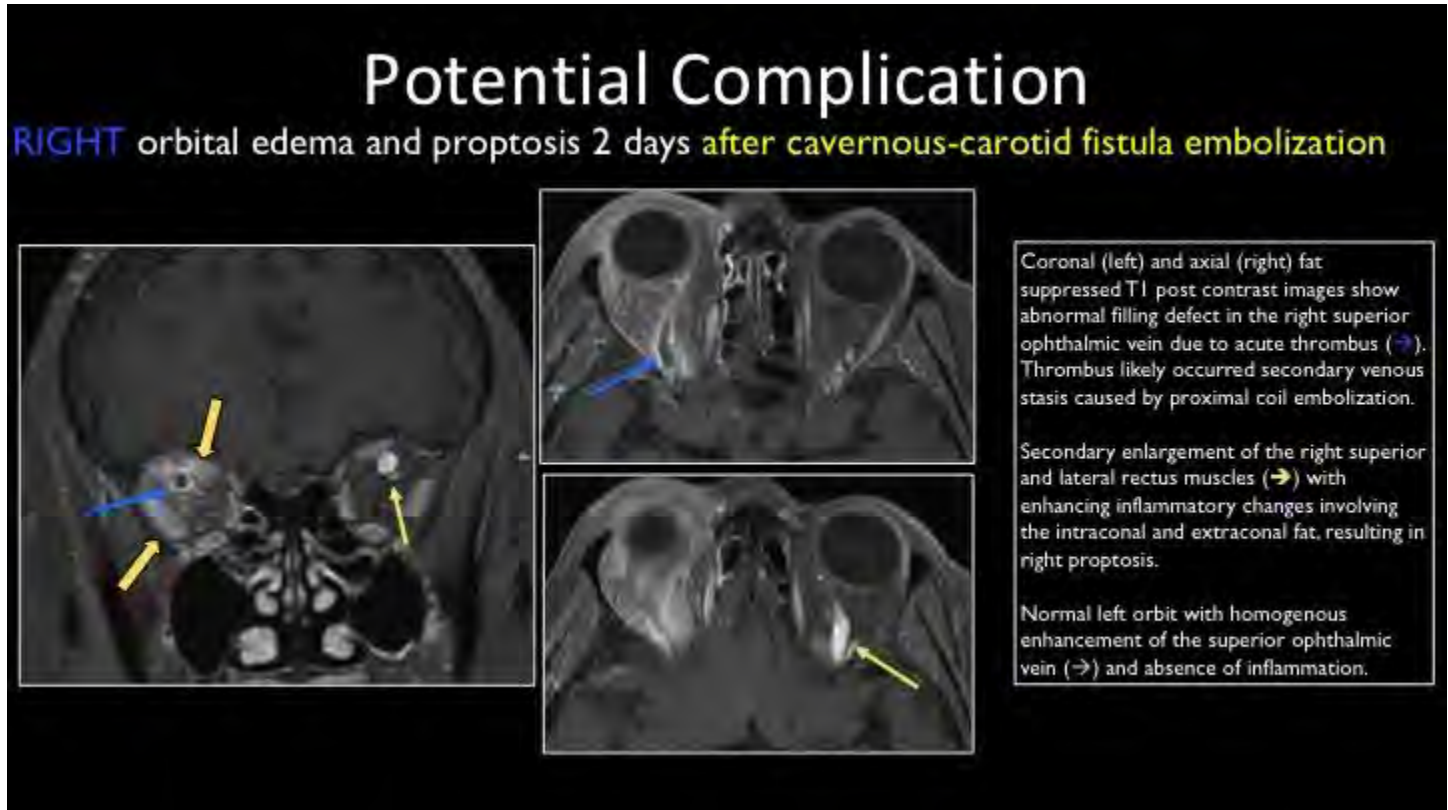
The purpose of this exhibit is to: - Review the clinical presentation, etiology and classification of carotid-cavernous fistulas (CCFs) - Demonstrate primary and secondary imaging features of CCFs on multiple modalities - Explore endovascular treatment of CCFs including procedural indications and techniques - Discuss expected post-treatment imaging of CCFs as well as potential complications

Results

N/A

Conclusions

N/A



(Filename: TCT_297_Slide5.jpg)

1581

Cosmetic injections: what radiologists need to know

V Andreu Arasa¹, O Sakai²

¹Boston Medical Center, Boston, MA, ²Boston Medical Center, Boston University School of Medicine, Boston, MA

Purpose

Cosmetic procedures, particularly filler injections in the face have become extremely common recently. Very few patients disclose prior or recent cosmetic interventions when they undergo CT and MR imaging studies of brain or head and neck for other reasons, or occasionally even when the current problem is secondary to complications from prior cosmetic interventions. In addition, filler injections may be performed after surgical reconstructions. Therefore, familiarity with these procedures and imaging findings are important not to mistaken as true pathologies and not to miss complications.

Materials and Methods

The purposes of this exhibit are 1) to learn various cosmetic injections recently performed in the US and outside of the US, 2) to be familiar with typical imaging findings after intervention, and 3) to learn common imaging findings of complications from cosmetic injections.

Results

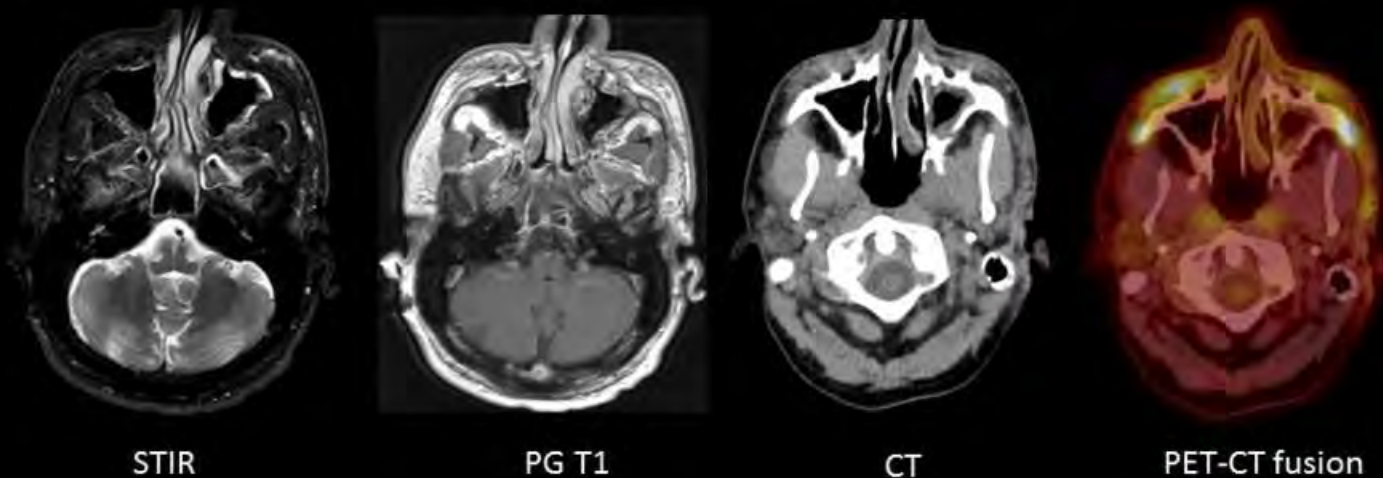
1) Review of common and uncommon cosmetic injection filler materials used in the US and other countries 2) Review of typical imaging findings of various filler materials 3) Review of imaging findings of complications from cosmetic injections including hematoma, seroma, infection, migration, fibrosis, and foreign-body reaction 4) Discussion not to overcall or miss true pathologies in patients who received cosmetic injections

Conclusions

The updated knowledge of filler injections currently used and familiarity with the common post-procedure imaging findings help radiologists not overcall or miss complications or true pathologies in patients who received cosmetic injections.

Collagen injection

Recurrent acinic cell carcinoma, right parotid, s/p surgery and collagen injections



(Filename: TCT_1581_ASNR2021_jpg.jpg)

1497

Cram your extramedullary intradural spinal lesions for good

S Velasco¹, P Puac Polanco¹, A Guarnizo², J Cruz³, F Moron⁴, F Rivas-Rodriguez⁵, C Torres⁶

¹University of Ottawa, Ottawa, ON, ²IMEXHS-RIMAB, Bogotá, Colombia, ³Universidad Católica/Instituto de Neurocirugía, Santiago, Chile, ⁴BCM, Houston, TX, ⁵University of Michigan, Ann Arbor, MI, ⁶University of Ottawa, Ottawa, AZ

Purpose

BACKGROUND INFORMATION Accurate imaging localization of a lesion in the spinal canal is essential for diagnosis and treatment planning, especially when minimally invasive approaches, such as hemilaminectomy, are required. Among the different compartments within the spinal canal, the intradural extramedullary space harbors the majority of the spinal pathology, according to the literature. While neoplasms predominate in this location, other less considered processes can also be encountered in daily practice, such as infectious and granulomatous lesions, among others. As such, a systematic imaging approach to these entities is required.

TEACHING POINTS/LEARNING OBJECTIVES: • To review the intradural extramedullary space lesions, emphasizing key imaging findings that lead to a diagnosis. • To illustrate the use of imaging landmarks to precisely localize a lesion in the intradural extramedullary space in challenging scenarios. • The use of different modalities, such as MRI, CT, and CT-myelography, will be discussed when appropriate. • Lesions associated with syndromes will be highlighted along with recommendations for further imaging workup.

Materials and Methods

The purpose of this exhibit is to review the imaging findings of common and uncommon lesions circumscribed to the extramedullary intradural spinal space through a case-based approach.

Results

Outline - Approach – etiology - Tumors: o Schwannoma, melanotic schwannoma, and associated syndromes o Neurofibroma,

neurofibromatosis o Meningioma o Myxopapillary ependymoma o Paraganglioma o Leptomeningeal metastases o Lymphoma o Solitary fibrous tumor o Malignant peripheral nerve sheath tumor (MPNST) - Non-neoplastic lesions o Tuberculosis o Migrated Disc o Cysticercosis o Abscess o Hemorrhage

Conclusions

SUMMARY/CONCLUSION Imaging approach to lesions in the spinal canal requires precise identification of anatomic landmarks, as recognizing the spinal compartment where a given lesion arises from allows to establish a proper and more accurate differential diagnosis. Being familiar with the key imaging features of masses centered within the intradural extramedullary space is essential for diagnosis and treatment planning.



Large expansile lumbar schwannoma. Sagittal T2 (A) as well as sagittal and axial T1W sequences post contrast with fat saturation (B,D) show a large heterogeneous intradural extramedullary mass with focal areas of extradural extension, demonstrating avid post contrast enhancement. The fat of the anterior (arrows in A and B) and posterior (arrowheads in A and B) epidural space is preserved confirming the intradural location of the lesion. Sagittal CT image of the lumbar spine in bone window (C), shows associated scalloping of the posterior walls of several vertebral bodies, with smooth sclerotic margins indicative of a slowly-growing mass. The tumour invades the lateral epidural space on the right and extends beyond the spinal canal into the right neuroforamen at L4-L5 level (arrow in D).

(Filename: TCT_1497_caseextramedullaryintradurallesions.jpg)

763

Craniofacial Manifestations of Renal Osteodystrophy

L Chien¹, N Kinger¹, R Peterson¹

¹Emory University School of Medicine, Atlanta, GA

Purpose

1. Discuss the pathophysiology of renal osteodystrophy 2. Demonstrate craniofacial manifestations of renal osteodystrophy on CT 3. Review common craniofacial osseous pathologies that can mimic renal osteodystrophy

Materials and Methods

Chronic kidney disease (CKD) is a common chronic illness affecting nearly 15 percent of the adult population in the United States. Disordered calcium and phosphate metabolism in CKD lead to elevated parathyroid hormone secretion and high bone turnover, resulting in renal osteodystrophy. Over time the osseous changes resulting from CKD can cause significant functional or cosmetic impairment. The purpose of this exhibit is to describe and illustrate different craniofacial manifestations of renal osteodystrophy.

Results

CT is superior in the evaluation of craniofacial osseous structures when compared to other imaging modalities. Renal osteodystrophy in the skull and facial bones has distinct radiographic manifestations which are well-characterized on CT. These include osteitis fibrosa cystica, diffuse ground glass appearance, and uremic leontiasis ossea. Osteitis fibrosa cystica shows cortical thinning, trabecular coarsening, and osteolysis. Mixed osteolysis and sclerosis result in widening of the diploic space and heterogeneous hypo- and hyper-attenuating nodular areas classically described as the "salt and pepper appearance" of the skull (Fig 1A). Areas of lytic and expansile bone loss suggest Brown tumors, which are foci of benign proliferative vascular and fibrous tissue (Fig 1B). The ground glass pattern is diffuse with poor corticomedullary differentiation (Fig 1C), in contrast to the asymmetric multifocal ground glass pattern in fibrous dysplasia. Uremic leontiasis ossea is characterized by osseous hypertrophy, cortical thinning, and feline serpiginous

tunneling of the bone marrow (Fig 1D). Common mimics include multiple myeloma, lytic metastases, Paget disease and fibrous dysplasia.

Conclusions

Renal osteodystrophy has characteristic craniofacial manifestations on CT, which may mimic other benign and malignant osseous pathologies. Early recognition is crucial to facilitate timely management and prevent worsening of functional and cosmetic disability.

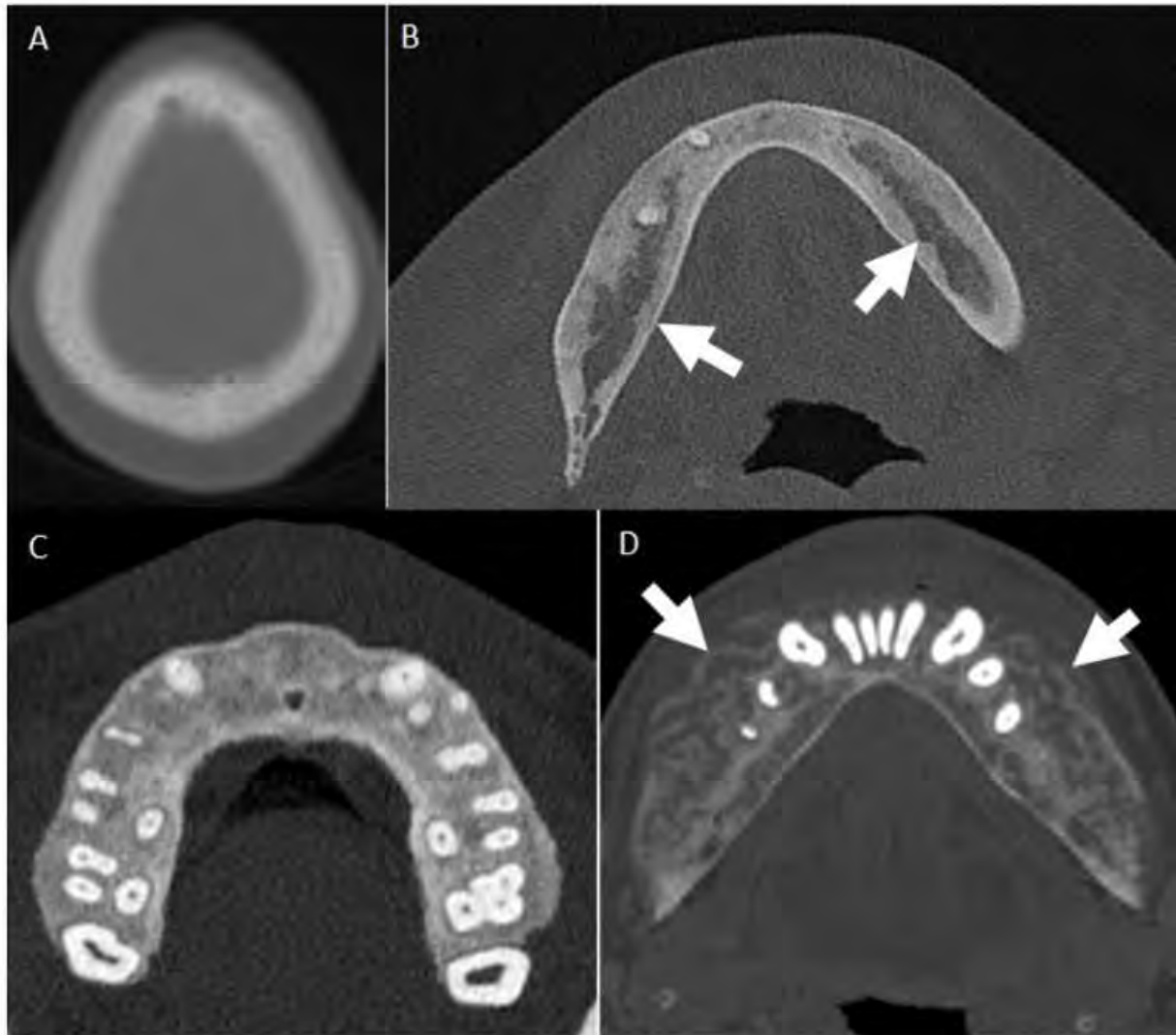


Figure 1. Different craniofacial imaging manifestations of renal osteodystrophy. A: Salt and pepper appearance characterized by innumerable tiny lucencies throughout the skull. B: Brown tumors of the mandible characterized by areas of lytic expansion (white arrows) with surrounding ground glass formation. C: Symmetric hypertrophy and ground-glass appearance of the maxilla. D: Uremic leontiasis ossea characterized by osseous hypertrophy and serpiginous stripe-like areas of bone formation (white arrows).

(Filename: TCT_763_ASNRRenalOsteodystrophyFigure1withcaption.JPG)

509

Creating Patient Specific 3D Printed Spines for Anatomy and Image Guided Procedure Teaching

V Cochran¹, C Wilson¹, M Bean¹, J Ormsby¹, M Mabray¹

¹University of New Mexico, Albuquerque, NM

Purpose

In this exhibit we show how to create patient specific 3D printed spines which can be used for anatomy and image guided procedure teaching. Our objectives are that the participant should learn the steps required to create a 3D printed spine and how that can be used for teaching including as a reusable model for performing image guided procedures.

Materials and Methods

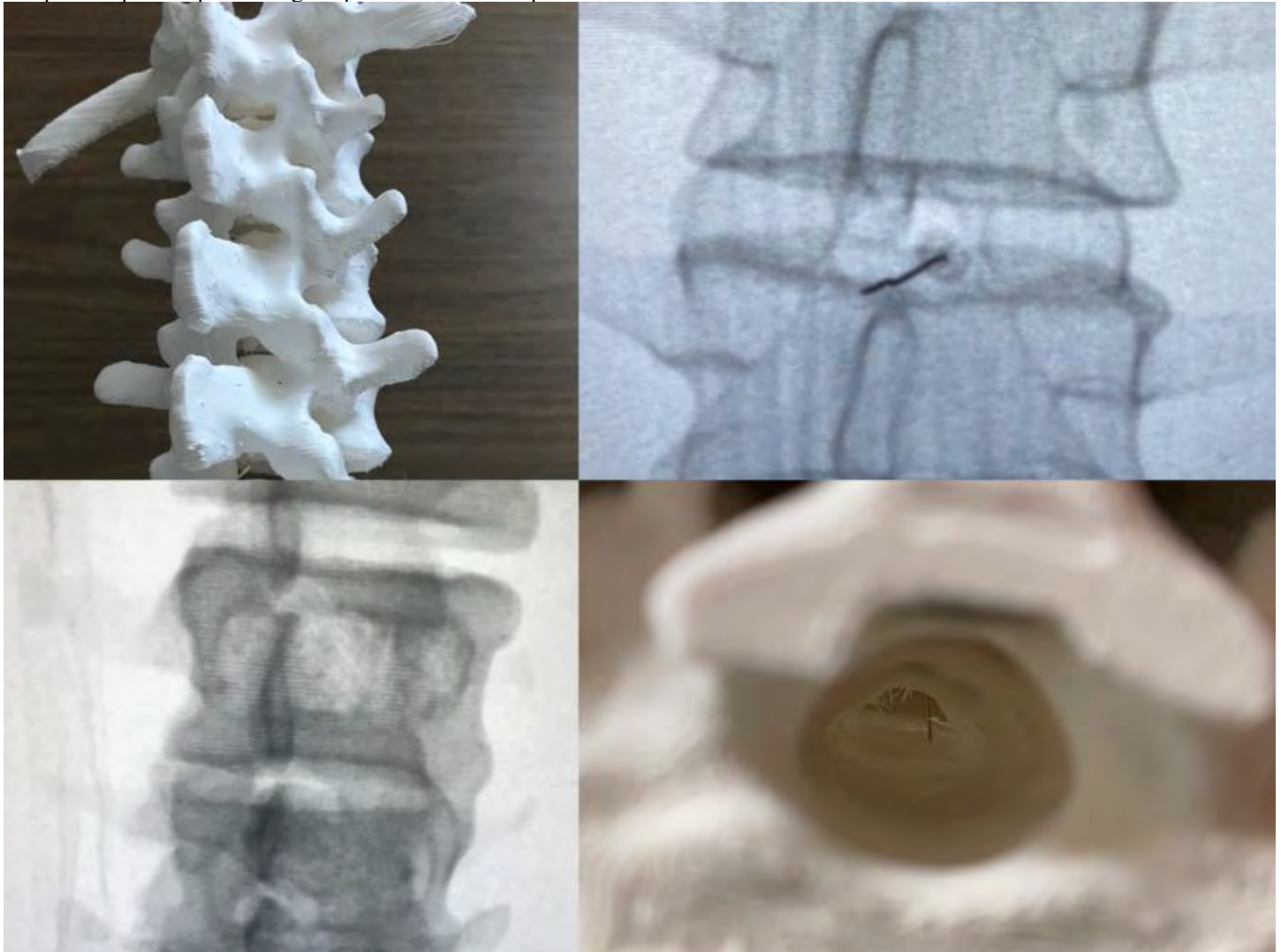
The purpose is to show how to create cost effective and reusable spine models for teaching and procedure training. These models which are visible under fluoroscopy allow radiology trainees to perform simulated fluoroscopy guided procedures such as lumbar punctures, thereby improving and demonstrating proficiency and minimizing the potential for patient harm.

Results

The exhibit reviews the steps to produce and use a patient specific 3D printed spine model. CT images of the lumbar spine were identified in PACS from patients with a normal lumbar spine and with a degenerated lumbar spine. DICOM images were transferred to our processing lab and software was used to convert the DICOM files to STL files. Printer specific software was then used to convert the STL file into the final print file utilized by the 3D printer. Print times can vary widely based on the size of the model as well as the density/resolution desired but these are print-specific settings that can be adjusted based on application. For the spine models here, print time was approximately 2-3 days. The patient specific 3D printed spine models were then used to review spinal anatomy with trainees and once confirmed to be visible under fluoroscopy were used to practice/simulate performing a fluoroscopically guided lumbar puncture. The spine was positioned prone on the fluoroscopy table with foam attached to the dorsal aspect and a fluoroscopically guided lumbar puncture was performed by the trainee with a 22 gauge spinal needle.

Conclusions

This exhibit demonstrates how patient specific 3D printed spines can be created and used as valuable tools for anatomy and procedure teaching. Prior simulation literature has focused on purchased commercial models and embedding in gel. These 3D printed models which are visible under fluoroscopy can serve as simple reusable models for practicing procedures such as fluoroscopically guided lumbar puncture. This can be integrated as part of a neuroradiology rotation for trainees to gain experience and demonstrate competence prior to performing the procedure on a live patient.



(Filename: TCT_509_SpinePicsASNR.jpg)

Cross-Border Teleradiology in Haiti as an Element of Neuroradiology Fellowship

K See¹, S Pinto¹, T Lu¹, G Hoang¹, S Patel¹, I Desai¹, S Zivin², A Parikh³, A Rajamohan¹, J Acharya¹

¹Keck School of Medicine of USC, Los Angeles, CA, ²Northwest Radiology Associates, Arlington Heights, IL, ³The Medford Radiological Group, P.C., Medford, OR

Purpose

Telemedicine is an invaluable asset, for its ability to transcend geographical boundaries, enable access to 24 hour coverage, increase interaction between subspecialists and reduce operational costs (1). A particularly advanced concept is cross-border teleradiology, which has been tried and tested in South Africa (2) and the European Union (3). There is still a paucity of data on the effectiveness of cross-border imaging in interpreting cross-sectional studies. At our institution, we partnered radiology fellows with board-certified attending radiologists to interpret neurologic and body CT studies through a portal in Port Au Prince, Haiti created between the locals and volunteers from a US non-profit organization. Our objectives were to evaluate the educational value of cross-border teleradiology during fellowship training, whether the project increases the participants' knowledge in the operational systems in cross-border teleradiology, and whether having participated in cross border teleradiology increases one's foreseeable likelihood in participating in similar global health endeavors in the future.

Materials and Methods

n/a

Results

Two ABR-certified attending neuroradiologists were coupled with 6 fellows in neuroradiology training. Each fellow signed up for a minimum of 3 volunteer shifts at Hospital Bernard Mevs in Port Au Prince, Haiti, utilizing an online platform set up by a non-profit organization. Hospital Bernard Mevs (HBM) is the only trauma and critical care hospital in Haiti, located in the Cite Militaire district of Port au Prince. A radiology department was set up in 2010 and 2011 in the aftermath of the earthquake, with a CT scanner and trained CT technologists. The fellows participated in 24-hour shifts, drafting reports for neurologic and/or body CT examinations, which were subsequently edited, along with images also directly interpreted by the attending Neuroradiologists at our institution. The reports were uploaded, and critical findings were discussed with the clinical team. The participating fellows then completed a survey after the completion of a minimum of 3 shifts. Questions of the survey include the following: On a scale of 1 to 10, how much did this exercise: Provide any educational value during fellowship training? Increase your knowledge in the operational systems in cross-border teleradiology? Increase your likelihood in participating in similar global health endeavors in the future?

Conclusions

n/a

841

Crucial Magnetic Resonance Imaging (MRI) Anatomical Landmarks for Correctly Staging Head and Neck Squamous Cell Carcinoma

G Guzman Perez-Carrillo¹

¹Mallinckrodt Institute of Radiology, St. Louis, MO

Purpose

The purpose of this educational exhibit is to illustrate the crucial head and neck anatomical landmarks in magnetic resonance imaging (MRI) utilized in the correct local staging of head and neck squamous cell carcinomas. The approach is based on anatomic localization, with an emphasis on the anatomy of the nasopharynx, oral cavity, oropharynx, hypopharynx, larynx, nodal levels, deep cervical spaces, pathways of perineural spread of disease and utilization of diffusion weighted images (DWI) to identify possible regions of locoregional tumor that need more meticulous characterization and evaluation. This is not designed to be a comprehensive review of all the anatomy of the head and neck, but to illustrate the most important anatomical landmarks to recognize in a comprehensive head and neck oncological imaging evaluation.

Materials and Methods

The purpose is to provide an educational exhibit with high-quality imaging that illustrates critical anatomical landmarks to recognize in a comprehensive MR imaging evaluation head and neck squamous cell carcinoma.

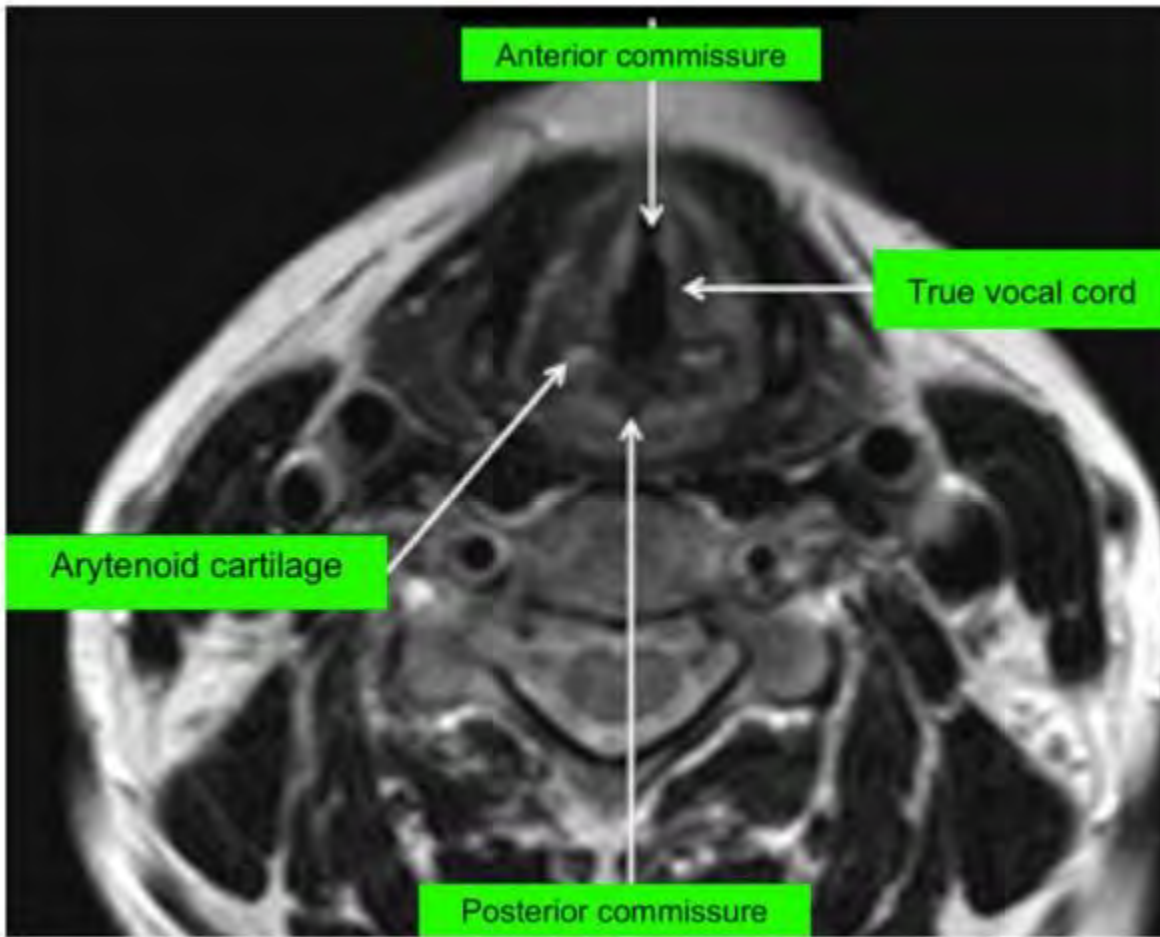
Results

This is a retrospective case review of a broad range of pathologically and clinically proven cases of head and neck neoplasms accumulated from 2000-2020 at multiple tertiary referral university medical centers and from a large private practice clinic with MRI service to the local university medical center. These are organized by location of the primary neoplasm and pertinent anatomy for the local staging. High quality anatomical and DWI images are used to illustrate the findings.

Conclusions

The viewer of this exhibit will gain or refresh information about critical MRI anatomy for the correct staging of head and neck squamous cell carcinoma that is useful in clinical practice and for certifying examinations. The images provided aid in recognition of

critical anatomical structures that must be thoroughly evaluated and categorized in order to arrive at the correct staging of head and neck squamous cell carcinoma. Staging of head and neck squamous cell carcinoma can present an imaging diagnostic challenge. Critical anatomy that needs to be recognized and evaluated for the correct staging of these tumors is fundamental to optimize patient care and outcome.



(Filename: TCT_841_ASNRHN2021.jpg)

1210

CT and Fluoroscopic Guided Epidural Injections: A Review of Current Indications, Techniques, Complications and Follow Up Care

P Joyce¹, E Velez¹, V Patel¹, A Rajamohan¹, P Kim¹, J Go¹, J Acharya¹

¹LAC + USC Medical Center / Keck School of Medicine USC, Los Angeles, CA

Purpose

The lifetime prevalence of developing spinal pain is reported between 54% and 80%, with oral therapy favored for short term relief and minimally invasive spinal intervention favored for longer term relief including epidural steroid injections. While CNS recurrence of non-Hodgkin's lymphoma is rare, ranging from 4% to 30%, patient outcome is severe when it occurs. Prophylactic administration of intrathecal chemotherapy can decrease recurrence, while studies on empiric therapy showing mixed results. With awareness of appropriate technique, patient selection criteria, contraindications, complications, and follow up care, interventionalists can provide these unique, safe and effective treatments for a wide range of patient populations. Objectives: ♣ Describe patient selection, preparation and contraindications ♣ Describe Fluoroscopic and CT technique while highlighting spinal anatomy ♣ Review appropriate pharmacology including recent literature on use of steroids, particulate vs nonparticulate steroid use and risk of chronic therapy ♣ Review complications and unique anatomic variants ♣ Review post-procedural and follow patient care

Materials and Methods

The goal of this exhibit is to familiarize radiologists, students and interested general practitioners with CT and fluoroscopic guided epidural injections with attention to patient selection, anatomy, techniques, complications and follow up care.

Results

Through literature review and our institution's experience, we will provide an image-rich presentation about patient selection, procedural technique, potential complications and tips to avoid them, and postprocedural/follow up care.

Conclusions

Epidural injections can be utilized for a broad range of patients ranging from reduction of spinal pain to instillation of chemotherapy. Prior studies reviewing epidural pain injections have shown that when image guidance is utilized by trained practitioners, complication rates range from 0.07% to 9.6%, with non-target injection occurring in 30% to 40% of cases when image guidance is not utilized. CT and fluoroscopic guided injections demonstrate varying rates of radiation exposure for both the interventionalist and the patient, thus requiring clinical judgment and experience to determine the most appropriate modality. Common procedural pitfalls include non-target injection into the retrodural space of Okada, intravascular injection, subdural injection, and intervertebral disc or spinal nerve injury.

158

CT Evaluation of Basilar Skull Fracture Patterns and Implication of Cranial Nerve Deficits

S Schoettler Woll¹, J Nickerson², J Thiessen²

¹Oregon Health and Science University, Portland, OR, ²N/A, N/A

Purpose

Skull-base fractures are a potentially devastating type of head trauma involving one or more of the three basal cranial fossae--anterior, middle, and posterior. Basilar skull fractures are most commonly seen in high impact traumas such as motor vehicle collisions, falls, and assaults. Depending on the specific fossae and bones involved in a basilar skull fracture, there are specific cranial nerves at risk. Computed tomography is most often the image modality of choice for initial investigation of basilar skull fractures. Using fracture patterns on CT imaging, diagnosticians can begin an evaluation of cranial nerves at risk. This educational exhibit describes different types of basilar skull fractures which put the 12 cranial nerves at risk, with CT examples.

Materials and Methods

This literature review is for educational purposes regarding development of critical knowledge for analysis of head CT for fractures and clinical picture that put specific cranial nerves at risk of injury.

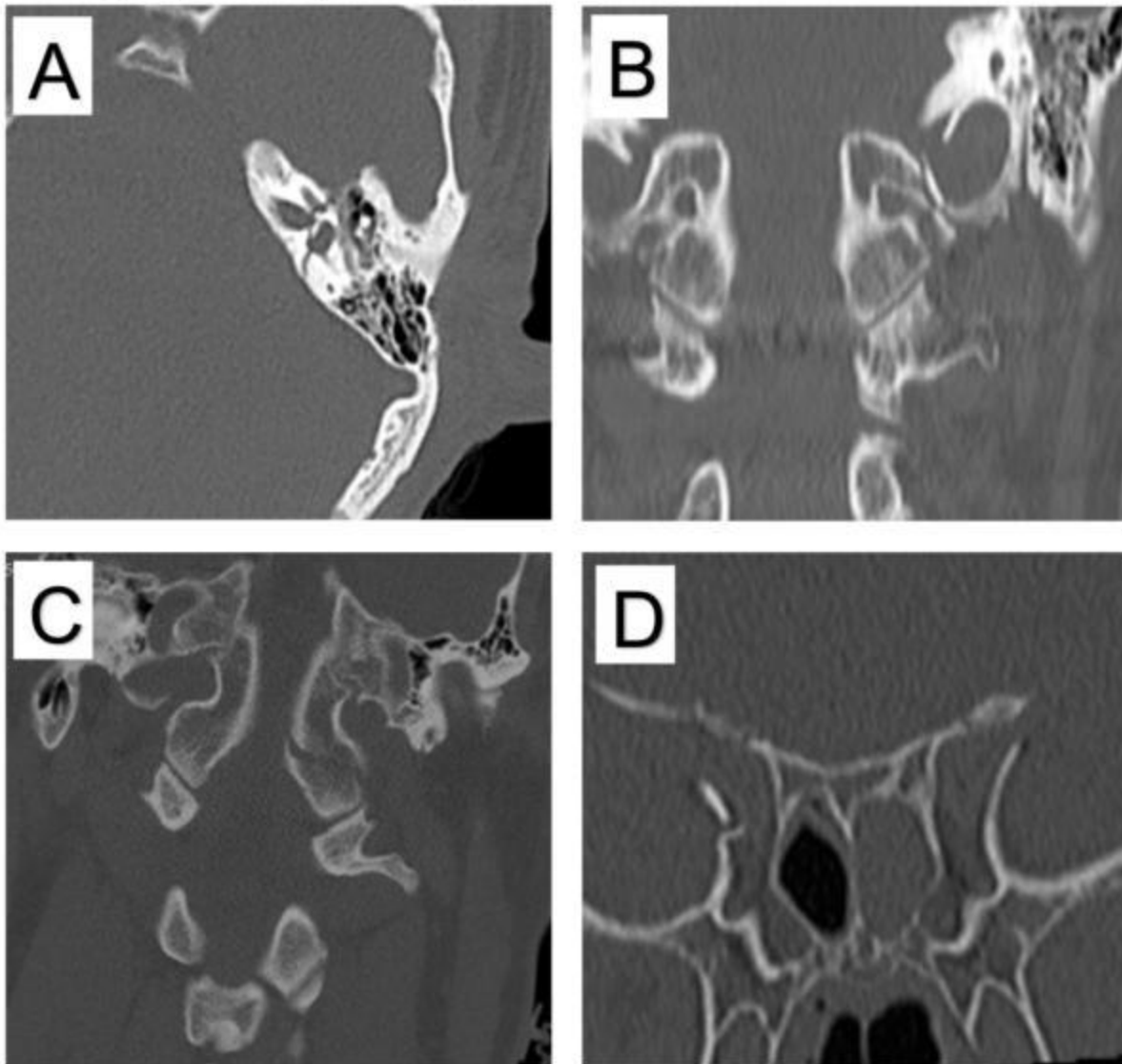
Results

Literature search of Pubmed database for articles for building an exploratory literature review on basilar skull fractures and associated cranial nerve deficits. Examples of fractures were obtained at Oregon Health and Science University.

Conclusions

The base of the skull has spatial relation to all twelve cranial nerves through the three cranial fossae. Cranial nerves I-VI are at risk in anterior fossa fractures, V-VIII nerves at risk in middle fossa fractures, and IX-XII nerves are at risk posterior fossa fractures. Evaluation of fracture extension near or through the calvarial foramen containing the exiting cranial nerve(s) can illuminate potential cranial nerve injuries. When approaching BSF, the first initial procedure for evaluation is a non-contrast head CT. Determining the anatomy that is affected by BSF can help indicate which cranial nerves are at risk of injury, whether it be direct entrapment by fragmentation of bone or through edema related to fractures. CT imaging findings can help correlate pathology with the clinical picture, and help determine the care plan for palsy or palsies. Additionally, when CT imaging does not show any pathology indicating nerve injury, but clinical features indicate a nerve palsy then MRI is the next step for evaluation.

Figure 1: (A) Axial non-contrast CT showing transverse fracture with fracture involving the internal auditory canal, and otic capsule concerning for CN 7 and 8 injury. (B) Coronal non-contrast cervical spine CT showing a complex left posterior fossa BSF extending into the left jugular foramen which puts CN IX-XI at risk. (C) Coronal non-contrast cervical spine CT showing left occipital condyle fracture extending through the inferior margin of the clivus and left hypoglossal canal putting CN XII at risk of impingement. (D) Coronal head non-contrast CT showing fracture of the right sphenoid traversing the right anterior skull base with extension across the right optic canal posterior right orbital roof.



CT-Guided Block and Radiofrequency Ablation of the C2 Dorsal Root Ganglion for Cervicogenic Headache: A Case Series

M Roytman¹, S Strauss¹, J Chazen¹

¹Weill Cornell Medicine/NewYork-Presbyterian Hospital, New York, NY

Purpose

Cervicogenic headache (CEH) is a secondary headache syndrome attributable to upper cervical spine pathology, with an estimated prevalence of 20% of patients with chronic headache. Due to the convergence of upper cervical segment nociceptive afferents with the trigeminal complex, pain from the upper cervical nerves may be referred to the occipital, orbital, frontal, and/or parietal regions. Potential culprit nerves include the greater occipital, lesser occipital and third occipital nerves, with the greater and lesser occipital nerves both receiving contributions from the C2 dorsal root ganglion (DRG). While CEH may occur from a variety of pathologies (e.g. tumors, fractures, infections, and arthritides), osteoarthritis of the lateral atlantoaxial joint with resultant C2 DRG irritation is an important, and potentially treatable, cause of CEH. We report a series of 7 patients in whom CT-guided C2 DRG block and radiofrequency ablation (RFA) was performed. Educational objectives of this exhibit include understanding the pathophysiology and diagnosis of CEH as well as recognizing the potential role and technical considerations of CT-guided C2 DRG RFA.

Materials and Methods

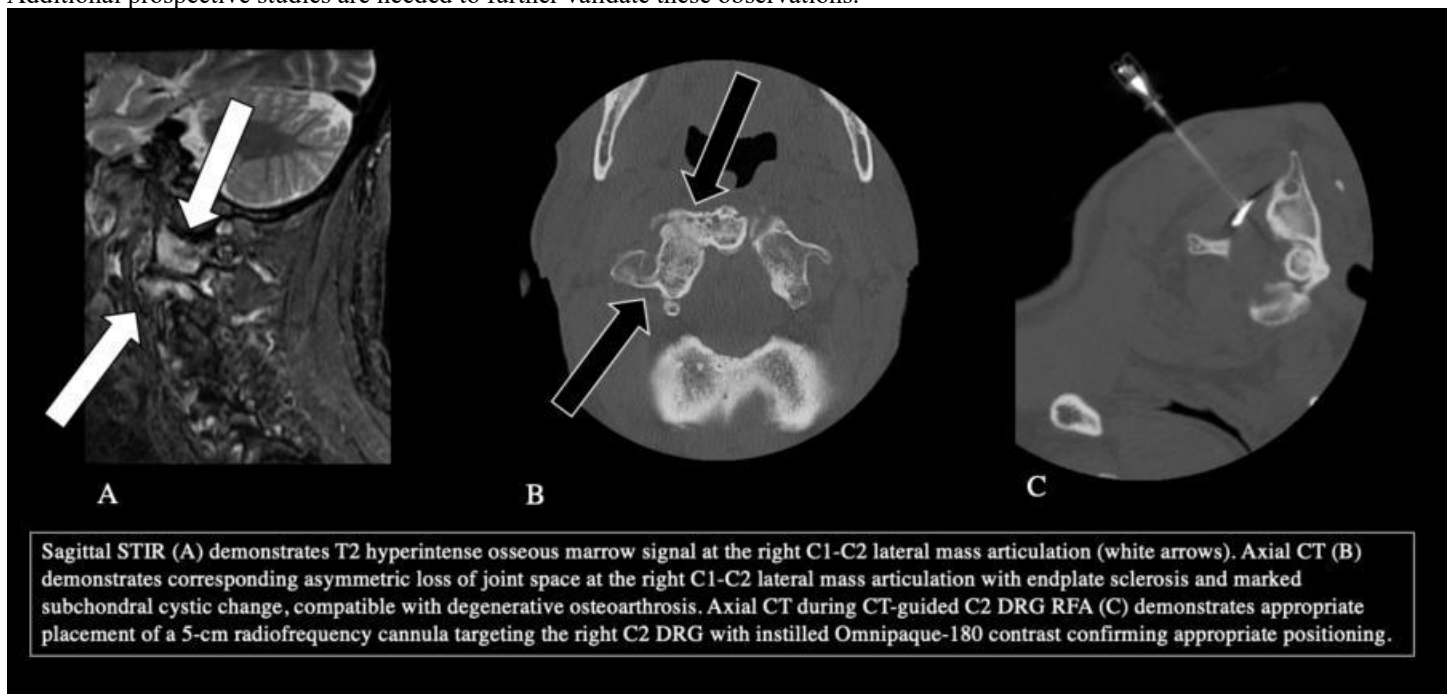
We present a series of 7 patients in whom CT-guided C2 DRG block and RFA was performed as well as describe technical considerations with a review of the pertinent literature for this procedure.

Results

Retrospective review of CT-guided C2 DRG block and RFA performed at our institution from 4/2014 through 9/2020. Seven C2 DRG RFAs were performed by a single radiologist with subspecialty training in neuroradiology. Patient cohort included 2 men and 5 women, with a mean age of 81.4 and standard deviation of 6.8 years (median, 79 years; range 73-92 years). CT-guided C2 DRG block was performed utilizing a standardized institutional technique, as previously reported [AJNR Am J Neuroradiol 40:1433–36].

Conclusions

All patients reported a reduction in subjective pain. Findings are in keeping with a single-center retrospective observational study of patients with refractory CEH and occipital neuralgia in which 16 patients underwent bilateral fluoroscopic-guided C2 DRG RFA with a 100% response rate; average of 78% pain reduction (median: 85%; range: 10-100%) for an average duration of 15 weeks (median: 25 weeks; range: 2-44 weeks) [Headache 2014;54:500-510]. These observations suggest a role for C2 DRG RFA in refractory CEH. Additional prospective studies are needed to further validate these observations.



(Filename: TCT_513_C2DRGRFAASNR.jpg)

Current Status and Future Challenges for Robotically Performed Neurointervention

W Crinnion¹, B Jackson¹, C Bergeles¹, H Liu¹, K Rhode¹, T Booth¹

¹Kings College London, London, London

Purpose

Introduction We present the benefits of robotically controlled endovascular intervention including reduction of radiation hazards to the operator and the possibility of remote intervention. **Overview of previous robotic systems used in cardiac and peripheral vascular intervention.** Current status in neurointervention **Presentation of the previous application of robotics to neurointervention.** **Limitations of current robotic systems** We describe the limitations of current systems and potential solutions including: haptic feedback, an appropriate master system, requirement for manual assistance and equipment compatibility. **Haptic Feedback and Master System Design** Haptic feedback is tactile feedback to the operator from the robotic master system. This is intended to simulate the feedback operators receive from endovascular catheters, guidewires and devices to safely navigate tortuous intracranial vasculature without complication. Currently no commercial robotic system incorporates haptic feedback. We summarise experimental attempts to incorporate haptic feedback into a robotic system. We discuss the methods for measuring forces applied to equipment including sensors at catheter tips, sensors in the slave device and model based solutions. Current commercial systems use joysticks however we present experimental systems which have designed controllers to more accurately mimic the movements performed by interventionalists. **Manual Assistance and Equipment Compatibility** All reported cases of robotically assisted neurointervention require manual assistance including the manual placement of a guide catheter close to the target pathology, manual manipulation of robotically incompatible equipment and manual deployment of certain devices. We describe the engineering capabilities required for a system to perform an entire procedure independently **Educational Objectives** • To understand the previous application of robotics to interventional procedures • To appreciate the current issues with available systems • To understand potential solutions for developing a fully functioning robotic platform for neurointervention

Materials and Methods

Recent advancements in robotic technology have led to the first in human robotically-assisted neurointervention [1] which paves the way for potential wider dissemination and the possibility of tele-operated intervention. Before this can be achieved a number of challenges must be overcome which we detail in this presentation.

Results

N/A

Conclusions

N/A

1536

Cystic Spinal Lesions: Spectrum of Imaging Findings

W Calderon¹, P Puac Polanco², C Torres², C Auger³, M Castillo⁴, A Rovira⁵

¹Hospital Universitari Vall d'Hebron, Barcelona, Catalonia, ²University of Ottawa, Ottawa, ON, ³Hospital Vall d'Hebron, Barcelona, Barcelona, ⁴Radiology, Chapel Hill, NC, ⁵Hospital Vall d'Hebron, Barcelona, Barcelona

Purpose

Summary: • Introduction. • Compartmental spinal anatomy. • Classification of cystic spinal lesions. • Imaging findings of cystic spinal lesions. **Objectives:** • To illustrate the anatomy of the different compartments in the spine. • To review & classify cystic spinal lesions based on their location & etiology. • To describe key imaging features of common & infrequent cystic spinal lesions using multimodality imaging. • To discuss the main differential diagnoses.

Materials and Methods

A wide variety of benign and malignant cystic lesions can involve the different compartments of the spine. Although an exact diagnosis may be challenging, distinct imaging features may be used in order to narrow the differential diagnosis and/or establish the exact diagnosis. In addition, spinal cysts can be divided into: intramedullary, intradural extramedullary, or extradural, depending on their location, which is extremely useful as well, as it helps to narrow the differential diagnosis. Magnetic resonance imaging (MRI) is the imaging method of choice to identify and characterize spinal cysts, and ultrasound (US) is often used as the initial imaging modality in pediatric patients. In this educational exhibit, we will review the key imaging features of common and infrequent spinal cysts, based on their location and etiology, using multiple imaging modalities.

Results

In this exhibit, key imaging findings of cystic spinal lesions will be reviewed. The lesions will be approached based on their location and etiology (i.e: neoplastic, congenital, degenerative, infectious, post-traumatic, and postsurgical). We will also review some of the mimics and differential diagnoses that should be considered.

Conclusions

Spinal cysts demonstrate different imaging features that vary depending on their location and etiology. Early detection, localization, and characterization of these lesions are key in order to decide patient management. Radiologists should be familiar with the common and infrequent types of cysts that can involve the spine, in order to guide further work-up and/or management.

Classification of meningeal spinal cysts



Type IA: extradural arachnoid cyst (no nerve root involvement)



Type IB: sacral meningocele



Type II: Perineural/Tarlov's cyst



Type III: intradural cyst

Nabors, MW, *et al.* J Neurosurg 1988; 68:366

(Filename: TCT_1536_Diapositiva2300.JPG)

802

Deadly Fungi: Imaging of Invasive Fungal Infections in the Head and Neck

C Tournade¹, T Moritani¹

¹University of Michigan, Ann Arbor, MI

Purpose

• Identify patient populations at risk for invasive fungal infections • Recognize imaging findings associated with invasive fungal infections • Identify complications of invasive fungal infections • Differentiate invasive fungal infections from other differential considerations

Materials and Methods

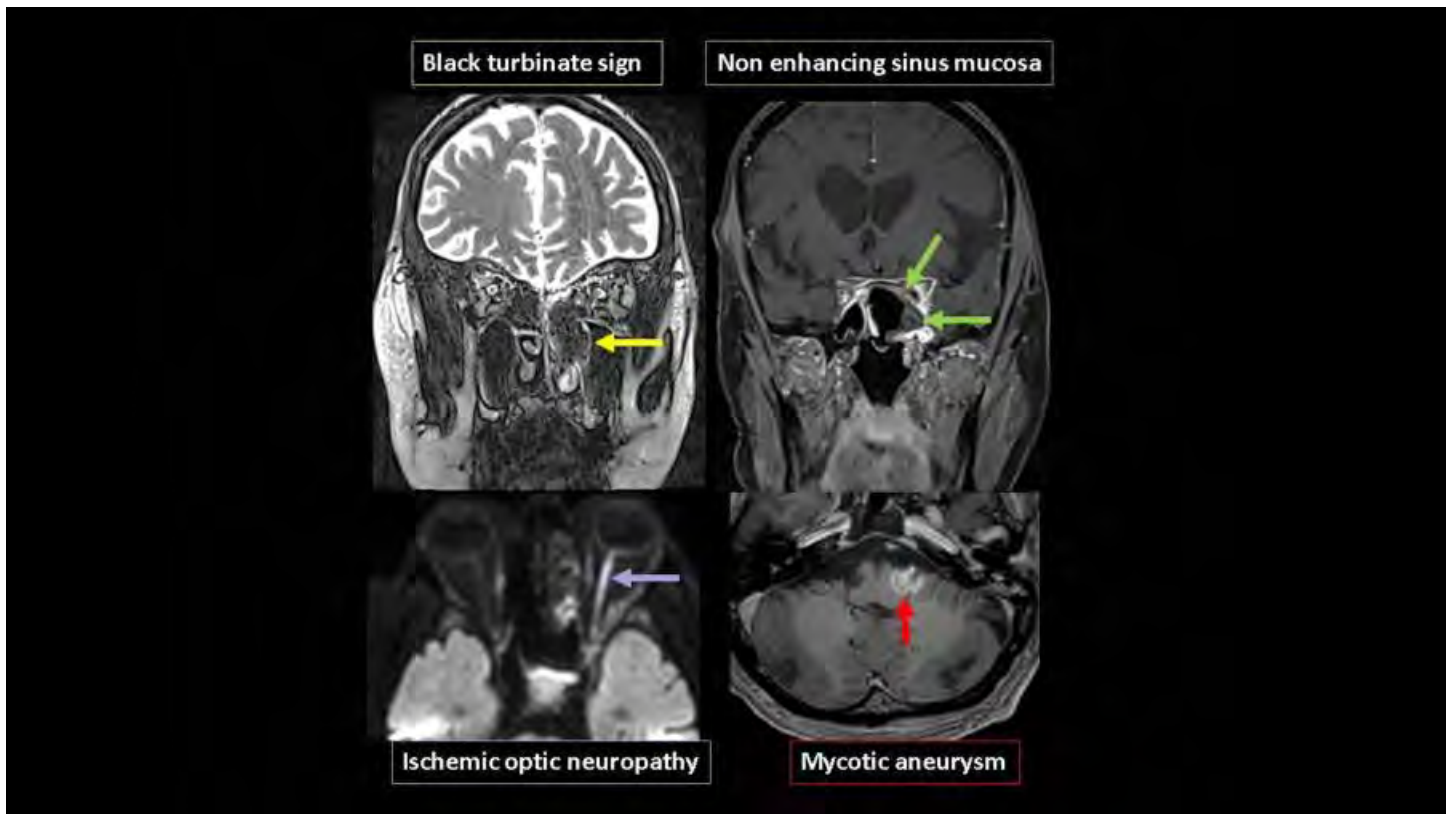
Fungal infections of the head and neck are most prevalent among patients who are immunocompromised and can lead to disastrous consequences if undiagnosed. These infections most often occur by direct extension or hematogenous spread and may lead to complications such as vascular invasion or intracranial or intraorbital extent. Early identification of these infections on imaging is critical to avoid significant morbidity and mortality in this patient population. It is similarly important to be aware of other potential pathologies which may appear similar to an invasive fungal infection in order to more expeditiously arrive at a diagnosis. By utilizing the clinical history, recognizing the associated imaging findings, and narrowing the differential from other potential processes, one can have a significant impact on patient care and management.

Results

Identify at risk patient populations to consider invasive fungal infections - Immunocompromised: Hematologic malignancy, organ or bone marrow transplant, immunodeficiency, diabetes, HIV, corticosteroid use Recognize imaging patterns and findings associated with invasive fungal infection -Aggressive nasopharyngeal disease -Black turbinate sign -Lack of enhancement of the nasal and sinus mucosa -Bone destruction -Orbital and periantral fat and extraocular muscle inflammation Identify complications associated with invasive fungal infections -Intracranial extension: Cerebral infarction and hemorrhage, abscess, leptomeningitis -Intraorbital extension: ischemic ophthalmopathy -Vascular invasion: septic vasculitis, mycotic aneurysm, cavernous or dural venous sinus thrombosis Recognize differential considerations

Conclusions

Invasive fungal infections can have a number of different imaging findings that may overlap with other diagnoses. Knowledge of these imaging findings with utilization of the clinical history to narrow the differential diagnosis will allow for faster identification of these disease processes on imaging in order to guide early patient treatment and prevent significant morbidity and mortality.



(Filename: TCT_802_Slide1.JPG)

350

Deciphering the clinical trials of immunotherapy in High-grade Gliomas: What a Neuroradiologist Needs to Know.

F Najmi Varzaneh¹, J Cui², J Ivanidze³, M Aboian¹

¹Yale New Haven Hospital, New Haven, CT, ²Brain Tumor Research Group, Yale University, New Haven, CT, ³Weill Cornell Medicine Radiology, New York, NY

Purpose

We review different types of immunotherapies including immune checkpoint inhibitors, oncolytic viral therapies, vaccines, and chimeric antigen receptor T cell therapy and their application in treatment of high-grade glioma. We focus on the outcomes of ongoing clinical trials regarding the effect of different immune checkpoint inhibitor agents on high-grade glioma. We also describe the imaging changes of high-grade glioma post immunotherapy and how iRANO criteria are being used.

Materials and Methods

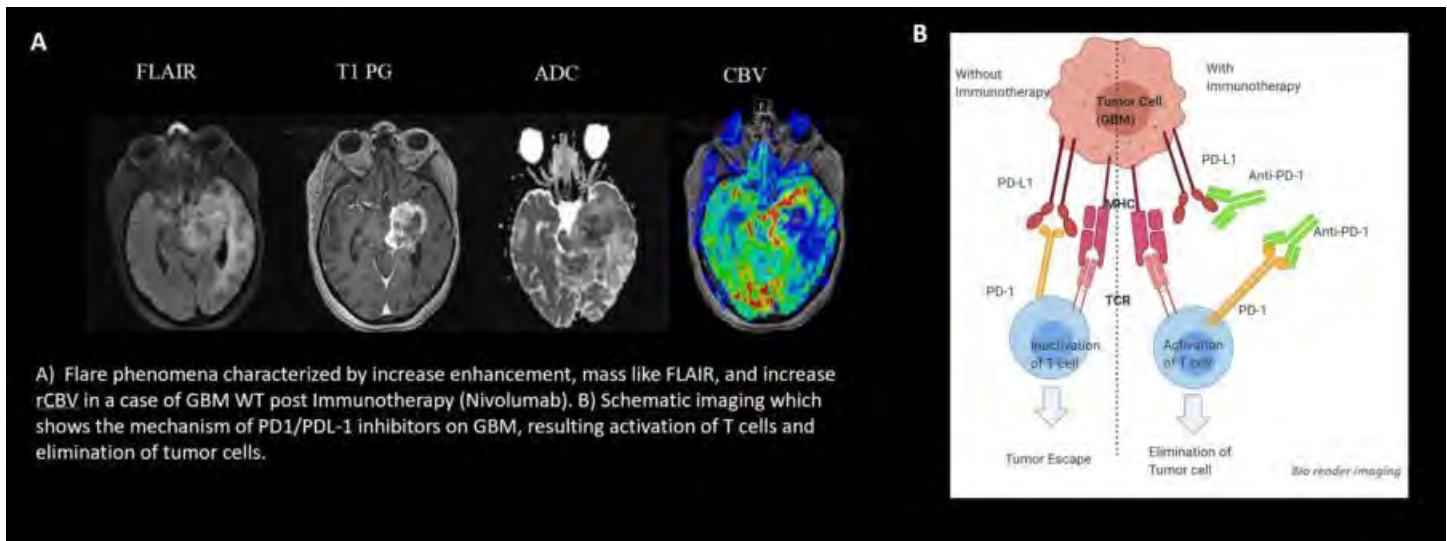
NA

Results

We review the literature and clinical trial protocols of immunotherapy approaches in treatment of newly diagnosed and recurrent glioma that are listed on clinicaltrials.gov. We also provide introductory curriculum for understanding immunology concepts and immunotherapy approaches.

Conclusions

Immunotherapy results in prominent flare phenomena which makes interpretation of standard and advanced MR imaging complicated and inconclusive. Our educational exhibit describes fundamental immunology concepts that are critical to understand immunotherapy. We provide detail information of past and current clinical trials including checkmate trials (143) which used immunotherapy as part of treatment in high grade glioma. We describe the MRI imaging criteria used in these trials (iRANO). We provide schema for interpreting standard and advanced MR imaging in high-grade glioma after starting different types of immunotherapy and step-by step guideline for imaging interpretation with respect to timing and imaging features.



(Filename: TCT_350_Capture-educaitona.JPG)

1440

Decoding the Mystery of Basal Ganglia and Thalamic Lesions

R HASSAN KARUVATH¹, B SINGH²

¹COLUMBIA ASIA, MALAPPURAM, KERALA, ²COLUMBIA ASIA REFERRAL HOSPITAL, BANGALORE, KARNATAKA

Purpose

Objectives: 1. To list the conditions that manifest as bilateral involvement of the basal ganglia and thalamus. 2. To describe the clinical, laboratory, and characteristic imaging features of these pathologies 3. Discuss the approach to narrow down the differential diagnoses for these conditions In our exhibit, we aim to provide a pictorial review of the pathologies that affect the basal ganglia and thalamus, and also provide an approach to narrow down the differential diagnosis.

Materials and Methods

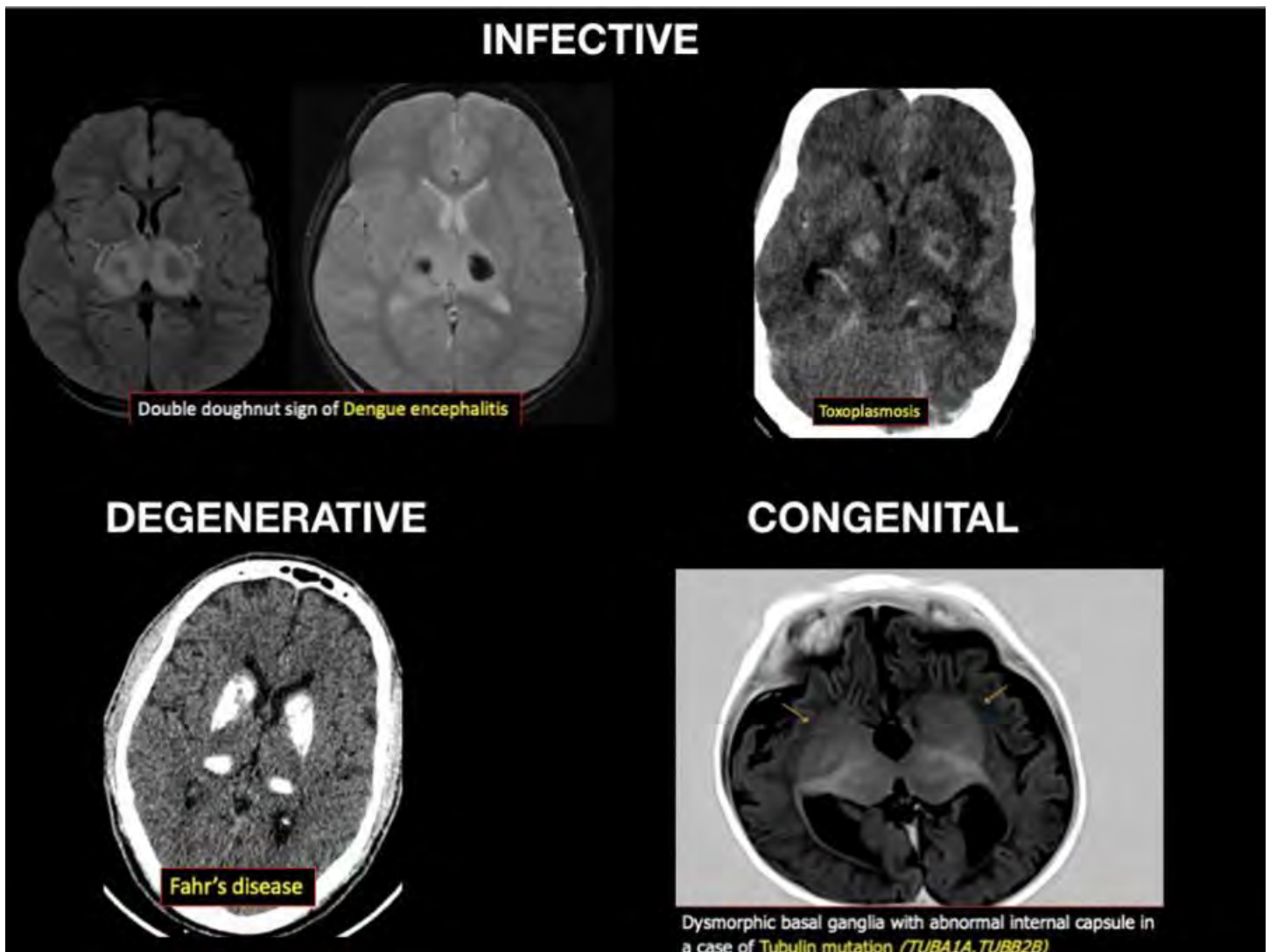
- The basal ganglia and thalamus are paired deep grey matter structures which form an integral part of the central nervous system.
- Both basal ganglia and thalamus are highly metabolically active and are involved in a variety of pathologies, the signal abnormalities of which can be quite intriguing and can be difficult to characterise.
- The pathologies affecting basal ganglia and thalamus can be broadly classified as systemic or local, which can be of acute or chronic onset and include metabolic, toxic, infectious, inflammatory, vascular, neuro degenerative disorders, neoplasms and miscellaneous disorders.
- In our exhibit we aim to illustrate and characterise the important pathologic conditions that manifest as signal abnormalities of basal ganglia and develop an approach to narrow down the differential diagnosis.

Results

- We retrospectively analysed the imaging characteristics of various basal ganglia and thalamic lesions in cases we came across in our hospital.
- The specific imaging features were reviewed with the clinical and laboratory details to diagnose and establish an approach to narrow down the differential diagnosis

Conclusions

Proper knowledge of the spectrum of pathologies and their differential diagnosis, careful assessment and correlation of other imaging findings with clinical and laboratory data is crucial to diagnose the spectrum of basal ganglia and thalamic abnormalities



(Filename: TCT_1440_asnrBG.jpg)

732

Deconstructing the Post-Treatment Neck - A Radiologist's Guide

H Saad¹, J Winkler¹, N Poyiadji¹, B Griffith¹, S Patel²

¹Henry Ford Health System, Detroit, MI, ²HENRY FORD HOSPITAL, DETROIT, MI

Purpose

Purpose: Imaging of the post-treatment neck is an important tool for detection of either complication or tumor recurrence in patients whose newly distorted anatomy prevents clinical detection of such complications. However, altered anatomy, post-operative scarring, and radiation effects also pose a challenge to interpreting radiologists when it comes to differentiating post-treatment change from tumor recurrence. The purpose of this exhibit is to simplify post-treatment image interpretation by reviewing treatment approaches in patients with head and neck malignancy, identifying types of neck dissection and surgical reconstruction, as well as acknowledging the potential complications of such interventions. A pictorial review of potential post-surgical and post-radiation complications and surveillance imaging findings will be presented in a case-based format, to help aid in the recognition of such findings on future post-treatment examinations. Approach/Methods: • We will review the indications for surgical intervention and radiation in patients with head and neck malignancy, and differentiate the different types of neck dissection (Fig 1) and surgical reconstruction, including relevant illustrations where needed. • We will provide a checklist for post-treatment imaging evaluation, including the primary treated malignancy, treatment type, and current clinical status. • Using a case-based format, we will provide a pictorial review of potential post-surgical complications including lymphocele (Fig 2), post-operative fistula (Fig 3), hematoma, and flap necrosis; post-radiation effects such as osteoradionecrosis (Fig 4), temporal lobe radiation necrosis, radiation induced vasculopathy and pseudoaneurysm, as well as cases of local and nodal recurrence and perineural spread of tumor. Summary/Conclusion: Evaluating the post-treatment neck on imaging can be challenging, and requires knowledge of not only the expected post-surgical and reconstruction neck appearance, but also an understanding of the potential post-surgical and post-radiation complications, as well as the appearance of disease recurrence.

This exhibit will provide viewers with an in-depth pictorial review of what to look for on future post-treatment neck imaging to ensure accurate interpretation.

Materials and Methods

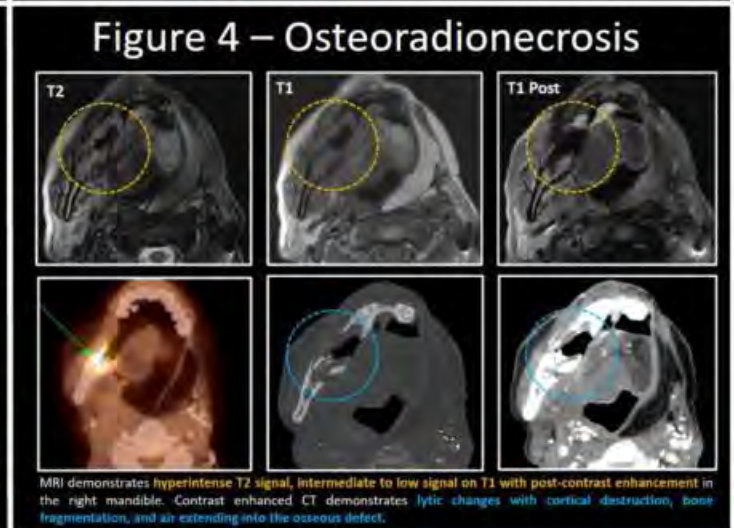
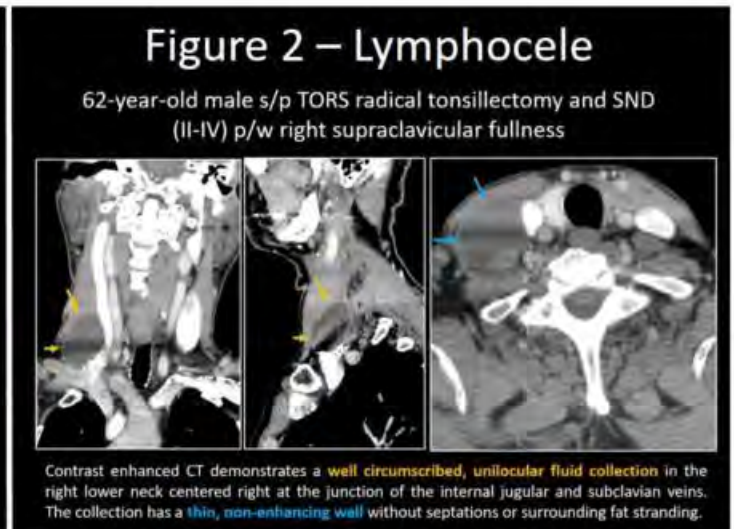
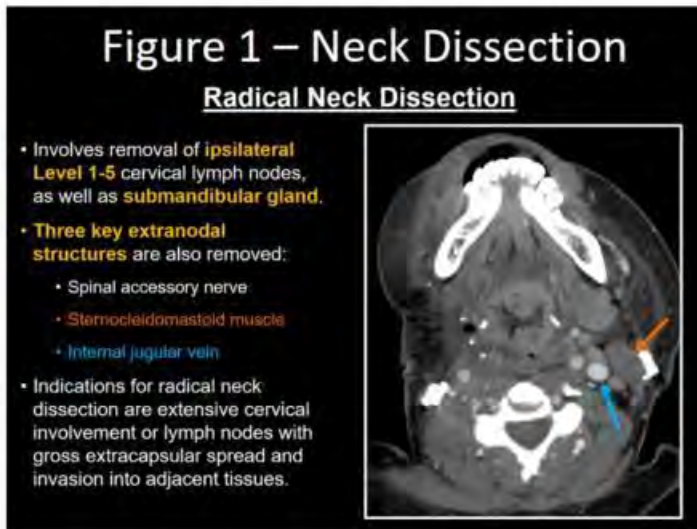
N/A

Results

N/A

Conclusions

N/A



(Filename: TCT_732_PostOpNeckFigureFinal.jpg)

1445

Deep brain stimulation: primer for neuroradiologists

M Hanaoka¹

¹University of Kentucky, Lexington, KY

Purpose

1. The basal ganglia and thalamus are vital subcortical structures involved in the regulation of autonomic, sensorimotor, associative, limbic, and endocrine functions. 2. Functional neurosurgery is an emerging field with a myriad of targets in the basal ganglia and thalamus to reversibly inhibit selected structures with deep brain stimulation (DBS) or ablate those structures using MR imaging-guided focused ultrasound. 3. Anatomic and functional understanding of key structures within the basal forebrain is essential for precise pretreatment localization and ideally posttreatment evaluation. 4. Susceptibility weighted MR imaging, advanced diffusion techniques and ultra-high-field in vivo MR imaging, and can improve target localization.

Materials and Methods

1. Describe the complex functional anatomy of the basal ganglia and thalamus on current clinical MR imaging and evolving advanced

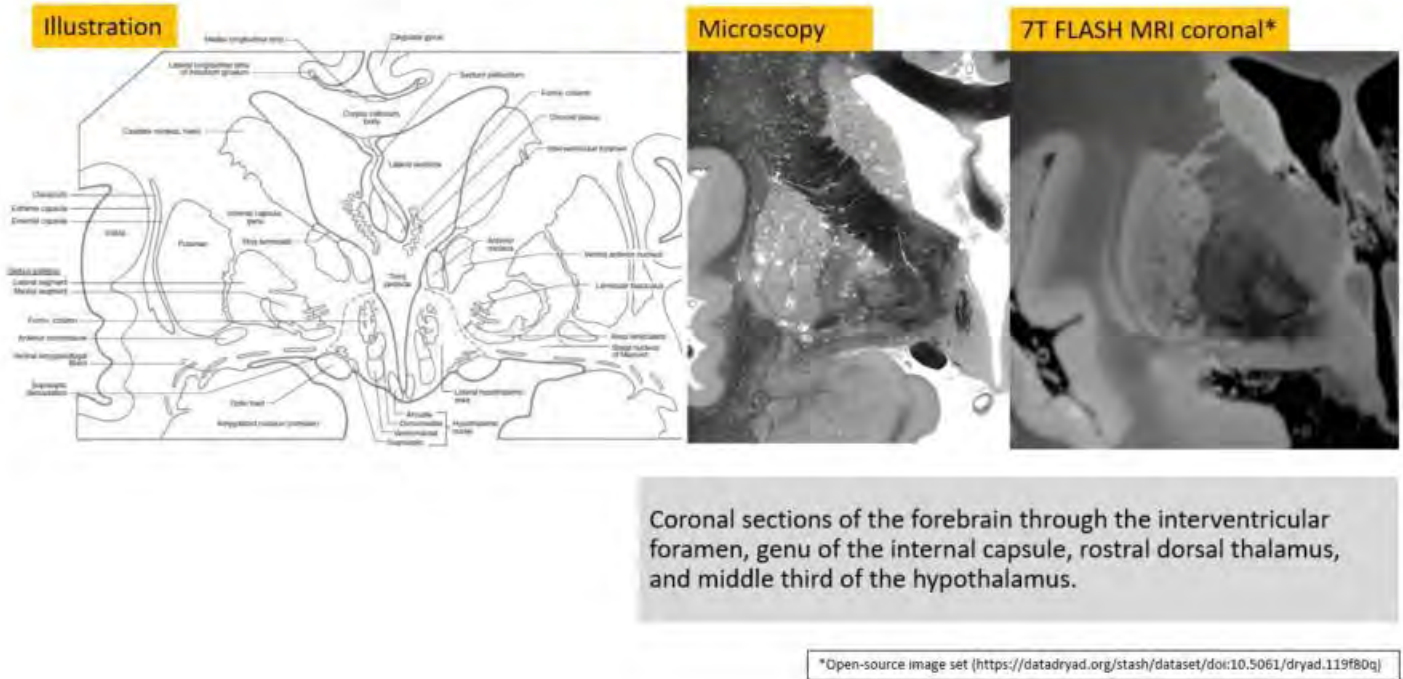
imaging techniques. 2. List common basal ganglia and thalamic pathologies amenable to treatment with functional neurosurgery, correlate them with their anatomic locations, and recognize their MRI findings. 3. Describe emerging functional neurosurgery applications with targets in the basal ganglia and thalamus

Results

NA

Conclusions

NA



(Filename: TCT_1445_1.jpg)

672

Demyelinating and Inflammatory Disorders of the Central Nervous System: A Case-based Review

S Lyo¹, R Minhas², V Velayudhan², Z Chaudhry³

¹SUNY Downstate Medical Center, Brooklyn, NY, ²SUNY Downstate Health Sciences University, Brooklyn, NY, ³State University of New York Downstate Medical Center, Brooklyn, NY

Purpose

Teaching Points The inflammatory and demyelinating disorders of the CNS are a heterogeneous group of disorders with significant clinical and neuroradiologic overlap. While most imaging findings are non-specific, certain imaging findings can suggest a specific diagnosis. We draw attention to these findings in a case-based quiz format while reviewing the spectrum of inflammatory and demyelinating CNS disease. Table of Contents/Outline • Inflammatory and demyelinating disorders • Autoimmune demyelinating - Multiple sclerosis (MS) -Neuromyelitis Optica Spectrum (NMO) -Tumefactive demyelinating lesion (TDL) • Infectious demyelinating -Acute disseminated encephalomyelitis (ADEM) -Progressive multifocal leukoencephalopathy (PML) -Differentiation from HIV Encephalitis/Toxoplasmosis • Inflammatory/Vascular -Sarcoidosis -Lupus -Susac syndrome -Autoimmune limbic encephalitis - Vasculitis -Cytotoxic lesions of the corpus callosum • Toxic metabolic -Marchiafava-Bignami -Osmotic demyelination • Comparison table highlighting key points

Materials and Methods

N/A

Results

N/A

Conclusions

N/A

Which of the entities listed below is the most likely diagnosis in this 18 y/o M with h/o fever, headache, altered mental status and recent viral illness?

- A) Marchiafava-Bignami disease
- B) Central Pontine Myelinolysis
- C) Acute obstructive hydrocephalus
- D) Acute disseminated encephalomyelitis (ADEM)**

ADEM

Etiology:

- Thought to result from cross reactivity of a viral antigen resulting in **autoimmune demyelination**
- Usually follows a recent viral illness or less commonly after vaccination (less than 5% of cases)

Imaging Findings:

- large white matter lesions
- involvement of **deep gray structures** (especially thalamus)
- Spinal lesions
- Calloseseptal interface typically spared

Treatment:

- High dose steroids, IV immunoglobulin (IVIG), and cyclophosphamide, if refractory
- Approximately 30% have permanent sequelae, usually seizure
- Small percentage have fulminant course with hemorrhage (acute hemorrhagic leukoencephalitis, Hurst variant)



FLAIR demonstrate confluent areas of abnormal signal in the **deep and periventricular white matter** of the frontal, parietal and occipital lobes, **corpus callosum** and **basal ganglia**. The **majority of lesions enhance**, on postcontrast MRI suggesting that this is a **monophasic disease**.

(Filename: TCT_672_DemyelinatingAndInflammatory-Question5.jpg)

109

Demystifying CNS Intravascular Lymphoma (IVL): Five Key Imaging Features For Prompt Diagnosis

M Isikbay¹, S Cha¹

¹University of California San Francisco, San Francisco, CA

Purpose

The key imaging features described here help keep CNS IVL on the differential. Other diagnosis to consider are: stroke, primary angiitis of CNS, and atypical infection. Definitive tissue diagnosis relies on prompt imaging diagnosis and radiologists to raise the suspicion CNS IVL. Key teaching points from this work include the following: 1. CNS IVL has a nonspecific clinical presentation. 2. Imaging features of CNS IVL can be variable and nonspecific however there are five key imaging features that aid in a prompt diagnosis. 3. Definitive tissue diagnosis can be expedited based on imaging features.

Materials and Methods

Central nervous system intravascular lymphoma (CNS IVL) is a condition that can affect the cerebral vasculature by causing occlusion of both arteries and veins throughout the anterior and/or posterior circulation. Given this pathophysiology the clinical presentation of this condition is varied, including symptoms ranging from cognitive impairment to paralysis. Similarly, there is a wide array of imaging findings that may also be seen in the setting of CNS IVL. This variability can make it a difficult diagnosis to consider, which is unfortunate given the importance of expedient identification for clinical management. The purpose of this work is to provide an organized framework for identifying key imaging features that help reliably make the prompt diagnosis of CNS IVL.

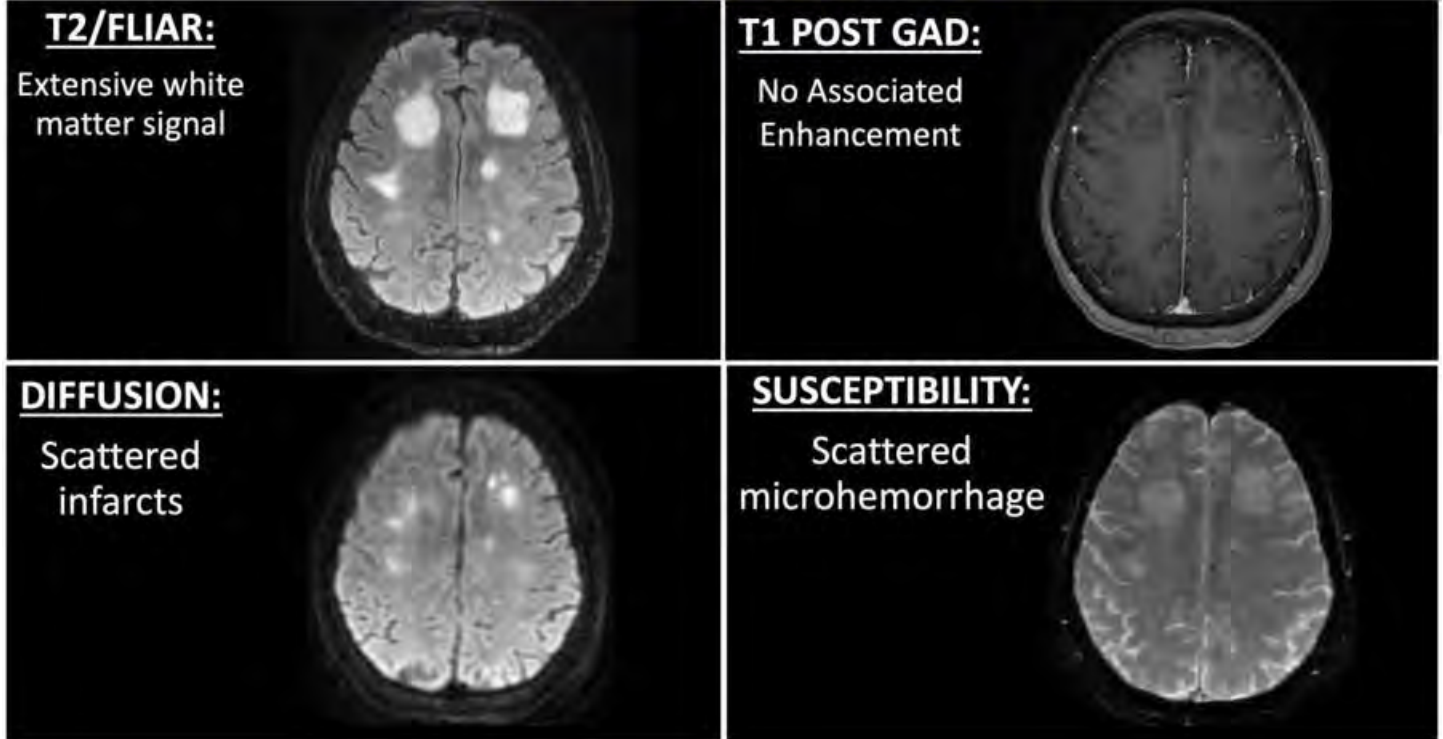
Results

Cross sectional imaging from 8 patients with biopsy confirmed CNS IVL was analyzed and organized by imaging findings relative to modality/sequence to highlight key patterns.

Conclusions

Standard MR imaging (including diffusion/susceptibility sequences) is necessary for the diagnosis of CNS IVL and there are five key imaging features for this condition which include: 1. Multifocal pattern of acute intra-parenchymal hemorrhage in non-vascular territories. 2. Atypical pattern of white matter lesions distinct from chronic microvascular ischemia on T2/FLAIR MR imaging. 3. Minimal to no contrast enhancement with white matter lesions. 4. Scattered acute infarcts on diffusion not always corresponding to white matter lesions. 5. Various patterns, size, and distribution of scattered microhemorrhages on susceptibility sequences.

MRI CHARACTERISTICS OF CNS IVL



(Filename: TCT_109_ASNR2021CNSIVLFigure.jpg)

1420

Demystifying Intricate Brachial Plexus and its Pathologies - MR Imaging Comes to The Rescue!

S More¹

¹K.E.M hospital, Mumbai, Maharashtra

Purpose

AIMS AND OBJECTIVES 1.To look for traumatic injuries to brachial plexus and categorize them into pre-ganglionic and postganglionic. To look for nerve injuries in continuity and without continuity and predict the prognosis. 2.To diagnose and differentiate benign from malignant lesions (tumors) of brachial plexus 3.Early diagnosis of Brachial plexitis 4.To differentiate radiation plexopathy from tumor recurrence 5.To rule out structural causes of TOS and look for dynamic compression in abduction position.

Materials and Methods

The brachial plexus is a complex neural network that supplies motor and somatosensory innervation of the arm, shoulder, and upper chest. In many cases, imaging has an important role in lesion localization and characterization and affects the management of traumatic and nontraumatic brachial plexopathies. In this exhibit we provide a case based review of different pathologies of brachial plexus.

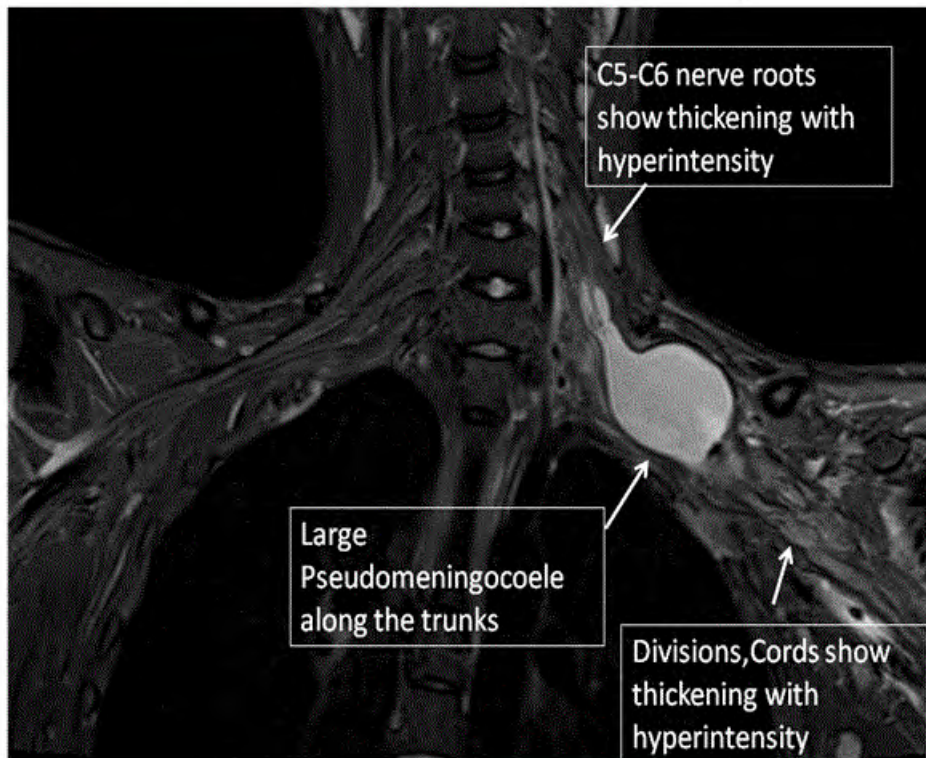
Results

In this study I reviewed cases of MRI brachial plexus for clinical symptoms, physical examination and electrophysiological findings along with imaging findings. MRI study consisted of both 2D and 3D MR imaging sequences. 3D fluid sensitive sequences specifically useful to assess preganglionic nerve root avulsion and to evaluate the entire extent of the injury.

Conclusions

MRI can evaluate both direct and indirect signs of nerve injury. Direct nerve injury is seen as T2/ STIR hyperintensity or nerve thickening or discontinuity or neuroma formation. Indirect signs of nerve injury i.e muscle denervation changes are seen as muscle edema (acute) or atrophy (subacute) or fatty replacement (chronic). Brachial plexopathies are broadly of two types: traumatic and non-traumatic pathologies. In traumatic group, MRI plays crucial role in early and accurate diagnosis, differentiating preganglionic and postganglionic, partial or complete injuries and in turn the appropriate management of these injuries. MRN depicts the nerve continuity with or without neuroma formation, or may show a completely disrupted/ avulsed nerve, thereby aiding in nerve-injury grading for preoperative planning. Non traumatic pathologies can be classified as neoplastic, brachial plexitis, degenerative and thoracic outlet syndrome (TOS). TOS can be vasculogenic or neurogenic or both.

Both- Preganglionic and Postganglionic Injury



(Filename: TCT_1420_ezgifcom-gif-maker1.gif)

1227

Demystifying the Central Skull Base Lesion: Core Anatomy and Case Review

M Chong¹, T Campion²

¹Royal London Hospital, London, United Kingdom, ²Barts Health NHS Trust, London E1 1BB, London

Purpose

Know the bony and foraminal anatomy of the central skull base and its parenchymal and neurovascular relations. List the major pathologies that arise from or involve the central skull base. Develop an approach that can help distinguish these diagnoses on the basis of imaging. Describe important potential complications of these pathologies with regard to involvement of structures in and around the central skull base.

Materials and Methods

To provide an educational review of the imaging appearances of central skull base pathology with a focus on relevant anatomy and real-life case examples.

Results

The range of pathologies that can affect the central skull base is diverse. This is an anatomically complex area with numerous foramina containing intricate neurovascular structures. It is essential that the reporting neuroradiologist has expert knowledge of common and uncommon lesions that may arise from or involve the central skull base in order that they can provide an appropriate differential diagnosis and help guide management by the multidisciplinary team. The neuroradiologist plays an invaluable role in the mapping of tumor anatomy to safely facilitate surgical intervention and tissue biopsy for histological analysis. Features that can assist in narrowing the differential include anatomical location, for example the tendency of chordoma to arise near the spheno-occipital synchondrosis, and the paramidline location of chondrosarcoma. MRI signal characteristics such as the T2 hyperintensity of chordoma and chondrosarcoma, the relative intermediate T2 signal of nasopharyngeal carcinoma and low/intermediate signal of plasmacytoma are additional useful features. The complementary use of CT and MRI imaging can further aid in diagnosis, for example in fibrous dysplasia where appearances on MRI may be variable, but a more typical ground-glass appearance is frequently demonstrated on CT.

Conclusions

In our educational presentation we review core concepts in the anatomy of the central skull base and its related neurovascular structures, the imaging features of important central skull base lesions and an approach to rationalising the differential diagnosis. This teaching is delivered using example cases of imaging from our Tertiary Neurosciences and Head & Neck centre.



Fig 1. Intracranial CT angiogram demonstrating a destructive central skull base lesion encasing the basilar artery. This proved to be a chordoma following surgical resection.



Fig 2. CT Head reveals an expansile, destructive lesion with soft tissue component involving the central and anterior skull base and ethmoid sinuses. This is an example of nasopharyngeal carcinoma.



Fig 3. CT Sinuses shows a mass infiltrating the central skull base involving the whole clivus. On MRI (not shown) there was encasement of the cavernous and supraclinoid segments of both internal carotid arteries. Surgical biopsy confirmed a pituitary macroadenoma.



Fig 4. CT Head demonstrates a large expansile central skull base lesion involving the clivus and basisphenoid. On MRI (not shown) T2 intermediate-low intensity was less in keeping with chordoma or chondrosarcoma. Following whole body CT and bone marrow biopsy this was confirmed to be a plasmacytoma (multiple myeloma).

Dental and Mandibular Lesions: Illustrative Review of an Easily Overlooked Topic

L Tu¹, M Adin², J Aslam³, W Zucconi⁴, A Mahajan², I Ikuta⁵, A Abou Karam⁶

¹*Yale School Of Medicine, New Haven, CT*, ²*Yale University, New Haven, CT*, ³*Yale University School of Medicine, Staten Island, NY*, ⁴*N/A, N/A*, ⁵*Yale University School of Medicine, New Haven, CT*, ⁶*Yale Medicine, New Haven, CT*

Purpose

Illustrative review of dental and mandibular lesions, with focus on details of interest to differing audiences - Acquired and common lesions - Common odontogenic and non-odontogenic tumors - Rare lesions and their pathologic classification - Congenital and miscellaneous lesions

Materials and Methods

Dental and mandibular lesions are often visualized on imaging of the brain, face, neck, and cervical spine. Often, these are incidental, and relate to dental/periodontal disease or trauma. Uncommonly, congenital and neoplastic lesions of the support structures of the teeth are detected. This topic may not be covered in depth by educational materials at the residency and fellowship levels. The purpose of this exhibit to provide an accessible, illustrative review at graded levels of detail for the trainee, general radiologist, and neuroradiologist.

Results

We first review the existing literature, which is summarized with regard to the role of imaging in the detection and evaluation of dental and mandibular lesions. The institutional radiology database at a large academic center is queried for common and uncommon pathologic lesions. Illustrative examples are presented via case review, with a focus on the differential of radiographically lucent abnormalities. Where relevant, lesions are correlated with the most recent WHO classification of Odontogenic and Maxillofacial bone tumors (4th edition, 2017).

Conclusions

First, normal radiographic anatomy of the tooth, support structures, and mandible are reviewed. Acquired lesions related to dental/periodontal disease, trauma, and their adjacent complications in the head and neck are discussed. Neoplastic lesions involving the teeth and mandible are reviewed next, with a focus on entities all imagers should have familiarity with. Brief review of the rare lesions and their pathological categorization, as might be in interest to subspecialists is also included. Odontogenic lesions covered include odontoma, ameloblastoma, and odontogenic carcinoma/sarcoma, among others; non-odontogenic lesions include osteoma, fibrous dysplasia, central giant cell lesion/granuloma, and squamous cell carcinoma (of the mandible) and others. Finally, non-neoplastic congenital and other/miscellaneous lesions are reviewed. Dental and mandibular lesions can be an easily overlooked topic in general and sub-specialty neuroradiology education. We present a case-based, graded review, tailored to the needs of varying audiences who will encounter these in head and neck, and other neuroimaging.

415

Diagnostic utility of Portable Ultra-Low Field Strength MRI in diagnosis of critical pathology in a neurological intensive care unit setting.

J Aslam¹, S Onderi¹, M Adin¹, K Sheth², M Mazurek², M Yuen², A Prabhat², B Cahn², I Chavva², G Sze¹

¹*Yale University School of Medicine, New Haven, CT USA*, ²*Yale University, New Haven, CT USA*

Purpose

Portable low-field-strength MR imaging is an emerging technique with promising results with regards to timely diagnosis of critical pathology in patients encountered in challenging settings. This is of particular importance in the neurological ICU where patients' mental status, difficulty with mobilization, time constraints and other limitations can potentially delay diagnosis and care. The ability to transport the scanner and perform diagnostically useful bedside MRI scans in the presence of numerous ferrous materials, and without the need for helium makes it a powerful addition to the care of patients in the critical care setting (1-4). In this pilot study, we found that a significant proportion of life-threatening intracranial pathologies can be meaningfully detected on portable MRI scan (70%).

Materials and Methods

To investigate the diagnostic performance of an ultra-low field portable MRI scanner in diagnosis of critical pathology in patients admitted to the neurological intensive care unit, compared to conventional high field MRI scan.

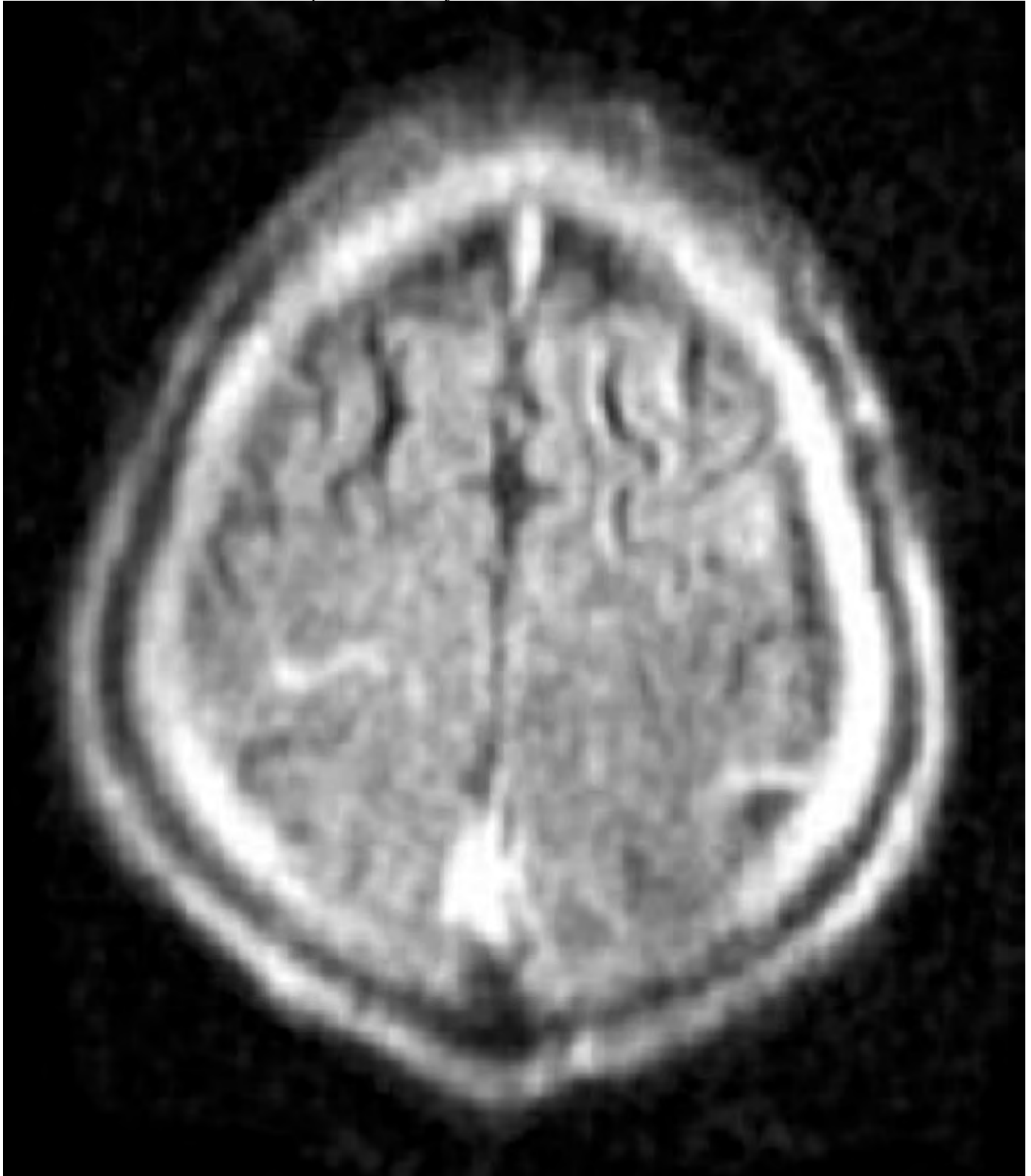
Results

Bedside point of care MRI scans (POC) were performed with a prototype 0.064-T MRI system (Hyperfine Research Inc) using an 8-channel head coil. Conventional standard of care MRI scans (SOC) were performed using one of the 1.5T or 3T scanners using a 32-channel linear arrayed head coil. Two neuroradiologists independently reviewed POC and SOC images using Radiant DICOM Viewer and PACS workstation respectively. Findings were classified as major and minor/lesion characteristics.

Conclusions

71 subjects (male=35, Age range: 19-90, median: 62, IR: 20) with intracranial pathology had both POC and SOC studies. POC scans were obtained within a few hours to a few days after the SOC scans which were used as a gold standard reference. 53 cases had major

findings diagnosed on SOC, 43(81.1%) of which were appreciable on POC images. 50 (70.4%) pathologies were identified on POC and 21 were not identified on POC MRI. Of these 50, 44 (88%) were major findings. Of 43 cases with major findings, 30 (70%) had at least one minor finding or lesion characteristics that were of diagnostic significance. Eleven of 20 hemorrhages (55%), 8 out of 11 infarcts (72%), 3 of 3 (100%) tumors were identified but not adequately assessed on POC MRI. Out of 10 major lesions that were not identified at POC MRI, two were due to patient related major artifacts and three were infratentorial lesions.



(Filename: TCT_415_POCMRI.jpg)

Different Faces of Parathyroid Adenoma: An Educational Primer on the Various Appearance of Parathyroid Adenomas using 4D CT

A Kumar¹, C Ge², A Kulkarni¹, S Dundamadappa¹

¹University of Massachusetts, Worcester, MA, ²University of Massachusetts Medical School, Worcester, MA

Purpose

Parathyroid adenomas are traditionally evaluated with ultrasound and nuclear medicine imaging, such as sestimibi scans. 4D CT is a relatively new method which clinicians are now employing to better assess the location of the parathyroid adenoma and provide precise anatomic details to assist with surgical planning. The classic imaging appearance of parathyroid adenomas on 4D CT is hypodense on noncontrast, arterial enhancement, and venous washout. This is not always the case. Often, these lesions do not demonstrate significant venous washout, some have delayed enhancement, and others are nonenhancing. The goal of this exhibit is to assist the neuroradiologist in evaluating parathyroid adenomas by demonstrating the classic appearance on 4D CT and also the many other faces which these lesions can demonstrate. Educational Objectives: 1. Understand the use of 4D CT to image parathyroid adenomas. 2. Identify classic imaging features of parathyroid adenoma using 4D CT. 3. Identify mimics and other imaging features of parathyroid adenoma using 4D CT.

Materials and Methods

N/A

Results

N/A

Conclusions

N/A

186

Differential Diagnosis of Unilateral Lesions in the Basal Ganglia and Thalamus

F Assunção¹, T Scoppetta¹, L Martins¹, L Freitas², E Narvaez², C Campos², B Inada², V Marussi², L do Amaral²

¹Hospital São Camilo, São Paulo, SP, ²BP - A Beneficência Portuguesa de São Paulo, São Paulo, SP

Purpose

The basal ganglia are involved in a variety of brain functions, including voluntary motor control, action gating, movement timing and procedural learning, among others. Their high metabolic activity explains the vulnerability to various conditions in which blood/oxygen/energy levels are diminished. As a consequence of its vulnerability, bilateral and symmetrical involvement of the basal ganglia is commonly seen. Bilateral presentation has already been widely discussed in the literature and does not escape from the usual well-known causes. The goal of this digital paper is to illustrate and discuss pathologies with unilateral involvement of the basal ganglia, including common conditions with atypical presentations.

Materials and Methods

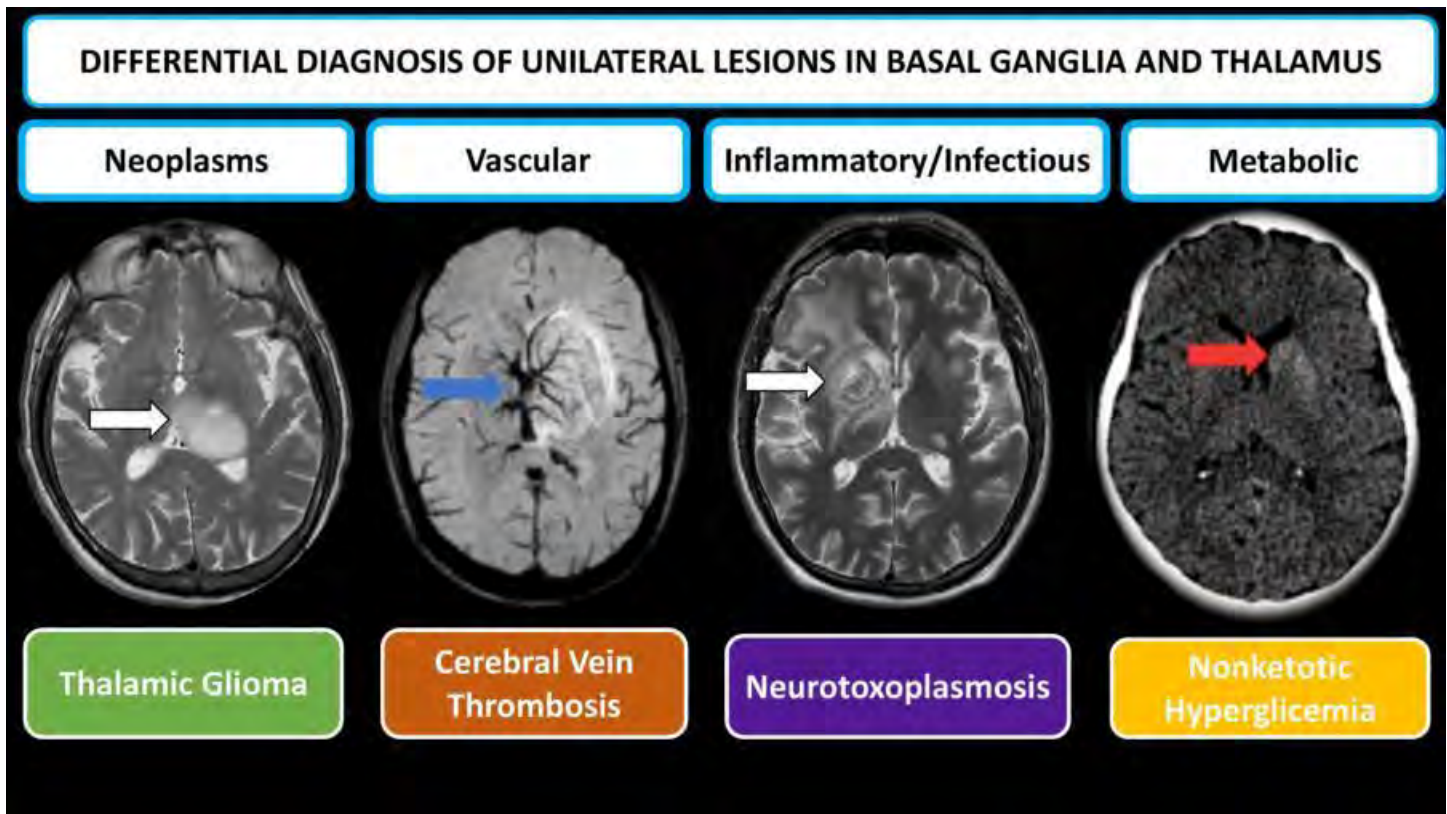
- To review the basal ganglia (BG) and thalamus anatomy. - To quickly revisit the main pathologies that present with basal ganglia involvement. - To approach the unilateral basal ganglia and thalamus involvement, highlighting the imaging clues for the differential diagnosis.

Results

We performed a retrospective and descriptive study of brain MRI of patients diagnosed with unilateral lesions in basal ganglia at our services.

Conclusions

We found several cases of unilateral involvement of the basal ganglia and thalamus and for better understanding we organize the pathologies in groups: neoplasms (thalamic glioma, lymphoma, metastasis), vascular conditions (hypertensive hemorrhage, cerebral deep venous thrombosis, ischemic stroke, cavernomas, arteriovenous malformation, capillary telangiectasia, developmental venous anomaly), inflammatory/infectious (neurotoxoplasmosis, neurocisticercosis, brain abscess, Rasmussen encephalitis), metabolic (nonketotic hyperglycemia induced hemichorea and Mitochondrial Encephalomyopathy with lactic acidosis and stroke-like episodes) and miscellaneous (Neurofibromatosis type I, Creutzfeldt Jacob Disease, contrast extravazation after thrombectomy and Perivascular Spaces). Bilateral involvement of the basal ganglia and thalamus has already been widely discussed in the literature and does not escape from the usual well-known causes, however unilateral involvement of the basal ganglia and thalamus can still be a diagnostic challenge for the radiologist physician.



(Filename: TCT_186_DIFFERENTIALDIAGNOSISOFUNILATERALLESIONSINBASALGANGLIAANDTHALAMUS.jpg)

1026

Differentiating CT/MRI Features of CNS Infections; How to Assist the Clinician

S Sevigny¹, A Emekauwa², V Jewells²

¹Campbell University School of Osteopathic Medicine, Lillington, NC, ²University of North Carolina at Chapel Hill, Chapel Hill, NC

Purpose

The etiologies of CNS infections that will be discussed include; viral {COVID-19, Herpes Simplex Virus (HSV 1, 2 & 6), John Cunningham (JC) Virus, Varicella Zoster Virus (VZV), Eastern Equine Encephalitis Virus (EEEV), West Nile Virus (WNV), Human Immunodeficiency Virus (HIV), Measles Virus, Rhabdovirus, Epstein-Barr Virus (EBV), Poliovirus, Rubella Virus, Cytomegalovirus (CMV), Nipah virus, Powassan virus, Human T- cell Leukemia Virus (HTLV-1), Zika virus}, bacterial {Streptococcus pyogenes, Methicillin-resistant Staphylococcus aureus (MRSA), Haemophilus influenzae, Listeria monocytogenes, Mycoplasma pneumoniae, Mycobacterium tuberculosis, Rickettsia rickettsii, Borrelia burgdorferi, Ehrlichia, Neisseria, Treponema pallidum, Brucella, Campylobacter}, fungal {Coccidioides, Aspergillus, Rhizopus, Mucor, Cryptococcus}, parasitic {Taenia solium, Toxoplasma gondii, Plasmodium, Toxocara, Trypanosoma cruzi, Babesia}, and prion disease.

Materials and Methods

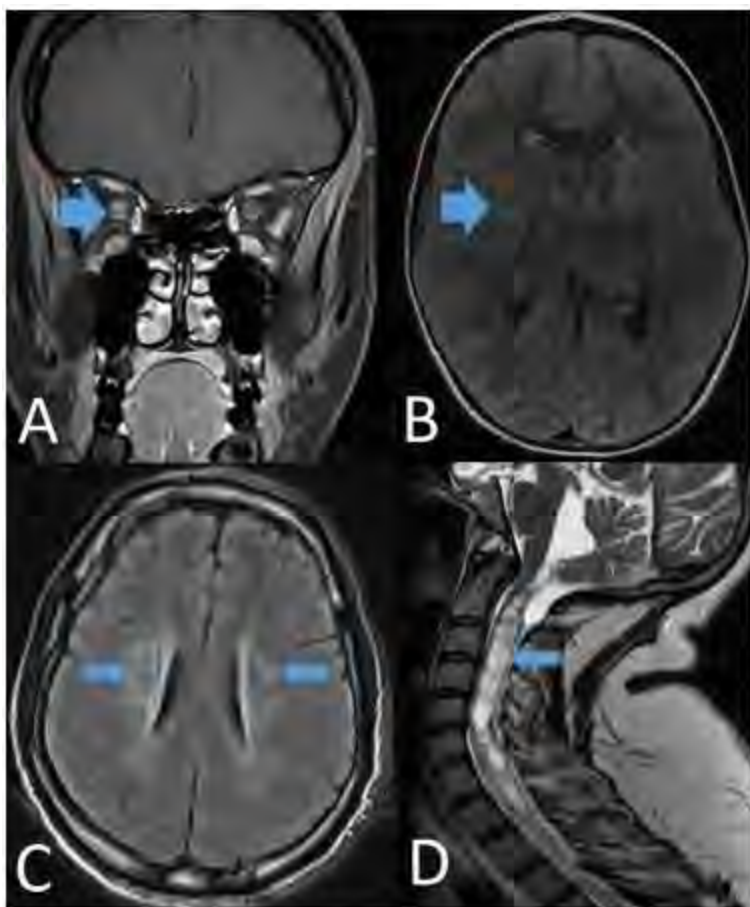
This exhibit is for the education of the readers with regard to the central nervous system findings seen on CT/MRI with infectious etiologies.

Results

IRB approval was obtained. After review of teaching files at our institution and a thorough literature review, cases were compiled into an electronic exhibit. Pertinent CT and MRI findings as well as appropriate clinical history were utilized to compile this exhibit with appropriate references. Diffusion and SWI imaging were performed in the majority of cases, and when applicable is discussed.

Conclusions

There is a broad differential of infectious CNS entities. Most of these processes are best imaged with MRI. Specific locations, appearance, and imaging features are helpful for differentiating infectious etiologies to allow the radiologist to assist the clinician for implementation of appropriate therapy and guidance for surgical intervention. Typical appearance of cerebritis, rhombencephalitis, hemorrhagic encephalitis, ventriculitis and empyema are also discussed as well as the double rim sign.



CNS infections can result in many different appearances.

- **Image A:** T1 +C image demonstrates optic nerve enhancement (arrow) originally mistaken for optic neuritis in a patient with Varicella Zoster. This infection is typically seen in immunocompromised individuals with activation of the virus in cranial nerves V and VII.
- **Image B:** FLAIR image demonstrates hyperintense signal within the basal ganglia and thalami (arrows) in a case of West Nile virus. This infection is typically seen in the elderly or young individuals. Associated hemorrhage is uncommon.
- **Image C:** FLAIR image demonstrates bilateral periventricular hyperintensities (also T2 bright-not shown) in a case of HTLV-1 secondary to human T-cell lymphotropic virus. This entity usually presents with mild lymphocytic pleocytosis as well as moderate protein and oligoclonal bands on CSF analysis. The key to diagnosis is testing for HTLV-1 antibodies. The imaging appearance can be mistaken for multiple sclerosis.
- **Image D:** Sagittal T2 image of the spine in a case of neurocysticercosis demonstrates multiple cystic lesions (vesicular phase) involving the central canal and mimicking a syrinx. This emphasizes the need for complete neural axis imaging in neurocysticercosis.

(Filename: TCT_1026_picDPI300.jpg)

1009

Diffuse Midline Gliomas: Multimodal and Advanced Imaging Characteristics and Molecular Pathways/Genetics

B Otemuyiwa¹, T Moritani¹, S Naganawa¹, M Ibrahim¹

¹University of Michigan, Ann Arbor, MI

Purpose

This educational exhibit is an overview of the advances in the molecular, genetic and imaging characterization of diffuse midline gliomas since their introduction in the 2016 WHO CNS tumor classification system.

Materials and Methods

To present an overview of diffuse midline gliomas, their molecular pathways and genetic features, and the various imaging modalities that are used to characterize these gliomas.

Results

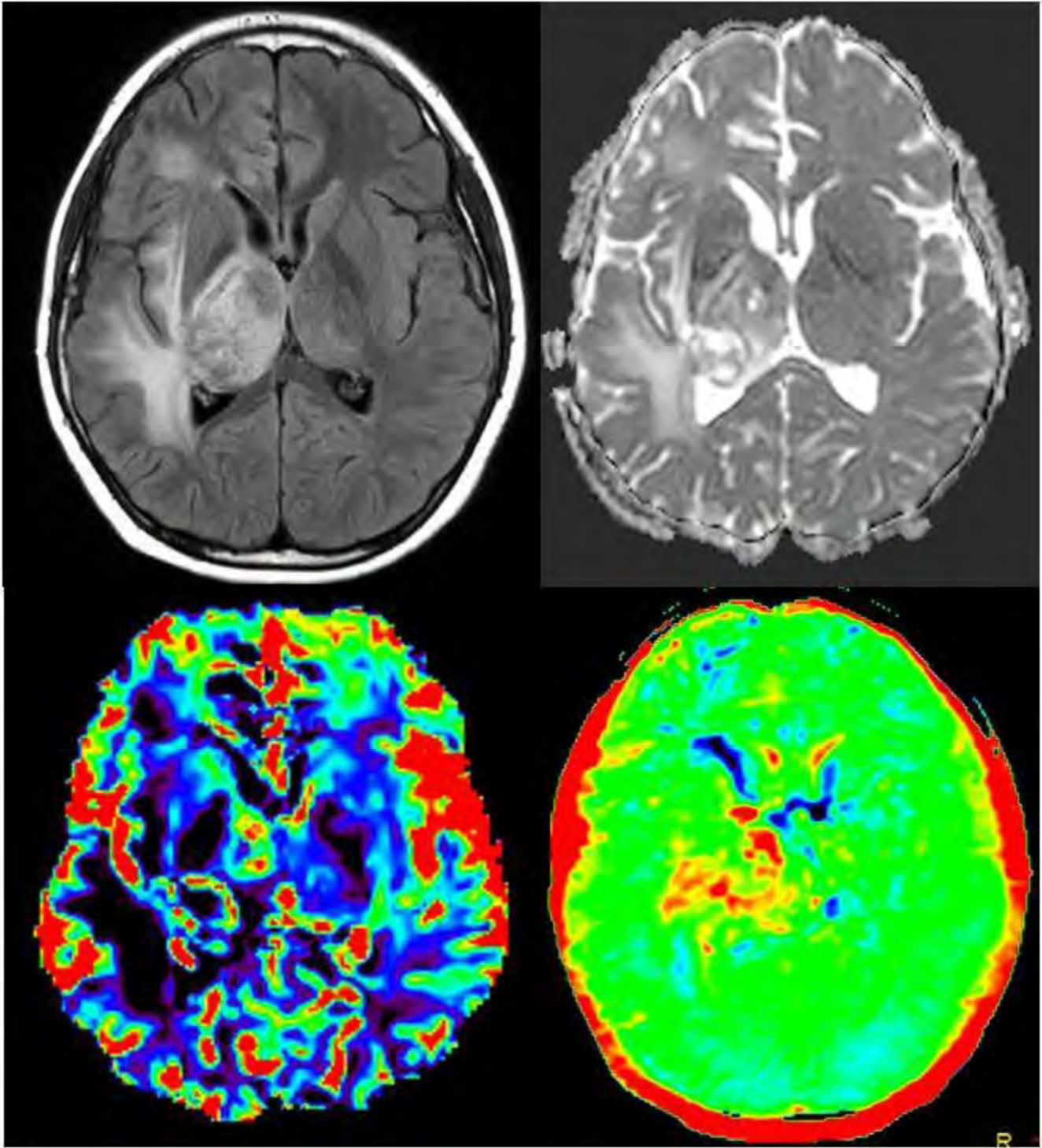
This educational exhibit will discuss diffuse midline gliomas as categorized by the WHO 2016 classification, with a particular focus on the molecular pathways/genetics and imaging characteristics. Multimodal imaging includes CT, MRI, DWI, PWI, MRI texture analysis, MR spectroscopy, APTw, and PET.

Conclusions

Diffuse midline gliomas are a new diagnostic entity defined by the 2016 WHO CNS tumor classification system. The H3 K27M mutation is present in most diffuse gliomas arising from the midline CNS, such as those involving the brainstem, thalamus, cerebellum, cerebrum and spinal cord. The H3 K27M mutation is associated with aggressive clinical behavior and has been found to be the major predictor of overall survival. CT has a limited role in characterizing these tumors as evaluation of brainstem lesions is often limited by mastoid beam hardening artifact. MRI is the gold standard for evaluating these lesions due to its superior soft tissue contrast and ability to delineate the extent of infiltrative disease. Advanced MRI techniques such as DWI and its derivative, ADC, APTw, MR spectroscopy and texture analysis can potentially noninvasively differentiate between mutant and wild-type H3 K27M diffuse gliomas, and are useful to evaluate treatment effects. Another imaging modality, PET, has also demonstrated the ability to discriminate between mutant and wild-type diffuse midline gliomas.

FLAIR

ADC



Corrected rBV

APTw

(Filename: TCT_1009_ASNRAbstract.jpg)

957

Diffusion Spectrum Imaging and Diffusion Kurtosis Imaging in Neurotrauma

C Yang¹, J Gajera¹, I Raza², B Major³, C Li¹, T Tan¹, H Kavnoudias⁴, J Tee¹, A Kam⁵

¹Alfred Health, Melbourne, VIC, ²Alfred Health, Melbourne, Victoria, ³Monash University, Melbourne, VIC, ⁴Alfred Hospital, Melbourne, AK, ⁵N/A, N/A

Purpose

In this review we explore the theoretical basis of DSI and DKI and its potential application to neurotrauma patients.

Materials and Methods

Non-invasive imaging biomarkers that may be employed as surrogates for the quantification of spinal cord injury severity are essential to guide further research in the prognostication and monitoring of patient's neurological recovery following traumatic brain injury (TBI) and traumatic spinal cord injury (tSCI). While conventional MRI techniques provide macrostructural information, they are non-specific and cannot reveal underlying microstructural changes that might indicate neurodegeneration and compensatory processes. Diffusion spectrum imaging (DSI) and diffusion kurtosis imaging (DKI) are advanced MRI techniques that characterize tissue microstructure via probability density function (PDF). Spinal cord Diffusion Tensor Imaging (DTI) metrics have been shown to correlate with neurological outcomes after tSCI and degenerative cervical myelopathy (DCM). DSI and DKI are emerging techniques that have the potential to further improve our understanding of the secondary reorganisation processes following TBI and tSCI.

Results

A search within EMBASE, MEDLINE, Web of Science and PubMed databases was conducted for articles relating to the use of DSI and DKI in TBI and tSCI. The citations of relevant articles were also searched for additional articles.

Conclusions

DTI metrics can be used to quantitatively perform DTI tractography using surrogate data, but its limitation is that it is unable to provide orientation of multiple fibres in an MRI voxel and fails to address the restriction on diffusion signal caused by complex microstructural organisation of the central neural system (CNS) (2). DSI adds a 3-dimensional Fourier encoding of water molecule displacements to DTI, and while the technique requires expertise in signal postprocessing, the resulting data can enable clinicians to visualise the orientation of the crossing fibres, and can resolve heterogeneity of fibre orientations in each voxel. DSI maps the complex 3D fibre passage of each MR voxel where DKI measures deviation from the unrestricted water molecule displacement. DSI's utility in the brain was discussed in previous research and validated in animal studies and DKI was experimentally studied on grey matter (GM) and white matter (WM); hence, we see an opportunity to extend its use in the spinal cord for tSCI patients.

1162

Disaster aVERTed: What does the spine surgeon need to know?

A Condos¹, J Vigilante¹, A Cho², D Hawley³, M Cathey⁴

¹Naval Medical Center San Diego, San Diego, CA, ²Naval Medical Center San Diego, san diego, CA, ³Naval Medical Center San Diego, Coronado, CA, ⁴N/A, N/A

Purpose

Vertebral artery injury (VAI) is the most common vascular injury in cervical spine surgery due to its variable course and proximity to areas of instrumentation. While VAI is rare, with the incidence ranging from 0.08%-0.5%, the potential consequences can be catastrophic leading to bleeding, neurological damage or death^{1,2,3}. Therefore, it is essential for radiologists to evaluate more than disc and arthritic degeneration on preoperative imaging, with the intent of helping to prevent complications from spine surgery.

Materials and Methods

The purpose of this exhibit is to: - Review cervical vascular anatomy, emphasizing the surgically important vascular anomalies using a case-based approach - Assist viewers to prospectively add value to the pre-operative imaging evaluation beyond disc and arthritic degeneration

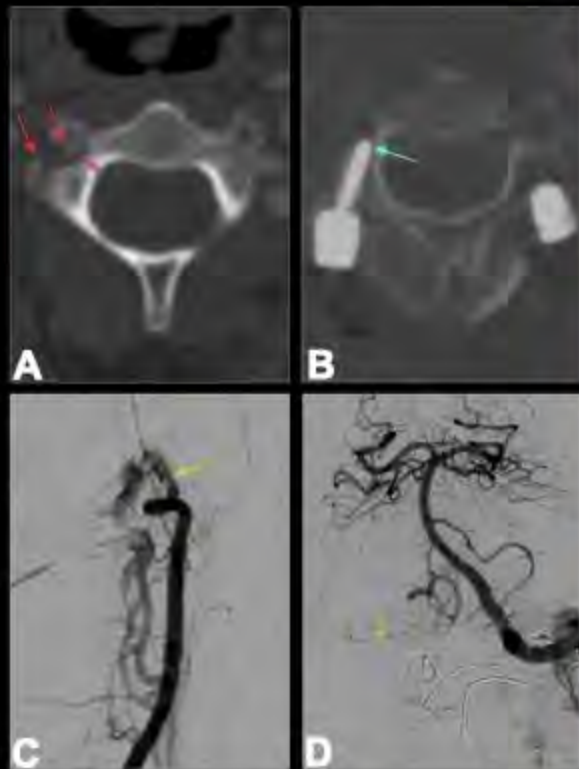
Results

Retrospective review of 3T MR and CT examinations performed for cervical radiculopathy over the last 10 years. A variety of cervical spine cases are presented which clearly demonstrate the pertinent imaging findings on high resolution cross-sectional imaging. Relevant anatomy is reviewed. Additionally, a literature review on vascular complications associated with cervical spine surgery was completed.

Conclusions

We will briefly review the normal vascular anatomy of the cervical spine, and then present cases highlighting surgically important vascular anomalies. Abbreviated review of normal vascular anatomy Surgically Important Vascular Anomalies of the Cervical Spine Aberrant Origin of the Vertebral Artery Aberrant Course of the Vertebral Artery High Riding Vertebral Artery High Entrance of the Vertebral Artery Duplicated Vertebral Artery Hypoplastic Vertebral Artery Fenestrated Vertebral Artery Vertebral Artery Loop Formation/Tortuous VA Retropharyngeal course of the Carotid Artery Aberrant Right Subclavian Artery Occult Internal Carotid Artery Stenosis Fibromuscular Dysplasia Vascular complications in cervical spine surgery are rare, but they have the potential to cause permanent neurological damage or even death. Vertebral artery injury is the most common vascular injury in spine surgery and most commonly occurs in posterior upper cervical spine instrumentation and anterior corpectomy. Radiologists can add value to the preoperative imaging evaluation beyond arthritic and disc degeneration by being aware of cervical vascular anatomy and anomalies. By drawing attention to these findings, the radiologist can potentially aid the surgeon in preventing catastrophic injury.

Case: Narrow C2 Pedicle Width



60 yo M s/p C1-C2 fusion secondary to Type II dens fracture with post-op vertigo

A. Pre-op CT shows a narrow C2 pedicle width (less than 4 mm) possibly secondary to VA tortuosity (red arrows)

B. Post-op neck CTA shows a short C2 pedicle screw. Despite short pedicle screws, the screw breached the posterior margin of the right TF (blue arrows), and concern for VAI was raised

C. RAO angiogram was obtained and shows R VA AVF (yellow arrow)

D. Post-op AP angiogram shows coil embolization (green arrows) of the R VA AVF

Teaching Point: If C1/C2 fixation is planned recognizing narrow pedicle width can help to prevent VAI

(Filename: TCT_1162_asnrimage.jpg)

1465

Diseases of the Intracranial Meninges

R HASSAN KARUVATH¹, S NAIK²

¹COLUMBIA ASIA, MALAPPURAM, KERALA, ²COLUMBIA ASIA, BANGALORE, KARNATAKA

Purpose

• To discuss the anatomy of meninges and the MR imaging technique when meningeal disease is suspected • To discuss the various meningeal pathologies with salient imaging features • To discuss an approach to narrow down the differential diagnosis

Materials and Methods

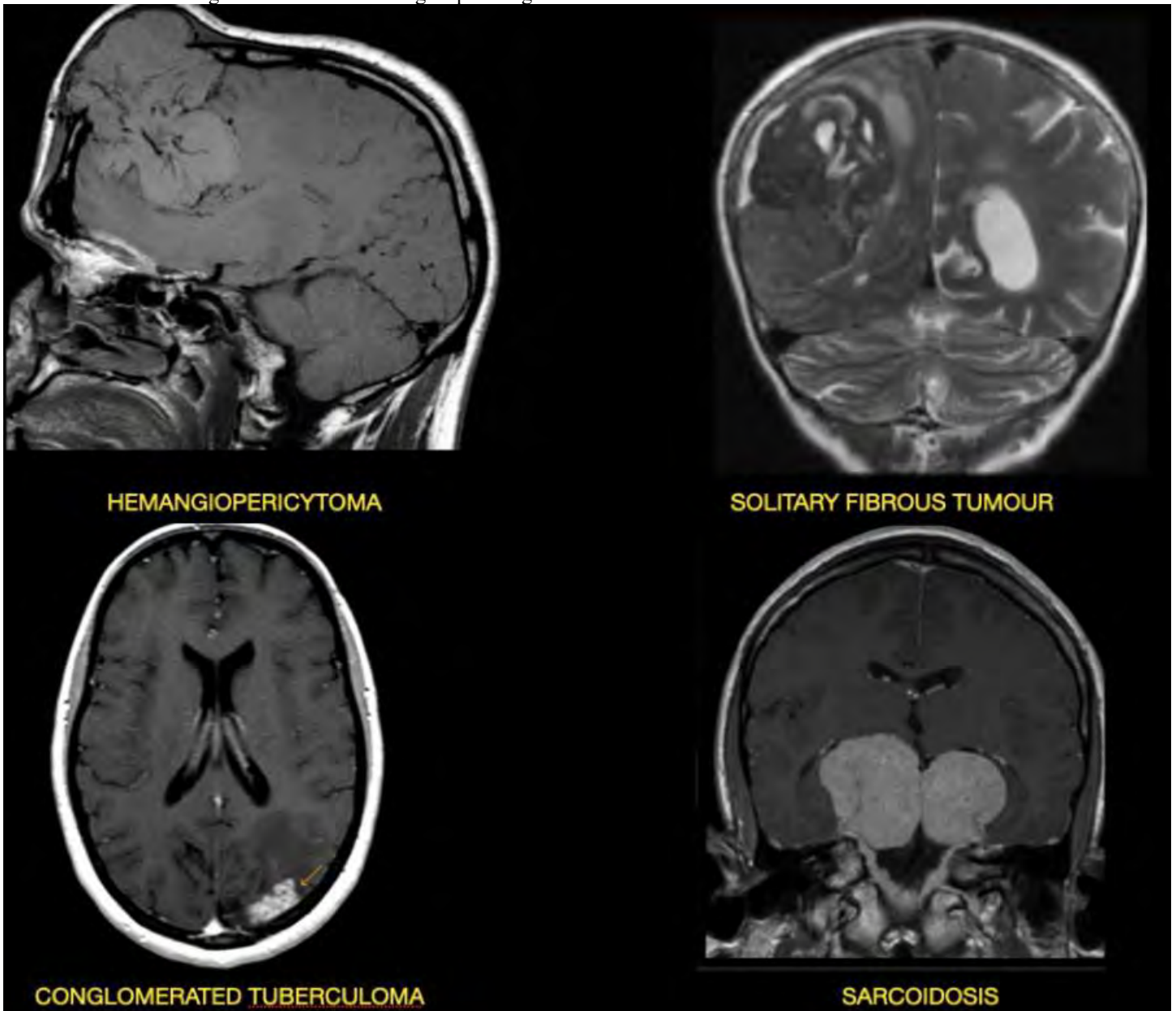
• There are various lesions which affect the meninges that include tumors, infections, cysts, and other lesions that primarily involve the meninges, also lesions that secondarily involve the meninges. • Knowledge of the anatomy of the meninges and their pathophysiology aids in an understanding of the various imaging appearances. • In our exhibit we aim to classify the various pathologies of meninges, discuss the salient imaging features and discuss an approach to narrow down the differential diagnosis

Results

- We retrospectively analysed the imaging characteristics of various meningeal pathologies in cases we came across in our hospital.
- The specific imaging features were reviewed with the clinical details to diagnose and establish an approach to narrow down the differential diagnosis

Conclusions

Knowledge of the pathophysiology, spectrum of meningeal disorders and their salient imaging features are very important for accurate characterisation and diagnosis of various meningeal pathologies.



(Filename: TCT_1465_aasnrmeninges.jpg)

1200

Dizziness and Vertigo - an Etiologic and Imaging Review

W Malak¹, M Hagiwara², V Nguyen¹

¹NYU Langone, New York, NY, ²NYU Langone Health, New York, NY

Purpose

Vertigo and dizziness are symptoms of a broad scope of diseases affecting the peripheral and central vestibular system. Neuroimaging is particularly valuable in cases which demonstrate neurologic signs/symptoms, and where imaging studies are appropriately requested

depending on suspected etiology. Frequent overlap in symptomatology necessitates a multidisciplinary approach towards diagnosis, image interpretation and management of these patients.

Materials and Methods

Review the definition of vertigo and dizziness. Review the differential diagnosis for patients presenting with these symptoms. Discuss the role of imaging in diagnosis and management of such diseases.

Results

We will review the clinical presentation, differential diagnoses, anatomy and imaging findings in patients presenting with dizziness and vertigo. A myriad of example cases will be exhibited. We will conclude with a brief highlight of a multidisciplinary approach to understanding dizziness and vertigo.

Conclusions

Dizziness and vertigo are prevalent symptoms and common complaints for patients presenting both in the primary care and emergency setting, resulting in a significant decrease in quality of life and a high cost burden to the US health care system. Frequently, duration and severity of symptomatology lead to additional subspecialty evaluation by neurologists and otolaryngologists. The etiology of these symptoms is often difficult to elucidate due to a wide range of pathophysiologic processes that frequently have overlapping manifestations. The broad differential diagnosis based on whether the disease process is central or peripheral, will be showcased. Imaging therefore, potentially plays a vital role in sifting through differential diagnoses; each differential will be categorized into neoplastic, infectious/inflammatory, structural, traumatic, and iatrogenic causes. CT, MRI and vascular imaging are frequently complimentary in providing meaningful information regarding diagnoses and guidance in management.

405

Down the Road Beyond Acuity of COVID-19: Delayed White Matter Anoxic Injury as Sequela of COVID-19

A Glover¹, D Dunaway²

¹Baylor College of Medicine, Houston, TX, ²N/A, N/A

Purpose

The Coronavirus Disease 2019 (COVID-19) continues to affect thousands and hospitalize hundreds each week throughout the world. Along with the severe acute respiratory syndrome coronavirus 2 (SARS-CoV-2) causing pneumonia and acute hypoxic respiratory failure of the lungs, multiple intracranial manifestations including acute anoxic injury, hemorrhagic encephalitis, and intracranial hemorrhage have been reported. In addition to the acute manifestations of COVID-19, we are now learning that patients may also suffer delayed consequences of this virus. One of these consequences is delayed post-hypoxic leukoencephalopathy (DPHL). DPHL results from cerebral hypo-oxygenation with subsequent white matter injury and brain edema. It is important to recognize DPHL for its prognostication for cognitive decline. A few case reports have discussed DPHL associated with SARS-CoV-2 infection, but due to the novelty of the virus, the incidence remains uncertain at this time. In addition to DPHL, other sequelae of the novel coronavirus include but are not limited to infarction, hemorrhage, olfactory bulb abnormalities, and vasculopathy. We present two cases of DPHL as it relates to COVID-19. These cases also demonstrate other intracranial findings of SARS-CoV-2 infection which are also highlighted. • To recognize and understand the importance of delayed anoxic white matter injury (DPHL) as sequela of COVID-19 • To educate the radiologist on other intracranial features of COVID-19, including infarction, hemorrhage, olfactory bulb abnormalities, and vasculopathy

Materials and Methods

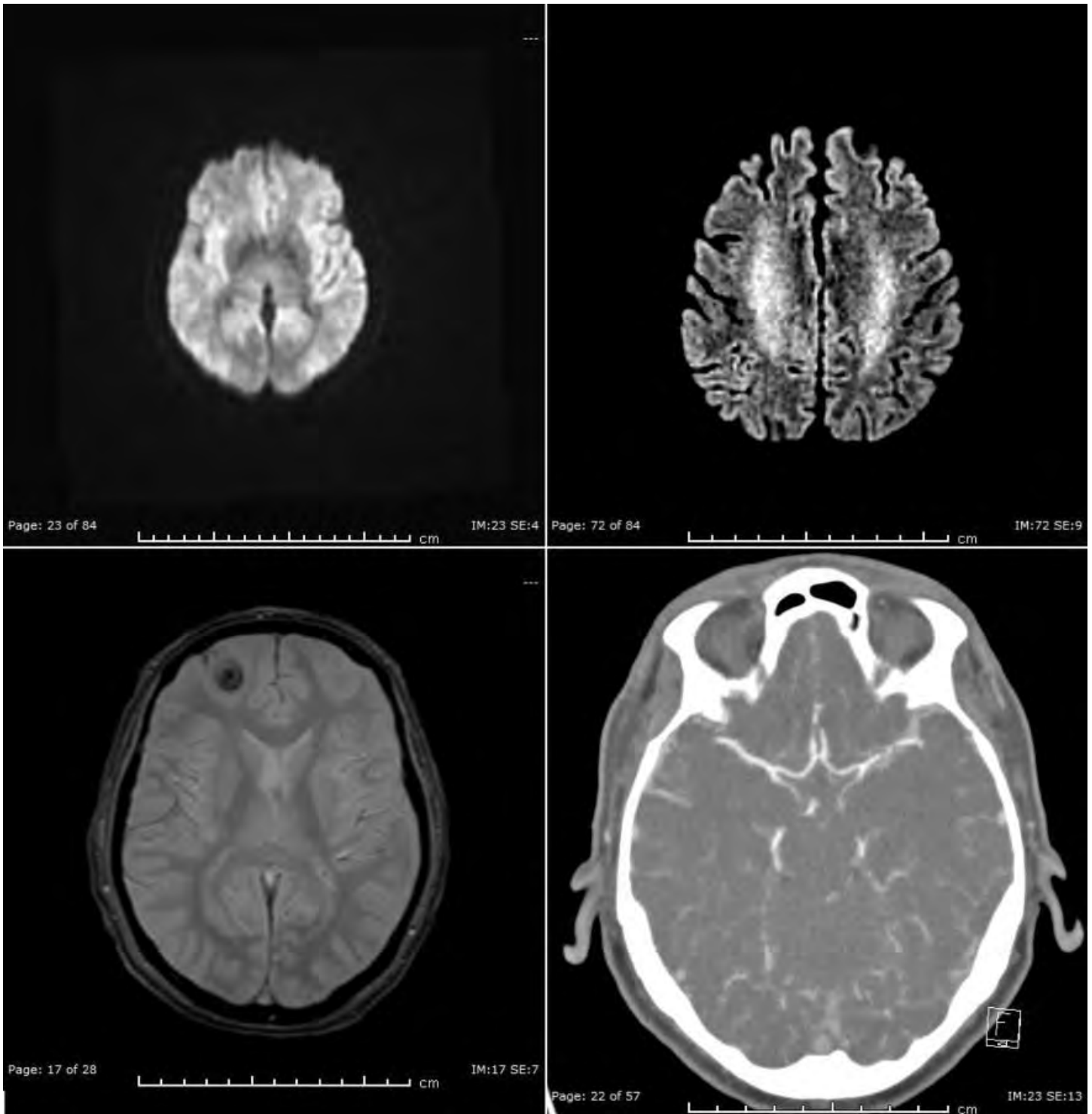
To educate the radiologist on intracranial manifestations of COVID-19. Specifically, to demonstrate and discuss delayed anoxic white matter injury (DPHL) as well as other manifestations such as infarction, hemorrhage, olfactory bulb abnormalities, and vasculopathy as manifested on CT, CT angiography, and MRI.

Results

We present two cases which demonstrate intracranial sequelae of COVID-19 infection in order to educate radiologists who read neuro-imaging.

Conclusions

Intracranial complications from COVID-19 are non-specific to SARS-CoV-2 but are paramount to recognize due to the long term prognostic implications even in the setting of relative resolution of pulmonary disease. DPHL is one intracranial complication which has been shown to result in patient decline. Therefore, it is important for the radiologist who reads neuroimaging to understand how COVID-19 can manifest intracranially.



(Filename: TCT_405_4image.jpg)

1414

Dual-energy Computed Tomography for Acute Ischemic Stroke Treatment

K NOGUCHI¹

¹University of Toyama, Toyama, Toyama

Purpose

NE-DECT has a potentially great utility for diagnosis of AIS. NE-DECT mages are playing an important role in diagnosis of AIS to make clinically important decisions for the treatment. We have believed that one-stop-diagnosis for AIS with a single acquisition of

NE-DECT is possible in many AIS cases. This protocol is very beneficial for AIS patients within 3 hours after the onset because of saving time (time is brain), in addition, decreasing total irradiation dose, and avoiding use of contrast-enhanced material.

Materials and Methods

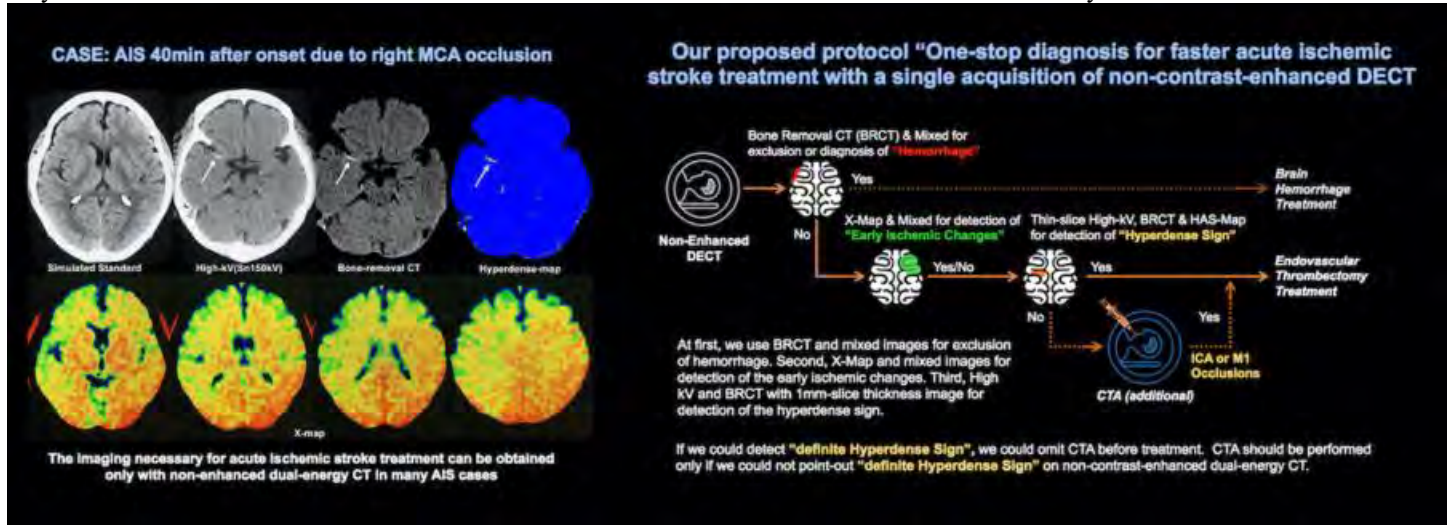
The major purpose of this educational poster is to show the utility of non-contrast-enhanced dual-energy computed tomography (NE-DECT) in the assessment of acute ischemic stroke (AIS) before and after endovascular thrombectomy treatment.

Results

1. Applications of NE-DECT for AIS Low kV CT, High kV CT, mixed, Monenergetic Imaging (from 40keV to 190keV), Bone-removal CT and Hyperdense-map (HAS-Map), Virtual non-contrast map (VNC) and Iodine-Map and X-Map 2. Patients with acute ischemic stroke within 3 hours after the onset

Conclusions

Roles of NE-DECT Imaging for AIS before and after Endovascular Treatment 1. Before endovascular thrombectomy 1) Exclusion of intracranial hemorrhage by mixed and BRCT 2) Diagnosis of acute arterial thrombus by BRCT, High-kV and HAS-Map 3) Evaluation of early ischemic changes by mixed and X-Map 2. After endovascular thrombectomy 1) Discrimination between hemorrhage and Iodine leakage by VNC and Iodine-Map 2) Evaluation of infarct volume after treatment by VNC and X-Map NE-DECT Imaging is very useful for the evaluation of acute cerebral infarction before and after endovascular thrombectomy treatment.



(Filename: TCT_1414_ASNR.jpg)

1360

Dural Based Masses: Expanding the Differential Past Meningioma

D Lehmkuhl¹, P Roth¹, R Bhatia¹, N Nagornaya¹

¹Jackson Memorial Hospital/University of Miami, Miami, FL

Purpose

The focus of this educational exhibit is to review the differential diagnosis for dural based lesions and to present a detailed overview of the pathology proven dural based lesions. We will highlight distinguishing imaging features, characteristic locations and elucidate key imaging findings that are of particular use to the clinician in order to guide appropriate follow-up and therapy.

Materials and Methods

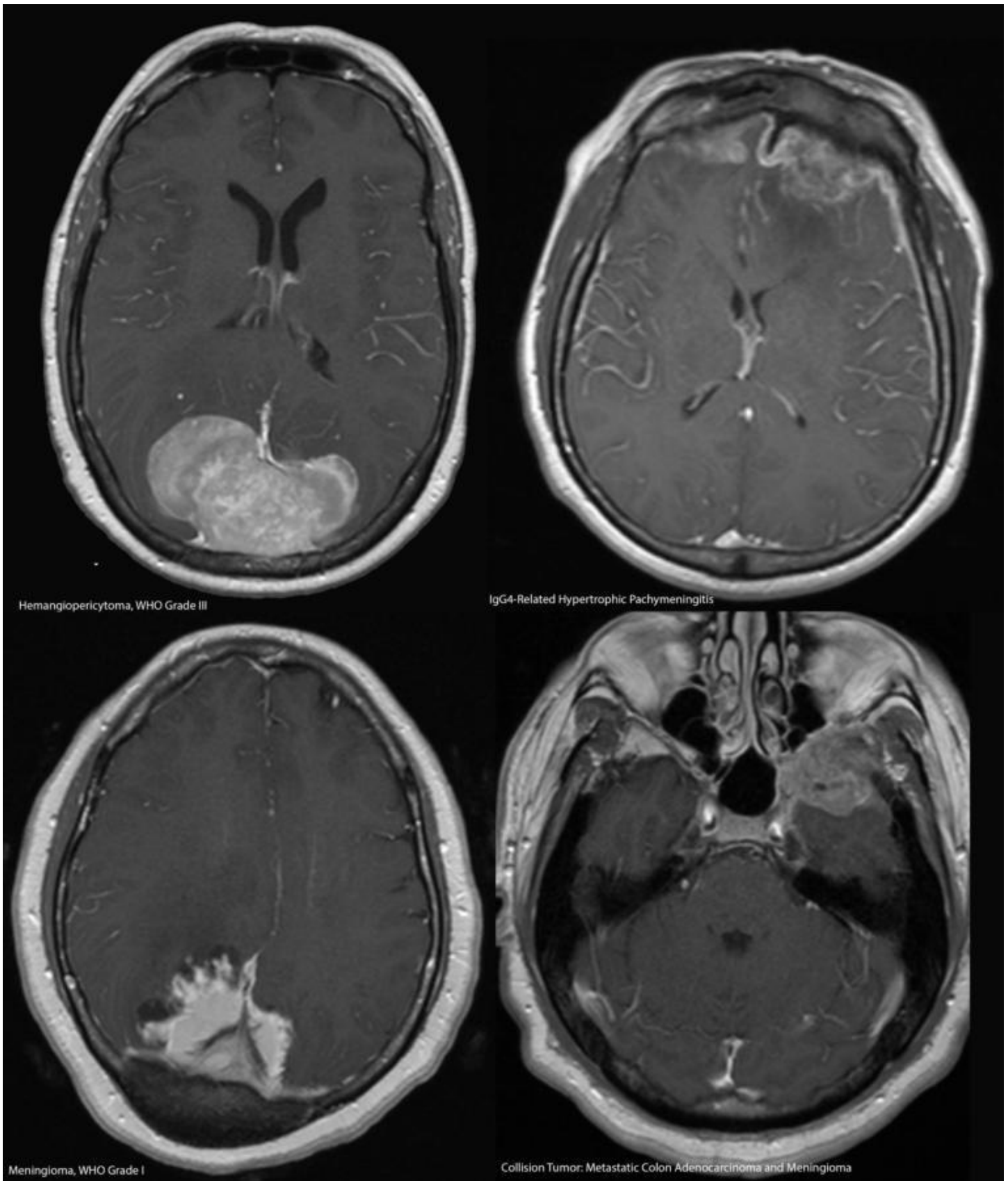
While meningiomas are the most common dural based tumor, there are a number of other dural based lesions that can have a similar appearance. Although meningiomas are often managed conservatively, other dural based lesions require timely intervention in order to maintain neurological function. Therefore, radiologists must be able to recognize meningioma imitators and diagnose dural based pathology accurately.

Results

Multiple examples of pathology proven dural based lesions were reviewed with MRI and/or CT images to describe the common imaging features of various dural based lesions. In addition, patient demographics and laboratory findings when appropriate will be discussed to help refine the differential diagnosis.

Conclusions

Although dural based lesions often have a similar appearance on imaging, the radiologist should be able to create a more refined differential diagnosis by recognizing distinctive imaging characteristics in order to guide clinicians to the appropriate treatment course and prognosis.



(Filename: TCT_1360_ASNRFigure.jpg)

138

Dural lesions: beyond the meningioma, a constellation of differential diagnosis!

Purpose

Knowing the various pachymeningeal pathologies and being able to differentiate them by its imaging patterns is essential for early diagnosis and for orientate the correct treatment by the attending physician.

Materials and Methods

The main differential diagnosis for pachymeningeal thickening, with nodule or plaque pattern, is meningioma, yet there is an infinity of other potential diagnosis that might be thought when you are interpreting a set of images in a patient presenting dural thickening. The etiology varies too, involving from neoplastic disorders to idiopathic diseases, passing by inflammatory/autoimmune and infectious diseases. Our purpose is to review and discuss the many differential diagnosis of meningiomas, showing a constellation of other possible diagnostics for pachymeningeal involvement, focusing on the various forms of presentation in the imaging.

Results

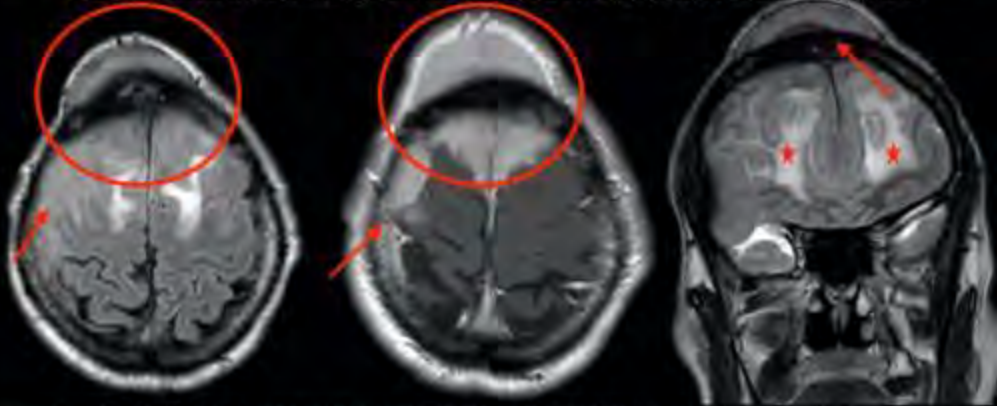
Based on the virtual teaching file of our quaternary hospital in Brazil, we reviewed several cases of pachymeningeal disorders, detaching lesions that might mimic meningiomas, and could lead to misdiagnosis, highlighting its main imaging characteristics that might aid in your recognition.

Conclusions

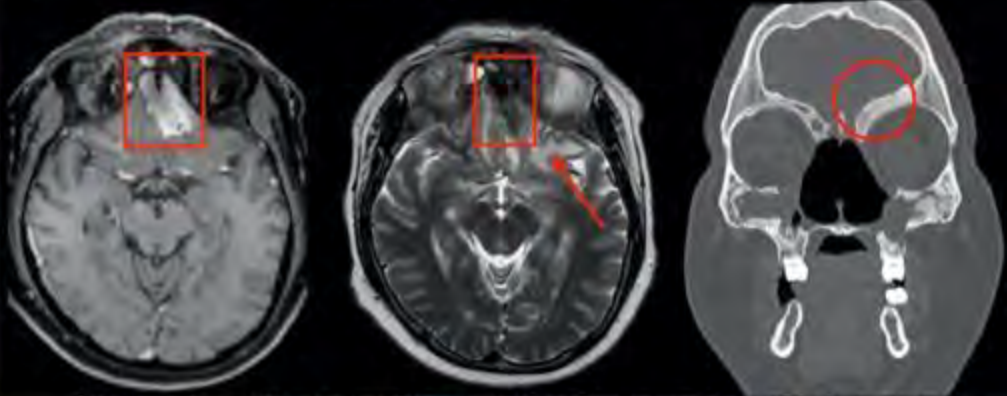
Meningiomas are not the only diagnostic for nodular or en plaque pachymeningeal thickening, but they are not the only one. There are many differential diagnostics for pachymeningeal diseases, each one with CT and MR imaging that allow the radiologist to orientate the correct diagnosis, aiding our clinical colleagues in the patient care. We discuss a fourteen different causes for meningeal thickening, with neoplastic (eg, meningeal myxofibrosarcoma, Burkitt lymphoma, matle cell lymphoma, hemagiopericytoma, plasmocytoma, metastasis), infectious disease (eg, tuberculosis, paracoccidioidomycosis), inflammatory disorders (granulomatosis with polyangiitis, sarcoidosis, Rosai-Dorfman disease) and spontaneous intracranial hypertension that might mimic meningiomas on imaging.



Diffuse dural lymphoma mimicking an plaque meningioma, hypointense on T1WI, strong enhancement after contrast administration and determining erosion of the nearby skull. The biopsy showed a Mantle Cell Lymphoma.



Extra-axial lesion isointense on T1WI; showing diffuse enhancement by the contrast media, presenting dural tail sign inferring meningeal attachment, and determining compressing effect on the cerebral parenchyma. The final diagnosis by biopsy was Rosai-Dorfman disease.



Pachymeningeal thickening showing avid contrast enhancement, hypointense on T2WI, and determining hyperostosis of the skull nearby. After biopsy, the diagnosis was granulomatosis with polyangiitis.



Multiple skull lesions, with dural extension mimicking pachymeningeal aggressive lesions, showing marked contrast enhancement, with hypointense on T2WI and restricted diffusion. Perfusion (not showed) demonstrated high rCBV values (a finding most consistent with meningioma). The patient was submitted to surgical biopsy and diagnosed with fungal lesions caused by *Paracoccidioides brasiliensis*.

(Filename: TCT_138_ASNR2021001.jpg)

Endovascular devices for the treatment of intracranial aneurysms and post procedure imaging

M LEE¹, A Brackett², W Brim³, M Aboian⁴, M Johnson³

¹YALE SCHOOL OF MEDICINE, NEW HAVEN, CT, ²Harvey Cushing/John Hay Whitney Medical Library, Yale University, New Haven, CT, ³Yale University, New Haven, CT, ⁴Yale University, Woodbridge, CT

Purpose

1. Review current published literature regarding endovascular therapy of intracranial aneurysm and post procedure imaging 2.

Describe the treatment and management of intracranial aneurysms

Materials and Methods

Introduce endovascular treatment methods of intracranial aneurysms for the purposes of reviewing post-procedural image findings and patterns. In addition, we performed a systematic review of current literature regarding endovascular treated intracranial aneurysms to purpose post-imaging recommendations.

Results

A systematic search of the literature was developed and executed by a clinical librarian. A total of four databases were searched: Ovid Embase, Ovid MEDLINE, Cochrane trials (CENTRAL), Web of Science-Core Collection. The search strategy used both keywords and controlled vocabulary combining the terms for: endovascular surgery, embolization coil, stents, postoperative period, computer assisted tomography, as well as related terms. The search strategy was independently reviewed by a second institutional librarian. Publications were screened in Covidence by a neuroradiology attending, radiology resident, and post baccalaureate student. The study was approved by the IRB.

Conclusions

Systematic review yielded 1,526 publications for initial screening. A total of 19 publications were included for full text review. Results demonstrated that the Guglielmi electrolytically detachable coil system (GDC), stent-assisted coiling (SAC), flow diverters (FD) are the primary endovascular devices utilized for the treatment and management of intracranial aneurysms. These findings highlight the significance of the following anatomic considerations: aneurysm size, wide neck aneurysms, aneurysm morphology and aneurysm location. The follow imaging modalities: DSA, CT/CTA and MRI/MRA are the most often utilized modalities in the peri-procedural period of endovascular treated IAs. However non-invasive modalities offer adequate sensitivity and specificity regarding treatment response (i.e. recurrence) and potential complications. Thus, recommendation for follow up imaging of endovascular treated IAs are as follows: 1) DSA remains the gold standard for follow up of coiled aneurysms. However, MRI/MRA is an adequate non-invasive alternative especially in the setting of routine surveillance. 2) To date there is no consensus or guidelines for follow up imaging of flow diverters or disrupters. However, it would be reasonable to utilize DSA on initial follow up.

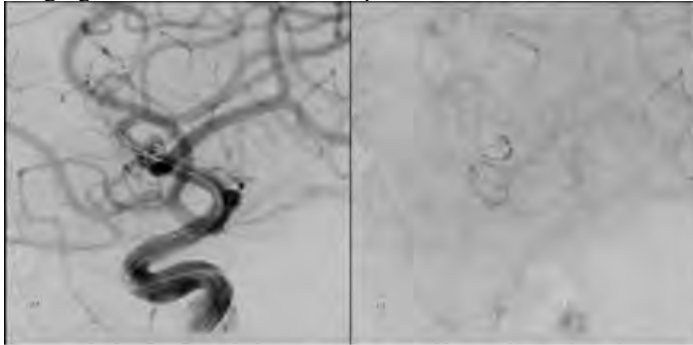


Figure 1 Intraoperative DSA demonstrating rupture of the R MCA aneurysm after placement of a 3D coil.

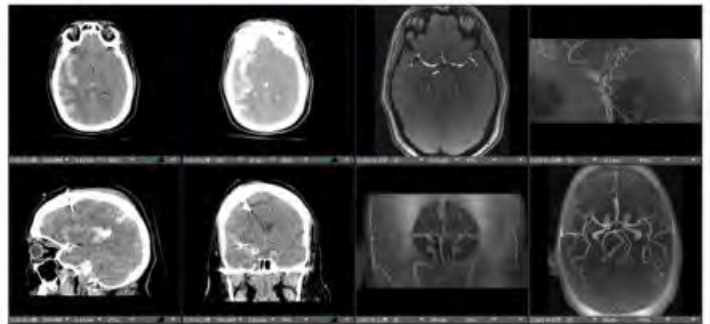


Figure 1 MRI 30 days post procedure demonstrating residual flow enhancement within the neck of the aneurysm and extending into the coil consistent with a class IIIa lesion.

Table 1 Modified Raymond-Roy classification

Class	
I	Complete obliteration
II	Residual neck
III	Residual aneurysm
IIIa	Contrast opacification within the coil interstices within the residual IA
IIIb	Contrast opacification outside the coil interstices within the residual IA

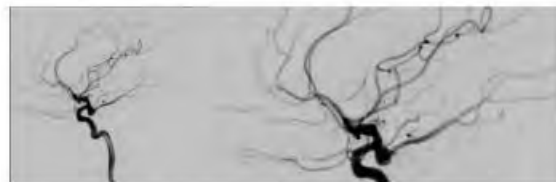


Figure 1 Distal embolization of clot into the left ACA and superior trunk of the MCA after withdrawal of the microcatheter and balloon catheter.

(Filename: TCT_1423_abstractgraphics2020_A.jpg)

H Sotoudeh¹, E Sotoudeh², A Sarrami³, Z Saadatpour⁴, A Rezaei⁴, M Tabatabaei⁵, A Singhal⁴
¹UAB, Birmingham, AL, ²Iranian Hospital in Dubai, Dubai, Dubai, ³Semnan University of Medical Sciences, Davis, CA, ⁴University of Alabama at Birmingham, Birmingham, AL, ⁵Arak University of Medical Sciences, Arak, Markazi

Purpose

Radiomics is a new era of precision medicine. It is a translational field of research aiming to find associations between qualitative and quantitative information extracted from clinical images and clinical data +/- genomics to improve the clinical decision-making. The basic concept of Radiomics is the fact that the anatomic and functional clinical images contain qualitative and quantitative information (which are not appreciable by human eyes), which may reflect the underlying pathophysiology of a tissue.

Materials and Methods

In this educational presentation the basic concept of Radiomics is reviewed for the neuro-radiologists.

Results

Radiomics analysis: The act of extraction of a high number of features from medical images. Analysis includes: size, shape, and textural features These radiomic features are further used in creating different predictive statistical models.

Conclusions

Oncologic imaging is the most common application of Radiomics. Evolution of Radiomics is related to accessibility of big datasets and AI. Radiomics analysis can be used as initial tomural evaluation or during treatment to evaluate the treatment response. Radiomics can evaluate the tissue heterogeneity : Radiomic features are strongly correlated with heterogeneity indices at the cellular level and this heterogeneity is related to the overall survival rate. Biopsies can capture heterogeneity within only a small portion of a tumor and usually at just a single anatomic site, Radiomics captures heterogeneity across the entire tumor volume. Radiomic features are therefore also associated with: A. Tumor aggressiveness B. Clinical endpoints such as survival and treatment response C. Genomic, transcriptomic, or proteomic characteristics.

3. Radiomic Features Extraction

- The features themselves are measures of the image heterogeneity within the ROI.
- Feature extraction is done by software.
- Each feature is number as an output of a mathematical formula.

Radiomics Pipeline

- Image Acquisition: Manual
- Segmentation: Semi-automated
- Feature Extraction: Automated
- Feature Selection: Shape, First order, Second order, High order, Deep
- Classification: PCA, Lasso, AI

Feature types: A. Shape features

- Shape features describe the 3D (or 2D) geometrical composition of the ROI :
- Size volume,
- Maximum diameter along different orthogonal directions,
- Maximum surface,
- Tumour compactness,
- Sphericity etc

Feature types: B. Histogram/First order features

- First-order: Statistics computed from image's histogram of voxel/pixel intensities.
- Average,
- Standard deviation,
- Skewness,
- Kurtosis,
- Energy
- Entropy
- First-order : distribution of individual voxel values without concern for spatial relationships.

Feature types: C. Texture/Second-order features

- Second order : Spatial relationship as statistical inter-relationships between neighbouring voxels .
- They provide a measure of the spatial arrangement of the voxel intensities, and hence of intra-lesion heterogeneity.
- Such features can be derived from the
- gray-level co-occurrence matrix (GLCM), quantifying the incidence of voxels with same intensities at a predetermined distance along a fixed direction,
- Gray-level run-length matrix (GLRLM), quantifying consecutive voxels with the same intensity along fixed directions.

Most common Texture features

- Gray-level co-occurrence matrix (GLCM)→the most commonly used texture feature→ Considering only voxels within a specific range of gray values, it produces a matrix of the spatial relationships of pairs of voxels.
- Joint intensity matrix (JIM)→evaluates the spatial relationships of pairs of voxels within given intensity ranges across different MRI sequences. This is in contrast to GLCM, which is restricted to a single MRI sequence.
- Neighborhood gray-tone difference matrix (NGTDM)→a description of the differences in signal intensity, or gray-tone, between each voxel and its neighboring voxels .
- Neighboring gray-level dependence matrix (NGLDM)→Similar to NGTDM, is computed from the gray tone relationship between every element in the image and all of its neighbors at a certain distance.
- Gray level run length matrix (GLRLM)→A matrix of all the voxels within the same gray level value .

(Filename: TCT_516_Fig1600.jpg)

1048

Expect the unexpected: Anomalies of venous development mimicking ischemia on transfontanellar ultrasound

M Figueiredo¹, M Kase¹, R Iquizli¹, F Benevides Silva¹, Y Sameshima¹, A Barbosa²
¹Hospital Israelita Albert Einstein, Sao Paulo, Sao Paulo, ²Hospital Israelita Albert Einstein, SAO PAULO, NY

Purpose

Ultrasound (US) is an effective modality for documenting abnormalities in the brain parenchyma in the neonatal period. While some lesions can often be readily distinguishable by their imaging characteristics, some require advanced imaging for a definitive diagnosis.

Materials and Methods

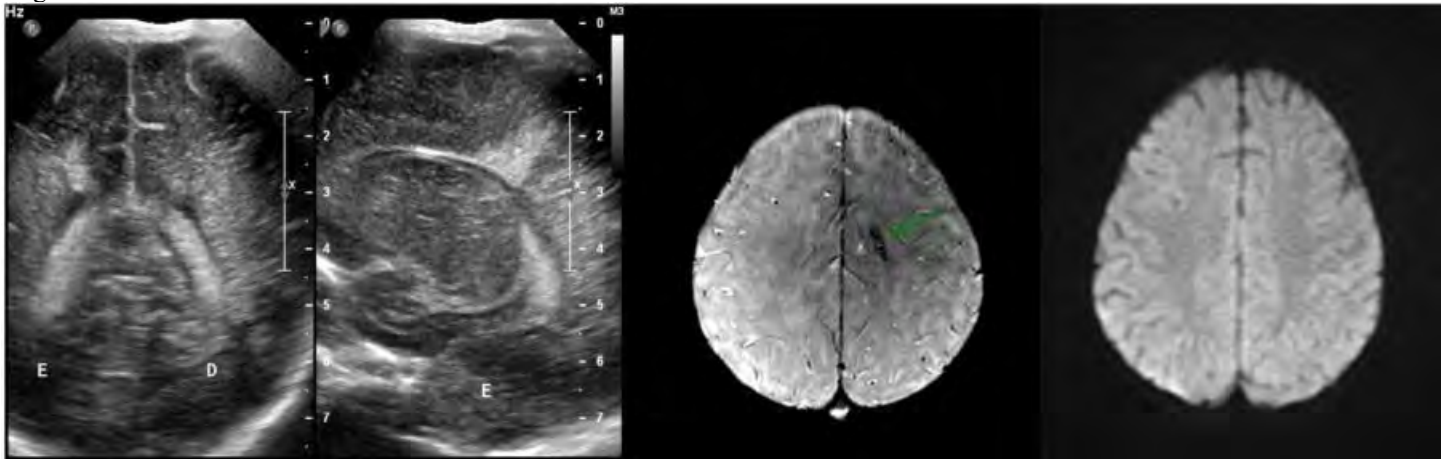
This exhibit will show an institutional case series of anomalies of venous development mimicking ischemia on transfontanelar ultrasound.

Results

Although magnetic resonance imaging (MRI) is the reference standard for infant brain imaging, it is expensive, often requires sedation, and may not be possible to perform on critically ill patients. Cranial US is relatively inexpensive, does not require sedation, and offers the important benefit of being portable. Additionally, in neonates the presence of several sonographic windows allows for effective US evaluation of many regions of the brain. The usual observation in cases of ischemia is a combination of diffuse increase in the echogenicity of brain parenchyma with associated obliteration of sulci/cisterns and focal reduction of adjacent ventricles. A few cases in our institution demonstrated what was originally thought to be an area of ischemia. However, additional imaging with MRI revealed anomalies of venous development, without signal abnormalities on T2 and diffusion in the adjacent parenchyma.

Conclusions

Transfontanelar US remains an important and frequently utilized technique in the evaluation of neonatal brain injury. Many specific clinical questions can be resolved by optimally utilizing this simple informative tool, as common lesions have distinguishing imaging characteristics that enable the diagnosis. However, in some cases, there is a need to perform advanced imaging to elucidate the diagnosis.



(Filename: TCT_1048_Images.jpg)

171

Fetal Brain Destructive Lesions – antenatal and perinatal imaging

S Kanekar¹, S Kanekar²

¹Hershey Medical Center, Hershey, PA, ²Brown University, Hummelstown, PA

Purpose

1. To classify and discuss the pathology and pathogenesis of the fetal brain destructive lesions. 2. To highlight the imaging findings and diagnostic pearls for these specific diagnosis in the antenatal and perinatal period.

Materials and Methods

Brain injury in mature and premature infants is of enormous public health importance because of the large number of such infants who survive with a serious neurodevelopmental disability, including major cognitive deficits and motor disability. Besides encephalopathy of prematurity (or PVL), various acquired or congenital malformation can lead to destructive brain lesions. With the increasing understanding of our knowledge regarding the neurogenetics of brain development, identifying these malformations is of critical importance to the long term developmental effects on the child and to the parents in regard to their future pregnancy.

Results

We retrospectively reviewed the imaging studies from our PACS system of 122 patients with the fetal brain destructive lesions, which forms the basis of this exhibit. All patients had an antenatal ultrasound. In addition, 36 patients also had a fetal MRI. All patients had CT and/or MRI scan of the brain in the perinatal period. For easy understanding, this exhibit is classified under the following categories: 1. Encephalopathy of prematurity 2. Hypoxic-ischemic injury 3. Toxic and metabolic disorders 4. Congenital infection - TORCH, 5. Brain damage due to vascular malformation: Vein of Galen malformation, AVM, Cavernous malformation, Capillary telangiectasia, 6. Maternal causes: Maternal or fetal coagulation disorders, Maternal hypoxia-trauma, sepsis, Hg, Mechanical conditions Placenta praevia, Complications of Monochorionic Twin Pregnancies-TTTS, Chorioamnionitis 8. Tumors: teratoma, astrocytomas, lipomas, choroid plexus papillomas (CPP), PNET, ATRT, Desmoplastic Infantile Tumors. 8. Congenital anomalies: corpus callosal dysgenesis; holoprosencephaly; hydranencephaly, posterior fossa Anomalies

Conclusions

With our increasing understanding of the neurogenetics of the congenital malformation of the brain, identifying of the

developmental malformations and encephalopathy of prematurity are of vital importance, to decide about its recurrence in the future pregnancies and if possible treat them intrauterine to decrease the damage to the developing neural structures. We discuss the neurogenetics, pathogenesis and imaging appearance of the fetal destructive lesions of the brain in this exhibit.

462

From Beginning to End, the Multi-Faceted Role of Radiology and Nuclear Medicine in Diagnosis, Management, and Treatment of Thyroid Malignancies.

A St. Claire¹, J Peacock¹, F Cloran², S Pettyjohn³

¹Brooke Army Medical Center, Fort Sam Houston, TX, ²San Antonio Uniformed Services Health Consortium, San Antonio, TX, ³USAF, Rockmart, GA

Purpose

Primary malignancies of the thyroid are the most common endocrine malignancy with common subtypes including papillary, follicular, medullary and anaplastic thyroid carcinoma, with a rising incidence of 17.6 cases per 100,000 individuals. (1) While the reported mortality rate is 0.5 deaths per 100,000 patients, mortality rates differ significantly based on histology, gender, and age. (1) The radiologist's role as a treatment partner is unique in that they are involved in the detection, diagnosis, staging, treatment and follow-up of thyroid malignancies; however, traditionally disparate disciplines within radiology are utilized. For example, radiologists practicing ultrasound (US) frequently are involved in the detection and biopsy of thyroid nodules, neuroradiologists may interpret associated Neck CTs and MRIs, and nuclear medicine imagers take part in detection and treatment of primary and metastatic disease. This Educational Exhibit provides a global approach to imaging in the diagnosis and management of thyroid malignancies. The following are the objectives for this image-rich exhibit: 1. To demonstrate the role of US in the evaluation of palpable or incidentally discovered thyroid nodules (Figure 1a) utilizing the American Thyroid Association (2) and/or Thyroid Imaging Reporting and Data System (3) guidelines to determine if a nodule needs imaging follow-up or biopsy. 2. To show the primary roles of CT and MRI including: a. Identifying anatomic evidence of nodal or distant metastases (Figure 1b) b. Staging of local thyroid malignancy, i.e., identifying anatomic extent of disease (when potentially underestimated on US, such as if substernal or greater than 3 cm in size) and assessing T4 status (Figure 1c) 3. To highlight the diagnostic and therapeutic roles of Nuclear Medicine including: a. Using I-123 and I-131 in the assessment of well-differentiated, radioiodine avid thyroid disease (for example, papillary or follicular thyroid carcinoma) (4) b. Administering high-dose I-131 in the treatment of known nodal metastases or in cases of residual disease c. Utilizing 18F-FDG PET-CT for non-radioiodine avid malignancies (such as medullary and anaplastic thyroid carcinoma) to assess local and metastatic extent (Figure 1d) (5) d. Showing the advent of 68Ga-DOTATATE in the assessment of well-differentiated medullary thyroid carcinoma and radioiodine-refractory thyroid carcinoma, and the potential treatment with Lu177- DOTATATE (Lutathera®) (5)

Materials and Methods

N/A

Results

N/A

Conclusions

N/A



Figure 1a



Figure 1b

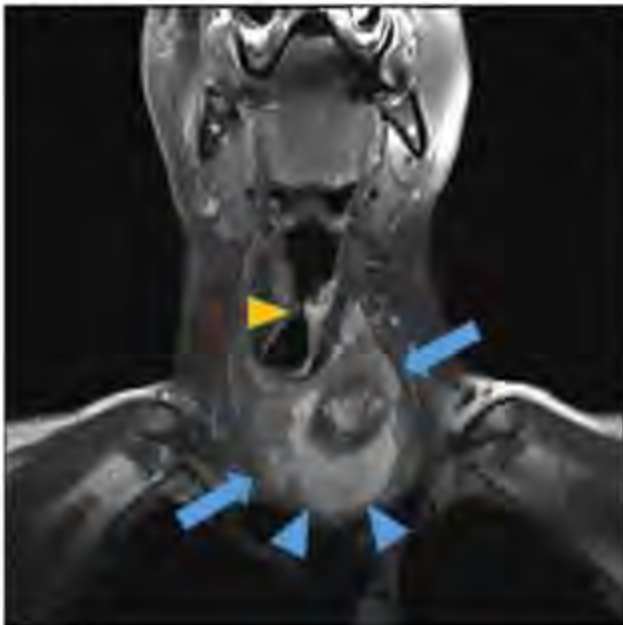


Figure 1c



Figure 1d

Figure 1. Imaging spectrum of metastatic thyroid carcinoma. **METASTATIC PAPILLARY THYROID CARCINOMA:** Longitudinal ultrasound image (Fig. 1a) in this 40 year old woman shows a solid, lobulated, taller than wide (on transverse image, not shown) hypoechoic nodule (blue solid arrows) measuring up to 2.0 cm x 1.6 cm x 1.0 cm within the right thyroid lobe with macrocalcifications (blue arrowhead); this is a TI-RADS 5 nodule requiring FNA. Coronal contrast enhanced CT image of the neck (Fig. 1b) in this same patient shows the calcified right thyroid nodule (blue arrowhead) as well as multiple partially calcified right cervical lymph nodes (Level III [orange arrowhead] and Level VI [green arrowhead] nodes shown), consistent with nodal metastases. **METASTATIC ANAPLASTIC THYROID CARCINOMA:** MRI coronal T2 fat-suppressed image (Fig. 1c) in this 84 year old man shows a large mass originating from the left thyroid lobe measuring up to 10 cm and demonstrating both solid (blue solid arrows) and necrotic (blue arrowheads) components. There is associated mass effect on the trachea as well as abnormal edema surrounding the left vocal cord (orange arrowhead), consistent with recurrent laryngeal nerve involvement (T4a disease). Cropped PET-CT maximal intensity projection in this same patient (Fig. 1d) shows a markedly avid mass centered within the lower neck (blue arrow) with decreased central avidity (blue arrowhead) corresponding to region of necrosis. There are numerous additional FDG-avid pulmonary metastases (orange arrowheads).

(Filename: TCT_462_RoleofRadiologyinThyroidMalignancy-Figure1.jpg)

From Skin to Skull: Imaging of Scalp injuries in the traumatic setting

C HonShideler¹, H Dasenbrock¹, M Abdalkader¹, V Andreu Arasa², B SETTY²

¹Boston Medical Center, Boston, MA, ²N/A, N/A

Purpose

Multiple anatomic structures overlie the calvarium to collectively form the scalp. In the traumatic setting, radiologists tend to focus on evaluating the more important intracranial structures and the skull, frequently overlooking injuries to the scalp. Scalp injuries can be described in various ways, based on the type of injury – blunt or penetrating; open or closed; acute and delayed complications. Birth related and iatrogenic scalp injury are important subsets. Different imaging modalities can be used for diagnoses and may require a multidisciplinary approach for treatment in certain situations. Awareness of these scalp injuries results in the use of appropriate imaging tools for correct diagnosis and successful treatment outcomes. EDUCATIONAL OBJECTIVES 1. Discuss various imaging modalities available to the interpreting radiologist. 2. Describe imaging features in blunt and penetrating traumatic scalp injuries, including degloving injuries. 3. Review imaging characteristics of birth-related scalp injuries. 4. Examine various treatment strategies for different types of scalp injuries. TABLE OF CONTENTS/OUTLINE 1. Review anatomy of the scalp. 2. Discuss common mechanisms and risk factors: birth related scalp injuries, penetrating and blunt scalp injuries. 3. Imaging armamentarium available for diagnosing scalp injuries. 4. Imaging characteristics of birth related scalp injuries such as cephalohematoma, subgaleal hematoma and caput succedaneum. 5. Discuss different scalp injuries ranging from the frequently encountered scalp hematomas to rarer complications such as degloving injury, pseudoaneurysms and arteriovenous fistulas. 6. Review the treatment of various scalp injuries. Materials and Methods

To raise awareness of the variety of scalp injuries that can occur during the traumatic setting and explore imaging modalities and treatment strategies available to the radiologist.

Results

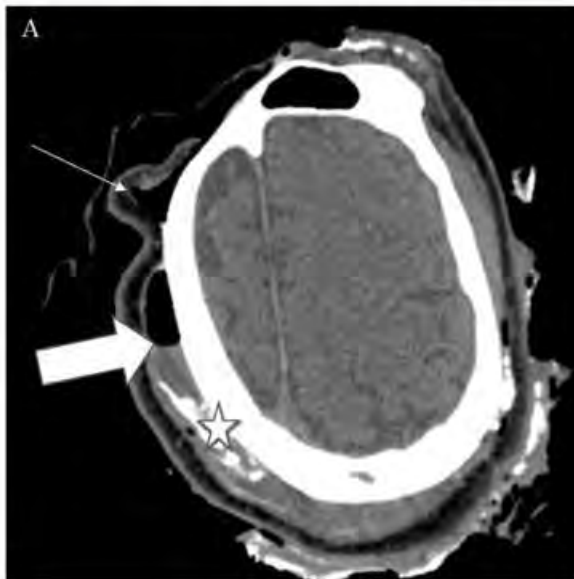
N/A

Conclusions

N/A

Degloving Injury of the Scalp

A 53 year old male s/p MVC with degloving injury of the scalp.



(A) Non contrast axial CT of the brain demonstrating a degloving injury (*thin arrow*) of the soft tissues with air fluid level (*thick arrow*) and debris (*asterisk*) in the right parietal region.



(B) Coronal reformatted image demonstrating the site of the degloving injury at the scalp (*thin arrow*).

(Filename: TCT_835_Degloving.jpg)

1047

From Tornwaldt Cysts to Echordosis Physaliphora and Sacral Cordomas. The Many Fates of the Notochord Remnants.

F Feltrin¹, M Alhasan², A Alhasan³, A Agarwal¹

¹UTSouthwestern Medical Center, Dallas, TX, ²UTSouthwestern, Dallas, TX, ³Taibah University, Madinah, United Arab Emirates

Purpose

There is a group of distinct pathological entities that share a common origin: the notochord remnants. Depending on whether the notochord cell remnant persists after birth, it can have different fates. Thorndwaldt cysts, Chordomas and Eccordosis Physaliphora are different entities that although share a common origin, have different clinical and radiological presentations, as well as a very different prognosis.

Materials and Methods

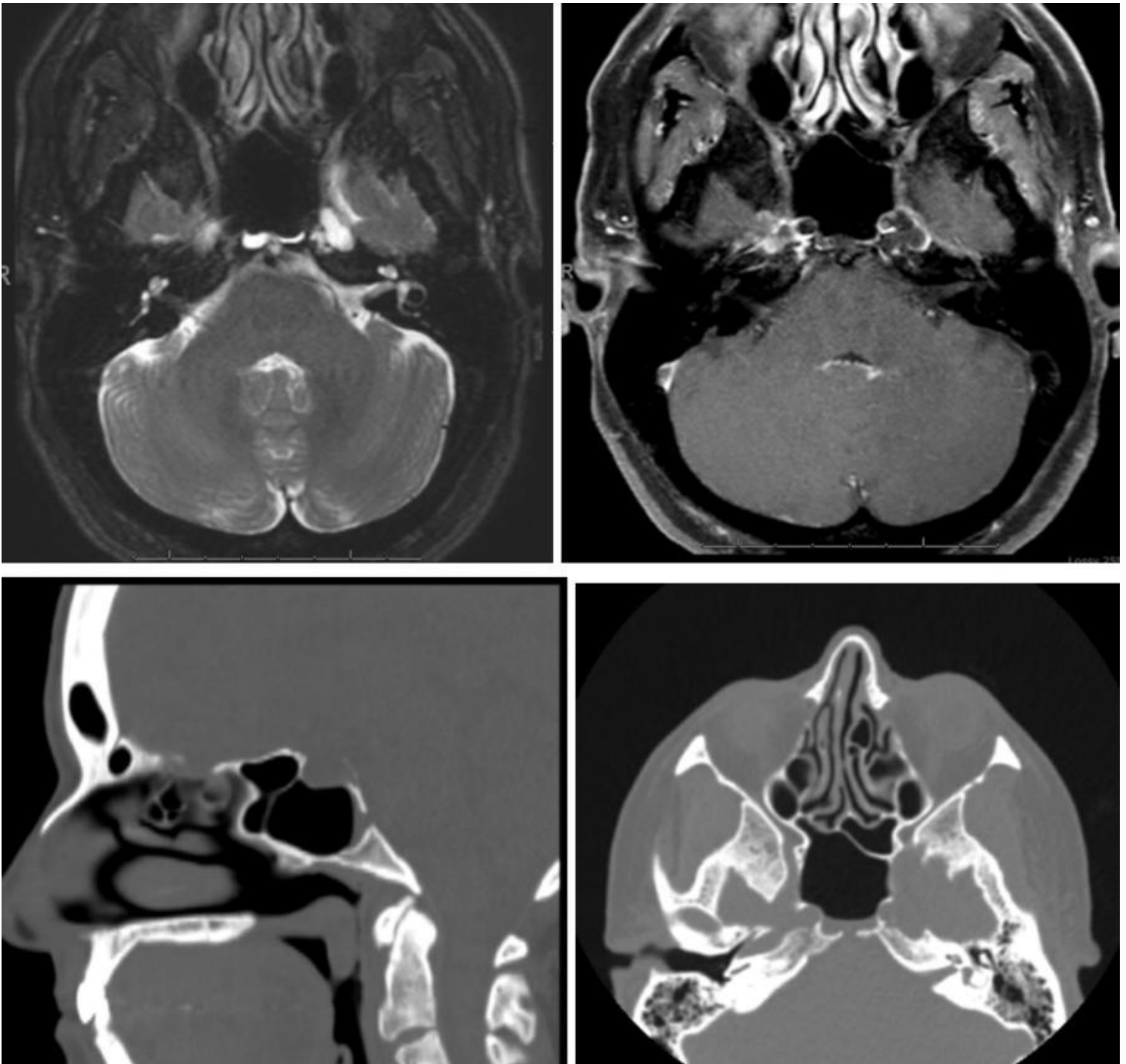
Our objective is to display these different entities according to location, most classic clinical and radiological presentation.

Results

Cases with classic presentation were collected from the archives of our institution. We described the classic clinical and radiological presentations, as well as we discussed the treatment options and prognosis.

Conclusions

We have found that Thorndwaldt cyst is an incidental finding, usually without clinical relevance. Characterized by variable T1, usually T2 hyperintense signal and without post contrast enhancement. Chordomas are found equally at the clivus or at the sacrum but can also be less frequently found at the vertebral bodies. They usually present as a well defined expansive and infiltrative lytic lesions, sometimes with intratumoral calcifications at CT. On the MR they usually have a pronounced high T2 signal, with variable T1 signal and variable post contrast enhancement. Eccordosis Physaliphora, on the other hand, are always located at the posterior aspect of the clivus, sometimes with an apparent calcified vascular stalk. Described on the pathology as a gelatinous cyst inside the CSF, at MR the same aspect can be found, represented by a small cyst with low T1 and high T2 signal, without enhancement, closely related to the clivus.



(Filename: TCT_1047_eccordosis.jpg)

974

Functional and Structural Neuroimaging in Frontotemporal Dementia

E Gil¹, L Coelho², L Godoy², L Lucato³, G de Carvalho Campos Neto², A Coutinho⁴, A Barbosa², R BERTANHA², L Bisolo², D Nunes⁵, L Bezerra⁶

¹Hospital Albert Einstein, São Paulo, Brazil, ²Hospital Israelita Albert Einstein, São Paulo, Brazil, ³Instituto de Radiologia, Hospital das Clínicas da Faculdade de Medicina da Universidade de São Paulo, São Paulo, Brazil, ⁴HCFMUSP, São Paulo, Brazil, ⁵InRad, São Paulo, Brazil, ⁶Hospital Israelita Albert Einstein, São Paulo, SP

Purpose

Frontotemporal dementia (FTD) is the third most frequent early-onset neurodegenerative dementia, but diagnosis and subtyping this disease may be challenging. Early diagnosis is essential to improve outcome, and functional and structural neuroimaging plays an important role in this scenario. This educational exhibit provides a practical overview of the atrophy patterns that may help the radiologist reach an accurate imaging diagnosis.

Materials and Methods

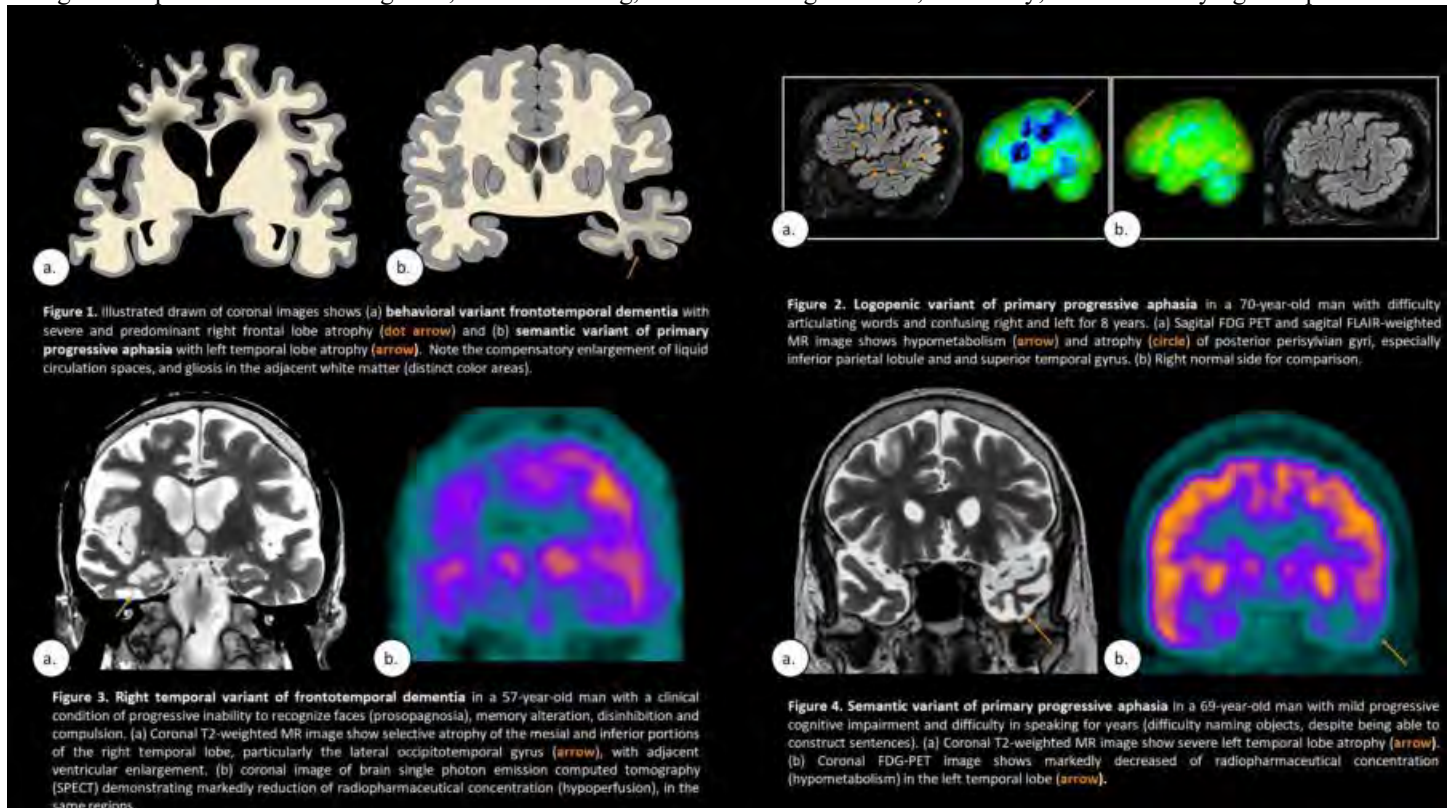
1-To review the pathophysiology of neurodegenerative processes and their typical clinical presentations. 2- Recognize the different nuclear medicine (FDG-PET and SPECT) and magnetic resonance imaging (MRI) patterns of frontotemporal dementia to help the radiologist avoid misinterpretations and improve diagnostic rate. 3- Demonstrate the main differences and key points on differentiating FTD from "normal aging" and other dementias. 4- Contribute to a multidisciplinary approach in the workup of FTD. 5- Briefly discuss the future perspectives of the main imaging modalities currently used in the research scenario, focusing on validation of neuroimaging biomarkers.

Results

Review of the current literature to identify the main characteristics and future perspectives of frontotemporal dementia, and a radiology database search and electronic medical record review for the following pathologies: behavioral variant frontotemporal dementia (bvFTD), right temporal variant of frontotemporal dementia and primary progressive aphasia (PPA). PPA may be further subdivided into subgroups including semantic variant PPA (svPPA), non-fluent variant PPA (nfvPPA) and logopenic variant (lvPPA).

Conclusions

Frontotemporal dementia is a diverse and clinically devastating group of diseases. It is fundamental that radiologists and nuclear medicine physicians recognize these conditions, thus helping the clinician to provide the patient appropriate treatment and best outcome. The ability to narrow diagnosis can also help the patients, so they can be correctly informed and prepared to avoid unnecessary hardship, both emotionally and financially. Recent research has shown the importance of pathobiology and molecular changes to improve methods of diagnosis, disease tracking, differential diagnosis and, ultimately, disease modifying therapies.



(Filename: TCT_974_FTD-ASNR.jpg)

288

Fundamentals of Cerebral Angiography: The Relationship Between Biplanar Projections and Cerebral Vascular Anatomy

M Isikbay¹, M Caton¹, A Baker¹, v halbach¹, M Amans¹

¹UCSF, San Francisco, CA

Purpose

1. Angiographic projections significantly alter the appearance of key anatomy 2. The impact of a projection on vascular anatomy is challenging to understand 3. No comprehensive resource exists which teaches this relationship clearly 4. Multiplanar reformats (MPRs) of CT angiography can be used to demonstrate this relationship

Materials and Methods

Utilizing appropriate projections during angiography is critical as it can dramatically alter the visualization of key anatomy. While available training resources do discuss common angiographic projections such as Townes', Waters', and Schuller's, no training

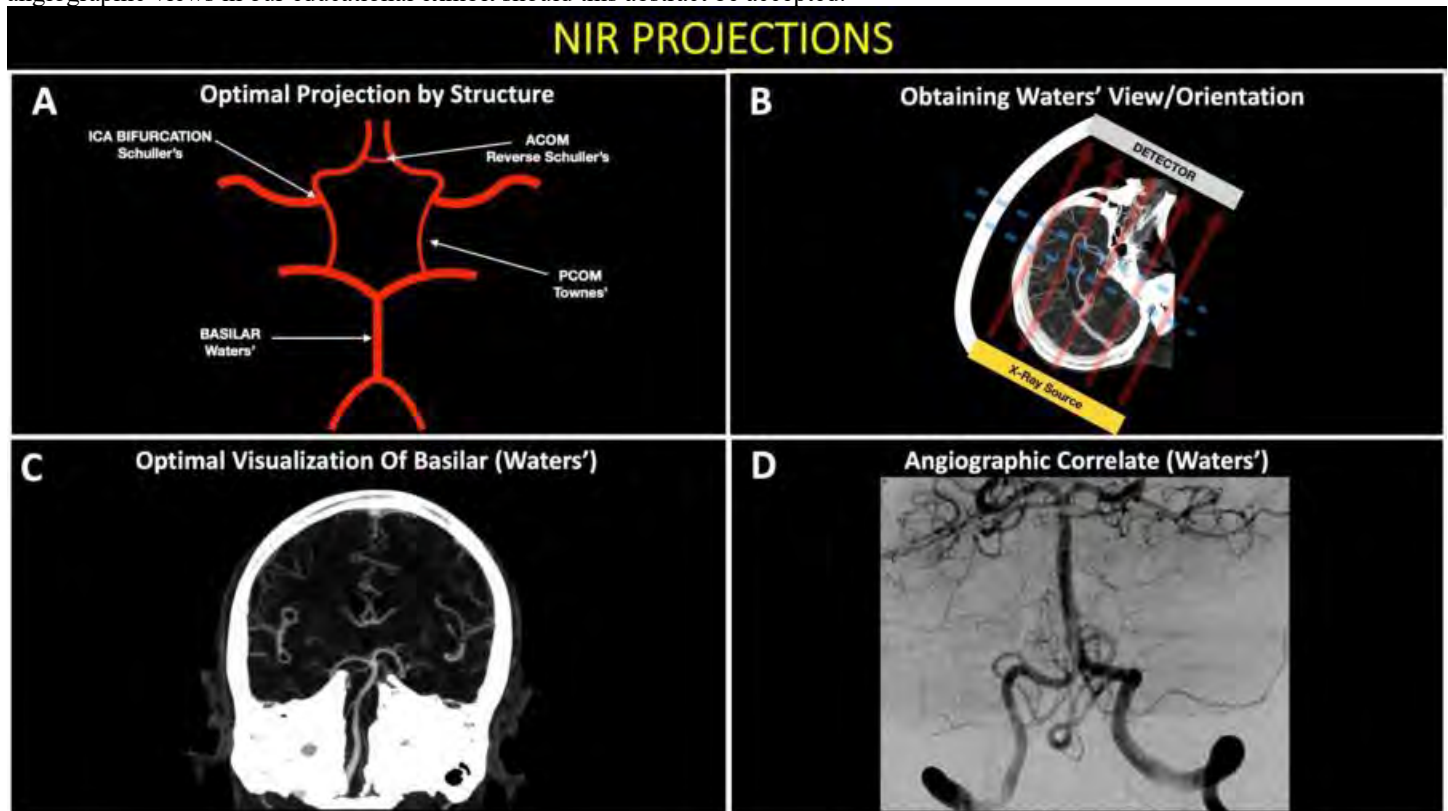
resource exists which clearly shows the impact each projection has on the appearance of vascular anatomy. We present an educational model here to address this issue which utilizes MPRs of a CTA that clearly demonstrates this relationship.

Results

Figures were created to demonstrate how angiographic projections were obtained. Then multiplanar reformats of a CTA of the brain were created that mimicked these angiographic projections. Representative thick slab MIP slices were utilized to create figures that demonstrated how each projection altered the appearance of various vessels.

Conclusions

The optimal angiographic projection for key cerebral vessels is outlined in Figure 1A. In this abstract the Water's is explored. Figure 1B shows the orientation of the X-ray source and detector to obtain this view relative to a sagittal CTA head MPR. The blue dotted lines demonstrate the orientation and level where a coronal thick slab MPR was created (Figure 1C) which demonstrates the effect this orientation has on the basilar artery. A corresponding image of the basilar artery obtained during angiography in Water's view is also provided (Figure 1D). The Water's view is best for visualizing the basilar artery because the long axis of the vessel is perpendicular to the path of the X-rays used (Figure 1B). This causes the basilar artery to appear "elongated" as the entire length of the vessel is optimally visualized (Figure 1C, Figure 1D). We believe this methodology of teaching the relationships between angiographic orientation and vascular anatomy helps make the 3-D spatial reasoning more intuitive. We plan to provide similar figures other angiographic views in our educational exhibit should this abstract be accepted.



(Filename: TCT_288_ASNR2021NIRProjectionFigure.jpg)

904

Getting Mental With Dental- Neuroimaging Review of Critical Anatomic Structures Affected by Dental Extractions

H Chengazi¹, S Ruggiero², C Kirsch¹

¹Northwell Health, New York City, NY, ²NEW YORK CENTER FOR ORTHOGNATHIC AND MAXILLOFACIAL SURGERY - Northwell Health, LAKE SUCCESS, NY

Purpose

Dental extraction pathology has unique anatomic and pathologic considerations due to variable course of the trigeminal inferior alveolar and lingual nerves. Understanding this critical oral cavity variable anatomy including adjacent structures and spaces allows for improvement in localizing injury, a prompt diagnosis and assistance in referring clinicians' treatment plans. This presentation reviews the critical variable anatomy, pathology, and radiographic findings of odontogenic disease secondary to dental extractions, specifically trauma to the neurovascular anatomy.

Materials and Methods

The purpose of the presentation is to radiographically demonstrate pathology that may occur from dental extractions performed for

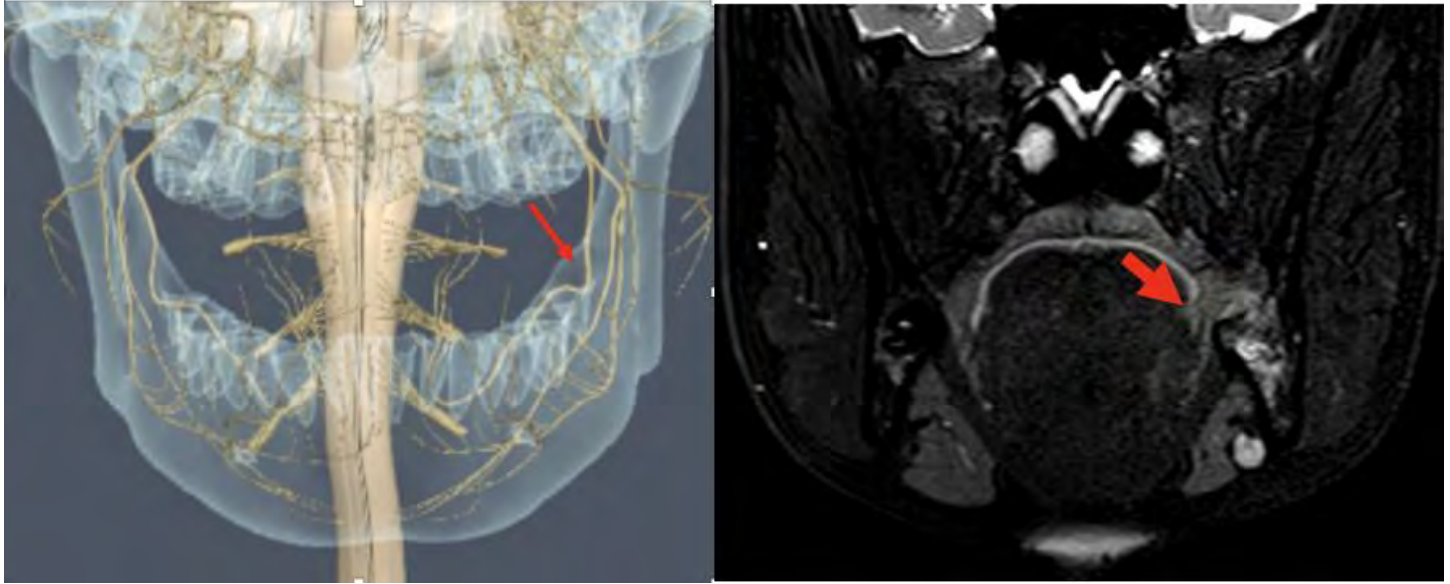
caries, periodontal disease and impacted third molars with resultant alveolar osteitis, infection, fracture and bone fragmentation, hematoma, oroantral fistulas, and especially paresthesias from trauma to adjacent inferior alveolar and lingual nerves

Results

Retrospectively cross-sectional CT and MRI review highlighting sequences demonstrating post-extraction pathology referred to our institution from 2015-2020. Specifically included is a detailed anatomic presentation of the variable course of the V3 lingual nerve branch at risk for injury during third molar extractions with a review of relevant and critical adjacent soft tissue anatomy.

Conclusions

Dental extractions for caries, periodontal disease and impacted third molars can lead to alveolar osteitis, infection, fracture and bone fragmentation, hematoma, oroantral fistulas, and paresthesia from inferior alveolar and lingual nerve trauma. This exhibit presents cross-sectional CT and MRI sequences highlighting post-extraction pathology referred to our institution from 2015-2020, with a detailed anatomic presentation of V3 lingual nerve branch with its variable course putting it at risk for injury during third molar extractions with a review of relevant and critical adjacent soft tissue anatomy.



(Filename: TCT_904_ScreenShot2020-11-01at105911PM.jpg)

983

Granular cell tumor of the sellar region

T Richards¹, K Salzman¹

¹University of Utah, Salt Lake City, UT

Purpose

Discuss the cell origin, histology, imaging features, clinical presentation, and surgical considerations for granular cell tumors of the sellar region. Discuss the key unique imaging features of each entity in the differential diagnosis for granular cell tumors.

Materials and Methods

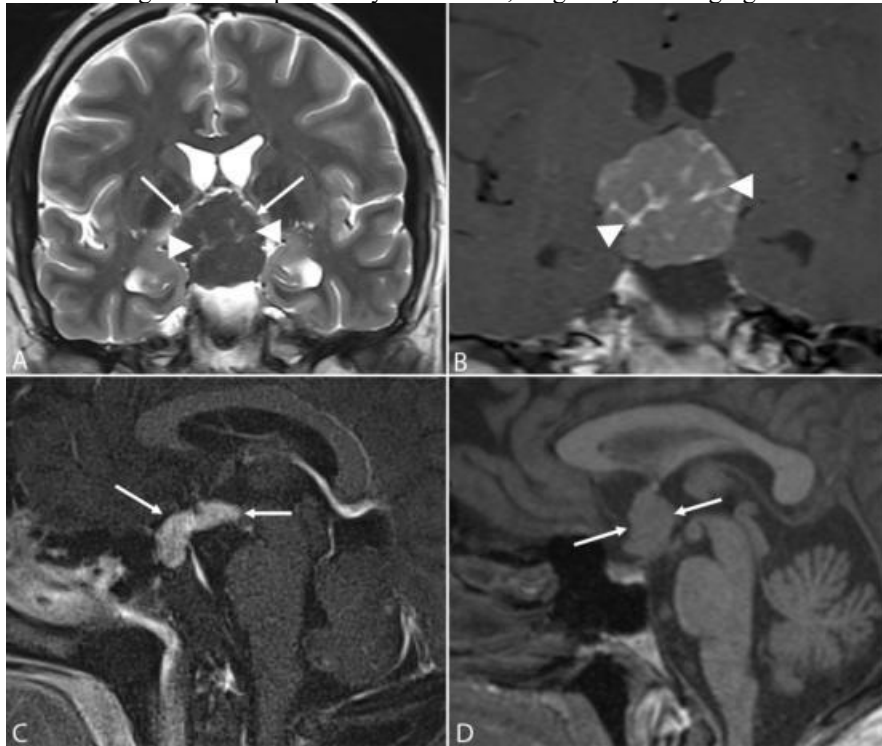
To educate neuroradiologists on this rare entity and instruct when the tumor should be included high on the differential diagnosis of a suprasellar and/or sellar mass.

Results

Cell origin and histology 1. Granular pituicyte 2. Usually TTF-1, vimentin, and S100 positive 3. PAS positive polygonal cells, perivascular lymphocytic infiltrates 4. Histopathologic images will be provided Clinical features 1. Mean age 49 2. Female predominance 3. Vision changes, hypopituitarism, headaches 4. Benign clinical course with recurrence common Imaging features 1. CT hyperdense, calcifications rare 2. MRI a. Typically enhances b. Star-like crack appearance c. T1 isointense d. T2 hypointense 3. Surgical tissue sampling needed for diagnosis Differential diagnosis 1. Primary sellar/suprasellar masses a. Craniopharyngioma i. Cystic T2 hyperintense changes ii. Calcification iii. T1 hyperintense areas iv. Enhancement b. Germinoma i. Calcification ii. CSF seeding iii. CT Hyperdense iv. Enhancement c. Glioma i. May be non-enhancing ii. Usually T2 hyperintense iii. Infiltrative d. Other TTF-1 positive tumors (often difficult to differentiate) i. Pituicytoma ii. Spindle cell oncocytoma iii. Sellar ependymoma 2. Pituitary adenoma a. Inseparable from the anterior pituitary lobe b. Enhancing 3. Hypothalamic hamartoma a. No enhancement b. Slightly T2 hyperintense c. Different origin 4. Sarcoidosis a. Other sites of involvement b. Chest radiograph abnormalities c. Typically coats or thickens infundibulum rather than mass-like lesion 5. Lymphocytic hypophysitis a. Thickened stalk rather than mass b. Clinical history such as immunotherapy helpful 6. Lymphoma a. Homogeneous enhancement b. Other sites of involvement 7. Metastasis a. Cancer history b. Usually more heterogeneous c. Other sites of involvement Treatment 1. Trans-sphenoidal resection 2. Surgically challenging, vascular & adherent tumor

Conclusions

Imaging features including T2 hypointense signal and a "star-like crack sign" may help suggest the diagnosis of granular cell tumor. Radiologists can include granular cell tumor in the differential diagnosis when imaging features are consistent, which can help prepare the neurosurgeon for the possibility of this rare, surgically challenging tumor.



T2 (A) and T1 post contrast (B) coronal images demonstrate a suprasellar mass that has T2 hypointense signal (arrows) and enhancement. Pathology was consistent with a granular cell tumor of the sellar region. Note the T2 hypointense and enhancing "star-like" crack sign (arrowheads) which has been described for this entity.

Sagittal T1 post contrast fat saturated midline image (C) demonstrates enhancement along the superior pituitary gland and infundibulum (arrows). The patient had additional leptomeningeal lesions in the brain and multiple lung nodules. Biopsy was consistent with neurosarcoïdosis.

Midline sagittal T1 MPRAGE image (D) demonstrates a T1 isointense mass (arrows) along the anterior aspect of the 3rd ventricle displacing the pituitary stalk posteriorly. Pathology of the mass was diagnostic of a chordoid glioma.

(Filename: TCT_983_ANSR_abstract_Granular_Cell_Tumor_figure.jpg)

580

Head and Neck Manifestations of Systemic Disease

K Werth¹, T Kennedy²

¹University of Wisconsin, Madison, WI, ²The University of Wisconsin, Middleton, WI

Purpose

Review pathophysiology and imaging findings associated with various multi-systemic disease processes that have manifestations in the head and neck. Review expected patterns of disease that will allow radiologists to look for clues to aid in the diagnostic work-up of a patient with systemic disease.

Materials and Methods

There are numerous multi-systemic disease processes that have imaging findings within the head and neck, which can either be an initial manifestation of a systemic diagnosis or sequelae of a known disease. The imaging findings can be focal or diffuse, and these cases can oftentimes be a diagnostic conundrum for radiologists as many of these diseases can appear very similar to infectious processes. Radiologists can play a pivotal role in the diagnostic work-up and outcomes of patients with underlying systemic illness by recognizing key imaging features and helping to circumvent possible complications or emergencies related to the systemic disease. The purpose of this electronic educational exhibit is to familiarize radiologists with the various imaging presentations of different multi-systemic diseases by utilizing a case-based approach.

Results

Case-based approach to reviewing imaging findings seen in the head and neck related to multi-systemic disease

Conclusions

This electronic educational exhibit will review the pathophysiologic issues and imaging findings related to various multi-systemic disease processes, including rheumatologic and mucociliary disease, metabolic and bone disorders, as well as disorders of immunodeficiency and malignancy. More specifically, this exhibit will use a case-based style to review granulomatosis with polyangiitis (GPA), eosinophilic granulomatosis with polyangiitis (EGPA), sarcoidosis, relapsing polychondritis (RPC), amyloidosis, IgG4 immunodeficiency, Gorlin syndrome, Gardner syndrome, cystic fibrosis, McCune-Albright syndrome, Paget's disease, and Kallman's syndrome. It is imperative for the interpreting radiologist to be aware of imaging findings in the head and neck related to common and uncommon multi-systemic diseases. Accurate recognition of these findings is important for further care of the patient as well as avoiding potential head and neck complications or emergencies that may result if unrecognized. The goal of this exhibit is to

educate radiologists on possible head and neck manifestations of multi-systemic disease processes while also reviewing their pathophysiology.

CASE 1: DIFFERENTIAL DIAGNOSIS

Malignant Otitis Externa

Septic Thrombophlebitis

Sarcoidosis

Amyloid

Granulomatosis with Polyangiitis

(Filename: TCT_580_ASNR2021HNManifestationsofSystemicDisease.jpg)

1043

High-risk Carotid Atherosclerotic CT Angiography Biomarkers: Imaging Findings and Significance

T Reher¹, A Kuner², J McNally³, J Manunga⁴, K Johnson⁵, L Eisenmenger⁶

¹University of Wisconsin Hospital and Clinics, Madison, WI, ²University of Wisconsin School of Medicine and Public Health, Middleton, WI, ³University of Utah, Salt Lake City, UT, ⁴Minneapolis Heart Institute, Chaska, MN, ⁵University of Madison - Wisconsin, Madison, WI, ⁶University of Wisconsin - Madison, Middleton, WI

Purpose

Review CT/CTA biomarkers of unstable carotid plaques Discuss the MRI/MRA correlates of CT/CTA carotid plaque features Present the potential implications of high-risk plaque features on patient risk stratification and management Evaluate what future clinical studies are needed

Materials and Methods

Worldwide, stroke is the second leading cause of death and large vessel atherosclerosis contributes to up to 25% of cases. Non-contrast head CT and CTA of the head and neck are a common method of initially assessing for stroke. Though MRI has superior soft tissue characterization and provides additional biomarkers of at-risk carotid atherosclerotic plaques, it's longer scan time, decreased accessibility outside of business hours, and prohibitive medical devices/foreign bodies restrict its use in many cases. For these reasons, there has been considerable investigation into CTA surrogate findings that may help to stratify a patient's risk of a carotid source stroke and guide management. The purpose of this educational exhibit is to highlight at-risk atherosclerotic plaque features that a radiologist needs to know and to characterize their clinical significance.

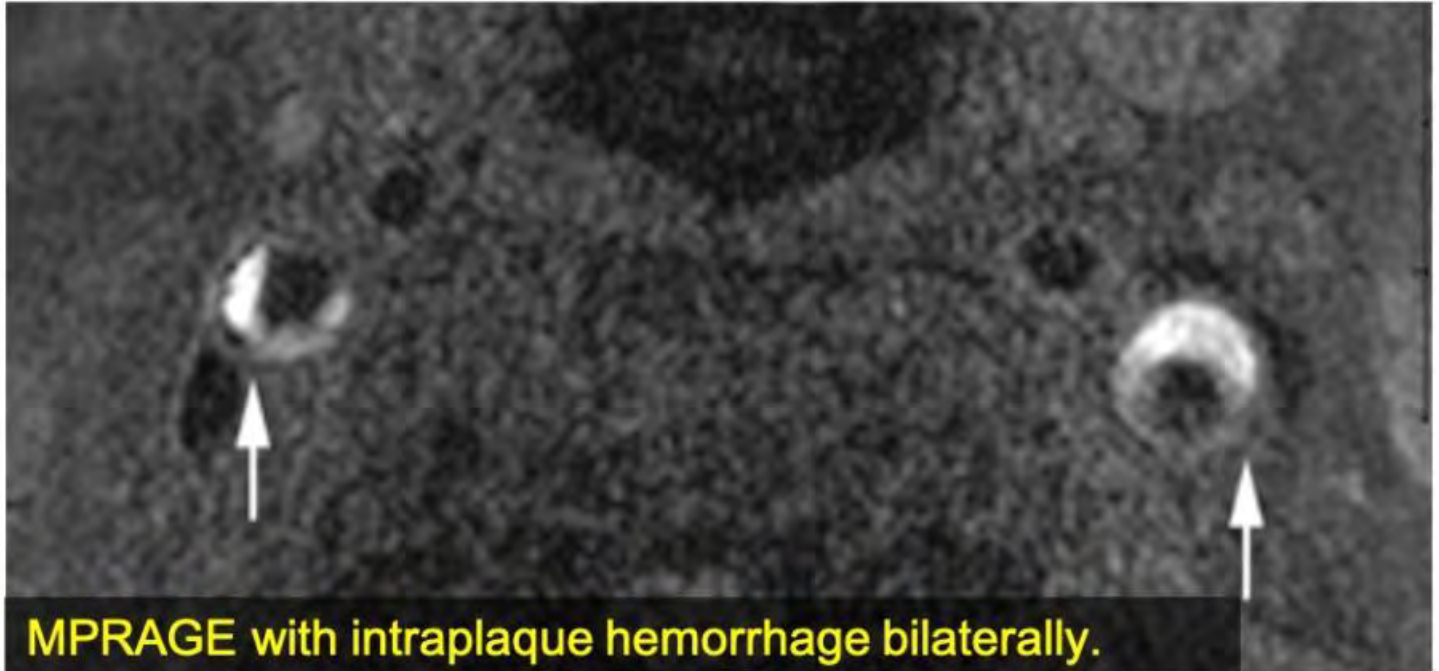
Results

We will present imaging of mild, moderate, and severe atherosclerotic stenosis, plaque ulceration as well as CTA rim-sign of intraplaque hemorrhage (IPH) and plaque enhancement as a marker of neovascularization or disrupted fibrous cap. We will touch on the importance plaque composition. In addition, we will describe corollary MRI/MRA findings for CTA plaque characteristics.

Conclusions

Owing to its superior spatial resolution, CT allows for plaque volume quantification. CTA outperforms ultrasound for subcomponent characterization (fatty, mixed, calcified) and detecting plaque ulcerations, defects >1 mm deep along the luminal surface. Plaque enhancement requires a pre-contrast scan and follows a previously established threshold of 10 Hounsfield units. Detection of IPH using CT is challenging and conflicting results have been reported; however, there is recent evidence that soft plaque and calcification morphology can predict the presence of IPH and stroke risk. The implications of calcification volumes and features still remains

complex. Multienergy CT offers advanced tissue characterization. CTA imaging can present carotid atherosclerosis biomarkers to aid in stratifying a patient's risk profile for stroke. To guide patient management, radiologists should take steps to optimize imaging protocols and become familiar with these findings.



(Filename: TCT_1043_CT_Plaque.jpg)

197

Hindsight is 20/20: A Review of Orbital Infection, Complications, and Mimics

D Hutchison¹, C Liang², N Miner¹, E KUOY¹, J Soun¹, D Florioli¹, E CHU¹

¹University of California, Irvine, Orange, CA, ²University of California Irvine Department of Radiological Sciences, Orange, CA

Purpose

Orbital and periorbital infections are relatively common with significant associated morbidities, including vision loss and sometimes even death. Treatment and prognosis vary based on anatomic extent of the infection. After reviewing the exhibit, the reader should be

able to distinguish preseptal from orbital cellulitis, identify complications requiring emergent surgical management, and distinguish orbital infection from other pathology.

Materials and Methods

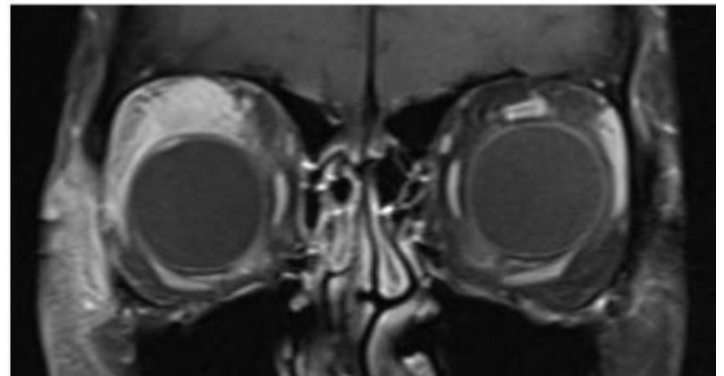
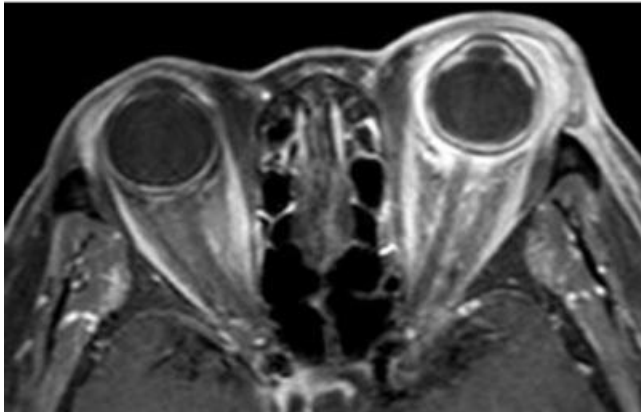
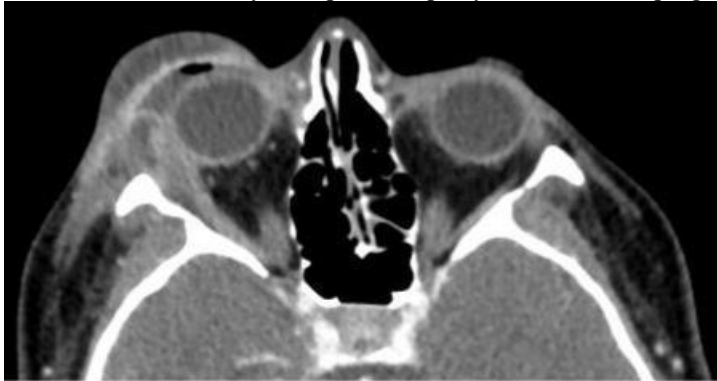
Overview of orbital infection, complications, and differential diagnosis.

Results

Case examples from our institutional database were used to create this educational exhibit.

Conclusions

This exhibit will focus on the three main clinical entities that encompass ocular and orbital infection: periorbital cellulitis, orbital cellulitis, and endophthalmitis. Key clinical and image findings of orbital infection will be reviewed, including route of spread, risk factors, pitfalls, and complications. Specifically, key distinguishing imaging features of each of the 5 stages of the Chandler classification of orbital infection will be presented, including: I. Preseptal cellulitis II. Orbital cellulitis III. Subperiosteal abscess IV. Orbital abscess V. Cavernous sinus thrombosis Furthermore, additional complications of ocular and orbital infection will be included: 1. Meningitis 2. Cerebritis 3. Intracranial abscess 4. Intraocular abscess 5. Panophthalmitis 6. Optic neuritis Additionally, clinical and imaging characteristics of important ocular pathologies that mimic orbital infections and their key differentiating features will be addressed, including: 1. Inflammatory: Sarcoid, orbital pseudotumor, granulomatosis with polyangiitis 2. Neoplastic: Lymphoma, retinoblastoma, rhabdomyosarcoma, metastasis 3. Vascular: Cavernous malformation, lymphatic malformation 4. Trauma: Orbital emphysema, retrobulbar hemorrhage 5. Systemic disease: Sickle cell disease with subperiosteal hematomas and bony infarcts 6. Endocrine disorder: Thyroid ophthalmopathy Treatment and prognosis of orbital and ocular infection will also be discussed.



(Filename: TCT_197_Figure.jpg)

769

Horner's Syndrome: A review of the oculosympathetic pathway

S Jetty¹, D Howard¹, A Shetty¹, A Kessler²

¹University of Rochester Medical Center, Rochester, NY, ²University of Rochester Medical Center, Rochester, NY

Purpose

Horner's Syndrome is a neurologic presentation in which disruption of the oculosympathetic pathway results in the classic clinical triad of miosis, ptosis, and anhidrosis. In these patients, imaging plays a key role in discovering the etiology of their symptoms. Educational objectives include: 1. Review the anatomy of the oculosympathetic pathway. 2. Review optimal imaging protocols to assess the pathway. 3. Review the various clinical presentations based on their sites of disease. 4. Discuss key sites of pathology within the pathway using a case-based approach.

Materials and Methods

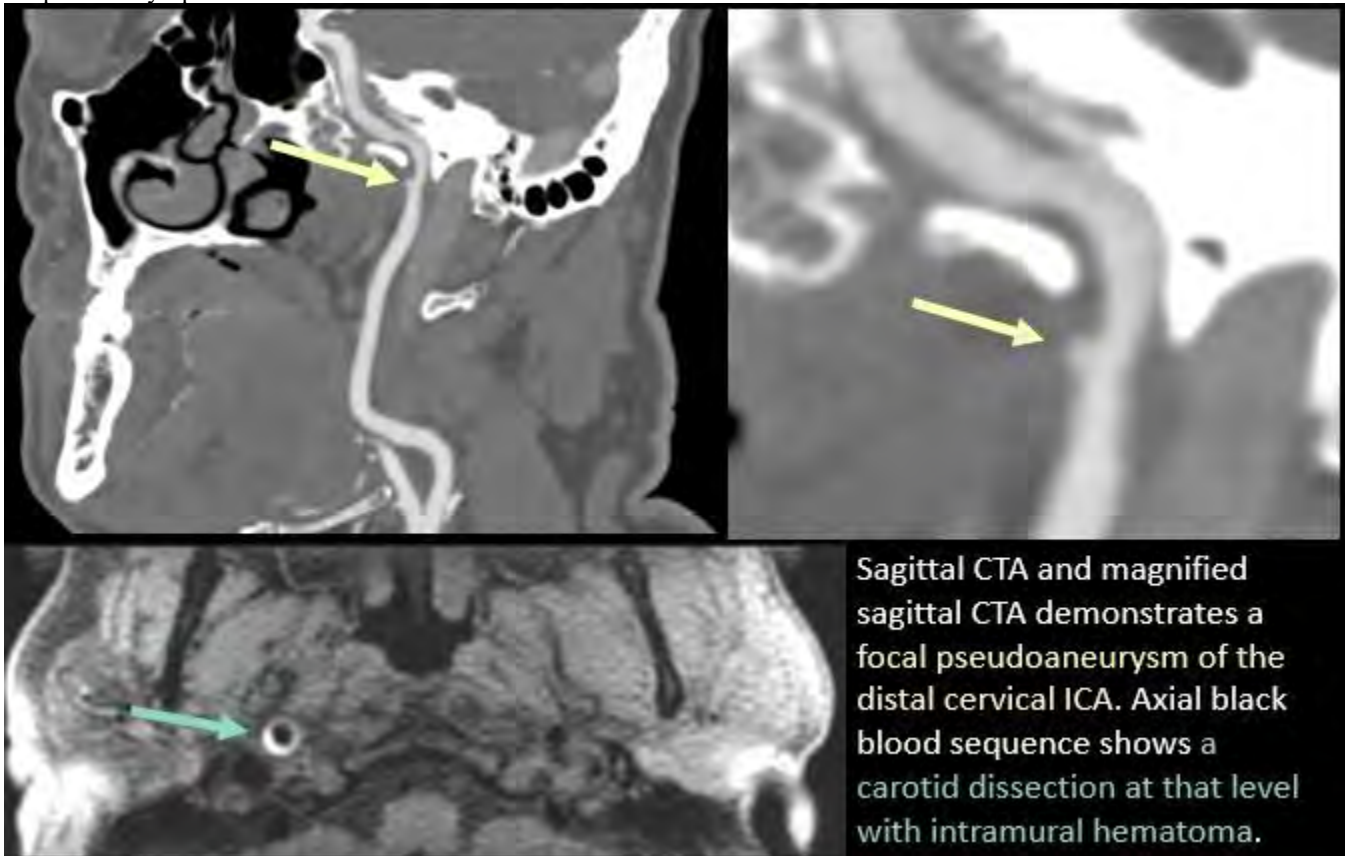
Horner's Syndrome was first described by Francois Pourfour du Petit in France in 1727 after experimentation on dogs. Horner's syndrome results from the disruption of the sympathetic innervation of the eye and classically presents with the clinical triad of miosis, ptosis, and anhidrosis. Other signs/symptoms such as enophthalmos and a narrow palpebral fissure can also be present. There is varied pathology, benign and malignant, which can affect this pathway and knowledge of the anatomical pathway and its associated clinical presentation can lead to prompt patient care.

Results

First-order (Central) • Hypothalamic lesions • Stroke, tumor, demyelinating diseases • Brainstem • Stroke, tumor, demyelinating disease • Cervical spine • Trauma, syringomyelia, trauma, myelitis • Vascular • Trauma, AV malformation • Infection Second-Order (Pre-ganglionic) • Lung • Pancoast tumor, infection • Vascular • Subclavian artery aneurysm, subclavian artery dissection • Thyroid • Malignancy, goiter • Cervical rib • Iatrogenic Third-Order (Post-ganglionic) • ICA • Trauma, carotid artery aneurysm, dissection, thrombosis. • Superior cervical ganglion • Jugular venous ectasia, trauma, iatrogenic • Skull base • Tumors, cavernous sinus thrombosis, infection, inflammation

Conclusions

Understanding the anatomy of the oculosympathetic pathway is critical in interpreting imaging on patient's with Horner's Syndrome. This knowledge, coupled with optimized imaging protocols, allows the radiologist to play a crucial role in diagnosing the etiology for the patient's symptoms.



(Filename: TCT_769_SubmissionGraphic.jpg)

771

How can CT help to narrow the differential diagnosis of some lesions in the CNS initially assessed by MR?

F Assunção¹, L Martins¹, L Freitas¹, E Agapito Valadares¹, B Nóbrega¹, L Scoppetta¹, T Scoppetta¹
¹Hospital São Camilo, São Paulo, SP

Purpose

CT and RM are complementary imaging methods, each with its advantages and disadvantages. The knowledge of how CT can add value to MRI in the diagnosis of different pathologies of the CNS in different clinical settings must be the domain of the neuroradiologist, avoiding that CT is misinterpreted as a screening tool. The advantages of CT are numerous, such as providing detailed evaluation of the cortical bone, allowing accurate detection of calcifications or metallic foreign bodies, allowing assessment of the density of pseudotumor lesions, etc. These characteristics can provide additional valuable information in the interpretation of lesions in the CNS initially assessed by MR. The aim of this study is to show many clinical and radiological cases in which CT played

an important additional role in the diagnosis of CNS diseases initially assessed by MRI, as well as to encourage neuroradiologists to better explore the method as a complementary tool.

Materials and Methods

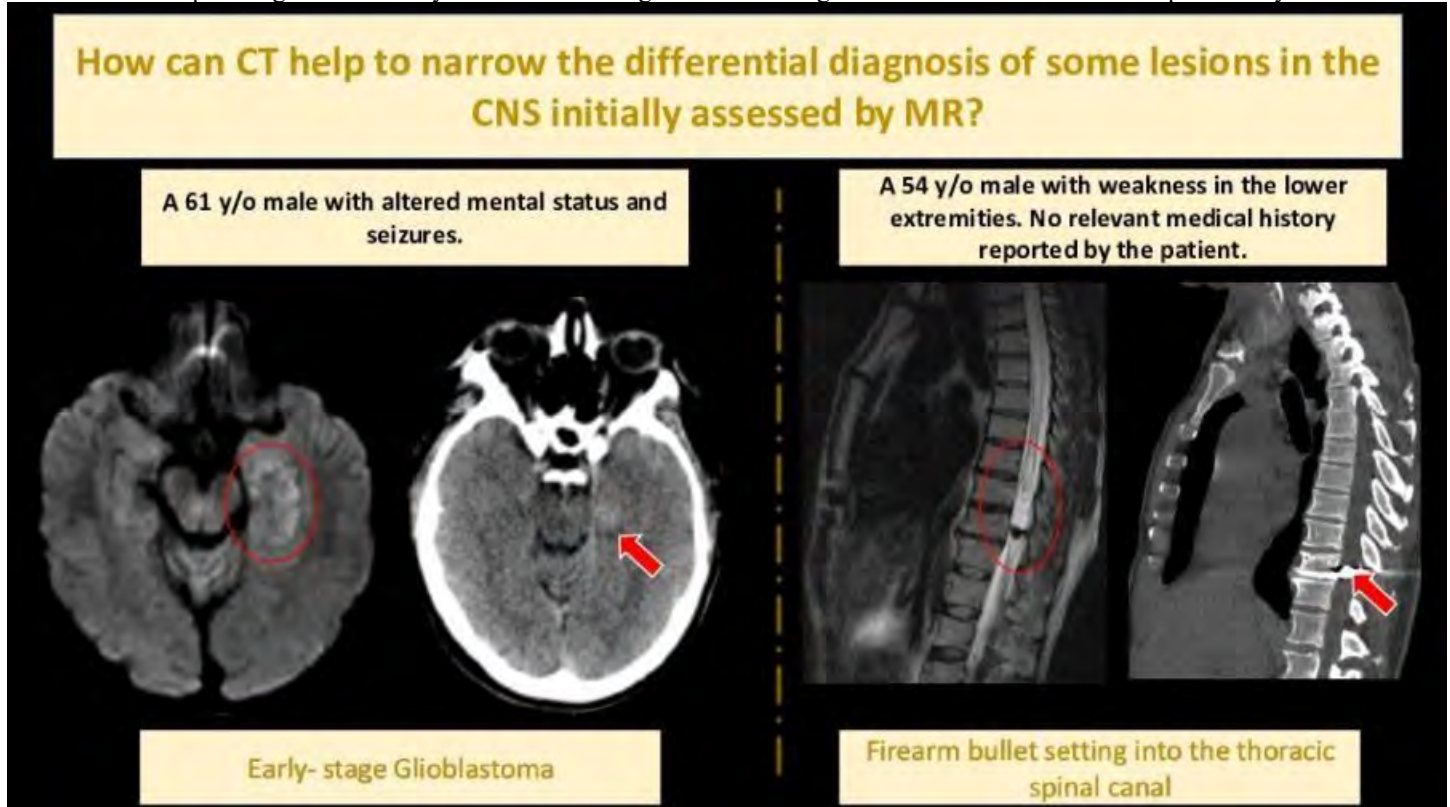
The purpose of the study is to show, through an approach with clinical cases, how brain computed tomography (CT) can help to narrow the differential diagnosis of some lesions in the central nervous system initially assessed by brain magnetic resonance (MR).

Results

We searched in our database for clinical cases of patients whose brain CT performed important role in the diagnosis or in the narrowing of the differential diagnosis of lesions in the CNS initially assessed by brain magnetic resonance (MR).

Conclusions

We found interesting cases in our database such as a pseudotumoral lesion in the spinal cord caused by a metallic bullet artifact (not mentioned in the patient's medical history) and whose CT helped us in the differential diagnosis. Another interesting case was in a patient with a hippocampal lesion identified on MRI as a T2 hypersignal lesion that allowed a wide differential diagnosis such as herpetic infection, post-epileptic status, glioma etc. and whose hyperdensity of the lesion on CT allowed us to narrow the differential diagnosis for primary tumor. In conclusion, this serie of cases reaffirms the potential additional value that CT has in the interpretation of different CNS pathologies assessed by MRI and encourages neuroradiologists to use this method as a complementary tool to MRI.



(Filename: TCT_771_filejpg.jpg)

371

How to begin your first AI project: A tutorial based on the diagnosis and management of gliomas

H Subramanian¹, W Brim¹, A Brackett², M Hans¹, M Johnson¹, A Malhotra¹, M Aboian¹

¹Brain Tumor Research Group - Department of Radiology & Biomedical Imaging, Yale School of Medicine, New Haven, CT, ²Harvey Cushing/John Hay Whitney Medical Library, Yale University, New Haven, CT

Purpose

1. Explain the process of conducting a systematic review. 2. Provide an example of systematic review methods applied to the use of AI in neuro-oncology. 3. Review the current literature published regarding the use of AI to diagnose and treat gliomas.

Materials and Methods

Applications of artificial intelligence (AI) have been increasingly studied in neuroradiology. We performed a systematic review to characterize the applications of machine learning in the diagnosis and management of gliomas. This will provide a comprehensive framework for neuroradiologists to develop research projects in machine learning applications to clinical practice.

Results

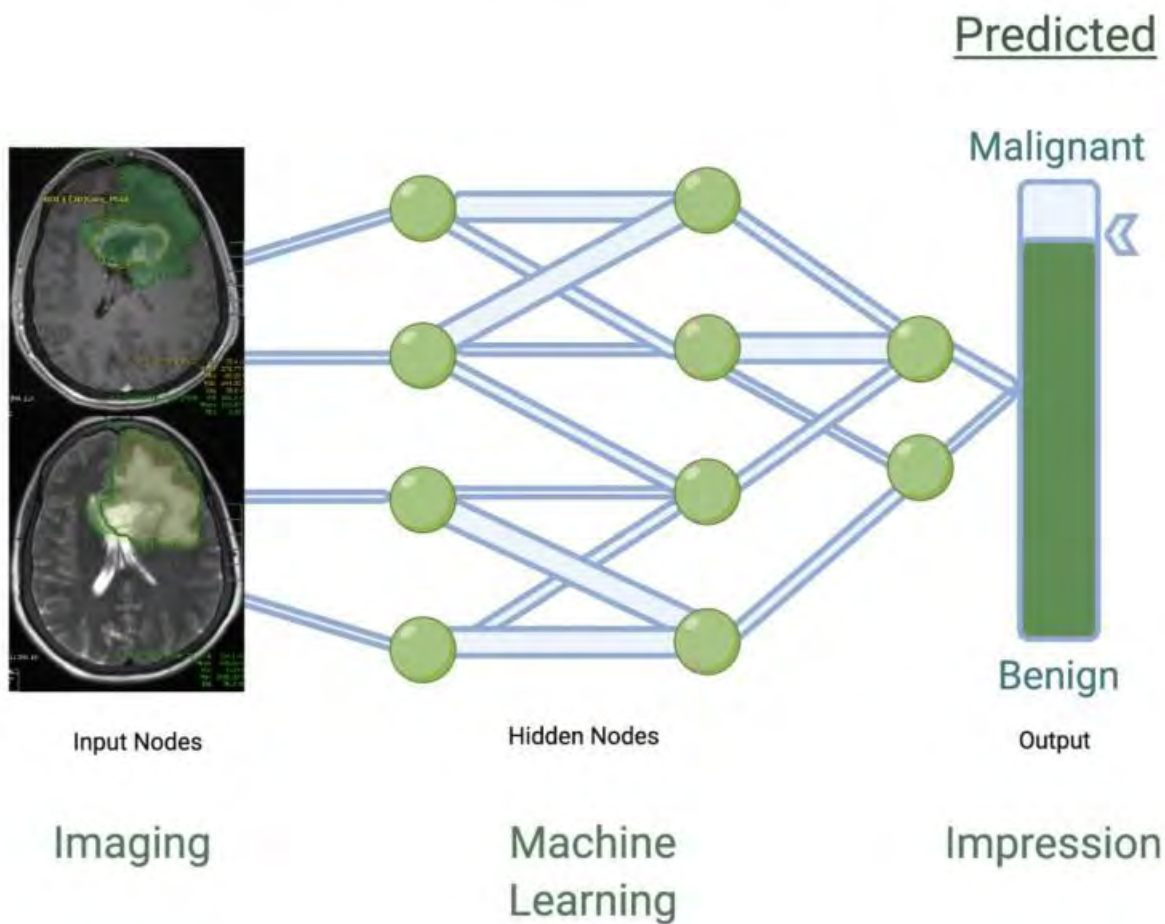
A systematic search of the literature was developed and executed by a clinical librarian. A total of four databases were searched: Ovid Embase, Ovid MEDLINE, Cochrane trials (CENTRAL), Web of Science-Core Collection. The search strategy used both keywords

and controlled vocabulary combining the terms for: artificial intelligence, machine learning, deep learning, radiomics, magnetic resonance imaging, glioma, as well as related terms. The search strategy was independently reviewed by a second institutional librarian. Publications were screened in Covidence by a neuroradiology attending, radiology resident, and post baccalaureate student. The study was approved by the IRB.

Conclusions

Systematic review yielded 11,238 publications for initial screening, and 88 conflicts were resolved by a neuroradiologist. Publications were screened to identify applications of machine learning in the diagnosis and management of gliomas. A total of 153 publications were included for full text review. Results demonstrated that machine learning approaches were used for the development of segmentation tools and the classification of tumors based on patient outcomes, WHO defined tumor subtypes, and molecular characteristics of tumors. Applications of machine learning in the diagnosis and treatment of gliomas include prediction of molecular subtype and classification by WHO grade, prediction of treatment response and disease progression, as well as prognostication and survival analysis. Systematic review is an effective method to review a large volume of literature in preparation for future research.

Training A Neural Network



Created with BioRender.com

(Filename: TCT_371_TrainingNeuralNetworks.jpg)

Hypothalamus and Pituitary Gland Embryology Including Radiological Cases of Developmental Anomalies

D Lee¹

¹*Staten Island University Hospital, Staten Island, NY*

Purpose

The hypothalamic-pituitary unit matures at approximately 20 weeks gestation. The pituitary gland has a dual embryological origin, the anterior lobe arising from an ectodermal evagination of the oropharynx and the posterior lobe arising from an evagination of the ventral hypothalamus and third ventricle. The aim of this exhibit will be to provide a visual illustration of the hypothalamic-pituitary unit development and its anatomy, as well as provide a radiology case series of developmental anomalies that was obtained at the author's institution. One example is a 32 year old female with a posterior pituitary cystic structure suspected to be a third ventricular diverticulum, likely a developmental abnormality involving the evagination of the third ventricle. Also included will be various cases of pituitary tumors obtained at the author's institution with radiology-pathology correlation to elucidate microanatomy of the pituitary gland. Educational objectives: -Discuss the embryological development of the hypothalamic-pituitary unit with visual pictorial and radiology illustrations. -Identify the normal macro- and microanatomy of the hypothalamic-pituitary unit. -Discuss various radiology cases including CT and MR images that demonstrate hypothalamic and pituitary developmental abnormalities. -Discuss various pituitary tumors with radiology-pathology correlation.

Materials and Methods

To illustrate the embryological development of the hypothalamus-pituitary unit by means of pictorial aids and CT/MR images. Cases obtained from the author's institution including CT/MR images of the sellar/suprasellar region will further understanding of hypothalamus/pituitary embryology and normal anatomy by demonstrating developmental abnormalities. Radiology images with correlating histopathology images of pituitary tumors will also further demonstrate pituitary microanatomy.

Results

Various visual aids will be utilized including: CT/MR images from cases obtained at author's institution, pictorial figures depicting embryological development of the hypothalamic-pituitary unit, and histological tissue samples obtained at author's institution for radiology-pathology correlation of pituitary tumors.

Conclusions

Following this educational presentation, the practicing radiologist will have a detailed knowledge of the embryology and development of the hypothalamus-pituitary unit. There will also be a better understanding of micro- and macro-anatomy via cases demonstrating developmental abnormalities and pituitary tumors.

1302

Image Based Analysis of Common Pitfalls in Brain CT Perfusion for Stroke

J Grenier¹, D Casey², M Igi³, L Murphy⁴, J Park⁵

¹*LSU Health Sciences Center New Orleans, New Orleans, LA*, ²*Louisiana State University Health Sciences Center, New Orleans, LA*, ³*Louisiana State University, New Orleans, LA*, ⁴*University of Pennsylvania, Philadelphia, PA*, ⁵*LSUHSC-New Orleans, New Orleans, LA*

Purpose

CT Perfusion has become an important component of the stroke workup in many centers, an adjunct to the non-contrast head CT and CT angiography (CTA). While the non-contrast CT is paramount for identifying potential ischemia or hemorrhage, and CTA for localization of a potential thrombus, CT perfusion plays an essential role in differentiating infarcted brain from salvageable ischemic tissue. While MR diffusion weighted imaging is more sensitive for early detection of cytotoxic edema in ischemic infarction, time is critical for successful intervention. CT Perfusion has therefore become more common in the typical stroke assessment, and has been integrated in stroke protocols. This reliance on CT Perfusion for crucial decision making has made it a necessity for the neuroradiologist and emergency radiologist to become proficient in interpretation. The classic CT Perfusion images of infarct core and surrounding penumbra is well established, however, an atypical scan could be problematic for the radiologist. Learning Objectives: · Review typical CT Perfusion images and parameters including cerebral blood flow, cerebral blood volume, mean transit time, and time to peak · Recognize abnormal CT Perfusion images · Review potential causes of abnormal CT Perfusion images, including incorrect bolus timing, atrial fibrillation, heart failure, motion artifact, incorrect placement of region of interest · Recognize incorrect time density curve · Review optimization of CT Perfusion protocol · Review possible post-processing techniques to resolve non-typical CT Perfusion images

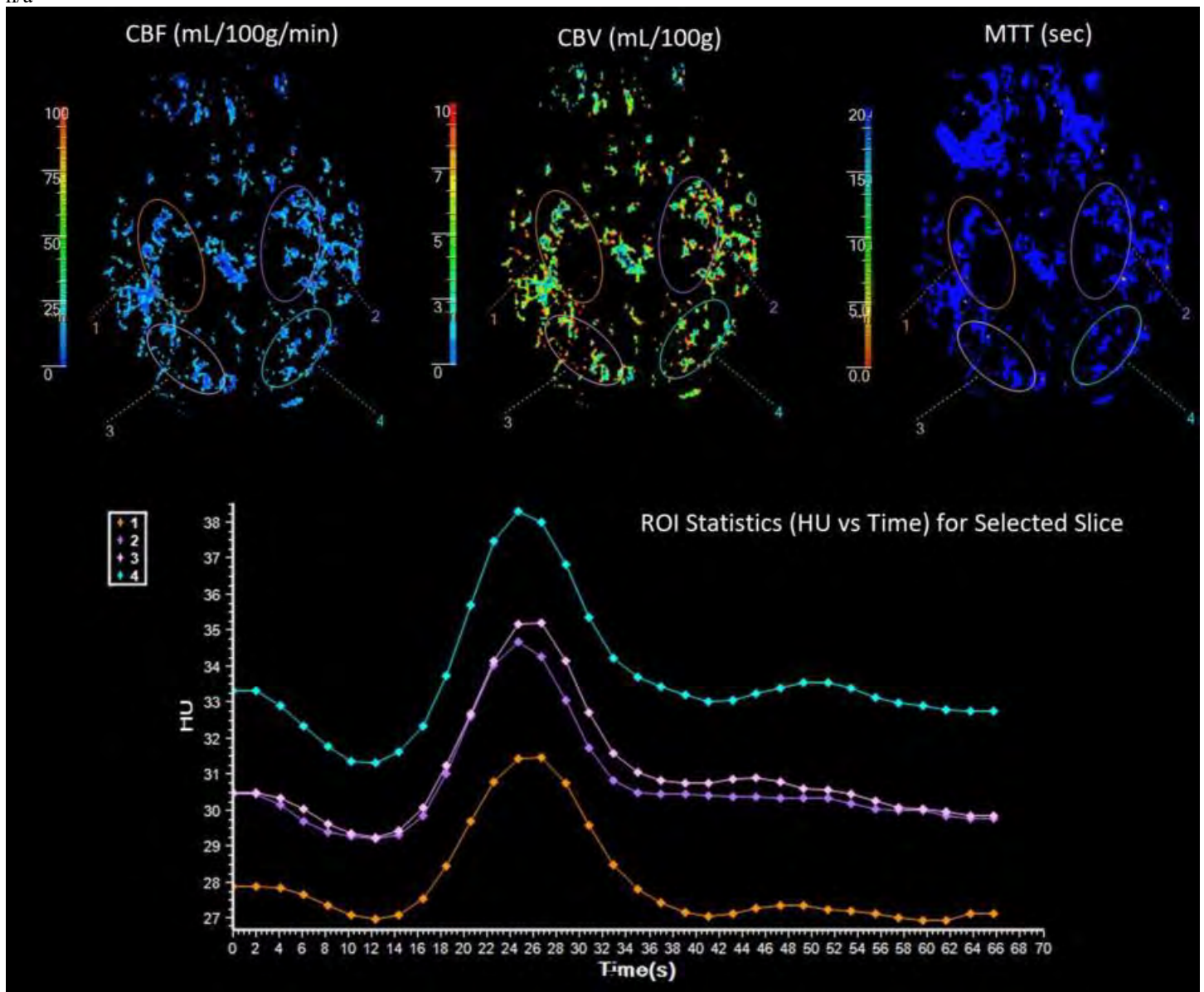
Materials and Methods

n/a

Results

n/a

Conclusions
n/a



(Filename: TCT_1302_CT CerebralPerfusionBolusMistiming.jpg)

367

Imaging Correlates Of Genotyping and Molecular Markers for Low And High-grade Glioma

S Kanekar¹, S Kanekar²

¹Hershey Medical Center, Hershey, PA, ²Brown University, Hummelstown, PA

Purpose

2016 CNS WHO classifications integrated the phenotypic and genotypic parameters of the brain tumors. Since then pheno- and genotyping has become the gold standard for characterizing the histologic and genetic make of the tumor which decide the surgical approach, the choice of the chemo and/or radiotherapy and in turn Overall survival and have a progression-free survival for the patient. Genotypic have their own limitations: of invasiveness, the cost, and limited availability. Noninvasive technique such as MRI (structural and molecular) imaging plays an important role in the radio-histogenomic classification of the brain tumor. Molecular imaging using various MRI techniques, DWI-ADC, MR spectroscopy, MR perfusion, and DTI has shown some promising results in understanding the genetic profile and the biological behavior of the tumor.

Materials and Methods

To discuss the gliomagenesis and associated molecular markers with various gliomas To correlate the imaging findings with the various Genotyping and molecular markers in low and diffuse glioma.

Results

We retrospectively reviewed the imaging studies from our PACS system of 55 pts with glioma (low, diffuse gliomas and glioblastoma), which forms the basis of this exhibit. All patients had undergone basic MRI along plus advanced imaging techniques such as MR spectroscopy, MR perfusion, DTI, fMRI, and ADC value. 46 of these tumors had a histopathology correlation with the imaging findings. Imaging parameters: site, size, margins, enhancing pattern, nonenhancing component, T2-FLAIR mismatch, necrosis area, percentage of necrosis area inside the enhancing lesion, ADC values, rCBV, multivoxel chemical shift MR spectroscopy, and FA and MD value calculations from DTI. Various imaging markers were correlated with the pheno and genotyping markers. For easy understanding, we have categorized this exhibit into: isocitrate dehydrogenase (IDH) status, O6-Methylguanine-DNA methyltransferase (MGMT), molecular genetics of glioblastoma and gliomagenesis, ATRX and TP53 mutations, 1p/19q codeletion as a marker for oligodendroglial tumors, Diffuse midline glioma and H3 K27M-mutant and TERT promoter mutations.

Conclusions

Various gene mutations reflect alterations in metabolism, cellularity, and angiogenesis, which manifest characteristic features on FLAIR-T2, DWI-ADC, MR spectroscopy, and DSC-PWI. Imaging, though at present cannot replace the genetic panel but has shown some promising direct and ancillary signs in identifying and diagnosing the types and subtypes of glioma.

1173

Imaging Evaluation of Orthostatic Headaches in the Pediatric Population

B Weston¹, S Strauss², J Chazen³, G Salama⁴

¹Cornell, New York, NY, ²Weill Cornell Medical Center, Manhattan, NY, ³Weill Cornell Medicine, New York, NY, ⁴Weill Cornell, New York, NY

Purpose

Definitive diagnosis in the setting of orthostatic headaches may be elusive, particularly in pediatric patients with underlying anatomic malformations or genetic conditions. Evaluation and management of positional headaches in children often requires a complex, multidisciplinary approach, and image guided procedures play a unique role by providing both diagnostic and therapeutic options for the patient. This educational poster will review potential etiologies of orthostatic hypotension in the pediatric population with a focus on CSF leaks and alterations in dural elasticity and compliance. The role of neuroimaging will be discussed with emphasis on technique and utility of CT myelogram, MR myelogram, and performing epidural blood patching as a diagnostic and therapeutic tool.

Materials and Methods

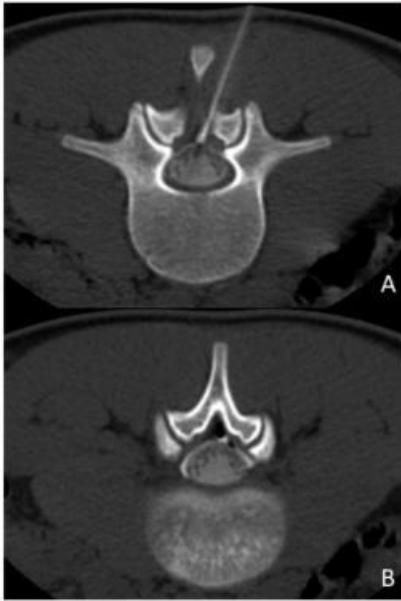
Upon completion of this educational poster, the radiologist/trainee will have a clinical and technical framework for evaluation of positional headaches in the pediatric population. Specific diagnostic entities to be reviewed include connective tissue disorders such as Ehlers-Danlos syndrome, Chiari type 1 malformation and its associated post-procedural complications, and spontaneous CSF leaks. The learner will become more familiar with the step-wise approach to diagnosis, and understand the role of CT myelography, MR myelography, and epidural blood patches in the pediatric population.

Results

A literature review of the epidemiology, presentation, diagnostic workup and therapy of CSF leak in the pediatric population was performed. This will be accompanied by a case-based review of the application of myelographic techniques in the work-up of orthostatic headache in the pediatric population. The role of CT-guided epidural blood patch in the pediatric population will also be elaborated.

Conclusions

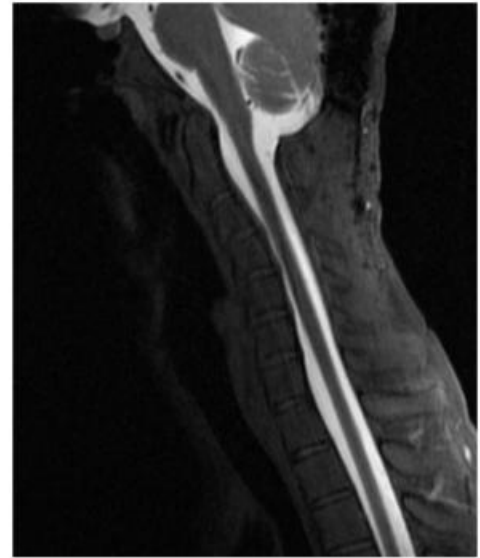
Neuroradiologists can play an essential role in the evaluation and treatment of pediatric patients with orthostatic headaches. CT myelogram and MR myelogram are often complementary in the evaluation of suspected CSF leak. Additionally, epidural blood patching can be a diagnostic tool when there is a high suspicion for CSF leak or intracranial hypotension, despite an inability to detect the leak on imaging. This is particularly salient when a connective tissue disorder is present, which may alter the compliance and elasticity of the dura and result in intracranial hypotension without a true CSF leak.



Axial prone images from an epidural blood patch post-myelogram demonstrates the needle tip in the epidural space (A) and a mixture of air and contrast confirming needle tip position in the epidural space (B).



Cross-table lateral image from a lumbar puncture for intrathecal administration of gadolinium demonstrates contrast filling the thecal sac.



Sagittal MRI Myelogram of the cervical spine demonstrates good opacification of the thecal sac and partially visualized occipital-cervical fusion hardware.

(Filename: TCT_1173_ASNRIImages.jpg)

1519

Imaging Features of Marginal Zone B-Cell Lymphoma (MZBCL) in the Head and Neck

K Grunseich¹, S Cha¹

¹University of California San Francisco, San Francisco, CA

Purpose

Summary: 1. MALT lymphoma in the brain, head, and neck: Marginal Zone B-Cell Lymphoma -Description of tumor characteristics and epidemiology -Clinical presentations- based on location, background inflammatory condition 2. Description of imaging characteristics with differential considerations and distinguishing features based on location. -Intracranial/Central Nervous System Compared to ddx: meningioma, solitary fibrous tumor, sarcoidosis, metastases -Orbits - Lacrimal gland, Nasolacrimal duct Compared to ddx: cellulitis, pseudotumor, sarcoidosis, IgG4, metastasis -Parotid Compared to ddx: sjogren's syndrome, sialadenitis, sarcoidosis - Thyroid Compared to ddx: simple goiter, primary thyroid cancer, thyroiditis (Hashimoto, Riedel), amyloidosis 3. Management and prognosis (integrated into each location of tumor) -Role of surgery, chemotherapy, radiation, and follow up Educational Objectives: 1) MZBCL MALT lymphoma is a rare tumor and has imaging features which should prompt the radiologist to suggest this entity. 2) Differential considerations on MRI based on its location and appearance in the head and neck. 3) Prompt imaging diagnosis is essential for clinical management and prognosis. Early administration of steroids for presumed alternatives can make subsequent biopsy nondiagnostic.

Materials and Methods

See Educational Objectives

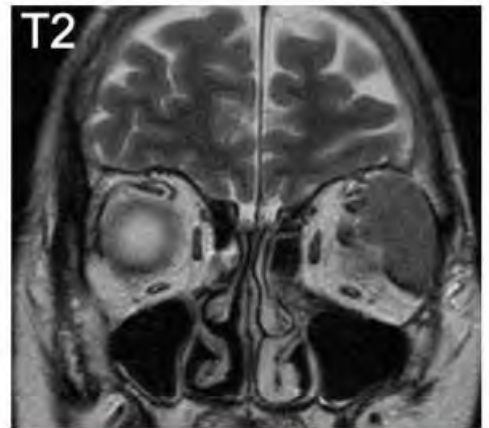
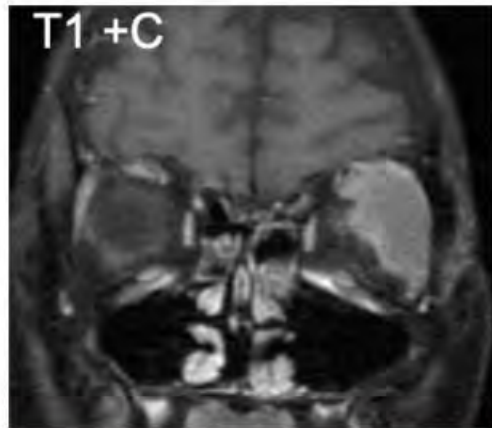
Results

Cited literature sources with images of cases seen at our institution.

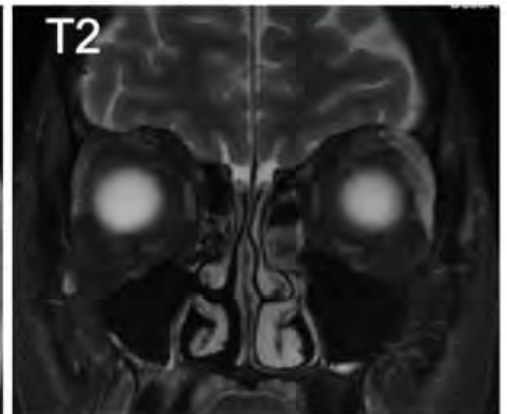
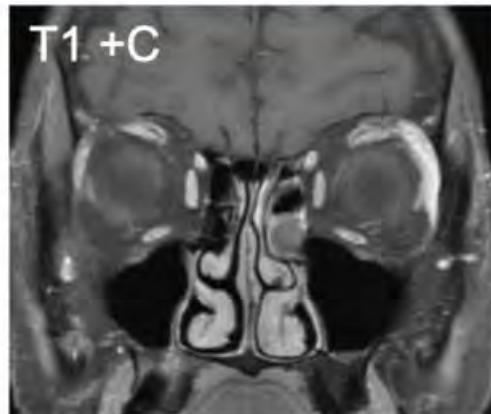
Conclusions

N/A

Pre Radiation



Post Radiation



(Filename: TCT_1519_ASNRSample.jpg)

1241

Imaging Findings in Idiopathic Intracranial Hypertension.

C Lee¹, D Oh¹, S Sampson², F Torres², J Acharya¹

¹Keck School of Medicine of USC, Los Angeles, CA, ²Kaiser Permanente Los Angeles Medical Center, Los Angeles, CA

Purpose

Summary: Idiopathic Intracranial Hypertension (IIH) is a clinical syndrome characterized by lack of identifiable cause of elevated intracranial pressures (ICP). Imaging plays an important role in the diagnosis of IIH with subtle signs and by excluding confounding causes. The overall incidence is rare – about 0.9 cases per 100,000 (1), making it an often underappreciated diagnosis. The typical presenting patient is a young to middle age obese female who presents with headache, visual problems, and occasionally papilledema. Diagnosis is invasive, requiring lumbar puncture to demonstrate elevated opening pressures. Treatment includes weight loss, acetazolamide, lumboperitoneal shunt (LPS), and optic nerve sheath fenestration (ONSF). Imaging is an essential first step in nearly all cases as a non-contrast head CT may be acquired in the setting of headache and typically required prior to lumbar puncture. This provides a unique opportunity for radiologists to add value in the clinical decision making process as opening pressures are not always obtained. However, the imaging findings of IIH can be subtle. MR imaging and venography are essential to exclude other causes of increased ICP, ranging from brain tumors to dural sinus thrombosis. MR/venography increases the diagnostic confidence of IIH (2,3). The imaging findings of IIH are suggestive but often not diagnostic and include flattening of the posterior aspect of the globes, protrusion of the intraocular portion of the optic nerve, optic nerve sheath tortuosity, partially empty sella turcica, and transverse sinus stenosis. Educational Objectives: To review clinical syndrome of IIH To review the diagnosis of IIH To review the medical and surgical treatment options To review the key imaging findings of IIH

Materials and Methods

N/A

Results

N/A

Conclusions

N/A

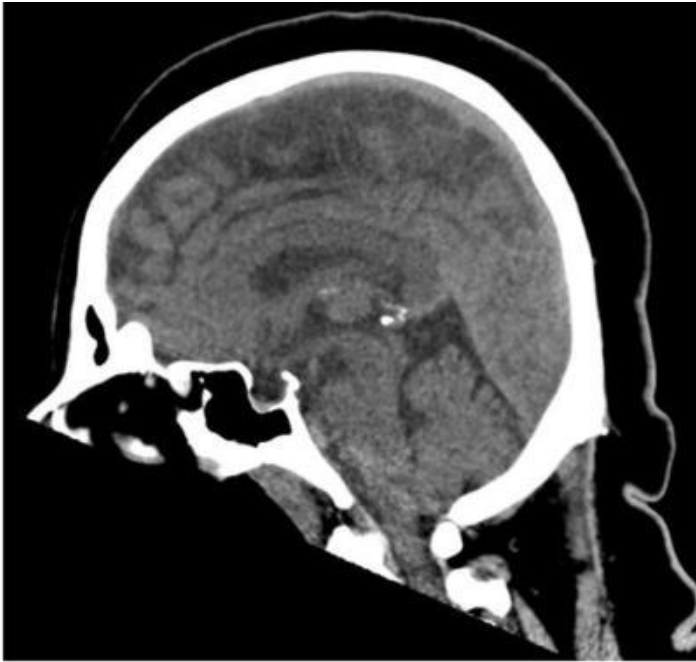


Figure 1. Empty Sella with thickening of the subcutaneous fat of the scalp and neck

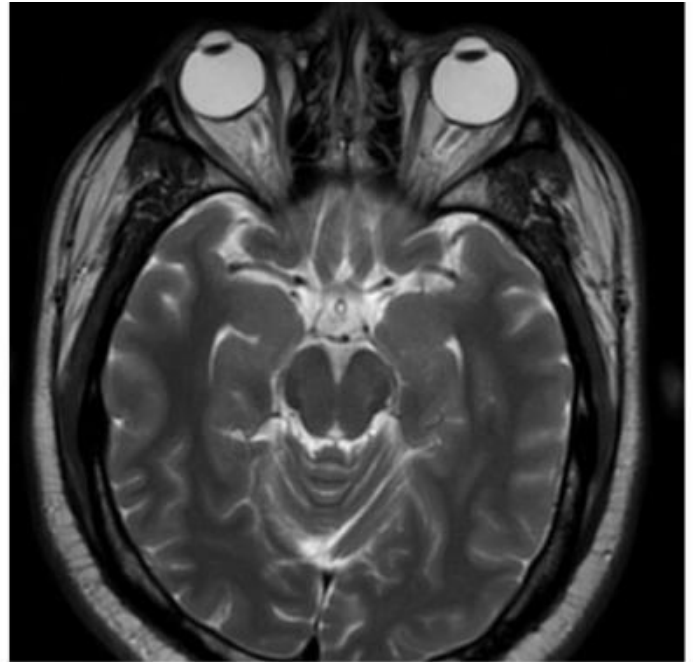


Figure 2. Flattening of the posterior sclera, fluid around optic nerve, and optic nerve tortuosity.

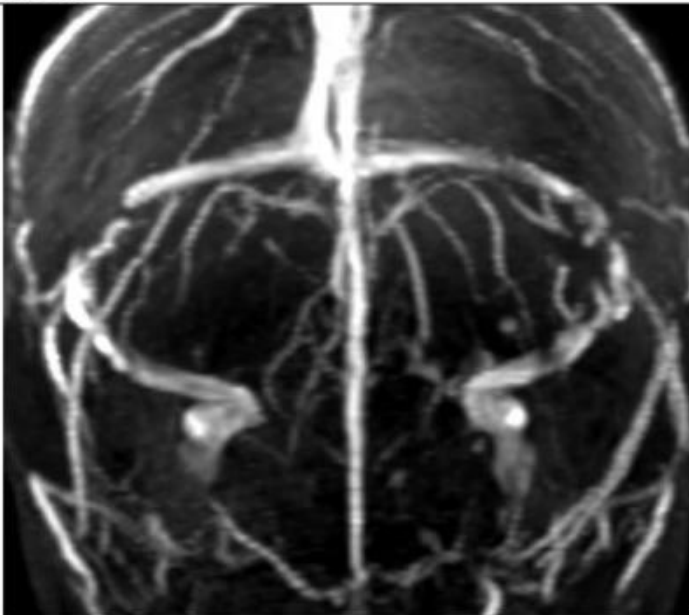


Figure 3. Narrowing of the lateral aspect of the bilateral transverse sinuses

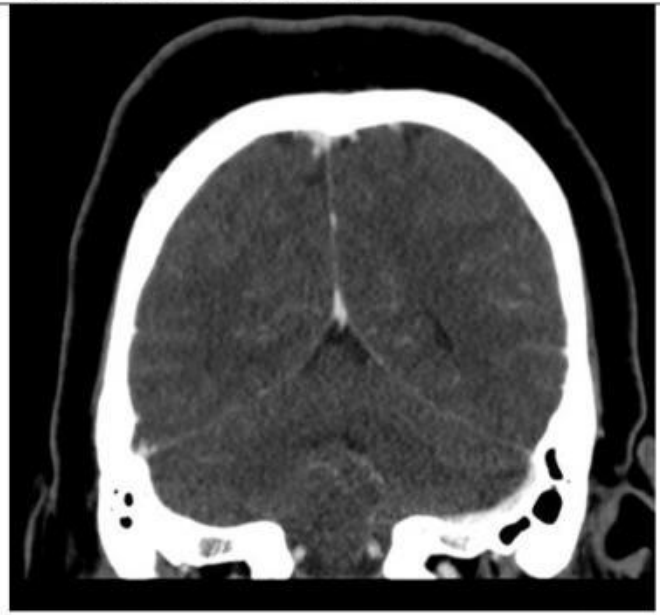


Figure 4. Narrowing of the bilateral distal transverse sinuses as indicated by loss of the delta sign

(Filename: TCT_1241_AbstractImages.jpg)

1467

Imaging Findings of Pineal Region Tumors

D Kaya¹, M Gule-Monroe²

¹UT Texas MD Anderson Cancer Center, Houston, TX, ²MD Anderson Cancer Center, Houston, TX

Purpose

Tumors of the pineal region can be divided histologically into several main categories: germ cell tumors (GCT), pineal parenchymal tumors, gliomas, primary pineal melanoma, metastases as well as extra-axial tumors including meningiomas and hemangiopericytomas, and rare entities such as cavernoma of the pineal region. WHO classifications of central nervous system tumors divides pineal gland tumors into four groups: • Pineocytoma • Pineal parenchymal tumor of intermediate differentiation (PPTID) • Papillary tumor of the pineal region (PTPR) • Pineoblastoma

Materials and Methods

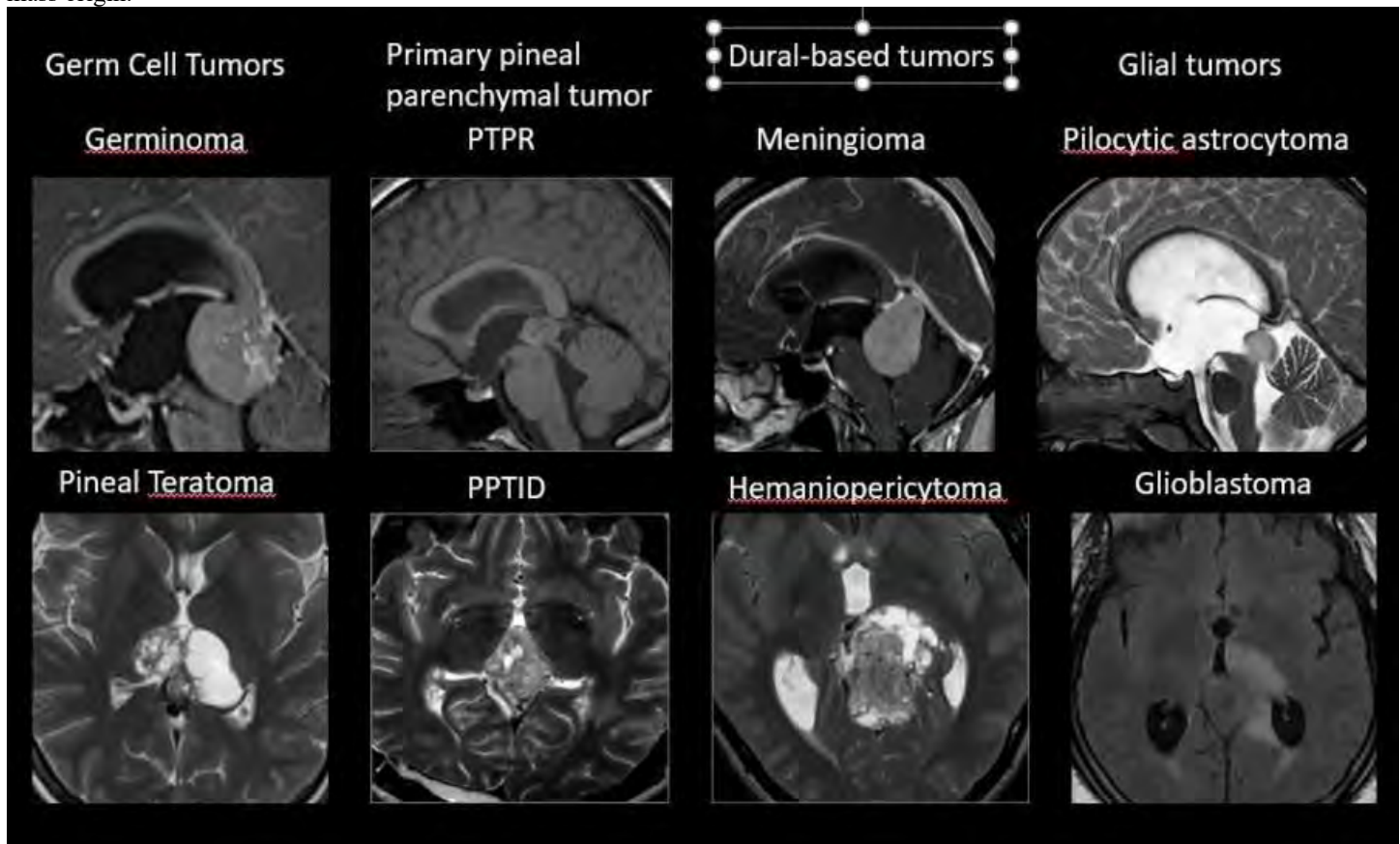
The purpose of this imaging rich educational exhibit is to review the anatomy of the pineal region, discuss and illustrate the common, uncommon, and rare adult and pediatric pineal region neoplasms with emphasis on imaging criteria for diagnosis.

Results

We will be reviewing cross-sectional imaging studies of pathologically confirmed cases. Tumor specific imaging features with an emphasis on differentiating characteristics and on an imaging differential diagnosis will be reviewed.

Conclusions

Each pineal region tumor will presented individually with its key features: a. Germinoma, pineoblastoma occur in pediatric patient. Pineal parenchymal tumor and meningioma common in adults b. Intrinsic T1 hyperintense signal is characteristic for PTPR and primary pineal melanomas but can also occur in PPTID. c. Cystic components in tumors are most frequent in nongerminomatous GCTs and PPTID d. Displacement of internal cerebral veins and position of pineal gland calcifications may add in discerning of pineal mass origin.



(Filename: TCT_1467_tumors1.JPG)

947

Imaging in CNS vasculitis

S Rathee¹, C Ahuja², V Gupta³, A Takkar², P Singh⁴

¹Dr.Ram Manohar Lohia Hospital, New Delhi, New Delhi, Delhi, ²PGIMER Chandigarh, Chandigarh, Chandigarh, ³Paras Hospital, Panchkula, Haryana, ⁴PGIMER, Chandigarh, Chandigarh, Chandigarh

Purpose

Vasculitis is inflammation of the blood vessels with or without necrosis. Primary CNS vasculitis affects small and medium size vessels and occurs as an isolated involvement of the CNS. Secondary CNS vasculitis occurs secondary to systemic illnesses including connective tissue disorders, infections, drugs, radiation and malignancy. Imaging plays a very important role in the diagnosis of CNS vasculitis as it finds a place in the diagnostic criteria for defining vasculitic conditions and is a non-invasive alternate of intracranial

biopsy. We therefore developed a high-resolution MRI based black blood imaging protocol for the diagnosis of CNS vasculitis. The main educational objectives of our presentation are to describe the imaging protocol and imaging findings in various CNS vasculitis.

Materials and Methods

The purpose of our study is to find out the imaging features of CNS vasculitis, to differentiate it from other vascular pathologies, and to differentiate between primary and secondary CNS vasculitis on basis of imaging.

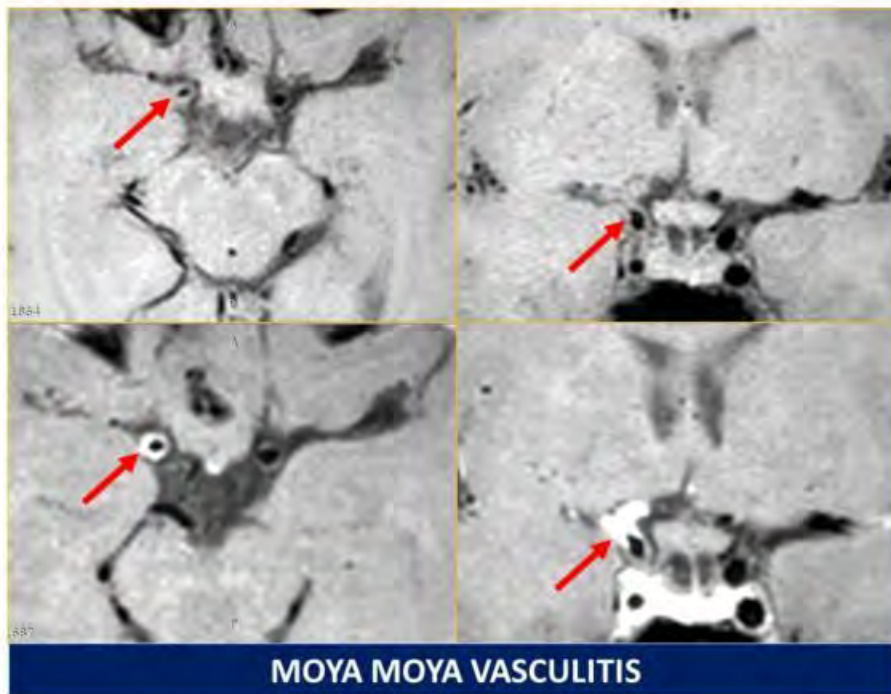
Results

Ours was a prospective observational study. Scanning was performed on 3T MRI scanner. We performed high resolution MRI, MR Angiography and pre- and post-contrast black blood imaging of 27 cases of probable CNS vasculitis, and compared the imaging findings of primary and secondary CNS vasculitis.

Conclusions

24/27 cases were given final diagnosis of CNS vasculitis. 8/24 patients (33.33 %) had systemic etiology of vasculitis and hence classified as secondary CNS vasculitis. These included 3 tubercular meningitis, 3 Polyarteritis Nodosa, 1 Takayasu arteritis, 1 Immune reconstitution syndrome related vasculitis. 16/24 patients were labelled as primary CNS vasculitis. All patients of intracranial vasculitis showed concentric wall thickening, which was segmental and grade 1 in majority (91.7 % and 62.5 % respectively), all except 1 showed wall enhancement which was concentric in all and grade 2 in majority (62.5 %). There were differences in thickening and enhancement patterns of primary and secondary CNS vasculitis but they were not significant. 2 patients of suspected CNS vasculitis showed vessel wall thickening without enhancement, and were given final diagnosis of RCVS. 1 patient showed no wall thickening or enhancement, and was given final diagnosis of moyo moyo disease. Vessel wall MRI serves well to demonstrate the changes of vasculitis. However it does not help to differentiate primary from secondary vasculitis.

CASE SCENARIO



- ❖ T1 pre and post contrast black blood images- **progressive narrowing** and **short segment concentric grade 1 thickening** of right supraclinoid ICA, with **grade 2 enhancement** of walls
- ❖ Patient was started on steroids on basis of vessel wall MRI findings, and improved significantly symptomatically.

Progressive narrowing of supraclinoid ICA with concentric wall thickening and enhancement
 ↓
 CNS vasculitis (Moya moya pattern)

(Filename: TCT_947_vasculitisimage.jpg)

1151

Imaging in HTLV-1 Central Nervous System Disease: A Pictorial Review

C McNamara¹, L Dixon¹, G Taylor², D Dhasmana², N Davies¹

¹Imperial College Healthcare NHS Trust, London, United Kingdom, ²Imperial College NHS Healthcare Trust, London, United Kingdom

Purpose

Human T-cell lymphotropic virus type 1 (HTLV-1) is a retrovirus which causes HTLV-1-associated myelopathy (HAM) in up to 4% of affected individuals. The imaging features of HAM are well described. There is however, now an increasing recognition of a wider range of CNS complications associated with the infection, including both acute myelitis and encephalitis. Despite 20 million people being infected worldwide the imaging features of these presentations are less well described. The objectives of this presentation are: 1. Provide a background and update to the epidemiology of HTLV-1 infection and the pathophysiology associated with CNS infection. 2.

A review of the classical imaging features associated with chronic HTLV-1 associated myelopathy. 3. A comparison between HTLV-1 associated myelopathy and other causes of myelopathy, with tips to help differentiate. 4. An overview of more novel imaging findings in HTLV-1 CNS infection, including: a. Acute HTLV-1-associated myelitis presenting with a longitudinally extensive myelitis and severe spinal cord swelling. b. HTLV-1 associated encephalopathy causing neurocognitive impairment accompanied by waxing and waning abnormal T2W hyperintense lesions in the cerebral white matter. c. HTLV-1 related abnormal signal in the cerebral corticospinal tracts. d. HTLV-1 related brainstem lesions localised to certain cranial nerve nuclei. 5. A review of the clinical and pathological features associated with HTLV-1 infection and how these correlate with specific imaging features at the time of presentation.

Materials and Methods

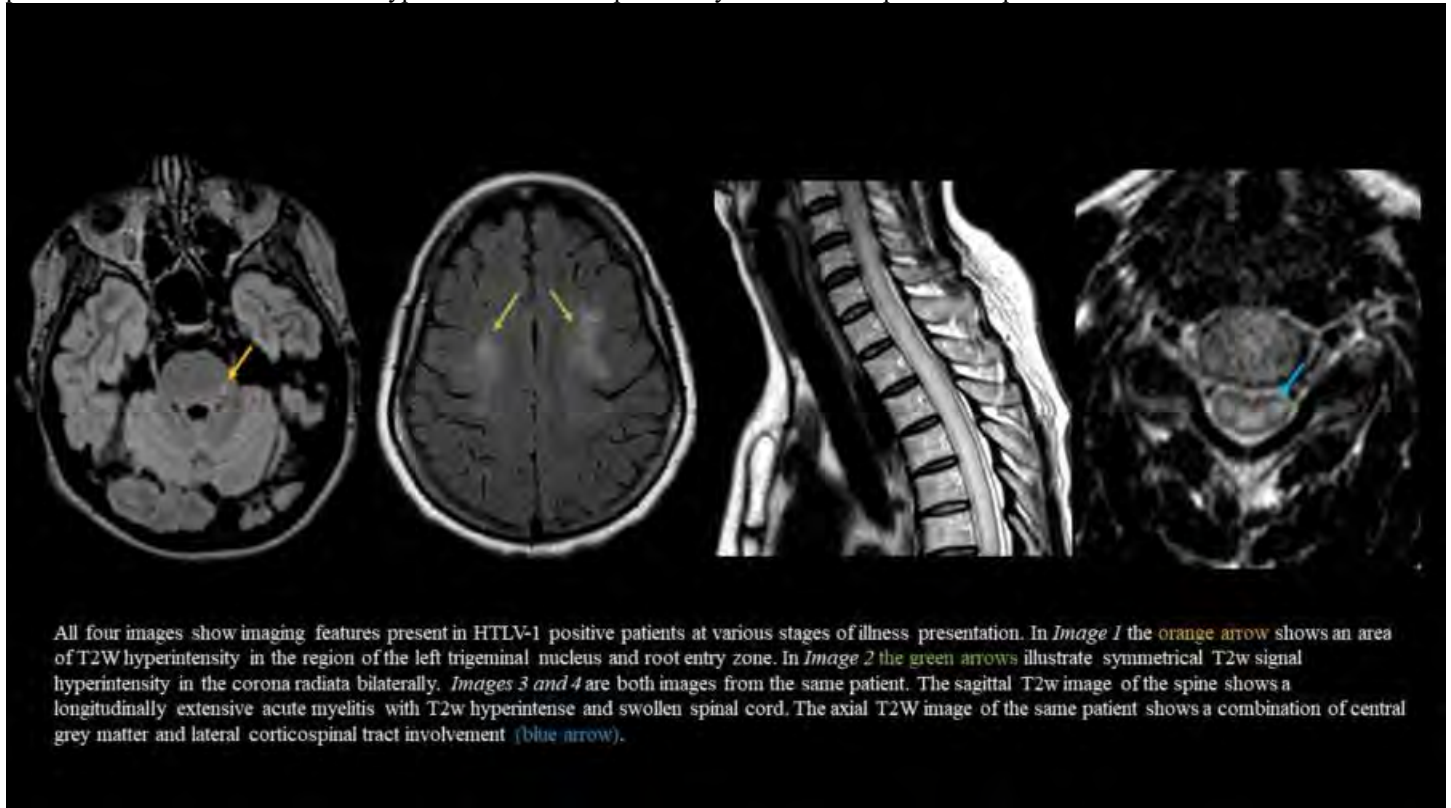
To provide a detailed pictorial review of the MR imaging features associated with HTLV-1 infection of the brain and spinal cord.

Results

A retrospective review of the MR imaging of patients with confirmed HTLV-1 infection presenting to a National Centre for Human Retrovirology.

Conclusions

HTLV-1 infection can cause inflammation of both the brain and spinal cord. This pictorial review covers several of the previously described features including; acute myelopathy, cord volume loss and imaging features of encephalitis. However, previously undescribed imaging features have also been covered including: high T2W signal at the root entry zone of cranial nerves, a unique pattern of subcortical T2W matter hyperintensities and a potentially characteristic pattern of spinal cord inflammation.



All four images show imaging features present in HTLV-1 positive patients at various stages of illness presentation. In *Image 1* the orange arrow shows an area of T2W hyperintensity in the region of the left trigeminal nucleus and root entry zone. In *Image 2* the green arrows illustrate symmetrical T2w signal hyperintensity in the corona radiata bilaterally. *Images 3 and 4* are both images from the same patient. The sagittal T2w image of the spine shows a longitudinally extensive acute myelitis with T2w hyperintense and swollen spinal cord. The axial T2W image of the same patient shows a combination of central grey matter and lateral corticospinal tract involvement (blue arrow).

(Filename: TCT_1151_HTLV_ASNRSubmission-Read-Only.jpg)

283

Imaging of Cerebral Venous Thrombosis: What Every Radiologist Should Know

I OLIVEIRA¹, F Pereira², V Jarry³, J de Castro⁴, F REIS⁵, J DUARTE⁶

¹UNICAMP, CAMPINAS, Brazil, ²State University of Campinas, Campinas, SP, ³Hospital de Clínicas da Universidade Estadual de Campinas, Campinas, São Paulo - Brasil, ⁴UNICAMP - University of Campinas, São Paulo - Brazil., Paulínia, Brazil, ⁵UNICAMP, Campinas, Sao Paulo, ⁶HCPA, Porto Alegre, Rio Grande do Sul

Purpose

Cerebral venous thrombosis (CVT) is an uncommon condition that is potentially reversible if it is diagnosed and promptly treated. Although CVT can occur at any age, it most commonly affects neonates and young adults. It is also more common in women, (pregnancy, postpartum status, and the use of oral contraceptives increase the risk of CVT). Clinical diagnosis is difficult because the clinical manifestations of CVT are nonspecific and pleomorphic, such as headache, seizures, decreased level of consciousness, and focal neurologic deficits. Therefore, imaging is crucial to diagnosis, and radiologists must be able to identify the findings of CVT and

to recognize potential imaging pitfalls that may lead to misdiagnosis. Hence, appropriate treatment (anticoagulation therapy) can be started early in the right patients to avoid complications, and even death. Although CT-scan is still often performed as first line investigation on an emergency, it is now well established that the best diagnostic tool is the combination of T1-weighted spin echo (T1SE) and T2SE MRI sequences to show the hyperintense thrombosed vessel and magnetic resonance venography (MRV) to detect the nonvisualization of the same vessel. Learning objectives: ILLUSTRATE THE ANATOMY OF THE CEREBRAL VENOUS SYSTEM; OUTLINE THE IMAGING FINDINGS OF CEREBRAL VENOUS THROMBOSIS (CVT) AND THE ASSOCIATED ABNORMALITIES IN THE BRAIN PARENCHYMA; REVIEW SUBTYPES OF CVT; HIGHLIGHT THE MAIN PITFALLS AT IMAGING OF CVT. DESCRIBE COMPLICATIONS OF CVT.

Materials and Methods

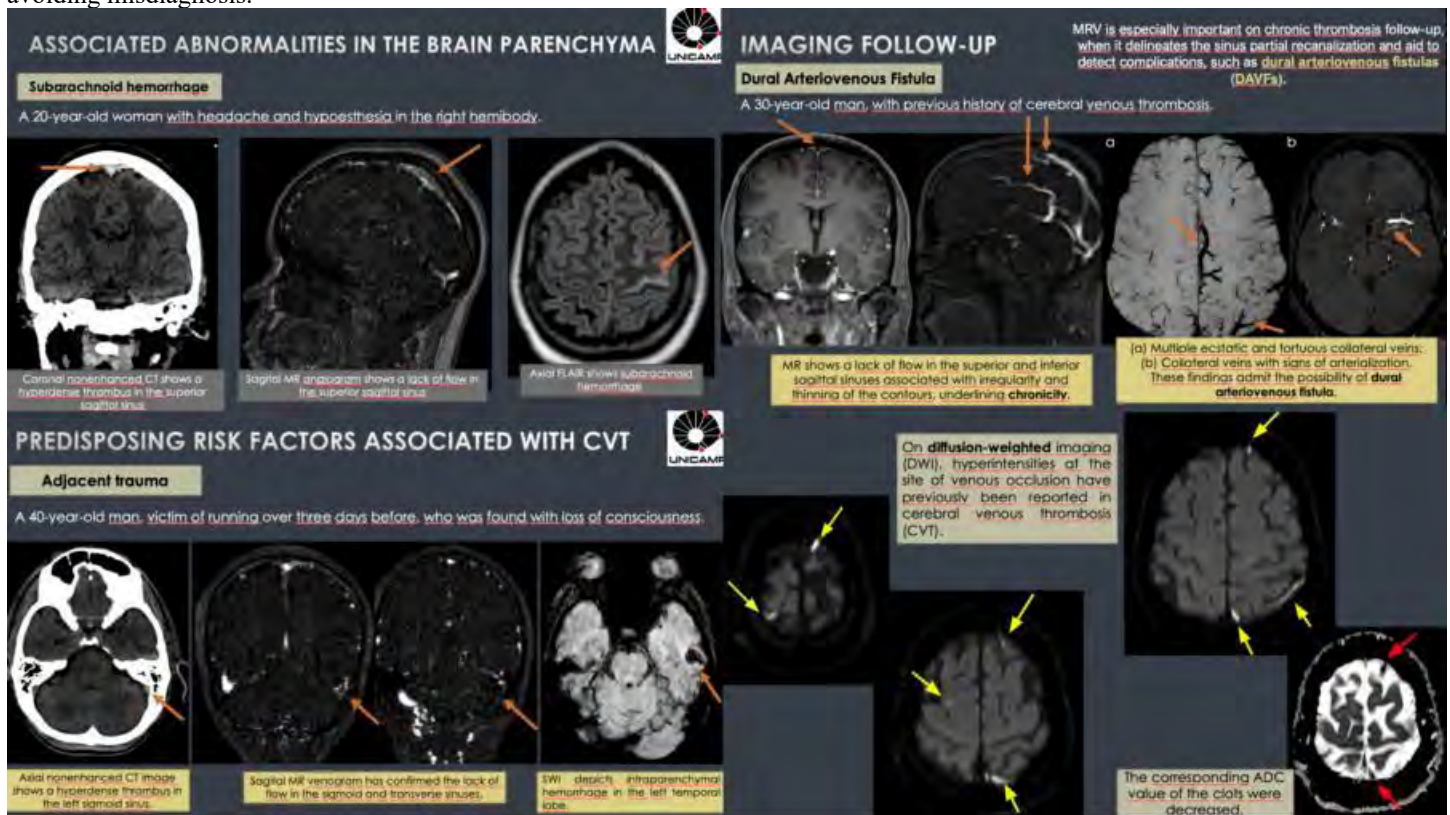
The objectives of this abstract are to illustrate the anatomy of the cerebral venous system; describe different subtypes of CVT, including dural sinus CVT, deep CVT and isolated cortical vein CVT; review the main imaging findings of CVT and the associated abnormalities in the brain parenchyma, also highlight the diagnostic pitfalls.

Results

All the cases are from Unicamp Clinical Hospital.

Conclusions

Cerebral venous thrombosis is a relevant cause of brain hemorrhagic infarct. Some scenarios may be associated to venous thrombosis as we previously demonstrated. Early treatment is essential to decrease the rate of complications and sequelae. Neuroimaging plays a relevant role to diagnosis and follow up in CVT, so radiologists must be aware of the imaging findings and with the pitfalls, thus avoiding misdiagnosis.



(Filename: TCT_283_CVTASNR2021.jpg)

1378

Imaging of Cervical Spine Ligamentous Injuries: Bridging the Gap between Neuroradiologists and Neurosurgeons

S Bhuta¹, A Prabhu², M Stanton²

¹Gold Coast University Hospital, Gold Coast, Australia, ²Gold Coast University Hospital, Gold Coast, QLD

Purpose

Magnetic resonance imaging (MRI) is integral in assessment of traumatic spinal injury, specifically assessing disco ligamentous structures to evaluate spinal stability and delineate any nerve root impingement or avulsion Spine classification system along with MR reporting template bridges the knowledge gap between Neuroradiologist and Neurosurgeons which in turn influences the patient management.

Materials and Methods

In the setting of acute spinal trauma, imaging delineates all osseous and soft tissue injuries and helps to guide potential surgical

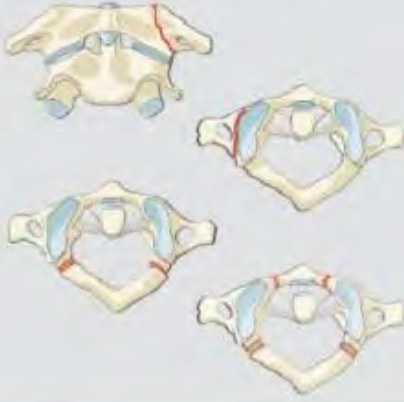
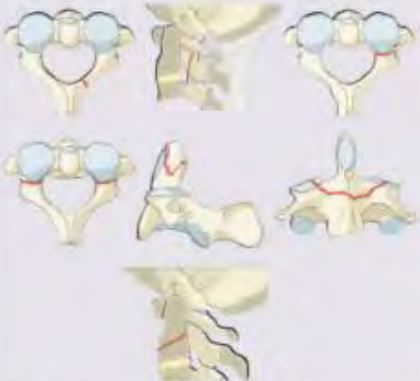
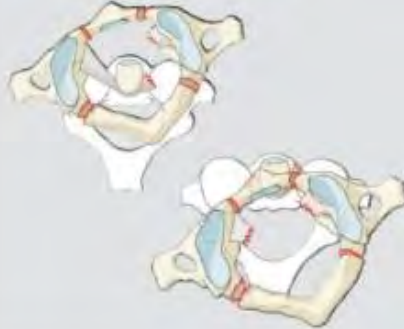
intervention. Computed tomography (CT) remains as modality of choice in the setting of acute trauma. However, magnetic resonance imaging (MRI) is integral in assessment of traumatic spinal injury, specifically assessing disco ligamentous structures to evaluate spinal stability and delineate any nerve root impingement or avulsion. Our aim is to describe the critical imaging parameters of cervical spine injuries in accordance with AO Spine classification system and how it influences neurosurgical management.

Results

MRI allows thorough assessment of disco-ligamentous structures in the setting of acute cervical spine trauma and injury to soft tissues otherwise not seen on CT. T2 FS sagittal and coronal images are valuable in assessing cervical spine ligaments (Anterior and posterior longitudinal etc). 3T MR offers advantage over 1.5T because of its superior resolution. It is important for the Neuroradiologist to identify the key MRI findings like Type B and C ligamentous injuries and utilizing a reporting template to avoid any discrepancies and errors.

Conclusions

AO Spine classification for cervical spine injuries is now widely used and is more robust and correlates well with MR imaging. Type A injuries are classically compression injuries and can be managed conservatively. Type B injuries are ligamentous injury. If anterior tension band (ie. ALL) or posterior tension band. (ie. posterior ligamentous complex) is injured (B2 or B3 injury) this fracture is less stable and is considered for internal or external fixation, surgical intervention or Halo immobilisation. B1 osseous injuries alone can be managed conservatively in hard collar. Type C injuries involve translation or displacement and have significant ligamentous injury and often requires surgical intervention(Fig.1). AO Spine classification system along with MR reporting template bridges the knowledge gap between Neuroradiologist and Neurosurgeons which in turn influences the patient management.

I. Occipital Condyle and Craniocervical junction	II. C1 Ring and C1-2 Joint	III. C2 and C2-3 Joint
<p>Type A Isolated bony injury (condyle)</p> 	<p>Type A Isolated bony only (arch)</p> 	<p>Type A Bony injury only without ligamentous, tension band, discal injury</p> 
<p>Type B Non-displaced ligamentous injury (craniocervical)</p> 	<p>Type B Ligamentous injury (transverse atlantal ligament)</p> 	<p>Type B Tension band / Ligamentous injury with or without bony injury</p> 
<p>Type C Any injury with displacement on spinal imaging</p> 	<p>Type C Atlantoaxial instability / Translation in any plane</p> 	<p>Type C Any injury that leads to vertebral body translation in any directional plane</p> 

(Filename: TCT_1378_AO.jpg)

782

Imaging of Complications After Spinal Surgery: What the Surgeon Wants to Know.

P Reddy¹, M Mian², S Vattoth³, S Viswamitra², R Ramakrishnaiah⁴, M Kumar², R Van Hemert⁵

¹University of Arkansas for Medical Sciences, Little rock, AR, ²University of Arkansas for Medical Sciences, Little Rock, AR, ³University of Arkansas for Medical Sciences, LITTLE ROCK, AR, ⁴Univ of Arkansas for Medical Sciences, Little Rock, AR, ⁵UAMS, Little Rock, AR

Purpose

The objectives of this presentation are: 1. To describe the normal imaging appearance and appropriate positioning of various spinal hardware. 2. To discuss the complications associated with spinal surgery based on time since surgery. 3. Discuss post processing techniques and artefact reduction techniques for spinal hardware evaluation. Summary of the presentation: 1. Introduction. 2. Types of spinal fixation. 3. Review of imaging appearance of common spinal fixation devices. 4. Evaluation of hardware failure. 5. Post operative fluid collections - CSF Leaks, seroma and abscess. 6. Evaluation for spondylodiscitis following spinal surgery. 7. Epidural fibrosis, arachnoiditis and recurrent disc herniation. 8. Adjacent segment disease. 9. Artifact reduction techniques. 11. Post processing and 3D techniques. 12. Conclusion.

Materials and Methods

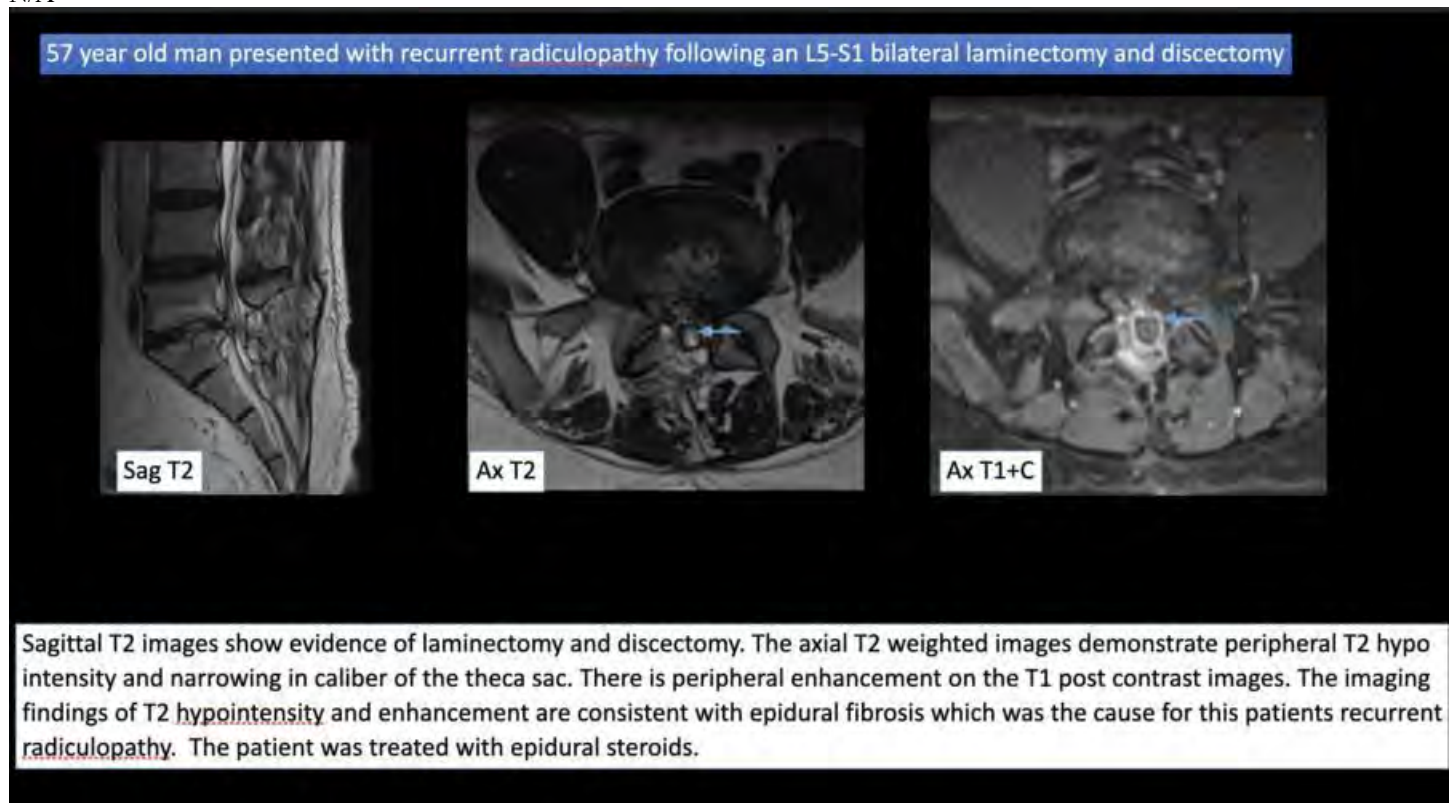
The purpose of this educational exhibit is to describe the expected imaging appearance following spinal surgery and then discuss the imaging of various complications such as implant loosening, hardware failure and post operative fluid collections with an emphasis on conveying clinically relevant findings to the surgeon using appropriate terminology.

Results

A retrospective review of the institute database was performed. Interesting and challenging cases were selected for the purpose of this review. The cases were discussed with the spine surgeon at our institute to determine which findings were most relevant.

Conclusions

N/A



(Filename: TCT_782_spinesurgery.jpg)

1569

Imaging of Complications Associated with Intrathecal Pump Catheters

A Spiro¹, A Weyer²

¹University of Pittsburgh Medical Center, Pittsburgh, PA, ²University of Pittsburgh, Pittsburgh, PA

Purpose

- Review radiographic access of the reservoir port
- Demonstrate catheter discontinuity, migration, and kinking on radiographs and catheter discontinuity, occlusion, and leak with contrast injection under fluoroscopy
- Illustrate the use of CT myelography for detection of delayed and subtle catheter leak, catheter discontinuity and kinking, subarachnoid loculations or adhesions, catheter-induced dural tear with CSF leak, and catheter-tip granuloma causing spinal cord compression

Materials and Methods

Implanted intrathecal pump catheter systems are utilized to treat various conditions such as intractable spasticity and chronic pain. Sequelae of device malfunction and complications can include medication withdrawal, inadequate pain control, infection, and spinal cord compression. We present a review of the imaging appearance of implanted intrathecal pump catheters with a focus on the appearance of common and rare complications associated with these systems.

Results

N/A

Conclusions

A range of complications may be associated with intrathecal pump catheter systems. Familiarity with the appearance of these complications on radiographs, under fluoroscopy, and on CT myelography will allow radiologists to detect the location and nature of the complication and thereby assist with planning for surgical revision or removal of the system.



(Filename: TCT_1569_try3.jpg)

713

Imaging of Duropathies: Primary and Secondary Conditions Involving the Pachymeninges

E Zamora¹, K Shifteh¹, C Zamora²

¹Montefiore Hospital, The Bronx, NY, ²UNC Department of Radiology, Chapel Hill, NC

Purpose

This educational exhibit presents an overview of dural anatomy and histology. It also provides a review of major conditions that may affect the dura with emphasis on characteristic imaging findings and relevant clinical features. After completing this exhibit, the reader should be able to: (1) Understand basic concepts of dural anatomy and histology. (2) Recognize characteristic imaging features and basic clinical aspects of various entities affecting the dura.

Materials and Methods

There is a wide spectrum of benign and malignant entities that can affect the dura. The aim of this exhibit is to familiarize the reader with the normal dural histology and anatomy as well as the imaging findings associated with relevant conditions.

Results

Although on gross inspection the dura appears to have a simple structure, electron microscopy demonstrates a fairly complex ultrastructural organization. Recently, five layers of varying thickness have been identified: bone surface, external median, vascular, internal median, and arachnoid. As the toughest membrane of the human meninges, the dura represents a major barrier for disease, and it is also the most important site for CSF turnover. However, it is also a site that is often involved by a wide range of benign and malignant conditions which may encompass various etiologies: (a) congenital—dural ectasia (NF-1 in spine and sphenoid, collagen vascular disease), giant arachnoid granulations; (b) inflammatory, infectious, and/or granulomatous—IgG4-related pachymeningitis,

granulomatosis with polyangiitis, rheumatoid arthritis, neurosarcoïd, tuberculosis; (c) traumatic, iatrogenic, degenerative and/or idiopathic—postoperative dural thickening, dural ruptures (intracranial hypotension, root avulsions with intraspinal pseudomeningoceles, CSF leak with or without superficial siderosis, spinal cord herniations), acute trauma (arterial and venous epidural hemorrhage), Hirayama disease; (d) vascular—dural fistulas, dural sinus malformations, chronic extra-axial hematomas (progressive calcification and dural thickening/organization), extramedullary hematopoiesis, (e) neoplastic/proliferative—pachymeningeal carcinomatosis, meningiomas, hemangiopericytomas, lymphoma/leukemia, Langerhans cell histiocytosis, Rosai-Dorfman disease, mimics (e.g. neoplasia simulating extra-axial hemorrhage); and syndromic: Gorlin syndrome.

Conclusions

This educational exhibit provides a review of major conditions that may affect the dura with emphasis on characteristic imaging findings.

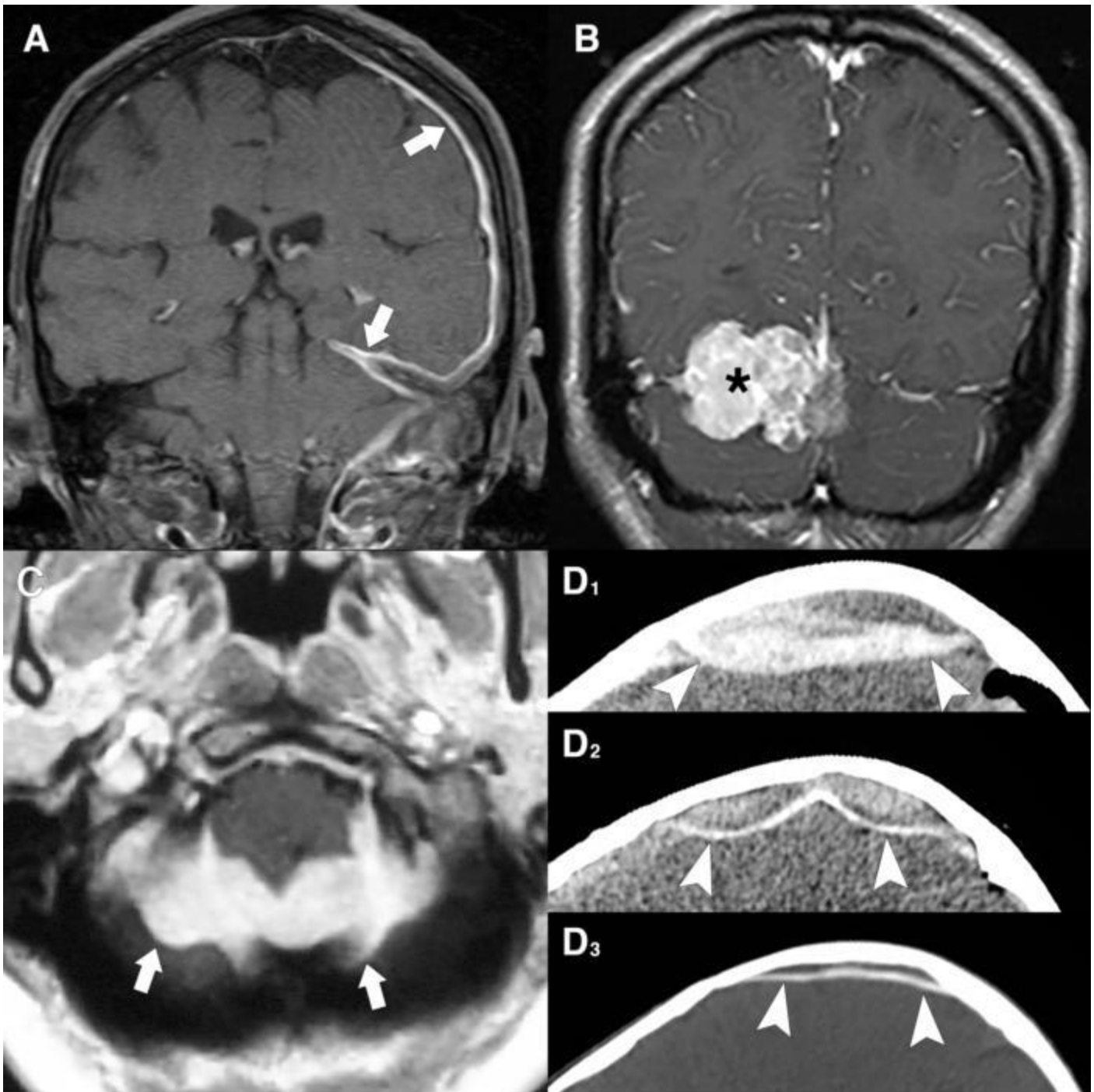


Figure Legend: Examples of select entities that may affect the dura. (A) Coronal post-contrast fat-saturated T1 shows extensive dural thickening and enhancement of a patient with granulomatosis with polyangiitis (arrows). (B) Coronal post-contrast T1 in a different patient with a solitary fibrous tumor shows a mildly heterogeneous, avidly enhancing mass (asterisk) centered in the right tentorium. (C) Axial post-contrast T1 in a different patient with Rosai-Dorfman disease demonstrates thick enhancing tissue in the posterior fossa (arrows). (D) Axial noncontrast CT images at various timepoints in a different patient show progressive dural calcification following an epidural hematoma (arrowheads).

(Filename: TCT_713_Figure.jpg)

Imaging of Free Flaps in Head and Neck Reconstruction Surgeries

A Agarwal¹, M Alhasan¹, B Heard²

¹University of Texas Southwestern Medical Center, Dallas, TX, ²UT Southwestern, Dallas, TX

Purpose

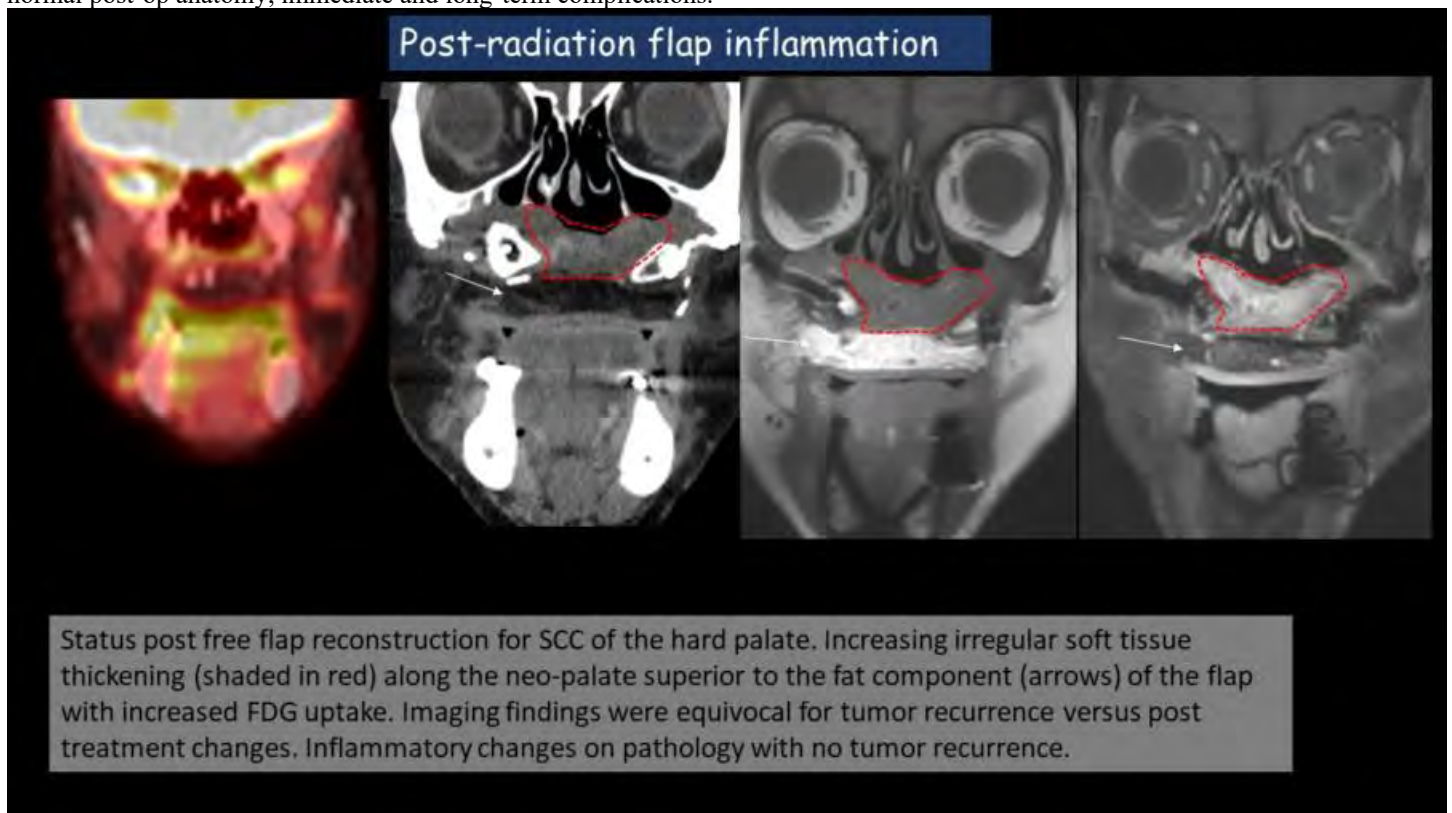
1. To provide basic understanding of the free flap reconstruction techniques for Head and Neck surgeries through schematic diagrams, intra-operative photos and their imaging correlate 2. To discuss the imaging findings in immediate and late complications of free-flap reconstruction surgeries 3. To discuss pertinent findings to help differentiate local recurrence from conditions which can mimic tumor

Materials and Methods
Imaging plays a vital role in evaluating postoperative status of pharyngolaryngeal cancers. Free flaps have become the preferred reconstruction method for most large head and neck oncologic defects. Interpretation of postoperative images is challenging because of the anatomical distortion and variability in treatment approach. Therefore, it is necessary for the neuroradiologist to understand the surgical techniques, post-surgical anatomy, immediate and long term complications associated with free-flap reconstruction surgeries.

Results
The contents will be organized as : 1. Types of Free-flap reconstruction surgeries 2. Post-operative anatomy 3. Immediate postoperative complications (ischemia, infection, bleeding, and dehiscence) 4. Long-term complications (infection, fistulas, hardware exposure, osteonecrosis, recurrence) 5. Conditions mimicking local recurrence

Conclusions

This exhibit provides an overview of free-flap reconstruction surgeries in Head and Neck cancers, provides case-based review of the normal post-op anatomy, immediate and long-term complications.



(Filename: TCT_256_FlapInflammation.jpg)

1284

Imaging of Optic Pathway Pathologies with Emphasis on Diffusion-Weighted Imaging

V KHARE¹, T Moritani², J Kim²

¹UNIVERSITY OF MICHIGAN, Ann Arbor, MI, ²University of Michigan, Ann Arbor, MI

Purpose

Upon completion of this exhibit, the reader will: - Become familiar with the anatomy of the optic pathway. - Utilize DWI as an

additional parameter to aid in diagnosis of pathologies ranging from inflammatory, infectious, vascular, and neoplastic in origin. - Help predict likely clinical course based on qualitative and quantitative DWI & ADC data.

Materials and Methods

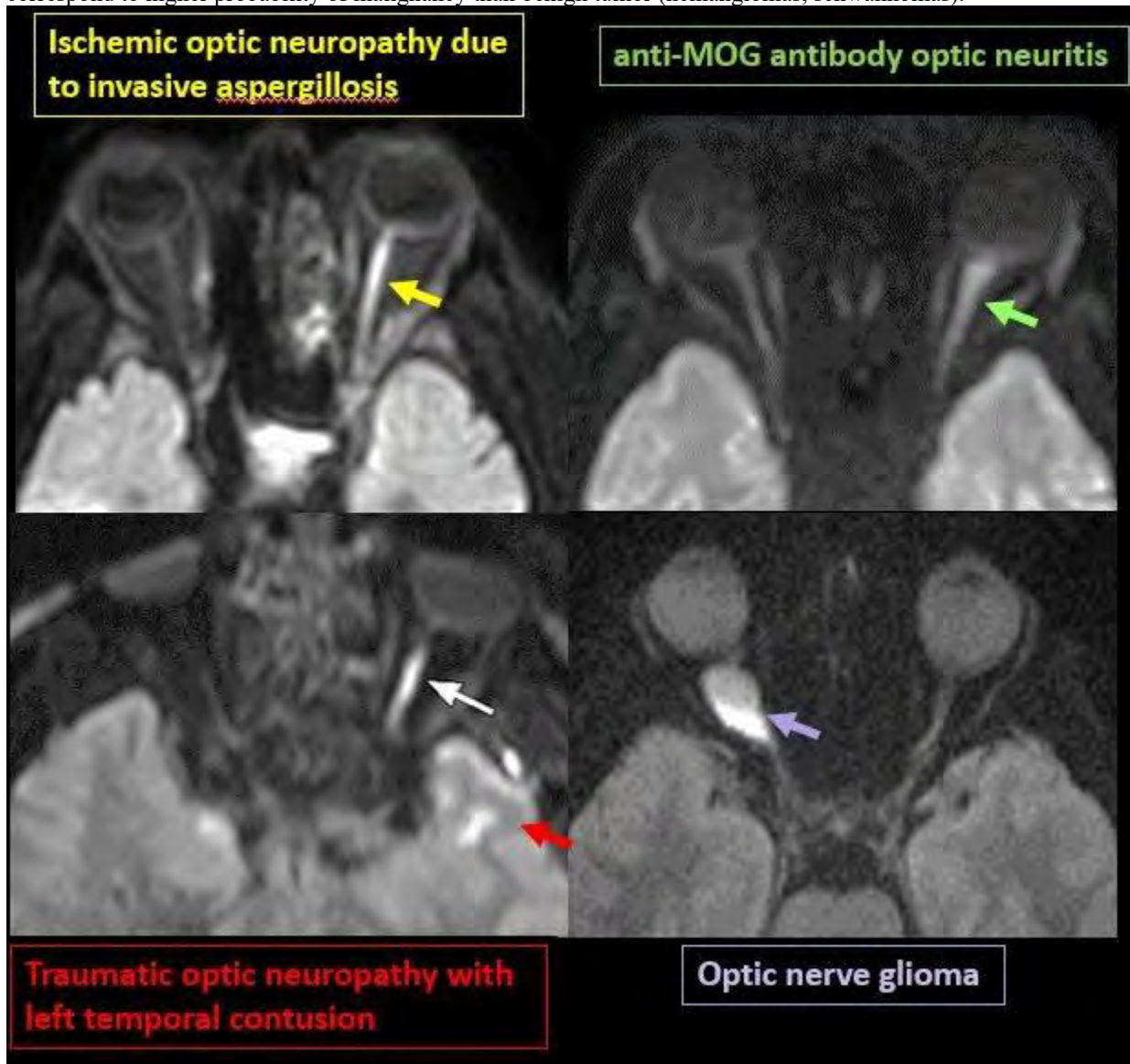
- Discuss various MR imaging findings for pathologies affecting the optic pathway, with emphasis on diffusion-weighted imaging (DWI).

Results

- Anatomic overview of the optic pathway - Discuss the use of various diffusion sequences including single and multi-shot EPI, and non-EPI with ADC maps - Discuss various common pathologies affecting the optic pathway (e.g., demyelinating processes, inflammatory processes, neoplastic entities, and optic nerve manifestation of global brain pathology) and how findings on DWI may help understand the overall clinical course.

Conclusions

- The location and laterality of optic nerve involvement can be differentiated by DWI. - Optic Neuritis (ON): ADC can differentiate between multiple sclerosis-related ON and neuromyelitis optica-related ON. In acute disseminated encephalomyelitis, lack of pathologic signal intensities on DWI with increased ADC maps are correlated with better clinical outcomes. - Ischemic Optic Neuropathy, Arteritic (giant cell arteritis, invasive aspergillosis) and Non-arteritic. DWI demonstrates bright signal with decreased ADC value, allowing for earlier differentiation and is usually associated with worse clinical outcome. - Traumatic Optic Neuropathy: Hyperintense signal in the optic nerve, with a predilection towards the posterior segment, can aid in diagnosing traumatic optic neuropathy, with a qualitative assessment being a surrogate for clinical outcome. - Papilledema/Increased Intracranial Pressure: In contrast, bilateral DWI hyperintensity within the optic nerve can serve as a useful marker for papilledema and qualitative DWI signal intensities correlate with clinical significance. - Optic Pathway Tumors: The use of DWI and ADC values can aid in prognostic and diagnosing malignant potential. DWI may help provide a predictive model for scoring probability of malignance of multiple optic pathway tumors (optic nerve meningiomas, gliomas, lymphomas, retinoblastoma, and metastasis), as lower mean ADC values correspond to higher probability of malignancy than benign tumor (hemangiomas, schwannomas).



1258

Imaging of Orbital Lesions: A Deeper Insight into Compartment-Based Pathologies.

M Hussein¹, T Rizvi¹

¹*University of Virginia, Charlottesville, VA*

Purpose

The objective of the presentation is to describe the key anatomical features of the orbit and to emphasize the role of imaging in detection and characterization of orbital compartmental pathologies. Thorough knowledge of orbital anatomy and the use of the compartmental approach in assessing orbital lesions helps a radiologist in arriving at the diagnosis or frame a differential diagnosis.

Materials and Methods

1. Review compartmental anatomy of the orbit. 2. Classify orbital lesions according to location into bulbar and retrobulbar with further sub classification of retrobulbar lesions into intraconal and extraconal lesions. 3. Review the role of imaging in differentiating orbital pathologies based on the signal characteristics and enhancement patterns with representative examples.

Results

We reviewed cases with orbital pathologies performed at our institution. We categorized them into bulbar and retrobulbar lesions with the latter being further subdivided into intraconal and, extraconal lesions

Conclusions

A compartmental approach to evaluating orbital disease can guide in making the differential diagnosis. MRI helps in determining the extent of disease, describing its exact localization according to the involved orbital compartments and guiding the referring ophthalmologist into making an informed decision. Knowledge of orbital anatomy is essential to developing an approach to orbital lesions. High-quality multislice CT with intravenous contrast provides good quality images; however, gadolinium-enhanced MRI is superior in its ability to differentiate soft-tissue structures from adjacent structures and provides more specific tissue characterization.

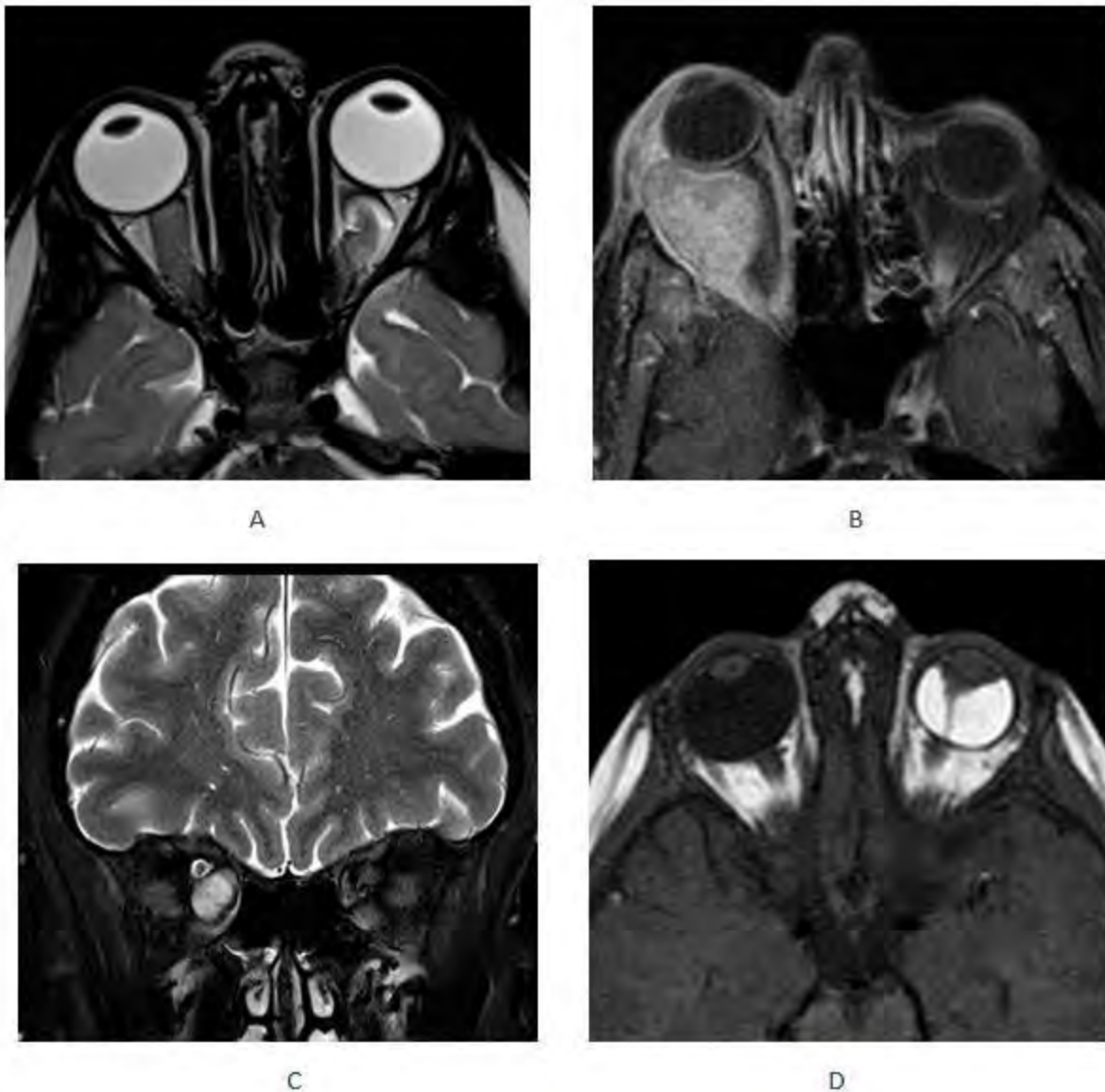


Figure 1: T2 axial image showing retrobulbar intraconal lesion arising from both optic nerves: Bilateral optic glioma in a case of NF-1 (A), T1 fat sat post contrast image showing extraconal intra-orbital lesion: Right lacrimal sac carcinoma (B), T2 coronal image showing vascular retrobulbar intraconal lesion: Right orbital hemangioma (C), Axial T1 image showing intraorbital bulbar lesion: Left persistent hyperplastic vitreous (PHPV) (D).

(Filename: TCT_1258_Orbitimages.JPG)

1130

Imaging of Paranasal Sinus Infections in Children: Unusual complications not to be missed!

G Orman¹, S Kralik¹, N Desai¹, A Meoded¹, J Vallejo², T Huisman², H Tran¹

¹Texas Children's Hospital, Houston, TX, ²Texas Children's Hospital and Baylor College of Medicine, Houston, TX

Purpose

Diagnosing PNS infections and complications in children requires knowledge of the unique anatomy of the nasal cavity and the PNS. In fetal life, nasal mucosa evaginations into the lateral nasal walls. initiate the development of the PNS. The PNS continue to develop

after birth and complete their maturation and pneumatization at different ages during childhood which makes the pattern of PNS infections determined by patient age. Complications are caused by direct spread of the infection to the orbit, face, intracranial or osseous structures or hematogenous spread of the infection to the intracranial structures. Emergent imaging studies are often necessary in the evaluation of the complications in pediatric patients when the symptoms persist for 10 days and/or if there is evidence of intracranial or orbital complications. In addition, immunocompromised children are especially vulnerable to developing unusual complications. Computed tomography is excellent for determining whether there is intraorbital extension of PNS disease. However, when the infection approaches the orbital apex, a magnetic resonance imaging study with contrast is necessary to assess spread into the cavernous sinus and the intracranial compartment.

Materials and Methods

Paranasal sinuses (PNS) infections are common in children. They may cause common and well-known complications, but also, unusual and potentially devastating complications. Our purpose is to review imaging findings of PNS infections including both common and unusual complications as well as development of the PNS and essentials of imaging techniques in children.

Results

n/a

Conclusions

The pattern of PNS infection is determined by the patient's age due to the continuous development of the PNS during childhood. PNS infections may spread and cause complications that are well-known and established in the literature. However unusual complications and potentially devastating complications may exist and all involved in care of these children should be familiar with the wide range of complications of PNS infections. Neuroimaging is essential for differential diagnosis and to exclude critical complications.

540

Imaging of Radiation-induced Brain Toxicity

C Soto¹, O Arevalo², S Khanpara³, S Calle², R Riascos³, K Shah⁴

¹National University of Colombia, Bogota, Colombia, ²The University of Texas MD Anderson Cancer Center, Houston, TX, ³University of Texas Health Science Center at Houston, Houston, TX, ⁴N/A, N/A

Purpose

Radiation therapy (RT) plays a key role in the treatment of patients with brain and H&N neoplasms. RT-related adverse events have been characterized based primarily on their time of onset from RT into three distinct categories as follows: acute reactions during the course of RT, early delayed complications which happen a few weeks to a few months after RT, and late delayed reactions which occur several months to years following RT. Objectives: 1. To describe the pathogenesis of cerebral radiation toxicity 2. To present a comprehensive case-based review of the imaging manifestations of the different stages of the radiation induced brain injury, with emphasis on advanced neuroimaging techniques 3. To highlight the imaging differences between early progression, pseudoprogression, and radiation necrosis

Materials and Methods

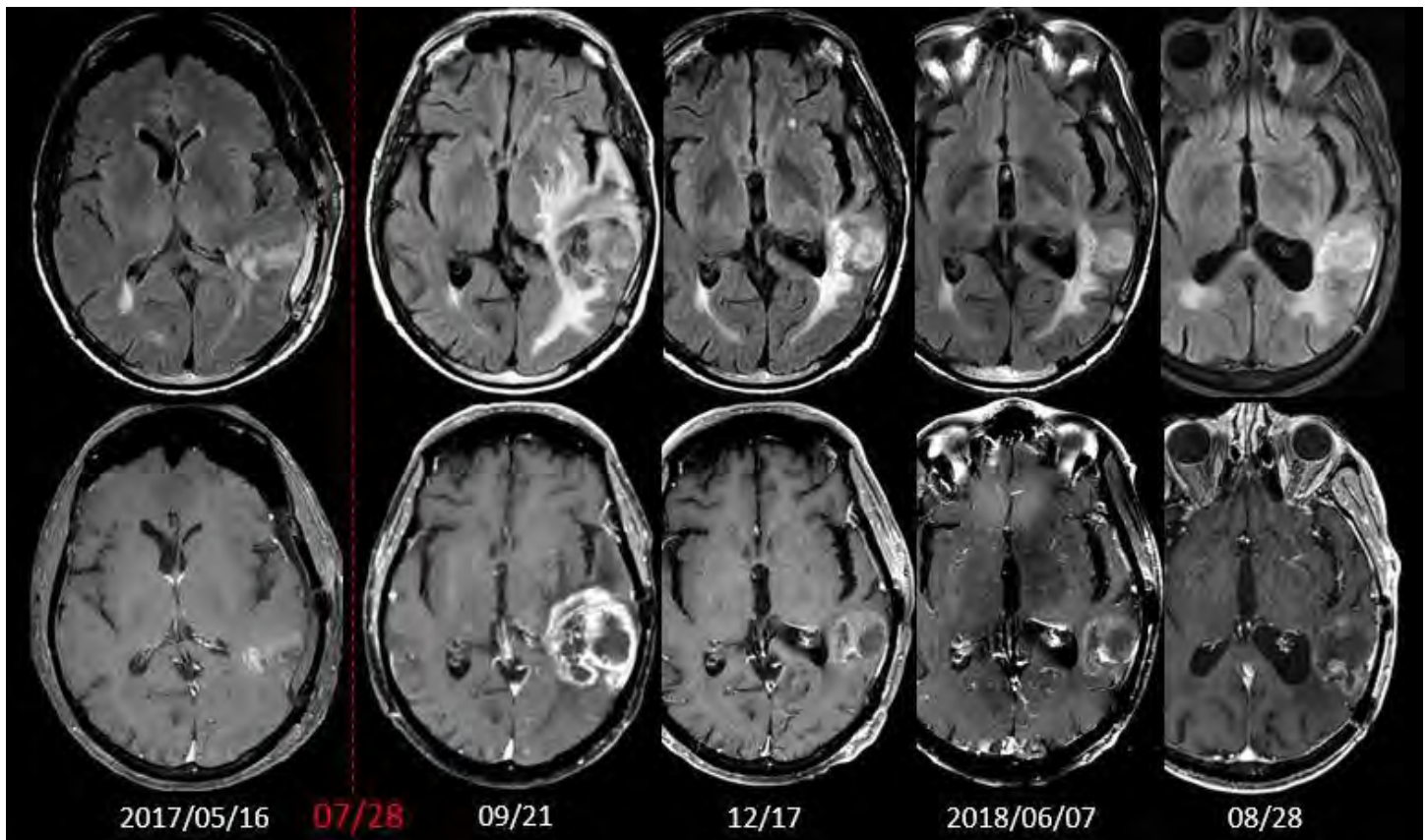
To present a case-based review of the gamut of imaging manifestation of cerebral radiation-induced toxicity.

Results

A comprehensive review of the literature will be performed, and a selected collection of cases will be presented including conventional imaging, advanced neuroimaging techniques, and pathology correlation.

Conclusions

Imaging is crucial for the diagnosis of pseudoprogression, progressive disease, and radiation necrosis. Although the imaging findings are mostly non-specific, there are some key radiographic and clinical features that may be helpful to discriminate between those entities. The advanced brain tumor imaging techniques are useful for challenging cases.



(Filename: TCT_540_Figure.JPG)

406

Imaging of Sellar and Parasellar Pathologies

A Jipa¹, V Jain²

¹MetroHealth Medical Center/Case Western Reserve University School of Medicine, Cleveland, OH, ²N/A, N/A

Purpose

Although physically small, the region of the pituitary and sella turcica can be affected by numerous pathologic processes. Imaging plays a key role in the evaluation of sellar pathology. The radiologist can often suggest a specific diagnosis based on imaging and basic clinical information. Radiologists should have a comprehensive knowledge of the imaging features of common diagnoses such as pituitary adenomas and be able to suggest rarer diagnoses as well. An important skill is accurate anatomic localization of the abnormality. Specifically radiologists should recognize true pituitary lesions and separate these from pathologies of the para-sellar structures such as the cavernous sinuses, skull base, hypothalamus, and sphenoid sinus. Neoplastic and non-neoplastic disease processes can often be distinguished by imaging. Accurately assessing for invasion of nearby structures by neoplastic processes is of special relevance to ordering clinicians.

Materials and Methods

The purpose of this presentation is to review common and rare disease processes of the pituitary gland and surrounding regions with a focus on MR. Representative images will be used to highlight various diagnoses and set up a systematic method for evaluating sellar abnormalities. The presentation is focused on radiology trainees but also aims to provide a high-yield review for practicing radiologists. A review of pituitary disease processes (adenoma, Rathke Cleft cyst, hypophysitis, hyperplasia, intrasellar craniopharyngioma, etc) will be provided along with a descriptions or parasellar processes (meningioma, skull base tumors, sphenoid sinus tumors, aneurysms, etc) that can have a similar radiologic appearance.

Results

This review includes images from previously unpublished cases to illustrate various sellar pathologies. Each image is completely de-identified.

Conclusions

Properly identifying sellar pathologies and differentiating them from para-sellar mimics is an important skill for the diagnostic radiologist. Understanding the normal MR anatomy of the pituitary gland and para-sellar structures and patterns of growth for sellar and para-sellar mass lesions provides a foundation for accurate diagnosis. Providing an accurate diagnosis can have important

implications for surgical planning. Diagnoses with possible non-surgical management such as hypophysitis should be suggested as appropriate.

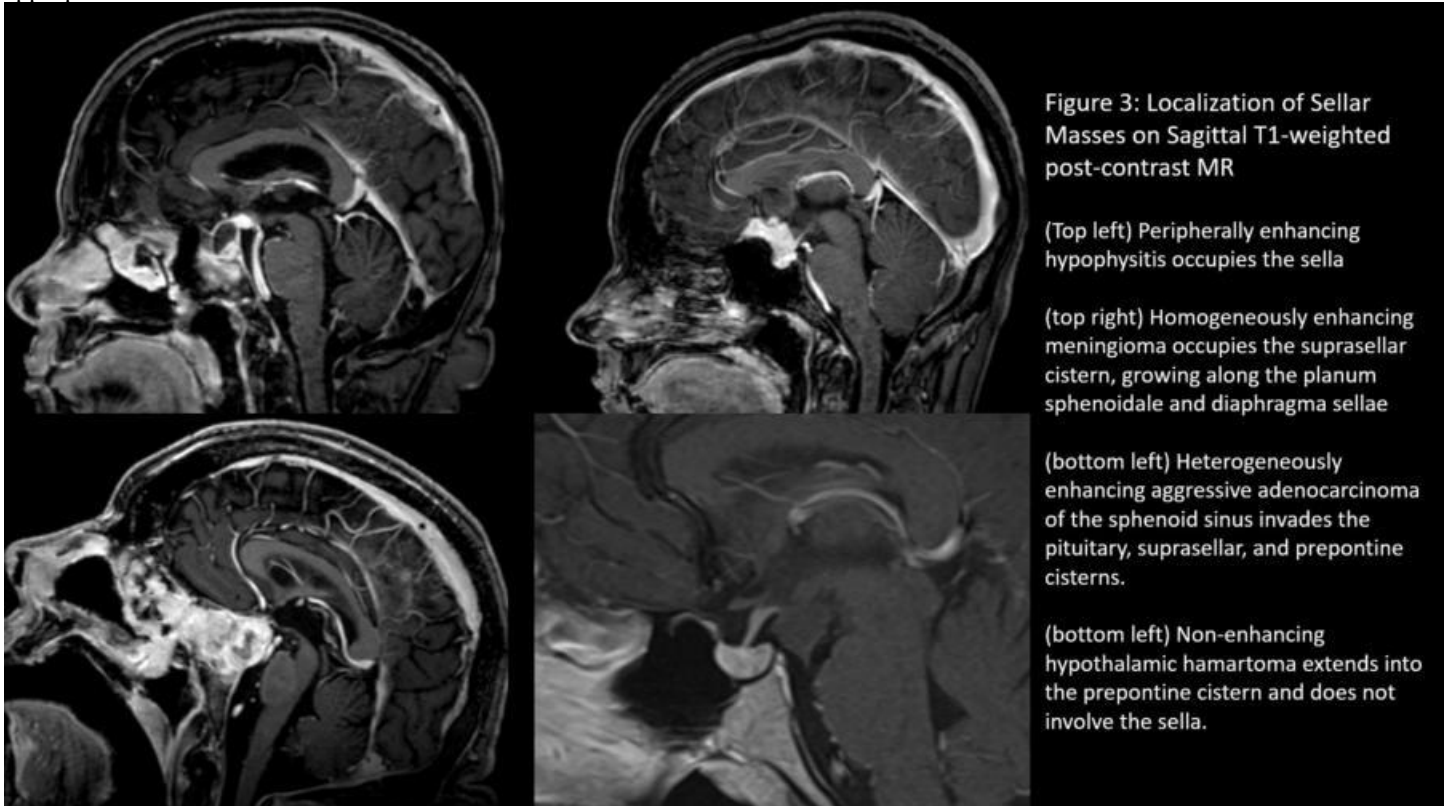


Figure 3: Localization of Sellar Masses on Sagittal T1-weighted post-contrast MR

(Top left) Peripherally enhancing hypophysitis occupies the sella

(top right) Homogeneously enhancing meningioma occupies the suprasellar cistern, growing along the planum sphenoidale and diaphragma sellae

(bottom left) Heterogeneously enhancing aggressive adenocarcinoma of the sphenoid sinus invades the pituitary, suprasellar, and prepontine cisterns.

(bottom left) Non-enhancing hypothalamic hamartoma extends into the prepontine cistern and does not involve the sella.

(Filename: TCT_406_PituitaryEducationalExhibitSampleSlide.jpg)

544

Imaging of the Masticator Space: A Pictorial Review

M Mansouri¹, R Fullerton¹, S Benitez¹, J Burns¹, J Bello¹, K Shifteh¹

¹Montefiore Medical Center, Bronx, NY

Purpose

Educational Goals/Teaching Points: 1. To identify the major anatomic landmarks and contents within the masticator space as well as surrounding anatomical spaces (buccal, parapharyngeal, parotid). 2. To identify CT and MR imaging findings of the common and uncommon disease processes of the masticator space and differential diagnosis. Introductory anatomy of the masticator space will be discussed, including identifying major anatomical landmarks and contents (muscles of mastication, nerves, bones) and surrounding anatomical spaces (buccal, parapharyngeal, parotid). Further, a case based approach will be provided to identify and differentiate major disease processes of the masticator space based on the following classification: * Benign: - Vascular/Congenital: Hematoma, AVM, Hemangioma, Lymphangioma - Infection: Odontogenic Abscess, Osteomyelitis, Chronic Infection - Acquired: Accessory Parotid Gland, Masseteric Hypertrophy, V3 Denervation, ALS - Mandibular Lesions: Odontogenic Keratocyst, Dentigerous Cyst, Ameloblastoma, ABC, Central Ossifying Fibroma - Neoplasms: Leiomyoma, Neural Sheath Tumor, JNA * Malignant: Sarcoma, Lymphoma, Rhabdomyosarcoma, Metastasis

Materials and Methods

The masticator space contains the mastication muscles, mandible, mandibular nerve, and inferior alveolar vein and artery. Inflammatory conditions of the space are particularly common and are usually odontogenic in origin. Lymphovascular malformations are also common specially in pediatric population. Benign and malignant tumors may arise from the different contents of the space. Since clinical assessment of lesions in this space may be difficult, CT and MR imaging is important for the characterization and mapping of the lesions.

Results

N/A

Conclusions

Masses of the masticator space (MS) are difficult to evaluate clinically, and CT and MR images are essential for the diagnosis and characterization of these lesions. Malignant tumors may or may not demonstrate bone erosion or violation of the fascia. Infections of the MS may cross the fascia and mimic neoplasms on imaging studies. Perineural spread may occur in tumors involving the MS and its recognition on imaging studies is essential to plan the appropriate treatment.

Imaging Spinal Fixation Hardware: A Guide for the Radiologist

D Lee¹

¹Staten Island University Hospital, Staten Island, NY

Purpose

The planned presentation will progress as follows: -Various spinal hardware including intervertebral disc replacement, plate-and-rod hardware, posterior fusion devices and how they are expected to be positioned -Indications for the placement of aforementioned various hardware -Normal radiographs/intraoperative fluoroscopic images/CT/MR images of spinal fixation hardware. Parts of hardware will be identified, as well as other fixation substrates used such as cement -Normal expected post-surgical changes on imaging -Various complications related to spine hardware and how they appear on various imaging modalities including CT/MR/nuclear studies not limited to infection, prosthetic and peri-prosthetic fractures, hardware loosening, and hardware misplacement -Discussion of various surgical approaches such as oblique lumbar interbody fusion (OLIF), extreme lateral approach, or direct lateral approach and associated complications with each approach. -The medical and/or surgical management of aforementioned hardware complications Objectives: -Identify various spinal hardware routinely found on various imaging modalities including radiographs, CT, and MR -Describe the proper placement of spinal hardware based on various radiographic views conventionally used to assess position, as well as other imaging modalities -Describe normal post-surgical changes on imaging - Identify frequently encountered spinal hardware complications on imaging and describe how they are managed

Materials and Methods

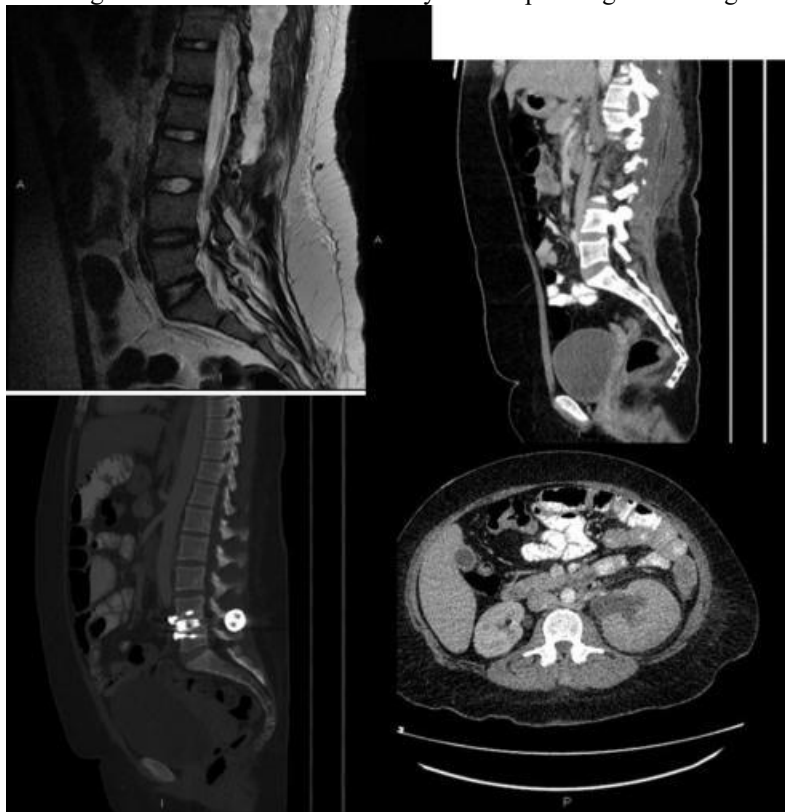
This is an educational review regarding spinal fixation hardware and complications. Following this study, the radiologist will be able to achieve the following: -Describe normal spinal fixation hardware placement and alignment on imaging -Describe various surgical approaches and associated complications -Describe spinal hardware complications and associated imaging findings, including nuclear studies -Describe normal imaging findings following placement of prosthetics

Results

Images from various modalities including radiographs, fluoroscopic images, CT, MR, nuclear studies, and pictorial illustrations of spinal hardware, taken from cases from the author's institution demonstrating post-surgical findings and complications.

Conclusions

Practicing radiologists will be able to identify spinal fixation hardware on imaging and recognize normal positioning of prosthetics. Radiologists will also be able to identify normal postsurgical findings and recognize complications associated with spinal hardware.



MR T2 lumbar spine immediately post-operation and CT lumbar spine with IV contrast one month post-operation. Initially, there is a moderate volume fluid collection in the dorsal paraspinous soft tissue. One month later, the fluid collection is rim-enhancing, suspicious for organizing infected fluid collection.

CT abdomen with sagittal and axial views following IV Contrast. Three weeks status post L4-L5 oblique lumbar interbody fusion with interspinous distraction device. Patient presenting with left flank pain, found to have left pyonephrosis secondary to mid-ureteral obstruction at the level of L4. Ureteral obstruction secondary to surgical complication could not be ruled out.

(Filename: TCT_1553_SpinehardwareASNR2021.jpg)

Imaging-based Classifications that May Enhance the Value of Contextual Neuroradiology Reports.

R Samant¹, J McCarty², R Riascos³

¹UT Health, McGovern School of Medicine, Texas Medical Center, Houston, TX, ²UTHealth Houston, Houston, TX, ³The University of Texas Health Science Center at Houston, Houston, TX

Purpose

Templates of Imaging-based Classifications when integrated in contextual reports may enhance the value of radiology reports. The objectives of this educational exhibit are to: 1. Present actionable imaging-based classifications in Neuropathology. 2. Demonstrate our institutional templates of these classifications that can be included in contextual reports. 3. Show some representative case-based examples of using these templates. 4. Provide a set of templates that we believe enhance the value of contextual Neuroradiology reports.

Materials and Methods

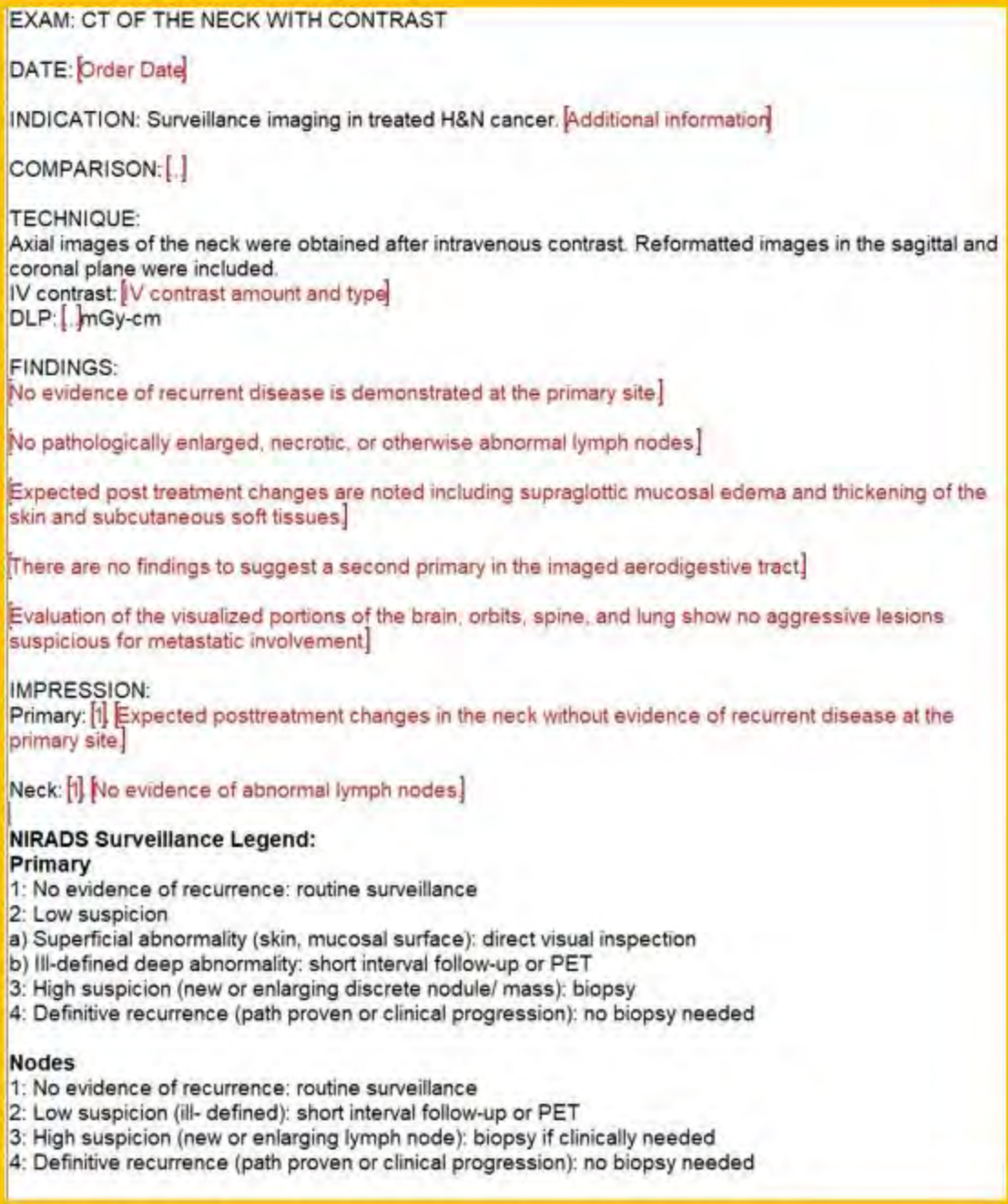
Contextual structured reports are tailored to the clinical situation, disease or examination indication. Such reports have the advantage of ensuring all pertinent points are addressed and have an intuitive approach for clinical interpretation for trainee education. The purpose of this educational exhibit is to encourage Neuroradiologist to further refine their contextual reports by including templates that address widely accepted imaging-based actionable classifications in Neuropathologies.

Results

After reviewing literature, we have collected a list of Imaging and Clinico-Imaging classifications of Neuropathologies that have been proposed. Examples include relatively well known and less known classifications such as NI-RADS Categories, Spinal Instability Neoplastic Score (SINS), Epidural Spinal Cord Compression (ESCC) scale, AO Spine Classification, Biffi Scale, CT-NASCET style stenosis, ASPECT Score, CTA collateral score, Castellivi classification etc. From this list, relatively well-accepted evidence-based actionable classifications were selected. Templates were structured on our speech recognition platform to include these classifications in contextual reports. These classifications, evidence supporting their application and our institutional templates for these classifications will be presented.

Conclusions

Including imaging-based classifications in contextual reports have a high potential of enhance the value of Neuroradiology reports.



(Filename: TCT_981_NI-RADS.jpg)

1587

Immunotherapy Clinical Trials in Melanoma: Imaging Melanoma Metastatic Disease During Treatment With Immunotherapy

J Sikder¹, M Aboian²

¹Yale University School of Medicine, New Haven, CT, ²Yale University, Woodbridge, CT

Purpose

1. To review different types of immunotherapy with focus on immune checkpoint inhibitor therapy and chimeric antigen receptor T cell therapy. 2. To highlight the outcomes of immunotherapy clinical trials in melanoma. 3. To highlight unique challenges of imaging brain and spine melanoma metastases

Materials and Methods

Approximately 100,350 people are diagnosed and 6,850 people die every year from melanoma. Historically, advanced stage melanoma has been correlated with poor prognosis with median overall survival of 8-10 months with a 5 year survival rate of 10%. Chemotherapy results are limited with short lived objective responses of less than <15%. Immunotherapy for melanoma has changed

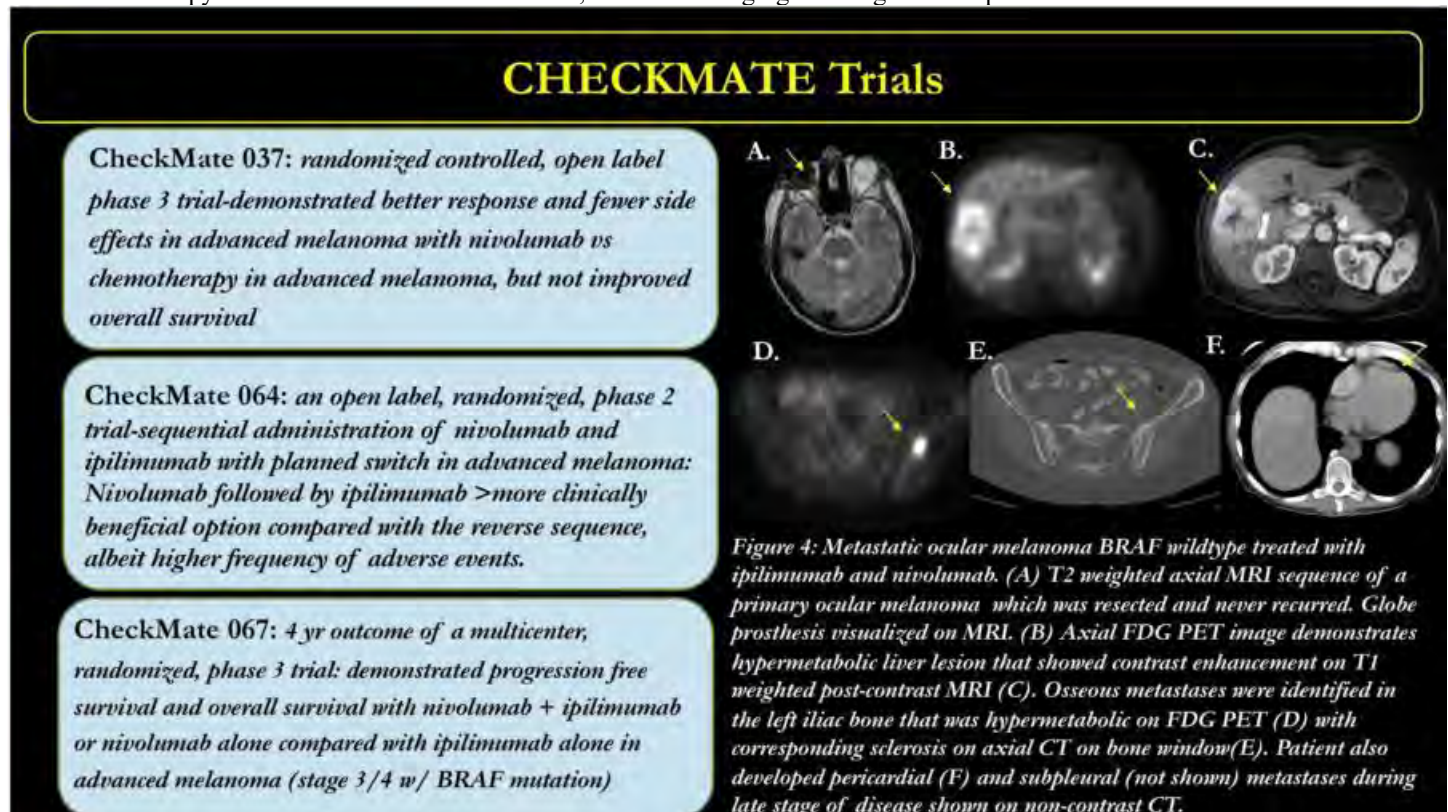
the outcomes in patients with metastatic melanoma, and in particular with metastatic disease to the brain. In our study, we describe imaging features of melanoma on different modalities before and after immunotherapy with focus on published research discussing the checkmate trials and their clinical and radiological scope.

Results

Comprehensive analysis with review of published literature on immunotherapy trials and outcomes with applications to clinical significance were pursued. Images of metastatic melanoma on differential modalities were reviewed by neuroradiology attending and radiology resident using Visage Imaging Software (Pro Medicus Limited, Visage 7). Correlation to pathology, patient's oncological history/treatments, and outcomes in conjunction with our imaging were conducted utilizing EPIC (Medical record system). Mpower (Montage-Clinical Analytics for medical imaging) was utilized to data mine for post immunotherapy images and side effects.

Conclusions

We present a comprehensive analysis of role of immunotherapy in treatment of metastatic melanoma with focus on brain metastases. We review the published literature and data mining to present the metastatic patterns of most common mutant subtypes of melanoma, the immunotherapy clinical trials with their outcomes, as well as imaging challenges and expectations.



(Filename: TCT_1587_ed_exh_figurecopy.jpg)

1140

Implantable Epilepsy Devices and MRI Safety: A Guide to Helping Patients Being Imaged

J Ormsby¹, D Lima¹, J Hallstrom¹, R Selwyn¹, G Lorenzo¹

¹University of New Mexico, Albuquerque, NM

Purpose

Summary Refractory epilepsy may be treated with implantable devices though MRI compatibility may limit future imaging. Nevertheless, imaging with MRI can be obtained when device safety profiles are adhered to, requiring understanding of devices, MRI physics, and well-developed institutional protocols. Objectives Review implantable devices used to treat epilepsy. Understand individual epilepsy device MRI safety profiles. Demonstrate protocols to effectively and safely obtain MR imaging.

Materials and Methods

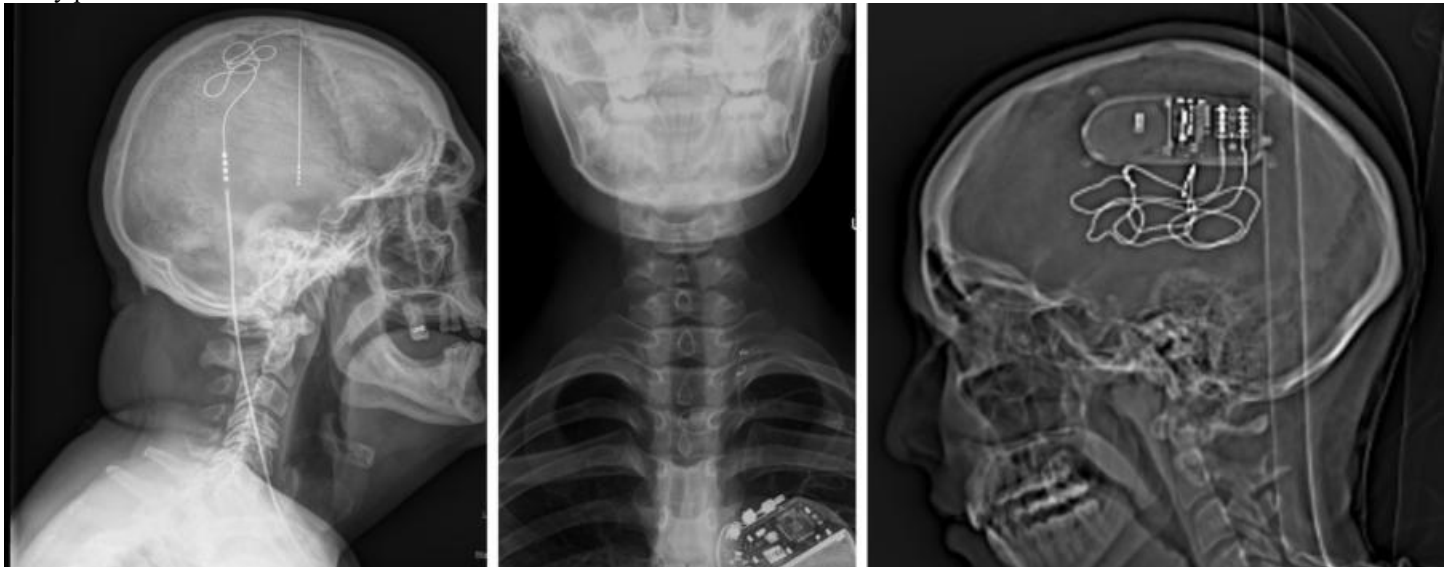
To inform neuroradiologists on MRI safety issues related to implantable epilepsy devices and how to develop protocols to successfully image within the safety parameters.

Results

We will review vagal nerve stimulators (VNS), responsive neurostimulation devices (RNS), and deep brain stimulators (DBS), all of which can be used for treatment of epilepsy, including their safety profiles, and how to understand the individual safety parameters. We will discuss choosing sequences and making changes to sequences to fall within the safety profile. We will describe how we have successfully done this at our institution and how it can be employed at other institutions.

Conclusions

Results Epilepsy can be difficult to treat and manage especially when patients become medication resistant. Unfortunately, many patients do not have an identified source on imaging to focus resection on. In these cases, implantable epilepsy devices can be used including VNS, RNS, and DBS. Like any indwelling foreign body, one must consider MRI safety issues for these devices and stay within certain limits to minimize risk of harm. This includes looking at what type of transmit coils can be used, maximum magnetic field strength, maximum spatial gradient, specific absorption rate (SAR) limits, and scan time as determined by the device manufacturer. Additionally, the neuroradiologist needs to know the indication for an MRI and if there are alternatives to answer the same clinical question. If MRI is still warranted, then the neuroradiologist should prioritize sequences and work with both medical physics and MRI technologists to create clinically useful imaging. When done successfully, this can provide great satisfaction for the patient, ordering clinician, and neuroradiologist. Conclusion It is imperative for the neuroradiologist to be aware of the different devices that can be used to help treat epilepsy and realize that many of these devices can be scanned in an MRI if able to adhere to the safety profile of these devices.



(Filename: TCT_1140_Epilepsydevices.jpg)

840

Infantile Subdural Hygroma and Venous Thrombosis as a Complication of Birth

j_scheller¹, J Mack²

¹Private Practice, Baltimore, MD, ²Penn State Hershey, Hershy, PA

Purpose

Cerebral venous thrombosis (CVT) in infancy poses particular diagnostic challenges due to the wide range of presentations and lack of specific symptoms. When thrombosis is accompanied by subdural collections, the possibility of abusive head trauma (AHT) is often raised. Recent radiologic reports (Choudhary and others) suggest that thrombosis in cortical veins is a unique feature of AHT. However, these articles do not articulate how thrombosis due to natural disease was excluded. In this presentation a group of 11 infants with subdural fluid collections and CVT are reviewed. None had accompanying evidence of trauma. Chronic subdural hygromas are accompanied by inflammatory markers in the dural compartment. Inflammation combined with the alterations in the anatomy can predispose to thrombosis in the absence of significant trauma. Review anatomy of meninges and physiologic derangements that may accompany chronic collections (chronic inflammation; repeated small volume bleeding that may accompany hygromas) Review risk factors and radiologic signs of focal CVT with particular emphasis on heme sensitive sequences Discuss importance of clinical findings, including any prodromal symptoms and/or change in head circumference over time

Materials and Methods

To document the presence and complications of infantile chronic subdural hygromas in the absence of trauma.

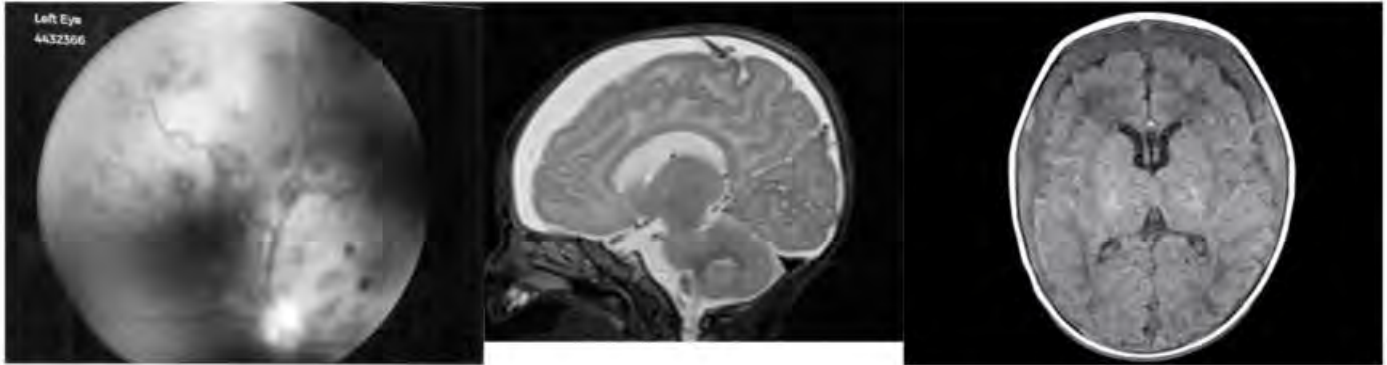
Results

Infants suspected of being victims of abusive head trauma were referred for a medical legal second opinion. All had undergone a thorough birth and pediatric history, a complete physical exam, routine blood work, 2 skeletal surveys, a head and cervical MRI, and an ophthalmologic exam. We chose those who had chronic subdural hygromas and cortical venous thromboses and excluded those with external or internal organ injury skull fractures or swelling, acute or healing bony fractures, and any evidence of cervical abnormality. Change in head growth from birth to diagnosis was documented as was presence or absence of retinal hemorrhages. Radiology studies were reviewed by a radiologist and neurologist.

Conclusions

There were 11 infants who were found to have chronic subdural hygromas and cortical vein thromboses. The average age was 4

months, 4/11 were born premature. 7/11 presented with vomiting, 3/11 presented with seizures. 10/11 were found to have retinal hemorrhages. All had normal development 6 months later. Chronic subdural hygromas can predispose to cortical venous thrombosis in infants in the absence of significant trauma.



Number	Increase in HC percent	Premature	Age in Months	Retinal	Vomiting	Seizures	Subdural Fluid
1	70	Yes		3 Bilateral	Yes	No	not tapped
2	30	Yes		8 Bilateral	No	Yes	not tapped
3	30	No		5 Unilateral	Yes	No	xanthochromic
4	20	No		7 Unilateral	Yes	No	dark fluid
5	25	No		2 Bilateral	Yes	No	orange fluid
6	80	No		3 Bilateral	No	Yes	not tapped
7	70	No		2 None	Yes	No	not tapped
8	40	No		2 Bilateral	Yes	No	blood tinged fluid
9	25	No		6 Unilateral	Yes	No	not tapped
10	50	Yes		5 Bilateral	No	Yes	not tapped
11	60	Yes		11 None	No	No	Not tapped

(Filename: TCT_840_Presentation1.jpg)

1033

Internal Carotid Artery Nomenclature: History, Evolution, and Clinical Utility

A Kuner¹, L Eisenmenger², A Grayev³, T Kennedy⁴

¹University of Wisconsin School of Medicine and Public Health, Middleton, WI, ²University of Wisconsin - Madison, Middleton, WI, ³University of Wisconsin, Madison, WI, ⁴The University of Wisconsin, Middleton, WI

Purpose

Internal carotid artery anatomic nomenclature systems have changed over the years, as treatment has evolved from surgical to endovascular intervention for vascular disease. These systems reflect the interventional methods of the time, and provide detail that is pertinent to intervention for treatable pathology. A detailed understanding of internal carotid anatomy is necessary for accurate recognition and clear communication of vascular pathology. In this exhibit we will review the most common internal carotid artery nomenclature systems, and highlight the purposes of their utilization. This will be illustrated with various examples of pathology in which anatomic detail and accurate localization helps determine an appropriate treatment. This includes, but is not limited to, determination of intra and extradural aneurysm location, variability in ophthalmic artery origin, and the carotid cave and the importance of the transitional segment. After reviewing this educational exhibit the reader will be more comfortable determining the accurate anatomic location of vascular pathology with an understanding of how the utilization of localizing nomenclature terminology will determine treatment.

Materials and Methods

The purpose of this educational exhibit is to review the most common nomenclature systems of the internal carotid artery, illustrate these anatomic details with clinical cases, and demonstrate how inclusion of appropriate localization can aid in the determination of treatment decisions.

Results

N/A

Conclusions

N/A

455

Intraoperative Ultrasound for Procedural Guidance During Cavernous Malformation Resection Surgery

L Mankowski Gettle¹, J Pitts¹, A Kuner², L Eisenmenger³, R Dempsey¹, D Dawkins¹

¹University of Wisconsin School of Medicine and Public Health, Madison, WI, ²University of Wisconsin School of Medicine and Public Health, Middleton, WI, ³University of Wisconsin - Madison, Middleton, WI

Purpose

Intraoperative ultrasound has been previously described as a tool for surgical localization. While utilization remains relatively low, it is most commonly reported for applications in the spine. It is utilized to assist in identifying intramedullary disease which can be difficult to detect upon superficial visual inspection. Additionally, traditional navigation systems are not useful in these scenarios where intraoperative decompression of the CSF and subarachnoid space causes shifts in the parenchyma that precludes confident image registration. At our institution, our neurosurgeons have regularly utilized radiologist-performed intraoperative ultrasound for intraoperative navigation during the resection of cavernous malformations from the brain, including both supratentorial and infratentorial locations. The benefits of this adjunct navigation technique includes optimization of a minimally invasive approach to address this non-malignant neoplastic disease. It also affords the surgeon the opportunity to identify an associated developmental venous anomaly that may be occult or difficult to visually identify at the time of resection, reducing the risk of complications. The goal of this electronic educational exhibit is to present a series of our cases, and describe our techniques and methods highlighting how radiologist-performed intraoperative ultrasound can be utilized for the resection of cavernous malformations.

Materials and Methods

The purpose of this electronic educational exhibit is to present a series of our cases to demonstrate how intraoperative ultrasound contributes to a more targeted and minimally invasive surgical approach, demonstrate the versatility of the technique illustrated by lesions in various locations of the brain parenchyma including both supra and infratentorial cavernous malformations, and provide technical tips and details for the radiologist performing ultrasound.

Results

N/A

Conclusions

N/A

1563

Intraosseous Basivertebral Nerve Ablation for the Treatment of Chronic Low Back Pain – A Review of Imaging Endplate Characteristics Indicative of Vertebrogenic Pain and Post Procedure Lesion Characteristics.

R Silbergleit¹, J Hirsch², J Lotz³

¹Beaumont Hospital, Royal Oak, MI, ²MGH, Boston, MA, ³N/A, N/A

Purpose

Summary of Planned Presentation: In this education session we propose to overview the clinical presentation of vertebrogenic pain including typical pain location and symptoms paired with interactive review of pre-procedure MRIs for vertebral endplate changes. Baseline MRIs will be paired with post-procedure MRIs in a discussion of targeting success and lesion characteristics post intraosseous BVN ablation. Education Objectives: • Describe the clinical characteristics of vertebrogenic pain. • Identify endplate changes on MRI indicative of vertebrogenic pain on baseline images. • Describe target location for intraosseous BVN ablation and rationale. • Discern typical lesion / vertebral body characteristics on MRI post intraosseous BVN ablation.

Materials and Methods

Background: Vertebral endplates, innervated by the basivertebral nerve (BVN), are increasingly recognized as a source of chronic low back pain (CLBP). When vertebral endplates are damaged or degenerate, chronic inflammation ensues and leads to nerve sensitization, with pain signals transmitted via the basivertebral nerve (BVN) located within the vertebral body.[1,2] These vertebrogenic sources of pain, from damaged endplates with resulting chronic inflammation, are readily visible as Modic changes (MC) on routine MRI, a highly specific biomarker for CLPB.[3] In two previously published randomized controlled trials, intraosseous radiofrequency ablation (RFA) of the BVN demonstrated superior efficacy and durability compared to sham and standard

care in patients with vertebrogenic CLBP diagnosed by endplate changes on MRI (Modic Type I or II).[4,5] Assessment of the lesion relative to the terminus of the BVN for each treated vertebral body was reviewed using the 6 weeks post-ablation MR image (T1, T2, and STIR time constants). Placement of the probe tip is targeted for 30-50% of the vertebral body from the posterior wall.

Results

Not applicable

Conclusions

Not applicable

1148

Intravascular large B cell lymphoma (IVLBCL)- Central Nervous System and other organs' manifestations – What radiologists should know.

H Nakamura¹, H Mimura², M Doi³

¹St. Marianna University Of Medicine, Kawasaki, Japan, ²St. Marianna University School of Medicine, Kawasaki, n/a, ³St Marianna University of Medicine, Kawasaki, n/a

Purpose

Summary, 1) Clinical profile of IVLBCL 2) Brain imaging. 3) Spinal cord imaging 4) Lung imaging 5) Adrenal gland involvement Educational objective. 1) We learn the highly variable brain and spinal cord lesions throughout the clinical course. 2) We learn the characteristic radiological findings other than CNS

Materials and Methods

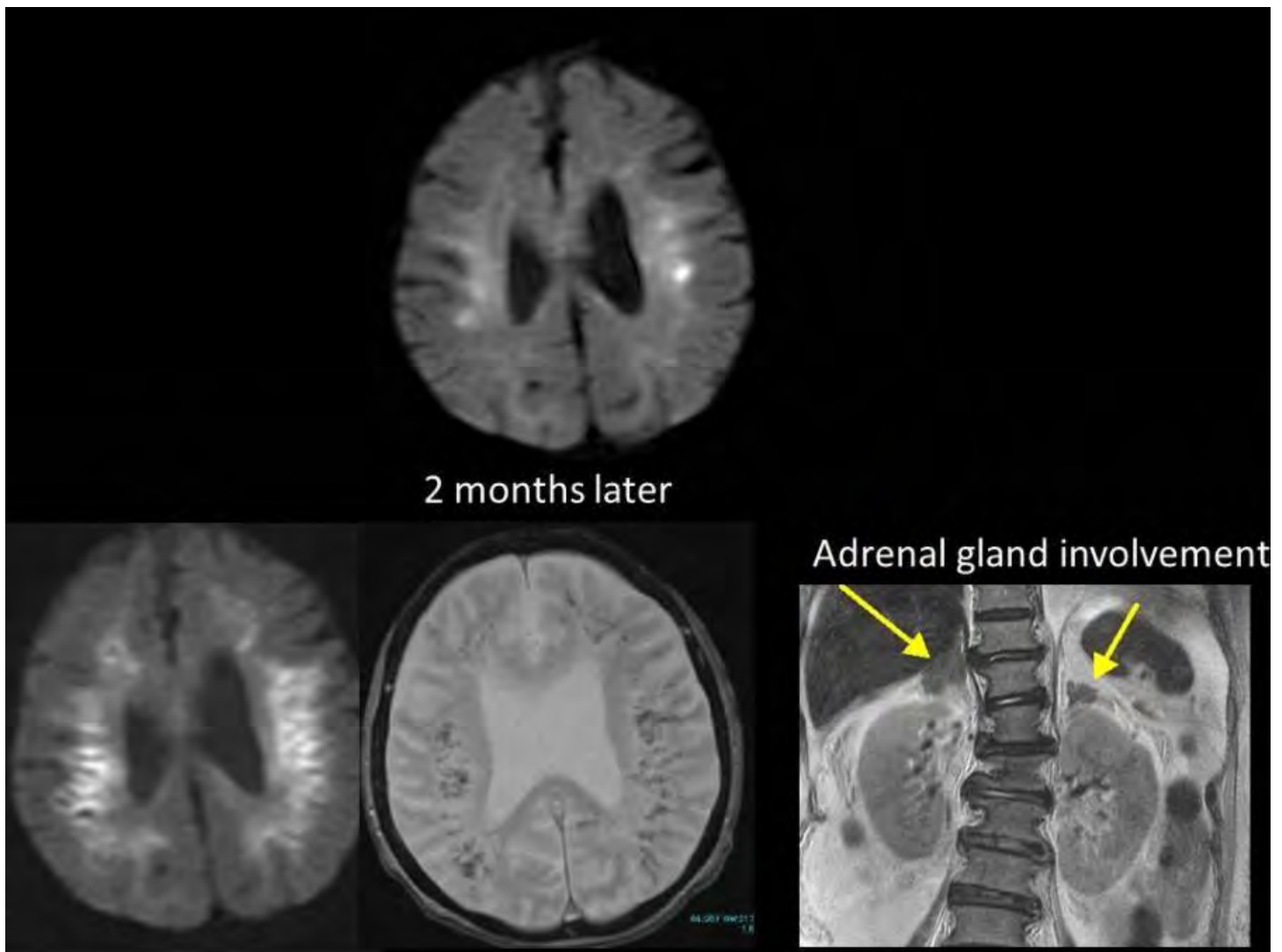
IVLBCL is a rare, clinically aggressive lymphoma entity characterized by almost exclusive growth of large cells within the lumen of all sized blood vessel. It is commonly involved in the central nervous system (CNS). The brain lesions are highly variable First of all, we would like to consolidate variable brain findings, which enable to differentiate many common entities such as cerebral infarction and acute disseminated encephalopathy. Secondary, longitudinally extensive spinal cord lesions would like to be differentiated from other entities such as sarcoidosis and neuromyelitis optica. Finally, characteristic findings other than CNS will be introduced.

Results

From 2012 and 2020, we examined the medical record of our hospital. We found pathology proven five cases (including two autopsy cases) and their radiological findings were reviewed.

Conclusions

1) Diagnosis of IVLBCL is frequently delayed because of the initial non-specific symptom and the absence of non-invasive diagnostic markers. 2) The most frequent involvement except for the cutis is the CNS. Brain MRI findings used to show various patterns, but we consolidate two major patterns. One is persistent hyperintensity on DWI, which enables us to differentiate from thrombotic infarction. The other is acute hemorrhagic leukoencephalopathy associated with non-enhancing areas of restricted diffusion, which would be differentiate from other common entities such as acute disseminated encephalopathy, autoimmune disease, leukemia and herpes infection 3) Longitudinally extensive spinal cord lesions involving the conus with old age patients, constitutional symptoms, anemia or thrombocytopenia may consider IVLBCL 4) Lung CT shows focal nodules, diffuse ground glass infiltrate or consolidation may consider IVLBCL when the patient has dyspnea and hypoxemia 5) An increase volume of adrenal gland may be an additional clue. Conclusion. 1) Variable brain lesions are majorly divided into two types. 2) Longitudinally extensive spinal cord lesions considering the ancillary finding only be differentiated. 3) We should also learn the radiological findings other than CNS, which may be a clue for the correct diagnosis.



(Filename: TCT_1148_2020ASNRpicture.jpg)

945

Is There Anything Hidden Underneath This Bleeding?

E Salvador¹, A Hilario¹, P Martin Medina¹, L Koren¹, E Barcena¹, J Alonso¹, A Domingo¹, A Martinez de Aragon¹, J Millan¹, A Ramos¹

¹Hospital Universitario 12 de Octubre., Madrid, SPAIN

Purpose

Objectives: ● To review different causes of secondary bleeding. ● To identify MRI biomarkers associated with secondary hemorrhage ● To recognize signs of underlying structural lesion at MRI, mainly tumors and vascular malformations. ● To review the different MR angiographic techniques when investigating a possible vascular malformation within a hemorrhage. Bleeding is classified as primary or secondary depending on the cause of the bleeding. The primary ones are most frequent and are due to degenerative processes secondary to arterial hypertension or amyloid angiopathy. The secondary ones are associated with tumors, endocarditis, vascular malformations, alterations in coagulation or drug abuse. The bleeding is caused by rupture of neofomed vessels, vessel wall inflammation, or by alterations in the coagulation system. Radiological signs that should lead to suspicion of an underlying tumor within an intracranial hemorrhage are: multiple stages of hematoma in the same lesion with debris–fluid level, atypical localization, persistent deoxyhemoglobin with absent hemosiderin and very important the presence of areas of inappropriate enhancement and the existence of perihematoma edema and disproportionate mass effect that persist in time. Patients with anticoagulation related hemorrhage will present with multiple stages of hematoma in the same lesion sometimes with a fluid level, hematoma expansion is common as well as the coexistence of multiple hematomas of different age and volume. In Cavernous hemangiomas MRI depict low intensity on T2WI GRE and SWI surrounding various circumscribed regions of hemorrhage as opposed to tumors, there is a complete rim of hemosiderin surrounding the cavernous hemangiomas. In hemorrhages caused by arteriovenous malformations the hematoma has a regular and homogeneous appearance and curvilinear flow voids can be visualized located at the periphery of the hematoma.

MRA is useful in mapping the AVM. In lesions that have high signal associated with adjacent hemorrhage, phase contrast MRA is necessary to provide the best details of AVM. Patients with substance abuse as the cause of the hemorrhage are usually young and usually angiography is necessary to rule out underlying vascular malformations.

Materials and Methods

N/A

Results

N/A

Conclusions

We will demonstrate in this exhibit how MRI together with Angio MR are essential tools to identify the cause of the hematoma enabling to establish the appropriate treatment

696

It's Not Just a Bump on the Head – A Pictorial Review of Calvarial Anatomy and Pathology

J Winkler¹, H Saad¹, N Poyiadji¹, S Patel², B Griffith¹

¹Henry Ford Health System, Detroit, MI, ²HENRY FORD HOSPITAL, DETROIT, MI

Purpose

Purpose: There are a wide range of both benign and malignant tumors that can affect the calvarium, as well as non-neoplastic conditions and anatomic variations that can be discovered on imaging. These often rare lesions are frequently discovered incidentally on CT and MRI imaging of the head that was ordered for unrelated indications. The radiologist must have a thorough search pattern and an awareness of the variety of pathology to make these diagnoses. This exhibit will provide a pictorial review of the normal anatomic variants and neoplastic and non-neoplastic lesions that involve the calvarium with an emphasis on key differentiating imaging features. Approach/Methods: • Using CT and MRI representative case files, we will review normal anatomic and congenital variants of the calvarium such as arachnoid granulations (Fig 1) and enlarged parietal foramina (Fig 2), as well as the associated relevant anatomy. • We will also use case files to show a variety of neoplastic and non-neoplastic calvarial lesions ranging from the more common fibrous dysplasia and multiple myeloma to the more rare osteosarcoma (Fig 3) and en plaque meningioma (Fig 4), as well as many in between. • There will be an emphasis on defining imaging characteristics that differentiate the various lesions and incorporating clinical information to formulate an appropriate differential diagnosis. Summary/Conclusion: An awareness of the variety of pathologies that can affect the calvarium, as well as an understanding of normal anatomic variants is necessary for the complete radiologic evaluation of head imaging. At the conclusion of this exhibit, viewers should be familiar with normal anatomic variants of the calvarium, as well as the defining imaging characteristics of both common and uncommon pathologies, and the incorporation of clinical information to formulate an appropriate differential diagnosis.

Materials and Methods

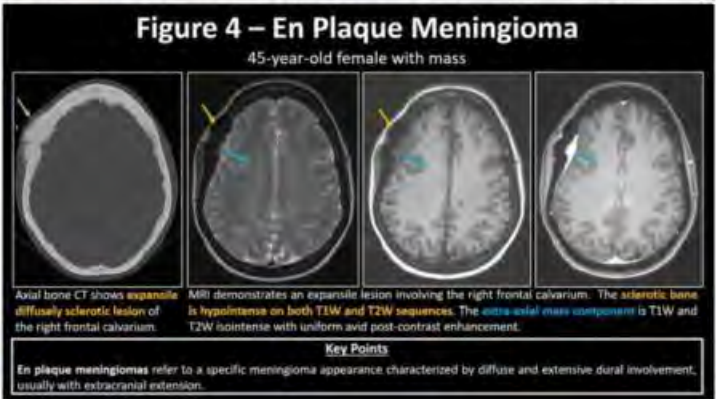
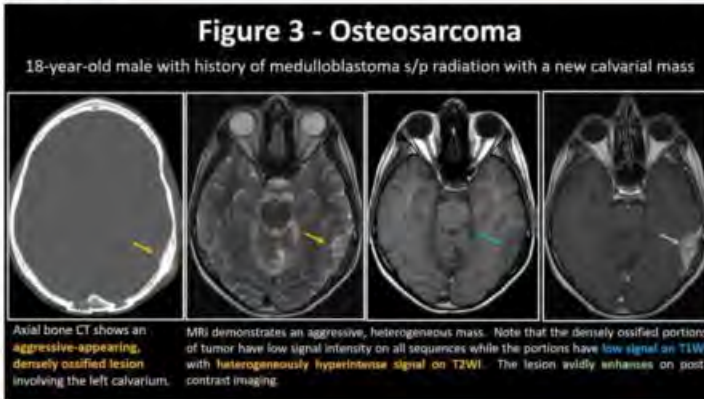
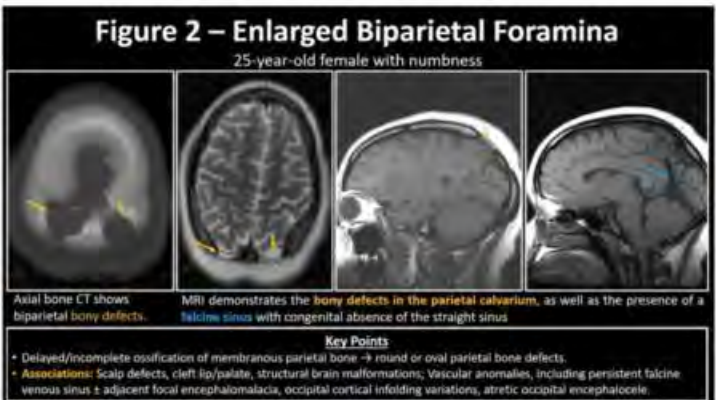
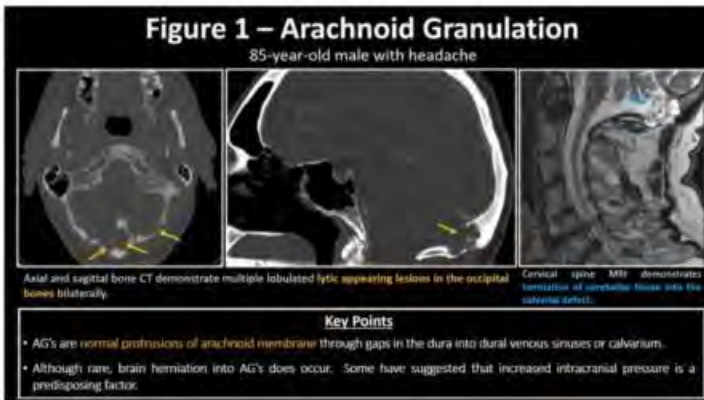
N/A

Results

N/A

Conclusions

N/A



(Filename: TCT_696_CalvarialLesionASNRFinal.jpg)

1064

Keeping it Basic: Central Skull Base Pathology

J Robison¹, D Gridley², J Hayden³

¹Creighton Phoenix Radiology Program, Phoenix, AZ, ²Creighton Phoenix, Paradise Valley, AZ, ³Creighton Phoenix Radiology, Phoenix, AZ

Purpose

A broad range of clinical diagnoses may result in central skull base abnormalities identified on imaging studies. Recognition of these abnormalities and providing a succinct, accurate differential diagnosis to ordering providers is a necessary skill for specialty trained neuroradiologists. This electronic exhibit reviews the imaging anatomy of the central skull base on cross sectional imaging and delineates the range of pathology seen in this location.

Materials and Methods

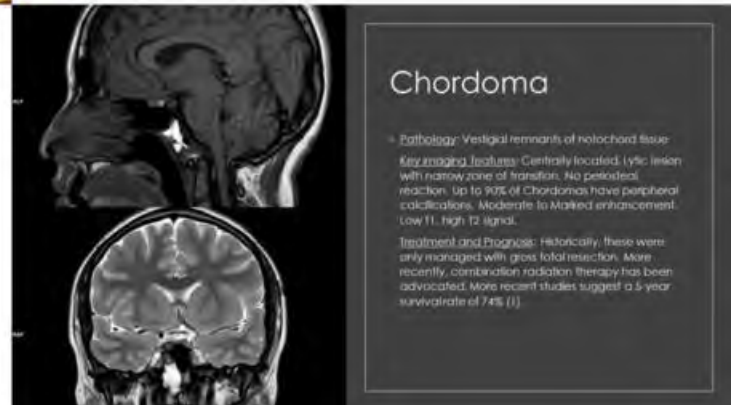
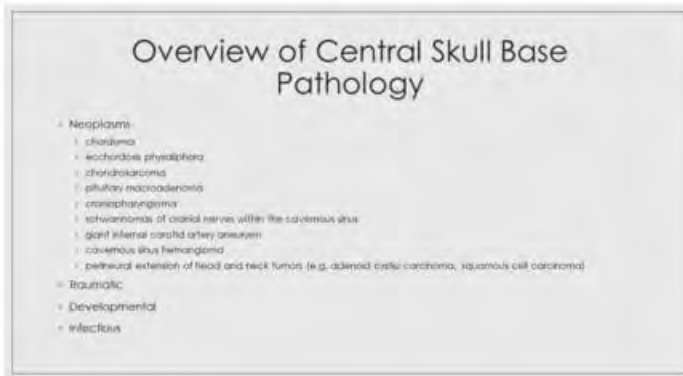
To provide a concise, pictorial guide of central skull base pathology for ordering providers and radiologists.

Results

We will use anonymized images obtained at our hospital with central skull base pathology. The accompanying descriptions, educational summaries, and figures will be obtained from well-referenced textbooks and scholarly articles on the subject.

Conclusions

The central skull base may be involved with a broad range of pathologic processes including congenital, metabolic, infectious, and neoplastic etiologies. Recognizing the normal anatomy and imaging appearance of the central skull base, in addition to possessing a basic familiarity with the various conditions found in this region can help radiologists provide a succinct and accurate differential diagnosis for clinicians to guide clinical management.



(Filename: TCT_1064_KeepingitBasicSkullBasePathology.jpg)

1238

Leptomeningeal and Pachymeningeal Diseases of the CNS

E Carrodeguas¹, S Cha²

¹University of California San Francisco, Redwood City, CA, ²University of California San Francisco, San Francisco, CA

Purpose

Educational objectives: 1. Recognize the difference in appearance of pachymeningeal and leptomeningeal enhancement 2. Understand the different pathophysiological mechanisms between pachymeningeal and leptomeningeal enhancement 3. Common differential considerations and distinguishing features in pachymeningeal enhancement 4. Common differential considerations and distinguishing features in leptomeningeal enhancement 5. Spectrum of CNS melanoma diseases and their characteristics
 Table of contents: I. Overview of the pachymeninges and of the leptomeninges A. Anatomy B. Pachymeningeal versus leptomeningeal enhancement 1. Mechanism 2. Characteristic imaging appearance II. Causes of pachymeningeal enhancement A. Infection 1. Tuberculosis/Fungal disease B. Neoplastic 1. Meningioma, Dural Lymphoma, Metastasis C. Intracranial Hypotension D. Inflammatory 1. Neurosarcoidosis 2. Granulomatosis with polyangiitis III. Causes of leptomeningeal enhancement A. Infection 1. Viral, fungal, bacterial B. Carcinomatosis 1. CNS Primaries 2. Metastatic Disease C. CNS melanocytosis/melanomatosis IV. Summary

Materials and Methods

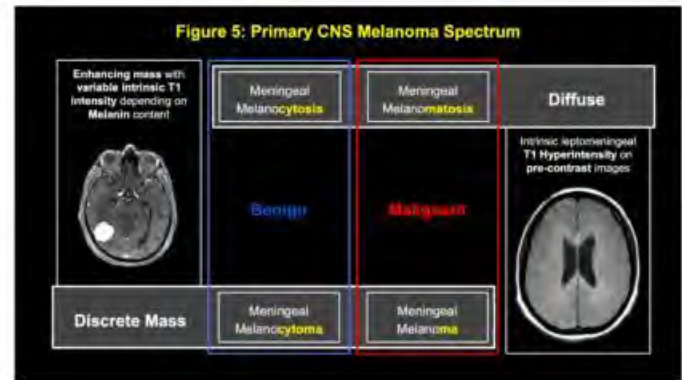
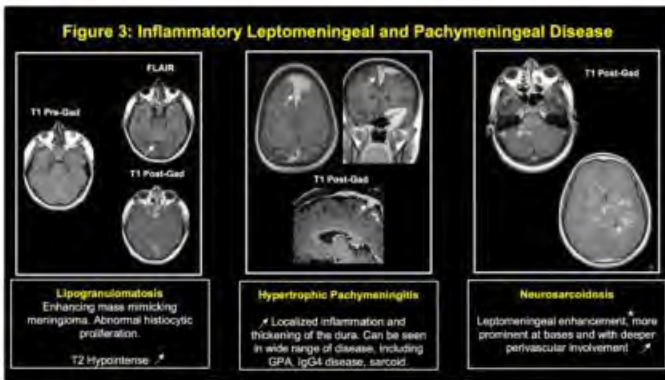
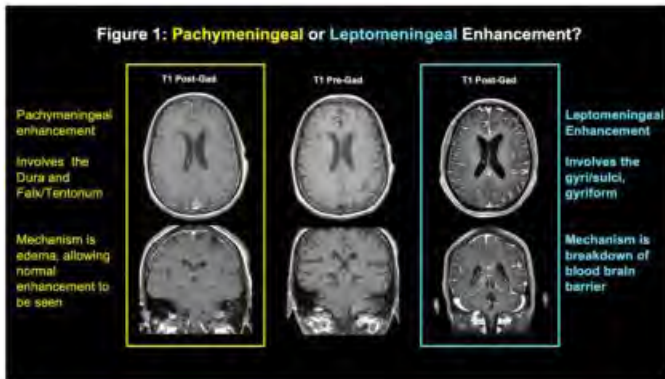
To deliver the aforementioned educational objectives (see below) in an impactful and clear way: Educational objectives: 1. Recognize the difference in appearance of pachymeningeal and leptomeningeal enhancement 2. Understand the different pathophysiological mechanisms between pachymeningeal and leptomeningeal enhancement 3. Common differential considerations and distinguishing features in pachymeningeal enhancement 4. Common differential considerations and distinguishing features in leptomeningeal enhancement 5. Spectrum of CNS melanoma diseases and their characteristics

Results

Not applicable

Conclusions

Not Applicable



(Filename: TCT_1238_ASNR.jpg)

1585

Lesion Localization in Neuro-Ophthalmology for Afferent Visual Pathways Disorders: Classic Ophthalmological Exam and Neuroimaging Correlates

R Patel¹, S Khanpara¹, A Kamali¹, R Samant¹

¹The University of Texas Health Science Center at Houston, Houston, TX

Purpose

A wide range of neurologic conditions can involve the afferent visual pathway. An understanding of common neurologic presentations of afferent visual pathway defects can help the radiologist in targeting their search pattern to specific area of interest that may otherwise go undetected. A good neuro-ophthalmological clinical evaluation followed by expert imaging evaluation by radiologist is crucial in determining lesion localization, appropriate diagnosis and its management. At the end of the exhibit, the viewer will become familiar with common clinical presentation, key Neuro-ophthalmological findings for Afferent Visual Pathway disorders and able to localize anatomical regions of interest for imaging.

Materials and Methods

1. To illustrate detailed anatomy and function of the afferent visual pathway. 2. To provide a clinically driven and image-rich interactive quiz featuring spectrum of pathologic conditions involving the afferent visual pathway.

Results

All cases related to afferent visual pathway defects will be presented with pertinent clinical history, detailed neuro-ophthalmology examination findings followed by quiz format Neuroimaging presentation with answers/discussion highlighting neuroanatomical region of interest and the relationship between the location of the lesion and the neuro-ophthalmology examination findings. A brief self-quiz at end will conclude the exhibit.

Conclusions

Neuro-ophthalmology is an interdisciplinary field which includes ophthalmology, neurology, and radiology to determine the visual implications of neurologic disorders. The afferent visual system consists of the retina, optic nerve, optic chiasm, optic tract, optic radiation, lateral geniculate nucleus and visual cortex. Imaging locations of disease are classified as pre-chiasmatic, chiasmatic, and post-chiasmatic. Clinical examination signs may reveal afferent pupillary defect, decreased visual acuity, and visual field deficits which help the neuro-ophthalmologist to localize anatomical regions of interest for imaging. Radiologist adds value not only by recognizing pathologic imaging features, but also by understanding the clinical examination findings that may result from what they observe, and likewise using findings from the clinical exam as a guide to accurately localize pathologic lesions.

1410

Lesions of the Greater Sphenoid Wing: Anatomy Review and Differential Diagnosis

T Kennedy¹, C Robson², D Shatzkes³, C GLASTONBURY⁴

¹The University of Wisconsin, Middleton, WI, ²Boston Children's Hospital, Weston, MA, ³Lenox Hill Hospital, New York, NY, ⁴N/A, N/A

Purpose

Summary: The greater wing of the sphenoid is an important component of the skull base and when involved by a meningioma, characteristic imaging findings include a sunburst pattern of osseous hyperostosis and surrounding plaque like enhancement that involves the lateral orbit, the dura of the middle cranial fossa and adjacent temporalis muscle. Not all masses within the greater sphenoid wing however are meningiomas. It is important to recognize that there is a differential diagnosis for lesions in this location which is dependent on the age of the patient and the specific imaging features on CT and MRI. This exhibit reviews the pearls and pitfalls of lesions occurring in this unique anatomic location. Objectives: 1) Review the anatomy of the greater sphenoid wing and adjacent structures 2) Review the differential diagnosis of lesions of the greater sphenoid wing including meningioma, primary bone/cartilaginous tumors, metastatic disease, myeloma, lymphoproliferative tumors, vascular malformations, fibro-osseous and developmental lesions. 3) CT, MR and Nuclear Medicine findings of these conditions will be discussed- highlighting overlapping and distinguishing imaging features.

Materials and Methods

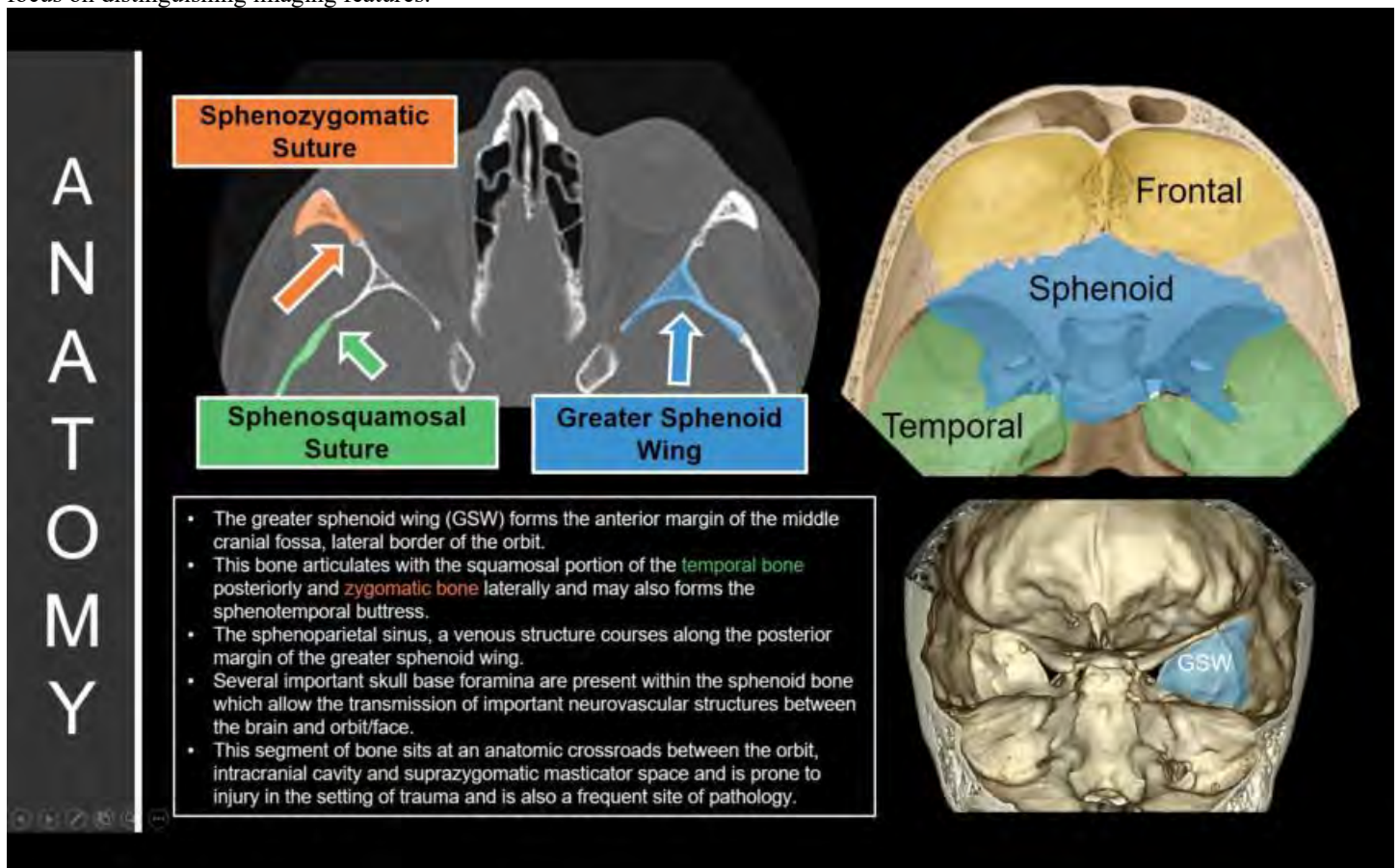
The purpose of this educational exhibit is to review the differential diagnosis of lesions that occur within the greater sphenoid wing.

Results

N/A

Conclusions

Meningiomas are common lesions to occur within the greater sphenoid wing and are known to cause hyperostosis of the adjacent skull reported to occur in up to 44% of cases. However when meningiomas occur within the greater sphenoid wing localized hyperostosis is seen in 90% of cases.¹ Based on histopathologic analysis, this characteristic feature within the GSW is felt to be related to tumor infiltration of the bone, which not typically seen elsewhere in the skull.¹ Other neoplastic and non-neoplastic lesions can mimic an intraosseous meningioma, particularly if they too result in hyperostosis. Primary bone/cartilaginous tumors, metastatic disease, myeloma, lymphoproliferative tumors, vascular malformations, fibro-osseous and developmental lesions will be discussed with a focus on distinguishing imaging features.



(Filename: TCT_1410_AnatomyGSW-ASNRsubmission.jpg)

Machine Learning and AI Applications in Stroke Detection: Review of Current and Upcoming Techniques

A Kadribegic¹, J Adhya¹, M Goldberg¹, C LI¹, L Eisenmenger², W CHANG¹

¹Allegheny Health Network, Pittsburgh, PA, ²University of Wisconsin - Madison, Middleton, WI

Purpose

In this presentation we will discuss types of applications using artificial intelligence (AI) in the evaluation of stroke, discuss currently available products, their approved indications, and effectiveness and discuss new and upcoming technologies applying AI/machine learning for the detection and evaluation of stroke. After viewing this presentation, the viewer will: 1) Learn about the currently available products using AI/machine learning for stroke evaluation. 2) Understand the basics of AI/machine learning in stroke detection and how the various product offerings work. 3) Discover upcoming/new innovations in AI/machine learning for stroke and their potential applications.

Materials and Methods

AI applications in radiology have blossomed with increases in computing power and improved algorithms in the last 2-3 years. Numerous applications focused on the detection of intracranial hemorrhage and acute ischemia on non-contrast head CT, helping prioritize potentially positive cases. Several MRI applications use diffusion weighted imaging to help determine NIHSS and prognostic factors such as mRS. Following the breakthrough trials DEFUSE-3 and DAWN, AI-assisted radiology applications such as RAPID CTP emerged to facilitate detection of perfusion abnormalities and triage stroke patients. In recent years, automated relative vessel density applications including RAPID CTA were developed to help in stroke detection and identification of LVO. In this presentation, we will discuss the different AI applications currently available for use in stroke, including automated vessel density detection (RAPID-CTA, RAPID-LVO, Viz LVO), automated ASPECTS scoring software for NCCT (e-aspects, RAPID ASPECTS), automated detection of hemorrhagic stroke and other hemorrhage (RAPID ICH, Aidoc Head, AI-CT, JBS-04K, AccipioDx, qER, etc), and MRI triaging software (RAPID MRI, JBS-01-2K).

Results

We conducted a literature search of relevant studies in the area of AI in stroke detection and evaluation, analyzed recent lectures from RSNA 2019 and ASNR 2020 on AI applications in stroke, and outlined our own clinical experience with AI applications in stroke detection and evaluation.

Conclusions

AI and machine learning can help triage important studies for timely interpretations and improve clinical efficiency and accuracy for radiologists. Many new applications are under development that have great potential for improving patient outcomes by prioritizing potentially positive cases and providing prognostic information.

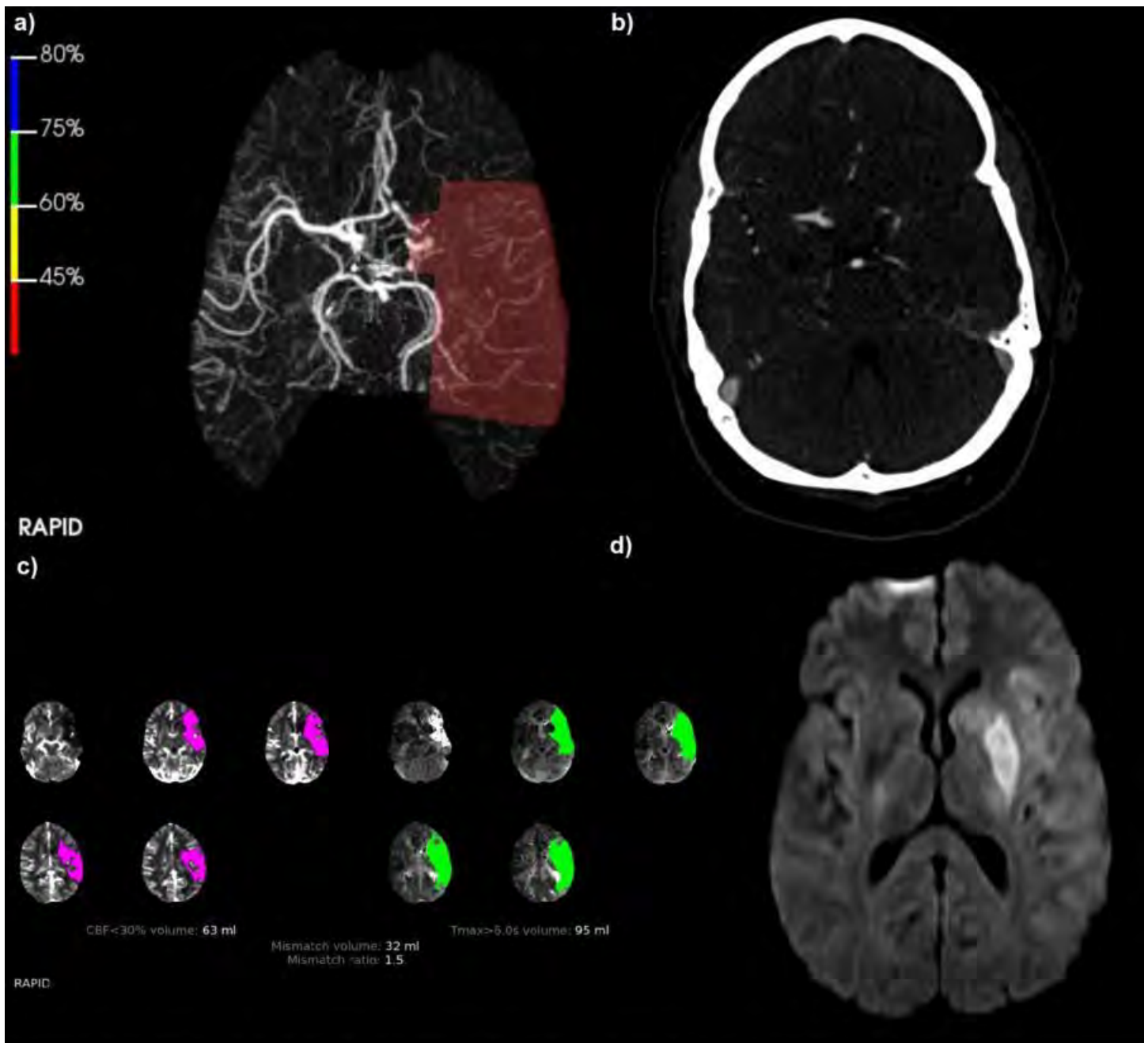


Figure 1: a) Rapid CTA output showing decreased vessel density in a Left ICA/MCA distribution. b) CTA showing occlusion of the left ICA terminus. c) Rapid CT perfusion output showing decreased cerebral blood flow and delayed perfusion in the left MCA territory. d) MRI after thrombectomy showing infarct in the left putamen.

(Filename: TCT_220_ai.jpg)

1593

Magnetic Resonance Imaging and Diffusion Tensor Imaging Anatomy of Cerebellum and Brain-stem: An Imaging Case Based Review

R Patel¹, S Khanpara¹, A Acin¹, Y Cai¹, R Samant¹

¹The University of Texas Health Science Center at Houston, Houston, TX

Purpose

Having detailed gross anatomical and Diffusion Tensor Imaging (DTI) knowledge is a key to accurately localize and interpret disorders affecting the brainstem and cerebellum. The DTI is a useful tool to better understand various developmental and acquired brainstem and cerebellar disorders. This exhibit will help the radiologist to understand the imaging anatomy of brainstem and cerebellum with DTI correlation and thereby encourage them to utilize DTI as a tool in their daily clinical practice.

Materials and Methods

1. To describe technique, physics, highlight the clinical applications of DTI. 2. To review detailed anatomy of the brainstem and cerebellum on high resolution MRI. 3. To review detailed DTI anatomy of the brainstem and cerebellum.

Results

All studies performed using Phillips Ingenia 3T machine, generating multiplanar high resolution T1 and T2-weighted images. High resolution diffusion tensor MRI was performed and color-coded vector maps were generated. The DTI MRI data were prepared and analyzed by anatomically-guided tractography methods using Dynasuite software to reconstruct the posterior fossa white matter tracts.

Conclusions

The brainstem consists of 3 parts anatomically, namely midbrain, pons, medulla. The cerebellum consists of three lobes anatomically, namely the occulo-nodular lobe, the anterior lobe and the posterior lobe with the anterior and posterior lobes further divided in a midline cerebellar vermis and right and left cerebellar hemispheres. The cerebellar vermis is divided into 9 lobules, namely lingula, central lobule, culmen, declive, folium, tuber, pyramid, uvula, nodulus. Cerebellar white matter (WM) connections to the central nervous system are classified functionally into the Spinocerebellar (SC), vestibulocerebellar (VC), and cerebrocerebellar subdivisions. The SC pathways project from spinal cord to cerebellum, whereas the VC pathways project from vestibular organs of the inner ear to cerebellum. Cerebrocerebellar connections are composed of feed forward and feedback connections between cerebrum and cerebellum including the cortico-pontocerebellar (CPC) pathways being of cortical origin and the dentate-rubro-thalamo-cortical (DRTC) pathway being of cerebellar origin. There is a huge clinical implications of knowing these tracts and applying these knowledge during imaging interpretations of congenital posterior fossa malformation, genetic disorders, neurosurgery planning, neurodegenerative diseases etc.

1207

Magnetic Resonance Imaging Applications for Post-Treatment Surveillance of Head and Neck Cancer

C Zuchowski¹, J Kemme¹, A Aiken¹, K BAUGNON¹, X Wu¹

¹Emory University School of Medicine, Atlanta, GA

Purpose

This presentation reviews the current uses of MRI in surveillance of post-treated head and neck (H&N) cancer. Overview of expected post-treatment changes and common locations of recurrence for H&N cancer subtypes most amenable for MRI surveillance. Review the MRI protocols in post-treatment H&N cancer surveillance.

Materials and Methods

H&N cancers recur at a rate of <10 to 50% in the first 2 to 3 years after treatment depending on the primary site and stage, and imaging plays an important role in the early detection of recurrence. Multiple imaging modalities, including CT, PET, and MRI, are used in H&N cancer surveillance imaging. Although there are several guidelines for post-treatment H&N cancer imaging, there is no unanimous consensus for optimal surveillance imaging modality or interval. Additionally, expected treatment-induced changes can be difficult to distinguish treatment complications from residual or recurrent tumor. With the new and improving imaging technologies, it is challenging for the treatment teams to request the most appropriate study for imaging surveillance. Therefore, a review of the H&N subtypes most suitable to post-treatment follow-up by MRI is needed to ensure that the correct study and protocol is obtained.

Additionally, understanding of the treatment strategies is necessary in order to evaluate the post-treatment changes and differentiate possible complications from true recurrence.

Results

A literature review of the current application of MRI in H&N cancer surveillance based on anatomic subsites will be conducted. An IRB approved, HIPAA compliant retrospective review of MR images for H&N cancer surveillance at our institution will be conducted to gather illustrative cases.

Conclusions

In the post-treatment period, the H&N cancer subtypes surveilled by MRI are sinonasal, salivary gland, nasopharyngeal, orbital, and skull base tumors at risk for perineural, orbital, or intracranial tumor spread. MRI offers superior soft tissue contrast for evaluation of the orbit, skull base, intracranial compartment, pterygopalatine fossa, and masticator space. Oropharyngeal, oral cavity, laryngeal, and hypopharyngeal cancers are not typically surveilled by MRI in part due to the presence of symptoms prompting earlier presentation to clinicians and lower likelihood of intracranial involvement. Radiologist familiarity with characteristic tumoral imaging features, treatment strategies, and typical posttreatment changes is critical for accurate early detection of recurrent disease.

1149

Magnetic Resonance Imaging Based Imaging Genomics of Nuclear DNA related Neuro-mitochondrial Disorders

S SENTHILVELAN¹, S Sekar², B Thomas³, C Kesavadas⁴

¹Sree Chitra Tirunal Institute For Medical Sciences and Technology, TRIVANDRUM, Kerala, ²SCTIMST, Trivandrum, Trivandrum, Kerala, ³Sree Chitra Tirunal Institute of Medical Sciences & Technology, Trivandrum, Kerala, ⁴Sree Chitra Tirunal Institute for Medical Sciences & Technology, Trivandrum, Kerala

Purpose

Nuclear mitochondrial disorders are a subgroup of mitochondrial disorders, common in children and follow Mendelian inheritance. They constitute 1)Respiratory chain disorders (complex I-V deficiencies), 2)Disorders affecting respiratory chain assembly, 3)POLG related disorders affecting the mitochondrial DNA maintenance The objectives of this exhibit are 1)to understand the complex genetics of these disorders, 2)to elaborate on the wide clinical features, 3)to identify the unique imaging features by MRI, thereby assist in targeted exome sequencing, which eventually provide an accurate diagnosis.

Materials and Methods

Review of genetics of various nuclear neuro-mitochondrial disorders and their clinical presentation. Imaging based algorithmic approach in understanding their genetics and thereby, provide pertinent differential diagnosis. Pictorial essay of imaging appearances of these disorders.

Results

Nuclear mitochondrial disorders are a distinct subgroup in children which often require genetic diagnosis. This retrospective review of genetic proven nuclear DNA related disorders are categorized using MRI imaging appearances with an algorithmic approach to arrive at a diagnosis or pertinent differential diagnosis. MRI were done using both 1.5T MRI (Seimens Magnetom, Germany) and 3T MRI (GE Discovery, USA).

Conclusions

The unique imaging features of these disorders include cortical, thalamic and posterior brainstem involvement in POLG related disorders; cavitory leukoencephalopathy are seen commonly with respiratory chain deficiencies; noncavitory leukoencephalopathis are associated with MNGIE, Optic atrophy plus syndromes (OPA-1) and aminoacyl t-RNA synthetase deficiencies; anterior brainstem involvement is seen with SURF-1 mutation. Thus, it is important to understand specific MRI patterns and to look for certain key areas in identifying these disorders and to suggest a targeted genomic sequencing.

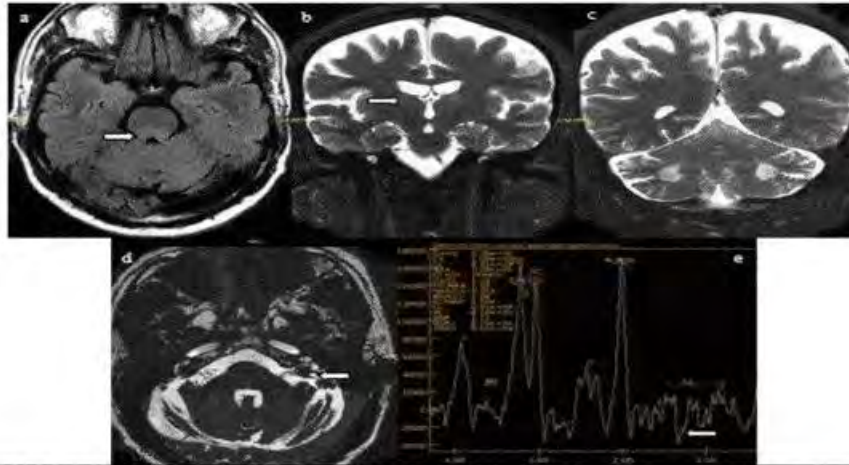


Fig.1 MRI in POLG mutation (MIRAS syndrome): Images depict thalamic, posterior brainstem, cerebellar involvement with prominent lactate in MRS.

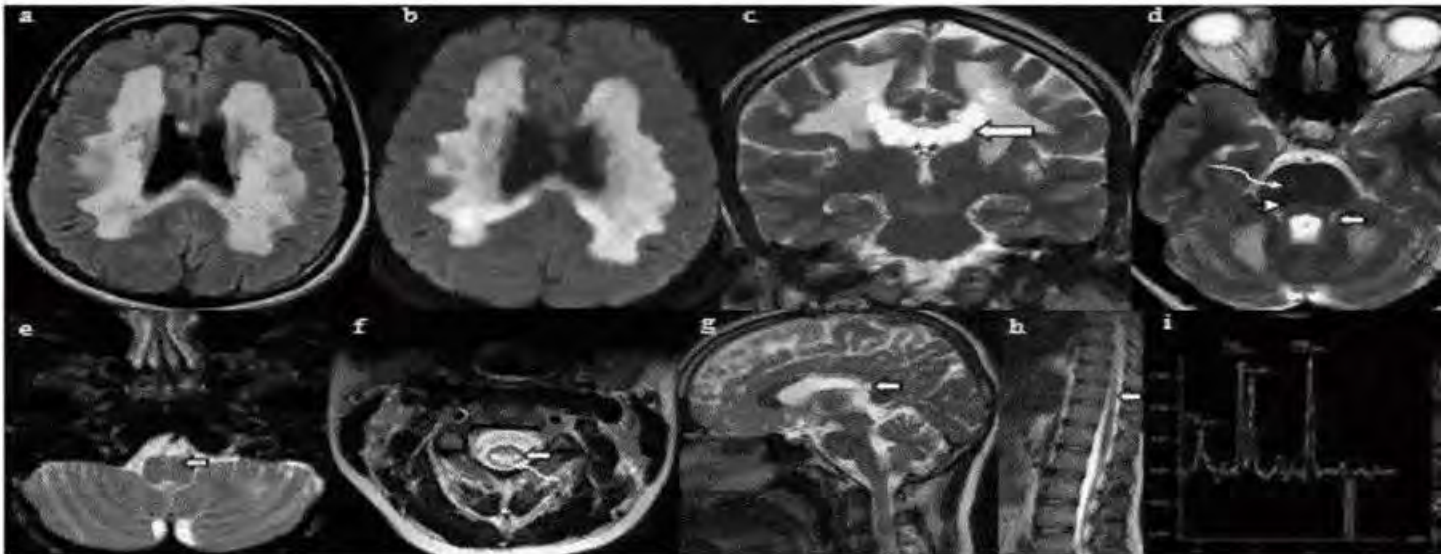


Fig.2 MRI in LBSL (DARS mutation): Images depict noncavitary leukoencephalopathy, corticospinal tract involvement (squiggly arrows in 'd'), lateral spinothalamic and posterior column tract involvement (arrows in 'f'), prominent lactate in MRS.

(Filename: TCT_1149_asnrimages.gif)

1521

Maple Syrup Disease: The First Weeks of Life Are the Most Important!

L Ávila Lessa Garcia¹, A Martins Maia Junior², C da Silva³, C Alves⁴, D Fragoso⁵, T SCOPPETTA⁶, T Freddi⁷, A Vossough⁸, F D'Arco⁹

¹HCFMUSP, São Paulo, SP, ²Irmandade da Santa Casa de Misericórdia de São Paulo, São Paulo, São Paulo, ³HCFMUSP - BRAZIL, São Paulo, São Paulo, ⁴Children's Hospital of Philadelphia, Philadelphia, PA, ⁵N/A, N/A, ⁶SANTA CASA DE MISERICÓRDIA DE SAO PAULO, SÃO PAULO, SAO PAULO, ⁷Hospital do Coração, São Paulo, São Paulo, ⁸CHOP-UPENN, Philadelphia, PA, ⁹Great Ormond Street Hospital for Children, London, London

Purpose

Review the imaging features of maple syrup disease (MSUD), correlating with the different pathogenic variants (mutations), the main clinical symptoms, and laboratory results observed in this disorder. The presentation will be divided into an introduction, literature review, materials and methods, cases/discussion, and conclusion.

Materials and Methods

Our purpose is to demonstrate, through clinical cases, the different imaging presentations of MSUD affecting the central nervous system (CNS). We aim to emphasize structural and metabolic changes based on imaging studies, correlating these findings with laboratory results, outcome, and different pathogenic variants. After this presentation, the reader will be able to identify the overall clinical and imaging features of MSUD, including recognizing the common and uncommon presentations of the disease.

Results

In the first step, the authors conducted an extensive search of the medical literature in English using the MSUD descriptor. All included articles (number) contained a description of neuroimaging studies. In a second step, the authors searched in their digital archives from 2005 to 2019 all the confirmed cases of MSUD and collected detailed data from the laboratory results, neuroimaging, and genetics of these patients.

Conclusions

A total of 25 patients were included. The main points observed able to increase the accuracy of the diagnosis were 1) Demographics, and main clinical symptoms, 2) Distribution of the lesions in the CNS, including corticospinal tracts, optic nerves, thalamus, posterior aspect of the brainstem, and spinal cord, and 3) imaging features depicted in the DWI sequence including the intra-myelinic edema, and the MR-spectroscopy showing branched-chain amino acids in 0.009 ppm, which is a potential molecular biomarker of this disease.

314

Mapping the Trajectories of the Major Afferent and Efferent Pathways of the Hypothalamic Nuclei in the Human Limbic System.

A Aein¹, S Mirbagheri², R Samant³, R Patel⁴, R Riascos⁴, A Kamali⁵

¹University of Texas Health Science Center at Houston, Houston, TX, ²Johns Hopkins University, Baltimore, MD, ³UT Health, McGovern School of Medicine, Texas Medical Center, Houston, TX, ⁴The University of Texas Health Science Center at Houston, Houston, TX, ⁵University of Texas Health Science Center Houston, Houston, TX

Purpose

The mammillary bodies and other hypothalamic nuclei have complicated connectivity with other limbic and non limbic structures such as the amygdala, hippocampus and thalamus. The hypothalamic nuclei and their connectivity play important role in emotion, learning, behavior and memory. The purpose of the current study is to demonstrate for the pictorial essay of the major limbic pathways originating from or ending in the hypothalamic nuclei along with their connectivity using high spatial resolution diffusion weighted imaging data.

Materials and Methods

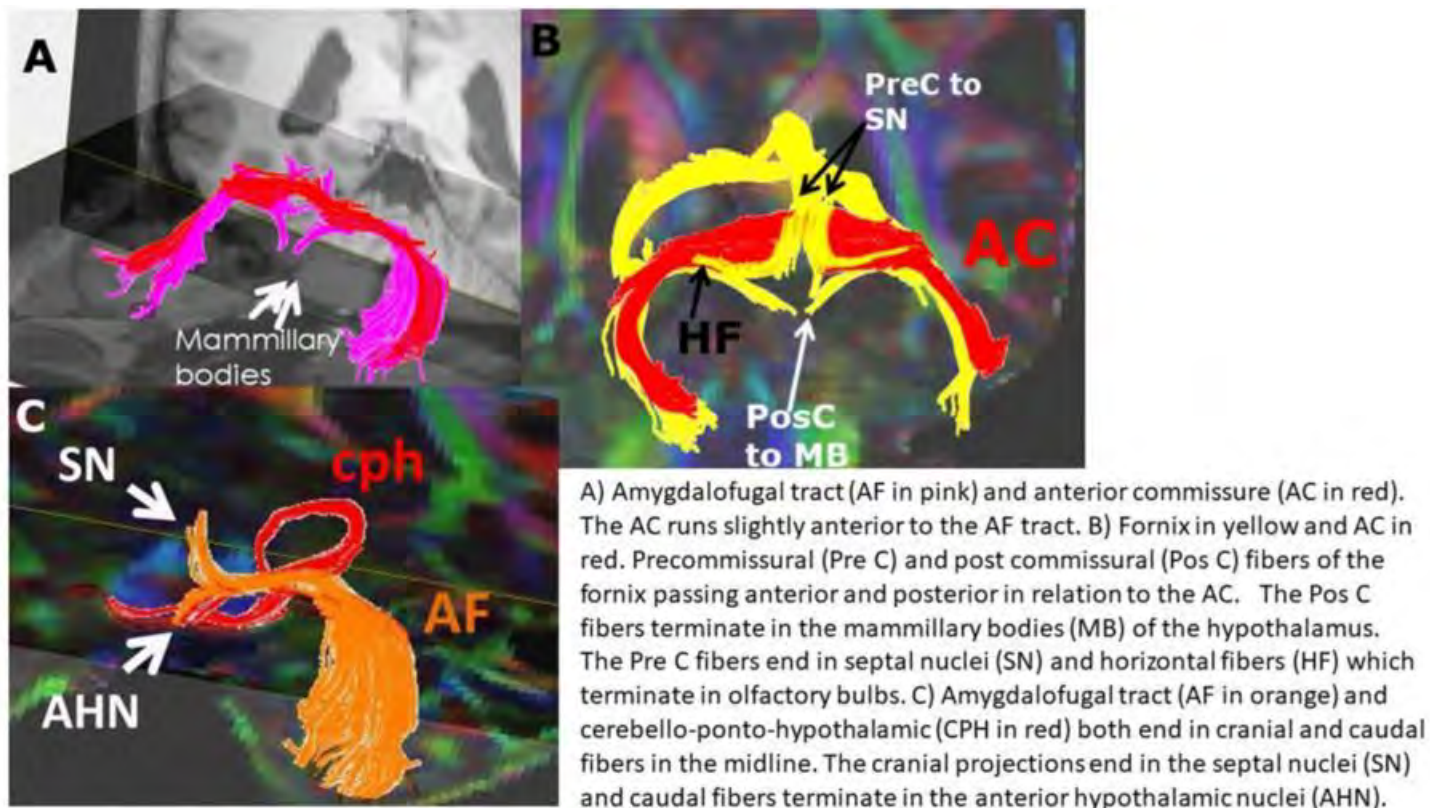
In recent years we have traced multiple limbic pathways originating from or terminating into the hypothalamic nuclei using high spatial resolution diffusion weighted tractography technique. These pathways include: the fornix, stria terminalis, amygdalofugal tract, dorsal thalamo-hypothalamic tract, mammillothalamic tract, parieto-occipito-hypothalamic tract and cerebello-hypothalamic tract. This is a short account of major hypothalamic pathways along with their connectivity in the human limbic system. The knowledge of the anatomy of these pathways is very important to understand the complicated circuits of the human limbic system which may be affected in many neurologic and psychiatric diseases.

Results

Fifteen healthy men (age range 24-37 years) were studied and written informed consent was obtained from all subjects. Conventional and DT-MRI Acquisition: Data were acquired using a Philips 3.0 T Intera system using a SENSE receive head coil. Diffusion-weighted image (DWI) data were acquired axially using single-shot multi-slice 2-D spin-echo diffusion with the balanced Icosa21 tensor encoding scheme. The b-factor = 500 sec mm⁻², TR/TE = 14460/60 msec, FOV = 256 mm x 256 mm and slice thickness / gap / #slices = 1 mm / 0 mm / 120. The EPI phase encoding used a SENSE k-space under sampling factor of two, with an effective k-space matrix of 112x112 and an image matrix after zero-filling of 256x256. Fiber Tracking: We used the FACT algorithm (DTIStudio) to reconstruct limbic structure fiber tracts with a fractional anisotropy (FA) threshold of 0.22 and angle threshold of 60 degrees.

Conclusions

We are presenting the pictorial essay of the major hypothalamic pathways anatomy in the human limbic system alongside with their connectivity. These pathways include: the fornix, stria terminalis, amygdalofugal tract, dorsal thalamo-hypothalamic tract, mammillothalamic tract, parieto-occipito-hypothalamic tract and cerebello-hypothalamic tract.



(Filename: TCT_314_Figure1.jpg)

1320

Masses, Mimics and Malignancy in the Skull Base: What the Surgeon Needs to Know.

A Stuckey¹, M McDonald²

¹UC San Diego Health System, San Diego Veterans Administration Medical Center, La Jolla, CA, ²N/A, N/A

Purpose

See Purpose section.

Materials and Methods

The past two decades have witnessed marked advancement in the management of skull base lesions due to parallel improvements in both imaging and surgical technique. Given that clinical assessment of the skull base is limited, imaging plays a critical role in the management of virtually all skull base lesions (1). Since many pathologies have overlapping imaging appearances, the most critical role of the radiologist lies in the accurate delineation of tumor margins and their relationship to critical neurovascular structures as guide for biopsy and radiation planning. In the course of this educational exhibit we will review the anatomy of the skull base with an emphasis on surgically relevant landmarks including: -variations of the floor of the anterior cranial fossa, sphenoid sinus and optic chiasm -anatomy of the sellar/parasellar region, with emphasis on the cavernous sinuses and cranial nerves -variant anatomy of the lateral and posterior skull base structures, including pneumatization of the petrous apices, skull base foramina and major neurovascular structures

Results

A retrospective review of our institution's imaging database will be performed to identify pathology-proven skull base neoplasms highlighting important patterns of disease spread. Index cases will include: -involvement of the periorbita/intraorbital compartment from sinonasal neoplasms -invasion of the cavernous sinus by sellar lesions such as macroadenomas and craniopharyngiomas - intracranial extension from anterior and central skull base lesions, including esthesioneuroblastoma -cerebellopontine angle neoplasms with emphasis on the decision points between translabyrinthine, middle cranial fossa and retrosigmoid approaches -posterior skull base neoplasms with discussion of combined posterior/transoral approach A review quiz will be supplied at the end of the exhibit to consolidate learning.

Conclusions

Limited clinical accessibility and complex regional anatomy ensures the vital role of radiology in the initial staging, work up and management of skull base lesions. After reviewing the present exhibit, the radiologist will be familiar with common intrinsic and extrinsic skull base pathologies as well as the key anatomic landmarks and patterns of local disease spread critical to management

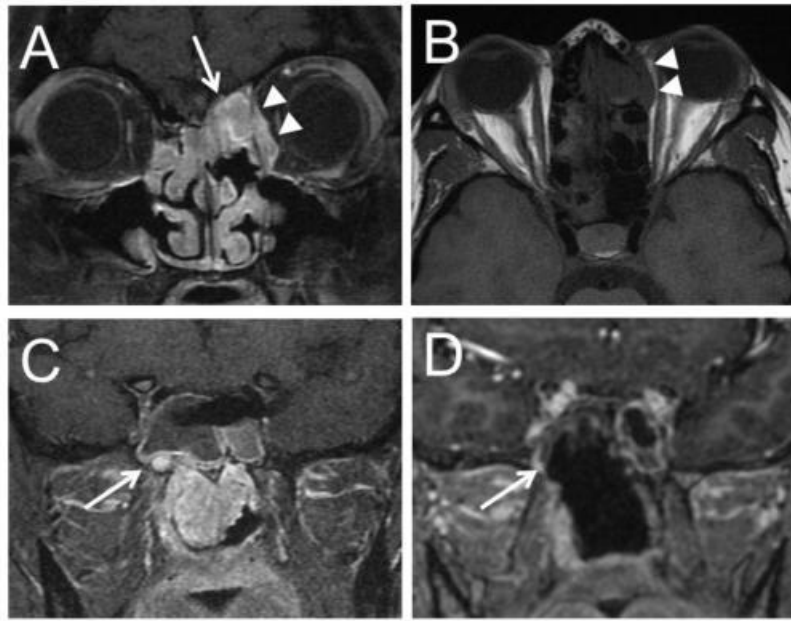


Figure 1. Extrinsic involvement of the skull base in pathology-proven sinonasal immature teratoma, including: invasion of the cribriform plate (A, arrow), left medial periorbita and extraconal fat (A and B, arrowheads) and left vidian nerve (C, arrow). After detailed radiographic analysis, the patient was treated with expanded endoscopic resection including combined left maxillectomy and left medial orbitotomy as well as unroofing of the left vidian canal for tumor debulking (D, arrow).

(Filename: TCT_1320_ASNRSkullBaseFig1.jpg)

1268

Medium Vessel Occlusions – the Next Frontier in Endovascular Treatment for Acute Ischemic Stroke

P Cimflova¹, M Kappelhof², N Singh¹, J Ospel³, N Kashani⁴, B Menon¹, M Almekhlafi¹, M GOYAL⁵

¹University of Calgary, Calgary, Alberta, ²Amsterdam UMC, University of Amsterdam, Amsterdam, Noord-Holland, ³University Hospital Basel, Basel, Basel, ⁴Foothills Medical Centre, University of Calgary, Calgary, Alberta, ⁵University of Calgary, CALGARY, ALBERTA

Purpose

Summary: Introduction, relevance, and natural history of medium vessel occlusions (MeVOs). Description of clinical and imaging findings (occlusions in the M2/M3, A2/A3, or P2/P3 branches of the middle, anterior, and posterior cerebral arteries, respectively). Overview of current treatment options for MeVOs and their results. Objectives: • Natural history of MeVOs is often poor. With the development of new and smaller endovascular devices, they are potential targets for endovascular treatment (EVT). • MeVOs have variable clinical presentation based on the location of the occlusion. • Knowledge of the vascular territory related to specific MeVOs is crucial for evaluation of the risks and benefits of EVT in patients with MeVOs and for a valid baseline image assessment.

Materials and Methods

• Why should we care about MeVOs? Introduction, MeVOs natural history, evolution of EVT in acute ischemic stroke and increasing relevance for MeVOs • Primary versus secondary MeVOs Primary MeVO – occurring "de novo" as first intracranial occlusion causing acute stroke symptoms, identified on baseline imaging Secondary MeVO – arise from large vessel occlusion when thrombus migrates, either before or during EVT; could be spontaneous or iatrogenic Conceptual and practical differences between primary and secondary MeVOs • Clinical presentation of MeVOs based on their location. (Each example with image) M2 anterior/superior and beyond - Contralateral arm and leg weakness, hemisensory loss, facial palsy, hemineglect (non-dominant hemisphere) or expressive aphasia (dominant hemisphere) - M2 posterior/inferior and beyond - Contralateral homonymous hemianopia or superior quadrantanopia, constructional apraxia (non-dominant hemisphere) or receptive aphasia (dominant hemisphere) - A2/A3 occlusions - Contralateral leg paresis, apathy, disinhibition, executive dysfunction - P2/P3 occlusions - Contralateral homonymous hemianopia, behaviour alteration (agitation, anger, paranoia), memory deficit • Challenges to identify MeVOs on baseline imaging Benefits of advanced imaging (delayed filling on multiphase CTA, colour-coded multiphase CTA, perfusion lesion on CTP or PWI) • Current EVT options and latest treatment perspectives Current state of EVT for acute ischemic stroke Technique overview – stent-retriever, contact aspiration, combined techniques Developments and progress in techniques for more distal occlusions Conscious sedation versus general anesthesia in MeVOs

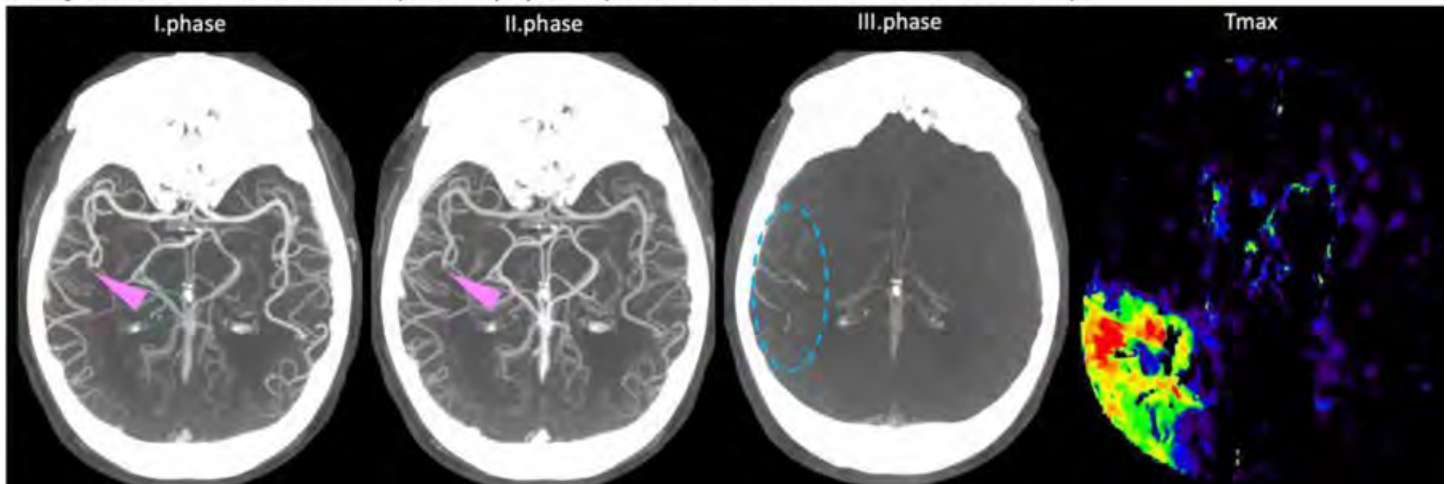
Results

NA

Conclusions

NA

Figure 1. Multiphase CTA with right MeVO (medium vessel occlusion) - M2/M3 MCA (pink arrowheads), delayed washout in the third phase (III) and perfusion lesion on Tmax CTP map.



(Filename: TCT_1268_ScreenShot2020-11-09at134957.jpg)

849

Meet the Outliers: Common and Uncommon Posterior Circulation Strokes & their Mimics

H Rajebi¹, G Fahimi²

¹Massachusetts General Hospital, Boston, MA, ²SUNY Upstate Medical University, Syracuse, NY

Purpose

Given the insubstantial role of non-contrast-enhanced CT and differences in clinical symptomatology, MRI and angiography play a pivotal role in early and accurate diagnosis of PC strokes. Although less frequent, thorough knowledge of PC infarcts in daily practice seems warranted for every neuroradiologist.

Materials and Methods

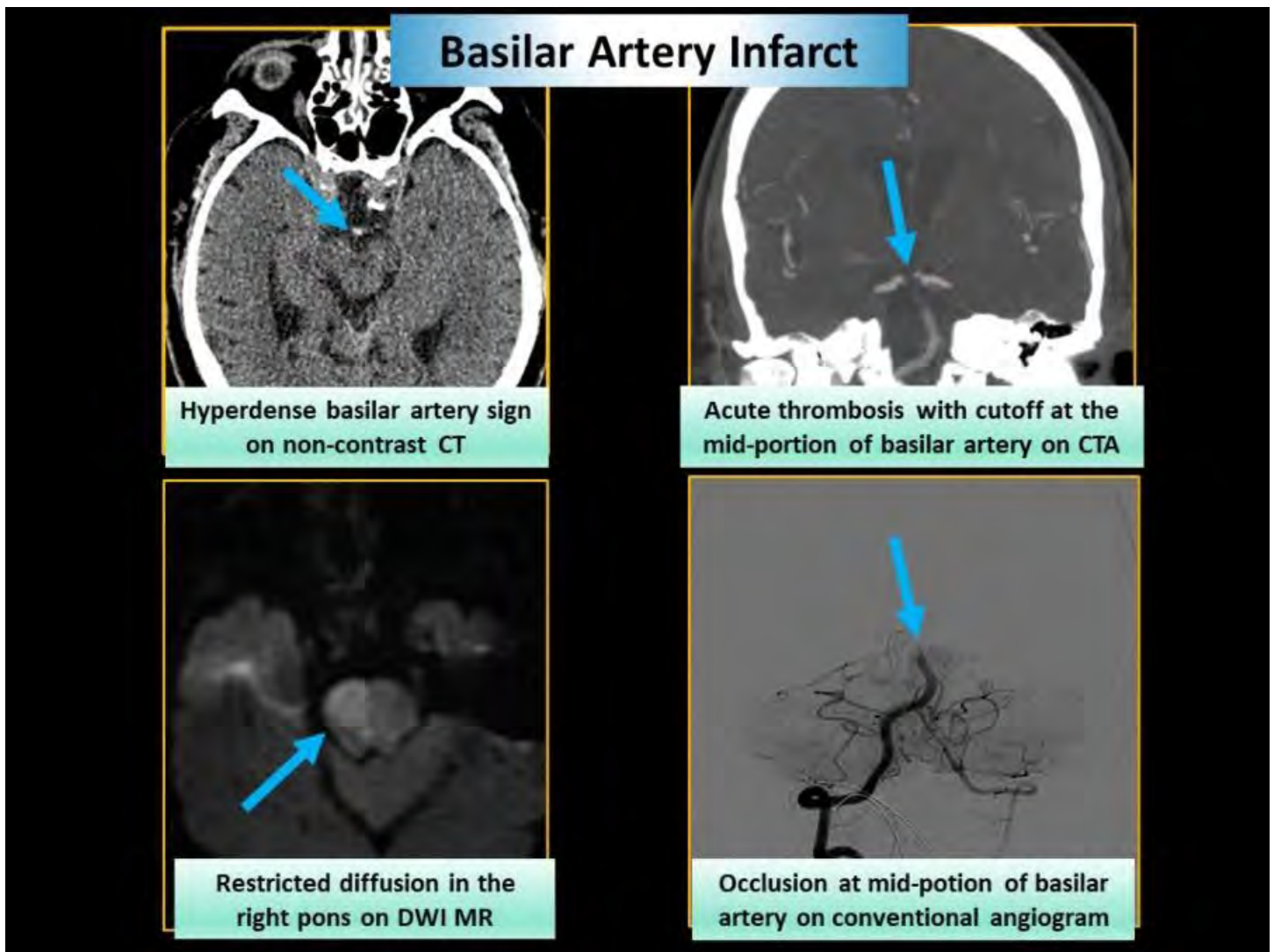
Posterior circulation (PC) stroke corresponds to any infarction eventuating within the vertebrobasilar vascular territory, which includes the cerebellum, midbrain, pons, medulla, thalami, and areas of temporal and occipital lobes. Although less common than anterior circulation infarcts, the precise diagnosis is challenging and more commonly delayed due to the limited sensitivity of the CT and screening neurologic examination. In this exhibit, we aim to review, discuss, and compare characteristic imaging findings and clinical symptomatology of the common and uncommon PC strokes.

Results

After a brief review of relevant PC anatomy and normal variants, a comprehensive institutional case-based review of the posterior circulation territory infarcts will be presented. Non-contrast CT head limitations with diagnostic hints and pitfalls will be illustrated in each case. CT angiogram, conventional angiogram, and MR images will also be demonstrated. Ultimately, a comprehensive classification of PC stroked based on clinical symptoms and detailed vascular territory will be presented. The mimics commonly misdiagnosed and their distinct radio-clinical features will also be discussed.

Conclusions

Cases of posterior cerebral, vertebral, basilar, superior cerebellar, anterior inferior cerebellar, posterior inferior cerebellar and anterior spinal arteries, and artery of Percheron territory infarcts will be discussed in detail. CT and MR images, and characteristic radiologic features for each entity will be described. CTA, MRA, and conventional angiography images will also be shown in relevant cases. Clinical symptoms, underlying predisposing conditions and signs of each infarct territory will be briefly reviewed.



(Filename: TCT_849_Slide1.JPG)

193

Memory fMRI for Pre-surgical Planning in Pediatric Epilepsy Patients: Where Are We and Where Are We going?

C Epps¹, B Huang¹, J Voyvodic²

¹University of North Carolina, Chapel Hill, NC, ²Duke University, Durham, NC

Purpose

This presentation aims to outline the current status and future direction of memory fMRI in planning temporal lobectomy in the pediatric epileptic population. After completing the presentation, the viewer should: 1. Understand the potential clinical uses of memory fMRI prior to temporal lobectomy. 2. Understand key differences in epilepsy effects on memory functional connectivity in children compared to adults. 3. Be aware of current literature concerning the use of memory fMRI pre-surgery to predict memory outcomes in the pediatric population and barriers to research 4. Understand differences between memory paradigms based on recognition versus recall. 5. Be familiar with a clinically feasible and practical recall-based functional memory paradigm.

Materials and Methods

Surgical intervention for temporal lobe epilepsy in children increases risk of long-term verbal learning and memory deficits highlighting the need for tailored resections. Memory fMRI is uniquely positioned to help limit post-surgical deficits by identifying language and memory organization patterns prior to surgery. Memory connectivity in children is relatively unexplored compared to adults. Early onset seizures interfere with normal circuit specialization and can result in unique patterns of memory connectivity distinctly different from those found in adults. fMRI has demonstrated efficacy in using language mapping to guide surgical intervention and predict functional outcomes. Stand-alone memory fMRI studies are rare. Pediatric studies have focused on language lateralization as proxy for memory re-organization as it is theorized that language and memory re-organization co-occur. However, some studies demonstrate that children do not consistently demonstrate language and memory co-lateralization raising the call for suitable memory fMRI paradigms. Many current memory fMRI paradigms use recognition-based paradigms. However, recognition

likely requires less encoding than recall. Therefore, consistent hippocampal activation is more likely with recall-based memory fMRI. Buck et al. have recently provided an example of a practical, recall-based memory fMRI paradigm. However, a substantial need remains for research in the use of recall-based memory fMRI paradigms in predicting post-surgical outcomes in pediatric epilepsy patients.

Results

N/A

Conclusions

Overall, this exhibit will review the current status and future direction of memory fMRI in planning temporal lobectomy in the pediatric epileptic population.

528

Meningioma or mimic: Look Twice and Save a Life

P Reddy¹, M Mian², S Viswamitra², S Vattoth³, R Ramakrishnaiah⁴, R Van Hemert⁵, M Kumar²

¹University of Arkansas for Medical Sciences, Little rock, AR, ²University of Arkansas for Medical Sciences, Little Rock, AR, ³University of Arkansas for Medical Sciences, LITTLE ROCK, AR, ⁴Univ of Arkansas for Medical Sciences, Little Rock, AR, ⁵UAMS, Little Rock, AR

Purpose

The objectives of this presentation are to 1. Describe the typical and atypical imaging features of meningiomas. 2. Discuss imaging features that should alert the radiologist that the lesion may not be a meningioma. 3. Discuss the imaging features of various diseases that mimic meningiomas. 4. Discuss the role of advanced imaging techniques such as MR perfusion, spectroscopy and elastography. Summary of the presentation is as follows 1. Introduction - Demographic information, anatomy of the dura and arachnoid granulations, discussion of type of capillaries in meningiomas 2. WHO classification of meningiomas 3. Discussion of imaging features of meningiomas a. Calcification b. Hemorrhage c. Metaplastic features d. Perilesional edema e. Cystic change f. En plaque meningioma g. Signal intensity on T2 weighted images h. Diffusion weighted imaging features 4. Histological subtypes of meningiomas. 5. Discussion of lesions mimicking meningiomas and differentiating features a. Lymphoma b. Metastasis c. Cavernoma d. Glioma e. Gangliocytoma f. Hemangiopericytoma/Solitary fibrous tumor g. EBV associated smooth muscle tumour. h. Rosai Dorfman disease i. Melanocytic neoplasms j. Tuberculoma k. Pituitary adenoma l. Schwannoma m. Plasma cell granuloma and IgG4 related disease n. Sarcoidosis 5. Meningiomas in unusual locations a. Optic nerve sheath meningioma b. Intraventricular meningioma c. Pineal region meningioma d. Jugular foramen meningioma e. Metastatic meningioma 6. MR perfusion, MR spectroscopy for differentiating meningiomas from other tumors. 7. Conclusion.

Materials and Methods

Meningiomas are the most common primary brain tumour and are commonly encountered in clinical practice. This may lead the radiologist to not consider other differential diagnosis when dealing with this condition. The purpose of this educational exhibit is to discuss the imaging appearance of meningiomas and conditions that mimic them. The emphasis will be on imaging features that help differentiate meningiomas from other dural based lesions. The utility of MR perfusion and spectroscopy for the same will also be discussed.

Results

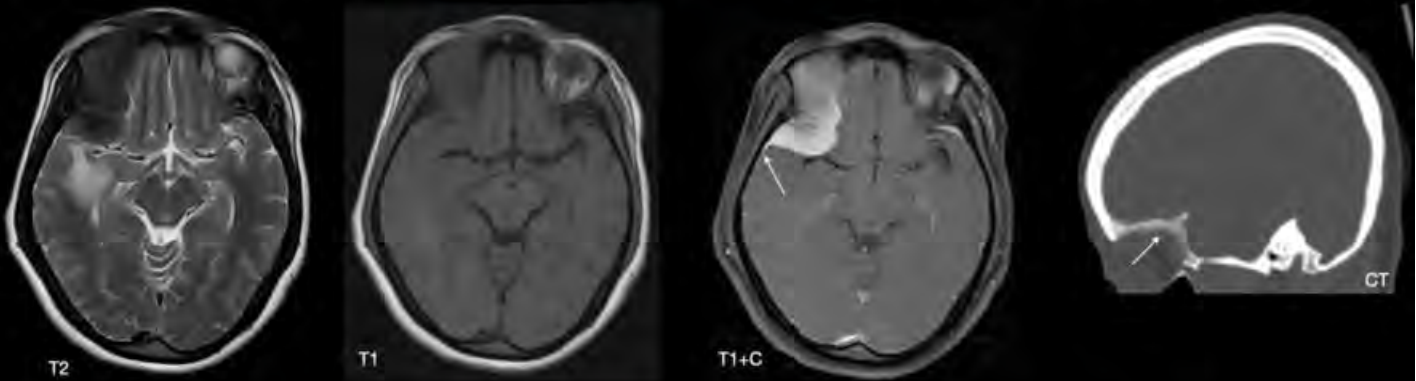
Review of the institute database was performed using a keyword search. Cases with interesting findings and cases which posed a diagnostic challenge were selected for the purpose of this review.

Conclusions

N/A

MENINGIOMA OR MIMIC?

This is a 39 year old lady who presented with history of progressive protrusion of right eye since 1½ years.



Dural based mass along the right orbital roof and temporal convexity with marked hypointensity on T2WI and homogeneous contrast enhancement. A dural tail (arrow) is seen. Marked hypointensity of the lesion on T2WI raises that suspicion that the lesion is not a meningioma. Sagittal CT reformat shows thickening and sclerosis of the underlying bone (arrow).

Diagnosis: Chronic fungal granuloma

(Filename: TCT_528_Asnrmeningioma002.jpg)

1455

Metagenomics and Neuroimage in the Etiological Diagnosis of CNS Infections: Finding a Needle in a Haystack

L Bezerra¹, L Coelho², R BERTANHA³, A Barbosa³, F Hirata³, L Godoy⁴

¹Hospital Israelita Albert Einstein, São Paulo, SP, ²Hospital Israelita Albert Einstein, São Paulo, IL, ³Hospital Israelita Albert Einstein, SAO PAULO, NY, ⁴Faculdade de Medicina da Universidade de São Paulo- FMUSP, Sao Paulo, Sao Paulo

Purpose

Subacute and chronic neuroinflammatory syndromes, including encephalitis and meningitis, may be a challenging diagnosis, given the wide range of potential infectious, autoimmune, neoplastic, paraneoplastic, parameningeal and toxic etiologies. Diagnosis rate for patients with encephalitis has remained poor, despite advances in pathogen-specific testing, such as PCR and antigen assays. Unlike traditional testing for a specific microbe or category of infection, metagenomic next-generation sequencing (mNGS) of cerebrospinal fluid (CSF) or brain tissue screens for all potential CNS pathogens, and can identify pathogens that were not part of the initial differential diagnosis, either because of the rarity of the infection, because the microorganism has not been previously associated with a clinical phenotype or because it is a newly discovered organism. This educational exhibit discusses the technical advantages and pitfalls of mNGS in the clinical scenario of patients with challenging diagnosis of subacute and chronic neuroinflammatory syndromes presenting with atypical imaging findings.

Materials and Methods

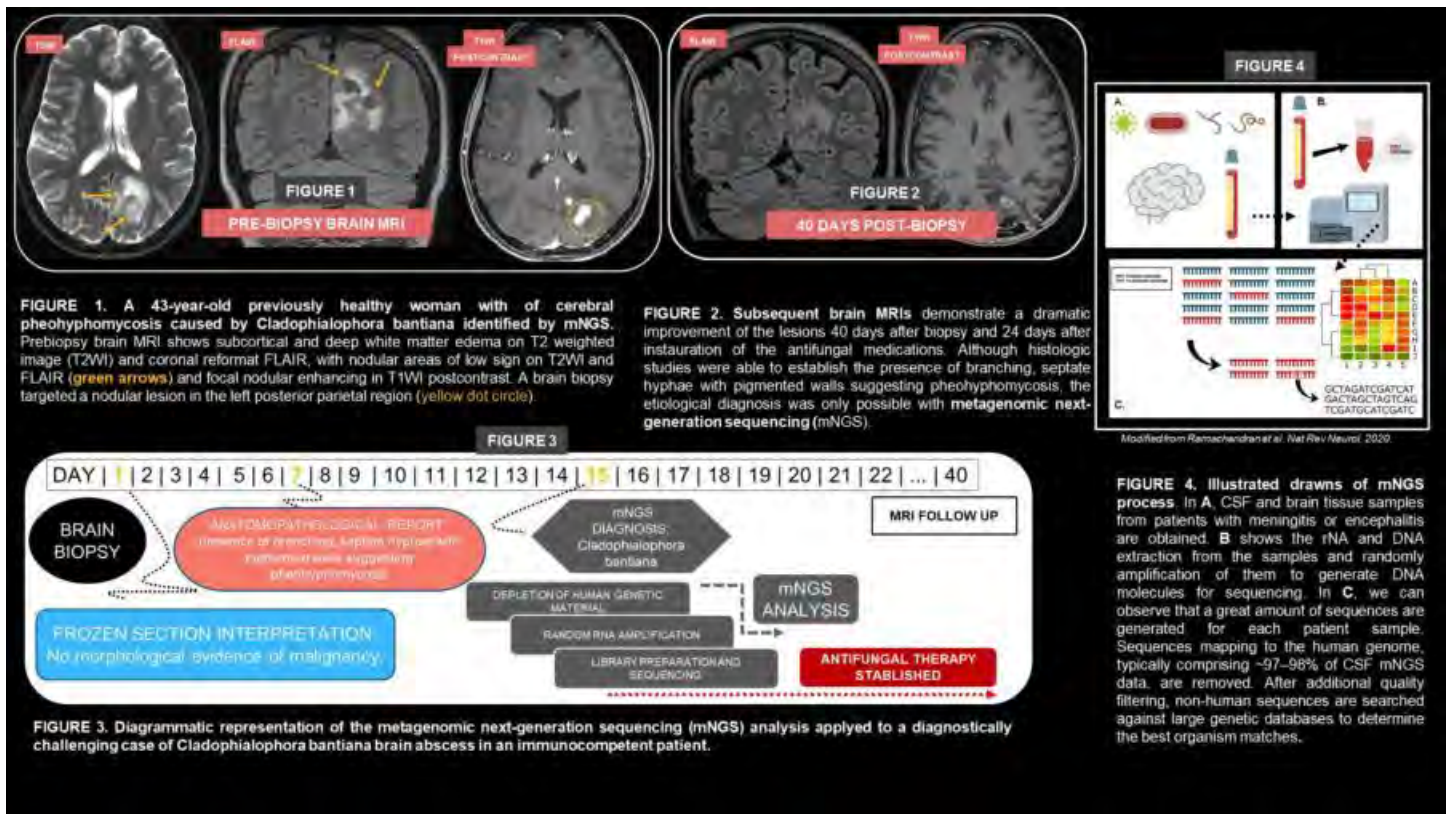
To review the use of metagenomic next-generation sequencing (mNGS) of CSF or brain tissue for the diagnosis of suspected infectious encephalitis. To present a case series of patients with challenging diagnosis of subacute and chronic meningitis in whom mNGS identified a pathogen or was crucial to rule out infection, illustrated by MR images.

Results

Case series of patients with challenging diagnosis of subacute or chronic meningitis / encephalitis, with neurologic problems indicating possible infection, but for whom conventional clinical and microbiologic studies yielded negative or inconclusive results. We performed mNGS on total RNA extracted from CSF or brain tissue in this patients, highlighting two cases in which mNGS identified a pathogen, including a case of cerebral pheohyphomycosis caused by *Cladophialophora bantiana* in an immunocompetent patient and a rare case of CNS vasculitis caused by *Brucella melitensis*. We also present an atypical case of autoimmune encephalitis in which mNGS ruled out infection.

Conclusions

Metagenomic NGS of CSF or brain tissue are powerful tools that offer the opportunity for dramatic improvements in our ability to detect (or rule out) a wide range of CNS pathogens, with potential benefits in timing and sensitivity. In this study, metagenomic obtained from patients with meningitis or encephalitis improved diagnosis and provided useful information in some cases.



(Filename: TCT_1455_MetagenomicJPEG.jpg)

1540

MOG Antibody Disease: Reviewing the imaging findings and differential diagnosis

A Alves Fonseca¹, R Pincerato², I Padilha³

¹Santa Casa de São Paulo / DASA / United Health Group, São Paulo, São Paulo, ²HOSPITAL SAMARITANO SP - UHG BRASIL, São Paulo, SP, ³Irmandade da Santa Casa de Misericórdia de São Paulo, São Paulo, São Paulo

Purpose

Myelin oligodendrocyte protein (MOG) antibody disease is an inflammatory demyelinating condition of the CNS characterized by a monophasic or relapsing course of neurological dysfunction. Clinical presentation includes optic neuritis (ON), myelitis, acute disseminated encephalomyelitis (ADEM) or ADEM-like presentation (such as brainstem attack).

Materials and Methods

The purpose of this review is to describe the imaging findings and differential diagnoses of MOG antibody disease.

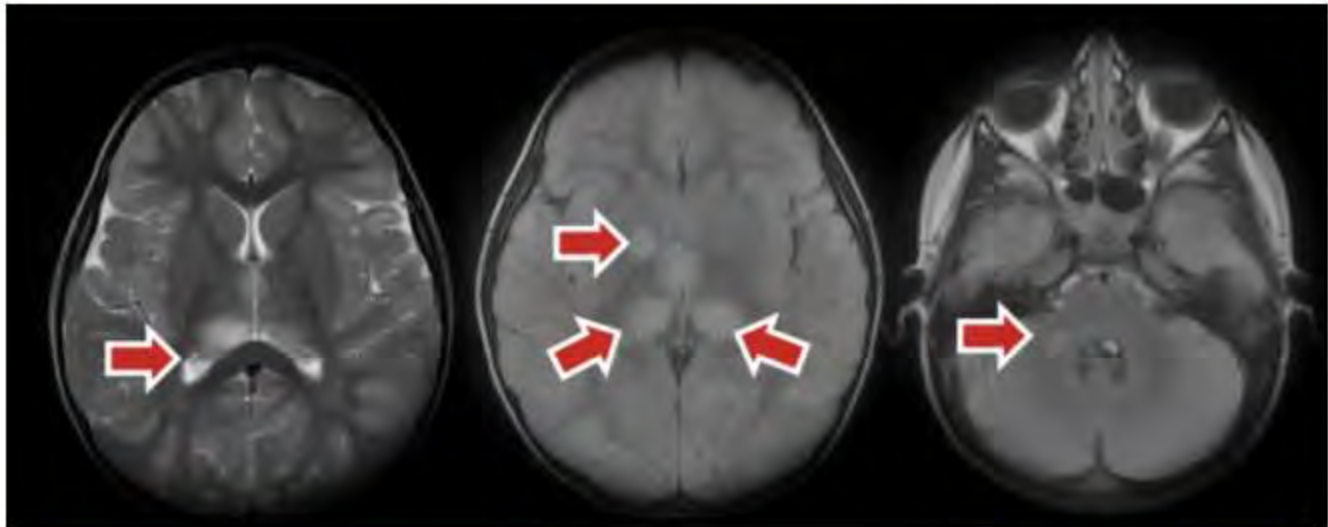
Results

After reviewing our institution teaching files, we selected cases demonstrating MOG antibody disease, the main imaging findings and differential diagnoses. We discuss the overlapping and differentiating features with other demyelinating diseases such as ADEM and NMOSD.

Conclusions

MOG antibody testing could be recommended by the radiologists in patients presenting with monophasic or relapsing acute optic neuritis, myelitis, brainstem encephalitis, encephalitis with radiological imaging findings of CNS demyelination. The suggestive radiological findings include: longitudinally extensive spinal cord lesions on MRI, conus medullaris lesions, longitudinally extensive optic nerve lesions, brain parenchymal lesions not suggestive of MS. Many cases of MOG encephalitis were likely to be previously diagnosed as ADEM or recurrent ADEM. MOG antibody positivity was thought to be a form of seronegative NMOSD but lately is shown that it is a distinct entity than NMO and is categorized as a separate demyelinating disease. In addition to distinct immunological target, MOG antibody disease is different from related autoimmune CNS diseases in its clinical course, radiological presentation and treatment responsiveness. The differential diagnosis of demyelinating disorders, mainly ADEM, MOG and NMOSD, requires an understanding of involvement patterns and its main pitfalls in order to prevent misinterpretation.

Brain Lesions in MOG



THALAMIC AND BASAL GANGLIA LESIONS

ADEM-LIKE

"FLUFFY LESION"

(Filename: TCT_1540_ASNR-Mog.jpg)

1219

MR Imaging of Benign and Malignant Lesions in the Oral Cavity

J Chi¹, M Hagiwara¹

¹NYU Langone Health, New York, NY

Purpose

Evaluation of lesions in the oral cavity can be challenging because of its complex anatomy in a confined space and apposition of mucosal surfaces. Magnetic resonance imaging is the imaging modality of choice to evaluate the complex anatomy of the oral cavity. An overview of MR imaging findings of common benign lesions in the oral cavity including congenital, vascular and inflammatory/infectious lesions will be reviewed. In addition, MR imaging findings of common benign and malignant oral cavity tumors will be presented. Objectives: ·Review the imaging anatomy of the oral cavity ·Review MR imaging characteristics of common benign lesions of the oral cavity ·Review MR imaging characteristics of benign and malignant oral cavity tumors

Materials and Methods

N/A

Results

N/A

Conclusions

N/A

1286

MR Imaging of Mitochondrial Encephalopathy, Lactic Acidosis, Stroke-like Episodes (MELAS) and other Mitochondrial Cytopathies with CNS Involvement

A Galstyan¹, S Wietstock², Y LI³

¹UCSF-School of Medicine, San Francisco, CA, ²UCSF Benioff Children's Hospital Oakland, San Francisco, CA, ³UCSF, San Francisco, CA

Purpose

N/A

Materials and Methods

The purpose of our educational exhibit is to illustrate the clinical manifestations of MELAS and other mitochondrial cytopathies, the distinguishing neuroimaging findings in these disorders, and the role imaging plays in the overall diagnosis and management of these patients.

Results

Mitochondrial cytopathies are a heterogeneous group of genetic disorders that occur as a result of pathogenic variants in nuclear or mitochondrial DNA, leading to a decrease in oxidative phosphorylation and cellular energy production. MELAS is the most commonly described mitochondrial cytopathy with CNS involvement. In this educational exhibit, we will discuss the following points: 1. The molecular genetic classification and pathogenesis of mitochondrial disorders. We will introduce mitochondrial cytopathies by discussing pathogenic mutations in mitochondrial DNA, as well as nuclear DNA that code mitochondrial subunits. We will discuss the generation of cellular ATP by oxidative phosphorylation, and how mitochondrial diseases disrupt this process. 2. The clinical presentation of mitochondrial disorders, focusing on MELAS. Mitochondrial diseases can manifest with single organ or multisystemic involvement. Using MELAS as a case example, we will focus on clinical features suggestive of mitochondrial disease. 3. The characteristic magnetic resonance imaging (MRI) features of mitochondrial disorders. MRI plays a key role in the diagnosis of mitochondrial disease, and we will describe key imaging features, as well as progression of these features over time, that are suggestive of the diagnosis. We will focus on MELAS and describe the distribution and symmetry of lesions in MELAS, using case examples. In addition, we will describe the MRI features of other less common mitochondrial cytopathies. 4. The important role of imaging in monitoring and management in patients with MELAS and other mitochondrial cytopathies. We will discuss the clinical management of these patients, the role of MRI in surveillance and detection of new stroke-like episodes.

Conclusions

MELAS and other mitochondrial cytopathies are rare but complex genetic disorders with multisystemic manifestations, commonly involving the CNS. Neuroimaging plays a key role in the diagnosis and workup in patients with suggestive presentations. In this educational exhibit, we review the imaging features, clinical presentation, and underlying pathophysiology of this group of disorders to facilitate recognition of these difficult-to-make diagnoses.

Introduction to Mitochondrial Cytopathies

Mitochondria '*power house*' of the cell
Most important generators of cellular ATP by oxidative phosphorylation
Includes ETC complexes I-IV and the ATP synthase complex V

Primary mitochondrial disorders (PMDs)

- Inherited disorders of energy metabolism due to mutations in mitochondrial DNA or nuclear DNA
- Results in *mitochondrial oxidative phosphorylation impairment*

Clinical presentation:

- Single-organ involvement (e.g., the eye)
- OR multi-systemic disease ****most common****

Classification:

- Mitochondrial DNA
 - 37 genes – all are essential to mitochondrial function
 - Genetic defects can be inherited or sporadic
 - Unique: *mutation distribution across tissues (heteroplasmy)*
↑ Mutation load → ↑ clinical symptoms
- Nuclear DNA
- Both

Most commonly affects:

1. CNS
Typically involve more than one CNS area → complex neurological signs and symptoms
Mimicking more common conditions (e.g., MS, stroke, or hereditary cerebellar ataxias)
2. Musculoskeletal system
Both have a *high energy demand* and as a result *increased mitochondrial density*

Alves, César Augusto Pinheiro Ferreira, et al. "Neuroimaging of mitochondrial cytopathies." *Topics in Magnetic Resonance Imaging* 27.4 (2018): 219-240.

(Filename: TCT_1286_EducationalExhibit.jpg)

1377

MR Imaging Spectrum of MOG Antibody Disease: Unravelling the Mystery of Demyelination

S Bhuta¹, A Prabhu², S Broadley²

¹Gold Coast University Hospital, Gold Coast, Australia, ²Gold Coast University Hospital, Gold Coast, QLD

Purpose

Myelin Oligodendrocyte Glycoprotein antibody disease (MOG- AD) is a newly described entity with similarities to MS and NMOSD.

MOG-AD presents as retrobulbar optic neuritis, extending into peri-optic nerve sheath and partially into orbital fat, longitudinally extensive transverse myelitis. These imaging features can alert a clinician to perform appropriate antibody tests.

Materials and Methods

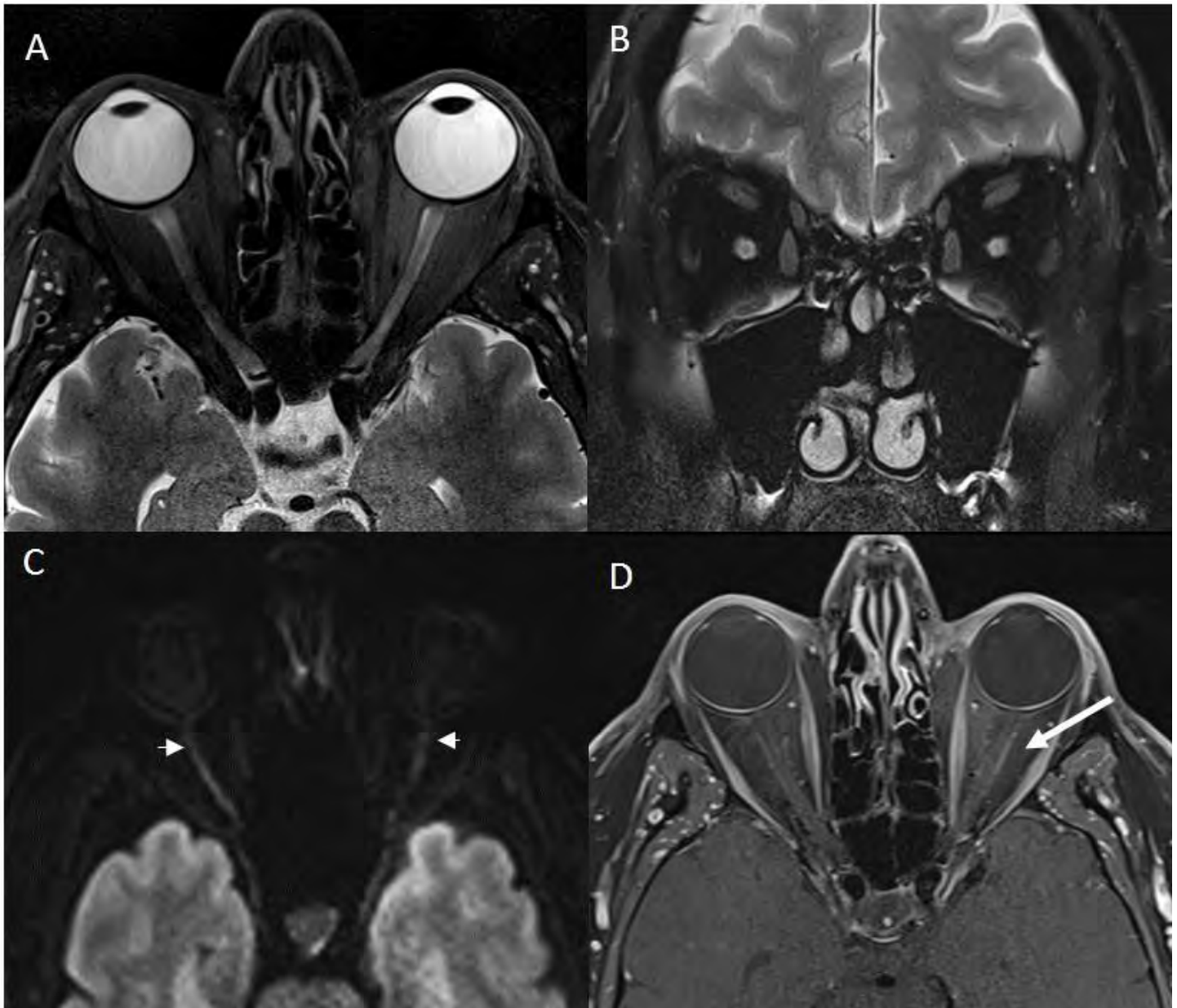
Myelin Oligodendrocyte Glycoprotein antibody disease (MOG-AD) is a newly described entity that shares features with Multiple Sclerosis (MS), Neuromyelitis Optica (NMOSD) clinically and radiologically. Purpose of this exhibit is to highlight typical imaging findings of MOG disease of the CNS and how MRI can play a critical role in establishing accurate diagnosis.

Results

The most common presenting feature is optic neuritis (ON) followed by myelitis. Relapsing pattern of ON is also seen. 3T MRI with dedicated imaging of the orbit is required apart from brain and spine imaging. T2 FS axial and coronal imaging of optic nerves along with Diffusion Weighted Imaging (DWI) is important. MR perfusion and Spectroscopy can be used in problem solving cases. T2 Sag or STIR imaging of spine is relevant to assess long segment cord lesions involving the conus. These findings can alert a neurologist to test for MOG-IgG.

Conclusions

We discuss unique imaging pattern of MOG-AD in terms of anatomical location, laterality, signal changes and temporal progression. MOG-AD often presents as bilateral retrobulbar optic neuritis, extending into peri-optic nerve sheath, retrobulbar fat and longitudinally extensive transverse myelitis. It predominantly involves the anterior segments of the optic nerve, the intra-orbital segments, while chiasm and retro-chiasmatic pathways are generally spared which are typically involved in NMOSD. Restricted diffusion can be seen in the optic nerves on DWI along with papilledema. Retrobulbar fat stranding and optic nerve or nerve sheath enhancement is a crucial finding usually not seen in MS or NMOSD (Fig.1). MS presents with periventricular, infratentorial lesions, discrete lesions in spinal cord. MOG-AD has key imaging features such as bilateral extensive oedematous and inflammatory anterior optic neuritis or longitudinally extending myelitis with a predilection to the conus. Knowledge of these imaging features will aid the neuroradiologist to direct the clinician to favour one antibody testing over the other in a timely fashion especially in certain regions of the world where resources are limited.



(Filename: TCT_1377_MOGAD.jpg)

495

MRI of Craniospinal Bone Marrow Disorders--Sifting Through the T1 Darkness: An Educational Review

K Seifert¹, M Shahrzad¹, A Trinh¹, H Dahmouh², M Wintermark³, S Hashmi⁴, T Massoud¹

¹Stanford University School of Medicine, Stanford, CA, ²Stanford University, Stanford, CA, ³Stanford, Stanford, CA, ⁴N/A, N/A

Purpose

Normal bone marrow (BM) is red (cellular) or yellow (fatty). MRI patterns of BM vary with ratios of red and yellow BM, age, pathologies, and therapies. Interpretation of craniospinal BM can be challenging because of low specificity when focal or diffuse hypointense T1 signal is seen. Without clinical information, the differential diagnosis is long and includes many benign and malignant BM disorders. Additional pulse sequences also aid in deciding between physiological and pathological BM.

Materials and Methods

We comprehensively review MRI findings in a wide spectrum of axial skeleton BM disorders, and categorize these by etiology.

Results

We illustrate BM appearances when using different FSE and advanced MRI sequences. Normal yellow (hyperintense T1) and red (slightly T1 hyperintense) BM display higher signal intensity than muscle and intervertebral disc, whereas pathological BM is relatively hypointense. Physiological red to yellow marrow conversion in vertebral bodies occurs into late adulthood in four variable Ricci patterns (I-IV). BM changes include: (1) Reconversion from yellow to red BM, or red BM hyperplasia, occurs with increased

hematopoiesis, e.g. chronic anemias, respiratory diseases, after chemotherapy, heavy smoking, long-distance running, obesity, and at high altitudes. This is usually diffuse, except when focal nodular hyperplasia is rarely encountered. (2) Infiltration, when hematopoietic cells multiply excessively in benign (primary amyloidosis and mastocytosis) or malignant (multiple myeloma and leukemia) diseases. (3) Replacement, when BM implantation by non-native benign or malignant cells leads to inflammatory (osteomyelitis) or neoplastic (metastases and lymphoma) disorders. (4) Depletion, after total replacement of normal red BM with yellow BM, occurring after viral infections, drugs, chemotherapy, and radiotherapy. (5) Ischemia after microvascular occlusion, chemotherapy, and steroids. (6) Edema is non-specific and observed in trauma, infection, inflammatory diseases, ischemia, near neoplasia, or secondary to systemic diseases. (7) Storage diseases result in BM cellular necrosis and fibrous proliferation, mainly in Gaucher's disease and iron storage pathologies (thalassemia, post-transfusion, and hemochromatosis).

Conclusions

Accurate MRI differentiation of normal or pathologic disorders of the BM is important clinically. This presentation will aid in neuroimaging interpretation of focal, multifocal, and diffuse craniospinal BM disorders to improve patient management.

511

MRI of the Temporomandibular Joints: Case Review and Systematic Approach

L Tu¹, J Aslam², M Adin³, A Malhotra⁴, A Abou Karam⁵, I Ikuta⁶

¹Yale School Of Medicine, New Haven, CT, ²Yale University School of Medicine, Staten Island, NY, ³Yale University, New Haven, CT, ⁴Yale University School of Medicine, New Canaan, CT, ⁵Yale Medicine, New Haven, CT, ⁶Yale University School of Medicine, New Haven, CT

Purpose

We provide a practical approach to MRI of the temporomandibular joints (MRI TMJ): * Review indications for MRI TMJ * Review common and uncommon TMJ pathologies * Suggest a systematic approach to the MRI TMJ

Materials and Methods

MRI of the temporomandibular joints (MRI TMJ) is an uncommonly performed exam. The purpose of this work is to review indications, pathologies, and a systematic approach for this infrequent study.

Results

The radiology report database at a large academic institution was queried for all MRI of the temporomandibular joints via CPT code for the period 11/1/2015 – 11/1/2020. All reports were reviewed and categorized according to pathology. A representative selection of common and uncommon pathologies is presented via illustrative review. These are described in the context of a brief literature review. A systematic approach is described.

Conclusions

Within our institution, only 179 MRI TMJ exams have been performed in the last 5 years (11/1/2015 – 11/1/2020). This represents less than 0.07% (179/265,930) of all MRI exams. Of all MRI TMJ exams, 110 were found to have pathology of the temporomandibular joints, most commonly osteoarthritic degeneration. 60 exams described disc subluxation and other motion abnormalities. 15 exams described other, uncommon pathologies. These include inflammatory and infectious arthritis, neoplasia, and developmental anomalies. Representative cases/images of the common and most "interesting" pathologies are provided in the full presentation. A systematic approach is suggested, based on expected and incidental pathologies. Steps of study quality assurance, anatomic search pattern, disc motion/internal derangement assessment, and a brief checklist for associated/incidental findings are presented. Familiarity with MRI of the temporomandibular joints (MRI TMJ) requires dedicated review of cases and the existing literature given the low frequency of request in many practices. This exhibit provides an updated review of the relevant pathology and a practical approach.

400

MRI Perfusion Techniques: Beyond Dynamic Susceptibility Contrast

K Capel¹, M Jen¹, W CHANG², A Kuner¹, A Samsonov¹, J Holmes¹, K Johnson¹, L Eisenmenger¹

¹University of Wisconsin, Madison, WI, ²Allegheny Health Network, Pittsburgh, PA

Purpose

- Review general approach for MR perfusion
- Define DCE, DSC, BOLD, and ASL perfusion
- Discuss clinical applications, advantages, and pitfalls of each technique
- Explore challenges of non-contrast techniques (BOLD and ASL) with in-vivo applications
- Highlight differences between selective slab, slice-based, and motion based ASL techniques

Materials and Methods

Tissue perfusion acts as an important physiological marker for many neurological diseases including stroke, neurodegenerative diseases, and cancer. Dynamic susceptibility contrast (DSC) is well-established for measuring tissue blood flow and volume; however, quantification with DSC is challenging due to uncertainty with arterial input function measures, non-linear contrast relaxivity, and

water and contrast agent transport from intra to extravascular spaces. Our exhibit will review DSC and alternative MRI perfusion techniques, focusing on methodology, advancements, and applications essential for neuroradiologists.

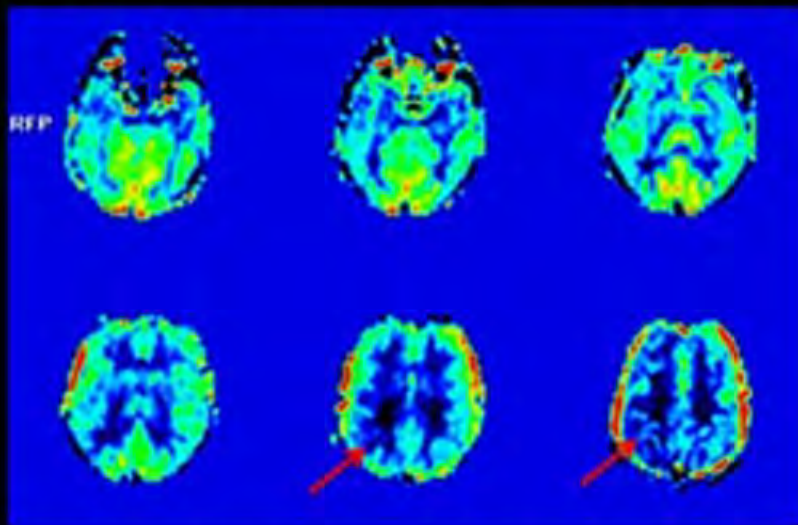
Results

We will define MRI perfusion terminology, parameters and principles related to DSC, and advanced imaging techniques such as dynamic contrast enhancement (DCE), blood oxygen level dependent (BOLD), and types of arterial spin labeling (ASL). Methodology advances, specific clinical applications, as well as advantages and potential pitfalls of the different techniques will be discussed.

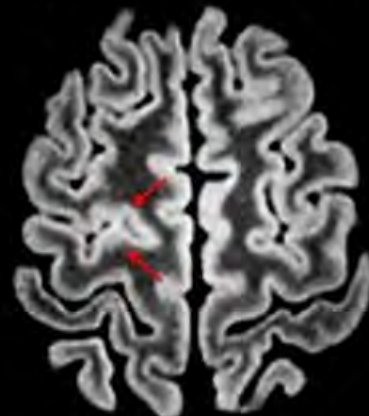
Conclusions

DSC is the traditional workhorse of MRI perfusion, including clinical differentiation between tumor and radiation necrosis; however, DSC is limited by its inability to provide quantitative data. BOLD imaging utilizes $R2^*$ differences between oxy and deoxy hemoglobin and is typically used in functional MRI to measure neuronal activity or refers to resting state in research settings; however, regional blood flow, levels of neuronal/astrocytic enzymes regulating vessel diameter, astrocyte morphology, and neurovascular coupling can impact BOLD signal. DCE MRI is T1 based with limited intracranial use in tumor evaluation due to higher noise levels and complex modeling. ASL is perhaps the most quantitative of MR perfusion methods with potential applications in longitudinal studies (Image A). ASL can be slab-based, slice-based, or motion based, each with advantages and disadvantages (Image B). MRI perfusion, both without and with contrast, is critical for evaluation of many neurologic presentations. Understanding the principles, advantages, disadvantages, and pitfalls of various perfusion techniques is essential for practicing radiologists.

A ASL Future Applications: Seizures, Focal Cortical Dysplasia in Pediatrics



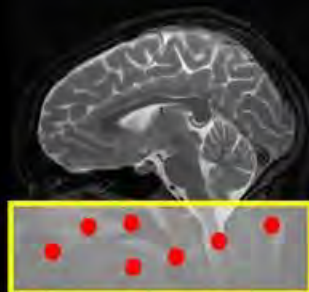
Spatial Arterial Spin Labeling (ASL) showing focal hypoperfusion in right perirolandic region at location of FCD.



15 year-old female with 6-year history of generalized tonic clonic seizures. Focal cortical dysplasia is seen on axial T2/FLAIR at the right premotor sulcus.

B Arterial Spin Labelling Types

Selective Slab Based
(PASL, FAIR, STAR)



Blood in the slab tagged and moves into volume

Slice Based
(CASL, PCASL)



Blood that passes through plane is tagged

Motion Based
(VS-ASL)



Blood that moves is tagged

(Filename: TCT_400_PerfusionFinal.jpg)

1102

MS and it's so-called Variants: A Pictorial Review

A Aggarwal¹, S Malik², M Oad³, S Lev³

¹Nassau University Medical Center, Fresh Meadow, NY, ²New York Institute of Technology College of Osteopathic Medicine, Glen Head, NY, ³Nassau University Medical Center, East Meadow, NY

Purpose

Recognize MS and variants on imaging Identify key features of MS and variants Identify mimics and radiological pitfalls

Materials and Methods

To illustrate the broad spectrum of MS and its so-called "variants", which include atypical demyelinating disorders and idiopathic

inflammatory demyelinating lesions (IIDLs). We discuss key features and mimics, highlighting pitfalls in radiological diagnosis. We review pathophysiology and clinical presentation and stress an algorithmic approach with tailored protocols.

Results

We retrospectively reviewed the imaging of patients with suspected MS, seen at our ED during the past 10 years. We organize by etiology, MS, other neuroinflammatory demyelinating diseases and mimics (e.g. infectious or post-immunization entities).

Conclusions

Multiple sclerosis (MS) is a chronic inflammatory disease of the CNS characterized by deficits separated in space and time. It typically presents with blurry vision and motor symptoms. Tailored MR protocols are useful to assess demyelinating plaques. The variants (Balo's, Tumefactive, Marburg, and Schilder) are rare and difficult to differentiate via imaging. NMO (Devic's Syndrome), now considered a separate entity rather than an MS variant, affects only the spinal cord and optic nerve. At least three vertebral segments of the cord are affected, centrally and symmetrically, unlike MS, with more peripheral lesions. Balo's Concentric Sclerosis (BCS) is more mass-like and resembles a "whirlpool" of concentric rings, reflecting varied states of demyelination. Tumefactive MS, often mistaken for abscess or neoplasm, may be single or multiple, with an incomplete ring of enhancement and little mass effect or edema. Schilder disease (SD) affects younger populations and occasionally progresses to MS. The only definitive diagnosis is brain biopsy. Marburg disease, (acute fulminant MS) has less than ten reported cases. Developmental venous anomalies are present along with portions of demyelination. Acute disseminated encephalomyelitis (ADEM) affects children after an infection/vaccination and presents with diffuse symmetric white matter lesions. The cortical and deep grey matter may be affected as well. Although typically monophasic, recurrent forms of ADEM do exist. The variants of MS are difficult to diagnose due to their sparsity and subtle differences. It is imperative that radiologists be aware of their existence and radiological work-up to positively impact patient management.

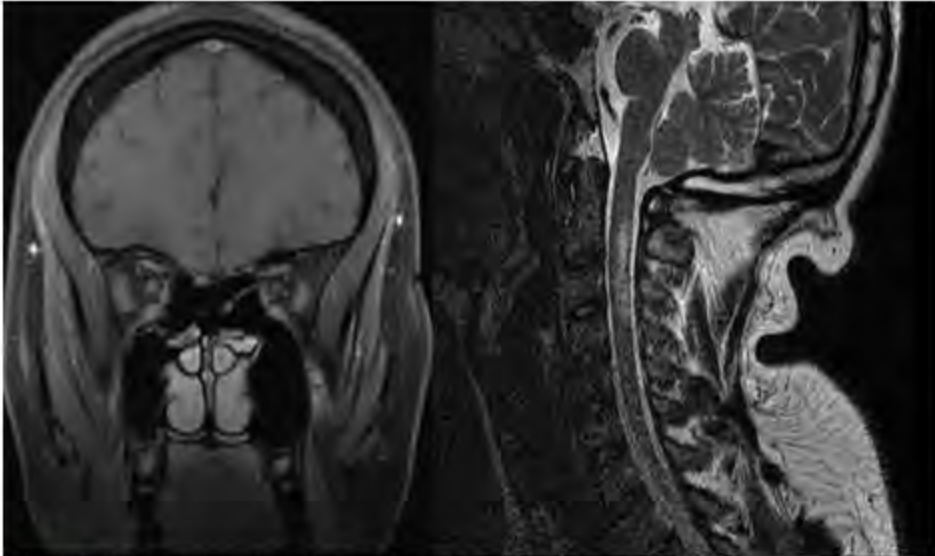


Figure 1. (A) Coronal post gadolinium T1 weighted image demonstrating asymmetric enhancement of the right optic nerve compatible with optic neuritis. (B) Sagittal T2 weighted fast spin echo demonstrating bright signal intensity and swelling of the upper cervical cord. In conjunction with white matter lesions, optic neuritis, these findings are characteristic of neuromyelitis optica (NMO).

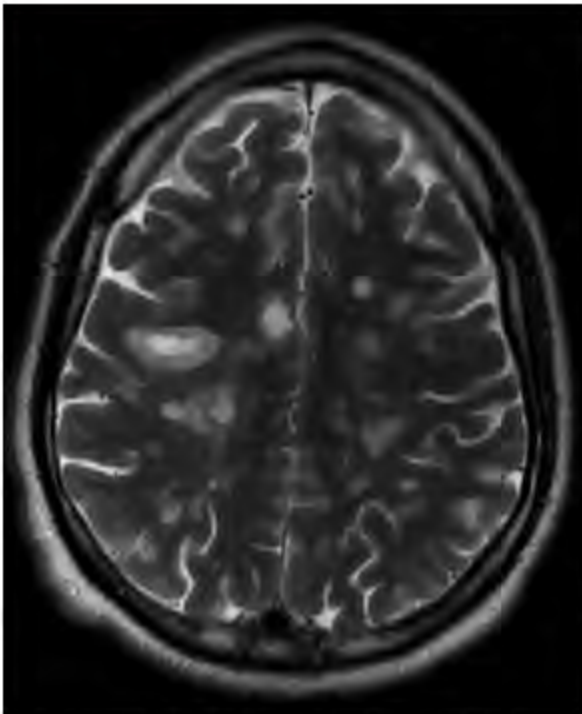


Figure 2. Axial T2 weighted MR image demonstrates multiple scattered ovoid lesions within the periventricular and subcortical white matter, many of which have a concentric ring pattern characteristic of Balos concentrics sclerosis.

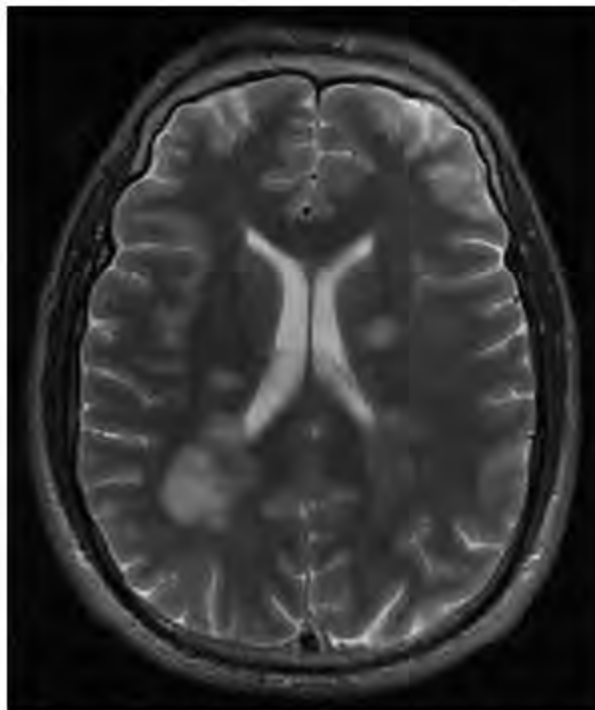


Figure 3. Axial T2 weighted FLAIR sequence demonstrates multiple confluent bright signal intensity foci in the white matter. Adjacent to the posterior aspect of the right lateral ventrical is a larger lobulated, confluent mass-like region of increased signal intensity characteristic of tumefactive MS.

(Filename: TCT_1102_MSvariantspictures.JPG)

216

Multidelay ASL: Pediatric Applications

M H¹

¹Nationwide Children's Hospital, Dublin, OH

Purpose

1. Review technique and postprocessing of multidelay arterial spin labeling (MDASL). 2. Compare multidelay and single-delay ASL with regard to interpretive pitfalls and artifacts. 3. Present multiple clinical cases of MDASL to demonstrate utility in pediatric brain imaging.

Materials and Methods

To provide technical understanding, interpretive guidelines, and clinical pearls for MDASL in pediatric brain imaging.

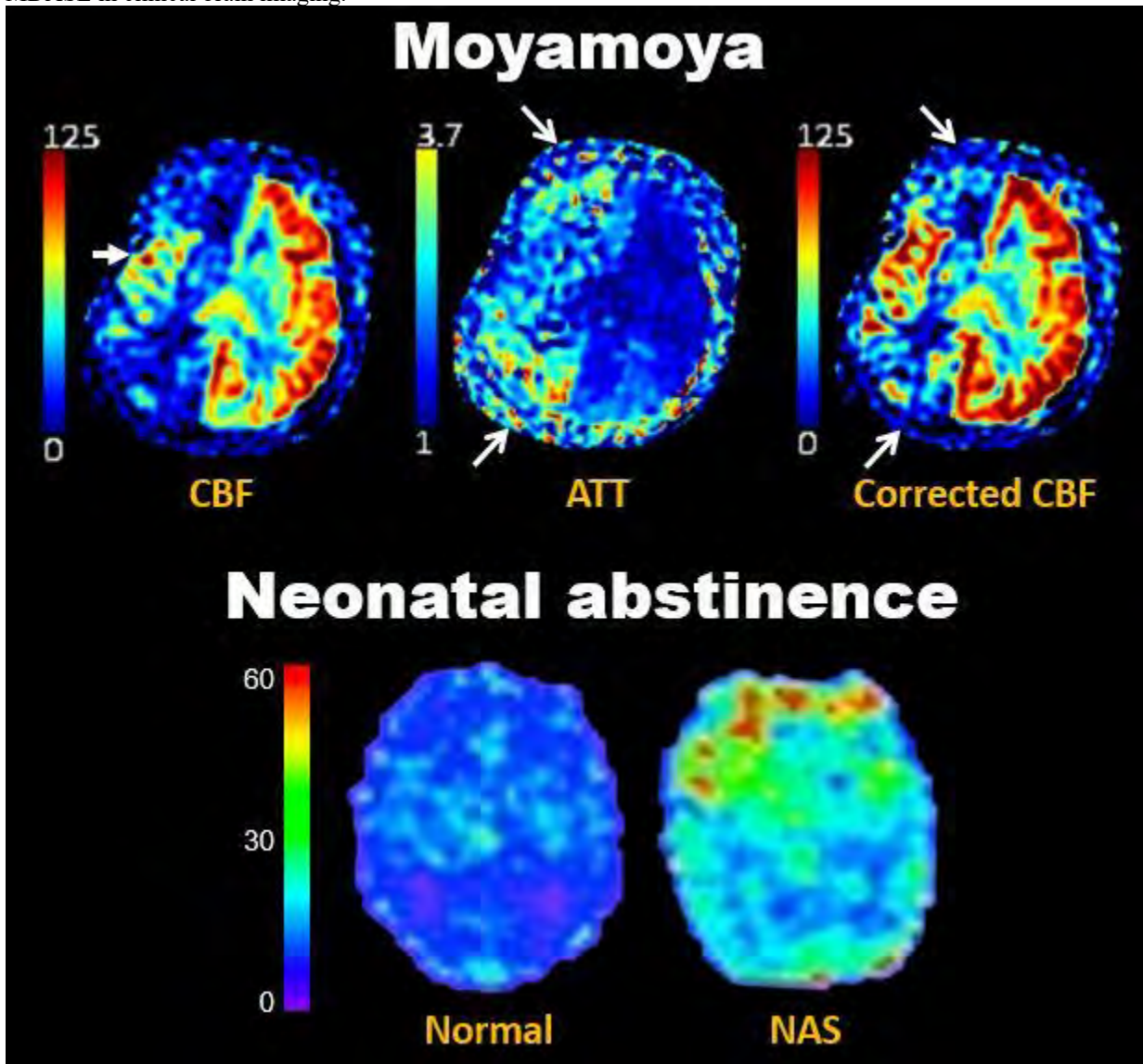
Results

We will discuss the technical basis of MDASL technique with regard to number and duration of postlabel delays, approaches to curve fitting, and quantitative generation of cerebral blood flow, arterial transit time, and cerebral blood volume maps. Benefits and disadvantages relative to single-delay ASL and other perfusion techniques will also be discussed, including potential technical artifacts and pitfalls. Subsequently, we will present selected teaching cases from our institutional experience of 162 patients, with clinical indications for imaging as follows: 41 neonatal abstinence syndrome, 25 seizure, 19 stroke, 15 tumor, 14 vasculopathy, 14 perinatal injury, 8 trauma, 7 headache, 6 congenital heart disease, 6 congenital anomalies, 4 infection, and 3 developmental delay. Key teaching examples will include: Vascular disease - Large artery infarction - Small artery infarction - Venous infarction - Moyamoya vasculopathy - Congenital heart disease Perinatal brain injury - Neonatal abstinence syndrome - Preterm brain injury - Term hypoxic-ischemic injury Tumors Epilepsy Migraine Trauma Infection

Conclusions

MDASL is a viable tool for pediatric neuroimaging that augments the diagnostic value of conventional MRI. The most promising applications for this technique are in slow-flow conditions including perinatal injury, stroke, vasculopathies, and migraine.

Understanding of technical concepts and potential pitfalls will enable radiologists to appropriately utilize both single- and multidelay MDASL in clinical brain imaging.



(Filename: TCT_216_MDASL.JPG)

Multimodality evaluation of the CNS compression neuropathies of a vascular nature: Pictorial review

M Gupta¹, M Kulzer², M Goldberg³, C LI³, W CHANG³, C Singh⁴

¹Allegheny General hospital, Pittsburgh, Pittsburgh, PA, ²Allegheny Health Network, PITTSBURGH, PA, ³Allegheny Health Network, Pittsburgh, PA, ⁴Allegheny General Hospital, Pittsburgh, PA

Purpose

CNS compression neuropathies of the vascular etiology have been noted to be a rare cause among various neuropathies. Neuroradiologist should search for the possible vasculopathy in order to correct diagnosis and timely management.

Materials and Methods

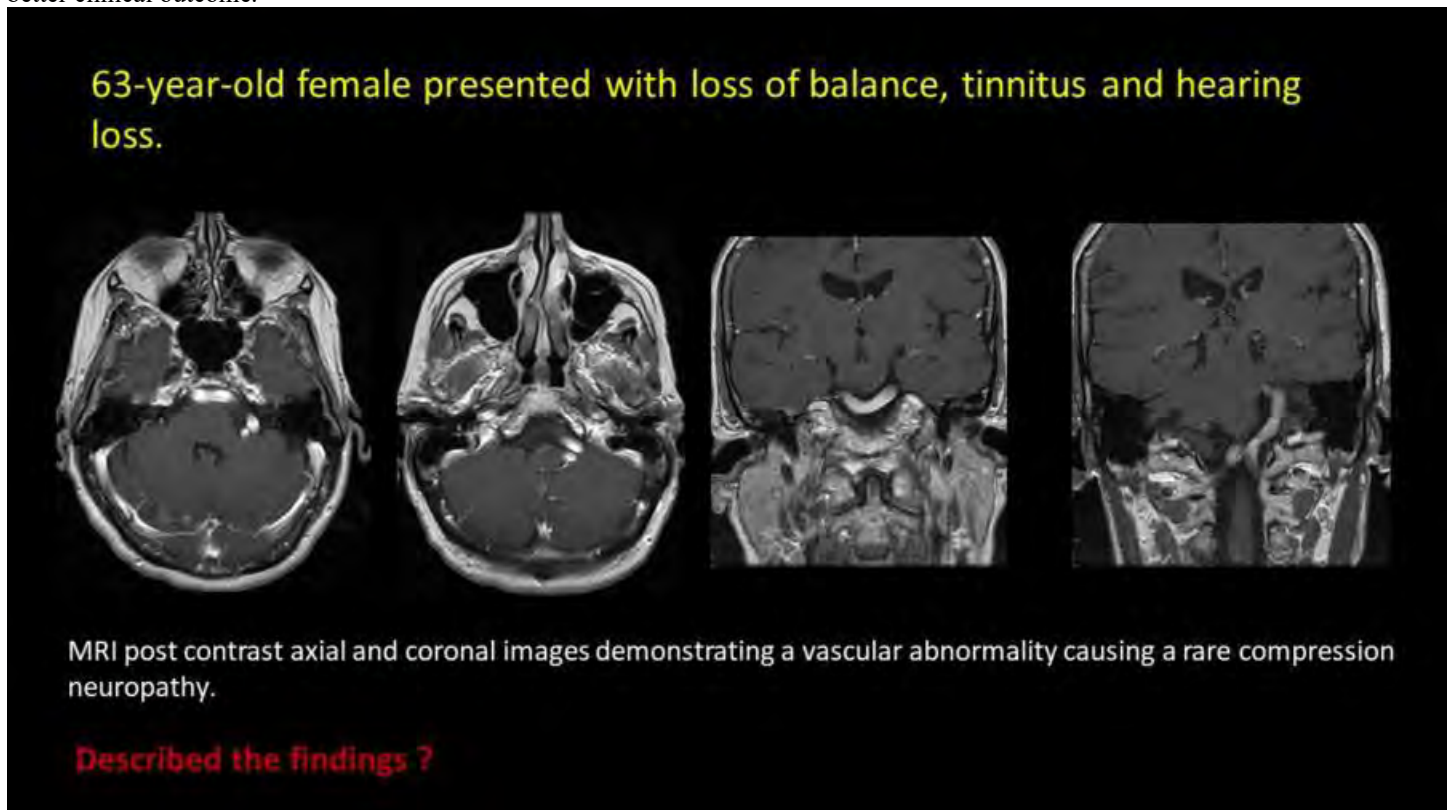
By completing this presentation, Radiologist will better understand the imaging manifestations of the various CNS compression neuropathies in different imaging modalities.

Results

This presentation will expose you to multiple CNS compression Neuropathies cases through quiz based (cases) and matching questions. For each of them, brief description, interpretation, imaging appearance, differential diagnosis and pitfalls will be described and teaching points/pearls will be made/highlighted.

Conclusions

By recognizing different vascular disorders as a cause of various CNS compression neuropathies, will increase diagnostic accuracy for better clinical outcome.



(Filename: TCT_1528_ASNRCompressionneuropathy.jpg)

1294

Mycobacterial Mayhem! A Case Based Review of Head and Neck Manifestations of Mycobacterial Disease

G Carpenter¹, E Sechrist², M Bashir³

¹Loyola University Medical Center, Chicago, IL, ²Loyola University Medical Center, Maywood, IL, ³Loyola University Medical Center, Maywood, IL

Purpose

Tuberculosis and other nontuberculous mycobacterial diseases represent a rare and often overlooked cause of head and neck lesions. Timely diagnosis and treatment of these curable infections is crucial as they can lead to severe debility and death if left untreated. Unfortunately, the appearance of head and neck mycobacterial disease by CT and MRI can be variable and can mimic other

pathologies. The aim of this educational exhibit is to illustrate the imaging findings of head and neck mycobacterial infections and to discuss the common clinical features that should prompt their inclusion in a differential diagnosis. Several pathologically-confirmed case examples will be reviewed.

Materials and Methods

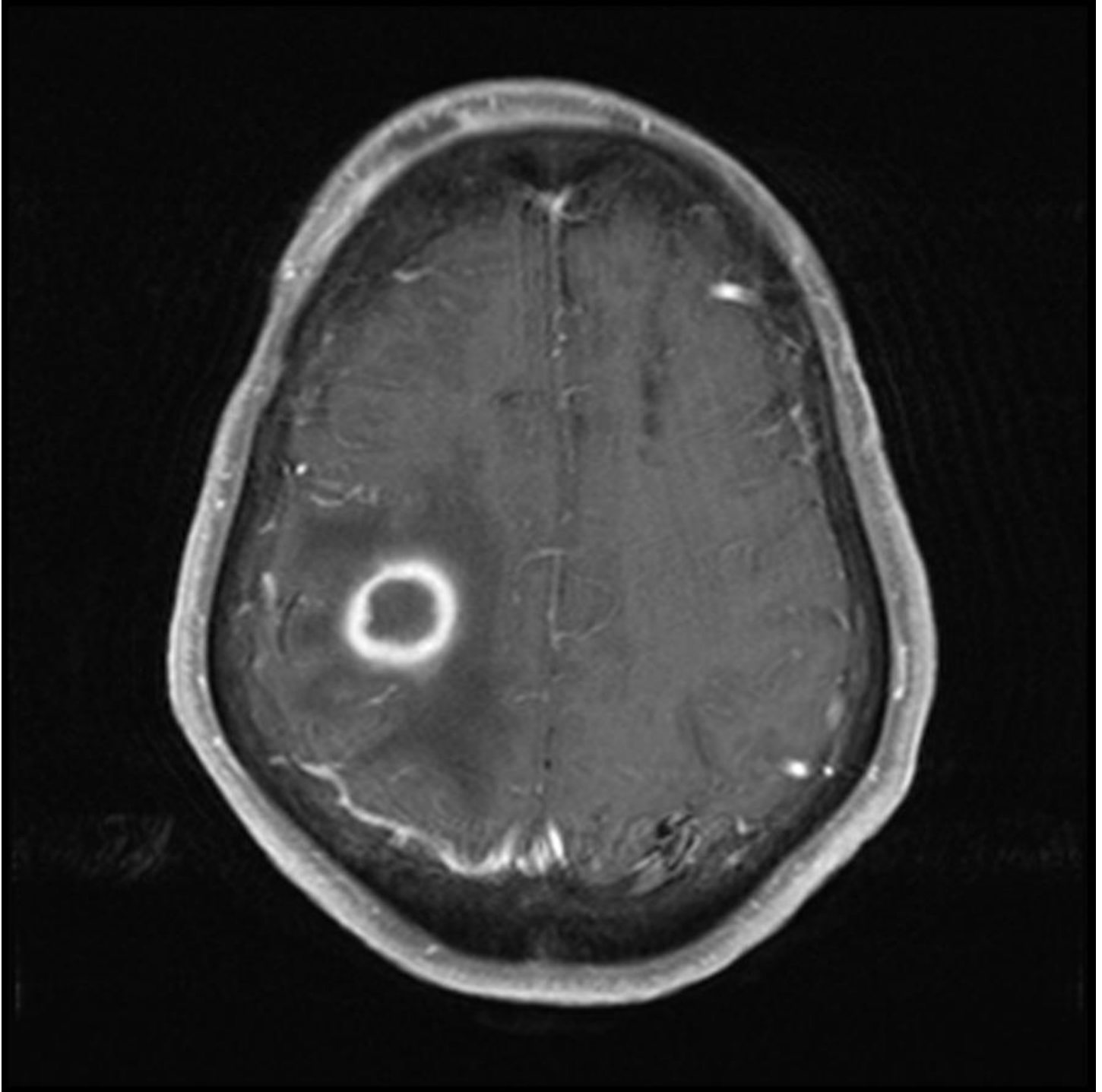
N/A

Results

N/A

Conclusions

N/A



(Filename: TCT_1294_T1post14767000001.jpg)

228

Name That Posterior Fossa Cyst! A Review and Approach for the Suspected Dandy Walker Malformation

Purpose

1. Review embryology of cerebellar development with an emphasis on the rhombic lip, a progenitor region vital to posterior vermian expansion with absence or dysfunction of this structure recently linked to the Dandy Walker Malformation (DWM) 2. Describe and illustrate the radiographic findings of classic DWM and its variants. 3. Discuss differential diagnosis of cystic posterior fossa structures including Blake's Pouch cyst, Mega Cisterna Magna, and posterior fossa arachnoid cyst. 4. Define clinical implications and prognostic outcomes in patients with DWM with regards to imaging findings utilizing a review of the literature and discussion of experience at our institution. 5. Review recent discoveries regarding the genetic underpinnings of inferior vermian malformations.

Materials and Methods

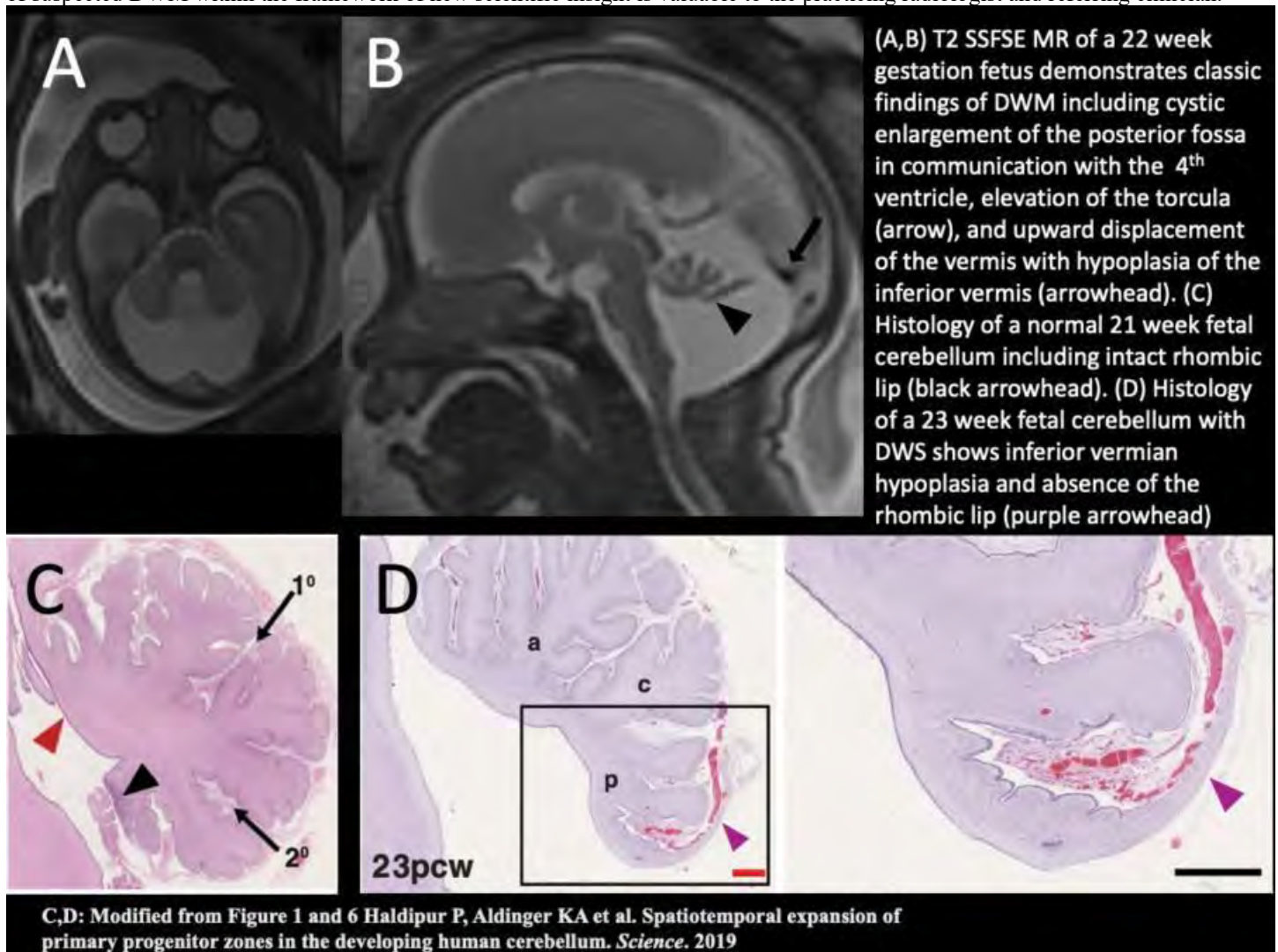
The Dandy Walker phenotype is the most common posterior fossa malformation. DWM and other cystic posterior fossa structures can be a diagnostic dilemma to the radiologist. Furthermore, accurate description and diagnosis of this malformation, its mimics, and ancillary findings is critical for clinical prognostication and management. Recent histologic, molecular, and genetic research has further defined the pathogenesis of this condition and will be reviewed.

Results

Our exhibit will draw upon approximately 25 cases from our institution of prenatally and postnatally diagnosed Dandy Walker Malformation and its variants with examples including prenatal ultrasound, CT, and fetal and postnatal MRI. We will use embryologic and genetic data to help explain common imaging findings seen alongside cystic posterior fossa structures.

Conclusions

Understanding of the pathogenesis of cystic malformation of the posterior fossa continues to evolve. Interpretation of imaging in cases of suspected DWM within the framework of new scientific insight is valuable to the practicing radiologist and referring clinician.



(Filename: TCT_228_Images.jpg)

Neuro-Oncology MR Imaging Workflow for Treated Gliomas

G Guzman Perez-Carrillo¹

¹Mallinckrodt Institute of Radiology, St. Louis, MO

Purpose

Differentiating post-treatment change from tumor recurrence in treated gliomas is one of the most challenging tasks a neuroradiologist faces. The objective of this educational exhibit is to improve the diagnostic accuracy of trainees and practicing neuroradiologists through the utilization of a neuro-oncologic diagnostic imaging algorithm using multiparametric MR imaging markers.

Materials and Methods

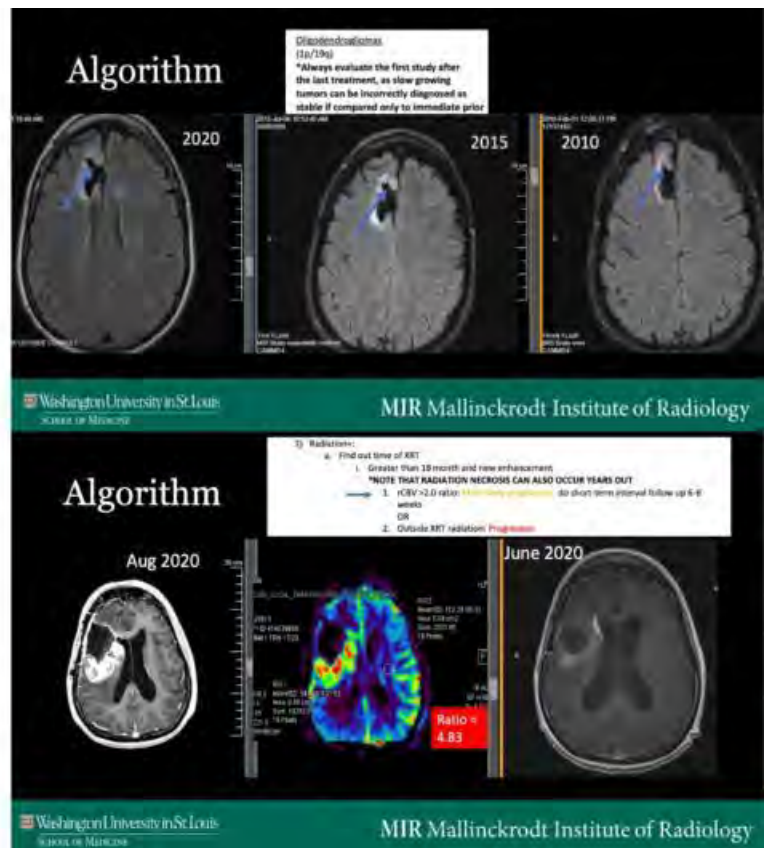
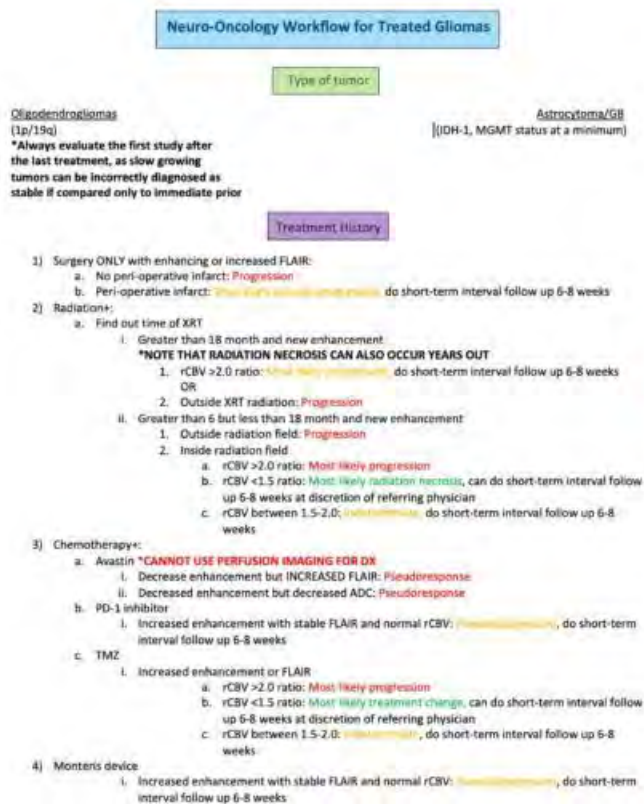
The purpose is to provide an educational exhibit with high-quality images that provides a workflow algorithm using MR multiparametric markers to correctly arrive at a diagnosis of post-treatment change versus tumor recurrence in treated brain gliomas.

Results

This is a retrospective case review of a broad range of pathologically and clinically proven cases of treated brain gliomas accumulated from 2014-2020 at multiple tertiary referral university medical centers. These are organized by type of brain glioma and treatment course. High quality anatomical, perfusion and diffusion-weighted images are used to illustrate the findings.

Conclusions

The viewer of this exhibit will gain or refresh information about critical MRI anatomical and physiological (i.e. perfusion and diffusion) findings integrated as a neuro-oncological imaging algorithm for the evaluation of treated brain gliomas that is useful in clinical practice and for certifying examinations. The images provided aid in recognition of critical anatomical and physiological findings that must be thoroughly evaluated and categorized in order to arrive at the correct diagnosis of glioma tumor recurrence or post-treatment change. Correct differentiation of post-treatment change versus tumor recurrence in treated gliomas presents an imaging diagnostic challenge. A comprehensive multiparametric neuro-oncological MR imaging algorithm is fundamental to optimize patient care and outcome.



(Filename: TCT_1346_ASNR2021AlgorithmFigure1.jpg)

280

Neurodegeneration with Brain Iron Accumulation (NBIA) in Children: a Clinico-radiological Approach

M D. Soldatelli¹, P Hanagandi², E Narvaez¹, V Marussi¹, L do Amaral¹

¹Beneficência Portuguesa de São Paulo, São Paulo, Brazil, ²King Abdulaziz Medical City, Ministry of National Guard Health Affairs, Riyadh, Riyadh

Purpose

Neurodegeneration with brain iron accumulation (NBIA) encompasses a heterogeneous group of rare inherited disorders characterized by progressive accumulation of iron, specifically in the basal ganglia with a predilection for the globus pallidus (GP) and substantia nigra (SN). The disease manifestations exhibit childhood onset with progressive extrapyramidal symptoms. This educational exhibit will illustrate and discuss the various NBIA subtype and highlight the clinico-radiological features, underlying genetic basis and current literature on the role of molecular mechanisms. We intend to propose a step-by-step approach that would assist the radiologist in diagnosing these rare pathologies.

Materials and Methods

1. Describe the various NBIA subtypes and their molecular mechanisms. 2. Illustrate the key radiological and clinical features with genotype-phenotype correlation. 3. Propose a diagnostic algorithm with step-by-step approach that would help the radiologist in making the presumptive imaging diagnosis.

Results

Retrospective analysis of MRI findings in genetically confirmed cases was performed at our tertiary referral institution. The following NBIA subtypes and their key imaging and clinical features will be discussed in this presentation: • Pantothenate kinase-associated neurodegeneration (PKAN) • Phospholipase A2-associated neurodegeneration (PLAN) • Mitochondrial membrane protein-associated neurodegeneration (MPAN) • Beta-propeller protein-associated neurodegeneration (BPAN) • Fatty acid-hydroxylase-associated neurodegeneration (FAHN) • Kufor-Rakeb syndrome (KRS) • CoASY protein-associated neurodegeneration (CoPAN) • Adult-onset NBIA: Neuroferritinopathy and Aceruloplasminemia Relevant genotype-phenotype correlation of the following entities is included: • Enzymes responsible for coenzyme A production: PANK2, CoASY • Proteins related to lipid metabolism: PLA2G6, FA2H, SCP2, CRAT, C19orf12 • Proteins involved in autophagy: WDR45, ATP13A2 • Proteins associated with vesicle trafficking: RESP1, AP4M1 • Unclear function: GTBP2, C2orf37

Conclusions

Radiologist's awareness of the NBIA Imaging spectrum would help in narrowing down the list of differential diagnoses and thereby facilitate targeted genetic work up. We believe our proposed clinic-radiological algorithm will enhance the understanding of this rare disease spectrum. Although the treatment remains symptomatic and supportive, new strategies could be developed with an increase in the detection and understanding of these conditions.

Key Clinico-radiological Differential Features in NBIA			
<p>Rapid psychomotor regression, profound hypotonia and visual disturbances</p> <p>Predominant cerebellar atrophy, Claval hypertrophy, optic chiasm thinning</p> <p>PLAN</p>	<p>X-linked; biphasic: static encephalopathy in childhood (developmental delay, epilepsy, sleep disorder) and neurodegeneration in adulthood</p> <p>Early and predominant substantia nigra (SN) involvement. High T1 signal in the SN with a band of T1 hypointensity ("hamburger sign")</p> <p>BPAN</p>	<p>Spasticity, cognitive impairment, obsessive-compulsive disorder, normal ophthalmological exam</p> <p>Symmetrical "eye-of-the-tiger" sign in the globus pallidi with central hypointensity</p> <p>CoPAN</p>	<p>Initially described in Jordanian family; juvenile-onset, supranuclear gaze palsy, cognitive features (visual hallucinations and dementia)</p> <p>Decreased nigrosome 1 and neuromelanin; bilateral symmetrical decreased striatal ¹²³Iflupane uptake</p> <p>Kufor-Rakeb Syndrome</p>

(Filename: TCT_280_ASNR2021NBIA.jpg)

909

Neuroexcitotoxicity and Cortical Spreading Depolarization/Depression: Imaging findings and mechanisms

Y Ota¹, R Kurokawa², A Baba³, A Capizzano¹, T Moritani¹

Purpose

We reviewed MRI findings and mechanisms of neuroexcitotoxicity and cortical spreading depolarization/depression (CSD) and their mimics. List of educational objectives: 1. Mechanisms of neuroexcitotoxicity and cortical spreading depolarization/depression 2. CSD related diseases 3. Review of imaging features of each disease and condition 4. Case presentations and mimics

Materials and Methods

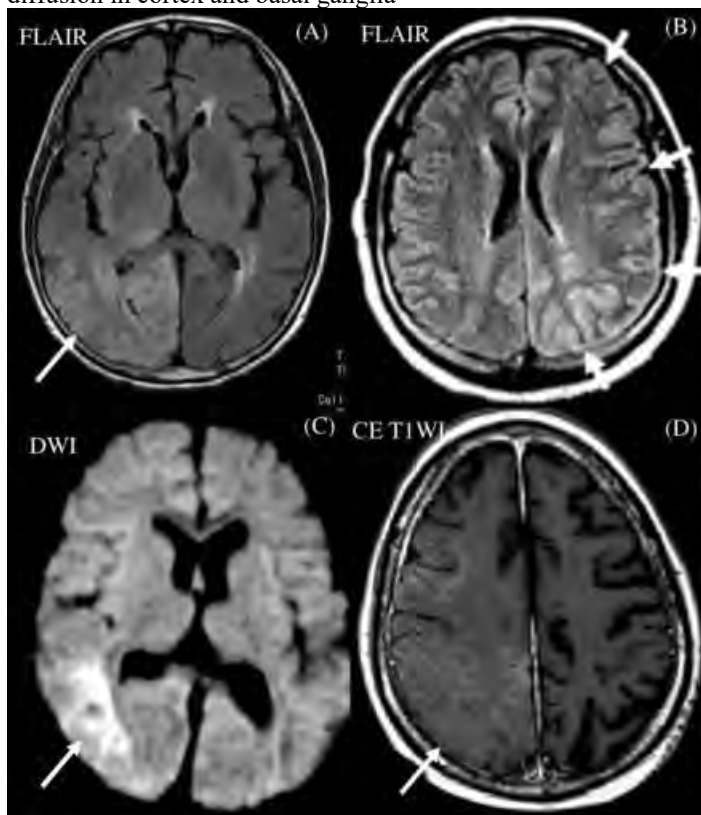
1. To review mechanisms of neuroexcitotoxicity and cortical spreading depolarization 2. To discuss different diseases and conditions with cortical spreading depolarization/depression 3. To demonstrate imaging features of each disease

Results

We reviewed mechanisms of neuroexcitotoxicity and cortical spreading depolarization/depression and MRI findings of each disease and condition. CSD related diseases - Status Epilepticus - Migraine - Hypoxic ischemic encephalopathy - Abused head injury Mimics - Autoimmune mediated encephalitis, Rasmussen encephalitis - SMART syndrome - herpes encephalitis - CJD

Conclusions

• Mechanisms of neuroexcitotoxicity and CSD • MRI findings - Status Epilepticus: Reversible FLAIR hyperintensity with diffusion restriction along the cortex, involvement of hippocampus and pulvinar - Migraine: Reversible: FLAIR hyperintensity and diffusion restriction along the cortex, without pulvinar involvement - Abused head injury: Subdural hematoma with surrounding cerebral white matter FLAIR hyperintensity with diffusion restriction - Hypoxic ischemic encephalopathy: Cortical FLAIR hyperintensity with restricted diffusion extending into the surrounding white matter, splenium, and thalami - MELAS: Reversible FLAIR hyperintensity and diffusion restriction along the cortex, classic lactate peak in MRS, and recurrence - Autoimmune mediated encephalitis: Involvement of hippocampus and basal ganglia as well as the cortex - SMART syndrome: FLAIR hyperintensity and diffusion restriction in the cortex with leptomeningeal and cortical enhancement, and recurrence - Herpes encephalitis: T2WI/FLAIR hyperintensity and restricted diffusion are seen in the bilateral mesial temporal lobe - CJD: FLAIR hyperintensity with restricted diffusion in cortex and basal ganglia



(A) 50-year-old female with status epilepticus. FLAIR hyperintensity along the right parieto-occipital cortex is seen. The right pulvinar is affected.

(B) 37-year-old female with migraine. FLAIR hyperintensity along the left fronto-temporo-occipital cortex is seen. The pulvinar is not involved.

(C) 9-month-old boy with abused head trauma. DWI hyperintensity in the right occipital white matter is seen.

(D) 54-year-old male with SMART syndrome. Gyral enhancement in the fronto-parieto-occipital cortex is seen.

(Filename: TCT_909_CSD-fig.jpg)

1209

Neuroimaging in Perinatal Stroke and Mimickers

J Scaggiante¹, M Yazdani¹, M Trevino¹, M Matheus¹, V Spampinato¹

¹Medical University of South Carolina, Charleston, SC

Purpose

A stroke occurring from 28 weeks of gestation to postnatal day 28 is widely defined as perinatal stroke [1]. Arterial ischemic infarctions represent about 80% of perinatal cases, and occur in up to 1 over 3500 newborns, an incidence 6 times higher than in childhood. The remainder of perinatal strokes are caused by cerebral sinovenous thrombosis (CSVT) and intracerebral hemorrhage. Newborns with perinatal stroke present with seizures, acute encephalopathy, and altered mental status. Presumed perinatal strokes are also diagnosed later in life during the workup of a focal neurological deficit. Neuroimaging findings of perinatal stroke and stroke mimickers vary among preterm and term neonates due to different degrees of brain maturation [2,3]. Our objectives are the following:

- Review of epidemiology and classification of perinatal stroke
- Review of brain maturation and mode of presentation
- Review of MR imaging protocol for neonatal stroke
- Case-based review of neuroimaging findings of neonatal stroke
- Review of neuroimaging mimickers of neonatal stroke

Materials and Methods

Our purpose is to provide a didactic review of perinatal stroke and stroke mimickers according to brain maturation and mode of stroke presentation.

Results

We will present perinatal stroke cases and mimickers from our teaching file. Our presentation will include stroke cases in preterm and term neonates, specifically cases of arterial ischemic infarct, CSVT, and intracranial hemorrhage, including subpial hemorrhage. We will also review imaging findings of stroke mimickers such as metabolic and infectious diseases, as well as imaging findings of hypoxic-ischemic brain injury, periventricular leukomalacia, germinal matrix hemorrhage. Cases will be accompanied by multiple-choice questions in an interactive format.

Conclusions

Imaging plays an important role in the diagnosis and management of perinatal stroke, and provides valuable information to rule out mimickers, such as metabolic diseases. It is important for radiology trainees to gain familiarity with perinatal stroke imaging findings in preterm and term neonates.

425

Neuroimaging Manifestation of Autoimmune Glial Fibrillary Acidic Protein (GFAP) Astrocytopathy; A pictorial Review.

H Sotoudeh¹, Z Saadatpour², A Rezaei², A Sarrami³, A Singhal²

¹UAB, Birmingham, AL, ²University of Alabama at Birmingham, Birmingham, AL, ³Semnan University of Medical Sciences, Davis, CA

Purpose

Autoimmune glial fibrillary acidic protein (GFAP) astrocytopathy is a rare inflammatory disorder of the CNS. Meningoencephalitis is the dominant presentation, and the inflammation can affect many regions, from the optic nerve to the spinal cord. The clinical symptoms are caused by meningitis, encephalitis, myelitis, and optic disc papillitis. Elevated GFAP-immunoglobulin G (IgG) levels in CSF (more reliable) and serum are characteristic of these patients. Up to 25% of patients have underlying malignancies, especially ovarian cancer. MRI is almost always abnormal in these patients. In 50% of cases, there are foci of T2 hyper signal intensities in the brain, and in 2/3 of cases, there are abnormal findings on post-contrast T1. In about half of patients, there is a characteristic linear, radial perivascular pattern of enhancement, through the cerebral white matter, emanating from GFAP-enriched peri-lateral ventricular regions. Other patterns of abnormal enhancements are leptomeningeal, punctate, serpentine, and ependymal. Despite the abnormal pattern of enhancements along the vessels, the DSA angiogram is always negative.

Materials and Methods

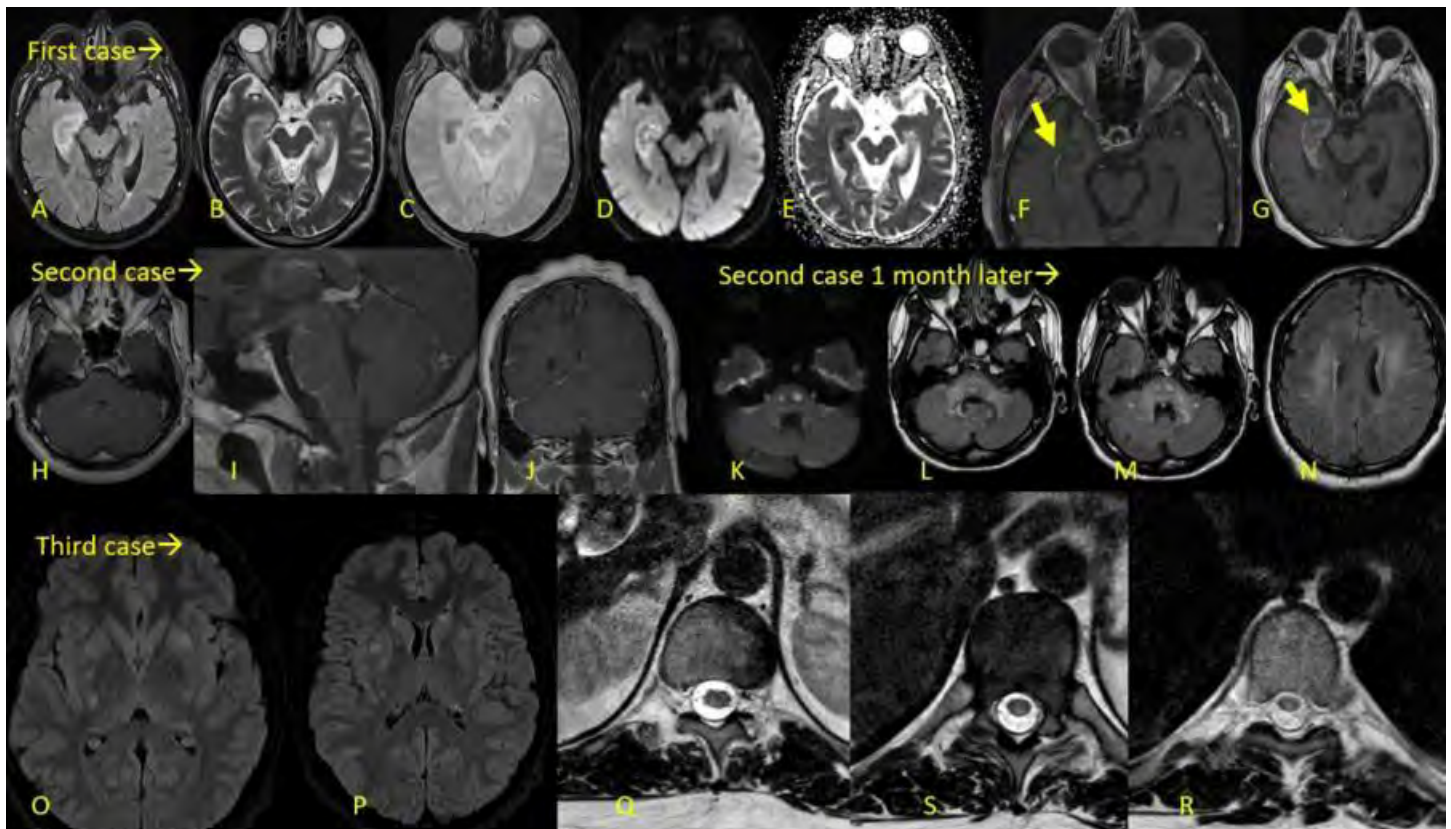
This presentation is a pictorial review of the neuroimaging presentations of GFAP astrocytopathy.

Results

Imaging findings of patients with GFAP astrocytopathy are summarized in this educational presentation.

Conclusions

The classical imaging features of GFAP Astrocytopathy on imaging include: Foci of T2 hyper signal intensities in the white matter A characteristic linear, radial perivascular pattern of enhancement, through the cerebral white matter, at the GFAP-enriched peri-lateral ventricular regions. Abnormal leptomeningeal enhancement.



(Filename: TCT_425_GFAPfinalimage300.jpg)

384

Neuroimaging Manifestation of COVID-19; A Pictorial Review

H Sotoudeh¹, A Rezaei², Z Saadatpour², A Sarrami³, A Singhal²

¹UAB, Birmingham, AL, ²University of Alabama at Birmingham, Birmingham, AL, ³Semnan University of Medical Sciences, Davis, CA

Purpose

Various neurological symptoms have been described in COVID-19 patients. Headache, dizziness, impaired consciousness, and acute cerebrovascular events are among the most common neurological manifestations of this infection. Although most of the COVID-19 patients have normal neuroimaging studies, intra-axial and extra-axial abnormalities can be seen in some patients. Ischemic and hemorrhagic strokes, encephalomyelitis, meningitis, demyelinating disorders such as acute disseminated encephalomyelitis (ADEM), meningitis, and acute myelitis are among the CNS complications which can be detected on neuro-imaging. Also, peripheral nervous manifestations of COVID-19, such as Guillain-Barré syndrome, Bell's palsy, and skeletal muscle manifestations such as rhabdomyolysis can be encountered by the neuroradiologists.

Materials and Methods

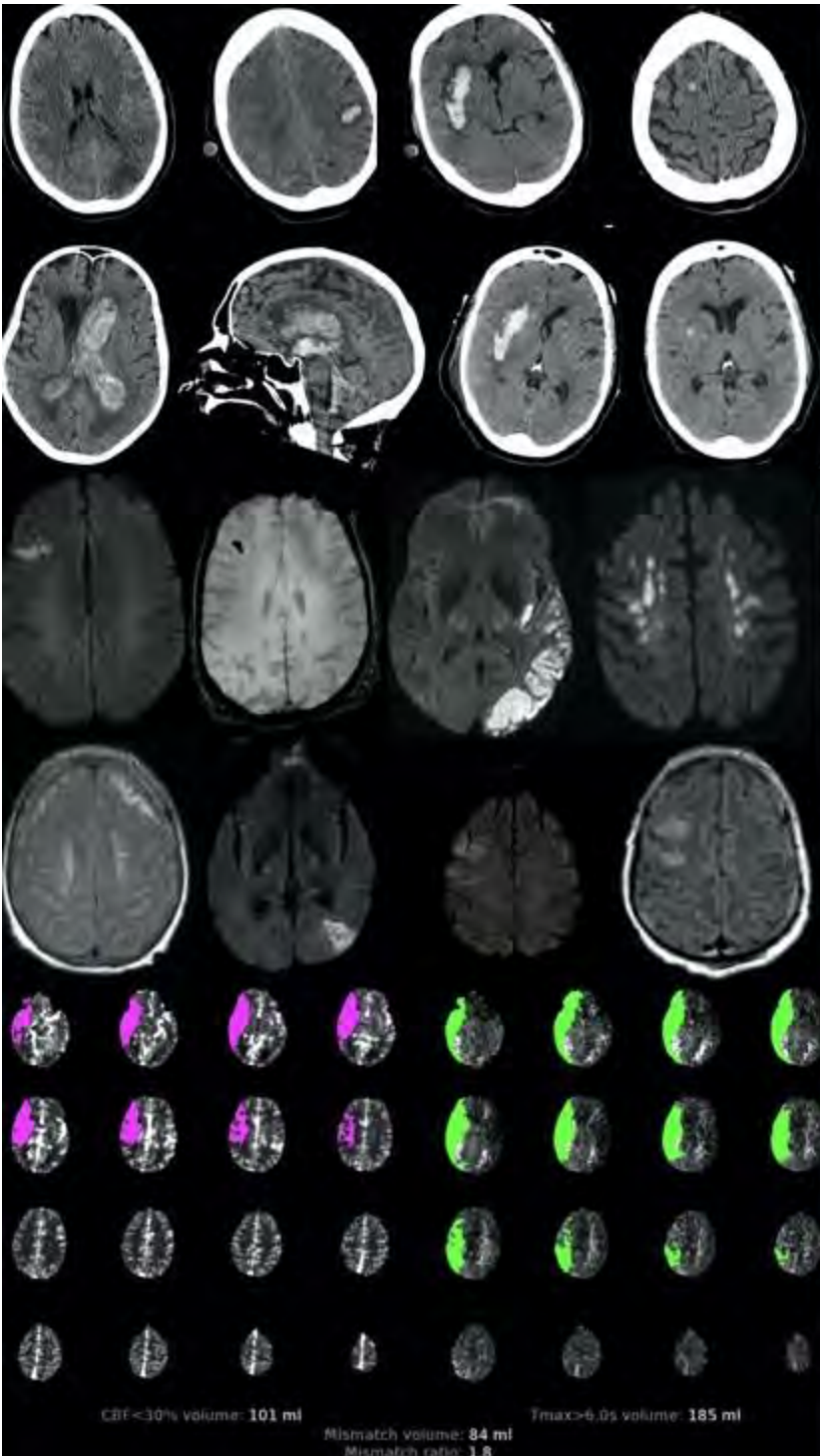
This presentation is a pictorial review of the neuroimaging manifestation of the COVID-19 infection in patients referred to a tertiary university hospital since the beginning of the pandemic.

Results

All patients diagnosed with the COVID-19 infection who underwent neuroimaging studies have been included in the dataset. The patients with positive findings have been divided into different classes (e.g. Ischemic cerebrovascular stroke, Hemorrhagic stroke, Lacunar infarctions, Micro-infarctions, Parenchymal hematomas, Microhemorrhages, Subarachnoid hemorrhage, Intraventricular bleeding, Subdural hemorrhage, meningitis, encephalitis, myelitis, inflammatory disease/ADEM). From each class, the classical imaging findings are being reviewed.

Conclusions

The pictorial review includes: Ischemic cerebrovascular stroke, Hemorrhagic stroke, Lacunar infarctions, Micro-infarctions, Parenchymal hematomas, Microhemorrhages, Subarachnoid hemorrhages, Intraventricular bleeding, Subdural hemorrhages, Meningitis, Encephalitis, Myelitis, Inflammatory disease/ADEM CNS complication of ECMO Artifacts of the neuroimaging in critical and intubated COVID-19 patients Large vascular occlusion Cytotoxic lesions of the corpus callosum (CLOCCs) Hypoxic encephalopathy Guillian-Barre syndrome PRES Also, our dataset is constantly updating, and the new imaging presentations will be added to this collection.



(Filename: TCT_384_COVIDCNDmanifestation.jpg)

434

Neuroimaging Manifestations of Parry Romberg Syndrome and Linear Morphea

A Ramachandran¹, P Rajagopalan², C Lindan³, O GLENN², Y LI¹

¹UCSF, San Francisco, CA, ²N/A, N/A, ³UCSF, Mill Valley, CA

Purpose

PRS and linear morphea are often underdiagnosed or misdiagnosed due to the relative rarity of these diagnoses and the difficulty in identifying its clinical features. MR imaging is essential for evaluating intracranial involvement. The imaging findings are variable, and may include white matter abnormalities, parenchymal calcifications, and brain atrophy. In our educational exhibit, we will describe key imaging features and a search pattern that will help you to clench this difficult-to-make diagnosis.

Materials and Methods

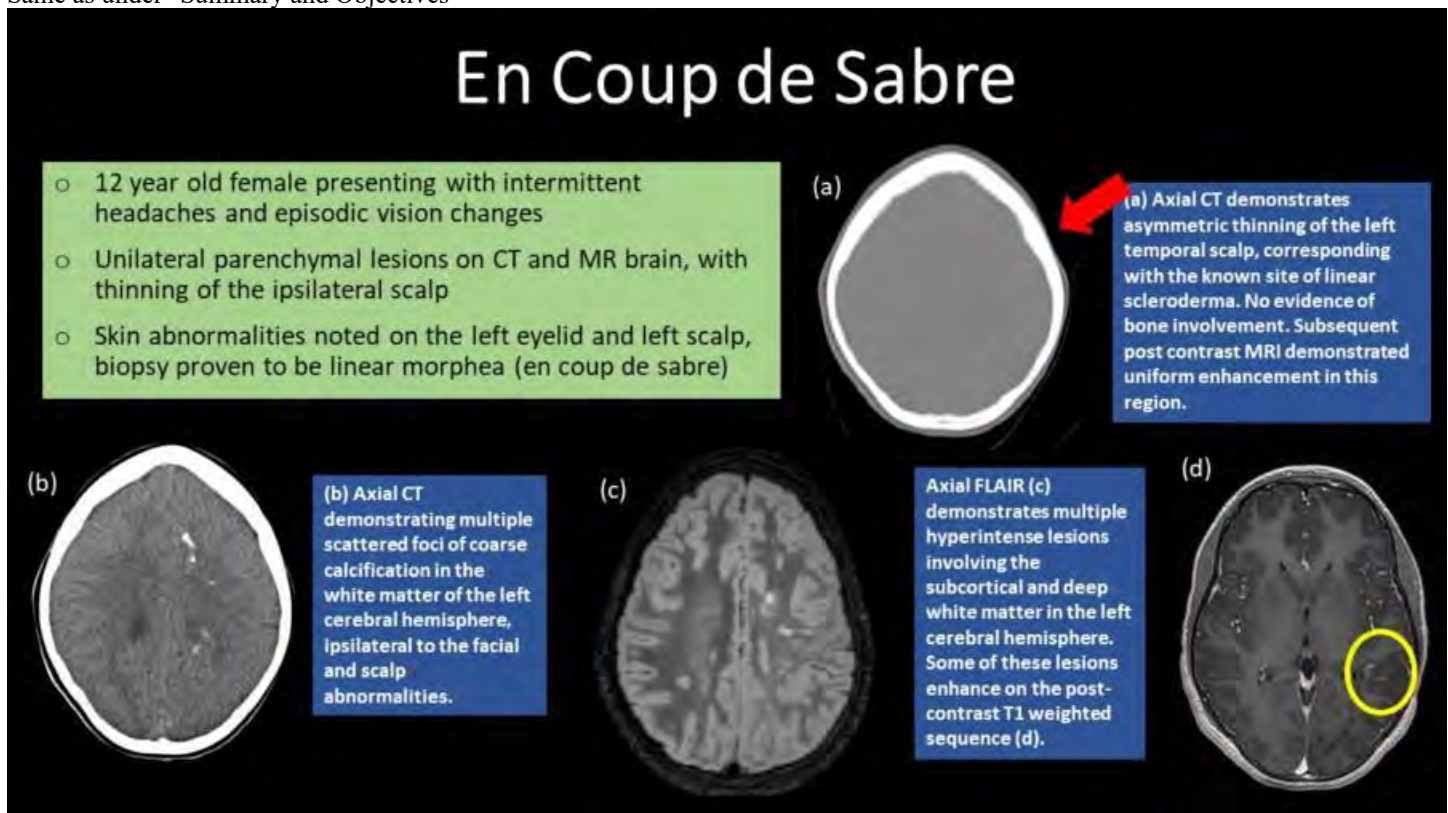
Describe the clinical manifestations of and review cases of Parry Romberg syndrome and linear morphea to illustrate various head and neck and intracranial findings

Results

Parry Romberg syndrome (PRS) is a rare, slowly progressive but self-limiting neurocutaneous disorder resulting in hemiatrophy of the face. PRS may be on a spectrum of fibrotic disorders including morphea en coup de sabre, a variant of linear scleroderma. Although the underlying pathophysiology is not clearly understood, PRS is likely an immune-mediated inflammatory process, possibly associated with vasculopathy. In this educational exhibit, we will discuss: 1) The clinical manifestations of PRS and linear morphea. Headaches and seizures are the most frequently reported neurological symptoms and can be refractory to treatment. 2) The facial soft tissue findings associated with PRS and linear morphea. PRS characteristically involves atrophy of the skin and subcutaneous connective tissues and can progress to affect the deeper tissues such as musculature, cartilage, and bone. We will provide imaging examples of hemifacial atrophy and en coup de sabre, focusing on a search pattern and key imaging features to make this diagnosis. We will provide complementary dermatologic pictures to describe the visual features of this diagnosis. 3) The intracranial neuroimaging manifestations of PRS. Typical findings on brain imaging are most often supratentorial, unilateral and ipsilateral to the affected side of the face. These include white matter hyperintensities on T2-weighted MRI sequences, intracranial calcifications and brain atrophy. Associated vascular abnormalities such as microhemorrhages, malformations, stenoses, and aneurysms have also been reported. Neuroimaging is also useful to exclude other etiologies, monitor disease progression and evaluate response to treatment.

Conclusions

Same as under "Summary and Objectives"



(Filename: TCT_434_PRS.jpg)

1348

Neuroimaging of Epilepsy Treatment

M Adin¹, A Herlopian², D Eyiymisi³, L Tu⁴, J Gerard³, R Bronen⁵

¹Yale University School of Medicine, New Haven, CT, ²Yale University School of Medicine, new haven, CT, ³Yale University, new haven, CT, ⁴Yale School Of Medicine, New Haven, CT, ⁵N/A, N/A

Purpose

Intractable seizures occur in 30% of patients with focal epilepsy despite an adequate trial of anti-epilepsy medications, necessitating surgical or additional interventional treatment. Over the last decade, the availability of interventions has increased considerably and it is important for neuroradiologists to be familiar with the different types of surgical approaches, their indications, and the imaging findings or complications associated with these. A variety of microinvasive treatment options and neuromodulation techniques bring unique challenges in imaging interpretations.

Materials and Methods

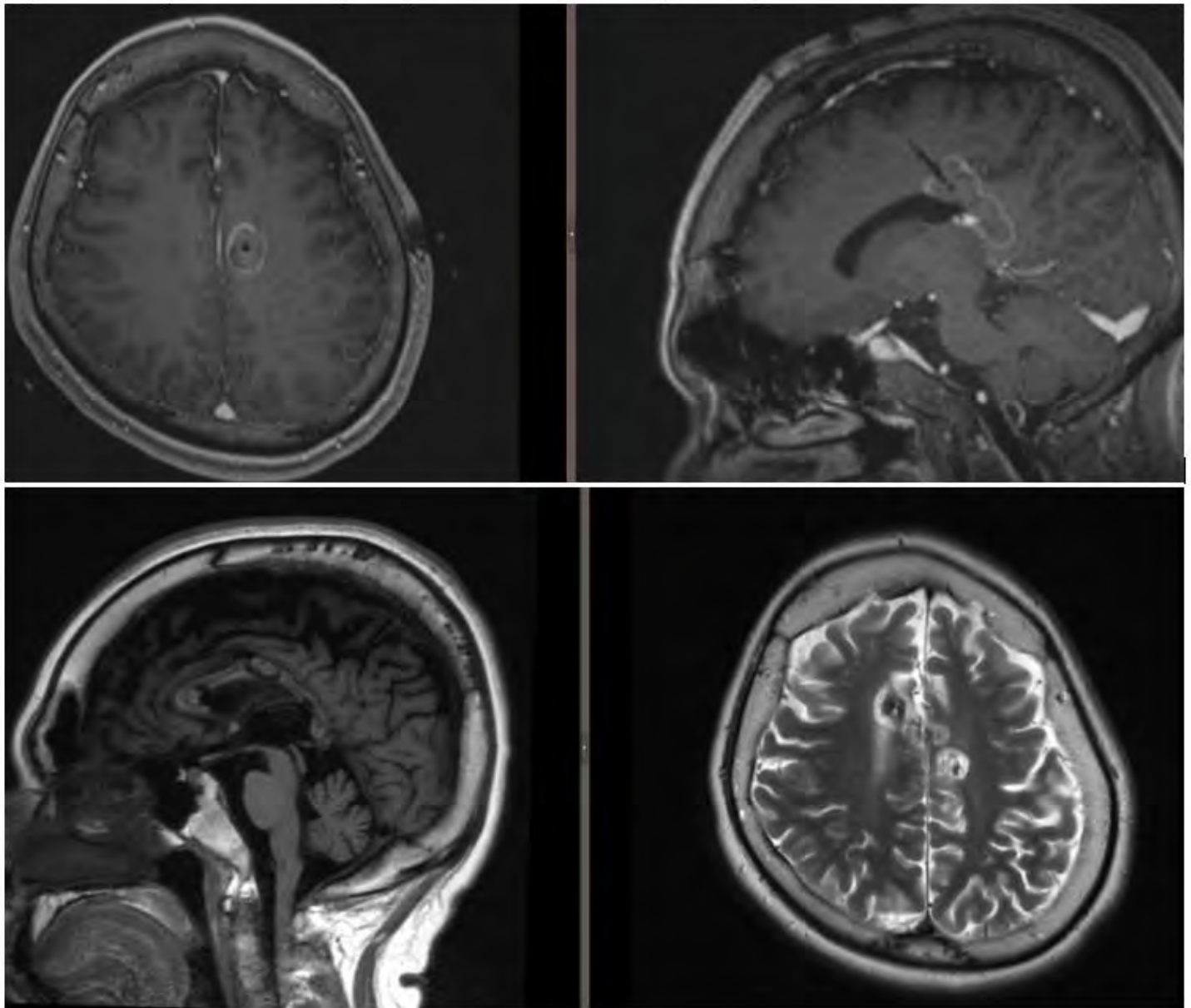
In this educational exhibit, we present multimodality peri- and post-procedural radiological findings of contemporary epilepsy treatments in a variety of cases and demonstrate how some of these change their imaging characteristics over time.

Results

We reviewed neuroimaging of epilepsy cases that were treated in a comprehensive epilepsy center.

Conclusions

1- Intracranial Electrodes – subdural, grid, and depth electrodes used to determine epileptogenic focus/network, surgical treatment and extent of surgery 2- Surgical treatment – traditional surgical resective techniques now include ablative techniques as well as limited transection techniques: • Focal Resection • Temporal Lobe Resection • Extratemporal Resection (frontal, parietal, or occipital) • Lesion resection • Multiple Subpial Transections. • Laser Interstitial Thermal Therapy. • Functional Hemispherectomy • Corpus Colostomy • Stereotactic Radiosurgery 3- Microinvasive neuromodulation - typically applied to a certain anatomical focus or network circuitry. There are three main types of neuromodulation in epilepsy that are approved by FDA • Vagus Nerve stimulation • Thalamic stimulation • Responsive focus stimulation Representative figure Figure 1. Laser ablation. No identifiable seizure focus found despite extensive investigation. Peri-operatively (top): peripheral enhancement with the hypointense laser tract centrally. 1-year later (bottom): Multiple foci of ablation and severe volume loss in corpus callosum. Callosotomy can help stop rapid bi-hemispheric seizure spread, that leads to catastrophic drop attacks.



(Filename: TCT_1348_callosotomy.jpg)

1322

Neurological Complications Related to Multiple Sclerosis Treatment: MRI Findings

W Calderon¹, P Puac Polanco², C Torres², A Vidal Jordana³, J Escudero-Fernandez⁴, J Castelló³, J Río³, C Auger⁵, A Rovira⁶
¹Hospital Universitari Vall d'Hebron, Barcelona, Catalonia, ²University of Ottawa, Ottawa, ON, ³Hospital Universitari Vall d'Hebron, Barcelona, Catalonia, ⁴N/A, Barcelona, Barcelona, ⁵Hospital Vall d'Hebron, Barcelona, Barcelona, ⁶Hospital Vall d'Hebron, Barcelona, Barcelona

Purpose

Summary: • Introduction. • Pathophysiology and phenotypic classification of multiple sclerosis. • Disease-modifying therapies: Mechanism of action, indications and side effects. • Imaging findings of neurologic complications. Objectives: • To review the pathophysiology and phenotypes of multiple sclerosis. • To discuss the mechanism of action, indications and associated risks of drugs usually prescribed in multiple sclerosis. • To illustrate the clinical presentation and imaging findings of treatment related complications in multiple sclerosis.

Materials and Methods

Multiple sclerosis (MS) is an idiopathic chronic inflammatory demyelinating disease of the CNS. Usually occurs between 20 and 50 years of age; with a highest prevalence in North America and Europe. The incidence of neurologic complications following MS treatment is extremely low. Serial MRI has allowed not only to assess the disease activity and therapeutic response, but also detect imaging abnormalities associated with immunomodulatory drugs. In this exhibit, we illustrate the neurological complications related to MS treatment based on our clinical experience.

Results

Our exhibit is focused on recognizing the relevant imaging features of neurological complications related to MS treatment, such as PML, PML-IRIS, Aman, aseptic meningoencephalitis, varicella-zoster meningovascularitis among other, through case-based discussions.

Conclusions

Disease modifying therapies for MS treatment are considered safe with few neurologic adverse events reported. Although rare, the most prevalent neurological complication is PML and PML-immune reconstitution inflammatory syndrome (IRIS). Serial MRI is useful for monitoring MS activity and for detecting treatment-induced complications.

Varicella-zoster meningovascularitis



Relapsing MS patient under NTZ treatment with continuous holocraneal headache and a new unsteady gait. Contrast-enhanced T2-weighted FLAIR images obtained after 12 infusions of NTZ (A) and after 72 infusions (B). The development of small leptomeningeal nodular lesions in both frontal lobes and left parietal lobe (arrows) were seen. Similar lesions were identified on the posterior fossa and spinal cord (not shown). MR angiography (C) showed irregularity of the proximal segments of the right middle and posterior cerebral arteries, and segmental fusiform dilatation of the proximal segment of the left middle cerebral artery and of its anterior temporal branch (arrows). MRI of the brain performed 3 weeks later (D) demonstrated multiple small deep acute infarcts on DWI, one of which involved the corpus callosum (arrow). A follow-up brain MRI performed 3 months later showed resolution of the leptomeningeal enhancement (E).

(Filename: TCT_1322_ASNR2021300.jpg)

380

Neuronal and Mixed Neuronal Tumors: How, When and Where? A Review Based On New WHO 2016 and cIMPACT-NOW update 6

A Ayres¹, S Ferracioli², J Takahashi³, R Moreno⁴, L Lima⁵, L Godoy⁶, G Bandeira⁷, C da Silva⁸, L Lucato⁹

¹ICESP- FMUSP, São Paulo, Sao Paulo, ²InRad - HC- FMUSP, Sao Paulo, -- SELECT --, ³HCFMUSP, São Paulo, SP, ⁴Department of Radiology, Memorial Sloan Kettering Cancer Center, New York, NY, ⁵ICESP - FMUSP, Sao Paulo, SC, ⁶Faculdade de Medicina da Universidade de São Paulo- FMUSP, Sao Paulo, Sao Paulo, ⁷Faculadde de Medicina da Universisdae de São Paulo, Sao Paulo, Sao Paulo, ⁸HCFMUSP - BRAZIL, São Paulo, São Paulo, ⁹N/A, N/A

Purpose

In the revised fourth edition WHO Tumor Classification of the Central Nervous System and cIMPACT-NOW update 6, the classification "neuronal and mixed neuronal-glial tumors", has expanded and now includes dysembryoplastic neuroepithelial tumor (DNET), gangliocytoma, ganglioglioma, Lhermitte–Duclos disease, desmoplastic infantile astrocytoma/ganglioglioma, papillary glioneuronal tumor, rosette-forming glioneuronal tumor, diffuse leptomeningeal glioneuronal tumor, central /extraventricular neurocytoma, multinodular and vacuolating neuronal tumor, and cerebellar liponeurocytoma. There are a growing number of entities included in this category, especially with the advent of molecular tools. In this educational exhibit, we will review the imaging, histopathology and immunohistochemical findings of our cases of neuronal and mixed neuronal-glial tumors.

Materials and Methods

To illustrate the typical imaging findings with with histopathological and IH correlations of neuronal and mixed neuronal tumors, with cases from our tertiary hospital. Also a literature review will be made.

Results

We will review illustrative cases of histologically proven neuronal tumors (gangliocytoma, Lhermitte–Duclos disease, central and extraventricular neurocytoma) and mixed neuronal-glial tumors (DNET, ganglioglioma, ganglioglioma anaplastic, papillary glioneuronal tumor, rosette-forming glioneuronal tumor, diffuse leptomeningeal glioneuronal tumor, multinodular and vacuolating neuronal tumor) from our hospital. The neuroimaging findings of each tumor were highlighted with histological and IH correlation.

Conclusions

As a group, neuronal and mixed neuronal-glial tumors are morphologically and genetically diverse, yet they share several similar features. They are characterized by the presence of neuronal cells (neurocytes or ganglion cells) and variable amounts of glial elements. Immunohistochemical findings reflect the presence of this double population, with variable positivity for GFAP or OLIG2 in the glial component and synaptophysin, MAP2 and NeuN in the neuronal component. Commonly, they may present with malformative vessels, calcifications, a loose background with cystic degeneration and extension to the subarachnoid space. The neuroimaging findings varies according to each tumor type. The location of the tumor is information that could contribute to narrow the diagnosis. In addition, they usually have little or no expansive effect, and may have typical image findings, as DNET.

Neuronal and Mixed Neuronal Tumors: How? When? Where? A Review Based On New WHO 2016 and cIMPACT-NOW update 6

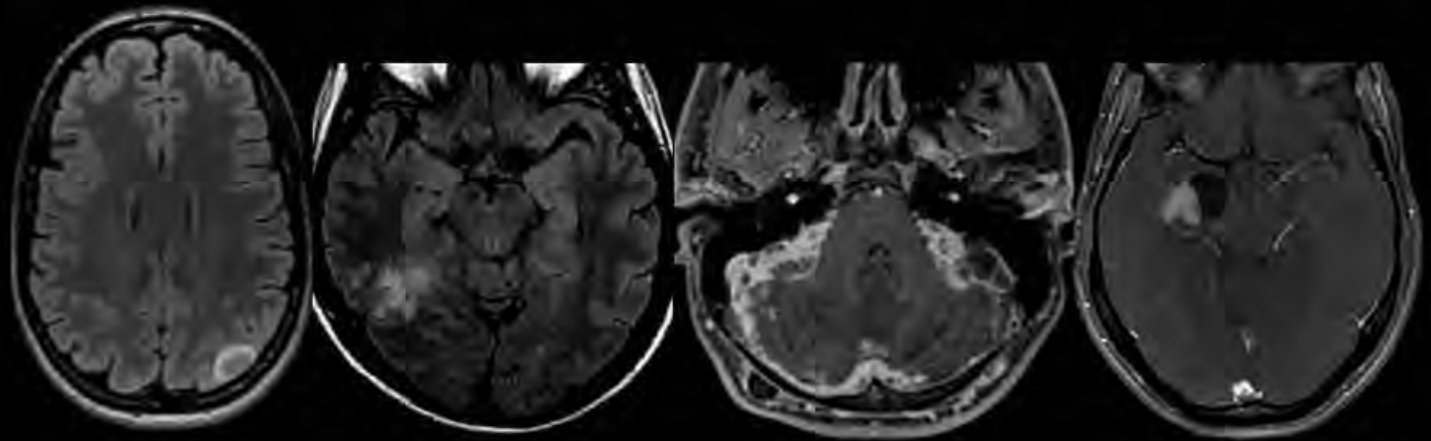


Figure 1:

- A. DNET.** Axial FLAIR image show an hyperintense expansive lesion in the corticosubcortical region of the left parietal cortex . This lesion is characterized by mismatch sign.
- B. Diffuse leptomeningeal glioneuronal tumor.** Axial post-contrast T1WI show multiple expansive lesions in the subarachnoid space, with post contrast enhancement.
- C. Multinodular and vacuolating neuronal tumor.** Axial FLAIR image with hyperintense multi cystic subcortical lesion in the right temporal lobe, with no mass effect.
- D: Ganglioglioma (grade I).** Axial post-contrast T1WI show an expansive cystic lesion in the right hippocampus, with a solid mural nodule, with post contrast enhancement.

(Filename: TCT_380_ASNRv2.JPG)

281

Neuroradiological Manifestations of Hematological Malignancies

A Pozdnyakov¹, S Lee², F Salehi²

¹McMaster University, Hamilton, Ontario, Canada, ²Juravinski Hospital, Hamilton, Ontario, Canada

Purpose

The primary objective of this educational exhibit is to present different radiological manifestations of central nervous system involvement in the setting of hematological malignancies. Secondary objectives include: a) formulate differential diagnoses for CNS abnormalities in patients with pre-existing hematological malignancies; b) identify key features that can characterize the abnormality by the primary malignancy origin; c) recognize iatrogenic pathologies that are associated with treatment of hematological malignancies.

Materials and Methods

This educational exhibit will provide neuro-radiologists with important differential considerations in patients with known hematological malignancies, as well as provide an overview of the imaging findings associated with various hemato-oncological CNS pathologies.

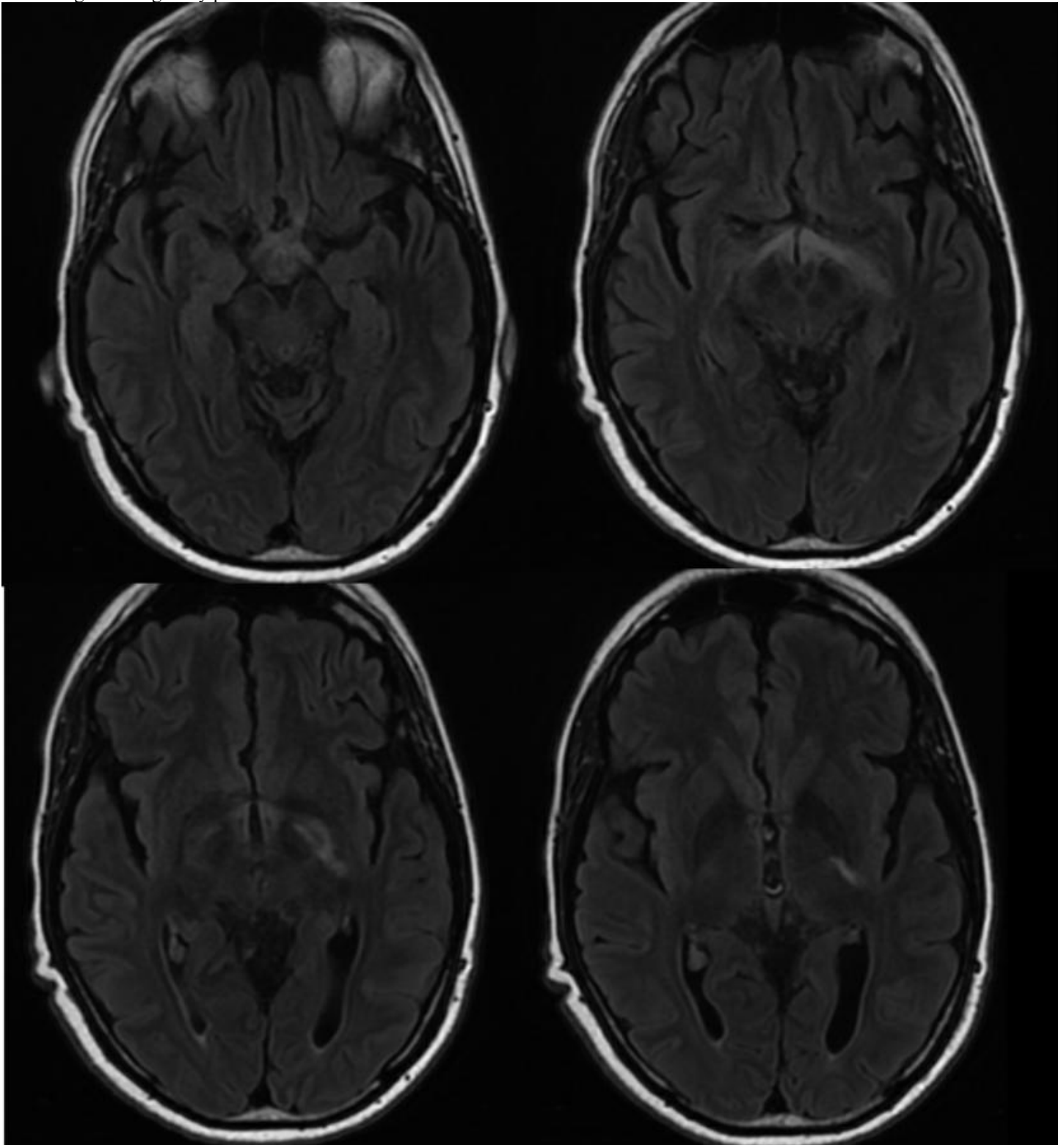
Results

This educational exhibit will be presented in a multi-slide PowerPoint format. Each category of the hematological malignancy will be presented in a respective section of the presentation and key findings will be accompanied with imaging illustrations selected from the database of our teaching hospitals, including our tertiary cancer center. The presentation will be divided into the following sections: a) Introduction and classification of hematological malignancies; b) primary CNS lymphoma; c) secondary CNS lymphoma; d) leukemia and myelogenous sarcoma; e) plasma cell neoplasms; f) histiocytic malignancies; g) post-transplant complications; h) treatment-associated complications; i) differential diagnoses of non-neoplastic origin in hematological oncology patients. Images included in the

abstract demonstrate a case of CNS leukemia (ALL) in a post stem cell transplant patient with enhancing nodules in the optic chiasm, optic tract and the mammillary bodies that responded to treatment.

Conclusions

This educational exhibit will be a valuable overview for radiologists who train or work in cancer centers with large populations of hematological malignancy patients.



(Filename: TCT_281_leukemiawithCNS.jpg)

M Mitry¹, S Strauss², D Holzwanger³, J Chazen⁴, G Salama⁵

¹New York Presbyterian Hospital-Weill Cornell, New York, NY, ²Weill Cornell Medical Center, Manhattan, NY, ³New York Presbyterian-Weill Cornell, New York, NY, ⁴Weill Cornell Medicine, New York, NY, ⁵Weill Cornell, New York, NY

Purpose

Image-guided interventions in neuroradiology play an integral role in both the diagnosis and treatment of many oncologic conditions. This educational exhibit reviews the range of image-guided interventions performed by neuroradiology as part of the care team for cancer patients, with specific discussion of indications and techniques for diagnostic and therapeutic procedures.

Materials and Methods

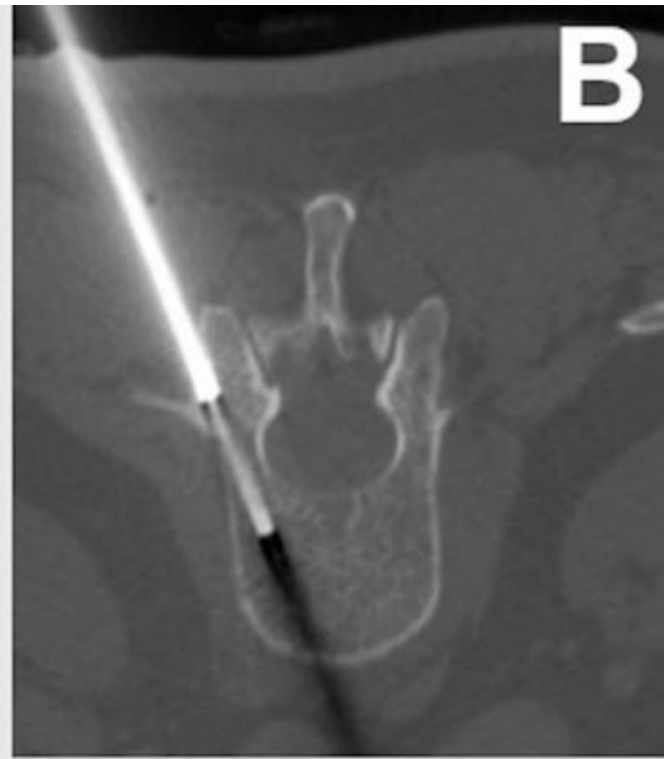
See "Summary and Objectives"

Results

Using a case-based approach, a variety of image-guided interventions in neuroradiology will be reviewed. Indications, techniques, and complications of these procedures will be discussed. Patient examples with intra-procedural and additional relevant imaging will be provided to demonstrate technique and pertinent anatomy.

Conclusions

Oncologic Image-Guided Interventions: Image-guided interventions aid in diagnosis, presurgical planning, and treatment of metastatic and primary disease in the head, neck, and spine as well as neuropathic cancer-related pain. CT-guided or MR-guided biopsy may be performed as part of initial investigation or evaluation for disease recurrence (1) (Figure 1A, B). CT myelogram and CT-guided fiducial placement play an integral role in radiation and surgical planning, and can help to reduce wrong level surgery and OR time (2). In terms of therapeutics, image-guided ablations and nerve and/or ganglion blocks and ablations can effectively reduce pain and improve function in patients with painful bone metastases or neurogenic pain (3) (Figure 1C). Both radiofrequency and cryoablation examples will be discussed. Finally, the indications and use of kyphoplasty, both balloon and implant, in the management of pathologic vertebral body fractures, will be reviewed (Figure 1D). **Conclusion:** Neuroradiologists often play an integral role in the delivery of oncologic care. A variety of image-guided interventions aid in diagnosis and treatment of a variety of conditions in the head, neck, spine, and paraspinal tissues. Familiarity with intervention techniques, relevant anatomy and indications allows neuroradiologists to offer diagnostic and therapeutic options for an often complex patient population, for which other treatment options have been ineffective or suboptimal.



(Filename: TCT_1469_Figure_ASNR.jpg)

1482

Neuroradiology Interesting Cases- a Ghanaian Perspective

K Twum¹, R Dwivedi²

¹Komfo Anokye Teaching Hospital, Kumasi, Africa, ²Worldwide Radiology & Salford Royal NHS Trust/Greater Manchester, Salford, Greater Manchester

Purpose

This educational exhibit provides a unique opportunity to share a selection of interesting neuroimaging cases from West Africa, as part

of a pictorial review with opportunity for interaction. We hope to demonstrate the scope for teleradiology mentoring for improving subspecialty training in radiology, particularly in low and middle income country settings, where radiology infrastructure including personnel is not sufficient to meet population demands.

Materials and Methods

To demonstrate the scope for teleradiology mentoring for improving subspecialty training in radiology

Results

A sample of cases, from the variety of neuroradiology studies discussed within the interesting case forum, have been presented. The four chosen studies aim to reveal the breadth of neuroimaging cases within the Ghanaian context. We highlight educational points and relevant differential diagnosis. Opportunities for discussion would be welcome.

Conclusions

Results Cases include neoplastic, infective aetiologies of the brain and spinal cord, in adult and paediatric populations. Conclusion This educational exhibit provides a unique opportunity to share a selection of interesting neuroimaging cases from West Africa, as part of a pictorial review with opportunity for interaction.

1479

Nodular Fasciitis in the Head and Neck

A Allen¹, S Ceglar¹, L Ledbetter², N Pham¹

¹UCLA, Los Angeles, CA, ²David Geffen School of Medicine, Los Angeles, CA

Purpose

Nodular fasciitis is a rare and challenging clinical entity to diagnose in the head and neck. Both clinically and histopathologically, the rapid progression and cellular composition can mimic malignant tumors. Thus, it is important to include this mass in the differential diagnosis, especially in a rapidly growing mass with antecedent trauma. Objectives: •To review the etiology, histology, and pathophysiology of nodular fasciitis in the head and neck. •To demonstrate the imaging patterns of nodular fasciitis in the head and neck. •To examine the salient imaging and clinical features of key differential diagnoses. •To review the natural history and treatment of nodular fasciitis.

Materials and Methods

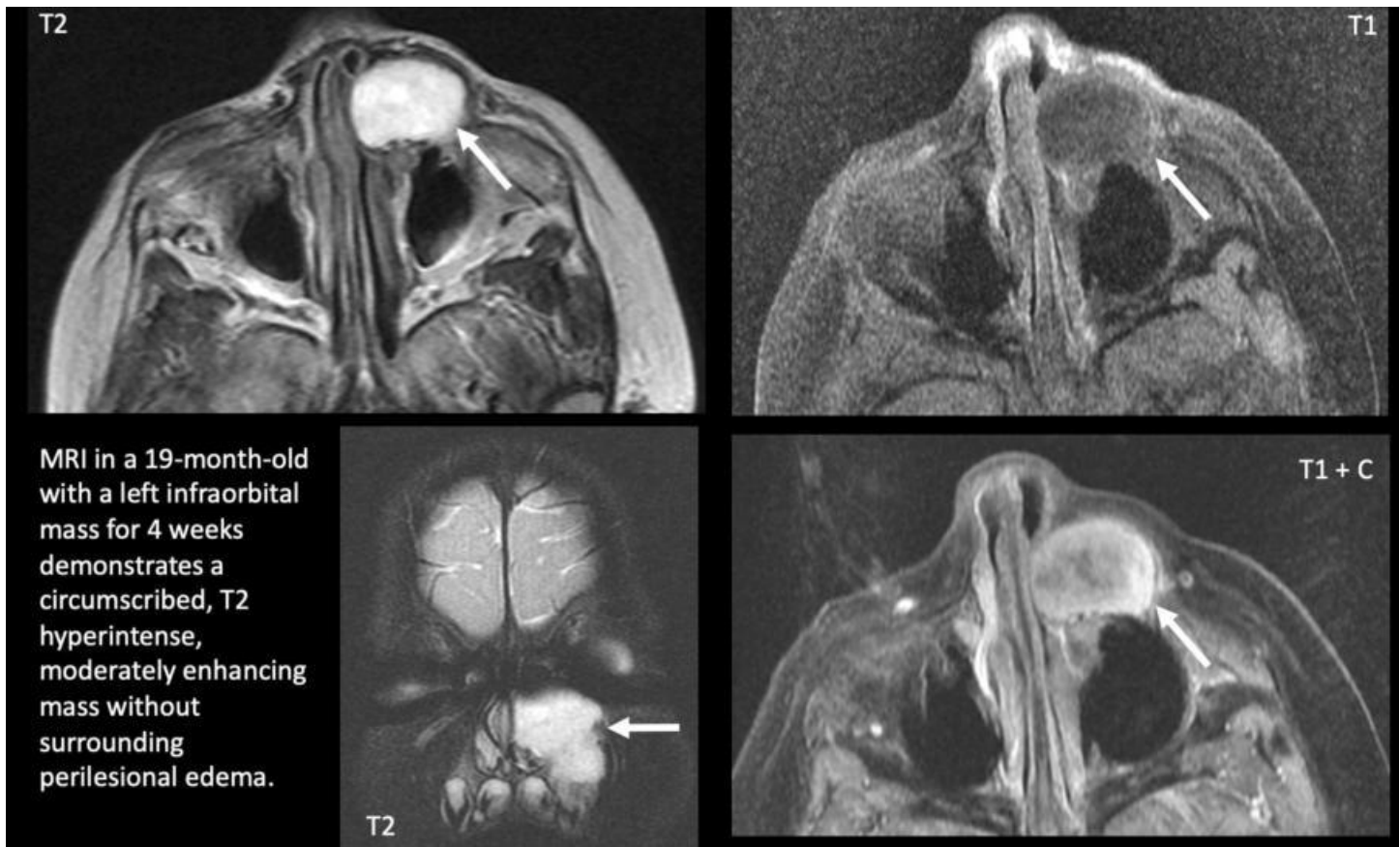
Nodular fasciitis is a benign tumor-like fibroblastic proliferative process often effecting the superficial soft tissues. Although the pathogenesis is unknown, antecedent trauma has been a proposed inciting factor (1). Nodular fasciitis most frequently involves the upper extremities, followed by the trunk and head and neck, which is a more common site in infants and children (1). It typically presents as a rapidly growing mass with pain and tenderness. Subtypes are based on anatomic location including subcutaneous, intramuscular and intermuscular locations (1). Treatment with surgical resection is often curative, however a trial of steroid injections and observation may be attempted. Histology demonstrates a tumor of variable cellularity with an extracellular matrix ranging from myxoid to collagenous. The lesion is composed of spindle stellate cells in a loose fibromyxoid stroma with a fascicular to storiform pattern. Contrast enhanced CT often demonstrates a well-defined soft tissue mass with moderate to avid enhancement in a superficial location. Cystic lesions can be seen and usually demonstrate peripheral, nodular or rim-like enhancement. On MRI, the signal intensity is variable and dependent on the amount of collagen, cytoplasm and water content (1). Most lesions demonstrate higher signal intensity than muscle on T2-weighted imaging due to abundant collagen. In contrast, fibrous lesions show reduced signal intensity on all pulse sequences.

Results

N/A

Conclusions

Nodular fasciitis of the head and neck can present as a discrete solid or cystic mass, which can frequently mimic malignant tumors. Although rare, it is important to have an awareness of this entity in the appropriate clinical context, as the diagnosis is often difficult to make by imaging or pathology alone.



(Filename: TCT_1479_NodularFasciitisCase.jpg)

238

Noninvasive Imaging of Treated Intracranial Aneurysms – A Comprehensive Pictorial Review of Current CTA and MRA Techniques

C Liang¹, S Walia¹, J Woo¹, V Patel¹

¹University of Pennsylvania, Philadelphia, PA

Purpose

N/A

Materials and Methods

Conventional CT and MR angiography (CTA/MRA) are powerful noninvasive imaging tools to detect cerebral aneurysms; however, artifacts can diminish their ability to detect residual or recurrence after surgical and endovascular treatment. Digital subtraction angiography, the gold standard for follow-up, still carries a low but non-zero risk of complication. Hence, there is growing interest in methods to improve noninvasive imaging techniques to follow treated aneurysms, with an increasing number of studies demonstrating their effectiveness. The topic is complicated by no clear consensus on the imaging test of choice, and significant variations between institutions. Knowledge of these techniques and their efficacy can assist the radiologist in selecting, recommending, or performing the best imaging test for patients with treated aneurysms.

Results

We start with a review of aneurysm treatment devices, including some recently approved. We then discuss numerous published methods to improve standard CTA and MRA techniques.

Conclusions

We first review various aneurysm treatment devices, including surgical clipping and endovascular therapy such as coiling, flow diverters/Pipeline, and flow disruptors/WEB devices. We then review the noninvasive imaging techniques, including their advantages and limitations, with review of the literature for: conventional and dual-energy CTA, time-of-flight (TOF) MRA including ultrashort echo-time (TE), and conventional and time-resolved (TR) contrast-enhanced (CE) MRA. Briefly, in addition to adjusting conventional CTA scanning parameters, dual energy CTA has shown reduced artifact while also optimizing contrast. Iterative metal artifact reduction algorithms improve the unenhanced but not CTA appearance after clipping/coiling. CTA is more limited after coiling compared to MRA due to beam hardening artifact from the coil mass, whereas it is more useful after clipping or stenting. Short TE further reduces coil susceptibility artifact on TOF MRA. CE-MRA has shown improved visualization over TOF after coiling and flow diverters, with further advantages of TR CE-MRA over both TOF and conventional CE-MRA. We highlight these differences via an

image-rich format throughout the exhibit. Noninvasive imaging techniques are increasingly utilized to follow treated aneurysms. Readers of this exhibit will learn the available techniques and better understand their advantages/limitations, helping to optimize image interpretation and patient management.

428

Normal Maturation Anatomy and Variants of the Pediatric Cervical Spine

p aouad¹, M Serhal², S Moum³, P Assaad³, S Palasis³

¹*northwestern university, chicago, IL*, ²*Lebanese University, Beirut, Lebanon*, ³*Ann & Robert H. Lurie Children's Hospital of Chicago, Chicago, IL*

Purpose

Knowledge of the normal development and common variants in the pediatric cervical spine is crucial to avoid pitfalls in evaluating traumatic spinal injury. The morphology, normal parameters, and patterns of injury of the cervical spine in children are different than in adults.

Materials and Methods

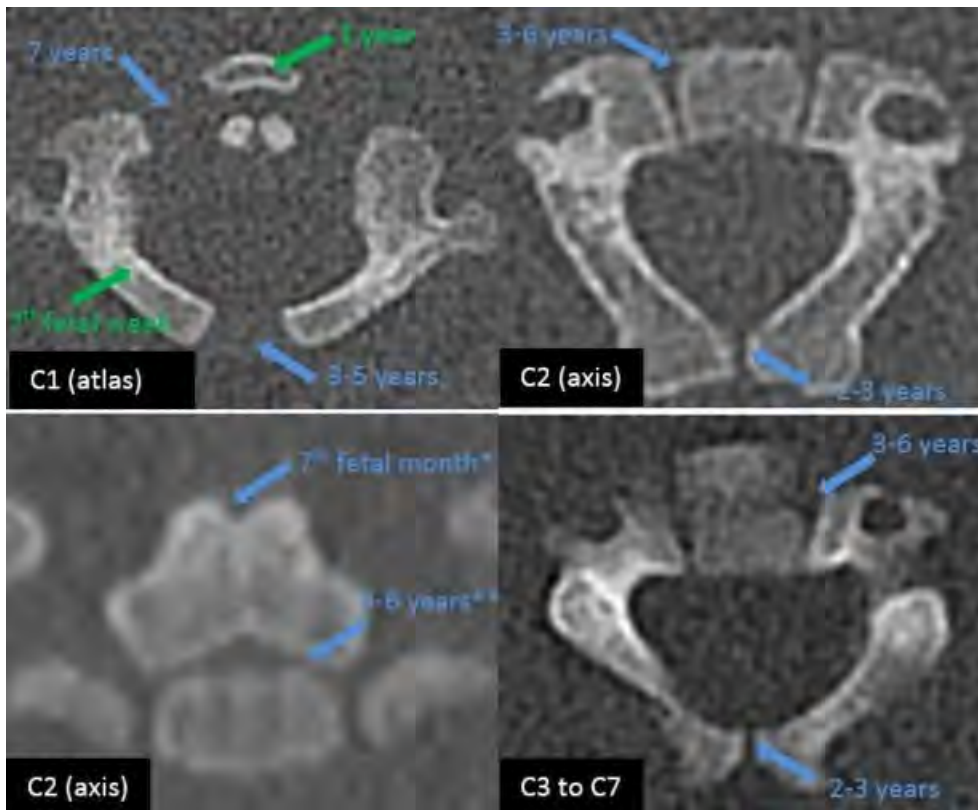
Review the developmental anatomy, normal variants and common types of injury found in the pediatric cervical spine. Differences between pediatric and adult cervical spine imaging will also be reviewed.

Results

Normal development: • C1 (i.e. atlas) has three ossification centers: the anterior arch and two neural arches. • C2 (i.e. axis) has six ossification centers: two for the dens, right and left; two neural arches; the centrum; and the tip of the odontoid. • C3 through C7 have three ossification centers: one centrum and two neural arches (1). Normal parameters, variants, and pitfalls: • Synchondroses are regular, corticated and occur in predictable locations. Acute fractures are irregular, not sclerotic and can occur in any location. • Secondary ossification centers occur at the tip of the transverse and spinous processes and can be seen up to the 3rd decade. • Secondary ossification centers can be seen at the superior and inferior aspects of vertebral bodies and can persist to early adulthood. • "Pseudo-Jefferson fracture" defined as displacement of the lateral masses relative to the dens on open-mouth view <6 mm occurs in children until 4-7 years of age. • C2-C3 pseudosubluxation defined as normal mild anterior positioning of C2 relative to C3 is common before 8 years of age. If the anterior edges of the spinous process of C1, C2 and C3 are 2 mm or more of each other, bilateral pars interarticularis fracture of C2 are likely present ("Hangman's fracture"). • The posterior intraspinous distance should be ≤ 1.5 times the intraspinous distance one level above or below. Widening of the distance between the C1 and C2 spinous process tips is normal on flexion radiographs. • The posterior ring of C1 can remain cartilaginous. The ossification center of the C1 anterior arch may not form or may be bipartite or multiple. • Anterior wedging of the vertebral bodies up to 3 mm can be normal, most pronounced at C3. • Widening of the prevertebral soft tissues can be normal during expiration (1, 2).

Conclusions

Recognition of the normal development and anatomic variants of the pediatric cervical spine is essential to avoid pitfalls and unnecessary work-up.



CT images of C1, C2, and a lower cervical vertebra (C3 to C7) illustrating the age of appearance of ossification centers (in green) and fusion of the synchondrosis (in blue). Note that the sagittal synchondrosis of the dens fuses during the 7th fetal month but may remain visible (*). The synchondrosis between the dens and the centrum fuses at 3-6 years but a remnant may remain visible until 11 years (**). The tip of the dens is a secondary ossification center that appears at 3-6 years and fuses with the dens at 10-12 years (not shown).

(Filename: TCT_428_figurecervicalspine300.jpg)

1487

Not Just a Pipe Dream: Multimodality Vascular Imaging Techniques in Neuroradiology

G Singh¹, E Mtui², A Famuyide³, V Spektor⁴

¹Newark Beth Israel Medical Center, Newark, NJ, ²New York Presbyterian, New York City, NY, ³New York-Presbyterian, Columbia, New York City, NY, ⁴New York-Presbyterian Hospital, Columbia Campus, Radiology, Rockaway, NJ

Purpose

Multiple angiographic imaging techniques have been introduced and refined over the years. Vascular imaging techniques are used in nearly all imaging modalities to answer a variety of questions. Vascular imaging is encountered in acute and outpatient settings, academic and non-academic, and requires general and neuroimaging specialists to be aware of their uses. We will provide an overview of vascular imaging techniques in neuroradiology and outline the major indications, advantages, and disadvantages of CT and MRI-based vascular imaging techniques.

Materials and Methods

Imaging technology constantly evolves. The existing techniques improve, new techniques are developed, and new paradigms become available within the arsenal of medical tools. DSA, MRI, and CT were once reigned as the options available and were under Neuroradiologist's purview. As those techniques have evolved, several new technologies have appeared as well, and some of them are mainly driven by other specialists. It is important for us not only to keep up and understand our technologies but also to learn about other technologies available for patient care. MRI remains the single most important tool in the entire neurologic diagnostic armamentarium. One reason it gained this role is incredible versatility and variety of MRI. Choosing the right sequence or a set of sequences became a daunting task. Several MRA techniques are readily available for our use, each with its own set of advantages and limitations. In addition, we now have several different techniques to do MR Perfusion, Permeability imaging, and vessel wall imaging. CTA has also evolved, and what used to be a purely intraluminal imaging technique is now developing new abilities to provide high-resolution structural information and even dynamic information. Trans-cranial Doppler ultrasound is now widely used in neurological intensive care units, and while it is primarily outside of neuroradiologist's daily work, we should learn to understand it. The purpose of this educational poster is to provide an update and resource for trainees and radiologists at all stages of their careers.

Results

Literature review of neuroradiology, neurology, and neurosurgery literature was conducted to select the most important imaging methods. The methods are summarized, including fundamental physics principles, utility, and potential pitfalls, including examples of each technique.

Conclusions

N/A

Not Just Another Number: Laboratory Values and Their Use in Diagnosing Disease in the CNSD Luu¹¹*Staten Island University Hospital, Northwell Health, Staten Island, NY***Purpose**

Patient care is multifaceted and nuanced, requiring that physicians have all available information at their disposal. This is especially applicable to neuroradiologists, as they make countless difficult diagnostic decisions with each image they view. These images, taken at face value with no history or labs for background, would often be indiscernible. For example, take meningitis. The most common CT finding associated with meningitis is hydrocephalus. This finding alone has a multitude of differential diagnoses, ranging from the relatively benign normal pressure hydrocephalus to more sinister etiologies like obstructive tumors or meningitis. In contrast, if this hydrocephalus was assessed in conjunction with a lumbar puncture showing decreased glucose, elevated protein, and a positive Gram stain, it would be surprising if any neuroradiologist did not indicate bacterial meningitis to be the most likely diagnosis in their impression. A neuroradiologist may not be able to personally see and assess each patient, but lab values can provide invaluable tools to streamline differentials and provide more accurate impressions, leading to improved patient care.

Materials and Methods

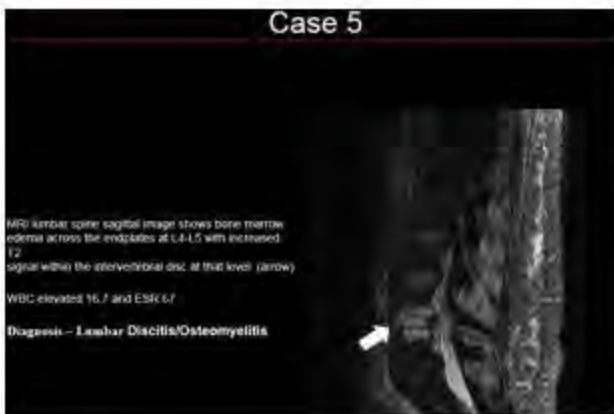
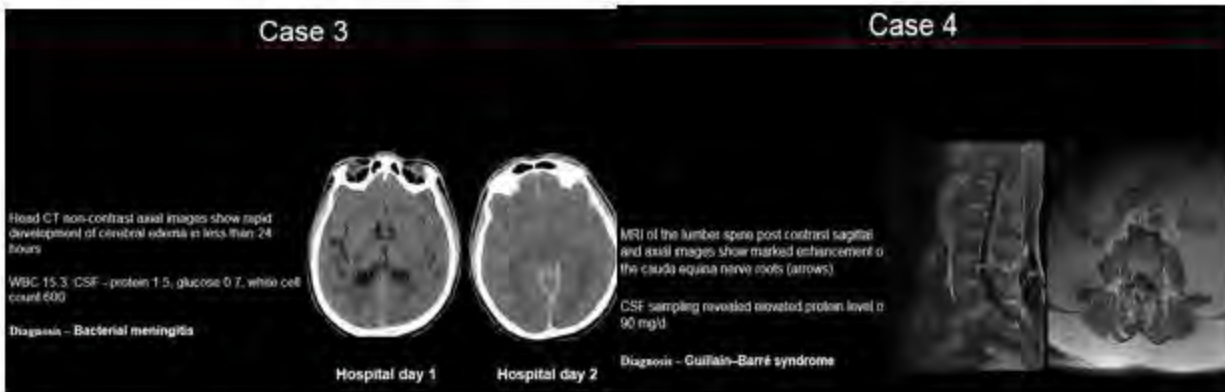
The purpose of this exhibit is to emphasize the importance of viewing images in the context of the patient. This is both to encourage neuroradiologists to explore the clinical picture behind each patient's image, as well as to provide insight to non-radiologist practitioners about what labs they can order to assist a neuroradiologist when requesting studies.

Results

Presentation of 5 cases where laboratory values along with imaging findings work together to help make the diagnosis. 1. Blood tests – WBC, ESR, vitamin B12, IG4, hematocrit, Prolactin 2. Lumbar puncture – oligoclonal antibodies, NMO antibodies, Lyme markers, glucose/protein/WBCs 3. Antibodies – anti-Ro/La, lupus antibodies, beta-2 transferrin antibodies, HLA B27 4. Miscellaneous – SPEP/UPEP

Conclusions

We may not be able to personally see and assess each patient. However, values can provide invaluable tools to streamline differentials and provide more accurate impressions, leading to improved patient care.



(Filename: TCT_301_Cases.JPG)

676

Ocular and visual disturbance – inside the brain, what remain?

I Alves¹, A Vieira², G Chaves², C Roca², C Amancio², C Leite³

¹Hospital Sírio-Libanês, São Paulo, Brazil, ²Hospital Sírio-Libanês, São Paulo, São Paulo, ³University of São Paulo, São Paulo, São Paulo

Purpose

Neuro-ophthalmic disorders have a broad spectrum of differential diagnosis and many diseases with ophthalmic manifestations may have a normal orbit evaluation. The optic tract and its connection are long and each involvement point has a different clinic manifestation, including brain diseases. The objective of this pictorial essay is to review optic tract anatomy, focusing on the encephalic paths and discuss the brain disorders with ophthalmic manifestations.

Materials and Methods

1. Review optic tract anatomy 2. Correlate ophthalmic clinical findings with optic tract lesion 3. Describe the afferent and efferent visual pathway 4. Discuss the pathologies differential diagnosis of brain disorders with visual manifestations

Results

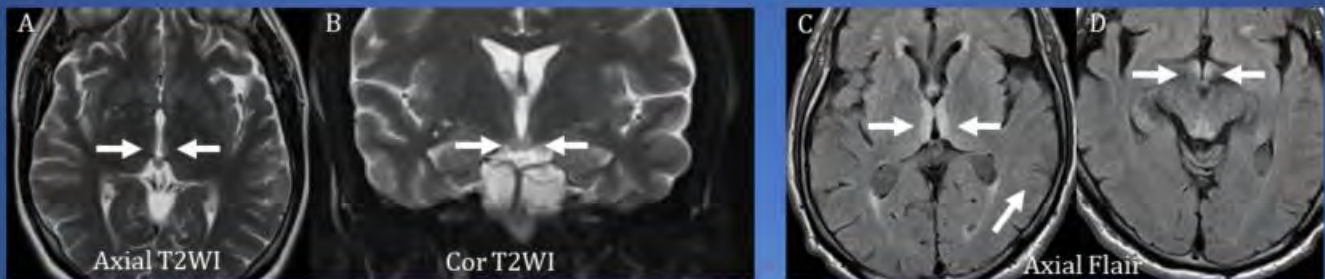
The eye has been described as a window to the brain, many visual manifestations are associated with brain disorders. The retrochiasmatal visual pathway is composed by optic tracts, lateral geniculate bodies, optic radiations and visual cortices while the brainstem and cerebellum are involved in efferent visual function. Therefore, many pathologic processes can show as visual disturbances, such as demyelination, trauma, hemorrhage, osmotic myelinolysis, neurodegenerative diseases, hypoxic/ischemic injury, tumors, infections and vascular malformations.

Conclusions

Localizing the cause of visual disturbances sometimes requires looking beyond the eyes. The clinical findings may help to localize where is the disturbance and the neuroradiologist should understand these clinical manifestations to know where to search. The whole afferent and efferent visual pathway may be involved and neuroimaging is a fundamental tool to ancillary the diagnosis.

OCULAR AND VISUAL DISTURBANCE

Inside the brain, what remain?



Nystagmus. Two different cases but same pathology. Notice the hypersignal on Flair and T2WI on medial thalamus (A and C) and mammillary bodies (B and D), suggestive of Wernicke encephalopathy.

(Filename: TCT_676_ImagensASNR.jpg)

912

Odontoid: Development, Anomalies and Disease Processes.

M Krycia¹, F Memon²

¹Henry Ford Hospital, Royal Oak, MI, ²Yale University, New Haven, CT

Purpose

Summary: Development, relevant anatomy, congenital anomalies and disease processes affecting the odontoid are discussed.

Objectives: 1. Discuss embryologic development of the odontoid. 2. Discuss relevant anatomy including pertinent ligaments. 3. Discuss congenital anomalies of the odontoid. 4. Discuss common as well as rare disease processes affecting the odontoid.

Materials and Methods

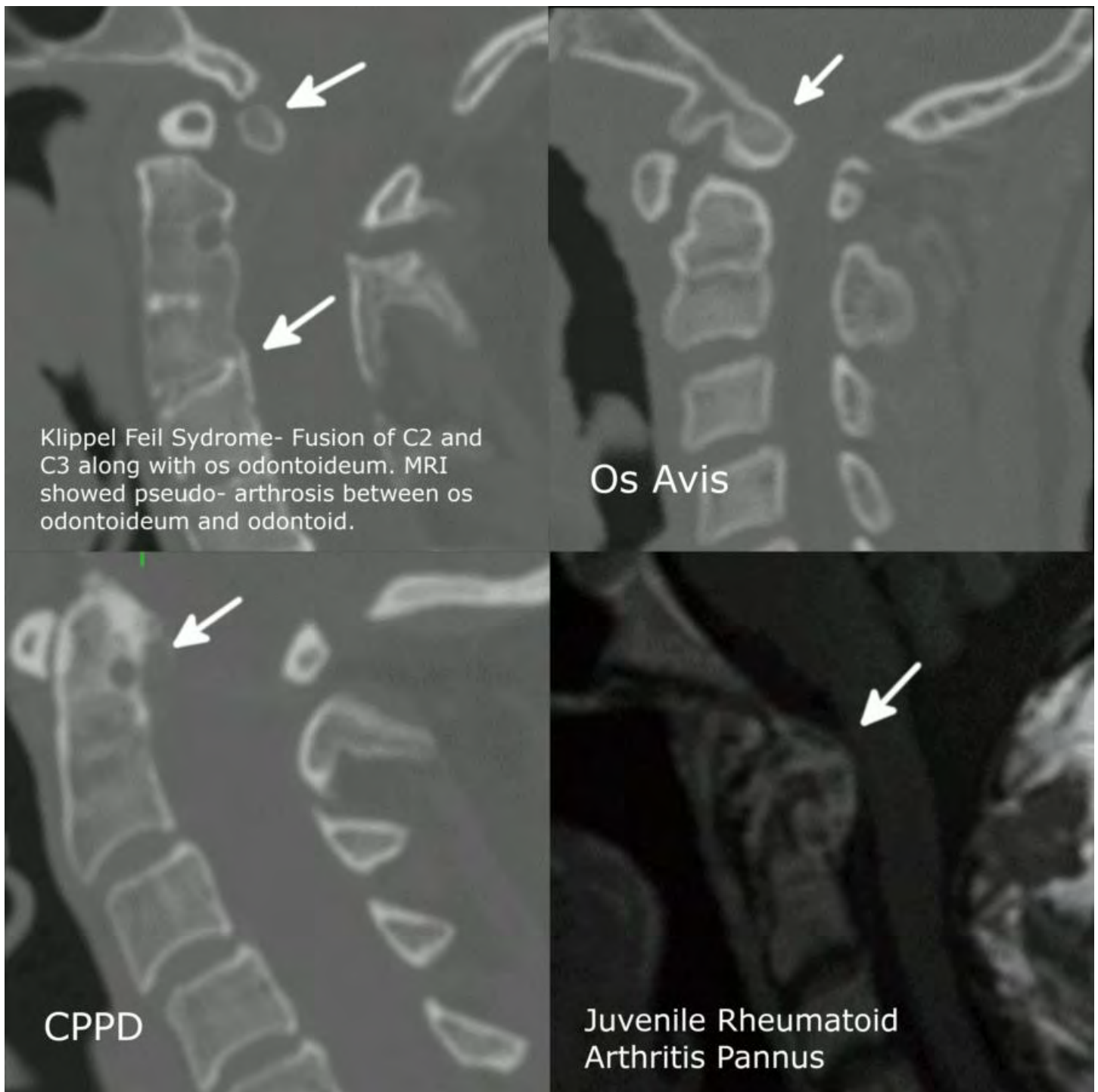
To discuss development of the odontoid as it pertains to congenital anomalies. To provide a detailed account of common and rare disease processes affecting the odontoid with emphasis on sharing images for all diseases discussed.

Results

The Yale university case archives for the last 20 years were searched with key search word 'odontoid'. All available reports were studied and all abnormal cases were studied. Observations were made and recorded. Existing text and literature was studied.

Conclusions

Knowledge of relevant embryology and anatomy aids in the understanding of congenital anomalies affecting the odontoid. Disease processes affecting the odontoid can have typical and non-typical appearances. This aims to familiarize readers with different radiologic appearances of a vast variety of common and rare anomalies and disease processes affecting the odontoid.



(Filename: TCT_912_Odontoid.gif)

749

Optimizing Communication and Patient Care with Common Data Elements in Spine Reporting

R Frederick¹, W Gibbs²

¹Mayo Clinic Arizona, Phoenix, AZ, ²Mayo Clinic, Scottsdale, AZ

Purpose

Teaching points 1. Discuss the evolution of the radiology report, and the potential to improve communication and patient care, to enhance our value by facilitating integration of evidence and guideline based management recommendations, and to prepare for future requirements of artificial intelligence and natural language processing. 2. Describe the concepts of standard terminology, common data elements, and CDE macro sets. 3. Detail specific use cases in spine radiology Table of Contents/Outline I. Introduction A.

Radiology reporting: past present and future B. What is standard terminology and why is it vital for humans and machines C. How does use of standard terminology benefit the patient, surgeon, and radiologist in spine care D. Common Data Elements (CDE) and CDE macros II. Case 1: Osseous spinal metastatic disease A. Rationale behind creation B. Spinal Instability Neoplastic Score C. Epidural Spinal Cord Compression Scale D. NOMS Criteria for individualized patient management in spine oncology III. Case 2: Cervical spine deformity A. Rationale behind creation B. CDE Macro: C2-7 SVA, C2-7 Cobb, T1 slope, CBVA C. Added radiology value and collaboration with spine surgeons in optimizing surgical planning, minimizing patient risk, and building machine learning algorithms predicting outcomes

Materials and Methods

Please see summary and objectives.

Results

Use cases are presented that detail rationale behind creation, literature support, images/ cases as explanatory examples.

Conclusions

Please see summary and objectives.

Cervical Deformity

- **Rationale:**
 - Adult spinal deformity (due to degenerative change) affects up to 68% of people over 65 years, as well as younger patients with ankylosing spondylitis, rheumatoid arthritis, and scoliosis
 - Deformity has substantial debilitating effects on patients' general health and quality of life
 - Compensatory mechanisms that occur are primarily focused on maintaining horizontal gaze
 - Treatment planning is based on clinical (gait & posture) assessment + radiology assessment
- **Macro components:**
 - C2-7 Cobb
 - C2-7 SVA
 - T1 Slope
 - **CBVA: Chin brow vertical angle characterizes loss of horizontal gaze, one of the most debilitating aspects of deformity, compromising all activities of daily living**



Patient: John Doe
EXAM: Cervical Spine radiographs
INDICATION: Neck pain., rheumatoid arthritis, preoperative evaluation.
FINDINGS: Chin on chest deformity. Pedicle screw and rod hardware fixation T1-T4. 12mm anterolisthesis C2 on C3. Moderate loss of disc space height at all cervical levels.

C2-7 Cobb:	Cervical deformity CDE macro
C2-7 SVA:	
T1 slope:	
CBVA:	

IMPRESSION:

(Filename: TCT_749_ASNRCDE.jpg)

320

Orbital Emergencies in a Blink: What the Radiologist Should Know

E Gil¹, R Loureiro², D Sumi², H Tames³, C Soares², K Oliveira², L Coelho², R Murakoshi², R Gomes², M Daniel²
¹Hospital Albert Einstein, São Paulo, Brazil, ²Hospital Israelita Albert Einstein, São Paulo, São Paulo, ³University of São Paulo, São Paulo, São Paulo

Purpose

Orbital emergencies are common in emergency departments, and the consequences of these pathologies may be devastating if not correctly diagnosed and treated. The radiologist plays a vital role in this process, therefore it is essential to recognize the main features and mechanisms involved. This educational exhibit provides a systematic approach and a practical overview of orbital emergencies.

Materials and Methods

1- Present an overview of the anatomy and mechanism involved in orbital emergencies. 2- To demonstrate the imaging appearances of typical and atypical orbital emergencies. 3- Develop a classification scheme with a list of pathologies based on the region of involvement and create a flowchart to help the radiologist avoid misinterpretations and improve diagnostic rate.

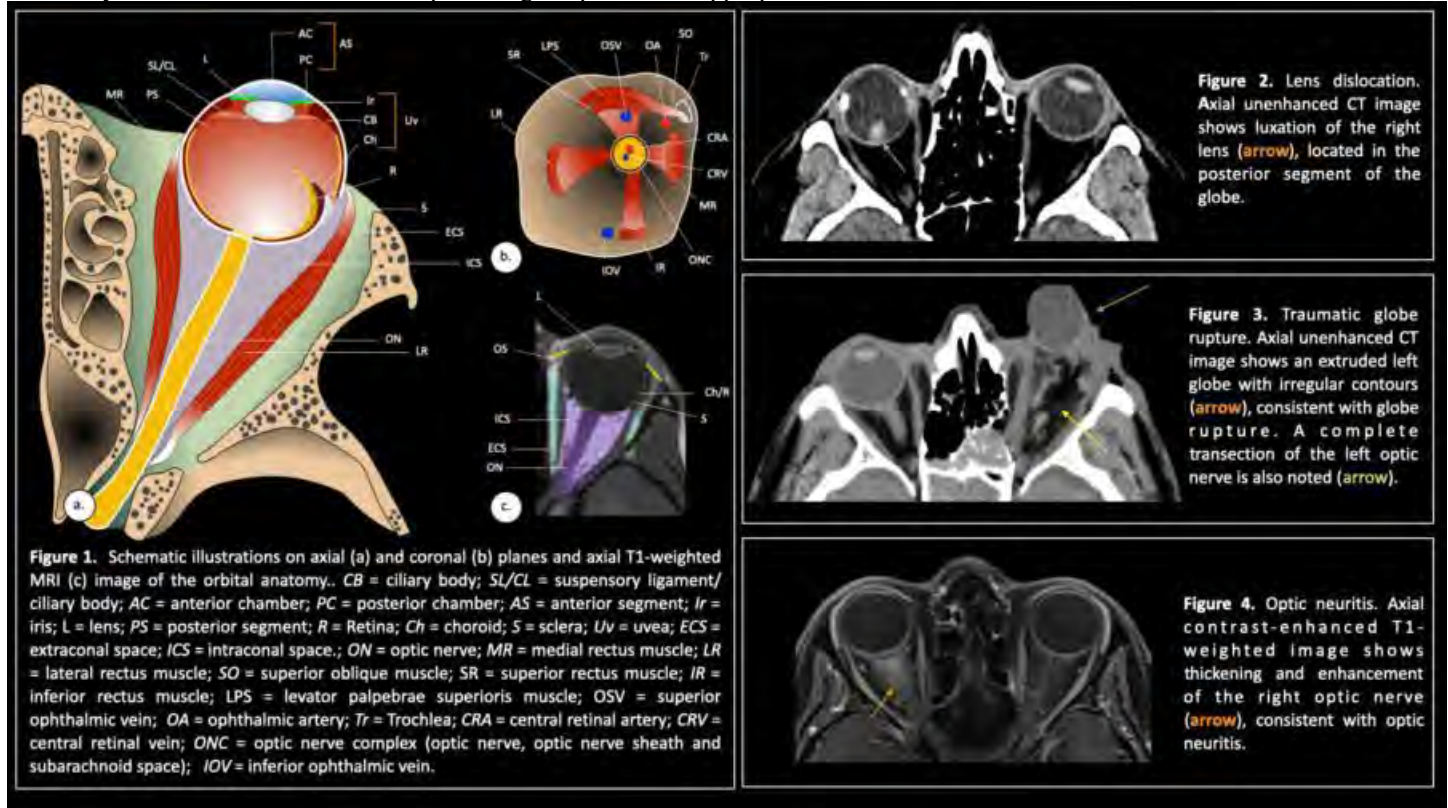
Results

Review of the current literature to identify the main characteristics of orbital emergencies, and a radiology database search and electronic medical record review for the following pathologies: hemorrhages, retinal, choroidal and posterior vitreal detachments, lens dislocations, foreign bodies, globe rupture, abscess, endophthalmitis, idiopathic inflammatory disease, immunoglobulin G4-related,

thyroid-associated orbitopathy, optic neuritis, graft-versus-host-disease, papilledema and pitfalls such as primary orbital amyloidosis and venous varix.

Conclusions

Emergency orbital pathology represents a significant number of emergency department consults. It is fundamental that radiologists accurately detect these conditions, thus providing the patient the appropriate treatment and best outcome.



(Filename: TCT_320_OrbitalEmergencies001.jpg)

1578

Orbital Pseudotumor Spectrum: A Pictorial Review

V Jirankali¹, S Patwari²

¹Columbia Asia Referral Hospital, Bengaluru, Bengaluru, India, ²Columbia Asia Referral Hospital, Bengaluru, Bengaluru, Bengaluru

Purpose

1. To recognize the key imaging findings of each orbital pseudotumor subtype. 2. To know the differential diagnosis of each orbital pseudotumor subtype and tips on arriving at a correct diagnosis.

Materials and Methods

1. To demonstrate the CT and MRI findings in idiopathic orbital inflammation. 2. To recognize the key imaging findings of each orbital pseudotumor subtype. 3. To know the differential diagnosis of each orbital pseudotumor subtype and tips on arriving at a correct diagnosis.

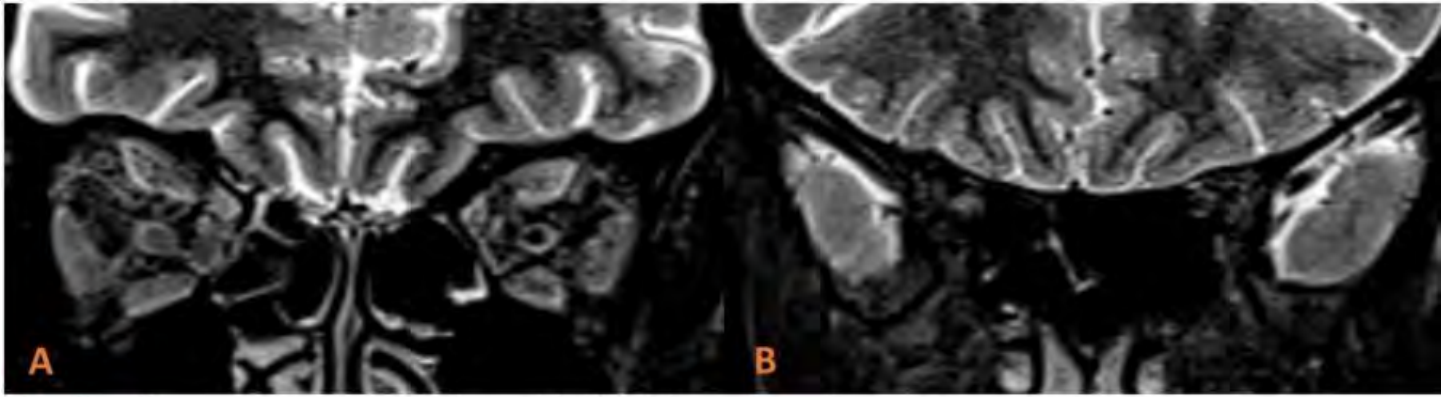
Results

We will present the spectrum of orbital pseudotumors using the representative cases of each subtype of orbital pseudotumor from our institution. Contrast CT scans of orbit and MRI scans of brain and orbits (T1/T2/STIR/T1 Fat sat and Post contrast T1 sequences) will be analysed for the orbital lesions.

Conclusions

Results: Following are the subtypes of orbital pseudotumors [1]: 1. Scleritis 2. Uveitis 3. Dacryoadenitis 4. Optic perineuritis 5. Optic neuritis 6. Myositis 7. Cellulitis In addition to the above subtypes, we have also found few multicompartmental diseases which involve more than one compartment as described above. We have encountered with all subtypes of pseudotumors as mentioned above except for dacryoadenitis. In few of the orbital pseudotumors which we reviewed, lacrimal gland was involved as a part of multi-compartmental disease process, but sole involvement of lacrimal gland (dacryoadenitis) was not found. Following approach was followed: 1. Radiological findings with clinical correlation to identify inflammation and to differentiate it from orbital infection and tumor. 2. Identification of radiological patterns and sites of involvement – so that the disease can be assigned to a particular subtype of pseudotumor. Conclusions: 1. There is significant overlap in the imaging findings of orbital pseudotumors, infection and neoplasms.

Hence, it is important to recognize the key radiological findings with clinical correlation so that correct diagnosis can be made and proper treatment can be initiated. 2. Utility of MRI helps in delineating the compartments of the orbit involved. .



A. Swollen extra-ocular muscles with STIR hyperintensity

B. STIR hyperintensity along posterior segment of right optic nerve

(Filename: TCT_1578_ASNR400.jpg)

365

Pachymeningeal Enhancement: A Case Based Review

N HYSON¹, B Griffith², S Patel³, P Doshi²

¹Henry Ford Hospital, Detroit, MI, ²Henry Ford Health System, Detroit, MI, ³HENRY FORD HOSPITAL, DETROIT, MI

Purpose

N/A

Materials and Methods

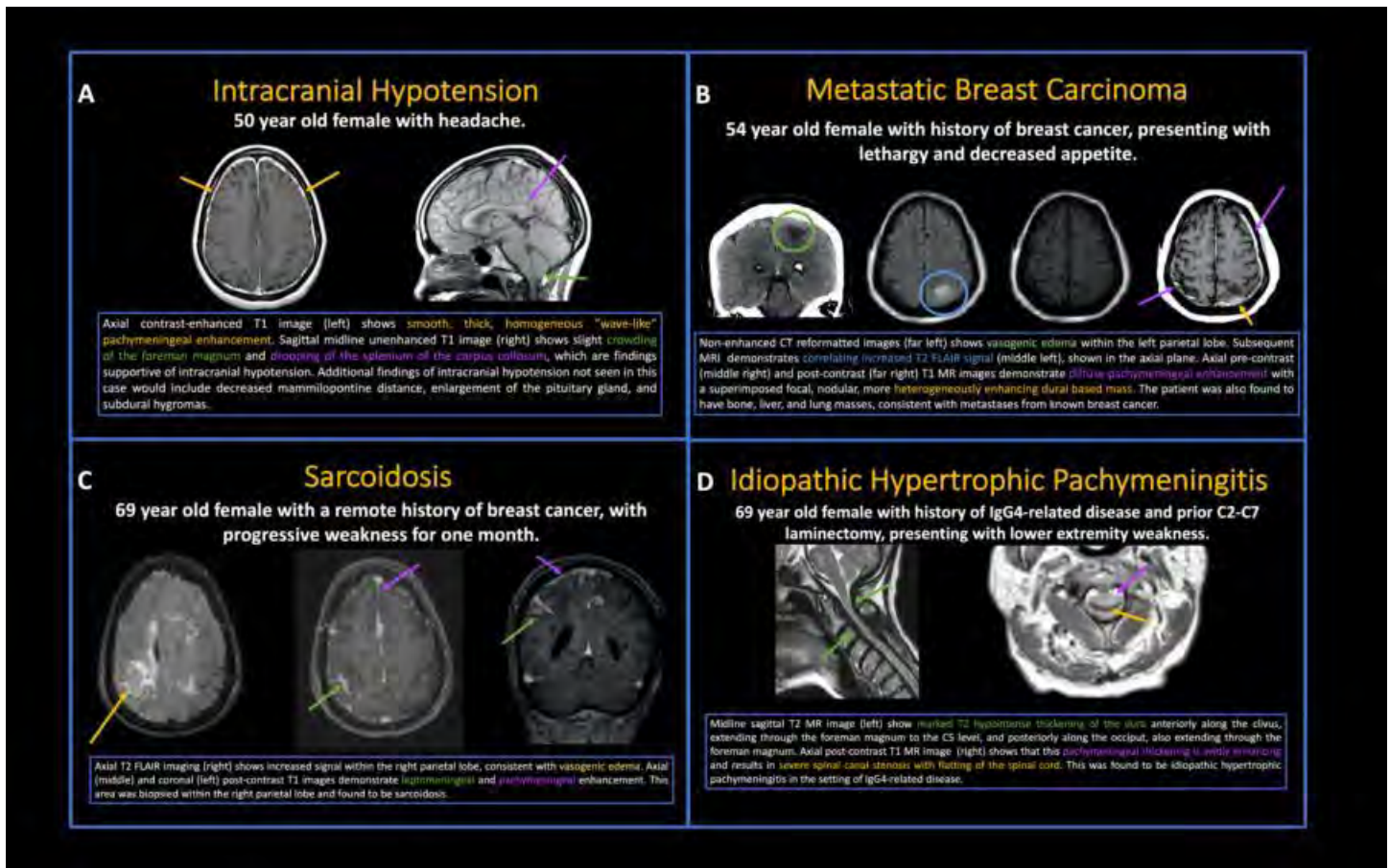
Pachymeningeal enhancement can be due to a broad range of causes – including both neoplastic and non-neoplastic. In this exhibit, we will present a series of cases from our teaching files on disease involving the pachymeninges. In doing so, we hope to broaden the radiologist's differential while providing clinical and imaging clues to aid in suggesting a diagnosis.

Results

- Using a case and image based approach we will present cases of infectious, inflammatory/reactive, and neoplastic etiologies of pachymeningeal enhancement.
- Etiologies will include benign causes such as intracranial hypotension, neurosarcoïd, idiopathic hypertrophic pachymeningitis, tumefactive fibroinflammatory lesion, and Tolosa-Hunt syndrome. Additionally, we will review malignant etiologies such as dural lymphoma and metastatic disease.

Conclusions

- Pachymeningeal enhancement – also called dural or dura-arachnoid enhancement – can be due to a variety of both benign and malignant etiologies.
- Normal pachymeningeal enhancement is thin, linear, and often discontinuous, and is most recognizable along the falx cerebri and tentorium cerebelli.
- Diffuse pachymeningeal enhancement can be seen secondary to benign etiologies such as chronic inflammatory or granulomatous diseases (Figure 1C), however can also be secondary to malignancy (1,2).
- Thick, continuous "wave like" pachymeningeal enhancement is particularly characteristic in MR imaging of intracranial hypotension (Figure 1A) (3).
- Irregular, relatively heterogeneous and focal nodular enhancement can be secondary to an underlying malignant process (Figure 1B), particularly with adjacent parenchymal changes and no known alternative etiology (1,2).
- Focal pachymeningeal thickening and enhancement can also be seen adjacent to a localized inflammatory process, such as adjacent to intracranial abscess/empyema or transiently in the postoperative setting (1). We show examples of focal pachymeningeal enhancement with cases of tumefactive fibroinflammatory lesion, Tolosa-Hunt syndrome, and idiopathic hypertrophic pachymeningitis (Figure 1D).
- Understanding the many causes of pachymeningeal enhancement, as well as the typical imaging appearance and associated imaging and clinical findings, is important to providing an appropriate differential diagnosis.



(Filename: TCT_365_PachymeningealASNRHyson.jpg)

1056

Parapharyngeal Space Masses: a Case Series and Imaging Review

N Vargas¹, R Assadsangabi¹, A Bewley¹, J CHANG¹, M Bobinski¹, O Raslan¹, A Ozturk¹, V Ivanovic¹
¹UC Davis Medical Center, Sacramento, CA

Purpose

Primary masses of the parapharyngeal space are encountered very infrequently and can pose a diagnostic challenge. Approximately 0.5% of head and neck neoplasms arise from this location. This educational exhibit will explore neoplasms of this space as seen in our case series and discuss their imaging findings. Educational objectives: 1. Review the anatomy of the parapharyngeal space. 2. Develop a differential diagnosis for masses found in this space. 3. Be able to describe imaging characteristics of these diagnoses. 4. Become familiar with the relative frequencies of each diagnosis.

Materials and Methods

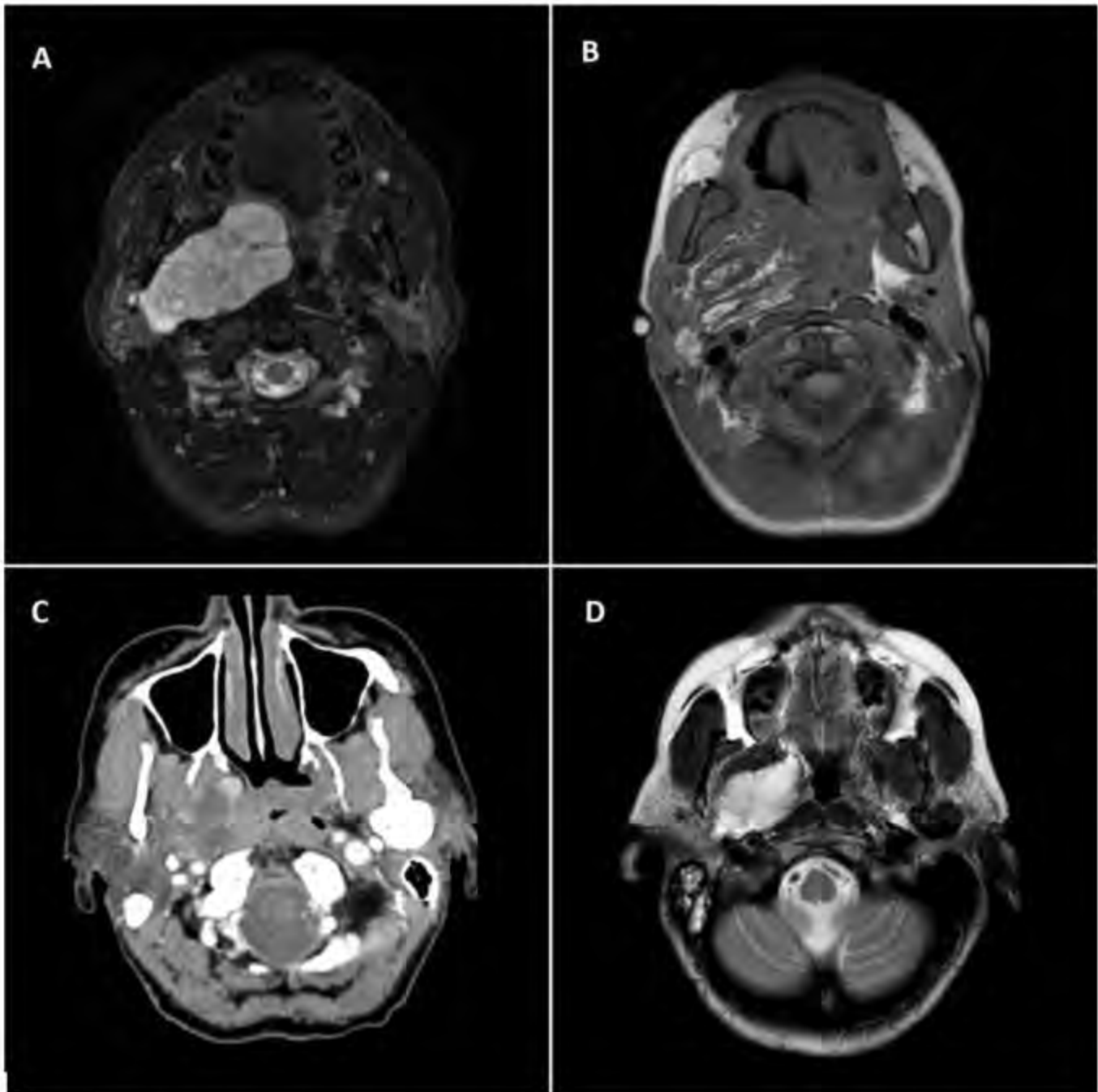
The purpose of this case series is to evaluate frequency of benign versus malignant parapharyngeal space masses, discuss the differential diagnosis and present imaging characteristics of the encountered pathologies within our patient population.

Results

Electronic Health Record was searched for parapharyngeal space masses that were surgically resected from 2015-2020. Cases with available pathologic diagnosis were included in the study.

Conclusions

Results: A total of 15 cases met the inclusion criteria. Pleomorphic adenoma was seen in 6/15 (40%) and carcinoma ex pleomorphic adenoma in 2/15 (13.3%) of cases. There was one case of giant cell fibroblastoma, hemangiopericytoma, schwannoma, Warthin's tumor, and lipoma (6.7%). Smooth peripheral tumor margins were seen in 13/15 cases; of these, 12/15 had a benign diagnosis and 1/15 was malignant. Irregular, infiltrative tumor margins were seen in 2/15 cases, both of which were malignant. Conclusions: In our case series, majority of resected parapharyngeal space masses (80%) were benign. Pleomorphic adenoma was the most commonly seen pathology. Irregular, infiltrative tumor margins might suggest a malignant etiology.



Parapharyngeal Masses Fig 1:

A. Axial STIR of pleomorphic adenoma seen as a large lobulated expansile mass in the right parapharyngeal space with homogenous hyperintensity. **B.** Axial T1WI of giant cell fibroblastoma presenting as a large heterogenous mass composed of fat and fibrous tissue in the right parapharyngeal space with mass effect on the oropharynx. **C.** Axial contrast enhanced CT of Carcinoma ex pleomorphic adenoma depicted as an ill-defined mass in the right parapharyngeal with heterogenous enhancement and central areas of necrosis. **D.** Axial T2WI of Carcinoma ex pleomorphic adenoma shown as a well circumscribed homogeneously hyperintense mass in the right parapharyngeal space with anterior displacement of pterygoid muscles and mass effect on nasopharynx.

(Filename: TCT_1056_ParapharyngealMassesFig1Fin.JPG)

Parasitic Worm Infestations of the Brain: A Neuroimaging Pictorial and Educational Review

E van Staalduinen¹, K Wang¹, B Dang¹, S Hashmi², M Wintermark³, T Massoud¹

¹Stanford University School of Medicine, Stanford, CA, ²N/A, N/A, ³Stanford, Stanford, CA

Purpose

Brain parasitic diseases (BPDs) may arise from macroscopic worm infestations (helminthiasis) or microscopic protozoal infections. Although helminths may remain asymptomatic for years, a higher organism burden correlates with greater morbidity and mortality. BPDs are prevalent in the tropics/subtropics but their world incidence is increasing owing to more global travel and immunosuppression; some even occur mainly in the U.S. (e.g. baylisacaris). Early recognition/treatment decreases BPD morbidity and the risk of secondary superinfection. Neuroimaging can complement clinical and laboratory tests to narrow the differential diagnosis. We review the neuroimaging findings of the main helminthic BPDs.

Materials and Methods

We comprehensively review the imaging findings in brain parasitic worm infestations, and categorize these by etiology.

Results

Parasites causing BPDs are many and diverse. The brain may be a severely affected organ. Helminthiasis are caused by three types of parasitic worms: cestodes (tapeworms), trematodes (flukes), and nematodes (roundworms). Tapeworms may exist in adult or larval forms, which are more pathogenic to the brain. They are ribbon-shaped, segmented, and with an anterior scolex for host attachment. Neurocysticercosis (*Taenia solium*, pork tapeworm) is the commonest epilepsy-inducing BPD worldwide. Infestation can be intra- and extra-axial. We will illustrate the neuroimaging appearances of its 4 stages: vesicular, colloidal vesicular, granular nodular, and nodular calcified. The other main brain cestodiasis are cystic hydatid disease (*Echinococcus*, causing ring enhancing grapelike clusters) and sparganosis (can see punctate "calcospherules" within parasites, ring enhancement, and changes in shape/location). The main brain trematodiasis are paragonimiasis, where brain complications rarely result in meningoencephalitis, and eventual clusters of calcification; and schistosomiasis (*Bilharzia*) where eggs in the brain induce a granulomatous response and necrosis ("arborized" appearance, with linear enhancement and surrounding enhancing nodules). We will also illustrate the main brain nematodiasis, including angiostrongylus (*Alicata's* disease), baylisacaris, gnathostomiasis, strongyloidiasis, and toxocariasis.

Conclusions

CT and MRI increases the likelihood of detection, proper treatment, and prevention of additional morbidity and mortality for clinically challenging BPDs. This presentation will aid in neuroimaging interpretation of brain helminthiasis to improve patient management.

776

Pathologies of the Cauda Equina: More Than Just a Syndrome

M Shriver¹, R Kurtz²

¹Hospital of the University of Pennsylvania, Philadelphia, PA, ²University of Pennsylvania, Philadelphia, PA

Purpose

Summary: The cauda equina consists of both ventral and dorsal nerve roots of the lumbar and sacral nerves as well as a single coccygeal nerve. The cauda equina can be affected by a number of different pathologies, many of which are unique to this portion of the neuraxis. Cauda equina syndrome is a rare, surgically emergent condition that results from severe compression of the descending lumbar and sacral nerve roots within the spinal canal. Failure to diagnose and untimely operative management can result in significant morbidity, with long-term neurologic sequelae. It manifests with an array of symptoms such as low back pain, asymmetric lower extremity weakness and sensory disturbances, perianal paresthesia, and/or diminished bowel and bladder function. A sample of cases that we present are: • A 44-year-old female with a large disc extrusion at L4-L5, resulting in severe spinal canal stenosis and compression of the cauda equina nerve roots (Figure A). • A 37-year-old male with a multiple cavernous malformations along the cauda equina following radiation therapy (Figure B). • A 63-year-old female with a myxopapillary ependymoma (Figure C). • A 19-year-old male with arachnoiditis ossificans (Figure D). Additional discussed pathologies include a large spinal canal schwannoma, conus medullaris infarct with enhancement of the ventral cauda equina nerve roots, leptomeningeal carcinomatosis, and epidural abscess with compression of the cauda equina. We will review the differences between cauda equina syndrome and conus medullaris syndrome both clinically and on diagnostic imaging. We will also review the essential MR sequences and a search pattern to appropriately evaluate the cauda equina for pathology and when to report critical findings to the clinician to foster appropriate, timely care.

Materials and Methods

N/A

Results

N/A

Conclusions

N/A



(Filename: TCT_776_Figure.jpg)

Pearls and Pitfalls in the Diagnosis of Pituitary Apoplexy

S Hu¹, A Jipa¹, V Jain¹

¹MetroHealth Medical Center/Case Western Reserve University School of Medicine, Cleveland, OH

Purpose

The knowledge of combining the typical imaging features of pituitary hemorrhage and infarction to relevant clinical manifestations is crucial to provide accurate diagnosis of Pituitary Apoplexy (PA) and direct prompt treatment. Hemorrhage and necrosis are not uncommon in large adenomas and shouldn't be over diagnosed as apoplexy in the absence of classic clinical picture and imaging features.

Materials and Methods

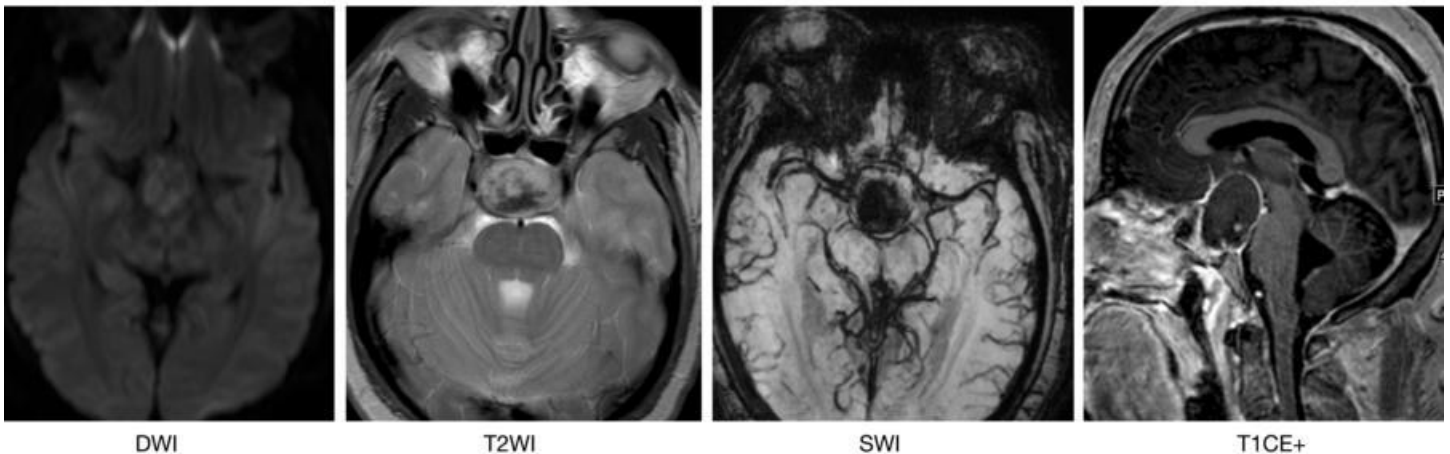
PA is a potentially life-threatening syndrome caused by acute onset, rapid enlargement of pituitary gland from acute hemorrhage and/or infarction, often within a pituitary adenoma or hyperplastic pituitary gland in peripartum period. Pituitary adenoma is one of the most common intracranial neoplasms, when nonfunctioning, may reached a significant size at the time of diagnosis, making them susceptible to hemorrhage and infarct in the setting of various triggering factors. Hemorrhage within the adenoma is mostly asymptomatic but may also be associated with the clinical syndrome of PA. Given the emergent and critical nature of PA, knowledge of imaging features of pituitary hemorrhage and understanding of the common clinical manifestations of PA is crucial for accurate diagnosis and prompt treatment.

Results

The imaging of multiple cases of pituitary hemorrhage were downloaded from PACS and relevant clinical information was also retrieved from EMR. The cases include asymptomatic pituitary adenoma hemorrhage and PA. Imaging modality used for comparison include CT and pre-/post-contrast MR.

Conclusions

Pituitary hemorrhage may lead to clinical syndrome of PA, however more frequently hemorrhage is subclinical and discovered incidentally. Combination of typical imaging features of pituitary hemorrhage to appropriate clinical setting is fundamental to arrive at a correct diagnosis of PA. Pituitary gland is generally enlarged and signals on T1/T2 WI are variable depending on the age of hemorrhage. In the acute phase, apoplexy will show characteristic absence of central enhancement with peripheral rim enhancement, high signal on diffusion weighted imaging (DWI), low signal on apparent diffusion coefficient (ADC). Hemorrhagic apoplexy will also show fluid-fluid levels, enhancement of sphenoid sinus mucosa/adjacent dura and sellar blooming on susceptibility (T2*) weighted and gradient echo (GRE) images. Detailed features will be shown in the exhibit. The clinical manifestations of PA include headache, vision change, cranial neuropathies, nausea/vomiting and acute endocrine abnormalities.



Pituitary apoplexy: Adenoma shows restricted diffusion (bright on b1000 and dark SI on ADC maps not shown), heterogenous low SI on T2, blooming on SWI and absence of contrast enhancement on the T1CE+ image. This adenoma showed contrast enhancement on an MRI performed few weeks before which is not shown here.

(Filename: TCT_773_pituitaryapoplexy.jpg)

1291

Pearls and Pitfalls of Carotid Vessel Wall Imaging

C McNamara¹, M Finnegan¹, R Quest¹, L Biasioli², P Jezzard², I honeyfield¹, N Rane¹

¹Imperial College Healthcare NHS Trust, London, England, ²University of Oxford, Oxford, United Kingdom

Purpose

Carotid vessel wall imaging is an increasingly important technique that has the potential to change both the way ischaemic stroke is risk assessed and subsequently managed. High quality MR imaging of the carotid wall is challenging for several reasons including; turbulent flow, vascular tortuosity, the nature of MR sequence acquisition and artefact degradation. Over the past two decades, there has been an increasing recognition of the importance of measuring not only the degree of luminal stenosis but also plaque morphology associated with atherosclerotic disease. This in turn has called for further improvements in imaging methods that can define the vessel wall with increasing fidelity. One such advance has been the attempt at quantification of plaque characteristics using advanced T2-mapping techniques which have been validated ex-vivo against pathological samples. The ultimate goal in this regard is to establish a reproducible biomarker that allows for a non-invasive measure of plaque risk and plaque response to emerging medical therapies. The objectives of this exhibit are to: 1) Briefly review the challenges associated with carotid vessel wall imaging with a special emphasis on specific anatomical regions such as the bifurcation which are prone to artefact formation. 2) Provide an overview of the physical principles underpinning MR vessel wall imaging of the carotid arteries. This will include both contrast and non-contrast enhanced sequences with a special emphasis on emerging techniques such as T2W mapping and its application in assessing plaque characteristics. 3) Give an overview of how best to assess the quality of imaging; the typical imaging artefacts associated with particular sequences at classical anatomical locations with suggestions on how scanning technique can be best optimised in order to minimise these. 4) Provide a pragmatic review of optimal scan protocoling for accurate carotid vessel wall imaging. Optimal surface coil technique will also be reviewed in this section.

Materials and Methods

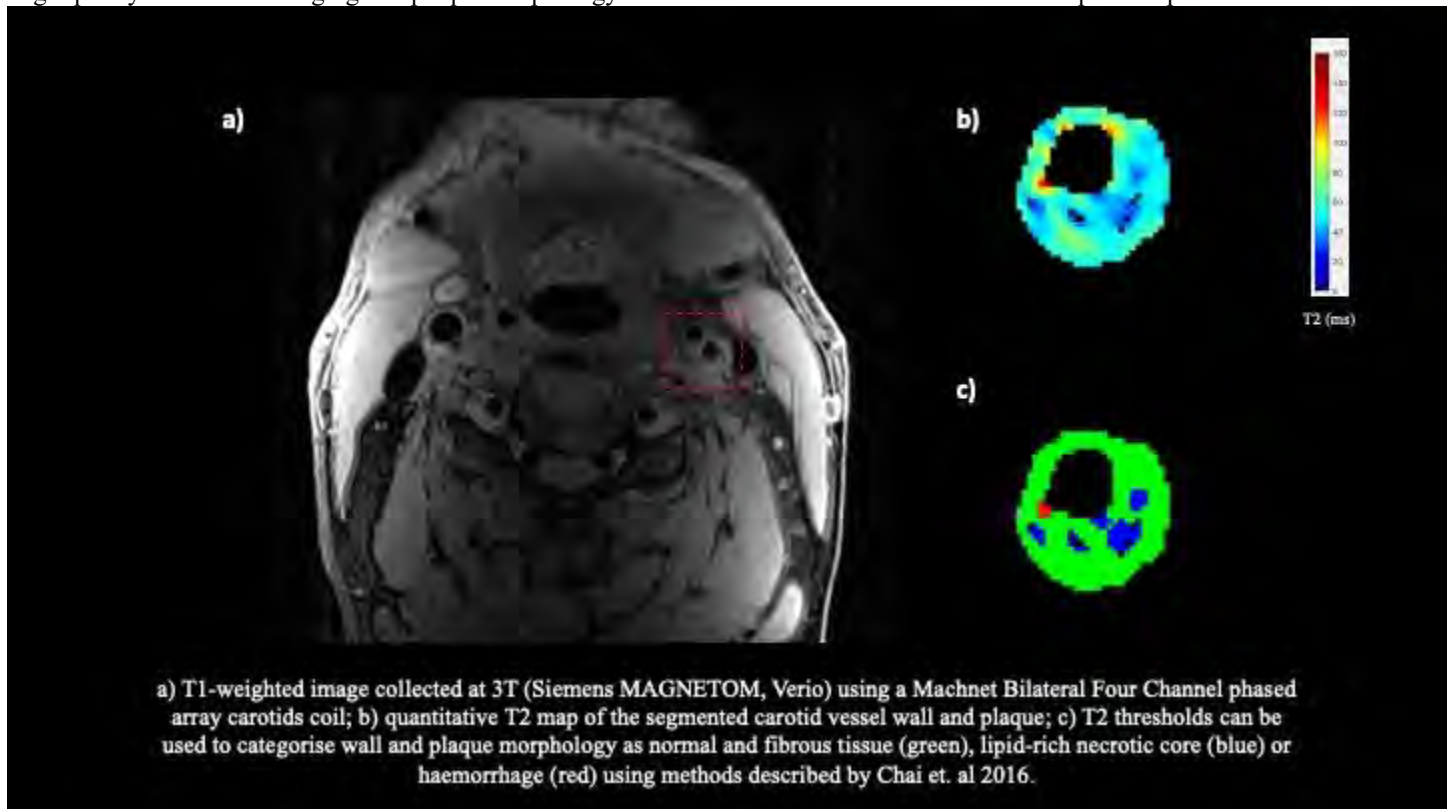
To provide an overview for the practising neuroradiologist of the physical principles and challenges associated with achieving high-fidelity carotid vessel wall imaging.

Results

A detailed literature review and direct input from the vessel wall imaging group at the radiological sciences unit in Imperial College Healthcare NHS Trust.

Conclusions

High quality vessel wall imaging and plaque morphology characterization is achievable with MR sequence optimisation.



(Filename: TCT_1291_CarotidImage.jpg)

1167

Pediatric Headache Patient Decision Aid (PDA)- A Shared-Decision Making Tool Guiding High-End Imaging Utilization

N Kadom¹, J Forte², S Gilyard¹

¹Emory University, Atlanta, GA, ²Children's Healthcare of Atlanta, ATLANTA, GA

Purpose

Patient decision aids (PDAs) are evidence-based tools which convey information to patients that pertain to a very specific decision they have to make. They list any pros and cons in a language that meets average literacy levels and often employ visuals [NQF 2016]. Using PDAs makes patients feel better informed, have a more accurate perception of risks, and be more likely to actively participate in decision making that is congruent with their personal values [Stacey 2017]. The use of PDAs can increase the use of high value care, such as screening tests, and reduce overutilization of low value testing [Fowler 2020].

Materials and Methods

To design an evidence-based decision aid that can be used to guide imaging use and clinical management in children with headaches and meets National Quality Forum (NQF) National Certification Standards for PDAs [NQF 2016].

Results

The guide was developed by a pediatric neuroradiologist and a pediatric neurologist headache specialist at a tertiary academic children's hospital following a local initiative that summarized existing evidence regarding imaging appropriateness in children with headaches [ACR Kadom]. We developed a pilot PDA for pediatric headache illustrating the National Quality Forum (NQF) National Standards for PDAs [NQF 2016].

Conclusions

A PDA was developed and annotated to illustrate how it meets NQF National Certification Standards for PDAs (Figure 1). The PDA features required to be considered for review are: Specific health condition named, target user identified, stated decision under consideration, description of available options, positive and negative features for each option, opportunity for patients to indicate preferences. The PDA features required for diagnostic test certification are: Description of what the test measures, next steps when test is positive vs. negative, description of consequences to detection of inconsequential findings, test positive and negative predictive value. As a next step, this PDA will be submitted for certification and piloted in our institution's pediatric headache clinic.

Headache in children <18 years old:

Should I (or my child) get imaging for headache?

Most children with headaches have a "primary headache". A primary headache means there is no worrisome cause for the headache.

A few patients with headaches have a disease that causes the headache. For example, a bleed in the brain, an infection of the head or brain, an aneurysm, or a blood clot in the brain can cause headaches. Rarely, a headache can be the first symptom of a brain tumor. Diseases like this can be found with imaging studies.

Doctors have a lot of experience in treating headaches. They also know what to look for to know whether you/your child needs imaging. Doctors will look for a "red flag" when examining you/your child. Patients with red flags should have imaging.

Your doctor will check which red flags, if any, apply to you/your child. Review the list with your doctor and say whether you agree when imaging is needed or not.

After you decide about imaging, your doctor will talk with you about next steps.

	Image within 24 hours	Image within 4 weeks
Systemic	<input type="checkbox"/> Fever/chills/night sweats/myalgia, weight loss, jaw claudication <input type="checkbox"/> Altered level of consciousness <input type="checkbox"/> Anticoagulation <input type="checkbox"/> Cancer <input type="checkbox"/> Immunosuppression <input type="checkbox"/> HIV infection <input type="checkbox"/> New onset or change during pregnancy	
Neurologic	<input type="checkbox"/> Papilloedema <input type="checkbox"/> Asymmetric cranial nerve function <input type="checkbox"/> Asymmetric motor function <input type="checkbox"/> Abnormal cerebellar function <input type="checkbox"/> New seizure <input type="checkbox"/> Focal findings on exam <input type="checkbox"/> Change in behavior/personality <input type="checkbox"/> Transient visual obscuration <input type="checkbox"/> Pulsatile tinnitus	
Onset	<input type="checkbox"/> Recent or sudden (peak intensity <1 minute)	<input type="checkbox"/> Age <6 years old
Occipital		<input type="checkbox"/> Occipital back of head
Pattern	<input type="checkbox"/> Triggered by Valsalva <input type="checkbox"/> Progressively worse over time or change in characteristics	<input type="checkbox"/> Postural aggravation <input type="checkbox"/> Changes with position <input type="checkbox"/> No family history
Phenotype of rare headache	<input type="checkbox"/> Trigeminal autonomic cephalgia <input type="checkbox"/> Hypnic <input type="checkbox"/> Exercise, cough- or sex-induced	
Aneurysm screening	<input type="checkbox"/> Patient has 2 (two) 1 st degree relatives with a history of aneurysm <input type="checkbox"/> Patient has a genetic diagnosis with predisposition for aneurysms	

Adapted from: Dohlik [1] and Goldstein [2]

Test Performance			
CT Head (diagnostic accuracy) ¹	Sensitivity: 88%	Specificity: 72%	<input type="checkbox"/>
CTA Head (aneurysm) ²	PPV: 100%	NPP: 83%	<input type="checkbox"/>
MRI Head (diagnostic accuracy) ¹	Sensitivity: 99%	Specificity: 28%	<input type="checkbox"/>
MRA Head (aneurysm) ²	PPV: 92%	NPP: 98%	<input type="checkbox"/>

I agree that imaging is *not* necessary
 I agree that imaging *is* necessary
 I disagree

Patient Signature: _____ Date: _____

(Filename: TCT_1167_PDAPage1.JPG)

1481

Pediatric Intracranial Hemorrhage: an Anatomical Approach.

E Penailillo¹, T Becker¹, S Bravo-Grau¹, F SEPULVEDA², D Araneda Castiglioni¹, J Cruz³

¹Pontificia Universidad Catolica de Chile, Santiago, Chile, ²Instituto de Neurocirugia, Santiago, Chile, ³Pontificia Universidad Catolica de Chile / Instituto de Neurocirugia, Santiago, Chile

Purpose

Introduction: More than half of strokes in the pediatric population correspond to intracranial hemorrhage and a large proportion of them have secondary causes. Different imaging techniques play a key role in the initial workup and follow-up of these patients. The

etiology, management, prognosis, and complications vary greatly depending on the affected compartment, which justifies a location/pattern-based approach that can be determined on the initial study. An anatomical classification is proposed, highlighting the most relevant causes of bleeding in each compartment in the pediatric population. Educational objectives: - To review the role of imaging in pediatric hemorrhagic stroke. - To examine classic and uncommon causes of intracranial hemorrhages in different compartments on pediatric patients. - To introduce new patterns that are fundamental to suspect unusual entities or modify patient management, including intraventricular hemorrhage, posterior fossa/spinal subarachnoid hemorrhage (SAH) and subpial hemorrhage. - To illustrate imaging pearls on noninvasive techniques that allow prospective diagnosis of relevant causes of intracranial hemorrhages, including vascular malformations, with correlation with invasive modalities. - To propose a novel classification scheme of intracranial hemorrhage. Table of contents/Outline: - Introduction: Relevance of pediatric hemorrhagic stroke. Role of CT, CTA, MR, MRA, DSA. Classic patterns. - New location-based patterns of hemorrhage: intraventricular, spinal/posterior fossa SAH, subpial. - Pearls on differential diagnosis according to location (classic and new patterns), with a focus on uncommon but relevant causes. 1. Epidural: Traumatic epidural hematoma 2. Subdural: Non-accidental trauma, coagulopathy 3. Subarachnoid (SAH): Aneurysmal, Arteriovenous malformations (AVMs), Arterial dissection 4. Subpial: Neonatal subpial hemorrhage 5. Intraventricular: AVMs, moyamoya syndrome, choroid plexus hemorrhage 6. Intraparenchymal: AVMs, Cavernomas, Metabolic disorders (hypernatremic dehydration), Coagulopathy, Venous sinus thrombosis - Conclusion

Materials and Methods

N/A

Results

N/A

Conclusions

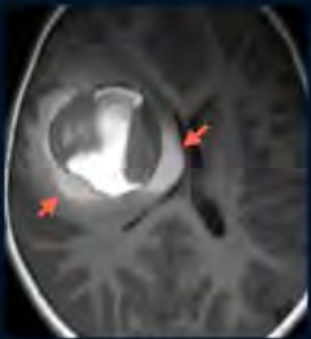
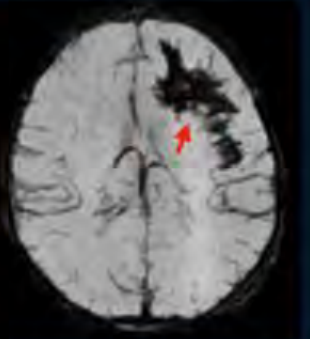
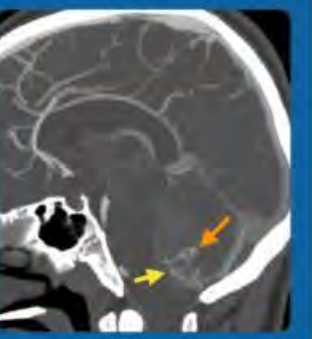
N/A

PEDIATRIC INTRACRANIAL HEMORRHAGE

An Anatomical Approach

TEACHING POINTS

- More than half of strokes in the pediatric population correspond to **intracranial hemorrhage**, and a large proportion of them have **secondary causes**.
- Etiology, management, prognosis and complications vary greatly depending on the **anatomical compartment involved**, which justifies a **location based approach**.

INTRAPARENCHYMAL	SUBPIAL	INTRAVENTRICULAR
 <p>Cavernoma</p> <p>Slow flow vascular malformations.</p> <p>The T1 hyperintense perilesional signal is a reported sign that may be useful to differentiate cavernomas for other hemorrhagic masses.</p>	 <p>Hypernatremic Dehydration</p> <p>Hypernatremic dehydration can cause serious neurological injury in neonates.</p> <p>Linear and confluent hemorrhagic foci may aid in its diagnosis (as shown in SWI)</p>	 <p>Neonatal subpial hemorrhage</p> <p>A pattern unique to neonates. Typical findings are:</p> <ul style="list-style-type: none"> - Hemorrhage following cortical surface - Adjacent cytotoxic cortical edema - Absence of SAH - Temporal location
		 <p>Ruptured arteriovenous malformation</p> <p>In the presence of intraventricular hemorrhage, always consider a ruptured subependymal AVM or moyamoya.</p> <p>Also, if an AVM is detected, weak points should be actively sought, specially perinidal aneurysms.</p>

(Filename: TCT_1481_Pediatricintracranialhemorrhage.jpg)

1128

Pediatric Nasopharyngeal Carcinoma Imaging Features

G Orman¹, H Tran¹, N Desai¹, A Meoded¹, S Kralik¹, V Smith², J Hicks¹, C Kirsch³, T Huisman⁴

¹Texas Children's Hospital, Houston, TX, ²Baylor College of Medicine, Houston, TX, ³Northwell Health, New York City, NY, ⁴Texas Children's Hospital and Baylor College of Medicine, Houston, TX

Purpose

Pediatric nasopharyngeal carcinoma (NPC) is a rare epithelial origin tumor associated with undifferentiated histology, Epstein-Barr virus (EBV) infection, and genetic risk factors. Childhood NPC is usually clinically silent, often presenting with advanced

locoregional compromise, including skull base invasion and cervical lymphadenopathy, and has a better prognosis than adult NPC. Educational objectives are: 1. To discuss neuroimaging features of NPC in a cohort of 28 children. 2. To discuss differential diagnosis of adolescents presenting with a nasopharyngeal mass, emphasizing key imaging characteristics of NPC.

Materials and Methods

Pediatric nasopharyngeal carcinoma (NPC) is a rare epithelial origin tumor associated with undifferentiated histology, Epstein-Barr virus (EBV) infection, and genetic risk factors. Childhood NPC is usually clinically silent, often presenting with advanced locoregional compromise, including skull base invasion and cervical lymphadenopathy, and has a better prognosis than adult NPC. Our purpose is to describe computed tomography (CT) and magnetic resonance imaging (MRI) features in a cohort of 28 pediatric NPC patients.

Results

A retrospective review was performed among children with histopathology proven NPC diagnoses between 1996 and 2019 for this study. The electronic medical records were reviewed to determine demographics, EBV serology, and World Health Organization (WHO) type. Nasopharyngeal CT and/or MRI at presentation for tumor spread as well as density and/or intensity, lymphadenopathy, postcontrast enhancement and diffusion characteristics before treatment were evaluated.

Conclusions

Twenty-eight patients (21 males, 7 females) were included. The mean patient age at diagnosis was 13.3 (range 7 to 17) years. EBV was positive in 71.4% of patients. The majority of patients (78.6%) had a WHO type III tumor, unilateral fossa of Rosenmuller involvement (71.4%). Neuroimaging features were CT isodensity, T1-isointensity, T2-hyperintensity, and heterogeneous postcontrast enhancement for all patients (100%) and restricted diffusion (90%). In conclusion, although uncommon in pediatric patients, NPC should be in the differential diagnosis of adolescents presenting with a nasopharyngeal mass. Recognizing key imaging characteristics is helpful in the diagnosis of NPC.

252

Pediatric neuro-oncology brain MRI imaging: apart from the tumor itself, what else should we look for?

M Shapira Rootman¹, O Konen², H Toledano²

¹*Schneider children's medical center of Israel, Petach Tikva, Israel,* ²*Schneider Children's medical center of israel, Petach Tikva, Israel*

Purpose

Follow up brain MRI studies of pediatric neuro-oncology patients is primarily aimed at detecting tumor recurrence (either local or metastatic spread) and assessment of response to therapy (stable disease, tumor progression or response). Nevertheless, there are potentially multiple additional imaging findings that might be of clinical significance. These include post radiation changes (such as radiation induced vascular malformations, moyamoya disease), shunt-related complications, post-operative complications (such as pseudo-meningocele) in addition to other less common complications like cranial nerve injury, signs of an underlying cancer predisposition syndrome, development of secondary tumors, optic nerve atrophy and so forth. In this educational exhibit we intend to present potential clinically relevant imaging findings (other than tumor recurrence and assessment to therapy) on brain MRI studies of pediatric neuro-oncology patients.

Materials and Methods

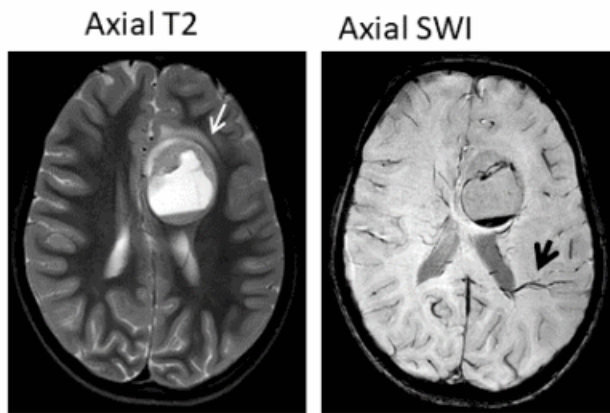
The purpose of this educational exhibit is to present the various complications that radiologist might encounter while reviewing brain MRI studies of pediatric neuro-oncology patients.

Results

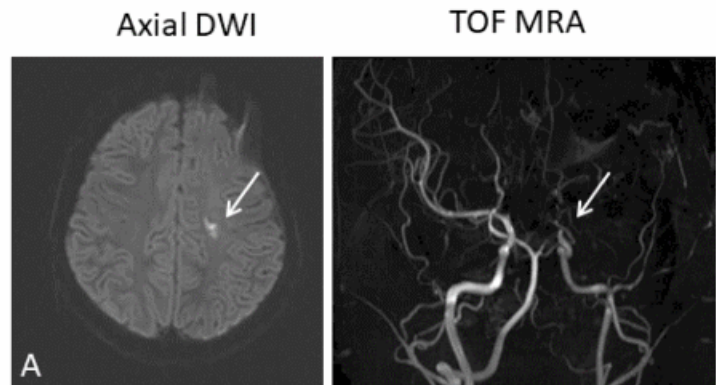
All complications will be presented according to major categories: post radiation/chemoradiation, shunt-related, post-surgical, infectious/inflammatory, ischemic and so forth.

Conclusions

Imaging findings on brain MRI of pediatric neuro-oncology patients will be discussed. These include post treatment changes Shunt related complications clues for cancer predisposition syndrome development of secondary malignancies



8.5-year old girl with left frontal hemorrhagic mass lesion. Multiple DVAs are suggestive of CMMRD (one is shown in panel B). Pathology revealed GBM.



12-year old girl with remote history of left frontal ependymoma. S/P surgical resection & radiotherapy. Presented with sudden right arm weakness. MRI revealed a small left frontal infarct. MRA study revealed significant narrowing of the distal left ICA secondary to prior irradiation.

(Filename: TCT_252_1.GIF)

1371

Pediced Glandulo-Fascial Flap Reconstruction: Review of the Radiographic Appearance of Novel Surgical Techniques and Potential Pitfalls in Imaging Interpretation

B Meyer¹, D Zander², V Potigailo¹, C Oliver¹, F Chowdhury³

¹University of Colorado, Aurora, CO, ²University of Colorado, Englewood, CO, ³University of Colorado, Aurora, CO

Purpose

Novel variations of PGFFR may show an unfamiliar imaging appearance. Recognition is important to reduce over-diagnosis of head and neck tumor recurrence or new primary.

Materials and Methods

Pediced glandulo-fascial flap reconstruction (PGFFR) describes various surgical techniques in which glandular tissue is relocated following resection of head and neck tumors. Traditionally, PGFFR was limited to submandibular gland (SMG) transfer for oral and oropharyngeal cancers to shield the gland from radiation therapy. However, there are now novel anatomic variations of PGFFR into other locations for reconstruction which have not been described in the radiologic literature. Variations include relocation of the SMG into the oropharynx or parotid bed, or relocation of the thyroid gland as an adjunct to other reconstructive flaps. Post-operative imaging findings of gland relocation may be unfamiliar to imagers.

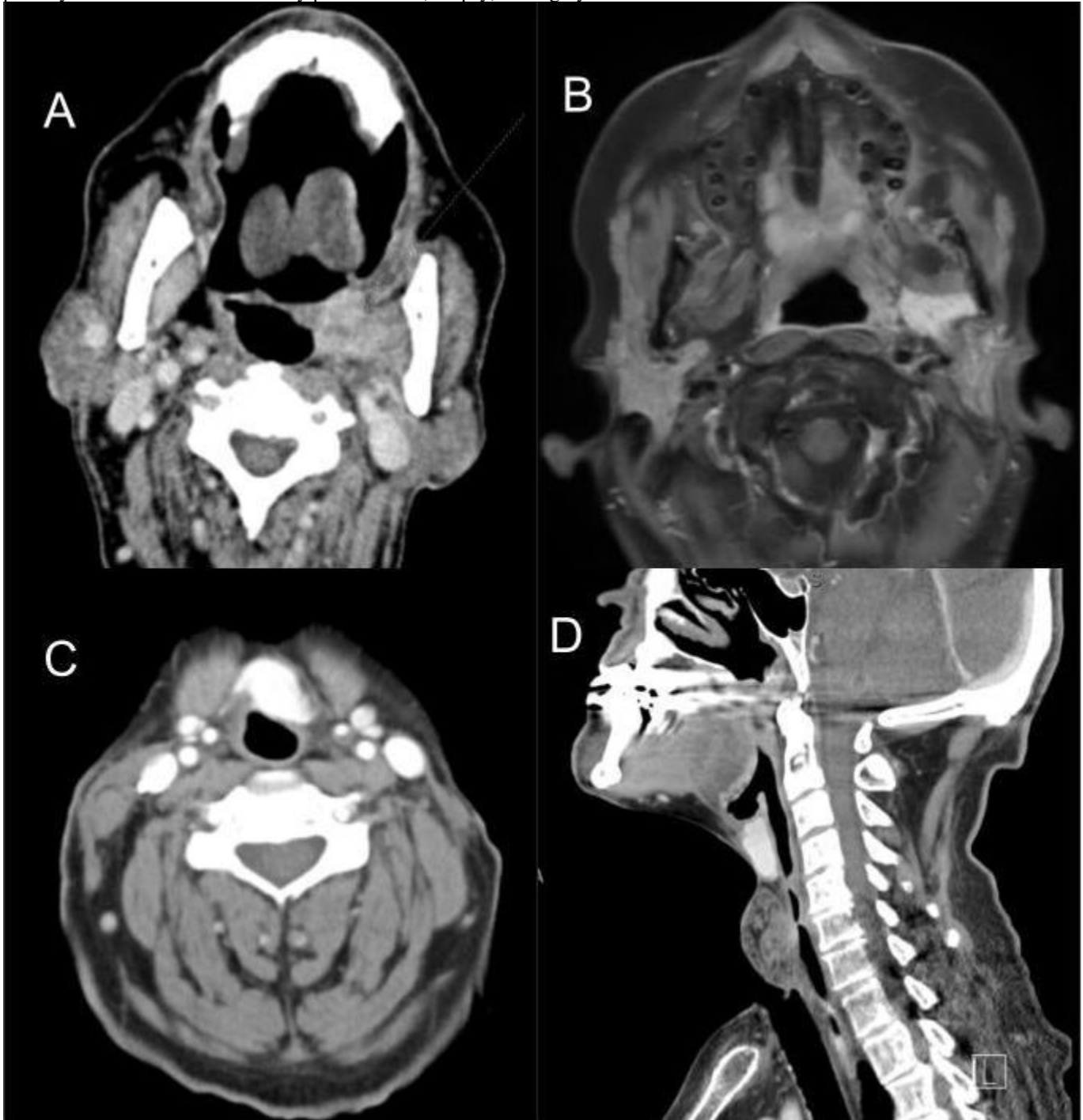
Results

Patients with post-operative imaging at our institution were identified who had undergone PGFFR. Imaging modalities included contrast-enhanced CT and pre/post contrast MRI. Chart review was performed to establish clinical context.

Conclusions

Eleven patients with imaging after PGFFR were identified including 10 cases of SMG relocation and 1 thyroid gland relocation. Patients were treated for oral or oropharyngeal cancers, parotid tumors and one for pterygopalatine fossa sarcoma. Thyroid relocation

was performed in conjunction with total laryngectomy. The most common appearance after SMG relocation by CT was focal asymmetric hyperattenuation within the surgical bed as seen along the left oropharynx on image 1a. The morphology of the ectopic gland was variable. By MRI, the relocated SMG corresponded to asymmetric enhancing tissue in the surgical bed (as seen in a different patient in the left parotid bed on image 1b). The ectopic glands showed MRI characteristics and enhancement consistent with the contralateral normal submandibular gland. For the thyroid gland relocation, contrast CT showed a hyperattenuating, circumscribed structure anterior to the neopharynx (images 1c and 1d). In all cases the anatomic gland was absent. In conclusion, novel variations of PGFFR are characterized by asymmetric homogeneous enhancement in the resection bed in the setting of an absent ipsilateral anatomic gland. Recognition of this appearance should prompt review of the surgical record before diagnosis of recurrence or second primary so as to reduce unnecessary patient alarm, biopsy, or surgery.



(Filename: TCT_1371_GFFRImage1.jpg)

J Gajera¹, M Yeo², J Seah¹, J Maingard³, I Raza¹, C Yang¹, C Li¹, B Major⁴, J Tee¹, H Asadi⁵, H Kavvounias⁶
¹Alfred Health, Melbourne, VIC, ²University of Melbourne, Melbourne, VIC, ³N/A, N/A, ⁴Monash University, Melbourne, VIC, ⁵Austin Health, Melbourne, VIC, ⁶Alfred Hospital, Melbourne, AK

Purpose

In this review we explore the available performance metrics used to undertake a fair comparison of deep learning models.

Materials and Methods

There is a growing interest in employing the use of artificial intelligence (AI) programs to perform classification tasks in neuroradiology to improve clinical decision support systems. Convolutional neural networks have the potential to leverage modern data-rich neuroimaging methods, automating image analysis and driving the development of reliable clinical decision support systems. However, to improve the reliability of a particular model it is necessary to employ standardized metrics to evaluate an algorithm's performance. Clinicians must perpetually learn new skills to incorporate AI advances into everyday practice in order to stay up-to-date. This review explores the means to interpret evidence from AI radiology peer-reviewed literature.

Results

A search within EMBASE, MEDLINE, Web of Science and PubMed databases was conducted for articles relating to the use of performance metrics in AI research. The citations of relevant articles were also searched for additional articles.

Conclusions

Findings/Discussion: Multiple methodologies are used to gauge an algorithm's performance in artificial intelligence research including accuracy (ratio of the number of correct predictions to total number of predictions), logarithmic loss (measure of uncertainty), the confusion matrix (table that visualizes the performance of a classification algorithm), precision (TP/(TP+FP)), recall (TP/(TP+FN)), the F1-score (harmonic mean of precision and recall), Matthews correlation coefficient (single value metric for binary classification problems that accounts for all true and false, positives and negatives in the confusion matrix) and the area under the receiver operator characteristic, or AUC. AUC is equal to the probability that the classifier will rank a randomly chosen positive example higher than a randomly chosen negative example, with the advantage of being independent of the prevalence of positive cases. Furthermore, we explore other statistical measures of inter-rater reliability such as Cohen's Kappa, other methods of performance assessment including regression metrics (i.e. mean absolute error and mean squared error), and discuss the concepts of overfitting and underfitting.

Summary/Conclusion: Clinicians should be aware of standardized performance metrics to compare the outcomes generated from deep learning models in the literature.

1022

Perineural Tumor Invasion: Hiding in Plain Sight

M Hussein¹, T Rizvi¹, S Mukherjee¹
¹University of Virginia, Charlottesville, VA

Purpose

This exhibit will review anatomy of cranial nerves which serve as pathways for perineural tumor spread. Knowledge of perineural spread is important as it is a bad prognostic sign for head and neck cancer.

Materials and Methods

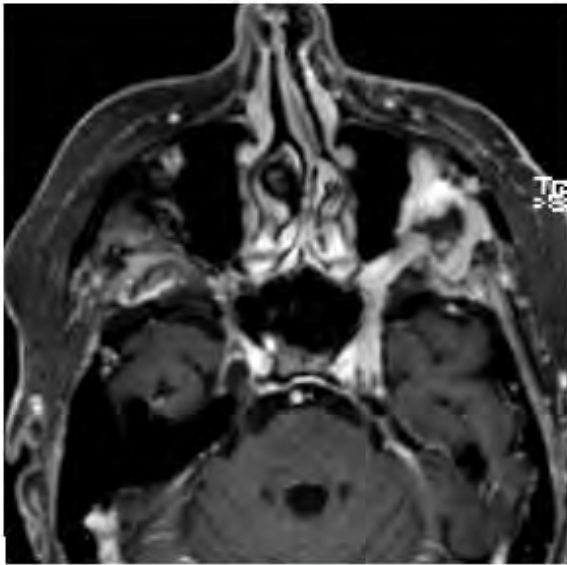
1. Review relevant cranial nerve anatomy pertinent to head and neck lesions 2. Review imaging features of perineural tumor spread in head and neck malignancies

Results

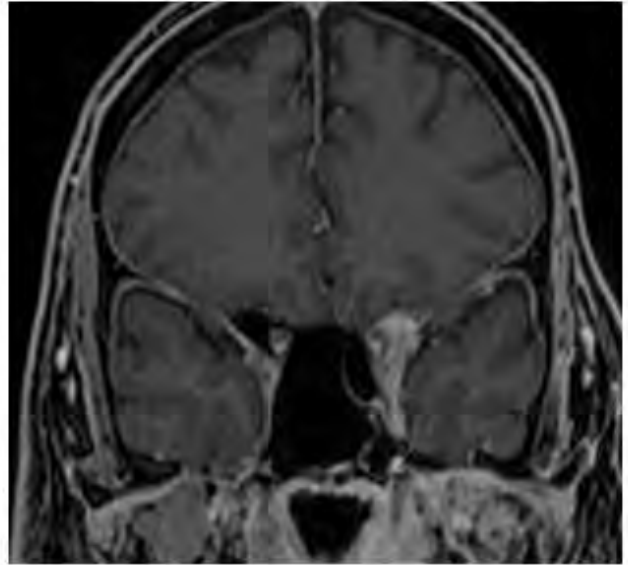
We reviewed cases of perineural tumor invasion at our institution where MRI was of great help in depicting high resolution images of cranial nerve course and perineural spread of tumor.

Conclusions

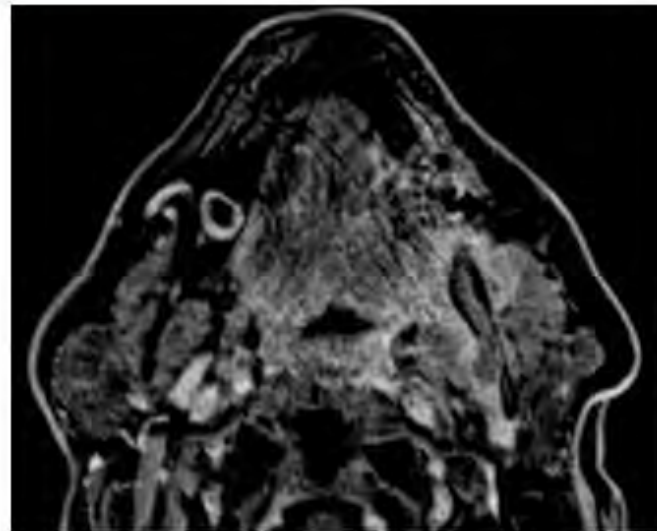
Perineural spread is an important adverse prognostic indicator in the staging of head and neck malignancies, which influences the planning of the surgical approach and treatment regimen. Imaging plays a critical role in the assessment and delineation of perineural tumor spread. A comprehensive knowledge of the pertinent anatomy of the cranial nerves, and the typical imaging features of perineural tumor spread is therefore essential in the imaging of head and neck oncology.



A



B



C

Figure1. T1 fat saturated post contrast axial image in a known case of spindle cell cancer of left orbit shows perineural spread along left V2 division of trigeminal nerve (A). T1 fat saturated post contrast coronal image in a known case of basal cell carcinoma shows perineural spread along the left V1 division of trigeminal nerve (B). T1 fat saturated post contrast axial image showing perineural spread along the left V3 branches (inferior alveolar nerve) in a case of left mandibular squamous cell carcinoma (C).

(Filename: TCT_1022_Perineuralimages.JPG)

599

PET/MRI in Pediatric Neuroimaging: Primer for Clinical Practice

C Pedersen¹, S Messina², H Daldrup-Link³, A FRANCESCHI⁴, M Aboian⁵

Purpose

PET/MRI is a promising new modality that combines exquisite soft tissue information from MRI with functional data provided by PET all in a package with minimal radiation penalty. As such, this modality is particularly useful in pediatric neuroimaging and can be used to diagnose a variety of childhood cancers and epilepsy. Even though PET/MRI has become more widely available, challenges in clinical implementation still remain and our educational exhibit will provide recommendations on combined hybrid protocols that have been successful in clinical practice in several tertiary centers across the country. Educational objectives: 1. Considerations regarding available PET/MRI systems, protocols, and dose reduction techniques will be addressed. 2. Diagnosis and follow-up of common pediatric malignancies will be illustrated with 18F-FDG PET, 11C-MET, 18F-DOTATATE and MRI. 3. Utility of PET/MRI in epilepsy diagnosis will be highlighted and illustrated with cases. 4. Current challenges in PET/MRI will be discussed. 5. Future trends and AI in pediatric neuroimaging.

Materials and Methods

A unique challenge in pediatric cancer patients is to balance the need for serial imaging with avoiding excessive radiation. PET/MRI is especially promising in pediatric neuroimaging since the functional and soft tissue characterization provided by these two modalities is achieved with a very low radiation dose. Disadvantages such as longer scan time and sedation can be mitigated with optimal protocol selection and use of synchronous systems. PET/MRI can advantageously be used to diagnose epileptogenic foci as well as diagnose, stage and follow malignancies in the brain, head, neck and spine.

Results

Review of published literature on use of PET/MRI in pediatric neuroimaging was performed and key articles were identified. Protocols and clinical uses of PET/MRI were obtained from multiple tertiary institutions based on publications and using personal communication with radiologists at these institutions, in addition to the authors' own experience.

Conclusions

In this case-based educational exhibit we illustrate the utility of PET/MRI in diagnosis of pediatric patients with a wide range of malignancies as well as epilepsy. Dose reduction techniques and tracer selection are covered, sequential versus synchronous PET/MRI systems explained and considerations behind MRI protocol design will be discussed. Additional radiotracers such as MIBG, DOTATATE, and amino-acid based tracers will also be covered.

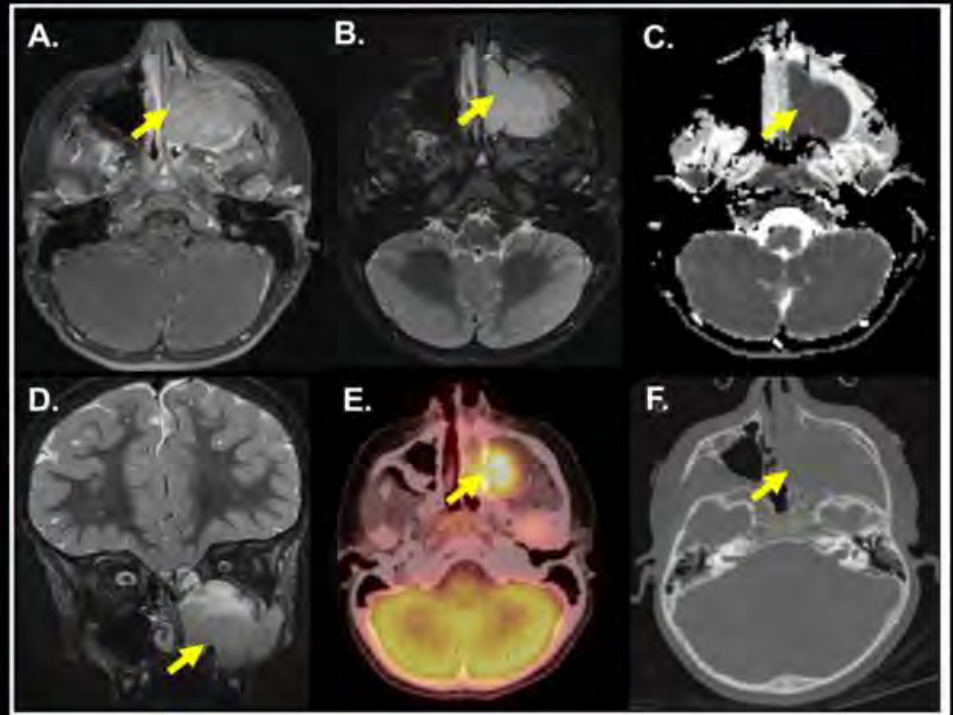
Value of FDG-PET/MRI in Staging and Follow-up

Case

An enhancing, T2 hyperintense mass with restricted diffusion (A,B,C) is involving the left maxillary sinus, with mass effect on the left orbit (D), osseous destruction (F) and hypermetabolic activity on ¹⁸F-FDG PET (E, SUV max 8.0). The mass was alveolar rhabdomyosarcoma upon resection.

MRI & FDG-PET are complimentary in head and neck evaluation of rhabdomyosarcoma. *MRI*: Non-contrast and non-fat suppressed T1 and postcontrast T1 are useful to evaluate for perineural extension, while *FDG PET* is effective to characterize extent of disease, nodal metastases and tumor recurrence.

**! Teaching Point:
Rhabdomyosarcoma of the
head and neck requires
multimodal evaluation**



(Filename: TCT_599_ASNR.jpg)

1431

Pictorial Review and Approach to Sellar and Parasellar Lesions

B Singh¹

¹Columbia Asia Referral Hospital, Yeshwantpura, Bangalore, Bangalore, India

Purpose

Tumours and tumour-like-lesions can involve sellar and parasellar regions and anatomic localisation of these lesions is necessary in arriving at a differential diagnosis. MRI, especially with a sella protocol is necessary for localisation, characterisation and determining the extent of these lesions. CT scan can be used as an additional tool to see bony changes if any.

Materials and Methods

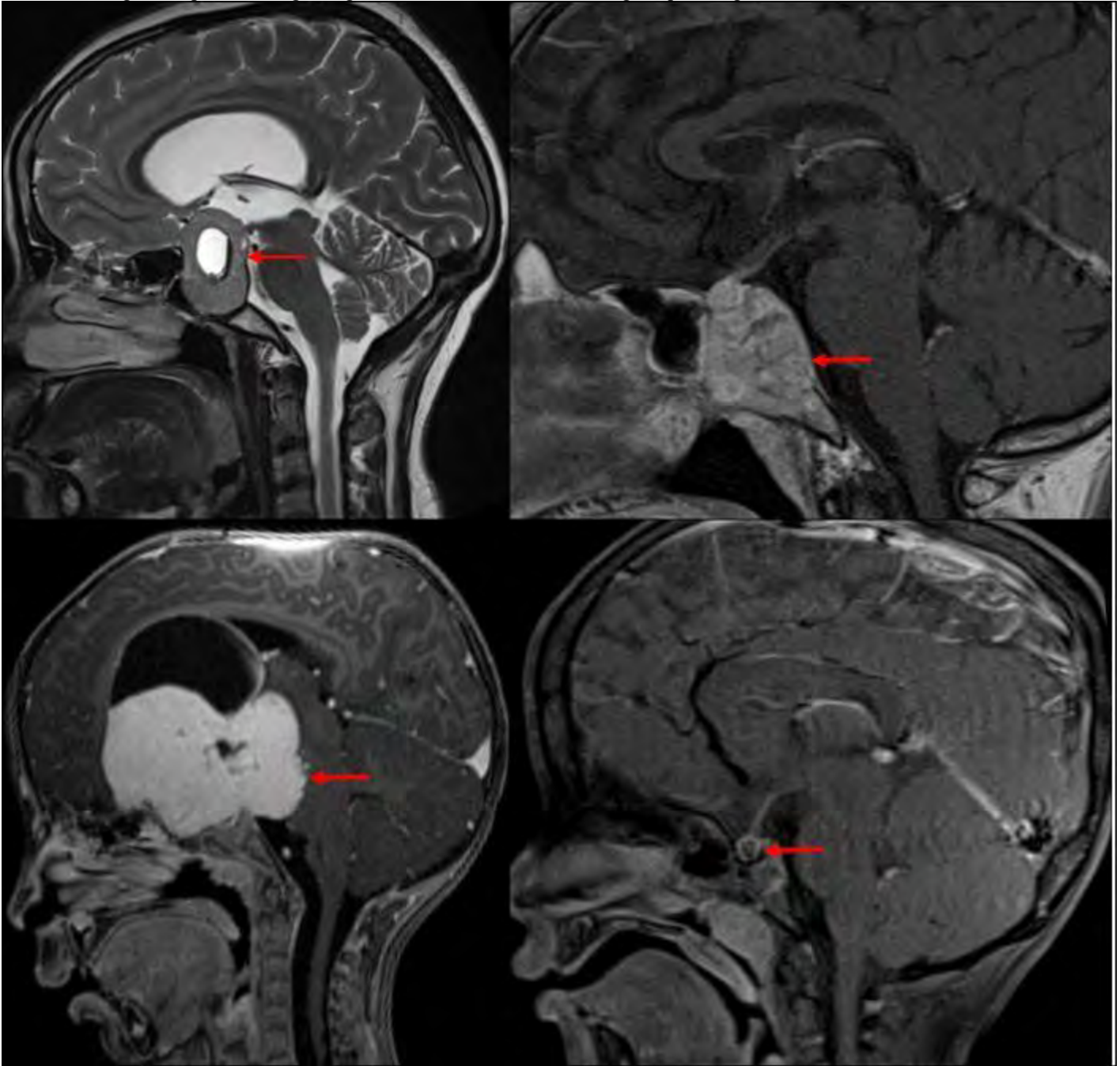
1. To review the anatomy of sellar and parasellar regions. 2. To discuss the approach of localising the sellar and parasellar masses which helps in narrowing the differential diagnosis. 3. To review important congenital, neoplastic, inflammatory/infectious and miscellaneous lesions of sellar and parasellar regions.

Results

Following approach was followed to evaluate the sellar/parasellar masses – 1) Identifying pituitary gland and sella turcica. 2) Determining the epicentre of the lesion – sellar/suprasellar/parasellar/infrasellar. 3) Analysing the lesion – for signal intensity, whether the lesion is solid/cystic, does it contain flow voids/calcifications 4) Establishing the differential diagnosis. Following lesions were reviewed: Solid lesions: • Lateral structures origin – aneurysm, Meningioma. • Hypothalamic-chiasmatic/tuber-cinerium origin – glioma, germinoma, hamartoma, histiocytosis, Sarcoid • Clival – chordoma. • Metastasis, Ectopic neurohypophysis. Cystic lesions: • Empty sella • Arachnoid cyst • Rathke cleft cyst • Craniopharyngioma • Epidermoid

Conclusions

Radiologist's awareness about the complex anatomy of sellar and parasellar region, differential diagnosis of sellar and parasellar lesions is of a great importance in guiding the treatment decisions and surgical planning.



(Filename: TCT_1431_SELLARSUPRASELLAR.JPG)

965

Pictorial review of Cavernous Haemangiomas of the Cavernous Sinus

M Nasralla¹, R Saqib², J Cain², S Mathur³

¹Royal Preston Hospital, Preston, United Kingdom, ²Royal Preston Hospital, Preston, Lancashire, ³Lancashire Teaching Hospitals, Preston, UK

Purpose

To review the imaging findings of cavernous haemangiomas of the cavernous sinus. The role of dynamic-contrast enhanced MR sequences and nuclear medicine as a problem-solving tool in cases of diagnostic uncertainty.

Materials and Methods

Cavernous haemangiomas are rare lesions of the cavernous sinus. These usually present with neurological deficits relating to compression on the cranial nerves within the cavernous sinus in addition to non-specific symptoms such as headache. Accurate diagnosis of these lesions is important as biopsy or surgery of these lesions is often complicated by haemorrhage. Reliable diagnosis is possible in a large proportion of these lesions which demonstrate reproducible features with conventional MR sequences. Dynamic contrast enhanced sequences is useful in more challenging cases where atypical presentations of more common lesions such as meningiomas or schwannomas are considered or where firm exclusion of an aggressive pathology such as chordomas is required. While MR is the main modality used for characterisation, Tc99-pertechnetate labelled RBC scintigraphy may also be of benefit in selected patients.

Results

This is a retrospective review of cases of cavernous haemangiomas of the cavernous sinus within our radiology department over a period of 10 years. These cases were discussed and managed in our regional skull base multidisciplinary meeting.

Conclusions

CT demonstrates a well-defined isoattenuated mass in the cavernous sinus region with homogeneous enhancement. Adjacent bony structures demonstrate a benign pattern of remodelling. Calcifications are typically absent. Characteristic MR Findings include marked T2 hyperintense signal and T1 hypointense / isointense signal. Morphological features include well-defined, lobular margins (figure 1). Variable encasement of the ICAs without stenosis is a commonly reported feature. In our cases where there was diagnostic uncertainty or clinical need for further characterisation, dynamic contrast enhanced sequences were obtained demonstrating typical early heterogeneous enhancement with 'filling-in' on subsequent delayed sequences (figure 2). In one case Tc99-labelled RBC SPECT-CT was obtained to confirm the presence of cavernous sinus haemangiomas (figure 3). In a further case where a haemangioma was suspected, scintigraphy demonstrated corresponding 'cold' activity which favoured an alternative diagnosis.

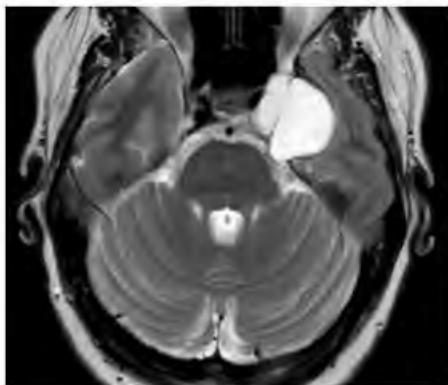
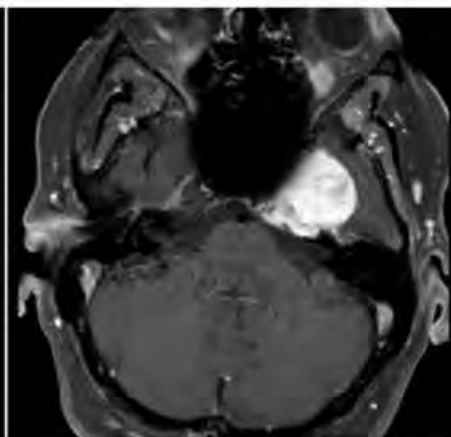
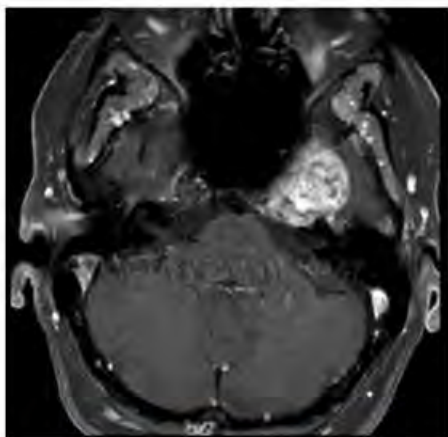


Figure 1: Axial T2 weighted sequence demonstrates a well-defined, lobular lesion arising centred in the left cavernous sinus, which returns markedly high T2 signal.



Figures 2a and 2b: Dynamic contrast-enhanced T1 fat-saturated sequences demonstrated early heterogenous enhancement of the cavernous sinus lesion (a).

Subsequent sequences show centripetal contrast enhancement with homogenous enhancement demonstrated on the final delayed sequence (b).

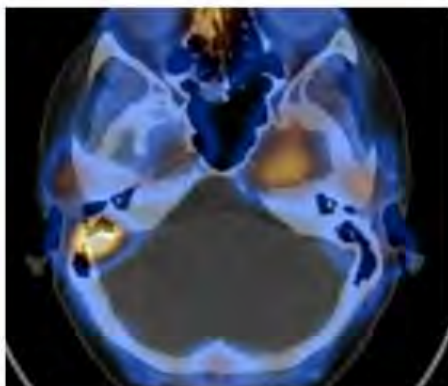


Figure 3: Tc99m-pertechnetate labelled RBC SPECT-CT demonstrating corresponding avid tracer activity of the left cavernous sinus.

(Filename: TCT_965_Images.jpg)

181

Pictorial review of common and uncommon imaging presentations in idiopathic intracranial hypertension

P Felix¹, X Li¹

¹Emory University School of Medicine, Atlanta, GA

Purpose

• Review the concept of altered intracranial pressure disorders. • Briefly discuss the epidemiology and the disease theories. • Summarize the Idiopathic Intracranial Hypertension (IIH) syndrome and the clinical presentation phenotypes. • Highlight the radiologic findings in MRI that are more prevalent and frequently encountered in patients with chronically elevated intracranial pressure, particularly in a highly prevalent community such the one our practice is established in. • Become familiar with the typical and atypical imaging presentations of increased intracranial pressure to suggest this diagnosis and guide appropriate treatment for the clinical team. A few interesting examples include spontaneous CSF-filled outpouchings of the dura (cephaloceles) [Figures 1 and 2], low lying cerebellar tonsils that can be confused with Chiari I variant [Figure 3], more commonly encountered findings as empty or partially empty sella [Figure 3] and transverse venous sinus stenosis [Figure 4]. • Review the current options, including conservative, pharmacologic, and surgical approaches, available and in use by different medical specialties to manage IIH.

Materials and Methods

Explore the common and uncommon imaging presentations of Idiopathic Intracranial Hypertension (IIH). A concise, yet comprehensive overview of IIH, will first be discussed, including basic concepts, pathophysiology, management, and recent updates. This will be followed in an interactive manner by a pictorial review of the usual findings of this condition followed by examples of more atypical manifestations.

Results

N/A

Conclusions

IIH is a misunderstood disease. Patients may present initially to a wide variety of providers, like optometrists or ophthalmologists for blurry vision, PCPs and neurologists for neurologic deficits, tinnitus, or headaches and even otolaryngologists or neurosurgeons for spontaneous CSF leak. Imaging excludes masses, hydrocephalus, venous sinus thrombosis, as well as additional orbital, skull base and venous imaging findings. A routine brain MRI protocol is frequently order by clinicians and is our responsibility recognizing the characteristic findings of IIH. If additional suspicion is raised for the presence of IIH, a coronal fat suppressed T2W images of the orbit and contrast enhanced MRV to evaluate the venous sinuses are highly recommended. This condition is highly prevalent in our community, thus, our institution has implemented a protocol to minimize the incidence of reimaging and hospital stay.

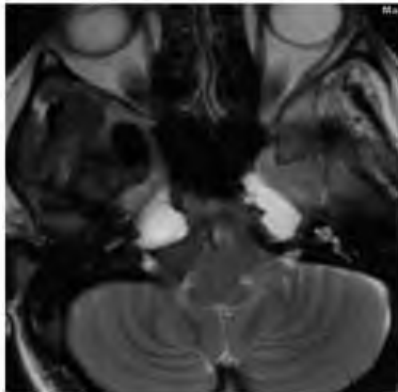


Figure 1 Axial T2 weighted image in a 31 year-old-female demonstrating bilateral enlarged Meckel caves.

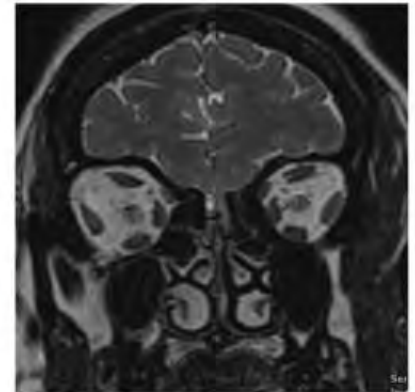


Figure 2 Coronal T2 weighted image in a 44-year-old female with rhinorrhea and chronic headache demonstrating an encephalocele of the left gyrus rectus through the cribriform plate, found later to have Idiopathic Intracranial Hypertension

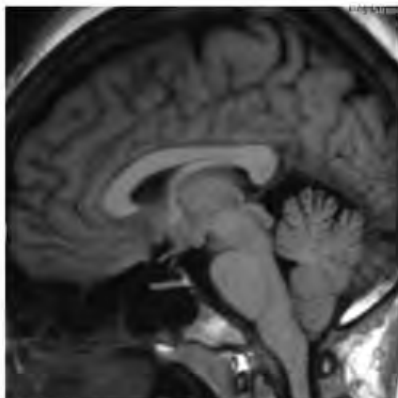


Figure 3 Sagittal T1 weighted image in a 31 year-old-female with chronic headaches and elevated opening pressure on LP demonstrating an empty sella configuration, abnormal for her age and borderline cerebellar tonsils below the foramen magnum

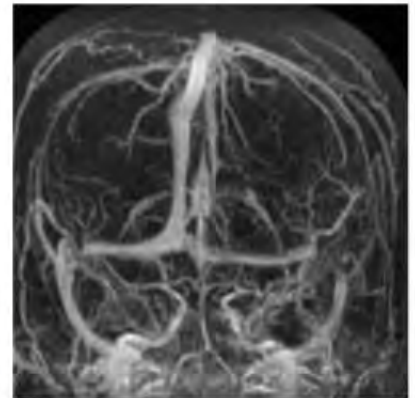


Figure 4 MR venography showing bilateral stenotic transverse sinuses in 37 year-old-female with elevated intracranial pressure and chronic headache and concomitant empty sella

(Filename: TCT_181_graphicIIH300.JPG)

605

Pilomatricoma and Superficial Soft-Tissue Masses of the Head and Neck: A Pictorial Review

C Ju¹, N Pham¹

¹UCLA, Los Angeles, CA

Purpose

Pilomatricomas are common benign tumors. Radiologic encounters with this entity, however, are rare given the infrequent use of imaging in diagnosis and management. This educational exhibit will describe pertinent background, histology, and imaging features of pilomatricoma and distinguish it from other superficial soft-tissue masses that may be encountered. 1. To review background information, sites of occurrence, histopathologic and imaging features of pilomatricoma in the head and neck. 2. To review the differential diagnoses for pilomatricoma and associated histopathologic and imaging features.

Materials and Methods

Pilomatricomas are benign tumors arising from hair follicle matrix cells and commonly present in the neck and periorbital, scalp, and preauricular regions of the head. Though pilomatricomas make up less than 0.5% of skin tumors overall, they comprise approximately

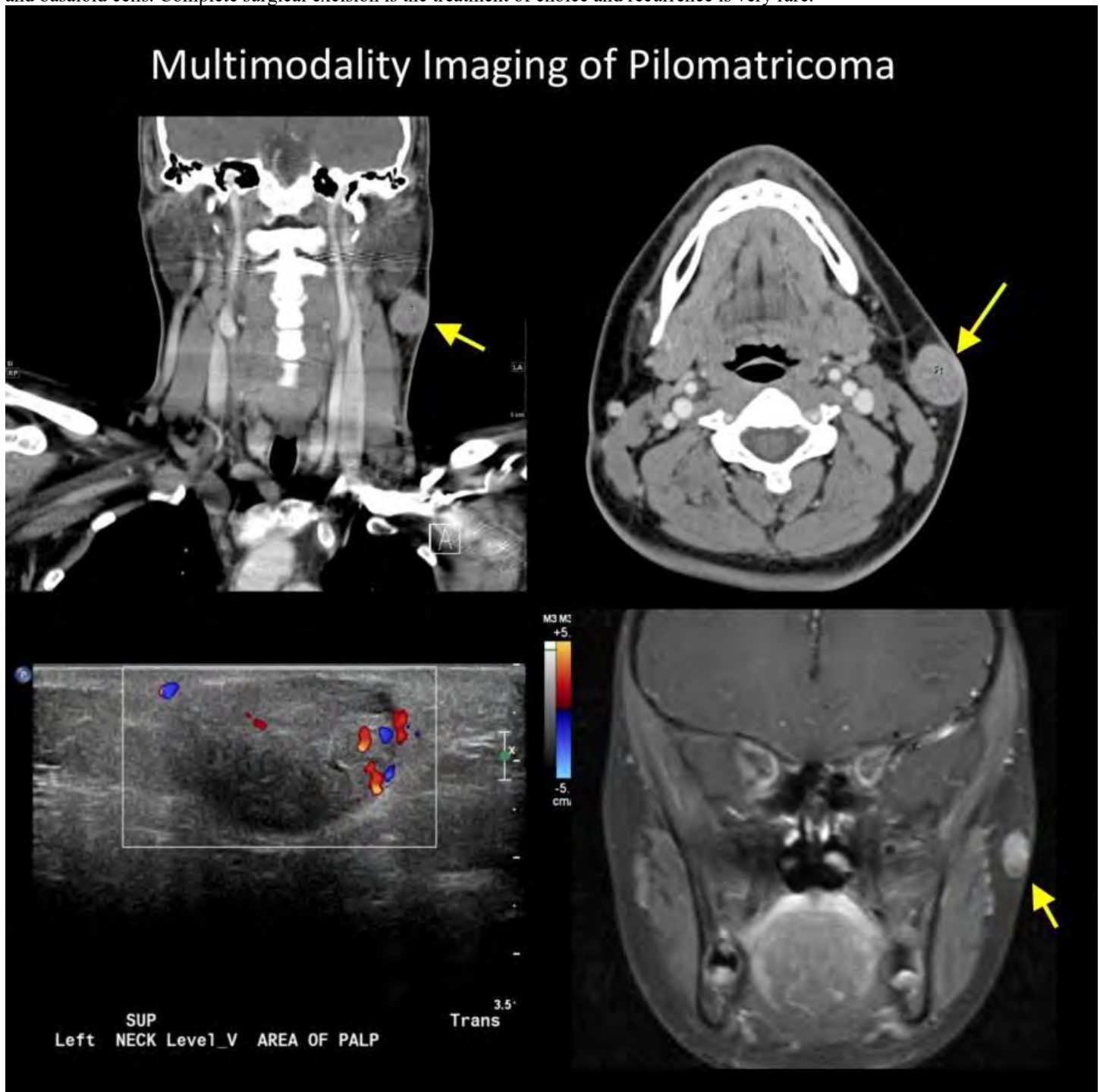
10% of superficial masses seen by pathologists. Other mimicking superficial soft-tissue masses include sebaceous cyst, dermoid cyst, ossifying hematoma, adenopathy, giant cell tumor, chondroma, degenerating fibroxanthoma, foreign body reaction, and osteoma cutis. Histologically, pilomatricomas appear as encapsulated dermal nodules. Dead cells that retain their shape are termed enucleated shadow cells, or ghost cells, and can be found in the center of these nodules. Ultrasound is often used as first-line imaging. Common features include hypoechoic connective tissue capsules with internal reticulations. On CT, the lesion is confined to skin and subcutaneous fat with various patterns of calcification, which may mimic dermoid or sebaceous cysts. On MRI, the lesion appears heterogeneously enhancing and without restricted diffusion, which distinguishes it from cystic lesions.

Results

A single institutional retrospective review was performed to identify cases of pilomatricomas of the head and neck. Subsequently, a comprehensive literature review was performed to elucidate pertinent background, histologic and imaging findings of pilomatricomas.

Conclusions

Pilomatricoma is a benign skin neoplasm derived from hair follicle matrix cells and commonly discovered in the neck, cheek, periorbital region, and scalp. Most cases occur in children and adolescents. The unique histopathologic findings are that of ghost cells and basaloid cells. Complete surgical excision is the treatment of choice and recurrence is very rare.



1432

Pituitary Apoplexy: Imaging and Clinical Features

E Sechrist¹, G Carpenter², M Bashir³

¹Loyola University Medical Center, Maywood, IL, ²Loyola University Medical Center, Chicago, IL, ³Loyola University Medical Center, Maywood, IL

Purpose

This educational exhibit will present real examples of pathologically-confirmed pituitary apoplexy. Imaging findings and clinical features of will be discussed.

Materials and Methods

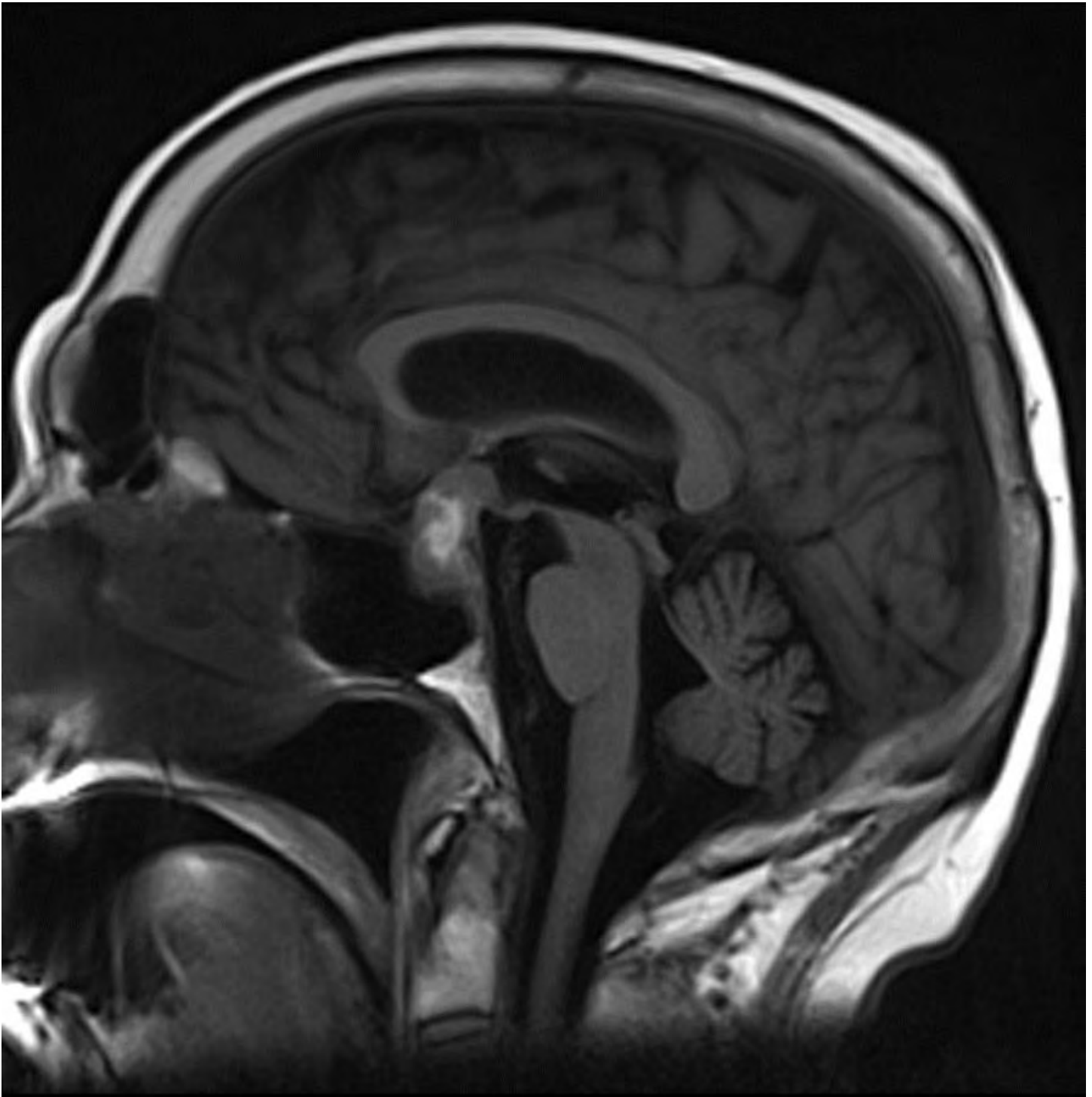
Pituitary apoplexy is a condition caused by hemorrhage or infarction of a normal or neoplastic pituitary gland. It is a clinical diagnosis with a constellation of symptoms including sudden onset of headache, nausea, vomiting, blurry vision, and ptosis. Due to its critical hormonal producing function, pituitary infarction caused by apoplexy can be fatal. While imaging features of apoplexy can be nonspecific, appropriate history with corroborating imaging findings can certainly aid in diagnosis. This educational exhibit will present real examples of pathologically-confirmed pituitary apoplexy. Imaging findings and clinical features of will be discussed.

Results

N/A

Conclusions

N/A



(Filename: TCT_1432_MRSagT1pre8.gif)

832

Planning and Evaluation of Pediatric Middle Ear Surgeries: What the Surgeon Needs to Know

R Smalley¹, K SODERLUND¹, N DiGeorge¹

¹Naval Medical Center Portsmouth, Portsmouth, VA

Purpose

After viewing this educational exhibit, the radiologist should be able to 1. Describe the surgical approach, appearance of common implants, and expected post-surgical appearance of the middle ear following several common middle ear surgeries. 2. Describe the common pathology requiring these surgeries, relevant findings relating to the extent and severity of these pathologies, and relevant variant anatomy and comorbid conditions that would affect surgical planning. 3. Describe common complications of these surgeries

including infections, implant failure, residual/recurrent disease, and injury to adjacent structures. 4. Provide the ordering surgeon a succinct and complete evaluation for the topics described above.

Materials and Methods

Pediatric conditions leading to middle ear surgery are relatively common, including tympanic membrane rupture, ossicular chain destruction, cholesteatoma, occult mastoiditis, chronic otitis media, and bilateral severe-to-profound sensorineural hearing loss. The middle ear is densely packed with anatomic structures that are visible on CT and MRI, with many well described anatomic variants that affect both surgical candidacy and the surgical approach to be taken. Additionally, there are sites of pathology that are not visible during endoscopic surgery which must be remarked upon during pre-operative imaging workup. Following surgery, the ordering surgeon will be well served by a report detailing the presence or absence of complications that may lead to treatment failure or the need for revision surgery.

Results

Correlating CT and MRI imaging from pre- and post-operative cases, endoscopic intraoperative photographs, ex-vivo photographs of surgical implants and tools, and medical illustrations of surgical approaches, the radiologist will gain a more complete understanding of common middle ear surgeries. These include tympanic membrane closure, ossicular chain reconstruction, antrotomy, mastoidectomy, cholesteatoma surgery and cochlear implantation.

Conclusions

The radiologist is provided a checklist of suggested items to address within the findings section of the radiology report on pre- and post-operative imaging. This includes anatomic variants of surgical significance, comorbid conditions, post-operative infections, and complications that may result in treatment failure or the need for revision surgery. The radiologist is also provided a list of suggested impression statements to succinctly convey the presence or absence of these findings.

774

Post-operative Imaging in Moyamoya Disease: CT Angiography and MR/CT Perfusion.

P Reddy¹, M Mian², S Viswamitra², M Kumar², R Van Hemert³, R Ramakrishnaiah⁴, S Vattoth⁵

¹University of Arkansas for Medical Sciences, Little rock, AR, ²University of Arkansas for Medical Sciences, Little Rock, AR, ³UAMS, Little Rock, AR, ⁴Univ of Arkansas for Medical Sciences, Little Rock, AR, ⁵University of Arkansas for Medical Sciences, LITTLE ROCK, AR

Purpose

The objectives of this presentation are to: 1. Review the treatment options for Moyamoya disease 2. Review the expected postoperative imaging features 3. To recognize the complications of surgery 4. To understand the hemodynamic changes that occur post treatment and their assessment with imaging. The summary of the presentation is as follows: 1. Introduction 2. Treatment options - direct bypass procedures, indirect bypass, combine procedures 3. Normal postoperative imaging appearance after direct and indirect procedures and changes over time 4. Surgical complications a. Cerebral ischemia b. Hyperperfusion syndrome c. Significance of the Ivy sign d. Graft occlusion and failure 5. Post operative perfusion imaging 6. Conclusion

Materials and Methods

The purpose of this educational exhibit is to describe the normal expected post operative imaging features following surgery for Moyamoya disease as well the complications associated with surgery. A brief review of the various surgical techniques will be followed by a discussion of the imaging features. The role of postoperative perfusion imaging for determining prognosis will also be discussed.

Results

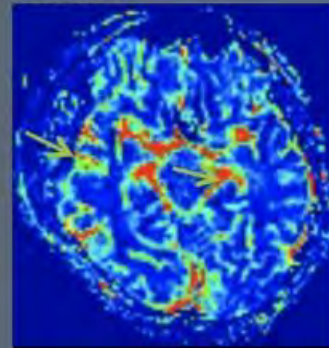
A retrospective review of the institute database for interesting and challenging cases was performed using a keyword search.

Conclusions

N/A

Pathophysiology of hyperperfusion syndrome in MMD

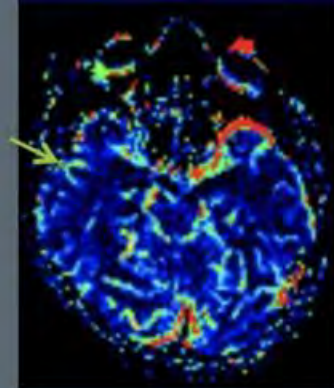
Vaso-paralysis under chronic ischemia
Aberrant neoangiogenesis – fragile wall structure
Poor pial collateral flow
Raised pro inflammatory factors



STA – MCA bypass

Reperfusion

Reactive oxygen species production
Further increase in pro-inflammatory cytokines



Focal hyperperfusion
Local vasogenic edema

Focal neurological deficit
Hemorrhagic conversion

Preoperative (bottom) and postoperative (top) MR perfusion CBV maps in the same patient showing increased CBV in the right temporal lobe as compared with the pre op scan suggestive of hyperperfusion.

(Filename: TCT_774_MMDpost.jpg)

1389

Practical fMRI Data Analysis Tutorial

L Daftari¹, S Mirbagheri¹, S Agarwal¹, S Gujar¹, J Pillai², H Sair³

¹Johns Hopkins University, Baltimore, MD, ²Johns Hopkins Univ. School of Medicine, Baltimore, MD, ³Johns Hopkins University School of Medicine, Baltimore, MD

Purpose

Practical fMRI data analysis tutorial supplemented by clinical cases intended primarily for neuroradiologists, radiology residents and fellows with beginner level fMRI experience.

Materials and Methods

The increasing importance of FMRI to answer clinically relevant and scientifically interesting questions has led to a demand for analysis techniques which allow radiologists and investigators to interrogate the acquired data in informative and convenient manner. One of the widely used software for fMRI data analysis is FSL (FMRIB Software Library). FSL is a free suite of applications from Oxford's Functional Magnetic Resonance Imaging of the Brain (FMRIB) laboratory. It can be used on Mac OS X and Linux, and Windows in a Virtual Machine environment. The purpose of this presentation is to provide a practical step-by-step post-processing and data presentation of BOLD fMRI using FSL (FMRIB Software Library) software.

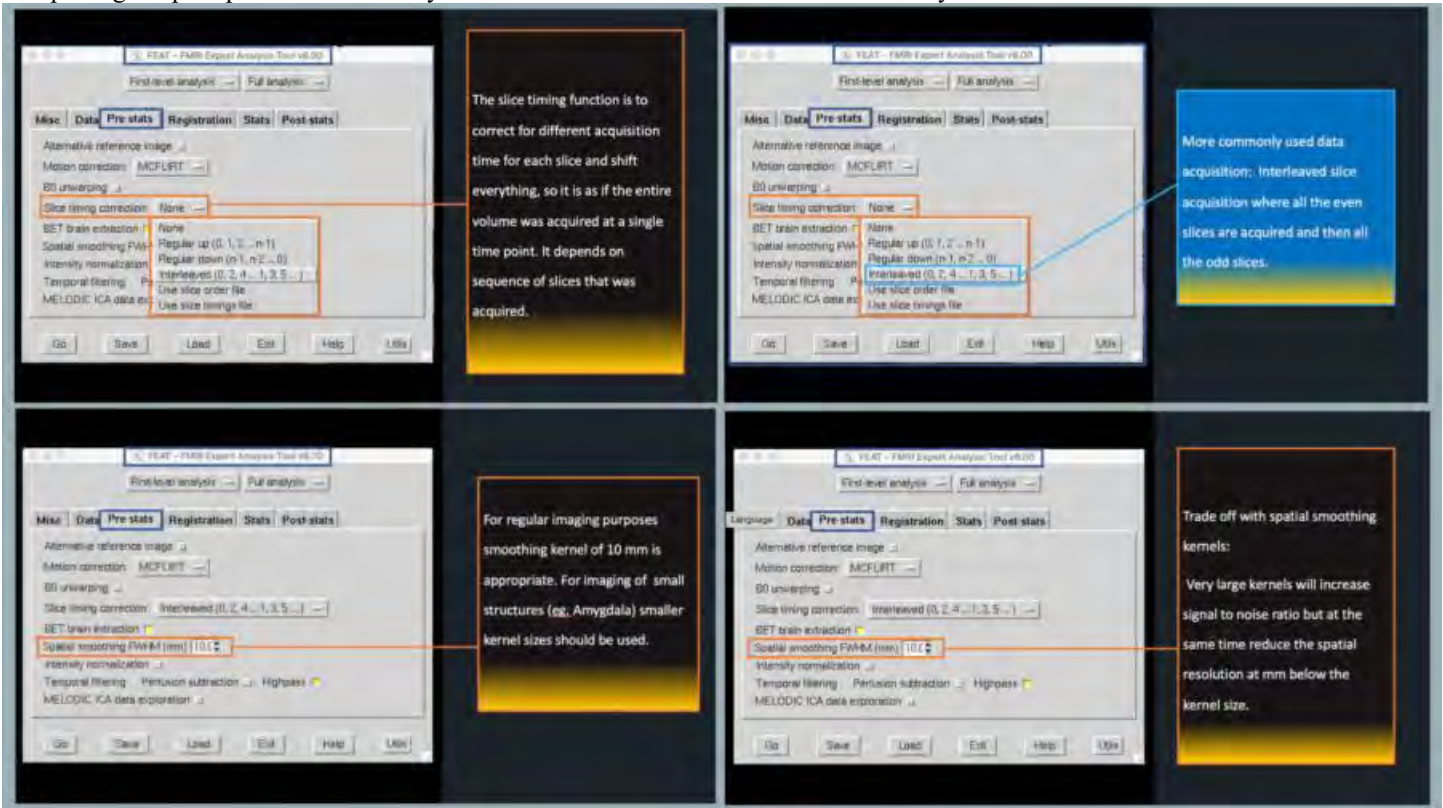
Results

This presentation provides a practical step-by-step post-processing and data presentation of BOLD fMRI of both task-based language and sensory-motor cortex and resting state studies using FSL software. The presentation underscores how to think about fMRI data and the steps of analysis in addition to details of how to perform each step.

Conclusions

The techniques available for the interrogation and analysis of neuroimaging data have a large influence on flexibility, sensitivity, and

scope of the findings and interpretation of the data. Also, particularly for the resting state fMRI that no commercially available software exists, FSL and other research packages are essential. Thus, it is very important that the neuroradiologists who are interpreting the post-processed and analyzed results be familiar with the fMRI data analysis.



(Filename: TCT_1389_Sampleslides.jpg)

1142

Practical Guidelines and Pitfalls on how to implement MR Spectroscopy in the Clinical Practice

R Riascos¹, S Khanpara¹, A Aein¹, O Arevalo², R Patel¹

¹University of Texas Health Science Center at Houston, Houston, TX, ²MD Anderson Cancer Center, Houston, TX

Purpose

N/A

Materials and Methods

MR proton Spectroscopy (MRS) is a technique that has been utilized for three decades; however, implementing it in a Clinical Setting has multiple challenges. We will review the main technical challenges and demonstrate through cases an easy guide on how to implement MRS. This exhibit should help radiology residents and technologists to understand the approach to basic MRS imaging and identify the major challenges to obtain a high quality study.

Results

Introduction to MRS Why is PRESS the most frequently used technique? Should I use long or short TE; should I use Multi or Univoxel MRS? How to correctly place the voxel Shimming and pitfalls Clinical Scenarios where MRS is mostly utilized MRS in pediatric brain Changes with age Demyelinating and Developmental disorders MRS in adult brain Role of MRS in Advanced Brain Tumor Imaging Questions Tumor or non neoplastic Tumor type Tumor grade White matter infiltration vs Edema Tumor recurrence vs Necrosis Other Pitfalls Multivoxel corner Incomplete water saturation in CSF contamination Postprocessing

Conclusions

We will present cases to demonstrate the imaging challenges.

772

Pre-operative Imaging in Moyamoya Disease: A Pictorial Review.

P Reddy¹, M Mian², S Viswamitra², R Van Hemert³, R Ramakrishnaiah⁴, M Kumar², S Vattoth⁵

¹University of Arkansas for Medical Sciences, Little rock, AR, ²University of Arkansas for Medical Sciences, Little Rock, AR, ³UAMS, Little Rock, AR, ⁴Univ of Arkansas for Medical Sciences, Little Rock, AR, ⁵University of Arkansas for Medical Sciences, LITTLE ROCK, AR

Purpose

The objectives of this presentation are: 1. To understand the pathophysiology of Moyamoya disease 2. To review to diagnostic criteria for Moyamoya disease 3. To review the imaging characteristics of Moyamoya disease in various modalities 4. To review the causes of Quasi Moyamoya disease The summary of the presentation is as follows: 1. Introduction 2. Pathophysiology 3. Clinical features 4. Diagnostic criteria 5. Staging 6. Collateral pathways on DSA 7. Significance of PCA lesions 8. MRI findings in Moyamoya disease 9. Preoperative perfusion imaging - diamox challenge, MR perfusion and ASL 10. CT findings in Moyamoya disease. 11. Case examples of Quasi Moyamoya disease 12. Conclusion.

Materials and Methods

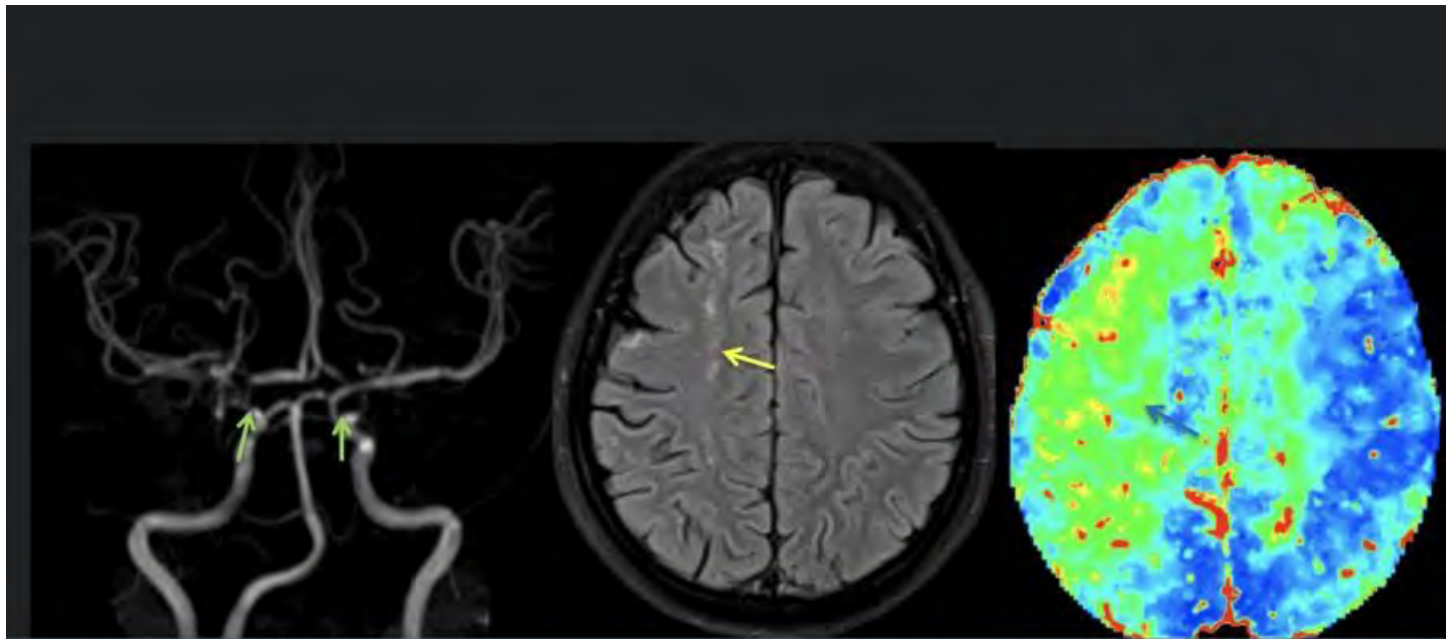
Moyamoya disease is rare condition with characteristic imaging manifestations. Imaging play an important role in diagnosis of Moyamoya disease and exclusion of quasi Moyamoya disease. MR and CT perfusion helps defined disease severity and set a based line for cerebral hemodynamics before surgery. The purpose of this review is to describe the imaging manifestations of Moyamoya disease with an emphasis on the role of pre operative perfusion imaging.

Results

A retrospective review of the institute database was performed using a key word search. Cases with characteristic findings and cases which posed a diagnostic challenge were selected for the purposes of this review.

Conclusions

N/A



MRA shows severe stenosis of the bilateral supraclinoid ICA's and proximal MCA's. There is a deep watershed infarct on the left. The CT perfusion MTT map shows prolonged transit time in the MCA territory which is an area of impaired CVR at risk for infarction and likely to benefit from revascularization.

(Filename: TCT_772_MMDpre.jpg)

259

Preoperative Functional MRI: A primer for Radiology Residents and Neuroradiology Fellows

M Trevino¹, B Langdon², M Spampinato¹

¹MUSC, Charleston, SC, ²Medical University of South Carolina, Charleston, SC

Purpose

Blood-oxygen-level-dependent (BOLD) functional magnetic resonance imaging (fMRI) is widely used to map eloquent brain areas for presurgical planning and neuronavigation, in conjunction with tractography. BOLD fMRI takes advantage of "neurovascular coupling", a property of the cerebral vasculature resulting from neuronal activity. Neuronal activity triggers a hemodynamic response that creates localized changes in brain blood oxygenation. The BOLD technique can localize changes in tissue oxygen content due to alterations in the local magnetic properties of oxyhemoglobin (diamagnetic) and deoxyhemoglobin (paramagnetic) secondary to the hemodynamic response (vasodilation) to neuronal activation. Our objectives are the following: • Review basic principles of task-based fMRI. • Review of the recommended ASFNr fMRI paradigms to test motor function, language, and vision. • Case-based review of common applications of fMRI. • Review of limitations and pitfalls of fMRI, including susceptibility artifacts and neurovascular uncoupling.

Materials and Methods

Our purpose is to provide a didactic review of clinical fMRI in a case-based review format.

Results

We will present fMRI cases performed for presurgical planning selected from our teaching file. Tractography will also be reviewed when available. Our presentation will include pediatric and adult cases of brain tumor, arteriovenous malformation, cavernoma, and malformation of cortical development. Cases will be accompanied by multiple-choice questions in an interactive format.

Conclusions

fMRI has a key role in preoperative mapping of eloquent brain regions adjacent to a resectable brain tumor, vascular malformation, or epileptogenic focus. fMRI provides unique information to plan surgery while minimizing the risk of inducing permanent neurological deficits, especially when sulcal anatomy is distorted due to tumor infiltration. The sensitivity and specificity of fMRI for mapping language and motor are greater than 80%, with higher false negative rates in GBMs due to neurovascular uncoupling with loss of the BOLD response. fMRI is a valuable alternative to the WADA test for the evaluation of language hemispheric dominance in epilepsy. The role of the Neuroradiologist has gone beyond mere anatomical assessment to the use of fMRI for presurgical localization of eloquent brain regions. It is important for radiology trainees to gain familiarity with functional mapping techniques.

1315

Preoperative radiological evaluation in cochlear implantation – A systematic approach

S Hiremath¹, D Schramm¹, S Chakraborty¹

¹University of Ottawa, Ottawa, Ontario

Purpose

Computed tomography and magnetic resonance imaging (MRI) appearances of imaging findings in inner malformations will be described in a case-based format, illustrating the salient features. We need to be aware of the basic anatomy of the inner ear and congenital and acquired inner ear pathologies. There is an increasing need to be aware of surgical methods used to treat sensorineural hearing loss, particularly cochlear implantation, and the factors influencing surgical methods and approach.

Materials and Methods

This educational exhibit aims to: • Review the basic anatomy of the inner ear, including the cochlear, vestibule, and semicircular canals • Describe the imaging findings that influence the choice of surgery in inner ear malformations • Illustrate the findings in congenital and acquired causes of sensorineural hearing loss that are amenable to cochlear implantation • Depict the anatomical factors that influence surgical approach during cochlear implantation

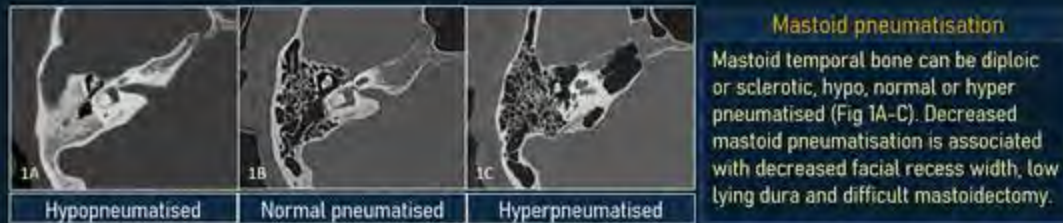
Results

Computed tomography and MR imaging complement each other in evaluating the inner ear anomalies and factors affecting surgical management and prognosis. It is of utmost importance as it may guide in surgical decision making and reduce complications. We will demonstrate the role of CT, cone beam CT and MR imaging, including multiplanar reformats and high-resolution T2W imaging, in the evaluation of the sensorineural hearing loss and likely surgical candidates. We will illustrate the utility of imaging modalities as problem-solving tools in identifying the conditions that influence surgical decision making and reduce complications. Particular focus will be placed on the common and infrequent anatomical variants involving facial nerve, jugular fossa, and sigmoid sinus along with rare arterial variations. We will also highlight the extent of the mastoid pneumatization and its secondary effects, including durameatal distance and facial recess width. We will also describe in brief the radiological assessment of cochlear duct length, width and round window accessibility.

Conclusions

There are many inner ear malformations, common and infrequent anatomical factors that influence cochlear implant surgery. As radiologists, we need to be aware of the anomalies and variants to facilitate optimal decision making and minimize surgical complications.

Anatomical factors influencing cochlear implant surgery



(Filename: TCT_1315_Cochlearimplants.gif)

1299

Preventing and treatment of acute allergic reactions to Gadolinium-Based Contrast Agents

A Heshmatzadeh Behzadi¹, A Megahed², A Saeed Bamashmos³, K Elfatairy⁴, G Parmar⁵, G Muro⁶

¹Yale New Haven Health-Bridgeport Hospital, Milford, CT, ²Yale New Haven Health, Bridgeport Hospital, Bridgeport, CT, ³Yale New Haven Health Bridgeport Hospital, Bridgeport, CT, ⁴Yale New Haven Health-Bridgeport Hospital, Bridgeport, CT, ⁵Yale New Haven Health/Bridgeport Hospital, Bridgeport, CT, ⁶Yale New Haven Health-Bridgeport Hospital, Bridgeport, CT

Purpose

Immediate-type allergic reactions to gadolinium based contrast agents (GBCAs) are known to be very rare. Compared with iodinated contrast for which serious reactions such as anaphylaxis have been reported in 0.02% to 0.04% of intravenous procedures, GBCA reactions are much less frequent on the order of 1:10,000. Despite the low incidence of immediate-type gadolinium-based contrast agent (GBCA) allergic reactions, preventing these reactions, and properly managing them to reduce their adverse sequelae can improve the already favorable GBCA safety profile.

Materials and Methods

Educational Goals/Teaching Points This Presentation will help those who manage the administration of GBCA contrast agents, particularly in screening, recognizing, monitoring, and treating the allergic reactions intrinsic to their use.

Results

Areas of focus include factors indicating increased allergic reaction risk, patient selection strategies, skin testing, premedication, and treatment of adverse events.

Conclusions

GBCAs are extraordinarily safe and useful for contrast-enhanced MRI examinations. The extremely low incidence of immediate-type allergic reactions to GBCAs and nearly nonexistent death rate (1 per million injections) can lure practitioners into complacency. But severe allergic reactions to GBCA can occur and this risk can be mitigated by remaining vigilant and prepared for reactions. Higher risk patients can be imaged at hospitals with code teams during the daytime making it easier to manage adverse events if they do occur. Patients with a history of surviving a severe GBCA reaction can undergo skin testing to identify specific GBCA which might be tolerated. Several studies suggest that nonionic linear agents may have the lowest rate of severe reactions. Premedication with steroids and antihistamine for high-risk patients may be helpful but breakthrough reactions can occur. Epinephrine IV (0.1 mg administered as 1 ml of 1:10,000 dilution) or IM (0.3 mg administered as 0.3 ml of 1:1000 dilution) is the drug of choice for anaphylaxis.

258

Primary Melanocytic Tumors of the Central Nervous System in Children: Imaging Features with Pathological Correlation

M Quinn¹, J Aw-Zoretic², N Wadhvani³, A Jaju⁴

Purpose

Primary melanocytic tumors of central nervous system in children are rare neoplasms arising from proliferation of the multipotent melanin containing neural crest cells found in the leptomeninges. These can have a wide range of manifestations, and are subclassified by the WHO based on a diffuse or focal pattern and pathologic aggressiveness, into following four subtypes: meningeal melanocytosis, meningeal melanomatosis, meningeal melanocytoma and meningeal melanoma. The radiology literature on the primary melanocytic tumor imaging is limited to mainly case reports, with few focusing on the pediatric population. The goal of this presentation is to illustrate the imaging appearance of entire spectrum of diffuse and focal primary melanocytic tumors of the brain and spine in pediatric population, supplemented with correlating histopathological slides, clinical context, and prognostic information. Diffuse types of primary melanocytic tumors are more common in children, often in association with neurocutaneous melanosis. Diffuse meningeal melanocytosis and melanomatosis demonstrate sulcal hyperdensity on CT that can mimic subarachnoid hemorrhage. MRI can demonstrate intrinsic T1 hyperintensity and loss of the normal CSF signal within the sulci. Diffuse leptomeningeal enhancement is characteristic. Malignant degeneration into a melanoma has been described in 40-62% of cases. Meningeal melanocytoma is a benign nodular leptomeningeal growth which occurs most commonly in the cervical and thoracic spine, the posterior cranial fossa, and Meckel's cave, likely related to the higher density of pigment producing neural crest cells in these regions. Meningeal melanoma is the malignant form of this process. On imaging, both melanocytoma and melanoma appear as dural based, well-defined masses with intrinsic hyperintensity on T1 weighted imaging, although concentration of melanin is variable. On T2 weighted imaging, they usually demonstrate iso- to hypointense signal and variable postcontrast enhancement. Associated hemorrhage demonstrating hyperdensity on CT and susceptibility on MRI is commonly seen. Differential considerations for diffuse disease include subarachnoid hemorrhage, meningitis, leptomeningeal carcinomatosis, and neurosarcooidosis. Several other primary and metastatic central nervous system masses can contain melanin, including metastatic cutaneous melanoma, melanotic meningioma, melanotic schwannoma, and even sometimes melanotic medulloblastoma.

Materials and Methods

NA

Results

NA

Conclusions

NA

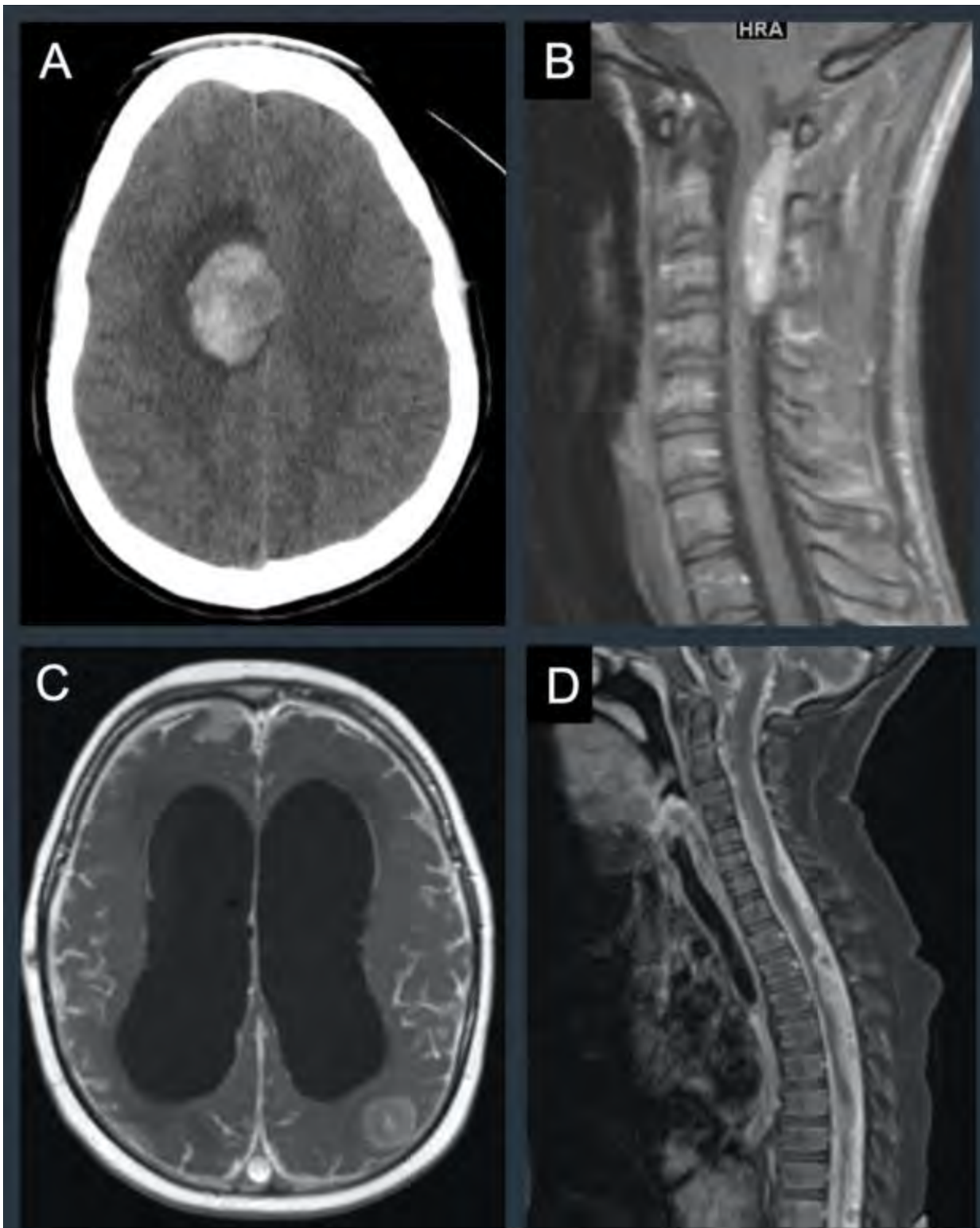


Figure 1. Pediatric primary melanocytotic disease. (A) CT demonstrates a hyperdense mass in the right paramedian frontal lobe of a teenage patient. This was a primary melanoma of the CNS complicated by hemorrhage. (B) Sagittal postcontrast T1-weighted image in a second teenage patient shows an extramedullary intradural enhancing cervical mass that was found to be a melanocytoma. This mass demonstrated intrinsic T1 hyperintensity (not shown). (C) Axial postcontrast T1-weighted MRI image in a child with diffuse melanomatosis demonstrates leptomeningeal enhancement and an enhancing left parietal lesion, which was likely leptomeningeal disease with parenchymal invasion. (D) Sagittal post contrast T1 cervical spine in the same patient shows diffuse extensive leptomeningeal enhancement.

(Filename: TCT_258_MelanocyticTumorsinPediatricPopulation_ASNRAbstract_Figure1.jpg)

Pseudolesions of The Head and Neck: A Pictorial Review

O Alharbi¹, A Aljebreen¹, M Almushayqih¹, M Nicolas-Jilwan²

¹King Faisal Specialist Hospital and Research Centre, Riyadh , AK, ²King Faisal Specialist Hospital and Research Centre, Riyadh, Saudi Arabia

Purpose

Knowledge of the potential pseudolesions of the head and neck is a fundamental prerequisite for a safe interpretation of imaging studies of this region. This pictorial review is intended to familiarize the reader with the most commonly encountered entities.

Materials and Methods

Anatomy of the head and neck is complex and challenging. The complexity is compounded by the juxtaposition of multiple crucial structures, the diverse devices that can be surgically implanted and variations of the normal anatomy. Pseudolesions of the head and neck refer to a wide range of normal anatomical variants, normal but ectopic structures, and implanted devices which should not be mistaken for pathology. This will avoid unnecessary additional explorations and patient anxiety. We present a wide range of these pseudolesions, the knowledge of which is crucial for a safe interpretation of head and neck imaging.

Results

We selected cross sectional examinations demonstrating several of the known pseudolesions of the head and neck. These include a patient with arrested pneumatization of the sphenoid sinuses as well as two cases with anatomical variations of the musculature: asymmetry of the anterior bellies of the digastric muscles and a patient referred for evaluation of a "parotid mass" who had a normal but large masseter muscle. Among variations of the salivary glands, we present a case of bilateral herniation of the sublingual glands and a child with facial microsomia, absent parotid gland and asymmetrically large accessory parotid along the masseter muscle. Two cases of vascular variants commonly mistaken for pathology are shown, including asymmetry of the pterygoid venous plexi and prominent suboccipital veins. We highlight the imaging features of a cervical ectopic thymus in a pediatric patient. We also show a neck CT illustrating the classical features of an ectopic thyroid gland. Finally, we present the CT of an obturator prosthesis post palatectomy, misdiagnosed as a recurrent tumor.

Conclusions

Among all potential pseudolesions of the head and neck, we selected examples of those most commonly mistaken for pathologies and highlighted their key features. We included all major categories encompassing bony, muscular and venous variants as well as variations of the salivary glands and ectopic glands. Among the numerous implants that can be encountered, we highlight the CT appearance of an obturator prosthesis as many radiologists are unfamiliar with these rarely used devices and the variations of their CT features.

718

Radiological Imaging in Anatomical Pharyngeal Dysphagia: A Case Based Review

M Jayakumar¹, N BR²

¹AMD Imaging Systems, Chennai, Tamilnadu, ²Bangalore Medical College, Bangalore, Karnataka

Purpose

Dysphagia is the perception that there is an impediment to the normal passage of swallowed material. When there is difficulty in moving the bolus from the mouth to the esophagus, it is termed oropharyngeal dysphagia. Difficulty in initial phases of swallowing can be due to anatomical or neuromuscular causes. This article discusses the various imaging findings in abnormal states of the pharynx, an anatomically and functionally complicated segment of the gastrointestinal tract. Learning Objectives: 1. Discuss the anatomy of swallowing pathway with special focus on the pharynx 2. List imaging techniques that may be used in the evaluation of patients with dysphagia, discuss the spectrum of common and uncommon causes and develop a clinico-radiological approach to oropharyngeal dysphagia 3. Describe the imaging findings of disease entities that may produce anatomical pharyngeal dysphagia with emphasis on MDCT

Materials and Methods

Dysphagia can be classified as high/oropharyngeal or low /esophageal dysphagia based on the location of pathology. Oropharyngeal dysphagia is either structural/anatomical or functional/neuromuscular. Barium swallow is the initial investigation in most patients presenting with dysphagia. MDCT allows for anatomical assessment of hypopharynx, providing a global perspective of the surrounding structures, aiding in detection, localisation and diagnosis of both intrinsic and extrinsic pathologies. This poster aims to provide an overview of dysphagia anatomy, pathology, imaging and facilitate appropriate clinical management. It presents a case based review of various anatomic causes of pharyngeal dysphagia.

Results

Barium swallow and MDCT images of patients who presented to our department of radiology with clinical diagnosis of mechanical dysphagia over a period of 1 year were reviewed retrospectively. 68 patients had obstructive dysphagia due to pharyngeal causes. Selected interesting cases are presented in this educational exhibit.

Conclusions

This pictorial review illustrates few interesting pathologies that cause structural pharyngeal dysphagia. Malignant tumors of swallowing pathway were the most common cause in our study. Other pathologies included diverticula, lesions causing extrinsic compression (lymph nodes, thyroid, cervical osteophytes), foreign bodies, infective processes and benign tumors. Knowledge of the imaging spectrum of disease entities that cause pharyngeal dysphagia and comprehensive radiologic assessment will help in reaching the accurate diagnosis.

1368

Radiologist's Guide to Orthognathic Surgery

M Lum¹, S Strauss¹

¹Weill Cornell Medical Center, New York, NY

Purpose

See below

Materials and Methods

Orthognathic surgery, or corrective jaw surgery, encompasses techniques aimed at improving maxillo-mandibular alignment for a variety of dentofacial conditions. Advances in surgical technique as well as the advent of computed tomography and anatomic 3D modeling led to increase in its utilization since the 1980s. As the discipline of oral and maxillofacial surgery continues to expand, it is important for radiologists to be familiar with modern orthognathic surgical techniques. At most centers, routine preoperative and postoperative imaging is performed and interpreted by oral surgeons in the office with dental radiographs and cone-beam CT, and conventional maxillofacial CT is usually only performed when postoperative complication is often suspected. However, there is a relative paucity of radiology literature reviewing expected and unexpected findings after orthognathic surgery. In this exhibit, we highlight normal and abnormal perioperative imaging findings in the setting of orthognathic surgery, and underscore key imaging descriptors relevant to surgical management.

Results

This image-based electronic exhibit will focus primarily on maxillofacial CT as the mainstay of perioperative evaluation for orthognathic surgery with emphasis on CT-based 3D modeling. The presentation will begin by introducing the most common surgical techniques including LeFort 1 osteotomy, LeFort 3 osteotomy, bilateral split sagittal osteotomy, and genioplasty. This will lead into an overview of indications for orthognathic surgery, including malocclusion, obstructive sleep apnea, and syndromic craniofacial anomalies (e.g. Pierre Robin sequence). The normal postoperative CT appearance for these surgeries will be presented utilizing CT images, 3D models, and corresponding schematic diagrams. Finally, we will conclude with a case-based review of common postoperative complications including nonunion/malunion, infection, and hemorrhage with integration of clinical history.

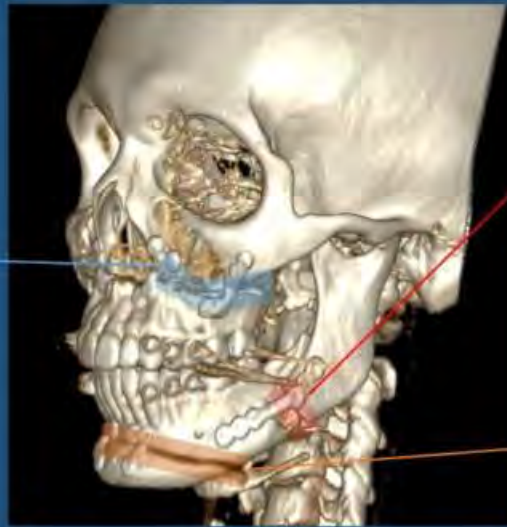
Conclusions

Orthognathic surgery, which focuses on improving maxillo-mandibular alignment, is increasingly utilized for both functional and cosmetic purposes. Due to the prevalence of in-office imaging by oral and maxillofacial surgeons, radiologists are not always routinely involved in the perioperative evaluation of patients undergoing orthognathic surgery. An understanding of modern surgical techniques and clinical indications is necessary in order to recognize the normal and abnormal postsurgical findings.

3 Common Components of Orthognathic Surgery

1. LeFort1 Osteotomy

- Similar to the eponymous fracture pattern
- Horizontal osteotomy traverses the maxillary ridge, lateral nose, and inferior maxillary sinus
- Allows for the mobilized segment to be moved in any plane.
- Pterygoids are involved to allow midface separation.



2. Bilateral Sagittal Split Osteotomy

- Vertical osteotomy through the mandibular body-ramus junction
- Allows for advancement or retraction of the mandible
- Used to correct mandibular excess, deficiency, or asymmetry

3. Genioplasty

- Adjunctive technique involves a horizontal parasymphseal osteotomy
- Enables chin augmentation

(Filename: TCT_1368_RadiologistGuidetoOrthognathicSurgery.jpg)

833

Recognizing and Classifying Hypomyelinating Leukodystrophies

A Foust¹, E Yang², S Prabhu³

¹Boston Children's Hospital, Boston, MA, ²Boston Children's Hospital, Jamaica Plain, MA, ³Boston Children's Hospital, Wellesley, MA

Purpose

Purpose: To describe a systematic approach to recognizing and classifying hypomyelinating leukodystrophies. Educational Objectives: 1. The reader will recognize normal and abnormal myelination patterns on MRI during the first two years of life. 2. The reader will understand how to systematically approach a case of hypomyelinating leukodystrophy and suggest specific diagnoses. Description: Hypomyelinating leukodystrophies (HLD) present a diagnostic challenge due to their relative rarity, overlap of clinical and imaging features, symmetry of imaging abnormalities, and presentation in very young patients expected to have incomplete myelination. Furthermore, the increased use of whole exome sequencing (WES) has facilitated diagnosis of HLD, but also has increased the importance of correct radiographic diagnosis when encountering variants of uncertain significance. Given the potential implications of a HLD diagnosis (ie intellectual disability, cognitive/neurologic decline, reduced life expectancy, risk for future pregnancies), it is important for neuroradiologists to be aware of the imaging findings in these disorders. This educational exhibit briefly reviews normal myelination patterns observed in early childhood and differences between dysmyelination, hypomyelination and demyelination. We then utilize several illustrative cases to describe a systematic approach to differentiating between various forms of HLD. We integrate relevant clinical, imaging, and genomic information where relevant/available. Disorders illustrated include Pelizaeus-Merzbacher disease (PMD), POL III related leukodystrophies, hypomyelination with atrophy of the basal ganglia and cerebellum tubulinopathy (H-ABC/TUBB4A), trichotiodystrophy, 18q deletion syndrome, hypomyelination with brain stem and spinal cord involvement and leg spasticity (HBSL), Aicardi-Goutieres syndrome, non-ketotic hyperglycemia, treatable hypomyelinating disorders like hypothyroidism and other unusual hypomyelinating disorders. This systematic approach will not only improve accuracy in identifying currently described HLDs, but will also aid in differentiating these entities from other forms of pediatric leukodystrophy. Furthermore, this approach illustrates how imaging, clinical, and genetic data can be potentially mined for machine learning algorithms. Conclusion: A systematic and holistic algorithm enables recognition and proper classification of hypomyelinating leukodystrophies.

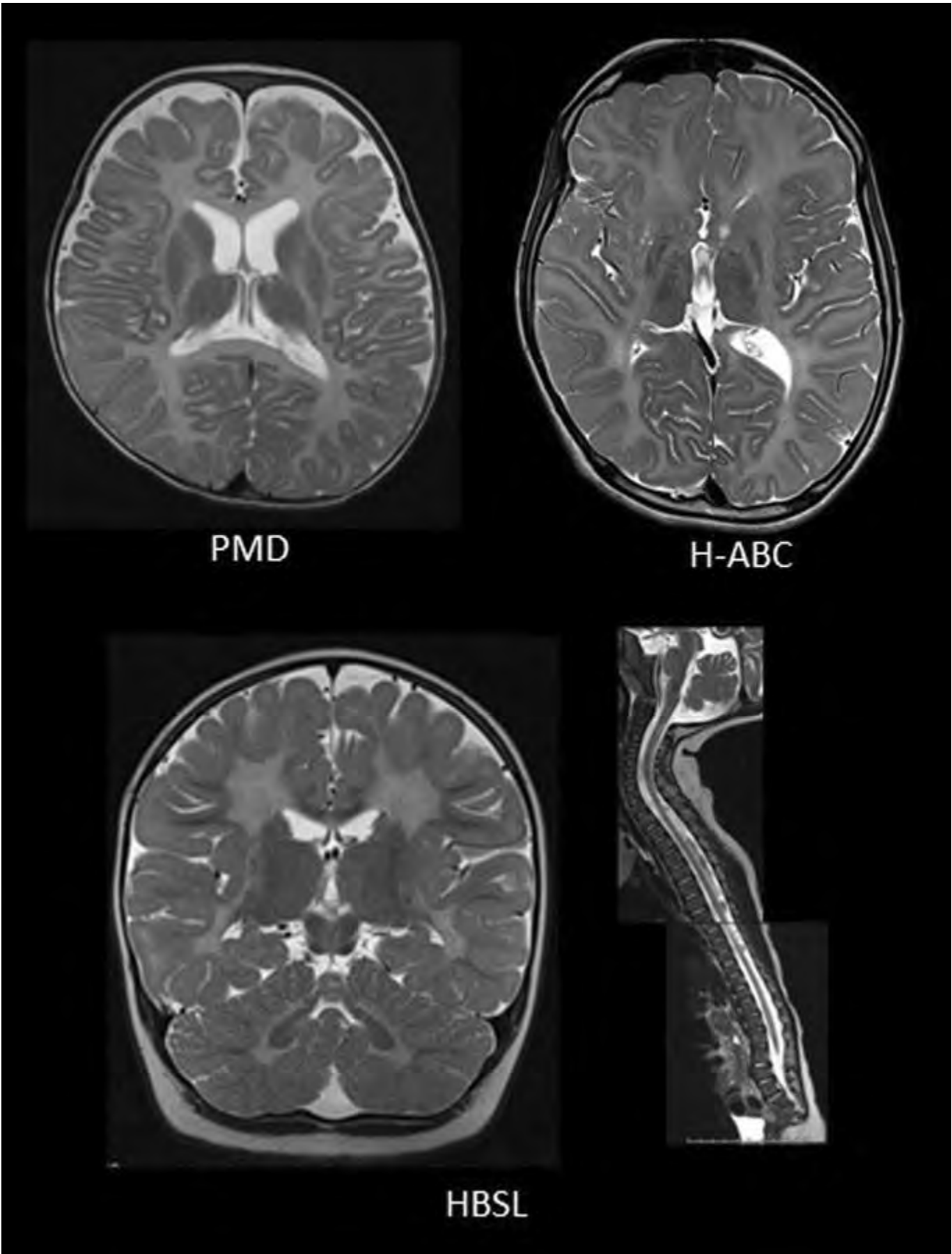
Materials and Methods

N/A

Results

N/A

Conclusions
N/A



Redrawing the Glioma Family Tree, Where do we stand in 2021?

O Arevalo¹, C Soto², S Khanpara³, S Calle¹, R Riascos³, K Shah¹

¹The University of Texas MD Anderson Cancer Center, Houston, TX, ²National University of Colombia, Bogota, Colombia, ³University of Texas Health Science Center at Houston, Houston, TX

Purpose

The Consortium to Inform Molecular and Practical Approaches to CNS Tumor Taxonomy (cIMPACT-NOW) has proposed some modifications to the current classifications of the diffuse gliomas in light of the rapid progress in molecular insights into these neoplasms. These changes will likely be included in the upcoming edition of the WHO classification for the CNS neoplasms to be official released in the 2020 winter. Objectives: 1. To review the proposed molecular classification of gliomas highlighting the changes to the WHO 2016 edition. 2. To illustrate the new entities with conventional and advanced neuroimaging techniques

Materials and Methods

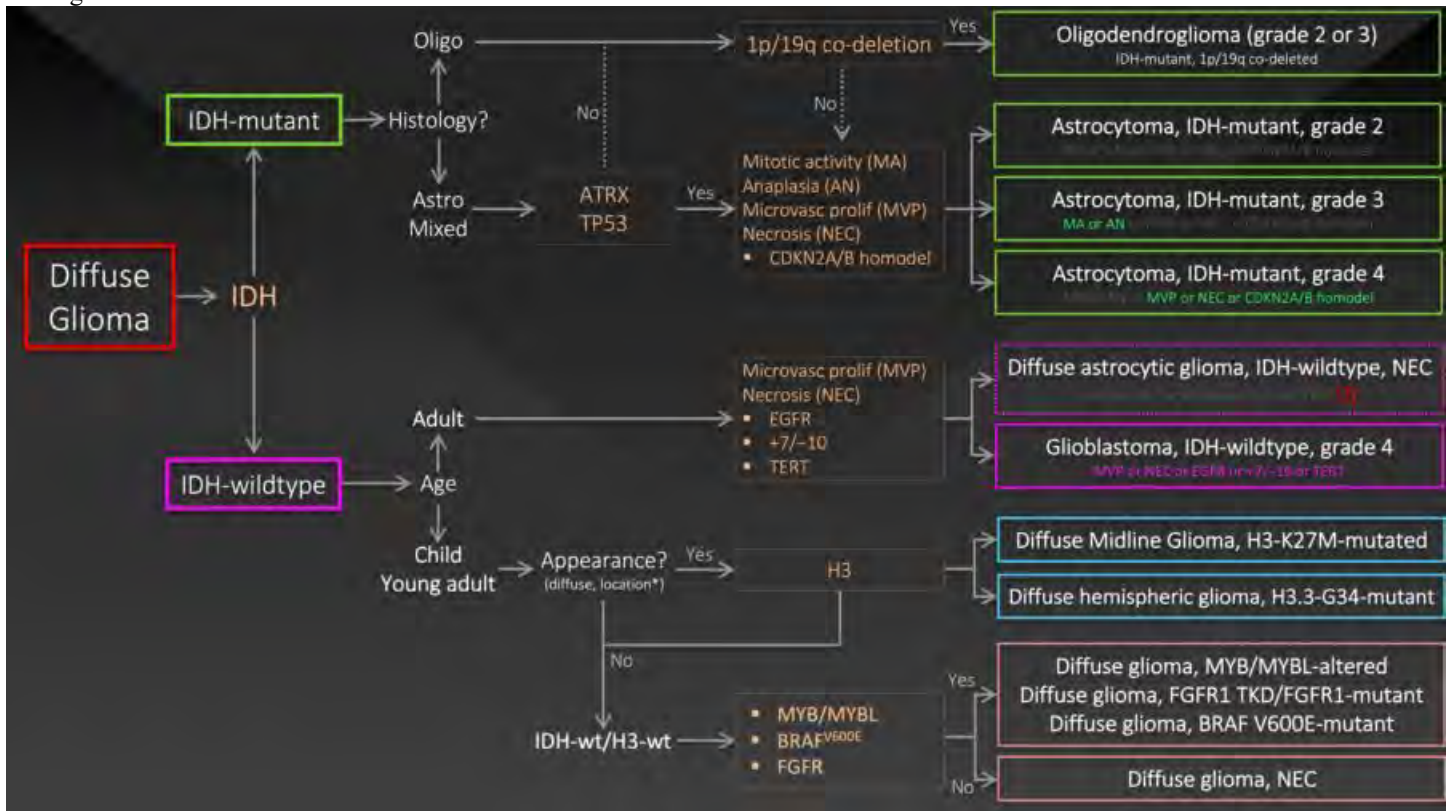
To present a case-based review of the proposed classification for gliomas

Results

After the 2016 World Health Organization (WHO) classification of central nervous system (CNS) tumors, there has been a steady growth in understanding how the genotype influences the CNS tumor typing and grading. The proposed updated classification system incorporates novel molecular markers to create tumor subgroups, which have been shown to better correlate with tumor biology, behavior and patient's prognosis. This exhibit reviews these updates, provides a practical overview of the important genomic markers of gliomas, and reviews imaging features of various genomic subgroups of adult gliomas.

Conclusions

The discovery of key genetic markers of gliomas has translated into the development of a novel tumor classification in 2016, to be updated in late 2020, resulting in a new perspective in the diagnosis and classification of gliomas. It is important for the neuroradiologists to become familiar with the new classification systems to better collaborate with the neuropathology, neurosurgery and neuro-oncology teams. Recent publications have shown association between certain genomic phenotypes and some imaging findings.



(Filename: TCT_507_Figure.jpg)

Relationship Between Alzheimer's Disease and Neurovascular Dysfunction

A Peret¹, A Kuner², J Yu³, G Roberts⁴, M Jen⁵, K Johnson⁶, L Eisenmenger⁷, C STROTHER⁸

¹UW Madison, Madison, WI, ²University of Wisconsin School of Medicine and Public Health, Middleton, WI, ³University of Wisconsin School of Medicine and Public Health, Madison, WI, ⁴University of Wisconsin - Madison, Madison, WI, ⁵University of Wisconsin, Madison, WI, ⁶University of Madison - Wisconsin, Madison, WI, ⁷University of Wisconsin - Madison, Middleton, WI, ⁸UW Madison, MADISON, WI

Purpose

Review the relationship of AD to vascular disease Present the current standard of care when performing and evaluating MRIs in AD Discuss advanced vascular MRI/MRA sequences and research supporting more direct imaging of vascular dysfunction

Materials and Methods

Alzheimer's disease (AD), a chronic neurodegenerative disorder characterized by insoluble beta-amyloid deposition in extracellular senile plaques and abnormal accumulation of hyperphosphorylated tau proteins in neurofibrillary tangles, is the leading cause of dementia. In the last two decades, numerous sources supported the hypothesis that AD and neurovascular dysfunction are intricately related. This exhibit will highlight the relevant studies highlighting this relationship, the imaging techniques commonly employed and innovative AD imaging approaches, as well as the future directions for this area of research.

Results

We will present the relationship of AD to systemic vascular disease, cerebrovascular disease, and specific cerebrovascular disease metrics, focusing on current clinically available MRI sequences as well as highlight more advanced MRI sequences currently under investigation.

Conclusions

The so-called "vascular hypothesis" suggests that several neurovascular anomalies play a role in the development and progression of AD, contributing to neuronal loss and cognitive impairment. Indirect signs of vascular pathology are the most commonly described both clinically and in research such as microhemorrhages (Fig. 1-A), white matter hyperintensities (Fig. 1-B), and decreased cerebral blood flow (CSF); however, direct measures of vascular disease such as increased blood flow pulsatility, decreased vessel wall compliance, and increased blood brain barrier permeability may be more sensitive markers of vascular disease. In preclinical AD, vascular biomarkers occur before cognitive impairment and before detectable increases in standard AD biomarkers. Advanced magnetic resonance imaging (MRI) techniques like dynamic contrast-enhanced MRI (DCE-MRI), 4D-flow MRI (Fig. 1-C,D), functional MRI (fMRI), and arterial spin labeling (ASL) MRI can provide a more comprehensive analysis of hemodynamic variables. The use of these imaging techniques to evaluate vascular biomarkers could provide a non-invasive tool in managing patients at risk of AD, allowing early detection of the disease and stratification of selected patients according to risk for dementia.

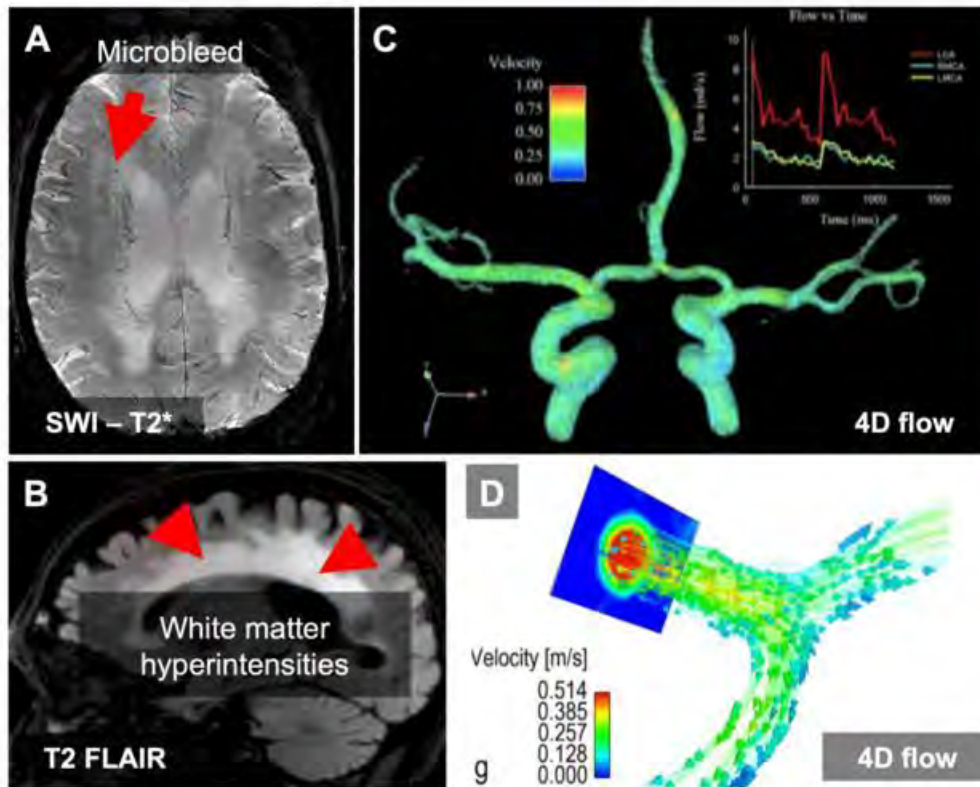


Fig. 1 - Imaging features of Alzheimer's Disease (AD). Multiple imaging signs are typically described in AD, including microbleed (A) and white matter hyperintensities (B). 4D-flow MRI is an advanced and innovative MRI technique used to study the cerebral blood flow parameters in AD (C, D).

(Filename: TCT_1034_Abstract2-Figure1.jpg)

1126

Review of Imaging Features in Type 1 Focal Cortical Dysplasia (FCD)

C Wheeler¹, J Black¹, S Gaddamanugu², S Singh³, M Goyal³

¹UAB School of Medicine, Birmingham, AL, ²Veterans Affairs Medical Center, Birmingham, AL, ³Children's Hospital of Alabama, Birmingham, AL

Purpose

Discuss the embryology and updated classification of cortical dysplasia. Review a case series to elucidate imaging findings of type 1 FCD. Discuss presurgical diagnostic techniques utilized to identify type I FCD epileptogenic foci.

Materials and Methods

FCD is one of the most common causes of medically intractable epilepsy. Furthermore, type 1 FCD remains a challenging entity to identify due to its subtle imaging features. We aim to present a case series reviewing imaging findings of type 1 FCD, a highly epileptogenic lesion. The purpose of this study is also to emphasize that dysplastic lesions may present as a mixed-type histopathology.

Results

A retrospective analysis was performed of 5 pediatric patients, who were treated operatively for drug-refractory focal seizures and had a biopsy-proven diagnosis of either type 1 FCD or mixed-type 1 and 2 FCD by histopathology. Multimodality imaging and related diagnostic studies were surveyed, including anatomical characterization with high-resolution MR sequences, metabolic analysis by interictal FDG-PET, ictal and interictal SPECT co-registered to MRI with MIM software, and electroclinical localization with EEG and/or stereoelectroencephalography (SEEG).

Conclusions

In all cases, a final diagnosis of type 1 or mixed-type FCD was confirmed and correlated with MR imaging findings. Three major

criteria of type 1 FCD were subtle cortical thickening, blurring of the gray-white matter junction, and asymmetric, shallow (U shape) or deep sulcation. In some mixed-type FCD, we observed T2 hyperintensity with heterogeneity and mild volume loss of subcortical white matter. Decreased metabolism on FDG-PET was more extensive than structural abnormalities on MRI. In several cases, further evaluation by SPECT subtraction or invasive SEEG placement was performed. When there was high etiological concurrence between anatomic imaging, metabolic analysis, and SEEG, the epileptogenic focus was resected. Our patients had excellent seizure control after surgical management. Imaging plays an essential role in the presurgical identification of type 1 focal cortical dysplasia. During multimodality evaluation, subtle findings of type 1 FCD can be perceived. While a conclusive histopathologic correlate cannot necessarily always be achieved on imaging, familiarity with characteristic features can lend greater confidence in recognition, increase interobserver specificity, and decrease imaging of negative seizure cases.

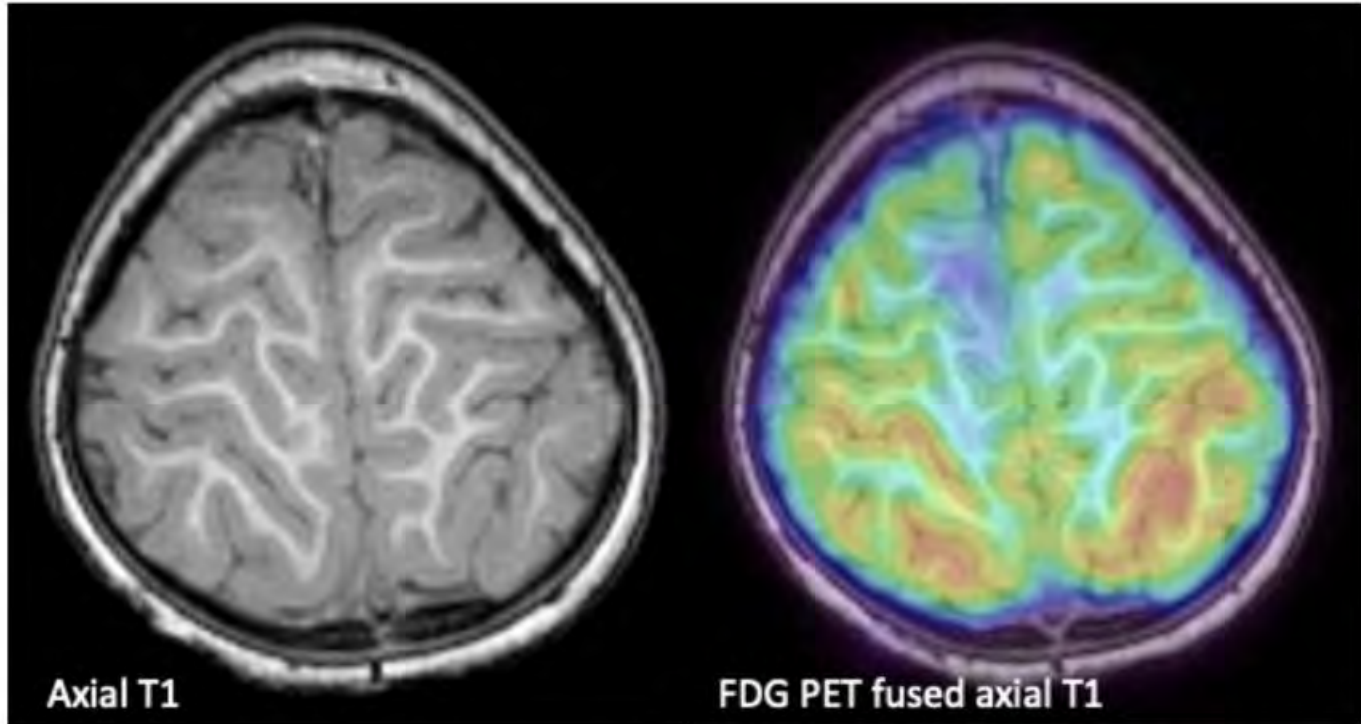


Figure 1. (A) Axial T1WI demonstrates subtle cortical thickening and blurring of the gray-white matter junction in the superior right frontal lobe. **(B)** PET shows reduced metabolism in these locations.

(Filename: TCT_1126_ScreenShot2020-11-10at110207PM.jpg)

1204

Revisiting Hybrid Phakomatoses: A pictorial review

S Jayappa¹, R Ramakrishnaiah², M Kumar³, S Vattoth¹, R Van Hemert⁴, C Glasier⁵, A Choudhary¹

¹University of Arkansas for Medical Sciences, LITTLE ROCK, AR, ²Univ of Arkansas for Medical Sciences, Little Rock, AR, ³University of Arkansas for Medical Sciences, Little Rock, AR, ⁴UAMS, Little Rock, AR, ⁵Arkansas Children's Hosp., Little Rock, AR

Purpose

Hybrid Phakomatoses are rarely encountered in neuroimaging practice. Knowledge of the different Hybrid Phakomatoses syndromes and their associated imaging findings is important for accurate diagnosis, avoid potential pitfall, and improve patient management. We present a detailed pictorial review of imaging findings of hybrid Phakomatoses with brief discussion on clinical presentation, genetic work up and complications.

Materials and Methods

Hybrid phakomatoses is the occurrence of two neurocutaneous syndromes in the same patient. Although neurocutaneous syndromes are common inherited disorders simultaneous occurrence of two neurocutaneous syndromes in the same patient is rare and not well described in literature. The purpose of this scientific exhibit is to provide a pictorial review various imaging findings of hybrid phakomatoses with brief discussion.

Results

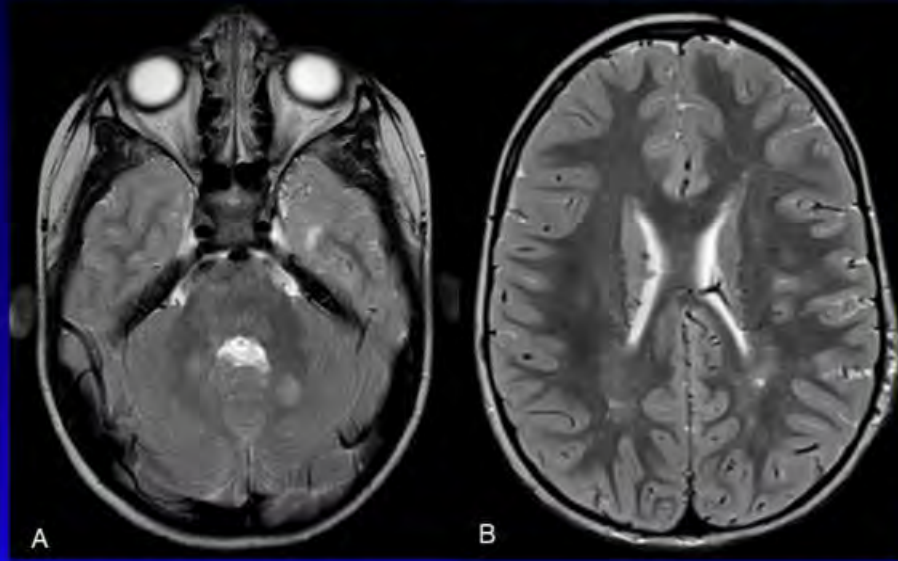
Patients with hybrid neurocutaneous syndrome will be selected from a teaching data base at a tertiary care pediatric hospital. A

detailed pictorial review and a brief discussion will be displayed under the following headings: Clinical presentation, genetic work up, imaging findings, unusual complications and clinical management.

Conclusions

Hybrid phakomatoses are rarely encountered in neuroimaging practice. Knowledge of the different Hybrid phakomatoses syndromes and their associated imaging findings is important for accurate diagnosis, avoid potential pitfall, and improve patient management.

FASI (NF 1) & Tubers (TSC) in a 5yr-old-male



UAMS
University of Arkansas for Medical Sciences

Arkansas
Children's
Hospital

(Filename: TCT_1204_Fig1.jpg)

1233

Role of Integrated PET/MRI in neurodegenerative disease

N Soni¹, M Ora²

¹UIHC, Iowa, IA, ²SGPGIMS, LUCKNOW, UP

Purpose

Routine use of MRI and PET supports the clinical diagnosis of neurodegenerative diseases (NDDs). MRI is a more widely available, albeit less sensitive, alternative to FDG-PET. Integrated PET/MRI provides concordant holistic molecular, functional, and structural information, highlighting the potential pathophysiology of various NDDs simultaneously and at different levels.

Materials and Methods

To review existing scientific literature about the integration of both qualitative and quantitative multimodal brain PET/MR biomarkers in the clinical setting of NDDs.

Results

We searched the PubMed and Medline databases (between 2011 and 2020) with the keywords "PET/MRI, PET, MRI biomarkers" and "neurodegenerative diseases.

Conclusions

Recently, a few small integrated PET/MRI studies have been published, including patients with neurodegenerative dementia. They have shown improved diagnostic accuracy in identifying and distinguishing dementia from healthy controls (Table 1). Hybrid FDG-PET/MRI revealed 35% more vascular pathology, changed the PET interpretation in 17% of patients, and altered management in 22% of patients. The higher reader confidence of FDG-PET findings improves the assessment of the structural correlates of MRI. FDG-PET/MRI helped in overall clinical diagnosis and management in 19 (90.5%) patients, especially with early-onset dementia. In the MCI group, it indicated underlying etiology, and in the dementia group, it helped in subtyping. Simultaneous amyloid-PET/MRI is feasible and provides high patient/caregiver and referrer acceptance of a new one-stop-shop dual AD biomarker (amyloid-beta load and MTLA) delivery approach.

Table 1: Integrated PET/MRI studies in Neurodegenerative Diseases.

Sr.No.	Author's name, year, Country, Study Design	Number of patients (M: F) [Clinical diagnosis]	Simultaneous Techniques	PET/MRI	Result/Conclusion
1	Moodley et al, 2015, UK, Prospective	24 (17:7) [AD, atypical AD with PCA,bvFTD, nvPPA, svPPA, rtvFTD]	¹⁸ F-FDG-PET/MRI		More widespread changes were identified using quantitative methods than on visual rating. The marked differences in atrophy-hypometabolism reflect differences in the molecular pathologies.
2	Schütz et al, 2016, Germany, Retrospective	100 (54:46) [MCI-51, possible/probable-AD-44, FTD-5]	¹⁸ F-florbetaben or PIBPET/MRI		MCI subjects-39% showed amyloid load, and 53% MTLA. Possible or probable ADD, in whom 61 % or 81 % amyloid-beta positivity was found, as well as 70 % or 69 % MTLA, respectively. Simultaneous amyloid PET/MRI supplement the clinical diagnosis of MCI due to AD and AD dementia.
3	Anazodo et al, 2018, Canada, Prospective (Pilot)	10 -FTD(5:5); 10-HC (4:6)	ASL-MRI	¹⁸ F-FDG-PET/	Visual assessments revealed lower sensitivity, specificity and inter-rater reliability for ASL (66.67%/ 62.12%/0.2) compared to FDG-PET (88.43%/90.91%/0.61). ASL performed lower than FDG-PET in discriminating patients from controls (AUC: ASL = 0.75 and FDGPET = 0.87). In patients with AD, pulsed ASL-MRI revealed abnormalities similar to ¹⁸ F-FDG PET with a reduced extent.
4	Riederer et al, 2018, Germany, Retrospective	45-AD (20:25), 20-MCI (10:10), 11-HC (5:6)	ASL-MRI	¹⁸ F-FDG-PET/	In patients with MCI, ¹⁸ F-FDG PET exclusively demonstrated quantitative hypometabolism and a component in the precuneus, indicating higher sensitivity to detect preclinical AD compared with ASL.
5	Nasrallah et al, 2018, USA, Prospective	5-PCA, 4-IvPPA, 6-AD, (6:9) 6-HC	¹⁸ F-florbetapir PET/MRI		There were moderate to high correlations between regional GM atrophy and ¹⁸ F-florbetapir uptake and both correlated to cognition.
6	Kaltoft et al, 2019, Denmark, Retrospective	78 (32:46) [35-AD, 2-eAD, 4-DLB, 1-FTD, 1-other, 7-VaD, 13-Mixed, 13-other abnormal, HCs-9]	¹⁸ F-FDG-PET/MRI		MRI lead to significantly higher Fazekas scores, higher medial temporal and global cortical atrophy scores, and identified more patients with infarcts (28 vs 8, p<0.001) compared to CT. MRI changed PET classification in 13 (17%) patients.
7	Mukku et al, 2019, India, Retrospective	21 (18:3), MCI-5, Dementia-16	¹⁸ F-FDG-PET/MRI		Additional findings and change of interpretation of PET/MR compared to PET/CT were considered to influence patient diagnosis or management in 17 (22%) of the patients
8	Ceccarini et al, 2020, Belgium, Prospective (Pilot)	27-AD, FTD, DLB, 30-HC	eASL-MRI	¹⁸ F-FDG-PET/	¹⁸ F-FDG-PET/MRI helped in diagnosis and management in 19 (90.5%). In MCI group it indicated underlying aetiology and in dementia group it helped in subtyping.
					On visual analysis- equal specificity (70%) between PET and MRI for differentiating normal and abnormal cases, but higher sensitivity (93%), confidence rating and interobserver agreement for ¹⁸ F-FDG PET compared with eASL.

(Filename: TCT_1233_ASNR_ABSTRACT_2021_NDD_TABLE.gif)

480

Schmorl's Nodes: Not Always Here to Stay!

J Aslam¹, Z Aslam², L Tu¹, A Mahajan¹

¹Yale University School of Medicine, New Haven, CT USA, ²Private, Staten Island, NY

Purpose

Schmorl's nodes are generally regarded as insignificant by radiologists on imaging exams. Here, we try and outline the evolution of Schmorl's nodes using a Case based approach. Schmorl's nodes undergo the same dynamic changes of other types of bone injury and can undergo healing over time. Schmorl's nodes go through the stages of: Formation (Acute), Repair (Subacute) and Healed (Chronic).

Materials and Methods

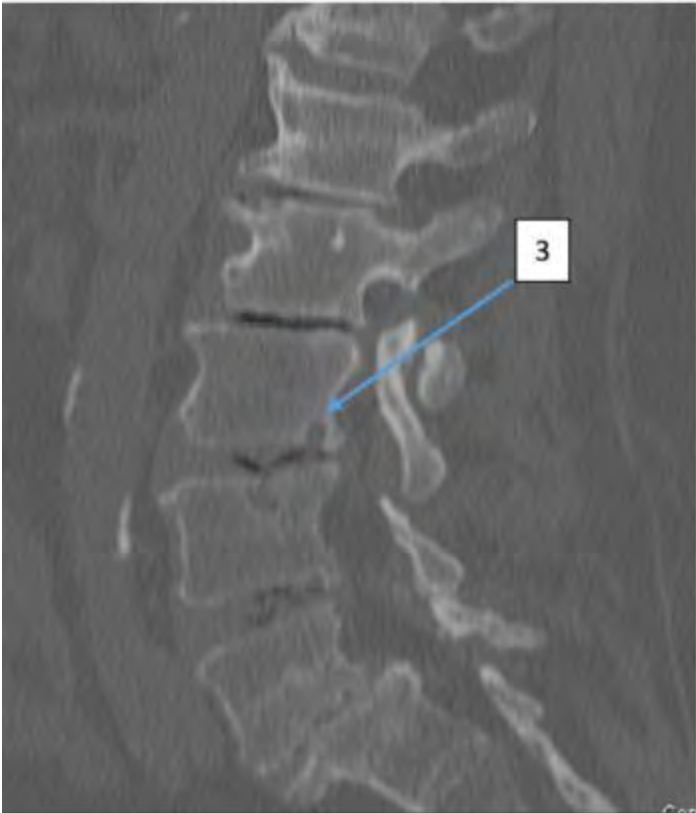
Stages of Schmorl's node evolution over time are not well understood radiologically. Our exhibit illustrates these changes over time to make the radiologist aware of this evolutionary process.

Results

Cases showing the evolution of Schmorl's nodes were collected at Yale New Haven Hospital in New Haven, Connecticut were reviewed and presented. CT and MR changes depicting these stages are outlined in this presentation.

Conclusions

Results: Acute phase may not demonstrate any enhancement or may show some mild enhancement. During the subacute phase (over 6months), there is similar T1 hypointensity, and T2/STIR hyperintensity. However, there is increased enhancement compared to the acute phase. During the chronic phase, the Schmorl's node returns to same intensity as the disk without any enhancement. On CT, it most often shows as lytic/lucent lesion however in some cases it can heal completely and become sclerotic. Conclusion: During acute phase Schmorl's node demonstrates T1 hypointensity, and T2/STIR hyperintensity. As the Schmorl's node evolves it undergoes various signal intensities on T1, T2 and post contrast images which can be used to assess the phase (acute, subacute and chronic). In addition, Schmorl's node can also go under various changes on CT from lytic lesion to sclerotic upon complete healing.



(Filename: TCT_480_HealingSchmorlsNodes.jpg)

Scrambled Synapses: A Case Based Review of Acute Seizure Evaluation

B Weston¹, A Sohn¹, C LI¹, M Goldberg¹, W CHANG¹

¹Allegheny Health Network, Pittsburgh, PA

Purpose

On completing the case-based review of this educational exhibit, the radiologist or trainee should be familiar with the clinical presentation, imaging evaluation, and management of the most common causes and "do not miss" causes of new onset seizures.

Materials and Methods

First time seizures are a common reason for Emergency Department visits and imaging is critical for the initial patient assessment. Computed Tomography and Magnetic Resonance Imaging evaluation provides a diagnostic challenge due to the overlapping radiologic features of many pathologies. Discriminating critical diagnoses, recognizing associated complications, and integrating advanced imaging techniques, can help the radiologist improve patient outcomes.

Results

N/A

Conclusions

Results: This presentation will review common emergent conditions which may initially present with new onset seizures. Cases will illustrate the spectrum of different epileptogenic etiologies including stroke/hypoxia, metabolic disorders, and encephalitis/infections, with an emphasis on differentiating between these categories. Representative cases from each category will focus on imaging findings that can add specificity to the diagnosis and potentially guide treatment decisions or further diagnostic evaluation. Complications such as abscesses, venous sinus thrombosis, and hemorrhage will be reviewed. Treatment and management will be discussed where appropriate. Conclusion: Diagnosis and management of new onset seizures often hinges on the imaging studies. Radiologists can play a key role in improving patient outcomes by timely recognition of specific diagnoses and evaluation for associated complications.

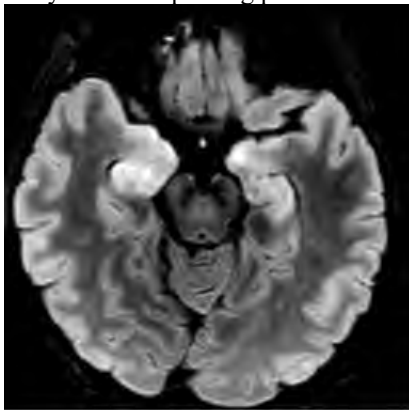


Figure 1: Axial T2 FLAIR image showing cortical and subcortical T2 hyperintensity in the bilateral temporal lobes in a patient with HHV6 Encephalitis.

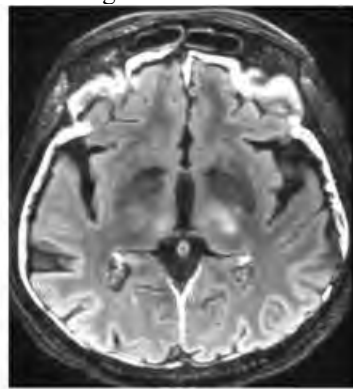


Figure 3: Axial post-contrast T2 FLAIR image demonstrates abnormal T2 hyperintense signal in the bilateral thalami extending into the posterior limbs of the internal capsule. Bilateral subdural fluid collections are also noted in this patient with viral encephalitis and seizures.

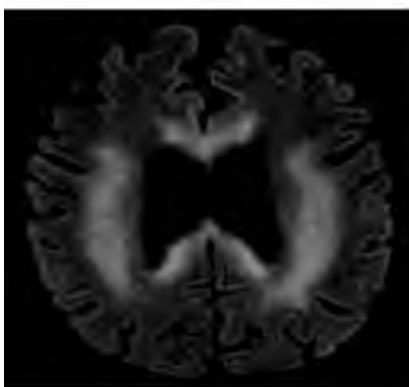


Figure 2: Axial T2 FLAIR image demonstrates confluent periventricular T2 hyperintense signal with extensive involvement of the corpus callosum in this patient with seizures and Marchiafava-Bignami.

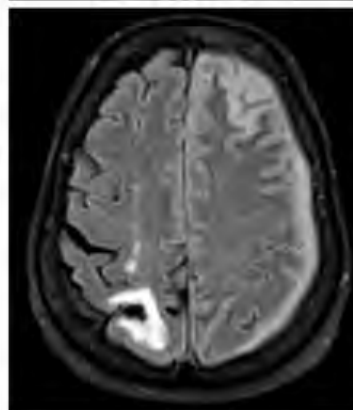


Figure 4: Axial T2 FLAIR image demonstrates a subdural fluid collection and cortical T2 hyperintensity in this patient with Pott's Puffy Tumor with underlying cerebritis who presented with seizures.

(Filename: TCT_461_ASNRImages.jpg)

Sellar Masses and Mass Like Lesion: A Pictorial Review of Uncommon Sellar Lesions.

P Reddy¹, M Mian², S Vattoth³, R Van Hemert⁴, M Kumar², R Ramakrishnaiah⁵, S Viswamitra²

¹University of Arkansas for Medical Sciences, Little rock, AR, ²University of Arkansas for Medical Sciences, Little Rock, AR, ³University of Arkansas for Medical Sciences, LITTLE ROCK, AR, ⁴UAMS, Little Rock, AR, ⁵N/A, N/A

Purpose

The objectives of this educational exhibit are to 1. Describe the imaging features of uncommon Sellar lesions using a quiz based approach 2. Elucidate the differentiating features between pituitary adenomas and other Sellar lesion 3. Describe a pattern based approach to come to a diagnosis when dealing with a Sellar lesion. The summary of the presentation is as follows 1. Case 1: Macroadenoma 2. Case 2: Rathke cleft cyst 3. Case 3: Giant ICA aneurysm 4. Case 4: Papillary craniopharyngioma 5. Case 5: Germ cell tumor 6. Case 6: Pilocytic astrocytoma mimicking craniopharyngioma 7. Case 7: Optic pathway glioma 8. Case 8: Hypothalamic hamartoma 9. Case 9: Dermoid 10. Case 10: Epidermoid 11. Case 11: Sellar angioliopoma 12. Case 12: Non adenomatous pituitary tumors - pituicytoma, spindle cell oncocytoma and granular cell tumour 13. Case 13: Chordoma 14. Case 14: Chondrosarcoma 15. Case 15: Granulomatous hypophysitis 16. Case 16: Sellar tuberculoma 17. Case 17: Lymphocytic hypophysitis 18. Case 18: Chronic fungal granuloma 19. Case 19: Rosai Dorfman disease 20. Case 20: Langerhans cell histiocytosis 21: Case 21: Giant cell reparative granuloma 22: Case 22: Paraganglioma 23: Pattern based algorithm

Materials and Methods

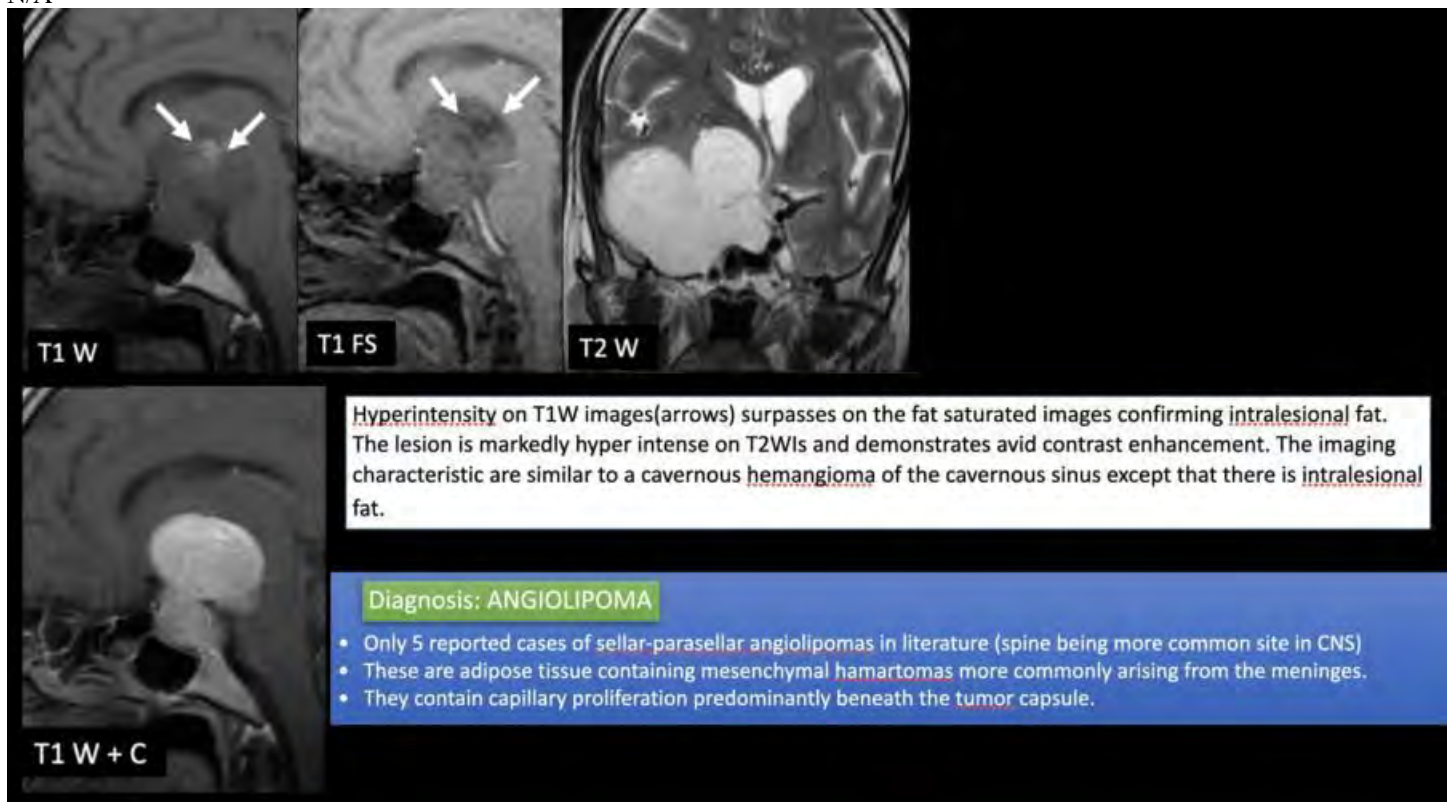
The purpose of this presentation is to describe the imaging features of uncommon Sellar and suprasellar lesions and develop a pattern based approach to narrow the differential diagnosis.

Results

A retrospective review of the institute data base was performed. Interesting and challenging cases were selected for the purpose of this quiz based review.

Conclusions

N/A



(Filename: TCT_791_sellarlesions.jpg)

296

Signal Intensity Abnormalities of the Inner Ear

S Ferracioli¹, K Nakacima², G Bandeira³, L Araujo⁴, S Souza⁵, E Gebrim⁶, L Lucato⁷, C Leite⁸, C Zamora⁷, M Castillo⁹
¹InRad - HC- FMUSP, Sao Paulo, -- SELECT --, ²Inrad, São Paulo, São Paulo, ³Faculadde de Medicina da Universisdae de São Paulo, Sao Paulo, Sao Paulo, ⁴Inrad, Sao Paulo, Sao Paulo, ⁵InRad, Sao Paulo, Sao Paulo, ⁶University of São Paulo, São Paulo, São Paulo, ⁷N/A, N/A, ⁸University of São Paulo, São Paulo, São Paulo, ⁹Radiology, Chapel Hill, NC

Purpose

In this educational exhibit we describe the possible signal abnormalities of the inner ear on MRI, highlight features that suggest the correct diagnosis, review the pertinent literature and present an educational flowchart for the differential diagnosis of these entities.

Materials and Methods

Our purpose is to review imaging findings and propose a step by step approach to help us generate a differential diagnosis of signal abnormalities of the inner ear.

Results

For this exhibit we searched the teaching files of two academic institutions for signal abnormalities of the inner ear on MRI. We propose a step by step approach for narrowing the differential diagnosis, and also review and discuss the pertinent literature emphasizing distinguishing features for each entity.

Conclusions

Signal abnormalities of the inner ear have a list of differential diagnosis, due to involvement of the labyrinth by infectious, inflammatory or granulomatous processes, bone dysplasias, tumors, and intracochlear hemorrhage. These diseases may be characterized by the signal intensity: hyperintensity on T2 (with morphologic changes in abnormal development), hypointensity on T2 (e.g. fungal infection, syphilis, histiocytosis, ossifying labyrinthitis), hyperintensity on T1 (e.g. intracochlear hemorrhage, lipoma), restricted diffusion (e.g. cholesteatoma) and post contrast enhancement (e.g. labyrinthitis, intracochlear schwannoma). Here, we propose using these imaging features in conjunction with the clinical data in order to generate a differential diagnosis list which will enable us to achieve the right diagnosis. We will discuss imaging and clinical characteristics that may aid to refine the differential diagnosis and propose a flowchart in the summary.

Signal Intensity Abnormalities of the Inner Ear

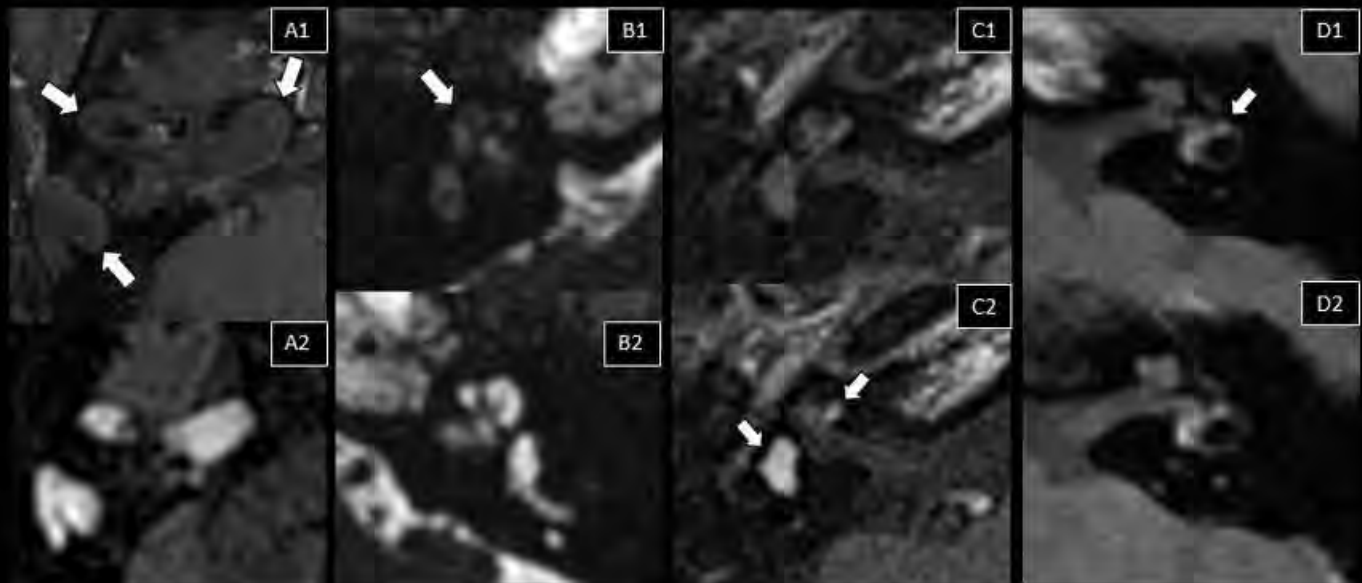


Figure 1:

A. Cholesteatoma. Axial post contrast T1 WI (A1) shows discrete non-enhancing masses (arrows) occupying the right external auditory canal as well as mastoid and petrous air cells with associated **restricted diffusion** (A2).

B. Ossifying labyrinthitis. Axial T2WI (B1 and B2) show partial obliteration of the right inner ear with associated **low signal** (B1). The normal appearance of the left inner ear is shown on B2.

C. Intra vestibular & cochlear schwannomas. Axial pre (C1) and post-contrast (C2) T1WI show a mass with **intense enhancement** in the right inner ear, localized in the vestibule and cochlea (arrows in C2).

D. Hemorrhagic labyrinthitis. Axial pre (D1) and post-contrast (D2) T1WI show **T1 hypersignal** in the left inner ear (arrow in D1), specially in the vestibule and semicircular canals, denoting a subacute hemorrhagic component (methemoglobin), with no discrete post contrast enhancement.

(Filename: TCT_296_ASNR2021.JPG)

573

Skull Base Infections and Their Complications

P Nguyen¹, R Assadsangabi², O Raslan³, A Ozturk⁴, M Bobinski³, V Ivanovic⁵, J CHANG³

¹University of California Davis School of Medicine, Sacramento, CA, ²University of California Davis, Sacramento, CA, ³UC Davis, Sacramento, CA, ⁴N/A, N/A, ⁵UC Davis Medical Center, Sacramento, CA

Purpose

Skull base infections (SBI) are life-threatening entities which require a high degree of clinical suspicion, prompt diagnosis, immediate antibiotic and antifungal therapy, and occasionally surgical debridement. However, diagnostic challenges often delay therapy due to non-specific presentations on imaging. Death in 9.5% and neurological dysfunction in 31% of cases (1), are due to intracranial extension and involvement of other intimate anatomies of the head & neck.

Materials and Methods

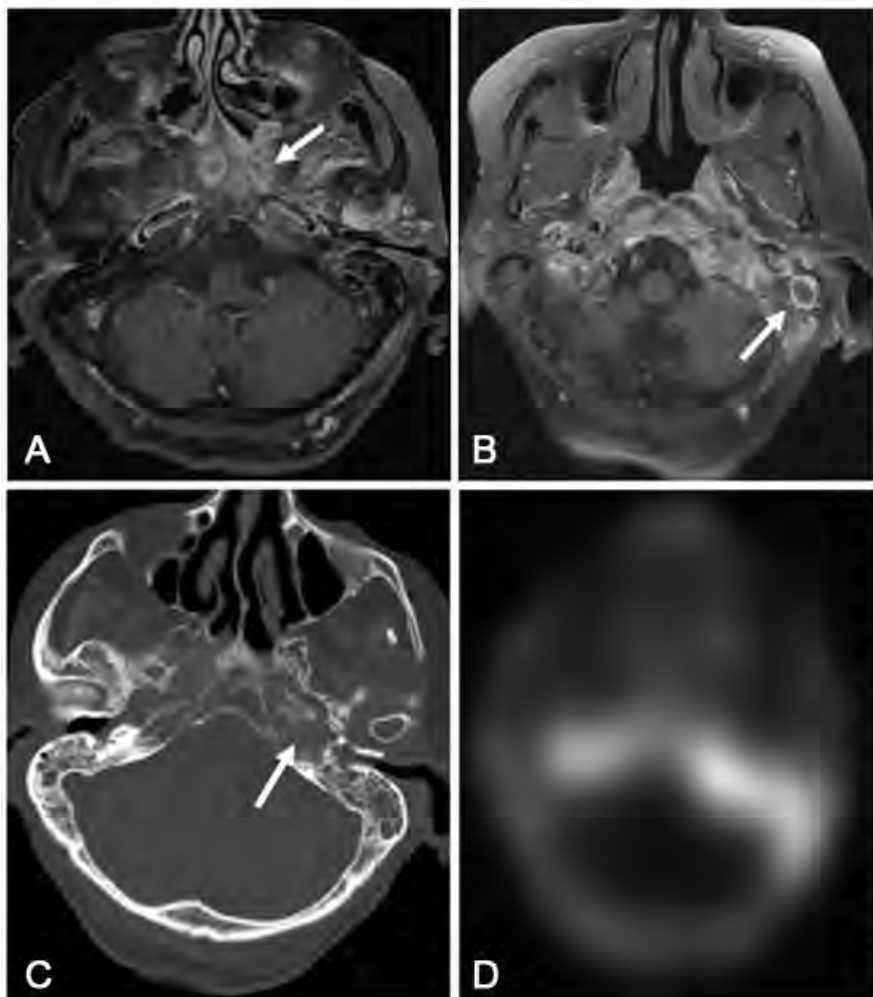
The purpose of this review is to highlight the imaging findings and diagnostic key points of skull base infections, their complications, and mimics.

Results

We reviewed relevant literature and retrospectively evaluated all patients from our PACS system with skull base infections which form this pictorial review.

Conclusions

SBIs commonly presents as osteomyelitis originating either from the paranasal sinuses or the external auditory canal. They are most strongly associated with immunocompromised patients and diabetics. Findings on CT include soft tissue swelling, demineralization, and bony erosions with attention to the skull base foramina (2). On MRI, key findings include marrow replacement with hypointense T1 signal (2,3), osseous and soft tissue enhancement, particularly on fat suppressed post contrast sequences, abscess formation and involvement of vascular structures (2). Radiologists must assess for dural or leptomeningeal involvement and associated intracranial complications such as cerebritis or empyema (2,3,4). SBIs are difficult to definitively diagnose due to their large overlap in presentation with other commonly considered differentials, including nasopharyngeal carcinoma (NPC) and metastatic diseases. A multimodal approach could facilitate correct diagnosis. Diffusion weighted imaging has shown to be diagnostically useful in differentiating between lymphoma and malignancies such as NPC with higher ADC values in SBO (5). Gallium scans correlate well with resolution of infection and can be helpful in monitoring treatment response (2,3). SBIs are life-threatening diseases requiring early interventions that are often delayed due to diagnostic difficulties on imaging. No pathognomonic radiologic findings are associated, and a multimodal approach with CT, MRI, and nuclear medicine is necessary to characterize soft tissue and bony involvement, extent of intracranial invasion, and therapeutic response. Here, we review the constellations of imaging findings to be aware of if clinical suspicion is high for SBI.



(A) Initial MRI showed mild osseous enhancement of basisphenoid (arrow) and left greater than right enhancing inflammatory tissues in infratemporal fossa. The diagnosis of skull base osteomyelitis was confirmed by Gallium scan and biopsy which revealed *Scedosporium* and *Staph aureus*. (B) Despite receiving treatment, symptoms progressed. Follow-up MRI demonstrated increased enhancement of skull base and surrounding tissue, wall thickening/enhancement of traversing internal carotid arteries, left coalescent mastoiditis and leptomeningeal enhancement in left middle cranial fossa (not shown). (C) CT scan showed erosions of the left petrous apex (arrow) and central skull base osteolysis. (D) Uptake on follow up Gallium-67 SPECT displayed the extent/progression of skull base osteomyelitis.

(Filename: TCT_573_SBO.jpg)

Soaking up Pediatric Hearing Loss: Otospongiosis/Otosclerosis and Other Temporal Bone Disorders

M Bean¹, J Hallstrom¹

¹University of New Mexico, Albuquerque, NM

Purpose

Our goal is to highlight a variety of pediatric temporal bone pathologies from recent cases encountered at our institution, including a 13 year old with osteogenesis imperfecta and bilateral otosclerosis/otospongiosis, a 5 year old with bilateral external auditory canal atresia, a 2 year old with bilateral enlarged vestibular aqueducts, and a 7 month old infant with complex anomalies including bilateral semicircular canal dysplasia. Our display will include representative images and discussion of pertinent findings.

Materials and Methods

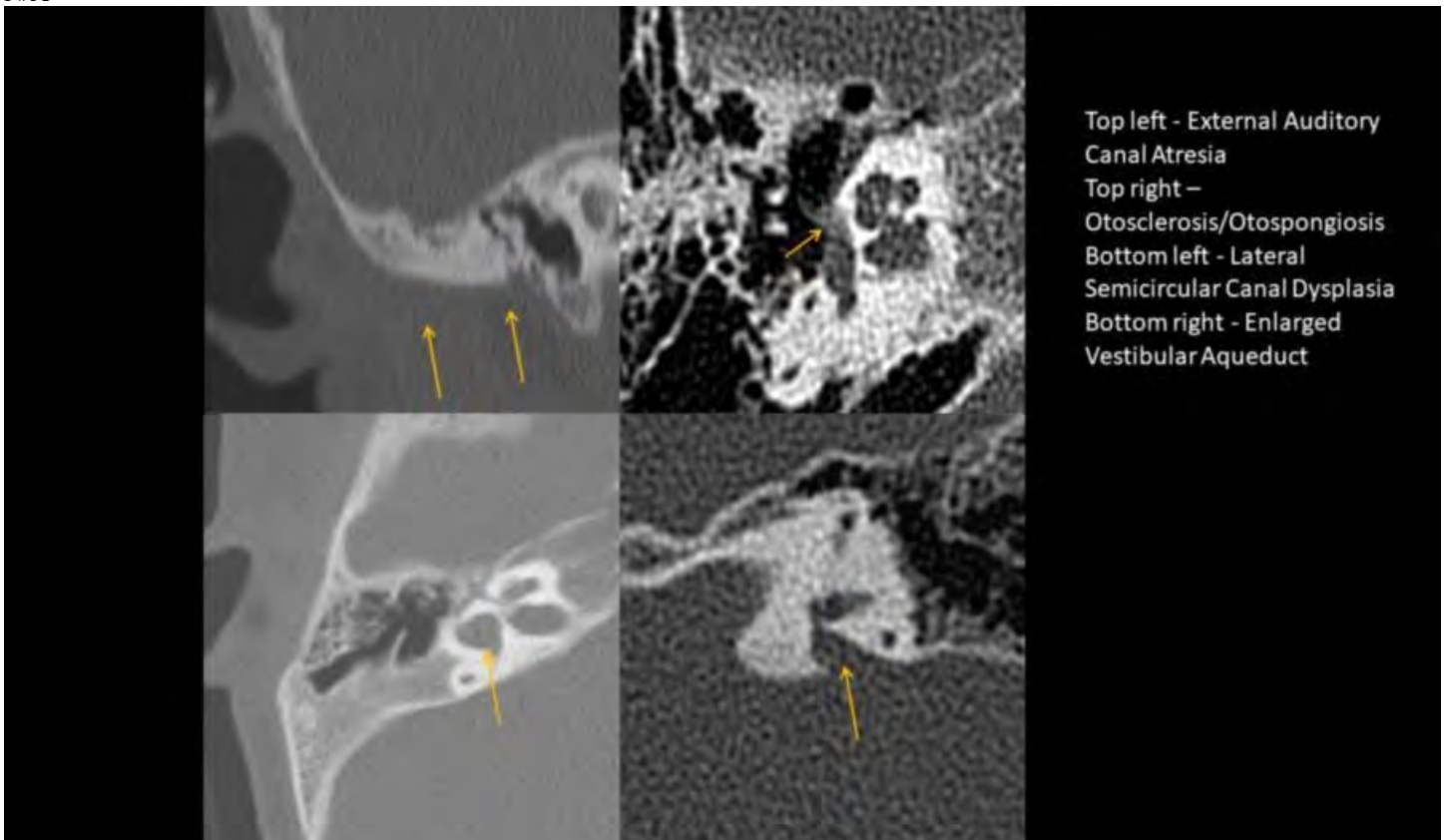
To teach about pediatric temporal bone pathologies, highlighting recent cases from our institution of otosclerosis/otospongiosis, external auditory canal atresia, enlarged vestibular aqueducts, and semicircular canal dysplasia.

Results

De-identified representative images from our PACS with annotations and brief text discussion.

Conclusions

N/A



(Filename: TCT_1189_ImagesforPediatrictemporalbonecases.jpg)

136

Spectrum Of Imaging Findings In Neurosarcoidosis

A Megahed¹, A Saeed Bamashmos², K Elfatairy³, A Heshmatzadeh Behzadi⁴, R Ismail¹, G Muro⁵, P Kochar⁶

¹Yale New Haven Health, Bridgeport, CT, ²Yale New Haven Health Bridgeport Hospital, Bridgeport, CT, ³Yale New Haven Health-Bridgeport Hospital, Bridgeport, CT, ⁴Yale New Haven Health-Bridgeport Hospital, Bridgeport, CT, ⁵Yale New Haven Health-Bridgeport Hospital, Bridgeport, CT, ⁶Penn State Hershey Medical Center, Hershey, Pennsylvania

Purpose

• Discuss the pathology of sarcoidosis. • Discuss the imaging findings of neurosarcoidosis in the brain. • Discuss the imaging findings of neurosarcoidosis with cranial nerve involvement. • Discuss the imaging findings of neurosarcoidosis in the spine.

Materials and Methods

Discuss the pathology and spectrum of imaging findings of neurosarcoidosis through review of patients with known neurosarcoidosis from our health care system with correlation with review of literature.

Results

- Pathology of sarcoidosis and incidence of neurological involvement. -Manifestations of neurosarcoidosis in the brain: a) Leptomeningeal involvement b) Dural involvement c) Brain parenchymal involvement d) Hypothalamic involvement e) Pituitary involvement f) Skull involvement -Manifestations of neurosarcoidosis related to the cranial nerves. -Manifestations of neurosarcoidosis in the spine: a) Intramedullary involvement b) Leptomeningeal and dural involvement c) Bone involvement

Conclusions

Knowledge of the imaging features of sarcoidosis affecting the neurological system is paramount for diagnosis of central nervous system involvement in patients with known sarcoidosis, also, neurological symptoms may be the presenting symptoms in patients with unknown sarcoidosis.

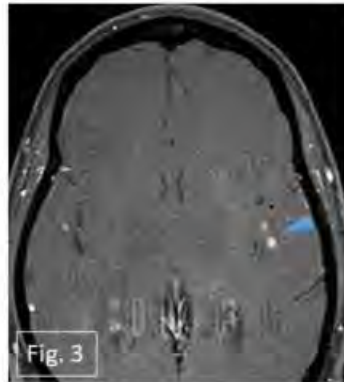
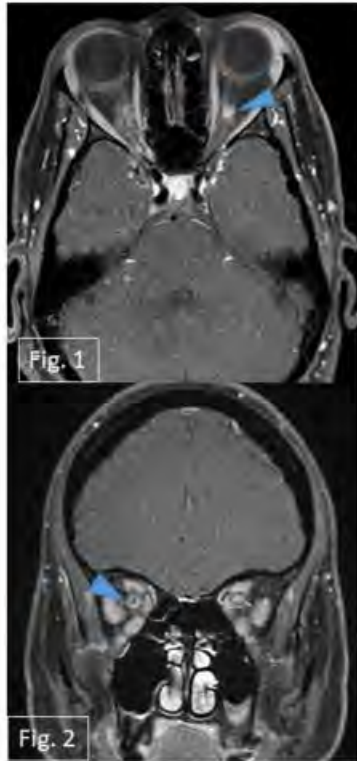


Fig. 1 is an axial post contrast T1 MRI image of the orbit showing thickening and enhancement of the left optic nerve (blue arrow head)

Fig. 2 is a coronal post contrast T1 MRI image of the orbit showing thickening and enhancement (blue arrow head)

Fig. 3 is an axial post contrast T1 MRI image of the brain showing foci of contrast enhancement along the left Sylvian fissure (blue arrow head)

Fig. 4 is a sagittal post contrast T2 MRI image of the lumbar spine showing enhancement along the anterior aspect of the conus medullaris (upper blue arrow) and nodular enhancement along the cauda equina roots (lower blue arrow)

(Filename: TCT_136_Presentation1.jpg)

842

Spelunking in the Cavernous Sinus: Quiz Based Review of Rare Cavernous Sinus Lesions.

P Reddy¹, **M Mian**², **S Viswamitra**², **S Vattoth**³, **R Ramakrishnaiah**⁴, **R Van Hemert**⁵, **M Kumar**²

¹University of Arkansas for Medical Sciences, Little rock, AR, ²University of Arkansas for Medical Sciences, Little Rock, AR, ³University of Arkansas for Medical Sciences, LITTLE ROCK, AR, ⁴Univ of Arkansas for Medical Sciences, Little Rock, AR, ⁵UAMS, Little Rock, AR

Purpose

The objectives of this presentation are to 1. Review the anatomy of the cavernous sinus 2. Describe imaging features of cavernous sinus lesions 3. Develop an algorithmic approach for narrowing down the differential diagnosis for a cavernous sinus mass The summary of the exhibit is as follows 1. Introduction 2. Cavernous sinus anatomy 3. Clinical features - cavernous sinus syndrome 4. Case 1: Cavernous hemangioma, cavernous sinus 5. Case 2: Chronic fungal granuloma - aspergillosis 6. Case 3: Invasive fungal sinusitis 7. Case 4: Tuberculoma 8. Case 5: Schwannoma 9. Case 6: meningioma 10. Case 7: epidermoid 11. Case 8: Invasive macro adenoma 12. Case 9: Inflammatory pseudotumor 13. Case 10: Giant ICA aneurysm 14. Case 11: Carotid cavernous fistula 15. Case 12: Cavernous sinus thrombosis 16. Summary of algorithmic approach to cavernous sinus lesions

Materials and Methods

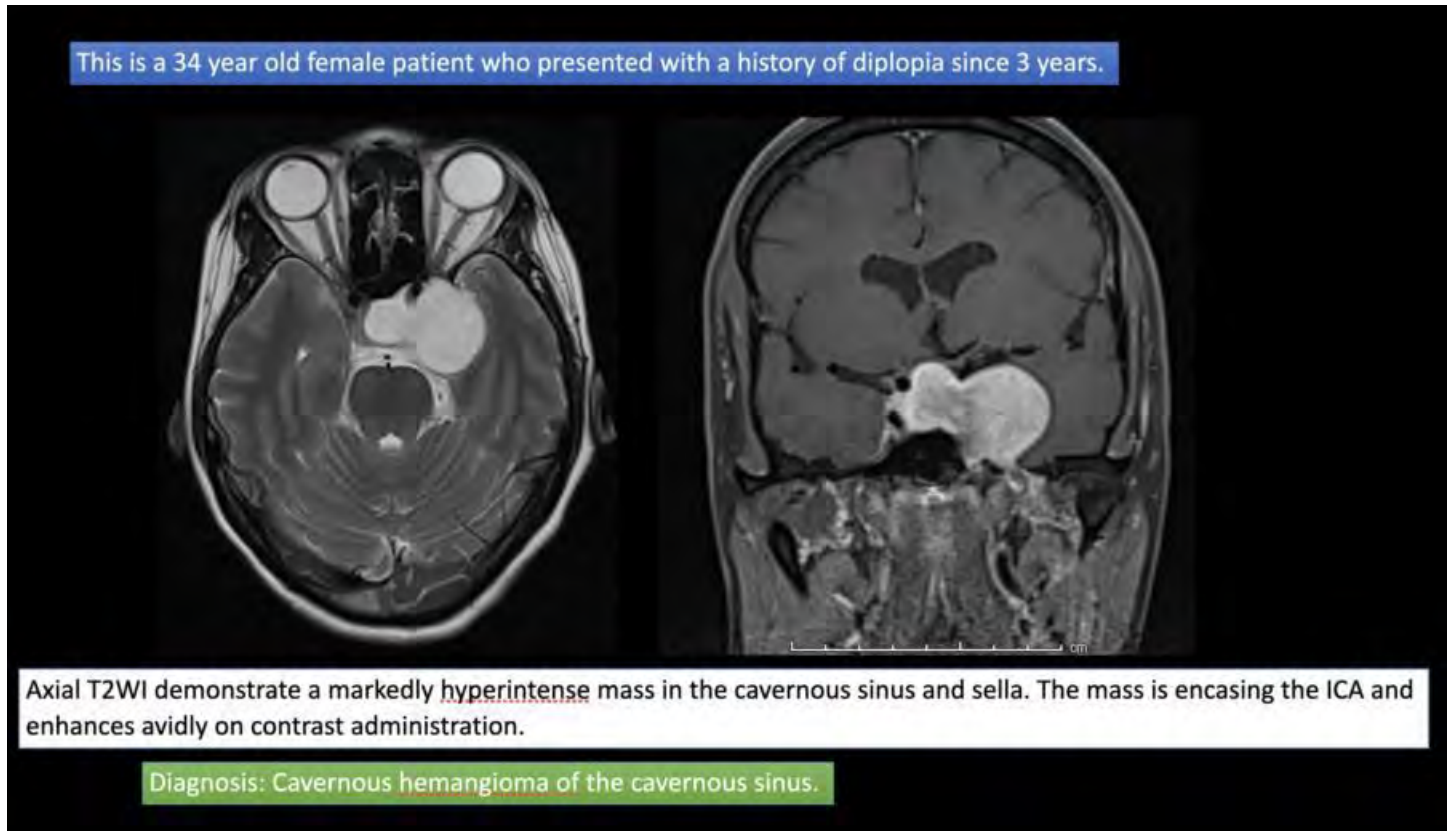
The purpose of this presentation is to describe the imaging features of cavernous sinus lesions and develop an algorithmic approach to narrow down the differential diagnosis.

Results

A retrospective review of the institute data base was performed. Interesting and challenging cases were selected for the purpose of this review.

Conclusions

N/A



(Filename: TCT_842_Cavernoussinus.jpg)

337

Spinal Cord Infractions

D Patel¹, B Langdon², M Yazdani²

¹MUSC, Ladson, SC, ²Medical University of South Carolina, Charleston, SC

Purpose

We describe the pathophysiology and imaging findings of spinal cord infraction including a range of imaging findings in anterior spinal artery territory infarction, posterior spinal artery territory infarction, fibrocartilaginous embolism, and spinal venous infarction.

Objectives: Become familiarized with anterior and posterior spinal anastomosing system Understand the pathophysiology of spinal cord infarction Become familiar with the imaging findings of spinal cord infraction

Materials and Methods

Spinal cord infarction is a rare event with the most common etiology being aortic surgery. Most radiologists are familiar with the typical imaging appearance of spinal cord infarction, being edema and restricted diffusion (if DWI sequence obtained) in the anterior gray matter of the spinal cord, sometimes referred to as "snake eyes or owl's eyes". However, with increasing severity, edema can spread posteriorly to involve the posterior horns and infarction of the whole cross section of the spinal cord can sometimes be seen in severe cases. We attempt to show a wide variety of spinal cord infractions with focus on infractions involving more than just the anterior horns of the spinal cord. We will attempt to discuss the pathophysiology behind this diversity of imaging findings.

Results

Using a series of illustrative spine MRI cases from our didactic imaging files we will show different manifestations of spinal cord infarction. We will start by describing the anterior and posterior spinal anastomosing system and review the segments most vulnerable to ischemia. We review the patient population most prone to this rare event. We will illustrate our points by showing multiple cases of anterior spinal artery territory infarction (with varying degree of spinal cord involvement), posterior spinal artery territory infarction, Fibrocartilaginous embolism, and spinal venous infarction. We also review the natural progression of the imaging findings of spinal cord infarction. Finally we review the differential diagnosis including multiple sclerosis, transverse myelitis, anti-MOG encephalitis, and vascular malformation.

Conclusions

The herein presentation expects to improve awareness, description, and identification of spinal cord infarction to all radiologists with an illustrative and instructive approach.

481

Spinal Dural Arteriovenous Fistula: Role of Imaging from Diagnosis to Treatment

A Ahmed¹, A Aly¹, M Ali¹, E Pedersen¹

¹Creighton university, Omaha, NE

Purpose

Learning Objectives: • Describe basic vascular anatomy of the spinal cord and its relation to spinal dural arteriovenous fistula (dAVF) • Discuss pathophysiology and subsequent clinical presentation in cases of spinal dAVF. • Review Imaging findings in cases of spinal dAVF. • Discuss Management options and prognosis of spinal dAVF. **Background:** Spinal dAVF is a rare slowly progressive disorder caused by abnormal connection between radicular artery and vein at the nerve root. Despite being rare, spinal dAVF is the most common spinal vascular malformation compromising about 60- 70% with the majority found in the thoracolumbar region. Spinal dAVF is underdiagnosed condition that can lead to paraplegia if left untreated due to progressive myelopathy resulting from increased spinal venous congestion. Clinical presentation of spinal dAVF is vague and non-specific making the neuroradiologist the first line in raising the possibility of this diagnosis. **Findings:** Combination of dedicated MRI and MRA is essential for diagnosis. Standard T2 Fast spin echo allows visualization of cord edema and signal voids on the dorsal aspect of the cord. T1WI shows the swollen cord and diffuse cord enhancement in the T1 post contrast images. Heavy T2 weighted sequences allows better visualization of the signal void vascular structures and detection of pulsation artifacts that might be confused with vascular signal voids. First pass contrast enhanced MRA can help in fistula localization. Digital subtraction angiography is still the gold standard in diagnosing and localizing the fistula and is essential for delineating the vascular anatomy before surgical or endovascular intervention. **Conclusion or teaching points:** Spinal dAVF is a treatable cause of paraplegia. The non-specific clinical presentation makes imaging essential in diagnosis. MRI is a noninvasive imaging modality that permits diagnosis and detailed assessment. Digital subtraction angiography is the gold standard for confirming the diagnosis, localizing the fistula and preoperative planning.

Materials and Methods

N/A

Results

N/A

Conclusions

N/A



Sagittal STIR (A), and T2W (B) images of the cervical cord. Axial T2W images of the medulla (C) and cervical cord (D) showing cervical cord edema (arrows) that extends into the medulla (dashed arrows). There are also multiple flow voids (dashed circles) which are consistent with AV fistula.

Spinal Facet Related Cysts, Analysis of Etiology, Composition, Imaging, and Treatment

Z Walker¹, M Aftab²

¹Michigan State University College of Osteopathic Medicine, East Lansing, MI, ²Ascension Genesys, Grand Blanc, MI

Purpose

Summary: Spinal facet related cysts are benign outgrowths of the spine. These cysts have not been extensively studied, yet pose a significant burden to the patients they affect. They can cause a variety of symptoms including back pain, radiculopathy, neurogenic claudication, and even cauda equina syndrome (1, 2). Cysts present most often in the sixth decade of life with a slight female predominance, with an incidence of approximately 0.5% of the general symptomatic population (3). Throughout this educational exhibit, I will educate radiologists on the pathogenesis, composition, proper imaging modalities and present the need for a classification system to advance care of these cysts and help guide conservative or surgical treatment. Objectives: 1. Characterize the etiology of spinal facet related cysts 2. Discuss the composition of various spinal facet related cysts along with proper nomenclature for radiologists 3. Provide radiologists with the optimal imaging modalities to diagnose and these cysts 4. Emphasize a classification system to advance the current understanding of treatment and prognosis 5. Analyze optimal treatment options

Materials and Methods

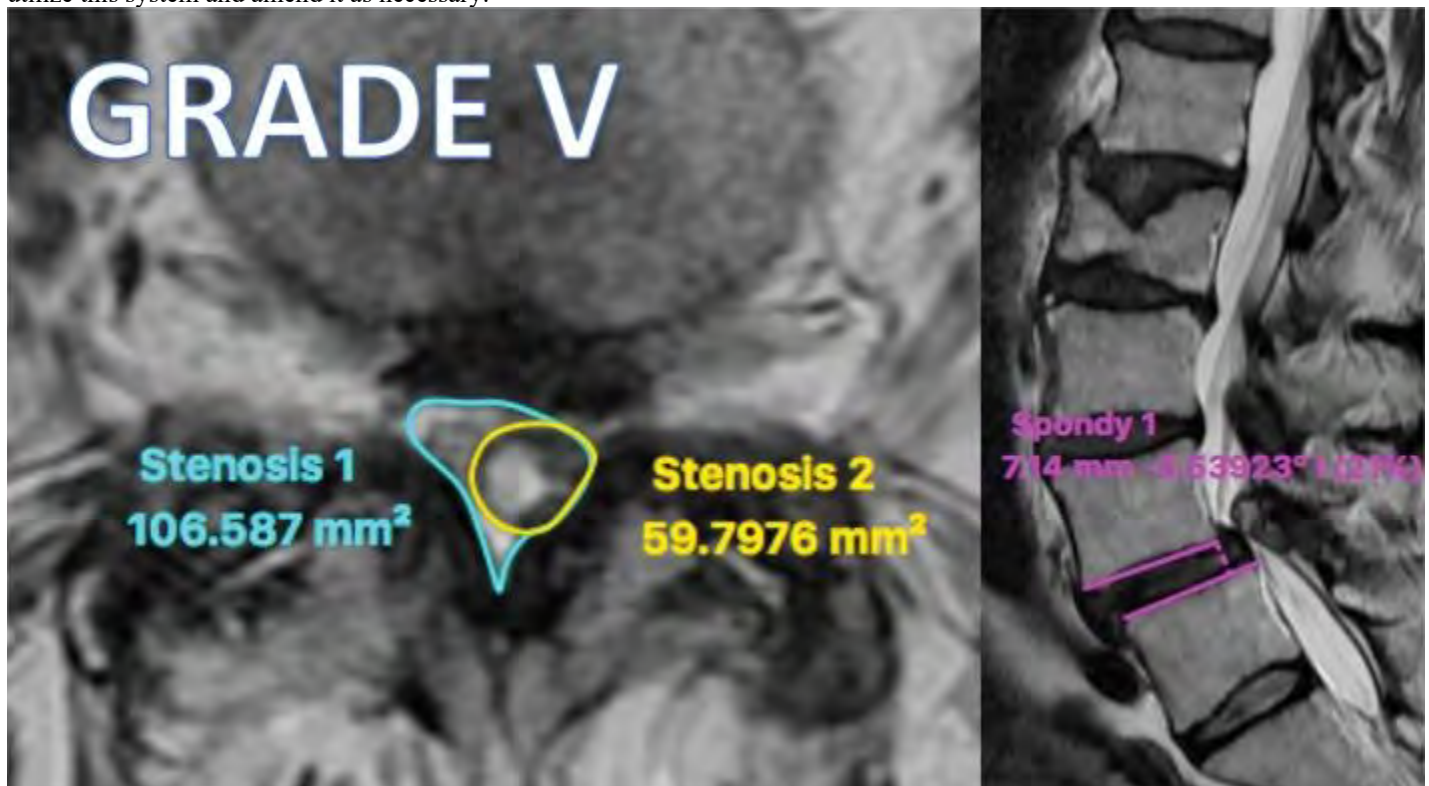
The purpose of this electronic educational exhibit is to provide a comprehensive review of spinal facet related cysts and provide radiologists the proper imaging modalities and classification to help guide treatment.

Results

N/A

Conclusions

The two most accepted ideas of cyst pathogenesis include spinal instability and trauma with wound healing (1, 3). The question remains, what is the proper nomenclature when radiologists refer to these cysts? Moreover, what do radiologists need to know when assessing them? The proper nomenclature should be juxtafacet cyst. Put simply, the term synovial cyst is not always accurate. MRI has emerged as the gold standard for imaging and it should remain so, noting that most juxta facet cysts appear isointense on T1 and hyperintense on T2 (1, 4). Going forward, radiologists as well as the treating physicians should adopt the NSURG classification system in order to advance the study of these cysts. A proper classification system is necessary in order for the radiologist to provide proper evidence-based recommendations to the treating physicians. We still do not know for certain whether this classification system will be efficacious in determining which patients develop complications during or post-surgery (5). Therefore future studies must utilize this system and amend it as necessary.



(Filename: TCT_780_NSURG_Grade_V.jpg)

Spinal Infections: From The Outside In

S Khan¹, S Eleti¹, T Campion¹

¹Barts Health NHS Trust, London, London

Purpose

To provide a reference and pictorial review of the spectrum of spinal infections across all compartments, from paravertebral tissues to intramedullary lesions.

Materials and Methods

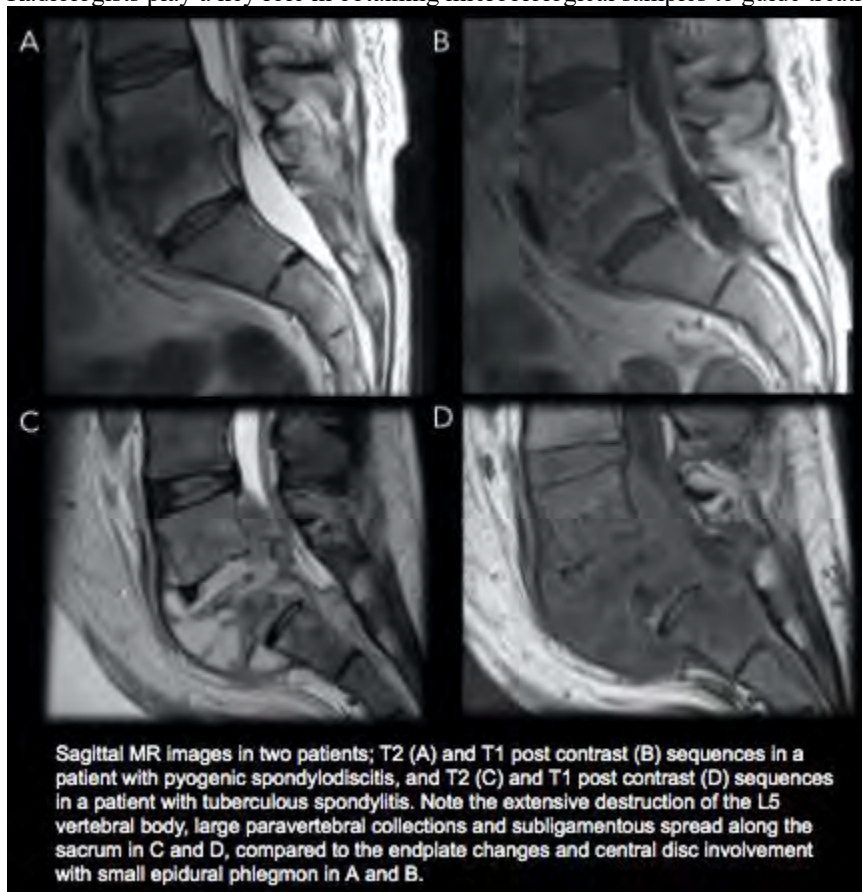
Spinal infections are a group of serious, life-threatening diseases, with an associated mortality rate ranging from 2-20% in developed countries. The incidence of spinal infections has increased in the past two decades, and account for up to 7% of musculoskeletal infections (1). Imaging plays a vital role in identifying spinal infection, particularly as the clinical presentation is often non-specific and findings can be observed after just 3 days of infection onset (2). Delay in diagnosis can result in significant neurological or structural deficit (3). Therefore, it is imperative that radiologists have a good understanding of the imaging features of spinal infection. There are many potential pitfalls in image interpretation including mimics such as degenerative or non-infectious inflammatory disease, delineating surgical versus non-surgical pathology and imaging in the postoperative setting. In addition, while the imaging appearances of particular infectious pathogens can be nonspecific, there are cases in which the radiologist can suggest likely causative organisms to appropriately guide therapy.

Results

Using a pictorial case series, we describe the salient radiological findings of various forms of spinal infection and their possible complications. This will include: • Paravertebral infective processes • Facet joint infection • Spondylodiscitis and osteomyelitis of the vertebral column • Epidural infection • Subdural and leptomeningeal infective processes • Infectious myelitis and cord abscesses. Additionally, we consider other processes that may mimic infection and describe methods that may be used to discriminate between them.

Conclusions

- Spinal infections are increasing in incidence and are associated with significant morbidity and mortality. Early diagnosis, aided by the use of imaging, is vital to improving patient outcomes.
- An awareness of the possible manifestations of spinal infection is crucial to guide appropriate imaging protocols to maximise sensitivity.
- While many pathogens present nonspecific imaging appearances, organisms such as tuberculosis, HIV, syphilis have more characteristic features which can be useful to guide empirical treatment.
- Radiologists play a key role in obtaining microbiological samples to guide treatment.



(Filename: TCT_325_PyogenicvsTB.jpg)

Spinal manifestations of Neurofibromatosis Type 1: The Perspective of a Tertiary Neuroscience Centre in the United Kingdom over Fifteen Years

L Nash¹, A Herwadkar²

¹Salford Royal NHS Foundation Trust, Northern Care Alliance, Manchester Clinical Neurosciences Centre, Greater Manchester, United Kingdom, ²Salford Royal NHS Foundation Trust, Northern Care Alliance, Greater Manchester Neurosciences Centre, Greater Manchester, United Kingdom

Purpose

N/A

Materials and Methods

Neurofibromatosis type 1 (NF1) is a phakomatosis caused by a mutation on the NF1 gene on chromosome 17. It is inherited in an autosomal dominant fashion but up to 50% of cases occur secondary to a sporadic mutation. It is a condition that involves many body systems including cutaneous, nervous, skeletal and vascular. The purpose of this educational exhibit is to demonstrate the widespread spinal manifestations that can occur.

Results

A combination of magnetic resonance and radiographic imaging is required for both the diagnosis of NF1 and the close monitoring of these patients for the development of NF1 related abnormalities in addition to any possible complications that may ensue. We, as a tertiary neuroscience centre, have a comprehensive caseload of NF1 patients with spinal manifestations over a timespan of 15 years, demonstrating pathologies from the common to the extremely rare.

Conclusions

The NF1 related spinal abnormalities in our exhibit are extensive and comprise but are not limited to the following: 1. Vertebral abnormalities (dystrophic versus non dystrophic changes); 2. Nerve sheath tumours (e.g. plexiform and spinal neurofibromas, malignant peripheral nerve sheath tumours) 3. Intramedullary spinal lesions (e.g. astrocytoma, unidentified bright object), 4. Rarer associated abnormalities (e.g. dural arterial venous fistula). We present a wide variety of cases demonstrating the extensive spinal manifestations of NF1. A thorough knowledge of these manifestations is crucial in understanding the natural history of disease to aid treatment and guide prognosis.

1341

Spontaneous Lateral Sphenoid Cephalocele: Getting It Right the First Time

E Fourgas¹, J Sodergren¹, T Singh¹, G Mongelluzzo², P Manickam³

¹Geisinger Health System, Wilkes Barre, PA, ²Radiology, Danville, PA, ³Geisinger, Danville, PA

Purpose

N/A

Materials and Methods

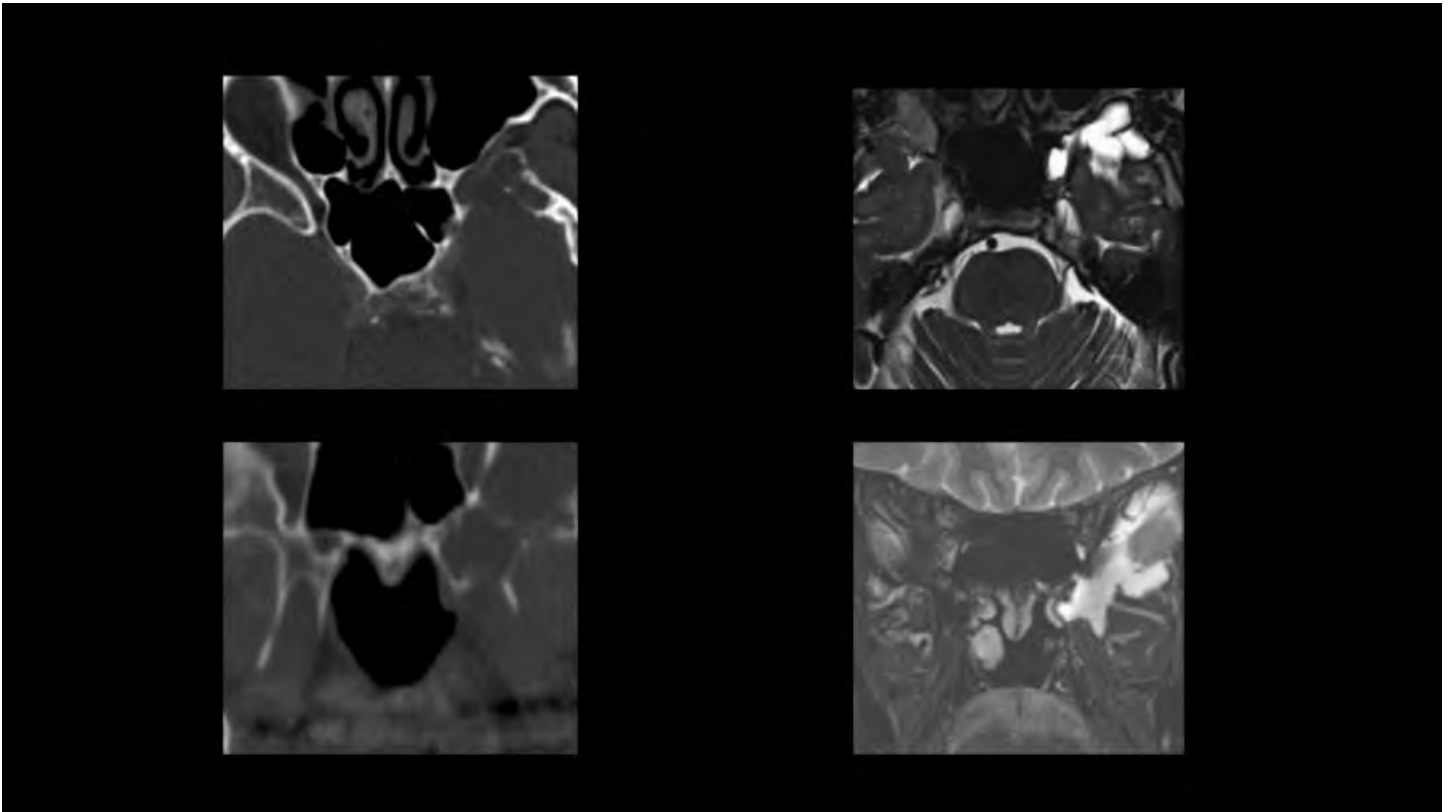
A spontaneous lateral sphenoid cephalocele is defined as a meningocele or meningoencephalocele that is caused by osseous defects in the lateral sphenoid bone. Although predisposing factors such as prior surgery, trauma or a mass are absent, there is an association with partially empty sella and arachnoid pits along the anterior middle cranial fossa. It may be discovered incidentally or present ominously with meningitis, seizures and headache. Since this diagnosis is rare and can be confounding at times, we present a spectrum of imaging findings in three patients with different clinical presentations to highlight the importance of early detection.

Results

CT and MR imaging were both performed in each of the 3 patients with a lateral sphenoid cephalocele. The clinical history and imaging of each patient was thoroughly reviewed.

Conclusions

In the first patient, the lateral sphenoid cephalocele was detected as an incidental asymptomatic finding with extensive scalloping of the left sphenoid bone on CT. The adjacent anterior temporal lobe was significantly distorted on MR. The second patient presented with seizures, an opacified sphenoid sinus and an anterior temporal lobe hypodensity on CT. The third patient had severe meningitis, fluid in the sphenoid sinus and a distorted left anterior temporal lobe on MR. The subsequent CT revealed a defect in the left lateral wall of the sphenoid sinus. All patients had a partially empty sella and arachnoid pitting of the anterior middle cranial fossa. In each case, the MR exam included a balanced SSFP (steady state free procession) sequence which enhanced the visualization of the abnormality. Early diagnosis of a lateral sphenoid cephalocele avoids a detrimental biopsy and guides the clinician towards proper management. An opacified sphenoid sinus should prompt a search for any osseous wall defects, signal abnormality and/or distorted anatomy of the adjacent temporal lobes as well as stigmata of intracranial hypertension. Furthermore, significant scalloping of the greater sphenoid wing may have a confusing imaging appearance, but an empty sella and distorted temporal lobe support the presence of a cephalocele. CT and high resolution MR are complimentary in characterizing this entity and both should be performed.



(Filename: TCT_1341_CephFinal.gif)

822

Sticky Spine!: A Review of the Imaging Findings for Arachnoiditis.

A Ottaiano¹, G Andreis¹, T Kotsubo¹, V Coelho², L Lessa³, N Ferreira¹, T Freddi¹

¹Hospital do Coração, São Paulo, São Paulo, ²Laboratório de Neuroimagem, FCM, UNICAMP., Campinas, São Paulo, ³HCFMUSP, São Paulo, SP

Purpose

Arachnoiditis is caused by the inflammation of the meninges and subarachnoid space and when it affects the cauda equina, it is referred as adhesive arachnoiditis. Objectives: 1. To review the pathophysiology and classification of arachnoiditis. 2. To describe the clinical presentations and imaging characteristics of arachnoiditis with representative cases from our institution. 3. To discuss its main complications.

Materials and Methods

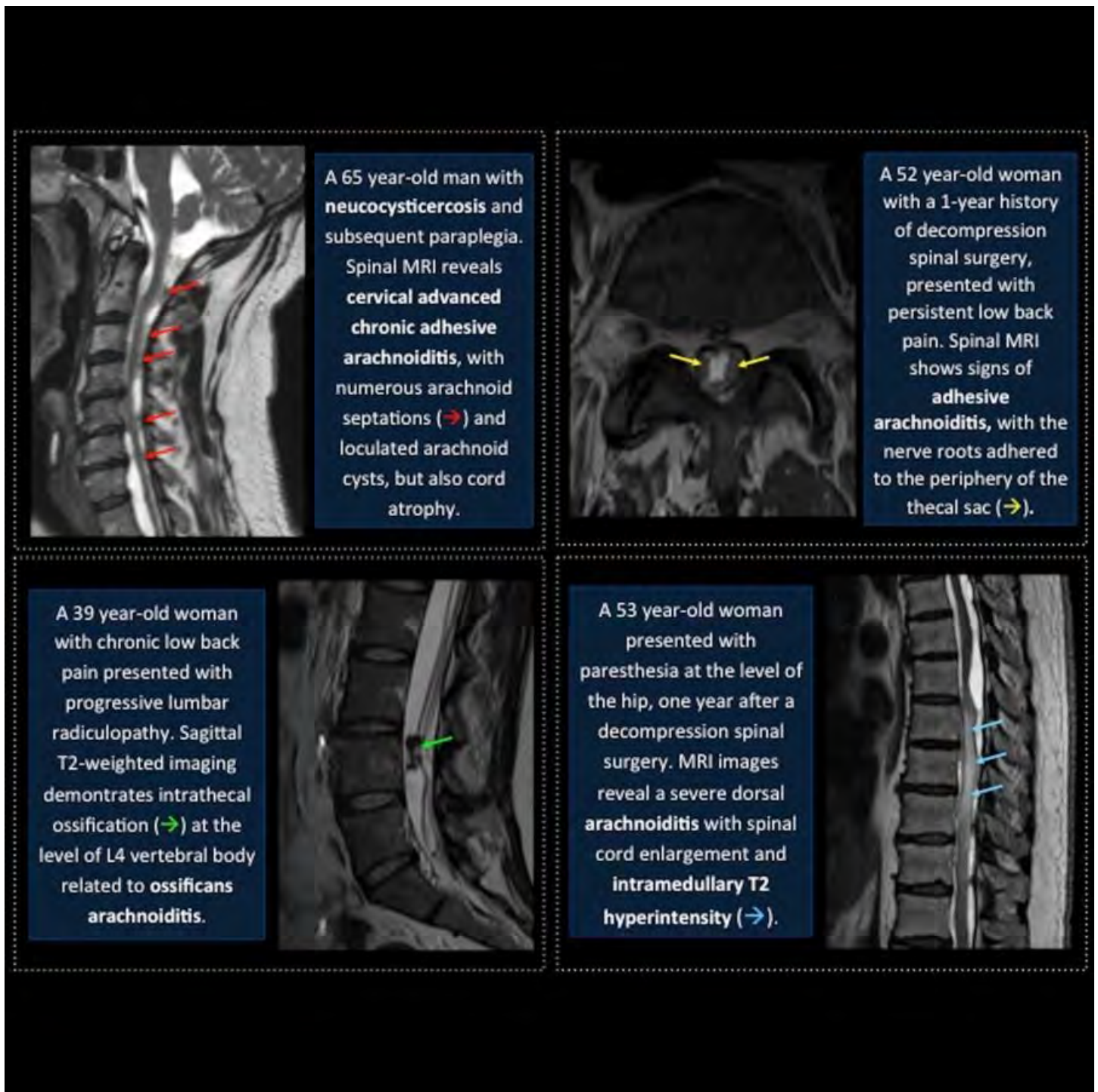
In this exhibit we provide a case-based review of the imaging characteristics of this entity and its main complications.

Results

Spinal and Brain MRI cases with imaging findings of arachnoiditis were retrospectively collected from our institutional database. For each case, the authors reviewed the clinical information and imaging features used to establish the diagnosis.

Conclusions

The pathophysiology of arachnoiditis is related to an inflammatory process that results in adherences of the nerve roots to each other and to the dura. Patients can experience a chronic and persistent back pain although, some cases can present with neurological impairment such as sensory disturbances in the extremities, motor weakness, urinary abnormalities or sexual dysfunction. MR is the imaging modality of choice for evaluation of these patients, and enables to classify this entity into three patterns on the basis of its appearance: (I) the nerve roots are clumped together and distorted; (II) the nerve roots are adherent to the periphery of the thecal sac, a large central soft-tissue mass replaces the thecal sac creating the "empty thecal sac" sign; and (III) a large central soft-tissue mass replaces the thecal sac. Rarely, chronic inflammation and fibrosis can progress leading to arachnoiditis ossificans. The complications of arachnoiditis include the formation of arachnoid cysts, myelomalacia and syringomyelia. Our pictorial review demonstrates that arachnoiditis may be secondary to a broad group of pathologic entities and may have a myriad of imaging appearance. Knowledge of the neuroimaging findings over the different phases of the inflammatory process and its precise description are essential to clinical counseling or even surgical treatment planning.



(Filename: TCT_822_ASNRArachnoiditis.jpg)

1363

Strike a Cord: Evaluating the Patient with Displacement of the Thoracic Spinal Cord

K Mathew¹, S Kumar¹, M Czaplicki¹, G Mongelluzzo¹, K Sargar¹, P Manickam²

¹Geisinger Medical Center, Danville, PA, ²Geisinger, Danville, PA

Purpose

Occasionally MRI of the thoracic spine performed for myelopathy or other indications may reveal a ventrally displaced thoracic cord with expanded CSF space posteriorly and no apparent mass. This leads to a diagnostic dilemma as there are a few possible conditions: ventral spinal cord herniation, spinal arachnoid cyst or dorsal arachnoid web. The surgical approach to manage these conditions varies significantly. For example, repair of a herniated spinal cord requires disruption of the dentate ligaments whereas removal of an

arachnoid cyst requires a less invasive approach. Therefore helpful imaging clues to differentiate among these etiologies are useful and will be reviewed in this exhibit through a series of cases. Modern MRI techniques, particularly aided by use of high-resolution steady-state free precession or volumetric 3D fast spin echo techniques allow for visualization of dural defects, membranes, and subtle changes in spinal cord morphology previously not achievable. For example, a discrete dural defect and spinal cord transgression may be apparent, confirming the diagnosis of a ventral spinal cord herniation. In certain circumstances CT myelogram can facilitate diagnosis. Cases of spinal cord herniation may demonstrate a lack of opacification ventral or lateral to the spinal cord or even direct leakage of contrast through the dural defect. In cases of dorsal arachnoid web, the contrast should opacify circumferentially around the spinal cord and demonstrate a 'scalpel sign' as on MRI. Arachnoid cysts will present as a filling defect or contrast-density gradient dorsal to the spinal cord that may fill in on delayed images.

Materials and Methods

To review imaging findings of three common etiologies of spinal cord displacement in the absence of an otherwise apparent extramedullary mass: ventral spinal cord herniation, arachnoid cyst and dorsal thoracic arachnoid web.

Results

We will review imaging of relevant cases from a tertiary care center to demonstrate how to differentiate these conditions and arrive at a diagnosis.

Conclusions

Differentiating between spinal cord herniations, arachnoid cysts and arachnoid webs is imperative for surgical planning. Modern MRI techniques, contrast myelography and awareness of the findings unique to each entity allows the neuroradiologist to arrive at a confident diagnosis and guide patient management.



(Filename: TCT_1363_combinedphoto.JPG)

Subpial Hemorrhage in Neonates: What Should We Know?

C Pinto¹, B Cunha², C Conceição²

¹Centro Hospitalar Universitário do Porto, Porto, Portugal, ²Centro Hospitalar Lisboa Central, Lisboa, Portugal

Purpose

The present exhibition will go through the main image findings of subpial hemorrhage in neonates, based in clinical cases from our institution. Educational objectives include: To understand the pathophysiology and presumed causative factors of this rare entity. To overview the radiologic presentation of subpial hemorrhage in neonates. To recognize the image pattern of this under-diagnosed pathology to raise awareness in the radiology community.

Materials and Methods

Subpial hemorrhage has become increasingly recognized as a distinct brain hemorrhage pattern in term neonates, especially in the presence of birth trauma and coagulopathies, but also in previously healthy neonates. It is a rare form of perinatal stroke, with few reports in the literature. The purpose of this exhibit is to review the typical image findings of this rare type of neonate brain hemorrhage; to stress out the image characteristics that can lead to the diagnosis; and to discuss the physiopathology of this peculiar type of hemorrhage.

Results

This educational exhibit provides an image-rich and case based discussion of imaging related to subpial hemorrhage, based on cases from our institution. After reviewing the exhibit the reader will be able to identify pertinent radiologic semiology of subpial haemorrhage in neonates.

Conclusions

Subpial haemorrhage occurs between the pia-mater and the cortical surface, although its pathophysiology is not yet fully understood. Bleeding from the outermost layer of the cerebral cortex into the glia limitans is so far the best explanation for hemorrhage in this potential space. Cortical vein congestion or thrombosis is another possible mechanism. The most common finding was both intra and extra-axial hemorrhage that did not respect an arterial territory. The temporal lobe was the most affect location and pooled hemorrhage was often present, in opposition to the smoothly spread seen in typical subarachnoid bleeding). Interestingly, all hemorrhages were associated with cortical and subcortical cytotoxic edema underlying the subpial hemorrhage. Medullary vein congestion was also a common feature. In the cases available, MRA showed no abnormalities. Summary/Conclusion: Through this exhibit, neuroradiologists will gain fundamental knowledge of the key image findings of neonatal subpial hemorrhage. This knowledge is important given the distinct pattern of this hemorrhage and the scarcity of literature reviews on this topic.

850

Successful Use of Intracranial High-resolution Black Blood Imaging for Diagnostic Evaluation of Patients with Autoimmune Disease and Neurological Symptoms

S Rogers¹, K Johnson¹, V Perovic¹, E Al Rabia¹, C Kidwell¹, J Becker¹

¹University of Arizona, Tucson, AZ

Purpose

After reading this presentation the reader should understand: 1. The clinical indications and potential benefits of black blood imaging. 2. The technique of black blood imaging of the vessel wall. 3. The advantages and limitations of performing black blood imaging when compared with other techniques for evaluation of the vessel wall in patents with autoimmune disease.

Materials and Methods

There is often diagnostic uncertainty when patients with autoimmune disease present with acute focal neurological symptoms and intracranial pathology. Black blood imaging allows for evaluation of the intracranial vessel walls in these patients to evaluate for acute vasculitis. We will present successful use of Dante Space black blood vessel wall imaging to increase diagnostic certainty prior to commencement of cytotoxic therapies in these patients, who are often young.

Results

We present a retrospective evaluation of black blood imaging in patients with autoimmune disease who underwent black blood vessel wall imaging as part of their clinical work up for acute neurological disease. We present the intracranial black blood vessel wall imaging technique performed with and without contrast.

Conclusions

We present case examples as well as the data obtained following our retrospective review and demonstrate the different intracranial appearances of vessel wall diseases such as atherosclerosis, inflammatory amyloid angiopathy, and acute vasculitis as well as negative studies in these patients. Black blood vessel wall imaging has become standard of care in the clinical work up of patients with autoimmune disease presenting with acute focal neurology at our institution and can accurately diagnose acute vasculitis from clinical

mimics. The success of this technique has meant that our rheumatological and neurological colleagues have come to rely on these imaging sequences in the routine work up of these patients.

488

Sympathetic Chain Paragangliomas of the Head and Neck: Clinical Presentation, Diagnosis, and Management of this Rare Clinical Entity

B Parnes¹, D Mayorga², A Khorsandi³, M Starc⁴

¹Mount Sinai West, New York, NY, ²Mount Sinai Health Systems, New York, NY, ³New York Eye and Ear Infirmary of Mount Sinai, New York, NY, ⁴Mount Sinai Hospital System, New York, NY

Purpose

Paragangliomas are neuroendocrine tumors derived from chromaffin cells. These rare tumors are described according to their location, however, there are only approximately twenty-one reported cases in the literature of cervical sympathetic chain paragangliomas.^{1,2} It is crucial to recognize the imaging features that are suggestive of cervical sympathetic chain paragangliomas, since these lesions may be managed with surgical resection. The objectives of this presentation are to provide a comprehensive review of clinical presentation, multimodality key imaging features, differential diagnoses, and management of this unique clinical entity. Clinically, cervical sympathetic chain paragangliomas present as slowly growing masses along the carotid sheath with regional mass effect and potentially Horner's syndrome.³ Characteristic imaging findings of cervical sympathetic chain paragangliomas will be emphasized including unique lateralization of the carotid sheath structures. A complete differential diagnosis including deep lobe parotid tumors, abnormal lymph nodes, vascular malformations, neurogenic tumors, and branchial cleft cysts will be presented. Imaging features of cervical sympathetic chain paragangliomas will be illustrated through multiple imaging modalities. CT, MRI, catheter angiography, as well as Gallium-68 Dotatate PET imaging findings will be reviewed. Surgical and pathological correlation of our index case will be demonstrated.

Materials and Methods

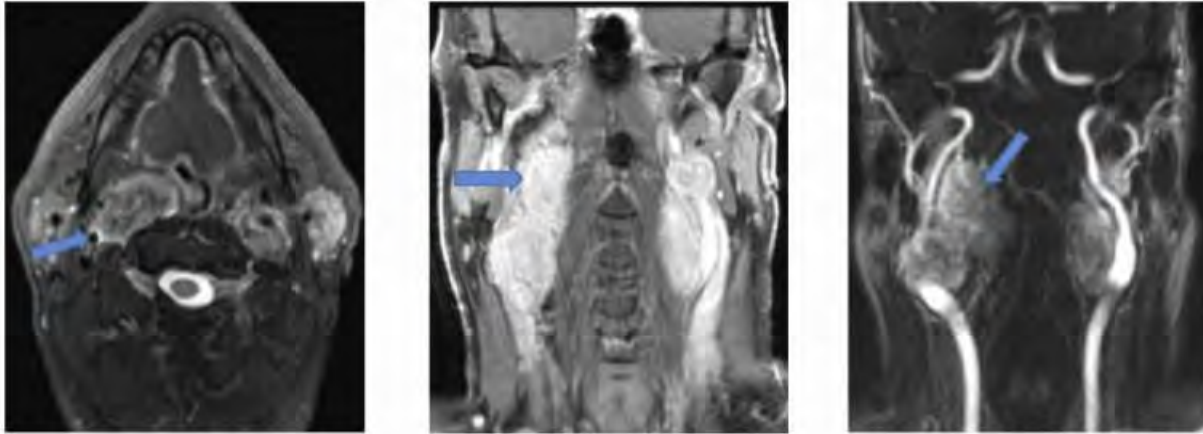
Classically, head and neck paragangliomas have been described as occurring in four general locations: carotid body, glomus tympanicum, glomus jugulare, and glomus vagale. The purpose of this presentation is to review the clinical presentation, key multimodality imaging features, differential diagnoses, and management of paragangliomas arising from the cervical sympathetic chain. By presenting a pathology-proven case as well as a thorough literature review, we hope to aid radiologists in gaining a better understanding of cervical sympathetic chain paragangliomas.

Results

N/A

Conclusions

Head and neck paragangliomas are classically described as arising from four typical locations. Our case-based presentation of cervical sympathetic chain paragangliomas illustrates this rare fifth subsite. Through a comprehensive review of clinical presentation, key multimodality imaging features, differential diagnoses, and management options, we hope to aid radiologists in gaining a better understanding of this unique entity.



(Filename: TCT_488_sympatheticchainparagangliomaimages.jpg)

1178

Symptomatic Non-stenotic Carotid Plaques(SyNC)

N Singh¹, J Ospel², M Marko³, M GOYAL¹

¹University of Calgary, University of Calgary, ²University of Basel, Basel, Switzerland, ³University of Vienna, Wien, Wien

Purpose

Teaching points: Definiton of symptomatic non-stenotic carotid plaques(SyNC) Risk of recurrent stroke/TIA in patients with SyNC High-risk plaque features Therapeutic implications of SyNC

Materials and Methods

Why do we need to identify non-stenotic carotid plaques? Determining stroke etiology is essential to provide adequate treatment for secondary stroke prevention. As per TOAST criteria, only >50% carotid stenosis is classified as "large artery atherosclerosis". Thus,plaques with <50% stenosis are classified as cryptogenic strokes. There is growing evidence that suggests non-stenotic carotid plaques are more common on ipsilateral side of stroke as compared to contralateral side implying association between the two. What are non-stenotic carotid plaques (SyNC)(with Image)? Non-stenotic carotid disease is defined as <50% carotid stenosis. The definition of "symptomatic" is based on the history of a ischemic stroke/TIA in the vascular territory supplied by the affected artery. Conversely, asymptomatic non-stenotic carotid disease(AsyNC) refers to non-stenotic carotid disease causing <50% carotid stenosis in the absence of clinical events consistent with ischemic stroke/TIA. Symptomatic non-stenotic carotid plaques have been proposed to be classified into definite, possible and probable SyNC by Goyal et al (1) What is the incidence & prevalence of non-stenotic carotid plaques in symptomatic and asymptomatic population? Pooled prevalence of ipsilateral non-stenotic carotid plaques has been reported to be 51%(95% CI: 45 - 59)(3). A recent meta-analysis showed the incidence of first-ever ipsilateral stroke/TIA was 0.5/100 person-years. The risk of recurrent stroke/TIA was 2.6/100 person-years and increased to 4.9/100 person-years if intra-plaque hemorrhage was present(2). What are the features of non-stenotic plaques with higher risk of stroke? High-risk plaque features include intra-plaque

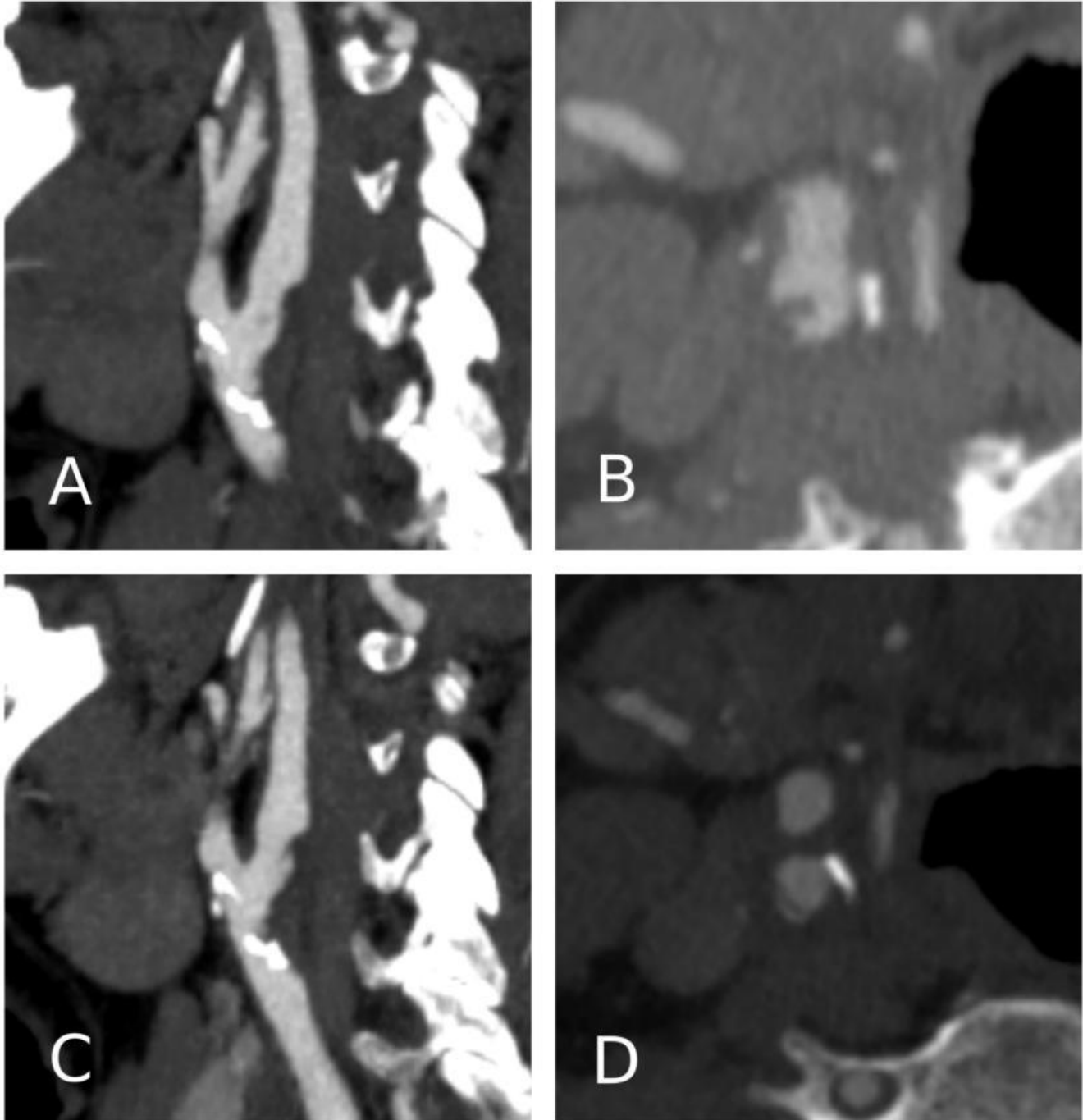
hemorrhage, plaque ulceration, plaque thickness (suggested cut-off of 3mm), fibrous cap rupture, lipid-rich plaque core and plaque echolucency. AHA lesion type >4 have shown to have the highest risk of recurrence(OR, 28.7; 95% CI,1.6-513.3)(2) What are implications of detection of SyNC Patients with SyNC who currently are a subgroup of ESUS population, would benefit from anti-platelet therapy over anti-coagulation. Acknowledging non-stenotic carotid plaques as a potential cause of stroke.

Results

NA

Conclusions

NA



(Filename: TCT_1178_ASNR_abstract_1.jpg)

1573

T-Boned, Now What? Assessing Acute Vascular Injury in the Setting of Temporal Bone Trauma

P Annigeri¹, R Nadgir²

Purpose

Using a case-based approach, we will discuss CT imaging findings that warrant further assessment of vascular integrity and review the various potential vascular complications of temporal bone trauma.

Materials and Methods

Temporal bone fractures are usually encountered in the setting of blunt force trauma and can be associated with vascular injuries that typically require early identification and urgent intervention. The purpose of this educational exhibit is to review normal CT anatomy of the temporal bone with emphasis on vascular anatomic considerations, discuss the imaging findings that should prompt assessment for vascular integrity, and provide a pictorial review of the numerous potential vascular complications of temporal bone trauma.

Results

• Using representative case files, we will review the CT anatomy of the vascular channels through the temporal bone and relationships to surrounding anatomic structures. • We will discuss CT imaging features that should raise suspicion for acute vascular injury and prompt further imaging. • We will review a broad spectrum of the potential vascular complications of temporal bone trauma including carotid artery dissection (A), vasospasm, pseudoaneurysm, extravasation, extrinsic vascular compression, venous thrombosis (B,C) and carotid-cavernous fistula (D).

Conclusions

Temporal bone anatomy is innately complex and a solid understanding of its normal fissures, sutures and foramina is important for evaluating acute temporal bone pathology. This exhibit will discuss the key imaging features that should prompt evaluation of the vasculature in the setting of temporal bone trauma. We will also provide a pictorial review of the various potential vascular complications of temporal bone trauma.

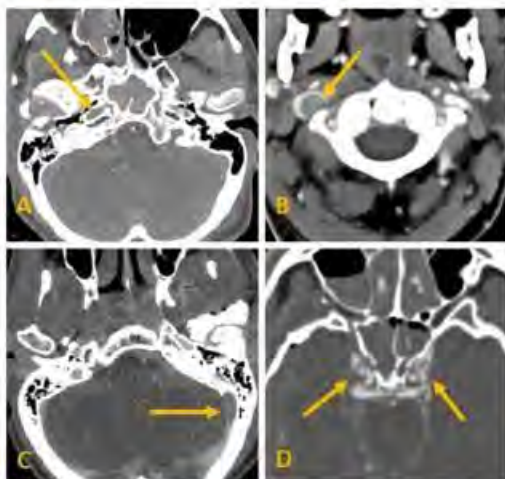


Figure A: Non-enhancement of the right petrous carotid artery compatible with carotid dissection with thrombosis

Figure B: Large non-occlusive thrombus in the right distal jugular vein

Figure C: Hypoattenuating in the left distal transverse sinus compatible with partial occlusion

Figure D: Opacification of bilateral cavernous sinuses on CT angiography compatible with carotid-cavernous fistula

(Filename: TCT_1573_t-bonefrxASNRcases.jpg)

1068

T2 Hypointense Lesions in the Head and Neck

A Singhal¹, H Patel¹, H Sotoudeh¹, V Prattipati¹, P Chapman²

¹University of Alabama at Birmingham, Birmingham, AL, ²Duke University, Durham, NC

Purpose

The presence of a pathology is often detected by abnormal T2 signal, typically hyperintensity. However, there are several pathologies throughout the body, including the head and neck that are characterized by T2 hypointensity. Identification of this T2 hypointensity can help streamline an otherwise broad differential diagnosis at different sites and therefore, help guide and in some cases even alter the expected pathway of patient management. There can be several causes of T2 hypointensity for e.g.- calcifications, fibrous or

ossific origin, granulomatous diseases, highly cellular tumors, blood, mucin, protein or air containing lesions or fungal infection. In this pictorial review, we will discuss several T2 hypointense head and neck lesions based on the various sites and features. Some of the sites discussed will include- skull base, sinuses, maxillofacial and orbital structures, aerodigestive tract, thyroid and other neck soft tissues.

Materials and Methods

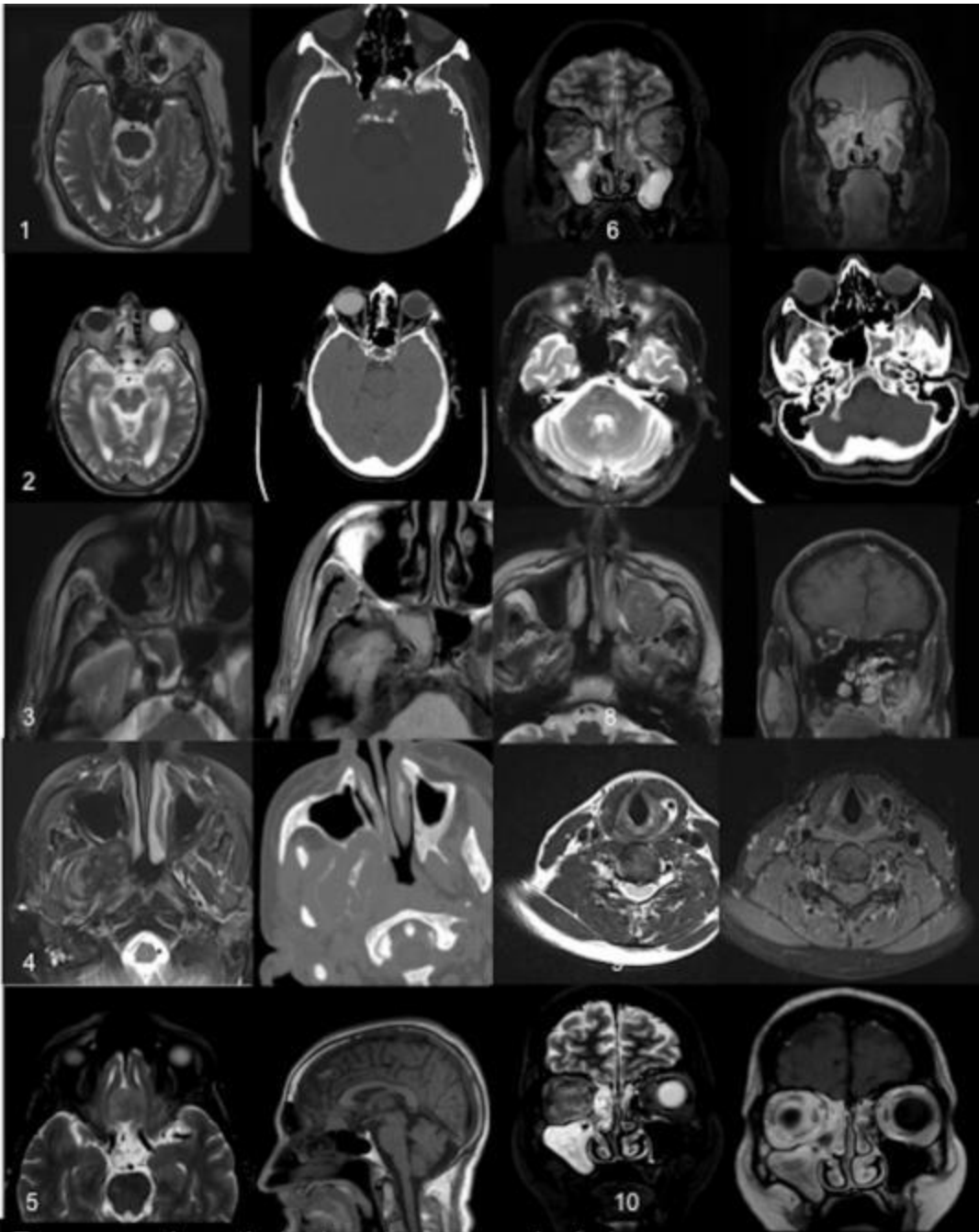
This presentation is a pictorial review of T2 hypointense lesions in the head and neck.

Results

Various cases will be presented depicting different T2 hypointense lesions in the head and neck at different sites. Few examples are shown in the included Figure.

Conclusions

Several lesions at various head and neck subsites can demonstrate T2 hypointensity. Identification of T2 hypointensity in head and neck lesions could help streamline a broad differential diagnosis for various sites.



Few example pathologies shown here include:

1. Pituitary adenoma with unusual calcifications
2. Globe silicone treatment for retinal detachment
3. Sphenoid sinusitis- inspissated secretions
4. Brown tumor in renal osteodystrophy
5. Meningioma
6. Sinus/orbit Granulomatosis with Polyangitis
7. Sphenoid mycetoma
8. Maxillary invasive non-keratinizing squamous cell carcinoma
9. Left piriform sinus laryngocele
10. Small focus of invasive fungal sinusitis

(Filename: TCT_1068_T2Hypo_HN.jpg)

Tandem Carotid Lesions in Acute Ischemic Stroke: Case Based Review

A Agarwal¹, A White¹, J Farag¹
¹UT Southwestern, Dallas, TX

Purpose

1. To discuss the hemodynamics behind tandem lesions in acute ischemic stroke 2. To discuss the role of non-invasive imaging for tandem carotid lesions 3. Case based review to discuss the management approach for tandem lesions in acute ischemic stroke

Materials and Methods

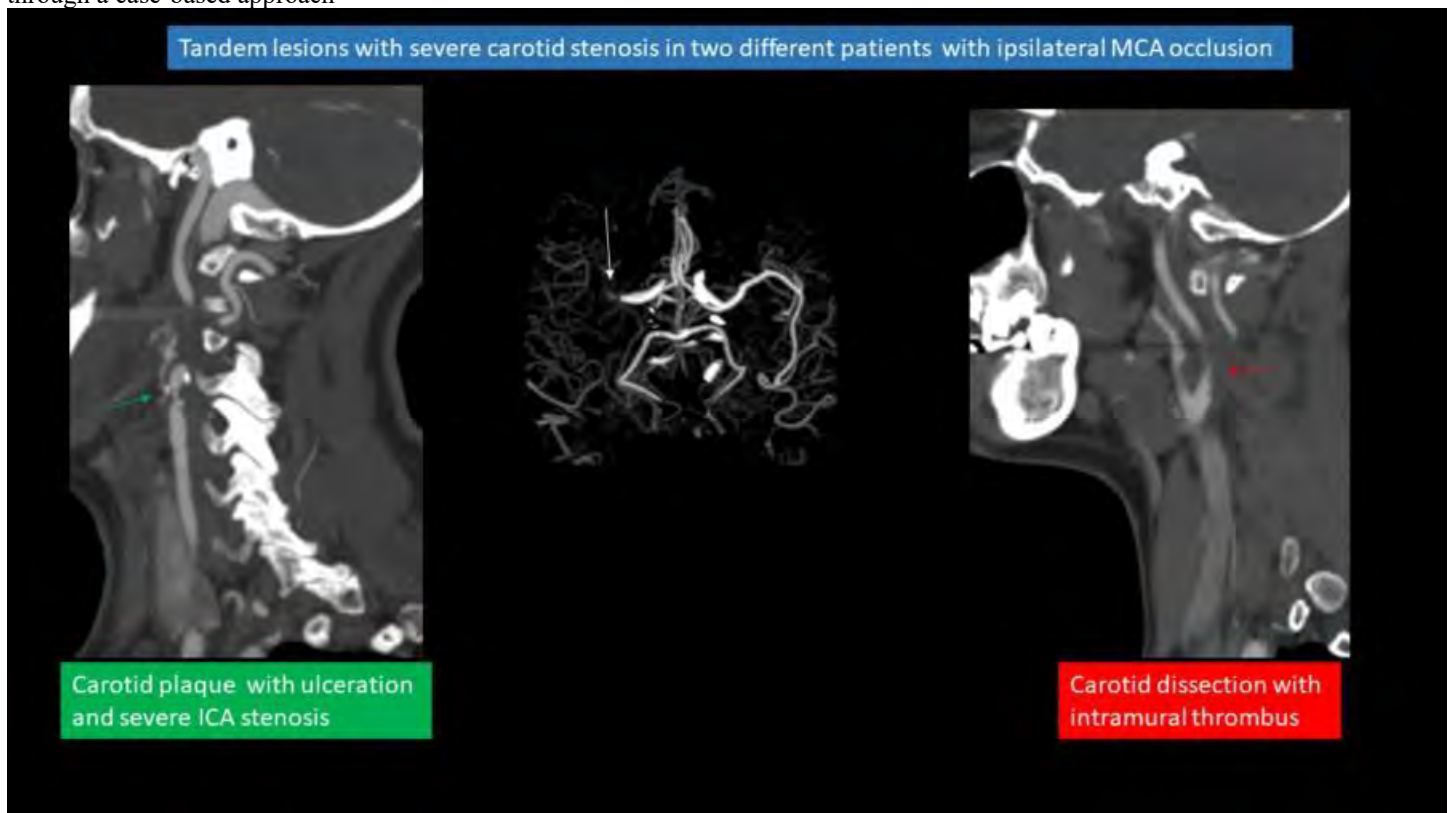
To provide a basic understanding of tandem carotid stenosis in acute ischemic stroke with case based- review

Results

1. Pathophysiology of acute ischemic stroke in tandem carotid lesions 2. Atherosclerotic Plaque versus Dissection 3. Radiologic differentiation of true carotid occlusion from near-complete occlusion 4. Management strategies for tandem carotid lesions: To stent or not to stent

Conclusions

This exhibit provides an overview of the diagnosis and management strategies for tandem carotid lesions in acute ischemic stroke through a case-based approach



(Filename: TCT_182_Tandem.jpg)

1083

Temporal Bone Masses from Benign to Malignant.

J Junn¹, M Schecht², L Eisenmenger³

¹Mount Sinai Hospital Icahn School of Medicine, NYC, NY, ²Mount Sinai Hospital, NYC, NY, ³University of Wisconsin - Madison, Middleton, WI

Purpose

Review salient temporal bone anatomy to localize the lesion Understanding imaging features of benign and malignant temporal bone pathologies

Materials and Methods

Understand imaging features and differential diagnosis for benign and malignant temporal bone masses.

Results

The temporal bone is often challenging for radiologists and trainees as it contains miniscule structures with intricate anatomy. Both benign and malignant masses may arise in or affect the temporal bone. This educational exhibit will highlight a spectrum of benign and malignant masses in the temporal bone by highlighting unique imaging findings to narrow the diagnosis. In this exhibit, we will discuss key imaging findings of benign and malignant pathologies encountered in this region including schwannoma, meningioma, epidermoid/dermoid, cholesteatoma, and cholesterol granuloma. Aggressive lesions including osteosarcoma/osteoblastoma, metastatic disease, intraosseous meningioma will be discussed. Non-neoplastic lesions with aggressive imaging features will also be highlighted such as pigmented villonodular synovitis.

Conclusions

Imaging and accurate interpretation are critical in the assessment of temporal bone pathology. Through this exhibit, the reader should ascertain useful imaging features to better assist patient management.

1339

The Acetazolamide Challenge Revisited: Multimodality Review of Technical Aspects and Clinical Applications.

F Feltrin¹, M Alhasan¹, W Moore¹, B Welch², M Pinho¹

¹University of Texas Southwestern Medical Center, Dallas, TX, ²UTSW Medical Center, Dallas, TX

Purpose

The noninvasive evaluation of cerebrovascular reserve (CVR) leveraging an acetazolamide (ACZ) challenge is a well established evaluation tool for patients with Moyamoya vasculopathy in some academic centers, both for preoperative planning as well as for post-surgical follow up. In recent years, new clinical applications have emerged, such as risk stratification for future stroke among patients with atherosclerotic disease and risk stratification of hyper perfusion syndrome among candidates for carotid revascularization. However, this tool is still uncommonly used in most radiology practices, likely due to lack of familiarity with the technical aspects and workflow.

Materials and Methods

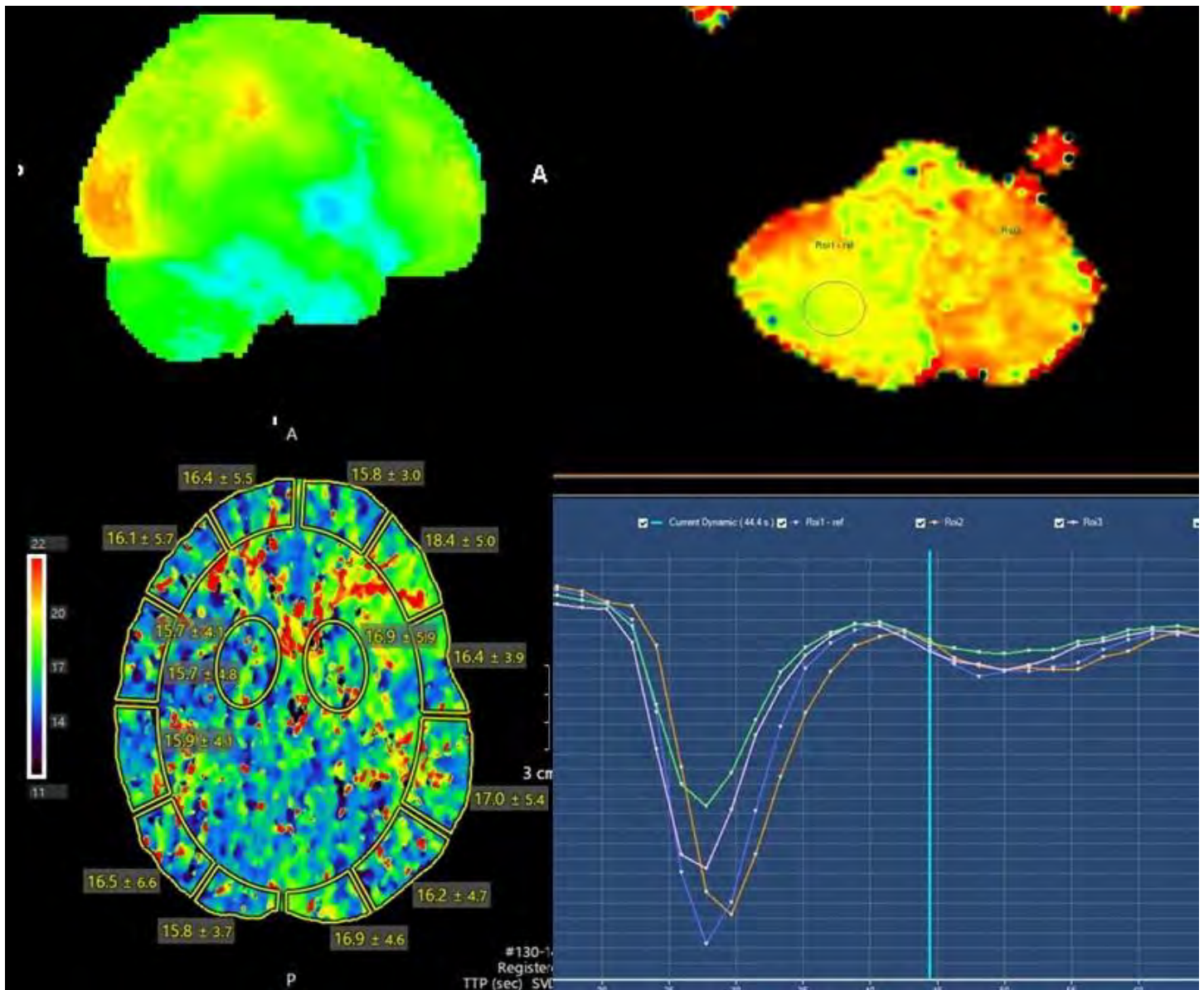
To provide a practical review of physiologic and technical principles, clinical applications, and expected results of multimodality clinical acetazolamide challenge perfusion imaging studies, including CT, MRI and nuclear imaging.

Results

Review of relevant peer reviewed literature focusing on the advantages, limitations, and differences in sensitivity, specificity, and accuracy of each method. Our discussion will feature representative cases from our experience to demonstrate the clinical utility and application of CT perfusion, MR DSC perfusion, MR ASL, and SPECT perfusion examinations, including imaging pitfalls. We will also include a summary and discussion of best practice technical parameters based on literature recommendations.

Conclusions

Our literature review suggests that most groups consider nuclear medicine as the gold standard for CVR evaluation with ACZ. Although MR (DSC and ASL) perfusion and CT perfusion are also commonly used, there is a concern that these methods may be less reliable due to a reliance on physiologic assumptions in calculation and/or technical challenges in the context of complex hemodynamics. "Steal" phenomenon after ACZ is the most reliable marker of poor CVR, and has been demonstrated to be a risk factor for future cerebrovascular events in patients with chronic cerebrovascular disease, including patients with Moyamoya and intracranial atherosclerosis. We also have found illustrative cases in our institution database which corroborate these concepts.



(Filename: TCT_1339_acetazolamide.jpg)

918

The Acute Neck: A Review of Common Nontraumatic Neck Emergencies

C Iv Kyrazis¹, J Wallace¹, E Hoeffner¹, R Lobo²

¹University of Michigan, Ann Arbor, MI, ²University of Michigan, Ann Arbor, MI

Purpose

Acute neck pain is a common presentation in the emergency setting. Computed tomography (CT) of the neck is often first-line in the imaging evaluation of nontraumatic neck emergencies, given the speed of acquisition and diagnostic accuracy with contrast-enhanced imaging. CT neck is often described as one of the most difficult imaging modalities to master in radiology, given the anatomic complexity and the range of emergent pathologies that require timely diagnosis. In particular, complications of deep neck infections are important to recognize early, as delayed diagnosis of a drainable abscess can result in increased morbidity and mortality, including development of septic shock, unplanned intubation, and prolonged hospital stay. (1) In this educational exhibit, our objective is to present an interactive electronic review of commonly encountered nontraumatic neck emergencies, important for both the general radiologist and neuroradiologist to understand. We will provide a review of neck anatomy, describing the superficial and deep cervical fascia, as well as their relevance to identifying and localizing pathologies within the deep spaces of the neck. We will include case-based imaging examples for each disorder with emphasis on reviewing the imaging findings, focusing on the neck CT, with a brief review of multimodality imaging features if relevant.

Materials and Methods

N/A

Results

Through the EMERSE (Electronic Medical Record Search Engine) application developed at our institution, we were able to search the electronic medical record and cross-match with radiology and pathology reports to identify representative examples of common nontraumatic neck emergencies. Our cases date from 2011 to 2020.

Conclusions

CT of the neck is commonly performed in the emergency setting to evaluate acute nontraumatic neck pain. Our educational exhibit seeks to clarify complex neck anatomy and review imaging features of common neck pathologies and their complications. Entities reviewed include odontogenic infections, Ludwig's angina, tonsillitis and tonsillar/peritonsillar abscess, Lemierre syndrome, retropharyngeal edema versus abscess versus suppurative adenitis, descending mediastinitis, epiglottitis, necrotizing fasciitis, TIPIIC syndrome, angioedema, and other entities. Reviewing this exhibit will increase knowledge on this topic and, subsequently, comfort with interpretation of the neck CT.

287

The Brain in Limbo: Spectrum of Autoimmune-mediated Encephalitis and Their Imaging Mimics Beyond Simple 'Limbic Encephalitis'

C Liang¹, E CHU¹, E KUOY¹, J Soun¹

¹UC Irvine Department of Radiological Sciences, Orange, CA

Purpose

Background Information: Autoimmune encephalitis, which encompasses various antibody-mediated inflammatory brain disorders, is increasingly being recognized as an important cause of new-onset altered mental status. The spectrum of imaging findings in autoimmune encephalitis is very broad and therefore often presents a unique diagnostic challenge. However, certain characteristic imaging and clinical findings can still help narrow down the list of differential considerations. Educational Objective/Purpose: This educational exhibit aims to review the spectrum of image findings of the major antibody subtypes of autoimmune encephalitis and their mimics.

Materials and Methods

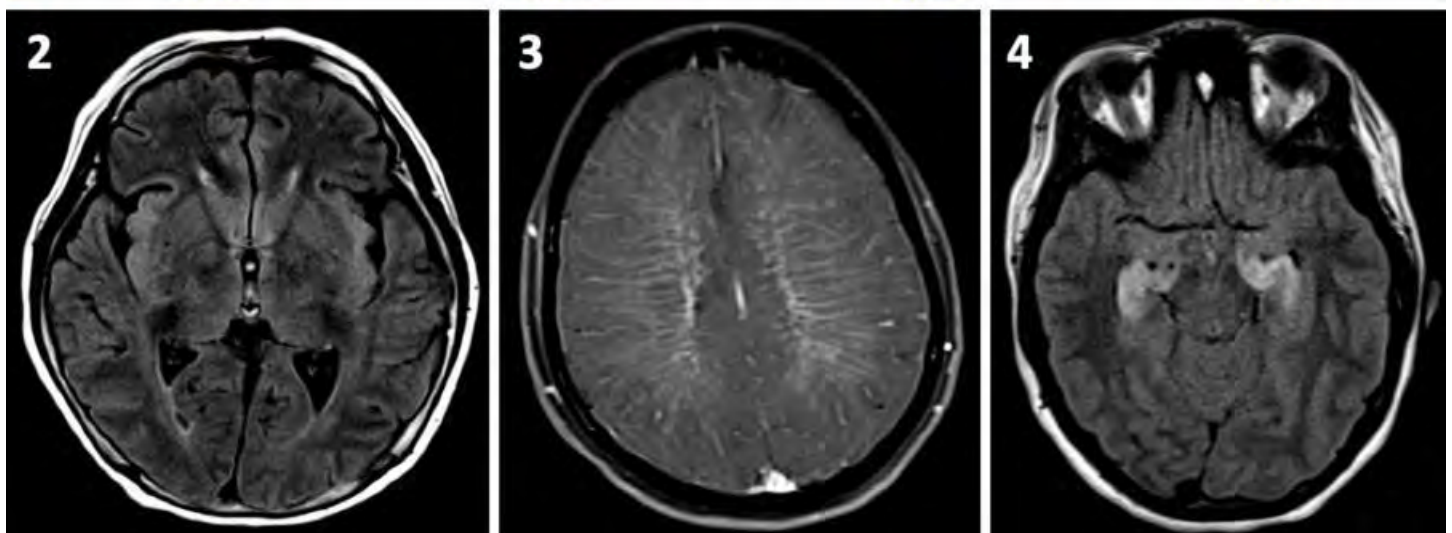
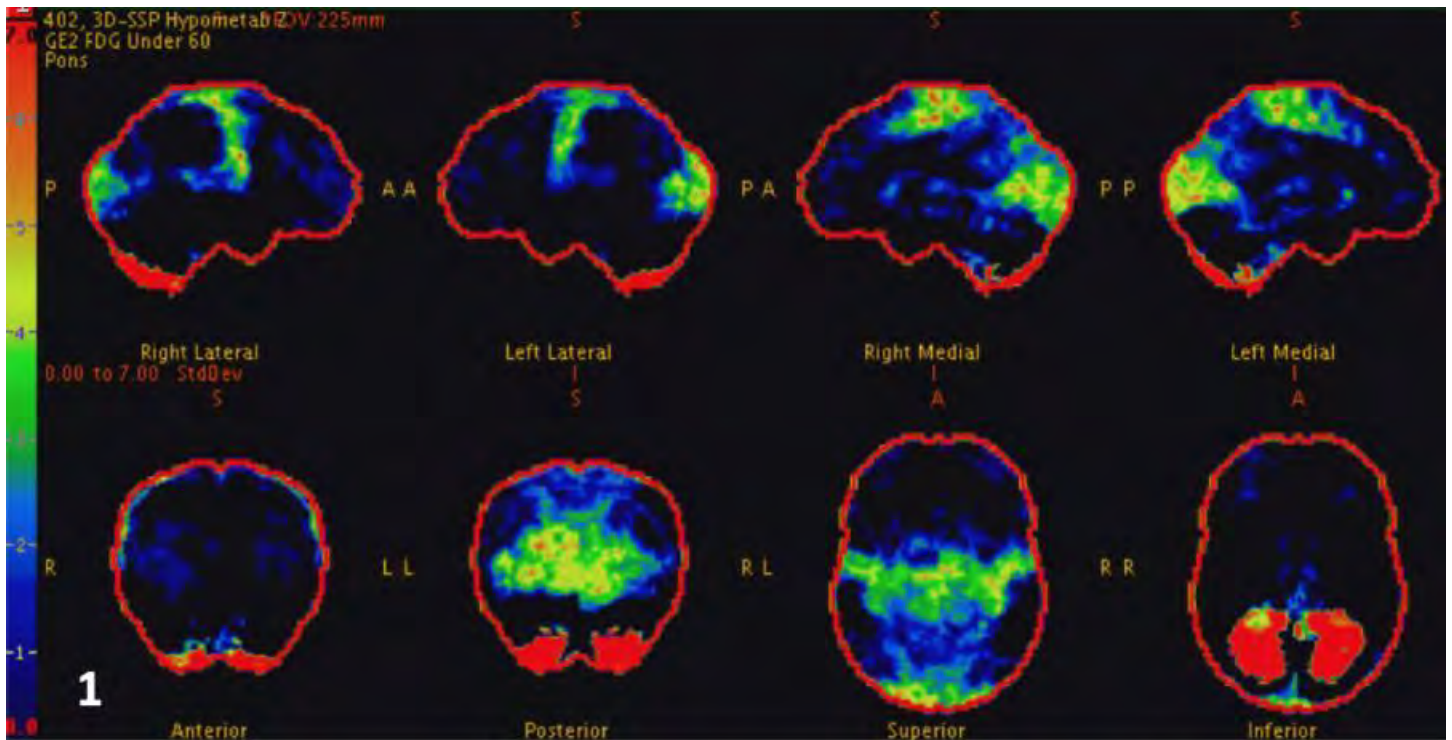
This exhibit also aims to suggest a diagnostic approach to the imaging of autoimmune encephalitis and its mimics.

Results

A review of literature on autoimmune encephalitis will be performed. Case examples will be obtained from our institutional database to create this educational exhibit in a case-based review format.

Conclusions

Table of Contents: I. Pathophysiology a. Paraneoplastic vs non-paraneoplastic b. Major malignancies associated with autoimmune encephalitis II. Major antibody subtypes of autoimmune encephalitis - imaging and clinical characteristics IIa. Group 1: intracellular antigens i. Anti-Hu ii. Anti-Ma/Ta iii. Anti-Collapsin response mediator protein 5 (CV2) iv. Anti-Glutamic Acid Decarboxylase (GAD) IIb. Group 2: extracellular antigens i. Anti N-methyl D-aspartate (NMDA) receptor 1. Without primary neoplasm 2. With primary neoplasm - ovarian teratoma ii. Anti-voltage gated potassium channel (VGKC) 1. Anti- Leucine-rich Glioma-inactivated 1 (LG1) subtype 2. Anti- Contactin-associated Protein-like 2 (CASPR-2) subtype iii. Anti-voltage gated calcium channel (VGCC) iv. Anti-Aminobutyric Acid Receptor (GABA_R) IIc. Other types of autoimmune encephalitis i. Anti-Glial Fibrillary Acid Protein (GFAP) Astrocytopathy ii. Systemic Autoimmune disorders with Encephalopathy III. Imaging mimics of autoimmune encephalitis and differentiating factors a. Infectious Encephalitis (i.e. HSV Encephalitis) b. Seizure-related changes/Status Epilepticus c. Diffuse astrocytoma d. Acute-subacute PCA infarct e. Chemotherapy toxicity f. Creutzfeldt-Jacob Disease g. Hypoxic Ischemic Encephalopathy IV: Proposed diagnostic approach to autoimmune encephalitis and its mimics Figure Legends: Figure 1: Anti-NMDA receptor encephalopathy Figure 2: Anti-VGKC encephalopathy Figure 3: Anti-GFAP astrocytopathy Figure 4: Seizure-related changes



(Filename: TCT_287_AbtractImagefile.jpg)

1476

The Design of a Neuroradiology Fellowship Boot Camp: Educational Gaps, Priorities, and Resources

L Tu¹, A Abou Karam², S Abi Fadel³, A Malhotra⁴, I Ikuta⁵, W Zucconi⁶

¹Yale School Of Medicine, New Haven, CT, ²Yale Medicine, New Haven, CT, ³Yale, New Haven, CT, ⁴Yale University School of Medicine, New Canaan, CT, ⁵Yale University School of Medicine, New Haven, CT, ⁶N/A, N/A

Purpose

Provide an structured, prioritized framework to prepare new neuroradiology fellows for: - Independent call - Uncommon exams - Mitigation of common errors

Materials and Methods

While the ANSR provides a sample fellowship curriculum, there is little guidance on a prioritized approach to educational resources or literature. The purpose of this work is to provide a framework for preparing new fellows for high acuity/complexity neuroimaging, with a focus on readiness for independent call and advanced exams not frequently seen in residency.

Results

Attending and fellow staff at a large academic center are surveyed to identify educational gaps occurring between residency and neuroradiology fellowship. The most common detection, diagnostic, and workflow errors made by new fellows are summarized. The

radiology report database is queried to identify uncommon and advanced neuroimaging exam types. The available literature is reviewed, with reference to diagnostic errors, uncommon study types, and the ASNR sample fellowship curriculum/educational resources. The resultant resources and advice are prioritized into three categories: 1) urgent/mandatory preparation for call 2) non-urgent, though high-priority educational needs 3) further reading. A practical guide to fellow education is thus outlined.

Conclusions

Significant and management changing errors made by new fellows follow distinct patterns, detailed in the full presentation. Uncommon exams where fellows are less likely to have had significant exposure during residency, though where is significant volume for fellows include: MRI of the temporomandibular joints, MRI of the brachial plexus, MRI of the lumbosacral plexus, perfusion CT, perfusion MR, CSF flow studies, fMRI, and MR spectroscopy. The most accessible/essential literature for each of these topics is arranged into prioritized reading lists. The ASNR provides a sample fellowship curriculum; however, a structured and prioritized approach to existing resources for new fellows is needed. Here, we present a model of a fellowship "boot camp" to provide this guidance, as well as to reduce the most common practical/workflow related errors made by new fellows.

825

The Diencephalon–Midbrain Junction: Anatomy, Normal Variants, Malformations, and Acquired Pathology

M McClure¹, J Estroff¹, E Yang¹

¹*Boston Children's Hospital, Boston, MA*

Purpose

The diencephalon-midbrain junction includes the epithalamus (pineal region), thalamus, hypothalamus, and dorsal midbrain. It defines the anatomical boundaries of the third ventricle, the cerebral aqueduct, and quadrigeminal cistern. Congenital malformations of this region were once thought to be uncommon compared to acquired pathology such as neoplasms. However, variant anatomy and congenital anomalies of the diencephalon-midbrain junction have been increasingly recognized and described with high resolution MRI. In this exhibit, we present the normal anatomy, anatomic variants, malformations, and acquired pathology seen in the diencephalon-midbrain junction. We begin with a review of the anatomy of this region with an emphasis on the lamina terminalis, infundibular recess, massa intermedia, habenular/posterior commissures, tectum, and superior medullary velum as key anatomic landmarks. We then present normal variants (e.g. cysts, interhypothalamic adhesions, deficiency of the tentorial incisura) that are commonly encountered. We contrast these variants with malformations of the diencephalon-midbrain region including abnormal fusion (e.g. in rhombencephalosynapsis, holoprosencephaly), congenital absence of normal structures (e.g. aqueductal stenosis), and hamartomas involving the hypothalamus as well as the tectum. Finally, we present important acquired pathology that affects this region including neoplasms, atrial diverticula, hemorrhagic/thrombotic sequela, demyelination (e.g. NMO), metabolic conditions (e.g. Wernicke encephalopathy), and postsurgical change (e.g. Wallerian degeneration along the fornices, lamina terminalis fenestration). Along the way, we review the embryology of this region and genetic conditions implicated in malformations as well as acquired pathology. By the end of this presentation the learner will be able to: (1) Recognize and identify on MRI the anatomic boundaries and key structural relationships of the pineal region (habenular/posterior commissures), third ventricle outlet, hypothalamus/ floor of the third ventricle, and quadrigeminal plate/ cistern. (2) Discuss key imaging features that assist in recognition of these malformations and variants and understand the basic embryology of these anomalies where relevant. (3) Describe key features of non-neoplastic acquired pathology unique to this region. (4) Reference some of the genetic bases of these malformations.

Materials and Methods

N/A

Results

N/A

Conclusions

N/A

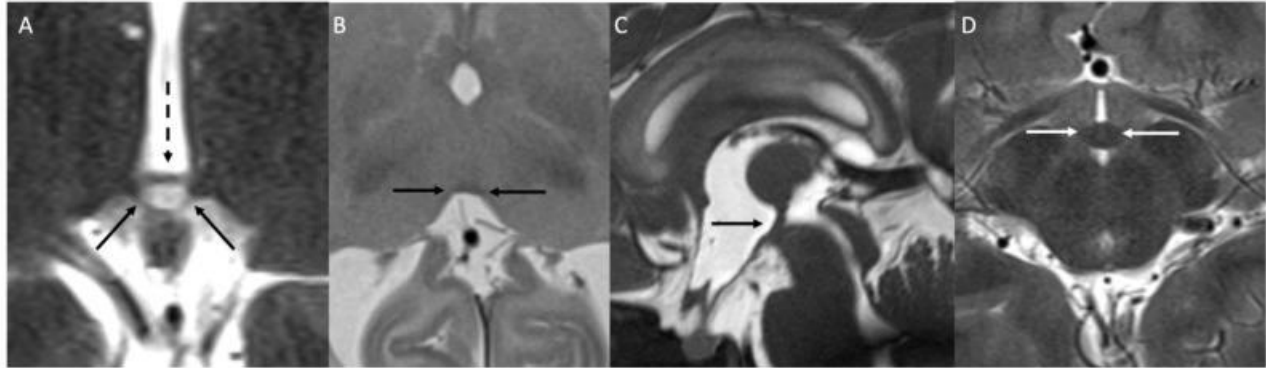


Figure 1. A. Axial T2 image of the pineal region demonstrates the habenular commissures (arrow) and posterior commissure (dashed arrow). B. Axial T2 of a newborn with broad massa intermedia demonstrates no normal habenular commissures or pineal gland, only a myelinated sheet suspected to represent the posterior commissure (arrows). C. Sagittal CISS imaging of a newborn with ventriculomegaly demonstrates an obstructing septum (arrow) between the massa intermedia and floor of the third ventricle. D. Axial T2 imaging of a patient with developmental delay demonstrates a single mammillary body (arrows).

(Filename: TCT_825_DMJdevelopmentalandcongenitalanomalies.jpg)

363

The diversity of imaging and clinical findings of stroke-like migraine attacks after radiation therapy (SMART) syndrome

Y Ota¹, A Baba², R Kurokawa³, A Capizzano⁴, T Moritani⁴

¹University of Michigan, Ann Arbor, MI, ²The Jikei University of Medicine, Minato, Tokyo, ³Graduate School of Medicine, The University of Tokyo, Tokyo, Japan, ⁴N/A, N/A

Purpose

After viewing this exhibit, the reader will be familiar with clinical presentation, typical and atypical MRI findings of SMART syndrome. Objectives • Clinical presentation • Typical and atypical MRI findings • Postulated mechanisms

Materials and Methods

• Highlight the clinical presentation of SMART syndrome • Present typical and atypical MRI findings of SMART syndrome • Review the postulated pathophysiology of SMART syndrome

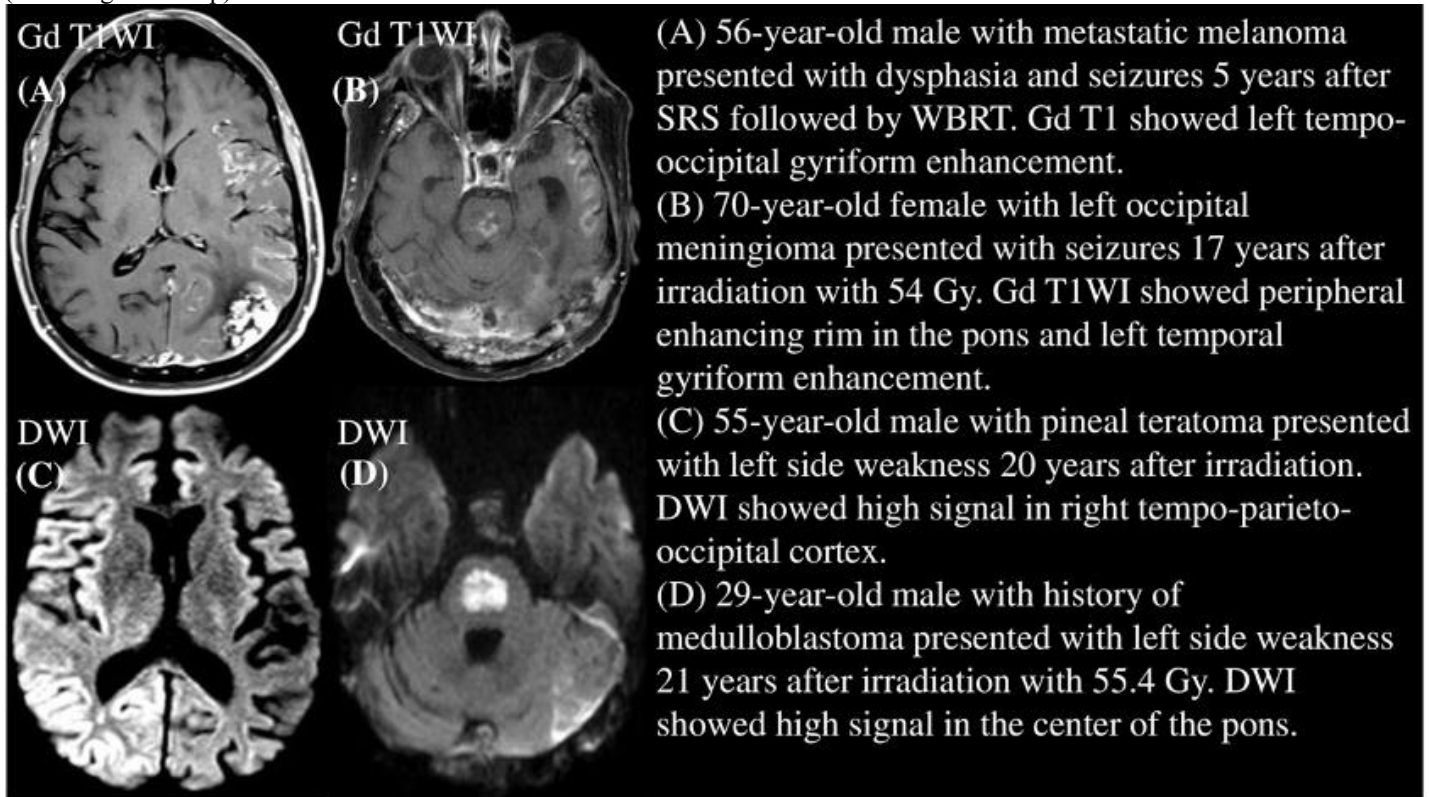
Results

• Clinical presentation -Symptoms -Original pathology and tumor location -Time period between radiation and diagnosis of SMART - Dose of brain irradiation • Typical and atypical MRI findings • Apart from classical gyriform enhancement, cases of brainstem enhancement and restricted DWI are presented • Postulated mechanisms -Late ionizing radiation effects upon mitochondrial DNA - Vessel narrowing or occlusion due to delayed radiation effects

Conclusions

SMART is a delayed complication of brain irradiation where patients have recurrent attacks of complex neurologic signs and symptoms. Pathophysiology is not fully understood. According to our cases, the time period between diagnosis and radiation dose ranged from 1 to 21 years and radiation dose from 34 to 60 Gy. Postulated pathophysiology includes mitochondrial DNA damage,

endothelial injury and spreading depression due to late radiation effects, but it has not been proven yet. Typical MRI findings include unilateral cortical T2/FLAIR hyperintensity with gyral cortical gray matter enhancement. These findings resolve when the symptoms alleviate, but permanent sequela is not uncommon. The distribution of MRI findings is not consistent with vascular territories but with the prior irradiation field. Atypical MRI findings include a central pontine T2 hyperintensity with peripheral rim enhancement and central DWI restriction. Representative cases are presented with conventional MRI findings, DWI, SWI, DSC- and DCE-MRI (including follow up) and MRS in one case.



(Filename: TCT_363_SMART.jpg)

950

The Draining Maze: A Review of Cerebral Venous Anatomy and Pathology

J Ruiz-Lopez¹, A Perez-Torres¹, L Garcia-Irizarry¹

¹UPR School of Medicine, San Juan, PR

Purpose

Educational Objectives: 1. Review Intracranial Venous Anatomy 2. Identification of the most common cerebral venous pathologies and their imaging findings on CT and MRI. 3. Overview of cerebral venous pathology mimics and pitfalls on imaging interpretation.

Summary: I. Introduction II. Review of Cerebral Venous Anatomy a. Dural Venous Sinuses b. Deep cerebral and cortical veins c. Venous Drainage Territories III. Pathology a. Cerebral Venous Thrombosis b. Venous Infarction c. Vascular Malformations 1. Low-Flow Vascular Malformations 2. High-Flow Vascular Malformations 3. Special Malformation Subtypes IV. Anatomical variants, mimickers and pitfalls V. Conclusion

Materials and Methods

Cerebral venous pathologies are oftentimes overlooked and difficult to suspect clinically due their varying or silent symptomatic presentation. Although venous occlusion and infarction are rare causes of intracranial hemorrhage, they may result in serious neurological damage and even mortality. Thus, prompt diagnosis is imperative as management may prevent some of the most severe outcomes. For these reasons imaging plays a primary role in the diagnosis of cerebral venous pathologies. The purpose of this educational exhibit is to review cerebral venous anatomy and describe the imaging characteristics of some of the most common associated pathologies, utilizing demonstrative radiological images as a guide. Important anatomical variants, mimickers, and potential interpretation pitfalls will also be highlighted with practical, case-based examples to further emphasize diagnostic accuracy.

Results

N/A

Conclusions

N/A

Dural Sinuses and Venous Plexuses: Posterosuperior Group



Figure 1: Contrast enhanced MRV and T1 3D reconstructions demonstrate the normal anatomical relationship between the posterosuperior group.

The inferior sagittal sinus (blue arrow) courses posteroinferiorly at midline, meeting the great vein of Galen at the falcotentorial apex to form the straight sinus (yellow arrow).

The superior sagittal sinus (red arrow) has a curved inferior trajectory following the skull's inner table at midline towards the torcular heterophilli, also known as the venous sinus confluence (green arrow).

Figure 2: The venous sinus confluence (green arrow) gives off the bilateral transverse sinuses (purple arrows).

The sigmoid sinuses (orange arrows) are continuations of the transverse sinuses coursing along the petrous temporal bones until ultimately draining into the internal jugular veins (light blue diamond) at the jugular bulb.

(Filename: TCT_950_CerebralVenousAPImage.jpg)

1356

The Fascinating Science of Chemical Exchange Saturation Transfer imaging: A Boon to Clinical Advances in Neuroimaging- Case based review

S Vankayalapati¹, K Kulanthaivelu², J Saini³

¹National institute of Mental health and Neurosciences, Bengaluru, Karnataka, ²National Institute of Mental Health and Neurosciences (NIMHANS), Bengaluru, Karnataka, ³NATIONAL INSTITUTE OF MENTAL HEALTH & NEURO SCIENCES, BANGALORE, India

Purpose

This exhibit will explain the basic physics and acquisition of Amide proton imaging (APT) sequence. This exhibit highlights the various clinical applications of this APT imaging in various CNS lesions. Also highlights the pathological basis of the imaging appearance.

Materials and Methods

Amide proton transfer (APT) or more generally chemical exchange saturation transfer (CEST) imaging is a novel molecular MRI technique that generates image contrast based on endogenous cellular proteins in tissue. Currently, APT-MRI holds great promise for abundant clinical molecular imaging applications

Results

Pictorial assay of 15 representative cases of various spectrum of intracranial space occupying lesions imaged with amide proton weighted sequence

Conclusions

Increased APT signal was observed in tumor tissues in all patients with grade III and IV. Elevation of APT signal was visible not only the Gd-enhancing core (solid portion) but also cystic portion (degeneration). Interestingly IDH-wildtype gliomas tended to have higher APTw value than IDH-mutant tumors. No elevation of APT signal was recognized in patients with grade II or grade I, which was benign histopathologically. No APT signal was visualized in chemo radiation-induced necrosis with Gd Enhancement, i.e. pseudo progression. Primary CNS Lymphomas had significantly lower APT signal than high-grade gliomas Tuberculoma had a periphery with higher APT ratios compared to the uninvolved parenchyma, the net increase was significantly smaller compared to the markedly raised APT in High grade glioma. APT signal was elevated in cystic lesions like colloid cyst, epidermoid cyst and Rathke cleft cyst. High APT signal is seen in the acute hemorrhagic lesions than subacute hemorrhage. Conclusion: APT imaging can be adjunct to anatomical MR imaging, diffusion and perfusion studies in various CNS space occupying lesions.

1069

The Gang's All Here: Parangliomas of the Head and Neck

M Crinnin¹, M Edquist², D Drumsta²

¹Jacobs School of Medicine and Biomedical Sciences, Buffalo, NY, ²University at Buffalo, Buffalo, NY

Purpose

Discuss the anatomy and embryology of paragangliomas of the head and neck. Give a brief overview of their epidemiology and presentation. Discuss the imaging characteristics of the major paragangliomas of the head and neck, including important mimics.

Materials and Methods

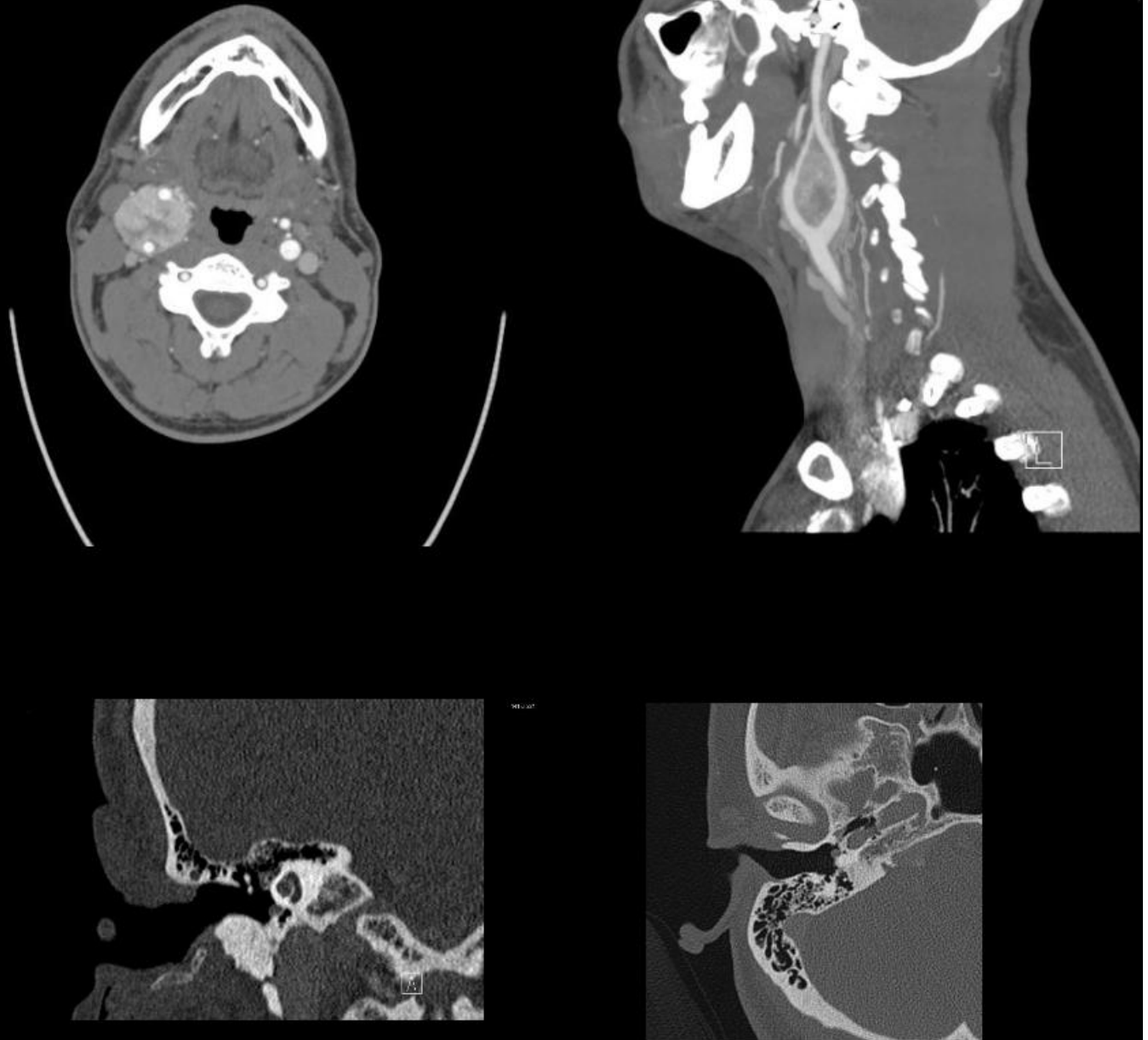
This educational exhibit aims to provide a brief overview of the anatomy, embryology, presentation, imaging findings, and common mimics of paragangliomas of the head and neck with included case examples from our institution as well as a thorough literature review.

Results

N/A

Conclusions

Head and neck paragangliomas are a group of neuroendocrine and vascular tumors including carotid body paraganglioma, glomus vagale, and glomus jugulotympanicum. They arise from neural crest cells and are associated with paraganglia of the parasympathetic nervous system. They can be sporadic or associated with Von Hippel-Lindau syndrome, MEN 2, NF type 1, and SDH mutations. They typically arise in middle-aged adults, with a roughly equal ratio of affected males to females with the exception of glomus vagale and glomus jugulotympanicum which have an increased prevalence in females. Although often benign, they can be hormonally active, which explains their clinical presentation. They are considered malignant only when metastatic. Depending on the location of the tumor, patients can present with a slowly growing mass in the neck, or with symptoms and signs often attributed to pheochromocytoma (an adrenal paraganglioma); including headaches, hypertension, tachycardia, and anxiety. Pulsatile tinnitus and hearing loss can be seen with glomus jugulotympanicum, and dysphagia and hoarseness in the case of glomus vagale. Imaging features include soft tissue density on CT with marked hyperenhancement. A "salt and pepper" appearance is seen on T1WI with mixed hyperintensity on T2WI. Local mass effect can occur respective to the location of the tumor. Differential diagnoses include: lymph nodes, ectasia of the carotid body or proximal internal or external carotid arteries, dehiscent jugular bulb, nerve sheath tumor, or cholesteatoma. Parangliomas of the head and neck are typically benign tumors that arise from neural crest cells associated with the parasympathetic chains in the head and neck. They have a characteristic imaging appearance of marked hyperenhancement on CT with a "salt and pepper" appearance on T1WI with mixed hyperintensity on T2WI with scattered flow voids. There are many mimics, including vascular and neoplastic etiologies.



(Filename: TCT_1069_combine_images.jpg)

348

The many faces and mimics of atypical skull-base meningiomas.

S Pinto¹, J Acharya², A Rajamohan³, V Patel³, C Liu⁴, T Lu², F Torres⁵, S Sampson⁶

¹Keck School of Medicine of USC, LOS ANGELES, CA, ²Keck School of Medicine of USC, Los Angeles, CA, ³University of Southern California, Los Angeles, CA, ⁴N/A, N/A, ⁵Kaiser Permanente, Los Angeles Medical Center, Los Angeles, CA, ⁶Kaiser Permanente Los Angeles Medical Center, Los Angeles, CA

Purpose

According to the 2016 WHO classification of central nervous system tumors, atypical meningiomas are histologically defined as tumors with a mitotic count of 4 or more per high power field or the presence of brain invasion (1). Atypical meningiomas comprise

approximately 5-7% of all meningiomas and present a unique diagnostic challenge (2). These neoplasms may demonstrate unusual imaging features such as cystic necrosis and internal hemorrhage (3). Atypical meningiomas of the skull base, in particular, are more locally aggressive than benign meningiomas in the same location (4). In the following exhibit, we will highlight the clinical presentation of multiple atypical skull-base meningiomas, which present clinically as facial masses. We will also discuss the imaging features of other aggressive skull base lesions which can present with extracranial extension and mimic the appearance of atypical meningiomas.

Materials and Methods

N/A

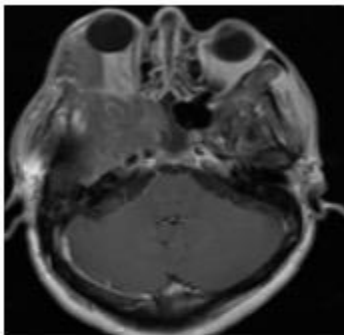
Results

N/A

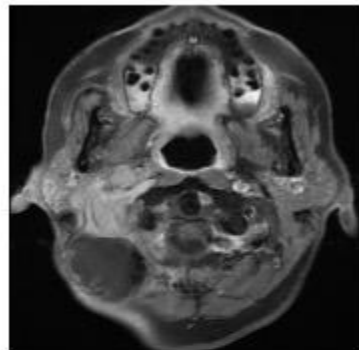
Conclusions

A total of four biopsy-proven skull-base atypical meningiomas, with extracranial extension were identified. All of these presented clinically as enlarging facial masses, with additional symptoms of airway compromise, cranial nerve palsies or proptosis. The tumors originated from the central or posterior skull base, with extension into the sinonasal, orbital or paravertebral spaces. They demonstrated aggressive imaging features, including hemorrhage, cystic degeneration and heterogeneous enhancement. Several other skull base lesions such as solitary fibrous tumors of the dura, chondrosarcomas and paragangliomas often demonstrate similar imaging characteristics and can have an extracranial pattern of spread. Solitary fibrous tumors of the dura have a heterogeneous pattern of contrast enhancement, similar to atypical meningiomas (5). These tumors may demonstrate calcifications and a lytic-destructive pattern of the calvarium with extracranial spread (5). Chondrosarcomas usually arise in the para-clival region and may extend into the paranasal sinuses or the nasopharynx (5). Paragangliomas of the skull base arise from the jugular foramen, the middle ear or along the vagus nerve. When these tumors invade the skull-base, they demonstrate a more infiltrative "moth-eaten" pattern of erosion. Recognition of the imaging features of atypical skull-base meningiomas and other aggressive skull-base tumors can help narrow the differential diagnosis and direct further management.

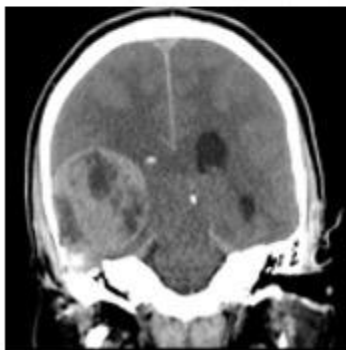
MIDDLE CRANIAL FOSSA ATYPICAL MENINGIOMA



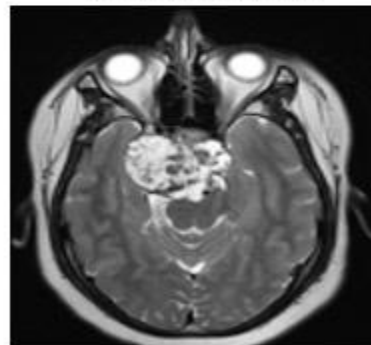
POSTERIOR CRANIAL FOSSA ATYPICAL MENINGIOMA



SOLITARY FIBROUS TUMOR OF THE DURA



CHONDROSARCOMA



(Filename: TCT_348_ASNR.jpg)

1537

The Many Faces of Central Nervous System Lymphoma: A Compartmental Approach

L Bisolo¹, L Coelho², E Gil³, M Camargo⁴, R BERTANHA⁵, F Hirata⁵, A Barbosa⁵, L Godoy⁶, F Nascimento⁷
¹Hospital Israelita Albert Einstein, Sao paulo, Sao paulo, ²Hospital Israelita Albert Einstein, São Paulo, IL, ³Hospital Albert Einstein, São Paulo, Brazil, ⁴Hospital isaraelita Albert Einstein, São Paulo, Sao Paulo, ⁵Hospital Israelita Albert Einstein, SAO PAULO, NY, ⁶Faculdade de Medicina da Universidade de São Paulo- FMUSP, Sao Paulo, Sao Paulo, ⁷Hospital Israelita Albert Einstein, São José dos campos, AK

Purpose

1. A brief review of lymphoma physiopathology 2. To demonstrate the imaging characteristics of typical and atypical central nervous system lymphoma (CNSL) in immunocompetent and immunocompromised patients, with a compartmental approach. 3. To show examples and compare with the main differential diagnosis. 4. To update with current radiogenomic concepts.

Materials and Methods

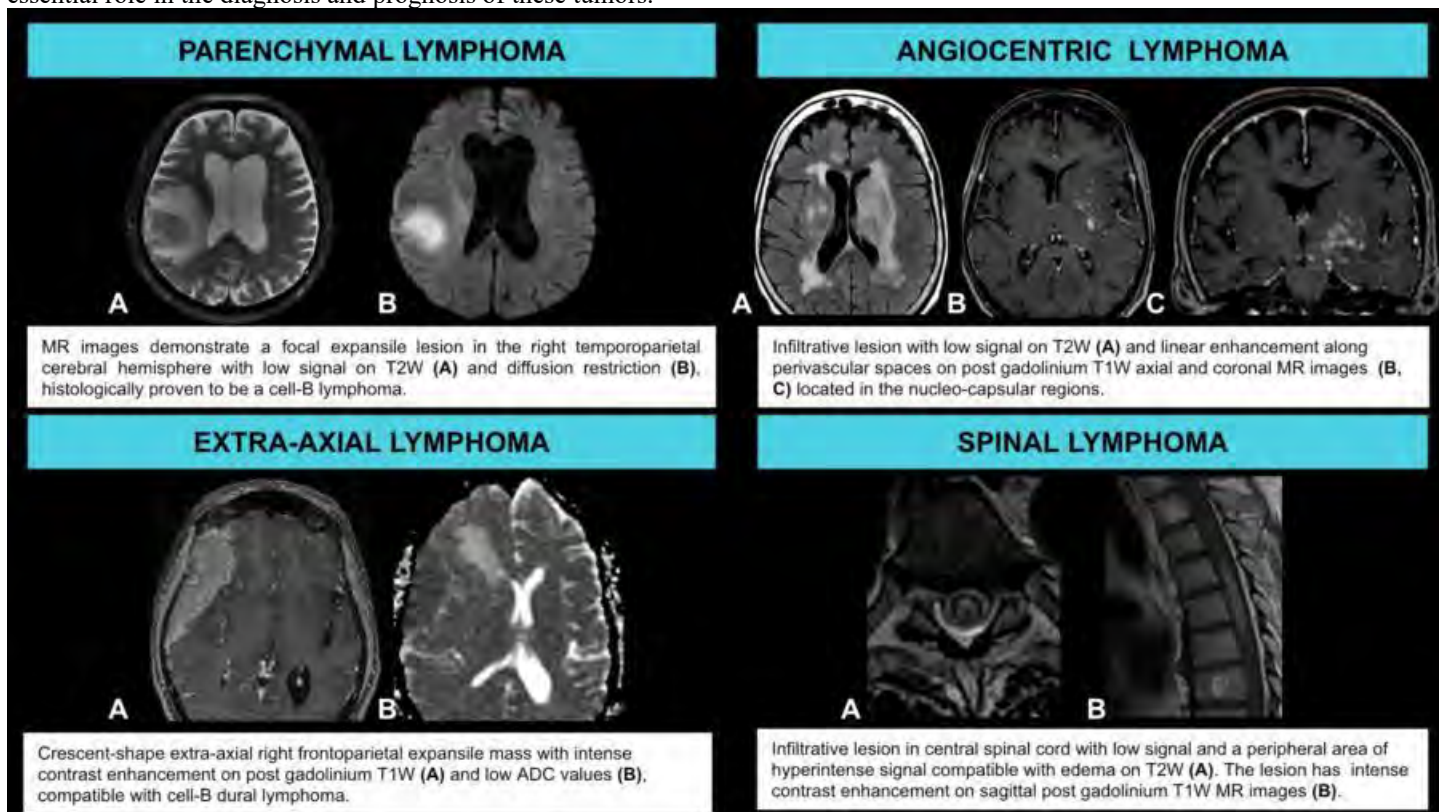
Central nervous system (CNS) lymphomas can be primary (PCNSL), when they are restricted to the brain, leptomeninges, spinal cord, or eyes, without evidence of disease outside the CNS at primary diagnosis or secondary to systemic disease. CNS lymphomas can present in immunocompetent and immunocompromised individuals with distinct imaging appearances. Our goal is to review the current literature and to demonstrate typical and atypical imaging features on CT, MR, and PET-CT of central nervous system lymphomas in immunocompetent and immunocompromised individuals.

Results

We reviewed the current literature about the imaging findings of central nervous system lymphomas with new radiogenomic concepts and will demonstrate multiple examples of CNS lymphomas after an analysis of 64 cases of our institutional database presenting as unifocal and multifocal lesions in the brain, in the extra-axial compartment, with necrotic and / or hemorrhagic areas, as lymphomatosis cerebri, lymphomatoid granulomatosis, angiocentric or intravascular lymphoma, and as post-transplant lymphoproliferative disorder.

Conclusions

CNS lymphomas may have multiple imaging presentations and may present in multiple compartments inside and outside the brain. The imaging characteristics are different if the patient is immunocompromised (HIV, HBV or autoimmune disease) or immunocompetent, eventually representing a diagnostic challenge when they present with necrotic or hemorrhagic areas, resembling glioblastomas, linear perivascular enhancement resembling granulomatous angiitis; or as an extradural mass, mimicking an epidural hemorrhage or a meningioma. The knowledge of the patient immune status, the typical imaging characteristics, and the possible localizations may orientate the radiologist to the appropriate diagnosis, especially when a biopsy is not possible. Emerging research has shown that radiogenomics can yield information about the underlying genetic alterations in lymphoma, so radiologists play an essential role in the diagnosis and prognosis of these tumors.



(Filename: TCT_1537_ASNR2.jpg)

1203

The Many Faces of Cryptococcus Infection in the Central Nervous System

J MATHIEU¹, J Talbott², J Narvid³

¹University of California, San Francisco, San Francisco, CA, ²UCSF and ZSFG, San Francisco, CA, ³N/A, N/A

Purpose

Summary This educational exhibit will begin by introducing the Cryptococcus pathogens, describing the mechanisms by which these agents cause disease, and discussing the clinical manifestations, with a focus on CNS infection. The majority of the presentation will be devoted to imaging. This exhibit will review examples of the following imaging presentations on CT and MRI, some of which may certainly overlap: hydrocephalus (C, D), nonenhancing T2/FLAIR parenchymal signal abnormality (A), dilated perivascular spaces/gelatinous pseudocysts (B), meningitis (C), choroid plexitis, and cryptococcoma (D). A discussion of the differential diagnosis will follow, including toxoplasmosis, tuberculosis, pyogenic abscess, JC virus encephalopathy, and lymphoma. The exhibit will conclude with the treatment and prognosis of this disease, specifically mentioning potential roles for the radiologist in the clinical management of these patients. Educational Objectives 1. Review the clinical presentation and pathophysiology 2. Discuss the imaging findings 3. Provide a differential diagnosis 4. Consider the radiologist's role in patient management

Materials and Methods

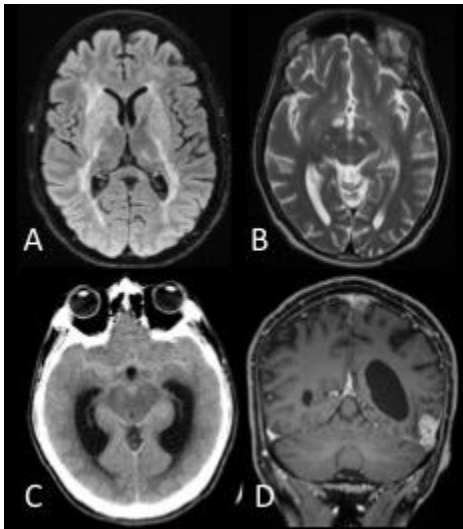
CNS Cryptococcus infections may present with various imaging findings and can arise in immunocompromised or immunocompetent hosts. The causative organisms include *C. neoformans* and *C. gatti*; infection typically results after inhalation of fungal spores, which are then spread hematogenously to the CNS from the primary pulmonary infection. Cryptococcus has a predilection for the perivascular spaces and tends to produce mucoid material to counter the host's immune response; therefore dilated Virchow-Robin spaces are frequently seen, which may coalesce to form gelatinous pseudocysts. Additionally, cryptococcus may present as meningitis, meningoencephalitis, or choroid plexitis. Direct invasion of the brain parenchyma in immunocompetent patients may result in the formation of cryptococcomas. However, in severely immunocompromised patients, brain involvement often does not enhance as these patients may not be able to mount a sufficient inflammatory response to elicit enhancement. The purpose of this presentation will be to review the basic pathophysiology of CNS Cryptococcus infection, to discuss the salient imaging findings, and to examine the radiologist's role in the treatment and follow up of these patients, which may include serial image-guided lumbar puncture (or lumbar drain placement) and repeat imaging.

Results

N/A

Conclusions

N/A



(Filename: TCT_1203_CryptococcusASNRAbstractFigure.jpg)

1300

The Mistaken Journey of Neurons: A Didactic Imaging Review on Cortical Malformations and their Association with Refractory Epilepsy!

M Brandão¹, A DE SOUSA², N Santos³, L Monteiro⁴, R Gabrig⁵, D Costa⁶, R Carvalho⁷

¹Hospital do Servidor Estadual de São Paulo, São Paulo, SP, ²Universidade Federal de São Paulo, São Paulo, São Paulo, ³Hospital Servidor Público Estadual de São Paulo, São Paulo, Brazil, ⁴Hospital Servidor Público Estadual de São Paulo- IAMSPE, São Paulo, SP, ⁵IAMSPE, São Paulo, São Paulo, ⁶Hospital Sao Luiz-Rede D'Or - Fleury group- Unifesp, São Paulo, São Paulo, ⁷Servidor Estadual de Sao Paulo Hospital, Sao Paulo, WY

Purpose

Malformations of cortical development (MCD) result from disruptions in the complex process of the human brain cortex formation and are highly associated to severe epilepsy, neurodevelopmental delay and motor dysfunction. The MCD has a cover wide spectrum of disorders that depend on the time of neuronal inhibition takes place, which may be during the stages of neuronal proliferation, migration and organization. Illustrate the classification of the disorders of cortical formation, and finally describe the main MR

imaging features with some didactical and original cases. Developed for current residents and fellows, we created an Illustrative guide intended to help easy search findings and make difference on the evaluation!

Materials and Methods

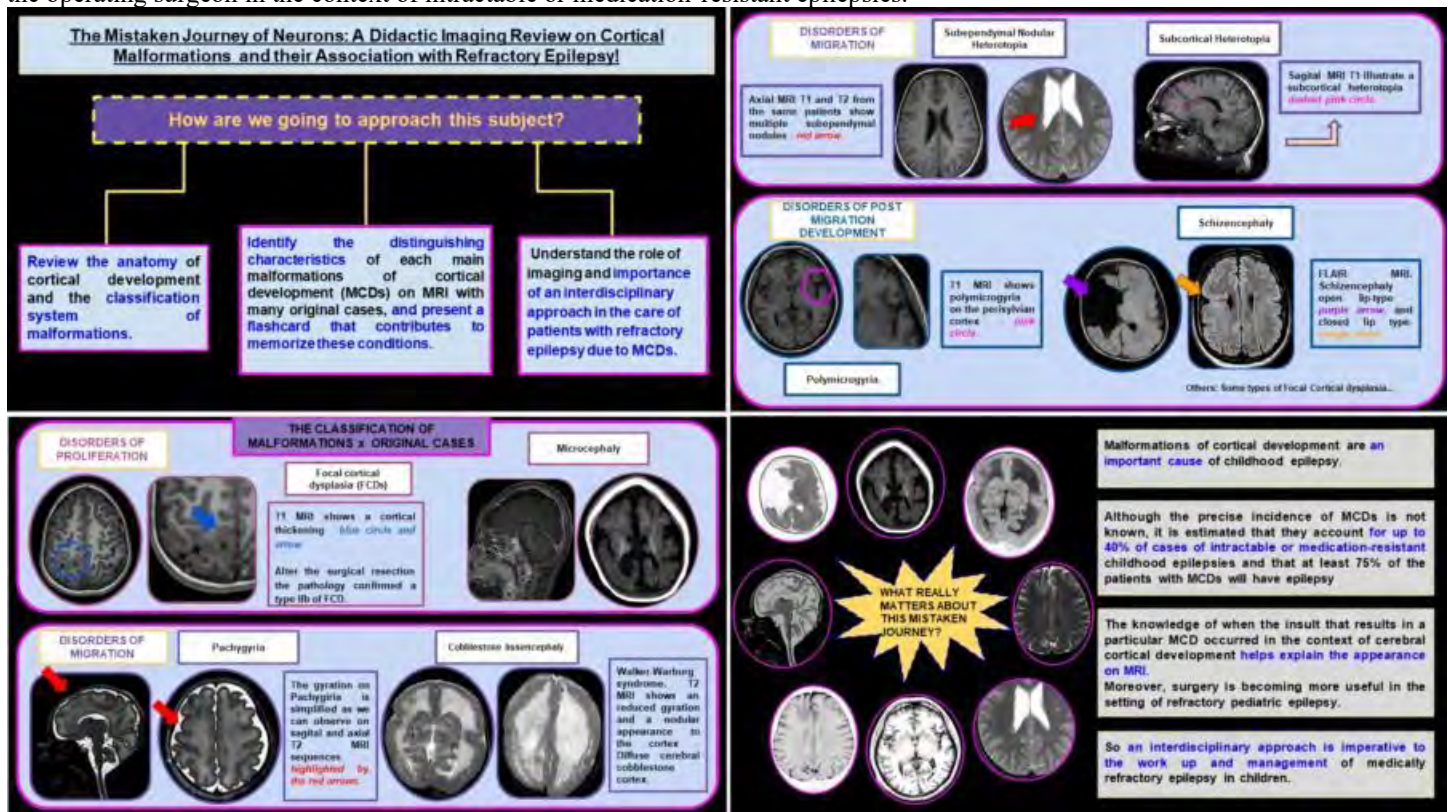
Identify the distinguishing characteristics of each of the major malformations of cortical development (MCDs) on MRI. Understand the role of imaging and importance of an interdisciplinary approach in the care of patients with refractory epilepsy due to MCDs. We will provide a pocket guide with the main cortical malformations associated with refractory epilepsy, seeking to assist Radiology and Neurologists residents and fellows.

Results

N/A

Conclusions

The knowledge of the wide imaging spectrum of MCD, familiarity with recent advances in imaging and an optimal radiological approach is essential for the radiologist to accurately diagnose and prognosticate MCD as well as provide the best surgical approach to the operating surgeon in the context of intractable or medication-resistant epilepsies.



(Filename:

TCT_1300_TheMistakenJourneyofNeuronsADidacticImagingReviewonCorticalMalformationsandtheirAssociationwithRefractoryEpilepsy.jpg)

1429

The Next Great Mimicker? A Case Series of Glioblastomas with Clinical and Imaging Features that Mimicked Other Pathologies

M Czaplicki¹, S Kumar², K Mathew¹, T Ly², A Moreno De Luca¹, K Sargar², G Mongelluzzo³, P Manickam¹

¹Geisinger, Danville, PA, ²Geisinger Medical Center, Danville, PA, ³Radiology, Danville, PA

Purpose

Glioblastoma, the most common primary intracranial neoplasm in adults, consists of a heterogeneous group of tumors which can demonstrate a variety of clinical presentations, histologic appearances, and imaging appearances. There may be significant overlap with other central nervous system pathologies including cerebrovascular accident, demyelinating disease, encephalitis, and others. Increasingly, molecular features of glioblastoma are incorporated into diagnosis and are well known to impact prognosis. It is also recognized that various molecular subtypes may influence the imaging phenotype. Clinically, patients with glioblastoma may present with a wide variety of symptoms, including symptoms of increased intracranial pressure, stroke like symptoms, and seizures or a Todd's paralysis, which may introduce biases into initial imaging interpretation. On imaging, glioblastoma typically presents as an irregular mass with thick enhancing margins, central necrosis, and surrounding infiltrative edema. Central hemorrhage and calcifications may be seen. Glioblastoma may occur anywhere in the brain, but has a predilection for subcortical white matter.

Multifocal disease is relatively common, occurring in up to a third of patients, and multicentric disease may also occur. Subependymal spread or CSF dissemination may be present on initial imaging. Diffusion restriction involving the solid non-necrotic portions of tumor is common. Elevation of relative cerebral blood volume is the rule. However, when GBM doesn't follow the expected pattern of imaging findings, uncertainty and misdiagnosis can ensue. Glioblastoma may not enhance. There can occasionally be significant overlap with other entities such as lymphoma, metastatic disease, demyelinating disease, encephalitis, cerebral abscess, and subacute infarction. It is important for neuroradiologists to be cognizant of the myriad ways that glioblastoma can appear on imaging and to familiarize themselves with the uncommon and unusual findings of this common pathology to avoid misdiagnosis.

Materials and Methods

Differentiating glioblastoma from mimicking entities is essential. The authors provide examples of such cases, and discuss methods to differentiate these entities.

Results

A total of 6 cases of pathologically-proven glioblastoma were reviewed, where the diagnosis was unclear initially, based on confounding clinical and imaging findings.

Conclusions

The authors have discussed a series of glioblastomas which mimicked other pathologies.

1446

The Oculosympathetic Pathway; Radiologic and Clinical Correlation

J Lang¹, N KIM², A Kuner³, T Kennedy⁴

¹University of Wisconsin - Madison, Madison, WI, ²University of Wisconsin Hospital and Clinics, Madison, WI, ³University of Wisconsin School of Medicine and Public Health, Middleton, WI, ⁴The University of Wisconsin, Middleton, WI

Purpose

EDUCATIONAL OBJECTIVES: 1. To review the important anatomy of the Oculosympathetic pathway with an emphasis on clinical and radiologic correlation to the relevant anatomy. 2. To introduce both common and uncommon disease processes as they relate to the Oculosympathetic pathway, and review the anticipated clinical features. 3. To provide a structured framework for the interpretation of imaging studies in patients with Horner syndrome.

Materials and Methods

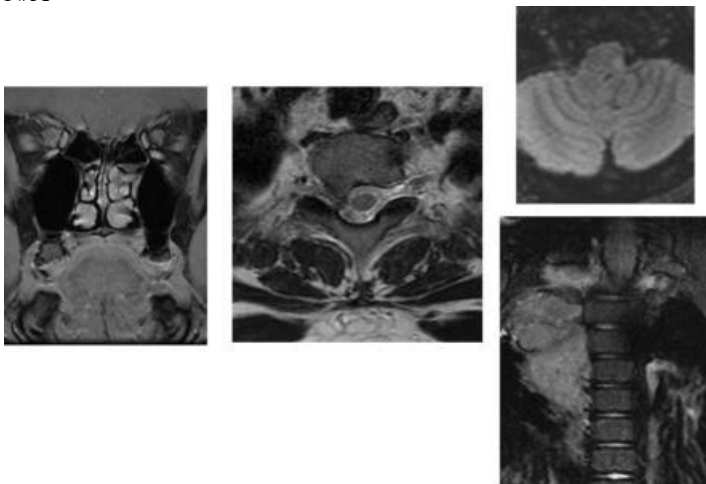
The radiologist is tasked with integrating a complex clinical history with (occasionally) subtle imaging findings to reach a specific diagnosis or focused differential. In patients with abnormalities of the Oculosympathetic pathway, clinical findings can vary depending on location of the affected neuron(s). A thorough understanding of the relevant anatomy and familiarity with common disease processes that can disrupt the Oculosympathetic pathway, not only is critical for the accurate interpretation of imaging studies in patients presenting with Horner syndrome, but also can aid in the discovery of subtle pathology with important treatment implications. After reviewing the anatomy of the Oculosympathetic pathway, we will give case examples demonstrating the heterogeneous pathology of the sympathetic chain, in addition to the relevant clinical presentation. Case examples include upper thoracic degenerative disc disease, lateral medullary infarct, paraspinal neuroblastoma, idiopathic orbital inflammatory syndrome, and internal carotid artery dissection.

Results

N/A

Conclusions

N/A



The Road to Success: Navigating Spinal Cord Tumors and their Mimickers

A Jain¹, O Schoeck², C Ko³, B Lee⁴, B Devenney⁵, J Li⁶, c chan⁷

¹Einstein Medical Center, Philadelphia, PA, ²Einstein medical center, Philadelphia, PA, ³Albert Einstein, Philadelphia, PA, ⁴Albert Einstein Medical Center, Philadelphia, PA, ⁵Einstein Medical Center Montgomery, East Norriton, PA, ⁶Einstein Healthcare Network, Wayne, PA, ⁷Einstein Healthcare Network, Philadelphia, PA

Purpose

Spinal tumors encompass a range of pathologies with varying morbidity and mortality rates as well as different treatment options. However, a variety of non-neoplastic pathologies can mimic spinal tumors requiring extensive work up, delays appropriate treatment and management, and may lead to incorrect and potentially dangerous pitfalls such as biopsy or resection. As magnetic resonance imaging is the crux of any initial work-up for spinal canal pathologies, identifying mimickers is essential in narrowing down the differential diagnosis and guiding proper management. 1. Gain familiarity with the spectrum of spinal pathologies mimicking tumors. 2. Develop a systematic approach to distinguishing non-neoplastic spinal lesions from tumor mimickers based on specific MR imaging features.

Materials and Methods

A pictorial review of a wide spectrum of spinal tumors and tumor mimickers will be presented. This exhibit will have emphasis on magnetic resonance imaging as it is the preferred imaging modality for evaluating the spinal cord and canal contents. We will present spinal lesions that may mimic tumors based on anatomic location: Intramedullary (syrinx, demyelination, abscess, vascular malformations, cord contusions, post traumatic myelocele, and cord infarct), intradural extramedullary (infection, sarcoid, vascular malformations, arachnoid cyst, severe arachnoiditis, tethered cord), and extradural (extruded and sequestered discs). We will also provide a systematic approach on how these lesions may be distinguished from spinal tumors based on specific imaging features and anatomic location.

Results

NA

Conclusions

Numerous lesions may mimic spinal tumors, either due to their location in the cord or due to compression of the cord. The first step is identifying the lesion location as intramedullary, intradural extramedullary, or extradural. The second is to identify characteristic MR imaging features of both tumors and mimickers. Reviewing case-based examples will highlight common mimickers and ultimately aid in creating a comprehensive and tailored differential diagnosis for spinal lesions and signal abnormality while avoiding pitfalls.

WHAT DO THESE CASES HAVE IN COMMON?



These are cases of various non-tumor pathologies mimicking tumors in the spine!

The Role of PET Imaging in Diagnosing and Improving Care of Dementia patients

A Ahmed¹, A Aly², M Ali¹

¹Creighton university, Omaha, NE, ²Creighton University, Omaha, NE

Purpose

Learning objectives: 1. Review the different types of primary dementia. 2. Describe normal neuronal FDG uptake and cerebral biodistribution. 3. Discuss FDG- PET protocol, pitfalls and limitations. 4. Recognize FDG-PET key imaging features in different types of dementia. 5. Review recent PET dementia tracers. Background: Dementia is a heterogenous group of neurodegenerative disorders characterized by gradual cognitive impairment. Early diagnosis and characterization of dementia is clinically challenging. Alzheimer's Dementia (AD), frontotemporal dementia (FTD) and diffuse Lewy body disease (DLB) are the most frequent causes of dementia. Recognition of the different types of dementia is essential because there are new emerging therapeutic regimens that might help with cognitive improvement. At the same time early diagnosis of dementia gives patients and their families enough time to seek support. Structural imaging as CT and MRI allows exclusion of secondary causes of dementia, however, has limited specificity in distinguishing primary causes of dementia. FDG-PET allows early diagnosis and differentiation of different types of dementia by showing characteristic metabolic pattern with each disorder. Findings: Brain highly utilizes glucose for metabolism. Dementia is associated with decreased neuronal metabolism in specific brain regions which can be detected by recognizing specific patterns of decreased FDG uptake. Metabolic changes occur before anatomic changes are evident by routine imaging. In AD FDG- PET uptake is decreased in the precuneus, posterior cingulate, temporoparietal, and occipital lobes. In DLB uptake is decreased in the occipital, temporal, and parietal lobes. In FTD- PET shows hypometabolism in the frontal and anterior temporal lobes. Several new PET tracers that bind tau proteins were developed and thus confirms the diagnosis and quantifies degree of brain damage. Disease specific tracers are used when FDG-PET findings are atypical. Conclusion and teaching points: FDG-PET is a useful modality in early diagnosis and characterization of different types of dementia through revealing distinct metabolic pattern of cerebral FDG uptake.

Materials and Methods

N/A

Results

N/A

Conclusions

N/A

1232

The Spectrum and Mimics of Contrast Surface Enhancement on Post-contrast Fluid-attenuated Inversion Recovery (FLAIR) Images, Including Hyper Acute Reperfusion Marker (HARM)

S Rogers¹, L Nagae¹, J Becker¹

¹University of Arizona, Tucson, AZ

Purpose

After reading this presentation, the reader should understand the following about Contrast Surface Enhancement on FLAIR (CSEF); seen as CSF, leptomeningeal, and brain enhancement on post-contrast FLAIR images: 1. The pathophysiology and imaging principles 2. Appropriate terminology, including history of the term hyper acute reperfusion marker (HARM) 3. The increased sensitivity of CSEF on post-contrast FLAIR compared to T1 weighted post-contrast images 4. The clinical significance and potential mimics

Materials and Methods

The significance and etiology of increased signal on post-contrast FLAIR images at the surface of and within the brain is often poorly understood by radiologists. Contrast Surface Enhancement on FLAIR (CSEF) within the leptomeninges, sulci and CSF spaces, and the brain may go unrecognized or ignored. This may be a consequence of T1 weighted imaging long being established as the workhorse of post contrast imaging, with relatively little attention comparatively received on post-contrast FLAIR imaging. However, post-contrast FLAIR imaging provides increased sensitivity for a wide spectrum of pathology that affects the blood brain barrier and blood CSF barrier, including after ischemia and reperfusion with HARM but also with other infectious, inflammatory, and neoplastic processes. Enhancement on FLAIR is not infrequently seen, once understood.

Results

An educational overview and a series of cases will be used to illustrate the pathophysiology, imaging principles, suggested protocol, and terminology of post-contrast FLAIR enhancement at the brain surface. We present comparison with T1, mimics of FLAIR enhancement, and the clinical importance of contrast surface enhancement on FLAIR images.

Conclusions

Post-contrast FLAIR allows detection of leptomeningeal and CSF enhancement, increasing sensitivity for disease processes that cause

inflammation, contrast leakage, and/or destruction of the blood brain barrier and blood CSF barrier. Familiarity with this finding will facilitate future research to improve our knowledge of neuro pathology and physiology.

491

The Vidian Canal and its Pathological Changes: A Neuroimaging Pictorial and Educational Review

K Wang¹, K Seifert¹, E Tong¹, M Wintermark², S Hashmi³, T Massoud¹

¹Stanford University School of Medicine, Stanford, CA, ²Stanford, Stanford, CA, ³N/A, N/A

Purpose

The vidian or pterygoid canal (VC) sits at the base of each medial pterygoid plate of the sphenoid bone. It extends anteroposteriorly from foramen lacerum to the pterygopalatine fossa, transmitting the vidian nerve (VN) and artery (a remnant of the first aortic arch). VN is an autonomic nerve formed by the greater and deep petrosal nerves. Its dysfunction may cause rhinitis, epiphora, Sluder's neuralgia, cluster headaches, and corneal ulceration. VC anatomy is important in surgical or endoscopic vidian neurectomy for treating intractable vasomotor rhinitis. VC can also be involved in several pathological conditions. Thus, a thorough neuroimaging evaluation of VC morphology is essential to understanding VN function and its disorders, and for selecting safe and appropriate surgical approaches that preserve VN. We provide a pictorial and educational review of the normal VC, its variants, and changes induced by different pathological alterations that are underreported in the radiological literature.

Materials and Methods

We comprehensively review the imaging findings of the normal and pathological VC.

Results

The VC is 0.9-2.7 mm in size and is clearly seen on coronal CT in the wedge-shaped area above the medial pterygoid plate. Foramen rotundum superolaterally, and the palatovaginal canal inferomedially can be mistaken for the VC. VC embeds into the sphenoid body in ~50%, or protrudes into the sphenoid sinus in ~50% (40% of these have bony dehiscence). Several pathologies involving the VC may be visible on neuroimaging, including: (1) Traumatic injury. VN injury after sphenoid sinus fractures through VC may be an underdiagnosed morbidity. (2) VN benign tumors. VN nerve sheath tumors (schwannoma or neurofibroma) are extremely rare. Preoperative CT and MRI reveal enhancing round masses in one or both VCs, with bony remodeling, enlargement, or erosion. (3) VN malignant tumors. Perineural spread along the VN in head and neck cancer results in VN and VC changes on MRI and CT. Direct VN invasion from sphenoid sinus malignancies can occur when VC is dehiscent. (4) Skull base tumors extending to VC. (5) Infection. Dehiscent VCs may put exposed VNs at risk of sphenoid sinus inflammation/infection. (6) Iatrogenic injury of the VN following endoscopic repair of CSF rhinorrhea and encephaloceles in the pterygoid recess.

Conclusions

We review the neuroimaging features of the normal VC and its pathological changes. This knowledge aids patient management especially in preoperative planning of endoscopic treatments.

383

The WHO 2020 Brain Tumor Classification: 10 New Entities You Need to Know

S Calle¹, O Arevalo², D Schomer², G Fuller³

¹The University of Texas MD Anderson Cancer Center, Houston, TX, ²N/A, N/A, ³MD Anderson Cancer Center, Houston, TX

Purpose

In light of the ever-growing insight into molecular features that drive central nervous system tumors, the Consortium to Inform Molecular and Practical Approaches to CNS Tumor Taxonomy (cIMPACT-NOW) released an update that highlights some of the new entities that will be introduced in the upcoming WHO 2020 Brain Tumor Classification. The educational objectives for this exhibit include: - To present various imaging studies of patients with primary central nervous system tumors encountered at our institution in order to allow the viewer to exercise the recognition of essential findings - To reveal the pathology results of each of these cases in a manner that is straightforward for the radiologist to understand - To identify the key diagnostic criteria for the specific entity - To compare the previously described diagnosis with the WHO 2020 update while illustrating the rationale for the modification - To deconstruct the change and display the information in a visual manner that is practical to grasp

Materials and Methods

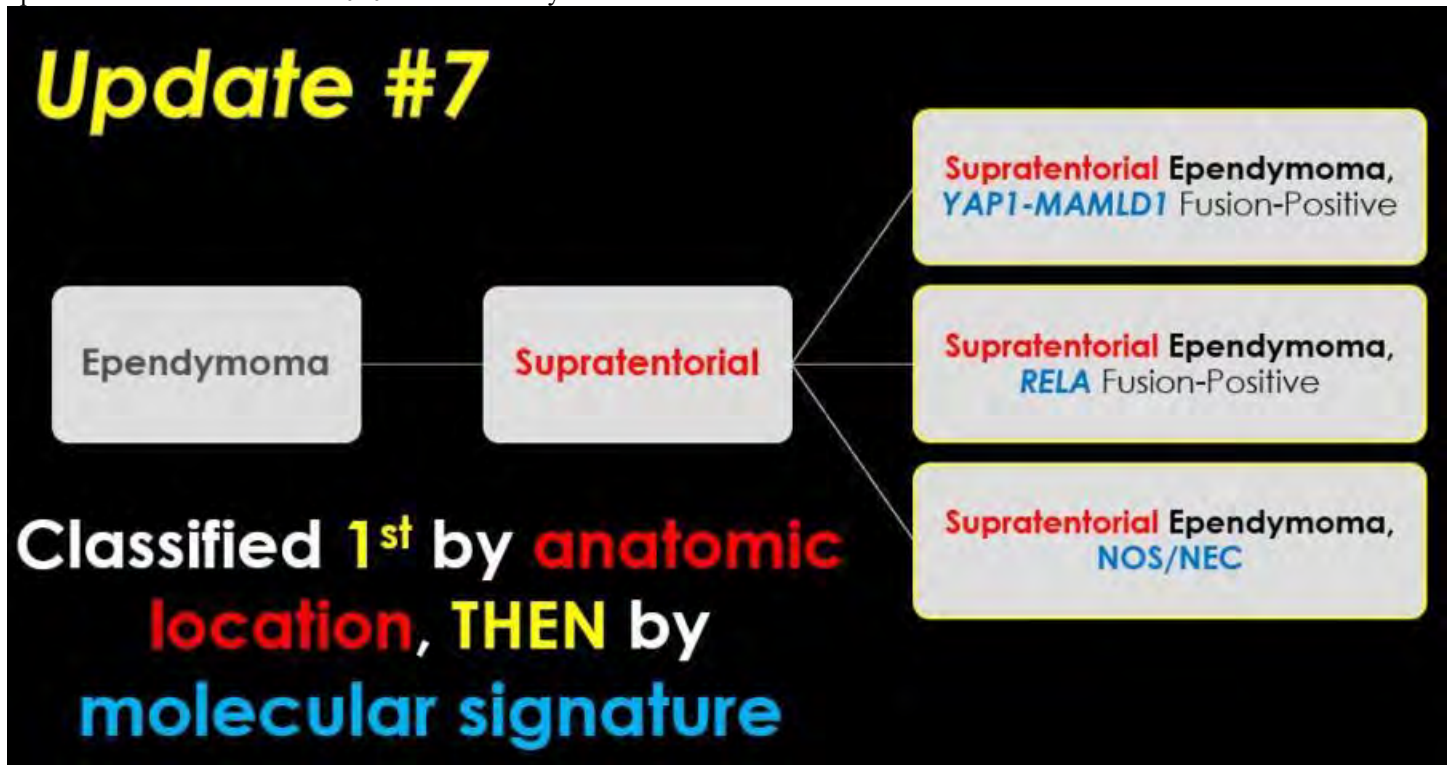
The purpose of this exhibit is to summarize ten of the newly recognized CNS tumor types/subtypes to be introduced in the future WHO 2020 brain tumor classification system with an emphasis on the principles that guide the updated recommendations and the imaging features that characterize these entities.

Results

We have collected cases that illustrate each of the selected entities to be highlighted for the purposes of the exhibit. Demographic information of the patients and the preoperative imaging was reviewed with the pertinent images selected for display. In collaboration with neuropathology, the pathology slides for each of these cases were included with a description of the diagnostic criteria for each tumor type/subtype. Comparative analysis of the current and proposed correct tumor name was described.

Conclusions

The incorporation of molecular signatures in the diagnosis, treatment and prognosis of CNS tumors has represented a leap in the understanding of the biology of these neoplasms. The radiologist can have a true impact on the clinical care of the patient by correctly identifying the key imaging features and by working in a collaborative interdisciplinary effort to correctly classify each case. It is our expectation that the information presented in this exhibit allows for the viewer to easily grasp these concepts in preparation for the updates included in the WHO 2020 classification system.



(Filename: TCT_383_Capture.JPG)

277

Therapeutic Head and Neck Interventions: More Than Just Biopsies!

A Hatef¹, J Job²

¹Ohio State University, Hilliard, OH, ²Ohio State University, Columbus, OH

Purpose

The head and neck radiologist plays an increasing role in patient management, with growing demand for image-guided therapeutic interventions such as highly precise percutaneous ablations. We present approaches for various targeted therapeutic interventions, commonly faced challenges, and show examples of cases performed at our institution. Objectives: 1. Methods for targeted therapy within the head and neck, including tailoring patient positioning, use of anatomical landmarks for safe approach, and techniques to expedite the case. 2. Discussion of commonly encountered challenges and how to work around them. 3. Examine therapeutic cases performed at our institution.

Materials and Methods

Demonstrate various techniques for image-guided therapeutic interventions within the head and neck, correlated with long term outcomes when appropriate.

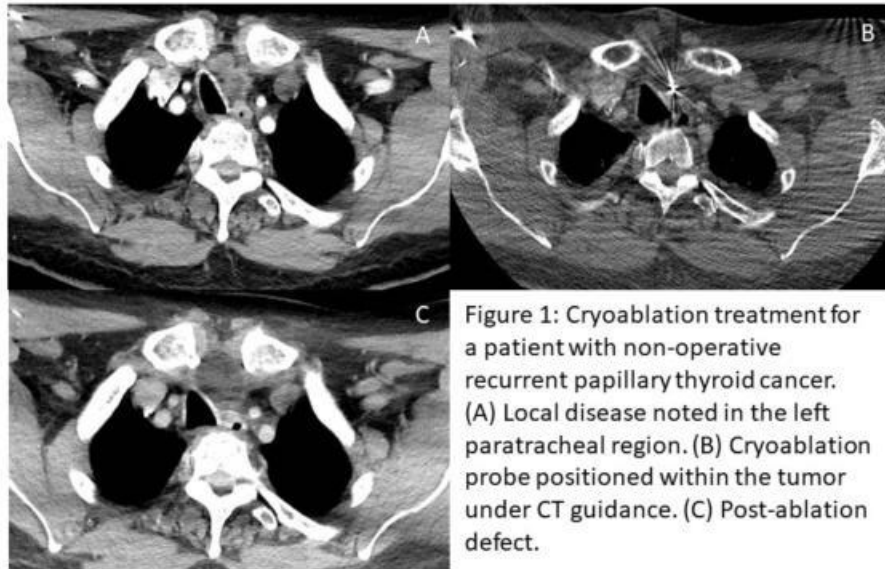
Results

Cases presented include: - Two cases of recurrent thyroid cancer s/p cryoablation - Alcohol ablation of a recurrent thyroid cyst - Botox injection of salivary glands for sialorrhea - Botox injection of anterior scalene/pec minor for thoracic outlet syndrome

Conclusions

Tailoring patient positioning and imaging technique is critical for visualization of the lesion of interest, safety, as well as ease of approach. For instance, when using CT guidance, either tilting the gantry or controlled patient head tilt can effectively eliminate common dental work/hardware related artifact from the plane of interest. Anatomical landmarks may be used to avoid critical structures, such as the styloid process when targeting a lesion in the prestyloid parapharyngeal space - keeping in mind that the major neurovascular structures lie in the post-styloid space. The tracheoesophageal groove and course of recurrent laryngeal nerve is another important anatomical landmark when targeting a lesion involving the central compartment of the neck. We review cryoablation cases for treatment in head and neck cancers, including our patient selection process at OSU and the appropriate outpatient follow up.

Additional cases including therapeutic botox injections and ethanol ablation will also be presented. There is increasing demand for targeted therapeutic interventions in the head and neck by the neuroradiologist and for close collaboration with referring subspecialties such as Endocrinology and Head and Neck Surgery.



(Filename: TCT_277_CryoablationFigure.jpg)

563

Thyroid Goiter Preoperative Imaging Evaluation: What the Surgeon Wants to Know

D Mayorga¹, B Parnes², A Khorsandi³, R Chai⁴, M Starc⁵

¹Mount Sinai Health Systems, New York, NY, ²Mount Sinai West, New York, NY, ³New York Eye and Ear Infirmary of Mount Sinai, New York, NY, ⁴Institute for Head, Neck, and Thyroid Cancer at the Icahn School of Medicine at Mount Sinai, New York, NY, ⁵Mount Sinai Hospital New York Eye and Ear Infirmary, New York, NY

Purpose

Through illustrative case examples, this presentation reviews the radiologic features of Thyroid Goiters (TG) that guide surgical management. Regional anatomic considerations, pitfalls, and findings suggesting malignancy are correlated with surgical outcomes and literature review. With this knowledge, the radiologist will have a positive impact on patient care by improving the quality of radiology reports, reducing operative time, and improving clinical outcomes.

Materials and Methods

TG is an abnormal enlargement of the thyroid gland that has garnered relatively little attention in radiology literature, perhaps due to its "benign" nature. This presentation highlights the critical imaging features that guide surgical management, based on literature review and case-based surgical-pathologic correlation at our institution.

Results

Known or suspected TG is a common indication for preoperative imaging at our institution. Multimodality imaging features are presented based on radiologic, surgical, and pathologic correlation. We review common clinical presentations of TG with functional or structural abnormalities, including hyperthyroidism and dyspnea. Indications for surgical resection include suspicion of malignancy, tracheal or esophageal compression, thoracic extension, and cosmesis. Pitfalls in diagnostic interpretation with critical management implications are presented.

Conclusions

TG typically presents as an abnormally enlarged multinodular thyroid or as asymmetric thyroid hypertrophy. Imaging provides useful anatomical and morphological information that guides management decisions. Identification of calcifications, cysts, scarring, and regions of hemorrhage is critical because these may increase surgical complexity. Key regional anatomic vascular variants and their relationship to the recurrent laryngeal nerve that affect surgical approach are illustrated. The presence of substernal extension and associated tracheal narrowing, generally a surgical indication, is reviewed in detail. Accurate cross-sectional imaging technique and

characterization of surgically significant substernal extension is demonstrated. Imaging features suggesting the need for thoracic surgical assistance are presented. Examples of TG in unusual locations are shown, including: retroesophageal, forgotten/ectopic mediastinal, pyramidal, thyroglossal, and lingual. Several "red flags" are illustrated that suggest malignancy, such as imaging evidence of vocal cord paralysis, extrathyroidal extension, and abnormal lymph nodes.



Fig. 1. Coronal unenhanced CT image of large TG with severe tracheal narrowing and a left lobe calcification.



Fig. 2. Sagittal contrast-enhanced CT image shows a large TG with retrosternal extension.



Fig. 3. Coronal contrast-enhanced CT image of an ectopic TG with no attachment to tissue in thyroid bed.

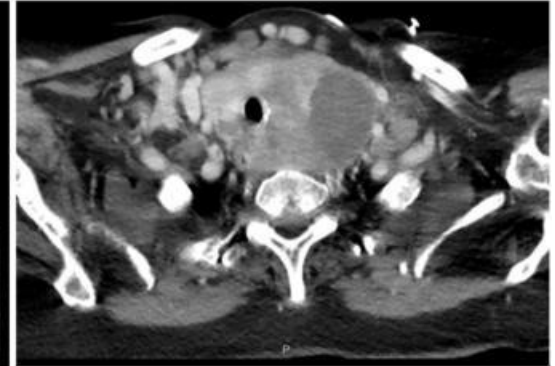


Fig. 4. Axial contrast-enhanced CT image of a pathologically-proven thyroid carcinoma. The TG is heterogenous with local lymphadenopathy.

(Filename: TCT_563_Slide1.JPG)

1063

Too Bright, Too Dark, or Just Right: Pearls and Pitfalls of ASL Perfusion Imaging

H Banchs Vinas¹, A Callen¹, M Caton², J Narvid²

¹University of Colorado, Aurora, CO, ²UCSF, San Francisco, CA

Purpose

Educational Objectives: -Understand arterial spin labeling perfusion imaging and its accepted clinical utility in neuroradiology. - Become familiar with different techniques of arterial spin labeling (pulsed, continuous, pseudo-continuous, and velocity selective) and the relative strengths/weaknesses of each. -Understand the importance of selecting an appropriate post-label delay (PLD) for a given patient and recognize the appearance of a PLD that was too long or too short. -Understand the orientation and location of the ASL labeling plane, how magnetic susceptibility in the neck or skull base as well as tortuous arteries may result in ineffective labeling and mimic pathology. -Recognize the labeling of things other than arterial blood and the pathophysiology that these findings may represent. -Identify structures which may be transiently hyperemic including nasal mucosa, choroid plexus and pituitary tissue and how these mimic pathology. -Recognize arterial transit artifact and its clinical implication.

Materials and Methods

Arterial spin labeling (ASL) is a widely used MRI sequence which measures tissue perfusion without the use of intravenous contrast. Increased availability of ASL has led to the identification of perfusion characteristics of multiple pathophysiologic states. However, ASL is prone to artifacts that can mimic pathology¹. This exhibit depicts the basic mechanisms behind ASL acquisition and illustrates several ASL artifacts. By understanding these, the neuroradiologist can both avoid misidentifying areas of altered perfusion and incorporate subtle pathophysiology to arrive at a correct diagnosis.

Results

We describe ASL technique and define brain perfusion terminology. Cases collected from two tertiary referral centers where there is apparent hypo- or hyper-perfusion are used to illustrate ASL acquisition and cerebrovascular pathophysiology.

Conclusions

Results: We identify nine unique ASL artifacts. Those artifacts which result in apparent hypoperfusion are contrasted with cases of stroke and hemiplegic migraine. Artifacts resulting in apparent hyperperfusion are depicted as potential pitfalls in the identification of tumor and pathologic arteriovenous shunting. Conclusion: ASL is a powerful tool in the armamentarium of neuroradiologists.

Understanding the potential artifacts related to both ASL acquisition and normal cerebrovascular physiology will prevent radiologists from suggesting incorrect diagnoses, and in some cases, allow for a more accurate diagnosis.

1190

Top 10 Eponyms in Neuroradiology and their Imaging Features

M Igi¹, J Grenier¹, J Park¹, D Casey¹, C Rigsbee²

¹Louisiana State University Health Sciences Center, New Orleans, LA, ²LSU HSC New Orleans, New Orleans, LA

Purpose

Eponyms, words derived from a person's name, have historically been used in medicine for centuries. The Hippocratic Oath, attributed to Hippocrates, for example, is thought to have first arisen in the 5th century B.C. Eponyms have been used extensively to describe normal anatomy, anatomic variants, and disease processes. Although, there is a growing trend to describe anatomy and diseases based on physiologic and pathologic descriptors, eponyms continue to permeate into medical textbooks and board examinations. More importantly, clinically, eponyms are found throughout medical charts, radiology and pathology reports, and procedural reports.

Therefore, an understanding of the most common eponyms remains essential for the successful physician. Educational Objectives: • Review common eponyms in neuroradiology • Review images from multiple modalities including magnetic resonance, computed tomography, and radiography • Review normal anatomy and anatomic variants in neuroradiology • Provide historical context to the eponyms, by providing background of the person for which the anatomy, variant, or disease is named • Review of multiple disease processes in neuroradiology • Provide alternative names for eponyms, based on pathologic and/or physiologic descriptors

Materials and Methods

Our goal is to review commonly encountered eponyms in neuroradiology and give their associated imaging features and historical background.

Results

N/A

Conclusions

N/A

494

Trigeminal Neuralgia Caused by Neurovascular Conflicts of Venous Origin: A Neuroimaging Review

M Shahrzad¹, E van Staalduinen¹, N Telischak¹, S Hashmi², M Wintermark³, T Massoud¹

¹Stanford University School of Medicine, Stanford, CA, ²N/A, N/A, ³Stanford, Stanford, CA

Purpose

Trigeminal neuralgia (TN) is a paroxysmal neuropathic facial pain syndrome that may result from vascular conflicts (abutment or compression) of the cisternal trigeminal nerve (CN5), usually by the SCA, AICA, PICA, and the superior petrosal vein and tributaries. Some 40% of TN patients undergoing microvascular decompression (MVD) have venous neurovascular conflicts, alone (10%), or with an artery (30%). Preoperative analysis of CN5-vein anatomical relationships is crucial for successful MVD. We provide an educational neuroimaging review of CN5-venous neurovascular conflicts that cause TN.

Materials and Methods

We comprehensively review the imaging findings in several types of CN5-vein conflicts causing TN, and categorize these by etiology.

Results

Venous conflicts are more common in younger patients. Vein adherence to CN5 arachnoid membrane and nerve sheath can cause nerve deformation, focal demyelination, ectopic impulses, and facial pain attacks. A vein contacting CN5 anywhere from Meckel's cave (MC) to its pontine entrance can cause a conflict. The root entry zone (REZ) has an area of transitional myelin, and is especially vulnerable. Since venous conflicts result in worse MVD outcomes than arterial ones, MRI determination of vessel type is crucial. However, it is more difficult to visualize CN5 contact by a vein than an artery, and venous conflicts may be missed on preoperative imaging. Assessment of CN5 using FSE and steady-state gradient echo sequences plus TOF MRA enables optimized assessment of venous conflicts and reliable differentiation of veins and arteries. Compressive veins belong to the superficial or deep superior petrosal venous systems (sSPVS or dSPVS). A vein from sSPVS, usually the transverse pontine vein, is compressive in 60%. Conflicts are situated at REZ, midcisternal (50%), and MC porus. The dSPVS is compressive in 40%, almost always by a vein traversing the MC porus. The veins of the cerebellopontine fissure and the middle cerebellar peduncle are other culprits. We will illustrate examples of CN5 conflicts with: (1) veins alone; (2) veins plus arteries; (3) rare intraneural veins; (4) developmental venous anomalies; and (5) DVs of petrotentorial AVFs.

Conclusions

Accurate differentiation of venous from arterial CN5 neurovascular conflicts is important clinically. Radiologists should suspect venous conflicts when MRIs reveal no typical arterial compression. This presentation will aid in neuroimaging interpretation of these conflicts to improve clinical management of TN.

Typical and atypical Image findings of Cavernomas and Potential Mimics

F Assunção¹, T Scoppetta¹, L Martins², L Freitas², E Narvaez², B Inada², S Omar², V Marussi², C Campos², L do Amaral²
¹Hospital São Camilo, São Paulo, SP, ²BP - A Beneficência Portuguesa de São Paulo, São Paulo, SP

Purpose

Cavernous malformations (CMs), also known as cavernomas or cavernous angiomas, are benign low flow vascular malformations composed of thin walled, dilated capillary spaces with no intervening brain tissue and filled with blood at various stages of stasis, thrombosis and calcification. MR findings of typical intra-axial CMs are usually enough to diagnose such lesions. However, extra-axial and multifocal CMs may mimic imaging findings of other diseases. Findings on CT are nonspecific and they may mimic a previous granulomatous infection, aneurysm, AVMs, subacute hematoma, or a hyperattenuating neoplasm such as meningioma or high grade glioma. Diffuse punctate hypointense lesions on SWI may be found in hemorrhagic metastasis, hemorrhagic embolus, amyloid angiopathy, radiation-induced telangiectasias or traumatic diffuse axonal injury. The objective of this study is illustrate typical and atypical imaging presentations of cavernomas and potential mimics of them.

Materials and Methods

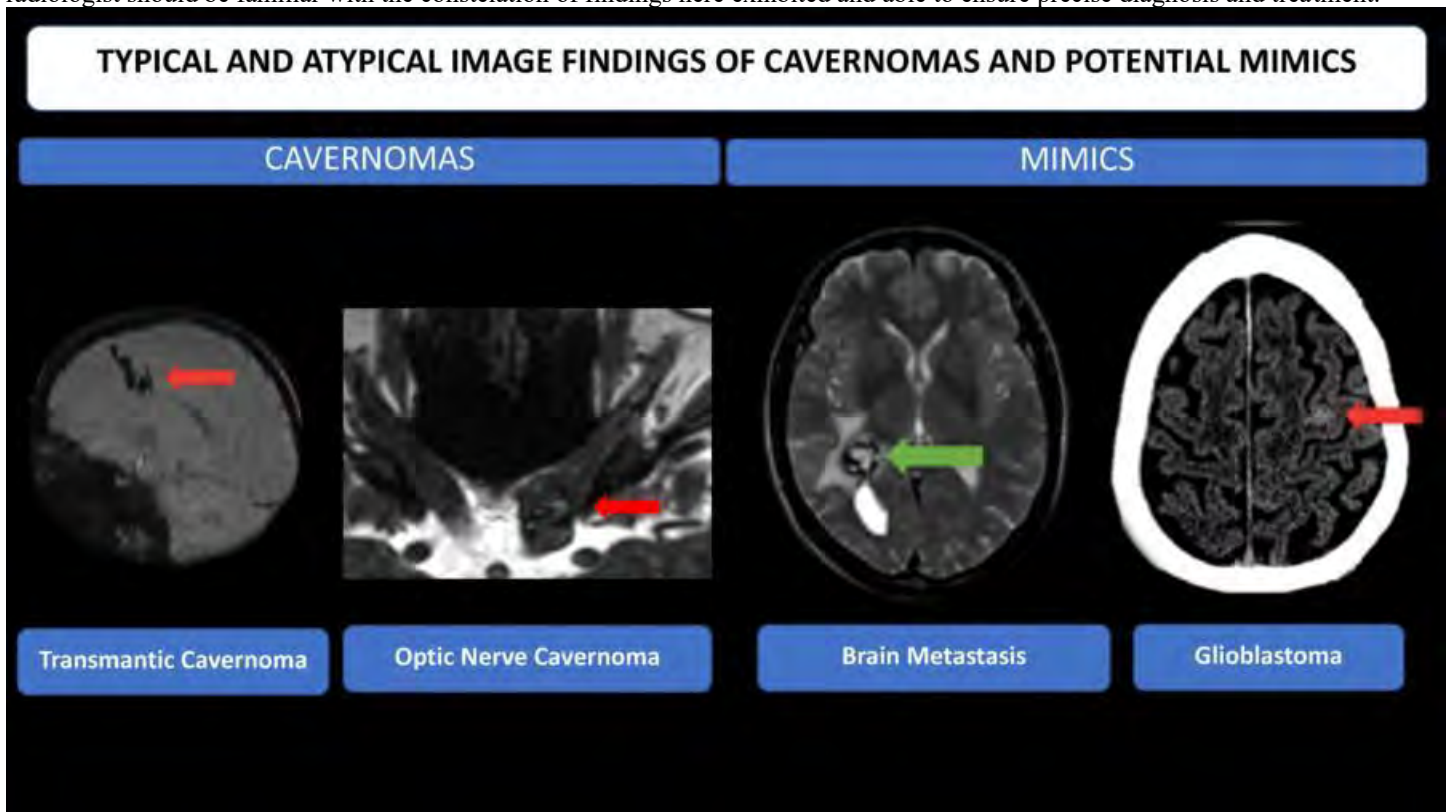
- To briefly review the definition, epidemiology, natural history, classification and imaging findings of cavernomas. - To illustrate typical and atypical clinical and imaging presentations of cavernomas. - To exhibit illustrative cases of potential mimics of cavernous malformations

Results

We performed a retrospective and descriptive study of brain MRI of patients diagnosed with cavernomas and mimics performed at ours services.

Conclusions

Cavernous malformations are a common benign lesion with vastly described imaging features that usually do not impose difficult in the diagnosis. However, atypical presentations (unusual characteristics and locations) and potential mimics can cross our worklist. The radiologist should be familiar with the constellation of findings here exhibited and able to ensure precise diagnosis and treatment.



(Filename: TCT_188_Cavernomas.jpg)

Typical and Not So Typical Pediatric Meningiomas: Pictorial and Educational Review

N Vaz¹, G Mendez², J Collins³, C Yang⁴

Purpose

The goal of this pictorial and educational review is to provide a general overview of pediatric meningiomas, focusing mainly on imaging features, and using cases from our institution to illustrate them. Recognition of certain findings may help the interpreting neuroradiologist to identify higher-grade tumors and, therefore, assist in guiding management.

Materials and Methods

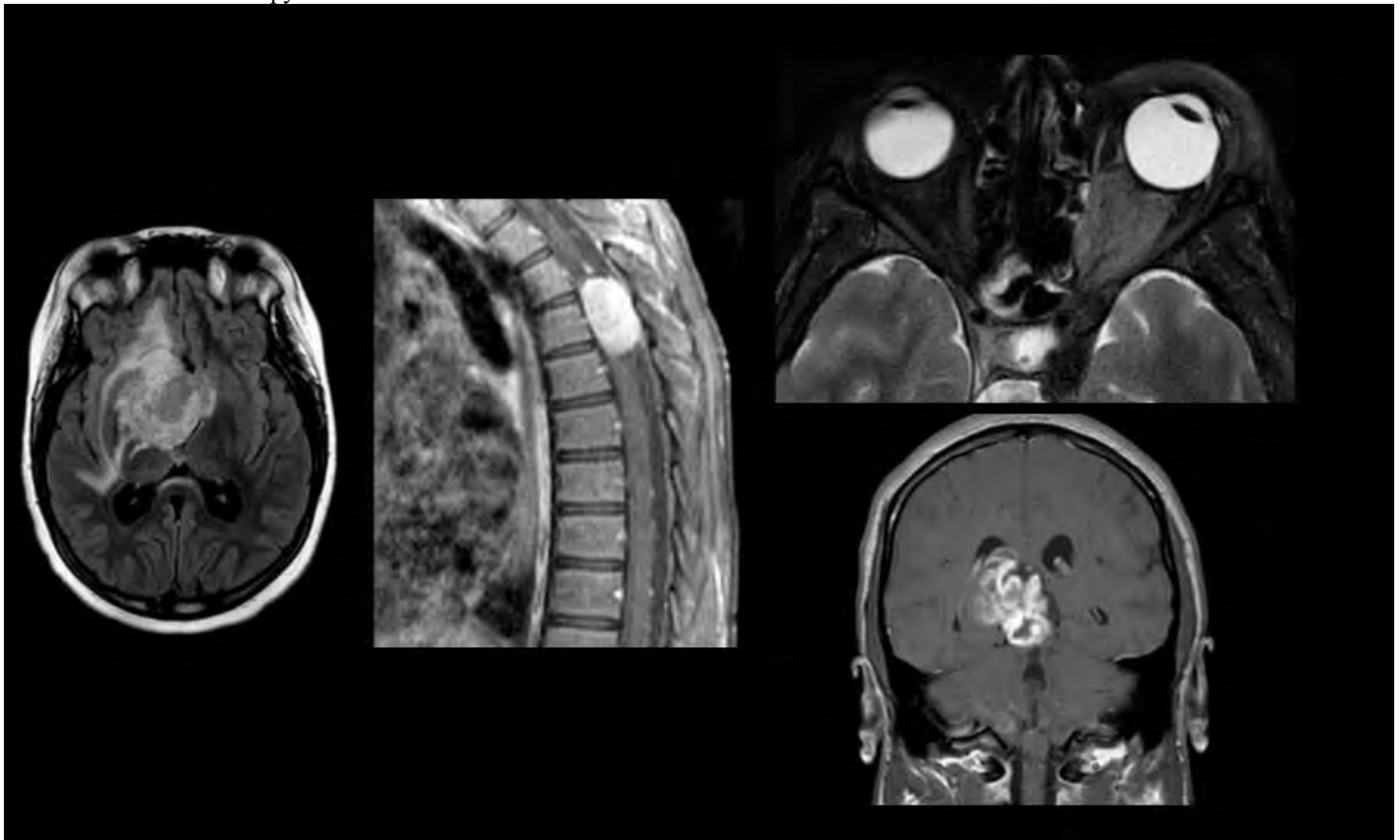
This exhibit aims to illustrate imaging findings of pediatric meningiomas. Drawing on cases from our institution, both typical and higher-grade pathology, we provide a brief overview of demographics, predisposing factors, histopathologic classification, treatment approaches and recommended follow-up of these tumors.

Results

Employing literature and case review to help classify general and imaging features of pediatric meningiomas.

Conclusions

Even though they represent the most common primary central nervous system (CNS) tumors in adults, meningiomas are exceedingly rare in the pediatric population. Pediatric meningiomas differ from their adult counterparts as they do not display the typical female predominance, and they include more spinal tumors. The majority of cases are seen in association with neurofibromatosis type 2, but may also be seen with other predisposing hereditary conditions such as Gorlin syndrome, or even sporadically. Radiation exposure is the only established environmental risk factor for meningioma. The classic meningioma is usually a sharply demarcated, extra-axial enhancing mass, commonly exhibiting a dural tail. The imaging diagnosis of meningiomas may be challenging if the classic imaging features are absent, which is more common in higher-grade cases. Certain imaging features may favor a high-grade tumor, with low ADC values being the most promising one. Tumors are classified histopathologically into 3 groups according to the WHO grading system. Grade I corresponds to common or typical meningiomas; grade II includes atypical, chordoid and clear cell histologies; grade III corresponds to the malignant meningiomas. Surgery is the mainstay of treatment for meningiomas. However, some small asymptomatic meningiomas may be followed with serial imaging. Radiation therapy may be useful in certain cases but must be used with caution. Chemotherapy has not been shown to be effective.



(Filename: TCT_330_PedMeningioma.jpg)

394

Understanding Tumor Metrics in Neuro-Oncology

H Dalla Pria¹, H Pokhylevych¹, A Hassan¹, A Ergin Sonmez¹, M Saleh¹, B Carter¹, K Shah¹, P Bhosale¹

Purpose

Objectives: A brief review of tumor metrics criteria and why they are essential for evaluating tumor response. Image-based approach with fundamental practical principles and educational points. Review of tumor criteria in neuro-oncology and current concepts - RANO HGG, RANO LGG, RANO LM, RANO BM, iRANO, NANO. Summary: History of tumor metric criteria Basic concepts of RANO HGG, RANO LGG, RANO LM, RANO BM, iRANO, NANO. Image-based approach: -The role of the radiologist in the assessment of the therapeutic response using tumor criteria in neuro-oncology. The evaluation of complete response, partial response, minor response, stable disease, and progressive disease. -The differences in immune response evaluation. -Limitations and Confounders: pseudoprogression, pseudoresponse, post-treatment changes, recurrence, and the use of advanced brain tumor imaging sequences on equivocal scenarios -Limitations of current tumor criteria and new directions - integrating new techniques and functional imaging. Take-home messages.

Materials and Methods

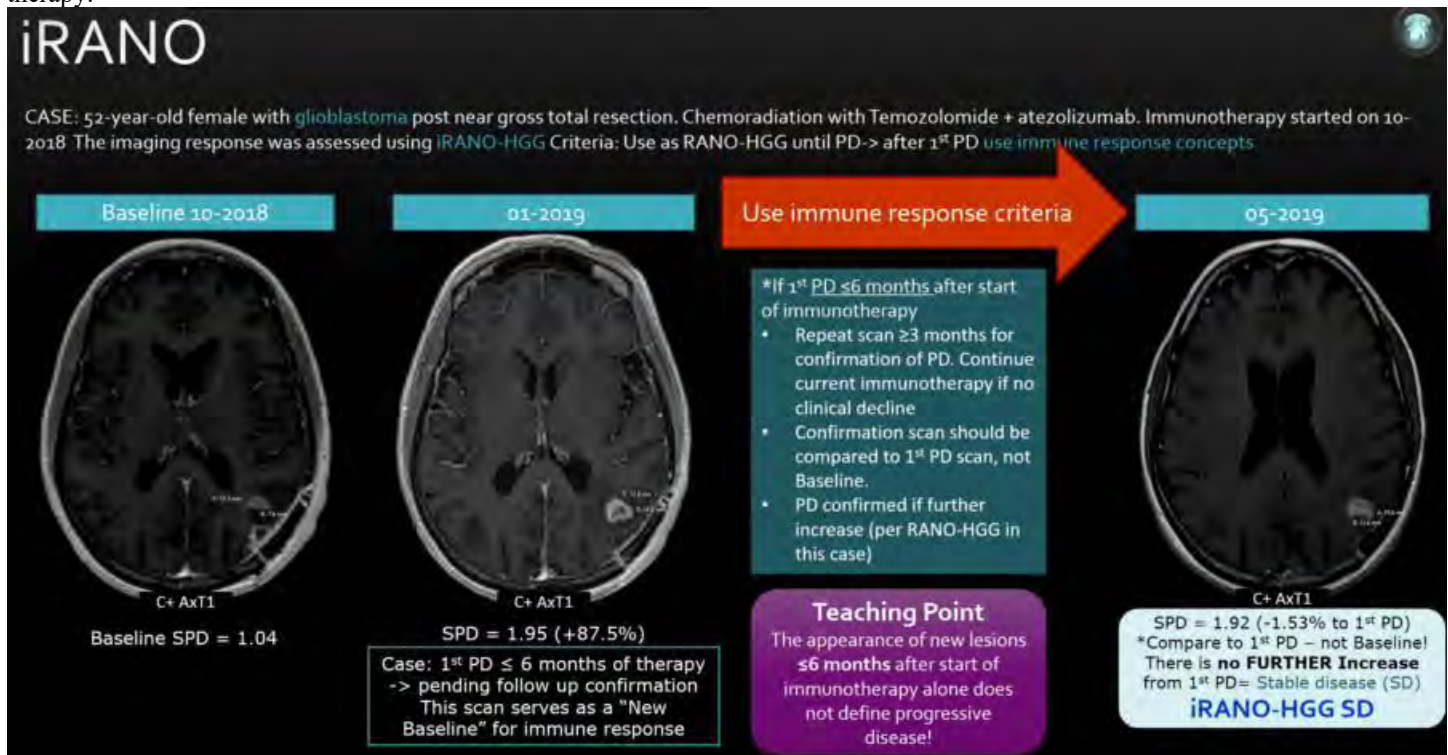
The purpose of this presentation is to conduct a broad review of current concepts in tumor metric criteria for neuro-oncology assessment. Our presentation will review the main theoretical points on tumor metric criteria for neuro-oncology. We will discuss the main practical questions, exceptions, and challenges of using tumor metric criteria using case-based scenarios.

Results

N/A

Conclusions

The early diagnostic and advance of novel therapeutics for primary brain tumors and brain metastases demanded the creation of specific tumor metrics criteria for neuro-oncology assessment. It's imperative to understand how to evaluate treatment response more than only know how to measure the tumors. An increase in size or enhancement is not always progression, and a subjective analysis can lead to disagreements and misinterpretations. Therefore, tumor metrics in neuro-oncology have a crucial role in uniformizing this evaluation for clinical trials. The radiologist must be familiar with each criteria specifics to avoid giving the wrong overall response. Misdiagnosing recurrence or progression is harmful to the patient since it would eventually lead to discontinuation or unnecessary change in the treatment. Misdiagnosing stable disease will delay the change in therapy. The radiologist's role is to use tumor metrics criteria for neuro-oncology for imaging response and ultimately help guide the best treatment for the patient – continuing or changing therapy.



(Filename: TCT_394_1300.jpg)

1554

Vascular Lesions of the Spine: a Simplified Diagnostic Approach.

D Aranedá¹, F Kara¹, S Bravo-Grau¹, E Penailillo¹, J Cruz²

¹Pontificia Universidad Catolica de Chile, Santiago, Chile, ²Pontificia Universidad Catolica de Chile/Instituto de Neurocirugia, Santiago, Chile

Purpose

Introduction: Vascular lesions of the spine and spinal cord are relatively rare, but diagnostic non-invasive imaging plays a major role in the initial diagnostic approach, localization of the involved segmental artery(ies) in cases of AV shunts, and follow-up in treated and non-treated patients. We aim to propose a simple yet comprehensive diagnostic approach with illustrative cases of the most relevant diseases and potential mimics centered on the MR imaging findings, and their correlation with the spinal DSA, so to provide an adequate framework for the neuroradiologist in the diagnostic process of these type of lesions. Educational objectives: -To review imaging findings focused on non invasive imaging, and diagnostic pearls of vascular tumors and vascular malformations of the spine. -To illustrate the different spinal arteriovenous shunts including AVM, DAVF and AVF. -To review spinal Cord Ischemia and its mimics. -To propose a practical approach to differentiate vascular lesions of the spine based on their imaging characteristics on non-invasive and invasive techniques. Table of contents/Outline: 1. Introduction: Relevance. Epidemiology. Clinical presentation. 2. Diagnostic techniques and protocols: Role of dynamic time-resolved MR angiography. Role of DSA. 3. Practical approach to differential diagnosis. How to identify the presence of an AV shunt. Diagnostic pearls. How to differentiate a vascular tumor from a vascular malformation. 4. Hypervascular Tumors. 5. Ischemia and its mimics (e.g. non-polio enteroviruses, anti-MOG disease). 6. Spinal Cavernous Malformation. 7. Spinal Aneurysm. 8. Spinal AV Shunts. Spinal DAVFs. Spinal AVM. Spinal AVF. -Macrofistula. -Microfistula. 9. Special cases. Spinal metameric syndrome. Mixed Epidural/Intradural Fistula. 10. Conclusion.

Materials and Methods

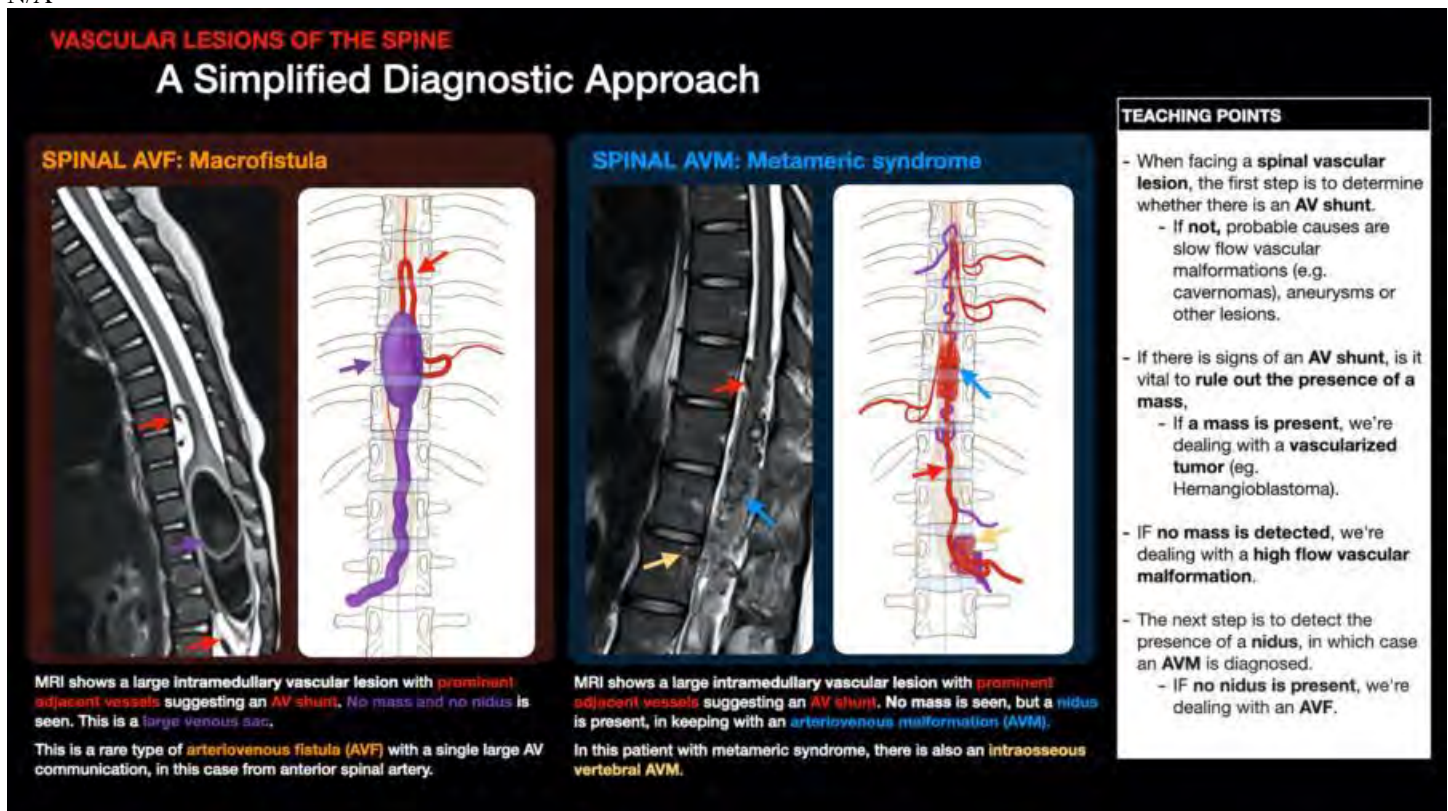
N/A

Results

N/A

Conclusions

N/A



(Filename: TCT_1554_ASNRvascularlesionspinediapo001.jpg)

807

Ventriculomegaly, Calcifications, White Matter Abnormalities...Can we differentiate Perinatal Brain Infections?

G Andreis¹, A Ottaiano², T Kotsubo³, V Coelho⁴, L Lessa⁵, N Ferreira¹, T Freddi¹

¹Hospital do Coração, São Paulo, São Paulo, ²Hospital of the Heart, São Paulo, São Paulo, ³Hospital do coração, São Paulo, São Paulo, ⁴Laboratório de Neuroimagem, FCM, UNICAMP., Campinas, São Paulo, ⁵HCFMUSP, São Paulo, SP

Purpose

Perinatal infections of the CNS include those in the tradicional TORCH (Toxoplasmosis, Rubella, Cytomegalovirus (CMV) and herpes simplex viruses (HSV), with a recent increasing interest for Zika virus as a congenital infectious agent, as well for neonatal

Chikungunya infection. This pictorial essay reviews the clinical information and imaging features of the main perinatal infections of the central nervous system. Objectives: 1. To review the main perinatal infections of the central nervous system (CNS). 2. Describe the clinical presentations and imaging characteristics of perinatal infections, with representative cases from our institution. 3. Describe the most characteristic imaging pattern of each etiological agent.

Materials and Methods

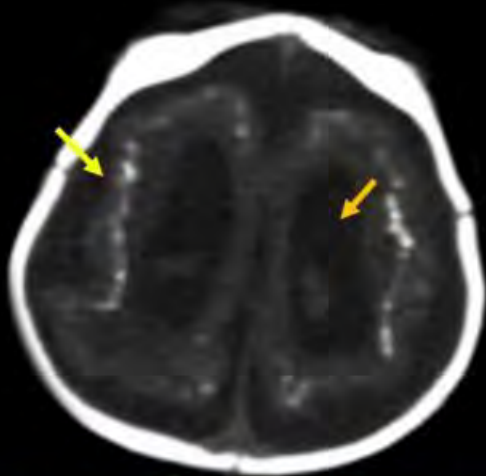
In this exhibit we provide a case-based review we emphasize the main imaging findings of the main perinatal infections.

Results

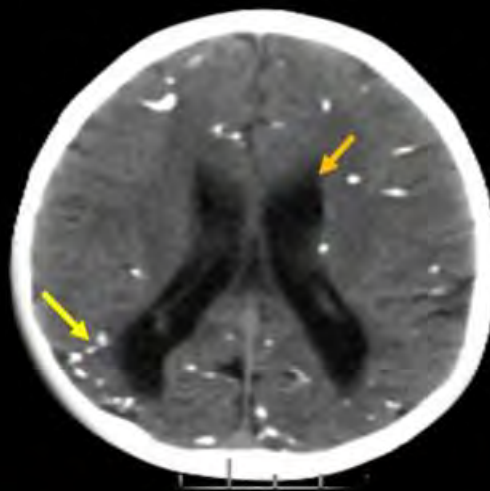
Brain CT and MRI cases of perinatal infections of the CNS were retrospectively collected from our institutional database. For each case, the authors reviewed the clinical information and imaging features used to establish the diagnosis.

Conclusions

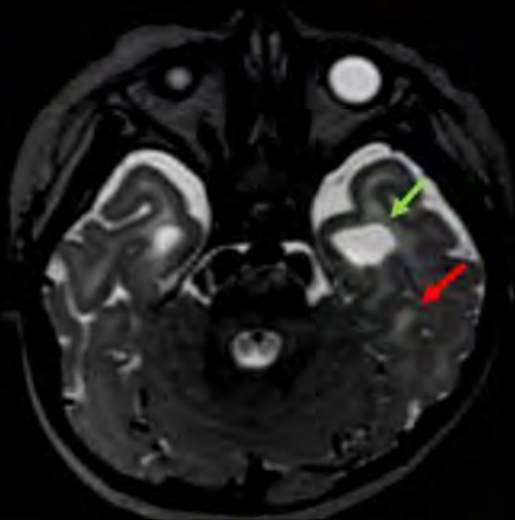
In patients with CMV infection, periventricular calcifications, anomalies of cortical development, white matter anomalies, temporal lobes cysts, microcephaly and ventriculomegaly were identified. In Toxoplasmosis, imaging findings are strongly associated with the timing of parasite transmission during pregnancy and may show hydrocephalus mainly involving the posterior parts of the lateral ventricles, porencephalic cysts and scattered calcifications. HSV infection demonstrates diffuse parenchymal involvement, with edema, diffusion restriction and necrosis. Children with congenital HIV may demonstrate basal ganglia calcifications, atrophy and vasculopathies. In congenital Zika virus infection, the most common imaging findings are extreme microcephaly, anomalies of cortical development, subcortical calcifications and ventricular dilation. In neonatal Chikungunya infection a distinct white matter diffusion restriction can be found. Our intention with this case based review is to demonstrate the most common CNS imaging findings of perinatal infections.



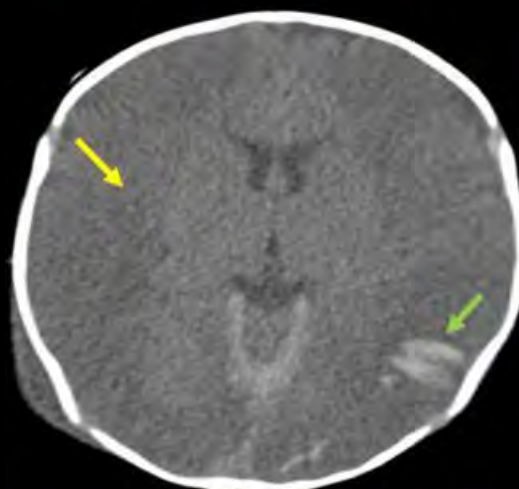
Cases of Zika virus infection showing **subcortical punctate calcifications**, **ventricular dilation**



Cases of Toxoplasmosis showing **sparse calcifications** and **ventriculomegaly**.



Cases of cytomegalovirus infection showing, **periventricular cysts (temporal poles)** and **white matter signal abnormalities**.



A 20 days-old boy with congenital herpes presenting fever and lethargy, showing **corticosubcortical diffuse abnormalities** and **hemorrhagic foci**.

(Filename: TCT_807_Imagens4.jpg)

1304

Watch Out! It May Be A Blister! The Importance Of Not Giving Up

C Parra-Farinas¹, J Diestro¹, J Spears¹, T Marotta¹

¹St. Michael's Hospital, University of Toronto, Toronto, Ontario

Purpose

Blister aneurysms are uncommon but well-recognized form of fragile intracranial vascular lesion. They have rapid growth and high bleeding rates. Initial investigations may be interpreted as negative. Further imaging is compulsory. This educational exhibit will show several cases of rapidly growing blister aneurysms. Our goal is to elucidate recognizable features on imaging from their early stages to help ensure a prompt diagnosis and correct management.

Materials and Methods

1. To show blister aneurysms radiological features with negative initial imaging findings 2. To list the advantages of the various imaging modalities used to properly diagnose this entity 3. To account the proposed pathophysiology leading to blister aneurysms development 4. To examine the relationship between radiological findings and treatment technique

Results

Blister aneurysms appear as small, subtle shallow and broad-based lesions. Initial imaging may be negative or equivocal. On short-term follow-up they show rapid growth which makes the diagnosis easier. Most false-negative studies, when evaluated in retrospect, reveal suspicious anomalies that could be well associated with a blister. The result is a delay in diagnosis and initiation of treatment which increases mortality rates. The evaluation usually starts with CT/CTA. It may underestimate the findings due to their small size, unusual location and proximity to the skull base. MRI vessel wall imaging is helpful as it can detect intramural hematoma on the dorsal surface of the vessel. Conventional angiography is the gold standard and should be performed whenever initial investigations prove to be negative in the correct clinical context. The pathophysiology remains poorly understood. There is consensus on the disproportionate fragility of blisters and their parent vessels. Arterial dissection, arteriosclerotic ulceration and hemodynamic stress have been described. Treatments techniques remains debatable. Both surgical and endovascular modalities can be used. Additionally, and even if an initial intervention proves successful, subsequent regrowth requiring further treatment has been commonly reported. Therefore, close follow-up is extremely important.

Conclusions

Blister aneurysms are extremely fragile and fast growing lesions before and after treatment, frequently underdiagnosed. A high index of suspicion, a familiarity with the initial subtle radiological features and the notion of the importance of repeat imaging will lead to a rapid diagnosis and accurate treatment.



(Filename: TCT_1304_CPF_ASNR2021.jpg)

777

Whac-A-Mole: Imaging Evaluation of CSF Leaks.

P Reddy¹, M Mian², S Vattoth³, R Van Hemert⁴, R Ramakrishnaiah⁵, M Kumar², S Viswamitra²

¹University of Arkansas for Medical Sciences, Little rock, AR, ²University of Arkansas for Medical Sciences, Little Rock, AR, ³University of Arkansas for Medical Sciences, LITTLE ROCK, AR, ⁴UAMS, Little Rock, AR, ⁵Univ of Arkansas for Medical Sciences, Little Rock, AR

Purpose

The objectives of this presentation are to: 1. Review skull base anatomy relevant to CSF leaks 2. Discuss the classification of CSF leaks 3. Discuss clinical presentation and diagnosis tests for CSF leaks 4. Discuss the Imaging approach to CSF leaks 5. Describe the imaging findings on CT and MR cisternography 6. Describe the pitfalls in interpreting these studies The summary of the presentation is as follows: 1. Introduction - Demographics and CSF physiology 2. Anatomy - common sites for skull base CSF leaks 3. Clinical features of CSF rhinorrhea 4. Diagnostic tests - Beta 2 transferrin, CT, MRI and nuclear medicine 5. Imaging technique - CT, MRI and role of heavily T2 weighted 3D imaging. 6. Imaging protocol for patients with suspected CSF leaks 7. Imaging findings - direct and indirect signs 8. Classification by etiology with case examples - spontaneous, congenital CSF otorrhea, iatrogenic, traumatic 9. Imaging pitfalls 10. Conclusion

Materials and Methods

The purpose of this educational exhibit is to discuss the causes, clinical presentation and imaging of CSF leaks with emphasis on good imaging technique and avoiding pitfalls. The utility of heavily T2 weighted 3D imaging sequences without intrathecal contrast will also be discussed.

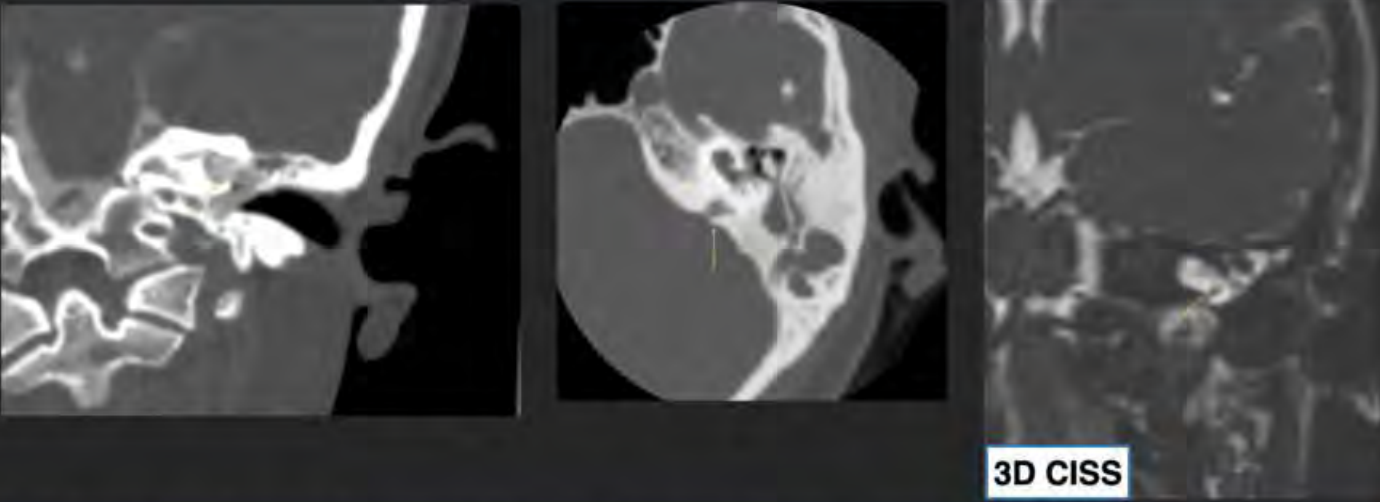
Results

A retrospective review of the institute database was performed for interesting and challenging cases which were included for this exhibit.

Conclusions

N/A

This is a 23 year old lady who presented with history of hearing loss and repeated episodes of meningitis.



CT cisternogram image shows a defect in the promontory with contrast opacification of the cochlea extending to the middle ear consistent with a CSF leak. HRCT temporal bone images demonstrate an enlarged vestibular aqueduct and absence of the spiral lamina in the cochlea suggestive of type 2 incomplete partition cochlear malformation. The defect in the promontory is also depicted on 3D CISS MR images.

Diagnosis: CSF Otorrhea associated with Type 2 incomplete partition cochlear malformation.

(Filename: TCT_777_cisternography.jpg)

1321

What is under the tent? Posterior fossa tumors in children, beyond the "usual suspects"

F Goncalves¹, L Tierradentro-García¹, A Zandifar¹, J Kim¹, A Ghosh¹, A Kashgari², S Goddu Govindappa³, A Bag⁴, C Saint-martin⁵, M Mohammadifard⁶, C Alves¹, S Teixeira¹, A Viaene¹, K Yeom⁷, S Andronikou¹, A Vossough¹

¹Children's Hospital of Philadelphia, Philadelphia, PA, ²King Abdullah specialized children hospital, Riyadh, WA, ³Apollo hospital, Bangalore Urban, Sheshadripuram, ⁴St. Jude Children's Research Hospital, Memphis, TN, ⁵Montreal Children's Hospital, Montreal, Quebec, ⁶Birjand university medical science, Birjand, South Khorasan, ⁷Stanford University, Palo Alto, CA

Purpose

Central nervous system tumors are common neoplasms among children. Tumors arising in the posterior fossa account for 45–60% of all pediatric central nervous tumors. Most posterior fossa tumors are discovered between 3 and 11 years old. The "usual suspects" are medulloblastoma (30–40%), pilocytic astrocytoma (25–35%), diffuse midline glioma (10–15%), ependymoma (10–15%), and atypical teratoid rhabdoid tumor (ATRT) (less than 1–2%). A wide variety of "unlikely suspects" represent 10–15% of posterior fossa tumors. The prevalence of the different types of tumors is, in fact, deeply influenced by their location.

Materials and Methods

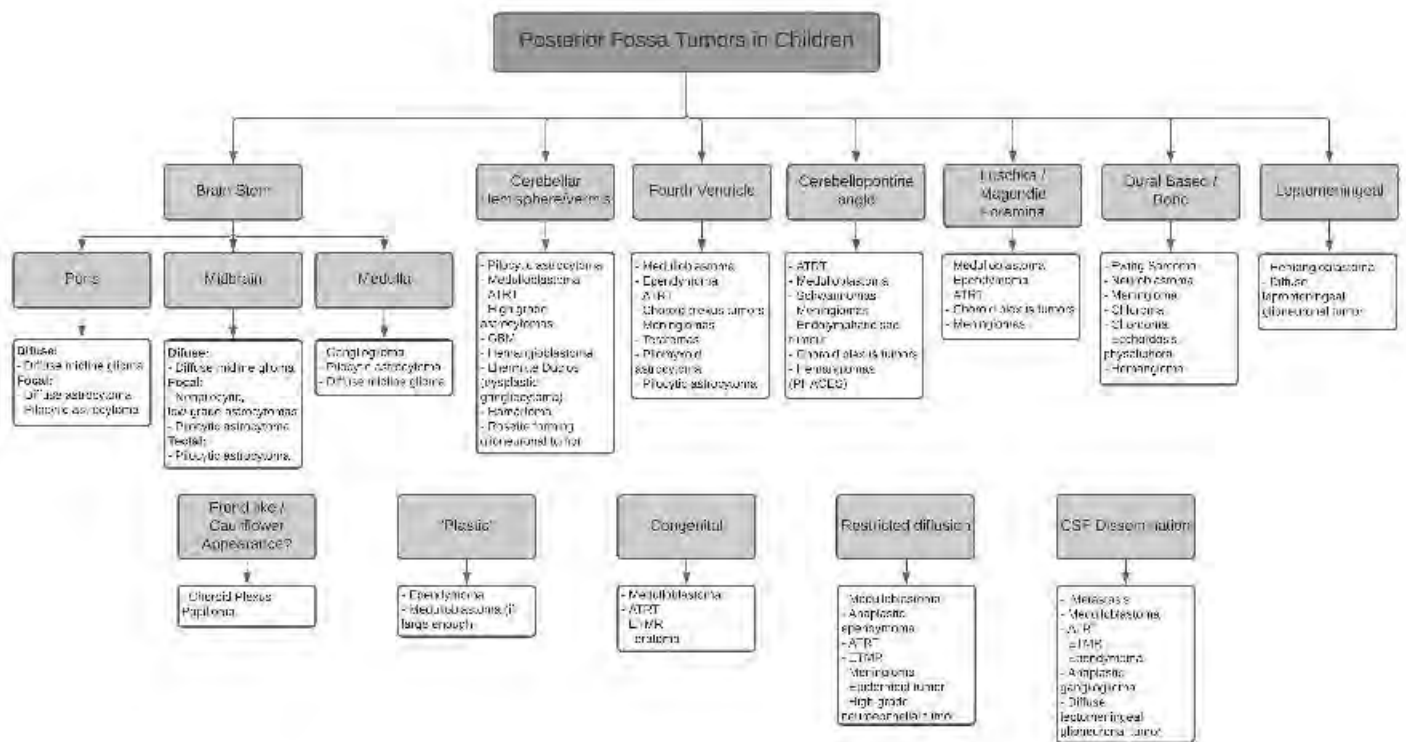
This electronic educational exhibit aims to review the most relevant neuroimaging findings of the most common posterior fossa masses and expand the differential diagnosis with uncommon entities.

Results

This exhibit comprehends the collective experience of pediatric neuroradiologists from multiple institutions worldwide. More than 20 posterior fossa tumors will be discussed, such as (in alphabetical order) angiocentric glioma, ATRT, choroma, choroid plexus tumors, diffuse leptomeningeal glioneuronal tumor, embryonal tumor with multilayered rosettes, ependymoma, Ewing sarcoma, ganglioglioma, GBM, hamartoma, hemangioblastoma, hemangioma, pilocytic astrocytoma, medulloblastoma, meningioma, midline pontine glioma, neuroblastoma, pilomyxoid astrocytoma, pseudotumors, rosette-forming glioneuronal tumor, and tectal glioma. First-order analysis will be performed based on topography. Masses will be divided into those arising in the brain stem (midbrain, pons, and medulla), cerebellar hemispheres/vermis, fourth ventricle, cerebellopontine angle, dural based / dural, and leptomeningeal. Subsequent order analyses will be performed based on typical neuroimaging findings and distinctive features on advanced imaging, age at presentation, clinical presentation, and ancillary findings.

Conclusions

Neuroimaging features on CT, conventional MRI, and advanced MRI imaging studies may help suggest the most likely diagnosis leading to early and appropriate treatment. Pre-surgical identification of the tumor type and its aggressiveness could be improved by the combined analysis of key imaging features with epidemiologic data.



(Filename: TCT_1321_POSTERIORFOSSATUMORS.jpg)

When can ASL technique make a difference in the evaluation of the high flow Brain Vascular Malformations?

F Assunção¹, T Scopetta¹, L Martins², M Soldatelli², L Freitas², E Narvaez², B Inada², V Marussi², C Campos², L do Amaral²
¹Hospital São Camilo, São Paulo, SP, ²BP - A Beneficência Portuguesa de São Paulo, São Paulo, SP

Purpose

Brain Vascular Malformations (BVMs) are considered a group of disorders that present with a wide variety of neurological symptoms and can even be found in asymptomatic patients. They can be divided into high and low flow malformations. High flow malformations include arteriovenous malformations (AVMs), cerebral proliferative angiopathy (CPA), dural arteriovenous fistulas and pial arteriovenous fistulas (DAVFs). The gold standard diagnosis is digital angiography, however brain MRI studies using the Arterial Spin Labeling (ASL) technique can be used in the diagnostic elucidation as well as in post-treatment control of these malformations. The goal of this digital paper is: - To review basic principles and applications of the ASL technique, - To discuss on typical imaging findings of high flow BVMs using the ASL technique - To discuss on when ASL technique makes difference in the approach of high flow Brain Vascular Malformations (post-embolization and radiosurgery control).

Materials and Methods

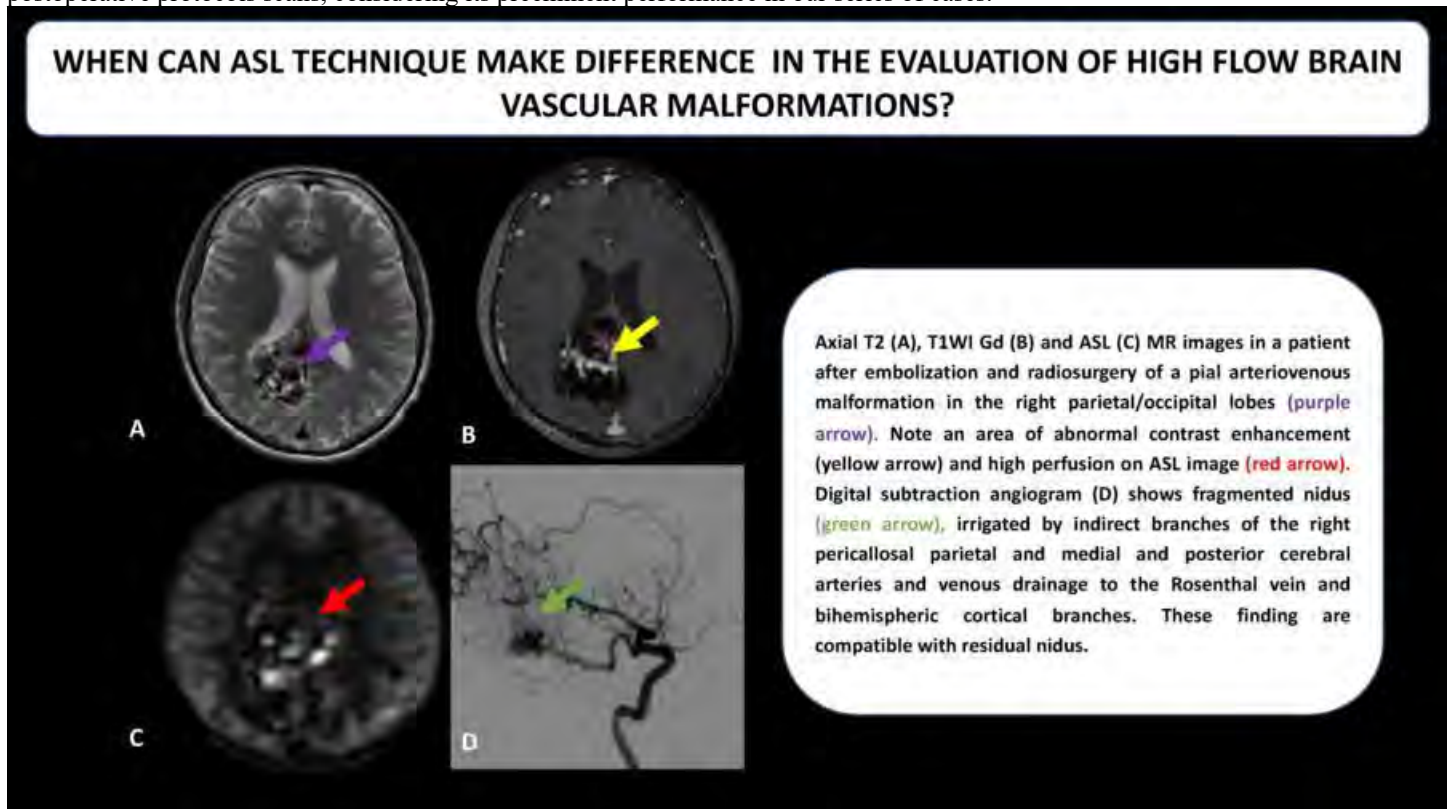
- To briefly review the clinical and imaging findings of brain vascular malformations (BVMs). - To describe and illustrate a series of cases of high flow CVMs in brain magnetic resonance imaging (MRI) studies, highlighting the support use of Arterial Spin Labeling (ASL) technique. - To demonstrate the applicability of ASL perfusion in the control evaluation after therapeutic embolization.

Results

We performed a retrospective and descriptive study of brain MRI of patients diagnosed with high flow CVMs performed at ours services.

Conclusions

High-flow BVMs are a group of disorders that is finest evaluated by digital angiography (DSA). However, ASL perfusion is a promising emerging technique. ASL technique has great applicability in the diagnostic elucidation as well as in the post-therapeutic evaluation of CVMs. Hot perfusion areas should be actively searched. Radiologist should become familiar with this standout perfusion technique to wisely use it in BVMs cases, restricting DSA to specific situations. Therefore, we reassure the use of ASL in the pre and postoperative protocols scans, considering its preeminent performance in our series of cases.



(Filename: TCT_187_MalformacoesVasculares.jpg)

392

When the Cochlea Goes Wrong: a "Sound" Review of Cochlear Anatomy and Malformations

H Tames¹, L Ramin¹, M Lemos¹, M Sarpi¹, C Toyama¹, R Gomes¹, E Gebrim¹

¹University of São Paulo, São Paulo, SP

Purpose

To review normal cochlear anatomy and landmarks. To classify cochlear malformations into aplasia, hypoplasia and incomplete partition types I, II and III. To identify accompanying imaging features of cochlear malformations. To discuss syndromes associated with cochlear malformations.

Materials and Methods

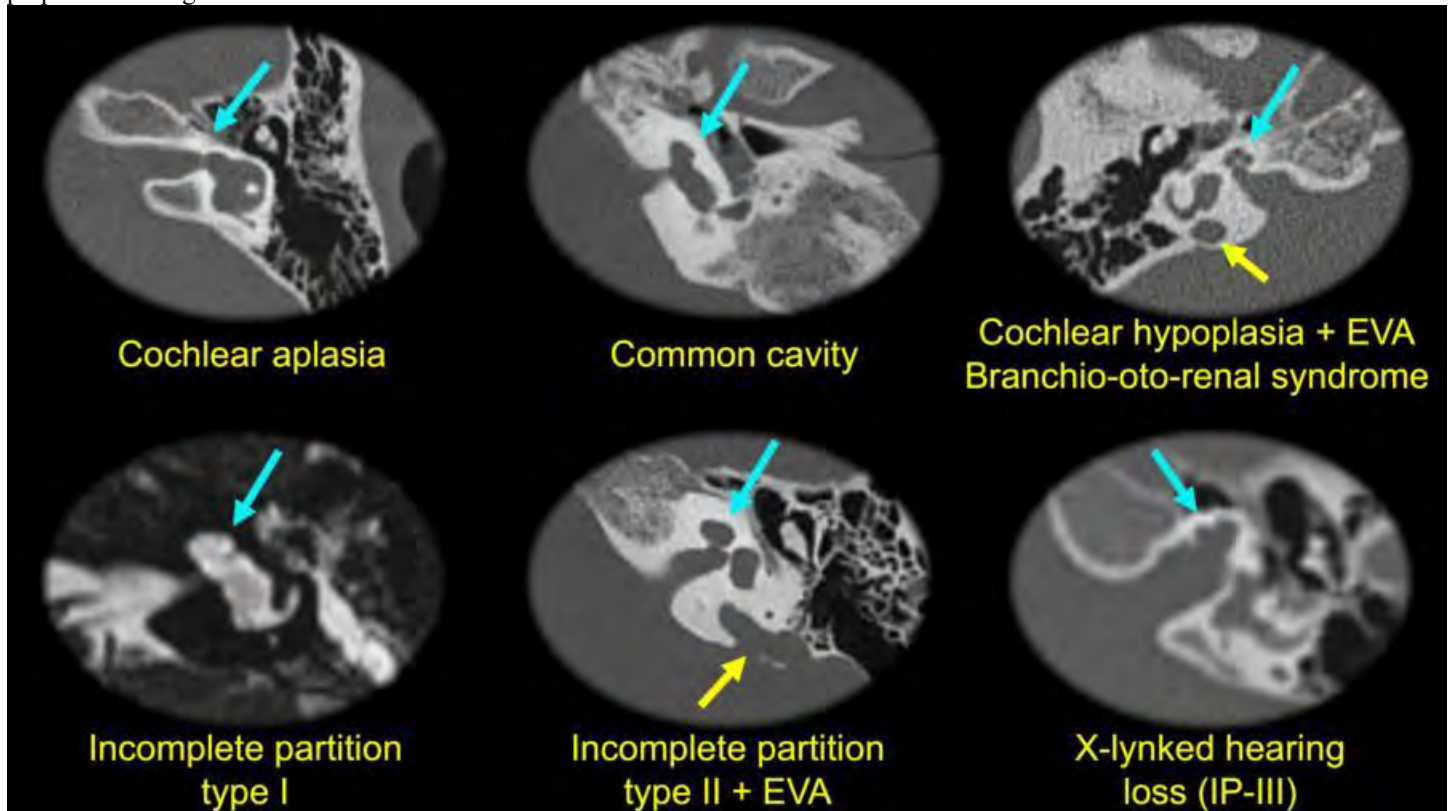
Imaging evaluation of the inner ear is frequently requested in cases of congenital sensorineural hearing loss. Although vestibule and semicircular canals malformations are frequently associated with cochlear malformations, the purpose of this exhibit is to focus on the normal anatomy and alterations of the cochlea, due to its impact in hearing prognosis and treatment planning. Accompanying features and associated syndromes will also be discussed.

Results

A literature and case-based review of the normal anatomy and malformations of the cochlea will be performed, illustrated with images from our institution.

Conclusions

Cochlear malformations can be a challenging topic. Recognition of the normal anatomy and spectrum of cochlear malformations is essential in cases of hearing loss, and adequate description of these findings impacts treatment planning, adding value to the well prepared radiologist.



(Filename: TCT_392_CochlearmalformationsASNR.jpg)

1530

“What is this lump on my head?” Evaluation of lesions of the scalp – A pictorial essay

A Alves Fonseca¹, R Pincerato², C Alves³

¹Santa Casa de São Paulo / DASA / United Health Group, São Paulo, São Paulo, ²HOSPITAL SAMARITANO SP - UHG BRASIL, São Paulo, SP, ³Children's Hospital of Philadelphia, Philadelphia, PA

Purpose

The adult scalp is affected by a wide array of pathology. Its important for radiologists to recognize and differentiate aggressive entities from nonaggressive or normal variants. Based on imaging findings is often possible for the radiologist to narrow down a list of differentials or even go further to elicit diagnostic hypotheses of systemic diseases from the characteristics of skull lesions.

Materials and Methods

The purpose of this study is to illustrate the main skull vault lesions and present a practical approach to understand the broad differential of them.

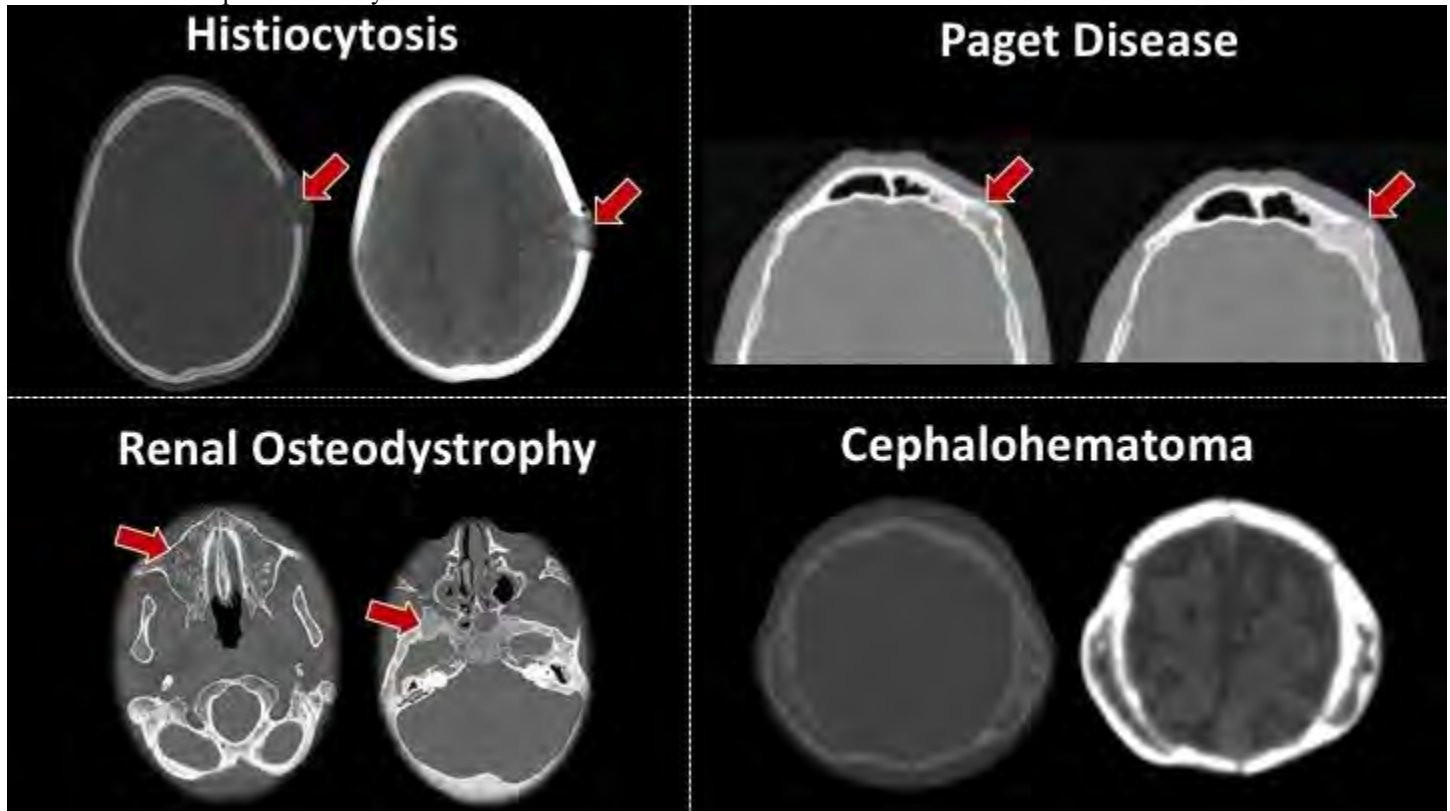
Results

The authors performed a search in Medline and PubMed database looking for "calvarial lesions" and "skull vault lesions" to make a review from the current literature. A retrospective analysis from our institution database was performed for selection of all cases demonstrating skull vault lesions. After that, a correlation with the presence of systemic diseases was done to clarify the importance of calvarial detection. The mainly imaging characteristics of calvarial lesions are highlighted herein. Laboratory findings and epidemiological data are also debated in each case. A retrospective analysis of 18 cases (10 men and 8 women, mean age 50,72) was

conducted. The examinations were performed on a 1.5 T equipment (GE Medical Systems) and 64 CT scanner (Siemens Somatom Sensation). All cases were pathologically proven. MR imaging revealed lymphoma [4 cases (22,2%)], metastasis [4 cases (22,2%)], multiple myeloma [1 case (5,5%)], plasmocytoma [2 cases (11,1%)], eosinophilic granuloma [2 cases (11,1%)], calcified cephalohematoma [1 case (5,5%)], neurofibroma of the scalp [1 case (5,5%)], exostosis [1 case (5,5%)], bone abscess [1 case (5,5%)] and Paget disease [1 case (5,5%)].

Conclusions

The cases were analyzed with regards to location and imaging characteristics. Potential places of origin of the injuries are the different layers of the scalp such as skin, connective tissue (subcutaneous), aponeurosis, periosteum and bone. Masses in the scalp and skull are not always neoplastic. Congenital, posttraumatic, and inflammatory lesions frequently present as masses of the calvarium. An extremely wide range of pathology may appear in this location. It may be difficult to render an etiologic diagnosis of lesions of the scalp and calvarium. Imaging methods can be used to evaluate these lesions. MR imaging is preferable to CT for evaluating soft tissue masses and CT is superior for bony masses.



(Filename: TCT_1530_Skulllesions.jpg)

Electronic Posters (ePosters)

576

3D amplified MRI

I Terem¹, L Dang², A Champagne³, J Abderezaei⁴, S Holdsworth²

¹Stanford, Menlo Park, CA, ²University of Auckland, Auckland, ³Queen's University, Kingston, ⁴Stevens Institute of Technology, Hoboken, NJ

Purpose

Amplified Magnetic Resonance Imaging (aMRI) has been introduced as a new brain motion detection and visualization method [1,2]. However, the original aMRI approach was a 2D post-processing approach which does not take into account motion in all three planes. Furthermore, it has only been applied to multi-slice data which typically only supports thick slices. Here, we strive to improve aMRI by introducing 3D aMRI post-processing algorithm and by applying it on volumetric data.

Materials and Methods

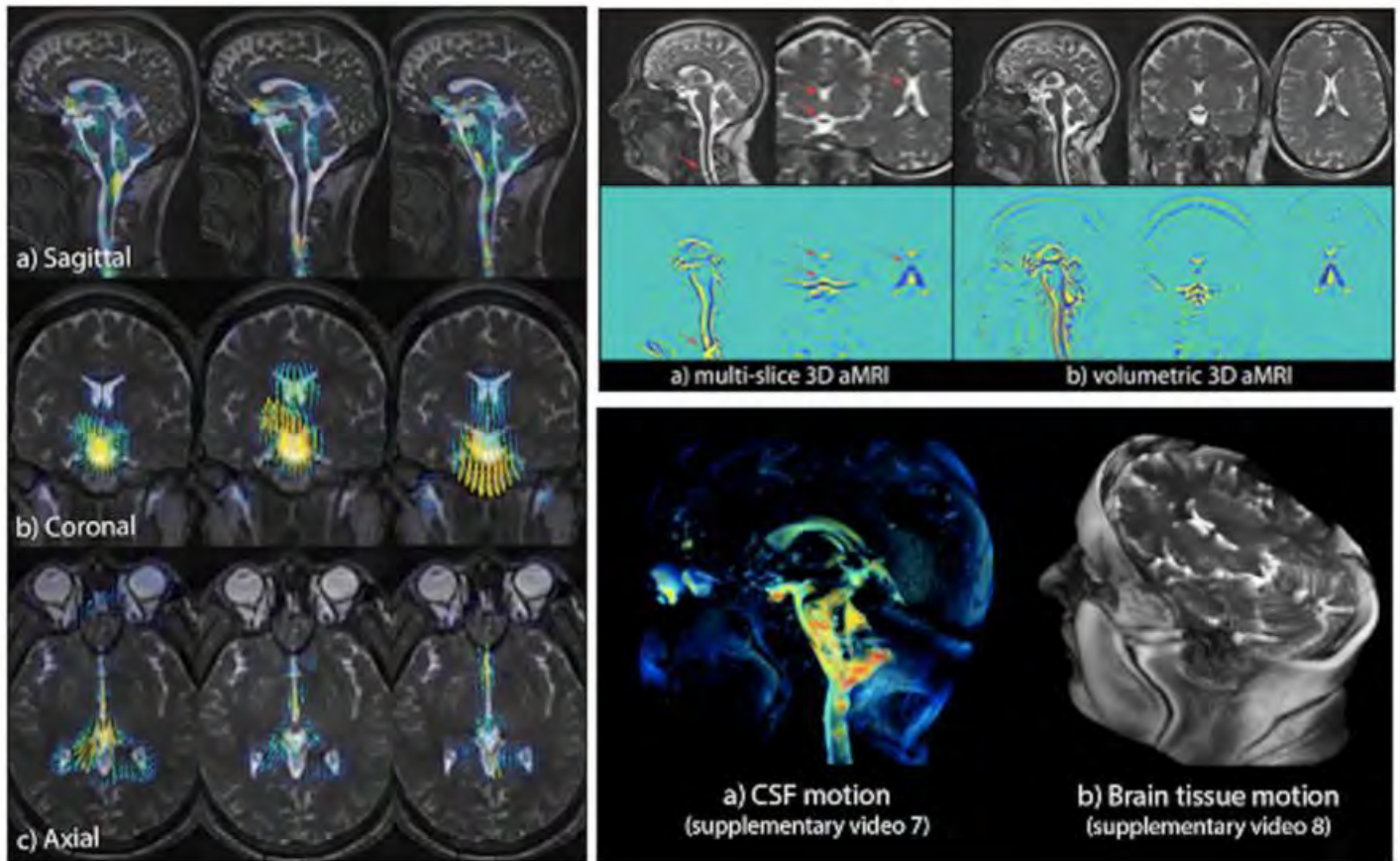
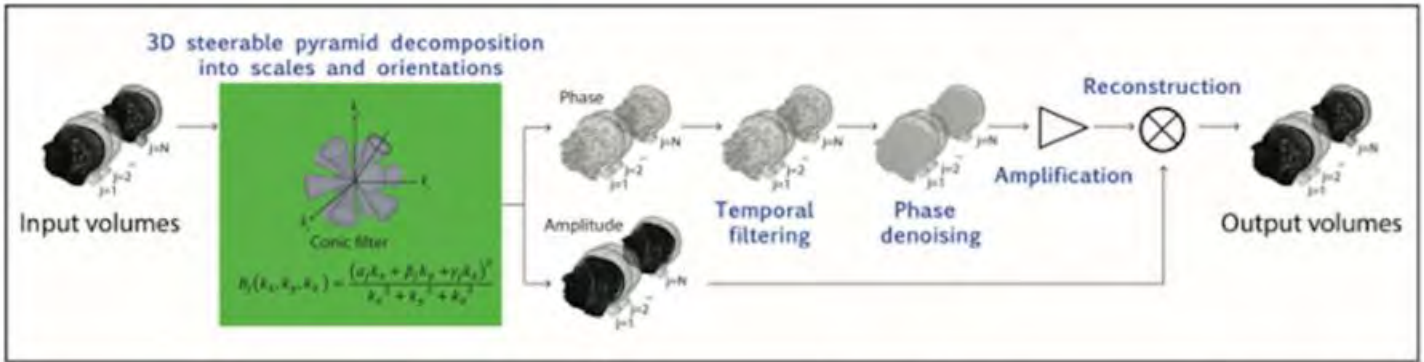
Scans were performed on a 3T MAGNETOM Skyra system using a 32-channel head coil on a normal brain (adult volunteer 44yr/F). Pulse oximetry was used for gating, and a balanced steady-state free precession (bSSFP) sequence was performed with the following parameters: multi-slice: matrix size = 192*192, TR/TE/flip-angle=35ms/1.7ms/43°, acceleration factor = 3, #slices = 25 (resolution = 1.2 x 1.2 x 3mm) and 25 cardiac phases. 3D volumetric: matrix size = 194x240, flip angle/TR/TE=50/1.7ms/26°, acceleration factor = 3, #slices = 104 (resolution of 1.2 x 1.2 x 1.2mm), and 13 cardiac phases. Motion amplification: 3D aMRI decomposes the volume into scale and orientation using the 3D steerable pyramid [3]. The amplification is achieved by temporally manipulating the decomposition output, which results in a 4D movie with motion magnification within the desirable frequency range. Optical flow maps [4] of 3D aMRI were generated using built-in MATLAB function to help to visualize the distribution of apparent velocities. In addition, 4D animation movies were produced to visualize the whole brain tissue and CSF motion using IMARIS 6.4.3.

Results

Both 2D and 3D aMRI considerably enhanced the pulsatile motion of the brain, however, 3D aMRI has superior ability to capture in through plane motion, and shows reduction in artifacts with superior pulsatile image quality. Optical flow together with 4D animation show the complete pulsatile brain tissue and CSF motion, helping to highlight the 'piston-like' motion of the ventricles.

Conclusions

3D aMRI coupled with isotropic volumetric data exquisitely captures 3D brain motion, with better image quality and fewer artifacts. 4D animation together with optical flow maps may help understand the dynamics of what drives the passage of CSF through the ventricular system, and the extracellular fluid within the brain tissue, and open up exciting applications for a range of diseases and disorders that affect the biomechanics of the brain and brain fluids.



(Filename: TCT_576_3DaMRI.jpg)

760

3D Attention-Based Encoder-Decoder Deep Network to Predict PET Cerebral Blood Flow Maps from Multi-Contrast MRI

R Hussein¹, M Zhao¹, J Guo², D Shin³, K Chen⁴, Y Yu¹, A Fan⁵, M Khalighi⁴, M Moseley¹, G Zaharchuk¹

¹Stanford University, Stanford, CA, ²University of California, Riverside, Riverside, CA, ³GE Healthcare, Menlo Park, CA, ⁴STANFORD UNIVERSITY, STANFORD, CA, ⁵University of California Davis, Davis, CA

Purpose

Adequate cerebral blood flow (CBF) is essential for the diagnosis and assessment of cerebrovascular diseases such as stroke, carotid stenosis, and Moyamoya [1]. This study aims to improve the quality of MRI-based CBF measurements. We designed an encoder-decoder network with attention mechanisms to predict the gold-standard 3D oxygen-15 water PET CBF maps from structural MRI and single- and multi-delay arterial spin labeling (ASL) perfusion images.

Materials and Methods

Data were acquired from 16 healthy controls and 16 cerebrovascular disease patients (12 with Moyamoya disease and 4 with intracranial atherosclerotic steno-occlusive disease) on a 3.0T PET/MRI hybrid system (SIGNA, GE Healthcare). The MRI scans included structural MRI imaging (e.g., T1-weighted and T2-weighted FLAIR), single- and multi-delay ASL, and arterial transit time (ATT) maps. All images were co-registered and normalized to the Montreal Neurological Institute (MNI) brain template, and then

scaled down to 96×96×64 voxels. We developed an attention-based encoder-decoder network that produces high-quality synthetic PET CBF maps from a set of MRI sequences. The proposed architecture consists of two convolutional networks: Encoder and Attention-Decoder. The encoder applies a series of 3D convolutions to compress the input MRI sequences into a single voxel of predefined dimensions. The decoder employs a selective attention mechanism that allows the system to focus more on the distinguished aspects of the input at the channel and spatial levels [2], thus yielding improvement in the quality of generated CBF maps.

Results

Reference CBF maps, corresponding synthetic CBF maps, and absolute error maps are shown in Figure 1. The results show that integrating multiple communicative MRI sequences can markedly improve the prediction of PET CBF maps for both healthy controls and cerebrovascular disease patients. An average SSIM, MSE, and PSNR of 0.92, 0.001, and 38.76dB were achieved, showing superior performance over existing PET CBF prediction methods [3].

Conclusions

This work demonstrates that a 3D encoder-decoder network integrating multi-contrast information from structural MRI and ASL perfusion imaging can synthesize high-quality PET CBF maps.

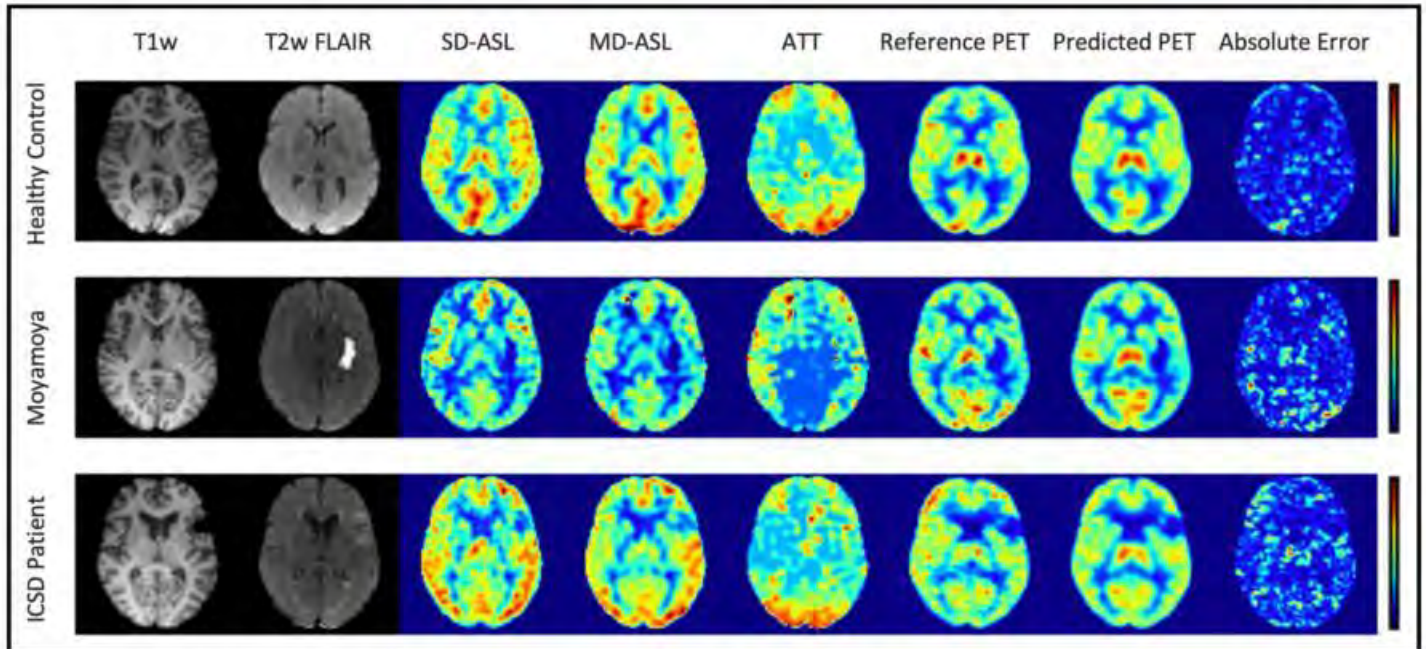


Figure 1. Examples of multi-contrast MRI sequences, reference PET CBF, corresponding synthetic PET CBF, and absolute error maps.

(Filename: TCT_760_Figure_ASNR2.jpg)

1372

4D MRI Viewer Facilitated Multidisciplinary Meeting Discussion in Patients with Multiple MRI Studies.

P Prendergast¹, F Gaillard²

¹Melbourne University, Melbourne, Victoria, ²Royal Melbourne Hospital, Parkville, Victoria

Purpose

While spatial MRI imaging is effective at showing the current state of a patient's condition, differences in factors such as head position, slice position, and window/level between scans can make it difficult for even trained neuroradiologist to detect changes over time when presenting the images side-by-side when the change is slow. Additionally a change in the tempo of progressive change, which may accelerate due to change in biological behaviour of pathology, can be difficult when follow-up scans are obtained at irregular levels. These tasks are even more difficult for clinicians and patients, which in turn can make it difficult to make informed management decisions.

Materials and Methods

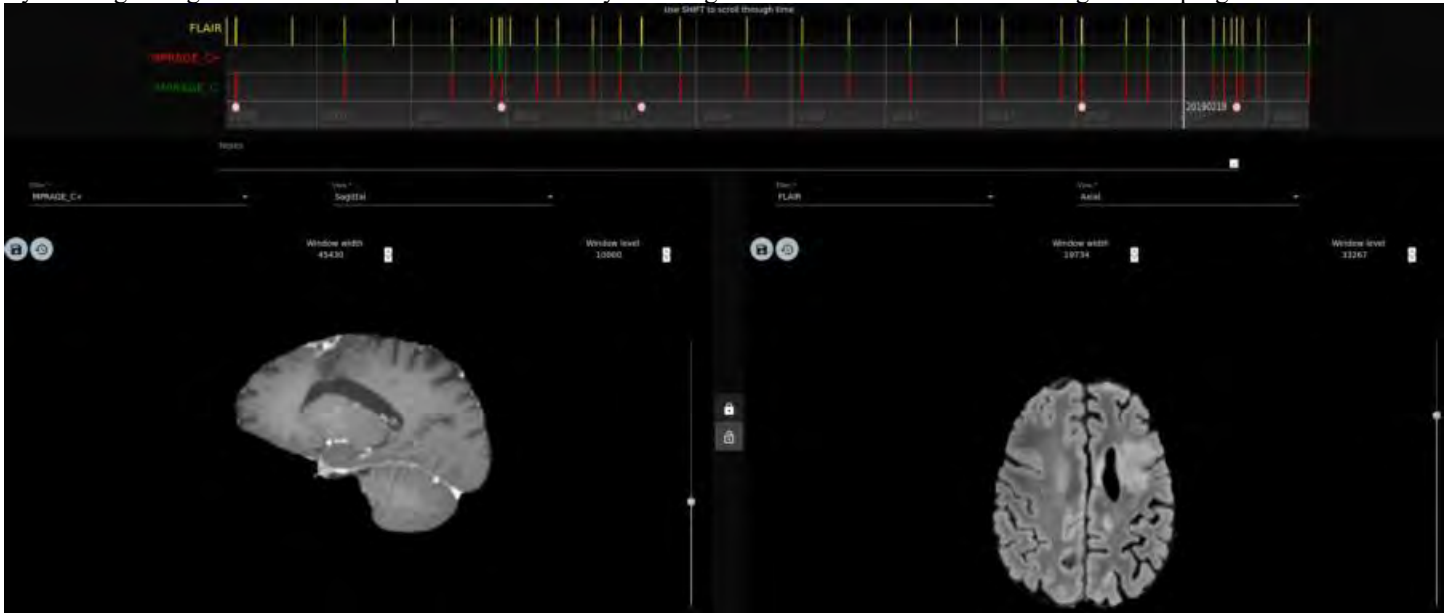
To address this, we have produced a '4D viewer' application (Figure 1), which allows the user to navigate not only through 3 spatial dimensions but also through time in a manner reminiscent of time-lapse photography, giving the radiologist, clinician and patient a better understanding of their progress. Previously, we have shown that by spatially registering and normalizing two scans, we were able to highlight new demyelinating white matter lesions in patients with MS with the result of a significantly increased success rate in the detection of disease progression[1], and that with the use of computer assisted visualization techniques, inexperienced readers such as medical students can perform to the level of a sub-specialty trained neuroradiologist when given this specific task[2].

Results

Preliminary results have shown positive responses to the application, with all respondents reporting that the longitudinal view presented by the application was an improvement on standard MDM case reviews.

Conclusions

By creating a longitudinal view of a patient's scan history we can gain a better intuitive understanding of their progress.



(Filename: TCT_1372_4D.jpg)

1270

A Case Report of Multicentric Chordoma

J Schmidgall¹, D Baskin¹, B Teh¹, S Fung¹

¹Houston Methodist Hospital, Houston, TX

Purpose

Chordomas are rare neuraxial tumors arising from notochord remnants, usually with low to intermediate grade metastatic potential, typically involving clival or sacrococcygeal regions. Very few cases involving multiple neuraxial regions (multicentric chordomas) have been reported. Here, we present a case of multicentric chordomas involving cervical and thoracic spine, sacrum, and possibly calvarium.

Materials and Methods

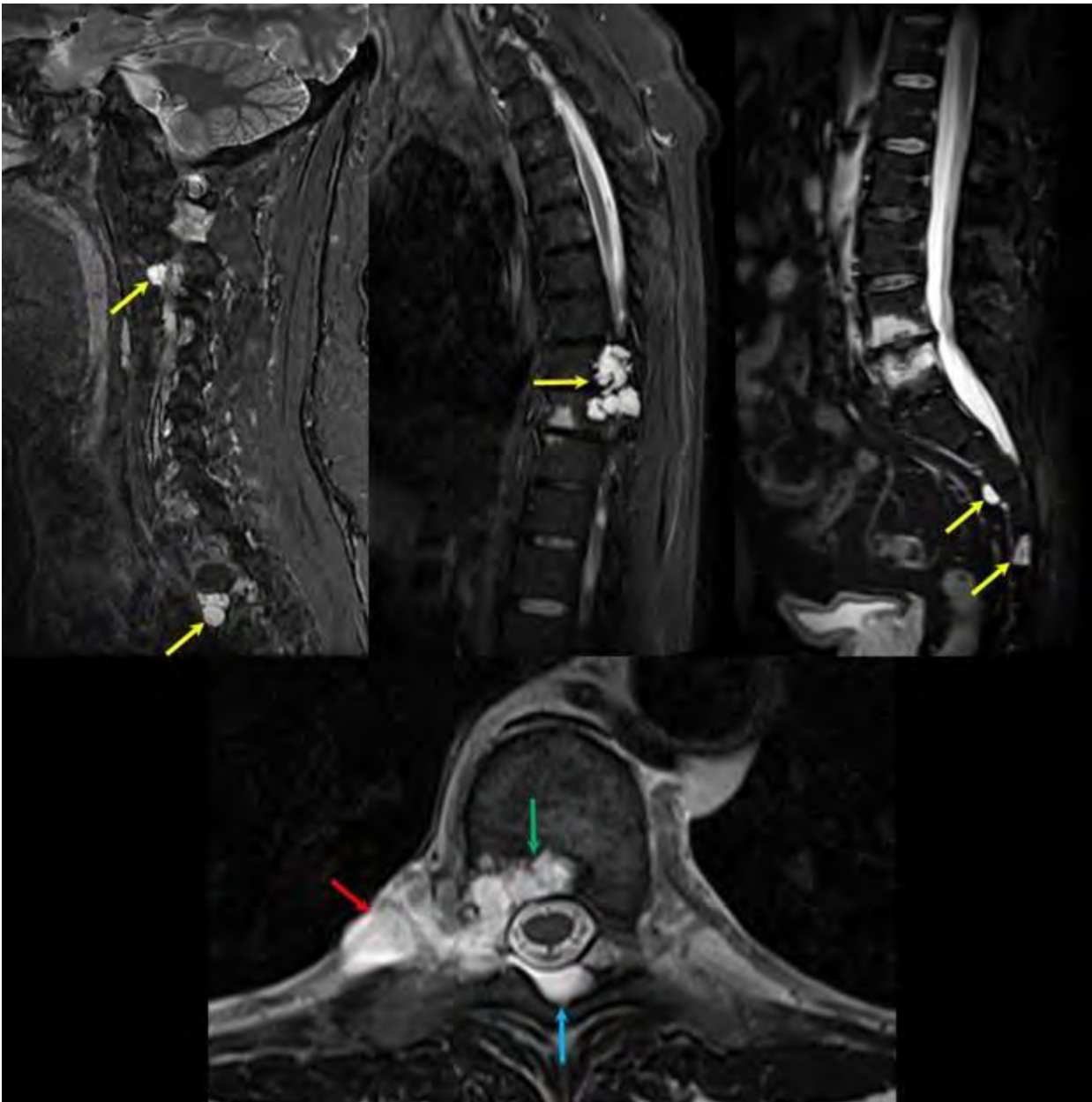
A 60 year-old man with no medical or cancer history had CT scan for colitis that incidentally showed lytic lesions of the spine. CT and MRI of the entire neuraxis was then performed showing multiple lesions involving the cervical and thoracic spine, sacrum, and left parietal scalp/bone. Biopsy of the dominant lesion at the T8-9 level showed chordoma. Patient is presently being evaluated for surgical excision of the T8-9 lesion enclosing the spinal canal and radiation treatment of the other lesions.

Results

MRI of the entire neuraxis shows multiple mildly enhancing spinal lesions with very high T2 signal best seen on STIR (figure yellow arrows) at C2-3, C3-4, C5-6, T2-3, T3-4, T8-9, S2-3, and S4 levels. These lesions have variable bone and soft tissue involvement. For example, axial image in figure centered on dominant lesion at T8-9 level shows lobulated T2-hyperintense lesion with well-defined margins involving bone (green arrow) with paraspinal (red arrow) and epidural (blue arrow) extension. On CT, bone lesion is osteolytic with thin sclerotic margins. Many of the smaller lesions are predominantly paraspinal with minimal cortical involvement. Presacral lesion at S2-3 is attached to periosteum without bone involvement. S4 lesion has similar MRI characteristics but is sclerotic on CT. Brain MRI shows plaque-like deep scalp lesion attached to outer table of left parietal bone with similar MRI characteristics. Sacral and scalp lesions are hyperintense on DWI with mildly reduced ADC.

Conclusions

Due to the rarity of multicentric presentation of chordomas, there is potential for misdiagnosis on initial workup. For instance, multiple vertebral body lytic and T2 hyperintense lesions may be misinterpreted as metastases or multiple myeloma. Periosteal or exophytic lesions, which may be in atypical chordoma locations, could be mistaken for benign cysts. Lesser-known imaging features of chordomas require more investigation in the future, such as variable levels of diffusion restriction, and presence of intratumoral calcification/bony debris, which may cause lesions to appear sclerotic on CT.



(Filename: TCT_1270_ChordomaFigure.jpg)

161

A Comparison of CT-Guided Bone Biopsy and Fluoroscopic-Guided Disc Aspiration as Diagnostic Methods in the Management of Spondylodiscitis

S Ahmad¹, M Jhaveri¹, M Mossa-Basha², M Oztek³, J Hartman³, S GADDIKERI¹

¹Rush University Medical Center, Chicago, IL, ²University of Washington, Seattle, WA, ³University of Washington, Seattle, WA

Purpose

Percutaneous tissue biopsy is a key step in the diagnosis and management of spondylodiscitis. CT-guided bone biopsy (CTB) and fluoroscopic-guided disc aspirations (FGA) are common noninvasive techniques, often chosen due to institutional preferences¹. Our objective was to characterize the advantages / disadvantages of each to guide decision-making in choosing a modality.

Materials and Methods

103 patients in 2 cohorts underwent FGA (n=47) or CTB (n=46) for diagnosis of spondylodiscitis. Patient and imaging data were gathered to ensure matched cohorts. Interventional and post-procedural data included radiation exposure, procedure time, complications, and microbiological details. Yield was calculated using MRI findings as the gold standard for infection.

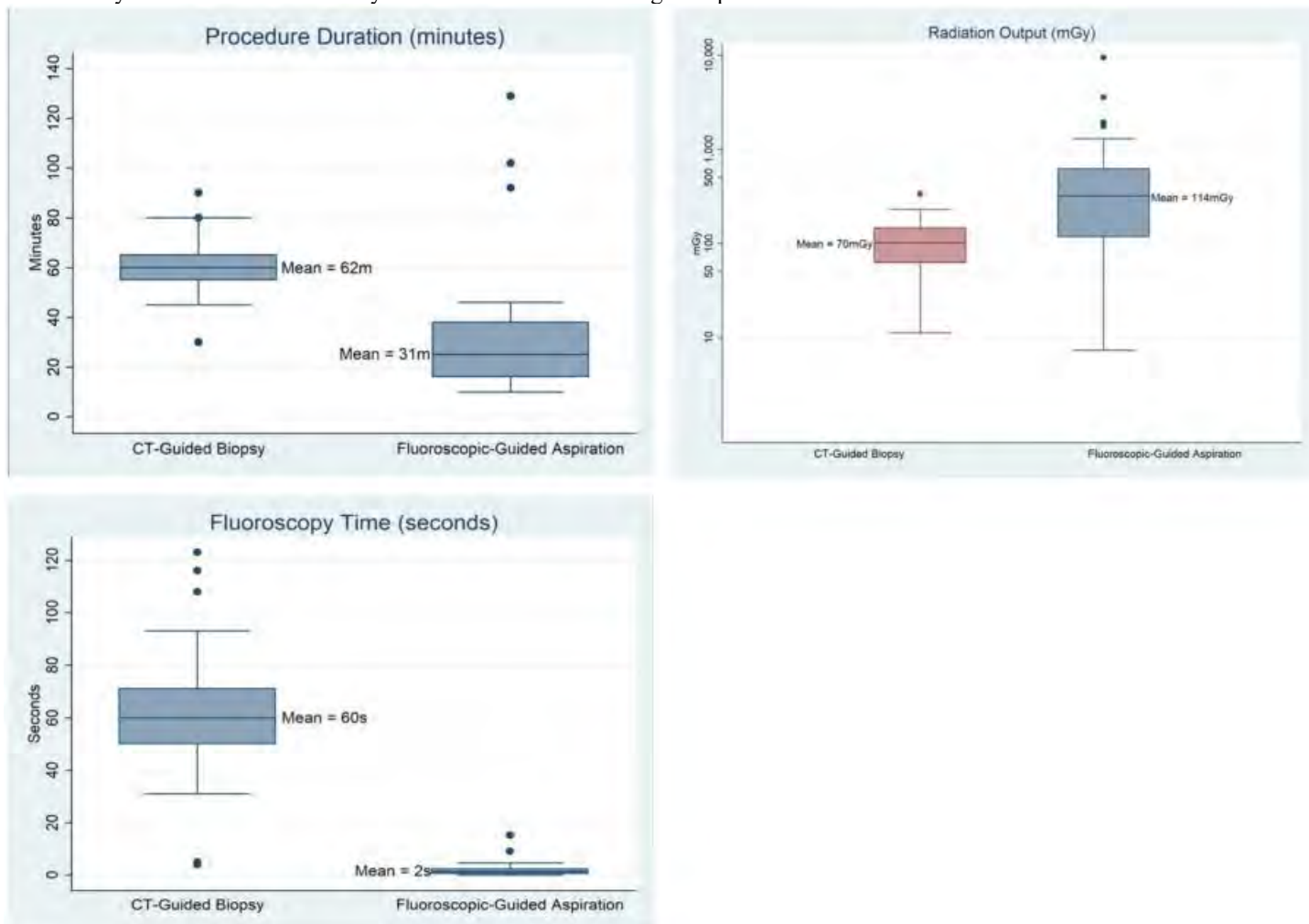
Results

There were no significant differences between the cohorts in terms of demographics, symptom duration, or pre-procedure antibiotics

use. CTB required more anesthesia (26% general anesthesia vs 0%, $p < 0.001$), had longer radiation exposure time (60 ± 24 seconds vs 2 ± 3 seconds, $p < 0.001$), radiation dose (114.4 ± 71.6 mGy vs 70.4 ± 147.2 mGy), and procedure time ($62\text{m} \pm 14$ vs $31\text{m} \pm 23$, $p < 0.001$) than FGA. There was no significant difference in yield (32% in FGA group vs 34% in CTB group, $p = 0.661$), and it was not affected by antibiotic use.

Conclusions

Both FGA and CTB have similar utility in isolating the causative organism in suspected case of spondylodiscitis. Our results suggest that increased radiation exposure, longer procedure time, and increased anesthesia use are relative disadvantages of CTB without an increase in yield. Controlled trials may be beneficial in determining the optimal choice in different scenarios.



(Filename: TCT_161_GraphsCombined.jpg)

1313

A Multi-Layer Realistic Fluoroscopy-Guided Lumbar Puncture Phantom Utilizing 3D Printing with Soft Tissue Tactile Feedback

R Javan¹, D Barreto², M Liu³, A Osorio⁴

¹George Washington University Hospital, Washington, DC, ²George Washington University, Arlington, VA, ³George Washington School of Medicine and Health Sciences, Washington, DC, ⁴The George Washington University, Washington, DC

Purpose

The purpose of this project was to develop a hyper-realistic simulation phantom for fluoroscopy-guided lumbar punctures. The realism goal is both with respect to the appearance under fluoroscopy and especially the soft tissue tactile feedback.

Materials and Methods

CT images of a normal lumbosacral spine study was imported into Materialise InPrint. The interlaminar space was digitally progressively made smaller to increase level of difficulty in the upper lumbar spine compared to the lower spine. This was done in Autodesk 3D Studio Max. The final 3D model extended from T12 to the mid-sacrum Gypsum-based 3D printing was used to create the radiodense hollowed bony anatomy with cortical thicknesses ranging from 2 to 5 mm to allow for visualization of the intricate anatomy with the ability to distinguish cortex and marrow. A semi-rigid rubber tube was inserted in the spinal canal to recreate the

CSF filled dura, with one end sealed and connected to a pressured syringe. The osseous model was immersed in 3 different consistencies of silicone rubber to recreate muscle, fat and skin. However, a cube-shaped space/defect was left in the soft tissues at the L3-L4 and L4-L5 levels. This space is filled for each use with material made by combining polyvinyl acetate glue, contact lens saline solution, and sodium bicarbonate, mixed with water containing hydrogel beads and covered by a taut layer of silicone.

Results

A multi-layer realistic phantom was developed using commercially available low-cost 3D printing technology along with molding techniques for the purpose of teaching and practicing fluoroscopy-guided lumbar punctures. This phantom simulates 5 distinct tissues.

Conclusions

The fluoroscopic appearance of the osseous structures, the realistic soft-tissue tactile sensation provide a great tool to introduce and improve trainees' lumbar puncture skills.

1577

A novel approach to safely perform a percutaneous biopsy of lesions of the petrous apex: An anatomic study on 3D-simulations and printed specimens.

J Core¹, R Pooley¹, V Gupta², A Desai¹, P Vibhute¹

¹Mayo Clinic, Jacksonville, FL, ²Mayo Clinic Florida, Jacksonville, FL

Purpose

The petrous apex has been considered unsafe for percutaneous biopsy as the petrous internal carotid artery resides immediately anterior to the petrous apex. Open surgery, remains the only option available for biopsy of the petrous apex. This study explores feasibility and safety of image-guided percutaneous trajectory to the petrous apex using virtual 3D simulations. Based on the hypothesis that the contralateral approach will be in direct "line of sight" to the petrous apex and posterior to the ipsilateral carotid artery, this study investigates the feasibility of a subzygomatic - mandibular sigmoid (coronoid) notch approach contralateral to the petrous lesion.

Materials and Methods

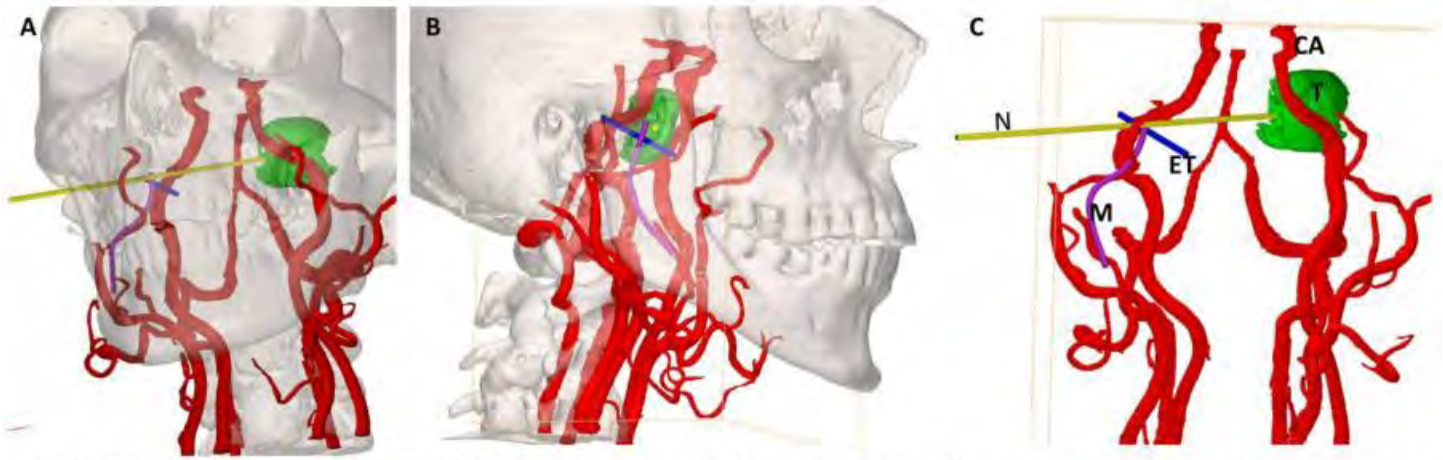
Radiology database was searched for patients with petrous apex lesion who had high resolution CT (whenever available MRI data sets). A total of 14 patients were identified. The DICOM data sets were anonymized and transferred to Materialise segmentation software. Segmentation was performed of the skull base and internal carotid artery using thresholding tools set a specific Hounsfield unit range. The mandibular nerves and Eustachian tubes were created with the "spline" function tool using a fixed diameter of 2.5 mm, to remain faithful to actual anatomy. Internal maxillary artery was not segmented as this invariably courses below the level of mandibular notch. Stereolithography files are generated to enable 3D printing of the phantoms. The Ultimaker S5 desktop 3D printers are to be used for phantom production. For virtual simulations 3 mm thickness biopsy needle was created also using the "spline" function tool. For each specimen virtual percutaneous needle placement simulation was performed in to the petrous apex lesion from the contralateral side via the subzygomatic - mandibular sigmoid (coronoid) notch approach. Placement was considered successful if the needle tip could be successfully placed in the center of the lesion without violating (injuring) all the chosen 3 critical structures.

Results

In all 14 specimens, virtual simulation of needle placement into the petrous apex was consistently possible without injuring the 3 critical structures.

Conclusions

A percutaneous approach to lesions centered in the petrous apex appears to be feasible, though further simulation with 3D phantoms and cadaver specimens are currently ongoing to determine safety and efficacy.



3D Simulation: Needle placement in left petrous apex chondrosarcoma via right subzygomatic-mandibular notch approach. Needle (N): yellow, Tumor (T): green, Carotid artery (CA): red, Mandibular Nerve (M): purple, and Eustachian Tube (ET): blue

(Filename: TCT_1577_PetrousApexBiopsy.jpg)

1100
A Novel Hybrid Human-Machine Interoperability Approach to Quality Assurance in Neuroradiology – Efficiently Identifying Missed Intracranial Hemorrhage Cases in Emergent Care Non-Contrast Head CT

A Wismueller¹, D Shrier¹
¹University of Rochester Medical Center, Rochester, NY

Purpose
 To develop and evaluate a novel hybrid human-AI quality assurance (QA) approach for evaluating radiologists' performance on accurately reporting intracranial hemorrhage (ICH) in emergent care setting head CT scans.

Materials and Methods
 A total of 1936 consecutive non-contrast emergency-setting head CT scans from 2 CT scanners at a large academic hospital were prospectively acquired over 47 consecutive days. Immediately following image acquisition, scans were automatically analyzed for ICH using commercially available software (Aidoc, Tel Aviv, Israel). Cases rated positive for ICH by AI (ICH-AI+) were automatically flagged in radiologists' reading worklists, where flagging was randomly switched off with probability 50%, see e.g. [1]. For ICH-AI+ cases, radiologists' missed ICH detection rates (ratio of number of missed ICH cases and number of all true ICH-AI+ cases) was calculated and compared between flagged and non-flagged ICH-AI+ cases, where images of all ICH-AI+ cases with ICH-negative results detected by natural language processing (NLP) of final radiology reports (ICH-AI+NLP- cases) were re-analyzed by an experienced neuroradiologist to identify true ICH+ cases missed by original radiology readings.

Results
 Among all 1936 CT scans, 381 ICH-AI+ cases were found, of which 190 cases were flagged. A total of 29 ICH-AI+NLP- cases were found, where 6 had been reported ICH+ by the radiology report. Of the remaining non-reported 23 ICH-AI+ cases, neuroradiology expert review identified 6 non-reported true ICH+ cases, where 5 cases were non-flagged, and only 1 case was flagged. This yields radiologists' missed ICH detection rates of 0.52% and 2.5% for flagged and non-flagged cases, respectively.

Conclusions
 Our results suggest that flagging ICH-AI+ cases on radiologists' worklists may decrease the rate of missed true ICH+ cases, although this was not found statistically significant based on small numbers of discordantly reported cases. Yet, our novel method of human expert review of ICH-AI+NLP- cases successfully revealed true ICH+ cases missed by original radiology reports with minimum human effort, and can therefore provide valuable contributions to neuroradiology QA programs as an efficient hybrid human-AI approach. We conclude that combining AI image analysis with NLP-based pre-selection of cases for targeted human expert review can efficiently identify missed findings in radiology reports and thus expedite neuroradiology QA programs.

1031
A Paradigm Shift in Diagnostic Radiology Education via Simulation Training: A Survey

L Shu¹, E Estades², R Thakkar³, D Barreto⁴, M Taheri⁵, R Javan⁵, F Huda⁶
¹Warren Alpert Medical School of Brown University, Providence, RI, ²George Washington university hospital, Silver Spring, MD, ³George Washington University Hospital, CABIN JOHN, MD, ⁴George Washington University, Arlington, VA, ⁵George Washington University Hospital, Washington, DC, ⁶Boston University Medical Center, Boston, MA

Purpose

Currently, radiology training is quite passive for medical students through shadowing experience. In addition, the variety of important and high-yield cases that radiology trainees are exposed to may be limited in scope depending on the institution. We evaluated the usefulness of a freeware, platform-independent, non-workstation dependent secure image database named "Weasis" to take a step towards a more hands-on and active radiology education.

Materials and Methods

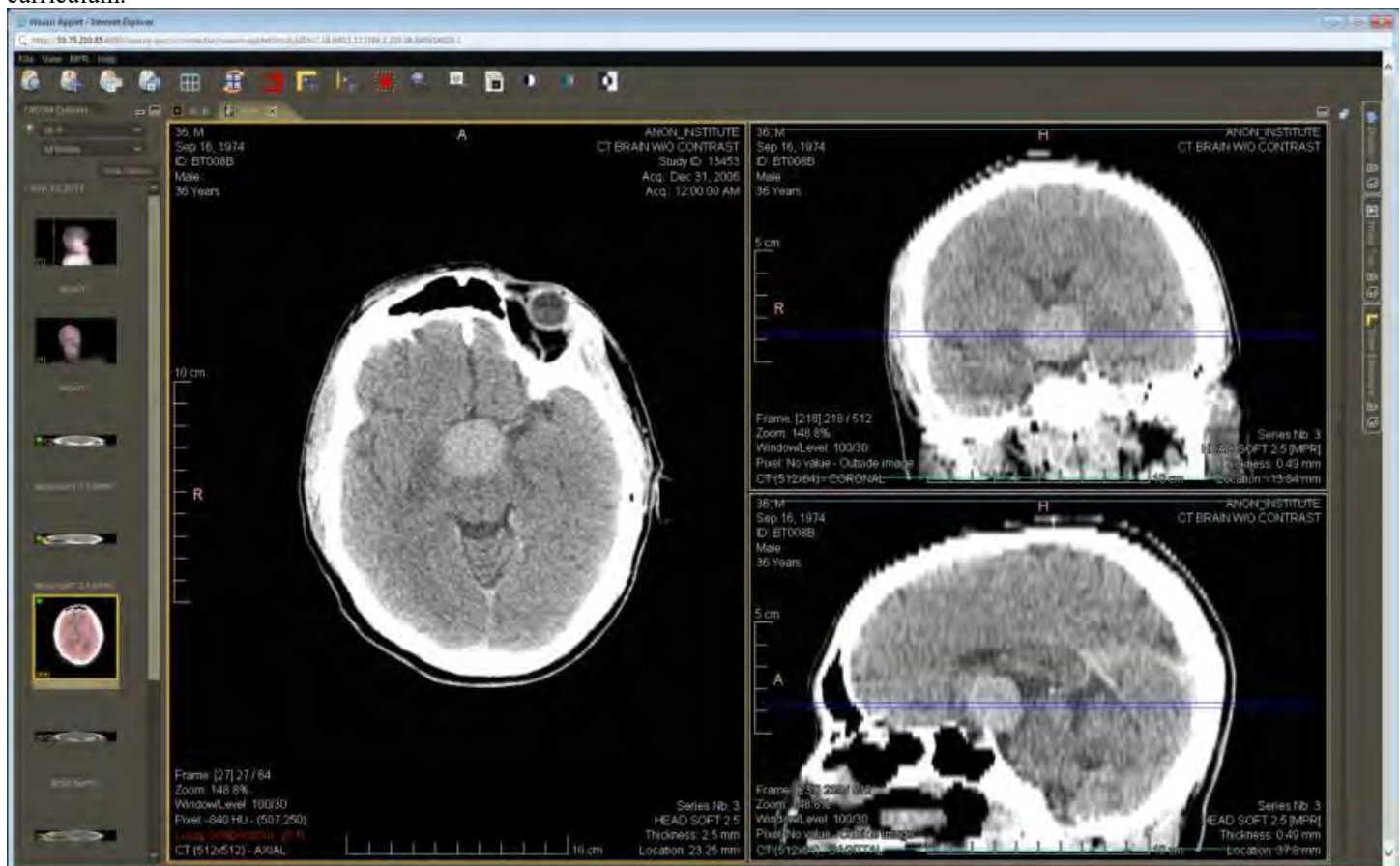
We utilized an open-source dem4chee -based PACS named " Weasis " in order to simulate a radiologist's practice in the real world, using anonymized report-free complete cases that could easily be uploaded live during read-outs for training purposes. MySQL was used for database management and JBOSS as application server. A survey was done over a one-year period of its use.

Results

A total of 40 trainees, 20 medical students and 20 residents/fellows participated in an online survey. Out of the 20 medical students, 19 would like more active learning during the radiology rotation and 17 would like PACS practices. 11 out of 20 of the students who responded to the survey had used Weasis. Out of those 11, 10 would recommend their peers to use Weasis and 9 believe that Weasis is superior to the traditional method (passive shadowing) of radiology training. All 20 residents and fellows surveyed had used Weasis and would recommend it to their peers. 18/20 believe Weasis improved their image interpretation skills, 19/20 would like to continue using Weasis, only 1/20 found it difficult to navigate Weasis, but he/she would still like to continue to use Weasis. 15/20 think Weasis should be incorporated into their residency/fellowship training curriculum.

Conclusions

Utilization of such a low-cost and versatile tool allows training programs to offer medical students an active and more realistic radiology experience, junior radiology residents with potentially better call preparation and senior resident/fellows with the ability to fine-tune high-level specialty-level knowledge. Survey results showed: 1. Most medical students wanted more hands-on (I.e. PACS) experience, 2. Residents/Fellows liked Weasis and think it improves their image interpretation skills, 3. Neither medical students nor residents thought it was difficult to navigate Weasis, 4. Both medical students and residents wanted Weasis to be incorporated into the curriculum.



(Filename: TCT_1031_WeasisBrainTumor-LymphomaCT1.jpg)

1115

A Practical Implementation of a Pipeline for Automatic Glioma Segmentation: Towards Clinical Integration?

E Lotan¹, B Zhang², S Dogra³, D Wang⁴, Y Lui⁴

Purpose

There is a growing body of literature demonstrating the potential of machine learning models for brain tumor segmentation. Furthermore, there is mounting evidence that accurate segmentation of tumor sub-regions (enhancement, edema) can offer the basis for quantitative image analysis towards precision medicine and improvements in individual prognostication. Bringing such tools to clinical reality requires thoughtful implementation. Here, we describe the components required towards clinical deployment of a deep learning-based glioma segmentation model and comment on the challenges.

Materials and Methods

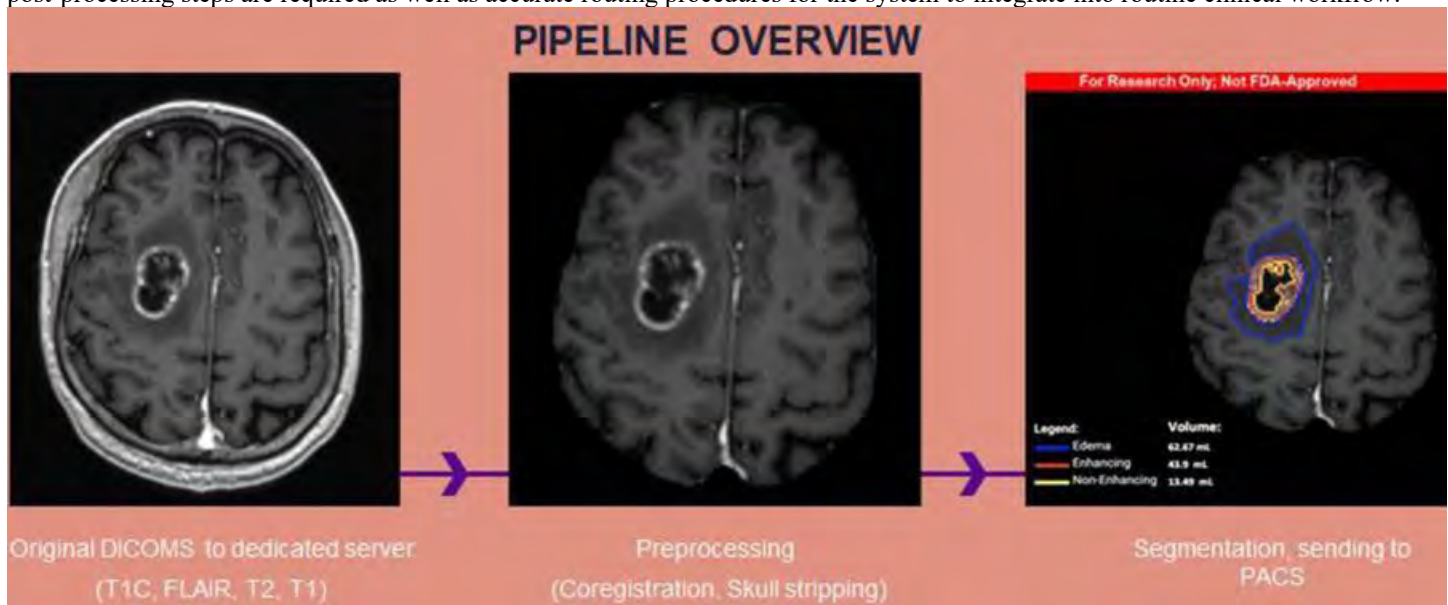
An end-to-end pipeline was constructed to route brain tumor DICOM, automate the segmentation algorithm, and push quantitative results back for clinical viewing. The pipeline operates using two servers: data transmission and inference. The latter is composed of 3 modules: (1) pre-processor for DICOM to NIFTI conversion, coregistration and skull-stripping; (2) segmentation using an in-house deep learning model to produce segmentation for enhancing tumor, necrotic tumor core and whole tumor [1]; (3) post-processor for tumor volume quantification, island-removal and hole-filling operation, followed by reversion to DICOM. A result incorporating segmentation visualization and volumetrics is routed to the clinical PACS environment. Of note, the in-house model is based on fusion of 2 individual models, a cascaded anisotropic convolutional neural network (CACNN) [2] and autoencoder regularization model [3], previously published by separate groups, additionally trained using 100 manually segmented internal postoperative cases and 335 preoperative cases from the 2019 BraTS open-access repository. Our regularized CACNN model achieved dice scores of 0.83 ± 0.09 , 0.84 ± 0.08 and 0.72 ± 0.12 for whole tumor, tumor core and enhancing tumor sub-regions, respectively including both preoperative and postoperative follow-up cases.

Results

Overall total processing time for 1 case is ~7 min including data routing (~1min), preprocessing/segmentation (~4-5min) and post-processing (~1min). An outline of the pipeline and PACS visualization are shown in Figure 1.

Conclusions

We show feasibility for clinical implementation of a deep learning-based model for glioma segmentation. Several pre-processing and post-processing steps are required as well as accurate routing procedures for the system to integrate into routine clinical workflow.



(Filename: TCT_1115_Pipeline_Fig1_300dpi.jpg)

1338

A Prospective Reappraisal of Motor Outcome Prediction in Acute Stroke Patients Using Atlas-Based Diffusion Tensor Imaging Biomarkers

Y Chen¹, S Cheng¹, K Hsieh², C CHEN³, D Kuo¹

¹Taipei Medical University Hospital, Taipei, N/A, ²Taipei Medical University Hospital, Taipei, Taiwan, ³TAIPEI MEDICAL UNIVERSITY HOSPITAL, TAIPEI, TAIWAN

Purpose

Diffusion tensor imaging (DTI) biomarkers can assess and quantify microstructure changes of cerebral white matter (WM) following injuries. This study aimed to determine prospectively whether atlas-based DTI-derived metrics obtained within first week after stroke can predict motor outcomes at 3-month follow-up.

Materials and Methods

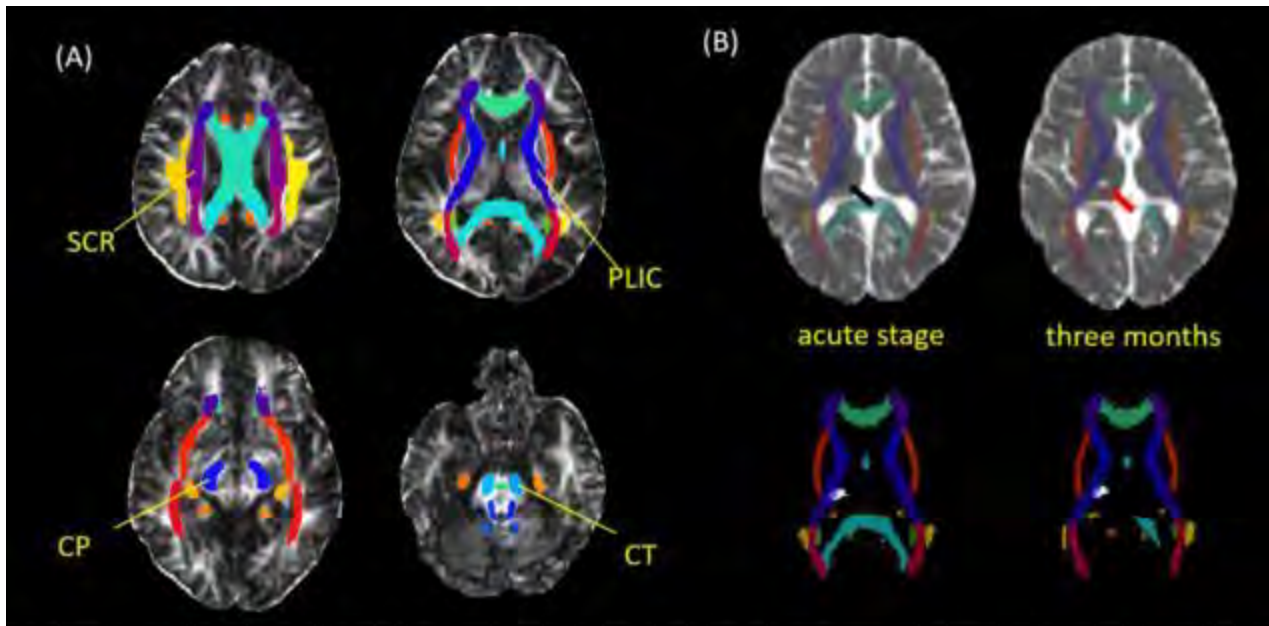
Forty patients with small acute stroke (2-7 days after onset) involving the corticospinal tracts were prospectively included in this study. Each patient underwent magnetic resonance imaging (MRI) exams within seven days and at three months after stroke, respectively, and evolutions using DTI-derived metrics between the two MRI exams were compared using WM tract atlas-based quantitative analysis. All clinical outcomes were measured at three months using the modified Rankin Scale (mRS), National Institutes of Health Stroke Scale (NIHSS) and Barthel index (BI); mRS results were divided into good (0–2) vs. poor (3–5) outcomes.

Results

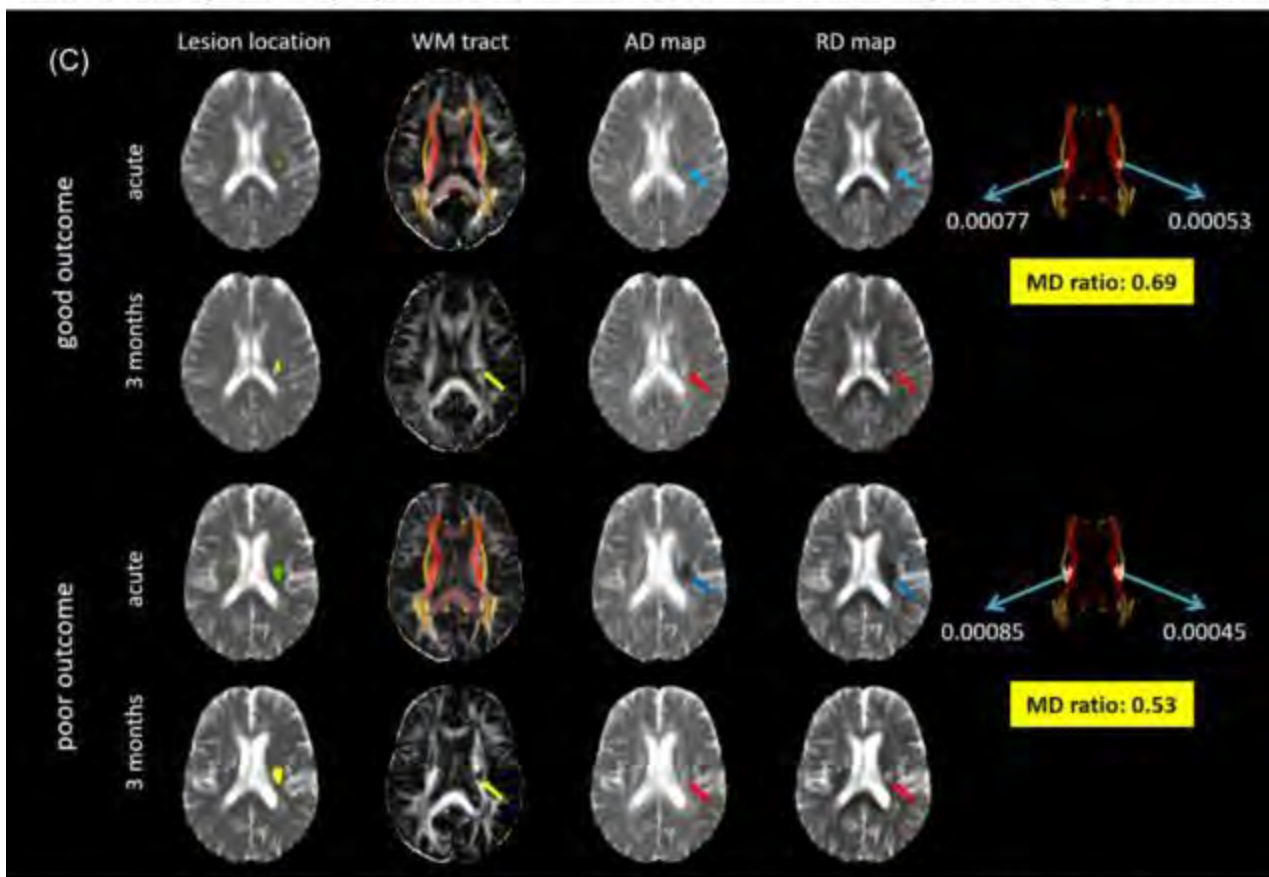
Thirteen (32.5%) of 40 patients who had lower BI, higher mRS and NIHSS had poor prognosis outcomes (mRS 3-4) at three months follow-up after stroke onset. DTI-derived metrics such as axial diffusivity (AD) and mean diffusivity (MD) ratios obtained at acute stage were significantly lower in patients with poor prognosis as compared to those with good prognosis (median MD ratio 0.66 vs. 0.72, $p = 0.049$; median AD ratio 0.58 vs. 0.67, $p = 0.021$). MD, AD, and radial diffusivity (RD) ratios increased significantly from acute stage to three months, regardless of good or poor prognosis (all p -values <0.001). Significant decrease was observed in fractional anisotropy (FA) ratios in lesions involving the posterior limbs of internal capsules (PLIC) and superior corona radiata (SCR) from acute stage to three months. Similarly, the area under the curves of MD, AD, RD ratios in PLIC and SCR were 0.875 ($p=0.002$), 0.868 ($p=0.003$), and 0.836 ($p=0.007$), respectively, for predicting three-month outcome.

Conclusions

Atlas-based DTI-derived metrics at acute stroke may provide objective and comprehensive evaluation of injured WM and are good surrogate indicators for predicting motor outcomes at three months in patients with stroke. For subgroup of patients with stroke involving PLIC and SCR, the DTI metrics may provide further therapeutic stratification for individualized rehabilitation programs.



(A) Four anatomical levels that form part of the CST pathway were selected in the individual atlas. In the telencephalon, SCR indicates superior corona radiata; PLIC indicates posterior limb of internal capsule. In the midbrain and brain stem, CP indicates cerebral peduncle; CT indicates corticospinal tract. (B) Individual atlas produced in acute stage and at three months were projected onto DTI-derived maps (i.e., FA, MD, AD and RD) in acute stage and at three months, respectively. The infarct showed lower SI (black arrow) on the MD map in acute stage while higher SI (red arrow) was shown at three months. The infarct is depicted manually (white-colored area) in acute stage, which was superimposed onto the individual atlases in (A) Four anatomical levels that form part of the CST pathway were selected in the



(C) Lesion locations were depicted manually on MD maps in acute stage (green-colored area) and then placed on MD maps required at three months (yellow-colored area) to evaluate changes in DTI metrics within three months. Markedly decreased AD and RD on the PLIC as compared with the contralateral side reflects the loss of axonal integrity (blue arrows). At three months, markedly increased AD and RD were observed (red arrows), while FA remained decreased (yellow arrows). In our series, patients with a MD ratio greater than 0.653 had good outcomes.

(Filename: TCT_1338_Fig1.jpg)

A Rare Case of Pediatric Brain Tumor: Congenital Glioblastoma

A Lima Júnior¹, J Rodrigues², P Coimbra¹, N De Abreu¹, L Gomes³, M Buratti Leal¹, A Sampaio Clarindo¹

¹Hospital Antonio Prudente, Fortaleza, Ceará, ²Antonio Prudente Hospital, Ceará, Fortaleza, ³UniRV, Goianésia, Goiás

Purpose

Congenital brain tumors are considered extremely rare, accounting for about 0.5 - 1.9% of all pediatric brain tumors. Among these neoplasms, congenital glioblastoma (GBMc) has a prevalence of 2 to 9% of these tumors. The case to be discussed is that of a newborn with a diagnosis of congenital glioblastoma, with an emphasis on clinical history, imaging and histopathological findings.

Materials and Methods

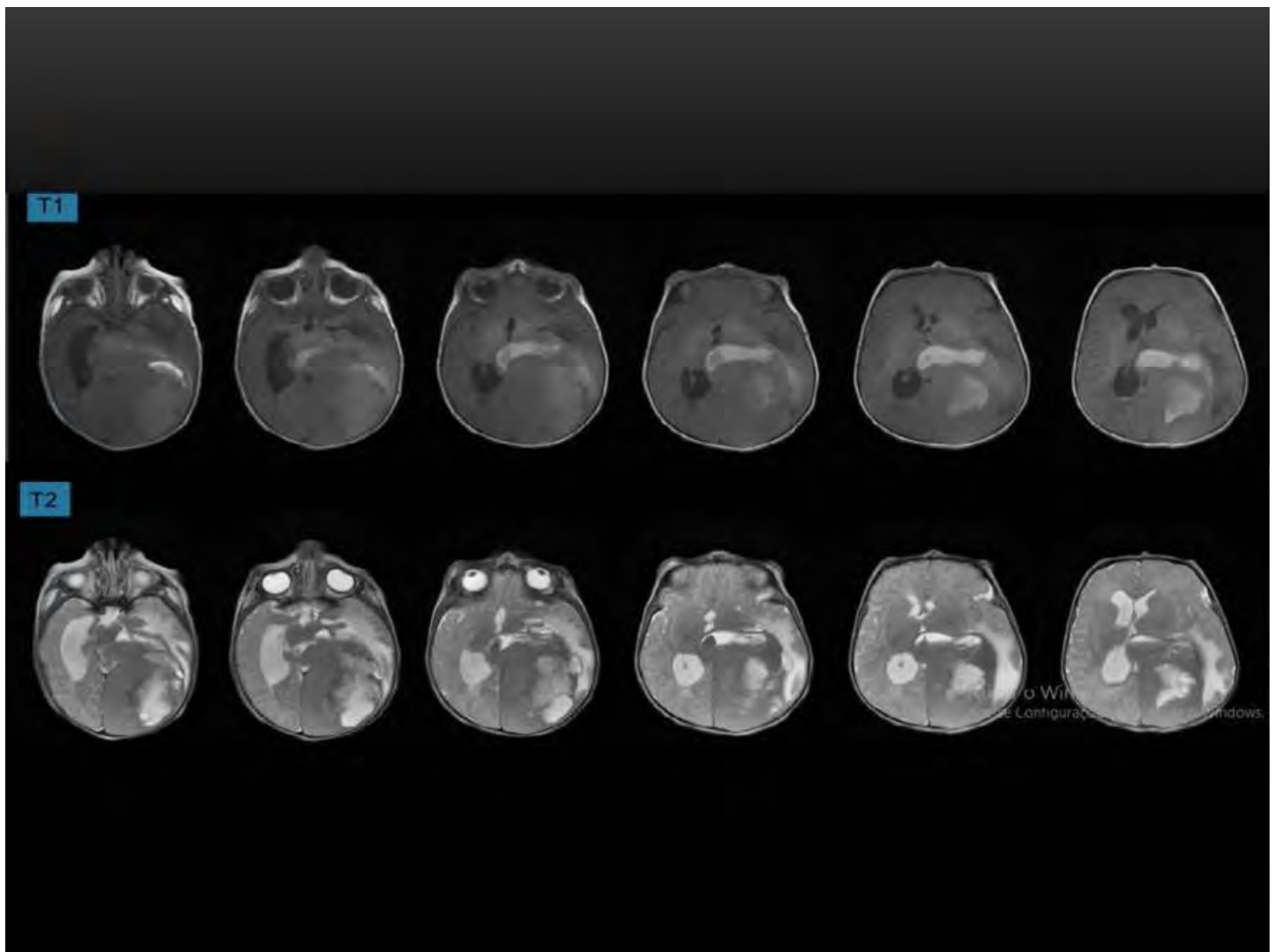
The case reported is that of an asymptomatic child, 20 days old, when, during a routine consultation with a pediatrician, an increase in head circumference was observed. Undergoing transfontanellar ultrasound that showed hydrocephalus, extensive parenchymal hematoma and expansive formation. MRI was performed to better evaluate the formation that showed a massive infiltrative lesion, with heterogeneous enhancement, delimiting central areas of necrosis with hematic material inside, determining a compressive effect on the adjacent parenchyma. Immunohistochemistry and methylation of tumor DNA were performed, which were compatible with glioblastoma.

Results

Congenital glioblastoma is one of the rarest types of congenital brain tumor, with less than 50 cases reported in the literature. It is a tumor histologically similar to other GBMs, presenting with high cellularity associated with necrosis, vascular proliferation and increased mitotic activity. Our case can be classified in the category probably congenital, since the initial findings were in the third week of life. Most pediatric tumors have an infratentorial location, while GBMc has a supratentorial predilection, a fact similar to the case in question.

Conclusions

Transfontanellar ultrasound was performed, which demonstrated extensive parenchymal hematoma, associated with expansive formation and hydrocephalus. Magnetic resonance imaging (MRI) show voluminous infiltrative lesion, with heterogeneous enhancement, delimiting central areas of necrosis, with the presence of hematic material inside it, involving a large part of the left cerebral hemisphere, associated with the important compressive effect of the adjacent parenchyma. Although there has been an improvement in prenatal diagnosis over the past few years, adequate clinical, pre and post-surgical management remains quite challenging, mainly due to the rarity of the disease, generating limited information for the production of adequate protocols in the treatment of this condition.



(Filename: TCT_712_Slide1.JPG)

629

A Retrospective Review of the utility of Gadolinium Contrast imaging in evaluation of Seizures in a Pediatric population.

R Hegde¹, A Vegunta¹, G Parmar¹, R Ismail¹, A Malhotra²

¹Bridgeport Hospital Yale New Haven Health system, Bridgeport, CT, ²Yale University School of Medicine, New Canaan, CT

Purpose

In a recent survey by Society of Pediatric radiology for evaluation of seizures, 11% respondents favored always using Gd contrast, 13% did it usually and 32% using Gd sometimes. Repeat administration of contrast in patients with chronic seizure disorders is an emerging concern. The purpose of this study was to estimate the prevalence of contrast enhanced MRI brain studies performed for evaluation of seizures at our tertiary care center and to identify whether contrast was of significant utility in terms of diagnostic outcomes.

Materials and Methods

Retrospective review of our imaging database was performed from Oct 2016 to Oct 2020 to identify all the MRI brain studies ordered for seizures and epilepsy in patients up to 18 years. A total of 2122 MRI imaging reports were reviewed after excluding non-diagnostic/limited diagnostic studies. These reports were separated into noncontrast and contrast studies. Studies performed with contrast were divided into negative studies; positive studies classified into 2 groups- contrast was beneficial in reaching the diagnosis or as contrast was not of additive benefit. Noncontrast studies were classified as negative; positive studies were classified into 2 groups- cases where diagnosis could be reached without aid of contrast or cases where subsequent evaluation with contrast was needed or recommended.

Results

2122 MRI brain imaging reports were reviewed. Age distribution of the cohort was 252 neonates/infants (under the age of 1), 645 between ages 1-5 and 1225 ages 5-18 years. 971 studies (45.7%) were performed with contrast and 1151 were noncontrast (54.3%).

Contrast studies were classified as negative (n=533), positive but contrast was of no additive benefit (n=271) and positive and contrast was beneficial in diagnosis (n=167). Noncontrast studies were classified as negative (n=638), positive where further contrast evaluation was not required (n=482) and positive with need or recommendation of further evaluation with contrast (n=31). The percentage of negative cases and cases where contrast was not beneficial from the total contrast enhanced studies was 82.8% (804/971). Only 2.7 % of the noncontrast studies had need or recommendation for subsequent contrast evaluation.

Conclusions

Contrast should be reserved for specific clinical scenarios or when noncontrast imaging demonstrates underlying abnormality. Routine use of gadolinium contrast should be restricted especially given as yet unknown long-term concerns for gadolinium deposition.

389

A Retrospective Study of the Unexplained Phenomenon of the Wandering Carotid Arteries

A Nayate¹, J Durieux²

¹University Hospitals Cleveland medical center, Cleveland, OH, ²University Hospitals Cleveland Medical Center, Cleveland, OH

Purpose

Change of position of the cervical carotid arteries, termed the wandering carotid artery (WCA), on serial neck imaging has no clear etiology. Exact knowledge of the location of the cervical carotid arteries is critical to avoid surgical mishaps. In our clinical practice, we noticed that carotid arteries move primarily in obese patients on serial scans. Therefore, we hypothesized that an increased body mass index (BMI) is associated with an increased prevalence of WCA.

Materials and Methods

We retrospectively analyzed CT/MRI neck scans for 56 random patients who had imaging between 2012-2017 and no history of prior extensive neck procedures. We determined the position of the common and internal carotid arteries at the level of the thyroid cartilage, hyoid bone, and suprahyoid region. Location of the carotid arteries were labeled as lateral to the border of the pharynx, marginally retropharyngeal, and retropharyngeal and change in position was denoted when the carotid arteries moved at one of these locations on serial scans. We correlated patients' demographic and medical information including age, gender, history of type 2 diabetes and hypertension, carotid atherosclerosis, abdominal circumference (AC), and BMI as well as position of the aortic arch with the prevalence of a WCA. To determine if there are differences between groups, independent t-test or Wilcoxon-Mann-Whitney test was used for continuous variables and chi-square or Fisher's exact tests for categorical measures. Logistic regression with profile-likelihood estimation and Firth adjustment were used to determine the magnitude of the relationship between BMI and WCA.

Results

Mean age of patients was 55.23±19.04 years and 51% (29/56) were female. The estimated prevalence of wandering artery was 42.86 (95%CI: 29.48–56.23). The AC and BMI were higher in patients with WCAs compared to patients without (AC= 102.9±14.13 cm vs. 91.61±13.9 (p=0.01) and BMI= 34.27±8.58 (obese) vs 26.21±4.89 (overweight) (p=0.0001)). After adjusting for age, gender, hypertension, diabetes, atherosclerosis grade, and aortic arch location, the odds of WCA increase by 23% (95%CI:1.1-1.44) for every one-unit increase in BMI.

Conclusions

There is a higher prevalence of WCAs in obese patients with large abdominal circumference irrespective of age, gender, and history of diabetes, hypertension, or carotid atherosclerosis. Radiologists and clinicians should be aware of this relationship avoid potential surgical mishaps and incorrect diagnoses.

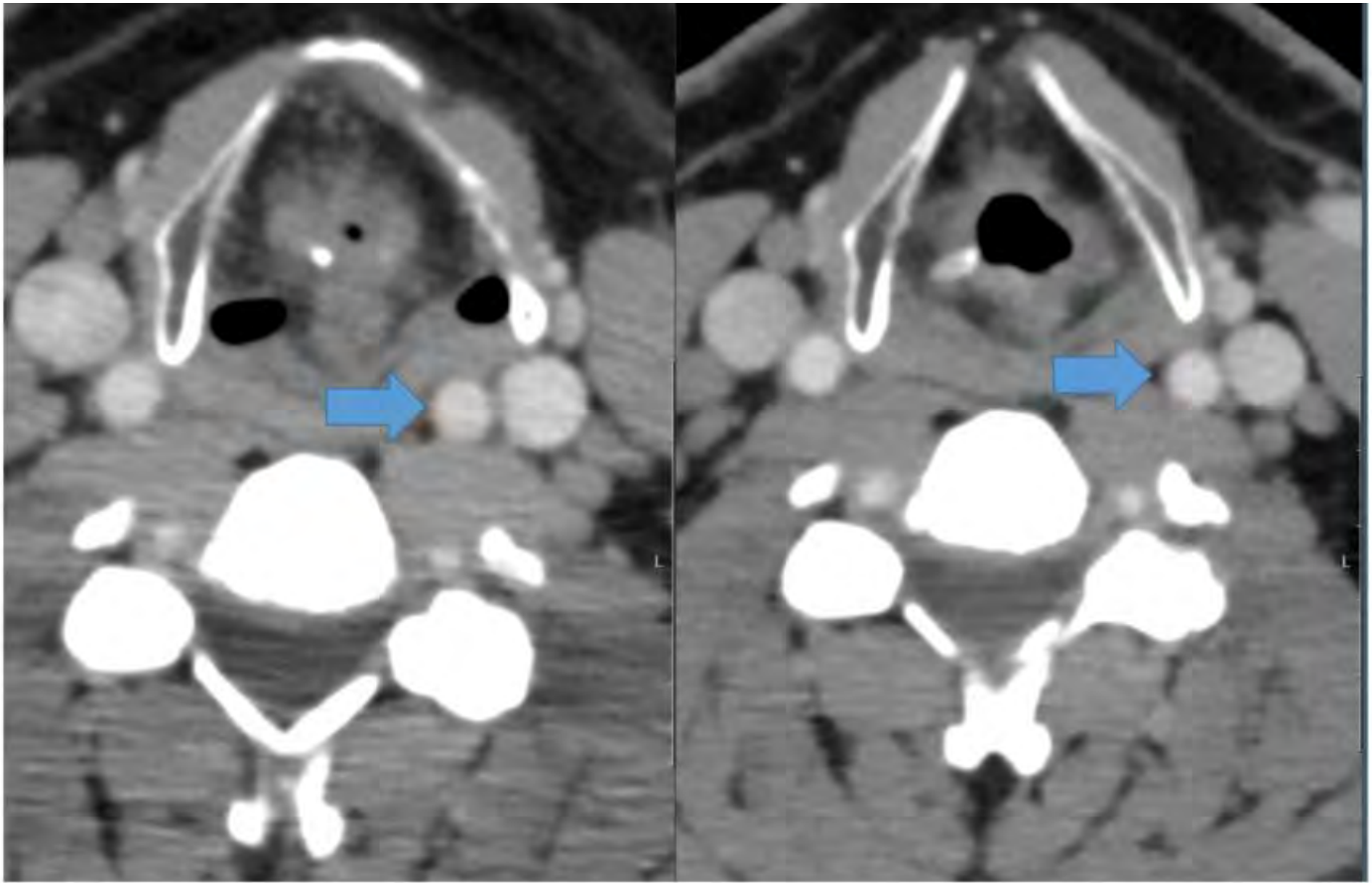


Figure 1: Example of the wandering carotid artery. Movement of the left common carotid artery (blue arrow) on 2 CT neck studies performed approximately 5 months apart.

(Filename: TCT_389_Picture1.jpg)

210

A solitary hypothalamic metastasis from prostatic cancer mimicking a giant thrombotic aneurysm and presenting with intraventricular hemorrhage and acute hydrocephalus.

H Sotoudeh¹, Z Saadatpour², A Rezaei², A Singhal³, K Tavakol⁴

¹UAB, Birmingham, AL, ²University of Alabama at Birmingham, Birmingham, AL, ³N/A, N/A, ⁴Howard University, Washington DC, DC

Purpose

Despite the high prevalence of prostate cancer, its brain parenchymal metastasis is not common and intracranial hemorrhage due to such a metastasis is even less common. This report presents a challenging case of solitary brain metastasis secondary to prostate cancer that gave rise to intraventricular hemorrhage and acute hydrocephalus mimicking a giant aneurysm.

Materials and Methods

Case Presentation: A 77-year-old man with a history of prostate cancer, hypertension and morbid obesity presented to the emergency room with severe headache. He was afebrile with a blood pressure of 144/79 mmHg, alert, without any sign of sensory or motor deficit. Shortly after admission, he became unresponsive and was immediately intubated. His blood tests revealed hypernatremia at 154mmol/L, otherwise the lab data including the COVID-19 screening proved normal. The cerebral CT and MR images, with and without contrast, were interpreted as a giant thrombotic aneurysm extending to the supra-sellar region by the emergency radiologist. Also, moderate intraventricular hemorrhage, acute hydrocephalus, and sub-ependymal interstitial edema were observed. Upon further evaluation of images, the lesion was determined to be an exophytic hemorrhagic hypothalamic mass, and the subsequent biopsy was consistent with prostate cancer metastasis.

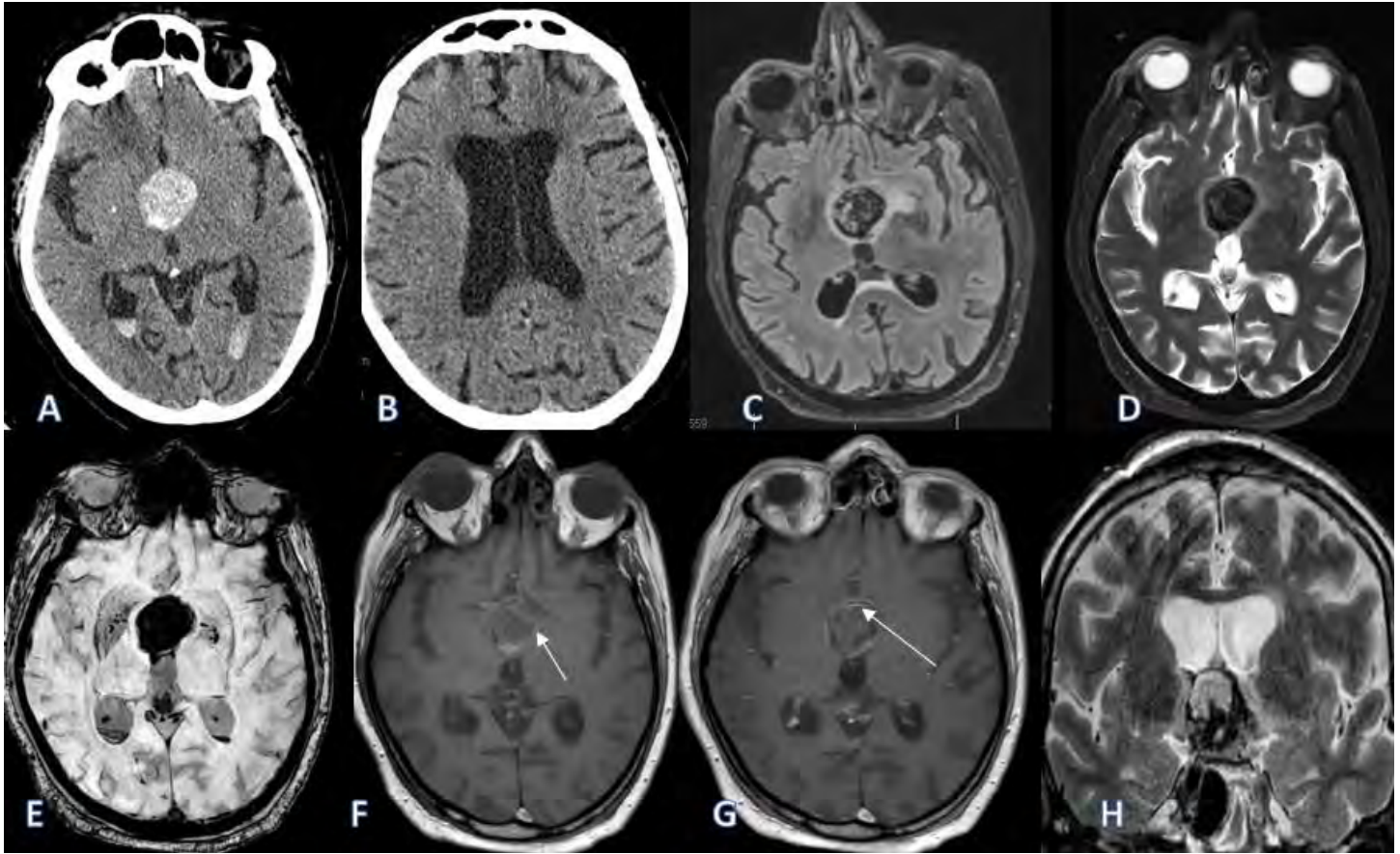
Results

Figure 1: Axial non-contrast CT shows a well-defined hyperdense lesion in the supra-sellar cistern associated with intraventricular hemorrhage and acute hydrocephalus (A & B). The lesion is seen to have low signal on FLAIR (C) and T2 (D) with a signal drop on

SWI (E). The lesion shows laminar morphology on T1 (F) and post-contrast T1 (G) but without enhancement. On the coronal T2 (H), the lesion appears to be an an exophytic mass from the hypothalamus with peripheral parenchymal edema.

Conclusions

An exophytic hemorrhagic hypothalamic metastasis can mimic a ruptured aneurysm on imaging. Given the improved survival of patients with prostate cancer, radiologists may encounter such unusual cerebral metastases from prostate cancers more frequently in the future.



(Filename: TCT_210_Fig110-15-2020.jpg)

1443

A workflow efficient PACS based automated brain tumor segmentation and radiomic feature extraction

M Aboian¹, K Bousabarah², W Holler², E Kazarian³, A Mahajan¹, A Malhotra¹, M Lin⁴, M Westerhoff²

¹Yale University School of Medicine, New Haven, CT, ²Visage Imaging GmbH, Berlin, Germany, ³Brain Tumor Research Group, Yale University School of Medicine, Greenwich, CT, ⁴Yale University, New Haven, CT

Purpose

The concept of personalized medicine includes individual assessment of a patient's imaging study characteristics that informs an individually tailored treatment. Extraction of imaging biomarkers from a region of interest has shown promise in predicting molecular features and treatment outcomes in glioblastoma (GBM), but progress has been limited due to time intensive manual segmentation process. Deep learning artificial intelligence is a powerful tool for automated segmentation although integrating this tool into the clinical workflow has been challenging. In this work, we implemented a deep learning-based algorithm for automated brain tumor segmentation and embedded it into PACS to accelerate a supervised, end-to-end workflow for radiomic feature extraction.

Materials and Methods

An algorithm was trained to segment primary brain tumors on MRI FLAIR images using BRATS dataset with multi-institutional and multi-sequence MRI scans of glioblastoma and lower grade glioma. The U-Net deep-learning network architecture was employed and algorithm was embedded into Visage 7 (Visage Imaging, Inc., San Diego, CA) diagnostic workstation. The automatically segmented brain tumor was pliable for manual modification. PyRadiomics (Harvard Medical School, Boston, MA) was natively embedded into Visage 7 for feature extraction from segmentations in form of JSON files. Time for segmentation, feature extraction, and quality of the segmentations was compared to a board-certified neuroradiologist.

Results

On our system (Titan Xp, NVIDIA, Santa Clara, CA) the AI brain tumor segmentation took on average 35.8 ± 1.4 seconds and the

median dice similarity coefficient was good at 86%. Finally, extraction of radiomic features took on average 5.8 ± 0.01 seconds. Both steps can be performed automatically before the radiologist opens the study in a future implementation. The integration of the automated segmentation algorithm into the standard PACS viewer and the ability to use the viewer's standard tools to adjust the segmentation if needed, has proven to make advanced quantitative image volume analysis much more accessible in clinical practice.

Conclusions

Integration of advanced image-based algorithms and extraction of imaging biomarkers into PACs systems can accelerate translation of research into development of personalized medicine applications in the clinic. The ability to use familiar clinical tools to revise the AI segmentations on the diagnostic workstation reduce the time needed to generate ground-truth data.

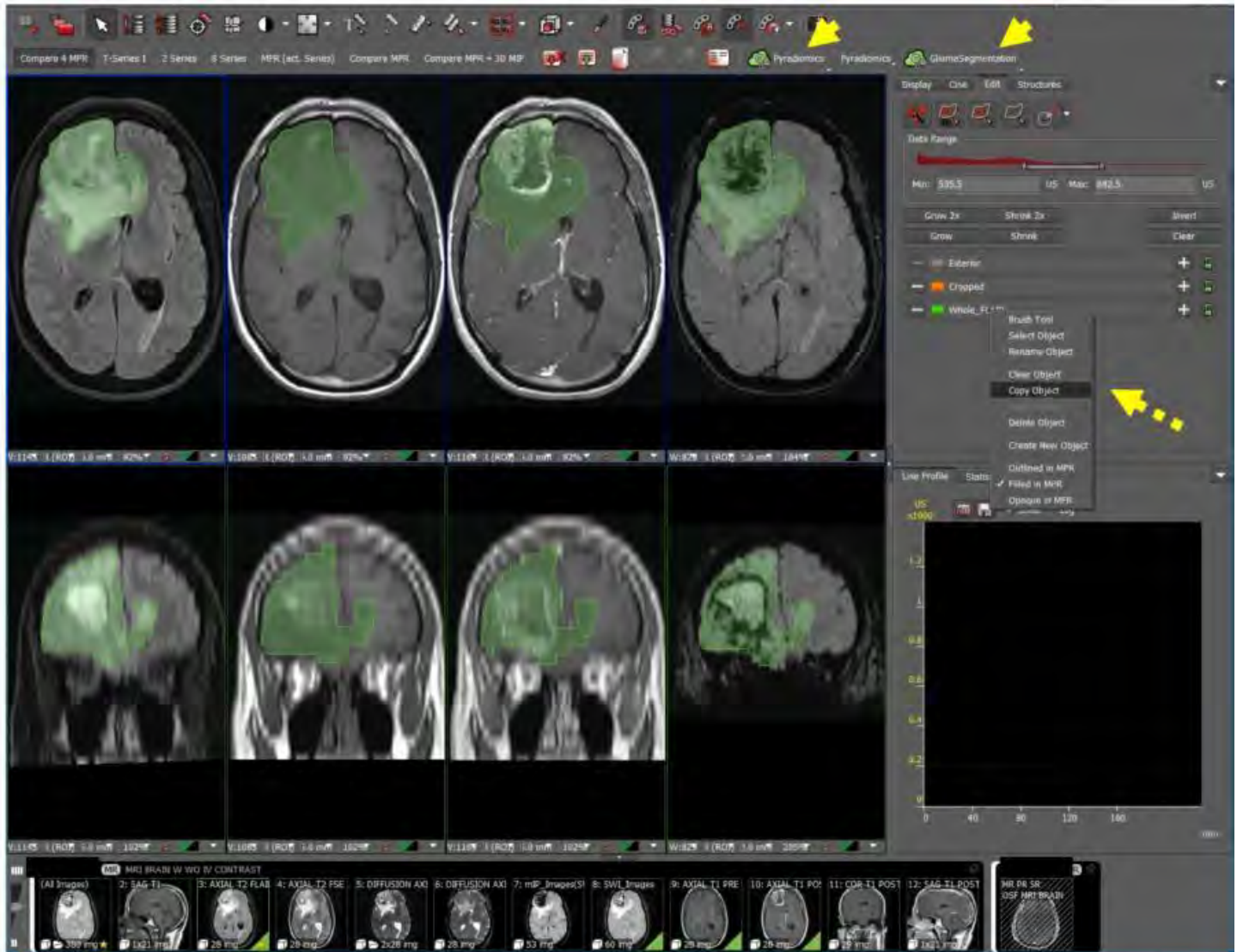


Figure 1: Auto-segmentation and feature extraction tool on clinical PACS station allows incorporation of radiomic based analysis into clinical workflow. Auto-segmentation and PyRadiomics feature extraction buttons are incorporated into the user interface (yellow arrowheads). The auto-segmentation of tumor and surrounding edema is performed on FLAIR images and can be copied onto other sequences using copy object feature (yellow dashed arrow).

(Filename: TCT_1443_GBM_segmentation_figurecopy2.jpg)

752

Absence of Pontine Perforators in Vertebrobasilar Dolichoectasia on Ultra-high-resolution Cone-Beam Computed Tomography

T Dobrocky¹, P Mordasini²

¹Inselspital, Bern, Switzerland, ²Inselspital, Bern, Bern

Purpose

Vertebrobasilar dolichoectasia (VBDE) is a rare type of non-saccular intracranial aneurysm, with poor natural history and limited effective treatment options. Visualizing neurovascular microanatomy in patients with VBDE has not been previously reported, however may yield insight into the pathology, and provide important information for treatment planning.

Materials and Methods

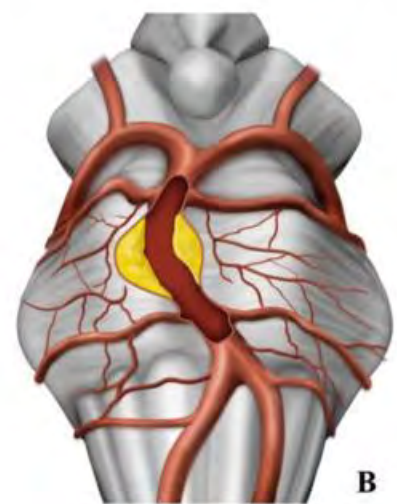
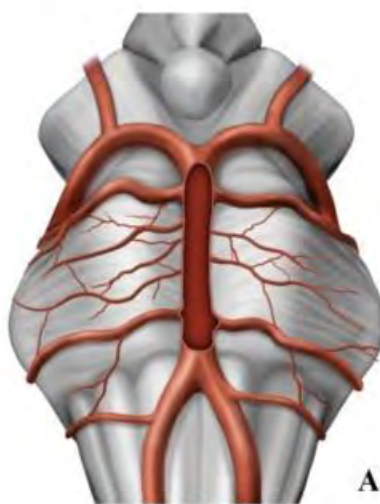
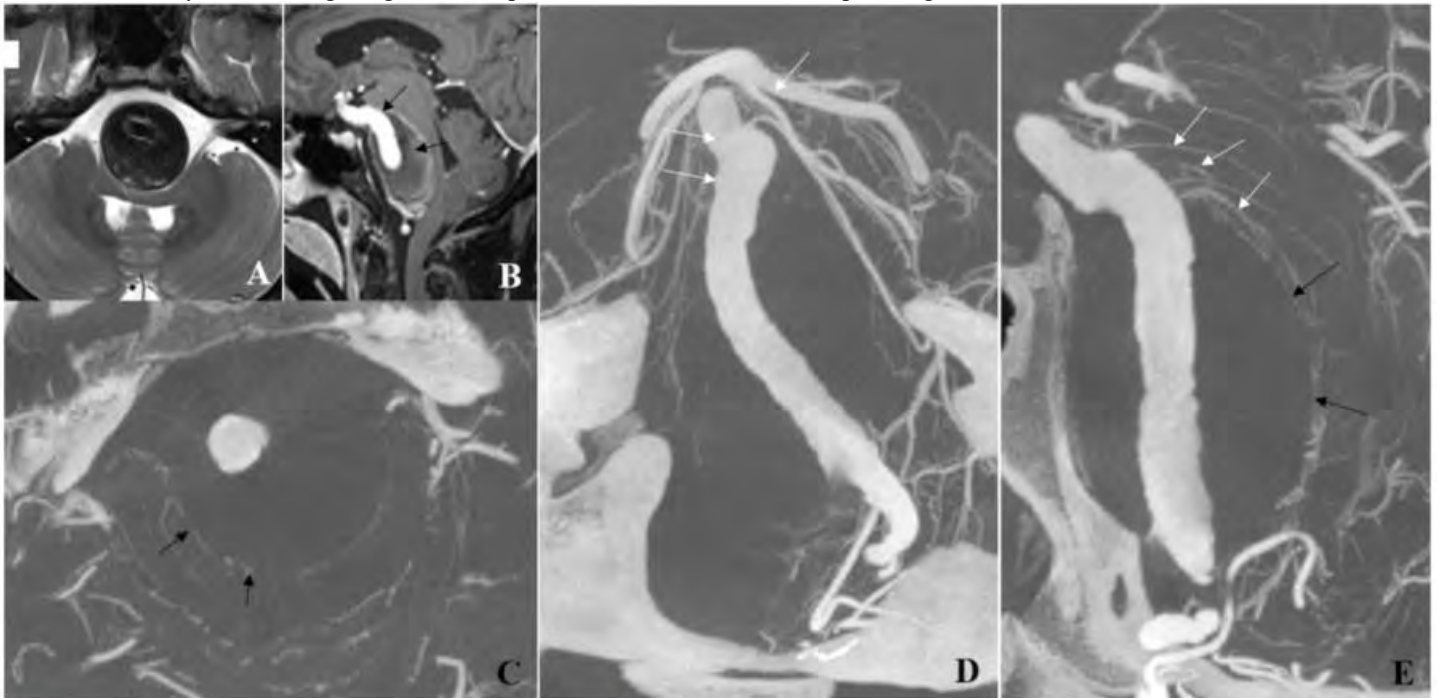
Ultra-high-resolution cone-beam computed tomography (UHR-CBCT) was performed in 7 patients (mean age: 59 years; 2 female) with a VBDE, and in 14 control patients with unrelated conditions.

Results

The mean maximum diameter of the fusiform vessel segment was 29 mm (range: 9 – 36 mm), and the mean length of the segment was 38 mm (range: 15 – 50 mm). In all VBDE patients UHR-CBCT demonstrated an absence of perforating arteries in the fusiform arterial segment and a mean of 3.7 perforators arising from the unaffected vessel segment. The network of interconnected superficial circumferential pontine arteries (brainstem vasocorona) were draping around the aneurysm sack. In controls, a mean of 3.6, 2.5, and 1.2 perforators were demonstrated arising from the distal, mid, and proximal basilar artery, respectively.

Conclusions

The absence of pontine perforators in the fusiform vessel segment of VBDE is counterbalanced by recruitment of collateral flow from pontine perforators arising from the unaffected segment of the basilar artery, as well as collaterals arising from the AICA/PICA and superior cerebellar artery (SCA). These alternative routes supply the superficial brainstem arteries (brainstem vasocorona) and sustain brainstem viability. Our findings might have implications for further treatment planning.



(Filename: TCT_752_ASNR.jpg)

Absence of susceptibility vessel sign is associated with aspiration-resistant fibrin/platelet-rich thrombi

J Darcourt¹, C Garcia², F Bonneville¹, B Payrastra², C Cognard¹

¹Toulouse University Hospital, Toulouse, France, ²INSERM, U1048 and University Toulouse 3, I2MC, Toulouse, Toulouse, France

Purpose

The composition of the thrombus influences its retrievability by mechanical thrombectomy (MT). The purpose of our study was to report on thrombi resistant to aspiration, regarding susceptibility vessel sign and histologic composition.

Materials and Methods

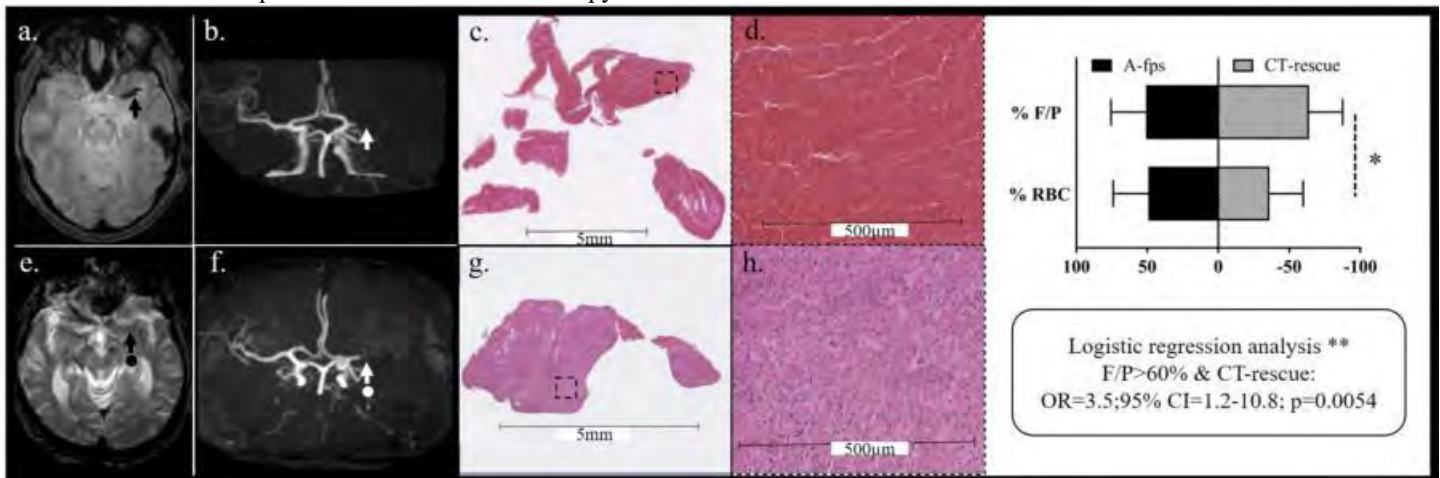
This observational study was based on a prospective database of acute anterior circulation ischemic strokes treated by MT. Endovascular first line strategy was aspiration (A-fps) and in case of failure, combined therapy (CT-rescue) was performed. The positivity of SVS (SVS+) or its negativity (SVS-) was assessed on T2* sequences. The thrombus composition was analyzed with hematoxylin eosin staining.

Results

Histological analysis was performed on 102 clots. Thrombi with SVS- were significantly richer in fibrin/platelets (F/P), $p=0.04$. Out of 210 MT, A-fps was performed in 131/210 (62%) patients. CT-rescue was needed in 37% of A-fps cases ($n=131$). Clots retrieved CT-rescue were richer in F/P 63.9% versus 50.8% for A-fps, $p=0.03$. Logistic regression analysis showed that F/P-poor clots (<60%) were significantly more likely to be recanalized by A-fps compared to F/P-rich clots (>60%) that were more likely recanalized by CT-rescue after A-fps failure (OR=3.5;95% CI=1.2-10.8; $p=0.0054$).

Conclusions

Our results confirm that SVS- clots are rich in F/P and suggest that these "white clots" are less likely to be retrieved by aspiration alone and more often require the use of combined therapy.



(Filename: TCT_515_Figure3V3.jpg)

1542

Accelerating AI: Mining Historical Image Annotations for Automated Tumor Detection on Brain MRI

N Swinburne¹, V Yadav¹, J Kim², K Juluru¹, D Gutman¹, A Ilica¹, A Holodny¹, R Young¹

¹Memorial Sloan Kettering Cancer Center, New York, NY, ²Weill Cornell Medical College, New York, NY

Purpose

Artificial intelligence (AI) applications for cancer imaging conceptually begin with automated tumor detection, which can provide the foundation for downstream AI tasks, including tumor segmentation, genomic classification, and treatment response assessment (1). Performing dedicated post-hoc image labeling is burdensome and costly. Here we data mine tumor annotations already present in our PACS, providing large quantities of training data for detection models (2) to establish multi-modality cancer detection tools.

Materials and Methods

We mined our cancer center's PACS for all annotated brain MRIs acquired from 2012-2017 (3). Our curation pipeline converted line measurement annotations to boxes, merged overlapping boxes, and excluded boxes <1 cm (likely too small for accurate downstream segmentation) or >7 cm (often drawn to measure brain midline shift). The resulting boxes were used for supervised training of object detection models using RetinaNet (4) and Mask R-CNN (5) architectures. To contend with incomplete labeling of tumors in our training dataset (reflecting "reporting bias" common in clinical radiology), the best performing detection model trained from our mined dataset was then used to detect unannotated tumors on the training images themselves ("bootstrapping"), thus automatically

correcting many of the missing labels on these images. After bootstrapping, a new model was trained from scratch using this expanded training dataset. All models were scored on a held-out ground truth test dataset comprising 754 manually labeled brain MR images from 100 patients with enhancing tumors.

Results

The initial PACS query extracted 31,150 individual axial post-contrast T1 image line annotations, yielding 11,987 boxes meeting inclusion criteria. This mined dataset was used to train models attaining 91.1% (RetinaNet) and 91.6% (Mask R-CNN) average precision (AP; minimum 0.5 intersection-over-union). Bootstrapping identified an additional 12,352 boxes for training, yielding models with 94.6% and 95.7% AP, respectively.

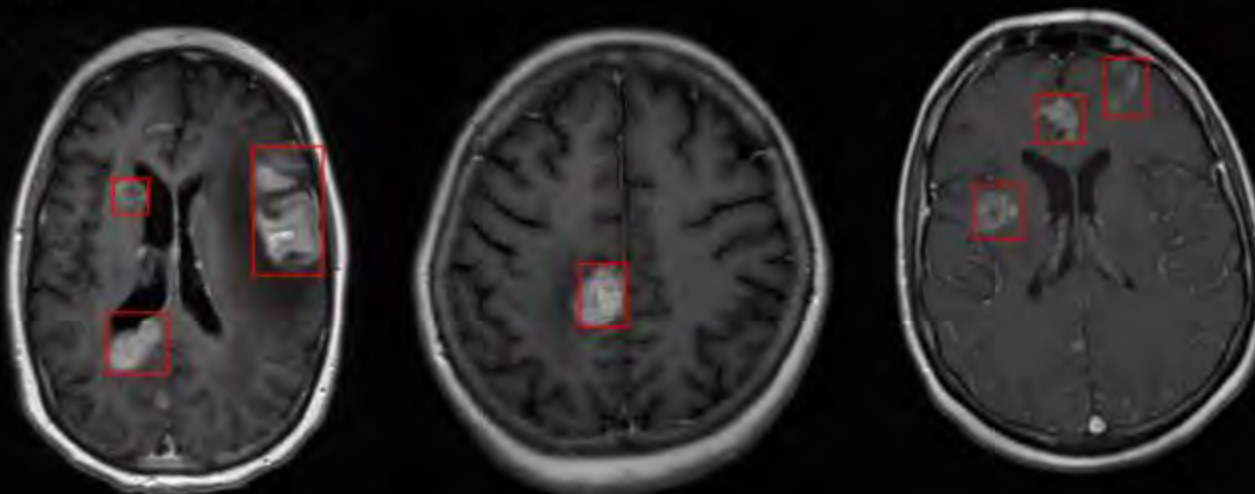
Conclusions

Utilizing only mined historical image annotation data, our best-performing tumor detection model achieved an excellent AP of 95.7%. This data curation and supervised training pipeline can be extended for other radiologic imaging modalities, repurposing vast amounts of existing and otherwise unused data to potentially enable automated tumor detection across radiologic modalities without the need for any de novo image labeling.

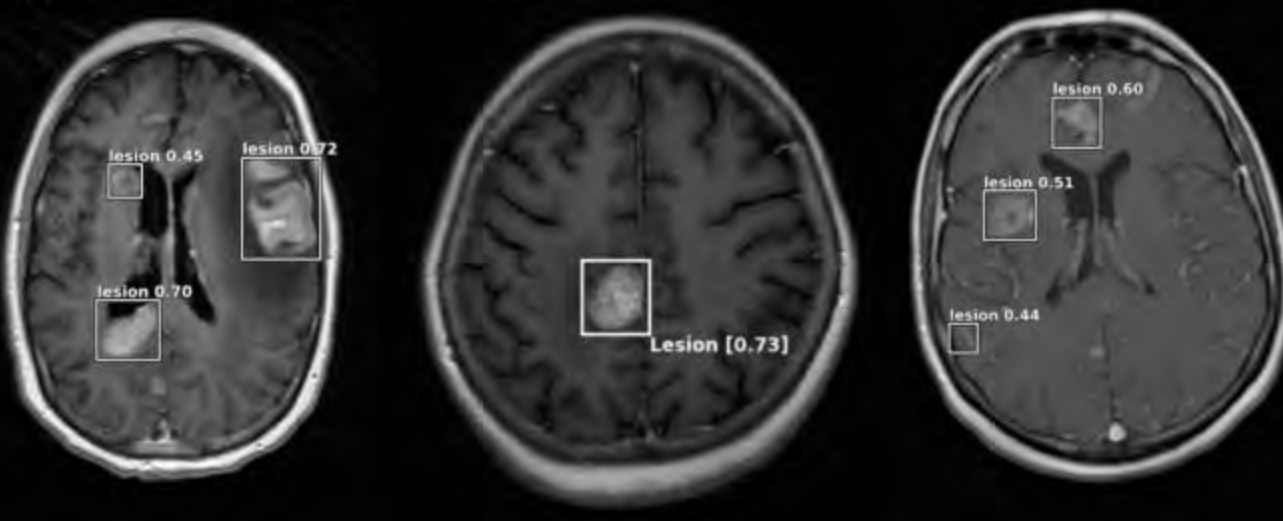
(a) Converting and merging ground truth boxes



(b) Ground Truth Boxes



(c) Predicted boxes (RetinaNet)



(Filename: TCT_1542_ASNR.jpg)

Accelerating Multiple Sclerosis Imaging with Deep Learning-based Image Synthesis

B Wiestler¹, T Finck¹, H Li², N Sollmann¹, T Loehr², M Bussas³, C Zimmer¹, J Kirschke¹, M Mühlau³, B Menze²
¹Dept. of Neuroradiology, School of Medicine, Technical University of Munich, Munich, Germany, ²Image-Based Biomedical Modeling, Technical University of Munich, Garching, Germany, ³Dept. of Neurology, School of Medicine, Technical University of Munich, Munich, Germany

Purpose

Advances in Deep Learning allow for the synthesis of MR contrasts from multi-modal input data, omitting the need for costly physical acquisition of sequences such as Double Inversion Recovery (DIR) and thus reducing scan times. However, in particular for diseases like Multiple Sclerosis (MS), targeted synthesis of the frequently small lesions requires domain knowledge-driven adaptation of image translation frameworks to achieve reliable image synthesis.

Materials and Methods

Advancing our prior work on unpaired image synthesis [1,2], we included an additional L1-norm loss for lesions based on automatic lesion segmentation masks into the cycle-consistency loss of the network. This loss focuses the network on translation of lesions, which otherwise contribute only little to the training error. Using this architecture, we trained a network to synthesize DIR and FLAIR images from input T1w and T2w sequences of 50 MS patients from a prospective MS cohort. Two readers independently counted lesions separately in T2w as well as acquired and synthetic FLAIR and DIR images of another 50 patients, blinded to the image origin. Lesions were grouped into locations outlined in the McDonald criteria (periventricular, (juxta)cortical, infratentorial, subcortical). In addition, we compared lesion-to-background ratios between acquired and synthetic sequences.

Results

Both readers detected significantly more lesions in DIR images compared to either FLAIR or T2w images, irrespective of the image source (acquired or synthetic). This difference was most pronounced in (juxta)cortical lesions, but was also seen in periventricular and infratentorial lesions. When comparing acquired and synthetic images, both readers detected more lesions in specific (periventricular, (juxta)cortical, infratentorial) locations in the acquired compared to the synthetic FLAIR (Figure). For DIR images however, this difference was not significant. In parallel, the lesion-to-background ratio was highest for DIR images and comparable between acquired (median 33.0) and synthetic (median 32.0) DIR images.

Conclusions

Lesion-targeted image synthesis is able to generate high-contrast DIR images from input T1w and T2w images in MS patients. Importantly, lesions (in particular (juxta)cortical) are well translated in this framework, comparable to the original DIR. In combination with compressive sensing, this could lead to a reduction of scan time in our setting from roughly 24 minutes (for T1w, T2w, FLAIR and DIR images) to less than seven minutes.

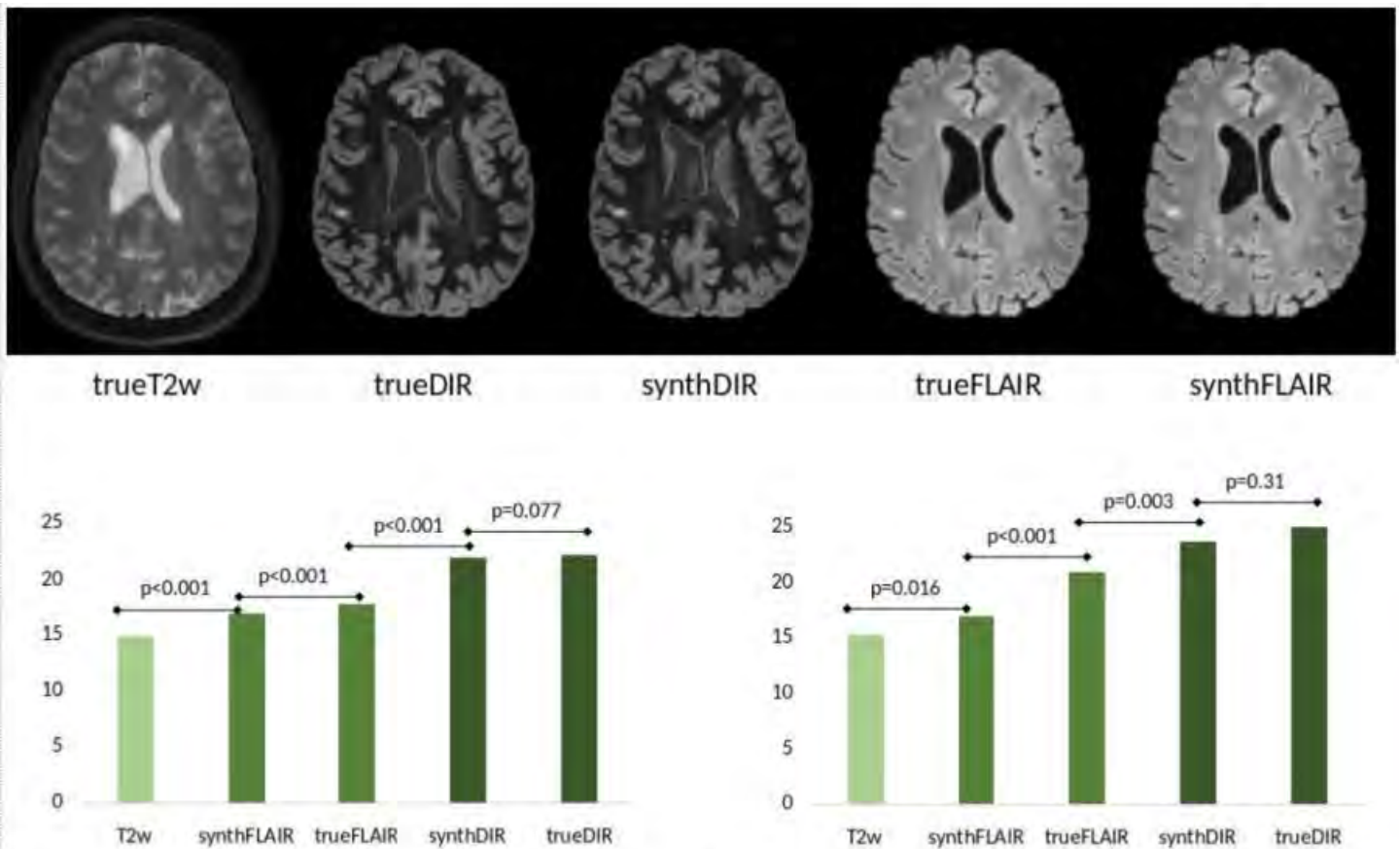


Figure: Top row, example of acquired (“true”) and synthetic (“synth”) images. Bottom row, box plot for lesion counts in specific locations (periventricular, (juxta)cortical, infratentorial) for reader 1 (left) and reader 2 (right). p values are results of signed rank tests
(Filename: TCT_603_figure1.jpg)

857

Accuracy of CT Angiography in Detection of Acute Cervical Arterial Dissection

R Patel¹, R Bhadelia², K Manzoor¹, T Sotman¹, P Mehta¹

¹Beth Israel Deaconess Medical Center, Boston, MA, ²Beth Israel Deaconess Medical center, Boston, MA

Purpose

CT angiography (CTA) is often considered to be equal to MRA/axial T1 fat suppressed images (MRA/T1FS) in detection of cervical arterial dissection (1, 2). However, it is our experience that CTA findings are often ambiguous in differentiating acute from chronic dissection and MRA/T1FS is then requested for confirmation before definitive anti-coagulation therapy is started. Our purpose was to assess accuracy of CTA as compared to MRA/T1FS images in detection of acute cervical arterial dissection.

Materials and Methods

Using electronic database, we identified 73 cases suspected of acute cervical arterial dissection between 2010-2020 with both CTA and MRA/T1FS images within 24 hours of each other. Two neuroradiologists evaluated CTA and MRA/T1FS images to determine presence or absence of acute dissection by consensus. An acute dissection was considered to be present when an intramural thrombus was visualized on MRA/T1FS images. The consensus reading was used as a gold standard to determine how often CTA was true positive (TP), false positive (FP), true negative (TN) and false negative (FN) in detecting acute dissection.

Results

35/73 patients had acute cervical arterial dissection with an intramural thrombus. The CTA detected acute dissection: TP =31/73, FP =18/73, TN=20/73 and FN =4/73. The accuracy of CTA in detecting acute dissection was: sensitivity = 88.6 %, specificity =50%, positive predictive value =63.3 % and negative predictive value =81.8%.

Conclusions

Our results show that low specificity of CTA in detecting acute dissection may often require confirmation by MRA/T1FS images prior to starting definite therapy. Although CTA can be more easily obtained due to scanner availability, we believe that initial and

exclusive evaluation with MRA/T1FS for the detection of acute dissection should be considered when such limitations or MRI contraindications are not present.

196

Acute Infarction in COVID-19 Positive Patients – A Single Institution Review

R Gray¹, A Charlie¹, N DiSanti², D Singh², B Hershey¹, V Sethi¹

¹*Department of Radiology, Temple University Hospital, Philadelphia, PA,* ²*Lewis Katz School of Medicine at Temple University, Philadelphia, PA*

Purpose

Neurologic manifestations of coronavirus disease 2019 (COVID-19) have been widely reported, including ischemic infarction and intracranial hemorrhage, among other outcomes. The purpose of our study was to investigate findings of acute infarction in a cohort of COVID-19 positive patients in a large, academic hospital located in an underserved community that treated more COVID-19 patients than any other hospital in the greater Philadelphia area.

Materials and Methods

We performed an IRB-approved retrospective study on all patients 18 years and older with a confirmed diagnosis of COVID-19 who presented to our hospital between March 1, 2020 and October 20, 2020. Out of all 1872 patients, 445 underwent CT and/or MR imaging of the brain, which were primarily examined for acute infarction and hemorrhagic conversion.

Results

Among 1872 patients with confirmed COVID-19, a total of 445 patients were identified with neurologic symptoms and underwent neuroimaging, of which 23/445 (5%) patients had acute infarction. The median age of patients with infarcts was 67 years; 15/23 (65%) were male and 8/23 (35%) were female. Of the patients with acute infarcts, 21/23 (91%) were ischemic and 2/23 (9%) were hemorrhagic on initial imaging and 8/23 (35%) died during their admission. Of the acute ischemic infarcts, 6/21 (29%) developed hemorrhagic conversion within 7 days. Of the acute infarcts, 9/23 (39%) were in the anterior circulation, 7/23 (30%) in the posterior circulation, 4/23 (17%) were multi-territorial, and 3/23 (13%) were lacunar infarcts.

Conclusions

We found a high incidence of acute infarcts in COVID-19 positive patients with high mortality. Our results strengthen the need for appropriate imaging at the first onset of symptoms. Further studies need to be done to better understand mechanism(s) and distribution. Public awareness also needs to be elevated, as some reports suggest that some symptomatic patients delayed or withheld medical evaluation during the pandemic.

153

Added value in stroke imaging: Accuracy and utility of additional coronal diffusion weighted imaging

M Baggett¹, D Helmy¹, J CHANG¹, M Bobinski¹, R Assadsangabi¹

¹*University of California, Davis, Sacramento, CA*

Purpose

Prior studies have investigated thin-slice diffusion imaging to improve detection of small infarcts. No study has evaluated adding a second imaging plane with the same slice thickness as the axial plane. Our goal was to evaluate adding coronal images with the same slice thickness as the standard axial images to improve detection of small infarcts.

Materials and Methods

We retrospectively studied axial and coronal diffusion weighted images (4 or 5-mm thick, 1-mm gap) in two rounds of data collection. During the first round, two radiologists were presented with 29 patients and identified sub-centimeter infarcts on axial DWI only during one sitting, and on coronal DWI only during a second sitting. During the second round, the two radiologists were presented with 61 separate patients. The two radiologists reviewed axial DWI only during a first sitting, and both axial and coronal DWI during a second sitting. All cases were then reviewed by an expert reviewer with axial and coronal DWI simultaneously, utilizing information from the patients' electronic medical records, and follow-up imaging, to determine the true infarcts and the artifacts. Relative contrast-to-noise ratios (rCNR) and relative mean ROI (rROI) within each lesion on both projections were measured and compared via linear regression.

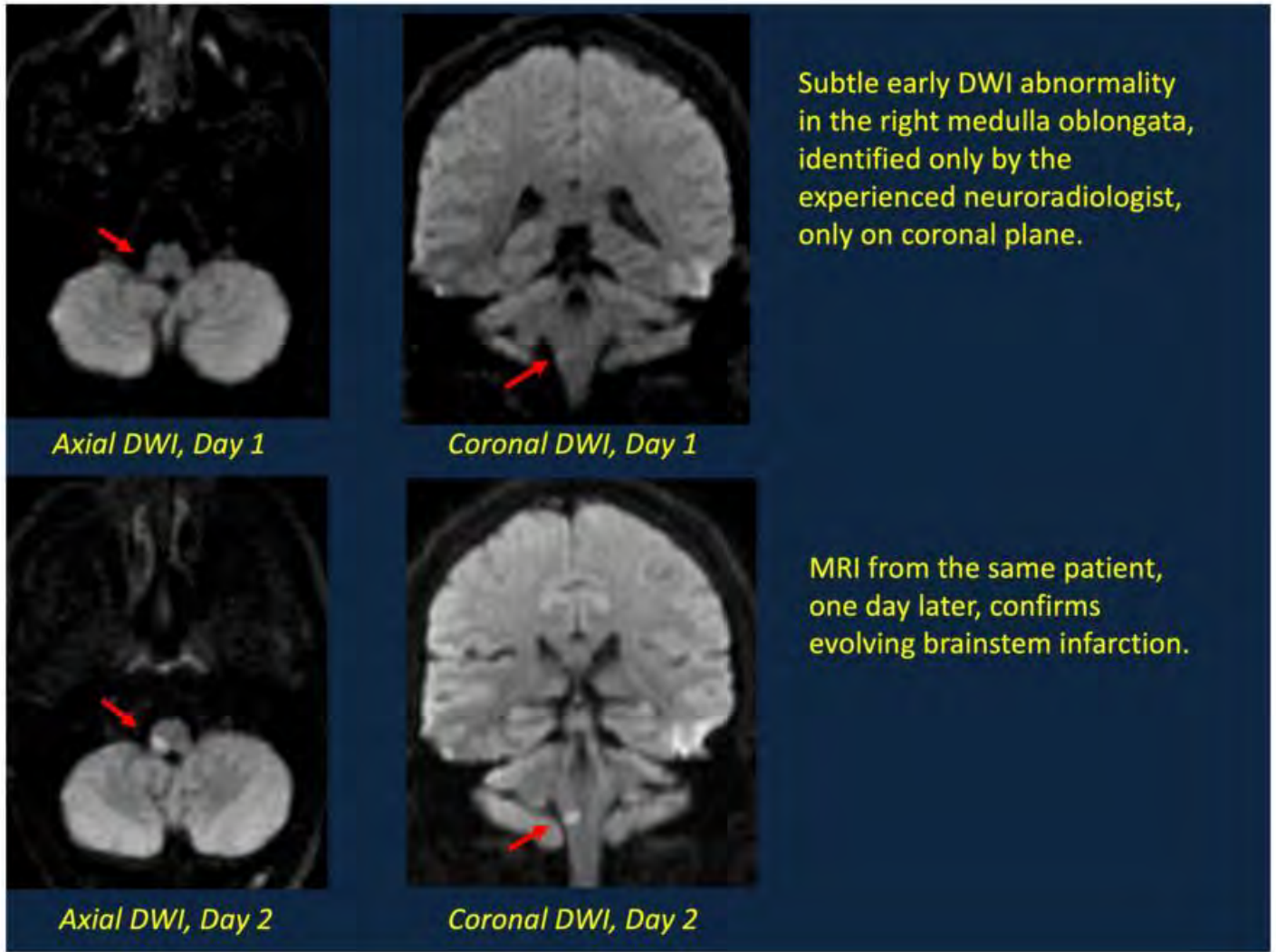
Results

During the first round of data collection, sensitivity for infarct detection was similar for the two readers: 92.7% and 100% on axial DWI, and 95.1% and 92.7% on coronal DWI. During the second round of data collection, sensitivity was improved when reviewers were provided both axial and coronal image: 88.9% to 98.1% for both radiologists ($p = 0.03$). Specificity also improved but did not reach statistical significance ($p = 0.06$ and 0.12). The false negative and false positive lesions tended to be more subtle, with lower rCNR and rROI values.

Conclusions

Including both axial and coronal DWI images with the same slice thickness in the stroke protocol improves detection of small infarcts,

which can be misdiagnosed on a single imaging plane. The second imaging plane is particularly useful for subtle foci of diffusion restriction. We show improved detection of small infarcts by adding a second imaging plane with the same slice thickness, which requires less time to acquire than thin-slice images.



(Filename: TCT_153_ASNRfigureDWI2021.jpg)

505

Additional value of coronal STIR sequence in MRI imaging of the lumbar spine

H Kale¹, V Kamble¹, M Munshi¹, V Nakshiwala¹

¹Kokilaben Dhirubhai Ambani Hospital, Mumbai, Maharashtra

Purpose

Back pain and radiculopathy are common indications for performing an MRI of the lumbar spine. Back pain may however be produced by a variety of pathology related to both spinal and extra-spinal causes. There is increased interest regarding incidental findings on MRI of the lumbar spine and their management. We evaluate the additional benefit of obtaining a T2 STIR coronal sequence on routine lumbar spine MRI imaging.

Materials and Methods

The T2-STIR coronal sequence was retrospectively evaluated in a total of 270 consecutive lumbar spine MRI's performed over a period of 6 months. Evaluation was performed by 3 radiologists (20, 20, 5 years of experience). The studies in which T2-STIR coronal sequence provided additional information were identified. The extra-spinal(outside of the lumbar spine) findings were classified as major and minor depending on whether the findings would require further imaging, follow-up or treatment. Consensus was used if there was uncertainty in major or minor classification.

Results

A total of 116(42.8%) extra spinal findings were identified predominantly on coronal T2-STIR imaging. Of these 58(21.4%) findings

were classified as minor and 58(21.4%) were considered major. Minor findings mostly consisted of adnexal cysts, simple-appearing renal cysts and perinephric fat infiltration. The major findings were the classified into three subcategories : 1.Abdominal organs(renal, liver, gall bladder etc.)-8%, 2. Gynecological-2% 3. Other bony/para spinal lesions-14%. 7 patients had >1 major finding.

Conclusions

A coronal T2-STIR sequence provides substantial benefit in evaluation of the lumbar spine. Additional pathology may be revealed or become more apparent with this sequence.Overall, 21.6% patients had additional findings which warranted either additional imaging, follow up or treatment.

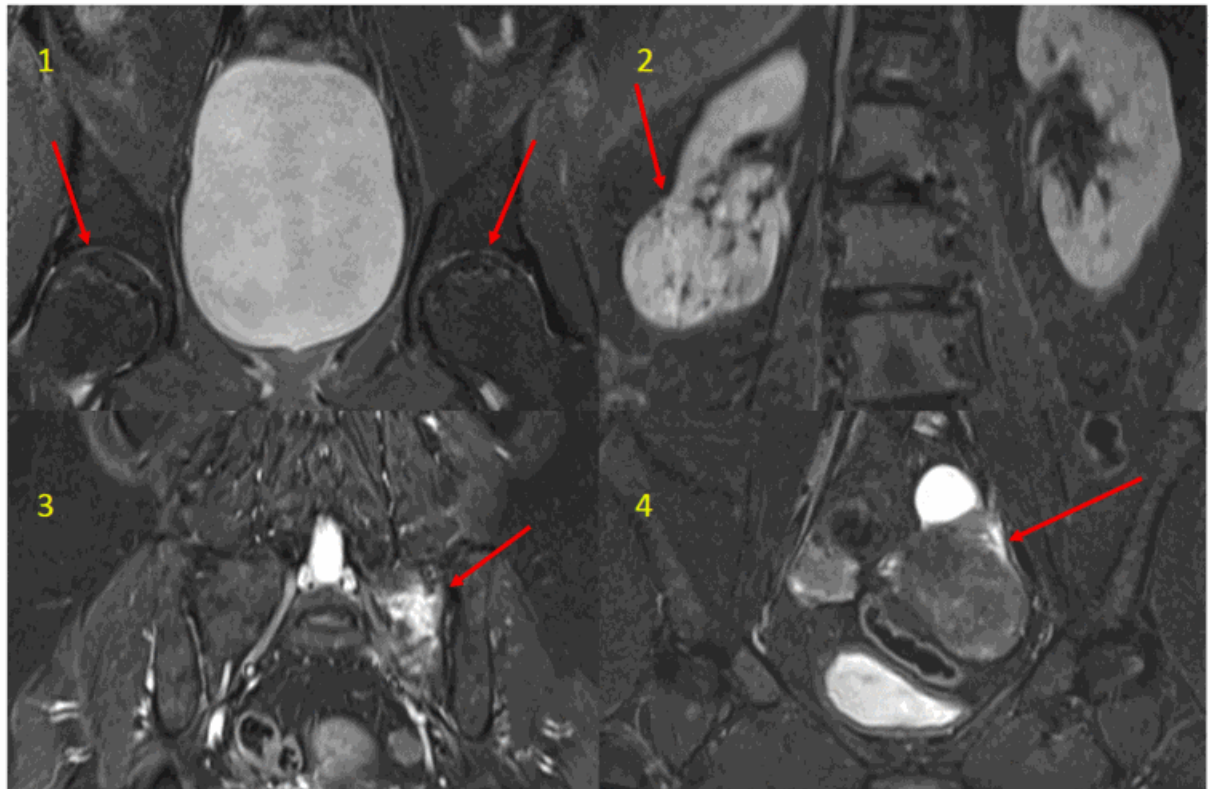
Figure legends

Figure 1: Avascular necrosis of the femoral heads

Figure 2: Right kidney solid renal mass

Figure 3: Insufficiency fracture left left sacral ala

Figure 4: Uterine fibroid and cystic solid adnexal mass



(Filename: TCT_505_ASNR2021final.gif)

442

Age-related Changes in Ocular Lenses on Dual-Energy CT

J Sachs¹, K Hiatt², G Bomar³, T West⁴, P Bunch⁵, M Benayoun⁵, C Lack⁵

¹Wake Forest School of Medicine, Winston Salem, NC, ²Wake Forest Baptist Medical Center, Winston Salem, NC, ³Wake Forest Baptist Health, Winston-Salem, NC, ⁴Wake Forest Baptist Medical Center, Winston-Salem, NC, ⁵Wake Forest School of Medicine, Winston-Salem, NC

Purpose

On single-energy CT the lenses are relatively homogeneous structures that fall within the expected range of soft tissue attenuation. Relatively little has been written about the use of CT for diagnosis of cataract¹, but traumatic cataracts are known to be relatively hypodense. Nuclear sclerotic cataracts are the most common form of age-related cataract², thought to be related to cumulative age-related insults to the lens including ultraviolet light. These are typically diagnosed clinically by visual confirmation of lens cloudiness or discoloration, suggesting that the ocular lens over time absorbs more photons in the visible light portion of the electromagnetic spectrum. DECT allows for assessment of energy dependent changes in photon attenuation³. We hypothesize that age-related changes in photon attenuation of the lens may be detectable using DECT.

Materials and Methods

Retrospective, HIPAA-compliant, IRB-approved. CTs of the head reviewed. Inclusion criteria: 1) DECT acquisition; 2) >18 years old; 3) one native ocular lens. Two cohorts formed: 18-27 year olds, the other 75 years or older. 100 total lenses in each cohort. ROIs spanning 3-5 mm² were placed over the native ocular lenses. Mean and SD HU values were recorded at 40 keV, 70 keV, and 190 keV. Mean HU values were calculated for each cohort at each energy. Absolute differences between the high (190) and low (40) keV were calculated. Comparison between cohorts was performed using unpaired t-tests.

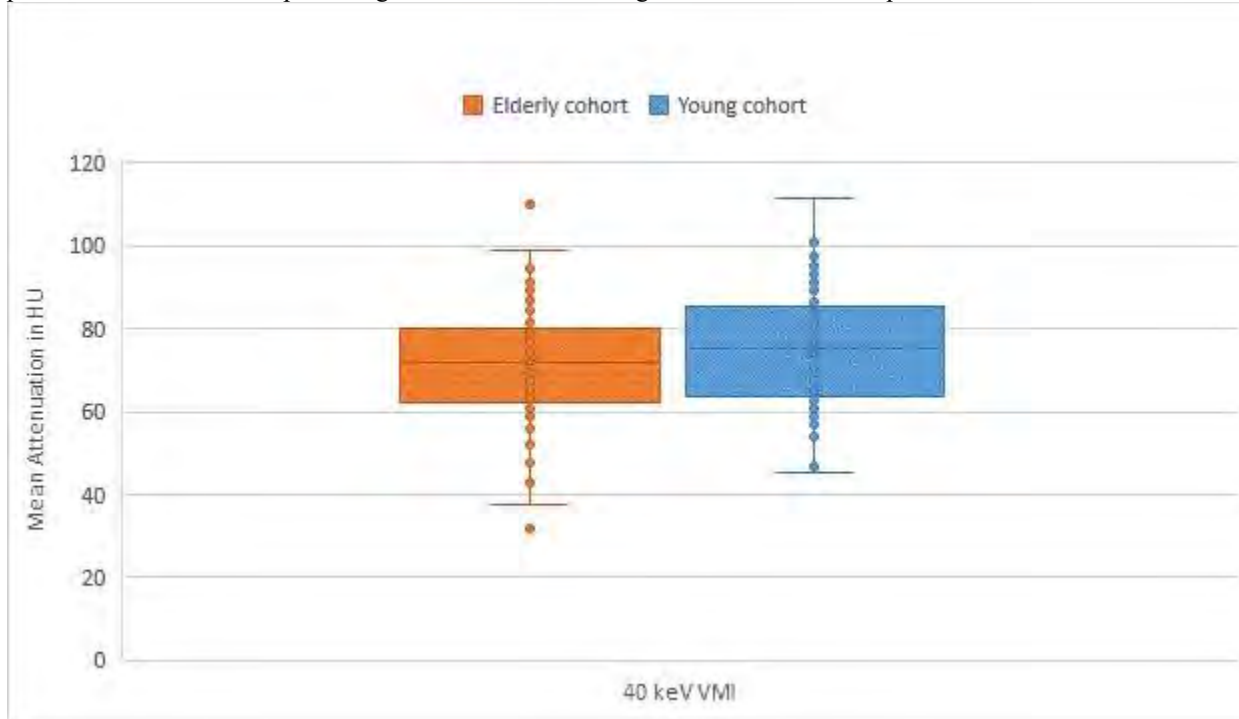
Results

Mean HU attenuation values were significantly different between the young adult (75.33, SD 13.42) and more elderly cohort (71.02, SD 13.59) at 40 keV (p = 0.0244). The summary data is depicted in Figure 1. Differences in mean HU values between the cohorts at

the 70 and 190 keV energy levels did not reach statistical significance. No statistically significant difference was found between the cohorts when comparing the absolute differences in HU attenuation at 190 versus 40 keV.

Conclusions

Though a statistically significant difference in mean HU attenuation of the ocular lens was found between a young adult and elderly cohort at 40 keV VMI, the considerable overlap between cohorts in HU attenuation at all energy levels precluded identification of a practical HU threshold to predict age of an ocular lens using current DECT techniques.



(Filename: TCT_442_Figure1.jpg)

711

Alterations in Thalamic Functional Network Connectivity in Infants with Prenatal Opioid Exposure

Z Guckien¹, R Vishnubhotla¹, P Zhang¹, J Dietrich¹, D Haas¹, S Sadhasivam¹, R Radhakrishnan¹

¹Indiana University School of Medicine, Indianapolis, IN

Purpose

Prenatal opioid exposure (POE) has been shown to adversely affect neonatal and childhood outcomes. Infants with POE may develop Neonatal Opioid Withdrawal Syndrome (NOWS) that can prolong length of hospital stay (LOS). Studies have shown alterations in resting state functional MRI (rs-fMRI) connectivity in the amygdala in infants with POE, compared to healthy controls (1). However, alterations in other brain regions have not been studied. The aim of this study was to characterize alterations in thalamic rs-fMRI connectivity in neonates with POE.

Materials and Methods

In this prospective, IRB-approved study, 19 neonates with POE and 20 healthy, opioid naive (ON) controls underwent rs-fMRI during natural sleep at mean post-menstrual age (PMA) of 44.7 ± 2.6 and 44.6 ± 2.6 weeks respectively. Seed-based whole brain functional connectivity analyses were performed for each subject with the right (R) and left (L) thalamus as distinct seed regions. Unpaired mixed-effects group analyses between POE and ON groups were conducted for each seed region, corrected for PMA and sex.

Preliminary post hoc analyses in the POE group assessed the effects of maternal polysubstance use, smoking, and correlated LOS on thalamic functional connectivity. P value of $\leq .05$ was considered statistically significant.

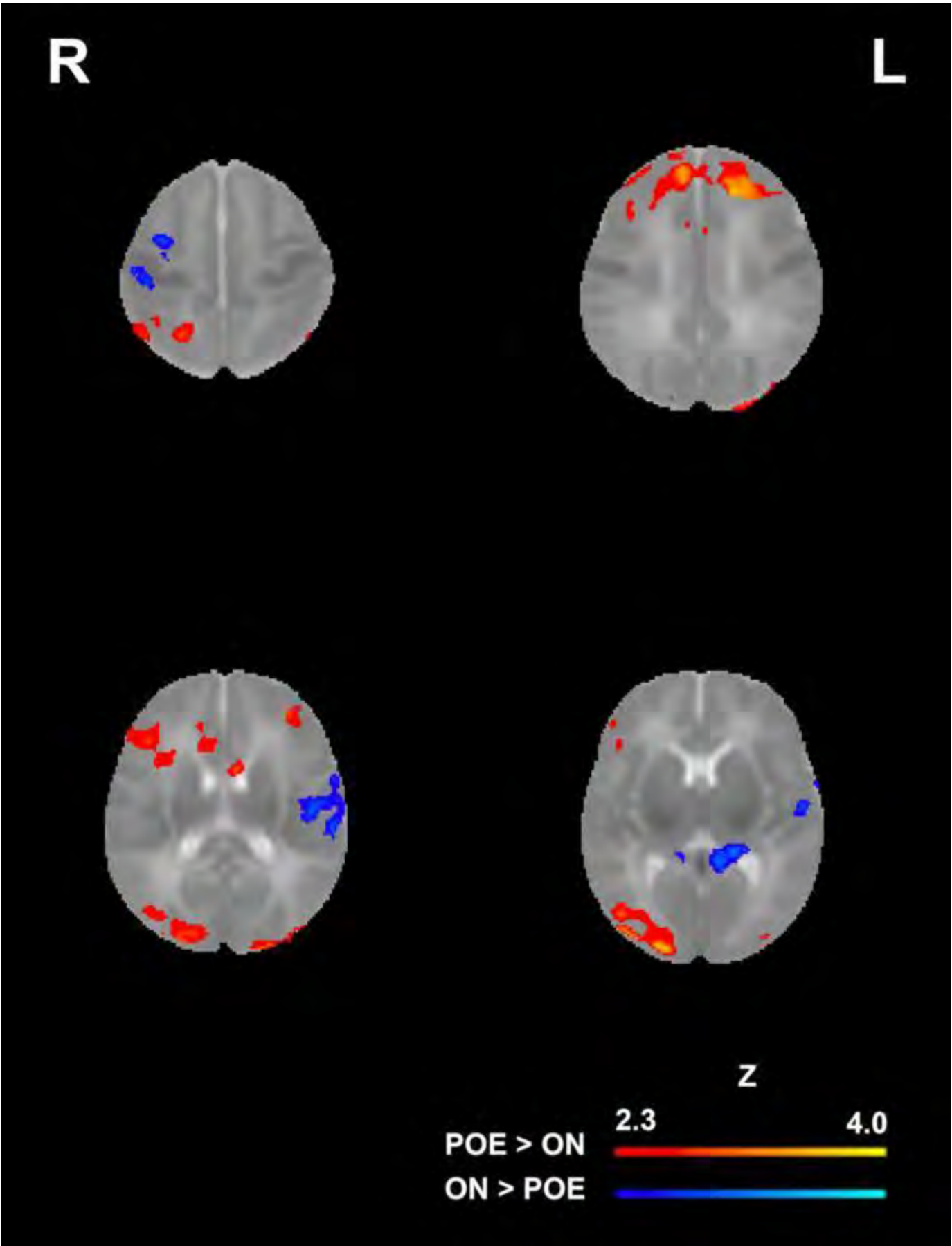
Results

Significantly altered thalamocortical connectivity was observed in the POE group compared to the ON control group (Figure 1). In infants with POE, alterations in functional connectivity of the R thalamus to the L occipital lobe ($P = .02$) and R superior parietal lobule ($P = .03$) were associated with maternal polysubstance use. Connectivity of the L thalamus to the R superior parietal lobule was associated with maternal smoking ($P = .04$). There were positive correlations between LOS and connectivity of the R and L thalamus to the L posterior cingulate gyrus and isthmus (Right: $R = 0.57$, $P = .006$; Left: $R = 0.43$, $P = .03$) and negative correlation between LOS and R thalamus connectivity to the R occipital lobe ($R = -0.5$, $P = .015$).

Conclusions

In POE neonates compared to ON controls, we show novel and significant alterations in thalamocortical functional connectivity that

may be influenced by maternal polysubstance use and smoking, and may reflect the severity of postnatal withdrawal given the correlation with LOS. Thalamocortical connectivity may have implications in informing risk stratification and treatment for POE-related neurodevelopmental outcomes that can be explored in future longitudinal studies.



(Filename: TCT_711_Thalamus_ROI_slices_HD.jpg)

Altered Resting-State fMRI Brain Connectivity Correlates with Objective Postural Stability Measures in Patients with Subacute Post-Concussion Vestibular Impairment

A Trofimova¹, J Smith¹, M Hajiaghamemar², M Seidi², V Ahluwalia³, S Akhnouk⁴, R Gore⁵, J Allen¹

¹Emory University, Atlanta, GA, ²Georgia Institute of Technology, Atlanta, GA, ³Georgia Institute of Technology, ATLANTA, GA, ⁴Emory University School of Medicine, Palm Harbor, FL, ⁵Shepherd Center, Atlanta, GA

Purpose

To correlate resting-state fMRI (rs-fMRI) connectivity and postural stability measures in subacute post-concussive vestibular impairment (PCVI).

Materials and Methods

IRB approved study. 15 subjects with subacute PCVI and 13 healthy subjects (HC) underwent rs-fMRI, sensory organization test (SOT) and visual motion sensitivity task (VMST) on a force platform (BERTEC). rs-fMRI acquired on 3.0T research magnet, 32-channel head coil (2.5mm isovoxel, TR/TE=750/32ms, flip angle=52°). Preprocessing and ROI-to-ROI connectome analysis was done in CONN Toolbox. ROIs included: frontal eye field (FEF), inferior (IFG) and middle (MFG) frontal gyrus, parieto-insular vestibular cortex (PIVC), posterior hippocampus (pHC), anterior insula (aINS), multisensory orientation area (MSO), MT/V5, BA17/18, hOC5/V5. Maps were corrected for multiple comparisons using family-wise error correction ($p < 0.05$). Logistic regression analysis was applied to 78 postural stability metrics to find parameters based on Akaike's information criterion discriminating between HC and PCVI, used in correlation analysis with rs-fMRI. Null hypothesis rejected for $p < 0.05$.

Results

The best single discriminating postural stability metric (AUROC 0.87, sensitivity 80%, specificity 85%) was SOT condition 3 (sway-referenced-vision, fixed-surface), maximum sway angle (Par1). The best 3-parameter combination of postural stability metrics (AUROC 1.0, sensitivity 100%, specificity 100%) was standard deviation of medio-lateral center of pressure motion (ML-COP) during VMST easy/moderate (Par2) and difficult (Par3), and range of ML-COP during SOT condition 3 (Par4). Par1 and Par4 were significantly associated with enhanced correlations between left and right MSO, PIVC, right aINS, and left IFG; bilateral MFG; bilateral pHC; visual areas and left MSO-aINS-PIVC-IFG complex; right MT/V5 and left IFG. Par1, Par4 were associated with reduced correlations between MT/V5, HOC5/V5 and MFG, right MSO and IFG, left MSO and FEF. Par2 was associated with stronger correlations between MSO, aINS, PIVC, IFG; bilateral MFG; bilateral pHC.

Conclusions

Correlations between postural stability metrics and rs-fMRI connectivity in PCVI patients suggest inherent pathologic over-weighting of visual input, altered multisensory processing and spatial memory, which may account for symptom persistence. Validation of these findings in a larger cohort may provide the basis for future development of patient-centric therapeutic interventions specifically targeting these networks.

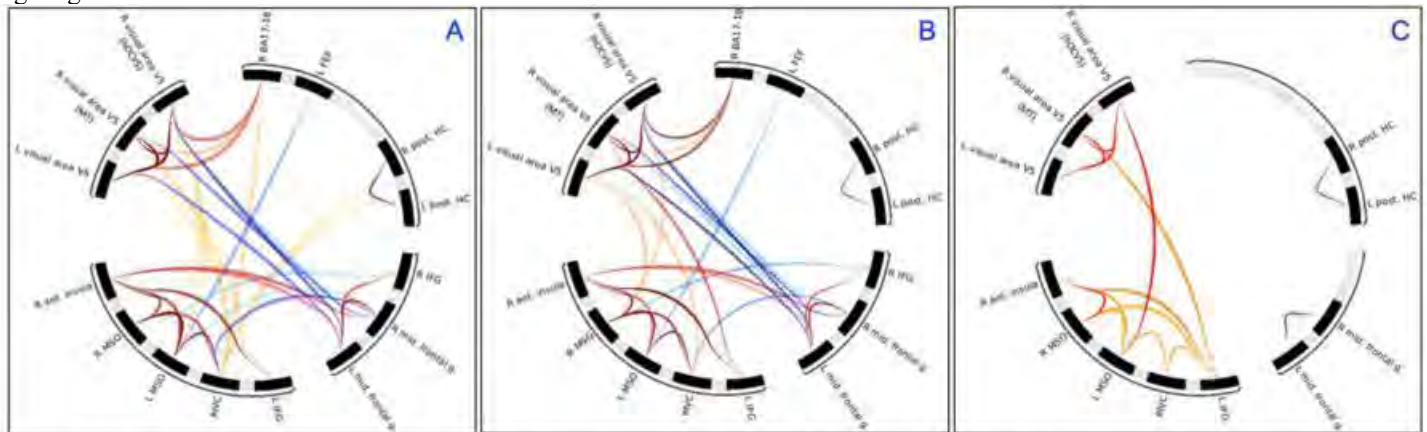


Figure 1. rs-fMRI functional brain connectivity correlations with best objective postural stability discriminators between healthy controls and subjects with post-concussive vestibular impairment. A) Parameter 1: maximum sway angle, sensory organization test (sway referenced vision, fixed surface), $p_{FDR} \leq .02518$. B) Parameter 4: range of center of pressure, medial-lateral direction, sensory organization test (sway referenced vision, fixed surface), $p_{FDR} \leq .0397$. C) Parameter 2: standard deviation of center of pressure, medial-lateral direction, visual motion sensitivity test (easy-moderate setting), $p_{FDR} \leq .03342$.

(Filename: TCT_577_Figure1.jpg)

Purpose

Rosai-Dorfman disease (RDD) is a benign disease of phagocytic histiocytes that predominantly affects adolescents. Patients typically present with lymphadenopathy and may have constitutional symptoms such as fever and night sweats. Extra-nodal involvement is seen in approximately 30% of patients and can involve the paranasal sinuses and orbits. Intracranial involvement is rare and typically affects the meninges. We present a case of a boy who initially presented with sinus congestion and through imaging, medical, and surgical workup was found to have involvement of the intra and extracranial portion of the trigeminal nerve with RDD. The patient subsequently developed involvement of the lacrimal glands with RDD.

Materials and Methods

This patient, a male boy, initially presented with recurrent sinusitis at 10 years old. A CT of the paranasal sinuses (Figure 1) demonstrated diffuse mucosal disease in the paranasal sinuses. At the ages of 11 and 13, the patient underwent endoscopic sinonasal surgery which demonstrated multiple nasal polyps and sinus mucosal disease. Pathology demonstrated nasal polyps with marked lymphocytic infiltration and mucosal disease with chronic inflammation. At the age of 14, the patient developed right facial numbness and a subsequent MRI brain demonstrated normal sized lacrimal glands and a right trigeminal nerve mass (Figure 2) which was classified as a schwannoma. The patient underwent removal of this mass and pathology demonstrated findings consistent with RDD. As a part of the workup, the patient underwent a PET/CT which demonstrated lymphadenopathy at multiple sites including in the cervical chain (Figure 3). A follow up MRI brain demonstrated symmetric and diffuse enlargement of the bilateral lacrimal glands, likely due to RDD (Figure 4).

Results

NA

Conclusions

This case demonstrates an unusual presentation of RDD involving the paranasal sinuses, intra and extracranial portions of the 3rd division of the right trigeminal nerve, and cervical lymphadenopathy with subsequent involvement of the lacrimal glands. Unilateral involvement of the trigeminal nerve with RDD is rare and to our knowledge has been described in one prior case. On the first MRI, the patient demonstrated an isolated right trigeminal nerve mass which was thought to represent a trigeminal schwannoma but was proven to be a manifestation of RDD. This case highlights that RDD should be considered in pediatric patients with a mass involving the trigeminal nerve and extensive paranasal sinus disease.



Figure 1: CT paranasal sinuses

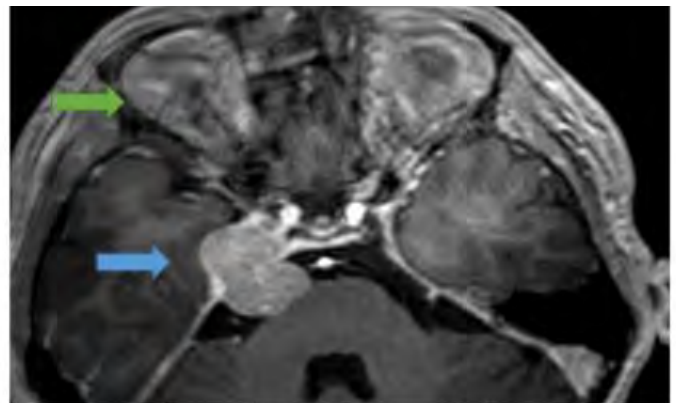


Figure 2: MRI brain with IV contrast

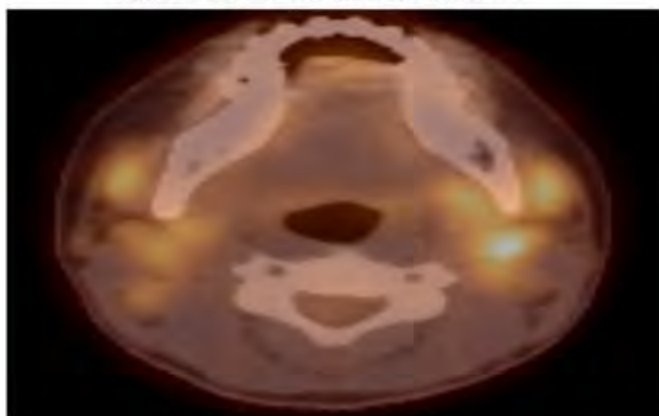


Figure 3: FDG PET-CT

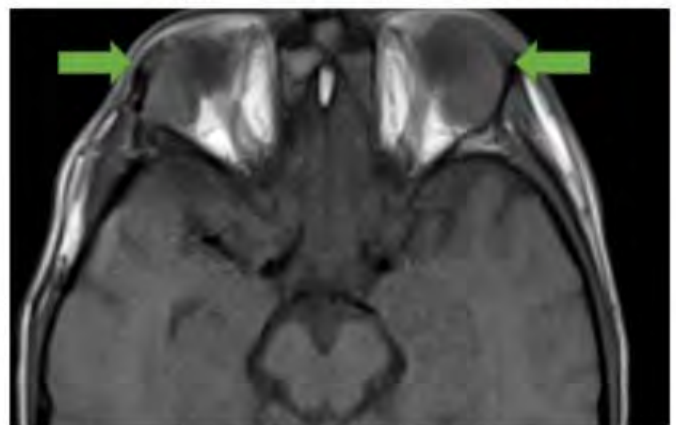


Figure 4: MRI brain T1-W

Analysis of Lesion Segmentations within White Matter, Gray Matter and Deep Gray Matter tissues using a 3D U-Net Convolutional Neural Network

R Saluja¹, D Weiss², J Rudie², A Rauschecker³, A Pradhan⁴, R Bryan⁵

¹Galileo CDS, Philadelphia, PA, ²University of California San Francisco, San Francisco, CA, ³UCSF Radiology, Mill Valley, CA, ⁴Galileo CDS Inc, Austin, TX, ⁵University of Texas Austin, Austin, TX

Purpose

Quantification and identification of brain tissues and lesions in neuroimaging plays a crucial role in diagnosis, disease staging, and treatment monitoring. With the revolution of AI systems in radiology and its improvement in identifying and segmenting lesions, quantitative tools have been working on WM lesions for evaluation. We sought to more carefully evaluate lesion segmentation performance in different tissue types. We developed and tested a 3D U-Net convolutional neural network (CNN) which segments lesions on FLAIR brain MRIs and evaluated its performance within white matter (WM), gray matter (GM) and deep gray matter (DGM) tissues.

Materials and Methods

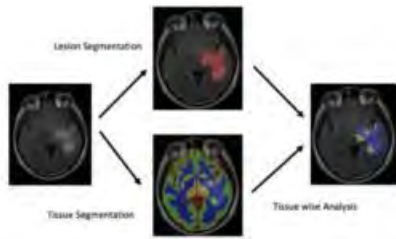
For lesion segmentation we use a U-Net that has been trained on an internal dataset of 386 FLAIR images and then used 97 cases for hyperparameter optimization and validation. The test set consists of another 35 FLAIR images. Two trained radiologists manually segmented the lesions using ITKSnap (version 3.6.0), which were used as the gold standard for comparative analysis. Volumes were preprocessed to 1x1x1 mm³ resolution. After lesion segmentation, we used corresponding T1 modality images to co-register the lesions to independently segmented brain tissues (GM, WM, CSF) performed by a tissue segmentation network, allowing the anatomic localization of lesions. We calculate the performance of our lesion segmentation separately within WM, GM and DGM (FIG1).

Results

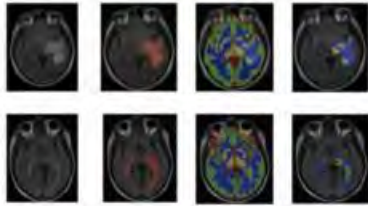
The median dice score for segmenting lesions in the whole brain was 0.74, while the median dice scores for lesions located in the white matter, gray matter and deep gray matter was 0.76, 0.69 and 0.69 respectively (FIG2). We further analyzed the total number of lesions, volume of lesions and volume of the largest lesion, within tissue type, as compared to ground truth. We further obtain cosine similarity of >90% for lesion volume, volume of largest component and number of lesions within each tissue and observe a high correlation with ground truth segmentations.

Conclusions

Our CNN network performs lesion segmentation and quantification well within all brain tissues and performs well in terms of volume similarity, dice scores and predicting the number of lesions within tissue types. With an increase in training cases with even more spatial and tissue type heterogeneity, the overall performance may increase. Quantitative imaging tools such as this automated volumetric measurement tool have the potential to improve clinical workflows by decreasing manual human measurement and labeling.



(a) Workflow for experimentation



(b) Examples of our analysis

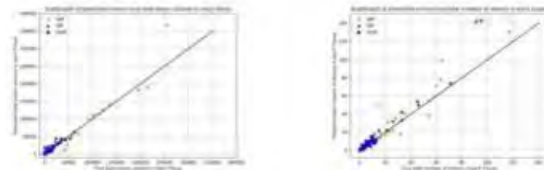
Figure 1: Tissue Analysis Workflow and Examples

Feature	MR1	MR2	MR3
Total Volume	0.993228607	0.960213866	0.944979576
Number of Lesions	0.9499993113	0.982119099	0.879836141
Volume of Largest Lesion	0.996117660	0.995393361	0.913818862

Figure 3: Compilation of Pearson correlation metrics

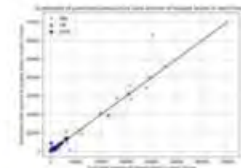
Metric	MR1	MR2	MR3	MR4
Dice Score (Lesion)	0.799112	0.757482	0.682775	0.690289
Sensitivity (Lesion)	0.786549	0.738318	0.636817	0.474398
PPV (Lesion)	0.83225	0.809156	0.807881	0.679934
Lesion Similarity (Dice Volume)	0.90679	0.99881	0.98882	0.917407
Lesion Similarity (Volume of Largest Lesion)	0.99542	0.99662	0.991889	0.881271
Lesion Similarity (Dice Number of Lesions)	0.949801	0.972389	0.965467	0.944677

Figure 2: Compilation of performance metrics



(a) Lesion volume

(b) Number of lesions



(c) Volume of largest lesion

Figure 4: Scatterplot of predicted-versus-true for individual tissues

(Filename: TCT_1634_0001.jpg)

671

Analysis of Perceptual Blind Spots in Imaging of Head and Neck Pathology

A Ferguson¹, V Ivanovic¹, M Bobinski², J CHANG², O Raslan², A Ozturk³, R Assadsangabi⁴

¹University of California, Davis, Sacramento, CA, ²UC Davis, Sacramento, CA, ³University of California Davis, Sacramento Medical Center, Sacramento, CA, ⁴University of California Davis, Sacramento, CA

Purpose

Misses in radiology occur in approximately 3-6% of imaging studies. Errors can be broken down into two broad categories: perceptual (70-80%) or interpretive (20-30%) errors. We focused on analysis of Neuroradiology Attending errors in H&N pathology at a single tertiary care center.

Materials and Methods

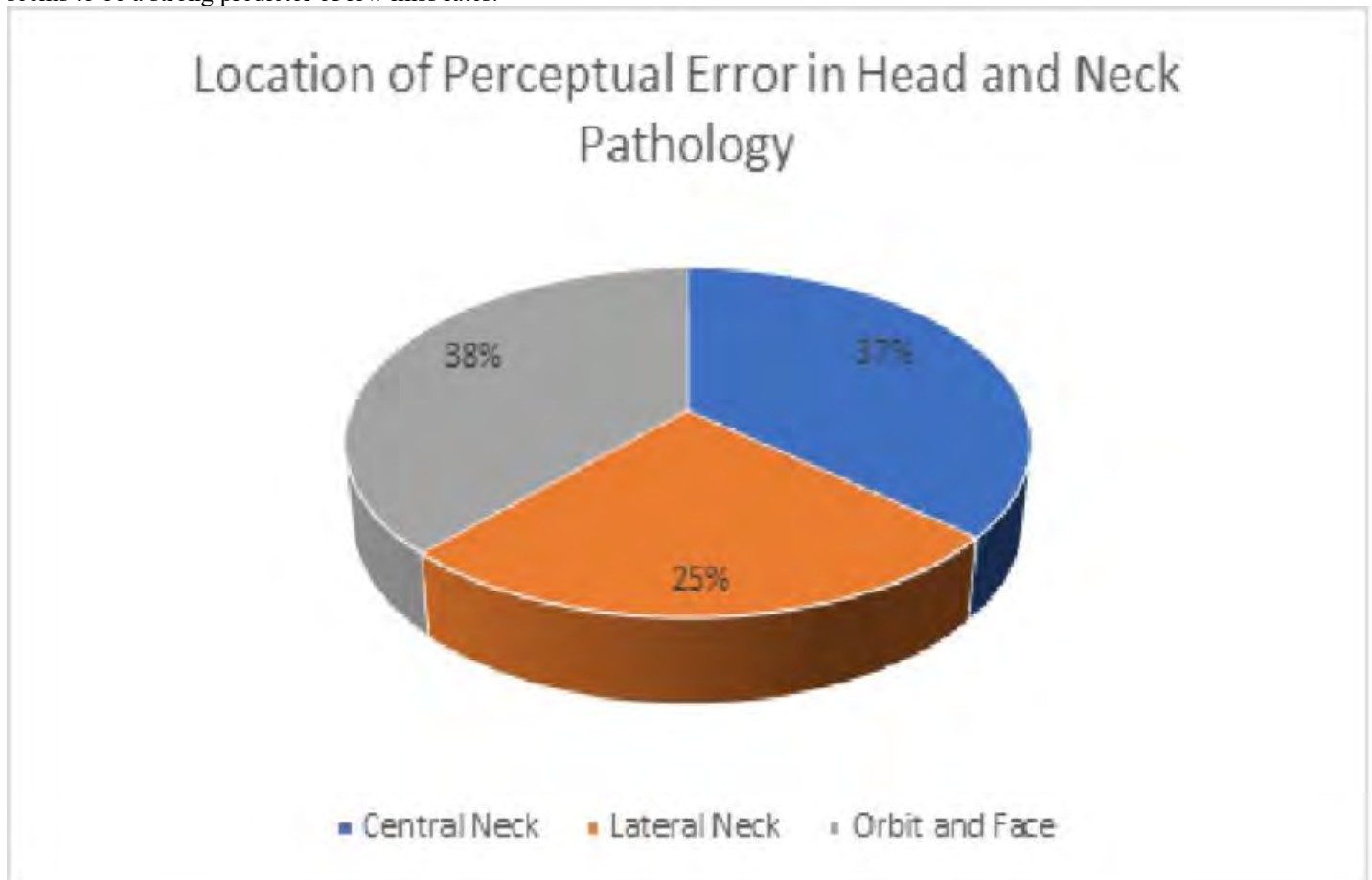
Neuroradiology Quality Assurance Database of missed cases from 20 attending physicians was searched for misses of H&N pathology from 2014 – 2020. Cases included misses on exams performed for primary H&N indications, or when imaging was performed for other reasons and H&N pathology was an incidental finding. All misses were confirmed by two attending radiologists or during our quarterly Quality Improvement conference. Only CT and MRI reports were included in the study. We collected data on specific missed pathologies as well as the frequency of attending radiologist H&N tumor board participation as the presenting radiologist during the study period. Misses were categorized as perceptual or interpretive. Misses were categorized into three anatomic compartments in order to facilitate creation of a checklist of 'blind spots'. Compartments included: central neck (thyroid gland, aerodigestive tract), the lateral neck (salivary glands, lymph nodes, soft tissues), and face (orbits, sinuses, masticator space). We correlated yearly H&N miss rate per attending radiologist with frequency of their H&N tumor board participation.

Results

Total of 74 H&N misses were identified; 86% were perceptual and 14% interpretive errors. Distribution of errors was: face (38%), central neck (37%) and lateral neck (25%). Most commonly missed pathologies were in the aerodigestive tract (13/74), orbit (12/74), parotid gland (9/74) and thyroid gland (8/74). There was a strong correlation between low yearly H&N misses and high frequency of H&N tumor board participation, $\rho = -0.75$.

Conclusions

Perceptual errors represent a higher percentage of total H&N errors in our study compared to what is reported in the literature for general radiology errors. Majority of misses can be compartmentalized into spaces or organs, thus creating a 'blind spot' checklist that could help decrease the error rate frequency. Experience in H&N imaging, as measured by frequent H&N tumor board participation, seems to be a strong predictor of low miss rates.



(Filename: TCT_671_PerceptualHeadandNeck.jpg)

931

Analysis of Perceptual Errors in Skull Base Pathology

S Vong¹, J CHANG¹, M Bobinski¹, R Assadsangabi¹, A Ozturk¹, O Raslan¹, V Ivanovic¹

¹UC Davis, Sacramento, CA

Purpose

Medical errors result in significant mortality/morbidity. In Radiology, errors are divided into two categories: perceptual and interpretative. Most errors are perceptual, ranging from 60-80%. Many studies have analyzed factors affecting radiologic errors and methods to reduce them. To our knowledge, no study has specifically evaluated skull-based errors in Neuroradiology. Thus, the purpose of this study was to analyze skull-based errors at a single tertiary institution and offer strategies to reduce errors in this region.

Materials and Methods

An IRB approved retrospective chart review was conducted from January 2014 to December 2019 at UC Davis and included all CT and MRI imaging exams. A total of 4000 addended reports and pre-existing Mortality & Morbidity conferences were reviewed by two Attending Neuroradiologists. Errors were separated into four subcategories: tumor, trauma, vascular, and congenital.

Results

A total of 94 skull-based errors were identified. Most errors were perceptual (87%), not double read by trainees (66%), occurred during a weekday (90%), and comparable between emergency/inpatient (52%) and outpatient (48%) rotations. Lower annual misses were strongly correlated per Attending and frequency of Head & Neck tumor board participation ($r=-0.74$). Over half of errors were tumors (55%), followed by trauma (24%), vascular (10%), and congenital (7%). Missed tumors included: vestibular schwannoma/meningioma at the cerebellopontine angle and metastatic lesions in the clivus and occipital condyle. Missed trauma included: retroclival hematoma, occipital bone fracture, and atlantooccipital dissociation. Missed vascular findings included: dural venous thrombosis. Missed congenital findings included: Chiari malformation and enlarged vestibular aqueduct. These diagnoses accounted for 50% of skull-based errors. Strategies to reduce errors focused on windowing, algorithmic search patterns, and evaluation of region of interests in multiple sequences/planes.

Conclusions

This retrospective review of skull-based errors at a single tertiary institution analyzed patterns of common errors and types of missed pathology. Most errors in our study were perceptual and experience in skull-based imaging, as measured by frequent tumor board participation, appeared to be a strong predictor of low miss rates. Strategies to reduce errors included searching for commonly overlooked pathologies in specific anatomic sub-compartments. Recognizing the region of interest and pathology may help to reduce future errors.

1383

Application of Apparent Diffusion Coefficient Histogram Radiomic Metrics for Differentiation of Posterior Fossa Tumors in Pediatric Patients

A Zandifar¹, L Tierradentro-García¹, F Goncalves¹, J Kim¹, A Ghosh¹, C Alves¹, S Teixeira¹, S Andronikou², A Vossough²
¹Children's Hospital of Philadelphia, Philadelphia, PA, ²University of Pennsylvania - Children's Hospital of Philadelphia, Philadelphia, PA

Purpose

Presurgical diagnosis of posterior fossa tumors in children can be challenging. Conventional MRI features such as T1- and T2-weighted signal and contrast enhancement may overlap among different types of posterior fossa tumors. This study aimed to evaluate the application of apparent diffusion coefficient (ADC) histogram analysis and radiomic metrics to differentiate the various posterior fossa tumors in children.

Materials and Methods

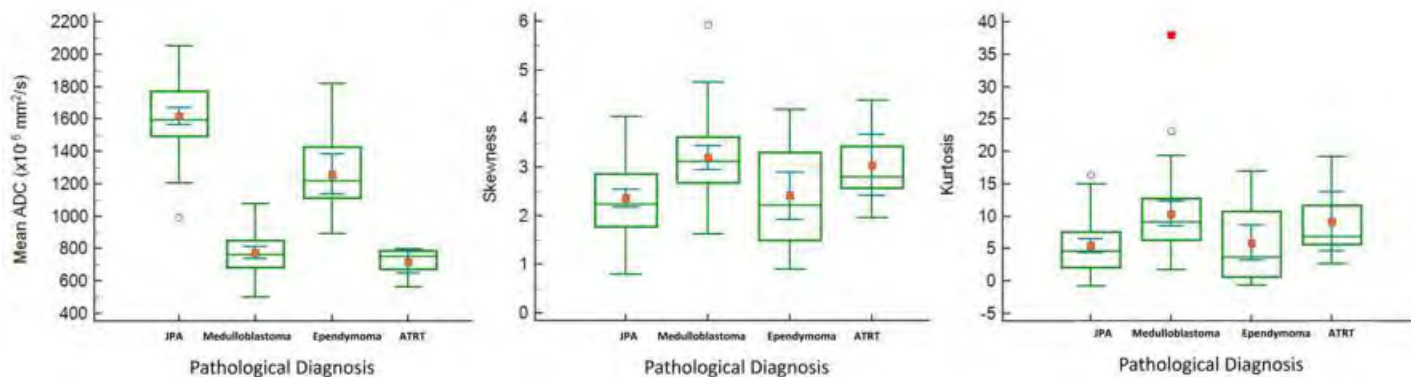
In this retrospective study, MRI data of 135 children with posterior fossa tumors were evaluated. These were histologically 65 pilocytic astrocytomas (PA), 43 medulloblastomas, 9 atypical teratoid rhabdoid tumors (ATRT), and 18 ependymomas. All evaluations were performed using diffusion-weighted imaging (DWI) and manual segmentation was done using an in-house developed parametric (pMRI) software. Diffusivity metrics were automatically calculated on a pixel-by-pixel basis. Only solid components of lesions were included in the analysis. The following first-order histogram radiomic metrics were calculated: ADCmean, ADCkurtosis, and ADCskewness. We used the Kruskal-Wallis test with post hoc comparison for determining the differences among the tumor types.

Results

The ADCmean showed overall significant differences between the four major tumor groups: 1.62 ± 0.21 vs. 0.77 ± 0.12 vs. 0.72 ± 0.90 vs. 1.26 ± 0.25 10^{-3} mm²/s ($p < 0.001$) in PA, medulloblastomas, ATRTs, and ependymomas, respectively. We also found significantly different values for ADCkurtosis: 5.41 ± 4.21 vs. 10.41 ± 6.38 vs. 9.22 ± 5.91 vs. 5.87 ± 5.48 ($p < 0.001$); and ADCskewness: 2.36 ± 0.74 vs. 3.19 ± 0.79 vs. 3.04 ± 0.82 vs. 2.41 ± 0.98 ($p < 0.001$). Post hoc analysis showed significant pairwise differences of ADCmean between medulloblastomas and ependymomas and also between ATRTs and ependymomas. Mean ADC had an area under the ROC curve (AUC) of 0.98 in differentiating ependymomas from medulloblastomas with a cut-off value of $>0.89 \times 10^{-3}$ mm²/s, demonstrating 100% sensitivity and 83.7% specificity in differentiating both of them.

Conclusions

ADC histogram analysis can be considered a useful tool for neuroradiologists to differentiate between the four common posterior fossa tumors in children.



(Filename: TCT_1383_abstractADCposteriorfossa.jpg)

1653

Association Between Resting-State Brain Oscillatory Activity and Global Cortical Atrophy

Z Brinson¹, A Proskovec¹, F Yu¹, A Longoria¹, H Rossetti¹, B Kelley¹, J Berry¹, J Maldjian¹, E Davenport¹

¹University of Texas Southwestern Medical Center, Dallas, TX

Purpose

Previous magnetoencephalography (MEG) studies have shown that individuals with mild cognitive impairment and Alzheimer's disease (AD) demonstrate increases in δ and θ [1,2], decreases in α and β [1], and lower ratios of relative power between high and low frequency bands[3] compared to controls. The aim of this study is to investigate the association between global cortical atrophy, a measure of neurodegeneration[4], and MEG resting-state oscillations in cortical regions that show early AD neuropathology.

Materials and Methods

Forty adults (median age=66.0 years, 48/52% female/male, 62/38% white/nonwhite, 25/75% cognitively impaired/nonimpaired) completed a 6-minute resting-state MEG scan and a T1w structural brain MRI scan. MEG data underwent standard preprocessing (Signal Space Separation, 0.5-150Hz band pass filtering, and artifact rejection), source localization with a beamforming approach, and normalization using 3 minutes of empty-room data. Brain activity was filtered into canonical frequency bands and mean relative power (MRP) and α/δ , α/θ , β/θ , $(\alpha+\beta+\gamma)/(\delta+\theta)$ ratios[3] were computed for 6 AAL atlas[5] regions: angular gyrus, anterior cingulum, hippocampus, parahippocampal gyrus, posterior cingulum, and precuneus. Global cortical volumes (GCV) normalized by intracranial volumes were computed using FreeSurfer 6.0. Linear mixed effects modeling was performed using R package nlme for each frequency band per region, with MRP or spectral ratio as the outcome and normalized GCV as the predictor. Age and sex were covariates and cognitive status was included as a random effect.

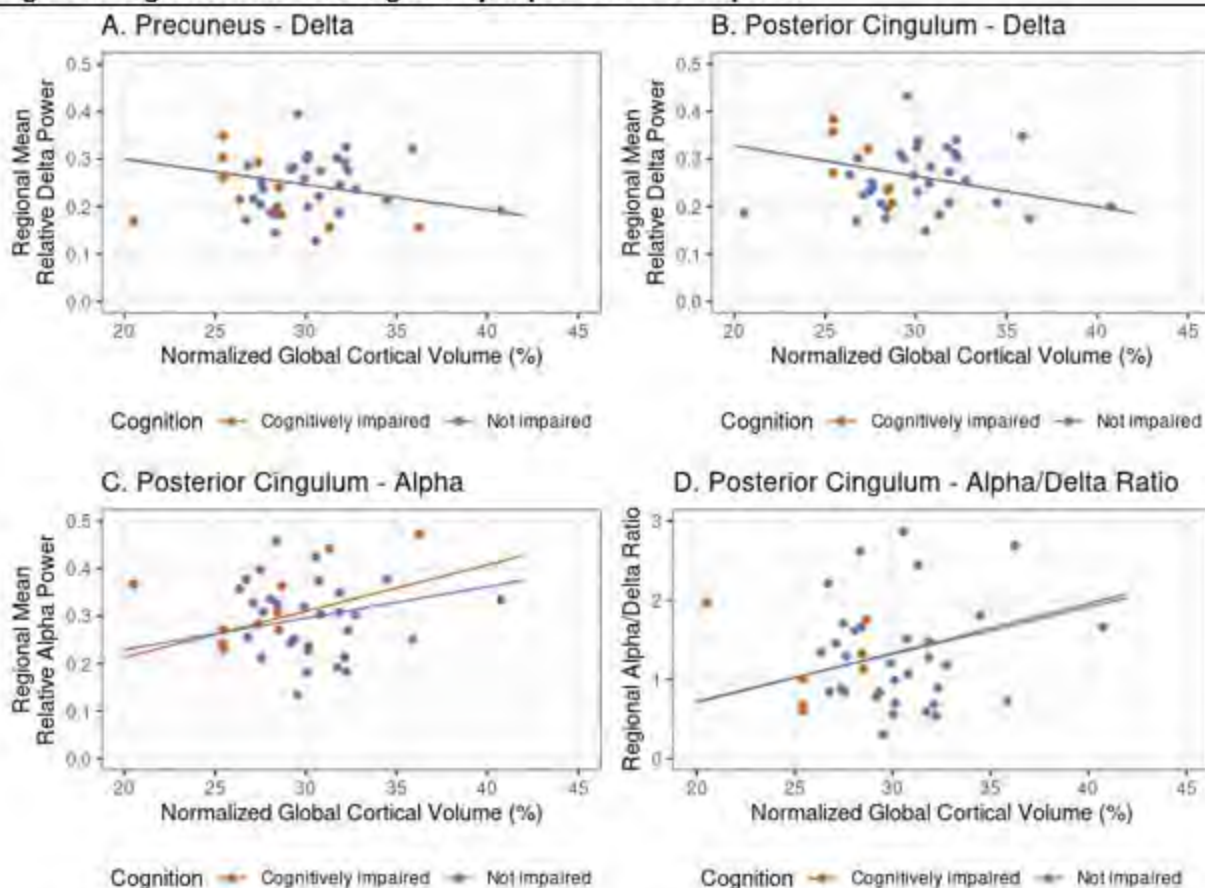
Results

Normalized GCV was negatively associated with MRP- δ in the precuneus ($\beta=-0.0054$, $p=0.084$) (Figure 1A) and posterior cingulum ($\beta=-0.0064$, $p=0.048$) (Figure 1B). The posterior cingulum also demonstrated higher beta coefficients for the cognitively impaired vs. nonimpaired for MRP- α ($\beta=0.0097$ vs. 0.0066) (Figure 1C) and α/δ ratio ($\beta=0.0624$ vs. 0.0593) (Figure 1D). Marginal associations for MRP- α ($\beta=0.0082$) and α/δ ratio ($\beta=0.0609$) did not reach significance.

Conclusions

Stronger spontaneous δ activity in the posterior cingulum is associated with global cortical atrophy, a known AD biomarker. MRP- α and the α/δ ratio in this region may be able to distinguish cognitively impaired from nonimpaired subjects and help in determining those at risk for AD.

Figure 1. Regression lines for cognitively impaired vs. nonimpaired



Note: Regional mean relative power in the delta frequency band is negatively associated with normalized global cortical volume in the precuneus (A; $\beta = -0.0054$, $p = 0.0837$) and posterior cingulum (B; $\beta = -0.0064$, $p = 0.0481$). Beta coefficients are higher for cognitively impaired vs. nonimpaired in the alpha frequency band (C; $\beta = 0.0097$ vs. 0.0066) and for the alpha/delta ratio (D; $\beta = 0.0624$ vs. 0.0593). Depicted regression lines are for a 66-year-old female.

(Filename: TCT_1653_ZabeccaBrinsonASNRLateBreakingAbstract2021-Figure1.jpg)

851

Atypical Finding of Magnetic Resonance in a CLN Type 5 Patient

A Lima Júnior¹, A Sampaio Clarindo¹, P Coimbra², N De Abreu¹, M Buratti Leal¹, L Gomes³, J Rodrigues⁴, A Pessoa⁵
¹Hospital Antonio Prudente, Fortaleza, Ceará, ²Hospital Antônio Prudente, Fortaleza, Brazil, ³UniRV, Goianésia, Goiás, ⁴Antonio Prudente Hospital, Ceará, Fortaleza, ⁵Hospital Infantil Albert Sabin ; Universidade Estadual do Ceará - UECE, Fortaleza, Ceará

Purpose

Ceroid neuronal lipofuscinosis (CLN) is a group of autosomal recessive neurodegenerative diseases, characterized by the lysosomal accumulation of an autofluorescent lipopigment with lipofuscin properties. Ceroid neuronal lipofuscinosis 5 (CLN5) was provided as a Finnish variant of late infantile CLN (Finnish vL1CLN). With the identification of the molecular defect, CLN5 now refers to CLN caused by a mutation in the CLN5 gene. Signs and symptoms usually develop between the ages of 4.5 and 7 years, although cases of late onset have been reported. Symptoms range from visual loss, ataxia, myoclonus and cognitive impairment. MRI findings are usually the main cause of atrophy of the cerebellum, in addition to increased signal intensity of the periventricular white substance in T2 weighting. This study refers to a case report of a patient with CLN5, with emphasis on MRI findings.

Materials and Methods

Case report for a prospective study of an 11-year-old patient who started, at 5, cognitive impairment accompanied by progressively difficult to control epilepsy using high doses of clobazam, lamotrigine and sodium valproate.

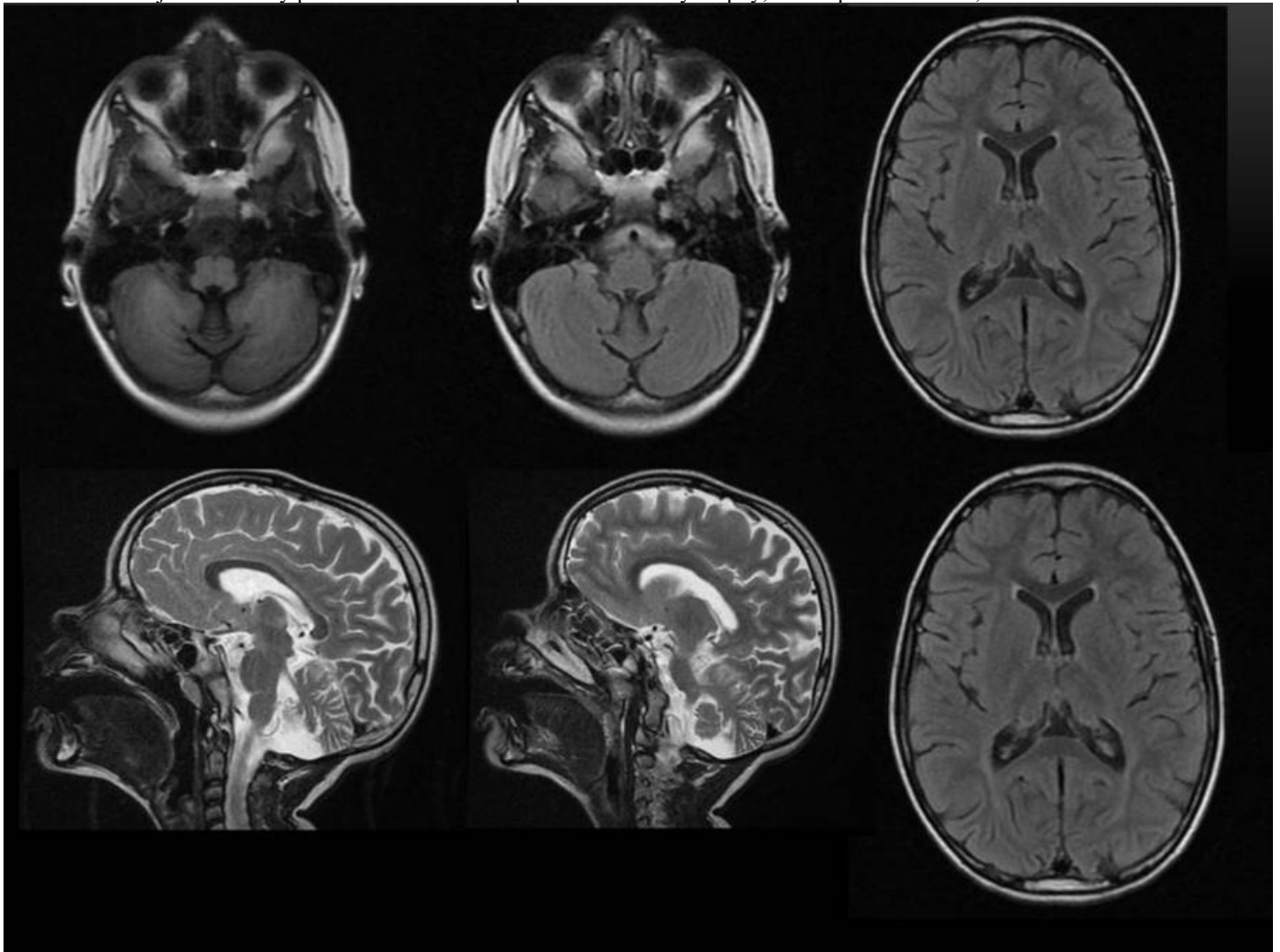
Results

An analysis of MRI images made at 7 years of age allows us to state that the patient, at the time, had a T2-weighted axial and sagittal

section, reduced fibers and commissures of the corpus callosum accompanied by a reduction in the mantle of the periventricular white substance in its later aspect.

Conclusions

Some clinical and radiological characteristics are typical of this disease, such as age, cognitive retardation and the appearance of changes in the periventricular white matter sign, however, there are particularities that draw attention, mainly the image, due to the absence of one of the main signs found in CLN5 patients, which would be the important atrophy of the cerebellum, therefore, we should not stick just to already previous classics to suspect some leukodystrophy, in this particular case, CLN5.



(Filename: TCT_851_Slide4.JPG)

888

Automated Estimation of Ischemic Core Volume on Non-Contrast-enhanced CT via Machine Learning

I Chen¹, B Tsui¹, J Qiao¹, W Hsu¹, L Sharma¹, M Bahr-Hosseini¹, M Nour¹, D Kim², N Rao³, N Salamon⁴, J Saver¹, D Liebeskind¹, K Nael¹

¹University of California, Los Angeles, Los Angeles, CA, ²UCLA, Santa Monica, CA, ³David Geffen School of Medicine at UCLA, Los Angeles, CA, ⁴University of California Los Angeles, Los Angeles, CA

Purpose

Accurate estimation of ischemic core on baseline imaging has treatment implications in patients with acute ischemic stroke (AIS). Machine learning (ML) algorithms have shown promising results in estimating ischemic core using routine non-contrast CT (NCCT). We used a ML-trained algorithm to quantify ischemic core volume on NCCT and compared the results to concurrent diffusion MRI as the reference standard in patients with AIS.

Materials and Methods

We analyzed consecutive anterior circulation AIS patients who had baseline (pretreatment) NCCT and MRI (DWI). Ischemic lesion volume was calculated on MRI-DWI using an automated software (Olea Medical SAS, La Ciotat, France). An automatic segmentation

approach using a combination of traditional 3D graphics and statistical methods, and ML classification techniques (Brainomix, Oxford, United Kingdom) was used to identify ischemic core voxels on NCCT. Total ischemic core volumes on ML-NCCT and DWI-MR were quantitatively compared by Bland-Altman plots and Pearson correlation.

Results

A total of 50 patients (27 female, 23 male, mean age 72.6 years) were included. Baseline imaging was performed within 173 ± 143 minutes (mean \pm SD) from symptom onset. The mean time difference between MRI and NCCT was 72 min. The baseline NIHSS was 14, 8-21 (Median, IQR). Algorithm-segmented ischemic core volume detected on NCCT was median 12.7 mL, IQR 3.5-26.0 mL. Ischemic core volume on DWI MRI was median 8.8 mL, IQR 3.2-34.0 mL. ML-NCCT core volumes significantly correlated with DWI MRI core volumes, $r=0.61$, $p<0.001$. The mean difference between the ML-NCCT and DWI MRI core volumes was 12.4 mL, $p=0.81$. For the reperfusion treatment threshold of an ischemic core volume within 70 mL, while no patients would have been excluded using our algorithm, five patients would have been incorrectly dichotomized as having an ischemic volume of <70 mL compared to MRI.

Conclusions

This ML-approach accurately quantifies ischemic core volume on NCCT compared to the reference standard of diffusion MRI in patients with AIS.

819

Automated Labelling of Radiologic Findings in Head Computed Tomography Reports via Natural Language Processing

M Iorga¹, M Drakopoulos¹, A Naidech², T Parrish², V HILL²

¹Feinberg School of Medicine, Chicago, IL, ²Northwestern Medicine, Chicago, IL

Purpose

Machine learning algorithms which analyze images to extract diagnostic features have become increasingly popular in radiology research. Gathering large labeled datasets is one of the primary challenges in training successful machine learning models. High-fidelity labelling is often performed manually, which can place large burdens on clinical or research personnel. In this work we explore automated labelling of head computed tomography scans by training a natural language processing algorithm to analyze radiology reports.

Materials and Methods

An institutional data warehouse search identified 97,552 head CT reports collected at Northwestern Medicine between 2008 and 2019, from which 1002 were randomly sampled for labelling. Each report was manually analyzed to determine if it describes (1) any abnormal findings, (2) any emergent findings, or (3) any new hemorrhage. Labels were initially created by a medical student and confirmed by a neuroradiologist. For natural language processing analysis, each report was processed into a frequency vector of unigrams, bigrams, and trigrams. Three logistic regression classifiers were trained (one independent classifier per label type) to predict if each report describes abnormal findings, emergent findings, or hemorrhage based on the n-gram frequency vector using L2 regularization and five-fold cross-validation.

Results

779 reports were manually labeled as abnormal; 363 reports as emergent; and 215 reports as acute intracranial hemorrhage. Report embedding produced 2,415 unigrams, 13,447 bigrams, and 19,117 trigrams across the entire corpus (34,979 features in total). Classifier performance was assessed using the area under the receiver operating characteristic curve (AUC), Dice similarity coefficient (DSC), and Fisher's exact test for two-way tables: hemorrhage (AUC: 0.981, DSC = 0.862, $p \ll 0.01$), emergent findings (AUC = 0.941, DSC = 0.810, $p \ll 0.01$), any abnormal findings (AUC = 0.967, DSC = 0.830, $p \ll 0.01$). ROC curves for each model are displayed in Figure 1.

Conclusions

High-performance models were trained for each label type, with all models performing significantly better than chance. When compared to previous work, our models underperformed on detecting emergent reports (AUC 0.941 $<$ 0.966), but outperformed on detecting both abnormal reports (AUC 0.967 $>$ 0.957) and hemorrhage (AUC 0.981 $>$ 0.961). Combining n-grams with logistic regression is a synergistic and robust approach to labeling head CT reports.

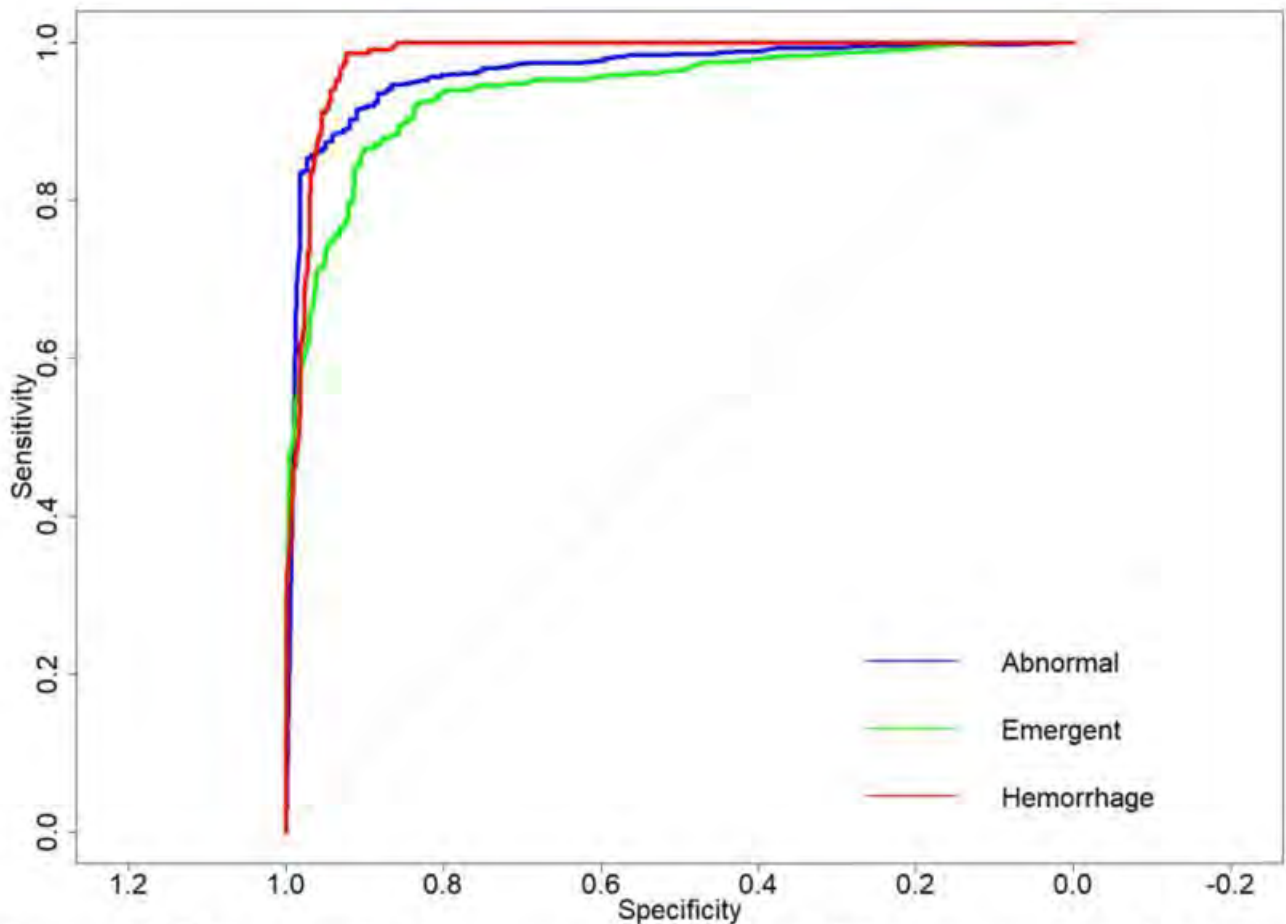


Figure 1: ROC Curves. Receiver operator characteristic (ROC) curves are shown for abnormal (blue), emergent (green), and hemorrhage (red) classifiers. ROC curves show generally strong performance across classifiers. The abnormal model (AUC = 0.967) has the steepest initial ascent, suggesting a high-specificity model is optimal while the hemorrhage model (AUC = 0.981) has the largest ascent, suggesting a higher sensitivity model. The emergent model (AUC = 0.941) typically underperformed the others but had more balanced performance across threshold values.

(Filename: TCT_819_IorgaASNRFigure.jpg)

587

Automated Severity Grading of Enlarged Periventricular Spaces in the Basal Ganglia Using an Interpretable, 3D Deep Learning Framework

B Williamson¹, V Khandwala¹, D Wang¹, L Wang¹, P Khatri¹, A VAGAL²

¹University of Cincinnati, Cincinnati, OH, ²University Of Cincinnati Medical Centee, Cincinnati, OH

Purpose

Enlarged perivascular spaces (PVS) is a key indicator of total small vessel disease (SVD) burden and, can aid in risk stratification including cognitive decline after acute stroke (Staals et al., 2016). Although white matter hyperintensities and lacunes have received research attention, PVS grading is a relatively underexplored entity in SVD. Development of automated scoring of PVS could aid research in the mechanisms of PVS and assist large studies evaluating PVS as a biomarker for clinical outcomes (Dubost et al., 2019). While automated methods for scoring PVS have been explored, they typically require high-resolution imaging that is untenable in acute stroke settings. The goal of our study is to develop a framework that can classify PVS severity with standard-of-care T2-w images.

Materials and Methods

We utilized the dataset from an ongoing population based acute stroke study (APRISE; R01 NINDS NS103824-01). We used a subset of 90 patients based on: presence of diagnostic axial T2-weighted image and presence of central read score for PVS severity at basal ganglia level. We first performed n4 bias correction, smoothing, alignment to an MNI template. We then split the data into a training

set (n=72) and a test set (n=18) used for final model evaluation. We binarized the PVS classification as 0 (none or mild; 0-10 PVS) and 1 (moderate to severe; 11+) PVS. A 50-layer 3D residual CNN was used for classification (Hara et al., 2017). During training, we performed a validation split of 20% to monitor network performance and implemented early stopping on validation F1 to decrease overfitting. A 3D Gradient Class Activation Mapping (3DGradCAM) was used to visualize the regions of focus for the final classification.

Results

Our model was able to classify PVS severity on the final test set (F1 = 0.69, Sensitivity = 0.725, Specificity = 0.53). More importantly, 3DGradCAM revealed a focus on the basal ganglia to make the classification (Fig 1). Notably, the whole T2 image was fed into the network, not just slices containing the basal ganglia, making the model more adaptable in clinical settings.

Conclusions

We successfully developed an interpretable model that was able to predict PVS grading with good accuracy. More data is available and will be included in final analyses. This is an important step towards the development of algorithms that can be applied to standard of care imaging to aid prognosis for SVD. Future work will aim to include clinical measures and multimodal imaging to improve model performance.

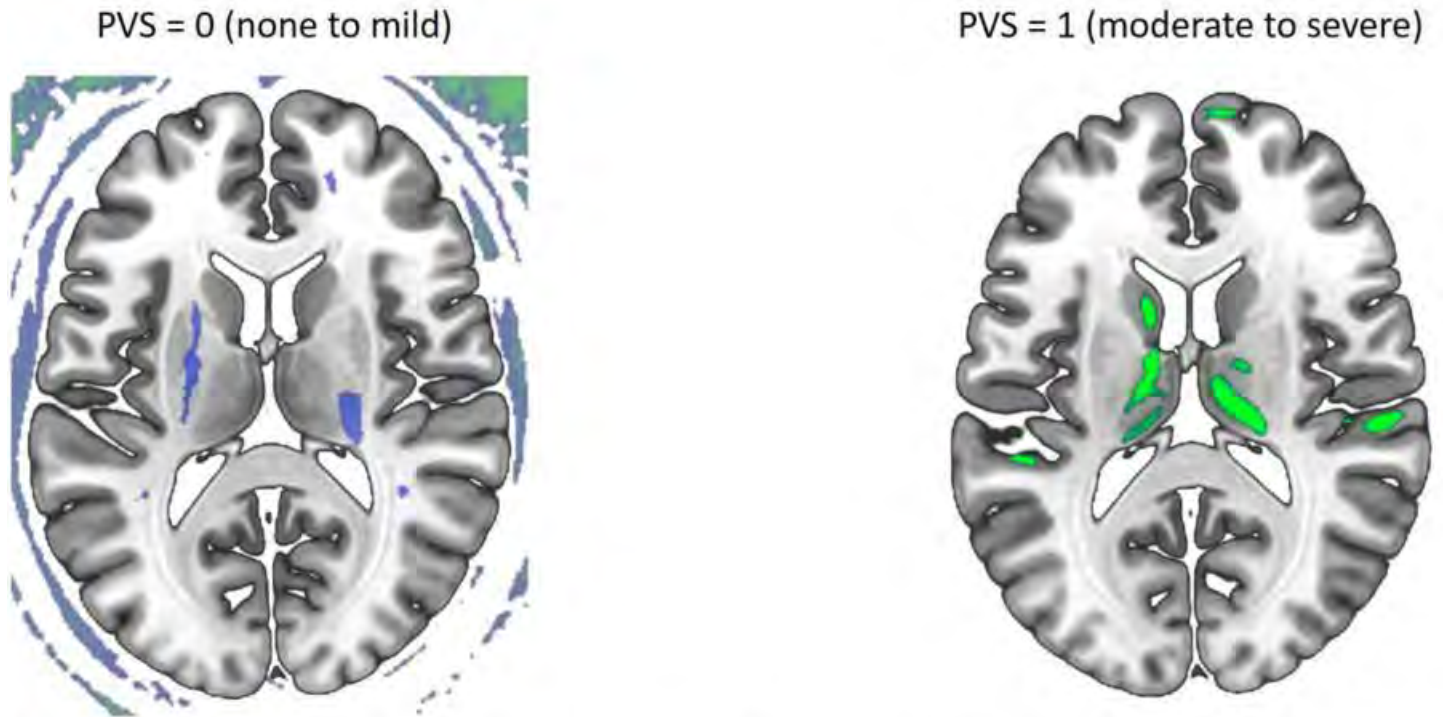


Figure 1. Examples of gradient activation maps showing the regions of focus for the network to classify each class. The color scale (blue to green) shows the relative importance of different regions compared to the rest of the brain within each subject. The network seems to weight the basal ganglia much more heavily when classifying moderate to severe PVS. This is consistent with the fact that PVS rating was determined by the number of PVS in the basal ganglia. The model looks to be comparing adjacent thalamic tissue to signal in the putamen to make its final decision.

(Filename: TCT_587_ASNR_Figure_1.jpg)

1641

Automated Software for Detecting the Hyperdense Vessel Sign in Acute Stroke

DV Giurgiutiu¹, A Filly², J Honce³, K Kwok⁴, B Mitchell⁵, K Copeland⁶

¹Augusta University Medical Center, Augusta, GA, ²Community Hospital of Monterey, Monterey, CA, ³University of Colorado School of Medicine, Aurora, CO, ⁴Central Valley Imaging Medical Associates, Manteca, CA, ⁵Charlotte Radiology, PA, Charlotte, NC, ⁶Boulder Statistics, Steamboat Springs, CO

Purpose

Rapid detection of large vessel occlusion (LVO) is essential for rapid triage for thrombectomy to salvage at-risk tissue. Early detection of LVO on noncontrast CT (NCCT) head would allow for initial triage and expedite advanced imaging. Rapid HVS, a new automated

software for detecting the hyperdense vessel sign (HVS), was compared to experienced radiologists for the early detection of LVO on NCCT.

Materials and Methods

Scans were selected from a database of 335 scans from three studies, of which 166 were selected for the study by stratified random selection. Images were evaluated by Rapid automated software, and six readers (three radiologists, and three neuroradiologists). There were two reads for each scan, 30 days apart. The Rapid algorithm returns a score between zero and one, and a threshold of 0.5 was applied to indicate a positive HVS. A scan rating confidence scale was used, from "very confident of absence," to "very confident of HVS," and a separate "technically inadequate" rating. The expert readers' scores were compared to the Rapid HVS score.

Results

Patient demographics: 54% of the sample were men. Ages ranged from 23 to 94 with a median of 65 years. GE, Philips, Siemens, and Toshiba scanners are represented in the sample. The median agreement with RAPID was 81%. An interchangeability analysis demonstrated that the Rapid software read was interchangeable with the results from the clinical readers. Among patients with CTA-confirmed LVO, 26-57% of human readers identified an HVS compared with 53% for the software. Among patients with no LVO, 90-100% of human readers did not detect an HVS compared with 85% for the software. Processing time was a median of 54 seconds, range of 44 to 74 seconds. The scan rating confidence grade by the experts correlated with the Rapid HVS score. Below a HVS algorithm score of 0.4 the proportion of LVO positive scans was 46% (indeterminant), between 0.4 and 0.6 the proportion of LVO positives scans was 62.5% (probable), and above 0.6 the proportion of LVO positive scans was 90% (likely).

Conclusions

Expert readers, and Rapid software, can both detect an HVS in about 55% of CT head images with an associated LVO on CTA. Rapid automated image processing facilitates faster triage of patients for more advanced imaging and therapeutic interventions.

1347

Automatic Detection and Segmentation of Gliomas using Deep Learning

S KIHIRA¹, X Mei¹, K Mahmoudi¹, C Liu¹, A Doshi¹, K Nael²

¹Icahn School of Medicine at Mount Sinai, New York, NY, ²UCLA, Los Angeles, CA

Purpose

Gliomas are the most common primary brain neoplasms accounting for roughly 40-50% of all malignant primary central nervous system tumors. Follow up surveillance of patients with glioma requires frequent MR imaging to monitor the size and extent. We aim to develop a deep learning-based framework for detection and segmentation of gliomas.

Materials and Methods

In this retrospective IRB approved study, patients were included if they 1) had a diagnosis of glioma with known surgical histopathology and 2) had preoperative MRI with FLAIR sequence. The entire tumor volume including FLAIR hyperintense infiltrative component and necrotic and cystic components was manually segmented by an expert neuroradiologist on FLAIR images. Deep learning-based U-Net framework was developed based on symmetric architecture from the 512 x 512 segmented maps from FLAIR as the ground truth mask. The input size was 256 x 256 x 3. The ReLU activation function was implemented on each convolutional layer. Max pooling was used after two consecutive convolutional layers in the downsampling path. A batch size of 32, Adam optimizer with a learning rate 1e-4, and binary cross entropy loss function was used. Stratified sampling was performed to split the database into training (n=98), validation (n=11), and testing (n=28). Dice similarity coefficient (DSC) was calculated to assess the deep learning-based segmentation map against ground truth segmentation using the intersection over the union between the masks.

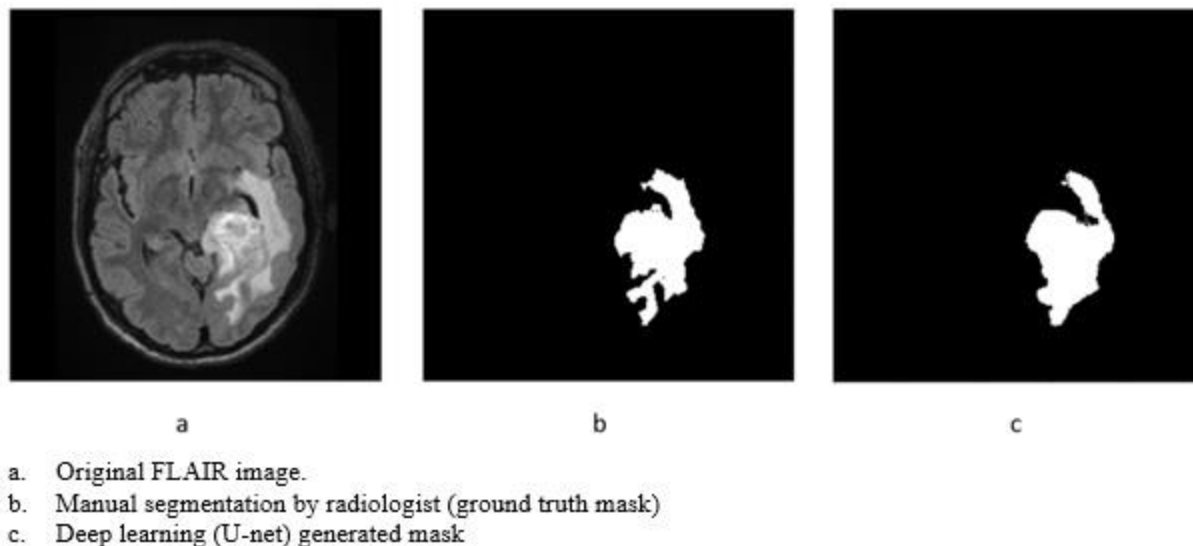
Results

A total of 137 patients (age: 59 ± 15, M/F 76/61) with 4/5/128 WHO grade II/III/IV gliomas were included. The mean (IQR) tumor volume was 37.7 (41.5) mL. The DSC of the generated mask compared to the ground truth mask on FLAIR was 0.8 in the testing group.

Conclusions

Our preliminary results showed that the described deep learning-based framework can detect and segment heterogeneous group of gliomas with a DSC of 0.8. If its potential is realized, this automated framework may provide a much needed consistency in quantitative assessment of tumor size in patients with glioma.

Figure:



(Filename: TCT_1347_Gliomasegmentationfigure.jpg)

1462

Automatic Identification of Emergent Findings on Head CT Scan using Deep Learning

Y Wu¹, A Adate¹, S Lalvani¹, M Iorga², T Parrish³, A Katsaggelos¹, V HILL³

¹Electrical Computer Engineering, Northwestern University, Evanston, IL, ²Feinberg School of Medicine, Chicago, IL, ³Department of Radiology, Northwestern University, Chicago, IL

Purpose

To implement a deep learning algorithm to automatically identify a patient as having an emergent finding (at least one of 21 different conditions) on a head CT study in order to create an efficient workflow in the reading room.

Materials and Methods

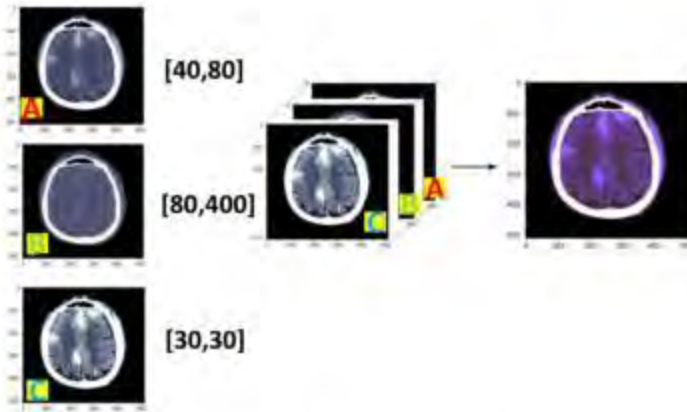
A total of 1405 CT scans were acquired from 997 subjects. Scan-based, whole brain labels were determined from the radiology reports and used as the gold standard to generate the patient's condition; emergent (e.g., hemorrhage, fractures, white matter disease, infarct, etc.) or non-emergent (e.g., chronic infarct, chronic small vessel ischemic change, volume loss). Five-fold cross-validation was used, including 80% as the training dataset and 20% as the validation dataset. For each scan, three window levels were applied to enhance the display of the brain, soft tissues and stroke using the pair of window and center of [80,40], [400,80] and [30,30] respectively. The concatenated inputs were normalized into the range of 0 to 1 and rescaled to the same volume size (48, 256, 256). A sequence to sequence model was designed to make the classification and generate slice-level attention weights[1]. Each CT slice was embedded into a shared 2D convolutional neural network (CNN) to extract feature vectors, which were passed into an attention layer to get a weight for each slice. Weighted average feature vectors were computed for each CT scan and fed into two fully connected layers, followed by the sigmoid activation function to predict the patient's status. A gradient back-propagation-based visualization method (Grad-CAM)[2] was applied to the volume to map the location of the emergent findings.

Results

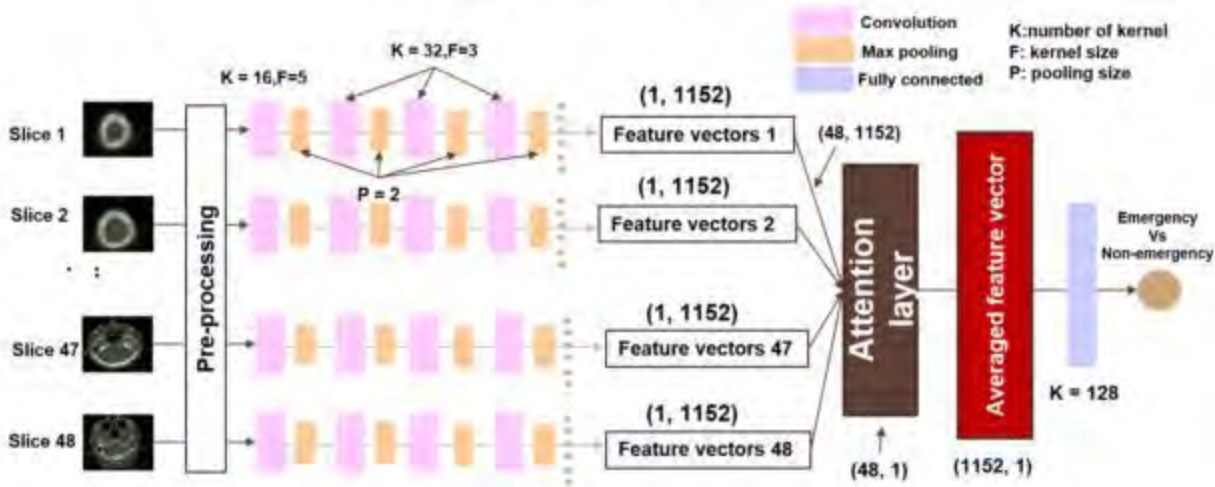
The sequence CNN model was able to identify the presence of any of the 21 conditions in the emergent category averaged across all five-folds with an overall accuracy of 0.848 ± 0.003 , sensitivity of 0.862 ± 0.003 , and ROC-AUC score of 0.872 ± 0.002 . The attention weights for each scan successfully identified the key axial slices and the Grad-CAM mappings from these slices demonstrated the discriminative locations used by the model.

Conclusions

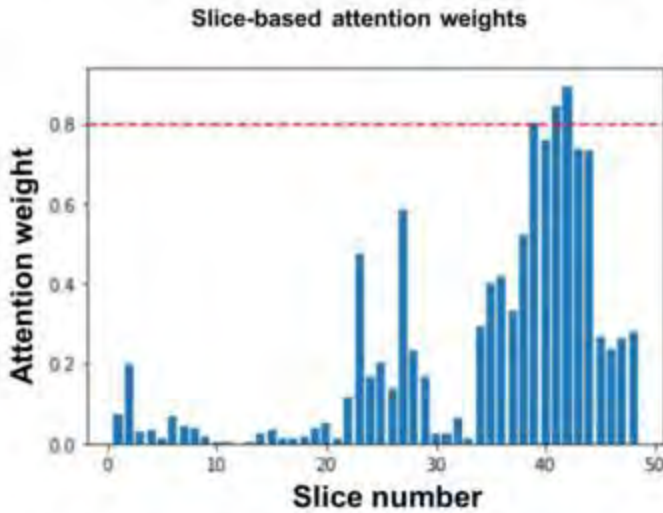
Our current sequence CNN model can successfully detect head CT emergencies and achieve comparable performance with current literature[3] with only the volume-level labels. The visual interpretation of the model provided an important way to alert radiologists of unexpected brain emergencies. In the future, we expect to scale up our experiment with the addition of 33,000 Head CT Scans and their corresponding radiology reports.



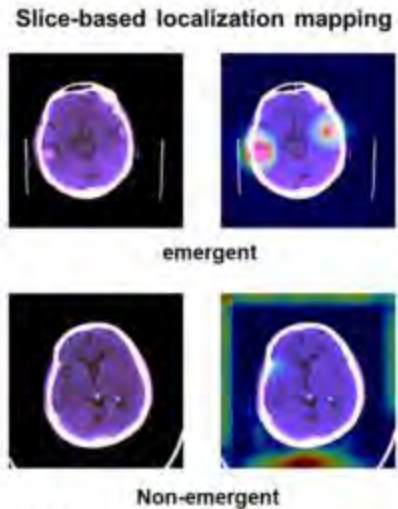
(A) Image Preprocessing



(B) Sequence Model Architecture



(C) Slice-based Attention Weights on a Scan



(D) Slice Visualization Mappings

Automatic Volumetric Segmentation of Postoperative Gliomas Using Machine Learning

E Lotan¹, B Zhang², S Dogra³, D Wang⁴, Y Lui⁴

¹New York University School of Medicine, New York, NY, ²NYU Langone Medical Center, New York, NY, ³NYU Grossman School of Medicine, New York, NY, ⁴NYU Langone Health, New York, NY

Purpose

Assessing changes in brain tumors over time is important for clinical evaluation, response to treatment. In particular, assessment of post-surgical imaging is challenging due to confounding appearance of resection cavities and brain distortions. Deep learning has shown great promise in assessment of preoperative gliomas [1]; however, similar tools for postoperative imaging are lacking. Here, we develop a machine learning model for automatic volumetric segmentation of postoperative gliomas.

Materials and Methods

The dataset consists of 335 preoperative cases from the BraTS 2019 dataset enriched using 100 postoperative cases manually-segmented (by two consensus review) (2). Each case comprises four 3D MRI contrasts (T1, T1 with contrast, T2 and FLAIR), rigidly aligned, resampled to 1 mm³ isotropic resolution and skull-stripped. The ground truth annotations follow methodology of the BraTS annotation protocol [1] with sub-regions: (1) enhancing tumor; (2) necrotic tumor-core; and (3) whole tumor ((1)+(2)+peritumoral edema). In order to address the labeling of any surgical resection cavities present, these areas were combined into sub-region #2. Dataset was split as follows: training (70% of in-house, 90% of BraTS cases), validation (10% of both in-house and BraTS cases) and test (20% of in-house postoperative cases). The model is based on fusion of a cascaded anisotropic convolutional neural network (CACNN) [2] and autoencoder regularization method [3] for preoperative glioma segmentation followed by hyperparameter optimization (learning rate, optimization function, dropout rate) and data augmentation (Fig. 1A). Dice score served as segmentation evaluation metric.

Results

The proposed regularized CACNN model achieved dice scores of 0.83 ± 0.09 , 0.84 ± 0.08 and 0.72 ± 0.12 for whole tumor, tumor core and active tumor sub-regions, respectively (Fig. 1B); compared to the baseline model's [2] dice scores: 0.81 ± 0.12 , 0.73 ± 0.25 and 0.62 ± 0.23 . The model takes ~3-5 minutes for segmentation and volume calculation.

Conclusions

Retraining and fusion of existing models that were designed to segment preoperative gliomas achieves high performance on both preoperative and clinically important postoperative cases. In fact, enhancing the fused model via hyperparameter optimization and data augmentation resulted in higher dice scores overall compared with results obtained by individual original models.

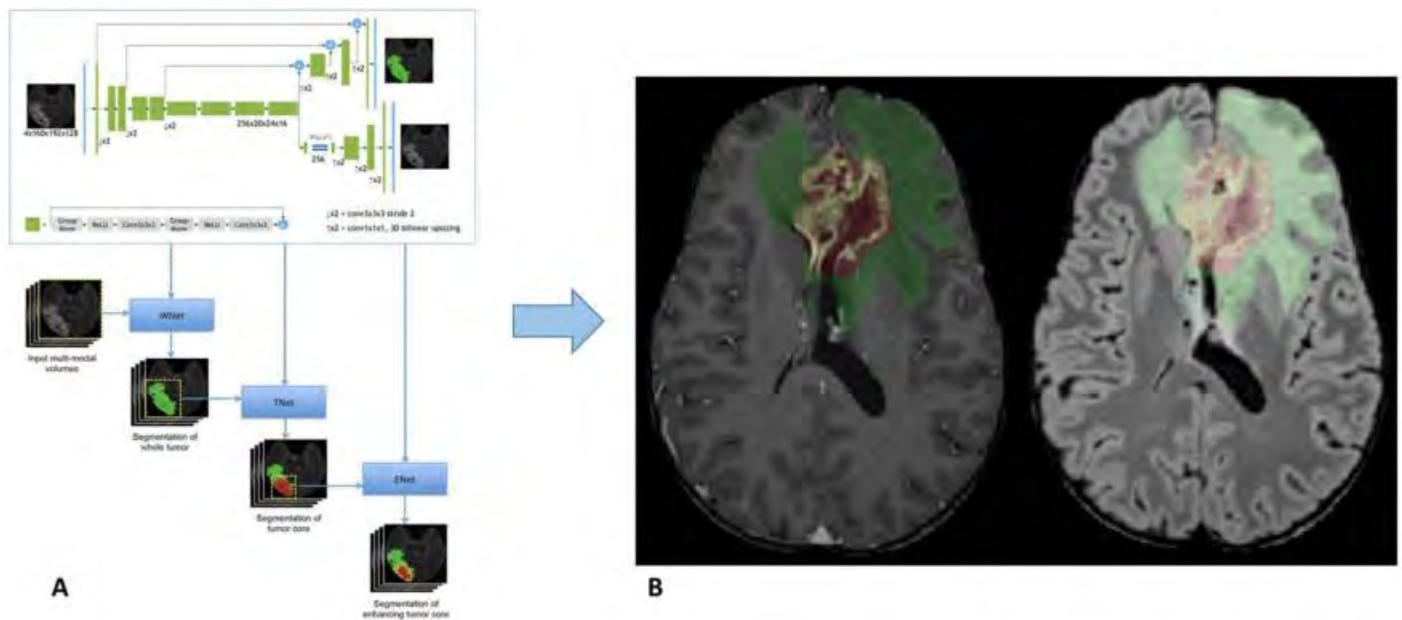


Fig. 1. Cascaded Anisotropic Convolutional Neural Networks using Regularized Autoencoder

(Filename: TCT_936_Seg_Fig1_300dpi.jpg)

Brain and Lung Imaging Correlation in COVID-19 Patients: Could the Severity of Lung Disease Reflect the Prevalence of Neuroimaging Abnormalities? A Global Multicenter Observational Study

A Mahammedi¹, A Ramos², N Bargallo³, M Gaskill⁴, L Saba⁵, H Carrete Jr⁶, A VAGAL⁷

¹University Of Cincinnati, CINCINNATI, OH- OHIO, ²Hospital 12 de Octubre, Madrid, Madrid, Spain, ³Hospital Clinic de Barcelona., Barcelona, Barcelona, ⁴University Of Cincinnati, CINCINNATI, OH, ⁵N/A, N/A, ⁶Universidade Federal de Sao Paulo, São Paulo, SP, ⁷University Of Cincinnati Medical Centee, Cincinnati, OH

Purpose

To study the association between chest and brain imaging abnormalities in COVID-19 patients with neurological symptoms.

Materials and Methods

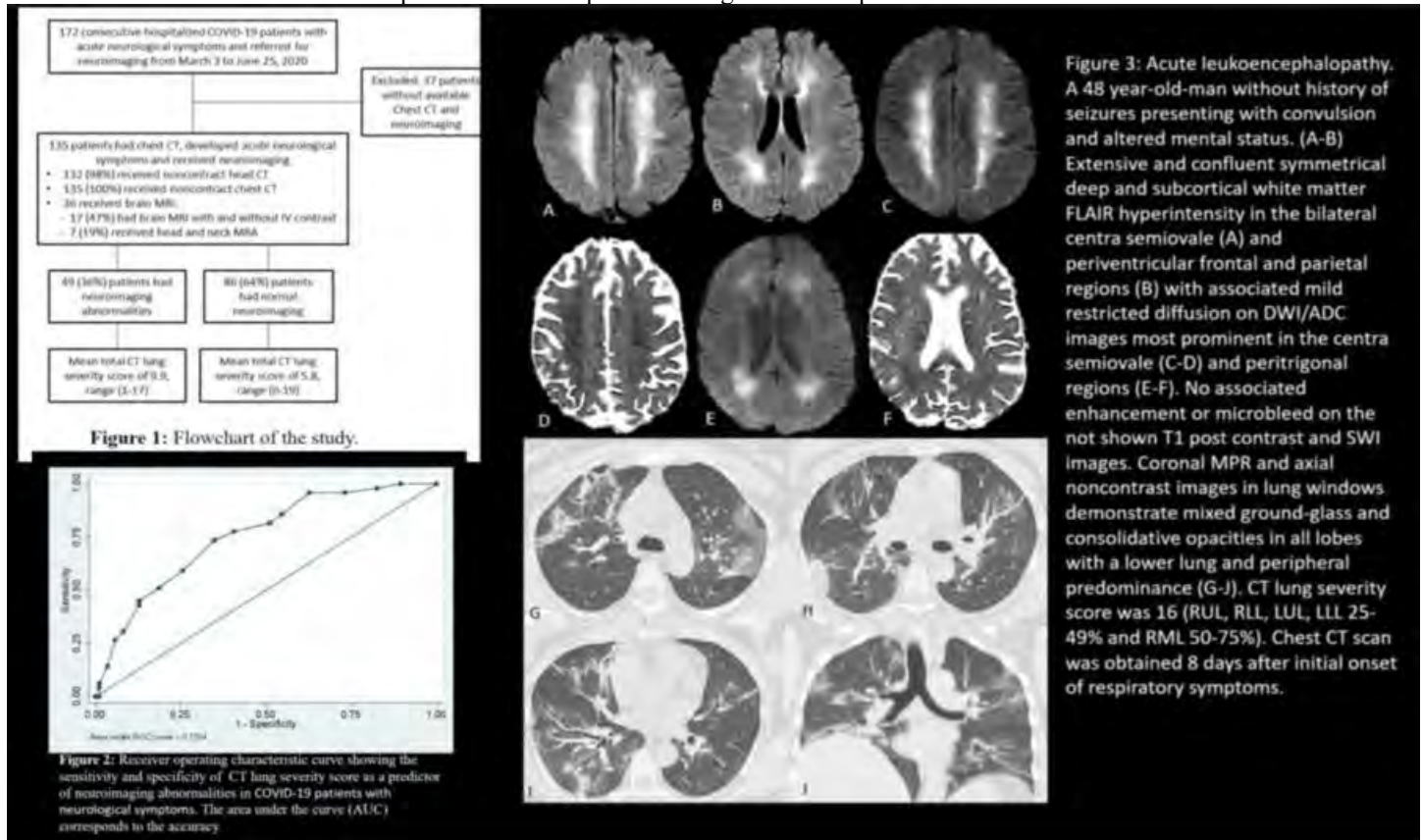
In this retrospective, international multicenter study, we reviewed the electronic medical records and imaging of hospitalized COVID-19 patients from March 3, 2020 to June 25, 2020. Our inclusion criteria were patients diagnosed with SARS-CoV-2 infection with acute neurological manifestations and available chest CT and brain imaging. The five lobes of the lungs were individually scored on a scale of 0 to 5 (0 corresponded to no involvement and 5 corresponded to more than 75% involvement). A CT lung severity score was determined as the sum of lung involvement, ranging from 0 (no involvement) to 25 (maximum involvement).

Results

A total of 135 patients met the inclusion criteria with 132 brain CT, 36 brain MRI, 7 MRA head and neck and 135 chest CT studies. Compared with patients without neuroimaging abnormalities 86 (64%), the 49 (36%) patients with neuroimaging abnormalities had a significantly higher mean CT lung severity score (9.9 versus 5.9, $P < 0.001$). These patients were more likely to present with ischemic stroke (40 [82%] vs 11 [13%], $P < 0.0001$) and were more likely to have either ground-glass opacities (GGOs) or consolidation (36 [73%] vs 73 [84%], $P = .01$) in the lungs. A threshold of CT lung severity score > 8 was found to be 74% sensitive and 65% specific for neuroimaging abnormalities. The neuroimaging hallmarks of these patients were acute ischemic infarct (28%), intracranial hemorrhage (10%) including microhemorrhages (19%), leukoencephalopathy with and/or without restricted diffusion (11%). The predominant CT chest findings were peripheral GGOs with or without consolidation.

Conclusions

CT lung disease severity may be predictive of acute neuroimaging abnormalities in COVID-19 patients with neurological manifestations. This can be used as a predictive tool in patient management to improve clinical outcome.



(Filename: TCT_1005_Figures.jpg)

G Sparacia¹, M Shahriari², R Cannella³, G Mamone⁴, G Parla¹, V Lo Re¹, I Petridis¹, L Maruzzelli¹, A Comelli⁵, A Iaia², R Miraglia⁴, A Luca¹
¹IRCCS-ISMETT, Palermo, Italy, ²Christiana Care Health System, Newark, DE, ³University of Palermo, Palermo, Italy, ⁴IRCCS-ISMETT, Palermo, Sicily, ⁵Ri.MED, Palermo, Italy

Purpose

Hepatic encephalopathy (HE) is a brain dysfunction which manifests with a wide spectrum of neuropsychiatry abnormalities that occurs in the setting of end stage liver disease. It is one of the most serious complications of liver cirrhosis and can be the first decompensating event in about 20% of these patients with a 5-year survival of about 20%. The aim of this study was to evaluate the performance of radiomics analysis for the diagnosis and staging of hepatic encephalopathy (HE) in adult cirrhotic patients undergoing brain MRI.

Materials and Methods

This retrospective IRB-approved study included adult patients with cirrhosis undergoing brain MRI on a 3T MR scanner between October 2018 and February 2020. Patients without history of chronic liver disease undergoing brain MRI on a 3T MR scanner in the same period of cirrhotic patients with the identical imaging protocol were selected as controls. HE was categorized according to the underlying liver disease, severity of clinical manifestation, and number of episodes. Texture analysis was performed on axial T1-weighted images by a radiologist blinded to any patients and clinical data using a freely available texture analysis software (LIFEx, version 5.10) by manually drawn a polygonal region of interest in the bilateral lentiform nuclei at the level of the foramina of Monro. A total of 43 texture features were automatically extracted and the most discriminative texture features were selected by using the statistical Benjamini-Hochberg procedure and used for multiparametric logistic regression models and classifiers for the diagnosis and grading of HE. The area under the receiver operating characteristics (AUROC) with 95% confidence interval (C.I.), p-value, and cutoff values were calculated. Statistical analysis was conducted using SPSS Statistics software package version 25 (SPSS, Chicago, USA) and the ROC curve fitting function version 2 under MatLab (The MathWorks Inc., Natick, MA, USA).

Results

The final study population consisted of 124 patients including 70 cirrhotic patients and 54 non-cirrhotic controls. The texture-based model provided an excellent diagnostic performance for the discrimination of cirrhotic patients with an AUROC of 0.971 (P<0.0001). The performance of radiomics features for the prediction of grade 1 HE was statistically significant (AUC 0.754; P <0.0001) as well as for the prediction of grade ≥ 2 HE (AUC 0.827; P<0.0001).

Conclusions

Brain MR radiomics allow to discriminate cirrhotic patients and to predict HE severity.

Radiomics features predictor for HE = 1

(AUC 0.754 [95% CI: 0.610, 0.897] P = <0.0001) (Fair test)

Cutoff	Sensitivity	Specificity	Accuracy	PPV	NPV
>-0.130	93.7%	59%	63.4%	90%	70%

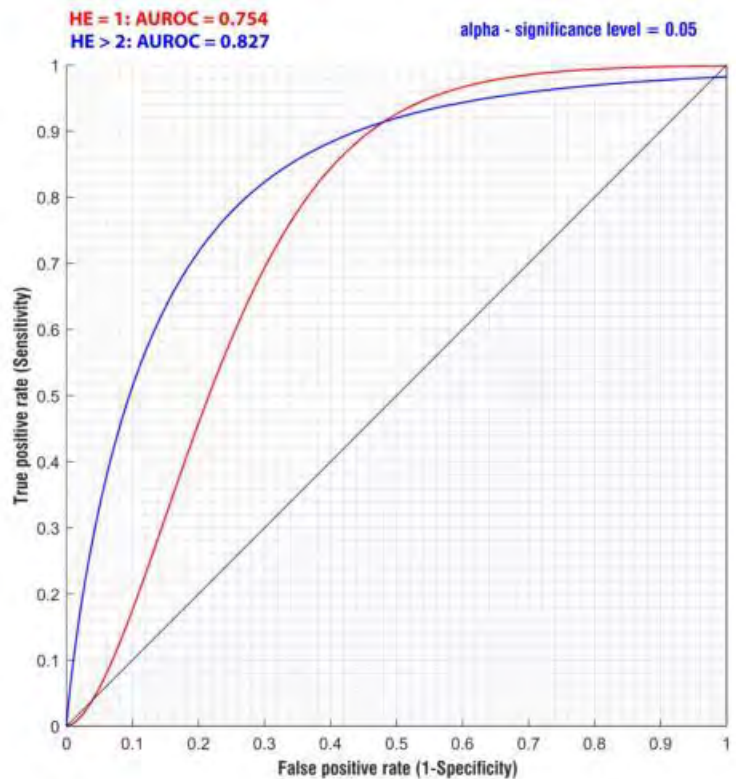
AUROC = Area under the receiver operating characteristics; CI = confidence interval; PPV = Positive Predictive Value; NPV = Negative Predictive Value

Radiomics features predictor for HE = >2

(AUC 0.827 [95% CI: 0.71686, 0.93772] P = <0.0001) (Good test)

Cutoff	Sensitivity	Specificity	Accuracy	PPV	NPV
>-0.089	95.4%	57.4%	64.2%	93%	67.2%

AUROC = Area under the receiver operating characteristics; CI = confidence interval; PPV = Positive Predictive Value; NPV = Negative Predictive Value



(Filename: TCT_1264_LOG_HE1_LOG_HE234.jpg)

Brain metastases in patients with non-small cell lung cancer without brain metastases at initial evaluation: cumulative incidence and risk factor analysis

M Kim¹, C Suh¹, J Park², J Guenette³, R Huang⁴, H Kim⁵

¹Asan Medical Center, Seoul, Seoul, ²Asan Medical Center, Seoul, Korea, Republic of, ³Brigham and Women's Hospital - Department of Radiology, Boston, MA, ⁴Brigham and Women's Hospital, Boston, MA, ⁵Asan medical center, seoul, seoul

Purpose

There are no established guidelines regarding the indication of surveillance brain MRI in non-small cell lung cancer (NSCLC). We aimed to establish cumulative incidence and risk factors associated with developing brain metastases in NSCLC patients without brain metastases at initial evaluation.

Materials and Methods

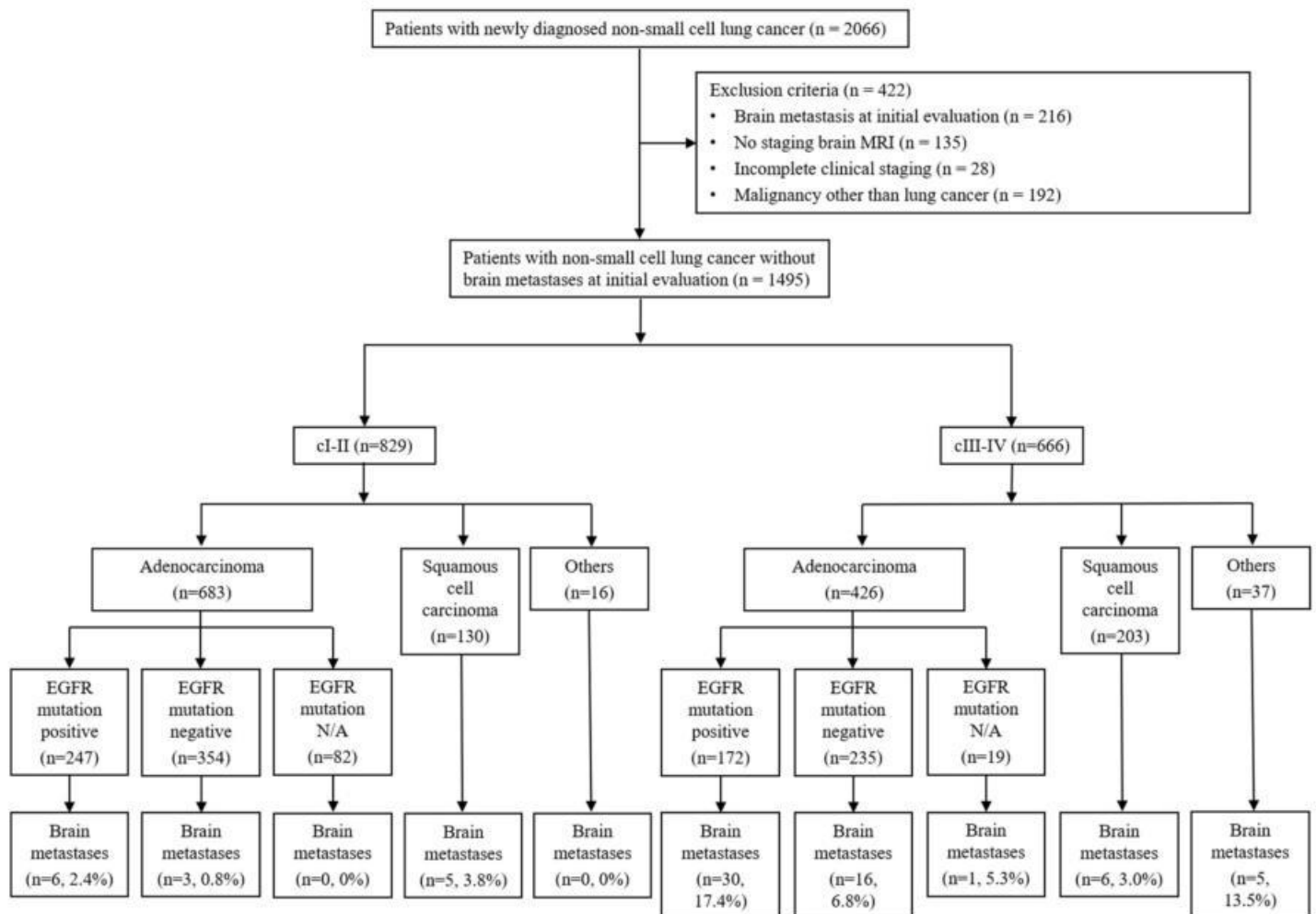
This retrospective, single institution study included patients 1495 NSCLC patients (mean age ± SD, 65 ± 10; 920 men) without brain metastases at initial evaluation. Cumulative incidence of brain metastases was determined with death as a competing risk and further stratified by clinical stage groups, cell types and molecular markers (epidermal growth factor receptor [EGFR] and anaplastic lymphoma kinase). Univariable and multivariable Fine and Gray regression analyses were performed to determine factors associated with developing brain metastases.

Results

The overall cumulative incidence of developing brain metastases at 6, 12, 18, and 24 months after initial diagnosis of NSCLC was 0.6%, 2.1%, 4.2% and 6.8% respectively. The corresponding cumulative incidence was higher in clinical stage III-IV (1.3%, 3.9%, 7.7% and 10.9%) than clinical stage I-II (0.0%, 0.8%, 1.2% and 2.6%) ($P < .001$). The corresponding cumulative incidence was higher in EGFR positive adenocarcinoma (0.7%, 2.5%, 6.3% and 12.3%) than EGFR negative adenocarcinoma (0.4%, 1.8%, 2.9% and 4.4%) ($P < .001$). Multivariable analysis revealed clinical stage III-IV (subdistribution hazard ratio [sHR], 7.2; $P < .001$) and positive EGFR mutation (sHR, 2.5; $P = .002$) as significant risk factors.

Conclusions

Clinical stage III-IV and EGFR positive adenocarcinoma are significant risk factors with higher cumulative incidence for developing brain metastases in NSCLC patients without brain metastases at initial evaluation.



(Filename: TCT_943_Figure1.jpg)

Brain Tumor IDH, 1p/19q, and MGMT Molecular Classification Using MRI-based Deep Learning: Effect of Motion and Motion Correction

S Nalawade¹, F Yu², C BANGALORE YOGANANDA³, G Murugesan¹, B Shah⁴, M Pinho¹, B Wagner¹, B Mickey², T Patel⁵, B Fei⁶, A Madhuranthakam², J Maldjian¹

¹University of Texas Southwestern Medical Center, Dallas, TX, ²UT Southwestern Medical Center, Dallas, TX, ³UNIVERSITY OF TEXAS SOUTHWESTERN MEDICAL CENTER, DALLAS, TX, ⁴UT Southwestern, Irving, TX, ⁵The University of Texas Southwestern Medical Center, Dallas, TX, ⁶UT Dallas, Richardson, TX

Purpose

Deep learning has shown promise for predicting the molecular profiles of gliomas using MR images. Prior to clinical implementation, ensuring robustness to real-world problems, such as patient motion, is crucial. We sought to evaluate the effects of motion artifact on glioma marker classifier performance and develop a deep learning motion correction network to restore classification accuracies.

Materials and Methods

446 glioma subjects with T2w images were selected from the TCIA. Out of 446 subjects, genomic data were obtained from the TCGA database for 214 subjects with IDH mutation status, 368 subjects with 1p/19q co-deletion status, and 247 subjects with MGMT methylation status. Simulated motion was added in the k-space domain along the phase encoding direction. Classifier performance for IDH, 1p/19q, and MGMT was assessed over a range of 0-100% corrupted k-space lines. The trained motion correction network was based on 2D Dense-Unet architecture comprised of densely connected convolution layers. To evaluate the generalizability of the network, a 3-fold CV was performed, dividing all subjects into 3 groups for training, in-training validation, and held out testing (~149 subjects). Data augmentation was used to increase the data quality and diversity, which helps to train networks with limited data. The training time for each network was approximately 120 hrs. The performance of the three glioma marker classifiers were then re-evaluated on the motion-corrected images.

Results

Glioma marker classifier performance decreased markedly with increasing motion corruption (Figure 1). Applying the motion correction network effectively restored classification accuracy for even the most motion-corrupted images. For IDH classification, 99% accuracy was achieved, exceeding the original network performance and representing a new benchmark in non-invasive MRI-based IDH classification. All three models achieved excellent performance with SSIM of over 0.99 and RMSE of less than 0.03 for all motion corruption levels.

Conclusions

We evaluated the effect of motion artifacts on glioma molecular classification networks, and the ability of motion correction networks to recover classification accuracy. We demonstrate that high-performing classification networks progressively lose accuracy with increasing motion-related image degradation and by incorporating motion correction prior to the classification step, recovery of classification network accuracy was possible even at the highest degrees of motion disruption.

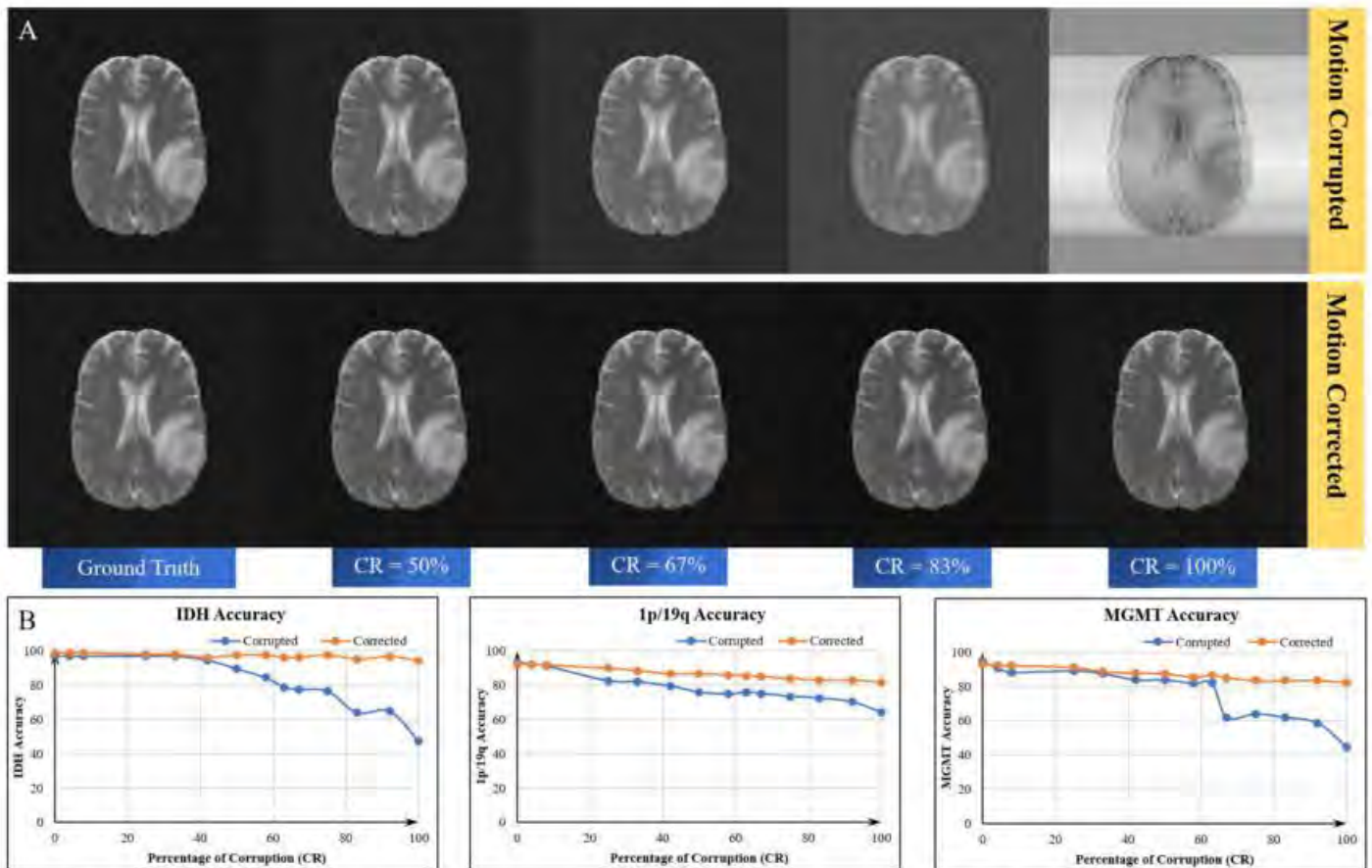


Figure 1.A Example of simulated motion and motion correction. Top Row: Simulated motion. From left to right, ground truth T2w image (column 1) and corrupted images for CR=50%, 67%, 83% and 100% (columns 2-5). Bottom Row: Motion correction using Model-1. From left to right, corrected output images for CR=0 %, 50%, 67%, 83% and 100%.

Figure 1.B IDH, 1p/19q, and MGMT classification accuracies for motion corrupted (blue lines) and Model-1 corrected images (orange lines) averaged across the 3 cross-validation folds for each molecular marker. Recovery of accuracy was best for IDH classification, boosting the accuracy to 99% for the baseline uncorrupted images and low-levels of motion corruption, and recovering the original 97% accuracy out to 92% CR.

(Filename: TCT_390_Figure1_1200dpi.jpg)

1062

Bridging Therapy with Alteplase for Stroke Patients with Low ASPECTS May Not be Beneficial and is Associated with Increased Risk of Symptomatic Parenchymal Hemorrhage

G BROOCKS¹, R McDonoug¹, U Hanning¹, J Fiehler², L Meyer¹

¹University Hamburg, Hamburg, NA, ²University Hospital Hamburg-Eppendorf, Hamburg, Hamburg

Purpose

The additional effect of intravenous treatment with alteplase (IVT) before mechanical thrombectomy (MT) in acute ischemic stroke patients with signs of extensive infarction on baseline CT is yet uncertain. The purpose was to evaluate the benefit of bridging IVT for patients with anterior circulation stroke and low Alberta Stroke Program Early Computed Tomography Score (ASPECTS) compared to direct MT.

Materials and Methods

This retrospective, observational multicenter study compares bridging IVT to direct MT for CT-based selection of patients with extensive baseline infarcts (ASPECTS \leq 5) attributed to large vessel anterior circulation stroke. Patients were selected from the German Stroke Registry (GSR) and three tertiary stroke-centers. Analyses of variance (ANOVA) and multivariable logistic regression analyses were performed to investigate the impact of IVT and MT on clinical outcome. Functional endpoints were the rates of good (modified Rankin Scale (mRS) score \leq 3) and very poor outcome (mRS \geq 5) at day 90. Treatment efficacy was evaluated with the modified

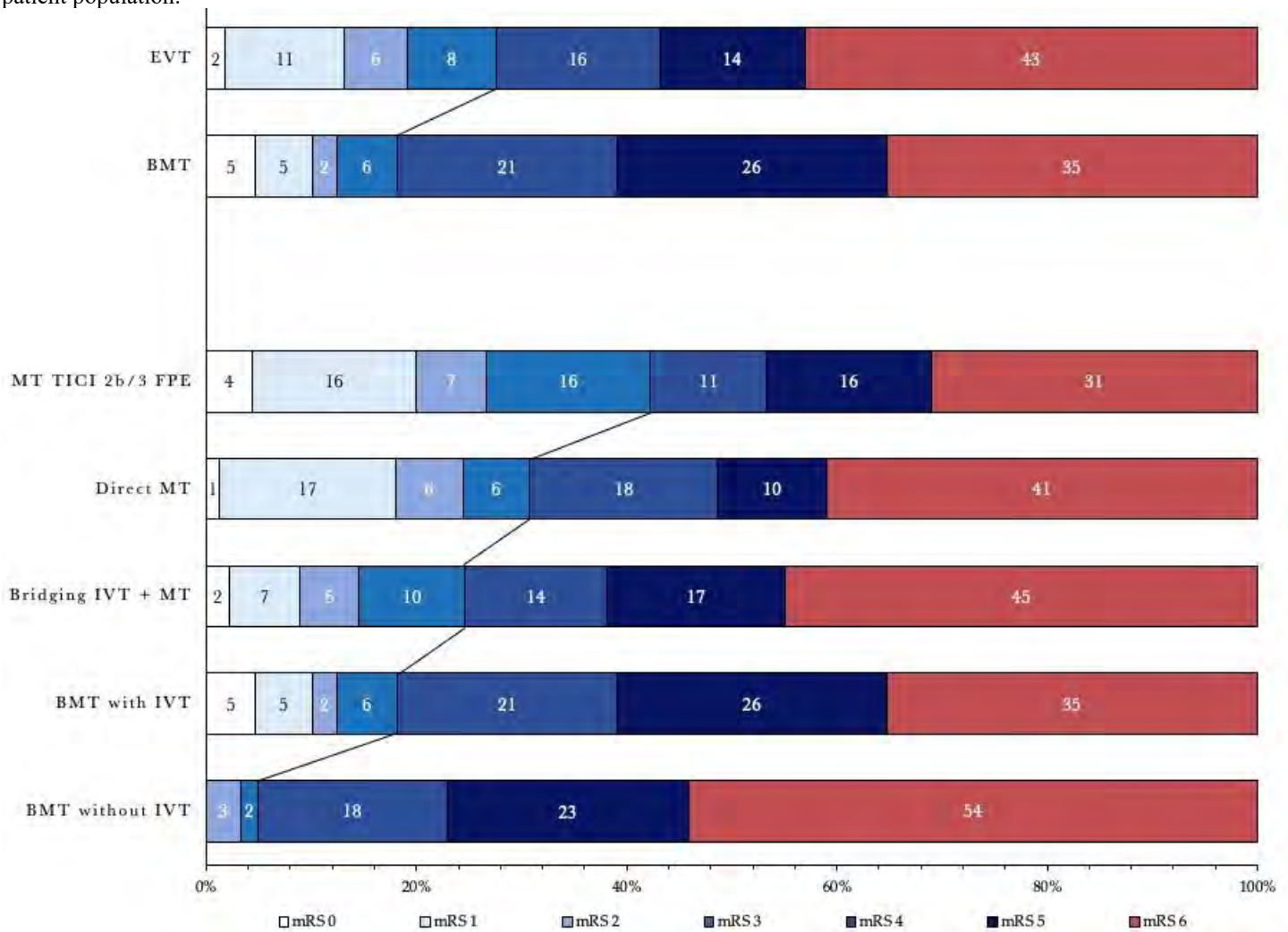
Thrombolysis in Cerebral Infarction (mTICI) scale. Safety endpoint was the occurrence of symptomatic intracranial hemorrhage (sICH).

Results

429 patients fulfilled the inclusion criteria and were analyzed. 290 patients (68%) received IVT and 168 (39%) patients received MT. Bridging IVT was not associated with better functional outcome compared to direct MT (mean mRS 4.6, 95%CI: 4.2-4.9 compared to 4.2, 95%CI: 3.8-4.6 in patients with direct MT). The rate of sICH was significantly higher in patients with bridging IVT compared to patients with direct MT (17.8% versus 6.4%, p=0.004). In multivariable logistic regression analysis, IVT was significantly associated with very poor outcome (odds ratio (OR): 2.22, 95%CI: 1.05-4.73, p=0.04) and was a significant and independent predictor for sICH (OR: 3.44, 95%CI: 1.18-10.07, p=0.02). Predictors of good functional outcome were successful reperfusion, age, and ASPECTS.

Conclusions

Bridging IVT in patients with low ASPECTS was associated with very poor functional outcome and increased risk for sICH. Hence, bridging IVT in low ASPECTS should only be considered carefully until randomized evidence supports the application of IVT in this patient population.



(Filename: TCT_1062_lysis_hades.jpg)

1067

Can Deep Learning Find the Ischemic Core on CT? Transfer Learning from Pre-trained MRI-based Networks

Y Yu¹, S Christensen², Y Xie¹, E Gong³, G Albers⁴, G Zaharchuk¹

¹Stanford University, Stanford, CA, ²GrayNumber Analytics, Lomma, Sweden, ³Subtle Medical Inc., Menlo Park, CA, ⁴Stanford University Medical Center, Palo Alto, CA

Purpose

Ischemic core prediction from CT perfusion (CTP) remains inaccurate compared with gold standard diffusion-weighted imaging (DWI). We evaluated if a deep learning model to predict the DWI lesion from MR perfusion (MRP) could facilitate ischemic core prediction on CTP.

Materials and Methods

Using the multi-center CRISP cohort of acute ischemic stroke patient with CTP before thrombectomy, we included patients with major reperfusion (TICI score \geq 2b), adequate image quality, and follow-up MRI at 3-7 days. Perfusion parameters including Tmax, mean transit time, cerebral blood flow (CBF), and cerebral blood volume were reconstructed by RAPID software. Core lab experts outlined the stroke lesion on the follow-up MRI. A previously trained MRI model in a separate group of patients was used as a starting point, which used MRP parameters as input and RAPID ischemic core on DWI as ground truth. We fine-tuned this model, using CTP parameters as input, and follow-up MRI as ground truth. Another model was also trained from scratch with only CTP data. 5-fold cross validation was used. Performance of the models was compared with ischemic core (rCBF \leq 30%) from RAPID software to identify the presence of a large infarct (volume $>$ 70 or $>$ 100ml).

Results

94 patients in the CRISP trial met the inclusion criteria (mean age 67 \pm 15 years, 52% male, median baseline NIHSS 18, median 90-day mRS 2). Without fine-tuning, the MRI model had an agreement of 73% in infarct $>$ 70ml, and 69% in $>$ 100ml; the MRI model fine-tuned on CT improved the agreement to 77% and 73%; The CT model trained from scratch had agreements of 73% and 71%; All of the deep learning models outperformed the rCBF segmentation from RAPID, which had agreements of 51% and 64%. See Table and figure.

Conclusions

It is feasible to apply MRP-based deep learning model to CT. Fine-tuning with CTP data further improves the predictions. All deep learning models predict the stroke lesion after major recanalization better than thresholding approaches based on rCBF.

Table 1	AREA UNDER CURVE (IQR)	DICE SCORE COEFFICIENT (IQR)	VOLUME DIFFERENCE, mL (IQR)	ABSOLUTE VOLUME DIFFERENCE, mL (IQR)
MRI MODEL	0.85 (0.80, 0.88)***	0.41 (0.25, 0.52)***	-3 (-38,41) **	41 (20, 65)
CT FINE-TUNED MRI MODEL	0.91 (0.87, 0.94)	0.51 (0.39, 0.63)	5(-24, 51)	36 (14, 68)
CT MODEL	0.93 (0.90, 0.94)***	0.52 (0.33, 0.62)	3 (-48, 42) **	44 (15, 63)
RCBF≤30%	N/A	0.12 (0, 0.25)***	-65 (-106, -33)***	65 (33, 106)***

* p<0.05, ** p<0.01, *** p<0.001. Paired Wilcoxon test was used to compare CT fine-tuned MRI model with other methods.

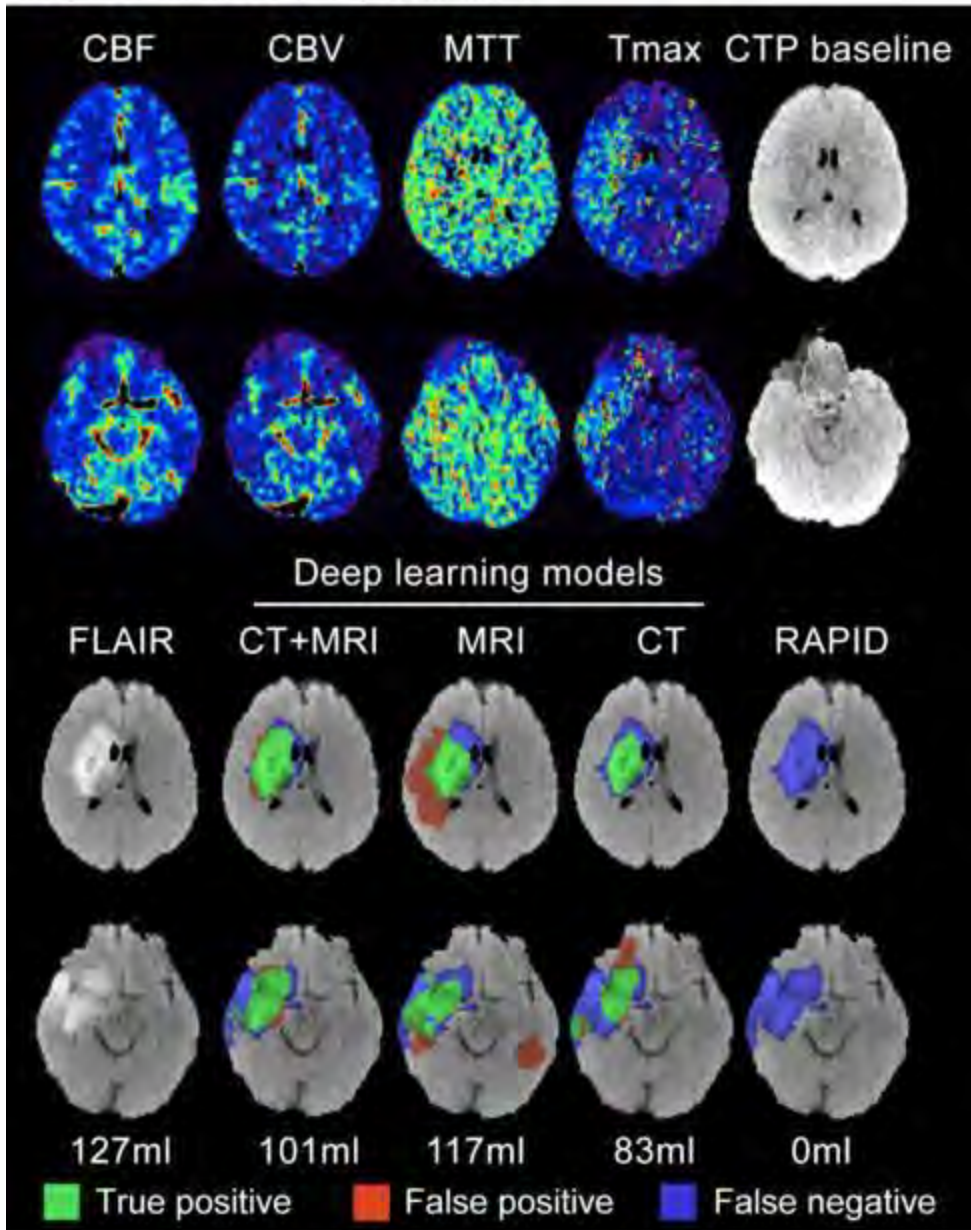


Figure 1. A patient with baseline NIHSS of 15 and TIC1 3. The top two rows are two slices of baseline CT perfusion images with cerebral blood flow (CBF), cerebral blood volume (CBV), mean transient time (MTT), Tmax, and pre-contrast CT. The bottom two rows are two slices of 5-day FLAIR, model prediction from CT fine-tuned MRI mode, MRI model, CT model, and rCBF≤30% segmentation on RAPID software. The green area represent true positive, blue area is false negative, and red area is false positive.

(Filename: TCT_1067_abstract-figure.jpg)

Can we see unruptured AVMs on non-contrast CT? Report of frequency of detection, typical findings, and predictable failures.

R MATTAY¹, L Miner², A Copelan³, K Davtyan⁴, J Schmitt⁴, A Mamourian²

¹HOSPITAL OF THE UNIVERSITY OF PENNSYLVANIA, PHILADELPHIA, PA, ²Penn State Milton S. Hershey Medical Center, Hershey, PA, ³Abbot Northwestern Hospital, Minneapolis, MN, ⁴Hospital of the University of Pennsylvania, Philadelphia, PA

Purpose

Cerebral arteriovenous malformations (AVMs) underlie 1 to 2% of all strokes and 9% of subarachnoid hemorrhages (1,2). While parenchymal blood from a ruptured AVM is evident on non-contrast CT (NCCT), detection of unruptured AVMs is known to be difficult but not quantified in the literature using multidetector CT. We report the appearance of NCCT scans of 25 patients from two academic hospitals with proven unruptured AVMs to determine their typical findings and if advances in CT have improved their detection when compared to prior literature (3,4).

Materials and Methods

Of 336 reports of NCCT with mention of AVM, only 25 (see Table 1 for demographic and clinical features) met our criteria of having angiography or MR proven AVM without hemorrhage, prior surgery, or other diagnoses. Demographic variables, clinical symptoms at presentation, abnormal CT imaging findings, attenuation of the superior sagittal sinus (SSS), and Spetzler-Martin Grade of each AVM were recorded. To test our hypothesis that decreased attenuation of the blood pool influences detection of AVMs we examined the relationship between AVM detection and SSS attenuation via Kruskal-Wallis test. Exploratory serial logistic principal components analysis (PCA) was then performed including demographic, presenting symptoms, and CT findings as features in the multivariate model.

Results

80% of the scans showed a relevant abnormality while 20% were completely normal. Logistic regression models indicate that clustered associations between several CT features, primarily calcifications, hyperdensity, and vascular prominence significantly predicted Spetzler-Martin grade (likelihood ratio 7.7, p= 0.006). The attenuation of the SSS was significantly lower in subjects with occult AVMs when compared to those with CT abnormalities (median 47 vs 55 HU, p-value <0.04).

Conclusions

We found that the NCCT scans were abnormal in 80% of our cases. A combination of findings such as hyperattenuation, vascular prominence, and calcifications was predictive of higher Spetzler-Martin AVM Grade. In patients with symptoms associated with AVMs, further imaging should be obtained when the SSS attenuation is less than 50HU since this was significantly associated with undetectable AVMs.

Demographics:	Center 1	Center 2	Total
N	16	9	25
Age (years)	47.4 (16.3)	44.0 (23.5)	46.2 (18.8)
Gender	12 M (75%) 4 F (25%)	7 M (78%) 2 F (22%)	19 M (76%) 6 F (24%)
Clinical Features:			
Headache	5 (31%)	5 (56%)	10 (40%)
Seizure	8 (50%)	2 (22%)	10 (40%)
Vertigo	1 (6%)	0 (0%)	1 (4%)
Visual Disturbances	2 (13%)	0 (0%)	2 (8%)
Sensorimotor	0 (0%)	1 (11%)	1 (4%)

Any abnormality	20 (80%)	Spetzler-Martin Grade:
		Grade 1: 9 (36%)
Calcifications	9 (36%)	Grade 2: 8 (32%)
Hyperdensity	20 (80%)	Grade 3: 7 (28%)
Vascular Prominence	14 (56%)	Grade 4: 1 (4%)
Parenchymal Edema	3 (12%)	
Adjacent Bony Change	1 (4%)	
SSS Density (HU)	58.4 (12.1)	

(Filename: TCT_636_Figure300.JPG)

B Dang¹, T Massoud¹

¹Stanford University School of Medicine, Stanford, CA

Purpose

Among the basal ganglia (BG), the caudate nucleus (CN) and putamen (P) are one developmental unit—the striatum. The caudolenticular (or transcapsular) gray bridges (CLGBs) connect CN and P across the internal capsule. Parkinson's disease (PD) is a neurodegenerative movement disorder entailing hindrance of BG processing. The CLGBs function as the primary efferent center from premotor and SMA cortex to the BG. However, a functional dichotomy exists between CN and P; CN is linked to mapping of higher cortical motor processes, and P assists in timing of movement execution. We hypothesized that baseline number and size of CLGBs may contribute to abnormal cortical-subcortical connectivity in PD. However, no studies have addressed the neuroimaging anatomy and morphometry of CLGBs. We investigated normative age-related MRI morphometrics of the CLGBs in healthy subjects, prior to future evaluations in PD patients.

Materials and Methods

We retrospectively analyzed axial and coronal 3T FSPGR images of 34 individuals for bilateral CLGB numbers, thickest diameter and greatest length (mm), symmetry, and axial areas of CN head and P (mm²). We calculated Evans' index (EI) to account for global brain atrophy. We tested the effect of sex as an independent variable on measured dependent variables using single factor ANOVA, and performed linear regressions with age as an independent variable for each dependent variable. We also calculated the Pearson correlation coefficient for linear correlations between all measured variables, with statistical significance set at $p < 0.05$.

Results

Study subjects were F:M=23:11 and mean age 49.9 years. All EI's were normal at < 0.3 . All but 3 CLGBs were bilaterally symmetrical with a mean 7.4 CLGBs per side. Mean results were: thickest and longest CLGBs = 1.0mm and 4.6mm, respectively; CN head and P areas = 205mm² and 382.0mm², respectively. Females had thicker CLGBs ($p=0.02$). There were no interactions between sex and CLGB length ($p=0.80$), CN head area ($p=0.60$), or P area ($p=0.45$); nor between age and CLGB thickness ($p=0.74$), CLGB length ($p=0.86$), CN head area ($p=0.10$), or P area ($p=0.20$). There were no correlations between CN head area and CLGB thickness or length ($p=0.77$ and 0.92 , respectively); nor between P area and CLGB thickness or length ($p=0.08$ and 0.16 , respectively).

Conclusions

This is the first report of normative MRI dimensions of the CLGBs to guide future studies on possible role of CLGB morphometry in PD predisposition or in success of rehabilitative movement therapy.

805

CBF in Term and Preterm Neonates: a pCASL Study

E Piccirilli¹, V Panara¹, M Treddenti¹, V Maruotti¹, M Colasurdo¹, M Caulo¹

¹University of Chieti, Chieti, Italy

Purpose

Cerebral blood flow (CBF) delivers oxygen and nutrients to meet metabolic demands. In the developing brain, CBF is the main determinant of brain maturation and its control involves complex neural and metabolic mechanisms: as newborns and especially preterms have underdeveloped or even impaired autoregulatory mechanisms due to immature vascular network and molecular signaling, their CBF can be significantly and negatively affected by several factors, influencing in turn brain maturation. Arterial spin labeling (ASL) and its evolution pCASL have proven to be reliable techniques to measure CBF in vivo and non-invasively in newborn babies. The aims of our study were to evaluate CBF values using pCASL in different brain regions in newborn babies of different gestational ages (GA) and how GA affects CBF.

Materials and Methods

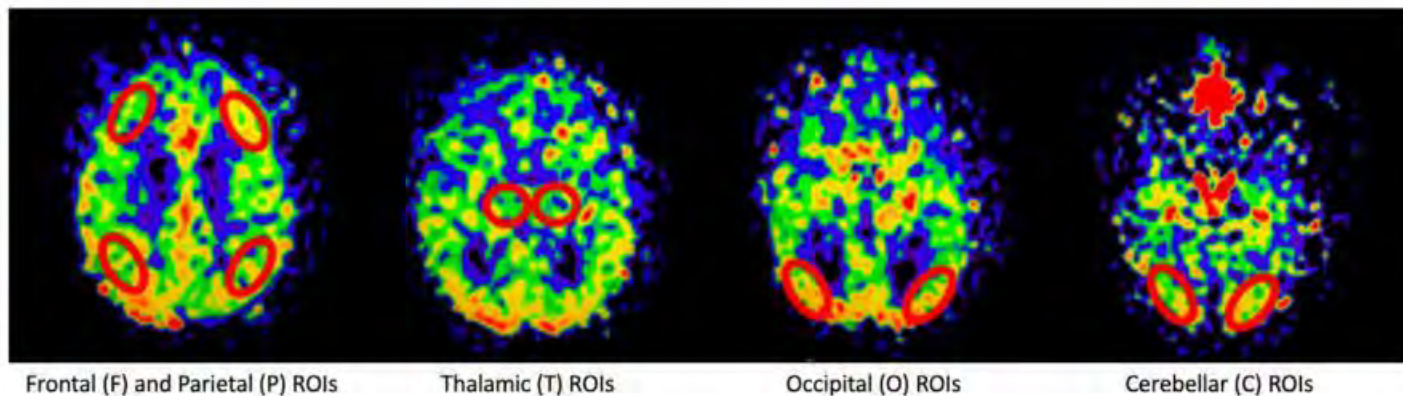
The brain MRI of 106 consecutive preterm and term neonates (acquired within 5 days of TEA and 5 days of birth, respectively) were included. The neonates were subsequently divided into 4 categories according to their GA. A standardized elliptic ROI was manually placed on the cerebral perfusion maps in the cortex of the frontal (F), parietal (P) and occipital (O) lobe, in the thalamus (T) and in the cerebellum (C) of each hemisphere, using the T2 TSE sequence as the anatomical reference. A two-sample t-test was applied to evaluate differences in CBF of each homologous ROI between hemispheres. Differences in CBF among ROIs (F, P, O, T and C) were assessed with One-way ANOVA. Pearson's correlation coefficient was calculated to evaluate the relationship between GA and mean CBF of each lobe and overall. Statistical analysis was performed with SPSS, with significance set at $p < 0.05$.

Results

No significant hemispheric differences in CBF were observed ($p=0.3$). Comparison of means indicated that there were statistically significant differences in CBF between F and P ($p=0.009$), F and T ($p < 0.05$), P and T ($p < 0.05$), P and C ($p=0.046$) and O and T ($p < 0.05$). The thalamus had the highest CBF overall followed by the frontal cortex, while the parietal cortex was the least perfused. A significant correlation between GA and CBF was observed, with overall CBF increasing with GA ($r=0.2$, $p=0.01$).

Conclusions

We demonstrated differences in CBF values among different cerebral grey matter regions in newborns, independently of their GA. The T was the region with the highest CBF, both in term and preterm neonates. Moreover, we demonstrated in vivo and non-invasively a significant correlation between CBF and GA.



(Filename: TCT_805_ASJ-ASNR.jpg)

877

Cerebral Perfusion in Posterior Reversible Encephalopathy Syndrome Measured with Arterial Spin Labeling MRI

S Fazeli¹, S Imbesi¹, D Bolar¹

¹University of California San Diego, San Diego, CA

Purpose

Pathophysiology of posterior reversible encephalopathy syndrome (PRES) remains controversial (1). Hypertension (HTN)-induced autoregulatory failure with subsequent hyperperfusion is currently the leading hypothesis, whereas an alternative theory suggests vasoconstriction leading to hypoperfusion as the underlying mechanism (1). Studies using contrast CT and MR perfusion imaging have yielded contradictory results supporting both theories (2). This study represents the first application of arterial spin labeling (ASL) to evaluate perfusion changes in PRES.

Materials and Methods

A search of MRI reports at our institution from July 2015 to September 2020 was performed with inclusion search terms of "PRES" and "posterior reversible encephalopathy syndrome". Of the resulting 103 patients, 17 patients with an unequivocal clinical and imaging diagnosis of PRES (based on FLAIR and DWI) and available diagnostic-quality ASL scans were included in analysis. Brain perfusion in affected brain regions was qualitatively assessed using ASL and characterized as hyperperfusion, isoperfusion, or hypoperfusion. The ASL perfusion imaging protocol consisted of the GE product pseudocontinuous ASL (PCASL) sequence with a 1.5s labeling duration and 2s post labeling delay, with parameters chosen based on ASL white paper recommendations (3). Additional demographic and clinical data including PRES etiology were extracted from the patients' electronic medical records.

Results

In the 17 patients with final clinical and imaging diagnosis of PRES, HTN was the most common etiology (n=11), followed by medications (n=4), renal insufficiency (n=1), and bone marrow transplant (n=1). ASL showed hyperperfusion in 13 and isoperfusion in 4 patients. Of those with HTN induced PRES, 82% had hyperperfusion on ASL. Table 1 summarizes the PRES etiology and ASL perfusion classification. Of note, none of the patients showed hypoperfusion. Figure 1 provides a representative example of a patient with PRES and hyperperfusion on ASL.

Conclusions

In this preliminary study of qualitative ASL findings in PRES, visually apparent hyperperfusion was seen in the majority (~76%) of patients, favoring the autoregulatory failure hypothesis as the predominant mechanism of PRES. Our data support that ASL provides a viable and practical way to assess perfusion in PRES and as such could potentially inform management strategies and allow noninvasive monitoring.

Table 1. PRES etiology and ASL perfusion classification

ASL perfusion	Etiology		
	HTN (n=12)	Medications (n=4)	Other (n=3)
Hyperperfusion	9	2	2
Isoperfusion	2	2	0
Hypoperfusion	0	0	0

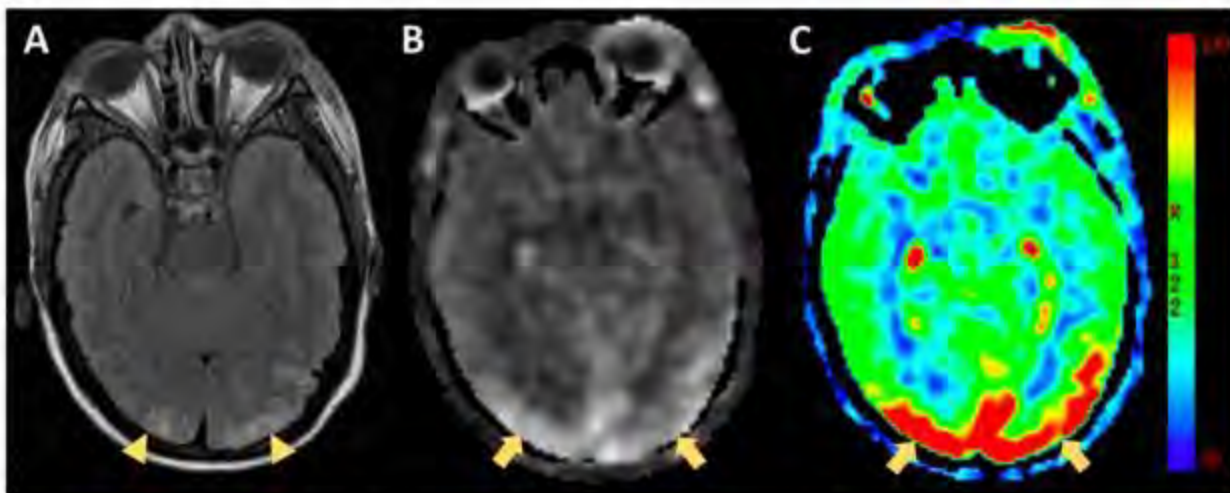


Figure 1. Axial T2 FLAIR (A), ASL grayscale (B) and ASL color (C) perfusion maps in a 23-year-old female with Tacrolimus induced PRES. Hyperperfusion (arrows) is noted corresponding to the regions of FLAIR hyperintensity (arrowheads). Color bar ranges from 20 to 130 ml/100g-min.

Cerebral small vessel disease score is associated with white matter disease progression

N Bareja¹, U Agarwal¹, L Okromelidze¹, M Demirel¹, B Erdal¹, E Middlebrooks¹, J Meschia¹, M Lin¹

¹Mayo Clinic, Jacksonville, FL

Purpose

Subcortical white matter disease (WMD) is prevalent, and it is associated with stroke and dementia. However, the rate and predictors of WMD progression are poorly described. Cerebral small vessel disease (SVD) score is a validated neuroimaging biomarker for global SVD burden. We hypothesize that high SVD burden may accelerate the progression of WMD. In this study, we aim to evaluate the association between baseline SVD score with the rate of progression of WMD volume.

Materials and Methods

Consecutive patients aged ≥ 50 years with white matter hyperintensities (WMD) on baseline MRI brain from 2016-2017 and follow-up MRI brain at least 1 year apart were included. Primary outcome was rate of WMD progression where fast progressor vs slow progressor was defined as annual change in WMD volume (cm³/year) above vs below the median. Markers of chronic SVD were rated for the extent of WMD, enlarged perivascular space (EPVS), chronic lacune, and cerebral microbleeds (CMB) using the STRIVE criteria. Severity of SVD was quantified by adding the presence of each SVD feature, with a total possible score of 0-4. WMD was segmented using the lesion predictive algorithm (LPA) tool in SPM, and WMD volume was quantified using MeVisLab (Figure1). Correlation analysis was performed to evaluate the relationship between SVD score and rate of WMD progression.

Results

Of the 22 patients, mean age was 72 ± 6 years old, and mean time between MRI brain scans was 2.50 ± 0.97 years. The annual rate of WMD progression was 4.1 cm³ (range 0.5 to 42.9) from a median baseline WMD volume of 17.8 cm³ (range 5.3 to 164.4 cm³). Fast progressors were more likely to be male, not on statin, history of intracranial hemorrhage, and had higher baseline WMD volume, compared to slow progressors ($p < 0.05$, Table 1). Higher baseline SVD score was associated with fast WMD progression (OR 3.16, 95% CI 1.00-9.95), and no patient with SVD score of 4 had slow WMD progression. Among SVD subtypes, fast WMD progression was associated with CMB (OR 3.71, 95% CI 0.54-26.04) and lacunar stroke (8.33, 95%CI 0.78-89.47) but did not achieve statistical significance.

Conclusions

Chronic cerebral small vessel disease burden is associated with faster white matter disease progression. A longitudinal study to evaluate whether intensive management of SVD risk factors may slow the progression of WMD and ameliorate future risk of clinical endpoints including stroke and dementia is ongoing.

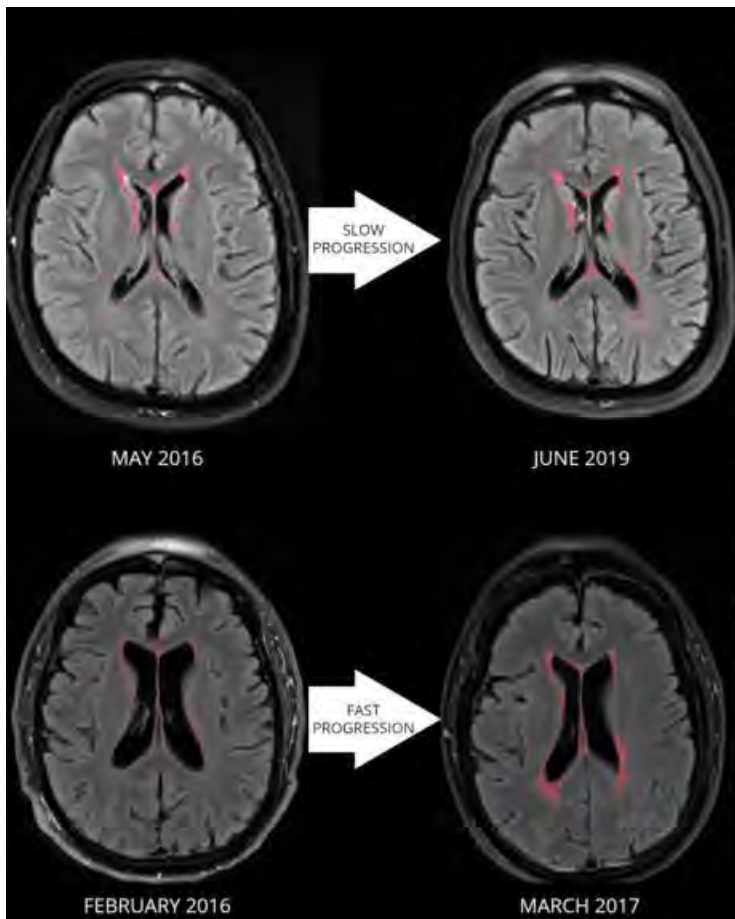


Table 1. Baseline patient characteristics January 2016 to March 2017

	Cohort N = 22	slow progressor N = 11 (50.0%)	fast progressor N = 11 (50.0%)	P-value
Mean age ± SD	72 ± 6.3	71.6 ± 8.0	72.7 ± 4.5	0.696
Female sex – no. (%)	9 (40.1)	7 (63.6)	2 (18.2)	0.030
Ever smoker – no. (%)	13 (59.1)	6 (54.6)	7 (63.6)	0.665
Comorbidities – no. (%)				
Hypertension	15 (68.2)	9 (81.8)	6 (54.6)	0.170
Diabetes	11 (50.0)	6 (54.6)	5 (45.5)	0.670
Hypercholesterolemia	12 (54.6)	8 (72.7)	4 (36.4)	0.087
CAD/MI	6 (27.3)	4 (36.4)	2 (18.2)	0.338
Atrial fibrillation	3 (14.3)	3 (30.0)	0 (0.0)	0.050
Congestive heart failure	1 (4.8)	1 (10.0)	0 (0.0)	0.283
Hx ischemic stroke	7 (31.8)	3 (27.3)	4 (36.4)	0.647
Hx intracranial hemorrhage	5 (22.7)	0 (0.0)	5 (45.5)	0.011
Hx dementia	3 (13.6)	0 (0.0)	3 (27.3)	0.121
Medications – no. (%)				
Antiplatelet	10 (45.5)	7 (63.6)	3 (27.3)	0.087
Anticoagulant	5 (23.8)	3 (30.0)	2 (18.2)	0.525
Statin	10 (45.5)	8 (72.7)	2 (18.2)	0.010
White matter disease volume				
WMD volume at baseline, median (range), cm ³	17.9 (5.3 to 164.4)	9.9 (5.3 to 19.7)	40.2 (5.4 to 164.4)	0.008
WMD volume at follow-up, median (range), cm ³	29.5 (6.1 to 202.9)	16.8 (6.1 to 30.4)	71.1 (18.5 to 202.9)	0.001
years between scans, mean ± SD	2.50 ± 0.97	2.59 ± 0.93	2.41 ± 1.05	0.678
change in WMD volume, median (range), cm ³	12.4 (0.8 to 139.2)	4.0 (0.8 to 11.8)	27.2 (13.0 to 139.2)	0.011
change in WMD volume per year, median (range), cm ³	4.1 (0.5, 42.9)	1.4 (0.5 to 3.8)	12.0 (4.4 to 42.9)	0.001
SVD markers on MRI brain				
any cerebral microbleeds	15 (68.2)	6 (54.6)	9 (81.8)	0.170
White matter hyperintensities	9 (40.9)	3 (27.3)	6 (54.6)	0.193
Enlarge perivascular space	21 (95.5)	10 (90.9)	11 (100.0)	0.306
Any lacunar infarct	6 (27.3)	1 (9.1)	5 (45.5)	0.056
SVD score				0.024
0	0 (0.0)	0 (0.0)	0 (0.0)	
1	4 (18.2)	4 (36.4)	6 (0.0)	
2	10 (45.5)	4 (36.4)	1 (54.6)	
3	4 (18.2)	3 (27.3)	1 (9.1)	
4	4 (18.2)	0 (0.0)	4 (36.4)	

(Filename: TCT_1082_ASNRImageSubmission.jpg)

739

Changes in Brain Functional Connectivity During Hypoglycemia and After Recurrent Hypoglycemic Episodes

W Wang¹, J Shimony¹, A Shimony¹, J Rutlin¹, C Anka¹, K Wharton¹, A Arbeláez¹

¹Washington University School of Medicine, St. Louis, MO

Purpose

Hypoglycemia is a common issue for patients with type 1 diabetes mellitus (T1DM). Antecedent hypoglycemia causes defective glucose counter-regulation and hypoglycemia unawareness to a second episode of hypoglycemia, known as hypoglycemia-associated autonomic failure (HAAF). This puts patients at risk for dead-in-bed syndrome and the precise mechanisms are unknown. We aim to study the neural mechanism of HAAF by examining brain functional connectivity in healthy individuals and in patients with T1DM undergoing study-induced hypoglycemia.

Materials and Methods

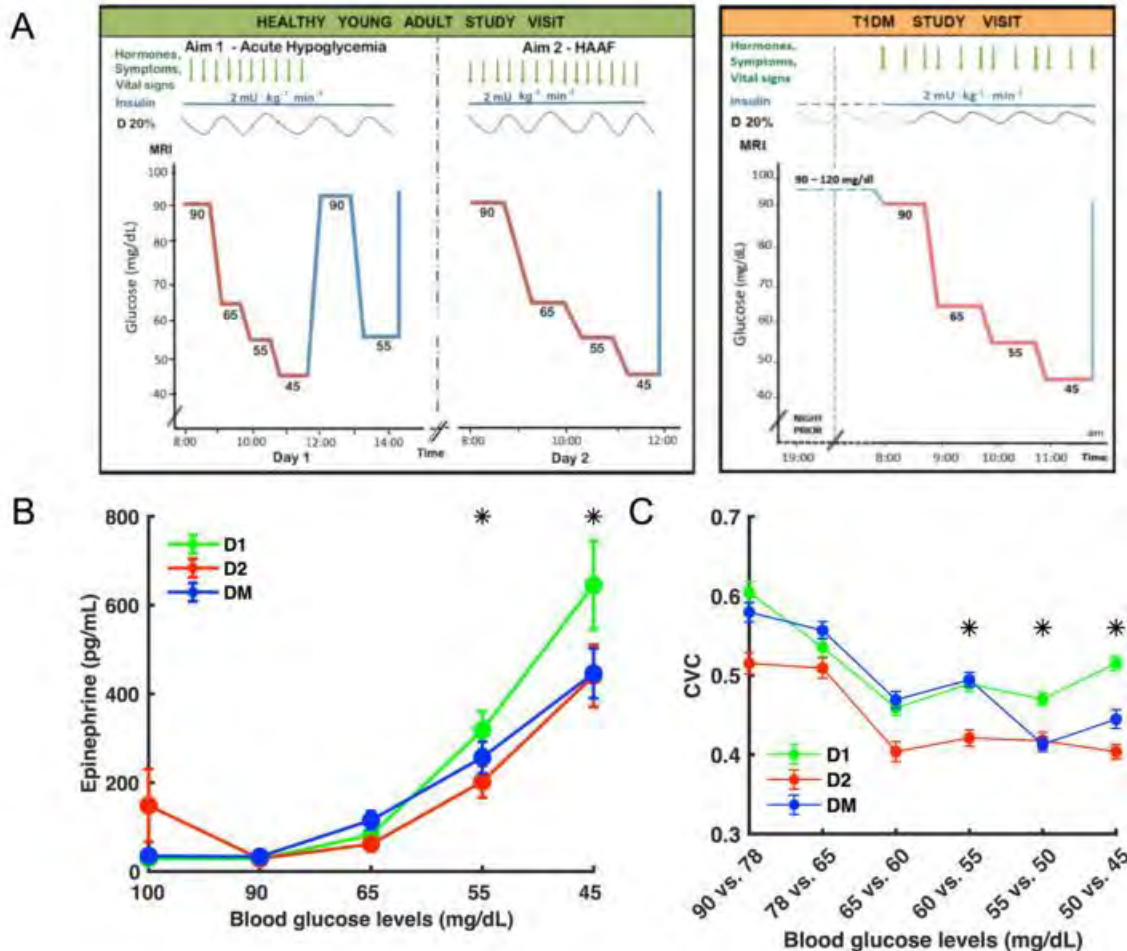
22 healthy adults underwent a 2-day study where their blood glucose levels were gradually decreased from 90 to 45 mg/dL (Panel A) each morning. In addition, they underwent an additional episode of study-induced hypoglycemia to 55 mg/dL in the afternoon of Day 1. 28 participants with T1DM without complications had a single-day study, and their blood glucose levels were gradually decreased and clamped at the same levels as the healthy individuals. Resting state fMRI (RS-fMRI), clinical hypoglycemic symptom scores and counterregulatory hormones (cortisol, epinephrine, and lactate) were measured at each clamped glycemic level. Time correlations of RS-fMRI data were computed between each pair of voxels, creating a functional connectivity matrix. For each voxel, correlation between its functional connectivity patterns to the rest of the brain at two different blood glucose levels were calculated and termed connectivity vector correlation (CVC), which quantifies similarity in functional connectivity between two glucose levels. CVC values from three study conditions, Healthy Day 1 (D1), Healthy Day 2 (D2), and T1DM (DM), were compared in 13 resting-state networks. Clinical measurements were examined as functions of blood glucose levels and compared among the three study conditions.

Results

Recurrent hypoglycemia in healthy individuals caused an attenuation of hypoglycemic symptoms and counterregulatory responses on Day 2 compared to Day 1, with Day 2's response similar to that of T1DM (Panel B). Recurrent hypoglycemia also caused an attenuation of CVC values for 12 of 13 resting state networks during hypoglycemia in healthy individuals on Day 2 compared to Day 1, with Day 2's CVC values closer to those of T1DM (Panel C).

Conclusions

Findings from this study suggest that impaired brain functional connectivity is associated with poor glucose counter-regulation and hypoglycemia unawareness, potentially causing HAAF.



(Filename: TCT_739_Figure.jpg)

1374

Characteristics And Outcomes Of Tmax > 6 Seconds Only Deficits In Patients With Acute Ischemic Stroke.

K RAGHURAM¹, W Choi¹, R Chaudhary¹

¹UTMB Galveston, Galveston, TX

Purpose

To identify characteristics and outcomes of ischemic lesions in patients with Tmax perfusion defect > 6 seconds but without CBF defects on CTP using the RAPID post processing platform and assess outcomes. Intention is to call to attention that M2 strokes can present with no CBF defects and should not be dismissed as benign oligemic tissue. Also, CT Perfusion must be considered in all patients with stroke to allow diagnosis of subtle M2 strokes.

Materials and Methods

To identify characteristics and outcomes of ischemic lesions in patients with Tmax perfusion defect > 6 seconds but without CBF defects on CTP using the RAPID post processing platform and assess outcomes.

Results

IRB approved retrospective review of all stroke patients with perfusion defect Tmax >6s in CTP without infarct core (CBF<30%) were performed. CTP studies with significant artifacts or bilateral scattered perfusion defects in a non-vascular territory were excluded. Volume of perfusion defects in T max >6s and CBF maps of < 30%, < 34% and < 38%, were recorded and compared with follow up MRI and CT. Patient's age, gender, NIHSS and presenting symptoms were recorded.

Conclusions

Results: Fifteen patients with Tmax >6s defects without infarct core (i.e. CBF < 30%) were included in the study. Eleven of these patients had distal arterial occlusion (M2 or M3 branches), four had proximal inflow artery stenosis. Of the eleven patients with distal occlusion, infarcts were identified in 9 (7 on DWI and 2 on CT). The Tmax >6s perfusion defect map corresponded to the location of the area of final infarct in all nine patients. Also in patients with proximal inflow vessel stenosis, in three out of four cases, the location of the Tmax defect corresponded to the area of diffusion restriction on MRI. In the fourth patient the CBF defect was seen in an area of chronic infarction. Conclusion: Tmax > 6 s defects without CBF defects were identified mainly in patients with distal MCA branch occlusions and in patients with significant inflow stenosis with progression to infarction in 12/15. The presence of detectable Tmax > 6s lesions may be an indication for considering endovascular intervention. Additionally, consideration should be given to expand CT perfusion examination to most stroke patients and not restrict its use to patients with NIHSS > 6.

1448

Characterization of Demyelinating Lesions in Multiple Sclerosis Using Highly Accelerated 3D Wave-CAIPI Susceptibility-Weighted Imaging and FLAIR

A Goncalves Filho¹, A Tabari², C Ngamsombat³, S Cauley¹, W Lo⁴, D Splitthoff⁵, P Schaefer¹, O Rapalino¹, E Klawiter¹, J Conklin¹, S Huang⁶

¹Massachusetts General Hospital, Boston, MA, ²Massachusetts general hospital, Boston, MA, ³Department of Radiology, Faculty of Medicine Siriraj Hospital, Mahidol University, Bangkok, Thailand, Bangkok, MA, ⁴Siemens Medical Solution, Charlestown, MA, ⁵Siemens Healthineers, Erlangen, Germany, ⁶Massachusetts General Hospital, Harvard Medical, Boston, MA

Purpose

Previous studies have suggested that the central vein sign (CVS) is specific for multiple sclerosis (MS) and that paramagnetic rims seen in chronic active MS plaques are associated with more aggressive disease (1,2). The goal of this study was to assess the frequency of paramagnetic rims and CVS using highly accelerated 3D Wave-CAIPI susceptibility-weighted imaging (Wave-SWI) and FLAIR (Wave-FLAIR) sequences for the adjunct characterization of demyelinating lesions in MS within clinically feasible scan times.

Materials and Methods

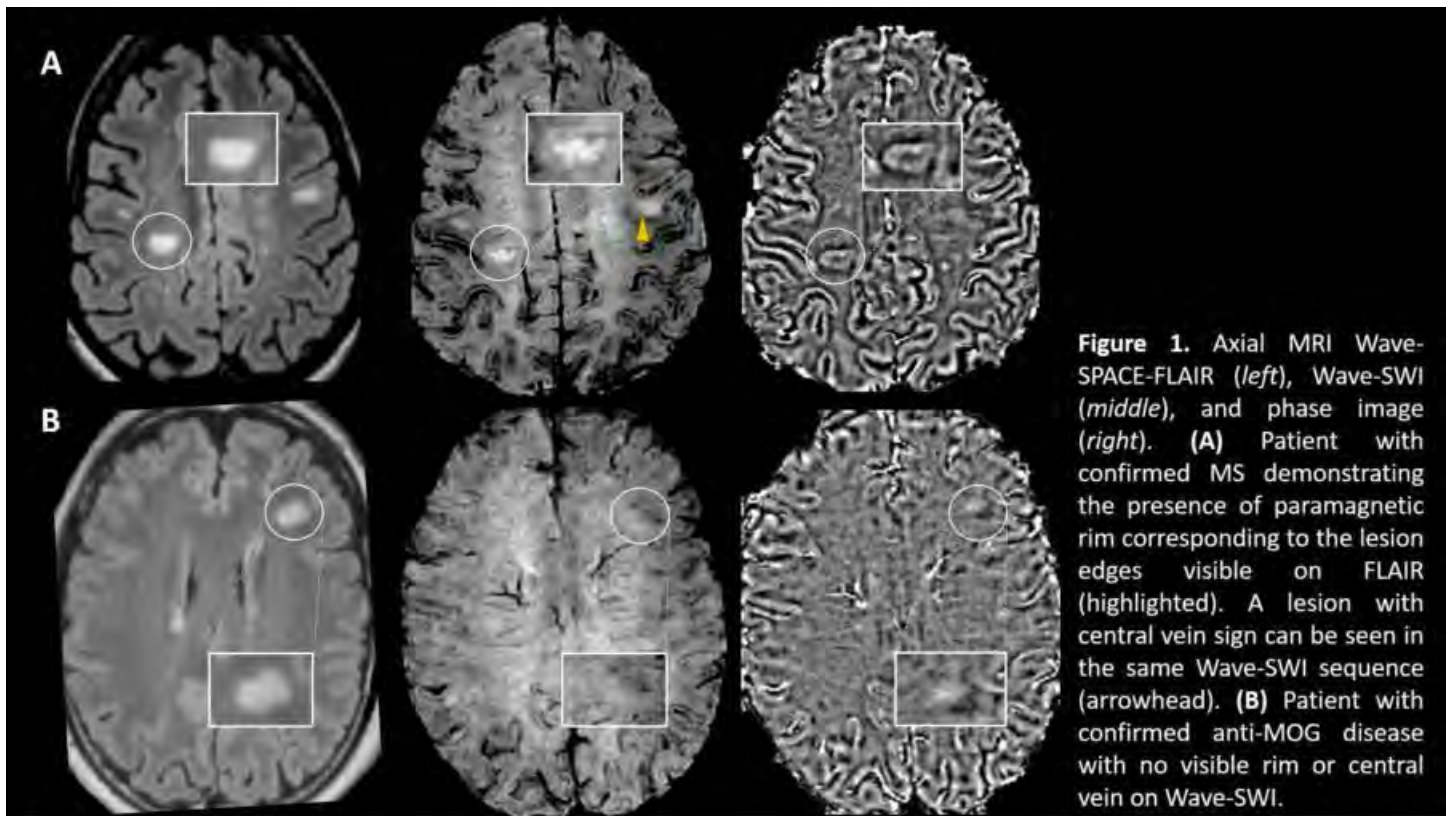
65 consecutive patients undergoing brain MRI for the clinical evaluation of demyelinating disease from June-October 2020 were scanned on 3T MRI scanners (Siemens Magnetom Prisma and Vida, Erlangen, Germany). The imaging protocol included accelerated prototype 3D Wave-SWI (R=6, acquisition time (TA)=1:58min, 0.8x0.8x1.8mm) and 3D Wave-FLAIR (R=4, TA=2:30min, 1x1x1mm) sequences, which in aggregate shortened the clinical MS protocol to <20 min. Each patient's Wave-FLAIR and Wave-SWI images were co-registered using built-in 3D registration software within the PACS (Visage). Two neuroradiologists (9 and 13 years of experience) independently reviewed the co-registered images and determined the number of lesions with paramagnetic rims and/or CVS. Discrepancies between raters were discussed, and consensus was reached on the number of lesions with paramagnetic rims and CVS per case.

Results

44 patients had confirmed MS by 2017 McDonald criteria, 7 had CIS, and the remaining 14 did not have MS. Of the 51 patients with MS or CIS, paramagnetic rims were identified in 23 cases (45%). 37 cases had at least one lesion with CVS (72.5%). There was substantial agreement between raters in the visualization of paramagnetic rims before consensus (89.23% - Cohen k = 0.75, p < 0.01). No paramagnetic rims or CVS were identified in the non-MS patients.

Conclusions

The frequencies of paramagnetic rims and CVS identified on highly accelerated 3D Wave-SWI and Wave-FLAIR sequences in our cohort were comparable to those reported by other groups using longer sequences with standard image encoding. The results support the use of highly accelerated Wave-SWI and Wave-FLAIR in clinical MS MRI protocols for the comprehensive evaluation of MS lesions. The combined time-savings afforded by Wave-CAIPI may enable the more widespread evaluation and adoption of imaging signs such as paramagnetic rims and CVS in the clinical follow-up and evaluation of patients with suspected and confirmed demyelinating disease.



(Filename: TCT_1448_PRSCVS4.jpg)

1397

Characterization of Fistulae and Fistula-Related Complications in the Neopharynx after Surgical Resection and Reconstruction for Head and Neck Cancer

C Chung¹, N Kinger¹, A Aiken², K BAUGNON², X Wu³

¹Emory University School of Medicine, Atlanta, GA, ²Emory University, Atlanta, GA, ³EMORY UNIV SCHOOL OF MEDICINE, ATLANTA, GA

Purpose

Total laryngectomy with myocutaneous flap reconstruction is routinely performed for primary and salvage treatment of advanced head and neck cancers. Pharyngocutaneous fistula, the most common complication after total laryngectomy, confers increased mortality can be readily diagnosed clinically via visualization of the fistulous tract. In contrast, fistulization to deep neck spaces and related osseous and vascular complications, which further contribute to mortality, may be apparent only on imaging. To better characterize the imaging and clinical features of fistula-related complications in the reconstructed neck, we performed a retrospective review of cases involving this entity within our institution.

Materials and Methods

A retrospective report search for 'neopharynx' and ('fistula' or 'fistulous' or 'fistulization') was performed on all radiology reports at our institution from January 2015 to October 2020 to identify consecutive cases of neopharynx-related fistula characterized on non-invasive imaging. Relevant fluoroscopic swallow study, contrast-enhanced CT neck, PET/CT and MRIs were reviewed to delineate imaging appearance of the fistulae, associated vascular and osseous compromise, and concurrent residual/recurrent malignancy. Patient charts were reviewed to identify relevant clinical and treatment history.

Results

36 patients with neopharyngeal fistulae and/or related complications were identified. 26 cases (72%) were initially identified on CT and/or PET/CT. Fistulization to the skin (Fig A), trachea, and prevertebral space were seen in 31, 4, and 2 cases respectively. Associated vascular (Fig B) and osseous (Figs C-D) involvement were identified in 7 (20%) and 4 (11%) cases. 5 cases involving residual/recurrent malignancy along the fistulous tract were noted. 29 patients (81%) were previously treated with radiation prior to surgical resection.

Conclusions

While neopharyngocutaneous fistulization is the most common type of fistulization, fistulous tracts to the trachea and prevertebral space can infrequently occur, with clinically significant consequences including aspiration and discitis/osteomyelitis. Vascular compromise with arterial exposure, narrowing, and luminal irregularity can also occur with risks of rupture and extravasation. The

majority of neopharyngeal fistulization is seen in patients who underwent radiation therapy prior to surgery, compatible with compromised post-surgical healing related to radiation induced vasculopathy.

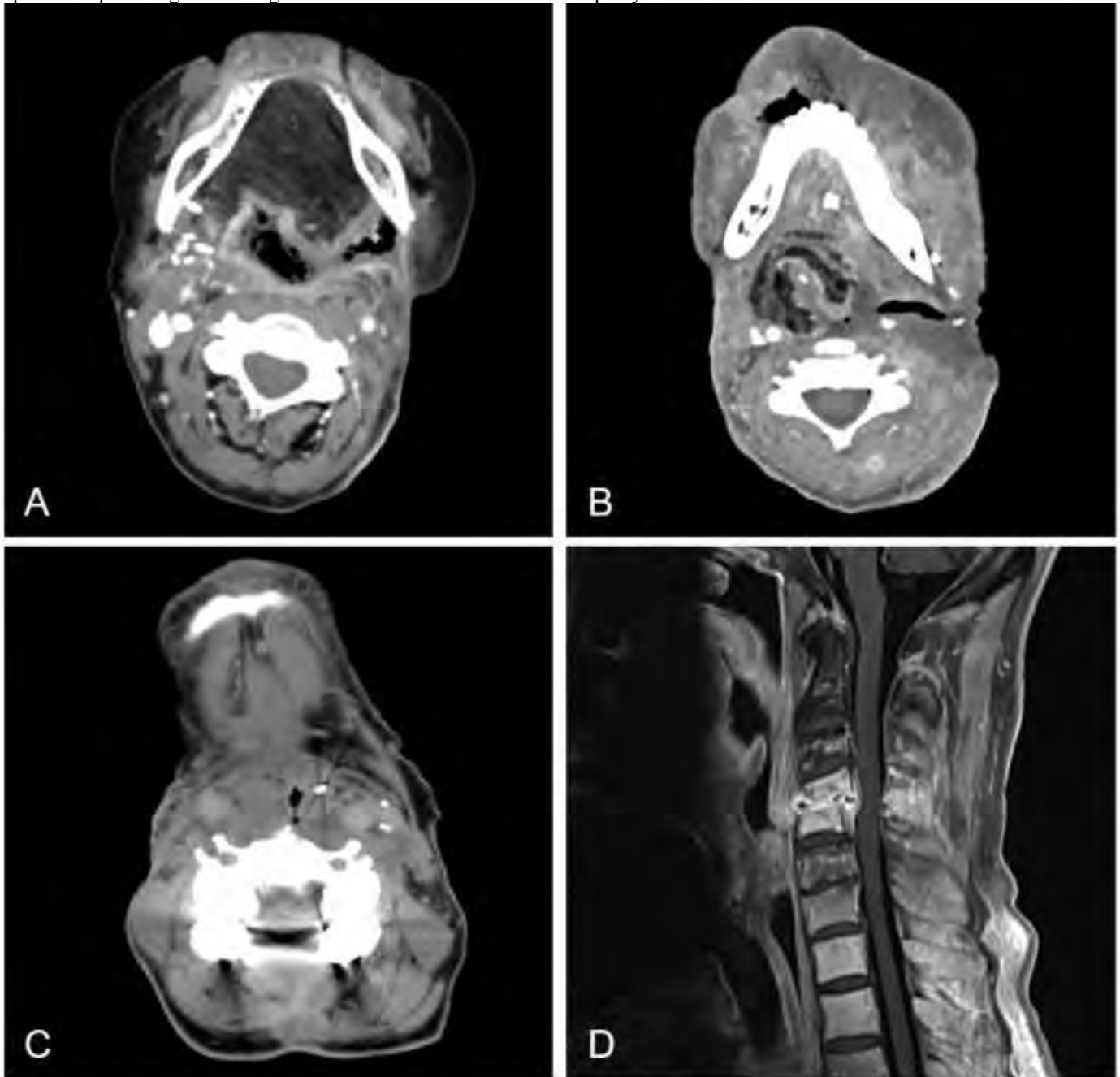


FIGURE. Imaging appearance of neopharyngeal fistulae and related complications. (A) Neopharyngocutaneous fistula extending to the lateral left neck. (B) Exposed left common carotid artery coursing through a fluid/air-filled neopharyngocutaneous fistula, with luminal irregularity concerning for mural thrombus and injury. (C) Air-filled fistulous tract from the neopharynx to the prevertebral space with extensive retropharyngeal/prevertebral edema. (D) Corresponding post-contrast sagittal T1-weighted MRI shows associated C4-5 discitis-osteomyelitis.

(Filename: TCT_1397_figure.jpg)

Characterization of Pediatric Cervical Spinal Fractures based on current AOSpine Classification System using CT, MRI and their association with Blunt Cervical Vascular Injury (BCVI) Grading: A Retrospective study at a single Level-I trauma center.

R Patel¹, S Khanpara¹, A Kamali¹, J McCarty¹, E Bonfante-Mejia¹, R Riascos¹, R Samant¹

¹The University of Texas Health Science Center at Houston, Houston, TX

Purpose

The incidence of blunt cervical vascular injury (BCVI) in children ranges widely between 1-9%. If not recognized promptly, as symptoms can be asymptomatic or not present for 10-72 hours after injury, it may lead to neurologic morbidity or death. In the adult population, specific screening criteria has resulted in less missed BCVI. When applied to children, a very liberal use of computed tomography angiogram (CTA) occurs carrying a high risk from radiation exposure. Main purpose of our study is identify and stratify cervical spine fractures based on AOSpine Classification System at high risk for BCVI in children which will help in screening algorithm for BCVI in children.

Materials and Methods

From our institutional IRB approved database of all children at our hospital who received imaging to screen for BCVI along with CT Cervical Spine from year 2008-2020 were included for study. We have reviewed MRI of Cervical Spine in our analysis where available. Among these patients, we have also included clinical markers including age, sex, Glasgow Coma Scale, mechanisms of injury, Injury Severity Score, seatbelt sign of the neck, focal neurologic exam. With help of CT and MRI of cervical spine, cervical spine fractures with and without ligamentous injury were classified using standard AOSpine Classification System. Using CTA Neck, we have characterized the BCVI grading using standard Biffle scale for BCVI. We have further characterized the different AOSpine fractures associated with BCVI in our cohort to create a specific algorithm for BCVI screening.

Results

Among the 375 children screened, 81 (21.6%) were found to have total of 98 cervical spine fractures with frequency of AOSpine Type A 58 (59.1%), AOSpine Type B 21 (21.5%), AOSpine Type C 19 (19.4%). 42 (11%) were found to have BCVI, one of the largest cohorts to date, in frequency of 14 (33.3%) internal carotid artery injuries and 28 (66.7%) vertebral artery injuries. There were 9 (21.4%) Grade I, 10 (23.8%) Grade II, 7 (16.7%) Grade III and 16 (38.1%) Grade IV cervical vascular injuries based on Biffle scale of BCVI. Our investigation has also concluded that AOSpine Type B (Tension Band type) injuries were most frequently 50% associated with BCVI followed by Type C (Translation type) injuries 27% and Type A injuries 23%.

Conclusions

By classifying high-risk cervical spinal fractures based on AOSpine Classification System associated with BCVI in children will help in the development of a more specific screening algorithm for BCVI.

1154

Characterization of Traumatic Blood-Brain-Barrier Disruption with Dynamic Contrast Enhanced MRI

J Ware¹, S Sinha¹, J Gugger¹, C Dabrowski¹, J Morrison¹, H Zamore¹, B Magdamo¹, J Kim², D Sandsmark¹, R Diaz-Arrastia¹

¹University of Pennsylvania, Philadelphia, PA, ²The City College of New York, New York, NY

Purpose

Traumatic Brain Injury (TBI) is a leading cause of disability worldwide, producing negative impacts on a range of health and social outcomes. Limitations in the ability to non-invasively detect TBI-related neuropathology pose a major barrier to the identification of patients at risk for cognitive decline and neurodegeneration after TBI, as well as to the development of disease-modifying therapies. Dysfunction of the blood-brain-barrier (BBB) has been implicated as a potential mechanism driving neurodegeneration after TBI by a number of animal studies, however human studies remain scarce leaving many questions unanswered. In this study, we examined the ability of dynamic contrast-enhanced (DCE) MRI to detect abnormal BBB permeability after TBI, and determine the relationship to TBI-related anatomical brain lesions.

Materials and Methods

3T DCE MRI was performed in the early post-injury period (median 21 days, range 6-37 days) in 29 adult patients who sustained TBI warranting hospitalization, as well as in 17 demographically-matched healthy control subjects. The Patlak 2-compartment model was used to derive whole-brain voxel-wise maps of permeability metrics including the volume-transfer coefficient (K_{trans}). Structural images were used to identify and segment TBI-related anatomical intracranial lesions. Mean K_{trans} values were compared between TBI and control subjects across the entire brain as well as within lesional, peri-lesional, and non-lesional regions. The number of voxels with abnormally elevated K_{trans} (>95th percentile value of control subjects, expressed as a percentage of all voxels) was also compared between groups.

Results

Among TBI subjects, 18 (62%) had at least one acute TBI-related positive finding, 14 (48%) of which had a parenchymal contusion. Compared to the control group, TBI subjects exhibited elevated K_{trans}, which was most pronounced within focal traumatic lesions

($p < 0.001$) but also present to a lesser degree in the peri-lesional region ($p < 0.01$). Within normal-appearing brain tissue mean Ktrans values did not significantly differ between TBI and control groups ($p > 0.05$), however the number of voxels with abnormally-elevated Ktrans was significantly higher in the TBI group ($p < 0.05$)

Conclusions

TBI is associated with elevated Ktrans values in the early post-injury time period, both within and outside of focal traumatic lesions. Compared to mean Ktrans, spatially-invariant voxel-based analysis may be more sensitive to low-level BBB disruption within normal-appearing brain tissue.

1391

Chordoid glioma: a rare old foe but a new pathological and radiological presentation

M Muneer¹, A Mohamed¹, M Vizcaino², P Vibhute¹

¹Mayo Clinic, Jacksonville, FL, ²Mayo Clinic, Jacksonville, MN

Purpose

To report two cases of Chordoid glioma (CG) with new presentation in terms of histopathology and location: a case of CG with osseous metaplasia, and another CG that was located in the posterior third ventricle. Chordoid glioma is a rare WHO Grade II neoplasm of the anterior third ventricle.

Materials and Methods

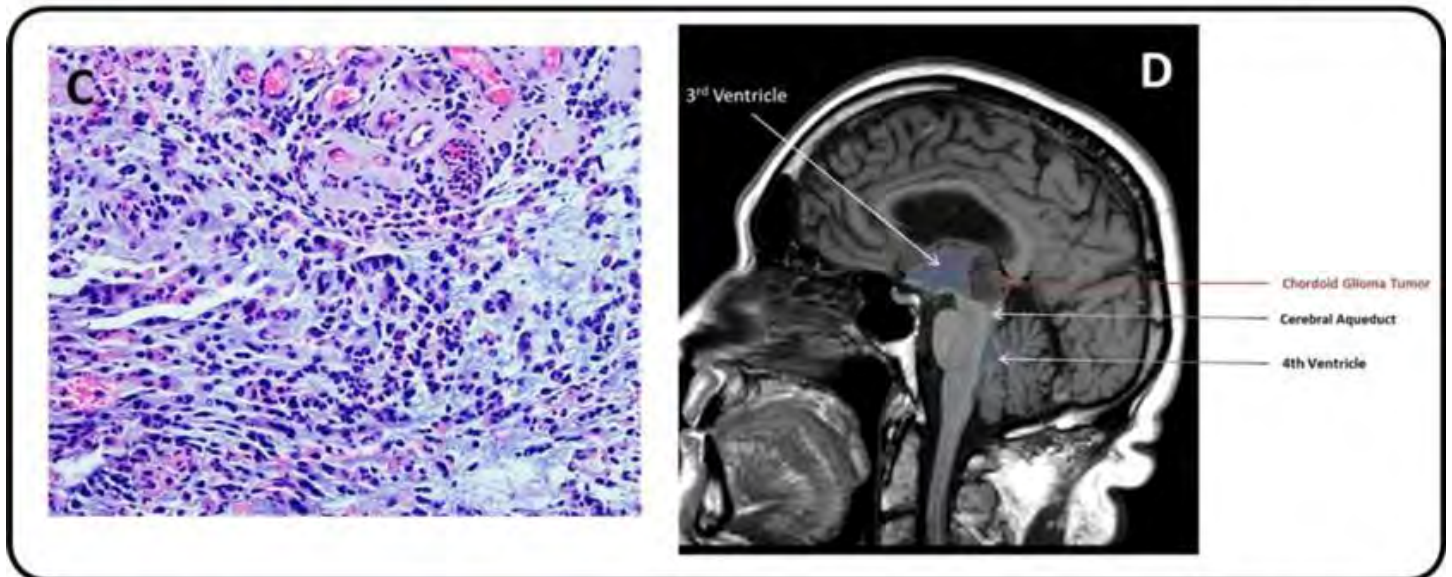
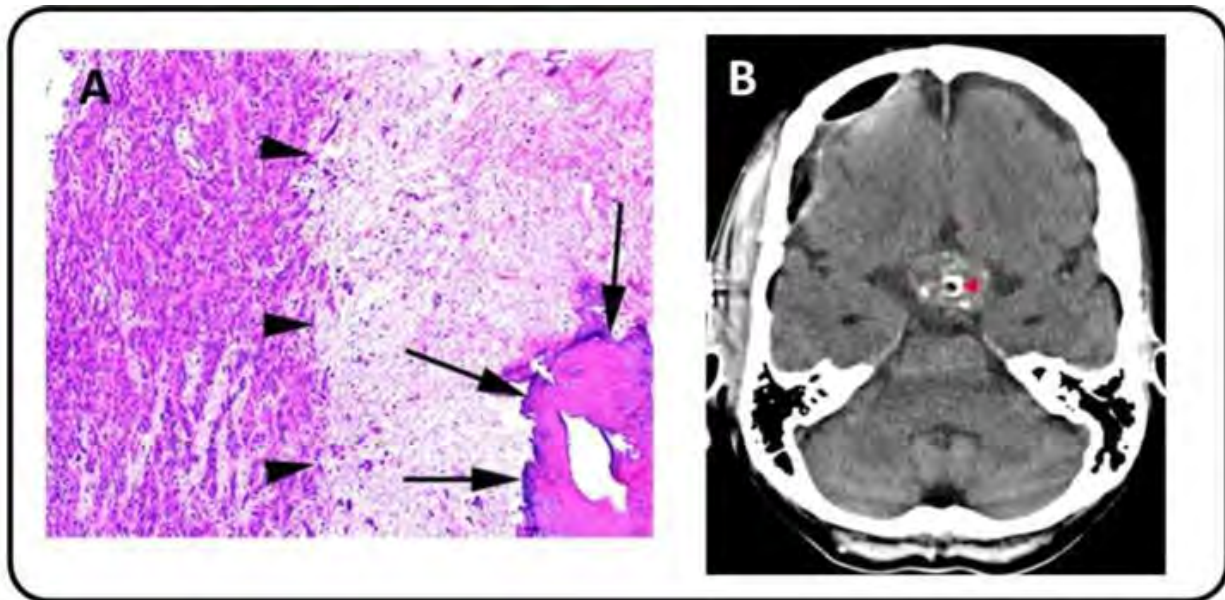
Descriptive study for two-patient case series with abnormal radiological and pathological presentations.

Results

The first case for a 70-year-old woman, which represents a unique case of chordoid glioma (CG) with osseous metaplasia seen on imaging and confirmed with in the biopsy specimen obtained from the tumor. MRI revealed heterogeneous tumor within the anterior third ventricle and demonstrated intense enhancement following gadolinium contrast administration with small non enhancing cystic or necrotic focus. Small nonenhancing cerebrospinal fluid (CSF) signal intensity peritumoral cysts were noted along tumor and brain interphase. The resected specimen showed central sclerosis with lamellar bone indicative of osseous metaplasia and remodeling. The second case for a 75-year-old man presented a unique presentation of CG arising in the posterior aspect of the third ventricle. MRI revealed a well circumscribed mass within the posterior aspect of the third ventricle resulting in obstruction of the cerebral aqueduct and hydrocephalus. The mass was clearly intraventricular as the pineal cistern was well preserved and the tumor had splayed the upper portion of the cerebral aqueduct with posterior displacement of the superior tectum (figure). While CG typically presents within the anterior third ventricle, this tumor has been reported in other locations such as the parieto-temporal lobe, corona radiata, and cerebellar hemispheres. To the best of our knowledge, CG arising from the posterior third ventricle has not been reported up to date.

Conclusions

The presented cases for the first time illustrate two different unique features of CG. The first case revealed a previously undescribed occurrence of osseous metaplasia within CG. The second case demonstrated the importance of considering CG in the differential diagnosis, when a sharply circumscribed mass is encountered within the posterior third ventricle.



Case 1 (A,B) with osseous metaplasia of the chordoid tumor. Hematoxylin and eosin stains (A) showed the central sclerosis (arrow heads) and the metaplastic bone (arrows). A non-contrast postoperative CT scan (B) shows hyperdense bone ossification and hypodense fatty marrow center on CT (red arrow head)

Case 2 (C,D) with abnormal location of the chordoid tumor. Histologic section demonstrate a low-grade glial neoplasm arranged in clusters and cords of epithelioid cells in a myxoid background with lymphoplasmocytic infiltrate and hyalinized blood vessels (C). A Sagittal T1-weighted MRI showing hypo-intense mass in posterior part of the third ventricle(D), which obstructs the cerebral aqueduct.

(Filename: TCT_1391_cggfinal300.jpg)

1337

Circulating microRNA profile as a moderator of aneurysm occlusion after flow diversion.

a eltanahy¹, J Ayers-Ringler², W Brinjkji², D Kallmes², R Kadirvel²
¹Mayo Clinic, rochester, MN, ²Mayo Clinic, Rochester, MN

Purpose

It is well established that patients with metabolic diseases are more than twice as likely to develop accelerated cardiovascular disease.

With the capability of transferring a regulatory message from donor to target tissues, microRNAs have emerged as stable biomarkers of physiologic and metabolic status, etiologic factors in complex disease, and potential therapeutic targets. We hypothesize that inter-individual variability in metabolic profiles is a major potential moderator of aneurysmal healing and occlusion via circulating miRNAs. The purpose of the study was to evaluate the expression of circulating miRNAs associated with the healing of intracranial, saccular aneurysms treated with flow diversion devices (FD).

Materials and Methods

Peripheral blood was collected from patients (n=8, pre-FD and at 6-12 month Follow Up (FU)). miRNA profiles were obtained by RNA sequence analysis. The t-test-based P values will be adjusted for multiple comparisons by using the false-discovery rate multiple-correction. Results were analyzed using the Ingenuity Pathway Analysis tool. qRT-PCR was used to validate RNAseq results.

Results

The total of 22 miRNAs differentially expressed at FU compared to baseline ($P < 0.05$ and fold change < -1.5 and > 1.5). Of these miRNAs, 11 were upregulated and 11 were down regulated. MiRNAs were associated with four major categories according to pathway analysis. 1) Dyslipidemia and insulin resistance (miR-4706, miR-410-5p, miR-129-5P, miR-9-3P, miR-642a-5p, miR-414-3P and miR-221-5P were upregulated, and let-7b-3p, miR-3659, miR-1976, miR-376b-39, miR-3200-5P, miR-8485 and miR-8085 were down regulated). 2) Senescence and ageing disorders (miR-642a-5p, miR-141-3P, miR-6790-5p and miR-5584-5P were upregulated and miR-1234-3P was downregulated). 3) Acute cellular stress and anti-inflammatory response (miR-3154, miR-3164 and miR-125b-1-3p were downregulated). 4) Phenotypic switch of vascular smooth muscle cells (miR-3653-3p and miR-5480-3p were downregulated).

Conclusions

Our results suggest that the downregulated miRNAs related to acute cellular stress and anti-inflammatory response, and vascular smooth muscle phenotype switch could be the pathways potential interest in aneurysm healing mechanisms. Understanding the influence that cardio-metabolic diseases and genetics exert on the regulation of circulating miRNA profiles should reveal the differential role circulating miRNAs play in aneurysm occlusion after flow diversion therapy.

1249

Clazosentan for Improvement of Time to Peak Perfusion in Patients with Angiographically Confirmed Severe Vasospasm

A Lai¹, C Tan², S Weidauer³, A Marr⁴, T Leslie-Mazwi¹, J Hirsch¹, S Roux⁴, R Gupta¹

¹Massachusetts General Hospital, Boston, MA USA, ²Harvard Medical School / Spaulding Rehabilitation Hospital, Cambridge, MA, ³Sankt Katharinen-Krankenhaus, Frankfurt, Germany, ⁴Idorsia Pharmaceuticals Ltd., Allschwil, Switzerland

Purpose

Clazosentan, an endothelin-1 receptor antagonist, has been shown to prevent the development of large vessel angiographic vasospasm after aneurysmal subarachnoid hemorrhage (aSAH). We hypothesized that clazosentan can improve cerebral perfusion for territories affected by angiographically confirmed vasospasm.

Materials and Methods

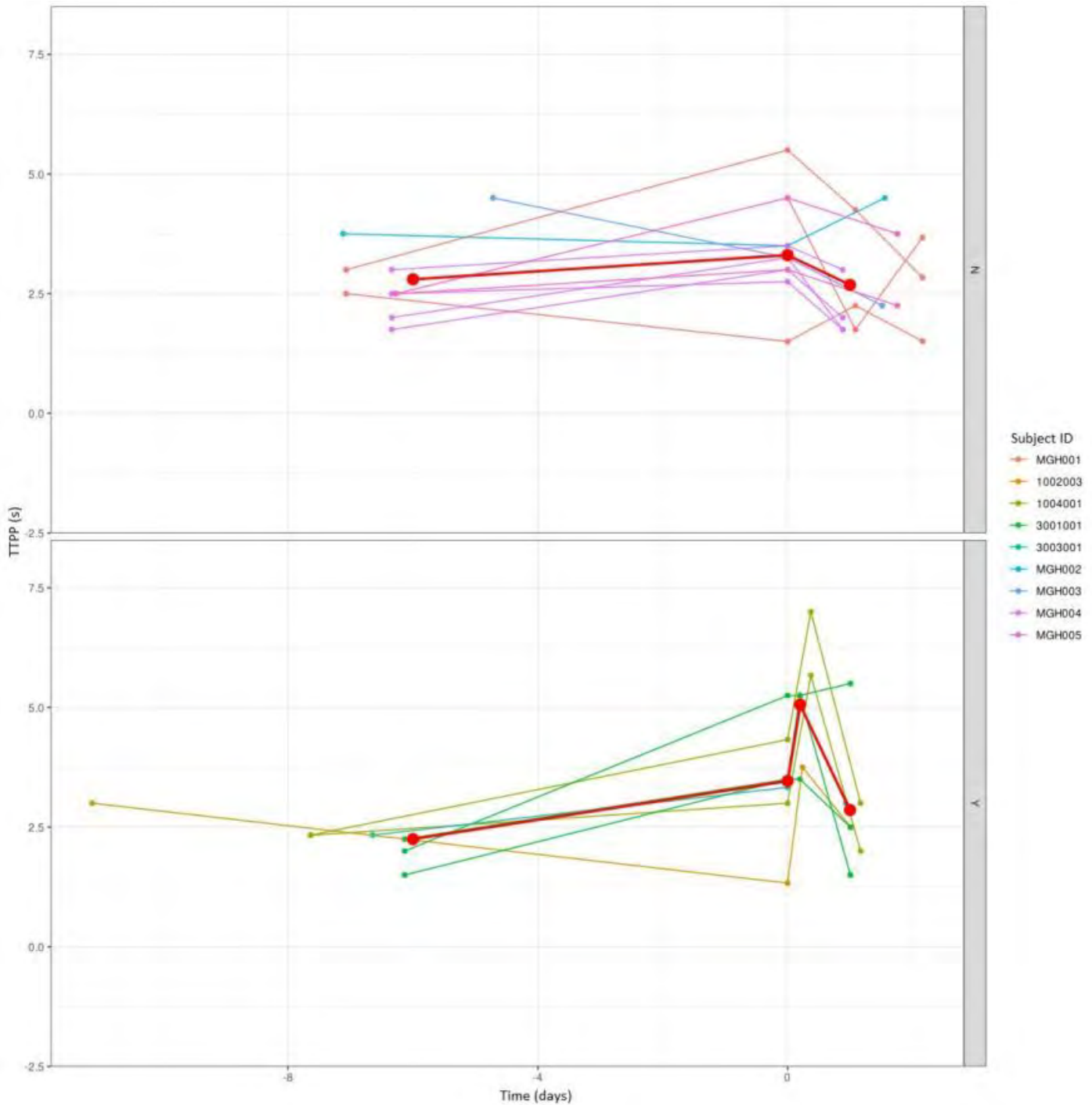
The REVERSE study was a prospective, multi-center, open-label, pilot-study of adult aSAH patients who received intravenous clazosentan after developing moderate-to-severe angiographic vasospasm. Using the radiographic data from the REVERSE study and additional retrospective radiographic data from our tertiary medical center, we compared the impact of intravenous clazosentan with intra-arterial vasodilator therapy (medical standard of care) on vasospasm reversal using Time to Peak Perfusion (TTPP; the time interval between the peak opacification of contrast dye in the main artery supplying an anatomically defined territory and in the parenchymal phase when the dye is diffusely present in the brain parenchyma).

Results

Both intravenous clazosentan (n = 7 vessels) and intra-arterial vasodilator therapy (n = 11 vessels) resulted in a statistically significant improvement in TTPP at 24 hours post-intervention when compared to the TTPP just prior to intervention for territories with angiographically confirmed severe vasospasm in the proximal arteries at baseline (linear mixed effect model, $p = 0.02$). The clazosentan and intra-arterial vasodilator therapy groups exhibited no statistically significant interaction term in our model ($p = 0.71$) suggesting similar temporal course of two therapies.

Conclusions

In our small pilot study, intravenous clazosentan administered for at least 24 hours had an effect comparable to that of intra-arterial vasodilator therapy in reversing angiographically confirmed severe vasospasm. Our results may indicate that clazosentan, in an appropriately selected patient cohort, could offer a noninvasive approach for alleviating vasospasm.



(Filename: TCT_1249_Figure1.jpg)

854

Clinical benefit of additional contrast-enhanced 2D T2-weighted fluid-attenuated inversion recovery image to detect leptomeningeal metastasis in lung cancer staging

H Kim¹, H Kim¹, J LEE², A Lee³, J Kim³, J Lee⁴, K Chang⁵

¹Soonchunhyang University Bucheon Hospital, Bucheon, Gyeonggi-do, ²SOONCHUNGHYANG UNIV HOSPITAL, BUCHUN, Korea, Republic of, ³N/A, N/A, ⁴Soonchunhyang University Bucheon Hospital, Bucheon, Gyeonggi-do, ⁵Human Medical Imaging and Intervention Center, Seoul, Seoul

Purpose

To evaluate the clinical benefit of 2D contrast-enhanced T2 fluid-attenuated inversion recovery (CE-T2 FLAIR) image to detect leptomeningeal metastasis (LM) in the brain metastasis work-up for lung cancer

Materials and Methods

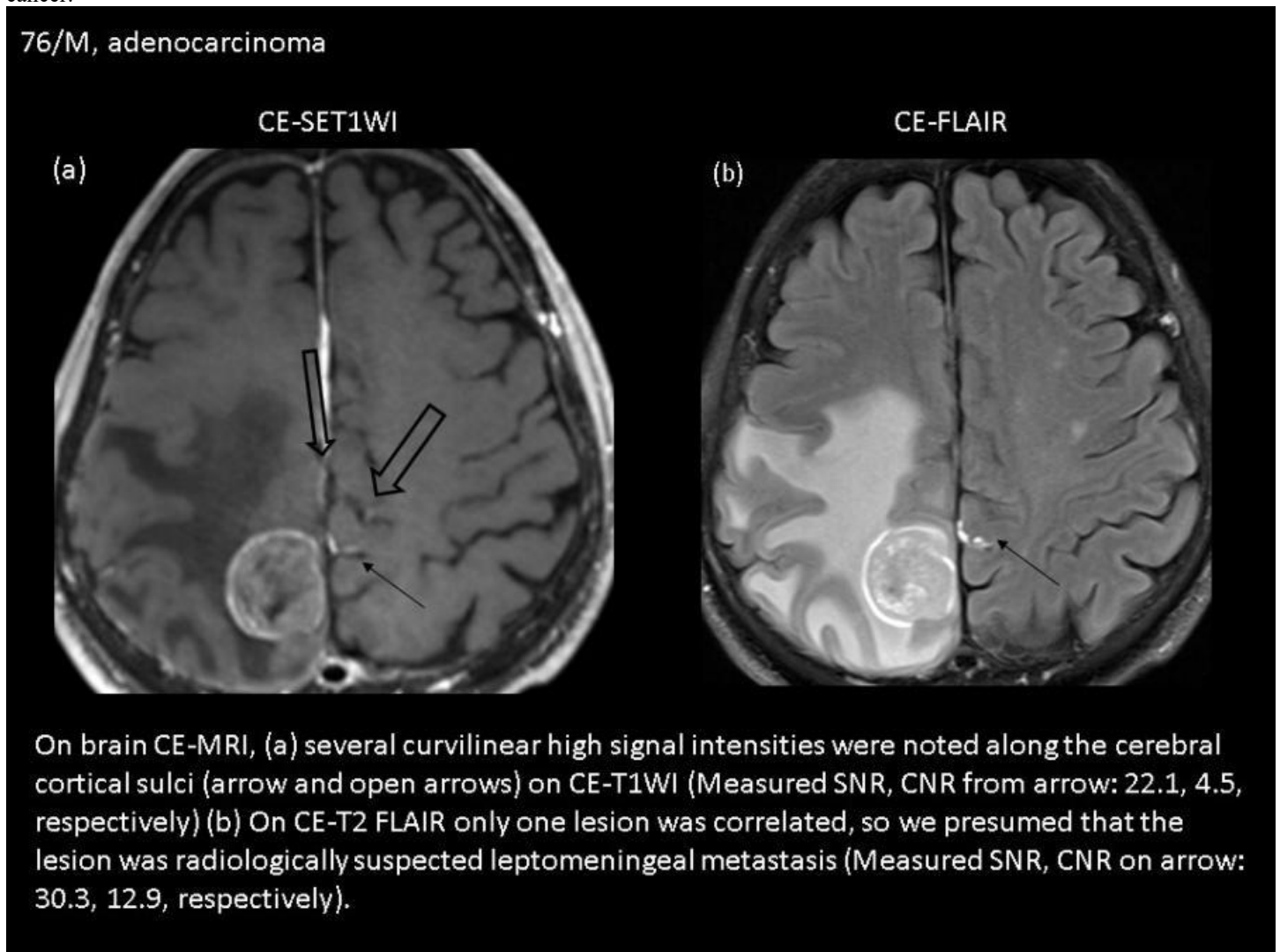
From June 2017 to July 2019, we collected lung cancer patients who had undergone brain MRI including 3D spin echo contrast-enhanced T1 weighted image (CE-T1) and CE-FLAIR. Among them, clinico-radiologically suspected leptomeningeal metastasis were found. Then, 2 independent readers analyzed presence of leptomeningeal metastasis across 3 sessions; CE-T1, CE-FLAIR and combined above two images. And diagnostic accuracy and inter-observer agreement were compared. For quantitative analysis, in patients with confirmed leptomeningeal metastasis, The ROIs were drawn in images which leptomeningeal metastasis was obvious, and contrast-to noise ratio (CNR) obtained from CE-T2FLAIR and CE-T1 were compared. In addition, the risk factor analysis was performed to find risk factors to increase diagnostic yield of CE-FLAIR.

Results

We collected 526 suspected lung cancer patients who underwent brain MRI and 77 patients were excluded (insufficient image protocol, unclear pathology, different contrast media, poor image quality). Of 449, 34 patients were clinico-radiologically suspected leptomeningeal metastasis, and among them, 23 were diagnosed to be true leptomeningeal metastasis according to NCCN guideline. The calculated diagnostic performance of CE-T1, CE-FLAIR, and combined analysis obtained from 34 suspected leptomeningeal metastasis were highest in combined analysis (AUC, 0.80, 0.82, and 0.89, respectively). The inter-observer agreement was also highest in combined analysis (0.68, 0.72, and 0.86, respectively). In quantitative analysis, CNR of CE-FLAIR was significantly higher than CE-T1 (paired t-test, $P < .05$). In risk factor analysis in all included patients ($n=449$), re-staging, presence of brain metastasis, and adenocarcinoma cell type were significant risk factor after initial lung cancer staging was corrected (OR, 9.71, 4.33, 8.41, respectively).

Conclusions

Adding CE-T2FLAIR may be added value in the leptomeningeal metastasis detection in the brain metastasis screening for lung cancer.



(Filename: TCT_854_ASNR_LJB.jpg)

1101

Clinical Characteristics Associated with Facial Meningoceles

B Hamilton¹, H Hanseler², S Gupta²

¹Oregon Health & Science University, WEST LINN, OR, ²OHSU, Portland, OR

Purpose

Our goal was to review all patients with suspected facial nerve meningoceles by imaging and correlate to clinical symptoms, gender, and body mass index (BMI). We hypothesized that facial nerve meningoceles are more common in patients with high BMI, which is a risk factor for idiopathic intracranial hypertension.

Materials and Methods

The purpose of this study is to identify factors patients with facial meningoceles have in common. This may help identify patients at higher risk for facial meningocele.

Results

We retrospectively reviewed all electronic radiology reports dating from 1999 to 2020 using the terms 'facial meningocele' or 'facial cephalocele', 'geniculate meningocele', and/or 'geniculate cephalocele' to identify potential cases. We then examined reports from temporal bone CT and internal auditory canal MRI studies. Cases without high resolution 3D T2 sequences on MRI, or with larger broad tegmen defects not isolated to the geniculate fossa were excluded. We reviewed all imaging studies for the size and signal intensity of the meningoceles on high resolution T2-weighted MRI, lack of enhancement on T1 post contrast MRI, and assessed for the presence and size of bone defect on temporal bone CT. We then correlated imaging to patient gender, age, BMI, and clinical findings identified via chart review.

Conclusions

There were a total of 11 patients ranging in age from 25 to 72 years of age, all of whom were female. Among the 11 patients, there were 19 total imaging studies reviewed, 11 CT (58%) and 8 MRI (42%). Of these, 1/11 (9%) patient had a normal BMI of 21.1, the remaining 10/11 (91%) patients had abnormally elevated BMI ranging from 26.30 to 54.89. Facial nerve symptoms were noted in 3/11 (27%) patients. 7/11 (73%) patients underwent surgery, one for repair of the meningocele, while the remainder were for unrelated indications. None of the patients had documented idiopathic intracranial hypertension. Facial nerve meningoceles on MRI and temporal bone CT appear more common in patients of female gender with elevated BMI. This finding adds to the knowledge base regarding the frequency of dural defects and meningoceles elsewhere along the skull base in patients with elevated BMI. While these may be discovered incidentally, the finding is important to document as symptomatic patients may require surgery.

419

Clinical Impact of a Quantitative MR Perfusion Pipeline on the Diagnostic Interpretation of Post-treatment Brain Tumors

G Yamin¹, B LANZMAN¹, E Tranvinh¹, C Patel¹, M Iv¹

¹Stanford University, Stanford, CA

Purpose

Quantitative perfusion MRI is an effective tool to differentiate between progressive tumor and treatment effect in previously treated brain tumors (1). However, its implementation in routine clinical practice can be challenging in large part due to workflow logistics. The purpose of this study is to evaluate the impact of a quantitative MR perfusion pipeline in the clinical workflow of an academic institution on the diagnostic interpretation of post-treatment brain tumors.

Materials and Methods

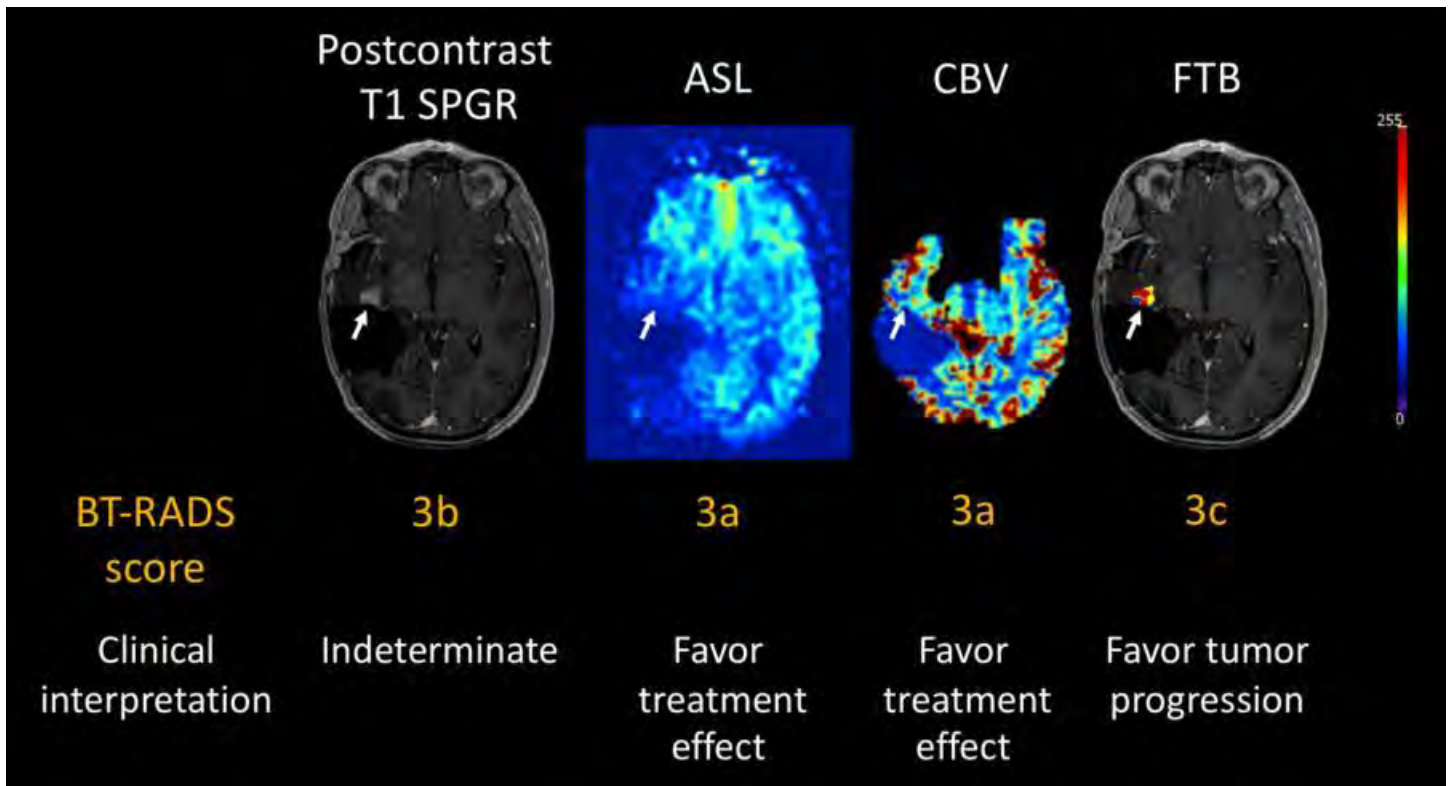
The brain tumor pipeline was implemented with support of our 3D Quantitative Imaging Laboratory, involving various steps, image processing, and quality control. To evaluate the pipeline's clinical impact, 50 patients with previously treated high grade gliomas, who had MRIs consisting of conventional and multiparametric perfusion (ASL, DSC) images processed through the pipeline, were retrospectively identified. Two neuroradiologists prospectively and independently provided brain tumor assessment scores, using the Brain Tumor Reporting and Data System (BT-RADS) (2). Raters provided scores of tumor status (BT-RADS) and confidence of tumor determination (1-to-5 point Likert, least-to-most confident), using conventional images first and then using respective ASL, rCBV, and fractional tumor burden (FTB) perfusion measurements and images. Inter-rater agreement of BT-RADS scores was assessed with Cohen's kappa. Descriptive statistics and one-way ANOVA with post-hoc analysis were used to compare BT-RADS scores with and without perfusion and to assess rater confidence scores.

Results

Inter-rater agreement was good-to-excellent for all modalities but lowest with conventional imaging (0.69) and highest with FTB (0.77). Use of ASL, rCBV, and FTB resulted in BT-RADS score changes in 3 (6%), 6 (12%), and 12 (24%) patients, respectively, for rater 1, and 8 (16%), 10 (20%), and 10 (20%) patients for rater 2. All but 1 score change for rater 1 and >60% of score changes for rater 2 were considered clinically significant (scores that resulted in a tumor status change). Of the 3 perfusion modalities, FTB was significant for yielding score changes for rater 1 (ASL-FTB, $p < 0.001$; rCBV-FTB, $p = 0.03$). For both raters, confidence scores were highest with FTB.

Conclusions

Implementation of a quantitative MR perfusion pipeline resulted in clinically significant diagnostic interpretation changes of post-treatment brain tumors in up to 24% of cases, with FTB being the preferred perfusion imaging.



(Filename: TCT_419_ASNRFTBfig11-1-2020.jpg)

129

Clinical, Radiographic, Pathologic Characterization and Survival Outcome of Rare NUT Carcinomas.

M VIRARKAR¹, M Mallery², M Saleh³, N Ramani³, A Morani³, P Bhosale³

¹UT Health Science Center, Houston, TX, ²UT Houston McGovern medical school, Houston, TX, ³MD Anderson Cancer Center, Houston, TX

Purpose

Nuclear protein of the testis (NUT) carcinoma (formerly NUT midline carcinoma) is an aggressive tumor with characteristic BRD4-NUTM1 translocation and a poor prognosis. The primary objective of this study was to describe the clinical and radiologic features, treatment response, and survival of NUT carcinoma (NC).

Materials and Methods

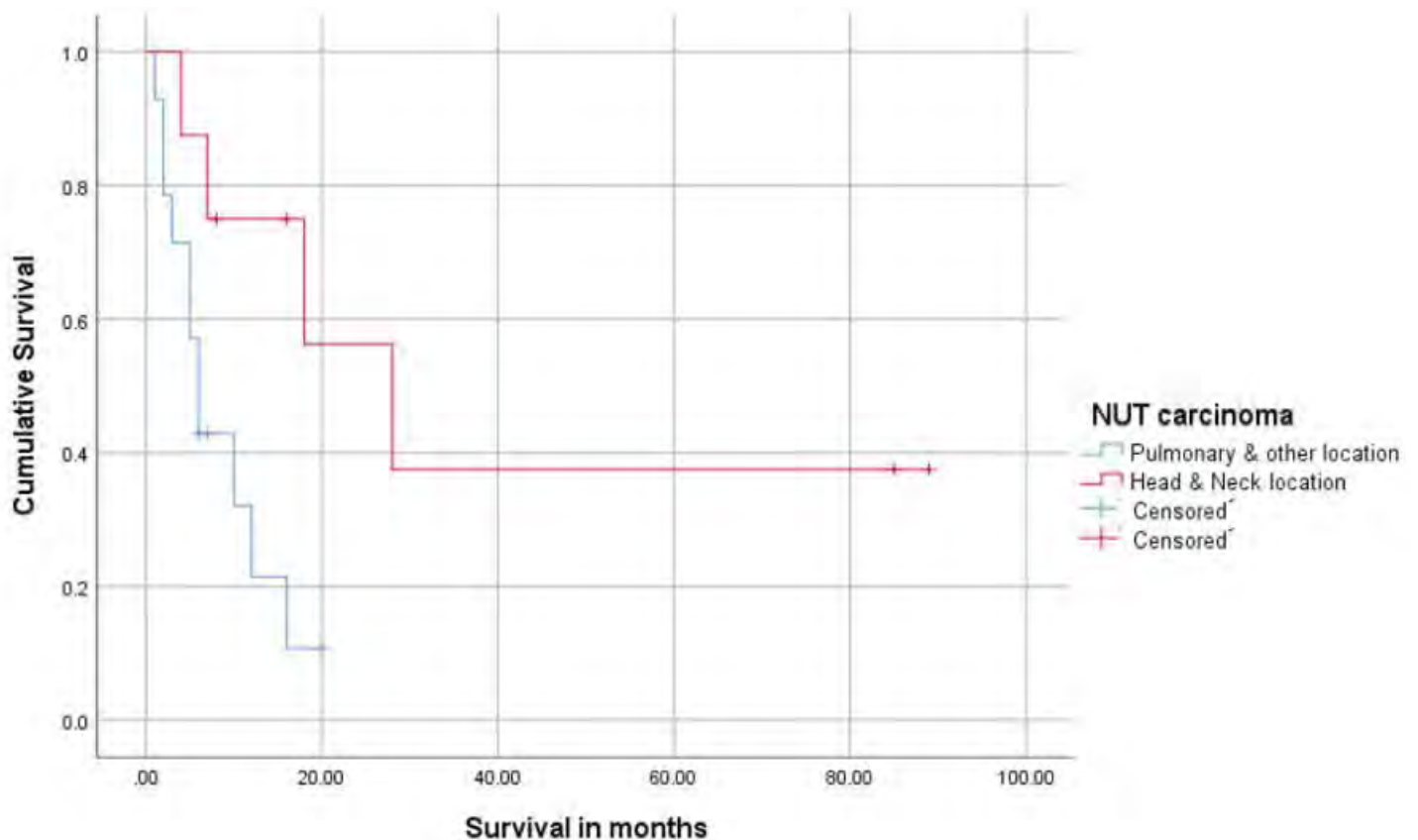
This retrospective single-center study was based on the review of medical records of NC patients with a specific genetic rearrangement or positive anti-NUT nuclear staining. Overall survival was analyzed according to primary tumor location.

Results

This series of 22 patients had a mean age of 36.27±2.68 years with 68% females and 32% males. The median age at diagnosis was 34 years (range: 17-55 years). The primary tumor was located in the chest (n=12/22; 55%), head and neck (n=9/22; 40%), and one patient had a renal tumor. About 68% (n=15/22) patients presented with regional lymph nodal involvement and 77% (n=17/22) had distant metastases. All the bone metastases were lytic (100%) with mixed lytic and sclerotic metastases in 5 patients. Only 18% (n=4/22) patients showed response to treatment, with progression in the remaining 18 patients. The median overall survival (OS) was 7 months. The OS was significantly (p = 0.024) more in patients with primary head and neck NC (n = 9, OS 16 months) versus those with pulmonary and other locations (n = 13, OS 6 months).

Conclusions

NC is an aggressive disease refractory to conventional therapy. Imaging with the complementary use of CT, MRI, and PET-CT is important for staging, guiding management, assessing the treatment response, and surveillance.



(Filename: TCT_129_11.jpg)

836

Coccygeoplasty A New Alternative For Treatment Of Refractory Coccygodinia In Patients With Coccyx Fracture, Hypermobility Or Luxation: Our Preliminary 12 Patients Experience

A De Vivo¹, I Gil², F Ventura³, H Alqatami⁴, L Manfre²

¹I.O.M., Catania, ITALY, ²N/A, N/A, ³IOM, catania, italy, ⁴Institute of Hamad Medical Corporation, doha, qatar

Purpose

Multiple factors can be responsible for coccydynia being fracture, sub-luxation and hypermobility of sacrococcygeal segments the most frequent etiology. Despite in the past multiple treatments had been proposed, most of patients remains symptomatic. Coccygeoplasty (CP) is a new minimally invasive treatment without relevant complication documented. We present the clinical results at 3 months' follow-up of a series of 12 patients with affected by coccygodinia treated with CP.

Materials and Methods

We retrospectively reviewed all patients that underwent CP for chronic coccydynia between January 2005 and October 2018. All patients had dynamic radiograms in standard and sitting position, conventional CT and MRI studies, for diagnosis of coccyx hypermobility, and exclude other pathologies that could contribute for the symptoms.

Results

Twelve patients affected by painful sacrococcygeal subluxation were treated in our center. There was significant improvement of clinical symptoms in 75% (n=9) of the patients, while the pain persisted in 25% (9/12). No complication occurred. FU CT control images showed optimal results in 75% (n=9) patients with fixation of the sacrococcygeal bone segments. No correlation was found between final imaging results and clinical outcome at 3 months (p=0.1).

Conclusions

Patients with coccyx sub-luxation submitted to CP showed a satisfactory pain relief at 3 months' follow-up. We fail to find a statistic relation between the final imaging results and clinical results, probably because of limited number of cases. More studies are needed to validate this technique and to find best indications for CP success.

1110

Collateral Delay Core (CDC) Score: A New Perfusion Metric Highly Predictive of Patient Outcome after Successful Thrombectomy

Purpose

To select and optimize a new tissue-based CT perfusion metric in patients with acute ischemic stroke based on its ability to predict short-term outcome and to compare that metric to the hypoperfusion intensity ratio (HIR)[1] in their ability to predict infarct growth rate, short- and long-term patient outcome in patients who underwent thrombectomy.

Materials and Methods

Out of 17 patients from the GENESIS cohort that underwent thrombectomy, the 14 that were successful (8 males and 6 females; five with TIC1 2b and nine with TIC1 3) were included. Patient characteristics: Age=68.1±15.4, baseline NIH Stroke Scale (NIHSS)= 16.7 ± 6.2, 24-hour NIHSS=14.1 ± 8.8, CTP to 24-hour CT time=26.8±2hrs, modified Rankin Scale (mRS) at 90 days=4.4±1.6. CTP perfusion software written in MATLAB previously used to compare different collateral flow metrics[2] and validated against Rapid iSchemaView[3,4] was used to calculate the size of ischemic core (CBF < 0.3*normal brain), penumbra (Tmax > 6s) and mismatch (penumbra-core) as well as the delay in perfusion (Tmax) in the same volumes compared to the contralateral hemisphere. A CDC score of the form CDC score = [ΔTmax (s)-T0] x vol (mL) was studied. The correlation coefficient of the scores to the change in NIHSS was calculated over delays (T0) of 0-20 seconds to find the optimal delay. The score with the highest correlation coefficient was chosen as the best. Infarct growth rate was determined as (24-hour CT hypodensity volume - CTP core size)/interscan interval. The correlation of the CDC score and HIR to the 24hr change in NIH stroke scale, infarct growth rate as well as 90 day mRS was compared.

Results

The volume in the core multiplied by the delay in the core provided the highest correlation to short-term patient outcome. A delay of 11s in the core provided the highest correlation coefficient. The CDC score was significantly correlated to infarct growth rate, short- and long-term patient outcome. The correlations were ~2x higher than HIR (see table).

Conclusions

The CDC score is a new tissue-based CTP metric that is ~2x more highly correlated than HIR to infarct growth rate, short- and long-term outcome after thrombectomy. A CDC score > threshold (100) provided 100% accuracy for determining whether patients improved or did not improve after thrombectomy and should be studied further as a way to further improve selection of patients for thrombectomy.

Table 1. Correlation coefficients (R²) and p-value of fits of tissue-based collateral flow metrics to infarct growth rate, short- and long-term patient outcome.

	Δ NIHSS	Infarct Growth Rate	90-day mRS	Dichotomized short-term outcome (ΔNIHSS≤0 vs. ΔNIHSS>0)	Dichotomized long-term outcome (mRS 0-2 vs. 3-7)
CDC score	R ² = 0.72 p = 0.0001**	R ² = 0.62 p = 0.004**	R ² = 0.28 p = 0.07	R ² = 0.61 p = 0.001**	R ² = 0.34 p = 0.06
HIR	R ² = 0.31 p = 0.04*	R ² = 0.37 p = 0.05*	R ² = 0.09 p = 0.39	R ² = 0.35 p = 0.03*	R ² = 0.03 p = 0.6

(Filename: TCT_1110_CDCscoretable.jpg)

1345

Comparing distribution of injury in isolated Basal-Ganglia-Thalamus (BGT) injury vs. combined Basal Ganglia-Thalamus-watershed (BGT-WS) pattern of neonatal hypoxic ischemic encephalopathy (HIE).

Purpose

Acute profound (AP) perinatal hypoxia is one of the common mechanisms of HIE that typically affects metabolically active structures as posterior putamen of basal ganglia (BG) and ventrolateral nucleus (VL) of thalamus – hence named BGT pattern. Partial prolonged

(PP) brain hypoxia can lead to other pattern of brain injury commonly involving watershed (WS) territories. When AP insult is superimposed on PP insult, a combined pattern of brain injury can occur. In prolonged labor it is also possible that thalami (especially pulvinars) become injured through hypoglycemia, contaminating the categorization with potential misdiagnosis. We aimed to compare the frequency and distribution of deep nuclei involvement in isolated BGT vs. combined BGT-WS pattern of injury.

Materials and Methods

We retrospectively reviewed MR exams of cerebral palsy patients aging 0-18 years with report diagnosis of isolated BGT or combined BGT-WS HIE. Location and extent of lesions (high T2 signal \pm atrophy) within BGT areas were compared between the 2 groups.

Results

We reviewed 772 MR exams – 437 (57%) isolated BGT and 335 (43%) combined BGT-WS patterns. Isolated BGT pattern showed BG involvement in 84% (368) vs 49% (163) for combined pattern. In particular, sole putamina lesions were more common in isolated BGT – 71% (310) – than combined – only 19% (63). Rest of BG combinations were not frequent and didn't differ significantly between groups. Frequency of thalamic involvement was closely similar between the 2 groups – 93% (408) in isolated BGT vs 95% (317) in combined. However, sole VL nucleus lesion was more common in isolated BGT – 67% (291) than combined – only 21% (69). Conversely, sole pulvinar lesions – 25% (82) vs. 6% (27) – and whole thalamus lesions – 49% (136) vs. 16% (69) – were more common in isolated BGT than combined group respectively. Posterior putamen & VL nucleus was the most frequent BGT lesion combination in isolated BGT (56.8%) but not in combined group (4.2%).

Conclusions

Significant differences between the 2 groups suggest that many cases defined as combined BGT-WS may in fact represent other injury accompanying PP insults, such as hypoglycemia which typically affects thalamic pulvinars. It is likely that cases in the combined group with isolated putamina or VL involvement may well represent combined BGT-WS injury but we suggest that WS injury with only thalamic injury outside VL region not automatically be assumed to represent BGT-WS combination as it may possibly represent WS-hypoglycemia combination.

Thalamus lesion	Isolated BGT pattern		Combined BGT - Watershed pattern		Chi-squared (X^2) test p value
	Number of cases	% from all cases (n=437)	Number of cases	% from all cases (n=335)	
Ventrolateral (VL) alone	291	[66.6%]	69	[20.6%]	0.000
Pulvinar alone	27	[6.2%]	82	[24.5%]	
Other nuclei alone	21	[4.7%]	30	[9 %]	
Whole thalamus	69	[15.8%]	136	[40.6%]	
Total cases with Thalamus lesion	408	[93.3%]	317	[94.6%]	

Table 1a comparing thalamic lesions in both isolated BGT and combined BGT-Watershed patterns regardless of BG involvement.

Basal Ganglia (BG) lesion	Isolated BGT pattern		Combined BGT - Watershed pattern		Chi-squared (X^2) test p value
	Number of cases	% from all cases (n=437)	Number of cases	% from all cases (n=335)	
Putamen alone	310	[70.9%]	63	[18.8%]	0.000
Dorsal striatum (Putamen & Caudate)	39	[8.9%]	41	[12.2%]	
Lentiform (Putamen & Globus pallidus (Gp))	3	[0.7%]	24	[7.2%]	
Striatum (Putamen, Caudate, and Gp)	16	[3.7%]	35	[10.4%]	
Total cases with BG lesion	368	[84.2%]	163	[48.6%]	

Table 1b comparing BG lesions in both isolated BGT and combined BGT-Watershed patterns regardless of thalamic involvement.

BGT lesion combination	Isolated BGT pattern		Combined BGT - Watershed pattern		Chi-squared (X^2) test p value
	Number of cases	% from all cases (n=437)	Number of cases	% from all cases (n=335)	
Putamen + Ventrolateral nucleus only	248	[56.8%]	14	[4.2%]	0.000
Any other BGT lesion combinations*	187	[42.7%]	313	[93.4%]	
Total cases with BGT lesion	435	[99.5%]	327	[97.6%]	

Table 1c comparing BGT lesions combinations in both isolated BGT and combined BGT-Watershed patterns.

*Other BGT lesion combinations includes cases with BG alone (e.g. Putamen alone), Thalamus alone (e.g. VL thalamus alone or pulvinar alone), or BGT but outside Putamen and VL nucleus combination (e.g. Putamen and pulvinar)

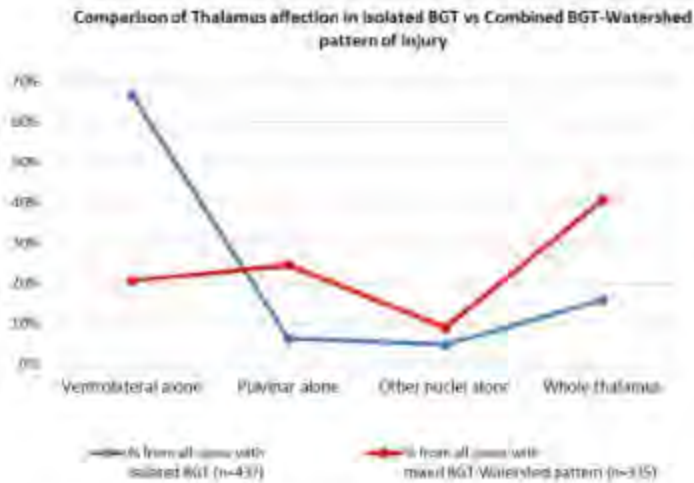


Figure 1a comparing thalamic lesions in both isolated BGT and combined BGT-Watershed patterns regardless of BG involvement.

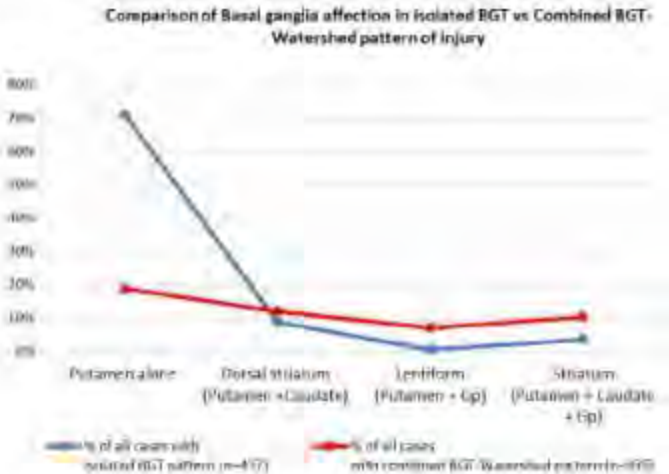


Figure 1b showing cases with BG lesions in both isolated BGT and combined BGT-Watershed patterns regardless of thalamic involvement.

Comparing Measures of Cortical Brain Structure in Treated HIV Infection

E O'Connor¹, J Becker², T Zeffiro¹

¹University of Maryland School of Medicine, Baltimore, MD, ²University of Pittsburgh School of Medicine, Pittsburgh, PA

Purpose

Background. Although many studies report cortical gray matter structural differences associated with HIV infection, the affected regions and serostatus effect sizes substantially vary. While some of this variation is due to sample heterogeneity, different measurement techniques may also contribute. Surprisingly, measurement differences as a possible source of inconsistency in the HIV neuroimaging literature has received little attention. To explore this possibility, we examined HIV associated cortical gray matter (GM) variation using both voxel based morphometry (VBM) and surface-based morphometry (SBM), including cortical thickness (CT), gyrification, fractal dimension and sulcal depth.

Materials and Methods

In a cross-sectional study, including 117 HIV+ seropositive and 90 demographically-matched, seronegative participants, we investigated serostatus effects on GM structure, applying computational VBM and SBM analysis to high resolution (1mm3), T1-weighted MRI data. Linear regression was used to model HIV serostatus effects on global structure, adjusting for age, CD4 nadir, drug use and total intracranial volume. CAT12/SPM12 and R were used for image processing and statistical modeling.

Results

HIV serostatus was associated with lower volume measures, including total GM (B = -15.1; 95% CI = [-28.8 – -3.49]), lower WM (B = -8.41; 95% CI = [-18.2 – 1.39]) and higher total CSF (B = 23.1; 95% CI = [6.45 – 39.7]). In contrast, no serostatus effects on surface structural measures were seen, including CT, gyrification, fractal dimension or sulcal depth.

Conclusions

Among volume and surface quantification techniques, total GM, WM and CSF volume were most sensitive to HIV infection, when adjusting for age and total intracranial volume. The finding that volume measures are better able to identify serostatus effects suggests that some of the variation in reported results across studies may have been related to measurement technique differences. Increased consistency in selecting computational methods may improve reliability and reproducibility in the HIV neuroimaging literature.

1254

Comparing the prognostic impact of age and baseline NIHSS in acute stroke due to large vessel occlusion: Results from the HERMES collaboration

J Ospel¹, S Brown², M Kappelhof³, W van Zwam⁴, T Jovin⁵, D Roy⁶, B Campbell⁷, Y Roos⁸, B Buck⁹, K Muir¹⁰, R du Mesnil de Rochemont¹¹, M GOYAL¹²

¹University Hospital Basel, Basel, Basel, ²Altair Biostatistics, St Louis Park, MN, ³Amsterdam UMC, University of Amsterdam, Amsterdam, Noord-Holland, ⁴Maastricht UMC+, Maastricht, Maastricht, ⁵University of Pittsburgh, Pittsburgh, PA, ⁶Centre Hospitalier de l'Université de Montréal, Montreal, Quebec, ⁷Royal Melbourne Hospital, Melbourne, Melbourne, ⁸Amsterdam University Medical Center, Amsterdam, Noord Holland, ⁹University of Alberta Hospital, Edmonton, Alberta, ¹⁰University of Glasgow, Glasgow, na, ¹¹University Hospital Frankfurt, Frankfurt, Hessen, ¹²University of Calgary, CALGARY, ALBERTA

Purpose

Little is known about the combined effect of age and National Institutes of Health Stroke Scale (NIHSS) in acute ischemic stroke, and it is not clear how the effects of baseline age and NIHSS on outcome compare to each other. The previously described Stroke Prognostication Using Age and NIHSS (SPAN) index adds up NIHSS and age to a 1:1 combined prognostic index. We added a weighting factor to the NIHSS/age SPAN index to compare the relative prognostic impact of NIHSS and age, and assessed endovascular treatment (EVT) effect based on weighted age and NIHSS.

Materials and Methods

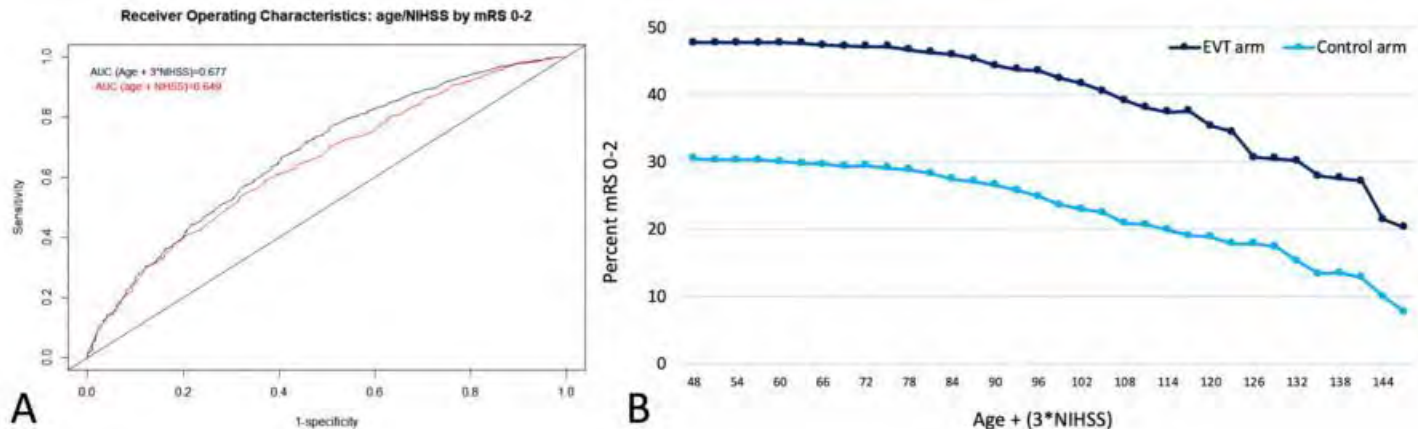
We performed adjusted logistic regression with good outcome (90-day modified Rankin Scale score 0-2) as primary outcome. From this model, the coefficients for NIHSS and age were obtained. The ratio between the NIHSS and age coefficients was calculated to determine a weighted SPAN index (wSPAN). The adjusted association of SPAN, and wSPAN with good outcome was compared, and proportions of good outcome and adjusted effect size estimates for EVT in patient subgroups defined by wSPAN increments of 3 were calculated to evaluate potential changes in treatment effect.

Results

We included 1750/1766 patients from the HERMES collaboration with available age and NIHSS data. Median NIHSS was 17 (IQR 13–21) and median age was 68 (IQR 57–76). Good outcome was achieved by 682/1743 (39%) patients. The NIHSS/age effect coefficient ratio was $([-0.0032]/[-0.111]) = 3.4$, which was rounded to 3, resulting in a wSPAN index defined as $([3*NIHSS]+age)$. The association with good outcome was slightly stronger for wSPAN, albeit not significant (figure 1A). Cumulative EVT effect size estimates across wSPAN subgroups consistently favored EVT, with a number needed to treat ranging from 5.3 to 8.7. Proportions of good outcome across the wSPAN spectrum are shown in figure 1B.

Conclusions

The impact on chance of good outcome of a 1-point increase in NIHSS roughly corresponded to a 3-year increase in patient age. EVT was beneficial across all weighted age/NIHSS subgroups.



(Filename: TCT_1254_Figure_ASNR_ageNIHSS.jpg)

800

Comparing Zero-TE MRI and CT: Diagnostic, Synthetic, and 3D Image Evaluation

M Ho¹, S Bambach²

¹Nationwide Children's Hospital, Dublin, OH, ²Nationwide Children's Hospital, Columbus, OH

Purpose

To compare the diagnostic effectiveness of zero-TE (ZTE) MRI and CT for cortical bone imaging in the pediatric head and neck.

Materials and Methods

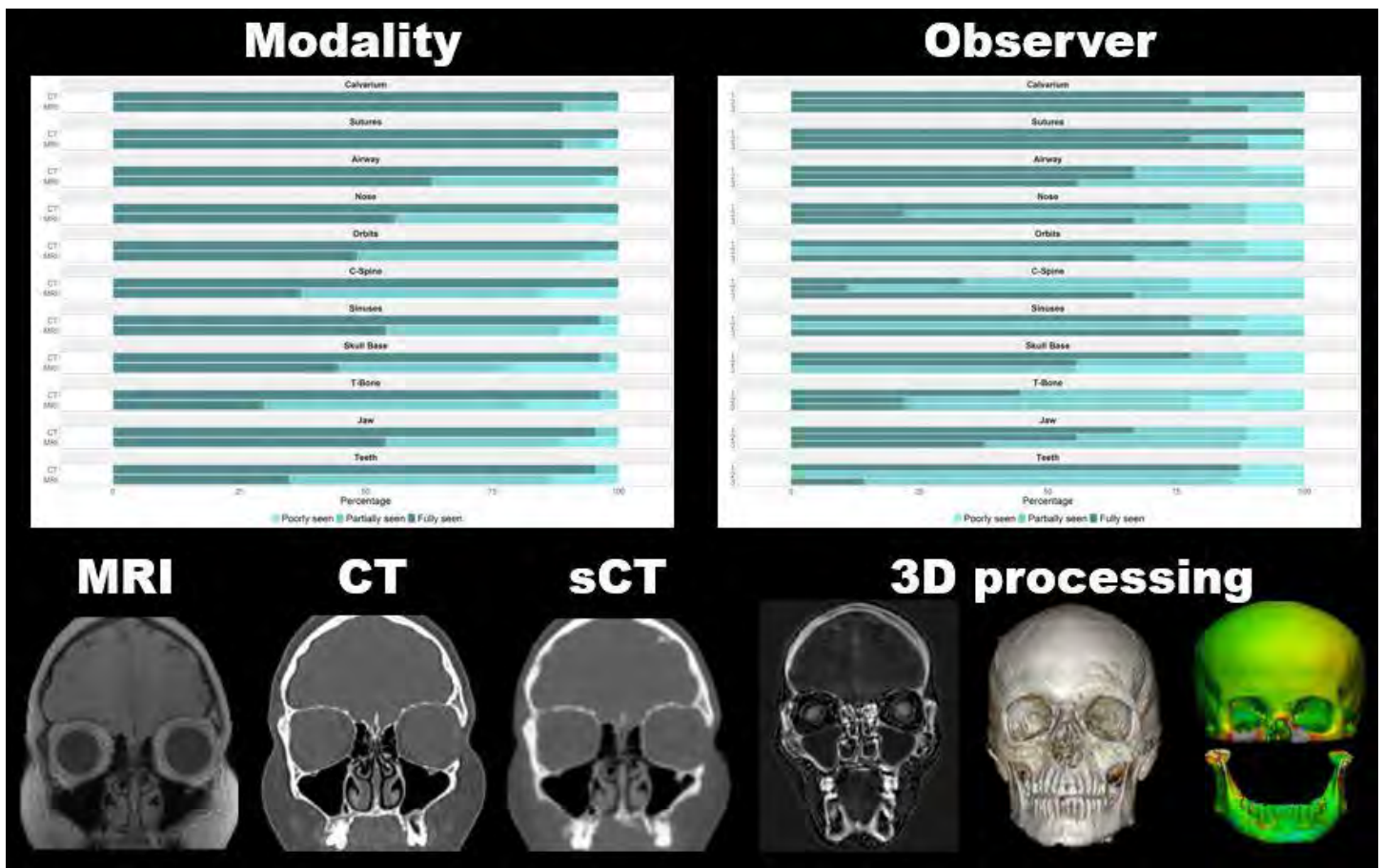
50 pediatric patients with a variety of brain, head, and neck pathologies requiring bone imaging were imaged using both conventional CT and ZTE MRI. CT and MRI examinations were co-registered using multiple-point affine transformation. 3-dimensional multiplanar reformats were generated in axial, coronal, and sagittal planes. Three board-certified pediatric neuroradiologists reviewed anonymized examinations and issued Likert scales for diagnostic visualization of prespecified landmarks. Diagnostic augmentation with 3D postprocessing and deep learning techniques for synthetic CT image generation were also implemented.

Results

ZTE MRI performance showed strong concordance with CT and high inter-observer consistency for evaluation of calvarium, sutures, and airway. Weaker correlations with greater inter-observer variability were noted for nose and paranasal sinuses, orbits, skull base and temporal bone, jaw and teeth, and cervical spine. Readers varied in diagnostic confidence using MRI, with areas of very thin bone and tissue interfaces producing the greatest interpretive dilemmas. During 3D processing, 95-98% of segmentable data points reached the surgical precision threshold of ± 2 mm in the majority of cases. MRI performance improved after excluding cases with major artifacts, including bulk motion and susceptibility. The implementation of deep learning techniques for synthetic CT image generation also improved reported ease of radiologist interpretation and 3D image postprocessing, although reference to raw image data was still necessary to ensure accuracy.

Conclusions

ZTE MRI shows promise as an alternative to CT for cortical bone imaging of the pediatric head and neck, particularly in the pediatric population for whom ionizing radiation exposure must be minimized. With appropriate clinical training, awareness of technical limitations and potential pitfalls, and the use of advanced postprocessing techniques, radiologists will be able to appropriately utilize and interpret ZTE MRI in clinical practice.



(Filename: TCT_800_ZTEresearch.JPG)

801

Comparing Zero-TE MRI and CT: Diagnostic, Synthetic, and 3D Image Evaluation

M Ho¹, S Bambach²

¹Nationwide Children's Hospital, Dublin, OH, ²Nationwide Children's Hospital, Columbus, OH

Purpose

To compare the diagnostic effectiveness of zero-TE (ZTE) MRI and CT for cortical bone imaging in the pediatric head and neck.

Materials and Methods

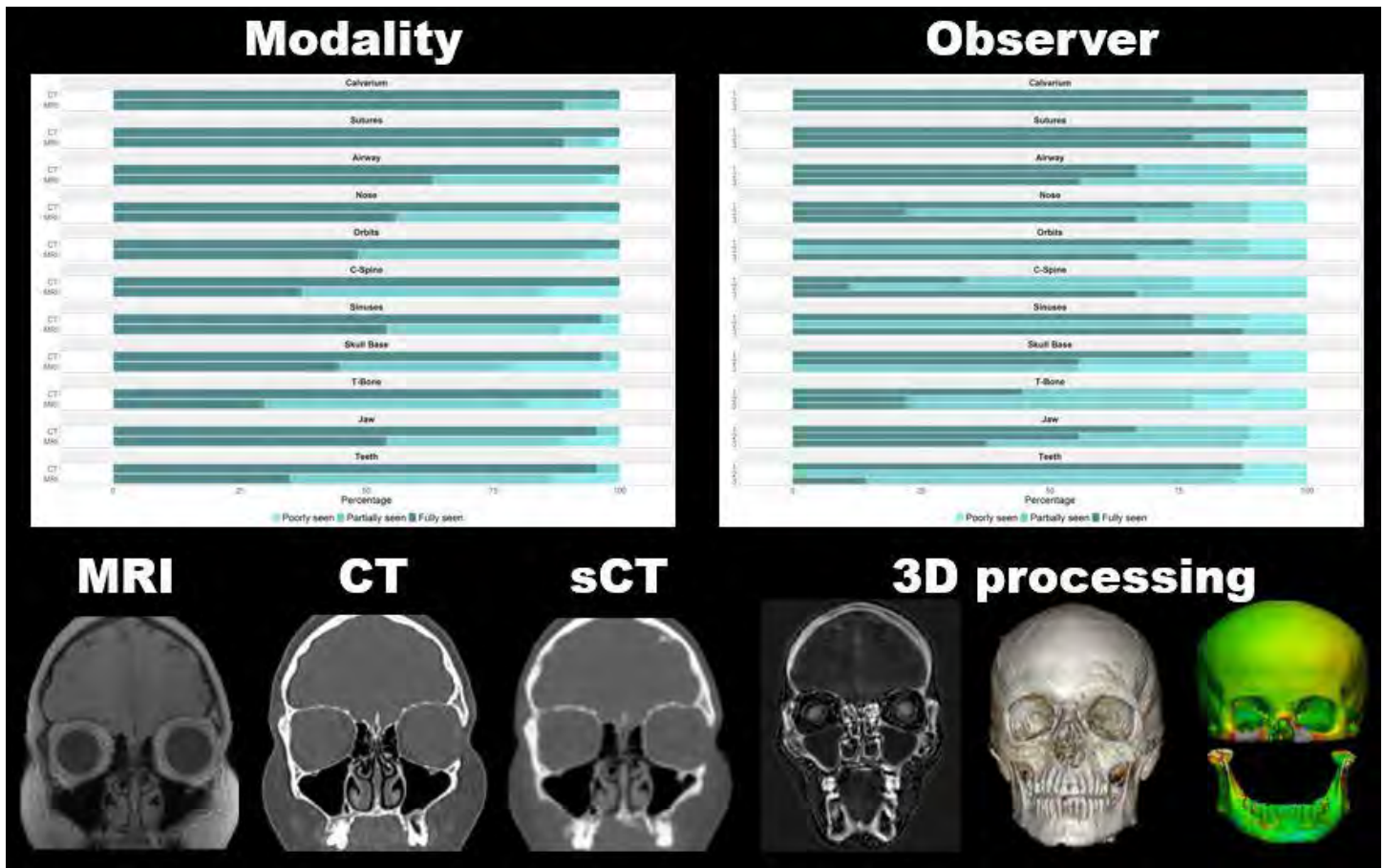
50 pediatric patients with a variety of brain, head, and neck pathologies requiring bone imaging were imaged using both conventional CT and ZTE MRI. CT and MRI examinations were co-registered using multiple-point affine transformation. 3-dimensional multiplanar reformats were generated in axial, coronal, and sagittal planes. Three board-certified pediatric neuroradiologists reviewed anonymized examinations and issued Likert scales for diagnostic visualization of prespecified landmarks. Diagnostic augmentation with 3D postprocessing and deep learning techniques for synthetic CT image generation were also implemented.

Results

ZTE MRI performance showed strong concordance with CT and high inter-observer consistency for evaluation of calvarium, sutures, and airway. Weaker correlations with greater inter-observer variability were noted for nose and paranasal sinuses, orbits, skull base and temporal bone, jaw and teeth, and cervical spine. Readers varied in diagnostic confidence using MRI, with areas of very thin bone and tissue interfaces producing the greatest interpretive dilemmas. During 3D processing, 95-98% of segmentable data points reached the surgical precision threshold of +/- 2 mm in the majority of cases. MRI performance improved after excluding cases with major artifacts, including bulk motion and susceptibility. The implementation of deep learning techniques for synthetic CT image generation also improved reported ease of radiologist interpretation and 3D image postprocessing, although reference to raw image data was still necessary to ensure accuracy.

Conclusions

ZTE MRI shows promise as an alternative to CT for cortical bone imaging of the pediatric head and neck, particularly in the pediatric population for whom ionizing radiation exposure must be minimized. With appropriate clinical training, awareness of technical limitations and potential pitfalls, and the use of advanced postprocessing techniques, radiologists will be able to appropriately utilize and interpret ZTE MRI in clinical practice.



(Filename: TCT_801_ZTEresearch.JPG)

919

Comparison of diffusion and susceptibility weighted MR imaging to differentiate primary CNS lymphoma from atypical glioblastoma: Correlation with major genomic biomarkers

K Ozturk¹, E Soylu², Z Cayci³

¹University of Minnesota, MINNEAPOLIS, MN, ²University of Minnesota Health, Minneapolis, MN, ³University of Minnesota, Minneapolis, MN

Purpose

We aimed to differentiate PCNSL from atypical GB without apparent necrosis using SWI along with DWI and to determine their relationship with major genomic alterations.

Materials and Methods

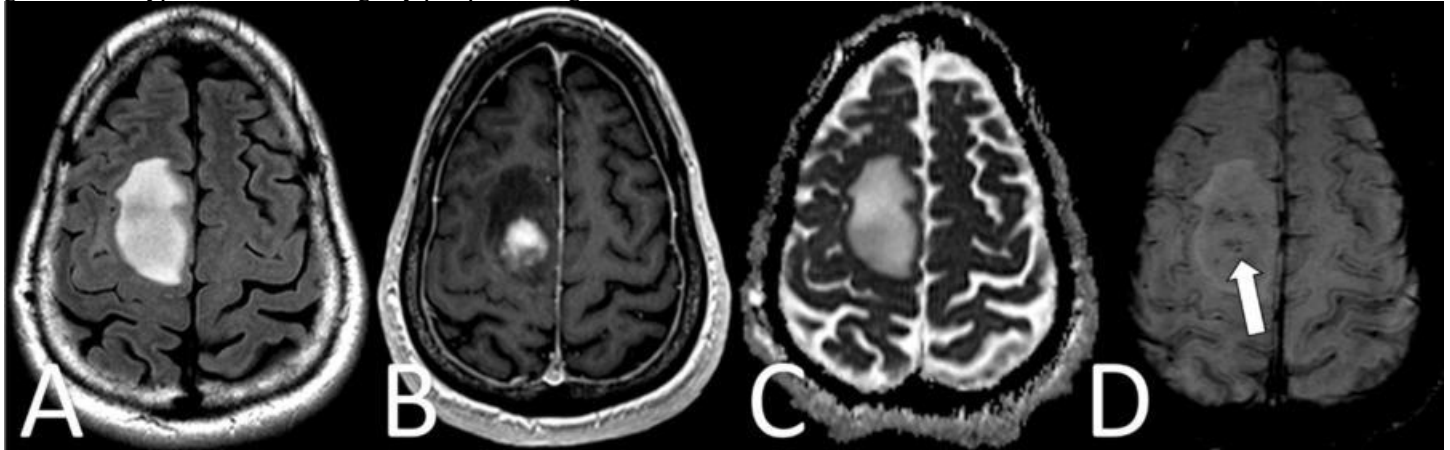
Thirty-one immuno-competent patients with PCNSL stratified by BCL2 and MYC rearrangement status, and 57 patients with atypical GB (solid enhancement with no visible necrosis) grouped according to IDH1 mutation status underwent 3.0-T MRI including DWI and SWI before treatment. ROI based analysis with ADC and SWI SI values of the lesions were normalized by dividing those of contralateral normal-appearing white matter (NAWM) and expressing the quotient as a ratio. The degree of intratumoral susceptibility signal intensity (ITSS) was determined on SWI. The independent-samples t-test and Kruskal Wallis test were used to compare parameters. The diagnostic ability of each parameter and their optimal combination for differentiating between PCNSL and GB according to their genomic alterations was evaluated by logistic regression analysis and receiver operating characteristic.

Results

rADCmean, rADCmin and rSWI revealed the highest area under the curve (AUC) on ROC analysis and were best discriminators of GB and PCNSL according to the major genomic alterations. PCNSL with rearrangement of both MYC and BCL2 (n=7) (mean rADCmean: 0.87 ± 0.06 , rADCmin: 0.72 ± 0.08) demonstrated significantly lower rADCmean, and rADCmin compared to other PCNSLs (n=24) (mean rADCmean: 1.19 ± 0.18 , rADCmin: 1.03 ± 0.17 ; $p < 0.001$) and GBs ($p < 0.001$). GB without IDH1 mutation (n=44) (mean rSWI value: 0.95 ± 0.15) demonstrated significantly lower rSWI value compared to GB with IDH1 mutation (n=13) (mean rSWI value: 1.13 ± 0.09 ; $p < 0.001$) and PCNSL ($p < 0.001$). Combining rADCmean and rSWI parameters distinguished GB with IDH1 mutation (AUC: 0.985) with sensitivity and specificity of 94.3 and 100% respectively; and PCNSL with rearrangement of both MYC and BCL2 (AUC: 0.982) with sensitivity and specificity of 100% and 95.4%, respectively.

Conclusions

Combined analysis of SWI and DWI could differentiate atypical GB from PCNSL in relation to their major genomic subtypes. These results support an integration of advanced MRI techniques to enable reliable differentiation of PCNSL from atypical GB stratified by genomic subtypes without causing any postprocessing work.



(Filename: TCT_919_Picture1.jpg)

1328

Comparison of gray matter and white matter integrity between multiple sclerosis and neuromyelitis optica spectrum disorders using cortical thickness and diffusion tensor imaging

I Hwang¹, S Kim², H Kwon², S Kim³, J Lee², J Kim¹, J Lee¹, R Yoo⁴, R Kang¹, T YUN¹, S Hong Choi¹, C Sohn¹

¹Department of Radiology, Seoul National University Hospital, Seoul, Korea, ²Department of Biomedical Engineering, Hanyang University, Seoul, Korea, ³Department of Neurology, Seoul National University Hospital, Seoul, Korea, ⁴Seoul National University Hospital, Seoul, Seoul

Purpose

To investigate the changes in cortical thickness and diffusion tensor imaging (DTI) parameters among multiple sclerosis (MS), neuromyelitis optica spectrum disorder (NMOSD), and control patients that reflect gray matter and white matter integrity, respectively.

Materials and Methods

This study prospectively enrolled MS (n = 25) and NMOSD (n = 20) patients between April 2014 and April 2020 in a single institution. The diseased control group (n = 21) also enrolled with patients visited the neurology clinic who were evaluated for the neurologic disease but not diagnosed with MS or NMOSD. The patients underwent three-dimensional T1-weighted images and DTIs using a 3-T MR scanner. We quantitatively evaluated cortical thickness in Montreal Neurological Institute (MNI) 152 space. The fractional anisotropy (FA) were also quantitatively analyzed using tract-based spatial statistics (TBSS) in normal-appearing white matters with masking of white matter lesions by manual segmentation. The group comparison analyses were performed for overall and anatomical region-of-interest (ROI) based cortical thickness, and DTI metrics by a non-parametric permutation test, with the age and sex as covariates. The significance level was corrected P-values less than 0.05.

Results

The mean ages in MS, NMOSD, and the control groups were 34 years, 47 years, and 41 years, respectively. The overall mean cortical thickness was significantly different among the three groups (P = .013), and the post-hoc test revealed MS had only significantly decreased cortical thickness compared to control (P = .001). By the anatomical ROI-based comparison, the cortical thickness was significantly decreased in the right lingual gyrus, right fusiform gyrus, and left inferior frontal gyrus opercular part in MS compared to the control group. However, there were no significantly different cortical areas between NMOSD and the control group. By the DTI TBSS analysis, there were significantly reduced FA areas in MS compared to the control group involving the corpus callosum, bilateral anterior and posterior coronae radiatae, bilateral posterior thalamic radiations, bilateral sagittal strata, and bilateral superior longitudinal fasciculi (minimum P = .002). However, there was no significant difference in areas between NMOSD and control.

Conclusions

There was significant cortical thinning and white matter damage in MS, while those were not evident in NMOSD, compared to the diseased control group.

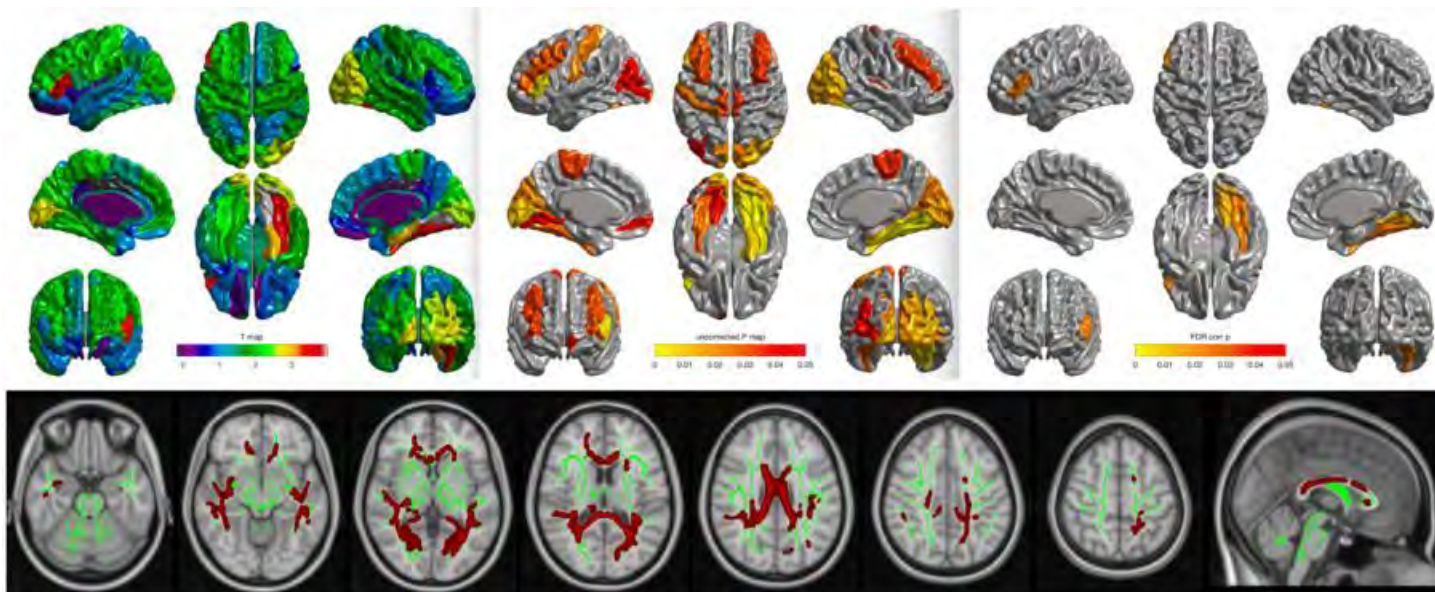


Figure. Cortical thickness (upper row: T, uncorrected p, and corrected p maps) and TBSS results (lower row) comparing between MS and the control groups.

(Filename: TCT_1328_ASNR_figure.jpg)

1224

Comparison of hypometabolism on 18F-FDG PET in left and right temporal lobe epilepsy based on a probabilistic brain atlas

HUETANI¹, H Tatekawa¹, A Hagiwara¹, I Ueda¹, B Ellingson¹, N Salamon²

¹University of California, Los Angeles, Los Angeles, CA, ²University of California Los Angeles, Los Angeles, CA

Purpose

18F-FDG PET is a useful diagnostic tool in patients with temporal lobe epilepsy (TLE). Little is known about the left-right differences of the extent of hypometabolism and the factors affecting it.1 This study identified differences in the extent of hypometabolism on 18F-FDG PET between left and right TLE patients using a probabilistic brain atlas. The relationship between the extent of hypometabolism and clinical and MRI findings was evaluated.

Materials and Methods

A total of 119 consecutive patients with unilateral pharmacoresistant TLE who underwent video-electroencephalography, MRI, and 18F-FDG PET were retrospectively included. Abnormal MRI findings and hypometabolism were qualitatively graded by two neuroradiologists. All hypometabolic regions of interest segmented by a neuroradiologist were summed to create a voxel-wise probability map.2 The stereospecific frequency of hypometabolism was analyzed statistically using the side of TLE, patient's characteristics, and MRI abnormalities.

Results

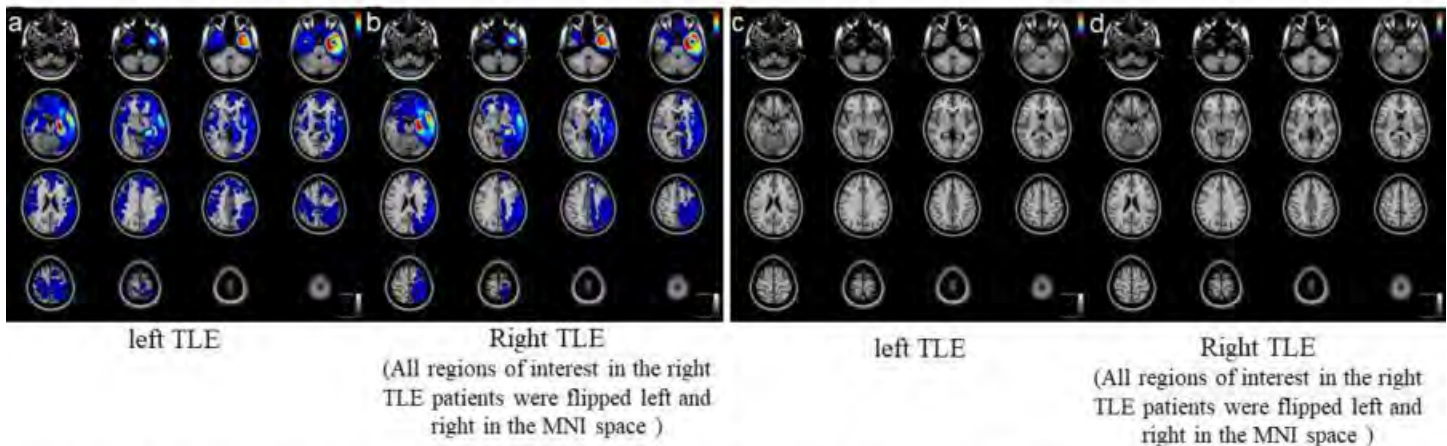
Left and right TLE included 61 and 58 patients, respectively. For visual assessment, hippocampal atrophy and hyperintensity were significantly more apparent in left than in right TLE ($P = .039$ and $.029$). As for 18F-FDG PET, hypometabolism in the contralateral hemisphere was significantly more frequent in left than right TLE ($P = .015$). A voxel-wise statistical brain atlas illustrated significant clusters occurring at a high frequency mainly in the bilateral insula, ipsilateral medial frontal lobe, and contralateral temporal pole in left TLE, and in the ipsilateral lateral temporal lobe, orbito-frontal lobe, and thalamus in right TLE. The extent of hypometabolism in the contralateral hemisphere was associated with elderly age at seizure and with history of febrile seizure in left TLE, and higher seizure frequency in right TLE. The extent of hypometabolism in the ipsilateral extratemporal lobe was related to apparent hippocampal atrophy and T2 weighted hyperintensity in both sides of TLE.

Conclusions

A probabilistic brain atlas demonstrated that hypometabolism was more extensive in the left TLE than in the right. Elderly age at seizure onset, history of febrile seizure, and higher seizure frequency were associated with extensive hypometabolism, and its effects differed according to the TLE side.

Voxel-wise frequency of hypometabolism on ¹⁸F-FDG PET

ADIFFI statistical analysis of hypometabolism on ¹⁸F-FDG PET



Voxel-wise brain atlas showed almost all cases had hypometabolism in the ipsilateral anteromesial temporal lobe and parahippocampal gyrus in both sides on TLE. Left TLE groups (a) had a larger extent of hypometabolism to the contralateral hemisphere than right TLE (b). ADIFFI statistical analysis illustrated significant clusters occurring at a high frequency in the ipsilateral insula, medial temporal lobe, superior temporal gyrus, medial frontal gyrus, thalamus, contralateral temporal pole, and insula in left TLE (c), and in the ipsilateral lateral temporal lobe, posterior insula, orbital gyrus, inferior frontal gyrus, and thalamus in right TLE (d).

TLE, temporal lobe epilepsy, ADIFFI, analysis of differential involvement, MNI, Montreal Neurological Institute

(Filename: TCT_1224_1.JPG)

239

Comparison of Machine Learning Classifiers to Predict Patient Survival and Genetics of GBM: Towards a Standardized Model for Clinical Implementation

L Pasquini¹, A Di Napoli², A Napolitano³, M Lucignani⁴, E Tagliente⁴, F Dellepiane⁵, A Romano⁶, A Holodny⁷, a bozzao⁵
¹Memorial Sloan Kettering Cancer Center, New York, NY, ²Sant'Andrea Hospital, La Sapienza University, Rome, Italy, ³Bambino Gesù Children's Hospital, IRCCS, Rome, Italy, ⁴Bambino Gesù Children's Hospital, IRCCS, Rome, Italy, ⁵Sant'Andrea Hospital, La Sapienza University, Rome, Italy, ⁶Sant'Andrea Hospital, La Sapienza University, Rome, ID, ⁷MEMORIAL SLOAN KETTERING CANCER CENTER, NEW YORK, NY

Purpose

Glioblastoma (GBM) is the most frequent and lethal primary malignant tumor for adults, with poor overall survival (OS) despite optimal treatment. Radiomic models have been shown to outperform clinical data alone for outcome prediction in GBM. However, clinical implementation is limited by lack of parameters standardization. We aimed to compare nine machine learning classifiers, with different optimization parameters, to predict OS, isocitrate dehydrogenase (IDH) mutation, O-6-methylguanine-DNA-methyltransferase (MGMT) promoter methylation, epidermal growth factor receptor (EGFR) VII amplification and Ki-67 expression in GBM patients, based on radiomic features from MRI data.

Materials and Methods

156 adult patients with pathologic diagnosis of GBM were included. Three tumoral regions were analyzed: contrast-enhancing tumor (CET), necrosis (NEC) and non-enhancing tumor (NET). Radiomic features were extracted with Pyradiomics and selected through Boruta algorithm. A Grid Search algorithm was applied when computing 4 times K-fold cross validation (K=10) to get the highest mean and lowest spread of accuracy. Model performances were assessed in terms of AUC-ROC. Nine ML classifiers were compared: AdaBoost (AB), Extreme Gradient Boosting (xGB), Gradient Boosting (GB), Decision Tree (DT) and Random Forest (RF), Logistic Regressor (LR), two Stacking classifiers (ST, ST_ABC), and KNeighbors (KN).

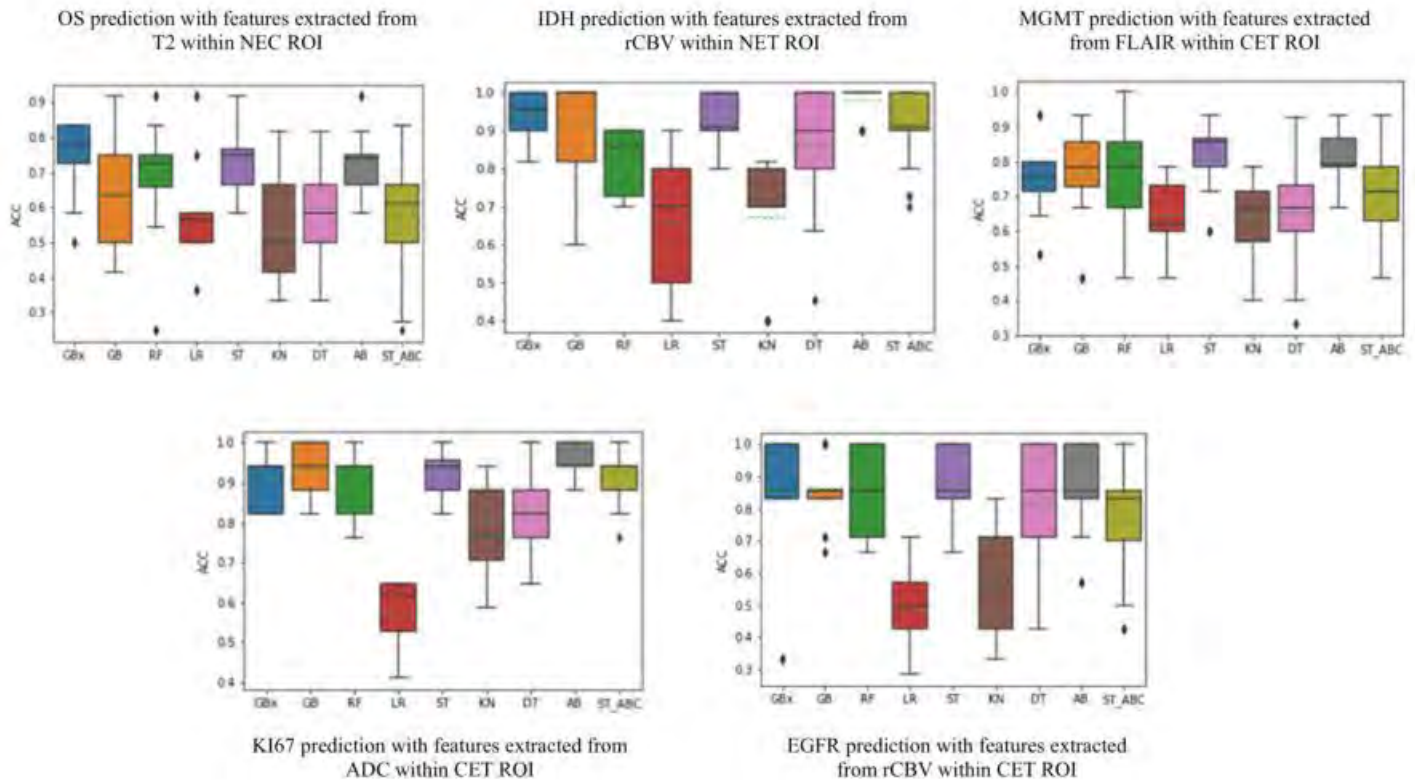
Results

xGB classifier obtained the best accuracy for OS with features extracted from NEC on T2 images (74.5%) and NET on ADC images (73.3%). AB classifier obtained the best accuracy for IDH mutation with rCBV-derived first order features (median, skewness) from NET (98%), MGMT methylation with FLAIR-derived texture features from CET (81.5%), Ki-67 expression with texture features extracted from CET on ADC images (95%), and EGFR amplification with T2 features on CET (93%). ST classifier also achieved good performance for prediction of EGFR amplification with rCBV-derived features from CET (88.4%)

Conclusions

xGB and AB classifiers showed the best performance across tasks. MRI features of peritumoral tissue were highly predictive of

patient survival in GBM, possibly representing a non-invasive tool to stratify patients for peritumoral resection radicality. Selected features from our analysis shed light on possible correlations between MR and tumor histology: 1) ki-67 expression with cellularity on ADC; 2) IDH mutation and EGFR amplification with neovascularization on rCBV; 3) MGMT methylation with tumor heterogeneity.



(Filename: TCT_239_figure.jpg)

1113

Comparison of Publically Available Top-Ranked Machine Learning Algorithms for Brain Tumor Segmentation on External Dataset

E Lotan¹, B Zhang², S Dogra³, D Wang⁴, Y Lui⁴

¹New York University School of Medicine, New York, NY, ²NYU Langone Medical Center, New York, NY, ³NYU Grossman School of Medicine, New York, NY, ⁴NYU Langone Health, New York, NY

Purpose

The MICCAI Brain Tumor Segmentation challenge (BraTS) has been running since 2012, identifying the best tools for volumetric segmentation of gliomas [1]. It is well known that due to differences in imaging and post-processing protocols, models may perform differently on real-life data than they do in challenges. Here, we compare 3 publically available top-ranked algorithms from the BraTS 2017 and 2018 challenges using an external dataset.

Materials and Methods

The best three top-ranked BraTS models were selected based on the availability of source code: (#1) a cascaded anisotropic convolutional neural network (CACNN) [2]; (#2) autoencoder regularization [3]; and (#3) Sequential 3D U-Nets [4]; these works are attributed originally to research groups from UCL, NVIDIA and MGH, respectively. We randomly split 335 cases from the 2019 BraTS open-access repository between training and validation datasets using 80:20 ratio. External dataset was composed of 40 preoperative gliomas unique cases manually annotated by two consensus review according to the BraTS protocol [1]: (1) enhancing tumor; (2) necrotic tumor-core; and (3) whole tumor ((1)+(2)+peritumoral edema). The whole external dataset was used for model testing. Mean dice scores served as our evaluation metric, and all cases were visually inspected.

Results

Model #1 outperformed the other models and was comparable to its published dice-scores in BraTS 2017 (Table 1). Figure 1 demonstrates a representative output of the models on one of the validation cases. Specific model hyperparameters were provided only by the authors of model (1). Model hyperparameters were not available for Models #2 and #3 and the performance was uneven, qualitatively and quantitatively, with lower dice scores computed here compared with their previously published results.

Conclusions

Implementation of brain tumor segmentation available source code is feasible. Despite, differences in imaging and post-processing protocol, reproducible performance can be achieved though is likely to depend on good hyperparameter optimization. To approach generalization across datasets, such optimization data need also be shared to public code repositories in order to facilitate cross-institutional adoption of successful deep learning-based tumor segmentation models.

Table 1

	Sub-regions	Model 1 (Wang, 2017) [*]	Model 2 (Myronenko, 2018)	Model 3 (Beers, 2017)
Dice Score on BraTS Test Data	Whole tumor	0.87	0.88	0.80
	Enhancing tumor	0.78	0.77	0.70
	Tumor core	0.77	0.82	–
Dice Score on External Validation Dataset	Whole tumor	0.88 ± 0.06	0.84 ± 0.05	0.56 ± 0.12
	Enhancing tumor	0.75 ± 0.27	0.72 ± 0.32	0.41 ± 0.16
	Tumor core	0.82 ± 0.16	0.78 ± 0.18	–
Inference speed on GPU		~ 90s	~50s	~70s

^{*} Hyperparameter optimization provided by the authors (Wang, 2017)

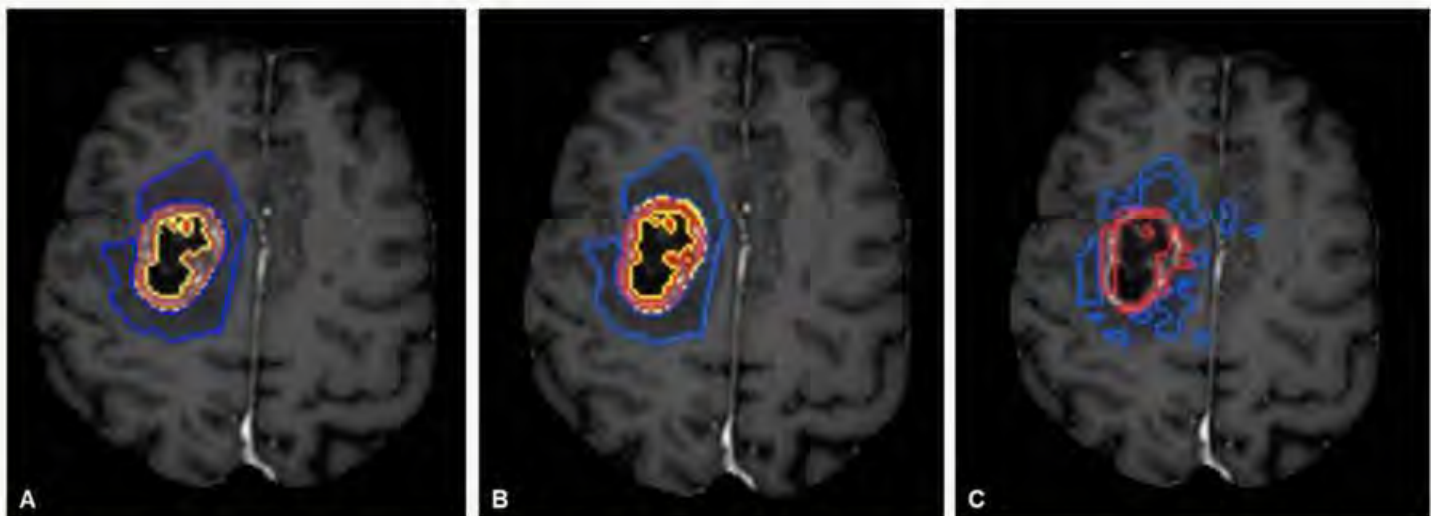


Fig. 1. Glioma sub-regions overlaying T1c axial image using : (A) model #1 (Wang, 2017); (B) model #2 (Myronenko, 2018); and (C) model #3 (Beers, 2017). The whole tumor is automatically segmented to peritumoral edema (blue), enhancing tumor (red) and necrotic core (yellow).

(Filename: TCT_1113_Comparison_Fig1_300dpi.jpg)

1037

Complications Secondary to Intradiscal Injections of Oxygen-Ozone Mixture. A Comprehensive Review of the Literature.

G GIANNATEMPO¹

¹SCIENTIFIC INSTITUTE "CASA SOLLIEVO DELLA SOFFERENZA", SAN GIOVANNI ROTONDO, FG

Purpose

Herniated disc is the commonest cause of back pain and/or sciatica and when patients fail to respond to conservative therapy, intradiscal injection of oxygen-ozone (O₂-O₃) mixture may be indicated, with a reported success rate ranging from 70% to 82% in long term follow up (12 months). However, controversy persists regarding the safety of the procedure.

Materials and Methods

To review all complications secondary to lumbar intradiscal ozone injection reported in literature.

Results

A comprehensive literature search was conducted using electronic database (PubMed) searching the keywords "ozone" and one of the following: "intradiscal", "lumbar", "disc", "disk", "herniated", "diskolysis", "nucleolysis", "discectomy", from 1980 through October 2020. Any studies that did not perform lumbar intradiscal injections or did multiple paravertebral injections were excluded.

Conclusions

Articles were divided in two groups, including a) complications reported in randomized trials and b) complications published as isolated case reports. Review of studies on large cohort of patients showed no complications or minor and transient adverse events, such as transitory paresthesia. Isolated case reports dealing with complications following intradiscal injection of ozone include: a case of transient cortical blindness, a case of transient vitreous-retinal haemorrhages, a case of nerve root injury with paresthesia and hypoesthesia, three cases of thunderclap headache related to pneumocephalus caused by accidental puncture of the thecal sac, a case of vertebro-basilar stroke and a case of paradoxical embolism causing anterior spinal cord syndrome and acute myocardial infarction. Regarding infections, only two cases have been reported: a case of L5-S1 discitis due to *Achromobacter xylosoxidans* and a fatal case of fulminating septicemia due to *E. coli*. Among long-term complications, a study on 23 patients surgically treated with microdiscectomy 12-24 months after ozone therapy, reported the presence of hard adhesions between soft tissues and bony structures, and between the nerve root and the dural sac. Conclusion. Intradiscal injection of O2-O3 mixture is safe and complications are very rare. It represents a safe, minimally invasive, well tolerated and low-cost procedure.

708

Comprehensive Analysis of Driver Mutation Profile in a Cohort of Lung Cancer Patients Using Targeted Gene Panel Analysis

M Kazarian¹, J Cui², A Mahajan², M Aboian³

¹Horace Mann School, Greenwich, CT, ²Yale University, New Haven, CT, ³Yale University, Woodbridge, CT

Purpose

Approximately 228,820 people are diagnosed annually with lung cancer diagnosis and 135,720 die from their disease. EGFR and KRAS targeted therapies have been shown to significantly improve treatment of non-small cell lung cancer (NSCLC), but they don't apply to the majority of patients. There's a critical need to characterize the molecular signature of patients with lung cancer and to define the proportion of patients eligible for novel targeted therapies.

Materials and Methods

Internal Review Board approval was obtained to retrospectively extract data from tertiary hospital tumor registry on all individuals diagnosed with lung cancer from 2011 to 2017, which included 4,159 patients screened. Data collected included patient demographics, oncomine results (50 and 150 gene panel), histology, and biopsy location in the final 2,203 patients. Python and visual basic code were used to generate the database.

Results

A total of 194 individual gene mutations were identified in this cohort, with 90.3% of patients having no detectable mutated genes. In this cohort, 49% of the patients had biopsy from the primary lung tumor, 8.5% from brain metastasis, 23.1% from lymph nodes, 6.6% from bone, including spine, and 5.7% from liver. Brain metastasis molecular signature was different from other biopsy sites and primary lung mass. Frequent driver mutations within brain metastases were TP53, NF1, KRAS, ATM, and ATRX. 10 out of 18 (55.5%) patients with brain metastases had 5 or more gene mutations, which has been correlated as a predictor of favorable response to immune checkpoint inhibitor therapy. TP53 mutations were commonly the sole mutation in the analyzed tumor sample, suggesting that it is sufficient for tumorigenesis. We found that 11 of the 137 patients with a TP53 mutation (8.03%) also had an EGFR mutation, which was only 8th most common in our cohort (0.82%). Among the patients with brain metastases, only one patient had EGFR mutation and it occurred in the setting with TP53 and PIK3CA mutation.

Conclusions

We present a comprehensive analysis of the molecular signature of lung cancer from a tertiary referral institution, which demonstrates that 90% of patients do not have a targetable mutation that corresponds to favorable treatment with EGFR targeted therapy, KRAS targeted therapy, and immune checkpoint inhibitor therapy. Lesions metastatic to the brain had different molecular signature from primary lung cancer and demonstrated hypermutated phenotype, which would be more susceptible to ICI therapy.

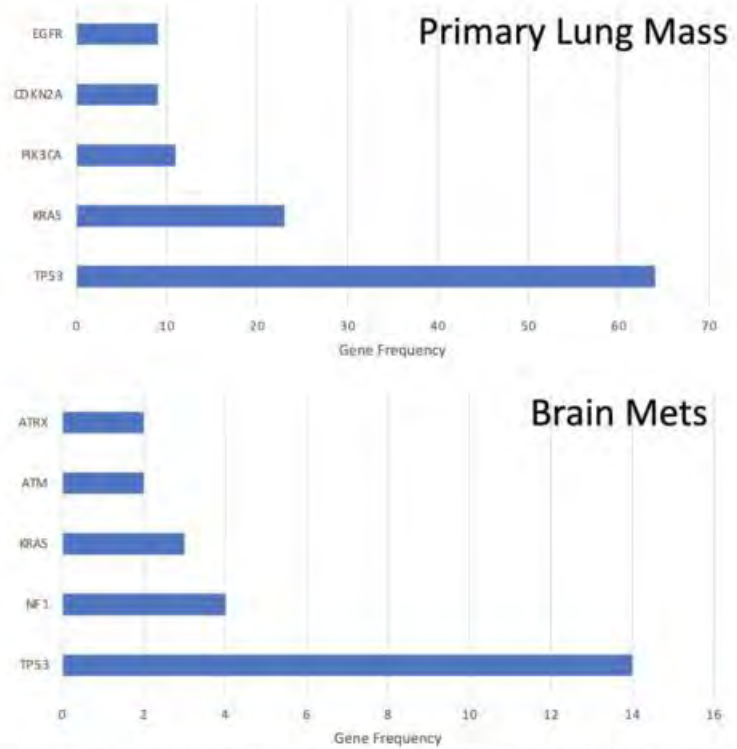
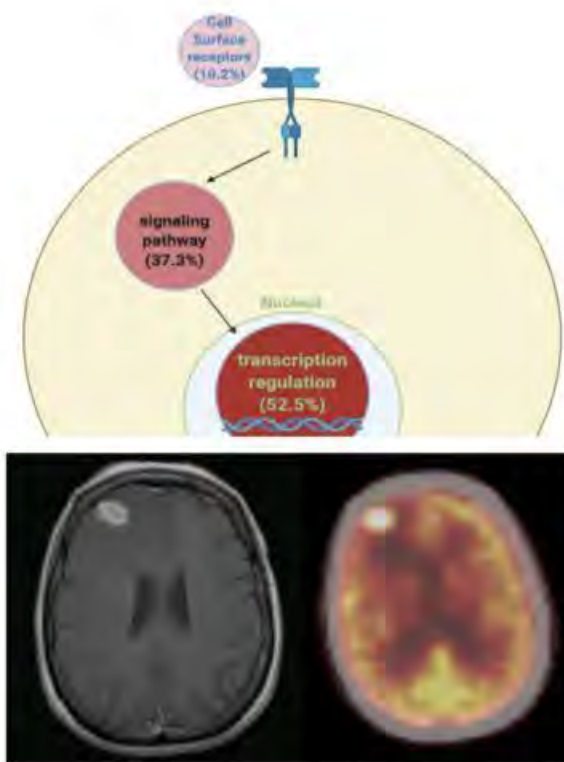


Figure: Molecular characteristics of lung cancer based on location of biopsy. Brain metastases demonstrate different distribution of mutations than primary lung mass. Majority of mutations occur in transcription regulation processes in primary and metastatic lesions.

(Filename: TCT_708_ASNR2021Figure2.jpg)

1281

Congenital Nasal Pyriform Aperture Stenosis: Evidence of Premature Midline Palatal Suture Fusion

D Mirsky¹, J Prager², T Wine²

¹Children's Hospital Colorado, Aurora, CO, ²University of Colorado School of Medicine, Aurora, CO

Purpose

Various etiologies have been theorized for the development of congenital nasal pyriform aperture stenosis (CNPAS). Imaging may shed light on this, possibly implicating abnormal fusion of the midline palatal suture and deficient lateral growth of the midface in affected neonates.

Materials and Methods

A single-center, retrospective study was performed at a tertiary care pediatric hospital involving children between 0 and 90 days of life. Maxillofacial computed tomography (CT) scans of children were reviewed. Abnormality of the palatal suture and midface transverse dimensions were measured and analyzed in patients with and without CNPAS.

Results

A total of 109 patients between 0 and 90 days of life had maxillofacial CT scans. Thirteen patients were classified as having CNPAS, 27 patients had normal scans (control group), and 69 patients were excluded due to the presence of other craniofacial anomalies. All patients with CNPAS had evidence of abnormal fusion of the midline palatal suture. Zero patients without CNPAS had a midline palatal suture abnormality. The mean width of the pyriform aperture was 5.7 mm (SD 1.7) in the CNPAS group and 13.1 mm (SD2.7) in the control group ($p < 0.0001$). The mean distance between the superior portions of the nasolacrimal ducts (NLD) was 9.1 mm (SD 2.1) in the CNPAS group, while the mean of the normal group was 13.4 mm (SD2.2), ($p < 0.0001$).

Conclusions

Patients with CNPAS have abnormal fusion of the midline palatal suture and exhibit lateral growth restriction of the midface. This may implicate synostosis of the midline palatal suture and abnormal midface growth.



(Filename: TCT_1281_Normalvsabnormal.jpg)

953

Conventional and Advanced Imaging Attributes of H3K27M mutation in Diffuse Midline Gliomas

R Chauhan¹, N Kathrani¹, K Kulanthaivelu², M Bhat¹, J Saini³, V Santosh¹, N Sadashiva¹

¹National Institute of Mental Health and Neurosciences, Bangalore, Karnataka, ²National Institute of Mental Health and Neurosciences, Bangalore, Karnataka, ³NATIONAL INSTITUTE OF MENTAL HEALTH & NEURO SCIENCES, BANGALORE, India

Purpose

Diffuse midline glioma (DMG), H3K27M-mutant is a newly described distinct class of clinically aggressive tumors categorized by 2016 World Health Organization classification of CNS tumors as grade IV irrespective of their histologic morphology. They carry an unfavorable outcome as compared to the wild-type (WT) counterparts. As the occurrence of H3K27M mutation may foresee an aggressive clinical course of tumor while concurrently giving a prospect for new targeted treatment methods, presence of these molecular alterations should be eagerly sought after. Our study aimed at evaluating the conventional (cMRI) and advanced MRI features that might aid in differentiating the H3 K27M-mutant DMGs from non-mutant/WT DMGs.

Materials and Methods

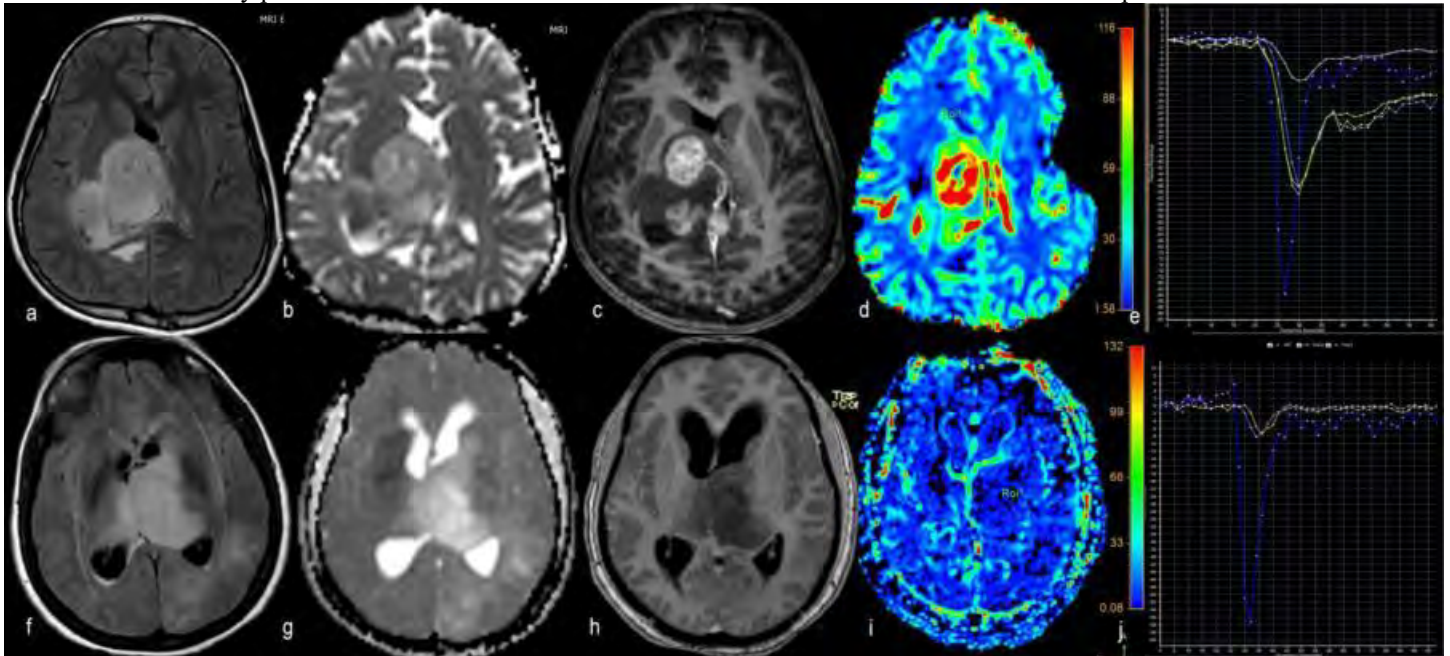
cMRI, DWI and DSC MR perfusion features of 123 patients who satisfied the inclusion criteria were evaluated after Institutional ethics committee approval. MRI was performed on 1.5 or 3.0 Tesla Scanners using 32 channel head coil. cMRI features based on VASARI (Visually AcceSable Rembrandt Images), Intra Tumoral Susceptibility Signal (ITSS) score, DWI (min ADC, peritumoral ADC, normalized tumoral and peritumoral ADC and fractional anisotropy (FA)) and DSC MRP (rCBV, rCBF, normalized rCBV, normalized rCBF, uncorrected rCBV, normalized uncorrected CBV, corrected CBV and K2) were assessed and compared between the groups. Statistical analysis was done using R software. $P < 0.05$ was taken as level of statistical significance.

Results

61 patients had H3K27M mutated gliomas while 62 patients had WT gliomas. Mutated DMG patients were significantly younger to WT group patients. On intergroup analysis, 6 of 28 cMRI features evaluated showed significant difference between the groups. These were enhancement quality ($P=0.032$), enhancing margin thickness ($P=0.05$), edema proportion ($P=0.002$), definition of non-contrast enhancing tumor margin ($P=0.001$), cortical invasion ($P=0.037$) & exophytic component ($P=0.013$). Of various diffusion parameters, peritumoral (PT)ADC and normalized PTADC were significantly higher in WT group ($P=0.033$ and 0.040). For thalamic gliomas, tumor min ADC was significantly lower in mutant DMGs ($P=0.042$). Among perfusion parameters, rCBV ($P=0.018$), rCBF ($P=0.017$) & normalized uncorrected rCBV ($P=0.019$) were significantly higher in the mutant group (Fig1a-e; WT-Fig1f-j). Subgroup analysis of thalamic, brainstem, pediatric and adult DMGs was also done.

Conclusions

MRI can noninvasively predict H3K27M mutation in DMGs based on various cMRI and advanced MRI parameters.



(Filename: TCT_953_Fig1.jpg)

160

Convolutional Neural Network Driven Automated Fazekas Scoring on Computed Tomography Head Scans

G Singh¹, S Kapse², C Lui¹, R Gattu¹, B Devanabanda¹, J Matthews¹, V Spektor³, P Prasanna⁴

¹Newark Beth Israel Medical Center, Newark, NJ, ²Indian Institute of Technology, Mumbai, NJ, ³Columbia University, New York, NY, ⁴Stony Brook University, Stony Brook, NY

Purpose

White Matter Lesion (WML) severity is a risk factor of hemorrhage and a potential predictor of clinical outcome after ischemic stroke. CT is the imaging modality of choice in acute stroke and trauma population. However, assessment of WML on CT is clinically challenging due to less distinctiveness of WM hypodensities (WMHs) compared to background WM. This further leads to inter-reader variability in WML grading on CT images. We present and evaluate a convolutional neural network for automated Fazekas scale grading on CT images.

Materials and Methods

CT head scans of 218 hypertensive patients were retrospectively acquired and were graded by 2 neuroradiologists R1, R2 with 19 and 11 years of experience and 1 fourth year radiology resident based on the Fazekas scoring (FS) system into four groups (FS0, FS1, FS2, FS3). Two 4-point scales were used for assessing periventricular lesions and deep WMHs (0, absence; 1, cap of pencil-thin PVH or punctate focal deep WMH; 2, smooth halo PVH or early confluence of focal deep WMH; 3, irregular PVH extending into the deep white matter or large confluent areas of deep WMH). Final score was given as an average of PV and deep WMHs. Highest Fazekas

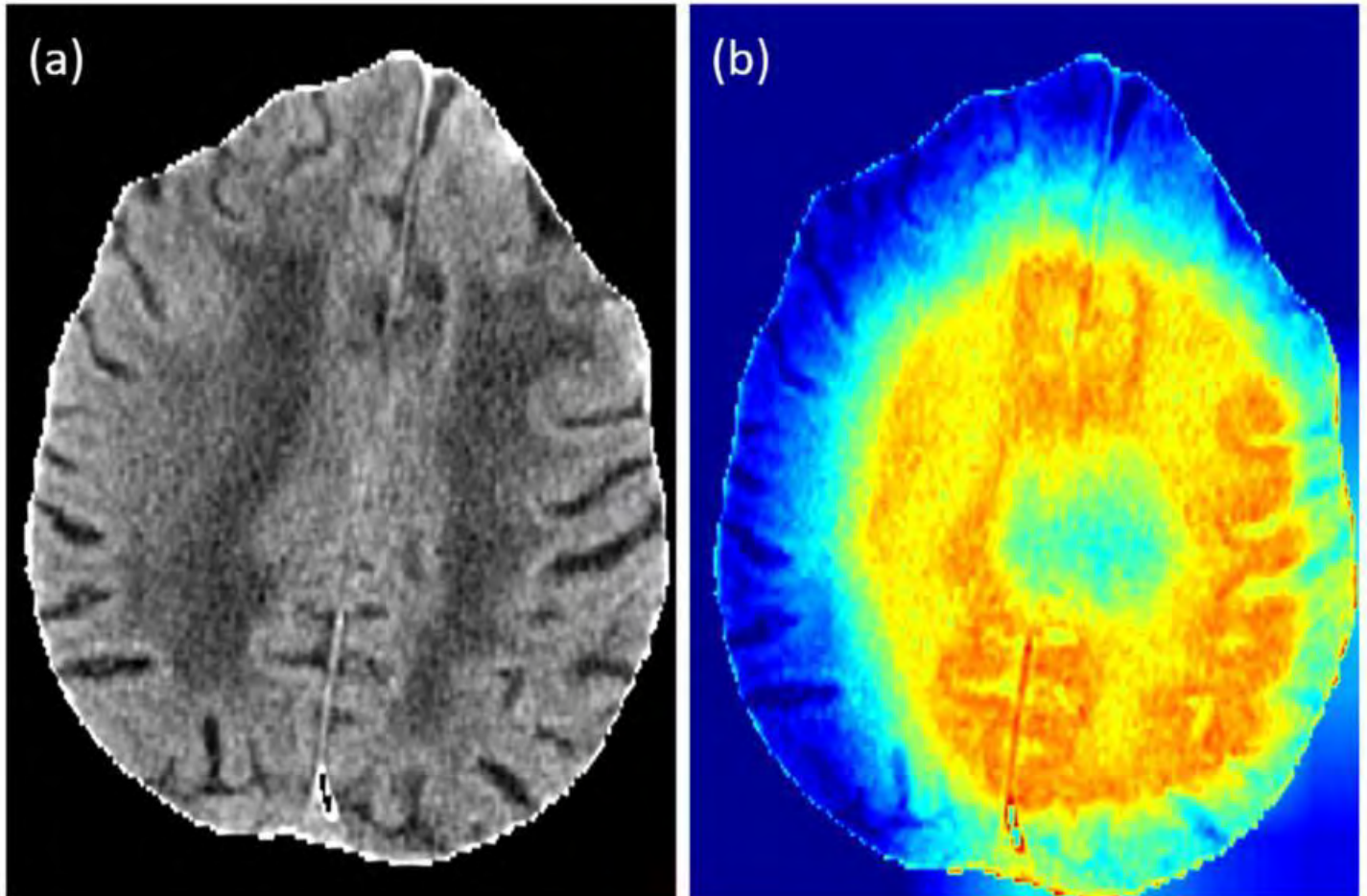
score was used as the ground truth (50 FS0, 103 FS1, 52 FS2, 13 FS3). After automatic brain extraction, three binary classifiers, M1, M2, and M3, were trained using a pretrained ResNet34 architecture to distinguish FS0 vs FS1, FS1 vs FS2, and FS2 vs FS3. The train/validation splits for the different FS groups were 35/15, 72/31, 37/15 and 10/3, respectively. A majority voting scheme was used to aggregate slice-level to patient-level decisions. Subsequently, we visualized the network activations on a spatial map.

Results

The accuracies for M1 was found to be 0.73 for FS0 and 0.80 for FS1. For M2, the accuracies were 0.58 for FS1 and 0.40 for FS2. For M3, the accuracies were 0.8 and 1 for FS2 and FS3, respectively. While M1 and M3 yielded moderate agreement with R1 (kappa >0.5), the model M2 yielded no agreement.

Conclusions

With a limited training set, the presented method was able to distinguish reliably between the two lower and the two higher Fazekas scales.



(Filename: TCT_160_Figure1.jpg)

910

Correlation between dynamic susceptibility contrast-enhanced perfusion MRI and genomic alterations in glioblastoma

K Ozturk¹, E Soylu², Z Cayci³

¹University of Minnesota, MINNEAPOLIS, MN, ²University of Minnesota Health, Minneapolis, MN, ³University of Minnesota, Minneapolis, MN

Purpose

To determine if dynamic susceptibility contrast-enhanced perfusion MR imaging (DSC-pMRI) with leakage correction can predict major genomic alterations in GB using retrospective imaging guided stereotactic tissue validation.

Materials and Methods

A total of 47 patients with GB (M/F: 23/24, mean age: 54, age range: 20-90 years) who had pretreatment DSC-pMRI with leakage correction and genomic analysis from enhancing tumor region were enrolled after inclusion and exclusion criteria. Stereotactic biopsy samples were taken from regions of interest (ROI) with highest rCBV values. DSC-pMRI maps and T2* signal intensity time curves were used to calculate mean rCBV, maximum rCBV, relative peak height (rPH), and percent signal recovery (PSR) by ROI analysis.

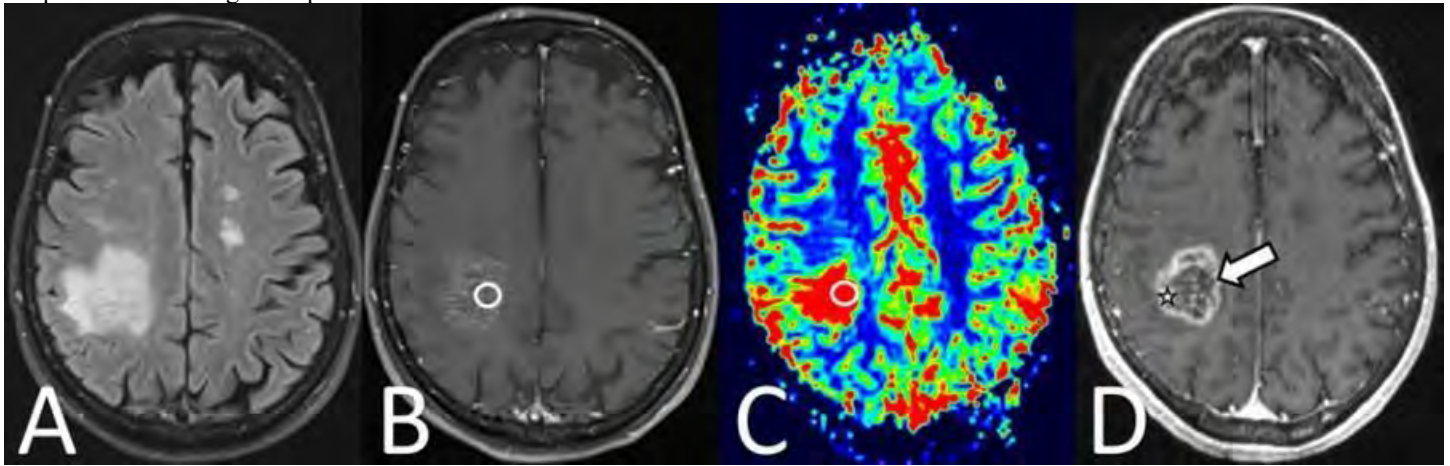
Major genomic alterations of IDH1-132H, MGMT, p53, EGFR, ATRX, and PTEN status were determined and correlated with DSC-pMRI derived parameters of GB. Statistical analysis was performed using the independent-samples t-test, and ROC (receiver operating characteristic) curve analysis. Significant variables from the univariate analysis were further analyzed in a multivariable stepwise regression model.

Results

Seven (7/47; 14.8%) patients had IDH1 mutation and MGMT methylation was present in 22 (22/47; 46.8%) patients. P53 mutation was present in 22 out of 34 (64.7%), ATRX mutation was present in 12 out of 27 (44.4%), PTEN mutation was present in 7 of 21 (33%), and EGFR amplification was positive in 12 out of 18 (66%) GBs. rCBVmean and rCBVmax was significantly different in relation to the IDH1, MGMT, p53, and PTEN mutation status (all $p < 0.05$). The rPH of the p53 mutation-positive (mean 5.8 ± 2.8) was significantly higher than those of the p53 mutation-negative group (mean 4.0 ± 1.5) ($p = 0.022$). Multivariable stepwise regression analysis revealed that the presence of IDH-1 mutation ($B = -2.81, p = 0.005$) was associated with decreased rCBVmean; PTEN mutation ($B = -1.21, p = 0.003$) and MGMT methylation ($B = -1.47, p = 0.038$) were associated with decreased rCBVmax; and ATRX mutation ($B = -1.05, p = 0.008$) was associated with decreased rPH.

Conclusions

Significant associations between DSC-pMRI derived parameters and major genomic alterations such as IDH-1 mutation, MGMT methylation, p53 and PTEN mutation status in GB suggests that expression levels of therapeutically relevant genomic alterations can be quantified utilizing DSC-pMRI.



(Filename: TCT_910_Picture3.jpg)

345

Correlation of National Institute of Health Stroke Scale (NIHSS) with Emergent Large Vessel Occlusion (ELVO) in Stroke Alert Patients – a Single Center Experience

Y Tang¹, C Cain²

¹Virginia Commonwealth University, Glen Allen, VA, ²Virginia Commonwealth University Medical Center, Richmond, VA

Purpose

NIHSS is the most commonly used clinical score to assess the severity of neurological deficits in acute stroke patients and has been used as a criteria for clinical trial enrollment. This pilot study is to evaluate the feasibility of using NIHSS to predict ELVO in stroke alert patients.

Materials and Methods

Study was approved by Institutional Review Board. 82 consecutive patients within 24 hours of stroke symptom onset who presented to our comprehensive stroke center from 1/1/2020 to 9/30/20 were diagnosed with anterior circulation (ICA, M1 and proximal M2) ELVO by CTA. 211 patients presented with stroke alert from 8/1/2020 to 9/30/2020 with negative ELVO on CTA were used as a comparison cohort. Patients with intracranial hemorrhage or other acute non-ischemic findings on head CT were excluded. NIHSS were recorded by stroke neurologists. Statistical analyses were performed using SPSS 26 software. NIHSS of ELVO and non-ELVO groups were compared using independent student's t-test. Receiver Operating Characteristic (ROC) Analysis was used to determine the best NIHSS cutoff to distinguish these two groups. For the LVO group, the size of ischemia ($T_{max} > 6s$) was estimated by CT perfusion using RAPID software. The relationship between NIHSS and size of ischemia was assessed by using Pearson correlation.

Results

ELVO group had a significantly higher NIHSS (17 ± 8 , mean \pm SD) compared to non-ELVO group (7 ± 7) ($p < 0.01$). However, there was significant overlap between these two groups. 22% of ELVO patients had NIHSS ≤ 5 , while 8% of non-ELVO patients had NIHSS > 20 . ROC analysis failed to identify a NIHSS cutoff value with acceptable sensitivity and specificity. For example, NIHSS of 10 had 80% of specificity but only 50% sensitivity in detecting LVO. NIHSS had a moderate correlation with the size of ischemia

detected on CT perfusion (Pearson correlation 0.517, $P < 0.01$). ELVO patients selected for mechanical thrombectomy had lower NIHSS (11 ± 7) than patients excluded from thrombectomy (16 ± 9) ($P < 0.01$).

Conclusions

Although NIHSS is positively correlated with presence of ELVO on CTA and size of ischemia measured on CTP, no threshold can be identified to detect LVO patients with acceptable sensitivity and specificity. Vascular imaging remains essential for all patients of suspected acute stroke regardless of symptom severity.

1070

Correlation of Spinal Cord Structural and Diffusion Tensor Imaging Biomarkers with Clinical Findings in Acute Cervical Spinal Cord Injured Patients

A Manmatharayan¹, N Jain², D Middleton³, M Alizadeh³, L Krisa³, A Flanders¹, F Mohamed³

¹Thomas Jefferson University Hospital, Philadelphia, PA, ²N/A, N/A, ³Thomas Jefferson University, Philadelphia, PA

Purpose

N/A

Materials and Methods

Diffusion tensor imaging can be used to evaluate microstructural changes in the spinal cord post injury [1]. The purpose of this study was to conduct a comprehensive analysis of the diffusion and structural measurements at five specific spinal cord levels in acute cervical SCI patients and correlate them with the American Spinal Cord Injury (ASIA) clinical grades.

Results

In this retrospective study, data from 42 acute cervical spinal cord injury patients was used. A board-certified neuroradiologist determined the levels of injury and stratified them into hemorrhagic cord (HC; n=16) and non-hemorrhagic cord (NHC; n=36). Axial gradient-echo sequence were used to measure the mean area (MA), antero-posterior diameter (AP) and right to left diameter (RL) using the Spinal Cord Toolbox (SCT). Diffusion Tensor Imaging (DTI) metrics were obtained from a single-shot echo planar imaging (EPI) sequence or a zonally magnified oblique multi-slice EPI technique. After preprocessing, various tensor metrics (Fractional Anisotropy, Axial Diffusivity, Radial Diffusivity and Medial Diffusivity) were extracted. ROIs were drawn at 5 levels: C2-3 disc level, injury epicenter, one vertebral level rostral to injury, one level caudal to the injury and two levels caudal to the injury. Spearman Correlation was used to correlate the imaging measurements with the ASIA grades A-D (1-4).

Conclusions

RESULTS: The data at the C2-3 level in HC injuries showed a moderate correlation with DTI indices AD ($r=-0.59$), MD ($r=0.6$), FA ($r=-0.44$), and RD ($r=0.48$). At one level rostral to the injury, HC injuries showed a moderate correlation with FA ($r=-0.61$) and RD ($r=0.5$). However, NHC injuries showed poor to no correlation of DTI metrics at all 5 defined levels. Most of the structural metrics in NHC injuries showed poor correlation below and at the injury site while in the upper levels, RL showed moderate correlation. **CONCLUSION:** Measurements of structural and diffusion metrics at levels above the injury epicenter in adult acute traumatic cervical spinal cord injury with hemorrhagic cord provided more correlation with clinical grades than at injury epicenter or below the injury site. This study shows the potential involvement of spinal cord injury regions well above the injury epicenter and advocates importance of diffusion and structural measurements away from the injury site.

LEVEL	ASIA	MA	AP	RL	FA	AD	MD	RD
C2/3	NHC	0.01	-0.29	0.43	0.26	0.31	0.18	-0.01
	HC	0.31	-0.08	0.34	-0.44	0.59	0.60	0.48
1 LEVEL ABOVE	NHC	-0.17	0.19	-0.38	-0.11	0.14	0.18	0.18
	HC	-0.08	-0.43	0.03	-0.61	0.14	0.28	0.50
INJURY EPICENTER	NHC	0.03	-0.02	-0.15	-0.04	0.14	0.16	0.19
	HC	-0.28	-0.52	-0.06	-0.34	0.05	0.25	0.27
ONE LEVEL BELOW	NHC	-0.16	-0.15	-0.07	-0.17	0.32	0.26	0.25
	HC	0.07	-0.17	0.19	-0.13	-0.26	-0.16	-0.16
TWO LEVELS BELOW	NHC	-0.15	-0.08	-0.23	-0.14	0.37	0.25	0.22

(Filename: TCT_1070_asnnnr.jpg)

916

Correlation of Thalamic Functional Connectivity with NICU Network Neurobehavioral Scale (NNS) in Infants with Prenatal Opioid Exposure

R Vishnubhotla¹, Z Guckien¹, P Zhang¹, J Dietrich¹, G Sokol¹, D Watkins¹, S Sadhasivam¹, R Radhakrishnan¹

¹Indiana University School of Medicine, Indianapolis, IN

Purpose

Prenatal opioid exposure (POE) may adversely affect neonatal and childhood outcomes. We reported alterations in resting state functional MRI (rs-fMRI) connectivity in infants with POE. [1] Implications of these rs-fMRI changes on neurobehavioral outcomes have not been studied. The purpose of this study is to compare differences in rs-fMRI thalamocortical connectivity between POE and healthy opioid naïve (ON) infants, and correlate connectivity changes with early neurobehavioral measures on the NICU Network Neurobehavioral Scale (NNS).

Materials and Methods

In this prospective, IRB-approved study, 19 infants with POE and 20 healthy opioid naïve (ON) controls underwent rs-fMRI during natural sleep at < 48 weeks postmenstrual age (PMA). Seed-based whole brain functional connectivity analyses were performed for each subject with right (R) and left (L) thalamus as seed regions. Unpaired mixed-effects group analyses between POE and ON groups were conducted for each seed region corrected for PMA and sex to identify regions of significantly altered thalamocortical functional connectivity in infants with POE compared to ON. 13 of these infants (6 POE, 7 ON) also underwent NNS assessment at mean PMA of 46.8 and 45.8 weeks respectively. In these infants, thalamocortical connectivity was correlated with NNS summary scores using Pearson correlation. Being a pilot analysis, P value of $\leq .05$ was considered statistically significant.

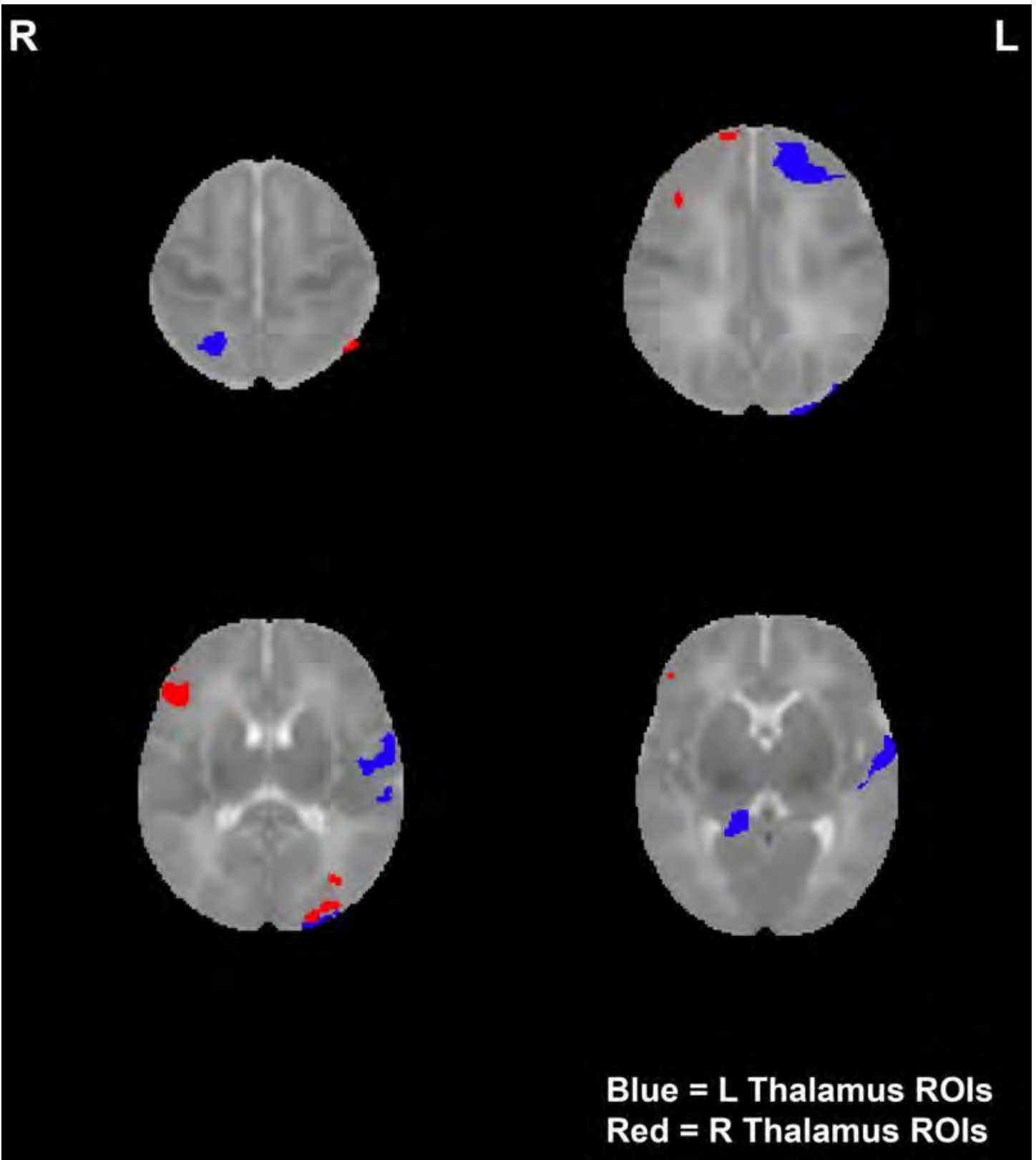
Results

Compared to healthy ON infants, infants with POE had significantly altered thalamocortical connectivity that correlated with multiple

NNNS summary scores (Figure 1). Specifically, in POE group, R thalamus - L superior parietal lobule connectivity was negatively correlated to NNNS arousal, excitability, handling and hypotonicity scores (all $P < .05$). In POE, R thalamus - R sensorimotor connectivity was negatively correlated to NNNS excitability scores ($R = -0.86$, $P = .03$), while in ON group, L thalamus - R sensorimotor connectivity had positive correlation with NNNS excitability score ($R = 0.78$, $P = .04$). R thalamus - L superior temporal gyrus connectivity had discordant, positive and negative correlations with NNNS handling score in POE ($R = 0.82$, $P = .047$) and the ON ($R = -0.89$, $P = .007$) groups respectively.

Conclusions

This is the first study to demonstrate altered neonatal rs-fMRI thalamocortical connectivity correlating with clinical outcomes in infants with POE. Large longitudinal studies would help in validating these findings and studying longer term outcomes.



(Filename: TCT_916_Thal_fMRI_NNNS.jpg)

1296

Cost-Effectiveness Analysis of DOTATATE PET/MRI in Patients with Intermediate-Risk Meningioma Undergoing Radiotherapy Planning: Incorporating Effects of Disability

J Rodriguez¹, S Mahase², M Roytman², G Madera², P Pan³, R Magge², S Pannullo², J Ivanidze²

Purpose

DOTATATE PET has demonstrated utility in meningioma diagnosis and post-surgical radiation treatment (RT) planning. While PET/MRI confers a higher cost of imaging compared to MRI alone, it has the potential of saving healthcare costs by decreasing RT doses, as well as reducing associated disabilities. Our purpose was to perform cost-effectiveness analysis (CEA) of PET/MRI in patients with intermediate-risk meningioma undergoing RT planning, using one-way and probabilistic sensitivity analyses (PSA) and incorporating the costs of disability.

Materials and Methods

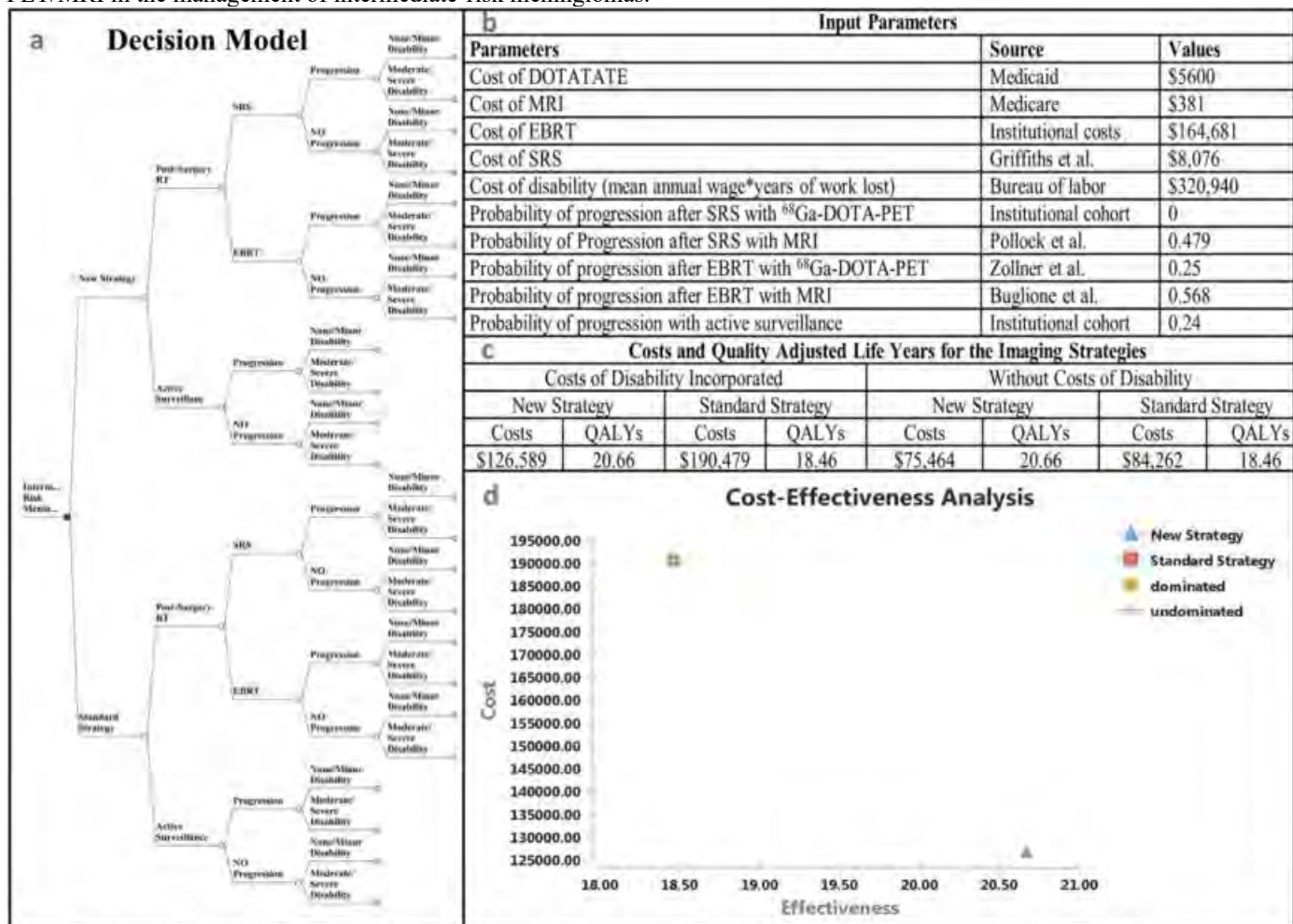
We built a decision model in TreeAge Pro software comparing health and economic consequences of two imaging strategies for intermediate-risk meningioma: DOTATATE PET/MRI (new strategy) or MRI alone (standard strategy). RT guidelines were based on RTOG0539. Probabilities for progression and outcomes were derived from the literature as well as from a prospective (PET/MR) and retrospective (MRI) cohort at our institution, respectively. Endpoint costs including RT, disability, and imaging were included. Disability costs were calculated based on mean US annual wage and mean number of working years after RT. PSA were performed on key variables. A willingness-to-pay threshold of \$100,000 was assumed.

Results

The new strategy was dominant over the standard strategy, resulting in lower cost (\$75,464 versus 84,262) and higher QALYs gained (20.66 versus 18.46); results remained robust when incorporating disability costs (Fig.1). PSA demonstrated that the new strategy remained cost-effective across all iterations of probabilities for disease progression and utilization of different treatment modalities. 79% and 54% of the iterations rendered the new strategy cost-effective when varying the input parameters for health utilities and the probability of disability, respectively.

Conclusions

Our CEA model demonstrated DOTATATE PET/MRI to be dominant over MRI alone, with higher QALYs and lower costs. Our findings remained robust when incorporating disability costs. PSA revealed that our model was most sensitive to variations in the input parameters of probability of disability and health utilities. Limitations of the study, to be addressed in future work, include the small cohort size and lack of long-term follow-up data of our institutional cohort. Our pilot data supports the use of DOTATATE PET/MRI in the management of intermediate-risk meningiomas.



(a) Decision Model. (b) Input Parameters. (c) Costs and QALYs for imaging strategies. (d) CEA.

Cost-effectiveness of Endovascular Thrombectomy in Acute Stroke Patients with M2 Occlusion

M Khunte¹, X Wu², A Malhotra³

¹Yale University, New Haven, CT, ²UCSF School of Medicine, San Francisco, CA, ³Yale University School of Medicine, New Canaan, CT

Purpose

The cost-effectiveness of endovascular thrombectomy (EVT) in patients with acute ischemic stroke due to M2 branch occlusion remains uncertain. The purpose of this study was to determine the societal impact of health outcomes and financial implications of EVT versus no-EVT in acute stroke patients with M2 occlusion.

Materials and Methods

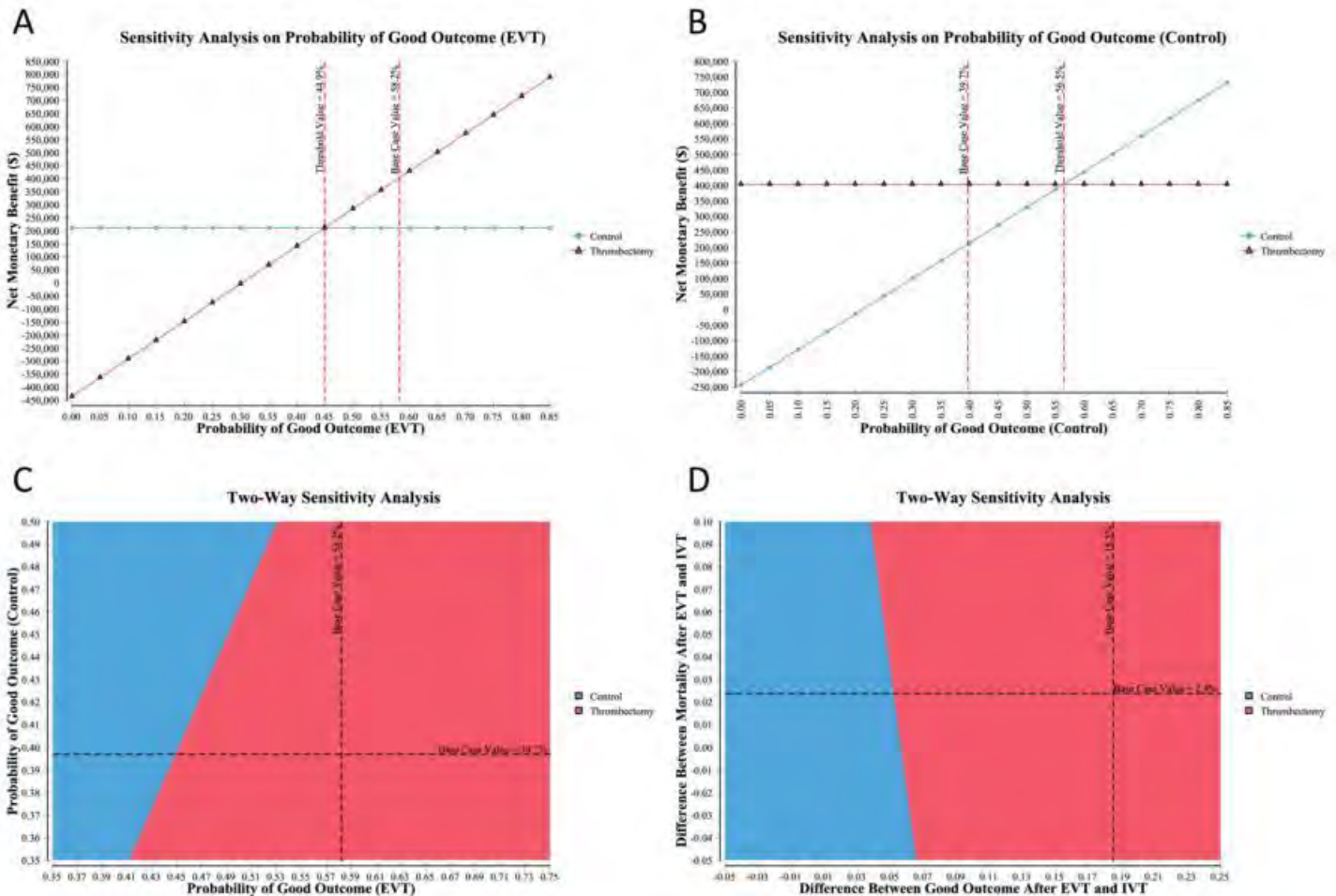
A decision-analytic study was performed with Markov modeling to estimate the lifetime quality-adjusted life years (QALYs) and associated costs of EVT-treated patients compared to no-EVT/medical management. The study was performed over a lifetime horizon with a societal perspective in the United States setting. Base case, one-way, two-way, and probabilistic sensitivity analyses were performed.

Results

EVT was the long-term cost-effective strategy in 93.37% of the iterations in the probabilistic sensitivity analysis, and resulted in difference in health benefit of 1.66 QALYs in the 65-years age groups, equivalent to 606 days in perfect health. Varying outcomes after both strategies shows EVT to be more cost-effective when the probability of good outcome after EVT was only 4 to 6% higher relative to medical management in clinically likely scenarios. EVT remained cost-effective even when its cost exceeded \$200,000 (threshold was \$209,111). EVT was even more cost-effective for 55-year old compared to 65-year old patients.

Conclusions

Our study suggests EVT to be cost-effective for treatment of acute M2 branch occlusions. Faster and improved reperfusion techniques would increase the relative cost-effectiveness of EVT even further in these patients.



Cost-Effectiveness of Perfusion Imaging in Select Patient for Acute Ischemic Stroke Treatment at 0-6 Hours

G Martinez¹, J Katz², A Pandya³, A Boltyenkov¹, J Wang², P Sanelli²

¹Siemens Healthineers, Manhasset, NY, ²Northwell Health, Manhasset, NY, ³Harvard T.H Chan School of Public Health, Boston, MA

Purpose

Two recent randomized clinical trials (RCT) demonstrated the safety and efficacy of endovascular therapy (EVT) for large vessel occlusion in the time window 6-24 hours from symptom onset time (SOT) by selecting patients with advanced imaging (CT perfusion or MR perfusion/diffusion). These studies emphasized the added value of advanced imaging in the identification of patients that may benefit most from EVT. However, most RCTs in the first 6 hours from SOT did not use advanced imaging for patient selection for treatment. Consequently, the main objective of this study is to analyze the risk-benefit tradeoff of advanced imaging given that there is uncertainty about its appropriate utilization in the SOT 0-6 hours window.

Materials and Methods

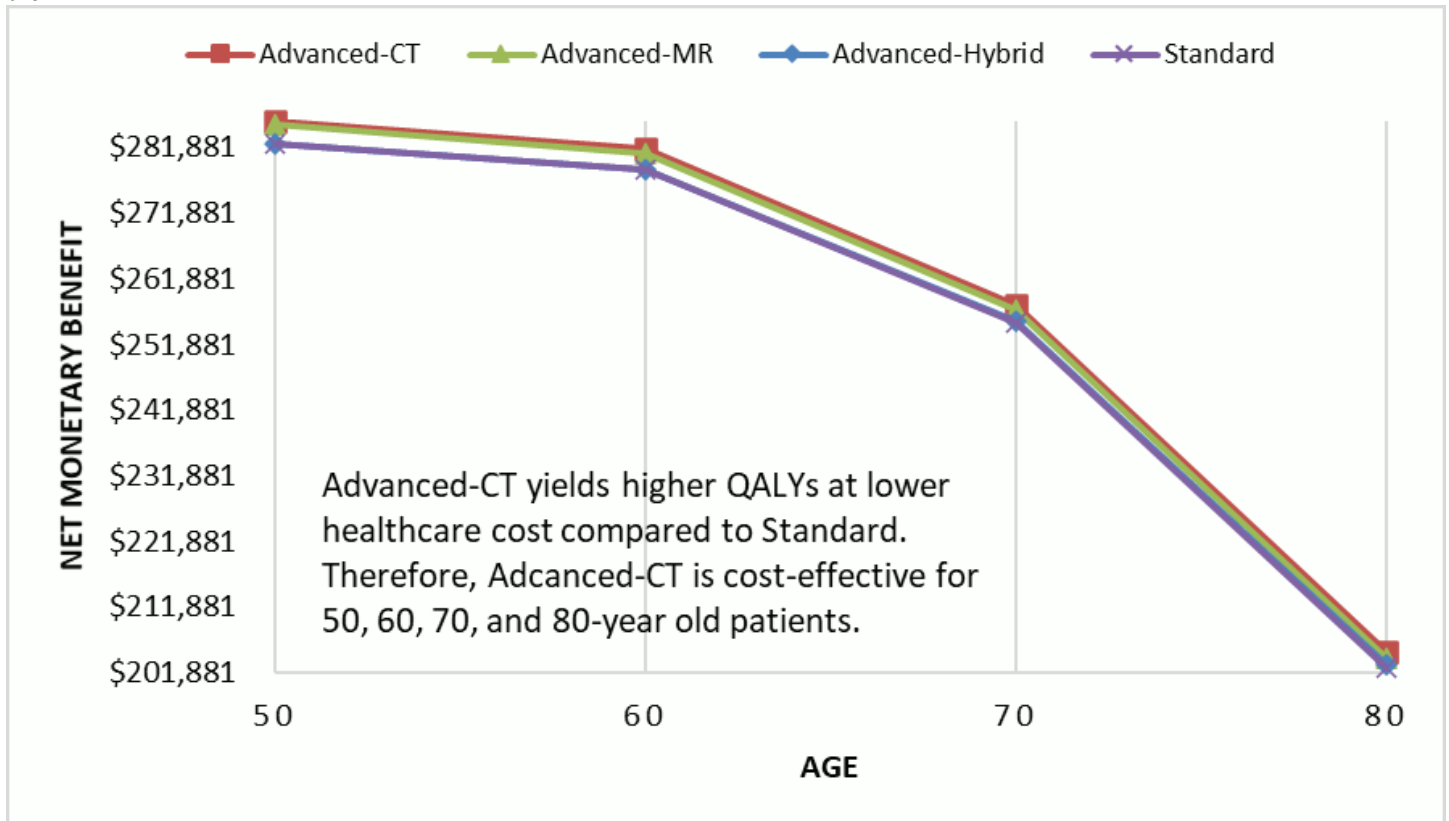
We developed a decision-simulation model representing different approaches to advanced imaging utilization for patient selection for EVT. More specifically, we compared the following approaches: a) Standard-CT: NCCT+CTA; b) Advanced-CT: NCCT+CTA+CTP; c) Advanced-MR: MR-DWI+MRA+MRP; and d) Advanced-Hybrid: NCCT+CTA+MR-DWI+MRP. The clinical-care pathways and treatment eligibility criteria were based on clinical metrics according to published stroke-care guidelines. The model includes time-dependent outcome to reflect the decline in functional outcomes associated with treatment delays caused by utilization of advanced imaging, and brain-cancer risk for radiation exposure from CT. We conducted cost-effectiveness analyses from a healthcare perspective, with the standard willingness-to-pay (WTP) thresholds (\$100,000/QALY and \$50,000/QALY). Model parameters were based on data from meta-analyses and RCTs.

Results

Our analyses determined that Advanced-CT and Advanced-MR yielded higher quality-adjusted life-years (QALYs) (4.81 and 4.82) at \$223,003 and \$224,280, respectively. However, Advanced-CT is cost-effective at both WTP thresholds. Furthermore, Standard-CT yielded lower QALYs (4.78) at \$223,690; thus, it was dominated by Advanced-CT. Sensitivity analyses on possible time-delays caused by advanced imaging determined that Advance-CT becomes dominated by Standard-CT if delays exceeded 60 minutes. Importantly, the benefits of Advanced-CT utilization outweigh brain-cancer radiation risks.

Conclusions

Performing Advanced-CT imaging at presentation for EVT selection in the first 6 hours is cost-effective, yielding higher QALYs at a lower cost compared to Standard-CT. Our findings highlight the added value of advanced imaging prior to treatment decisions at SOT 0-6 hours.



634

Coup and Contre-coup Injuries-Predictors of outcome in Traumatic Brain Injury

M Jayakumar¹, A Rangari²

¹AMD Imaging Systems, Chennai, Tamilnadu, ²SCTIMST, Trivandrum, Trivandrum, Kerala

Purpose

Focal brain injuries are found in approximately 50 % of all the patients with severe brain trauma and are responsible for nearly two-thirds of the deaths associated with head injury. Coup and contrecoup contusions comprise a group of focal brain injuries. Since the pathogenesis of the two are different, the outcomes also would therefore be expected to be different. With CT imaging, it is possible to precisely delineate the type, location and severity in the majority of traumatic brain injury (TBI) patients and to determine whether injuries are coup or contre coup. Since there are very few studies in literature comparing outcome in coup-contre coup injuries, this study aims to bridge the gap.

Materials and Methods

A retrospective study of 179 patients with traumatic head injuries who underwent CT scanning at our radiology department was carried out. The injuries were divided into three groups: Coup injuries with intraparenchymal injury (n=89), contrecoup injuries (n=44) and coup-contrecoup injuries (n=46). The groups were comparable with respect to age and GCS. Site of primary impact was determined by clinical and CT scan criteria. The mortality rates in each group were compared with respect to age, GCS and CT pattern. Outcome measured in this study was mortality during the same hospital admission. Using the Chi square test, the mortality rates were compared across the groups and then correlated with the GCS and age and conclusions were made based on the "p" value.

Results

The most common coup injury was depressed fracture with contusion ; followed by extradural hematoma with contusion. Patients with bilateral contusions and EDH with contusion formed the majority in the coup-contre coup group. There was a statistically significant difference in mortality between patients with coup injuries and patients with contrecoup (p< 0.005) and coup-contrecoup injuries (p<0.001). There was no significant difference in mortality between contrecoup and coup-contrecoup injuries (p = 0.1). Mortality in patients aged less than 60 years and patients with GCS > 8 was significantly higher in patients with contrecoup and coup-contrecoup injuries.

Conclusions

The present study shows that the presence of contrecoup contusions, with or without coup contusions, is associated with a poor prognosis across all GCS and age categories and may warrant closer monitoring and aggressive management. However, age more than 60 years, GCS > 8, and presence of acute SDH on CT scan was uniformly associated with a poor outcome.

869

COVID-19 and Anosmia, Retrospective Review of Critical Olfactory Anatomy and Pathology Affected by the SARS-CoV-2 Virus

G Keir¹, N Maria², C Kirsch³

¹Northwell Health, Manhasset, NY, ²Northwell Health Feinstein Institute for Research, New York City, NY, ³Northwell Health, New York City, NY

Purpose

Anosmia, phantosmia and dysgeusia are recognized symptoms of COVID positivity. The purpose of this IRB #20-0610 approved study was to retrospectively review cross-sectional neuroimaging in confirmed COVID positive patients with anosmia, dysgeusia and phantosmia, assessing olfactory bulb and tracts for presence or absence of volume loss, edema, micro-hemorrhages and enhancement. Findings are presented with review of olfactory tract anatomy, olfactory support cells and perivascular epithelium ACE-2 receptor anatomy, that may serve as potential entry sites for SARS-CoV-2 spike viral proteins and lead to the resultant pathophysiology.

Materials and Methods

All patients were 1) confirmed positive for SARS-CoV-2 by PCR or antibody testing, 2) had cross-sectional MRI or CT neuroimaging at time of disease, and 3) had electronic medical record (EMR) documenting anosmia, dysgeusia and phantosmia. A total of n=19 patients fulfilled all search criteria. Of n= 19 patients, n=9 patients had prior cross-sectional neuroimaging, obtained prior December 2019. Patients without confirmed PCR or antibody positivity, cross-sectional neuroimaging, or documentation of anosmia, dysgeusia or phantosmia in EMR were excluded.

Results

N=19 patients met all search criteria, n = 8 males, n=11 females, age range 9-79, average age 45.5 years, with 14 MRIs, 7 CTs, n=9 prior cross-sectional imaging demonstrated olfactory volume loss n=1, without prior imaging on MRI left olfactory tract encephalomalacia and total of n= 10 volume loss, n= 10 olfactory bulb and tract contrast enhancement, n=7 olfactory tract microhemorrhages and edema.

Conclusions

Experimental animal mouse models show SARS-CoV-2 viral spike proteins attach to ACE-2 receptors in olfactory support and perivascular cells, leading to olfactory tract infectivity. This retrospective neuroimaging study of 19 patients with 1) COVID-19, 2) anosmia, phantosmia or dysgeusia, and 3) cross-sectional neuroimaging, including 9 with prior imaging before infection, is one of the largest series to date. Neuroimaging of these patients demonstrated olfactory volume loss, edema, enhancement and microhemorrhages. Viral SARS-CoV2 infectivity via olfactory epithelial and perivascular ACE-2 receptors may lead to microvascular disruption, edema, and microhemorrhages with resultant olfactory tract encephalomalacia.



(Filename: TCT_869_ScreenShot2020-11-01at100743PM.jpg)

COVID-19: Cerebrovascular Occlusions and Posterior Circulation Stroke.

E Nimchinsky¹, C Jolstad¹, H Bueno¹

¹Rutgers New Jersey Medical School, Newark, NJ

Purpose

Anecdotal reports suggest that COVID-19 predisposes to thrombogenic complications, including stroke. The effect of COVID-19 on the incidence and types of cerebrovascular occlusions in a population is still unknown. We describe the effects of incidence and stroke subtype as well as vascular occlusions in our population as the pandemic swept through the region in order to help elucidate the relationship between stroke and COVID-19.

Materials and Methods

A single-center retrospective study was performed, including all patients presenting to our Comprehensive Stroke Center with signs and symptoms of stroke who received CT angiograms of the head, prior to and throughout the passage of the COVID-19 pandemic through the city of Newark, NJ, from December 1, 2019 to May 31, 2020. A novel hybrid technique using RT-PCR and chest imaging was used to assign probable COVID-19 status. Characteristics of the vascular occlusions and correlation with COVID-19 status were analyzed. Age, sex, COVID-19 status, presenting signs and symptoms, NIH stroke scale (NIHSS), laboratory values, CTA findings, and clinical outcomes were documented.

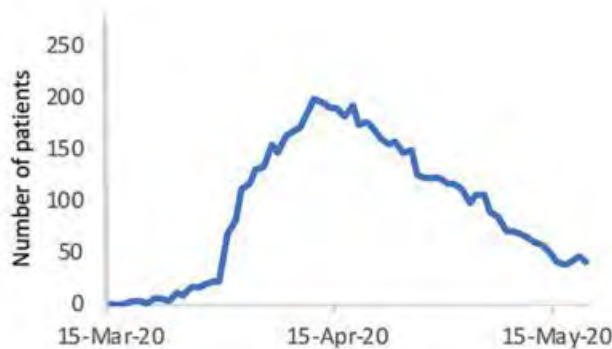
Results

358 patients met exclusion criteria. There was a significant increase in the incidence of vascular occlusions in April 2020, corresponding with the COVID-19 surge at our institution. The rate of clinical strokes did not increase, but the proportion with vascular occlusions increased from 29% in December through March to 50% in April (odds ratio 2.37, 95% CI, 1.30-4.31). There was a small but significant decrease in the mean age of patients with vascular occlusions. There was no difference in the incidence of large vessel occlusions (LVO) or multiple vessel occlusions in patients with and without COVID-19. Patients with COVID-19 were more likely to have a posterior circulation occlusion (odds ratio 5.96, 95% CI, 1.25-28.3) and more likely to die during hospitalization (odds ratio 8.1, 95% CI, 2.41-27.0).

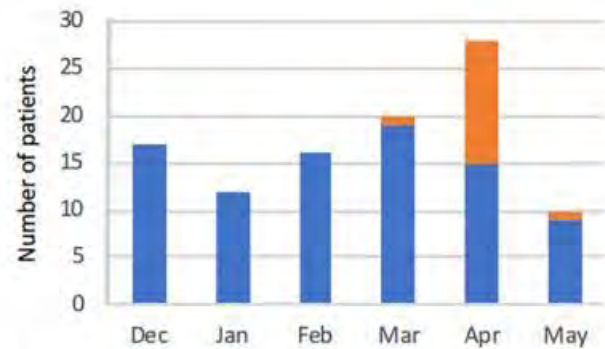
Conclusions

COVID-19 appears to be associated with an increased incidence of vascular occlusions at the population level. There also appears to be a decrease in mean age, with an increased risk of posterior circulation strokes and in-hospital mortality.

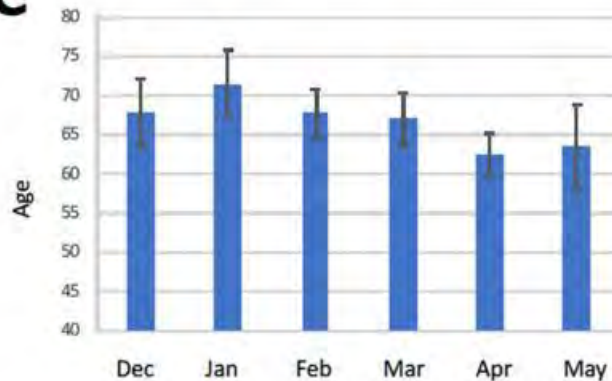
A



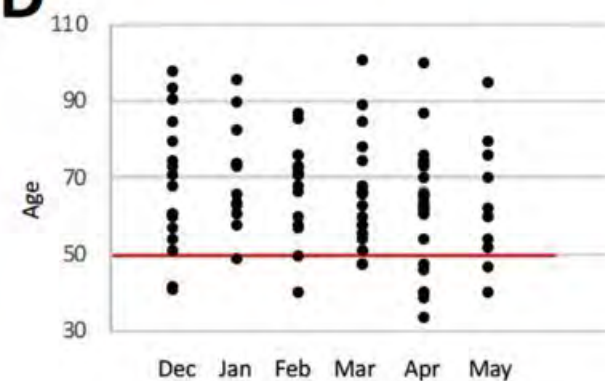
B



C



D



Cranial Nerve Cisternal Segment Enhancement in Multiple Sclerosis: Prevalence on 3.0-Tesla Volumetric T1 MRI and Clinical Associations

J Bowling¹, C Zamora², S Hung³

¹New York University Department of Radiology, New York, NY, ²UNC Department of Radiology, Chapel Hill, NC, ³University of North Carolina School of Medicine, Chapel Hill, NC

Purpose

Enhancement of the cisternal segments of cranial nerves (CN) III-XII is increasingly recognized in patients with multiple sclerosis (MS), particularly on volumetric T1 post-contrast sequences performed using 3.0-Tesla scanners, which have become standard of care in this population. However, the clinical associations and implications of such findings are poorly understood. Our primary aims were to determine the prevalence and characteristics of cisternal segment enhancement (CSE) and to examine clinical associations using patient data.

Materials and Methods

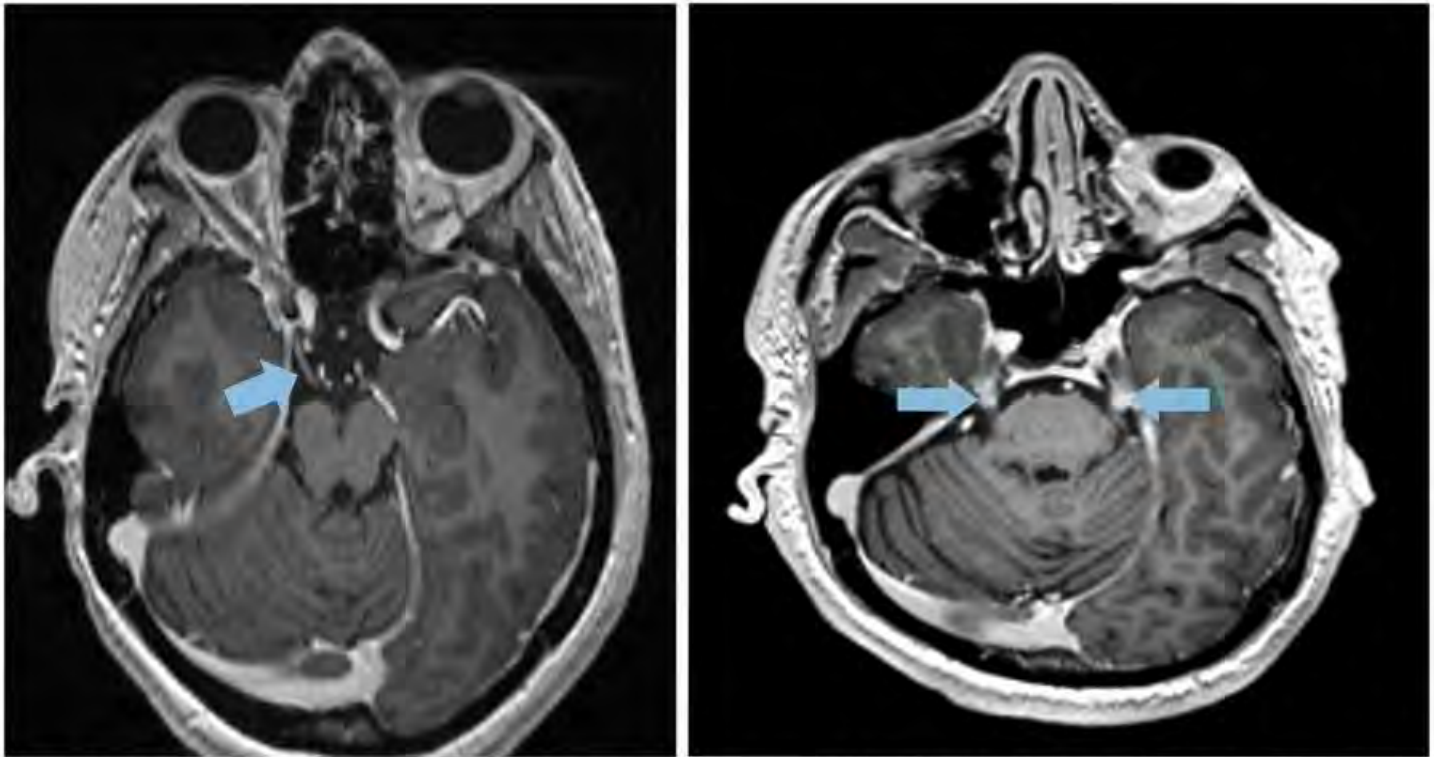
285 adult patients with MS and 3.0-Tesla brain MRI were studied retrospectively. Two neuroradiologists blinded to the clinical chart scored each patient's MRI for the presence and characteristics of CSE at each CN of interest (III-XII). A radiology resident blinded to the imaging abstracted clinical variables of interest at the corresponding time of imaging, including age, gender, race, MS type, disease-modifying drug use, history of trigeminal neuralgia, history of CN palsy, symptomatology, and Expanded Disability Status Scale (EDSS) score. CSE prevalence was determined. Interactions with clinical variables were calculated using two-sample T-tests, Fisher's exact tests, and logistic regression models. When available, imaging and patient data from a second time point was also analyzed to study the evolution of CSE.

Results

Case prevalence of CN-III (4.6%) and CN-V (3.9%) CSE was higher than demonstrated on previous reports (which used 1.5-T MRI). CSE prevalence at other CN (IV, VI-XII) was low (<1%) or zero. 60% of CSE was bilateral. Male gender was associated with CSE at CN-III ($p = 0.01$, OR 4.21), CN-V ($p = 0.002$, OR 8.89), and any CN ($p = 0.001$, OR 5.32). A history of trigeminal neuralgia was associated with CSE at CN-V ($p < 0.001$, OR 15.28). Other studied clinical variables were not associated with CSE. CSE was transient in most cases (mean follow-up time = 2.57 years) and was not associated with directly relevant symptomatology at the time of imaging.

Conclusions

CSE involving CN-III and CN-V was more prevalent in MS patients than previously reported, likely due to increased conspicuity on volumetric T1 sequences using 3.0-Tesla MRI. These findings were usually transient, were associated with male gender and a history of trigeminal neuralgia, and were not associated with directly relevant symptomatology at the time of imaging. CSE involving other studied cranial nerves (IV, VI-XII) appears to be rare in MS patients.



Left: 31-year-old female with an enhancing cysternal segment of the right oculomotor nerve (blue arrow). The patient's left oculomotor nerve does not enhance.

Right: 48-year-old male with enhancing cysternal segments of the bilateral trigeminal nerves (blue arrows).

(Filename: TCT_306_CNCSEFigure.jpg)

765

Craniocervical CT angiography at low kVp combined with iterative reconstruction algorithm and low-dose contrast medium

PLAI¹

¹*Kaohsiung Veterans General Hospital, Kaohsiung, Taiwan*

Purpose

To assess the image quality of 80-kVp craniocervical CT angiography (CCCTA) protocol combined with adaptive statistical iterative reconstruction-V (ASIR-V) and low-dose contrast medium (CM).

Materials and Methods

A total of 119 patients were randomly divided into three groups. For group A, 120-kVp protocol was followed with 60 ml CM and filtered back projection; for group B, 80-kVp protocol with 60 ml CM and ASIR-V; and for group C, 80-kVp protocol with 45 ml CM and ASIR-V. Both subjective and objective image quality and radiation doses were evaluated.

Results

Arterial attenuation, signal-to-noise ratio (SNR) and contrast-to-noise ratio (CNR) of the head, neck, and shoulder regions were significantly higher in groups B and C compared with group A. Group C yielded significantly better subjective image quality than that observed in groups A and B (both $p < 0.05$). As compared with group A, effective radiation dose and the iodine load of group C were reduced by 51.4% and 25%, respectively.

Conclusions

The CCCTA protocol with 80 kVp, ASIR-V, and 45 ml of CM injected at 3 ml/s significantly reduced the radiation dose, iodine load, and iodine delivery rate while providing better subjective and objective image quality, including higher arterial enhancement and a higher SNR and CNR compared with the 120-kVp protocol.

526

CT Perfusion Based Prediction of Core Infarct and Tissue At Risk: Can AI Help Reduce Radiation Exposure?

G Bathla¹, Y Liu², S Priya³, H Zhang⁴, N Le⁴, N Soni⁵, M Sonka⁶, C Derdeyn⁷

¹University of Iowa Hospitals and Clinics, Iowa City, IA, ²University of Iowa, Iowa City, IA, ³University of Iowa hospitals and Clinics, IOWA CITY, IA, ⁴The Iowa Initiative for Artificial Intelligence, Iowa City, IA, ⁵UIHC, Iowa, IA, ⁶The University of Iowa, Iowa City, IA, ⁷University of Iowa Hospitals & Clinics, Iowa City, IA

Purpose

CT/MR Perfusion (CTP/ MRP) plays a critical role in triaging patients with acute ischemic stroke (AIS) who present between 6-24 hours of last known normal (LKN). The increased radiation exposure with CTP remains a concern and is significantly greater than a single or multi-phase CT angiogram. The aim of the current study was to determine if an AI based solution could help reduce radiation exposure while maintaining diagnostic information.

Materials and Methods

Using retrospective CTP data from 59 patients, split as training/ validation (60/40%), we developed and validated separate 2D U-net models for cerebral blood flow (CBF) and time to maximum (Tmax) maps calculation to predict core infarct and tissue at risk respectively. The 4D-CTP images (28 time points) were used as input and color maps as output. Once trained, the full sets of 28 input images were sequentially reduced to smaller subsets of equitemporal 14, 10 and 7 time-points. The averaged structural similarity index (SSI) between the model derived images and ground truth (Rapid perfusion results) were compared. Volumes for core infarct and Tmax were compared using Pearson correlation coefficient.

Results

Both CBF and Tmax maps derived using 14 time points had comparable SSI (0.80-0.81, $p > 0.05$ for both). The maps derived from 10 and 7 time points were significantly different from ground truth ($p < 0.05$). The CBF and Tmax volumes derived from the model correlated well with ground truth volumes derived from Rapid software (0.69 for CBF and 0.74 for Tmax). The correlation between CBF (0.96) and Tmax (0.96) derived from 28 and 14 time points was excellent.

Conclusions

AI derived vendor-independent models show good correlation with Rapid derived volumes for CBF and Tmax with no significant difference in perfusion maps or derived volumes when using 14 time points instead of 28 time-points. Our findings suggest that the CTP radiation exposure could potentially be reduced by 50% while preserving the clinically relevant CTP information.

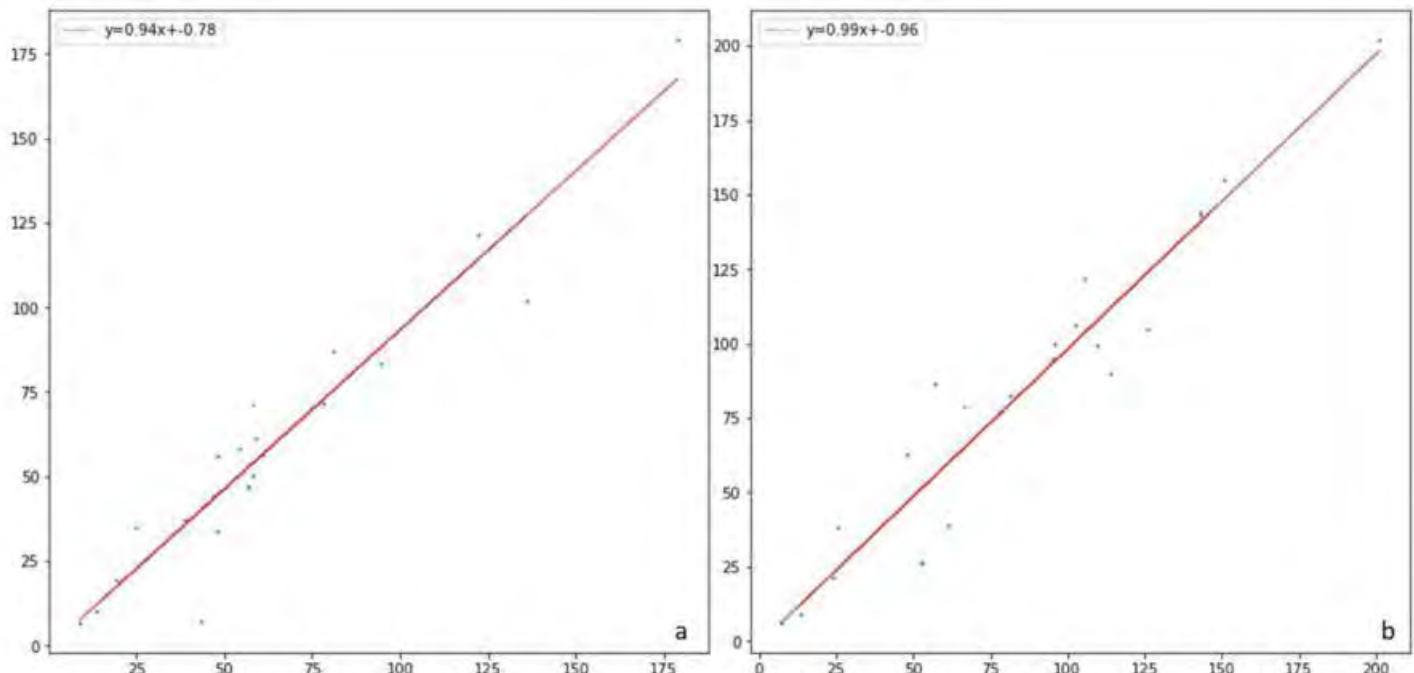
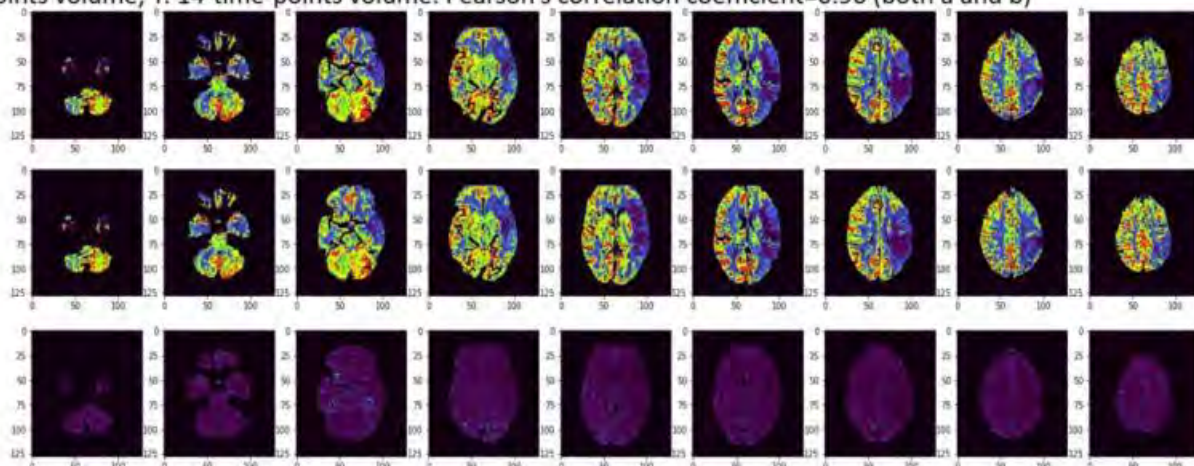


Figure 1(a, b). CBF (a) and Tmax (b) 28-time-points vs 14-time-points volume of affected brain scatter plot. X:28-time-points volume; Y: 14-time-points volume. Pearson's correlation coefficient=0.96 (both a and b)



CBF prediction results from a typical example patient (SSIM=0.98). Top row: ground truth; middle row: prediction; third row: differences.

(Filename: TCT_526_CTPF-1m.jpg)

122

CT-angiographic Appearance of Medullary Veins in Acute Ischemic Infarction Is Predictive of Outcome

A Drozdov¹, R Javan², C Leon Guerrero³, A Sparks¹, M Taheri¹

¹George Washington University Hospital, Washington, DC, ²N/A, N/A, ³George Washington University, Washington, DC

Purpose

A prior study demonstrated that decreased cortical venous drainage is predictive of poor clinical outcome in patients with acute ischemic stroke (AIS). An overlap of drainage between cortical and deep medullary veins (MV) exists, with selective, non-anastomotic drainage of the basal ganglia by deep MV only. The aim of this investigation is to test the hypothesis that a decrease in blood flow in MV on the initial CT angiogram (CTA) of patients with AIS can also be predictive of clinical outcome.

Materials and Methods

In this IRB approved study, we retrospectively reviewed a database of patients with AIS who were evaluated by multiphase CTA. Inclusion criteria: age above 18 yo, symptoms of AIS developed within preceding 12 hours, evidence of occlusion of the intracranial internal carotid artery, the M1 or M2 segment of the middle cerebral artery, or a combination of two occlusions. Exclusion criteria:

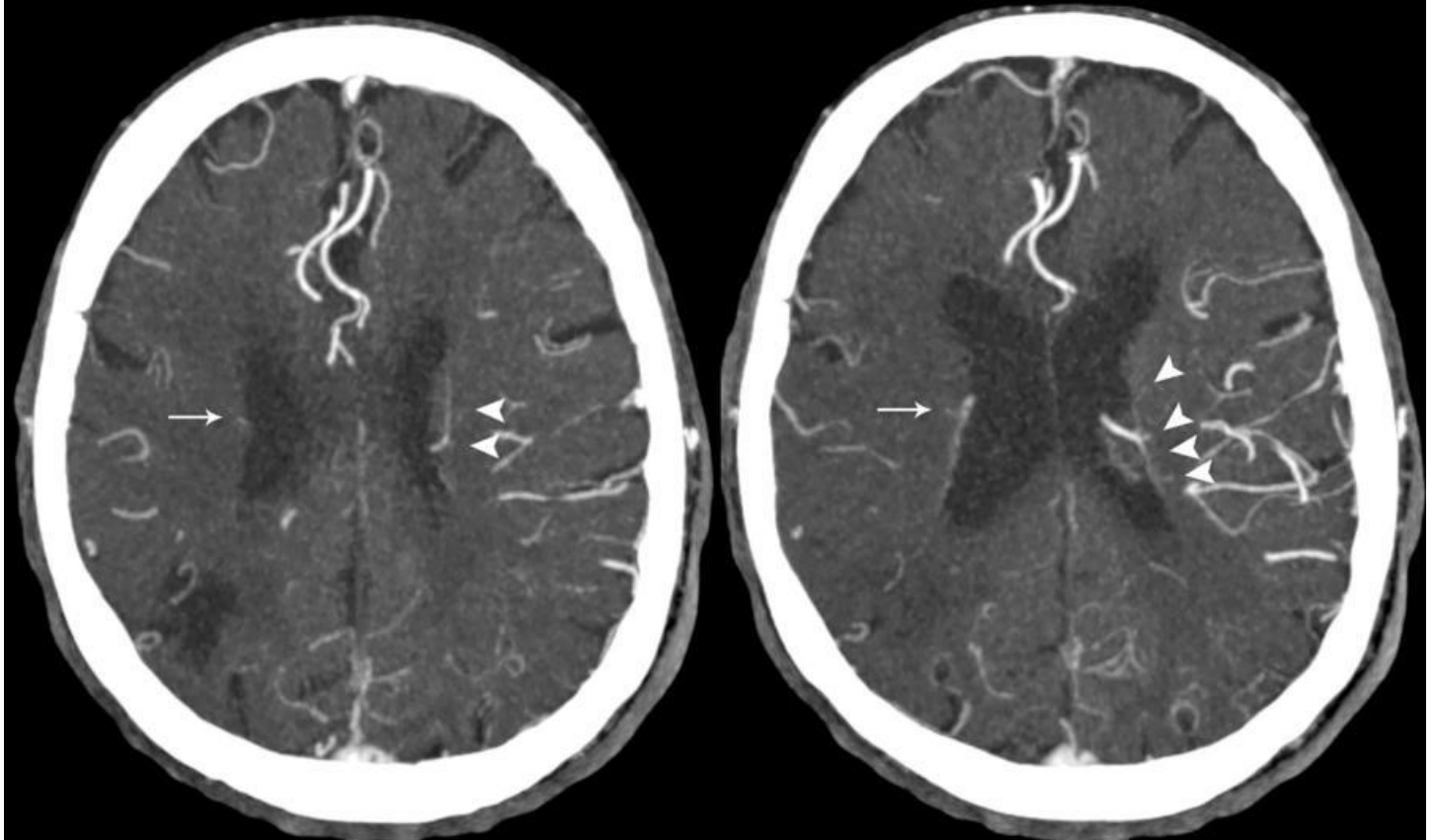
presence of intracranial hemorrhage, modified Rankin scale at baseline >2, or any terminal illness. The MV were assessed on 10mm axial MIP images from the basal ganglia to the highest section of the lateral ventricles. To characterize asymmetry of MV, we used a similar principle that was previously established for MV on SWI MR-images, with asymmetry defined as presence of 5 or more contrast-opacified MV in one hemisphere as compared to the contralateral side. Clinical outcomes were evaluated by mRS in 90 days. The Fisher Exact test was used to examine the significance of the MV asymmetry. Odds ratio and interrater variability were calculated.

Results

66 patients with AIS were included. The presence of asymmetry in MV was associated with a higher frequency of poor clinical outcomes (84.6% vs 50.9%); the OR was 5.3. Interrater agreement in assessment on MV was moderate in our study ($\kappa=0.55$). Figure 1 demonstrates asymmetric appearance of MV in patient with AIS.

Conclusions

This study shows that (a) medullary veins can be reliably assessed on multiphase CTA, (b) in patients with AIS, asymmetric appearance of MV is associated with poor clinical outcome. Validating novel neuroimaging biomarkers for treatment selection as well as predicting prognosis remains paramount for the improvement of care. The described sign has the potential to improve diagnostic accuracy and patient outcomes.



(Filename: TCT_122_MedVeinsAsymmetry.jpg)

302

CTP Core Volume Modifies the Predictive Value of ASPECT Scores in Stroke Outcome

C Sitton¹, A Sarraj², G Albers³, D Pujara⁴, R Riascos⁵

¹UT Health, Houston, TX, ²UT Houston, Houston, TX, ³Stanford University Medical Center, Palo Alto, CA, ⁴McGovern Medical School, Houston, TX, ⁵The University of Texas Health Science Center at Houston, Houston, TX

Purpose

While CT ASPECT scores predict clinical outcomes, the association between the scores and ischemic lesion volume is not linear as the subcortical regions involve small volumes while the cortical areas often involve large volumes. We evaluated whether ASPECTS and CTP ischemic core volume, modify each other's association with clinical outcome in patients undergoing endovascular thrombectomy (EVT).

Materials and Methods

In a prospective multicenter cohort study of imaging selection (SELECT), anterior circulation large vessel occlusion patients up to 24 hours from last known well were enrolled at 9 centers. All patients received a unified imaging profile (NCCT, CTA, and CTP with

ischemic core volume [rCBF <30%] by RAPID software). A blinded core lab adjudicated all images. Patients received standard of care IA or medical therapy at the discretion of the treating physician. Favorable outcome was defined by a 90 day MRS of 0-2.

Results

Of 445 enrolled, 284 received EVT and are included in this analysis. Median (IQR) ASPECTS was 8 (7-9), median (IQR) ischemic core volume 10 ml (0-33). Both ASPECTS and ischemic core volume independently correlated with good outcome after EVT. For ASPECTS, the probability of good outcome decreased by 14% per point (aOR 1.18, 95% CI 1.01-1.38, p=0.03). For CTP mRS 0-2 probability dropped by 25% for each 10 ml increase in core volume (aOR 0.75, 95% CI 0.67-0.84, P<0.001). The correlation between ASPECTS and good outcome was substantially altered when adjusted for ischemic core size (fig 1). Outcomes were poor irrespective of ASPECTS in patients with large core lesions while outcomes were generally favorable in patients with a small ischemic core, even with lower ASPECTS. In contrast, the relationship between CTP ischemic core and favorable outcome was not altered when adjusted for ASPECTS (pre-ASPECTS aOR: 0.75 (0.67-0.84), p<0.001 vs post-ASPECTS aOR: 0.75 (0.67-0.85), p<0.001) (fig 2).

Conclusions

ASPECTS association with clinical outcome after EVT was strongly modified by ischemic core volumes as determined by RAPID CTP thresholds. Favorable outcomes were achieved in patients with small ischemic core volume despite low ASPECTS.

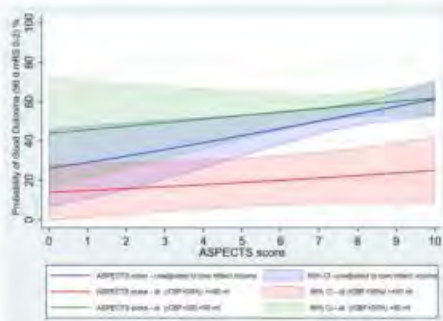
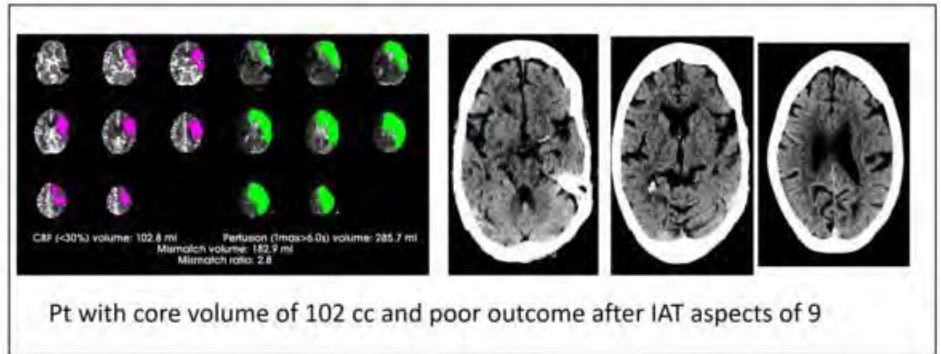


Figure 1. Probability of good outcome by CT ASPECTS unadjusted and adjusted to ischemic core volume, shows that probability of good outcome by ASPECTS score is substantially altered by ischemic core volume, both for small and large cores.



Pt with core volume of 102 cc and poor outcome after IAT aspects of 9

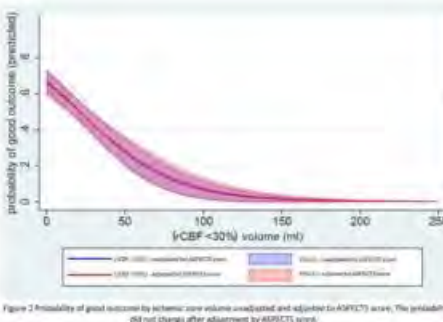
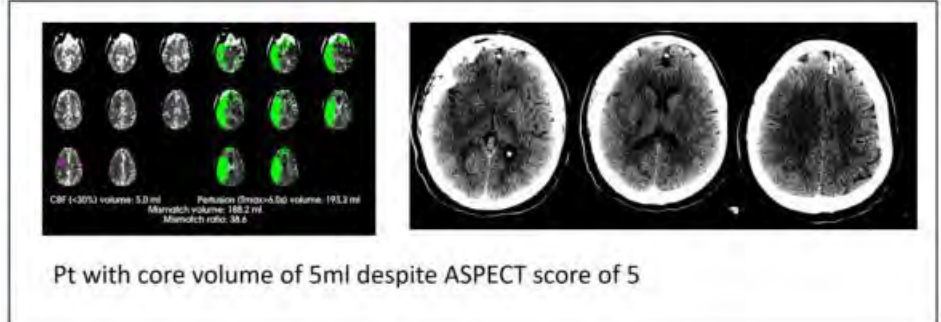


Figure 2. Probability of good outcome by ischemic core volume unadjusted and adjusted to ASPECTS score. The probability did not change after adjustment by ASPECTS score.



Pt with core volume of 5ml despite ASPECT score of 5

(Filename: TCT_302_CTPaspectsllideasn2021.JPG)

614

DCE Perfusion MRI of Meningiomas: Effect of Tumor Characteristics on Blood Brain Barrier Disruption in Subjacent Parenchyma.

S Glynn¹, M Roytman², E Sweeney¹, S Pannullo³, J Ivanidze⁴

¹Weill Cornell Medicine, New York, NY, ²Weill Cornell Medicine/NewYork-Presbyterian Hospital, New York, NY, ³New York-Presbyterian Hospital/Weill Cornell Medicine, New York, NY, ⁴Weill Cornell Medicine Radiology, New York, NY

Purpose

Meningiomas are the most common intracranial neoplasm (1,2). MRI is the gold standard for diagnosis and treatment planning, with PET and perfusion MRI representing adjunct modalities (3-5). Meningiomas express matrix metalloproteinases (MMPs) and other proteins hypothesized to affect the subjacent blood-brain-barrier (BBB), with important pathophysiologic and prognostic implications which are not adequately captured on conventional MRI. We investigated BBB permeability in parenchyma adjacent to meningiomas using dynamic contrast enhanced (DCE) perfusion MRI.

Materials and Methods

IRB approval was obtained. 21 patients with 35 lesions (27 meningiomas and 8 post-treatment change lesions) were enrolled as part of a prospective clinical trial. Patients underwent DCE-MRI according to our clinical protocol, and post-processing of parametric maps including VP, VE, KTRANS, and KEP was performed using Olea Sphere software. On postcontrast T1, regions of interest (ROI) were

placed in the parenchyma adjacent to each lesion and mirrored in the contralateral parenchyma. Wilcoxon matched-pairs signed rank test and 2-way ANOVA with Sidak's multiple comparisons test were performed to compare permeability metrics in meningioma-adjacent and contralateral parenchyma. Parenchyma adjacent to post-treatment change lesions was analyzed in an analogous fashion. To correct for multiple comparisons, a p-value of $p < 0.0083$ was used as the adjusted significance threshold.

Results

Clinical and demographic characteristics are shown in Table 1. Mean KEP and VE in meningioma-adjacent ROI were significantly higher compared to contralateral ROI ($p < 0.001$ and $p = 0.0061$, respectively; Figure 1A). There was no statistically significant difference in posttreatment-change adjacent ROI compared to contralateral ROI (Figure 1B). When stratified by WHO grade, there was higher KEP in WHO-I compared to WHO-II/III -subjacent parenchyma ($p = 0.0478$; Figure 2).

Conclusions

To our knowledge this is the first report evaluating the BBB in meningioma-adjacent brain parenchyma. We found BBB disruption in normal-appearing parenchyma subjacent to meningiomas, and this effect may be more pronounced in lower grade tumors, possibly related to differences in MMP secretion. Limitations include relatively small sample size and lack of long-term follow-up. Our findings may have pathophysiologic implications for meningioma treatment and response assessment.

Table 1. Clinical and demographic characteristics of the study population. *N=27

Characteristics	Study Population (N=21)
Mean Age (years)	58.4 (38-83)
Sex	
Female	15
Male	6
Lesion Type	
Meningioma	27
Post-Treatment Change	8
WHO Grade*	
Grade 1	16
Grade 2	6
Grade 3	2
Presumed	3

Figure 1. Region of interest placement. Representative T1-weighted image and VI parametric map of a 71-year-old man with WHO grade 3 meningioma and corresponding region of interest (ROI) placement.

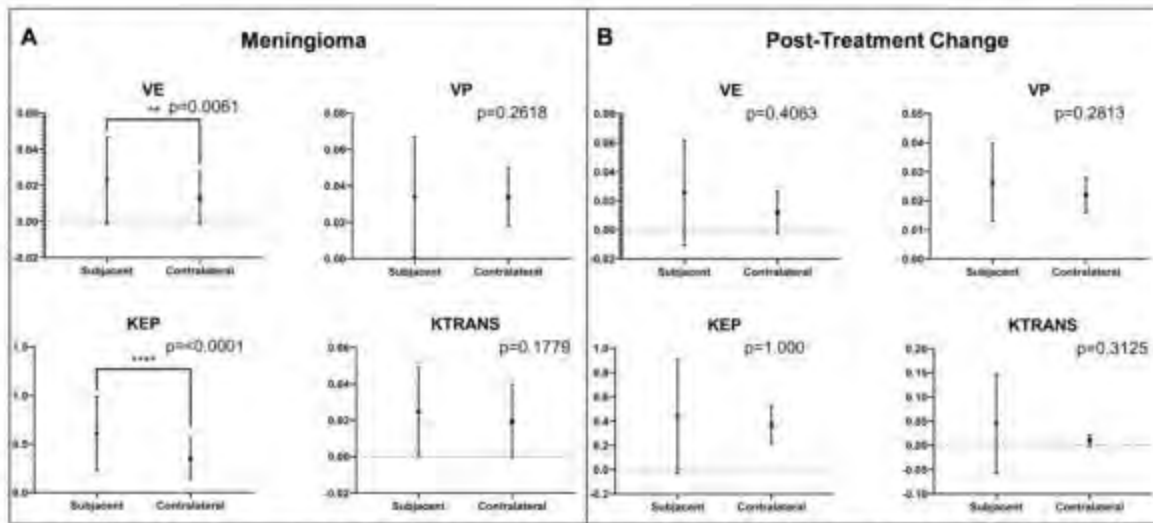
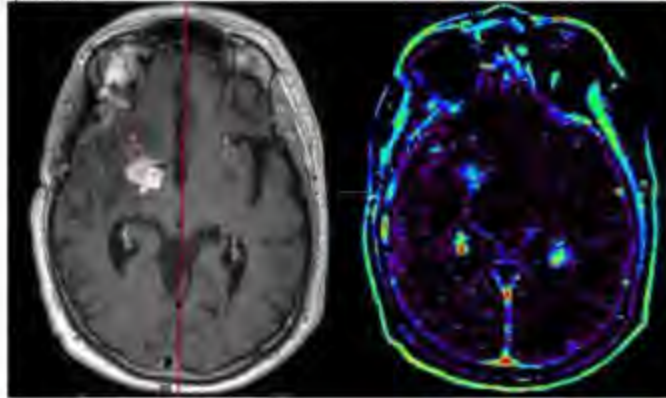


Figure 2. Permeability Parameters of Brain Parenchyma Subjacent and Contralateral to Meningiomas (Panel A) and Post-Treatment Change Lesions (Panel B). Statistical analysis of mean KTRANS (volume transfer constant from the blood plasma to extravascular extracellular space (EES)), KEP (rate of contrast movement from EES into the vasculature), VP (plasmatic volume per unit tissue volume) and VE (volume in the EES per unit of tissue volume) of parenchyma subjacent and contralateral to meningiomas (panel A) and post-treatment change lesions (panel B). Black asterisks indicate statistically significant values.

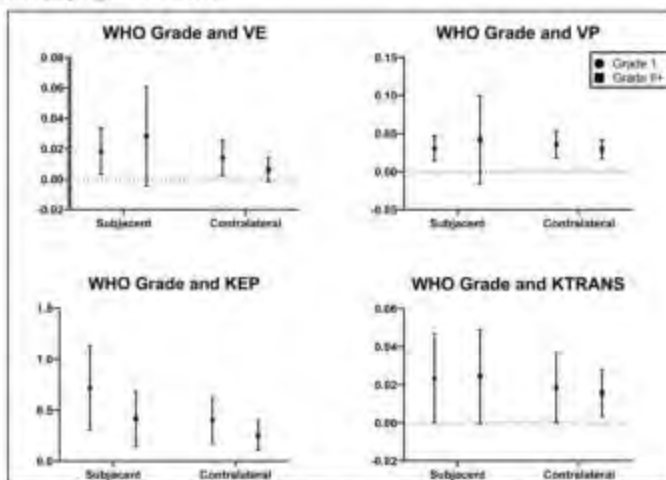


Figure 3. Permeability Parameters of Brain Parenchyma Subjacent and Contralateral to Meningiomas Stratified by WHO Grade. Statistical analysis of mean KTRANS (volume transfer constant from the blood plasma to extravascular extracellular space (EES)), KEP (rate of contrast movement from EES into the vasculature), VP (plasmatic volume per unit tissue volume) and VE (volume in the EES per unit of tissue volume) of parenchyma subjacent and contralateral to meningiomas, stratified by WHO grade.

Decreased rCBV and Permeability at the Margin of the Intracranial Glioblastoma Resection Cavity with GammaTile Implants Placement: A Preliminary Study

X Wang¹, K Ozturk², J Rykken¹

¹University of Minnesota, Minneapolis, MN, ²N/A, N/A

Purpose

GammaTile brachytherapy implants are a novel and FDA approved alternative treatment approach for patients with primary and recurrent brain tumors. It provides surgically targeted radiation therapy that begins working immediately on the residual surrounding tumor cells. Preliminary studies have shown that GammaTile implants exhibited good local control and improved median overall survival. Scant research has been performed on the hemodynamic vascularity changes in proximity to the resection cavity in patients with GammaTile Implants. The current study aims to noninvasively evaluate the rCBV and permeability changes following placement of GammaTile implants using DSC MRI. Similar evaluation was also performed on the patients with recurrent glioblastoma who underwent surgery only but without Gammatile implants.

Materials and Methods

Seventeen patients with recurrent glioblastoma status post-surgery and GammaTile placement were included. Another group of 8 patients with recurrent glioblastoma and surgery who did not have GammaTile implants were also evaluated. The available DSC MR images before and after the surgery with Gammatile placement were reviewed. Location of the implants was recorded.

Results

Figure 1 shows significantly decreased ($p < 0.05$) rCBV at the margin of the resection cavity post-surgery and GammaTile placement (1.54 ± 1.2) compared to the value prior to the intervention (2.25 ± 1.6). There was a qualitative perceived decrease in permeability/leakage at the margin of the resection cavity post-surgery and GammaTile placement in comparison with pre-surgical imaging. Figure 2 demonstrates decreased rCBV while perceivable slightly increased permeability/leakage at the margin of the resection cavity of 3 representative patients with ablation/surgery absent GammaTile placement. Table 2 summarizes the cerebral locations of the glioblastoma in both groups.

Conclusions

It is generally accepted that the microvascular blood volume and vascular permeability correlates significantly with tumor aggressiveness, and increased leakage/permeability is negatively related to overall survival. The decreased rCBV and permeability in proximity to the surgery and GammaTile placement in this preliminary study corroborate the efficacy of this novel and attractive treatment. It also provides further insight into the pathophysiology related to GammaTile implants and a potential mechanism of action, which is by preventing tumoral angiogenesis and altering the surrounding tissue permeability characteristics.

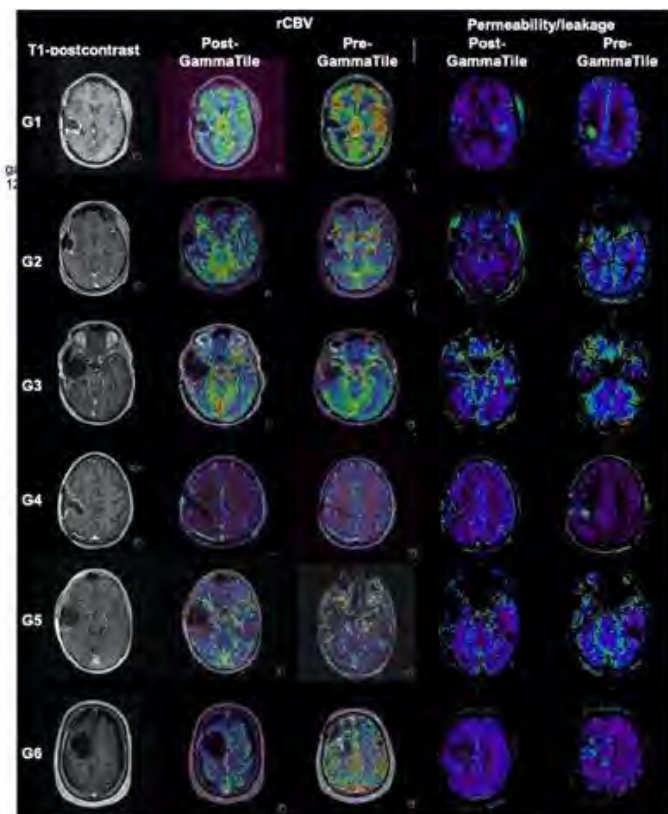


Figure 1 Axial MR post-contrast T1-weighted images of surgery and GammaTile placement, rCBV and permeability/leakage maps of post and pre GammaTile implants placement in 6 representative patients (G1-G6). There is significantly decreased rCBV at the margin of the resection cavity post-surgery and GammaTile placement in comparison with prior to the surgery. Perceivable decreased permeability/leakage at the margin of the resection cavity post surgery and GammaTile placement in comparison with prior to the surgery.

Table 1 Summary of sex and age information of both groups of patients.

	Surgery and Gammatile Implant group	Surgery only group
Number of patients	17	8
Male	13	7
Female	4	1
Age range (years)	36-74	50-69
Mean ± SD (years)	56.2 ±10.3	60.5 ±6.5

(Filename: TCT_234_ASNRnew.jpg)

310

Deep learning can differentiate IDH-mutant from IDH-wild type GBM

L Pasquini¹, A Di Napoli², A Napolitano³, M Lucignani⁴, E Tagliente⁴, F Dellepiane⁵, A Romano⁶, A Holodny⁷, a bozzao⁵
¹Memorial Sloan Kettering Cancer Center, New York, NY, ²Sant'Andrea Hospital, La Sapienza University, Rome, Italy, ³Bambino Gesù Children's Hospital, IRCCS, Rome, Italy, ⁴Bambino Gesù Children's Hospital, IRCCS, Rome, Italy, ⁵Sant'Andrea Hospital, La Sapienza University, Rome, Italy, ⁶Sant'Andrea Hospital, La Sapienza University, Rome, ID, ⁷MEMORIAL SLOAN KETTERING CANCER CENTER, NEW YORK, NY

Purpose

Mutations of isocitrate dehydrogenase (IDH) are frequent in secondary glioblastoma (GBM) (73%) and rare in primary GBM (3.7%), leading to better prognosis and longer survival. Distinction of IDH mutant and wildtype GBMs may be challenging on MRI, since conventional imaging features show considerable overlap. Previous studies attempted IDH prediction by means of supervised machine learning, with limited suitability in the clinical practice. While few studies employed unsupervised learning in a mixed low/high grade glioma population, a GBM-specific model is still lacking in the literature. Our objective was to develop an automatic model for IDH prediction in GBM by using Convolutional Neural Networks (CNN) on MRI data

Materials and Methods

We included 156 adult patients with pathologically proven GBM. MRI data included: unenhanced T1, T2, FLAIR, enhanced

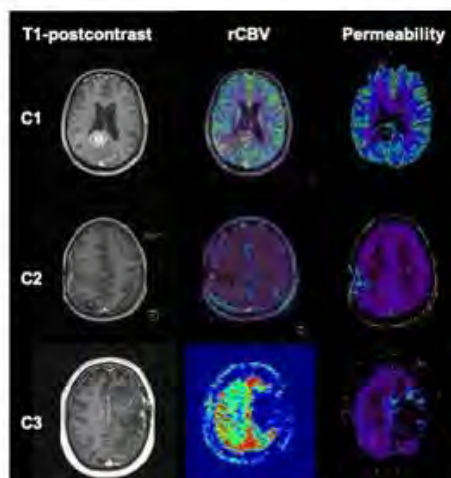


Figure 2 Axial MR post-contrast T1-weighted images, rCBV, permeability/leakage maps of 3 representative patients (C1-C3) with thermal ablation/surgery but without GammaTile implants placement. Interestingly, there is perceivable slightly increased permeability/leakage at the margin of the resection cavity, instead of decreased permeability/leakage identified in the group of patients status post GammaTile implants placement.

Table 2 Intracranial cerebral locations of recurrent glioblastoma of 25 patients.

Locations (lobe)	Numbers
Frontal	11
Temporal	6
Parietooccipital	3
Frontoparietal	2
Temporoparietal	2
Parietal	1

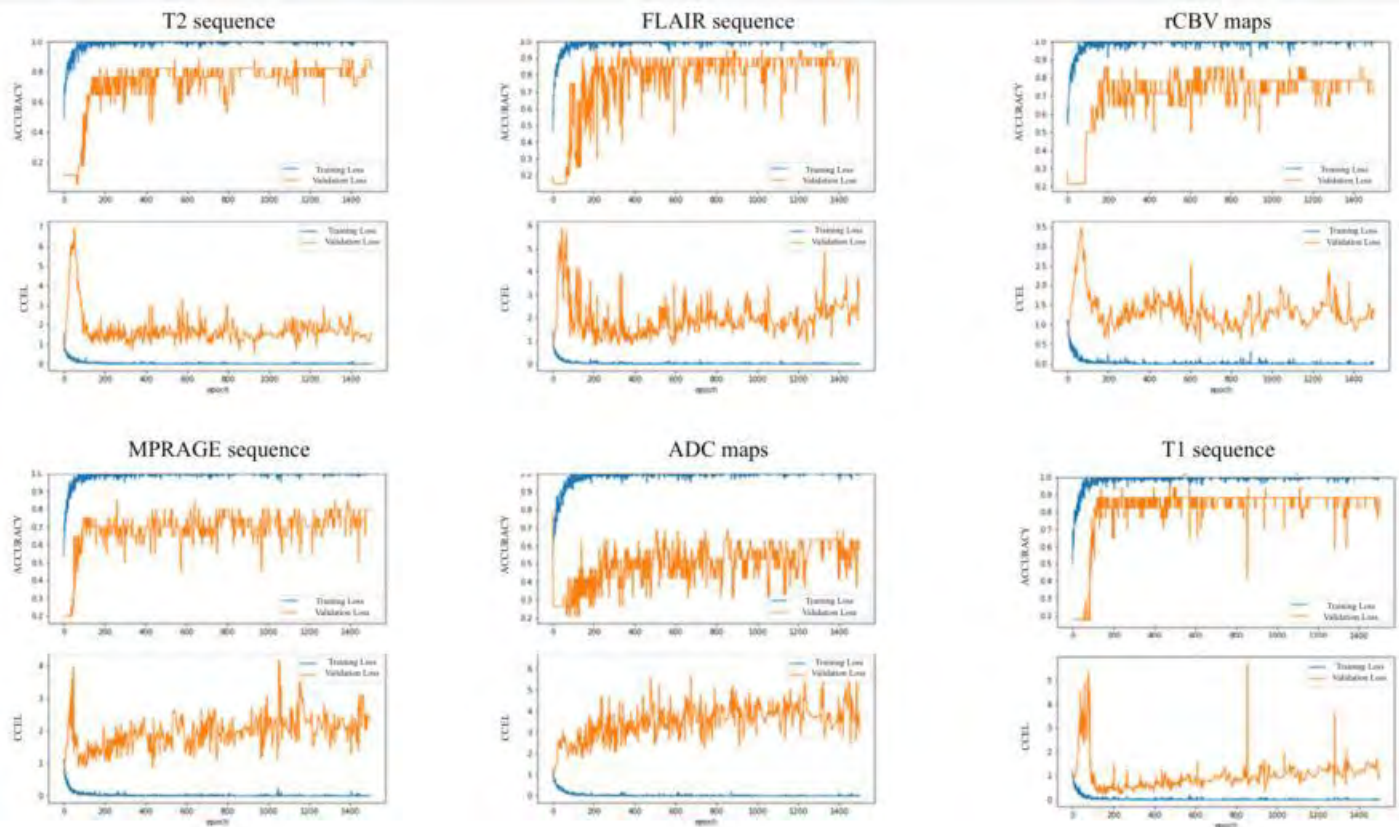
MPRAGE images, rCBV maps from DSC perfusion, ADC maps from DWI. Tumor area was obtained by a bounding box function on the axial slice with widest tumor extension on T2 images and was projected on every sequence. Data was split into training and validation (80:20) sets. Augmentation techniques allowed to fix class unbalance. A 4 block 2D - CNN architecture was implemented for IDH prediction on every MRI sequence. IDH mutation probability of each sample was calculated with softmax activation function from the last dense layer. Categorical cross entropy loss (CCEL) with two output nodes was evaluated on each epoch. Highest performance was calculated by accuracy and CCEL in the validation cohort

Results

To evaluate individual predictive performance, networks were trained for 1500 epochs separately on each MRI sequence. Our model achieved the following performance: T1 (accuracy 82%, AUC 0.8, CCEL 1.12), T2 (accuracy 82.3%, AUC 0.64, CCEL 1.56), FLAIR (accuracy 85%, AUC 0.86, CCEL 3.12), MPRAGE (accuracy 80%, AUC 0.62, CCEL 2.26), rCBV (accuracy 86%, AUC 0.88, CCEL 0.72). ADC achieved lower performance

Conclusions

We built a GBM-tailored deep-learning model for IDH mutation prediction, achieving accuracy of 85% with FLAIR images and 86% with rCBV maps. High predictivity of perfusion images may reflect the correlation between IDH, hypoxia inducible factor (HIF) and neoangiogenesis. The lower performance of ADC may be due to uniform values across GBM or confounding factors such as presence of blood products. The presented model may set a path for non-invasive evaluation of IDH mutation in GBM.



(Filename: TCT_310_Figure_1.jpg)

316

Deep Learning Enables 60% Accelerated Volumetric Brain MRI While Preserving Quantitative Performance – A Prospective, Multicenter, Multireader Trial

S Bash¹, L Wang², C Airriess³, S Dupont⁴, G Zaharchuk⁵, E Gong⁶, T Zhang⁷, A Shankaranarayanan⁴, L Tanenbaum⁸

¹RadNet, Woodland Hills, CA, ²Subtle Medical, Menlo park, CA, ³CorTechs Labs, San Diego, CA, ⁴Subtle Medical Inc, Menlo Park, CA, ⁵Stanford University, Stanford, CA, ⁶Subtle Medical Inc., Menlo Park, CA, ⁷Subtle Medical, Menlo Park, CA, ⁸RadNet, New York, NY

Purpose

In this prospective, multicenter, multireader study, we evaluate the impact on both image quality and quantitative image analysis consistency (NeuroQuant™) of 60% accelerated volumetric MRI scans processed with a commercially available, vendor agnostic, DICOM-based deep learning (DL) tool (SubtleMR™) compared to that of the standard of care (SOC).

Materials and Methods

With IRB approval and patient consent, 40 subjects underwent brain MRI exams on 6 scanners from 5 institutions. SOC and

accelerated (FAST) datasets were acquired for each subject. The FAST scans were then enhanced with DL processing (FAST-DL). Both SOC and FAST-DL were subjected to quantitative volumetric analysis with NeuroQuant™ and classification by a neuroradiologist into clinical disease categories based on results. Quantitative biomarker concordance of SOC and FAST-DL was assessed. To evaluate subjective image quality, randomized, side-by-side, multiplanar datasets (360 series) were presented blinded to 2 neuroradiologists. Images were preference rated on a 5-point Likert scale for apparent signal-to-noise ratio, image sharpness, artifacts, lesion conspicuity, image contrast, and gray-white differentiation.

Results

FAST-DL was statistically superior to SOC for perceived quality across all imaging features despite a 60% scan time reduction (all p-values <0.05). Both FAST-DL and SOC were superior to FAST for all quality features. There was high inter-reader agreement of the Likert image quality ratings between the 2 neuroradiologists. Paired T-test analysis demonstrated excellent agreement of quantitative data between the SOC and FAST-DL datasets. Linear Regression graphs and Bland-Altman plot graph analysis further demonstrated strong concordance in quantitative values across the range of conditions (normal, MCI, Alzheimer's Disease). There was 100% agreement in clinical disease classification for both the SOC and FAST-DL datasets (n=29 normal/MCI and n=11 dementia).

Conclusions

DL reconstruction allows 60% scan time reduction while maintaining high volumetric quantification accuracy, consistent clinical classification, and what radiologists perceive as superior image quality when compared with SOC. This trial supports the reliability, efficiency, and utility of DL based enhancement for quantitative imaging. Shorter scan times may boost utilization of volumetric quantitative MRI in routine clinical settings.

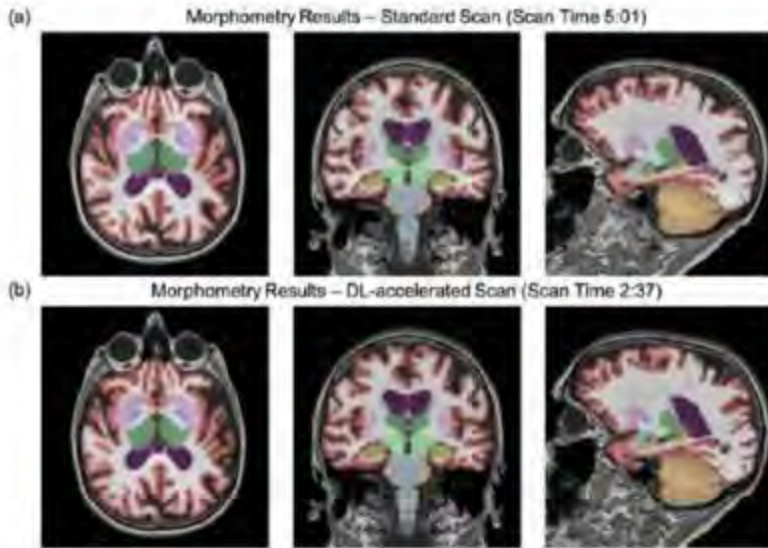


FIG 1. Representative 3D T1W multiplanar images with volumetric segmentation on a 3T scanner. [Left to right]: Axial, coronal, sagittal T1W images with SOC (scan time 5:01 min) on the top row (a) and FAST-DL (scan time 2:37 min) on bottom row (b).

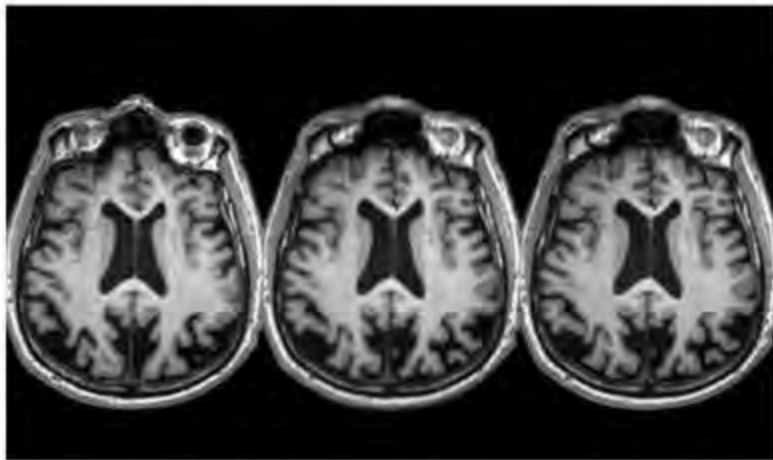


FIG 2. Representative axial 3D T1W images on a 3T scanner. [Left to right]: SOC (scan time 9:13 min), FAST (scan time 4:36 min), FAST-DL (scan time 4:36 min).

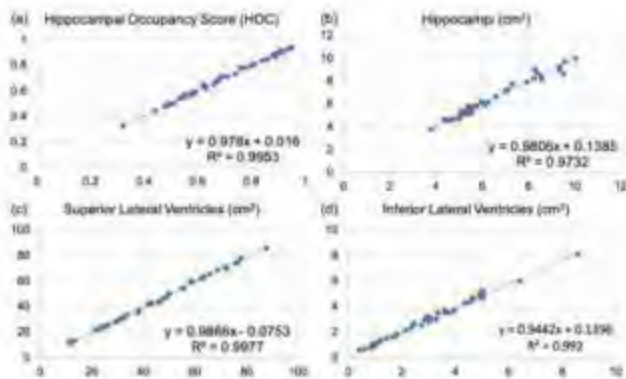


FIG 3. Linear Regression Results. The plot graphs demonstrate linear distribution without scatter, indicating consistent concordance between SOC and FAST-DL in quantitative assessment of HOC, HV, SLV volume and ILV volume.

(Filename: TCT_316_ASNR2021-DementiaAbstractImage.JPG)

Deep Learning Enables Accurate Quantitative Volumetric Analysis in Multiple Sclerosis at 40% Reduction in MR Scan Time – A Prospective, Multicenter, Multireader Trial

S Bash¹, H Gandhi², E Gong³, G Zaharchuk⁴, T Zhang⁵, A Shankaranarayanan⁶, L Tanenbaum⁷

¹RadNet, Woodland Hills, CA, ²Subtle Medical, Menlo park, CA, ³Subtle Medical Inc., Menlo Park, CA, ⁴Stanford University, Stanford, CA, ⁵Subtle Medical, Menlo Park, CA, ⁶Subtle Medical Inc, Menlo Park, CA, ⁷RadNet, New York, NY

Purpose

In this prospective, multicenter, multireader study, we evaluate the impact on both image quality and quantitative image analysis consistency of 40% accelerated volumetric MRI scans processed with a commercially available, vendor agnostic, DICOM-based deep learning (DL) tool (SubtleMR™) compared to that of the standard of care (SOC).

Materials and Methods

With IRB approval and patient consent, 22 subjects with multiple sclerosis underwent brain MRI exams. SOC and accelerated (FAST) datasets were acquired for each subject. The FAST scans were then enhanced with DL processing (FAST-DL). Both SOC and FAST-DL datasets were then post-processed using 2 different commercially available quantitative volumetric analysis tools (LesionQuant™ and icobrain™) for volumetric interrogation of plaque burden, whole brain, cortical gray matter, white matter, and thalami. Concordance of volumetric measurements was independently assessed for the SOC and FAST-DL datasets with both LesionQuant and icobrain. To evaluate subjective image quality, randomized, side-by-side, multiplanar datasets (198 paired series) were blindly presented to 2 neuroradiologists. Images were preference rated on a 5-point Likert scale for apparent signal-to-noise ratio, image sharpness, artifacts, lesion conspicuity, image contrast, and gray-white differentiation.

Results

FAST-DL was statistically superior to SOC for perceived quality across all imaging features despite a 40% scan time reduction (all p-values <0.05). Both FAST-DL and SOC were superior to FAST for all quality features. There was high inter-reader agreement of the Likert image quality ratings between the 2 neuroradiologists. Paired T-test analysis demonstrated excellent agreement of quantitative data between the SOC and FAST-DL datasets for both LesionQuant and icobrain. Linear Regression graphs and Bland-Altman plot graph analysis further demonstrated strong concordance in quantitative values.

Conclusions

DL reconstruction allows a boost in perceived image quality despite 40% scan time reduction while maintaining high volumetric quantitative accuracy in the evaluation of intracranial plaque burden and other regional anatomy across two independent commercially available quantitative tools. This study supports the reliability, generalizability, and efficiency of DL based enhancement for quantitative imaging.

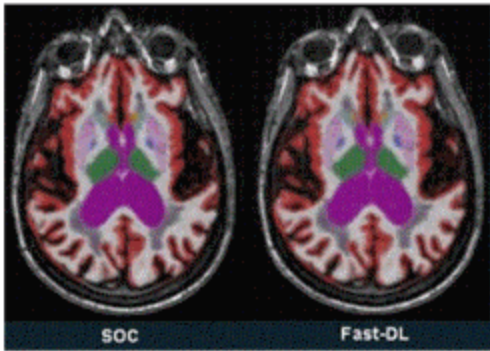


FIG 1. NeuroQuant™ axial 3D T1 segmentation of substructures of the brain [Left/right: SOC/FAST-DL].

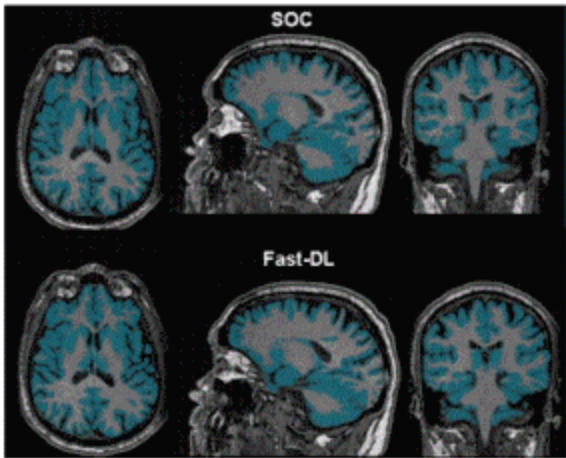


FIG 2. IcoBrain™ multiplanar 3D T1 segmentation of gray matter [Top/bottom: SOC/FAST-DL].

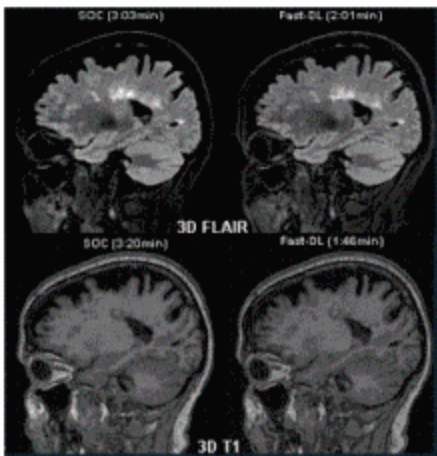


FIG 3. SubtleMR™ [Left/right: SOC/FAST-DL] [Top/bottom: 3D FLAIR/3D T1].

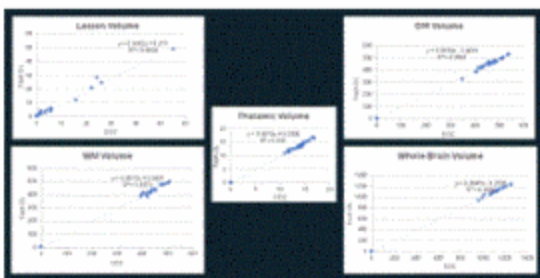


FIG 4. Linear Regression Results for quantitative volumetric concordance of SOC and FAST-DL datasets.

(Filename: TCT_343_Figs.GIF)

Deep learning improves the analysis of low-dose contrast-enhanced brain MRIs in neuro-oncology

S AMMARI¹, A Bône², L Dercle³, M Elhaik¹, E Chouzenoux⁴, C Balleysguier¹, J LAMARQUE¹, E Moulton⁵, P Robert⁵, E TALAB⁶, F Nicolas⁷, M Rohé⁸, N LASSAU¹

¹GUSTAVE ROUSSY CANCER CAMPUS, villejuif, FRANCE, ²Guerbet Research, Paris, Île-de-France, ³Columbia University Irving Medical Center New York, United States, NEW YORK, NY, ⁴Center for Visual Computing, CentraleSupélec, Inria Saclay, Université Paris-Saclay, Gif-sur-Yvette, Gif-sur-Yvette, FM, ⁵Guerbet Research, France, villepinte, villepinte, ⁶IGR, Paris, France, ⁷Guerbet Research, France, Villepine, Villepine, ⁸Guerbet Research, France, Villepinte, Villepinte

Purpose

Over three decades, gadolinium chelates have become almost unavoidable in neuro-oncology. If gadolinium-based contrast agents are considered safe, recent studies have shown evidence of their deposition and role in nephrogenic systemic fibrosis, fueling a growing interest for alternatives to standard injections at 0.1 mmol/kg. In these lines, this work proposes and evaluates a deep learning method able to synthesize brain contrast-enhanced T1-weighted (T1ce) MRIs from multiparametric scans obtained after a quarter-dose (0.025 mmol/kg) injection at most.

Materials and Methods

T1, Flair, diffusion, quarter-dose T1ce (low-T1ce) and standard-dose T1ce (ref-T1ce) sequences were acquired during 200 MRI exams of patients with mixed conditions. Our deep learning model was trained, using data from 150 exams, to synthesize a virtual image (vir-T1ce) as close as possible to ref-T1ce from all other imaging modalities. The model was then evaluated on 50 remaining exams: tumor regions on vir-T1ce and low-T1ce are analyzed in sub-regions by two radiologists (one expert and one trainee). The reference for sensitivity and false discovery rate were consensus tumor regions on ref-T1ce diagnosed jointly by both radiologists. Endpoints were to evaluate if vir-T1ce significantly outperformed low-T1ce in terms of sensitivity and false discovery rates, in nested evaluation configurations where only lesions larger than 0, 5, 7.5, 10, 15, 20 and 40 millimeters were successively considered.

Results

Out of 84 masses diagnosed on ref-T1ce, a significantly higher proportion was identified on vir-T1ce than on low-T1ce (60.1% versus 43.5%, $p=0.0001$). The rate of false positive finding was significantly higher for vir-T1ce than for low-T1ce (28.4% versus 12.0%, $p=0.004$). For both vir-T1ce and low-T1ce, no significant differences in the number or size of detected masses were found between examiners. Detection metrics improved when only larger lesions are considered. At the 7.5, 10 and 15 millimeters thresholds, the sensitivity for vir-T1ce remained significantly higher than for low-T1ce, but no statistical difference was found in terms of false discovery rate.

Conclusions

Our deep learning model significantly improves the lesion detection sensitivity when reading low-dose contrast-enhanced brain MRIs. Small lesions remain however difficult to identify, and small false positives are created. Future studies should evaluate the performance of our deep learning method on more homogeneous subgroups of patients.

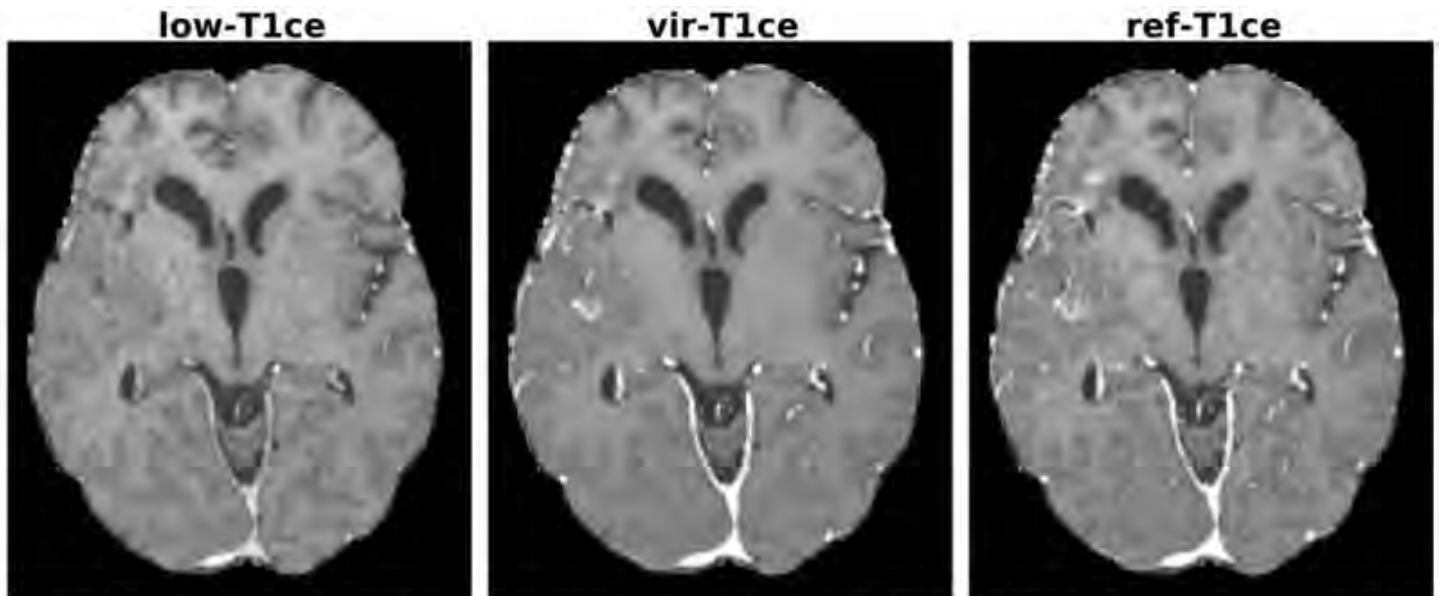


Figure 1: Example axial slices from corresponding low-dose (low-T1ce), virtual (vir-T1ce) and reference (ref-T1ce) contrast-enhanced T1 (T1ce) images. These images respectively play the role of input, output, and ground-truth for our deep learning method. The two first images are obtained after a quarter-dose injection of contrast agent at 0.025 mmol/kg, when the last one is obtained after a standard 0.1 mmol/kg injection.

Lesions	N	Size (mm)	Sensitivity (%)			False discovery rate (%)		
			low	vir	vir vs. low	low	vir	vir vs. low
All ($\geq 2.8\text{mm}$)	84	13.8 (std = 12.4)	43.5	<u>60.1</u>	$CI_{95} = [+8.5, +24.8]$ $p = 1.05 \cdot 10^{-4}$ [***]	<u>12.0</u>	28.4	$CI_{95} = [+5.1, +27.5]$ $p = 4.47 \cdot 10^{-3}$ [**]
$\geq 5\text{mm}$	66	16.4 (std = 12.7)	55.3	<u>73.5</u>	$CI_{95} = [+8.6, +24.8]$ $p = 3.21 \cdot 10^{-4}$ [***]	<u>12.0</u>	26.0	$CI_{95} = [+2.8, +25.0]$ $p = 1.41 \cdot 10^{-2}$ [*]
$\geq 7.5\text{mm}$	50	19.7 (std = 13.0)	65.0	<u>87.0</u>	$CI_{95} = [+10.1, +33.9]$ $p = 5.17 \cdot 10^{-4}$ [***]	<u>11.0</u>	18.7	$CI_{95} = [-3.1, +18.6]$ $p = 1.62 \cdot 10^{-1}$ [Ø]
$\geq 10\text{mm}$	43	21.5 (std = 13.2)	69.8	<u>87.2</u>	$CI_{95} = [+5.4, +29.5]$ $p = 5.60 \cdot 10^{-3}$ [**]	10.4	<u>8.5</u>	$CI_{95} = [-11.5, +7.6]$ $p = 6.93 \cdot 10^{-1}$ [Ø]
$\geq 15\text{mm}$	25	27.9 (std = 14.1)	74.0	<u>90.0</u>	$CI_{95} = [+0.6, +31.4]$ $p = 4.29 \cdot 10^{-2}$ [*]	5.1	<u>0.0</u>	$CI_{95} = [-11.7, +1.5]$ $p = 1.27 \cdot 10^{-1}$ [Ø]
$\geq 20\text{mm}$	17	33.0 (std = 14.5)	88.2	<u>97.1</u>	$CI_{95} = [-7.5, +25.2]$ $p = 2.69 \cdot 10^{-1}$ [Ø]	3.2	<u>0.0</u>	$CI_{95} = [-9.5, +3.0]$ $p = 3.06 \cdot 10^{-1}$ [Ø]
$\geq 40\text{mm}$	3	45.3 (std = 15.7)	<u>100.</u>	<u>100.</u>	$CI_{95} = [0, 0]$	<u>0.0</u>	<u>0.0</u>	$CI_{95} = [0, 0]$

Table 1: Average sensitivity and false discovery rate, in nested evaluation configurations where only lesions larger than some threshold (for their major axis) are considered. Best average metrics are in bold, and are further underlined if significantly different from their counterpart. Paired and unpaired t-tests are used for sensitivity and false discovery rate respectively. Confidence intervals at 95% and p-values are also reported. The symbols [Ø], [*], [**], [***] respectively denote the absence, or the 0.05, 0.01, 0.001 levels of significance.

(Filename: TCT_702_2020_10_22_ASNR21.jpg)

952

Deep learning models to automate the labelling of brain MRI datasets

D Wood¹, S Kafiabadi², A Al Busaidi³, E Guilhem⁴, J Lynch⁴, M Townend⁵, A Montvila⁴, N Gadapa⁴, M Kiik¹, G Barker¹, S Ourselin⁶, J Cole⁷, T Booth⁸

¹King's College London, London, UK, ²King's College Hospital NHS Foundation Trust, London, London, ³N/A, N/A, ⁴King's College Hospital, London, UK, ⁵Wrightington, Wigan & Leigh NHSFT, London, UK, ⁶King's College London, London, London, ⁷University College London, London, UK, ⁸Kings College London, London, London

Purpose

Deep learning is poised to revolutionize image recognition tasks in radiology. For MRI, a rate-limiting step to clinical adoption is the difficulty obtaining sufficiently large labelled datasets for model training. The purpose of this study was to automate dataset labelling by building a natural language processing (NLP) model to derive labels from neuroradiology reports and assign these labels to the corresponding MRI head scans at scale. We sought to validate the model by comparing labels predicted from reports with those generated on the basis of manual inspection of images by neuroradiologists.

Materials and Methods

In this retrospective study, 126,556 MRI images and radiology reports were obtained. Using pre-determined criteria, reference standard report and image labels were generated by a team of six neuroradiologists for model training and validation: 3000 reports and 250 images were labelled for the presence or absence of any abnormality; 2000 reports and 700 images were labelled for the presence or absence of 7 specialised categories of abnormality (acute stroke, mass, atrophy, vascular abnormality, small vessel disease, white matter inflammation, damage). A deep learning NLP model was trained on a subset of labelled reports and validated in two ways: comparing predicted labels to (i) reference standard report labels; and (ii) reference standard image labels. The area under the receiver operating characteristic curve (AUC) was used to quantify model performance. Accuracy, sensitivity and specificity were also reported.

Results

The model classified examinations as normal or abnormal with an AUC of 0.973 (reference standard image label evaluation). For 4 of the 7 specialised categories of abnormality the model achieved an image label AUC > 0.95. Once trained, the model assigned accurate labels to 121,556 images in under 30 minutes.

Conclusions

Our deep learning model can automate the labelling of large-scale MRI datasets for downstream computer vision model development.

827

Deep learning pharmacokinetic mapping of dynamic contrast enhanced perfusion MRI in recurrent glioblastoma

J Kim¹, M Bredel¹, B Nabors¹

¹University of Alabama at Birmingham, Birmingham, AL

Purpose

Dynamic contrast enhanced perfusion (DCE) MRI allows quantitative analysis of tumor vascularity, useful to evaluate biological activity of the recurrent GBM. Pharmacokinetic parameters (i.e. permeability [K_{trans}], extracellular volume fraction [V_e], and vascular volume fraction [V_p]) of DCE-MRI are most commonly calculated with nonlinear fitting of extended Tofts model [1], which is inherently ill-posed inversion problem and computationally expensive. We hypothesized a deep learning encoder model with convolutional neural network (CNN) can reliably estimate tracer kinetic parameters from noisy DCE-MRI data.

Materials and Methods

An in-house software written in Python-based deep learning framework (Keras with TensorFlow backend), and a Linux PC equipped with single GPU (NVIDIA RTX 2080 Ti) were used. We generated a Monte-Carlo simulated numerical phantom as training data set that consisted of synthetic concentration-time curves (n = 200,000) derived from Tofts-Kety tracer kinetic model with Orton arterial input function [2]. Ranges of random model parameter were predefined to emulate three different tissue conditions (i.e. tumor, normal and vessel). We built an 1D CNN model that encodes DCE time series data to 4 output parameters (contrast bolus arrival time, K_{trans}, V_e, and V_p). The model was constituted of concatenated 1D convolutional layer and 4 fully connected layers of feed forward neural network with leaky-ReLU and sigmoid activations. Adam algorithm was used for training optimization of neural network. Using trained model, tracer kinetic parameters of patient DCE-MRI were predicted. MRI (n=19) of recurrent GBM downloaded from "RIDER Neuro MRI" collection of the Cancer Imaging Archive (<https://wiki.cancerimagingarchive.net>) were used in this study. Output parameter maps were qualitatively analyzed and compared with those processed with Bayesian model fitting framework in Fabber software [3].

Results

Training and validation of the CNN model took approximately 45 min. Total parameter prediction time for whole brain (> 200,000 voxels) was less than 7 min. CNN-based method provided reliable parameter estimation, less susceptible to noise contamination compared to Fabber software.

Conclusions

Our proof-of-concept work demonstrated validity of CNN-based DCE-MRI analysis method capable of fast and robust tracer kinetic parameter mapping. This study lays the groundwork for further development of fully automated post-processing paradigm for DCE perfusion streamlined within clinical workflow.

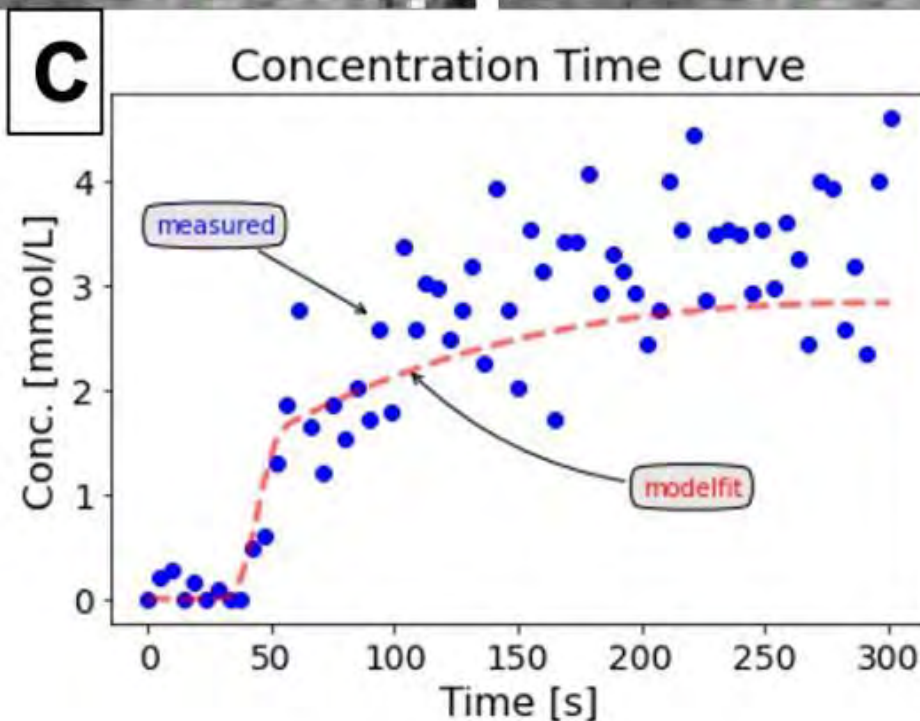
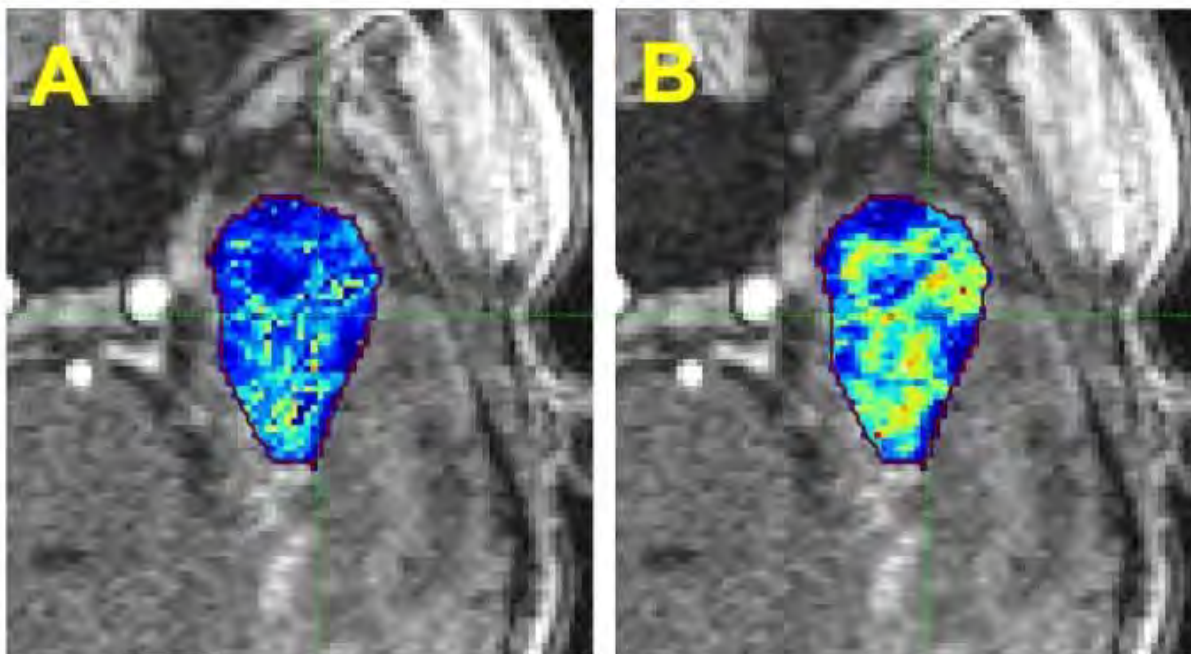


Fig. Example K^{trans} maps of DCE-MRI in recurrent GBM, processed with Bayesian model fitting software (A), proposed CNN-method (B) and predicted model fitting at single voxel (C).

(Filename: TCT_827_Picture1.jpg)

1505

Deep Learning tumor segmentation of metabolic images from Super-resolution MR Spectroscopic Imaging in Mutant IDH Glioma patients

U Neuberger¹, P Vollmuth¹, F Isensee², X Li³, B Strasser³, D Cahill⁴, J Dietrich⁵, M Bendszus⁶, O Andronesi⁷

¹University Hospital Heidelberg, Heidelberg, BW, ²German Cancer Research Center, Heidelberg, BW, ³Martinos Center for Biomedical Imaging, Boston, MA, ⁴MGH, Boston, MA, ⁵Massachusetts General Hospital, Boston, MA, ⁶University of Heidelberg, Heidelberg, WY, ⁷Massachusetts General Hospital, Harvard Medical School, Boston, MA

Purpose

To develop automated deep learning tumor segmentation of metabolic images obtained by super-resolution MR spectroscopic imaging (MRSI) in patients with mutant IDH glioma.

Materials and Methods

Mutant IDH1 glioma patients (n = 10) were scanned on a 3T MR scanner with a whole brain 3D MRSI protocol optimized for 2-hydroxyglutarate (2HG) detection using FOV=240x240x120 mm³ and matrix 46x46x10. The acquired low resolution MRSI metabolic maps were upsampled by a factor of 4 from an in-plane pixel size of 5.2x5.2 mm² to 1.3x1.3 mm² using a super-resolution method based on total variation and feature based non-local means [1]. Ground-truth segmentations of metabolic alterations were prepared using a semi-automatic region-growing segmentation method implemented in ITK-SNAP (www.itksnap.org). A U-Net convolutional neural network was trained on the super-resolution metabolic maps to delineate metabolic alterations in the tumor region of i) 2HG, glutamate and glutamine (HGG) and ii) total choline and n-Acetyl-aspartic acid (TCN) with a total of n = 20 metabolic maps using stratified 5-fold cross-validation [2]. The performance of the U-Net was evaluated calculating DICE coefficients and by comparing the intensity values of the ground truth masks and the segmentations created by the U-Net.

Results

Testing of the U-Net segmentations yielded an overall Dice coefficient of 0.90 (95% CI 0.87 – 0.94) (see Fig. 1). The mean intensity of the U-Net segmentations was not significantly different from the median intensity of the ground truth masks for both TCN (0.67 ± 0.32 vs. 0.76 ± 0.33 , $p = 0.5226$) and HGG (1.85 ± 0.30 vs. 1.96 ± 0.35 , $p = 0.4018$) maps (see Fig. 1).

Conclusions

Our results indicate that deep learning convolutional networks can be used for automated high-throughput and robust segmentation of metabolic images obtained by MRSI. Delineating tumor margins and measuring tumor volumes are important for treatment planning and the assessment of treatment response and can be augmented by including metabolic changes. Advances in MRSI to obtain high quality metabolic maps will improve the robustness of deep learning segmentation methods. The proposed methods might have great clinical potential for neuro-oncology, neuro-surgery and neuro-radiotherapy applications.

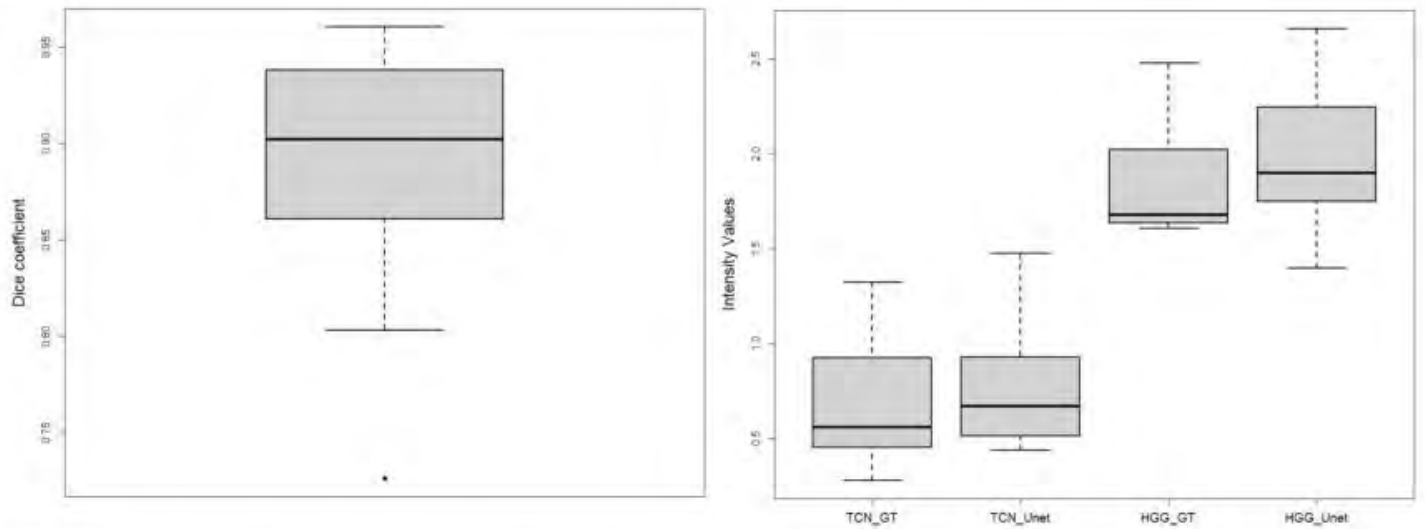
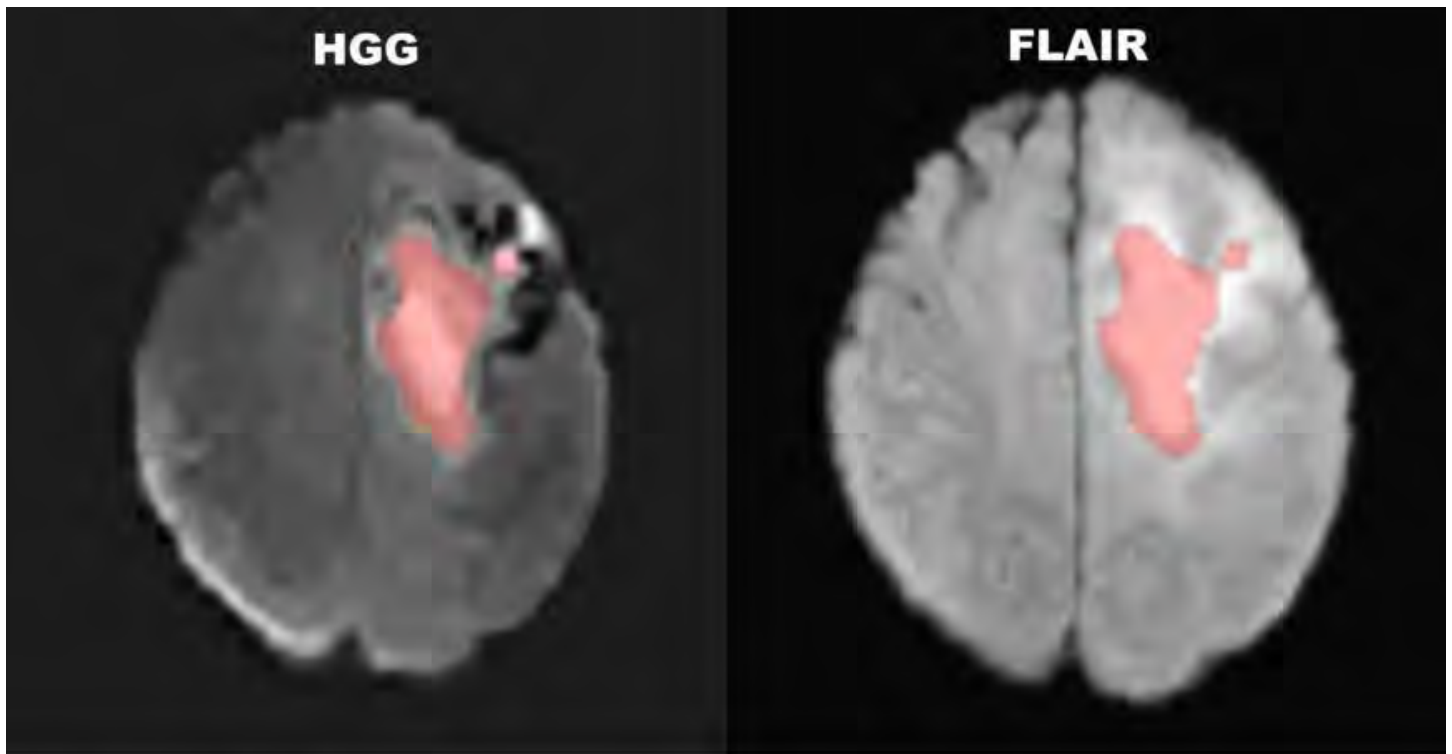


Figure 1:
 Top: HGG metabolic map with superimposed ground truth mask (left) and FLAIR image with superimposed segmentation of the Unet (right).
 Bottom: Boxplot of DICE coefficients of the segmentations produced by the Unet (left) and boxplots of intensity values of respective segmentation masks for the ground truth (GT) and the Unet (right).

(Filename: TCT_1505_Figure1_300dpi.jpg)

968

Deep Neural Network Analysis of CT Scans to Predict Outcomes in a Prospective Database of Severe Traumatic Brain Injury Patients

M Pease¹, A Dooman¹, D Okonkwo¹, S Wu¹
¹UPMC, Pittsburgh, PA

Purpose

Traumatic Brain Injury (TBI) is the leading cause of death and disability in young adults worldwide. Physicians and other validated

models predict long-term outcomes with only moderate success. Models such as IMPACT are designed to guide clinical trial design and are not intended to guide clinical decision-making. Machine Learning (ML) models identify abnormalities in radiographic images with a high degree of accuracy. We applied ML models to CT scans and clinical information from severe TBI to predict mortality. **Materials and Methods**

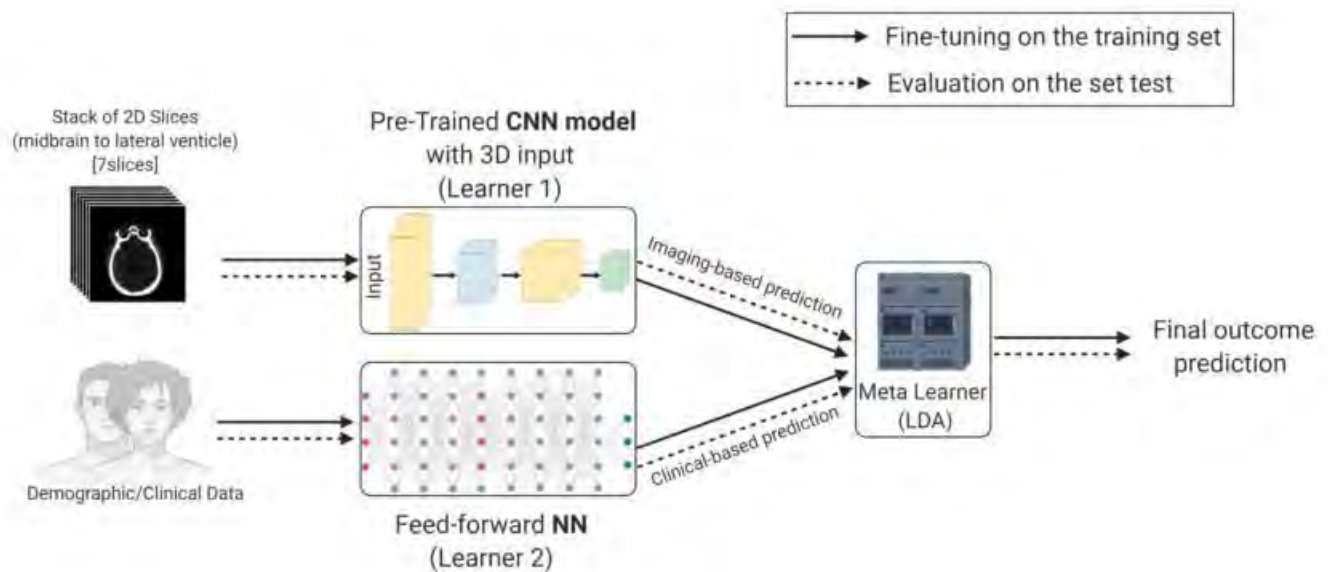
537 severe TBI patients from a prospectively collected database at a single institution from 2002-2018 had a CT scan prior to neurosurgical intervention and complete clinical information. We applied transfer learning and 3D convolutional neural network (CNN) to build a model using CT scans for mortality and unfavorable outcomes prediction. The CNN model was trained using a novel method to compensate for different CT head reconstruction filter kernels. The cohort was chronologically split into 70%, 10%, and 20% for training, validation, and independent test cohorts.

Results

The CNN model using CT scans alone predicted mortality in the independent test cohort with an AUC of 0.86 (95% CI: 0.72-0.91) and accuracy of 83%. For unfavorable outcomes, the AUC was 0.83 (95% CI: 0.72-0.91) with an accuracy of 81%. For the combined clinical and imaging model, the model's predictions for mortality (AUC 0.91; accuracy 88%; p<0.001) and unfavorable outcomes (AUC 0.90; accuracy 85%; p=0.01) were superior to IMPACT.

Conclusions

Deep learning CNN models of head CT scans predicted mortality outcome following severe TBI with a high degree of accuracy.



(Filename: TCT_968_ASNR.jpg)

1353

DeepResection: Automated Segmentation of Postoperative Epilepsy Imaging

R Muthukrishnan¹, T Arnold¹, A Gibson¹, K Davis¹, J Stein², B Litt¹

¹University of Pennsylvania, Philadelphia, PA, ²N/A, N/A

Purpose

To demonstrate a deep learning method for segmenting resections in postoperative MRI and the applications of this tool to epilepsy patient care.

Materials and Methods

Clinical (3T) T1 brain MR images (N=47) were collected from temporal lobe epilepsy patients that underwent resective surgery at the Hospital of the University of Pennsylvania (HUP). Resection sites were manually segmented in ITK-SNAP and reviewed by a neuroradiologist (JMS). A U-Net convolutional neural network (EfficientNet B1 backbone) was trained to segment surgical lesions in axial slices from these images. We performed a 5-fold cross-validation, where algorithm performance was assessed using the Dice-Sørensen coefficient (DSC) and quantified volume differences between manual and algorithmic segmentations. Finally, we developed an automated image processing pipeline that compares the resection segmentation to available preoperative anatomical labels, lesion segmentations or electrode locations to generate a custom report of resected regions and targets, such as the hippocampus (Figure 1).

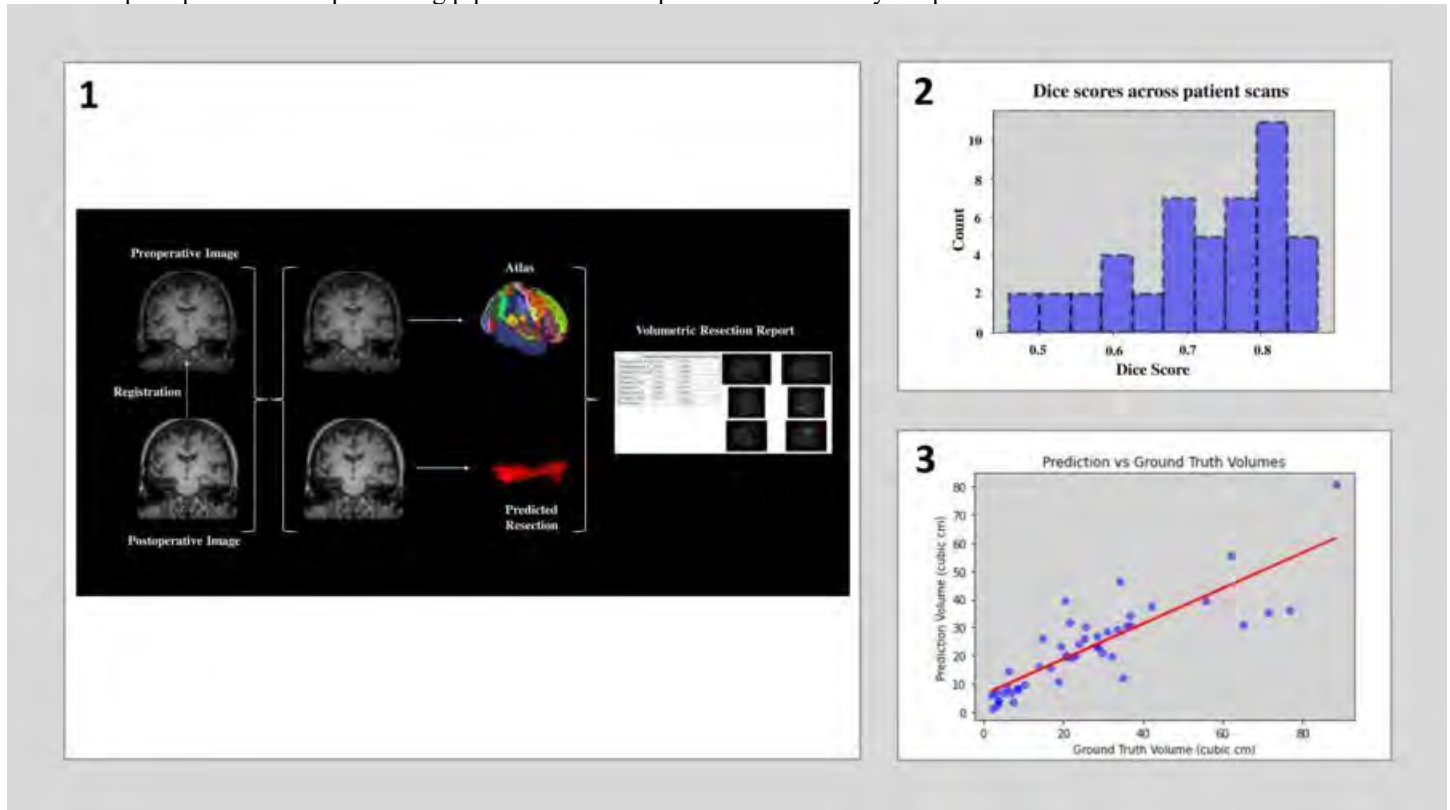
Results

Algorithm performance was measured using the Dice-Sørensen coefficient (DSC), a standard metric for image segmentation models that measures overlap between the ground truth and predicted labels. The average DSC per scan was 0.72 ± 0.11 (Figure 2),

comparable to the mean DSC for similar public segmentation challenges [BraTS 2013 (N = 65): 0.71-0.87, BraTS 2018 (N = 542): 0.80-0.88]. On average, predicted volumes were slightly lower than ground truth volumes with a strong correlation between the two volumes ($R^2 = 0.85$, Figure 3). There were 2 failure cases which involved under-segmentation of particularly large temporal lobe resections. Example outputs defining the hippocampal remnant are also presented.

Conclusions

In this study, a deep learning model was developed to segment temporal lobe resections with comparable overall performance to algorithms developed for other brain segmentation tasks. The model's performance supports its potential for incorporation in fully automated postoperative MRI processing pipelines and examples of clinical utility are provided.



(Filename: TCT_1353_figures.jpg)

673

Detecting Concurrent Bilateral Optic Neuritis with the Aid of an Image Post-processing Algorithm

A Schroeder¹, A Sharma², R Eldaya³, M Parsons², F Ofikwu², P Mazaheri², H Orlowski²

¹Washington University School of Medicine, St. Louis, MO, ²Mallinckrodt Institute of Radiology, St. Louis, MO, ³Mallinckrodt Institute of Radiology, St Louis, MO

Purpose

Identifying bilateral optic neuritis on MRI is difficult due to the symmetric nature of disease and relative inability to diagnose based on differences in locally paired structures. The purpose of this study was to test if an image-processing algorithm, previously shown to effectively detect unilateral disease, could be used to improve the diagnostic performance of radiologists in detecting bilateral optic neuritis.

Materials and Methods

In this retrospective case control study of 50 patients (30 controls and 20 cases bilateral optic neuritis, 41.4 +/- 22.1 yrs, 25M, 25F), coronal T2/FLAIR and CE-T1WI were processed with a proprietary algorithm designed to accentuate diseased optic nerves. Masked reviews of baseline and processed images were performed by 2 radiology residents, 2 neuroradiology fellows, and 2 neuroradiology attendings. Readers rated each nerve for presence of abnormal signal or enhancement on a 5-point Likert scale ranging from 1 (definitely normal) to 5 (definitely abnormal). The effect of processing on confidence rating and diagnostic performance was evaluated. Inter-observer reliability was assessed for each reader experience level.

Results

The algorithm accentuated 23/26 diseased nerves on FLAIR and 27/40 on CE-T1WI. There were no instances of accentuation in the control group. Confidence ratings increased in the diseased population after processing with the median (25th, 75th percentile) ratings increasing from 3.1 (2.4, 3.8) to 4.2 (3.8, 4.8) on FLAIR, and from 3.2 (2.5, 4.7) to 3.9 (1.2, 4.4) on CE-T1WI. Corresponding values for controls decreased from 2.0 (1.7, 2.3) to 1.3 (1.1, 1.7). Sensitivity improved from 45.5% to 77.6% on FLAIR and from 56.7% to

63.3% on CE-T1WI. Specificity improved from 87.2% to 96.2% for FLAIR and from 82.5% to 99.2% for CE T1WI. Interobserver agreement generally improved for all levels of training post-processing.

Conclusions

With selective accentuation of signal intensity of diseased optic nerves, image processing resulted in improved confidence of readers in identifying diseased and normal optic nerves, translating into an improved sensitivity, specificity, PPV, NPV, and inter-observer reliability.

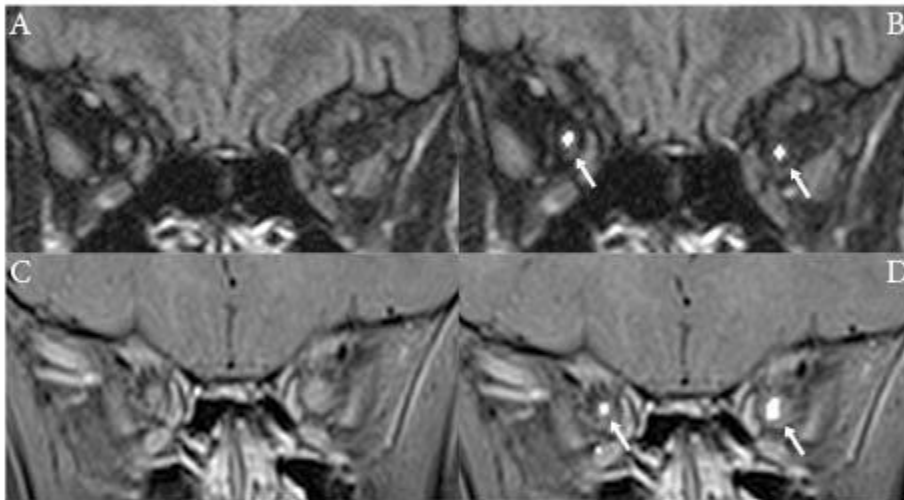


Figure 1. Representative coronal fat-saturated FLAIR (A,B) and coronal contrast-enhanced T1WI (C,D) from two different patients with concurrent bilateral optic neuritis before (A, C) and after (B, D) processing show accentuation of optic nerve signal intensity. In masked reads by 6 readers, detection rates of right (left) optic neuritis improved from 2 to 5 (4 to 5) on FLAIR and 2 to 5 (5, unchanged) on contrast-enhanced images.

Detection of microhemorrhages and enhancement in the wall of unruptured intracranial aneurysms on 3T MRI as predictors of increased rupture risk in patients presenting with sentinel headaches

P Gupta¹, S Kannath¹, B Thomas¹, K Chandrasekharan¹

¹Sree Chitra Tirunal Institute of Medical Sciences & Technology, Trivandrum, Kerala

Purpose

Characteristic presentation of patients with unruptured intracranial aneurysms is warning leak or sentinel headache (SH) due to a minor bleed in the wall of the aneurysm. Susceptibility weighted (SWI) MR imaging can show microbleeds in the wall of these aneurysms. Vessel wall imaging (VWI) may show variable wall enhancement correlated pathologically with wall inflammation. These sequences when independently evaluated provide a partial glimpse of cognates of pathological events in wall. We hypothesized that combination of VW MRI and SWI would be more informative to assess the changes in the wall of aneurysm in patients with sentinel headache and predict the future risk of rupture of the aneurysm.

Materials and Methods

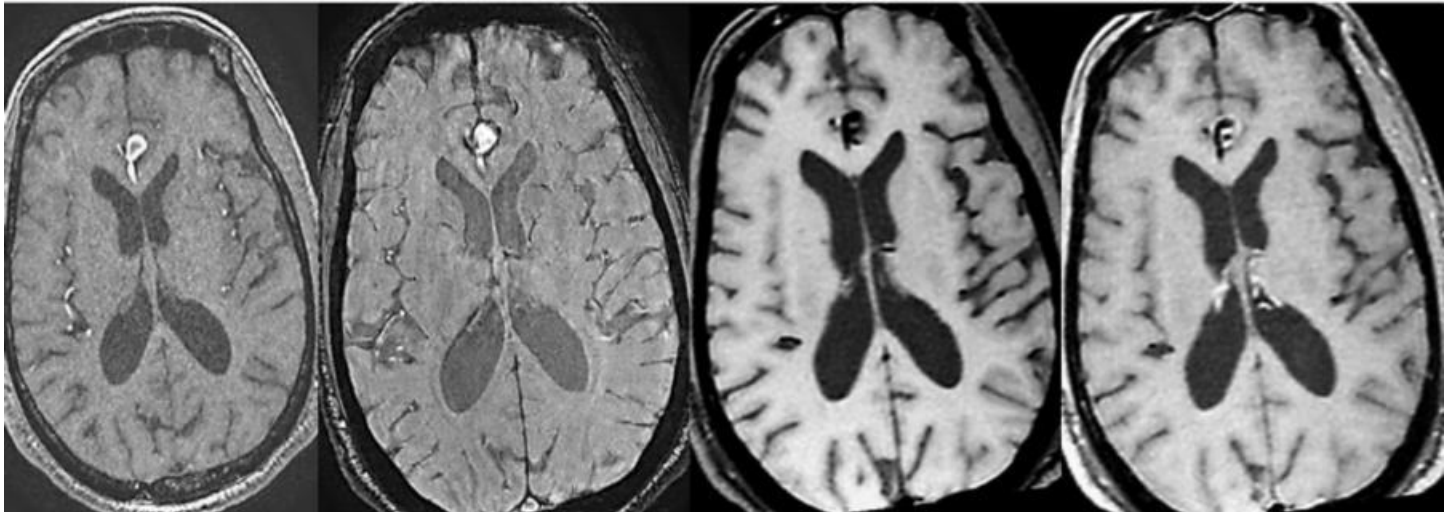
The SWI sequences and vessel wall imaging on MRI in patients of unruptured intracranial aneurysms presenting with sentinel headache can show microbleeds and inflammatory changes in the wall of the aneurysms and thus predict the future risk of rupture of the aneurysm.

Results

7 patients of intracranial aneurysms with history of SH underwent advanced MR imaging. SWI images were evaluated for presence of any hypointensity suggestive of microbleeds along the wall of aneurysm. The post contrast vessel wall images were evaluated for presence of any enhancement along the wall of the aneurysm.

Conclusions

Susceptibility foci on SWI in the wall was seen in all the 7 aneurysms suggestive of microbleeds. VWI showed enhancement of wall in 5 cases and nonenhancement in two cases. Enhancement was observed in all aneurysms imaged early after sentinel headache. However, one of the aneurysms which was imaged at 6 months showed presence of strong eccentric enhancement. This patient had 2 additional episodes of severe headache after 2 and 3 months of the sentinel headache Conclusion: Advanced MR imaging in patients with intracranial aneurysms presenting with sentinel headache can detect microhaemorrhages in the wall of the aneurysm which are indicative of minor bleeds occurring in the wall which may increase future risk of rebleed/rupture. Also, enhancement of the wall of the aneurysm is indicative of an active inflammatory process. Both these findings were present in the wall of aneurysms in our study in patients presenting with sentinel headache when MR imaging was done early. These findings are predictive of ongoing pathological changes occurring in the aneurysmal wall which place these aneurysms at increased risk of rupture and thus can help us plan an early intervention in these cases.



(Filename: TCT_757_Picture1.jpg)

388

Determining MGMT Promoter Methylation Status in Brain Gliomas Using MRI and Deep Learning

C BANGALORE YOGANANDA¹, B Shah², S Nalawade³, F Yu⁴, G Murugesan³, M Pinho³, B Wagner³, B Mickey⁴, T Patel⁵, B Fei⁶, A Madhuranthakam⁴, J Maldjian²

¹UNIVERSITY OF TEXAS SOUTHWESTERN MEDICAL CENTER, DALLAS, TX, ²N/A, N/A, ³University of Texas Southwestern Medical Center, Dallas, TX, ⁴UT Southwestern Medical Center, Dallas, TX, ⁵The University of Texas Southwestern Medical Center, Dallas, TX, ⁶UT Dallas, Richardson, TX

Purpose

To develop a highly accurate, fully automated deep-learning 3D network to determine the MGMT promoter methylation status using T2w images only.

Materials and Methods

Multi-contrast MR Images of brain glioma patients were obtained from the TCIA database. The corresponding genomic information was obtained from both the TCGA and TCIA databases. The datasets were screened for the availability of preoperative T2w MR images and known MGMT promoter status. The final dataset consisted of 247 subjects (163 methylated cases & 84 unmethylated cases). Tumor masks for 179 cases were available through previous expert segmentation. Tumor masks for the remaining 68 cases were generated by our previously trained 3D-IDH network & were reviewed by 2 neuroradiologists for accuracy. These tumor masks were used as ground truth for tumor segmentation in the training step. Ground truth whole tumor masks for methylated & unmethylated MGMT promoter type were labelled with 1s & 2s respectively. Data preprocessing steps included co-registration, skull stripping, N4BiasCorrection, & intensity normalization to zero-mean & unit variance. To determine the MGMT promoter status, Transfer learning was implemented using our previously trained 3D-IDH network. The decoder part of the network was fine-tuned for a voxelwise dual-class segmentation of the whole tumor with Classes 1 & 2, representing methylated & unmethylated MGMT promoter type respectively. To evaluate the generalizability of the network, a 3-fold cross validation was implemented. The dataset (247 subjects) was randomly shuffled & distributed into 3 equal groups. The 3 groups were alternated between training, in-training validation, & held-out testing groups such that each fold of the cross-validation procedure was a new training phase based on a unique combination of the 3 groups.

Results

The network achieved a mean cross-validation testing accuracy of 94.73% across the 3 folds (95.12%, 93.98%, & 95.12%, std dev=0.66). Mean cross-validation sensitivity, specificity, PPV, NPV & AUC for MGMT-net was 96.31% \pm 0.04, 91.66% \pm 2.06, 95.74% \pm 0.95, 92.76% \pm 0.15 & 0.93 \pm 0.03 respectively. The mean cross-validation Dice-score for tumor segmentation was 0.82 \pm 0.008.

Conclusions

We demonstrate high accuracy in determining MGMT promoter methylation status using only T2-w MR images that approaches that of invasive tissue-based molecular testing. This represents an important milestone toward using MRI to predict glioma histology, prognosis, and appropriate treatment.

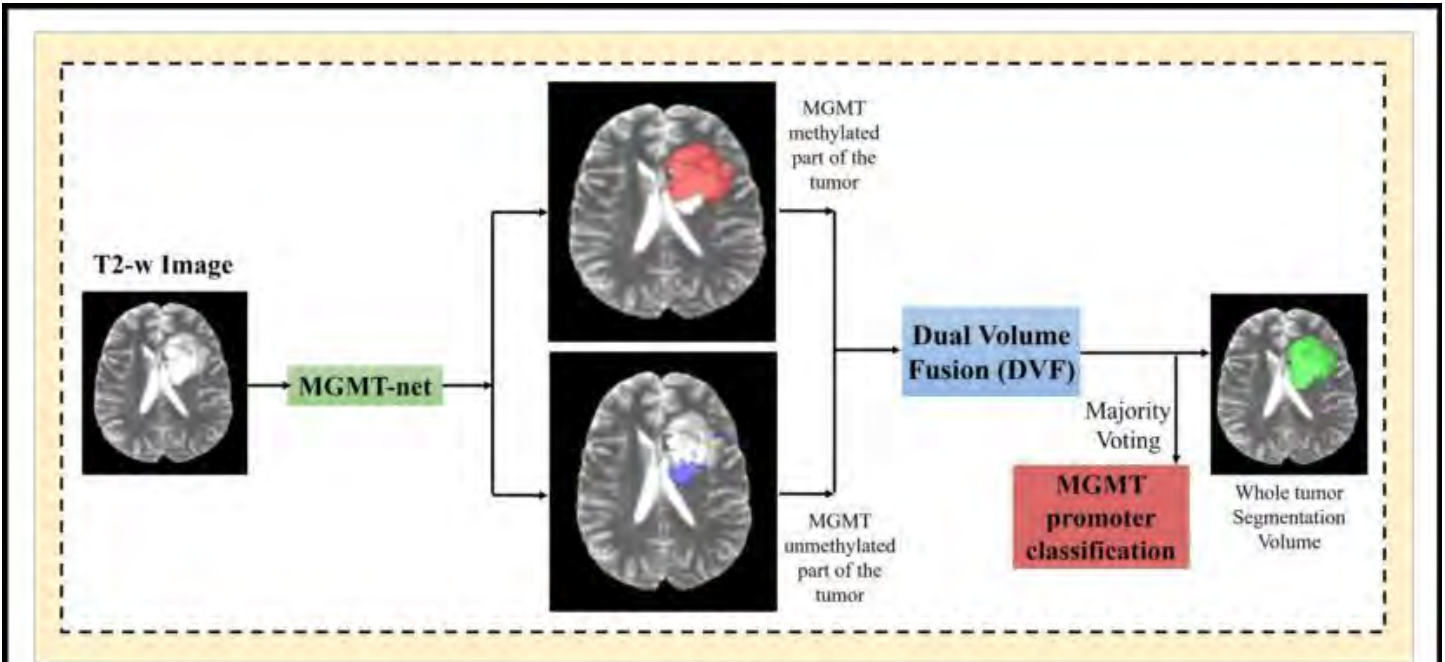


Figure 1: MGMT-net overview.

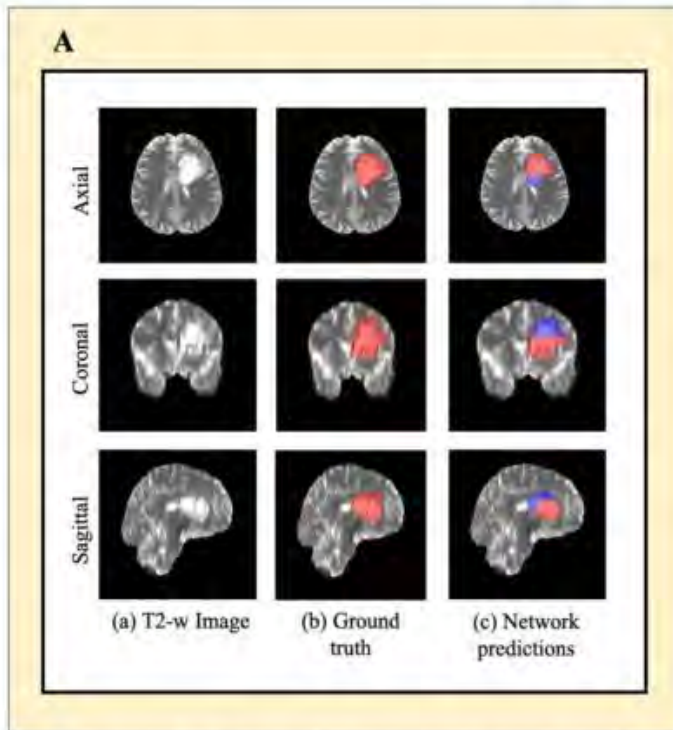


Figure 2: Example segmentation result

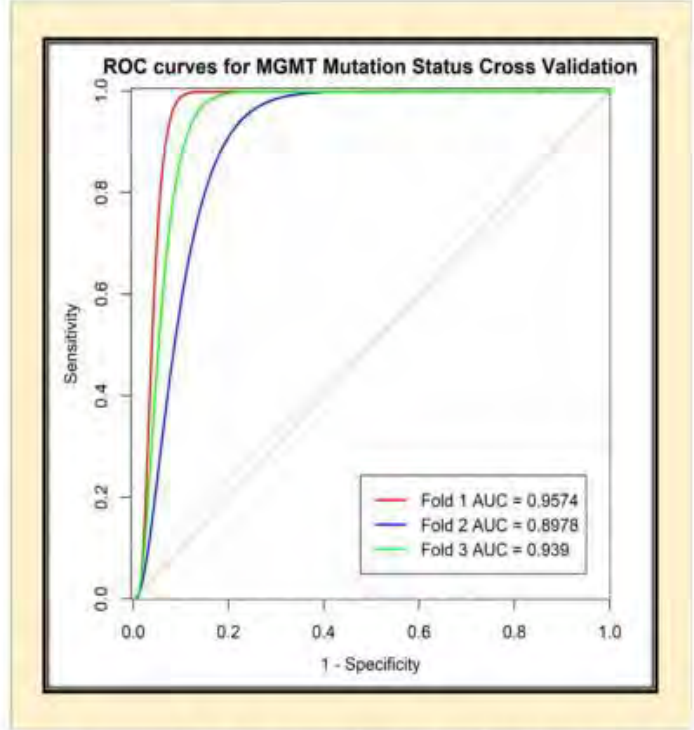


Figure 3: ROC analysis for MGMT-net

(Filename: TCT_388_Picture1.jpg)

Determining the Significance of Incidental Imaging Signs of Intracranial Hypertension with Corresponding Fundus Photography: A Prospective Study

A SAINDANE¹, B Meyer², B Chen², B Bruce², N Newman², V Biousse²
¹Emory University, Atlanta, GA, ²Emory University School of Medicine, Atlanta, GA

Purpose

MRI signs suggesting intracranial hypertension are common in patients with idiopathic intracranial hypertension (IIH), but also incidentally detected in asymptomatic patients and those with primary headache syndromes, prompting neuro-ophthalmology consultations and investigations (1-3). We aimed to prospectively identify the prevalence and significance of MRI signs of intracranial hypertension (MRI-IH) in patients imaged for any clinical indication.

Materials and Methods

Consecutive patients undergoing clinically-indicated outpatient brain MRI completed non-mydriatic fundus photography immediately following MRI, which were interpreted for papilledema. MRIs followed protocols tailored towards the clinical indication and were reviewed by a subspecialty certified neuroradiologist for signs of MRI-IH (2). Univariate analysis with Fisher's exact test or t-test was performed.

Results

296 consecutive MRI were completed for assessment of brain neoplasm (27.7%), multiple sclerosis (MS) and MS-mimics (18.6%), seizure (17.9%), headache (8.8%), and other non-headache neurologic symptoms (19.6%). Four patients (1.4%) had known IIH. MRI-IH (N; %) included: empty sella (98; 33.1%); enlarged Meckel cave (47, 15.9%); meningocele/cephalocele (4, 1.4%); transverse venous sinus stenosis (TSS) (7/198, 3.6%); scleral flattening (2, 0.7%); increased perioptic CSF (32, 10.8%); and increased optic nerve tortuosity (23, 7.8%). Overall, 51% patients exhibited no MRI-IH, 32.8% one sign, 10.8% two signs, 3.7% three signs, and 1.7% had ≥ 4 signs. Five patients (1.7%) had definite papilledema and two (0.7%) had questionable papilledema. Patients with definite papilledema had significantly increased average BMI (37.6 vs 27.5 kg/m²; P=0.038), history of IIH (40% vs 1%; P=0.001), increased optic nerve tortuosity (60% vs 7%; P=0.004), TSS (50% vs 3%; P=0.006), and ≥ 4 MRI-IH (40% vs 1%; P=0.002), compared to patients without papilledema. Other MRI-IH were not significant, nor were having one, two, or three signs.

Conclusions

MRI signs of intracranial hypertension were frequently encountered in almost half the patients in this prospective study. However, definite papilledema was only detected in 1.7% patients, questioning the need to perform systematic investigations for patients with incidentally detected MRI-IH.

403

Development of a Neck CT Anatomy Measurements Reference Dataset to Assist in the Design of Novel Transoral Thyroidectomy Instruments

R Nowrouzi¹, I Chong¹, Y Gao¹, B Crovetti¹, D Guffey¹, R Grogan¹, F Moron¹

¹Baylor College of Medicine, Houston, TX

Purpose

Neck anatomy varies widely depending on factors such as age, gender, race, ethnicity, and body mass index (BMI) (1,2). Currently, there are no reference datasets of standardized anthropometric measurements of the neck in the adult population (3). Transoral Endoscopic Thyroidectomy Vestibular Approach (TOETVA) surgery is a new surgical modality that allows for thyroidectomies to be performed without visible scars (4). Given its novelty, no surgical instruments have been specifically created for this procedure (5). Our aims are to create a Computed Tomography (CT) based neck anthropometric reference data set of TOETVA relevant neck anatomy and to measure population level variation in neck anatomy. This dataset will assist in the design of novel surgical instruments for TOETVA.

Materials and Methods

Patients who underwent contrast enhanced neck CT at Baylor College of Medicine (BCM) during the past 7 years and at Ben Taub Hospital (BTH) from January 2020 through July 2020 were retrospectively studied. Exclusion criteria included a history of neck surgery or head and neck cancer, age <18 years, incomplete demographic information, and inadequate image quality. Demographic information was collected from the electronic health record. 18 separate neck anatomic measurements were made. Demographics and CT measurements were correlated using pairwise Pearson's correlation. K-means 2-cluster analysis was used to aid in Wilcoxon analysis.

Results

The selection criteria yielded 458 patients: 192 from BCM and 266 from BTH (Table 1). Most of the 18 CT measurements followed a normal distribution (Figure 1). BMI and weight correlated strongly with CT measurements (Figure 2). K-means cluster analysis revealed significant BMI and weight differences between clusters (p<0.05). Analysis also revealed significant differences among most CT measurements between the 2 clusters (Figure 3).

Conclusions

Our results yielded the first adult reference dataset on neck anatomy to date. Statistical analysis of this dataset found a normal data distribution, which indicates the possibility of developing a single set of novel standardized instruments that would suit most patients. The possible benefit of a second set of instruments for obese individuals or a more versatile set of instruments should be investigated, since BMI significantly varied by cluster analysis. These novel instruments are needed to improve TOETVA surgical approach performance and outcomes.

		N total	N (%)
Gender	F	458	279 (60.9)
	M	458	179 (39.1)
Ethnicity	Hispanic	458	185 (40.4)
	Non-Hispanic	458	273 (59.6)
Race	African-American	458	84 (18.3)
	Hispanic	458	160 (34.9)
	Other	458	38 (8.3)
	White	458	176 (38.4)
BMI	Underweight	458	18 (3.9)
	Normal	458	131 (28.6)
	Overweight	458	139 (30.3)
	Obese	458	170 (37.1)

Table 1. Demographic and CT measurement information.

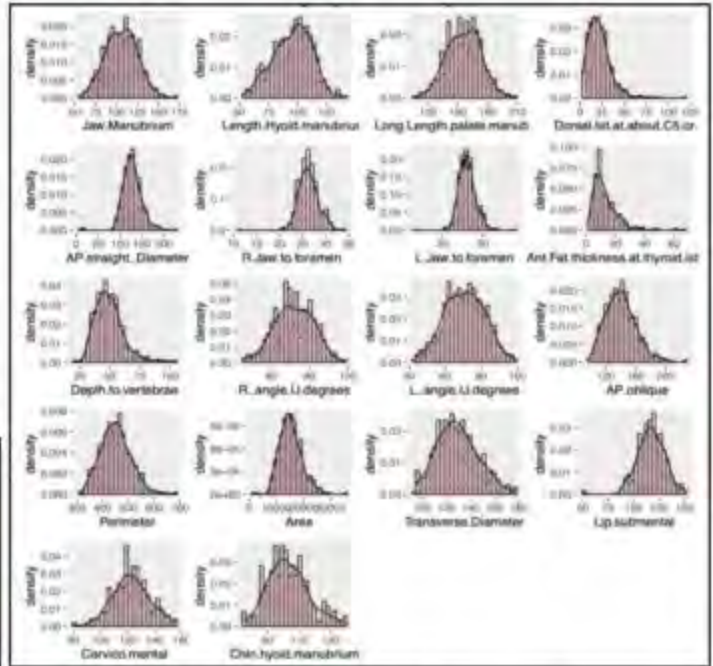


Figure 1. Histograms of the 18 CT measurements. Most CT measurements demonstrated normal distributions.

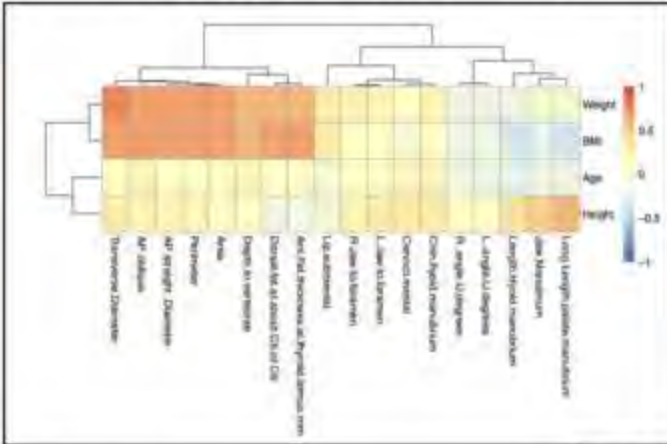


Figure 2. Heatmap showing Pearson correlation coefficients between CT measurements and continuous Demographic features. Weight and BMI correlated strongly with several CT measurements.

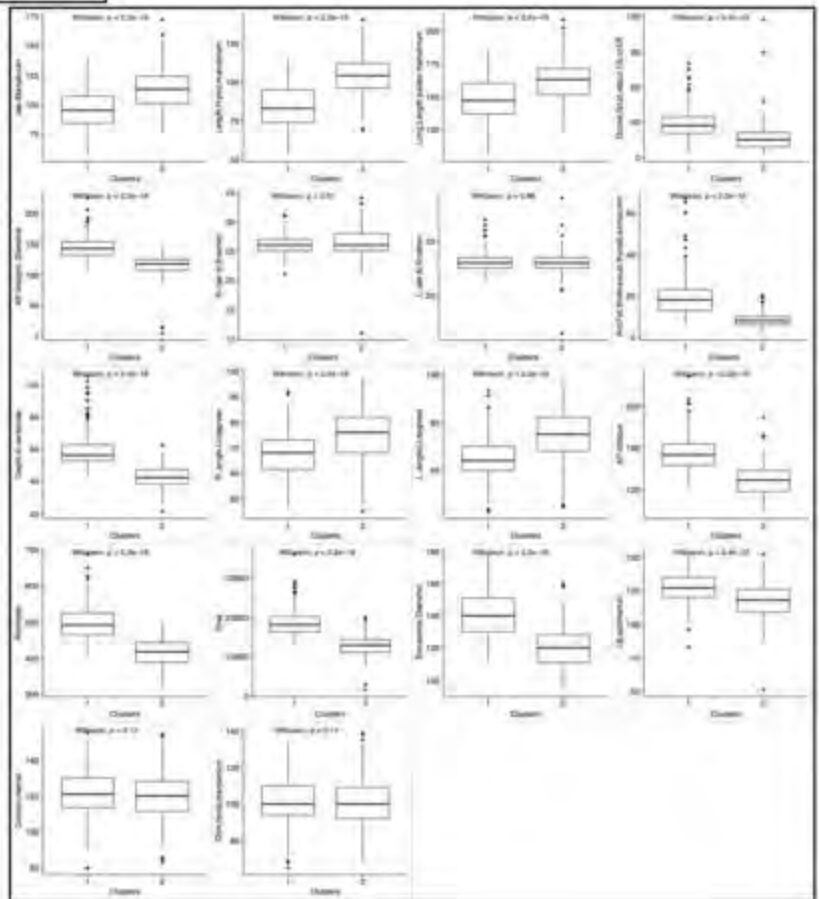


Figure 3. Wilcoxon analysis after k-means 2-cluster analysis. Most of the 18 CT measurements demonstrated significant differences between the 2 clusters.

Development of a Stationary Head Computed Tomography System

Y Lee¹, D Spronk², Y Luo², C Inscoe², J Lu¹, O Zhou²
¹UNC Chapel Hill, Chapel Hill, NC, ²UNC, Chapel Hill, NC

Purpose

Conventional computed tomography (CT) scanners utilize a single x-ray source and wide detector to capture fan-beam images around the body part of interest. CT systems are complex medical devices, and do not stand up well to the environmental conditions in low resource environments. However, the system imaging requirements to diagnose infarcts and hemorrhages in the brain are also some of the most stringent from an x-ray/CT physics perspective. The goal of this study is to develop a stationary head CT system with no moving x-ray sources or detectors. We will utilize carbon nanotube field-emission linear x-ray source arrays combined with linear detector arrays as the basis for system development.

Materials and Methods

Custom simulation software written in a combination of Matlab and Python were developed to explore potential imaging geometries for system development. Simulated hardware geometries were initially evaluated with hardware simulating the final system geometry using CNT linear x-ray source arrays with up to 100 individually addressable sources. An imaging field-of-view of 25 cm and 30 second scan time were targeted for the head scanning. A final system geometry was implemented with 50 cm linear x-ray source arrays and linear detectors. Iterative image reconstruction techniques were developed to account for the limited angle geometry.

Results

A final hexagonal based geometry was selected to maximize angular coverage for the limited angle CT approach. Z-axis coverage was performed through subject translation, similar to conventional CT scanners, representing the only mechanical motion within the system. Imaging dose of the final configuration was approximately one-fifth of conventional head CT, secondary to the limited angle coverage. Full system characterization is ongoing, but anticipated to be similar to portable head CT systems.

Conclusions

A stationary head CT imaging system has been developed based on the CNT linear x-ray source arrays, representing the first stationary x-ray system since the dynamic spatial reconstructor and electron beam CTs. First-in-human evaluation of the system is expected to begin in early 2021.

837

Diagnostic Accuracy of CT Angiography along with CT Perfusion in M2 Occlusions Compared to CT Angiography alone

R Pillenahalli Maheshwarappa¹, G Bathla¹, M Hayakawa², S Priya³, N Soni⁴, C Derdeyn⁵
¹University of Iowa Hospitals and Clinics, Iowa City, IA, ²University of Iowa Hospitals and Clinics, Iowa City, IA, ³University of Iowa hospitals and Clinics, IOWA CITY, IA, ⁴UIHC, Iowa, IA, ⁵University of Iowa Hospitals & Clinics, Iowa City, IA

Purpose

To evaluate the accuracy of CT angiography (CTA) along with CT perfusion (CTP) in diagnosing M2 MCA occlusion compared to CT angiography alone.

Materials and Methods

This is a single center IRB approved retrospective study. The study cohort included 70 patients who had both CT angiography and CT perfusion performed for symptoms of stroke from January 2017 to May 2020. 29 patients had M2 MCA occlusion, 21 had M1 MCA occlusion and 20 patients were normal. The conventional cerebral angiography was used as a reference standard for the M1/M2 occlusion and CTP for normal studies. Two blind readers in the first phase were given only the CTA to read. In the second phase CTA along with CTP was given. The accuracy of CTA alone compared to CTA+CTP to diagnose M2 occlusion was calculated. The time taken for both the phases (CTA alone and CTA + CTP) was also noted.

Results

The average age of the study population was 72 + 28 years, NIHSS was 13 and female to male ratio was 42:28. For Reader 1, the diagnostic accuracy to diagnose M2 occlusion with CTA alone improved from 79% to 93% when CTA + CTP both were used, for Reader 2 it improved from 89% to 97%. The average time taken by Reader 1 to diagnose occlusion improved from 61 seconds when CTA alone was used to 48 sec when both CTA + CTP were used. Similarly, the average time taken by reader 2 improved from 76 seconds with CTA alone to 68 sec when both CTA + CTP were used.

Conclusions

Concurrent use of CTP along with CTA increases the diagnostic accuracy in diagnosing M2 occlusion compared to CTA alone. In addition, there is decreased time taken to find the location of occlusion (normal, M1 and M2) when both CTA and CTP are used.

658

Diagnostic Accuracy of a Deep Learning Algorithm for the Detection of Intracranial Hemorrhage: Implications for Widespread Implementation

A Voter¹, E Meram¹, J Garrett², J Yu¹

¹University of Wisconsin-Madison, Madison, WI, ²UW Madison -Department of Radiology, Madison, WI

Purpose

Artificial intelligence decision support systems are increasingly popular and important tools to support radiologists managing increased imaging volumes. However, these tools have well known limitations, may have difficulty generalizing to different treatment settings, and their performance has not been rigorously evaluated.

Materials and Methods

This retrospective study included 3616 consecutive, emergent non-contrast head CT scans performed between 7/1/2019 and 12/30/2019 at our institution (49% male, ages 17-98, mean age of 62; 51% female, ages 18-105, mean age of 65). Each scan was evaluated for ICH by both a CAQ-certified neuroradiologist and Aidoc. We determined the diagnostic accuracy of Aidoc and performed a failure mode analysis with quantitative CT radiomic image characterization.

Results

Of the 3616 scans, 354 cases of ICH (9.8% of studies) were identified. The neuroradiologist and Aidoc interpretations were concordant in 97.2% of cases and the overall sensitivity, specificity, positive predictive value, and negative predictive value were 92.4%, 97.8%, 81.8% and 98.4%, respectively, with sensitivity and positive predictive values notably lower than in previous studies. Prior neurosurgery, single type of ICH, and male sex were all significantly associated with decreased Aidoc performance. Quantitative image characterization with CT radiomics failed to reveal significant differences between the concordant and discordant studies.

Conclusions

This study revealed decreased diagnostic accuracy of an AI DSS at our institution. Despite extensive evaluation, we were unable to identify the source of this discrepancy, raising concerns about the generalizability of these tools with indeterminate failure modes. These results further highlight the need for standardized study design to allow for rigorous and reproducible site-to-site comparison of emerging deep learning technologies

717

Diagnostic Evaluation of the Posterior Fossa using Antenatal and Postmortem MRI: An Unfolded View

N Gupta¹, C Martinez-Rios², N Barrowman³, D Demellawy³, E Miller³

¹CHEO Univ of Ottawa, Ottawa, Ontario, ²CHEO, Ottawa, Ontario, ³CHEO, Ottawa, Ontario

Purpose

Posterior fossa (PF) malformations are among the most common brain anomalies on antenatal imaging. The role of conventional neuro-autopsy (CNA) is undisputed, but poses difficulty with small, macerated fetuses and increasing parental refusal to autopsy. Alternatively, post-mortem magnetic resonance imaging (PMMRI) is less invasive and an acceptable technique for assessment of the brain. The objective of this study is to evaluate qualitative and quantitative differences of PF on PMMRI, when compared to antenatal MRI (ANMRI).

Materials and Methods

Retrospective, single-center study of ten fetuses referred for ANMRI and PMMRI from August 2010 to May 2018. PMMRI was performed between 0-5 days after termination of pregnancy (TOP). CNA was the gold standard. Fetuses without CNA were excluded. Qualitative evaluation was done to assess the brain abnormalities. Quantitative measurements included the trans cerebellar diameter, vermian length, brainstem thickness, maximum width of fourth ventricle and cisterna magna, skull base angles, and PF volume. All the measurements were evaluated by 2 pediatric neuroradiologists and a pediatric radiology fellow blinded to the clinical information and imaging reports. Statistical analysis evaluated the congruence between ANMRI and PMMRI.

Results

Twenty MRI exams were assessed. The ANMRI median gestational age was 21.7 weeks. The median age at TOP and PMMRI was 23.7 weeks. There was good congruence between ANMRI and PMMRI for qualitative findings further confirmed by CNA, with complete congruence in 50% of cases and 50% with partial congruence, frequently related to the presence of hemorrhage and ventricular dilatation in the PMMRI. No incongruence was noted. Quantitative evaluation in PMMRI compared to ANMRI showed a statistically significant enlargement of brain in the PF with smaller CSF-filled spaces (p-value < 0.05), with the exception of thickness of the medulla. The PF volume, bone to bone PF diameter and clival-supratentorial angle show no statistically significant change (p-value > 0.05).

Conclusions

Traditionally post-mortem diagnosis of fetal brain malformations has been provided by CNA, but the trend is declining due to less parental consent, leading to increase use of PMMRI as a promising alternative. Recognition of expected changes in the PF from altered fluid dynamics after fetal death is paramount, emphasizing the awareness of enlargement of the brain with consequent decrease in size of the surrounding CSF-filled spaces, when reporting PMMRI neuroimaging.

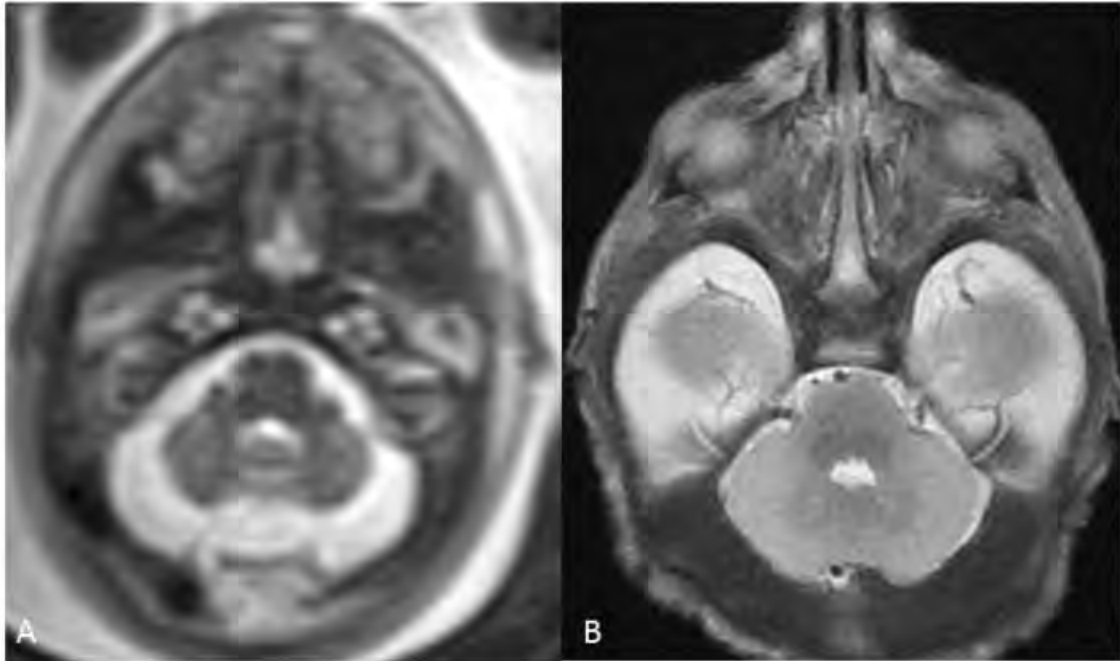


Figure A: ANMRI Axial T2 HASTE of a 27 weeks old fetus with IUGR, trans cerebellar diameter measures 2.1 cm with well defined extra-axial CSF spaces.

Figure B: PMMRI Axial T2 TSE of the posterior fossa of same fetus at 28.5 weeks, show increase in trans cerebellar diameter to 2.7 cm and now effacement of extra-axial CSF spaces

(Filename: TCT_717_ASNR2021ImageFinalGIF.gif)

1257

Diagnostic Performance of a Highly Accelerated Post-Contrast Wave-CAIPI 3D-T1 MPRAGE Compared to Standard 3D-T1 MPRAGE for Detection of Intracranial Enhancing Lesions on 3T MRI

A Goncalves Filho¹, J Conklin¹, C Ngamsombat², S Cauley¹, W Lo³, D Splitthoff⁴, J Kirsch¹, P Schaefer¹, O Rapalino¹, S Huang¹
¹Massachusetts General Hospital, Boston, MA, ²Athinoula A. Martinos Center For Biomedical Imaging, Bangkok, Thailand, ³Siemens Healthineers AG, Boston, MA, ⁴Siemens Healthineers, Erlangen, Germany

Purpose

To investigate the diagnostic performance of an accelerated post-contrast Wave-CAIPI T1 MPRAGE (Wave-T1 MPRAGE) sequence compared to a standard post-contrast T1 MPRAGE sequence for detection of intracranial enhancing lesions.

Materials and Methods

80 adult patients undergoing brain MRI with contrast were prospectively enrolled with IRB approval. The imaging protocol of all MRI scans included a standard post-contrast T1 MPRAGE (R=2, acquisition time (TA)=5min18s, 0.9 mm isotropic resolution) and a resolution-matched prototype post-contrast Wave-T1 MPRAGE sequence (R=4, TA=2min32s). 54 cases were acquired with the standard sequence before Wave, and 26 cases were acquired with Wave before standard. The studies were performed on 3T MRI scanners (MAGNETOM Prisma, Siemens Healthcare, Erlangen, Germany). Two neuroradiologists (8 years of experience each) blinded to sequence type performed an independent head-to-head comparison of the images. A predefined 5-point scale was used for grading intracranial enhancement (parenchymal, dural, leptomeningeal, extra-axial), motion artifacts, noise and overall diagnostic quality. Discrepancies among raters were adjudicated by a third reader.

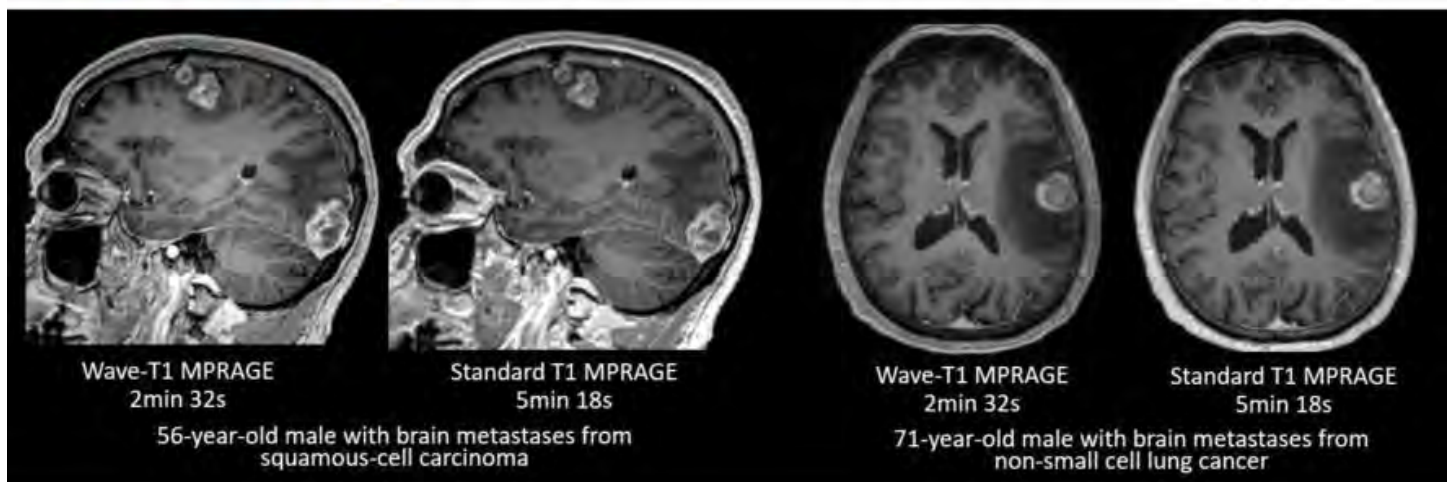
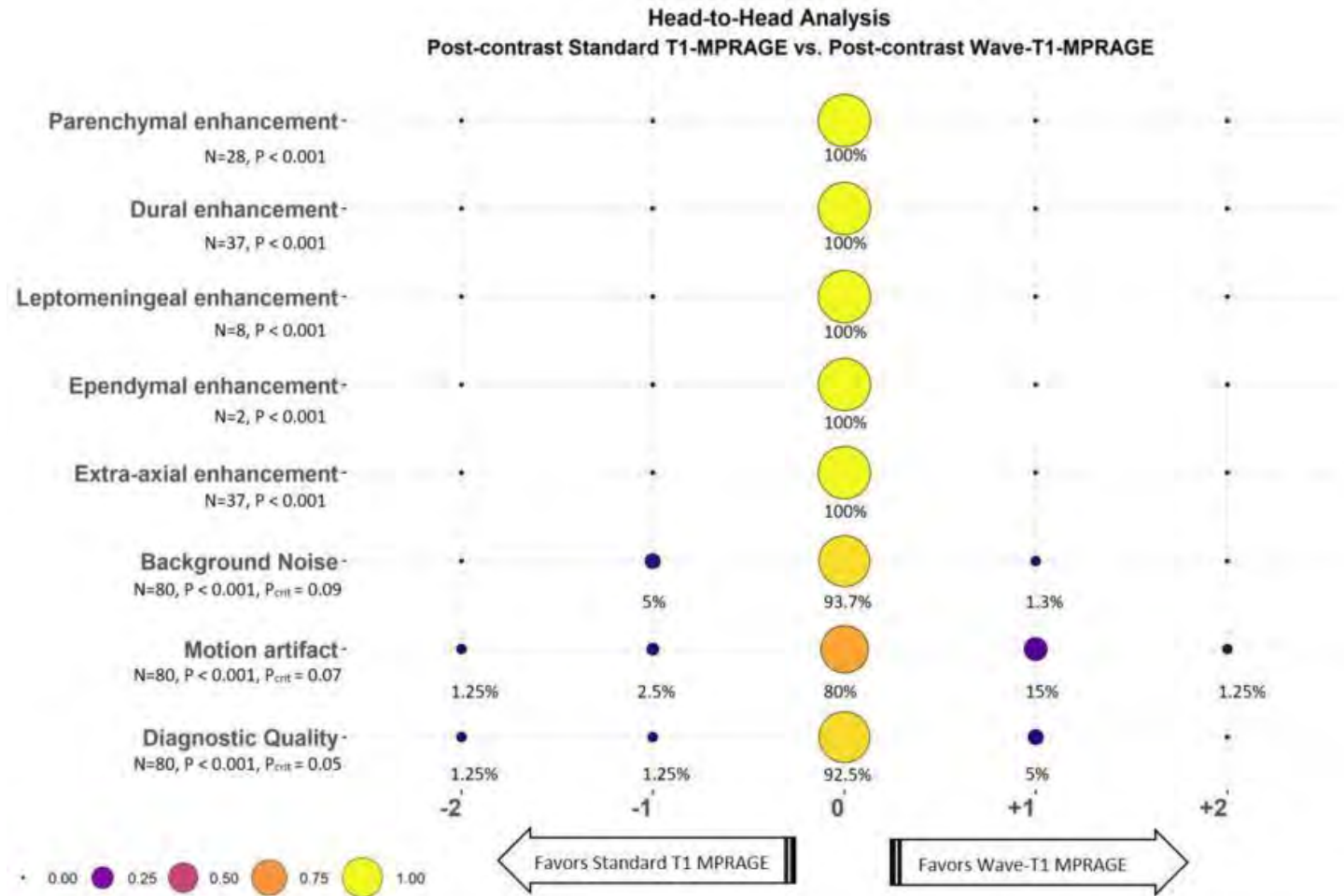
Results

The most common clinical indication for MRI examination was the investigation of neoplasms (64%), followed by vascular (10%) and inflammatory conditions (2%). Wave-T1 MPRAGE was equivalent to the standard sequence for detection of intracranial

enhancing lesions in all locations, with a reduction of TA by half (2:32 vs 5:18). Wave-T1 MPRAGE images were noninferior to the standard images in the perception of noise and motion artifacts ($P < 0.001$). Moreover, Wave-T1 MPRAGE presented less motion artifacts in 16% of cases, showing better performance compared to the standard sequence. The diagnostic quality of the standard and Wave sequences was also equivalent ($p < 0.001$).

Conclusions

Wave-CAIPI technology enables the acquisition of high-resolution 3D post-contrast T1 MPRAGE images in less than half the acquisition time, with equivalent diagnostic performance as a resolution-matched standard post-contrast T1 MPRAGE sequence. The faster scan has the added benefit of potentially reducing artifacts due to motion, particularly in motion-prone patients. The results support the assertion that Wave-T1 MPRAGE could replace a standard T1 MPRAGE sequence in clinical brain MRI protocols requiring contrast. The reduction in scan time and increased scan throughput will increase patient access and improve the utilization of MR imaging resources.



(Filename: TCT_1257_T1MPRAGE-Figure.jpg)

Diagnostic Role of Diffusion-Weighted and Dynamic Contrast-Enhanced Perfusion Magnetic Resonance Imaging in Paragangliomas and Schwannomas in the Head and Neck

Y Ota¹, A Capizzano¹, T Moritani¹

¹University of Michigan, Ann Arbor, MI

Purpose

Differential diagnosis of paragangliomas and schwannomas in the head and neck is challenging when conventional imaging features are overlapped between two tumors. This study was to design to assess the clinical usefulness of diffusion-weighted imaging (DWI) and dynamic contrast-enhanced perfusion magnetic resonance imaging (DCE-MRI) in differentiating schwannoma and paraganglioma in the head and neck.

Materials and Methods

From June 2016 to June 2020, 42 patients (mean age 46.0±16.5 years; 30 female), with pathologically diagnosed paragangliomas and schwannomas in the head and neck, underwent pre-treatment DCE-MRI with conventional MRI in a single-center. We assessed mean ADC, normalized mean ADC, quantitative and semi-quantitative parameters of DCE-MRI (Vp, VE, KEP, Ktrans, AUC, Peak enhancement, Wash-in, Wash-out, SER and TME) and tumor characteristics (presence of flow voids, percentage of cystic/necrotic change and enhancement pattern) between paragangliomas and schwannomas. Patients were scanned in 1.5T or 3.0T MRI scanners with axial T1WI, T2WI, axial and coronal contrast-enhanced fat-sat T1WI, and DWI. DCE-MRI sequences were performed using 3-dimensional T1-weighted images, with the administration of 20 ml of contrast. The freehand ROIs were depicted on the axial image, which predominantly showed solid enhancing portions on post-contrast T1-weighted images. The binary variables were compared by Fisher exact test, and the continuous variables were compared by Mann-Whitney U test. The multivariate stepwise logistic regression analysis was performed to identify the significant parameters to distinguish schwannomas and paragangliomas using the forward stepwise selection method.

Results

Vp and Kep from quantitative parameters (P= <.001 and .038, respectively) and TME, SER, Peak enhancement, and Wash-in from semi-quantitative parameters (P= <.001, <.001, <.001, and .002, respectively) showed statistically significant differences between two tumors. Presence of flow voids and enhancement patterns (homogenous or heterogenous) from tumor characteristics also showed statistically significant differences. There were no significant differences in ADC values. In the multivariate logistic regression analysis, Vp was identified as a most significant variable in the differentiation of schwannomas from paragangliomas.

Conclusions

DCE-MRI are non-invasive and can provide promising parameters that can differentiate paragangliomas and schwannomas in the head and neck.

Table 1 Patient's demographic and tumor characteristics

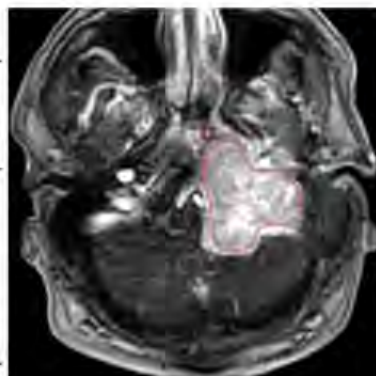
	Schwannomas	Parangliom as	P Value
No.	15	27	NA
Sex (male/female)	5/10	7/20	.73
Age (year)	42.2 ± 15.1	48.2 ± 17.2	.27
Maximum diameter (mm)	31.4 ± 15.4	32.3 ± 15.6	.76
Presence of vascular flow voids (Salt-and-pepper appearance)	2/15	18/27	.001 ^a
Cystic or necrotic change	5/15	14/27	.34
Enhancement pattern (homogeneous enhancement/total)	10/15	8/27	.027 ^a
Location (head lesion/total)	5/15	11/27	.75



A 41-year-old female with schwannoma. A heterogeneously enhancing tumor was seen in the left parotid space. Maximal diameter was 36mm. TME and VP were 202.1 and 0.08, respectively.

Table 2 ADC values and dynamic parameters

	Schwannomas	Paragangliomas	P Value
Mean ADC ($\times 10^{-3} \text{ mm}^2/\text{s}$)	1.17 ± 0.31	1.12 ± 0.26	.56
Normalized mean ADC	1.54 ± 0.43	1.44 ± 0.34	.46
Quantitative values			
Vp	0.06 (0.03 – 0.12)	0.40 (0.34 – 0.54)	<.001 ^a
Ve	0.42 (0.25 – 0.77)	0.28 (0.16 – 0.47)	.38
KEP (minute ⁻¹)	0.58 (0.36 – 0.67)	1.02 (0.43 – 2.27)	.038 ^a
Ktrans (minute ⁻¹)	0.15 (0.11 – 0.26)	0.31 (0.13 – 0.74)	.16
Semi-quantitative values			
Area under curve (mmol/minute/L)	5.6 × 10 ⁴ (1.95 × 10 ⁴ – 1.55 × 10 ⁵)	7.0 × 10 ⁴ (3.8 × 10 ⁴ – 4.1 × 10 ⁵)	.08
Peak enhancement	137 (75 – 220)	294 (266 – 300)	<.001 ^a
Wash-in	1.4 (0.74 – 3.8)	7.26 (2.54 – 42.6)	.002 ^a
Wash-out	3.4 (0.77 – 8.4)	1.0 (0.42 – 6.0)	.35
SER	53.9 (47 – 90)	146 (112 – 211)	<.001 ^a
TME (sec)	160 (108 – 239)	36.2 (27.7 – 77.4)	<.001 ^a



A 26-year-old male with paraganglioma. A homogeneously enhancing tumor was seen in the left jugular foramen. Maximal diameter was 50mm. TME and VP were 45 and 0.54, respectively.

(Filename: TCT_1307_ASNR2022perfusion.jpg)

Diagnostic yield of diffusion-weighted brain magnetic resonance imaging in patients with transient global amnesia: a systematic review and meta-analysis

S Lim¹, M Kim¹, C Suh¹, S Kim², W Shim¹, S Kim¹

¹Asan Medical Center, Seoul, ²University of Ulsan College of Medicine, Seoul

Purpose

Brain magnetic resonance imaging (MRI) including diffusion-weighted imaging (DWI) can support the diagnosis of transient global amnesia (TGA) by excluding alternative diagnoses and revealing typical hyperintense hippocampal lesions. However, the diagnostic yield of DWI in patients with TGA has not been systematically evaluated. Purpose: This study aimed to investigate diagnostic yield of DWI in patients with TGA and identify significant parameters affecting diagnostic yield.

Materials and Methods

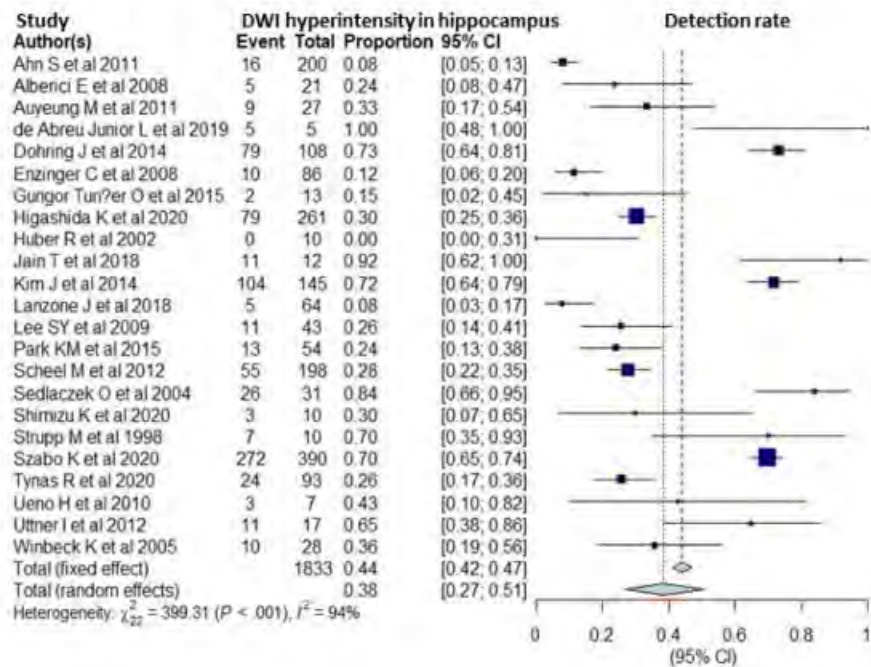
A systematic literature search using MEDLINE and EMBASE databases was conducted to identify studies assessing the diagnostic yield of DWI in patients with TGA (first search: July 25, 2020). The pooled diagnostic yield of DWI in patients with TGA was calculated using the DerSimonian-Laird random effects model. Subgroup analyses were also performed according to the slice thickness and magnetic field strength.

Results

Twenty-three original articles including 1,737 patients were included. The pooled incidence of right, left, and bilateral hippocampal lesions accounted for 33% (95% confidence interval [CI], 30%–37%), 42% (95% CI, 39%–46%), and 26% (95% CI, 24%–31%) of all lesions, respectively. The pooled diagnostic yield of DWI in patients with TGA was 40% (95% CI, 28%–53%). The Higgins I² statistic showed significant heterogeneity (I² = 94.3%). In the subgroup analyses, DWI with a slice thickness of ≤ 3 mm showed a higher diagnostic yield than DWI with a slice thickness of > 3 mm (pooled diagnostic yield: 61% [95% CI, 49%–72%] vs. 29% [95% CI, 16%–47%], P = 0.004). There was no difference in the diagnostic yield between DWI with 3.0 T and 1.5 T (pooled diagnostic yield: 31% [95% CI, 25%–38%] vs. 27% [95% CI, 16–40%], P = 0.543).

Conclusions

The pooled diagnostic yield of DWI in patients with TGA was 40% and DWI with ≤ 3 mm slice thickness is recommended to increase its diagnostic yield.



(Filename: TCT_379_Fig2.JPG)

938

Differential Diagnosis Of Tumor Recurrence And Radionecrosis In Patients With Brain Metastases After Stereotactic Radiosurgery Based On Perfusion-Weighted Magnetic Resonance Imaging And Blood Oxygenation Level Dependent Imaging Data

A Gryazov¹, O Chuvashova¹, C Davidson²

¹The State Institution "Romodanov Neurosurgery Institute, National Academy of Medical Sciences of Ukr, Kyiv, Ukraine, ²University of Utah, Sandy, UT

Purpose

To determine the effectiveness of differential diagnosis of relapse and radionecrosis of tumor recurrence and radionecrosis according to perfusion-weighted (PWI) magnetic resonance (MR) imaging and Blood oxygenation level dependent (BOLD) imaging after stereotactic radiosurgery (SRS) for brain metastases (BM).

Materials and Methods

Data of 88 patients with brain metastases were analyzed (36 patients with BM of non-small cell lung cancer, 28 patients with BM of breast cancer, 11 patients with BM of melanoma, 6 patients with BM of renal cell carcinoma, 4 patients BM of colorectal cancer, 3 patients with BM cervical cancer) who underwent SRS treatment at the Department of Radioneurosurgery of the State Institution of Neurosurgery named after acad. A.P. Romodanov. The cohort included only patients who were followed up for at least a year and in whom, according to standard MRI sequences, a presumptive diagnosis of tumor recurrence was made. Patients underwent a perfusion-weighted (PWI) magnetic resonance (MR) imaging and Blood oxygenation level dependent (BOLD) imaging programs.

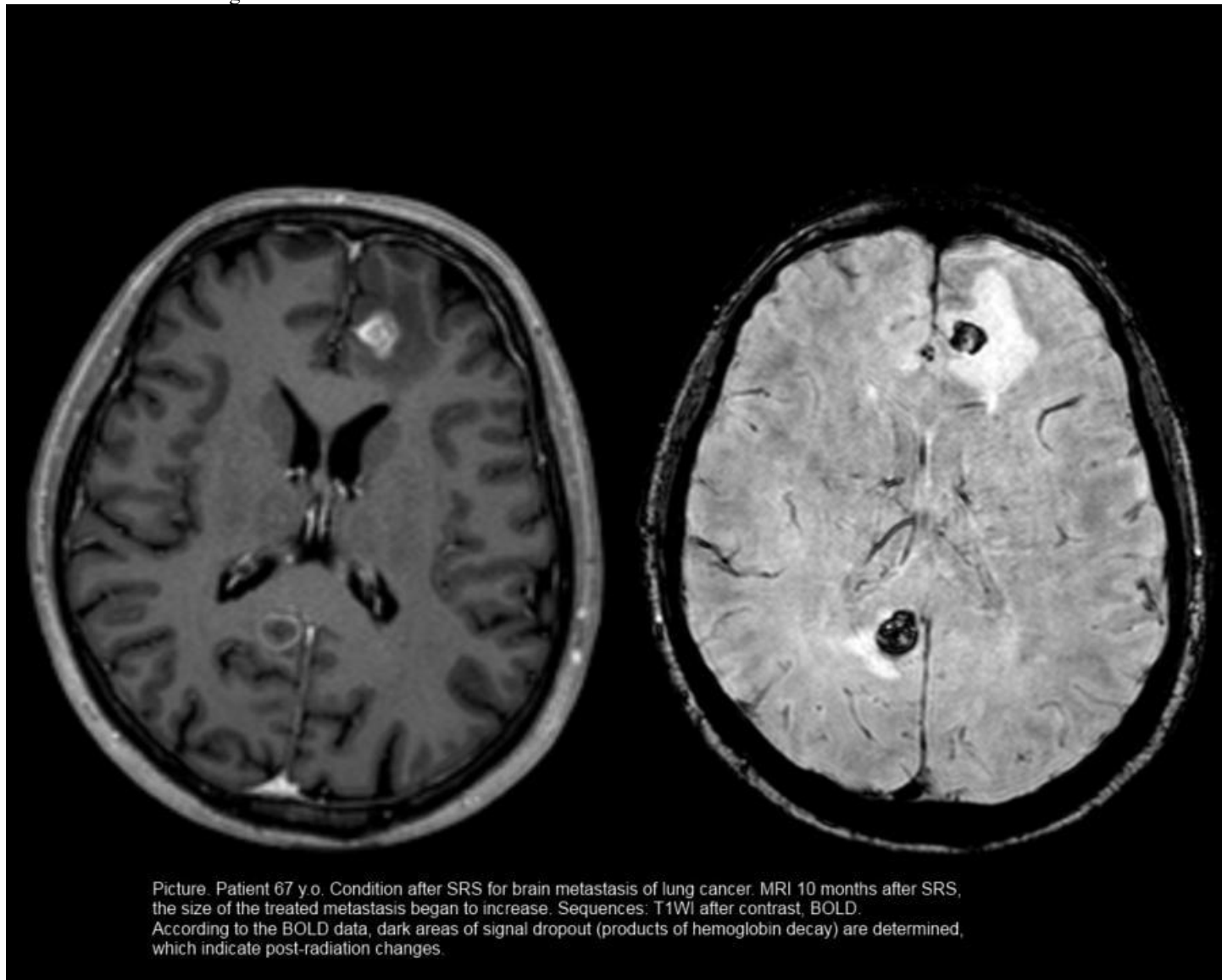
Results

Perfusion data (nCBV, 0.001) had sensitivity 87,7%, specificity 75,2% and accuracy 82,3%. ProBOLD data (<0.001) had sensitivity 77,3%, specificity 89,8% and accuracy 80,5%. The total data of both methods showed the following indicators: sensitivity 80,9%,

specificity 100%, accuracy 81.7%. Relapse had higher nCBV values than radionecrosis (5.88 versus 1.24, $P = 0.001$), radionecrosis had higher values according to proBOLD data (44.6 versus 7.7, $P < 0.001$). Multivariate logistic regression analysis using mean nCBV and proBOLD showed that nCBV and proBOLD were two independent variables to differentiate between relapse and radionecrosis.

Conclusions

The use of dynamically weighted perfusion and BOLD data weighted by susceptibility depending on the level of blood oxygenation allows with a sufficient degree of reliability to carry out differential diagnostics between the relapse and radionecrosis of brain metastases after radiosurgical treatment.



(Filename: TCT_938_00002.jpg)

309

Differentiating Radiation Necrosis from Ischemic Infarct Using Apparent Diffusion Coefficient Values in Post Treatment Patients with Glioblastoma.

A Kamali¹, S Mirbagheri², C Yalniz³, A Aein⁴, R Patel⁵, R Riascos⁵

¹University of Texas Health Science Center Houston, Houston, TX, ²Johns Hopkins University, Baltimore, MD, ³UTH McGovern Medical School, Houston, TX, ⁴University of Texas Health Science Center at Houston, Houston, TX, ⁵The University of Texas Health Science Center at Houston, Houston, TX

Purpose

Radiation necrosis and ischemic infarct are some of the possible complications of treatment with surgery, radiation or chemotherapy in glioblastoma patients. The appearance of these entities maybe confusing on conventional imaging since both may show linear enhancement and diffusion restriction on conventional imaging. Biopsy is the gold standard for diagnosis; however, it is costly,

invasive, and susceptible to sampling bias. We set out to investigate if the Apparent Diffusion Coefficient (ADC) values can differentiate these two pathologies from one another, noninvasively.

Materials and Methods

In this IRB approved retrospective study, the list of all glioblastoma patients who underwent radiation, surgery and chemotherapy from 2016-2020 was recorded. Subjects with history of treatment with Avastin and steroid were excluded from the study. A total of 100 patients between the age of 50-80 years were analyzed, including 50 patients with biopsy proven radiation necrosis, and 50 age- and-sex-matched patients with biopsy proven infarcts. The MRI scans were investigated and the ADC values of the areas of diffusion restrictions and normal appearing white matter (NAWM) from the contralateral hemispheres were measured by two neuroradiologists.

Results

Among the infarct group (n=50), the mean ADC value for the lesion (n=50) was 250.1 ± 57.2 mm²/s, and the mean ADC value for the NAWM was 730.0 ± 70.8 . Among the radiation necrosis group (n=50), the mean ADC value for the lesion was 479.0 ± 105.2 , and the mean ADC value for NAWM was 723.3 ± 64.0 . There is significant difference in ADC values of radiation necrosis and infarct (p value <0.001). These values are also significantly different (p value <0.001) from the mean ADC values of glioblastoma (0.789 ± 0.105) in our recent study (Stuart et al, 2019) using the same technique. The mean ADC values of the NAWM was comparable between the two groups (p value = 0.41).

Conclusions

This study shows that ADC values may be used as a noninvasive diagnostic imaging marker for differentiating radiation necrosis from ischemic infarcts in MRI scans of the treated glioblastoma patients.

1496

Differentiating Rathke Cleft Cysts From Pure Cystic Pituitary Adenoma: Contribution of Conventional Magnetic Resonance Imaging and Radiomics Based Machine Learning

C ALTINTAS TASLICAY¹, E DERVISOGLU¹, C Taslicay², I Mese³, A YALNIZ⁴, I ANIK⁵, Y ANIK¹

¹Kocaeli Universty School of Medicine, Kocaeli, TURKEY, ²Istanbul Technical University, Istanbul, TURKEY, ³Erenköy Mental Health and Neurological Disease Training and Research Hospital, Istanbul, TURKEY, ⁴Gebze Fatih State Hospital, Kocaeli, Turkey, ⁵KOCAELI UNIVESITY FACULTY OF MEDICINE, KOCAELI, Turkey

Purpose

Pure cystic pituitary adenomas (PCA) may mimic Rathke cleft cysts (RCC) when there is no solid enhancing component found on MR imaging, and preoperative differentiation may enable a more appropriate selection of treatment strategies. In this study, it was aimed to investigate the contribution of radiomics-based machine learning methods to MR imaging in differentiating RCC from PCA.

Materials and Methods

The study protocol was approved by the institutional ethics committee. 65 patients (28 RCC, 37 PCA) were included in this retrospective study. Preoperative MR images were evaluated using 7 semantic features. A total of 107 radiomics features were extracted from T2-weighted, postcontrast T1-weighted, and SPIR T1-weighted images. Using semantic and radiomics features, four models were created to distinguish RCC from PCA. Classifications were made with support vector machine, logistic regression, k-nearest neighborhood, naive Bayes, decision tree, random forest and neural network algorithms. Feature reduction was done with information gain method, and stratified 10-fold cross-validation was used as an internal validation technique. The performance of ML algorithms was evaluated with the area under the curve (AUC), sensitivity, specificity, and accuracy rates. p <0.05 was considered statistically significant.

Results

The naive Bayes algorithm had the best diagnostic performance in all classification models. The ML model using the radiomics features obtained from all sequences and semantic features showed the best results in distinguishing RCC from PCA (AUC:0.978). All models using semantic features showed better results than the model using radiomics features alone. When radiomics features were added to semantic features, only AUC of ML algoritms were increased minimally.

Conclusions

Preoperative distinguishing of RCC and PCC is very important to aid in treatment and surgical planning. The radiomics-based ML models might be a promising non-invasive tool in distinguishing RCC from PCA. However, ML using semantic features showed better results compared to ML using radiomics features alone. When radiomics features were added to semantic features, only AUC of ML algoritms were increased minimally but there was no statistically significant contribution to the performance of the model.

439

Differentiation of Chiari 1 Malformation and Spontaneous Intracranial Hypotension Using Objective Measurements of Midbrain Sagging

J Houk¹, P Kranz², T AMRHEIN¹

¹Duke University Medical Center, Durham, NC, ²Duke University Medical Center, Cary, NC

Purpose

Spontaneous Intracranial Hypotension (SIH) and Chiari 1 Malformation (CM1) are causes of headache with some overlapping clinical features. Cerebellar tonsillar ectopia (TE) can be present in both conditions; in SIH, TE is typically the result of brain sagging. These overlapping imaging features can lead to diagnostic confusion and unnecessary surgery, and therefore accurate differentiation of these entities on imaging is important.[1] The purpose of this investigation was to determine whether objective measurements of midbrain morphology can reliably discriminate SIH from CM1.

Materials and Methods

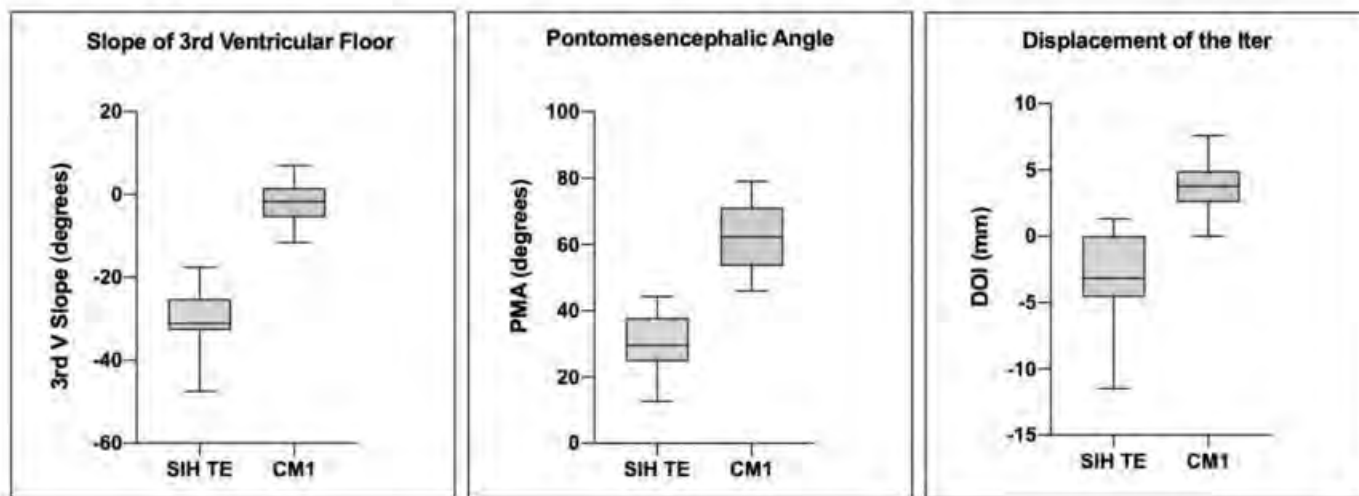
This retrospective case-control study included consecutive adult patients with SIH and CM1 (50 per arm). The following previously reported measurements [2-4] were obtained from brain MRI: TE, slope of 3rd ventricular floor (3rd V slope), ponto-mesencephalic angle (PMA), mammillo-pontine distance (MPD), lateral ventricular angle (LVA), internal cerebral vein-Vein of Galen angle (VHA), displacement of iter (DOI), and clivus length (CL). Comparison was made between subjects with CM1 and SIH. Additional subgroup comparison was performed on subjects with SIH with >5mm TE (termed SIHTE subgroup). After normality testing, statistical analysis was performed using t-test or Mann-Whitney test.

Results

Highly significant differences were observed between SIH and CM1 groups in the following measurements: TE, 3rd V slope, PMA, DOI, and CL (all $p < 0.0001$). Eight of 50 (16%) SIH subjects had TE >5mm; all of these subjects showed quantitative evidence of brain sagging. In this subgroup of subjects with TE, a cutoff value for 3rd V slope of -15° and PMA of $<45^\circ$ perfectly discriminated SIH from CM1. No subject with CM1 showed displacement of iter below the incisural plane.

Conclusions

Quantitative measures of brain sagging showed highly significant differences between subjects with SIH and CM1. Among subjects with cerebellar tonsillar ectopia, measurements of slope of the 3rd ventricular floor and the pontomesencephalic angle perfectly discriminated subjects with SIH from CM1.



(Filename: TCT_439_3rdVPMADOI.jpg)

369

Differentiation of glioblastoma from primary central nervous system lymphoma on post-contrast imaging using filtration based first-order texture analysis- Comparison of multiple machine learning models

G Bathla¹, S Priya², C Ward³, N Soni⁴, R Maheshwarappa¹, V Monga²

¹University of Iowa Hospitals and Clinics, Iowa City, IA, ²University of Iowa hospitals and Clinics, IOWA CITY, IA, ³Univ of Iowa, Iowa City, IA, ⁴UIHC, Iowa, IA

Purpose

To evaluate the diagnostic performance of multiple machine learning classifier models derived from first-order histogram texture

parameters extracted from T1W contrast-enhanced (CE) images in differentiating glioblastoma (GBM) and primary central nervous system lymphoma (PCNSL).

Materials and Methods

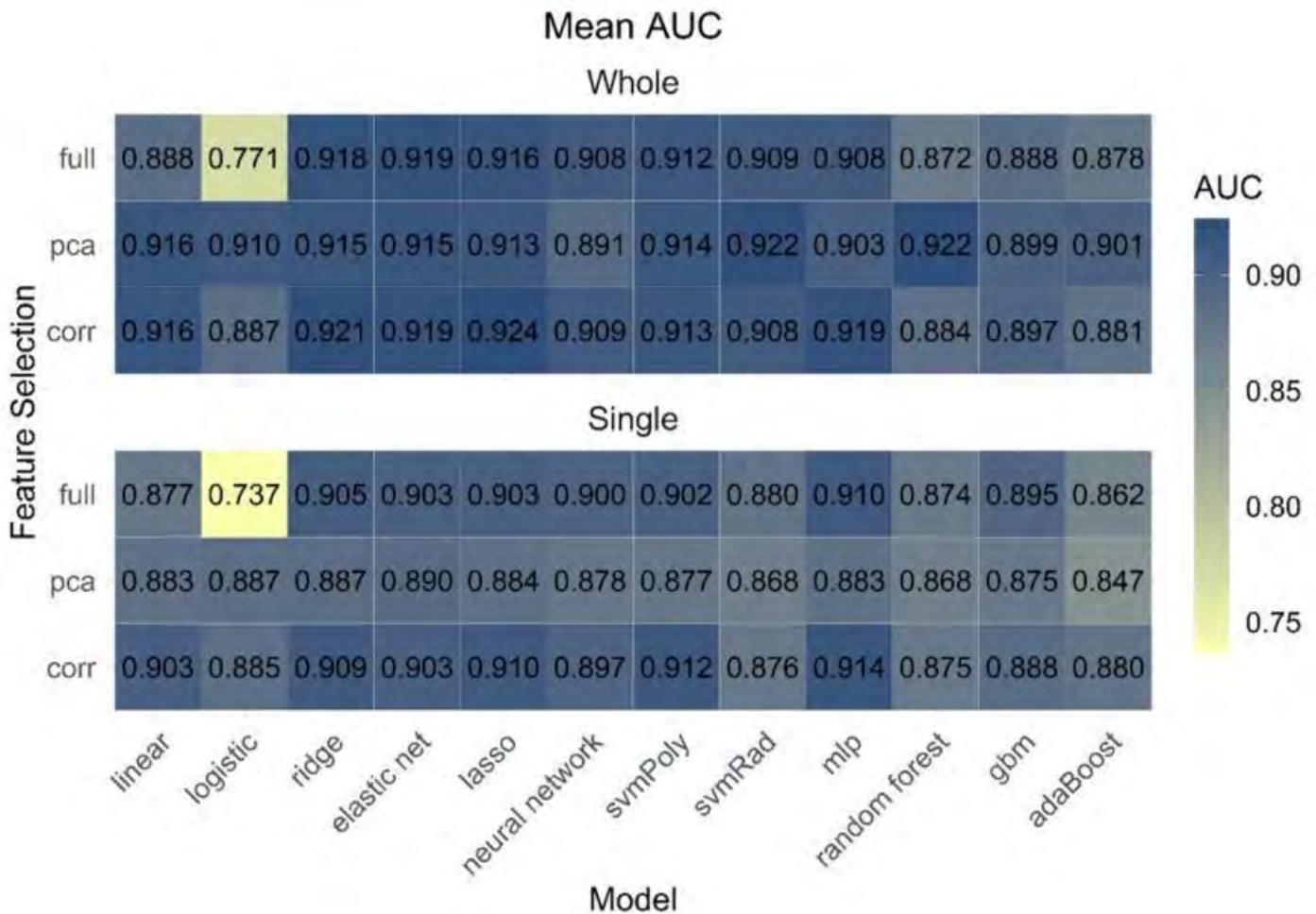
Retrospective study with 97 GBM and 46 PCNSL patients. Thirty-six different combinations of classifier models and feature selection techniques were evaluated. Five-fold nested cross-validation was performed. Model performance was assessed for whole tumor and largest single slice using receiver operating characteristic curve.

Results

The cross-validated model performance was relatively similar for the top performing models for both whole tumor and largest single slice (AUC- 0.909-0.924). However, there was considerable difference between the worst performing model (logistic regression with full feature set-AUC 0.737) and the highest performing model for whole tumor (LASSO model with correlation filter, AUC 0.924). For single slice, multilayer perceptron model with correlation filter had the highest performance (AUC 0.914). No significant difference was seen between the diagnostic performance of the top performing model for both whole tumor and largest single slice.

Conclusions

T1 contrast enhanced derived first-order texture analysis can differentiate between GBM and PCNSL with good diagnostic performance. The machine learning performance can vary significantly depending upon the model and feature selection methods. Largest single slice and whole-tumor analysis show comparable diagnostic performance.



(Filename: TCT_369_Fig-1.jpg)

1003

Diffuse Large B Cell Lymphoma with Neck Involvement, Nodal Imaging Characteristics

J Wilson¹, A Allen², B Ozgen Mocan¹

¹University of Illinois at Chicago, Chicago, IL, ²UCLA, Los Angeles, CA

Purpose

Diffuse large B-cell lymphoma (DLBCL) is the most common subtype of Non-Hodgkin lymphoma (NHL) in the United States. Classical imaging features of nodal non-Hodgkin lymphoma in the head and neck (H&N) are usually described as multiple enlarged cervical lymph nodes with homogeneous appearance despite their large size. Internal necrosis in an uncommon feature reported in 5-

13% of cases. However, atypical imaging features can also be seen especially with H&N DLBCL such as cystic or necrotic lymphadenopathy and heterogenous or infiltrative masses. We aim to further characterize the incidence of atypical imaging findings in H&N DLBCL at our institution.

Materials and Methods

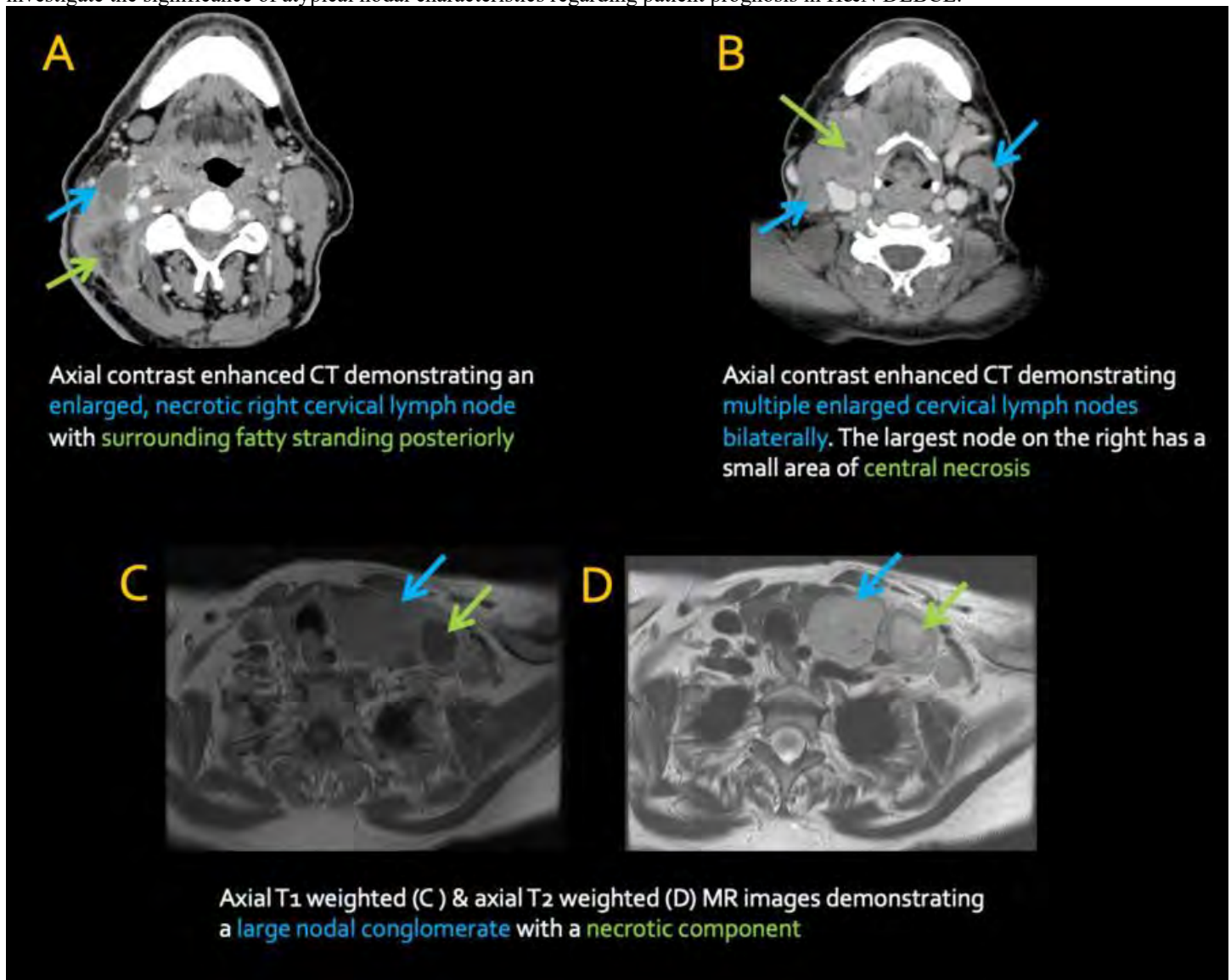
Retrospective chart review was performed and all individuals with pathology proven DLBCL with H&N involvement diagnosed at our institution over the past decade were identified. Individuals with lymph node involvement within the neck were then identified. Initial imaging was reviewed and nodal imaging characteristics were recorded including single vs multiple node involvement, maximal nodal size, nodal heterogeneity, nodal necrosis, and nodal hemorrhage. Additional characteristics include nodal location, laterality, presence/absence of bulky disease (defined as nodal conglomerates measuring >10cm), presence/absence of ill-defined nodal margins, and surrounding fat reticulation.

Results

24 individuals with DLBCL with neck nodal involvement were identified with an average age of 62 years at the time of diagnosis and gender distribution of 11 female patients to 13 male patients. Initial data obtained from imaging review determined that 71% of individuals presented with multiple involved nodes at the time of diagnosis and 54% of patients had at least one lymph node with evidence of internal necrosis. Involved lymph nodes demonstrated variable incidence of internal heterogeneity with ill-defined nodal margins identified in 57% of patients and 65% of affected nodes with surrounding fatty reticulation.

Conclusions

Our data demonstrates that atypical nodal involvement in H&N DLBCL may actually be more common than in classically taught. Previous work has suggested the possible prognostic potential of nodal necrosis on imaging and our ultimate goal will be to investigate the significance of atypical nodal characteristics regarding patient prognosis in H&N DLBCL.



(Filename: TCT_1003_ASNRabstractfigure.jpg)

Diffusion tensor imaging of the dentate nucleus after repeated administration of a macrocyclic gadolinium-based contrast agent gadobutrol in children

K Ozturk¹, D Nascene²

¹University of Minnesota, MINNEAPOLIS, MN, ²University of Minnesota, Minneapolis, MN

Purpose

The purpose of this study was to investigate possible signal changes in the dentate nucleus (DN) on diffusion tensor imaging (DTI) after administration of gadobutrol in a pediatric cohort.

Materials and Methods

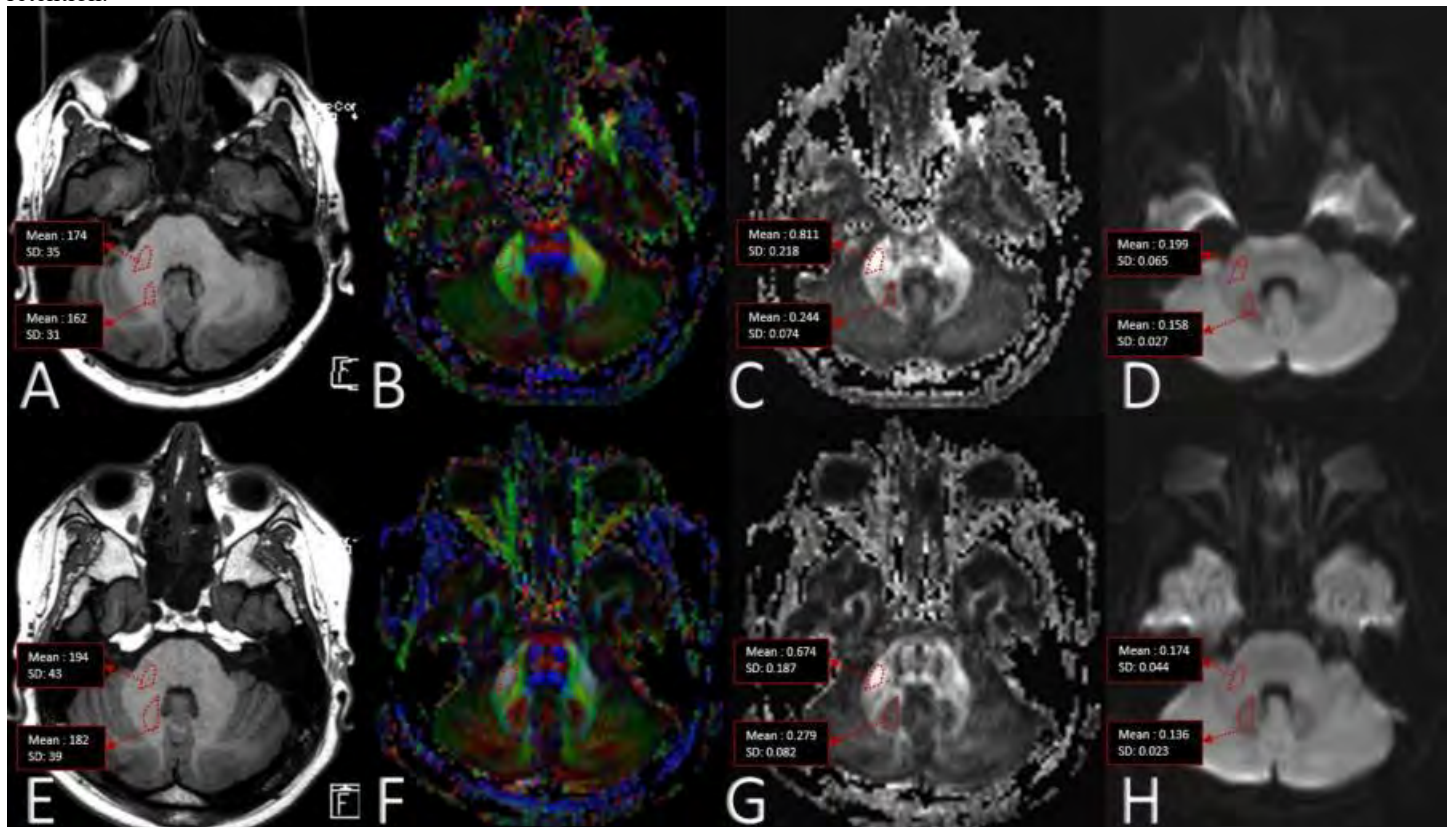
In this institutional review board approved study, we retrospectively identified 50 pediatric patients (mean age: 6.2 years, standard deviation: 4.3 years) with normal renal function exposed exclusively to the macrocyclic GBCA (mcGBCA) gadobutrol. We also identified 50 age- and sex-matched control patients with nonpathological neuroimaging findings (and no GBCA administration). All subjects underwent 3.0 Tesla MRI including unenhanced T1WI and DTI. Mean diffusivity (MD) and fractional anisotropy (FA) values were determined in the DN and middle cerebellar peduncle (MCP) in an ROI-based analysis. The DN-to-MCP SI ratios were then recorded and averaged. A paired t-test was performed to compare FA and MD SI ratios as well as SI ratio on unenhanced T1WI between children exposed to gadobutrol and controls. Pearson correlation analysis, one-way ANOVA or independent samples t-test were conducted to evaluate correlations between SI ratios and various confounding variables, including the number of mcGBCA-enhanced MRI, mean time interval between MRI, total mcGBCA dose, age, sex, and intrinsic disease.

Results

Patients underwent an average of 5.6 ± 5 gadobutrol injections (mean total dose, 14.3 ± 8.1 mmol) with a mean of 4.1 ± 3.2 months between each administration. The DN-to-MCP FA SI ratio was significantly lower for children with mcGBCA than in the control group ($p < 0.001$; non-GBCA group: 0.374 ± 0.03 ; mcGBCA group: 0.318 ± 0.06) but no significant difference of the DN-to-MCP SI ratio on unenhanced T1WI was noted between the mcGBCA group (0.937 ± 0.06) and the control group (0.946 ± 0.05 ; $p = 0.336$). There was also a significant MD SI ratio difference between mcGBCA group and control group ($p < 0.001$; non-GBCA group: 0.849 ± 0.12 ; mcGBCA group: 0.961 ± 0.14). A moderate negative correlation was identified between DN-to-MCP FA SI ratio and the number of mcGBCA administration (correlation coefficient = -0.356 , $p = 0.012$).

Conclusions

A mean of 5.6 consecutive administrations of the mcGBCA gadobutrol was associated with higher MD and lower FA values in DN suggesting a difference in tissue integrity between children exposed to mcGBCAs and control group, possibly relating to gadolinium retention.



(Filename: TCT_921_pics1.jpg)

Direct Comparison of Diagnostic Accuracy of Shuttle CT Angiography (CTA) versus Helical CTA in the Setting of Acute Stroke and Aneurysmal Subarachnoid Hemorrhage

N Smith¹, E Sweeney¹, A GUPTA¹, P Sanelli², J Ivanidze³

¹Weill Cornell Medicine, New York, NY, ²Northwell Health, Manhasset, NY, ³Weill Cornell Medicine Radiology, New York, NY

Purpose

CT-Angiography (CTA) imaging is critical in suspected aneurysmal subarachnoid hemorrhage (ASAH) and other neurovascular conditions (1,2). Traditionally, helical CTA (CTAh) has been used for the evaluation of vasospasm (VS) in ASAH patients. However, at present no studies directly comparing diagnostic accuracy of shuttle mode CTA (CTAs) to CTAh have been published. Advantages of CTAs over CTAh include lower radiation dose, less iodine contrast, and lower cost (3). Our purpose was to compare the diagnostic accuracy of CTAs and CTAh using a semi-quantitative scoring system with digital subtraction angiography (DSA) as the reference.

Materials and Methods

In this IRB-approved retrospective study, a total of 42 consecutive patients with suspected VS in the setting of ASAH or acute stroke underwent either CTAs or CTAh on a Discovery CT 750HD Scanner with follow-up DSA within 24 hours (reference standard) (Figure 1A). CTA were blinded and assessed for the presence of VS in the proximal cerebral arterial segments (bilateral A1/2, M1/2, P1/2) and basilar artery. VS was graded in each segment as follows: 1=none, 2=mild, 3=moderate, 4=severe. For each CTA or DSA, the sum score reflected overall degree of VS. Statistical analysis for the two patient cohorts were calculated in GraphPad Prism using the Wilson/Brown method.

Results

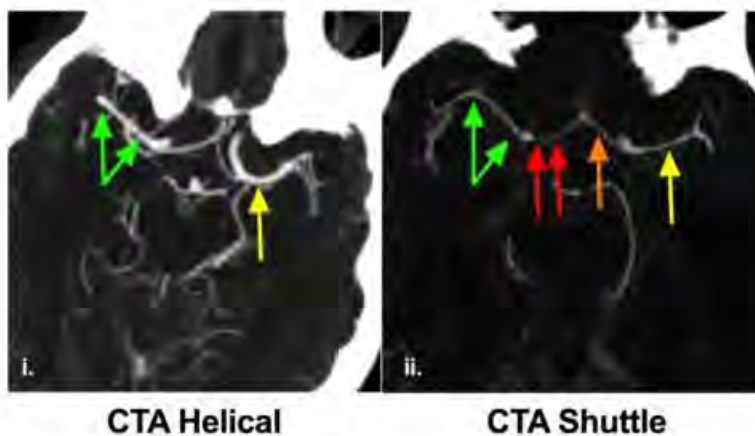
Examples of VS on CTAs and CTAh are shown in Figure 1B. ROC analysis demonstrated AUC 0.72 for CTAs (95% CI 0.56-0.88, $p=0.015$); AUC 0.70 for CTAh (95% CI 0.54-0.87, $p=0.028$) (Figure 1C). In patients with any degree of VS, CTAs demonstrated sensitivity of 95% (95% CI 77-100) and specificity of 14% (95% CI 5-35). CTAh demonstrated sensitivity of 100% (95% CI 84-100) and specificity of 10% (95% CI: 1.8-30). For moderate and severe VS (score > 2), CTAs demonstrated sensitivity of 62% (95% CI 41-79) and specificity of 62% (95% CI 41-79). CTAh demonstrated sensitivity of 65% (95% CI 43-82) and specificity of 70% (95% CI 48-85).

Conclusions

ROC analysis demonstrated comparable sensitivity, specificity and AUC in CTAs and CTAh. Limitations include the retrospective nature and small sample size; moreover CTAs and CTAh were performed in two separate cohorts. Advantages of CTAs include lower radiation, lower contrast volume, and lower cost. Our findings suggest a benefit of CTAs in the clinical setting particularly for monitoring of VS in patients with ASAH when multiple follow-up examinations are often necessary.

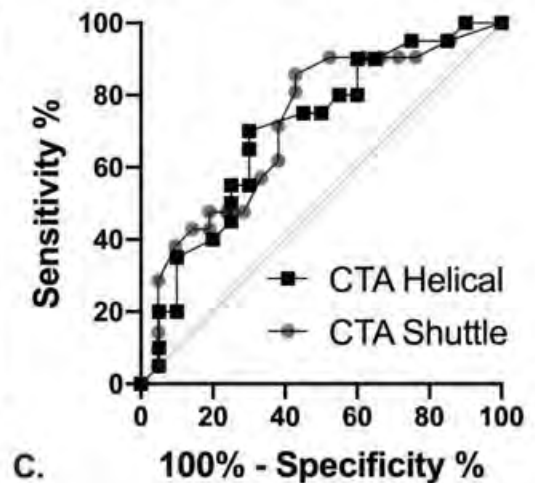
	CTA Helical vs DSA	CTA Shuttle vs DSA
Number of cases:	21	20
Number of patients:	19	17
Average age (years):	55.4	56.2
M:F	10:09	7:10
Mean number of hours between scans:	13.6	11.0
Diagnosis at presentation:		
SAH	15	15
Stroke	3	1
Other	1	1

A.



B.

CTAh vs CTAs



C.

Figure 1: A) Clinical and Demographic Characteristics of the Study Population. B) VS shown on axial MIP images derived from CTAh (i) and CTAs (ii). The arrows depict degree of VS as follows: green (no VS, Score = 1), yellow (mild VS, Score = 2), orange (moderate VS, Score = 3), and red (severe VS, Score = 4). The total score for each patient is the sum of the VS score in each of the 13 studied segments. C) ROC curves for degree of VS in CTAs and CTAh with DSA as gold standard.

(Filename: TCT_1516_Figure1forASNRAbstractFinal.jpg)

1610

Directed stimulation of the dentato-rubro-thalamic tract for deep brain stimulation in essential tremor: a blinded clinical trial

E Middlebrooks¹, C Lin¹, L Okromelidze¹, A Jain¹, R Carter¹, R Uitti¹, S Grewal¹
¹Mayo Clinic, Jacksonville, FL

Purpose

Connectivity-based observational studies have suggested that stimulation of the dentato-rubro-thalamic tract (DRTT) is the primary mechanistic basis for tremor improvement in deep brain stimulation (DBS) for essential tremor (ET). We designed a prospective, blinded crossover trial hypothesizing that DBS programming based solely on diffusion tractography (DT) of the DRTT would produce greater tremor control than standard-of-care (SOC) clinical programming and sham.

Materials and Methods

Prior to surgery, patients underwent 3T MRI including a robust, multiband spin-echo echo-planar imaging sequence with a total of 192 diffusion directions were asymmetrically sampled across three shells (b=1000, 2000, and 3000 s/mm²) in the anterior-posterior and posterior-anterior phase encoding direction giving a total of 404 diffusion scans per subject. Probabilistic tractography of the DRTT was performed. After coregistration of postoperative CT and localization of electrode contacts, a volume of tissue activated

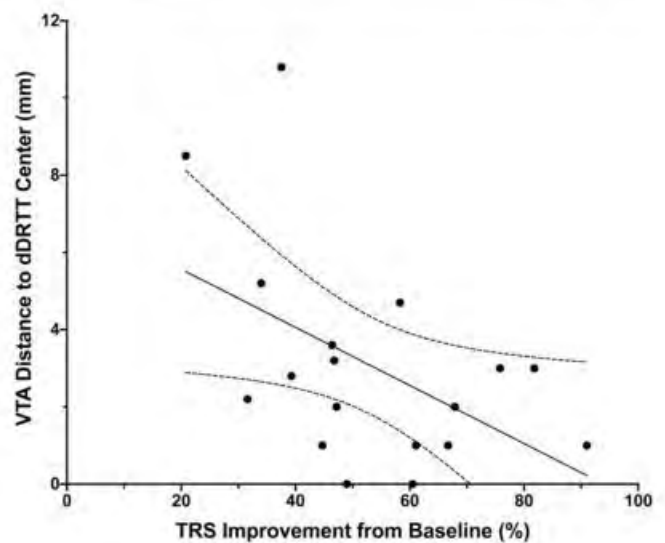
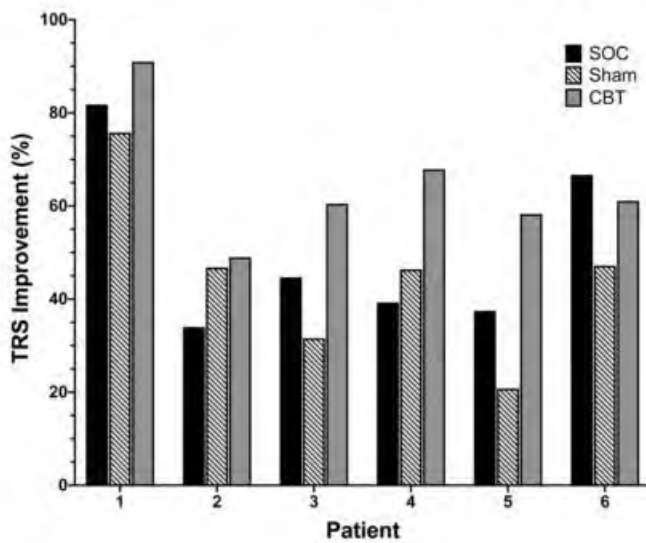
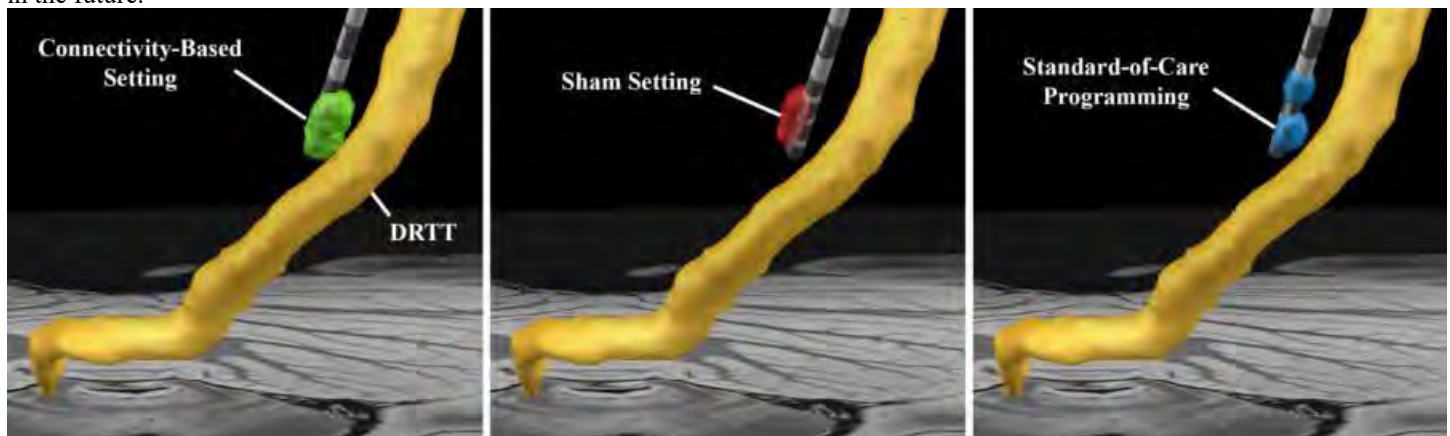
(VTA) was estimated using a finite element method (FEM)-based model. A connectivity-derived treatment (CDT) setting was derived using directional stimulation oriented towards the point of greatest DRTT probability. The sham setting was generated using directional steering to approximately 180 degrees from the treatment setting. All patients were initially programmed using current standard clinical programming methods for 3 months. At 3 months, each patient underwent blinded comparison for the three test programming settings: SOC, CDT, and sham and tremor rating score (TRS) recorded for each. Percentage improvement in TRS compared to baseline was the primary outcome variable.

Results

Six patients completed the trial. Mean TRS improvement was greater with the CBT settings (64.6% ± 14.3%) than with SOC programming (50.7% ± 19.2%) and sham (44.8% ± 18.6%). In 5 of 6 patients (83.3%), the CBT setting was superior to the SOC setting. The distance between the center point of the DRTT and the nearest VTA margin inversely correlated with the percentage improvement in TRS (R2=0.24; p=0.04).

Conclusions

Our phase I trial provides the first prospective, blinded sham evidence that DBS programming settings based solely on directionally targeting the DRTT defined by MRI tractography produced greater tremor improvement than current clinical practice and sham settings. Our findings suggest that there may be an increased role of DTI and radiology in optimizing DBS targeting and programming in the future.



(Filename: TCT_1610_et.jpg)

1401

Discrimination of tuberculomas using radiomics from its imaging lookalike high-grade gliomas

A Indoria¹, S Raju², D Mohan², S Vengalil², A Nalini², J Saini¹

¹Neuroimaging and Interventional Radiology, National Institute of Mental Health and Neuro Sciences, Bengaluru, India, ²Neurology, National Institute of Mental Health and Neuro Sciences, Bengaluru, India

Purpose

Non-neoplastic focal cerebral disorders, such as large tuberculomas and high-grade primary neoplasms of brain like Glioblastomas

can show overlapping clinical and radiological features. Usually tuberculomas appear as mixed intensity lesions on T2-weighted images, showing central necrosis and peripheral enhancement on post contrast T1W images. High-grade gliomas (HGG) may also present with similar imaging features. Management primary brain tumours and tuberculomas are entirely different and hence their differentiation is important. Previous studies have tried using magnetization transfer, MR spectroscopy, diffusion MRI and perfusion MRI for discrimination of tuberculomas and neoplastic lesions of brain. In absence of these specialized MRI methods, conventional MRI sequences can be exploited using radiomics for non-invasive discrimination of tuberculomas from neoplastic lesions like HGG. In this study we intend to discriminate tuberculomas non-invasively using radiomics from HGG.

Materials and Methods

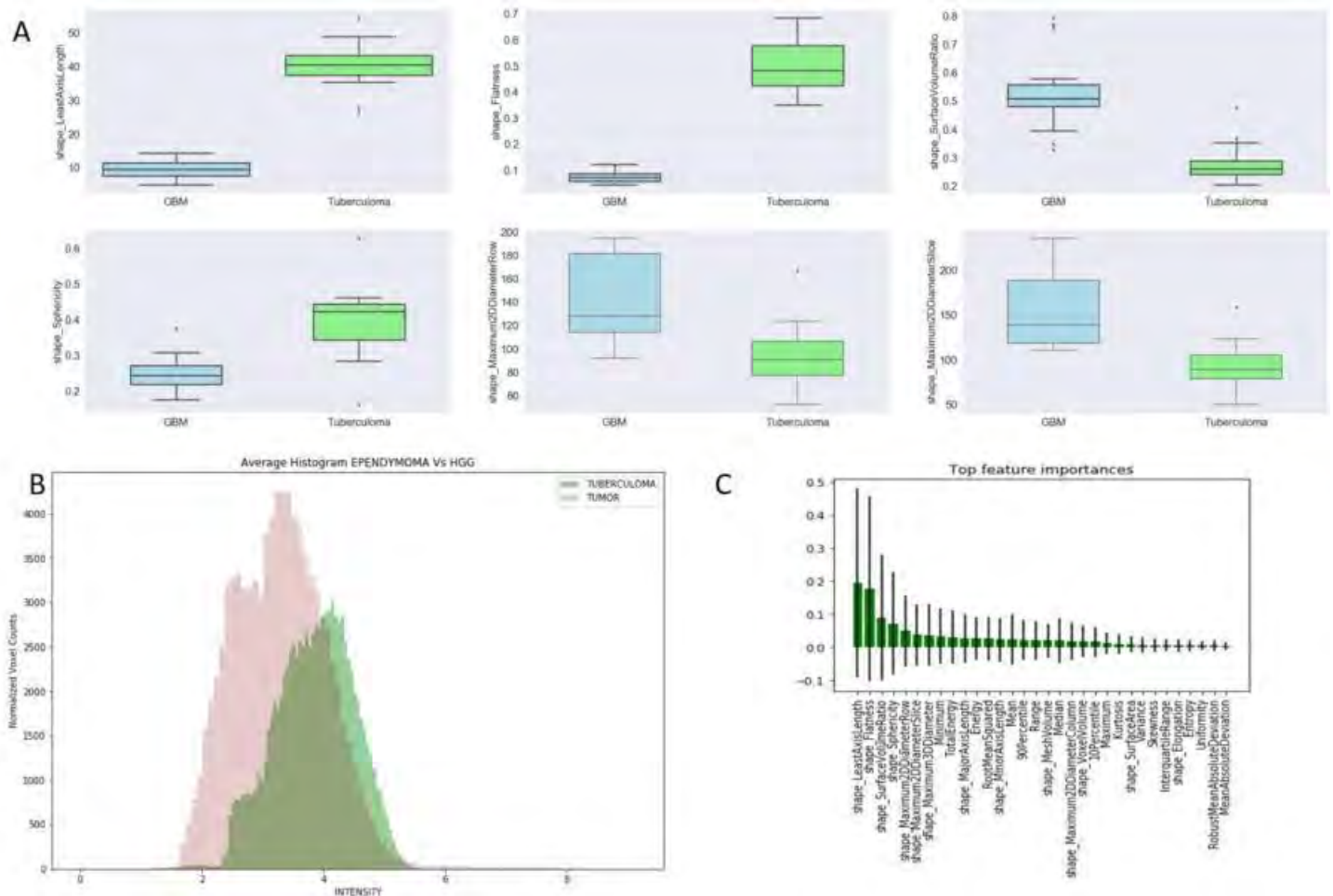
ROI was manually delineated on T2W FLAIR images using 3D slicer version 4.10.2. Images were z-score normalized for feature extraction. 32 features (Shape features and First order statistical features) were extracted using PyRadiomics. Feature importance was calculated using gini-index based method. Boxplots were created to study the relation of selected features with HGG and tuberculoma. Dataset was split into training and testing data. A Fourfold cross validation was carried out to obtain ROC-AUC score. Logistic regression classifier was trained on reduced feature set after hyper parameter tuning. Classifier performance was assessed on the basis of ROC-AUC score, Accuracy, Sensitivity, Specificity and F1 score.

Results

Boxplots indicate that the two groups (Tuberculoma and HGG) can be differentiated based on Radiomics features (Fig.1A). The shape features were proved to be more important in automated classification of Tuberculomas and HGG (Fig.1C) There was a significant difference in peak, center and height of the histograms that can be used to differentiate between the two groups (Fig.1B). 0.98 mean ROC AUC score was achieved after cross validation. The classifier also performed well on test dataset with accuracy, sensitivity, specificity, ROC-AUC score and F1 score of 1.0, 1.0, 1.0, 1.0 and 1.0 respectively.

Conclusions

We conclude that radiomics signature obtained from T2W FLAIR images has the potential of discriminating tuberculomas from HGG.



(Filename: TCT_1401_Picture2.jpg)

659

DIXON-T2WI Magnetic Resonance Imaging at 3 Tesla outperforms conventional imaging for thyroid eye disease

A Ollitrault¹, F CHARBONNEAU¹, M Herdan¹, K Zuber¹, J Savatovsky¹, A LECLER¹

Purpose

To determine the diagnostic performances of a single DIXON-T2WI sequence compared to a conventional protocol including T1-, T2- and fat-suppressed T2-weighted MRI at 3T when assessing thyroid eye disease (TED).

Materials and Methods

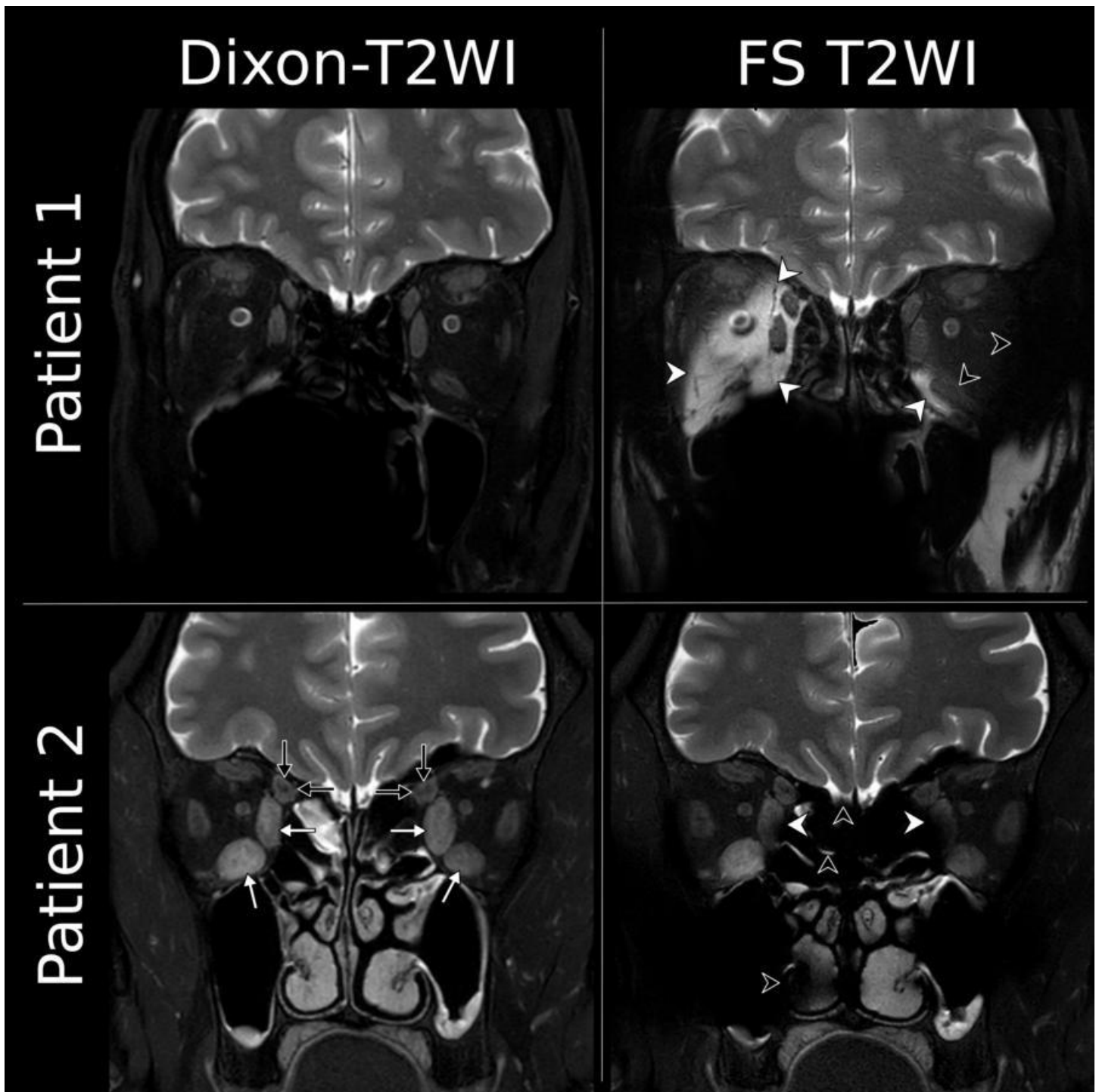
This IRB-approved prospective single-center study enrolled participants presenting with confirmed TED from April 2015 to October 2019. They underwent an MRI, including a conventional protocol and a DIXON-T2WI sequence. Two neuro-radiologists, blinded to all data, read both datasets independently and randomly. They assessed the presence of extraocular muscle (EOM) inflammation, enlargement, fatty degeneration or fibrosis as well as the presence of artifacts. A Wilcoxon signed-rank test was used.

Results

206 participants were enrolled (135/206 [66 %] women, 71/206 [34 %] men, age 52,3 +/- 13,2 years). DIXON-T2WI was significantly more likely to detect at least one inflamed EOM as compared to the conventional set: 248/412 (60 %) vs 228/412 (55 %) eyes, $p=0.02$. DIXON-T2WI was more sensitive and specific than the conventional set for assessing muscular inflammation: 100% versus 94.7 % and 71.2 % versus 68.5 %, respectively. DIXON-T2WI was significantly less likely to show major or minor artifacts as compared to FS T2WI: 20/412 (5 %) versus 109/412 (27 %) eyes, $p<0.001$ and 175/412 (42 %) versus 257/412 (62 %) eyes, $p<0.001$. Confidence was significantly higher with DIXON-T2WI than with the conventional set: 2.35 versus 2.24, $p=0.003$.

Conclusions

DIXON-T2WI showed higher sensitivity and specificity and showed fewer artifacts than a conventional protocol when assessing thyroid eye disease, in addition to higher self-reported confidence.



(Filename: TCT_659_Fig.jpg)

1518

Do Apparent Diffusion Coefficient Histogram Radiomic Metrics Differentiate Medulloblastoma Molecular Subgroups in Children?

L Tierradentro-García¹, A Zandifar¹, F Goncalves¹, J Kim¹, A Ghosh¹, C Alves¹, S Teixeira¹, S Andronikou², A Vossough²
¹Children's Hospital of Philadelphia, Philadelphia, PA, ²University of Pennsylvania - Children's Hospital of Philadelphia, Philadelphia, PA

Purpose

Medulloblastoma is the most common malignant CNS tumor in the pediatric population. Molecular subgroup classification can help determine the risk of metastasis, recurrence pattern, and prognosis. Conventional MRI sequences such as contrast T1- and T2-

weighted signals may not be adequate to establish differences among the subgroups. This study aimed to assess the application of apparent diffusion coefficient (ADC) histogram analysis and radiomic metrics to evaluate medulloblastoma subgroups.

Materials and Methods

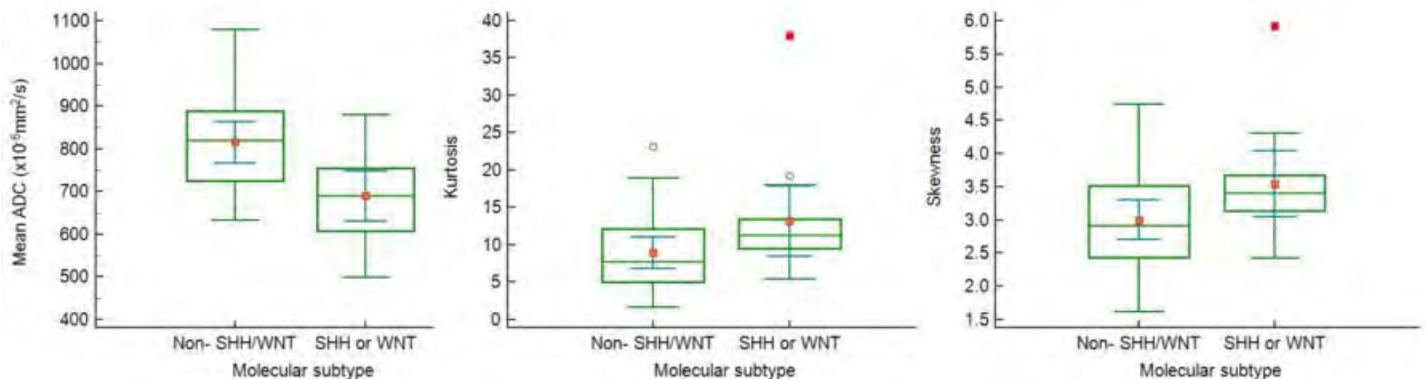
We retrospectively evaluated forty-three (43) medulloblastoma cases in children at our institution. We excluded four (4) patients that did not have a confirmed molecular diagnosis. We analyzed 39 subjects: WNT (n=4), SHH (n=10) and non-WNT/SHH (n=25). Based on the prognosis, patients were categorized into two groups: good prognosis (WNT and SHH, n=14) and poor prognosis (non-WNT/SHH, n=25). Tumors were assessed by DWI and manually segmented using an in-house developed parametric (pMRI) software. Diffusivity metrics were automatically calculated on a pixel-by-pixel basis. The following first-order histogram radiomic metrics were calculated: ADCmean, ADCKurtosis, and ADCskewness. Mann–Whitney U test was used to evaluate the differences between the two subgroups.

Results

Our data showed significant differences in ADCmean between the two medulloblastoma subgroups - good prognosis and poor prognosis: 690 ± 101 vs. 816 ± 117 $10^{-6} \text{mm}^2/\text{s}$ respectively, ($p < 0.002$). In terms of ADCKurtosis and ADCSkewness, we also found significant differences among the groups: 13.20 ± 8.11 vs. 8.92 ± 5.09 and 3.54 ± 0.86 vs. 3.00 ± 0.73 , respectively ($p < 0.05$).

Conclusions

ADC histogram analysis can be implemented as a complementary tool in the preoperative evaluation of medulloblastoma in children. This technique can provide valuable information for the differentiation of prognostic subgroups and aid in establishing a proper management approach, particularly in regions where easy access to molecular subtyping is not available.



(Filename: TCT_1518_abstractMedulloblastomasubtypes.jpg)

1559

Do not touch: A classic case of Multinodular and Vacuolating Neuronal Tumor (MVNT)

K Faiz¹, M Khan², E Kasper¹, J Provias¹, M Siddiqi³, F Salehi²

¹McMaster university, Hamilton, Ontario, ²McMaster University, Hamilton, Ontario, ³McMaster University, Mississauga, Ontario

Purpose

To display the characteristic MRI findings of MVNT which may obviate the need for surgical intervention for diagnosis.

Materials and Methods

A 25 years old female patient presented at our institution with headaches and blurry vision for 6 months. Brain MRI showed left parietal lobe gyriform, predominantly subcortical lesion with abnormal T2/FLAIR hyperintensity without significant associated volumetric expansion or mass effect. Close scrutiny of the periphery of the lesion demonstrated innumerable tiny T2 hyperintense punctate foci clustered together which were confluent centrally (towards the white matter) but appeared slightly more dispersed peripherally (towards the cortex). The lesion demonstrated increased diffusivity and minimal enhancement. MR spectroscopy at intermediate echo time demonstrated elevated choline within the confluent portion of the lesion centrally in keeping with low-grade neoplasm. The appearance of the lesion was most in keeping with a low grade neoplasm and in particular multinodular and vacuolating neuronal tumor (MVNT). Parietal craniotomy and microsurgical resection was scheduled. The procedure was uneventful and consisted of tan-grey soft tissue, cortex and white matter. It was sent for pathologic analysis. The tumor had a nodular architecture with a distinct microvacuolation. These nodules were comprised of a predominantly cellular population of medium to larger sized neuronal/ganglionic type cells. A thorough immunohistochemical analysis showed positivity for: CD56, CD34, p16 and Synaptophysin. The findings were consistent with multinodular and vacuolating neuronal tumour with an associated focal cortical dysplasia (ILAE Blumcke classification predominantly FCD3b). The patient has been symptom free after surgery with no signs of tumor progression.

Results

N/A

Conclusions

Our case displayed characteristic MRI findings of MVNT, with "aunt-Minnie" appearance of these typical findings which may obviate

the need for surgical intervention for diagnosis. We demonstrate that these rare lesions have typical features on standard MRI sequences indicative of biologically non aggressive lesions. Imaging characteristics did not change over time suggesting that patients with typical MVNT imaging features may not need surgical intervention for diagnosis.

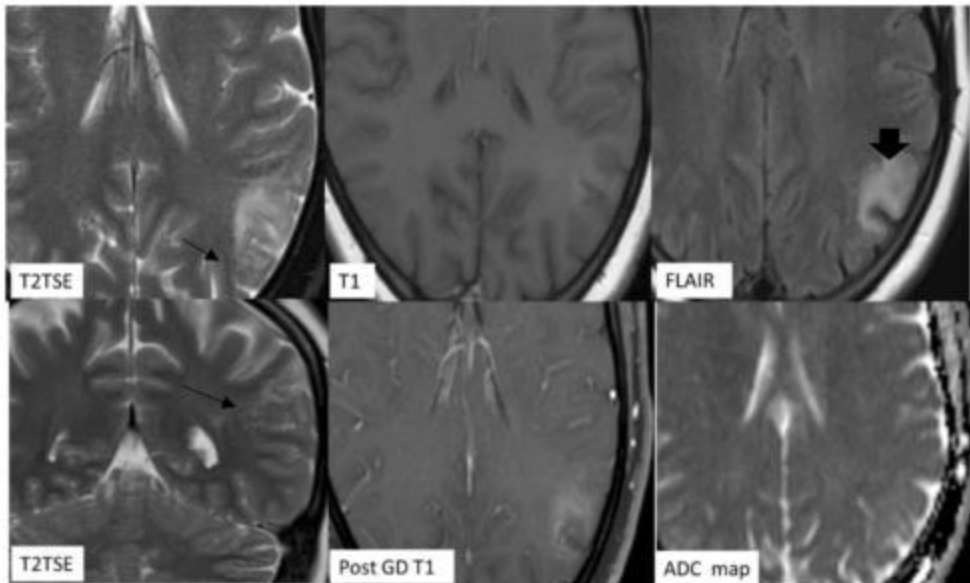


Fig. 1. Conventional MRI revealed a left juxtacortical parietal lesion, with partial involvement of the adjacent cortex. Close scrutiny of the periphery of the lesion demonstrated innumerable tiny T2 hyperintense punctate foci clustered together which were confluent centrally (arrow head) but appeared slightly more dispersed peripherally (arrows). These are hyperintense on T2 and FLAIR and hypointense on T1 sequences, with increased diffusivity and minimal enhancement.

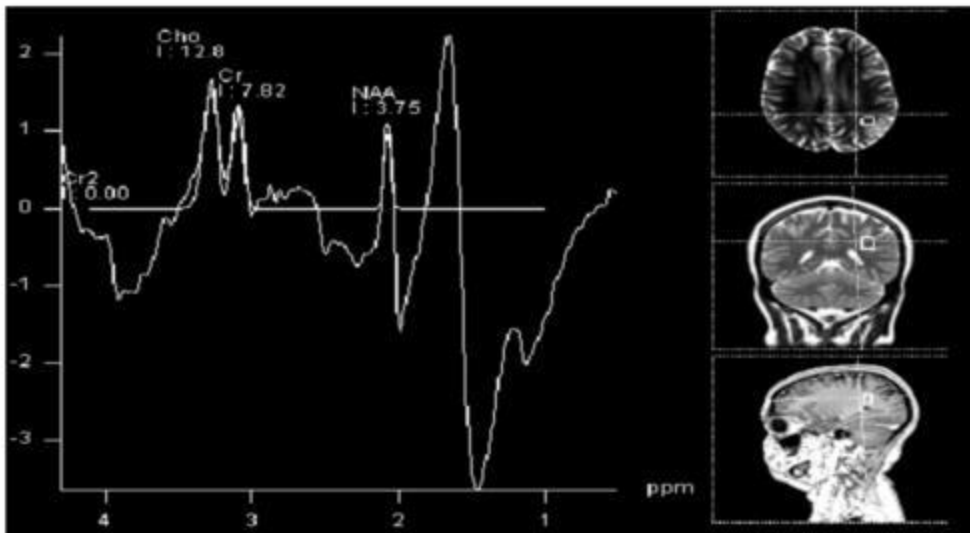


Fig. 3. MR spectroscopy at intermediate echo time demonstrated elevated choline within the confluent portion of the lesion centrally in keeping with low-grade neoplasm.

Does the Higher Relaxivity of Gadobenate Dimeglumine Permit Gadolinium Dose-lowering in MRI of the Central Nervous System (CNS)? Results of a Large Scale Parallel-Group Comparison

M DeLano¹, V Spampinato², E Chang³, R Barr⁴, R Lichtenstein⁵, B Cheong⁶, Z Wen⁷, C Colosimo⁸, J Vymazal⁹
¹Michigan State University, Grand Rapids, MI, ²MUSC, Charleston, SC, ³VA San Diego Healthcare System, San Diego, CA, ⁴Southwoods Imaging, Youngstown, OH, ⁵Sarasota Memorial Hospital, Sarasota, FL, ⁶St Luke's Medical Center, Houston, TX, ⁷Zhujiang Hospital, Guangzhou, China, ⁸Fondazione Policlinico Universitario "A. Gemelli", Rome, Italy, ⁹Na Homolce Hospital, Prague, Czech Republic

Purpose

Concern over possible long-term risks associated with Gd retention has encouraged the use of lower Gd doses at many imaging centers. The higher relaxivity of gadobenate dimeglumine (MultiHance) may be ideally suited to reduced dose protocols (1-5). We aimed to compare 0.05 and 0.1 mmol/kg BW doses of gadobenate at 1.5T and 3T in patients undergoing CE-MRI of the CNS.

Materials and Methods

352 patients who had received either 0.05 or 0.1 mmol/kg gadobenate for routine CE-MRI of the CNS, and had available pre- and postdose T1-SE/FSE, and/or T1-GRE, and T2-SE/FSE, and FLAIR MR images, were retrospectively enrolled at 7 centers in the USA. Images were prospectively reviewed by three blinded, independent neuroradiologists in terms of qualitative (delineation of lesion border, visualization of internal morphology, contrast enhancement of lesions; 4-point scales from 1=poor to 4=excellent) and quantitative (lesion-to-brain ratio, contrast-to-noise ratio) endpoints. The non-inferiority of the 0.05 mmol/kg dose was determined for each visualization endpoint based on the lower limit of the 95% confidence interval for the difference in pre + postdose means between the 0.05 and 0.1 mmol/kg doses. A non-inferiority margin of -0.4 was defined.

Results

181 patients (109M/72F; including 40 under 18 years) received 0.05 mmol/kg gadobenate while 171 (79/92F; none under 18 years) received 0.1 mmol/kg gadobenate. The mean change in visualization endpoint from predose to pre+postdose was in all cases significant ($p < 0.0001$). Readers 1, 2 and 3 evaluated 163, 165 and 164 patients and 304, 225 and 249 lesions in the 0.05 mmol/kg group, and 158, 161, and 160 patients and 382, 309 and 298 lesions in the 0.1 mmol/kg group. The lower limit of the 95% confidence interval for the difference in pre + postdose means was above the non-inferiority margin of -0.4 for all comparisons confirming that 0.05 mmol/kg gadobenate was non-inferior to 0.1 mmol/kg gadobenate for lesion visualization. This was true for sub-analyses at both 1.5T and 3T. Quantitative analysis confirmed significantly higher LBRs and CNRs with the higher dose.

Conclusions

A gadobenate dose of 0.05 mmol/kg is non-inferior to 0.1 mmol/kg gadobenate for lesion visualization and may be considered if Gd dose reduction is a priority.

420

Dual-Energy CT for Differentiating Hemorrhage from Iodine Extravasation after Mechanical Thrombectomy in Patients with Ischemic Stroke: Feasibility and First Results using a new Dual-Energy Technique

S Winklhofer¹, L Acu¹, R Terziev¹, T Schubert¹, S Wegener¹, Z Kulcsar¹, H Alkadhi¹, S Hakim¹
¹University Hospital Zurich, Zurich, Zurich

Purpose

Parenchymal hyperdensities in non-contrast computed tomography (CT) of the brain are frequently seen after mechanical thrombectomy in patients with acute ischemic stroke. These hyperdensities can be either hemorrhage or extravasation of iodinated contrast media into the ischemic core due to luxury perfusion during the intervention. Dual-energy CT (DECT) has been shown to be able to differentiate between these two etiologies (Ref. 1). TwinSpiral DECT is a recently introduced technique, which allows to acquire images at two different energy levels in two consecutive spiral scans allowing for a strong energy separation. The aim of this study was to evaluate the feasibility and accuracy of TwinSpiral DECT to distinguish between hemorrhage and iodine extravasation after mechanical thrombectomy in patients with acute ischemic stroke.

Materials and Methods

In this IRB-approved study, non-contrast TwinSpiral DECT scans of 35 consecutive ischemic stroke patients (20 males, 15 females, mean age 72 ± 12 years) 24 hours after mechanical thrombectomy were analyzed. The presence or absence of parenchymal hyperdensities suspicious for hemorrhage and/or iodine was assessed using the standard mixed images simulating single-energy CT. Virtual non-contrast (VNC) and corresponding iodine images were reconstructed from TwinSpiral DECT (tube voltages 80 and 150Sn kVp). In case of parenchymal hyperdensities, the presence of iodine and/or hemorrhage was assessed qualitatively using VNC and iodine images. Follow-up examinations (CT or MRI) were used as standard of reference. Sensitivity, specificity, and accuracy for the detection of hemorrhage in DECT images was calculated.

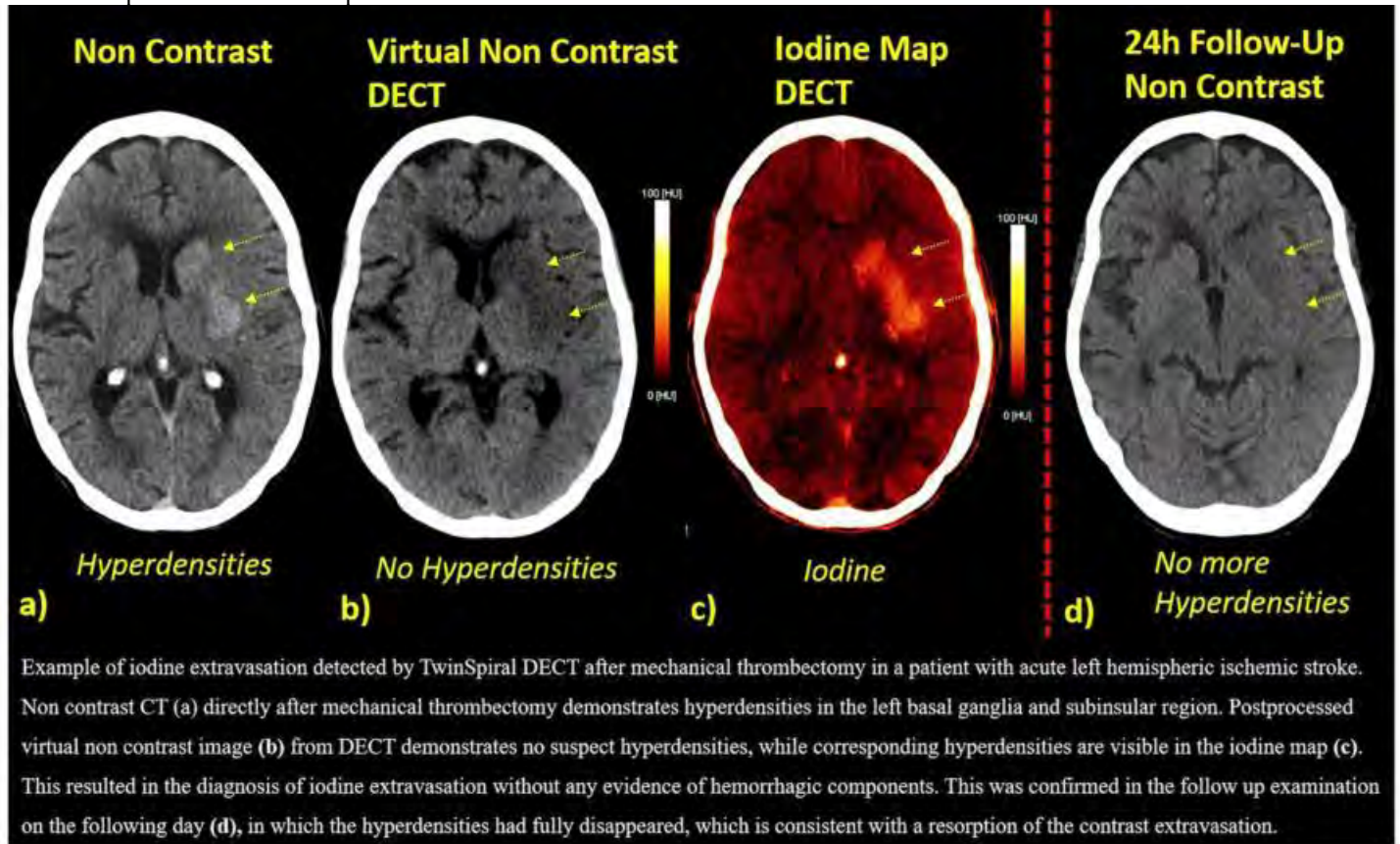
Results

The presence of parenchymal hyperdensities after mechanical thrombectomy was found in 16 of the 35 patients (46%). Hyperdensities

were classified by VNC and iodine images as hemorrhage in 3 (19%), as iodine extravasation in seven (44%), and as mixed (hemorrhage and iodine) in six patients (37%). The sensitivity, specificity, and accuracy for the detection of presence of hemorrhage in DECT images was 82%, 100%, and 88%, respectively.

Conclusions

TwinSpiral DECT demonstrates a high accuracy and excellent specificity for differentiating parenchymal hemorrhage from iodine extravasation in patients after mechanical thrombectomy. This technique is helpful for making the correct diagnosis and to guide further therapeutical decisions in patients with acute ischemic stroke.



(Filename: TCT_420_Figure_ASNR_DECT_Abstract_300.jpg)

1085

Dual-Energy CTA Iodine Map Reconstructions Improve Visualization of Residual Cerebral Aneurysms Following Endovascular Coiling

D Wolman¹, G Kuraitis², E Sussman³, B Pulli³, J Heit⁴

¹Stanford University Hospital, Palo Alto, CA, ²Stanford University, Los Angeles, CA, ³Stanford University, Stanford, CA, ⁴Stanford University, Los Altos, CA

Purpose

Dual-energy CTA (DECTA) is capable of material-specific decompositions which can highlight iodinated contrast, subtract predefined materials, and reduce beam hardening artifact.(1) We present a novel technique in which iodine map CTA (IM-CTA) reconstructions highlight iodinated contrast and subtract platinum coils, removing coil artifact when viewed as a MIP. We compare reference-standard cerebral angiography (CA) to conventional CTA (CCTA), MRA, IM-CTA, and IM-CTA MIPs to determine which method best detects aneurysm residua after endovascular coiling.

Materials and Methods

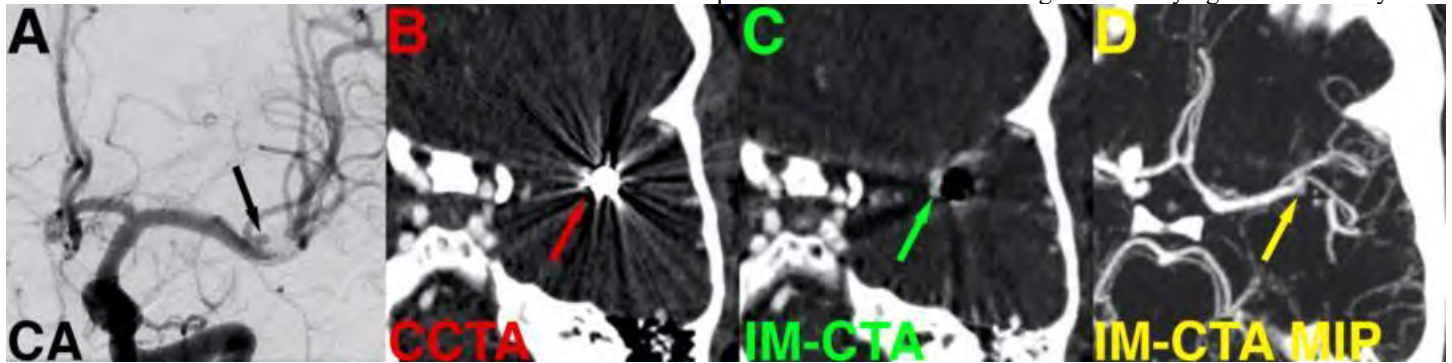
We included consecutive patients who underwent endovascular aneurysm coiling, follow-up DECTA and possible MRA, and DCA within 24 months of CT without intervening re-treatment. DECTA was performed 80- and Sn140-kVp tube voltages on a GE Revolution scanner with automatic generation of default CCTA and IM-CTA reconstructions. Blinded to CAs, all cross-sectional images were reviewed in consensus by 3 neurointerventionalists for residual aneurysms and respective modified Raymond-Roy classifications (mRRC). Sensitivity, specificity, and accuracy of each series is reported relative to DCA, and single-factor ANOVA and pairwise Spearman correlation coefficients were used to compare the accuracy of each series with regard to mRRC. Readers provided ROI measurements of HU deviation at the aneurysm neck within the parent vessel for quantitative noise assessment and qualitatively scored each series at that site on a 3-point scale ranging from uninterpretable to excellent image quality.

Results

Twenty-one patients with 25 coiled aneurysms were included, 10/21 of whom also underwent MRA. Mean time from DE-CTA to CA was 286 ± 212 days. IM-CTA and MIP IM-CTA most sensitively (89% and 90%) and specifically (93% and 93%) detected residual aneurysms, as compared to CCTA (6% and 86%) or MRA (67% and 50%). Relative to CA, IM-CTA and MIP IM-CTA most accurately detected (92% vs. 28% for CCTA) and classified residual aneurysms by mRRC ($\rho_{C-CTA} = -0.08$; $\rho_{IM} = 0.50$; $\rho_{MIP} = 0.55$; $P < 0.001$). Reader consensus reported the best image quality at the aneurysm neck with IM-CTA and MIP IM-CTA, with 56% of CCTAs considered uninterpretable vs. 0% of IM-CTAs. Image noise, defined as the mean SD near the aneurysm neck, was significantly lower for IM-CTA (34.5 ± 5.4 HU) or MIP IM-CTA (33.8 ± 8.7 HU) than CCTA (136.6 ± 7.1 HU; $P < 0.001$).

Conclusions

IM-CTA can subtract coil mass artifact and is more sensitive and specific than CCTA in detecting and classifying residual aneurysms.



(Filename: TCT_1085_201102_ASNR_DECTA-Coil_Figure2.jpg)

329

Dual-Energy Parathyroid 4D CT: Improved Discrimination of Parathyroid Lesions from Thyroid Tissue Using Noncontrast 40 keV Virtual Monoenergetic Images

A Pavlina¹, J Sachs¹, M Lipford¹, P Bunch¹

¹Wake Forest School of Medicine, Winston-Salem, NC

Purpose

Parathyroid CT commonly includes noncontrast, arterial, and venous phases (1). Up to 25% of parathyroid lesions (2) may appear nearly isodense to the thyroid on arterial and venous phases. In such cases, noncontrast images facilitate discrimination of parathyroid lesions from thyroid on the basis of thyroid iodine (K-edge 33 keV) content. However, primary hyperparathyroidism commonly coexists with thyroid disease (3), which may produce abnormal hypoattenuation of the thyroid due to decreased iodine, complicating CT interpretation. We hypothesize that dual-energy CT (DECT) 40 keV virtual monoenergetic images (VMI) will facilitate discrimination of thyroid tissue and parathyroid lesions by accentuating attenuation differences. Our purpose is to test this hypothesis through quantitative assessment of attenuation and contrast-to-noise ratios (CNR) between standard noncontrast images (70 keV VMI) and noncontrast 40 keV VMI.

Materials and Methods

Retrospective, HIPAA-compliant, IRB-approved. 15 parathyroid CT examinations met the following inclusion criteria: 1) DECT acquisition; 2) parathyroidectomy performed; 3) largest pathologically-proven parathyroid lesion at least 1 cm; 4) no prior thyroidectomy. Regions of interest (ROIs) were placed within the thyroid, largest pathologically-proven parathyroid lesion, and subcutaneous neck fat by a neuroradiology fellow on 70 keV and 40 keV VMI. Mean and SD HU attenuation were recorded. CNR was calculated for the thyroid relative to pathologically-proven parathyroid lesions using: $(ROI_{thy} - ROI_{par}) / SD$, where ROI_{thy} = mean thyroid HU attenuation, ROI_{par} = mean parathyroid lesion HU attenuation, and SD = subcutaneous fat HU attenuation SD.

Results

Absolute thyroid and parathyroid HU increases at 40 keV relative to 70 keV are summarized in Figure 1A. Figure 1B summarizes CNR of thyroid relative to parathyroid at 40 and 70 keV. Median and IQR CNR at 40 keV was 4.69 [3.85, 5.82] and at 70 keV was 4.06 [2.67, 4.64]. Median difference in CNR was 0.91 with IQR [0.25, 1.20]; significantly different from zero ($p = 0.0026$, Wilcoxon signed rank test).

Conclusions

40 keV VMI significantly increase CNR of thyroid relative to parathyroid, facilitating discrimination of parathyroid lesions from thyroid tissue on noncontrast images (Figure 1C, 1D). These findings are particularly relevant when parathyroid lesions exhibit isoattenuation to thyroid on arterial and venous phases and when coexisting thyroid disease causes relative decreased attenuation of the thyroid gland.

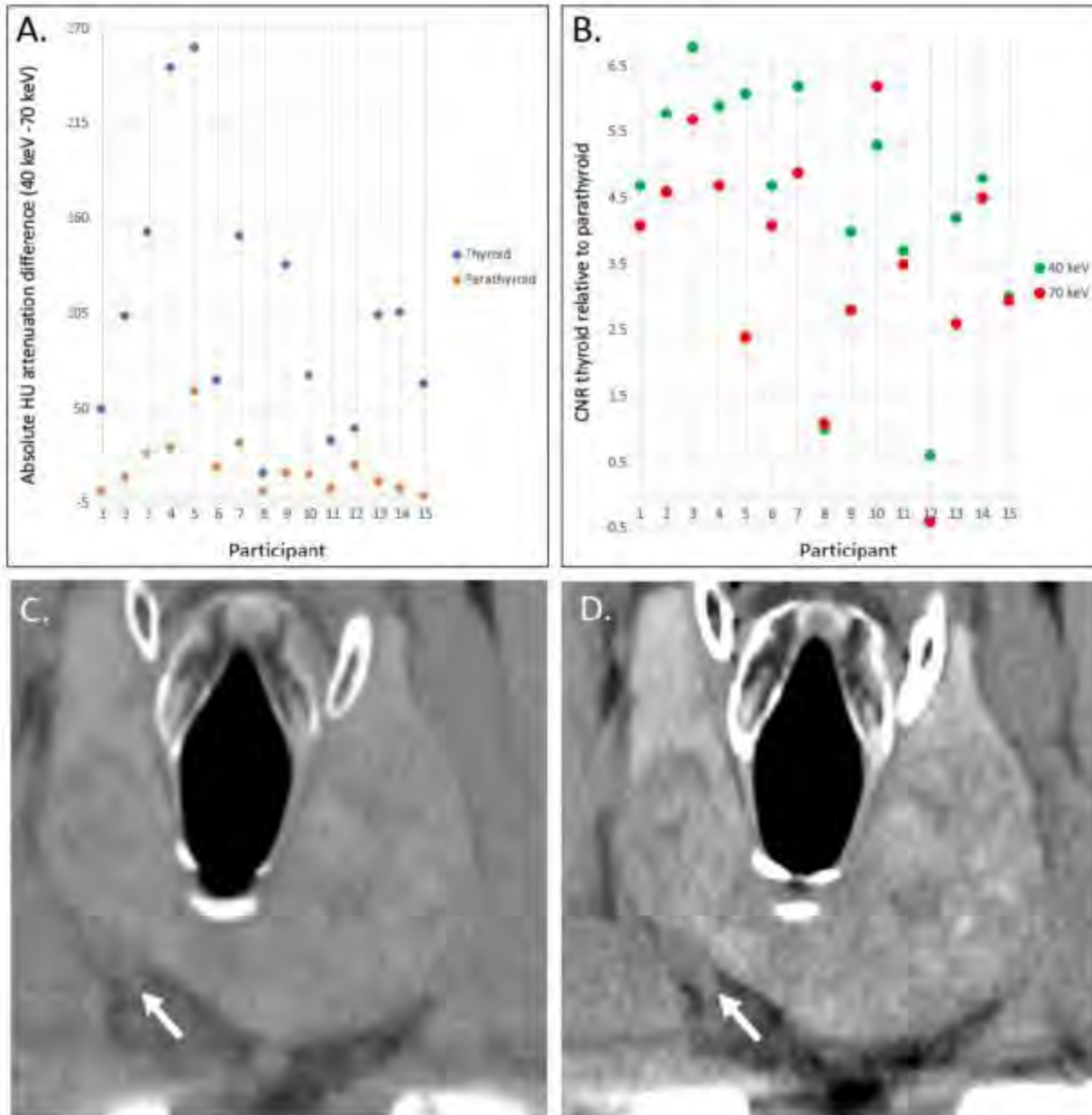


Figure 1. (A) Dot plot demonstrates the absolute HU attenuation difference between 40 keV and 70 keV for thyroid (blue) and pathologically-proven parathyroid lesions (orange) in each of the 15 study participants. **(B)** Dot plot demonstrates contrast-to-noise ratios between thyroid and pathologically-proven parathyroid lesions at 40 keV (green) and 70 keV (red) for each of the 15 study participants. **(C, D)** Coronal noncontrast 70 keV (C), and noncontrast 40 keV (D) images demonstrate a pathologically-proven right inferior parathyroid adenoma (arrows, C, D). Slice thickness (2 mm), window level (40 HU), and window width (400 HU) are identical for both images. Because the adenoma appeared isodense to the adjacent thyroid on the arterial phase image (not shown), it was uncertain whether the finding represented a parathyroid lesion or exophytic thyroid tissue. The adenoma appears slightly hypodense to thyroid on the standard (70 keV) noncontrast image (C); however, this attenuation difference is accentuated on the 40 keV image (D), increasing confidence that the finding represents a parathyroid lesion rather than exophytic thyroid tissue.

(Filename: TCT_329_Figure_abstract_final.jpg)

Dual-layer spectral detector CT of the brain: Normative data of electron density and effective atomic number

M Nakajo¹, K Kamimura², K Takumi³, Y Fukukura⁴, H Nagano⁵, T Yoshiura¹

¹Kagoshima University Graduate School of Medical and Dental Sciences, Kagoshima, Japan, ²Kagoshima University Graduate School of Medical and Dental Sciences, Kagoshima, Select a State or Province, ³N/A, N/A, ⁴Kagoshima University Graduate School of Medical and Dental Sciences, Kagoshima, Kagoshima, ⁵Kagoshima University Graduate School of Medical and Dental Sciences,, Kagoshima, Select a State or Province

Purpose

To describe electron density (ED) and effective atomic number (Zeff) values of the normal living brain tissues measured by dual-layer spectral detector CT (DLCT), and to evaluate their gray matter (GM) to white matter (WM) differentiation.

Materials and Methods

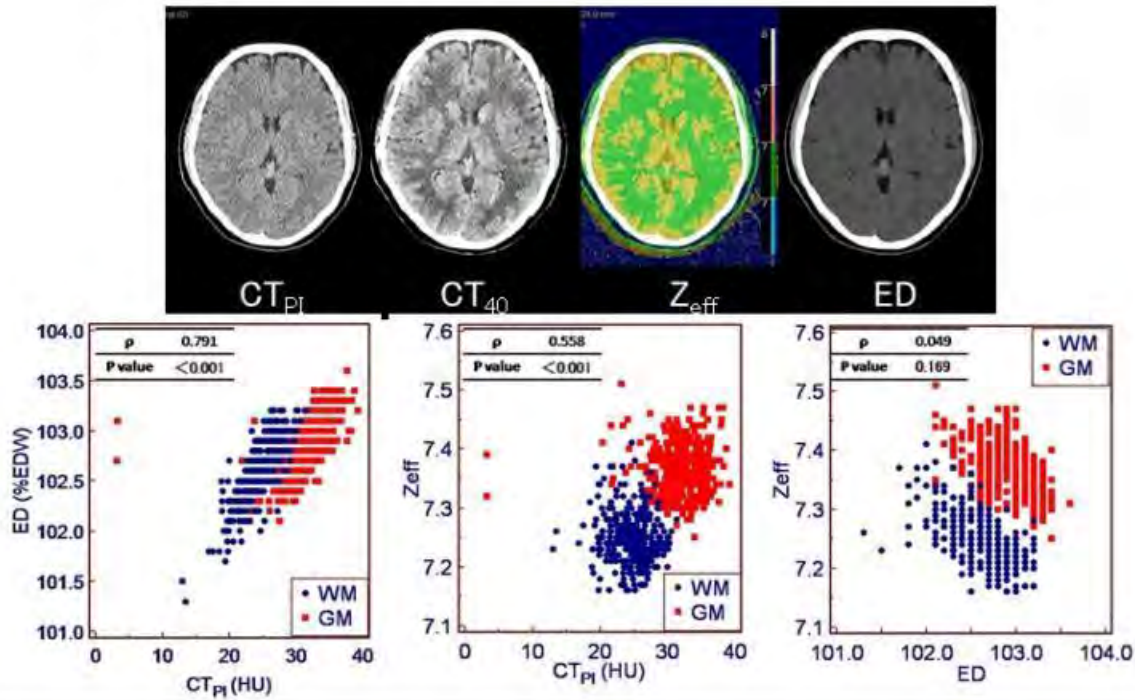
Non-contrast DLCT images of 50 patients (23 men and 27 women; age range 19-88 years; median 70 years) were retrospectively analyzed. Patients with any abnormal brain CT finding or medical history of any brain disease were excluded. In addition to conventional polyenergetic image (PI), virtual monoenergetic image (VMI) at 40 keV, and maps of ED (relative to water) and Zeff were generated. In each brain, elliptical ROIs were placed in 8 GM and 7 WM regions as well as in the CSF in the lateral ventricle to obtain the mean values. The mean values of ED and Zeff were compared among CSF, GM, and WM using Kruskal-Wallis test followed by Dunn test. Correlation between CT value on PI (CTPI), ED, and Zeff were evaluated using Spearman's correlation coefficient. Finally, GM/WM differentiation for each of CTPI, CT value on VMI at 40 keV (CT40), ED and Zeff was evaluated using area under the ROC curves (AUC).

Results

The mean ED (%) was highest in GM (102.91±0.30), followed by WM (102.62±0.32) and CSF (100.26±0.37) (P< 0.001, respectively), while the mean Zeff value was highest in GM (7.37±0.04), followed by CSF (7.31±0.05) and WM (7.25±0.04) (P< 0.001, respectively). We found a strong correlation between ED and CTPI ($\rho=0.791$, P<0.001) and a moderate correlation between Zeff and CTPI ($\rho=0.558$, P<0.001), whereas no significant correlation was shown between ED and Zeff ($\rho=0.049$, P=0.169). GM/WM differentiation was best performed by CT40 (AUC=0.997), followed by Zeff (0.971), CTPI (0.957), and ED (0.738).

Conclusions

Although both ED and Zeff are higher in GM than in WM, ED and Zeff have different contrast between brain tissues and CSF. Compared to conventional CT image, ED has poorer GM/WM differentiation, whereas Zeff may have equivalent to better GM/WM differentiation.



	Area under ROC curve*	Cutoff	Sensitivity (%)	Specificity (%)	Accuracy (%)
CT _{PI}	0.957 (0.940, 0.971)	>28.7	87.5 [350/400]	94.9 [332/350]	91.0 [682/750]
CT ₄₀	0.997 (0.990, 1.000)	>32.9	99.0 [396/400]	96.9 [339/350]	98.0 [735/750]
Z _{eff}	0.971 (0.956, 0.982)	>7.29	98.3 [393/400]	87.4 [306/350]	93.2 [699/750]
ED	0.738 (0.705, 0.769)	>102.7	69.0 [276/400]	64.0 [224/350]	66.7 [500/750]

Note-Data in parentheses are 95% confidence,

(Filename: TCT_593_ASNRfig.jpg)

721

Dural Arteriovenous Fistulas of the Foramen Magnum Region: Clinical and Angioarchitectural Phenotypes

M Caton¹, A Baker¹, K Narsinh¹, C Dowd¹, R Higashida², D COOKE¹, S Hetts³, v halbach², M Amans⁴

¹UCSF, San Francisco, CA, ²University of California, San Francisco, San Francisco, CA, ³N/A, N/A, ⁴Ucsf, San Francisco, CA

Purpose

Dural arteriovenous fistulas (dAVF) of the foramen magnum region (FMR) including fistulas of the marginal sinus (MS), hypoglossal canal, and condylar veins (CV)[1]. This subgroup of dAVF can present with a broad range of symptoms owing to variability and complexity in venous drainage pathways at the craniocervical junction [2]. It has been suggested that clinical phenotype may relate to venous angioarchitecture in this fistula subtype but this relationship is not well-described and current literature is limited to case reports and small series [3]. The purpose of this study was to describe a large, single-center experience with FMR-dAVF and to dissect the relationship between arterio- and venous angioarchitecture and clinical presentation.

Materials and Methods

We retrospectively reviewed a 10-year imaging database (Jan 2010-Aug 2020). Venous angioarchitectural features, arterial feeding vessels, and clinical presentation were extracted from the medical record. Angiographic risk was quantified using a modified version of the criteria proposed by McDougall et al [1]: Grade 1 = unrestricted sinus drainage, Grade 2 = Sinus reflux (including inferior petrosal sinus), Grade 3 = Reflux involving sinuses and cortical veins, Grade 4 = Restricted cortical vein outflow or perimedullary congestion.

Results

28 patients (mean age = 57.9, sex = 57.1% men) were diagnosed with 29 FMR AVF. These included 20 AVF of the MS and 9 of the CV (4 anterior CV, 2 posterior CV, 2 lateral CV, and 1 middle CV). Using our modified risk profile, there were 11 (37.9%) Grade 1, 9 (31.0%) Grade 2, 6 (20.7%) Grade 3, and 3 (10.3%) Grade 4. Pulsatile tinnitus was the most frequent symptom (82.1%) followed by

ocular symptoms (31.0%), subarachnoid hemorrhage (13.8%), CN XII palsy (10.3%), other CN palsy (6.9%), and asymptomatic (3.4%). The most frequent arterial supply was ascending pharyngeal artery (APA, 93.1%), posterior meningeal branch of vertebral artery (89.7%), occipital artery (65.5%), contralateral APA (55.5%), and ipsilateral internal carotid branches (meningohypophyseal and inferolateral trunk, together 48.3%). Relationship between venous risk profile and symptoms is summarized in Table 1.

Conclusions

We present the largest case series of FMR dAVF to date. Venous angioarchitectural features relate to clinical presentation: Orbital symptoms increase when sinus reflux is present, presumably due to pressurization of the cavernous sinus. Hemorrhage was only observed in grade III/IV fistulas.

**Clinical Presentation
(% of patients)**

Venous Angio-architectural Grade	<i>Pulsatile Tinnitus and/or Bruit</i>	<i>Orbital Symptoms</i>	<i>Hypoglossal Palsy</i>	<i>Myelopathy</i>	<i>Hemorrhage</i>	<i>Headache</i>
Grade I (n = 11)	90.9%	9.1%	0.0%	0.0%	0.0%	27.3%
Grade II (n = 9)	100.0%	44.4%	22.2%	0.0%	0.0%	44.4%
Grade III (n = 6)	66.7%	33.3%	0.0%	0.0%	16.7%	50.0%
Grade IV (n = 3)	33.3%	33.3%	0.0%	33.3%	66.7%	66.7%

(Filename: TCT_721_Figure1.jpg)

1598

Dural Sinus Narrowing and Ventriculomegaly as Predictors of Shunt-failure in Hydrocephalus Patients

B Rohr¹, F Knerlich-Lukoschus², O Jansen³, A Rohr⁴

¹University of British Columbia, West Vancouver, British Columbia, ²Asklepios Kinderklinik Sankt Augustin, St. Augustin, Nordrhein-Westfalen, ³University Hospital Schleswig-Holstein, Campus Kiel, Ki, Kiel, Schleswig-Holstein, ⁴Vancouver General Hospital, Vancouver, British Columbia

Purpose

Shunt-failure in hydrocephalus patients resulting in intracranial hypertension is a common and serious concern, however accurate diagnosis remains a challenge. The presence of enlarged ventricles on imaging is not considered reliable in predicting shunt-failure. Dural sinus narrowing has been proposed as an alternative marker and the purpose of our study was to compare ventriculomegaly and dural sinus narrowing as predictors of shunt-failure.

Materials and Methods

We analyzed 56 head MRIs/MRVs of children age 0-18 years (n=25) who presented with hydrocephalus and received CSF shunt procedures. Studies were included when f/u clinical data combined with intra-operative findings proved shunt-failure (positive Gold standard) or when a follow-up MRI was available when the child was well (negative Gold standard). The absence or presence of concerning hydrocephalus was diagnosed by an experienced blinded reader (A.R.). 3rd ventricle width, frontal horn diameters and greatest inner skull diameters on axial images were also measured and used to calculate Evan’s index and 3rd ventricular index. On MRV, the major dural sinuses were independently analyzed with respect to >50% narrowing, suggesting compression by increased CSF pressure. The presence / absence of ventriculomegaly and the presence / absence of significant dural sinus narrowing involving more than one of the major dural sinuses was correlated to the presence / absence of shunt failure as per Gold standard. Cochran Q test and descriptive statistics were used to find differences between the tests.

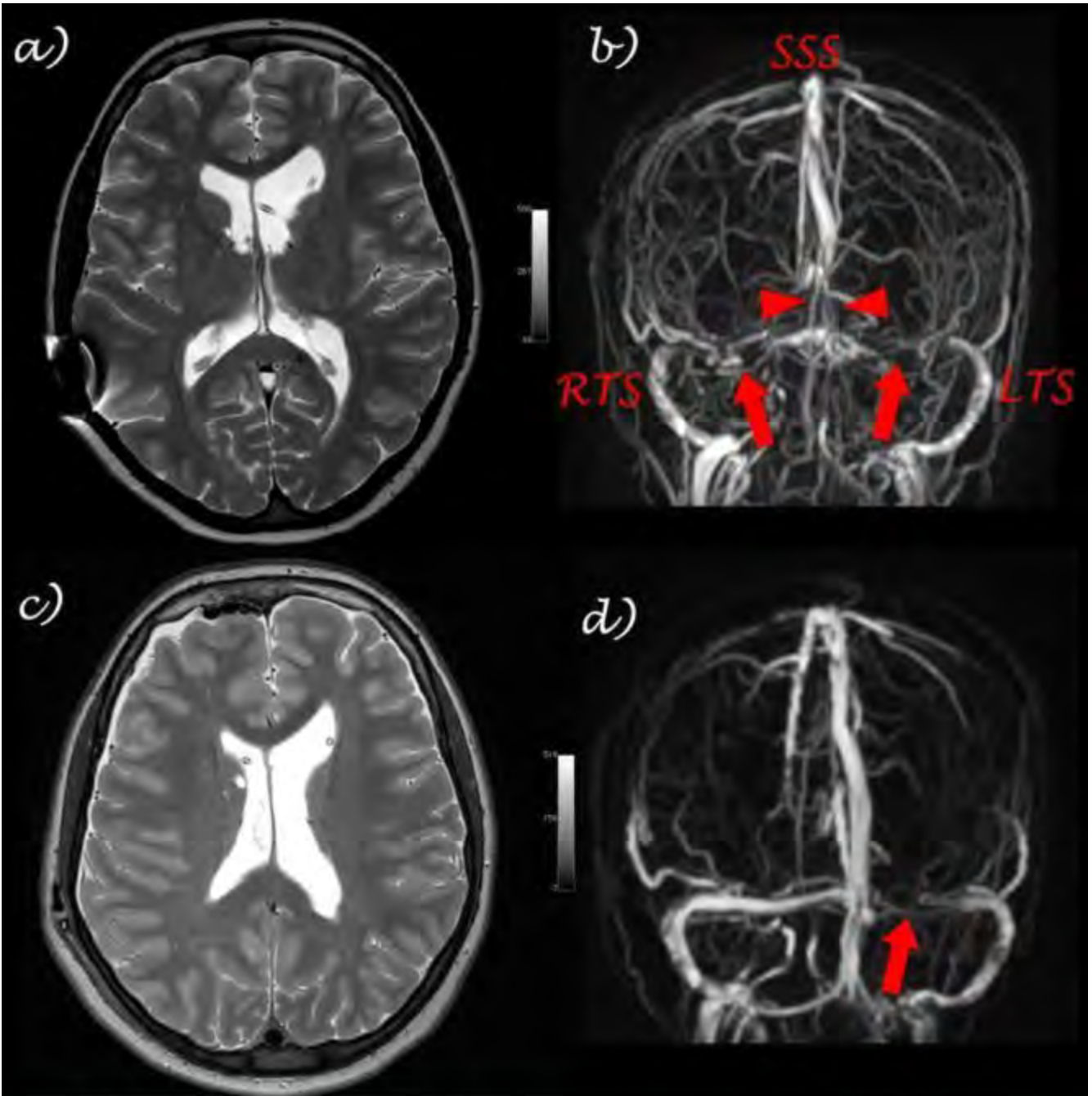
Results

20 MRIs/MRVs were available at time-points of shunt-failure and 36 were available when children were well. Dural sinus narrowing was more sensitive and specific in predicting shunt-failure than was ventriculomegaly (see table, p<0.05). Ventricle diameters and indices did not differ significantly between groups. Example figure: 17 year old girl with post-hemorrhagic hydrocephalus and ventriculo-peritoneal shunts. A first MRI when she presents with severe headache and vomiting shows normal ventricle size (a). MRV

(b) shows severe narrowing of the superior sagittal sinus (SSS, arrowheads) and of the left and right transverse sinuses (LTS, RTS, arrows). After shunt revision and improvement of symptoms, ventricle size has not changed significantly (c). MRV demonstrates normalization in the appearance of the SSS and RTS and residual narrowing in the LTS (d).

Conclusions

Dural sinus narrowing proved to be a more reliable marker compared to ventriculomegaly when diagnosing or excluding shunt-failure. Adding an MR venography to the standard protocol might therefore be considered in the workup of patients concerning for CSF shunt-failure and intracranial hypertension. This study has several limitations, including the retrospective character and limited number of patients and MRIs.



		Shuntfailure as per Gold standard					Shuntfailure as per Gold standard		
		Affected	Nonaffected	Total			Affected	Nonaffected	Total
Ventriculo-megaly	Positive	9	7	16	Sinus narrowing	Positive	14	5	19
	Negative	11	29	40		Negative	6	31	37
	Total	20	36	56		Total	20	36	56
Sensitivity	TP/(TP+FN)	0.45			Sensitivity	TP/(TP+FN)	0.70		
Specificity	TN/(TN+FP)	0.81			Specificity	TN/(TN+FP)	0.86		
PPV	TP/(TP+FP)	0.56			PPV	TP/(TP+FP)	0.74		
NPV	TN/(TN+FN)	0.73			NPV	TN/(TN+FN)	0.84		
Overall accuracy	(TP+TN)/(all)	0.68			Overall accuracy	(TP+TN)/(all)	0.80		

(Filename: TCT_1598_rohrupdate.jpg)

Dynamic Cerebral Perfusion Using C-Arm Flat Panel Detector CT in Angiography Suite: Comparison with Conventional Multislice CT Perfusion and MR Perfusion in Patients of Stroke

V Agarwal¹, A Kulkarni²

¹Christian Medical College, Ludhiana, UT, ²Christian Medical College, Ludhiana, Punjab

Purpose

To show the feasibility and comparability of flat panel detector CT perfusion in neuro angiography suite with conventional multi-slice CT perfusion and MR perfusion in patients of stroke

Materials and Methods

- Prospective study. Single Institutional Study - 15 patients of acute stroke presenting within 24 hours of last seen well were included - All patients underwent Digital Subtraction Angiography. Mechanical thrombectomy was done in 10 patients. - 10 patients underwent conventional CT perfusion (within 6 hours of onset) and 5 patients underwent post contrast DSC MRI perfusion (6-24 hours of symptom onset or wake up stroke) - All patients underwent Flat panel detector CT perfusion (FPD - CTP) in neuro angiography suite before mechanical thrombectomy. - Analysis was done by two senior Neuroradiologists.

Results

- Between Deceber 2020 to September 2020, 15 patients (10 men, 5 women; mean age, 62 years) admitted for acute ischemic stroke were included. - The analysis of FPD-CTP versus MSCT Perfusion versus MRP, by the reviewers revealed a high Pearson correlation coefficient in both reviewers for CBF (0.95 to 0.98) and CBV (0.95-0.98). - The perfusion abnormalities were comparable using FPD-CTP, MRP and MSCT Perfusion for CBF and CBV

Conclusions

- We have shown the feasibility and good comparability of perfusion parameter maps generated using FPD-CT perfusion in neuroangiography suite with conventional CT perfusion and MR perfusion in patients with acute stroke. - This FPD-CT application may be substituted for MSCT imaging in selected patients with acute stroke so that in the future, patients may be directly referred to the angiography suite to save time and avoid transportation - This might be of value in exposing less health care staff to the patients with unknown COVID status

339

Dynamic [68]Ga-DOTATATE PET/MRI of the Normal Pituitary Gland in a Prospective Cohort

S Kim¹, M Roytman¹, M Skafida¹, E Lin¹, N Karakatsanis¹, J Ivanidze¹

¹Weill Cornell Medicine/New York-Presbyterian Hospital, New York, NY

Purpose

Normal pituitary cells, as well as various pituitary neoplasms, demonstrate high but variable somatostatin receptor 2 (SSTR2) expression, which can be visualized with [68]Ga-DOTATATE, a PET radiotracer which targets SSTR2 with high affinity [1]. [68]Ga-DOTATATE PET has potential roles in preoperative and postoperative evaluations of pituitary neoplasms and in guiding molecular targeted therapy such as [177Lu]-DOTATATE. The purpose of our study was to evaluate static and dynamic [68]Ga-DOTATATE PET/MR characteristics in the normal adult pituitary gland in a prospective clinical cohort.

Materials and Methods

19 patients were prospectively imaged over 17 months for the purpose of evaluating meningioma, a SSTR positive tumor. [68]Ga-DOTATATE PET was acquired in 3D list mode over 50 minutes, beginning 5-15 minutes post injection. In the pituitary gland, dynamic activity data was obtained on a voxel-by-voxel basis through a volumetric analysis of the co-registered PET and MRI images at each five minute frame, using VINCI software (Max Planck Institute for Metabolism Research, Cologne, Germany). We used the standard Patlak graphical analysis to generate voxel-wise measurement of the [68]Ga-DOTATATE macro parameter of Ki, denoting the net influx rate constant.

Results

19 patients (17 PET/MR, 2 PET/CT) were analyzed (female=13, male=6, mean age=67.2). In women, older age was associated with significantly lower normalized SUV. In younger patients, female sex was associated with significantly higher normalized SUV ($p<0.005$). There was a significant interaction between sex and age on Ki ($F(1, 15)=5.058, p=0.04$) but post hoc analysis revealed no significant pairs. Age was a statistically significant predictor of normalized SUV ($R^2=0.28, p<0.05$). When stratified by sex, the effect of age was observed only in women. Dynamic time-activity curves for normalized mean SUV binned into 5-minute frames showed no apparent qualitative difference in uptake trends based on sex or age. Of note, the pituitary uptake of DOTATATE generally increased over time and sharply decreased after 50 minutes post injection, which was most pronounced in male subjects.

Conclusions

Demographic factors such as age and sex demonstrated significant influence on static and dynamic [68Ga]-DOTATATE PET parameters. Our findings represent the first in vivo investigation of pituitary biology with dynamic [68Ga]-DOTATATE PET and may help elucidate effects of sex hormones and physiologic lifetime change on SSTR signaling in normal pituitary tissue.

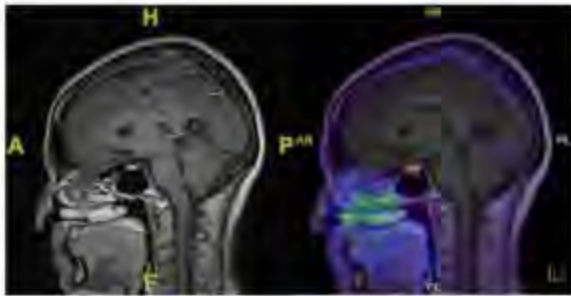


Figure 1: Sagittal T1 post contrast MRI of the brain (left) and fused DOTATATE PET/MR (right) demonstrating avid DOTATATE uptake in the sella turcica.

sPatlak Stratified by Age and Sex

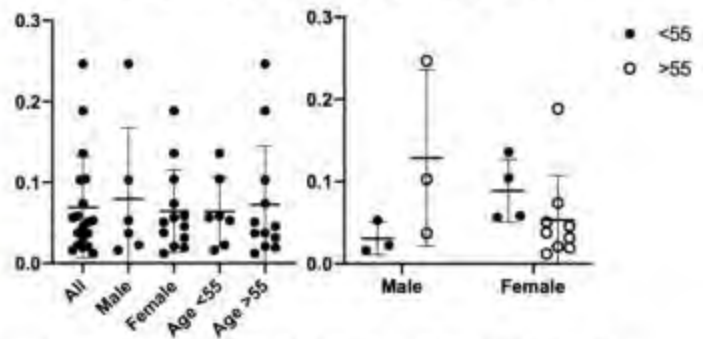


Figure 2: Distribution of sPatlak Ki with mean and std. deviations in the cohort stratified by age and sex.

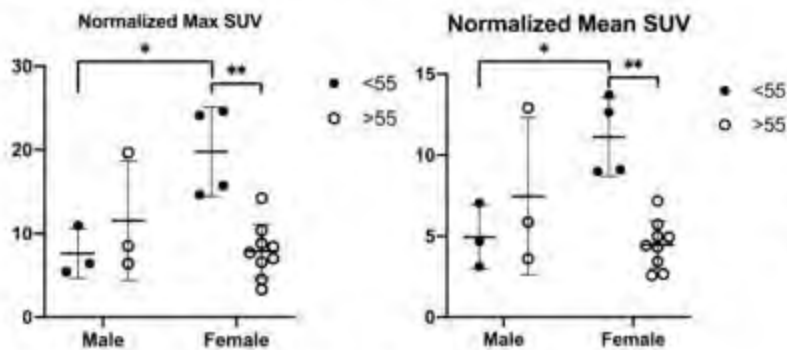
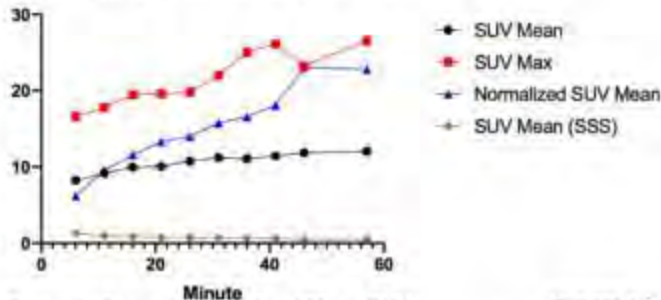
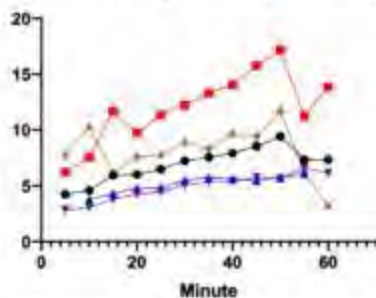


Figure 3: Distribution of normalized mean and max SUV with mean and std. deviations in the cohort stratified by age and sex.

Time Activity Curve of a 53 yo Female



Dynamic Average Normalized Mean SUV



Dynamic Average Normalized Mean SUV

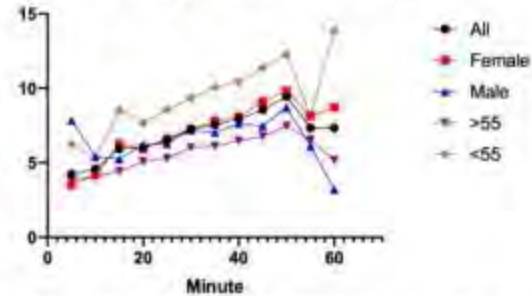


Figure 4: Dynamic time-activity curves of normalized mean SUV of a representative 53-year-old female patient as well as averaged SUV across the entire cohort stratified by age and sex.

Early Alzheimer's Detection from Structural MRIs using Convolutional Neural Networks

S Liu¹, A Masurkar², H Rusinek², J Chen², B Zhang², C Fernandez-Granda¹, N Razavian³

¹Center for Data Science, NYU, New York, NY, ²NYU Langone Health, New York, NY, ³NYU School of Medicine, New York, NY

Purpose

Early detection of Alzheimer's disease is critical for optimal intervention success. Structured MRI (T1) can provide a clinically scalable screening platform for this task. Existing methods rely on volumetric features to classify AD, using segmentation tools such as Freesurfer1. In this work we train and validate a deep convolutional neural network (CNN) model to classify three disease stages: cognitively normal (CN), mild cognitive impairment (MCI), and AD dementia (AD).

Materials and Methods

Data - Our study is based on two major Alzheimer's disease cohorts: Alzheimer's Disease Neuroimaging Initiative (ADNI)2, and National Alzheimer's Coordinating Center (NACC) 3. We restricted the analysis to scans acquired from subject ages of 65 to 85, and which had volumetric data available, leading to 423 subjects (1490 scans) in ADNI, and 319 subjects (357 scans) in NACC. We used data from 70% of the subjects in ADNI for training. Data from 88 subjects (301 scans) in ADNI were used for hyperparameter tuning. Final results were reported on two sets: 90 heldout subjects in the ADNI cohort; and the NACC data serving as external validation set.

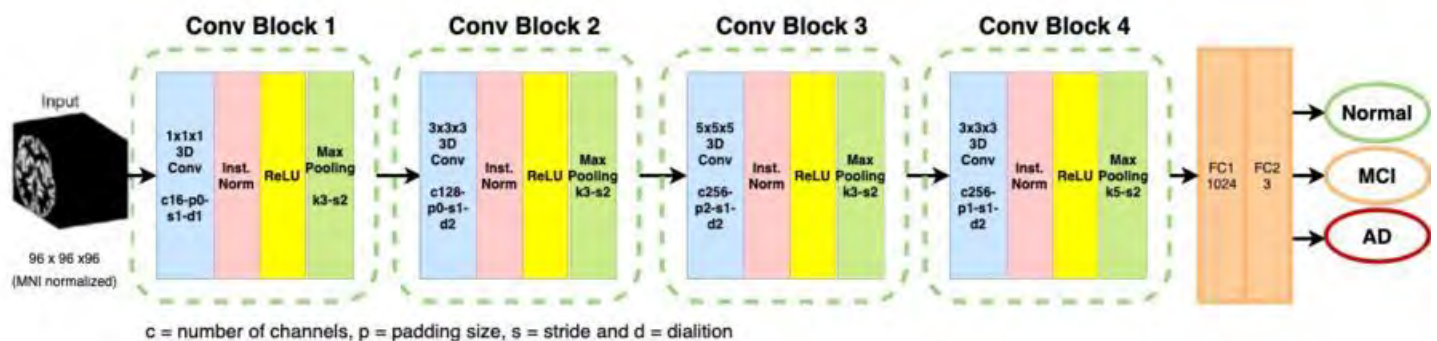
Modeling - We trained two models. A baseline logistic regression model over Freesurfer volumes of hippocampus, entorhinal cortex and medial temporal lobe (ICV normalized); and a 3D convolutional neural network, shown in Figure 1. We trained both models at the scan level for a 3-class classification task (CN vs MCI vs AD). Area under the ROC curve (AUC) of CN vs. [MCI or AD] serves as our evaluation metric.

Results

On the ADNI handout test set with 297 scans (89 CN, 111 MCI, and 97 AD), for classifying CN vs. MCI or AD, the proposed CNN model achieved AUC of 87.56 (95% CI: 87.1 - 88.02), compared to the baseline AUC of 84.45 (95% CI: 84.19 - 84.71). This model generalized well to NACC external validation data (357 scans: 190 CN, 80 MCI, and 87 AD), with an AUC of 84.16 (95% CI: 83.82 - 84.16). Baseline model AUC dropped to 78.54 (95% CI: 78.14 - 78.94) on the NACC cohort. On average, for one MRI, our CNN model requires 0.07s (15 min for NMI normalization), compared to 4-6 hours required for Freesurfer.

Conclusions

Compared to existing volume-based models, our proposed CNN model achieved better performance and exhibited stronger generalization to large external cohorts. Considering significantly lower computation time, our model can provide a potentially powerful screening tool based on T1 MRI for early Alzheimer's disease detection.



(Filename: TCT_546_AD_model.jpg)

Economic Impact of Workflow Image Processing to Reduce MR Contrast in Multiple Sclerosis Patients

R MATTAY¹, K Davtyan², J Rudie³, G Mattay², L Loevner², M Schnall², A Mamourian⁴, T Cook²

¹HOSPITAL OF THE UNIVERSITY OF PENNSYLVANIA, PHILADELPHIA, PA, ²Hospital of the University of Pennsylvania, Philadelphia, PA, ³N/A, N/A, ⁴Penn State Milton S. Hershey Medical Center, Hershey, PA

Purpose

A large percentage of multiple sclerosis (MS) patients experience "financial toxicity" due to imaging and other services, which can lead to loss of follow-up (1). Patients with MS typically routinely undergo serial contrast enhanced MRIs as often as every six months to every year (2). In light of recent FDA warnings of intracranial deposition of gadolinium from MR contrast, we previously implemented a quality improvement project wherein IV MR contrast would be reserved only for patients with evidence of new disease activity on pre-contrast brain imaging (3). Here we sought to explore the added positive economic impact brought about through this change in practice.

Materials and Methods

We previously implemented a protocol to determine the need for MR contrast agent administration in "real-time" by combining our in-house computer-assisted-detection software with 3-D Laboratory pre-processing of the pre-contrast T2/FLAIR imaging of the brain (3). As part of this study we compared scanner time and estimated Medicare reimbursement for imaging services using our current contrast conditional methodology versus calculated values for the prior protocol in which all patients should have received contrast injection as outlined in the standardized MR imaging protocol for MS.

Results

422 patients were imaged with this new protocol during a 5-month period and 60% of patients did not receive contrast injection. 75.1% of the total patients had imaging of the brain, cervical spine and thoracic spine, 15.6% had imaging of the brain and cervical spine, and 9.2% had imaging of the brain only. When compared to estimated scanner times and reimbursement for these same patients with the old protocol where all patients received contrast, the new contrast conditional protocol amounted to approximately 25% or 55.6 hours of scan time saved (222.7 hours vs. 278.3 hours) as well as a \$133,414 decrease in cost to the healthcare system (\$447,346.60 vs. \$580,760.06) which includes technical and professional fees. Calculations of net revenue to the hospital system per minute of scanner time used revealed \$33.48/min for the new protocol versus \$34.78/min for the old protocol.

Conclusions

This quality improvement project resulted in substantial economic benefit to the overall healthcare system. Although this may result in a loss of revenue to the radiology department and hospital for these set of patients, it is minimal when controlled for scanner time used, and is dramatically outweighed by other benefits to the patients.

	With Image Processing	Without Image Processing
Number of patients	422	422
Number of patients that received contrast	172	422
Estimated revenue based on Medicare reimbursement	\$450,836.08	\$588,950.64
Contrast costs	\$3,489.48	\$8,190.59
Net reimbursement (Reimbursement - Contrast)	\$447,346.60	\$580,760.06
Scanner Time	13,360.05 minutes	16,697.40 minutes
Net reimbursement per scanner time	\$33.48/minute	\$34.78/minute

(Filename: TCT_145_ASNRfigure300.jpg)

1091

Edge Density Imaging in MCI Patients Predicts Short-Term Conversion to AD

M Wang¹, T Benzinger², C Raji³

¹University of Pittsburgh/Carnegie Mellon University, Pittsburgh, PA, ²Washington University in St. Louis, Saint Louis, MO, ³Mallinckrodt Institute of Radiology Washington University in St. Louis, ST LOUIS, MO

Purpose

On average, 15% of patients with mild cognitive impairment (MCI) will develop Alzheimer's disease (AD) each year. The challenge lies in predicting which 15%. Clinically, being able to do so would give both prognostic utility in informing patients and a useful tool for detecting target populations for potential therapeutics that target the early stages of Alzheimer's. Scientifically, understanding the brain pathophysiology that foretells progression into Alzheimer's can help link how individual neuronal death leads to the macroscopic level changes we see in brain and behavior. With previous efforts in this field primarily focusing on grey matter changes, here, we utilized diffusion tensor imaging and edge density to identify changes in structural connectivity preceding Alzheimer's diagnosis.

Materials and Methods

We utilized a sample of 60 elderly subjects from the Alzheimer's Disease Neuroimaging Initiative dataset with mild cognitive impairment, 30 of which developed Alzheimer's disease within two years of the scan date. We generated edge density maps using diffusion tensor imaging. Edge density imaging shows the anatomical distribution and integrity of the white matter connectome and has been used in previous work to detect structural connectome perturbations. We utilized lasso to predict Alzheimer's conversion.

Results

We found that we could predict conversion to Alzheimer's with an accuracy of 82.5% using leave one out cross-validation. Receiver operator curve statistics are shown in Figure 1. Figure 2 shows which tracts are associated with conversion. We find that conversion is associated with decreased edge density in the left cingulum and extreme capsule, while positive association is seen in the right cortico-striatal pathway and the posterior commissure.

Conclusions

We find that we can accurately predict conversion to Alzheimer's disease in patients with mild cognitive impairment using edge density imaging. In comparison, other methods in the literature that utilize only a single imaging modality typically perform in the mid to high 70s on accuracy [1-3], requiring either multiple imaging modalities or other biomarkers such as CSF sampling to be used to enter into the 80s on the ADNI dataset. We believe this reflects an interesting direction towards early detection of dementia via analyzing changes in the connectome.

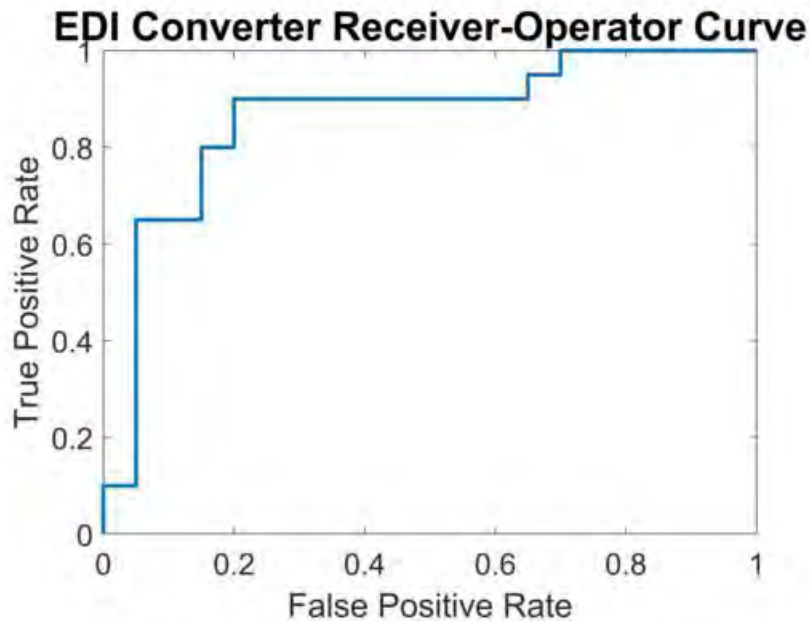


Figure 1: Classification accuracy using edge density imaging to distinguish between healthy controls and MCI->AD converters

(Filename: TCT_1091_ADConverters_EDI_Figure.jpg)

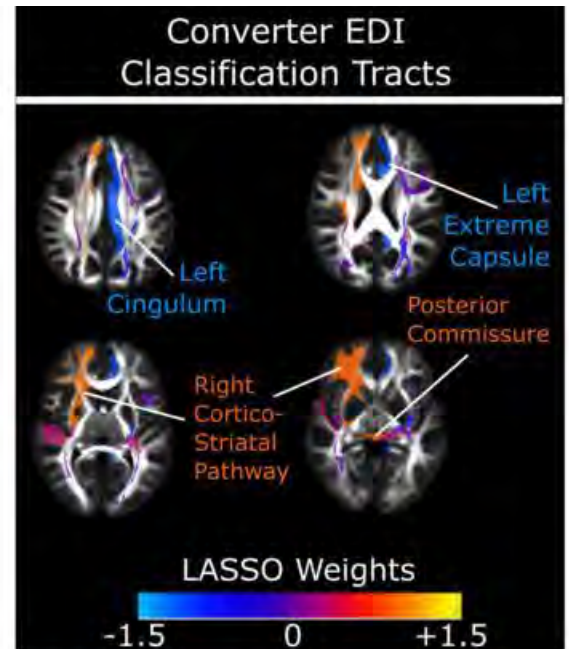


Figure 2: Tracts identified by lasso. Orange indicates increased edge density is a/w conversion, blue the opposite

1017

Edge Density Imaging Reveals Structural Connectome Reorganization associated with High BMI

M Wang¹, T Benzinger², C Raji³

¹University of Pittsburgh/Carnegie Mellon University, Pittsburgh, PA, ²Washington University in St. Louis, Saint Louis, MO, ³Mallinckrodt Institute of Radiology Washington University in St. Louis, ST LOUIS, MO

Purpose

While obesity's effect on traditional markers of brain structural integrity, such as regional volume and markers of vascular health, is well-demonstrated, its effect on the structural connectome is comparatively less understood [1,2]. fMRI studies have shown that subjects with high BMI show disrupted connectivity in both global resting networks and more localized emotional regulation ones purported to influence food-seeking behavior [3]. Given the vulnerability of white matter tracts to vascular disease, we sought to answer whether there was evidence of similar disruptions occurring in white matter connectivity, possibly leading to a feedback loop of obesity, resulting damage to structural connectivity, and ensuing vulnerabilities in functional behavioral regulation networks.

Materials and Methods

We utilized a sample of 60 elderly control subjects from the Alzheimer's Disease Neuroimaging Initiative dataset and utilized diffusion-tensor-imaging to compute edge density imaging using tractography. Edge density imaging shows the anatomical distribution and integrity of the white matter connectome and has been used in previous work to detect structural connectome perturbations. We utilized canonical correlation analysis to identify changes in edge density associated with high BMI.

Results

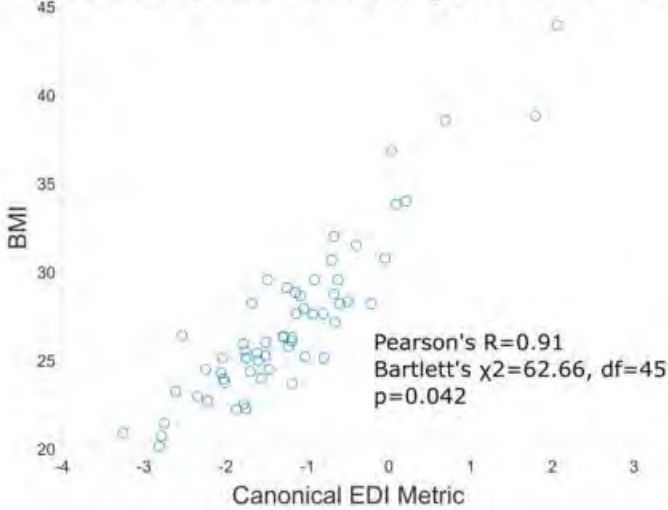
We found a linear combination of tract-averaged edge density that was statistically significantly correlated to BMI ($p=0.04$, multiple comparisons correction done via chi-squared), shown in Figure 1. We found that high BMI was associated with decreased edge density in deep periventricular tracts (namely the corpus callosum and fronto-/parieto-pontine tracts) but increased density in more peripheral, lateral zones as shown in Figure 2.

Conclusions

We find that obesity is associated with a reorganization of the structural connectome away from medial periventricular tracts towards lateral, peripheral ones. As obesity is associated with vascular damage of these periventricular tracts, we believe that this

reorganization indicates resulting compensatory changes. Furthermore, many of these tracts contain connections between regions such as the cingulate cortex, prefrontal inhibition control zones, and basal ganglia structures that are purported to be involved in food and reward processing and are known to have defective functional connectivity in obese patients [3,4]. We believe that this represents an interesting direction for future work in tying obesity-related neural damage to disrupted functional regulatory networks.

Canonical Correlation Analysis: EDI vs BMI



Canonical Coefficients of EDI to BMI Correlation

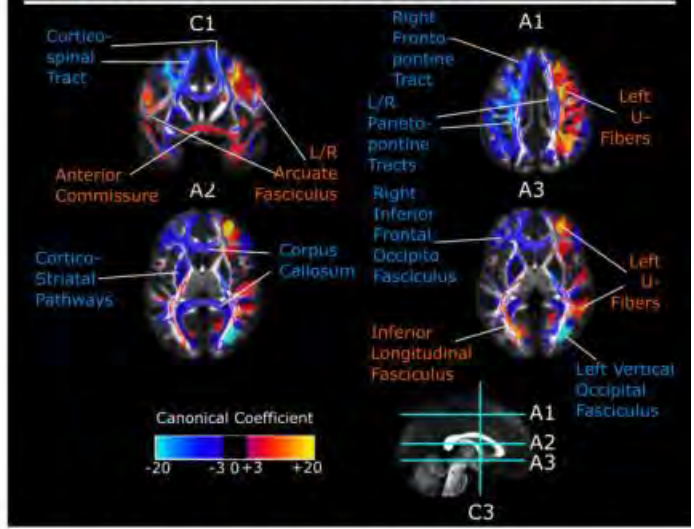


Figure 1: Correlation Analysis shows that changes in edge density imaging (EDI) can be statistically significantly linked to BMI

Figure 2: Tracts identified by canonical analysis. Orange indicates increased edge density is a/w high BMI, blue the opposite

(Filename: TCT_1017_Obesity_EDI_Figure.jpg)

1155

Effect of transcranial, near infrared light therapy on longitudinal evolution of white matter diffusion properties after moderate traumatic brain injury: Results of a randomized clinical trial

M Figueiro Longo¹, C Tan², J Man³, E RATAI⁴, A Yendiki⁵, M LEV⁶, R Gupta⁷

¹Massachusetts General Hospital, Boston, MA, ²Harvard Medical School / Massachusetts General Hospital, Cambridge, MA, ³Neuroradiology, Massachusetts General Hospital, BOSTON, MA, ⁴MGH ATHINOULA A MARTINOS CENTER FOR BIOMEDICAL IMAGING, CHARLESTOWN, MA, ⁵Athinoula A. Martinos Center for Biomedical Imaging, Department of Radiology, Massachusetts General, Charlestown, MA, ⁶MASS GENERAL HOSPITAL, Newton, MA, ⁷Massachusetts General Hospital and Harvard Medical School, BOSTON, MA

Purpose

Preclinical animal studies have demonstrated improved functional recovery from a traumatic brain injury (TBI) using Low-level Light Therapy (LLLT). [1] To assess neuro-reactivity of the injured brain to LLLT, we conducted a prospective, randomized, sham-controlled, interventional clinical trial of LLLT in the setting of acute moderate TBI in humans.

Materials and Methods

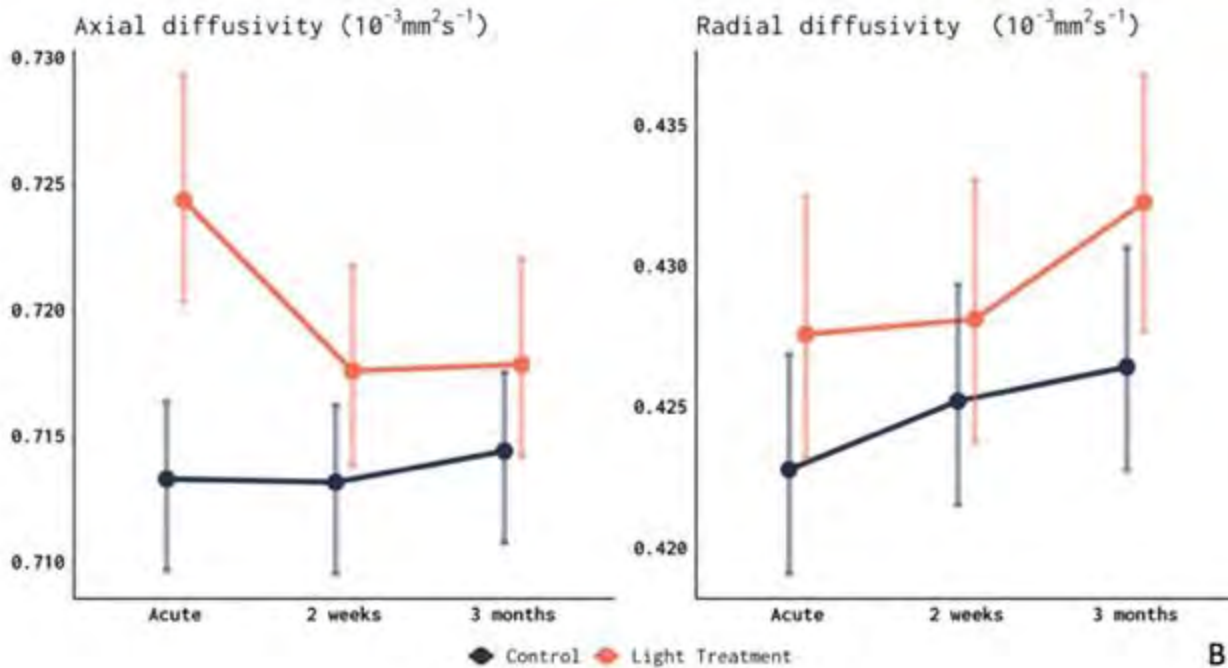
In this single-center trial, 68 patients (38 males, 49.7 +/- 18.8 years old) with acute, blunt moderate TBI were randomized to LLLT or sham groups within 72h after the trauma. Light therapy --- provided by a custom-built helmet delivering 810nm light uniformly to the skull (Figure A) --- was administered over 3 successive days via 20-minute session of donning the helmeting and turning the light on. MRI was performed in the acute (within 1 week), early sub-acute (2-3 weeks), and late sub-acute (~3 months) stages of recovery. Temporal evolution of radial (RD), axial (AD), mean (MD) diffusivity and fractional anisotropy (FA) was studied using region-base analysis based on Freesurfer white matter parcellation. A linear mixed effects model was used to assess the impact of LLLT longitudinally while accounting for variability between subjects and brain regions.

Results

40 subjects (18 in the LLLT group and 22 in the sham group) completed the study with at least two MRIs and were included in the final analysis. There were no adverse effect attributable to LLLT. The DTI analysis revealed that AD and RD tended to be higher in light treatment group across all time points ($P = 0.08$ for AD and $P = 0.11$ for RD), and there was a statistically significant (time x treatment) interaction for AD at all timepoints ($P < 0.001$) and for RD at 3-month time-point ($P < 0.001$). (Figure B).

Conclusions

LLLT was safe and affected longitudinal evolution of multiple diffusion tensor parameters in a statistically significant manner. Our study provides evidence that light therapy engages neural substrates that play a role in the pathophysiology of moderate TBI.



(Filename: TCT_1155_Figure.jpg)

1269

Efficacy of real-time intraoperative ultrasound in neurosurgery: Correlation to clinical outcomes and pre and post-operative imaging

A Nada¹, A Abdelrahman², M Northrup¹, E Mahdi¹, E Mahmoud³, C LEIVA-SALINAS¹, J Cousins¹, A Taha¹, A Humera¹
¹University of Missouri Healthcare, Columbia, MO, ²University of Toledo, Toledo, OH, ³National Cancer Institute, Cairo University, Cairo, Cairo

Purpose

Investigate the feasibility and value of real-time intraoperative ultrasound for resection of brain and spine masses and other pathologies. We will correlate intraoperative ultrasound findings with pre and postoperative imaging findings as well as the clinical outcomes.

Materials and Methods

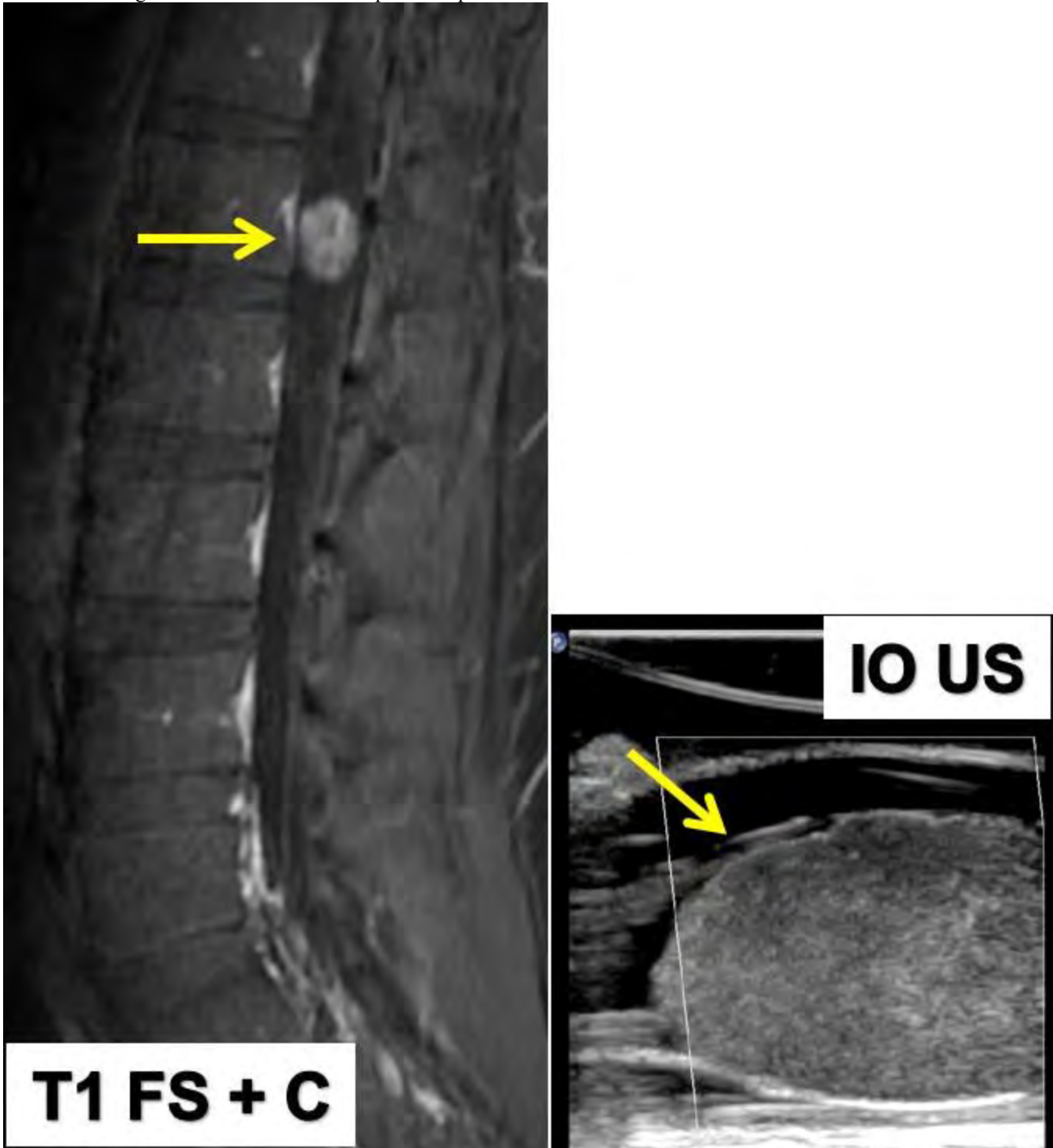
An IRB approve retrospective study was conducted for patients who underwent neurosurgery at our institution from January 2018 to August 2020. Fifteen patients has underwent real time intraoperative ultrasound at time of either brain or spine surgery. Efficacy of real-time for optimal localization and proper resection of CNS masses was evaluated and correlated to the patinets' clinical outcomes. The imaging findings of real-time intraoperative ultrasound also correlated to both pre and post-operative cross-sectional imaging.

Results

Our study included 15 patients (9 males, and 6 females) who underwent real-time intraoperative ultrasound at time of neurosurgery for brain and spine pathologies. The mean patients' age was 53 years (age range was 26-77 years). Complete mass resection with negative margins was achieved in 75% of brain masses (3/4) and 100% of intraspinal masses (7/7). Successful resection of the intraspinal arachnoid cyst and dorsal arachnoid web was achieved in 4 patients. We found strong positive correlation between the utility of real-time intraoperative ultrasound and patinets' clinical outcomes.

Conclusions

Real-time intraoperative ultrasound is an adjunctive helpful imaging tool for accurate localization and optimal resection of CNS tumors involving both intracranial and intraspinal compartments.



(Filename: TCT_1269_Fig.jpg)

934

Emergency Neuroimaging: Critical Result Frequencies Suggest Priority Scenarios for Clinical Decision Rules

L Tu¹, A Malhotra², A Venkatesh³, R Yaesoubi³, K Sheth⁴, H Forman⁵

¹Yale School Of Medicine, New Haven, CT, ²Yale University School of Medicine, New Canaan, CT, ³Yale University, New Haven, CT, ⁴Yale, New Haven, CT, ⁵Yale University, new haven, CT

Purpose

Emergency imaging is often used to mitigate against uncommon but high-risk pathologies which may harm patients. Clinical decision rules (CDRs) have been developed for many radiology indications in the ED setting, but few for neuroimaging indications beyond trauma and even fewer in common use. This work examines advanced imaging utilization, chief complaint for neuroimaging, and the rate of critical results to delineate scenarios where the development of CDRs may have the greatest impact on patient selection.

Materials and Methods

We queried the electronic medical record database at single large academic medical center for all imaging performed through the Emergency Department (ED) over a 4-year period (1/1/2014 to 1/1/2018). The most commonly performed exams are presented by rate of utilization. The distribution of ED chief complaints for patients who received a CT head and CTA head and neck exam is extracted. The ratio of critical results findings to total performed exams for common indications is calculated.

Results

A total of 290,030 advanced imaging exams (CT, MRI, PET) were performed through the ED between 1/1/2014 to 1/1/2018. The most common advanced imaging study was the CT head without intravenous contrast, comprising 23.0% of all such studies (n=66,707). CTA head and neck studies constituted 5.5% of advanced exams (n=13,916). The most common chief complaint for patients presenting to the ED receiving CT head imaging were altered mental status (9.4%), "neurologic problem" (7.8%), and fall (7.1%). For CTA head and neck, stroke (16.0%) and "neurologic problem" (13.1%) were among the most common chief complaints. The list extends far further than these above distributions and described in full in the presentation. Among the lowest yield scenarios for CT head imaging were studies performed for vertigo/dizziness (3.3%), hallucinations (1.8%), presyncope (0%), and delusions (0%). Among the lowest yield scenarios for CTA head and neck imaging were dizziness, (8.1%), generalized weakness (4.4%), and presyncope (0%). Finer grain details are presented in the full poster.

Conclusions

We identify scenarios with high utilization and low yield indicating an opportunity for improved efficiency and value via the development of CDRs. Priority scenarios include patients presenting with vertigo/dizziness, acute psychiatric presentations, and generalized weakness/fatigue.

1490

Emulating T2 Weighted MRI Data using T1 Maps and Susceptibility from STAGE Imaging

P Kokeny¹, D Utraiainen¹, S SETHI¹, K Ghassaban¹, Y Chen², E Haacke³

¹SpinTech, Inc., Bingham Farms, MI, ²Wayne State University School of Medicine, Detroit, MI, ³Wayne State University, Detroit, MI

Purpose

Clinical MRI has a growing need for fast quantitative brain imaging protocols. Many have been proposed and each has limits to the quantitative information it can provide. For those that provide maps of T1 and susceptibility ($\Delta\chi$) without T2 weighted imaging (T2WI) data, successfully emulating T2WI data may reduce total patient imaging time. The purpose of this work is to show how a T1 map, already very similar in contrast to a T2W image, can be further modified using $\Delta\chi$ to simulate high iron content regions comparable to conventional T2WI.

Materials and Methods

While relaxation times of biological tissues have a complex dependency on microstructure, there is still a general positive correlation to water content [1]. From the T1/T2/PD values of WM/GM/CSF, Table 1 shows why these tissues already look similar between a T1 map and T2WI data (see predicted values). While this works out nicely, iron also affects signal by decreasing T2. To compensate, a $\Delta\chi$ based weighting can be imposed on the T1 map to make iron rich regions and veins more comparable to T2WI data. Five cases from a previous study were used for analysis. Imaging was performed on a 3T GE Signa scanner. T2WI data was acquired sagittal with a 3D FSE sequence at 0.67x0.67x0.7mm³ and TE=109.5ms. T1 and $\Delta\chi$ maps were calculated using STAGE [2], acquired axial at 0.67x0.67x2mm³. The final emulated data was calculated by multiplying the T1 map with a $\Delta\chi$ weighted mask (see eqns 1 & 2 in [3], n=2). The CNR relative to WM of CSF, cortical GM, red nucleus (RN), and FLAIR lesions were compared between emulated and true T2WI data.

Results

CNR results are shown in Table 2. While CSF, cortical GM, and RN CNR are higher in the emulated data, the lesion CNR is about 2 times higher in the true T2WI data (see Figure 1). While some of the major arteries do have a shorter effective T1 from the time of flight effect, it is not always enough to match what is seen in the T2WI data (see Figure 1). This could possibly be fixed by tracking the arteries in the original STAGE data. Increased perivascular spaces are seen in the T2WI yet missed in the emulated data. This is likely due to the 3x larger voxel volume. A possible demyelinating lesion appears dark in both the emulated and true T2WI data (see Figure 1).

Conclusions

While a more rigorous analysis would be needed to validate the diagnostic capabilities of emulated T2WI data, this work shows promise in that the major brain tissue contrasts are comparable to the conventional T2WI scan.

	Assumed Tissue parameters			Predicted /CSF		Actual /CSF	
	T1 (ms)	T2 (ms)	PD	T1	$PDe^{-(T1/T2)}$	T1	T2WI
WM	900	70	0.71	0.20	0.15	0.18	0.18
GM	1600	100	0.81	0.36	0.28	0.30	0.29
CSF	4500	2500	1	1	1	1	1

Table 1: WM and GM signals relative to CSF predicted from the listed assumed tissue parameters and measured from the actual and emulated data (averaged over 5 cases). The predicted and actual values are within 20%. The emulated and true T2WI values are within 4%.

case	Emulated T2W						True T2W					
	reference		CNR				reference		CNR			
	WM (ms)	σ_{WM}	CSF	GM	RN	lesion	WM	σ_{WM}	CSF	GM	RN	lesion
1	804.9	41.6	71.1	14.3	-7.7	11.3	108.0	8.7	44.7	8.4	-6.7	16.3
2	846.3	51.9	73.4	11.4	-6.2	10.8	103.8	7.9	58.9	7.4	-4.5	23.5
3	801.6	48.3	78.3	8.2	-6.3	7.3	148.9	9.6	64.0	6.4	-2.2	14.3
4	847.3	51.0	85.1	9.5	-8.0	15.5	93.4	8.6	57.0	7.9	-5.1	27.8
5	816.5	55.5	64.8	9.1	-6.2	4.4	134.0	9.4	69.7	7.0	-5.3	11.6
Average	823.3	49.7	74.5	10.5	-6.9	9.8	117.6	8.8	58.9	7.4	-4.8	18.7

Table 2: CNR of different tissues relative to WM for five different cases from both emulated and true T2WI data.

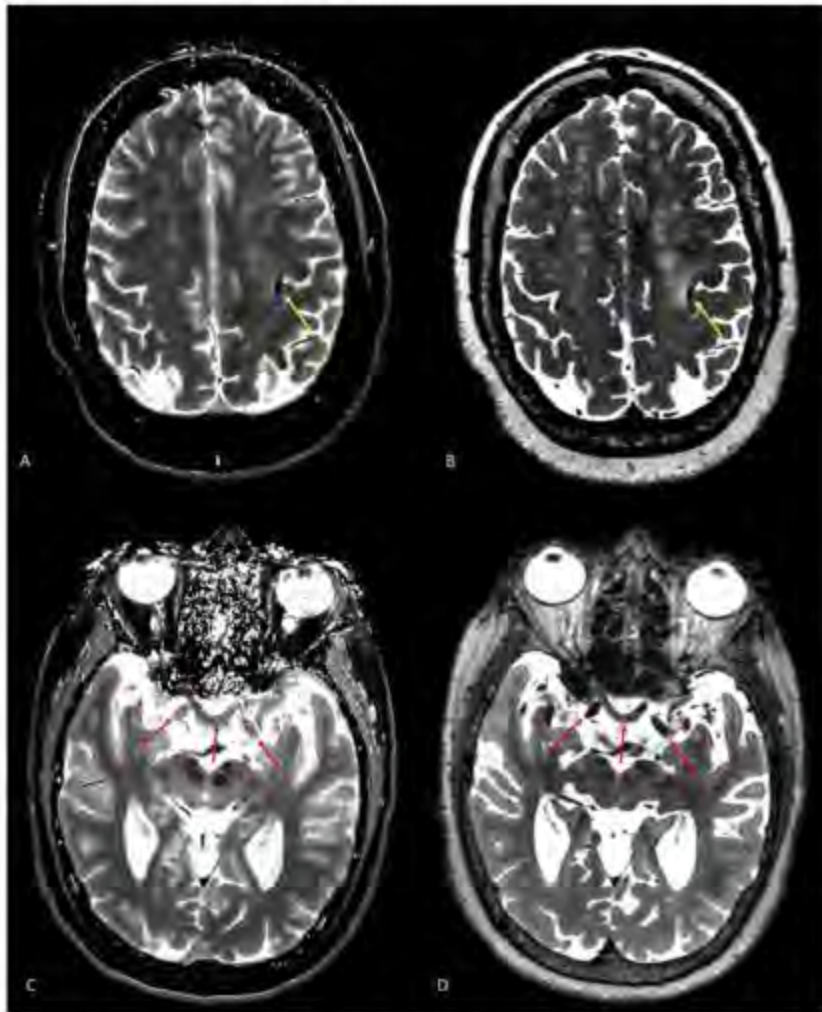


Figure 1: Slices of (A,C) emulated T2WI data and (B,D) true T2WI data from cases (A,B) #1 and (C,D) #5. The red arrows are pointing to the difference in arterial appearance. The yellow arrows are showing the similar appearance of a possible demyelinating lesion. Other lesions can be seen in the same slice and the higher contrast in the true T2WI is noticeable.

(Filename: TCT_1490_FigureALL_HR.jpg)

Endovascular Treatment of Wide-Neck MCA Aneurysms: Results from the SMART Registry

R Deleacy¹, D Bageac¹, K Woodward², M Park³, R Bellon⁴, A Spiotta⁵, O Zaidat⁶

¹The Mount Sinai Hospital, New York, NY, ²Vista Radiology, Knoxville, TN, ³University of Virginia, Charlottesville, VA, ⁴Radiology Imaging Associates PC, Englewood, CO, ⁵Medical University of South Carolina, Charleston, SC, ⁶Mercy Health, Toledo, OH

Purpose

Endovascular treatment of wide-neck aneurysms has been associated with higher recanalization and complication rates when compared to other subtypes. (1,2) We present results from the Assessment of the Embolization of Neurovascular Lesions Using the Penumbra Smart Coil (SMART) Registry evaluating clinical and angiographic outcomes following endovascular treatment of wide-neck MCA aneurysms.

Materials and Methods

A prospective, multi-center registry of patients treated in accordance with the cleared indications for the Penumbra Smart System, Penumbra Coil 400TM, and Penumbra Occlusion Device (Penumbra, Alameda, CA) was reviewed for cases of wide-neck MCA aneurysms. Primary outcome measures were investigator-adjudicated Raymond-Roy (RR) occlusion classification at 1-year, procedure-related serious adverse events, and retreatment.

Results

Seventy-two wide-neck MCA aneurysms were treated in separate patients. Average age was 62.3 years (SD 11.47) and 69% were female. Aneurysms were located at the MCA bifurcation in 69% (50/72), 9.7% (7/72) were previously treated, and 21% (15/72) were previously ruptured (60% Hunt & Hess 1-3; 40% Hunt & Hess 4-5). The longest axis averaged 6.8 mm (SD 3.7; range 1.8 – 19.0), and 15% (11/72) were large (> 10mm). Saccular aneurysms accounted for 87% (62/71). Treatment included unassisted coiling (43%), stent-assisted coiling (50%), and balloon-assisted coiling (13%). Radiographic and functional outcomes at 1 year were available for 83% and 61% of patients respectively. Clinical and radiographic outcomes are described in Table 1. Adequate aneurysm occlusion (RR I-II) was achieved in 95% of patients at 1 year. Procedure-related serious adverse events occurred in 11 patients (15%). One aneurysm (1%) required retreatment.

Conclusions

Endovascular treatment of wide-neck MCA aneurysms with Penumbra coils yielded high rates of successful occlusion, with a safety profile comparable to other endovascular treatment scenarios.

Primary Outcomes	All Subjects (N=72)	Ruptured (N=15)	Not Ruptured (N=57)
Post-Procedural RR Classification			
Class I to II	75.0% (54/72)	73.3% (11/15)	75.4% (43/57)
Class I	40.3% (29/72)	40.0% (6/15)	40.4% (23/57)
Class II	34.7% (25/72)	33.3% (5/15)	35.1% (20/57)
Class III	25.0% (18/72)	26.7% (4/15)	24.6% (14/57)
1-year RR Classification			
Class I to II	95.0% (57/60)	71.4% (5/7)	98.1% (52/53)
Class I	71.7% (43/60)	42.9% (3/7)	75.5% (40/53)
Class II	23.3% (14/60)	28.6% (2/7)	22.6% (12/53)
Class III	5.0% (3/60)	28.6% (2/7)	1.9% (1/53)
1-year Aneurysm Occlusion Compared to Post-Procedure			
Better (Progressive Occlusion)	43.3% (26/60)	28.6% (2/7)	45.3% (24/53)
Stable	50.0% (30/60)	57.1% (4/7)	49.1% (26/53)
Worse (Recanalization)	6.7% (4/60)	14.3% (1/7)	5.7% (3/53)
1-year modified Rankin Scale			
0	52.3% (23/44)	0.0% (0/8)	63.9% (23/36)
1	27.3% (12/44)	25.0% (2/8)	27.8% (10/36)
2	2.3% (1/44)	0.0% (0/8)	2.8% (1/36)
3	2.3% (1/44)	12.5% (1/8)	0.0% (0/36)
4	6.8% (3/44)	12.5% (1/8)	5.6% (2/36)
Deceased	9.1% (4/44)	50.0% (4/8)	0.0% (0/36)

(Filename: TCT_1606_ASNR_SMART_table.jpg)

1454

Enlarged perivascular spaces have the strongest association with future cognitive impairment

N Sheikh-Bahaei¹, G Barisano¹, F Seppehrband¹, J Acharya², A Rajamohan¹, P Kim¹, M Law³, A Toga⁴, H Chui¹
¹University of Southern California, Los Angeles, CA, ²Keck School of Medicine of USC, Los Angeles, CA, ³Alfred Health, Melbourne, VIC, ⁴USC Stevens Neuroimaging and Informatics Institute, Los Angeles, CA

Purpose

Although amyloid and tau are considered the pathological hallmarks of Alzheimer's disease (AD), there is discrepancy between development of clinical dementia and presence of abnormal proteins in the brain. Microvascular and glymphatic impairment may play a pivotal role in this process. Enlarged perivascular spaces (EPVS) are considered as a marker of glymphatic disruption. In this study we investigated the association between these microvascular changes and future development of dementia in Alzheimer's Disease Neuroimaging Initiative (ADNI)

Materials and Methods

Cases were initially recruited as cognitively normal who developed either MCI(n=64) or dementia(n=25) during their follow up and a group of matched controls (n=64) for sex, age, and follow up periods were selected. Number of EPVS in centrum semiovale(CS) and basal ganglia(BG)(1), number of lobar cerebral microbleeds, and severity of white matter hyperintensities using Fazekas scoring(2) were calculated. We also collected demographic data, APOE4, amyloid and tau levels, and cardiovascular risk factors(CVSRF) including diabetes, hypertension, high cholesterol and triglyceride at baseline. We compared the level of these factors between converters and non-converters when cognitively normal. Using multi-regression models, we investigated the association between the above and future development of cognitive impairment.

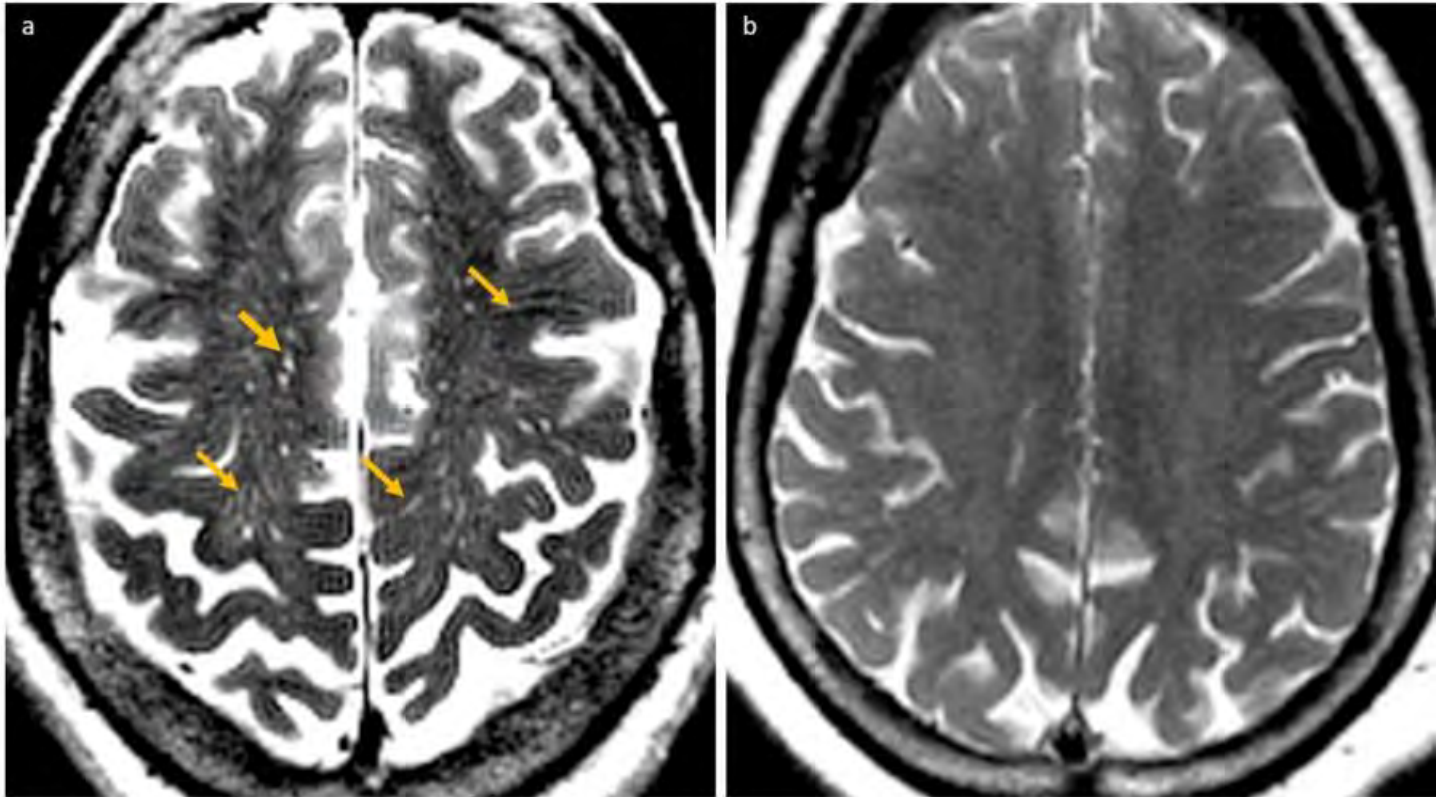
Results

Among the above variables, CS-PVS(p<0.0001), amyloid positivity(p=0.03) and hypercholesteremia(p=0.03) were significantly higher in future converters compared to non-converters. The association between PVS and future conversion remained significant

after adjusting for the demographic factors, CVSRFs, amyloid, and tau individually. More importantly, the effect of amyloid ($p=0.11$) and cholesterol ($p=0.85$) disappeared when added to the regression models with PVS. The Clinical Dementia Rating (CDR) at the time of conversion was also highly associated with SC-PVS ($p=0.02$) while its association with initial amyloid ($p=0.11$) and tau ($p=0.36$) were not significant

Conclusions

We found that presence of EPVS was the only factor significantly associated with future development of dementia. A Growing body of evidence has shown that glymphatic impairment and soluble amyloid might be one of the earliest changes in AD(3) and EPVS could be a potential imaging biomarker to investigate these underlying changes. It might have prognostic value at early stage of the disease when most of neurodegenerative biomarkers are still normal.



Enlarged Perivascular spaces (arrows) in centrum semiovale in a case converted to AD (a) compared to a matched non-converter control (b).

(Filename: TCT_1454_Picture1-V2.jpg)

1020

Estimating frequency of brain MRI abnormalities in patients with PCDH19-related epilepsy.

E Yang¹, L Smith¹, S Prabhu², C Harini¹, J Sullivan³, N Singhal³, A Poduri¹

¹Boston Children's Hospital, Boston, MA, ²Boston Children's Hospital, Boston, MA, ³UCSF, San Francisco, CA

Purpose

Variants in the X-chromosome gene PCDH19 represent one of the most frequent causes of developmental and epileptic encephalopathy (DEE). Females with PCDH19 pathogenic variants are obligate mosaics due to X-inactivation and affected to a variable degree with seizures, intellectual disability, and other comorbidities. Paradoxically, males with the same variants are typically asymptomatic unless there is mosaicism. PCDH19-related epilepsy usually presents in the first year of life as clustered or febrile seizures with focal or generalized onset. While historically PCDH19-related epilepsy has been considered 'non-lesional', recent reports have suggested cortical malformations can be present in affected females with pathogenic PCDH19 variants, a finding consistent with experimental data implicating nonfunctional, mosaic PCDH19 expression in aberrant cerebral cortex columnar organization.

Materials and Methods

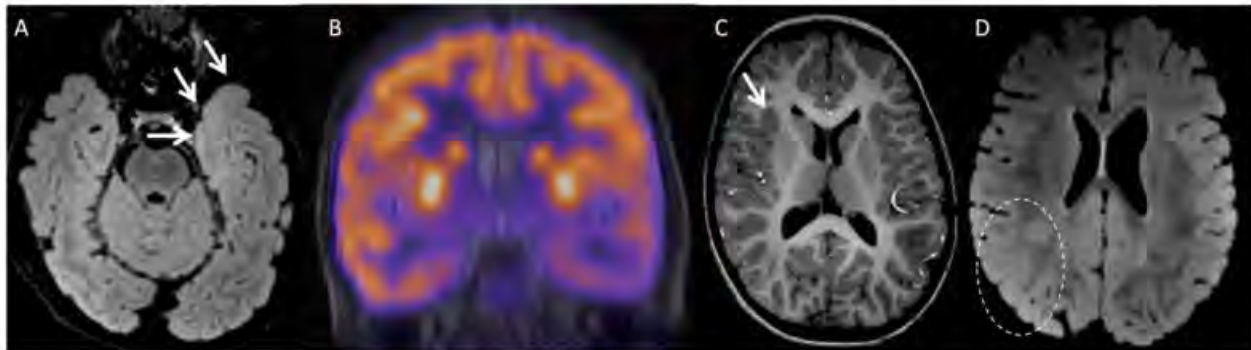
We ascertained cases from the Boston Children's Hospital site of the PCDH19 Registry. Among the 60 subjects, we had MRIs available for 19 (18 heterozygous females and 1 mosaic male). The brain MRIs of these patients were reviewed for structural abnormalities and correlated with EEG and nuclear medicine data where available.

Results

Of the 19 subjects, three had regional signal abnormality on their brain MRI suspicious for dysmyelination or focal cortical dysplasia, and all 3 signal abnormalities were concordant with electroclinical data. In two cases, there was hypometabolism on interictal FDG-PET imaging localizing to the MRI abnormality, and in one case the patient underwent resection which returned nonspecific gliosis. Although the 3 abnormal MRIs were performed on 3T magnets at a slightly older age than the other patients in our cohort, a statistically significant association of a lesional finding with scanner type ($p=.263$) or patient age ($p=0.79$) was not demonstrated.

Conclusions

We identified lesional abnormalities in a minority of patients with PCDH19-related epilepsy in our cohort. In the one patient with pathology, this signal abnormality was secondary to gliosis rather than a focal cortical dysplasia. Therefore, the abnormal signal seen in the brain MRIs from patients with PCDH19 variants may be a secondary marker of microstructural abnormalities, perhaps secondary to chronic epilepsy, rather than a cortical malformation. Whether this abnormal signal solely reflects PCDH19 mutation or additional somatic mutation in other genes is currently unknown.



Subject 1 axial T2 FLAIR SPACE (A) and coronal PET fused to FLAIR (B) demonstrates hazy FLAIR hyperintensity of the left temporal pole (arrows) and decreased FDG uptake in a wider region of the left temporal lobe. Left temporal lobectomy specimen demonstrated gliosis. Axial T1 MPRAGE imaging (C) from subject 2 demonstrates thickening and indistinct gray-white matter differentiation at the anterior right insula and frontal operculum (arrow). There was corresponding hypometabolism in this region on FDG-PET. Axial FLAIR SPACE imaging of subject 3 (D) demonstrates hazy signal in the right temporoparietal region (dashed oval).

(Filename: TCT_1020_PCDH19_ASNR2021fig.jpg)

1527

Evaluation of Pediatric Spinal Cord Infarct due to Fibrocartilaginous Embolism

L. Tierradentro-García¹, A Zandifar¹, J Kim¹, A Vossough²

¹Children's Hospital of Philadelphia, Philadelphia, PA, ²Children's Hospital of Philadelphia- University of Pennsylvania, Philadelphia, PA

Purpose

Fibrocartilaginous Embolism (FCE) is a rare cause of spinal cord infarct and the mechanism is fragmentation and migration of fibrocartilaginous nucleus pulposus into spinal microvasculature, typically due to mechanical compression and consequent intradiscal

pressure elevation. Only less than 30 pediatric patients have been reported in the literature, mostly in the form of single case reports. In some of these reports, the presence of a T2-hypointense disc near the cord infarct is taken as presumptive evidence of FCE. We sought to assess and present imaging features of FCE in a large pediatric cohort.

Materials and Methods

We evaluated patients with spinal cord infarct over a 15-year period. The definitive diagnosis of FCE is based on autopsy. The presumptive diagnosis of spinal cord infarct due to FCE in our patients was made based on a combination of clinical and imaging features, including the presence of an inciting event such as minor trauma, typical symptomatology of spinal cord infarct, course and rapidity of development of cord infarct symptoms, imaging findings typical of spinal cord infarct on conventional and diffusion-weighted imaging, presence of nearby intervertebral disc abnormalities, lack of other clear predisposing factors, negative inflammatory or other laboratory workup, and clinical follow-up. Imaging was compared to spine MRI of 65 age-group matched controls. Disc abnormalities, including annular fissure and T2-hypointense intervertebral discs, were also reviewed and the prevalence and association of these abnormalities were evaluated using Chi-Square and Fisher tests.

Results

There were 11 patients with a diagnosis of FCE. Six were female (54.5%). The mean age was 11.2 years (range 7-17). A posterior disc annular fissure was seen in 10/11 (90.9%) of FCE vs 2/65 (3.1%) of controls; odds ratio=315 (21 to 3805, $p<0.000001$), the majority in the cervical levels. The annular fissure was at or within one level of the spinal cord infarct levels in all patients. A T2-hypointense disc was seen in 1/11 (9.1%) vs 2/65 (3.1%) of controls; odds ratio=3.1 (0.26 to 38, $p=0.38$). In the single patient with a T2-hypointense disc near the cord infarct level, it was located adjacent to a disc level with an annular fissure.

Conclusions

In pediatric patients with cervicothoracic spinal cord infarct, an adjacent disc annular fissure is associated with a greatly elevated odds of FCE. A T2-hypointense disc adjacent to the spinal cord infarct was not associated with an elevated odds of FCE in our cohort.

1449

Evaluation of the Agreement of Metabolite Levels between PRESS and MEGA-PRESS Techniques in the Grading of Glioma Patients.

T Nguyen¹, G Melkus²

¹The Ottawa Hospital, Ottawa, ON, ²The Ottawa Hospital, Ottawa, Ontario

Purpose

The Mesher-Garwood (MEGA)-PRESS spectral editing technique has been used to identify 2-hydroxyglutarate preoperatively in glioma patients with isocitrate dehydrogenase mutation[1,2,3]. The main objective of this study is to evaluate the agreement of other metabolites (choline, creatine and NAA) between the MEGA-PRESS and PRESS sequences. A secondary objective is to evaluate the diagnostic accuracy of those metabolites in the preoperative grading of glioma.

Materials and Methods

In this prospective study, 39 consecutive patients with a newly diagnosed glioma were enrolled. All patients underwent a clinical examination with a 3T MR scanner. MEGA-PRESS parameters were: TR=2s, TE=60msec, 128 averages, voxel size=8cm³, duration =8.4min). The voxel was positioned to include the maximal amount of solid tumour tissue on FLAIR images. A PRESS sequence was performed in the same location with an identical voxel size. PRESS parameters were: TR=2s, TE=135 ms, 128 averages, duration=4:5 min). The MRS data were analyzed by an MR physicist using the LC model. Choline, creatine and NAA from the PRESS spectrum and from the MEGA-PRESS edit-off spectrum were evaluated. Metabolite levels from the edit-off spectrum were corrected for T2 relaxation using values previously published[4]. Reproducibility of metabolite levels between the two techniques were assessed using a Bland-Altman analysis. ROC analysis was performed to measure the diagnostic accuracy of different metabolite ratios in the diagnosis of high grade vs low grade gliomas.

Results

For all three metabolites, the level of agreement between the two techniques was higher when values from edit-off spectrum of the MEGA-PRESS sequence were corrected for T2 relaxation (Fig 1a). Without T2 correction, the difference in percentage between PRESS and MEGA-PRESS was -25.6% with limits of agreement of 243% (Fig 1b). With T2 correction, the difference in percentage for choline was 0.24% with limits of agreement of 3.1% (Fig 1c). For differentiation between high and low grade gliomas, the diagnostic accuracy of the Cho/Cr ratio (AUC=0.68, 95% CI 0.52 to 0.85) from PRESS was not statistically different from the ratios obtained from MEGA-PRESS without (AUC=0.67, 95% CI 0.50 to 0.83) and with T2 correction (AUC=0.66, 95% CI 0.48 to 0.83, $P>0.05$, Fig 1d).

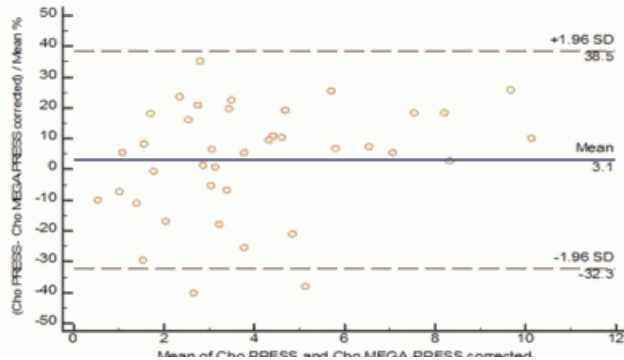
Conclusions

T2 corrected metabolite levels obtained from the edit off spectrum of the MEGA-PRESS sequence are in good agreement with those obtained from PRESS sequence.

Fig 1a. Comparison of metabolite levels obtained from PRESS and edit-off spectrum using Bland-Altman analysis

Metabolite comparison	Difference in %	Limits of agreement
Cho PRESS vs uncorrected Cho MEGA-PRESS	-26%	243%
Cho PRESS vs T2 corrected Cho MEGA-PRESS	3.1%	71%
NAA PRESS vs uncorrected NAA MEGA-PRESS	-56%	300%
NAA PRESS vs T2 corrected NAA MEGA-PRESS	-29%	223%
Cr PRESS vs uncorrected Cr MEGA-PRESS	-45%	218%
Cr PRESS vs T2 corrected Cr MEGA-PRESS	-3.1%	105%

Fig 1c. Bland-Altman plot of difference between Choline from PRESS and corrected Choline from MEGA-PRESS against a mean of Choline from PRESS and corrected Choline from MEGA-PRESS, with a mean absolute difference (bias) (solid line) and 95% confidence interval of the mean difference (limits of agreement) (dashed lines).



(Filename: TCT_1449_finalabstractASNR2021graphics.gif)

Fig 1b. Bland-Altman plot of difference between Choline from PRESS and uncorrected Choline from MEGA-PRESS against a mean of Choline from PRESS and uncorrected Choline from MEGA-PRESS, with a mean absolute difference (bias) (solid line) and 95% confidence interval of the mean difference (limits of agreement) (dashed lines).

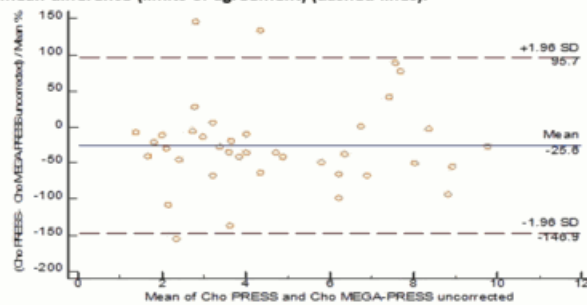
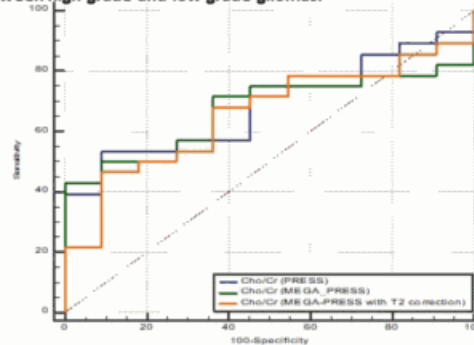


Fig 1d. Diagnostic accuracy of the Cho/Cr ratio in the differentiation between high grade and low grade gliomas.



1450

Evaluation of Ultrafast Wave-CAIPI 3D SPACE FLAIR Versus Standard 3D SPACE FLAIR for Epilepsy Imaging at 3T

A Goncalves Filho¹, C Ngamsombat², S Cauley¹, W Lo³, D Splitthoff⁴, J Kirsch⁵, P Schaefer¹, O Rapalino¹, S Huang⁶, J Conklin¹
¹Massachusetts General Hospital, Boston, MA, ²Department of Radiology, Faculty of Medicine Siriraj Hospital, Mahidol University, Bangkok, Thailand, Bangkok, MA, ³Siemens Medical Solution, Charlestown, MA, ⁴Siemens Healthineers, Erlangen, Germany, ⁵Massachusetts General Hospital, Charlestown, MA, ⁶Massachusetts General Hospital, Harvard Medical, Boston, MA

Purpose

To investigate the diagnostic performance of an accelerated Wave-CAIPI 3D SPACE FLAIR (Wave-FLAIR) sequence compared to standard 3D SPACE FLAIR in patients undergoing evaluation of seizures.

Materials and Methods

We enrolled 77 patients undergoing brain MRI for evaluation of seizures or established epilepsy under an IRB-approved protocol. All patients were scanned on 3T MRI scanners (MAGNETOM Prisma, Siemens Healthcare, Erlangen, Germany). In addition to conventional imaging sequences, all patients were scanned with a prototype isotropic 3D Wave-SPACE FLAIR (acceleration factor [R] = 9, acquisition time [TA] = 1:50 min on a 32-channel coil, or R = 6, TA = 2:45 min on a 20-channel coil) and standard SPACE FLAIR sequence (R = 2, TA = 7:15 min for both coils). Two neuroradiologists (9 and 8 years of experience) blinded to sequence type performed an independent head-to-head comparison of images. A predefined 5-point scale was used for grading findings relevant to the evaluation of epilepsy, including the visualization of cortical, white matter, deep gray matter, infratentorial, and hippocampal lesions. Raters also evaluated the presence of pulsation artifacts (due to blood or CSF flow), motion artifacts, noise, and overall diagnostic quality. Discrepancies were adjudicated by a third reader (>20 years of experience).

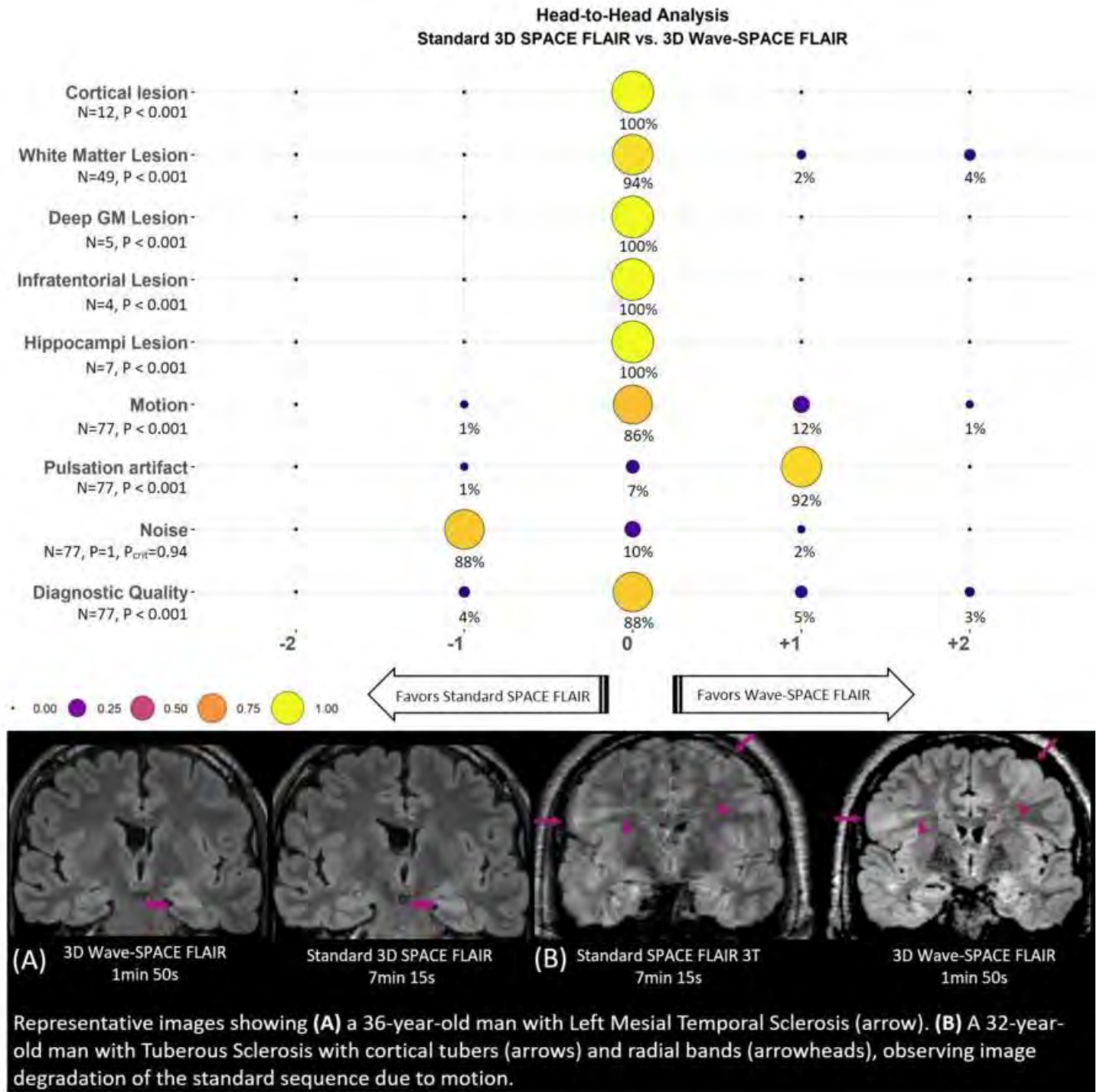
Results

Wave-SPACE FLAIR was non-inferior to conventional SPACE-FLAIR for detection of lesions in the cortex, white matter, deep gray matter, infratentorial compartment and hippocampi, despite being 4x faster with a 32-channel coil (1:50 min vs 7:15 min) and 2.5x faster with a 20-channel coil (2:45 min vs 7:15 min). Wave-SPACE-FLAIR was also non-inferior for motion and pulsation artifacts, as well as for overall diagnostic quality (P<0.001). In addition, Wave-SPACE-FLAIR was preferred over the standard sequence with fewer flow-related artifacts and motion artifacts. Standard SPACE-FLAIR was preferred over Wave-SPACE-FLAIR with respect to image noise.

Conclusions

An ultrafast Wave-CAIPI SPACE FLAIR sequence that is up to 4x faster than the standard sequence provides equivalent diagnostic performance with reduced motion and flow-related artifacts, at the cost of mildly increased image noise. High-resolution 3D imaging is central to the identification of structural lesions in patients with seizures, and deployment of accelerated imaging techniques may

improve the efficiency of these historically lengthy acquisition protocols, with benefits for patients, radiologists and radiology operations.



(Filename: TCT_1450_Wave-FLAIR-Epilepsy_ASNR21abstract.jpg)

762

Evaluation of Ultrasound core needle biopsy in the diagnosis of cervical lymph node lymphomas.

C Tsetse¹, A Khanal¹, J George¹, A Swarnkar², K Mirchia³

¹SUNY Upstate Medical University, Syracuse, NY, ²N/A, N/A, ³SUNY Upstate Medical University, Camillus, NY

Purpose

Ultrasound guided core needle biopsy (USCNB) of lymph nodes is increasingly recognized as an alternative to excisional biopsy in the diagnosis of lymphoma. It provides many advantages over surgical excision biopsy (SEB) such as reduced costs, decreased time to

initiate treatment and possible avoidance of complications associated with SEB. The objective of this study is to determine whether USCNB is adequate for histopathological diagnosis avoiding the need for SEB in cases of suspected head and neck lymphoma.

Materials and Methods

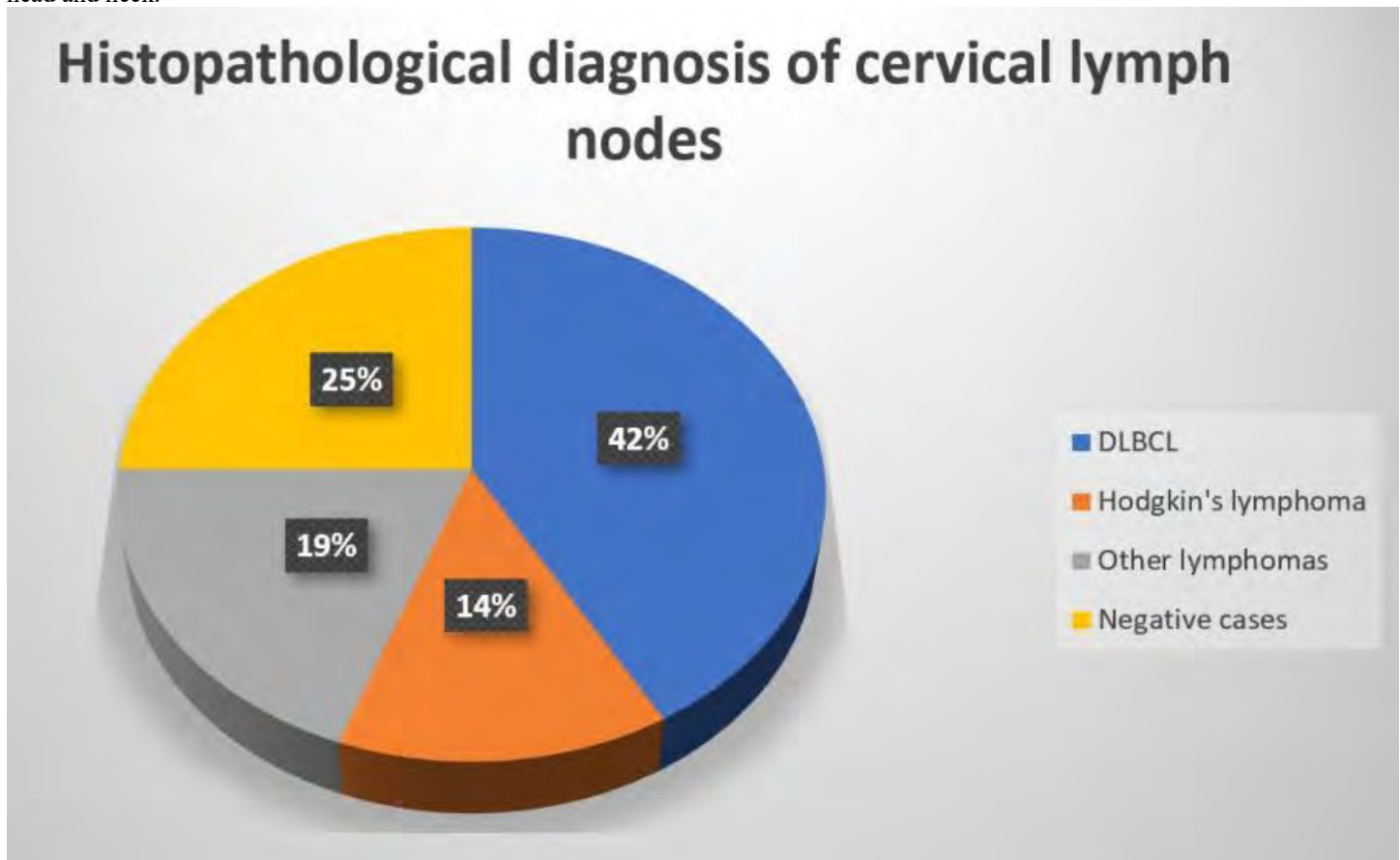
We reviewed retrospectively 42 suspected cases of lymphoma, referred for USCNB of cervical lymph nodes using lymphoma protocol at our institution, between 2016 and 2020. Patients electronic medical record, radiology and histopathology reports were reviewed. USCNB was performed on enlarged cervical lymph nodes (>1 cm) in all subjects. The biopsy needle size, the number of core samples obtained, and the core biopsy technique employed to establish a definitive diagnosis were documented. USCNB related complications, inadequate biopsies, and need for a SEB cases were noted for all cases.

Results

Of the 42 suspected lymphoma cases who underwent USCNB, 36 subjects (16 males and 20 females with mean age of 52 +/- 26 years) met the inclusion criteria. We achieved 100% success obtaining adequate samples from all 36 USCNB patients using a spring-loaded automated biopsy gun with 16-gauge needle diameter for definitive diagnosis of lymphoma. No further SEB was required in 35 of the 36 patients. In one case with a negative USCNB result, SEB confirmed benign lymphoid tissue. Histopathology and immunohistochemistry in 27 of 36 cases (75%) yielded a positive diagnosis of lymphoma whereas 9 of 36 cases (25%) yielded negative diagnosis for lymphoma. Additionally, FNA was performed in 25 of 36 cases (70%) for flow cytometry on the recommendation of the pathologist. All the FNA samples were also deemed adequate for flow cytometry. The size of lymph nodes biopsied range from 1.5cm to 8cm (mean 3.6cm, SD 1.7.) The total number of core samples obtained ranged between 2 and 12 depending on the quality of the core samples. No USCNB related complications were identified.

Conclusions

Ultrasound-guided core-needle biopsy is a safe and reliable first-line technique for definitive primary diagnosis of lymphoma in the head and neck.



(Filename: TCT_762_Fig2.JPG)

1433

Evolving Participation of Radiology Trainees in Brain Imaging: a Medicare Claims-Based Population Analysis

R Peterson¹, J Allen², J Hemingway³, E Rula⁴, E Rubin⁵, D Hughes⁶, R Duszak⁷

¹EMORY UNIVERSITY SCHOOL OF MEDICINE, NORCROSS, GA, ²Emory University, Atlanta, GA, ³Harvey L. Neiman Health, Reston, VA, ⁴Harvey L. Neiman Health Policy Institute, Reston, VA, ⁵Southeast Radiology, Ltd., Chester, PA, ⁶Georgia Institute of Technology, Atlanta, GA, ⁷Emory University School of Medicine, Atlanta, GA

Purpose

To assess temporal changes in the participation of radiology trainees nationwide in the interpretation of brain CT and MRI examinations.

Materials and Methods

Using national aggregated Medicare fee-for-service claims data from 1998 through 2018, we used Neiman Imaging Types of Service (NITOS) categorization to identify all billed brain CT (NITOS N31X) and brain MR (N41X) examinations. All services were work relative unit (wRVU) weighted to estimate work effort using annual Medicare Physician Fee Schedule files. Using GC claims modifiers, services rendered by radiology trainees were specifically identified. Utilization rates per 10,000 Medicare beneficiaries were calculated using annual Medicare enrollment files. Annual national work effort by trainees as a percentage of total work effort was calculated.

Results

Between 1998 and 2018, Medicare fee-for-service billed claims for brain CT and MRI increased from 2,795,087 and 795,344 to 5,806,117 and 2,309,017, respectively (+108% and +190%). Brain CT and MRI services rendered by trainees increased from 79,058 and 28,765 to 283,554 and 131,596, respectively (+259% and +356%). Per 10,000 Medicare beneficiaries annually, utilization rates of brain CT and MRI increased from 922 and 1,740 to 262 and 692, respectively (+89% and +164%). The overall percentage of trainee-rendered wRVUs for brain CT increased from 2.7% to 4.9% (+78%). The overall percentage of trainee-rendered wRVUs for brain MRI increased from 3.7% to 6.3% (+69%).

Conclusions

Over the last two decades, utilization of brain CT and MRI in the Medicare population has more than doubled. As examination volumes have increased, involvement of trainees in examination interpretations has increased disproportionately. Further work is necessary to identify appropriate trainee volumes to support national population brain imaging needs.

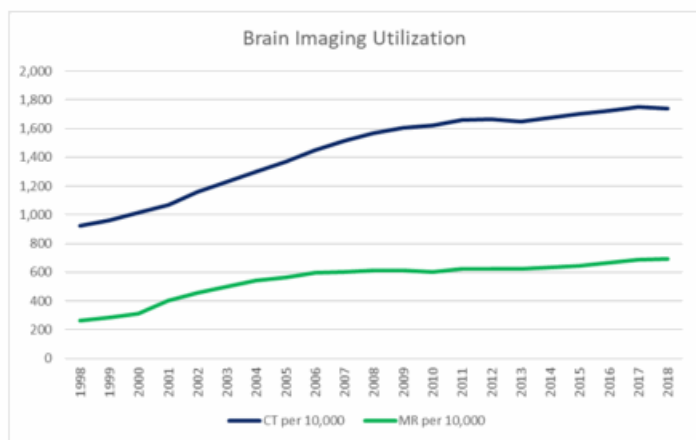


Figure 1a. Annual utilization of brain CT (blue) and MR (green) per 10,000 Medicare fee-for-service beneficiaries.

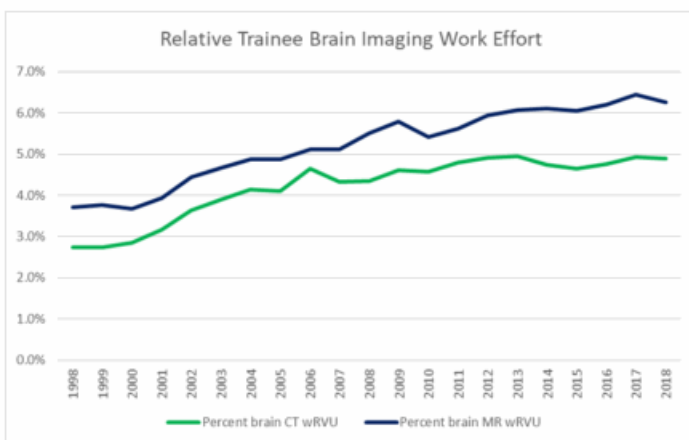


Figure 1b. Annual portion of work effort (in wRVUs) by radiology trainees, as a percentage of total services rendered nationally, for brain CT (blue) and MR (green).

(Filename: TCT_1433_Fig1.gif)

1546

Ex-vivo Post Mortem MRI of COVID-19 non-survivors

M Wangsgard¹, G Moonis¹, S Jambawalikar¹, P Canoll¹, K Thakur¹, A Khandji¹, A Lignelli¹

¹Columbia University Irving Medical Center, New York, NY

Purpose

Severe acute respiratory syndrome coronavirus 19 (SARS-CoV 19) demonstrates multisystem involvement beyond pulmonary manifestations. Many patients have significant neurological symptoms primarily related to cytokine storm and COVID coagulopathy with scant evidence to date for viral invasion into the CNS. One prior study performed post mortem imaging in-vivo in COVID-19 non survivors which showed hemorrhagic and PRES related brain lesions.[1] Our study aims to evaluate the ex-vivo post mortem brain MRI findings in patients that expired with a diagnosis of COVID-19.

Materials and Methods

Nine patients in a larger series of autopsy cases who expired between April and June 2020 in a single academic center with a diagnosis of COVID-19 were imaged ex-vivo. There were 6 males and 3 females with an average age of 74 (68-92). Primary presenting symptoms were respiratory distress/failure for all patients. The duration of time between admission and death ranged from 1 to 69 days (ave 40). 7 of 9 patients were intubated and 2 declined. The brain specimens were removed and placed in formaldehyde preparation and subsequently submerged in water. Imaging was performed on GE 3T premier MRI scanner with integrated spine array

and anterior aircoil. The following sequences were performed : 3D PD TR 2500, TE 27, ST = 0.6mm FOV 24 cm matrix 340340, 3D MP2RAGE (T1 weighted) TR=5s, TE=2 ms, TI=800 ms FOV 20cm Matrix 256x256, SWI TR=45, TE 21, ST=2mm FoV 24cm, matrix 320x320, MAGIC sequence (ST=4.0,FOV 24cm, matrix 320x256). T1 FLAIR, T1map, T2map, PSIR were derived from MAGIC.

Results

Of the 9 patients, 4 had antemortem neuroimaging (1/4 had subacute cortical infarcts 1/4 had global hypoxia on CT, 2/4 had normal neuroimaging). 5 patients did not have neuroimaging. In our ex vivo series, 6/9 patients (66%) demonstrated imaging findings of hemorrhage; 1/9 cortical (hemorrhagic infarcts), 3/9 intraventricular, 2/9 basal ganglia. T2 hyperintense basal ganglia signal abnormality was found in 3/9 (33%) possibly reflecting hypoxic injury. One of the cases with multiple parenchymal hemorrhages / hemorrhagic infarcts correlated with detailed pathologic examination [Figure 1b-d].

Conclusions

This is the first demonstration of ex vivo brain MRI imaging in patients who expired from COVID-19. All patients presented with respiratory distress and subsequent respiratory failure. Many of the patients demonstrated intracranial hemorrhage / hemorrhagic infarcts and hypoxic injury reflecting varied sequela of COVID infection.

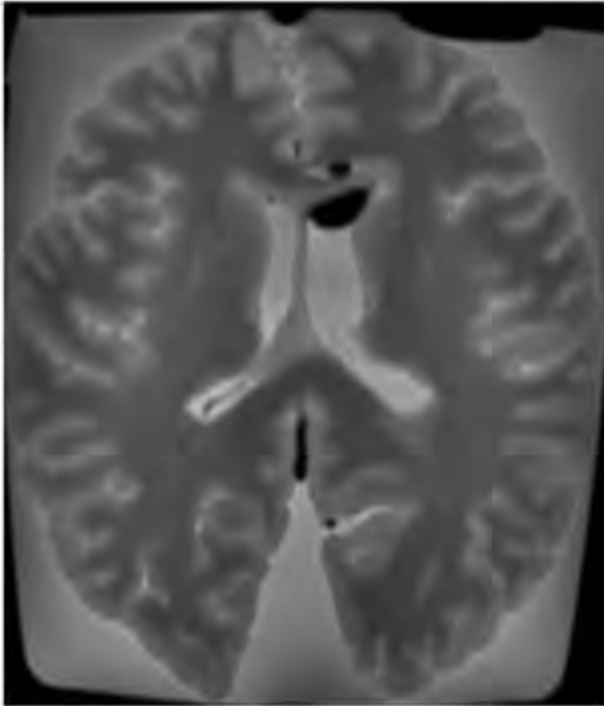


Figure 1a: Axial 3D FSE with intraventricular air related to preparation

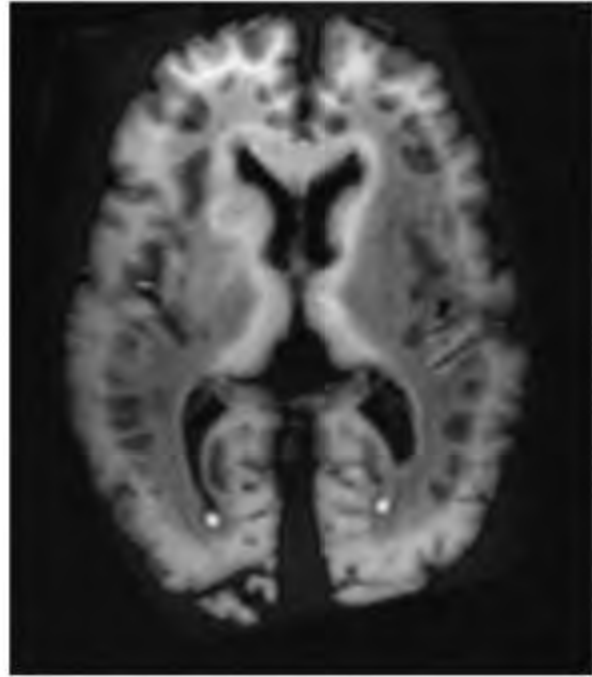


Figure 1b: Axial T1 Phase sensitive inversion recovery (PSIR) using MAGIC sequence with intraventricular hemorrhage

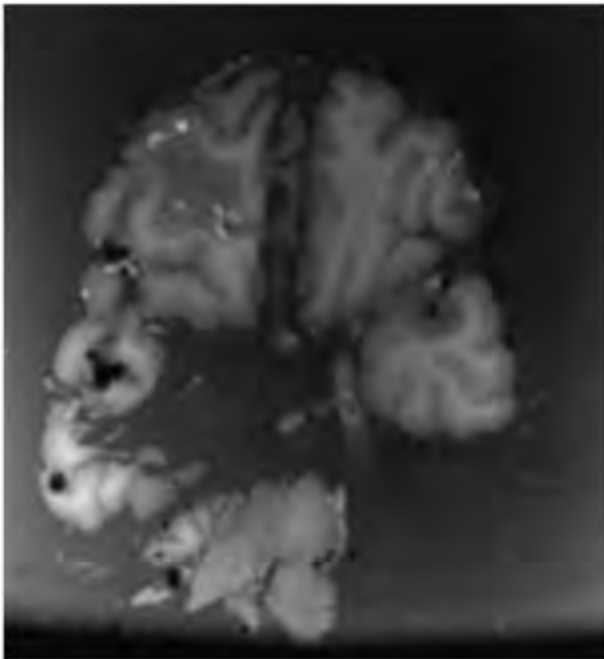


Figure 1c: Axial T1 MPRAGE demonstrating right inferior frontal hemorrhagic infarct

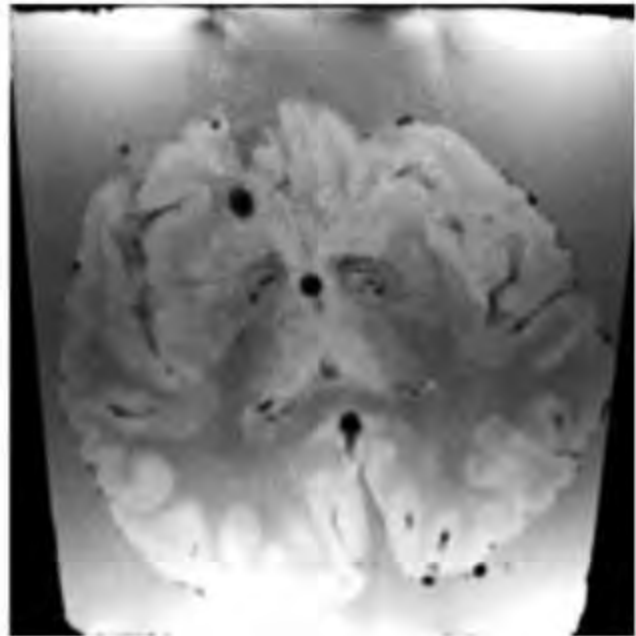


Figure 1d: Axial 3D PD demonstrating bilateral basal ganglia hemorrhage

Extracting Discriminating Information from Magnetic Resonance Subspectrum through Machine Learning

J Liu¹, I Benador², P Zhu³

¹Boston medical center, Boston, MA, ²Boston Medical Center, Boston, MA, ³Boston University, Brookline, MA

Purpose

Magnetic resonance spectroscopy (MRS) can be a powerful metabolomics tool, but its clinical use remains limited in part due to difficulty in interpretation of the complex and overlapping metabolite spectra. The purpose of this study is to elucidate whether valuable diagnostic information exists in visually complex metabolic peaks not traditionally considered, herein referred to as the 'subspectrum', using machine learning (ML).

Materials and Methods

For this proof-of-concept project, one hundred and seventy-eight spectra of pathology-proven grade I, II, III, and IV brain tumors from the eTUMOUR and INTERPRET database were manually processed using jMRUI with uniform processing parameters. To test the ability of ML to classify using only the subspectrum, the points corresponding to Creatine(Cr), Choline(Cho), Nacetylaspartate (NAA), lipids, and lactate(1.1-2.2 and 2.8-3.4 ppm), were removed from the input datasets. To test the ability of ML to classify using only the primary peaks (Cr, Cho, and NAA), all points outside of 1.8-2.2, and 2.8-3.4 ppm ranges were removed. We evaluated the performance of linear and nonlinear machine learning models on first classifying grades I-IV, and then again with the exclusion of the outlier class, grade III. To evaluate the comprehensive generalization performance, we used 5-fold cross validation to split the dataset and report the mean performance.

Results

We evaluated four machine learning models: logistic regression, linear SVMs, non-linear SVMs and K-nearest neighbor classifier, with non-linear SVM achieving best overall accuracy. Class-average accuracy for the classification amongst grades I-IV, was 0.61. With exclusion of grade III tumors, the class average accuracy for the classification of grades I, II, and IV was 0.74 using the subspectra, 0.77 using full spectra and 0.79 using primary peaks only.

Conclusions

Our current strategies of visual MRS interpretation may leave out important information which may be utilized for improved tumor classification. Machine learning techniques allow us to utilize that information without the need to identify individual metabolite peaks. With a minimal drop in accuracy using the full versus the subspectra, this study demonstrates that discriminating information exists within the MRS subspectra, and that it can be extracted using ML. However, further work is required to utilize this new information in augmenting the evaluation of the main peaks and to increase the overall diagnostic accuracy.

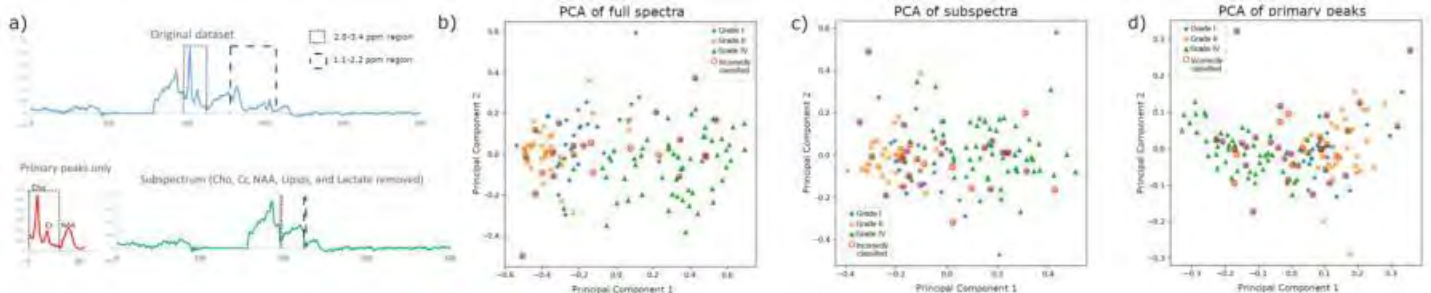


Figure 1: Graphical depiction of sample original spectrum, primary peaks, and subspectra dataset (a), plotted with relative intensity on vertical axis and numerical order of each datapoint on the horizontal axis, corresponding to the 7.1 to -2.7 ppm range. Zoned portion of the original dataset and subspectrum (points 110-157) correlates to zeroing of water signal on pre-processing, with dotted and dashed lines representing areas of removed spectrum for the evaluation of the subspectrum. Visualization of the clustering of full spectra (b), subspectra (c), and primary peaks (d), using principal component analysis, with mis-classified spectra indicated by red circles.

(Filename: TCT_971_finalfigure.jpg)

770

Feasibility of Imaging Blood Brain Barrier Dysfunction in Alzheimer Disease

J Ford¹, Q Zhang¹, A GUPTA¹, T Nguyen¹, J Ivanidze¹

¹Weill Cornell Medicine Radiology, New York, NY

Purpose

Emerging evidence is pointing to the role of blood brain barrier (BBB) dysfunction in the pathogenesis of Alzheimer disease (AD), a process that may involve matrix metalloproteinases degrading basement membrane and tight junction proteins critical to BBB integrity. Our group has optimized a novel non-contrast diffusion-weighted arterial spin labeling technique that magnetically labels intravascular water, which acts as an endogenous tracer. The technique exploits the unique diffusion properties of water (high diffusion in capillaries, low diffusion in tissues) and yields a map of the exchange rate of water across BBB (kW) for the entire brain. Given that water is 30-60 smaller than gadolinium-based contrast agents, this approach lays the groundwork for a more sensitive and

safer approach to evaluate BBB disruption. The goal of this pilot study is to generate kW maps in cognitively normal (CN) individuals and compare them to a patient with known AD.

Materials and Methods

Six CN subjects (23-29 years old, male) were recruited and underwent MRI with QPM to generate kW maps. The average kW for 12 Automatic Anatomic Labeling regions (bilateral frontal lobes, cingulate gyri, hippocampi, preneuni, temporal lobes, and cerebellar hemispheres) was obtained. Additional imaging was acquired from a patient with AD (56 years old, female).

Results

kW maps for the 6 CN and 1 AD subjects were successfully generated (Figure 1A). kW values for the AD subject were generally at the upper bounds of the kW ranges for CN subjects, particularly in the hippocampi and right cingulate (Figure 1B). The cerebellum, which is relatively spared in AD, was near the mean kW value for the CN patients.

Conclusions

This pilot study demonstrates the feasibility of non-contrast QPM to generate kW maps for both CN and AD subjects. It's possible that BBB disruption may not just be a downstream effect of AD pathology, but rather, may be an initial insult that sets off the neurodegenerative cascade. Further studies exploring the natural history of BBB disruption in AD patients could help elucidate its place in the disease process. Moreover, if QPM is established as a reliable probe for BBB integrity, this new tool could have future applications in other disease processes in which the BBB could be disrupted, including neoplasms, demyelinating disorders, movement disorders, or neuropsychiatric disorders.

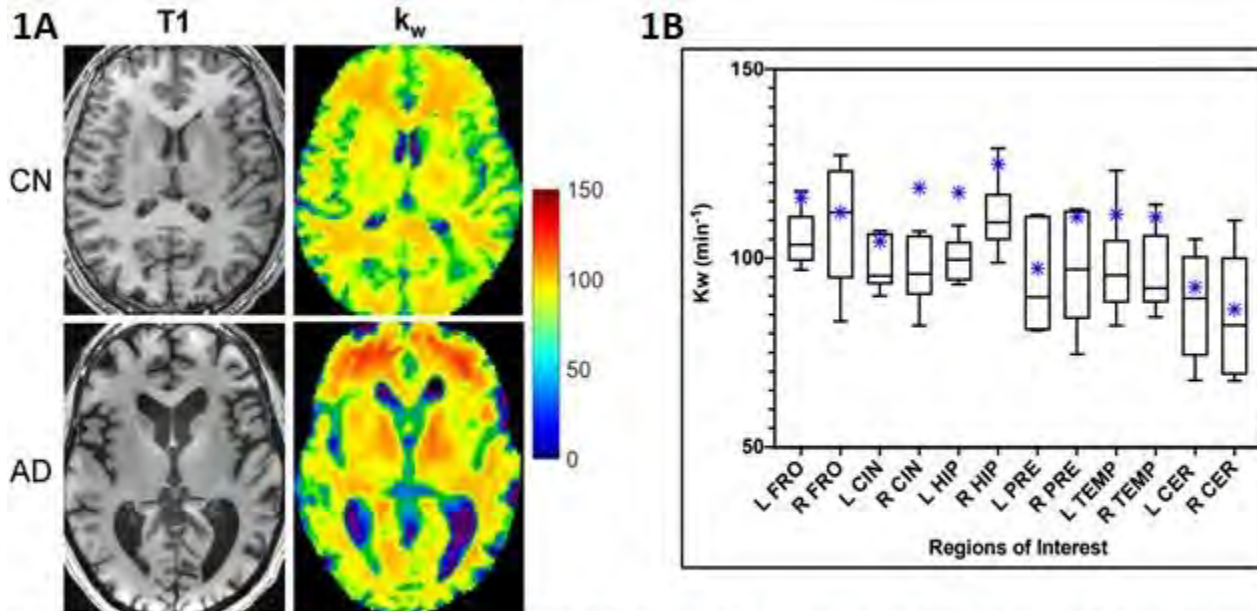


Figure 1A: T1-weighted images (Left) and k_w maps (Right) of CN subject (top) and AD subject (bottom). Figure 1B: Box plots of region-specific QPM-derived k_w values from CN subjects (n=6). Blue asterisks show corresponding k_w values for an AD patient. [FRO: frontal-orbital; CIN: cingulate; HIP: hippocampus; PRE: precuneus; TEMP: middle temporal gyrus; CER: cerebellum].

(Filename: TCT_770_KW.jpg)

273

Fetal MRI in Interferonopathies

D Prayer¹, C Mitter¹, G Yerlikaya-Schatten¹, F Laccone¹, G Gruber², G Kasprian³, M Cardoso Diogo¹

¹Medical University Vienna, Vienna, Vienna, ²Karl Landsteiner University, Krems, Lower Austria, ³MEDICAL UNIVERSITY OF VIENNA, VIENNA, Austria

Purpose

The term interferonopathy was introduced in 2011 (1), to define a group of Mendelian disorders associated with upregulation of type I Interferon (IFN). The common factor is an elevation of IFN levels that may have different pathophysiological backgrounds. MR patterns have not been evaluated in detail. Aim of this retrospective study is to demonstrate MR patterns in 7 cases with manifestations, interpreted as congenital infection-like phenotype (CILP).

Materials and Methods

7 Fetuses, aged from gestational weeks (GW) 22-32 with 10 in-vivo and 2 postmortem MRI examinations were included. In 2 cases pathohistological workup was available, in 1 fetus with additional NCAM-immunohistochemistry-based structure tensor analysis of developing fibers (5). Results of genetic examinations in accordance with the spectrum of changes associated with pseudotorch was proved in 4 cases (from 2 families). One patient was under interferon therapy because of hepatitis C during pregnancy. One had a florid Crohn's disease. One case showed characteristic signs on imaging studies with negative torch parameters. In all cases the

presence of torch-infections (especially CMV) had been excluded. Prenatal MRI examinations were performed at 1.5T or 3T fieldstrength. Protocols included T2-weighted (w) TSE sequences, T1-w, FLAIR, Epi/SWI, DWI and DTI Sequences in 2-3 planes, with a slice thickness of 2-4mm through the fetal brain, and T2-w, SSFP, T1-weighted, EPI/SWI, DWI sequences of the fetal body and extracerebral organs. Postmortem examinations were done at 3T, using isovoxel (CISS) T2-w sequences, T1-w, SWI, DTI Sequences over the fetal brain and body with 3-5mm slice thickness.

Results

Abnormal lamination and gyration was present in 10/10 exams, calcifications in 7/10, cerebral hemorrhage in 3/0, brain edema in 3/10, hepatosplenomegaly in 3/10, and placental changes in 7/10. Histology was available in 4cases (table 1)

Conclusions

The presented fetal MRI case series extends the known morphological findings of CILP to an "acute" manifestation with brain edema +/- hemorrhage. The strength of fetal MRI to visualize abnormalities of lamination and its advantage to identify acute DWI changes of the fetal brain may lead the path to the reduction of exposure to existing "teratogenic" effects and potentially to the initiation of novel therapies at early stages, preventing further harm to the developing central nervous system.

1575

Fetal MRI predictors of postnatal neurologic outcomes in patients with congenital vascular malformations.

A Goldman-Yassen¹, A Shifrin², A Pollock³, T Feygin³

¹Children's Healthcare of Atlanta, Atlanta, GA, ²North Shore Radiological Associates, Winchester, MA, ³Children's Hospital of Philadelphia, Philadelphia, PA

Purpose

1. To describe the prenatal imaging manifestations of congenital vascular malformations. 2. To determine the prenatal imaging findings associated with poor postnatal neurologic outcomes.

Materials and Methods

We performed an IRB approved search for fetal MRI with detected congenital vascular anomalies using keywords such as "vascular malformation", "vein of Galen", "dural sinus malformation", and "fetal MRI". Subjects were included if they had both prenatal and postnatal MRI, which were reviewed with focus on vascular and parenchymal pathology, and clinical data regarding neurologic outcomes accessible in the electronic medical record.

Results

Fetal MRI of 6 subjects with vein of Galen (VOG) malformations and 11 with tentorial dural sinus malformation (tDSM) were identified with available postnatal imaging and clinical follow up. 3/6 with VOG and 2/11 with tDSM demonstrated prenatal parenchymal injury and all had postnatal neurologic sequelae (from mild to severe). No subjects without parenchymal abnormalities on fetal imaging had postnatal neurologic sequelae (Fisher's exact test $p < 0.001$). Additional intracranial findings, such as extra-axial hemorrhage, ventriculomegaly, and varices, did not reach statistical association for association with abnormal neurologic outcomes ($p > 0.050$). One VOG and 8 tDSM cases spontaneously decreased in size or resolved upon postnatal imaging.

Conclusions

The presence of parenchymal injury on fetal MRI is a significant predictor of poor postnatal neurologic outcomes in subjects with congenital vascular malformations.



(Filename: TCT_1575_unnamed.jpg)

Firefighting and postural stability judgment impairment: An fMRI study

D Edmondson¹, R Zeiler², A Bhattacharya², K Cecil¹

¹Cincinnati Children's Hospital Medical Center, Cincinnati, OH, ²University of Cincinnati College of Medicine, Cincinnati, OH

Purpose

Over a million firefighters in the United States are exposed dangerous conditions including high temperature and smoky environments each year. Previous work has shown suboptimal environments can lead to cardiovascular, cognitive, psychological (1), and balance impairment (2). To identify whether multiple instances of intense heat from firefighting leads to difficulty assessing balance, we used fMRI to assess how well firefighters can judge static balance and postural gait.

Materials and Methods

Twenty-two, male firefighters (30-45 years old) were recruited. Firefighters were separated into two groups based on a work history survey: LOW (N=15) for firefighters with less than 10 structural fires or smoky conditions per year and HIGH (N=7) for firefighters with greater than or equal to 10 structural fires or smoky conditions per year. A Philips 3T MRI scanner equipped with a 32-channel head coil was used to acquire functional MRI (fMRI) while each participant watched two motor tasks. To assess static balance judgment ability, participants viewed and judged random images of actors in various degrees of stability and balance (3). To assess dynamic gait judgment ability, participants viewed and judged random brief videos (6 seconds duration) depicting actors walking with various degrees of stability. fMRI was processed using the FMRIB Software Library (FSL,4).

Results

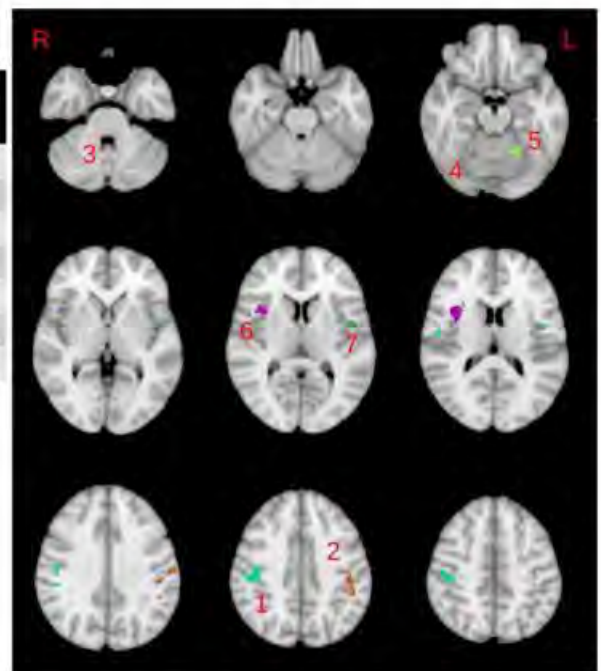
During the static balance judgment task, LOW had significant activation in bilateral cerebellum, operculum cortex, and postcentral gyrus when the actor was perfectly balanced (Figure 1). Areas of activation decreased until activation was found only in the right operculum cortex for an actor depicting bad balance. We did not find any significant activation during this task for HIGH. During the dynamic gait judgment task, LOW had significant activation in the right lateral occipital cortex and right occipital fusiform gyrus when the image had a perfectly balanced walk and bad balance walk. We did not find any significant activation during this task for HIGH.

Conclusions

LOW showed activation in regions of the brain common to the direct and indirect locomotor pathways (5) suggesting these regions of the brain are used to judge whether a subject is perfectly balance or not. The decreasing areas of activation suggests that less resources are necessary to identify someone out of balance than perfectly balanced. The lack of similar activation in HIGH compared to LOW suggests that firefighting may be impacting judgment of postural stability.

Regions of activation in Static Balance Judgment Task for LOW Group observing Perfect Balance

	Anatomical Location	Z-Max Location	Z-Max	Cluster Size (Voxels)	P-Value
1	R. Postcentral Gyrus	[21 52 57]	4.58	449	1.07e-06
2	L. Postcentral Gyrus	[76 54 53]	4.47	374	7.69e-06
3	Cerebellum Vermis	[45 27 19]	4.13	321	3.3e-05
4	R. Cerebellum	[34 33 27]	4.18	197	0.00144
5	L. Cerebellum	[57 35 26]	3.77	121	0.0218
6	R. Frontal Operculum Cortex	[26 69 42]	4.56	275	0.000125
7	L. Central Operculum Cortex	[68 62 42]	4.32	183	0.00231



Fluciclovine: A Not-So-Novel Novel Imaging Tracer Evaluating Intracranial Neoplasms

V Kuttappan¹, B Liu¹

¹Northwestern University, Chicago, IL

Purpose

Anti-1-amino-3-18F-fluorocyclobutane-1-carboxylic acid (18F-fluciclovine, 18F-FACBC) is a nonmetabolized leucine derivative that was developed to better identify gliomas with high radiotracer accumulation in tumor relative to normal brain. Since 2016, this radiotracer has taken an interesting course becoming FDA approved to image prostate cancer. This is a literature review of 18F-FACBC's original intended purpose as a diagnostic imaging agent for gliomas and other intracranial neoplasms.

Materials and Methods

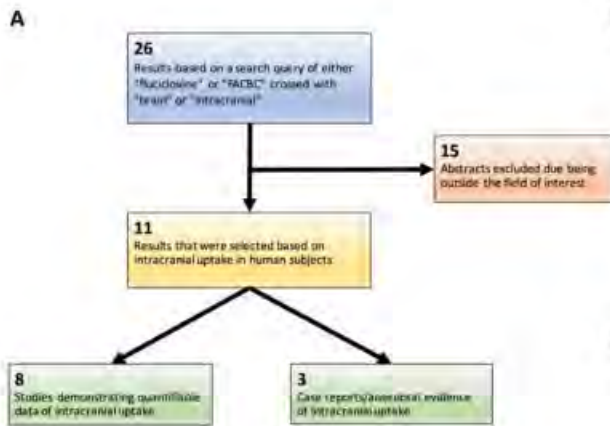
A literature search was performed in Pubmed for articles relevant to 18F-FACBC and any associated intracranial uptake. A search query of "fluciclovine" or "FACBC" was crossed with "intracranial" and "brain". All studies reporting patients with intracranial deposition of the 18F-FACBC PET in the clinical setting were included in this review. For each study, information was collected including but not limited to the type of study, number of subjects evaluated and the number of subjects showing uptake in their brain tumor.

Results

Eleven studies were selected satisfying the objective of this review which is to compile data on known 18F-FACBC intracranial uptake. Eight of these articles reported the efficacy of 18F-FACBC in gliomas. Three other studies pertained to case reports demonstrating uptake in meningiomas, a pituitary adenoma and the superior sagittal sinus. Of the glioma studies, 122/123 patients demonstrated PET positive uptake even with varying technical parameters including device used (i.e. PET/CT, PET/MRI or PET) and injected activity.

Conclusions

While contrast-enhanced MRI is the mainstay for detection of intracranial neoplasms, enhancement can only occur when the blood-brain barrier is disrupted or absent. 18F-FACBC utilizes amino acid transporters (LAT1 and ASCT2) to enter neoplasms regardless of blood-brain barrier integrity or presence. Gliomas are known to have elevated amino acid metabolism and upregulate amino acid transport which explain the results accrued in this review. Complementing the accessibility and well-established applications of contrast-enhanced MRI, 18F-FACBC could potentially be used to distinguish between types of gliomas, determine tumor volume and extent, plan treatment, guide biopsy and discriminate between residual/recurrent disease and treatment-related changes. And while nongliomatous intracranial uptake in this review is solely anecdotal, showcasing PET positive results may provide promise for the radiotracer's use in other applications.



B

Author	Year published	Type of study	Number of patients evaluated	PET Positive
Bosgrud	2019	Retrospective	21	21
Henderson	2019	Case Report	2	2
Karlberg	2019	Prospective	11	11
Kondo	2016	Prospective	5	5
Michaud	2019	Prospective	27	27
Parent	2016	Prospective	16	16
Tsuyuguchi	2017	Prospective	6	6
Wakabayashi	2017	Prospective	35	34
TOTAL			123	122

C

Author	Year Published	Type of Study	Number of patients evaluated	Intracranial Uptake
Nguyen	2016	Case Report	3	Meningioma
Oldan	2019	Case Report	1	Superior Sagittal Sinus
Wang	2020	Case Report	1	Pituitary Adenoma

FMRI Mapping of Frequency-Dependent Stimulation Effects of the Anterior Nucleus of the Thalamus during Deep Brain Stimulation for Epilepsy

E Middlebrooks¹, A Jain¹, L Okromelidze¹, C Lin¹, W Tatum¹, S Grewal¹

¹Mayo Clinic, Jacksonville, FL

Purpose

This is a prospective, single-center cohort study of epilepsy patients treated with ANT DBS evaluated with fMRI to determine binary effects of low- vs high-frequency stimulation on brain networks.

Materials and Methods

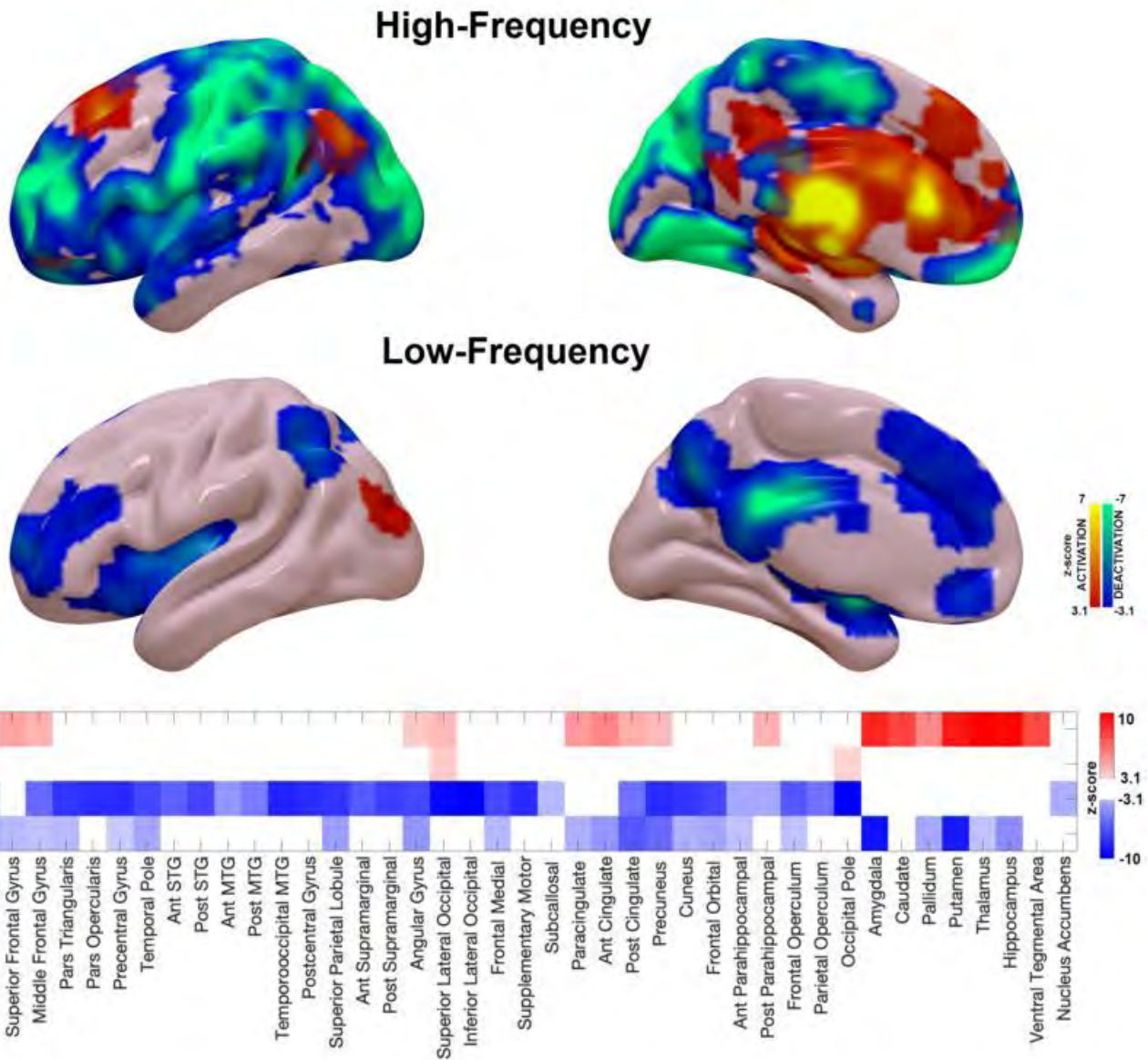
Five subjects were enrolled in this prospective cohort study scheduled to undergo bilateral ANT DBS for treatment of epilepsy. For fMRI acquisition, the DBS was set to cycle as "ON" for 30 seconds and "OFF" for 30 seconds. Two 7-minute fMRI runs were performed at high frequency (145 Hz) and two runs at low frequency (30 Hz) settings. An initial single-subject analysis of the fMRI data was performed for each run using a general linear model (GLM) for two contrasts: activation (DBS "ON" minus "OFF") and deactivation (DBS "OFF" minus "ON"). The single-subject COPEs for the two fMRI runs for each subject were combined using a fixed-effects analysis followed by a two-stage mixed effects analysis. Z-score statistical images and difference images were non-parametrically thresholded using a cluster threshold of $z > 3.1$ and a (corrected) cluster significance threshold of $p = 0.05$.

Results

High-frequency stimulation produced significant activation within multiple cortical and subcortical regions. In particular there was activation of the limbic network and regions of the default mode network (DMN). Low-frequency stimulation produced far less activation and failed to produce significant activation within these same DMN and limbic networks. High-frequency stimulation produced widespread cortical and subcortical deactivation that spared many of the previously mentioned limbic and DMN regions. There was deactivation, however, in the nucleus accumbens only with high-frequency stimulation. Meanwhile, low-frequency stimulation produced deactivation in the majority of the DMN and limbic structures. Interestingly, no activation or deactivation was present in ANT with low-frequency stimulation. The significantly different areas of deactivation with LF stimulation remained within many of the DMN and limbic regions.

Conclusions

High- and low-frequency ANT stimulation produced significantly different patterns of brain activation and deactivation, particularly affecting different regions of the DMN and limbic network. Given the current limited understanding of the differing effects of stimulation frequency in ANT DBS, as well as its role in affecting treatment outcome, our results show fMRI with active DBS stimulation to be a potentially powerful biomarker for patient-specific programming optimization.



(Filename: TCT_1609_FIG3copy.jpg)

1008

Fractional Anisotropy before and after interspinous process device implant: a feasibility study.

M Bellini¹, C Zini², L Monti³, L Manfrè⁴, s marcia⁵, G Sadotti⁶

¹Unit of Diagnostic and Functional Neuroimaging, Siena, Tuscany, ²Unit of Radiology, Hospital Santa Maria Annunziata, USL Centro, Firenze, FI, ³Diagnostic and Functional Neuroimaging Unit, Siena, Italia, ⁴Mediterranean Institute for Oncology, Viagrande, Catania, ⁵SS TRINITA' HOSPITAL, CAGLIARI, SARDEGNA, ⁶Unit of Radiology, Siena, SI

Purpose

To evaluate the fractional anisotropy (FA) before and after the placement of percutaneous interspinous process device (IPD) Lobster® (Techlamed, Firenze, Italy).

Materials and Methods

7 patients (2 male, 5 female, mean age 68 years old, range 57-81) with neurogenic intermittent claudication because of DLSS related to mono/bi-segmental lumbar central canal and/or foraminal stenosis were evaluated with 1.5 T magnetic resonance imaging (MRI) with axial DTI (SE-EPI, TR=5600 ms, TE 84 ms, ST =4 mm, matrix=136x152, FOV=300x270, NEX=6, b value= 0 - 800 s/mm²) before and 2 months after the IPD placement procedure. Technical success was defined as correct placement of the IPD; spinoplasty was accomplished in patients with BMD T-score < - 2.5.

Results

7 IPD (8 mm= 1; 10 mm=5; 12 mm=1) were implanted plus spinoplasty in 5 patients with 100% technical success; no major complications were registered. Before the IPD, the nerve root mean FA value at the levels affected by the central stenosis was $0,23\pm 0,03$ while the nerve root mean FA value at the same levels after the implant was $0,27\pm 0,04$ ($p<0.001$). In particular, before the implant the nerve root mean FA value at the levels of canal/foraminal stenosis was $0,23\pm 0,03$ (left) and $0,22\pm 0,03$ (right) without statistical difference comparing both sides ($p=0,42$); after the IPD implant the nerve root mean FA value at the levels of canal/foraminal stenosis was $0,27\pm 0,05$ (left) and $0,27\pm 0,03$ (right) ($p<0.001$). The nerve root mean FA value evaluated over the level of the stenosis with regular foramina and canal did not show statistical differences before and after the IPD placement ($p=0.17$). After the IPD, there is no statistical difference between the nerve root mean FA value at the levels former affected by stenosis $0,27\pm 0,04$ and the nerve root mean FA value at never affected levels $0,26\pm 0,04$ ($p=0,08$).

Conclusions

The nerve root mean FA value before and after IPD placement was different in central and foraminal stenosis ($p<0.001$) while no difference was found at the level of non stenotic level, suggesting that FA can be a viable method for the evaluation of neural disfunction.

998

Functional MRI Breath Holding Cerebrovascular Reactivity (CVR) Mapping in Patients with Drug-Resistant Epilepsy (DRE) under General Anesthesia

F Vedaeei¹, M Alizadeh¹, M Tantawi¹, S Thalheimer¹, V Romo¹, F Mohamed¹, C Wu¹

¹Thomas Jefferson University, Philadelphia, PA

Purpose

Cerebrovascular reactivity (CVR) is a potential indicator of vascular autoregulatory efficiency and directly affects blood-oxygen level dependent (BOLD) imaging in functional MRI (fMRI). Given the concern for neurovascular uncoupling (NVU) induced by inhalational anesthetics, we assessed CVR with fMRI and induced hypercapnia through a breath holding (BH) task in both awake and anesthetized states in human subjects. We then assessed differences in CVR induced by this standardized protocol of general anesthesia.

Materials and Methods

9 patients with drug-resistant epilepsy requiring MR imaging in both awake and anesthetized state for clinical purposes also underwent fMRI during each of these sessions. The awake and anesthetized fMRIs were acquired approximately 2 weeks apart. The standard anesthesia protocol consisted of two anesthetic agents including propofol (for initiation/induction) and sevoflurane (as the maintenance therapy) were used. The BH protocol consists of two separate BOLD acquisitions (5 minutes each) using echo-planar imaging (EPI) with 15 min gap between. The BH paradigm includes 5 repeated cycles of 40 seconds self-paced normal breathing followed by 20 seconds breath holding. After data acquisition and preprocessing, CVR maps were estimated from each patient's BOLD signal time series in each voxel of the gray matter and the thalamus. General linear model (GLM) was used to apply respiration response function (RRF) to BOLD fMRI signal in order to model the hemodynamic response to the breath holding task. A paired t-test was applied on regression coefficients for group comparison between awake and anesthetized states with a p value < 0.05. Clusters of at least 150 voxels were then identified.

Results

Overall CVR was not significantly different between the two states using student t-test (p -value=0.23, Figure 1). CVR group comparison between awake and anesthetized states resulted in 10 significant clusters ($p<0.05$) as shown in Figure 2. Under anesthesia state, higher CVR was seen in regions within frontal lobe, anterior cingulate, cerebellum, and superior temporal gyrus; however lower CVR was seen in the occipital lobe, cuneus, and middle temporal gyrus (Table 1).

Conclusions

Our findings suggest that inhaled anesthetics does not induce widespread NVU as the effect of anesthetic agent could be estimated through breath-hold task fMRI. The results also help understanding of the effect of inhalational anesthetics on CVR maps in patients with cerebrovascular and neurological diseases.

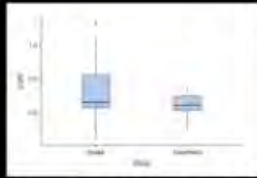


Figure 1. Plot of global CVR comparison between awake and under anesthesia states

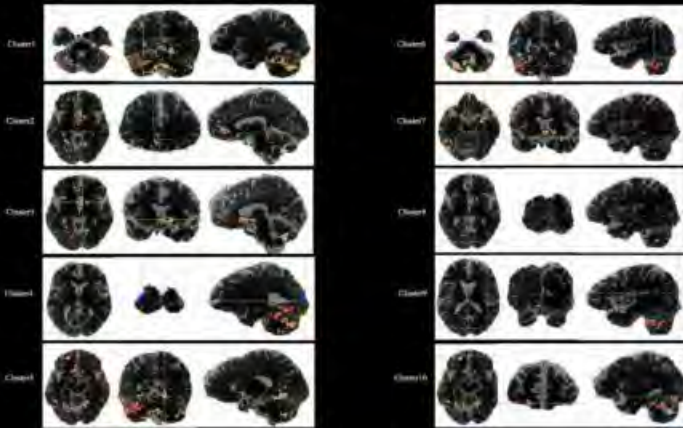


Figure 2. Group comparison of CVR map between awake and under anesthesia. Clusters in blue correspond to higher CVR in awake and red clusters correspond to higher CVR under anesthesia (paired t-test, $p < 0.05$, and minimum cluster size 150 voxels).

Cluster	Regions	Regression Coefficient (b-value)	Number of voxels	Volume (mm ³)	Coordination (Cmax)
Cluster1	Left Cerebellum	-4.4	3012	16142.43	(+29.1, +54.8, -25.8)
Cluster2	-Left Anterior Cingulate -Left Subcallosal Gyrus -Left Medial Frontal Gyrus	-1.2	351	1881.14	(+7.5, -28.2, -5.4)
Cluster3	-Right Caudate -Right Anterior Cingulate	-1.4	340	1822.18	(-6.4, -5.2, -4.0)
Cluster4	-Left Middle Occipital Gyrus -Left Cuneus -Left Lingual Gyrus	2.3	319	1799.64	(+23.1, +91.6, +5.2)
Cluster5	-Right Lingual Gyrus -Right Cerebellum	-0.63	231	1238.01	(-16.3, +53.7, -7.7)
Cluster6	-Right Cerebellum -Right Culmen	-3.11	224	1260.5	(-43.0, +46.8, -34.8)
Cluster7	-Right Superior Temporal Gyrus -Right Parahippocampal Gyrus -Right Subcallosal Gyrus	-1.2	231	1130.82	(-34.8, -3.7, -14.4)
Cluster8	-Right Middle Occipital Gyrus -Right Inferior Occipital Gyrus -Right Cuneus	1.85	174	932.53	(-36.7, +84.2, +1.8)
Cluster9	-Right Middle Temporal Gyrus -Right Middle Occipital Gyrus	1.1	173	927.17	(-43.8, +75.1, +12.6)
Cluster10	-Left Middle Frontal Gyrus -Left Superior Frontal Gyrus -Left Medial Frontal Gyrus	-1.9	160	905.73	(+21.7, -49.3, -9.0)

Table 1. List of clusters with significant level of 0.05. Positive b values represents higher CVR in awake, and negative values correspond to higher CVR under anesthesia

(Filename: TCT_998_BH_image.jpg)

1185

Geodesic Path Analysis of Neural Networks in the Alzheimer's Disease Connectome Project

N Adluru¹, V Nair¹, V Prabhakaran², S Li³, A Alexander⁴, B Bendlin¹

¹UW-Madison, Madison, WI, ²Univ. Of Wisconsin Hospitals and Clinics, Madison, WI, ³Medical College of Wisconsin, Milwaukee, WI, ⁴University of Wisconsin Madison, Madison, WI

Purpose

Neural networks derived from diffusion weighted MR imaging may shed light on disease progression and pathology propagation in Alzheimer's disease in vivo. Geodesic paths are fundamental in understanding key network phenomenon such as the propagation rates of information, infection or pathology. For example, the ubiquitous small-worldness property of natural occurring biological and social networks is based on having short path lengths between any pair of entities in the network. The purpose of this abstract is to provide preliminary analysis of the geodesic paths of neural networks derived from the Alzheimer's disease connectome project (ADCP).

Materials and Methods

Connectome imaging protocol based multi-shell diffusion weighted MRI data acquired from n=147 participants were analyzed (Table 1). Neural networks were extracted from the data using state-of-the-art image processing and tractography algorithms available in the MRtrix3 package [1,2]. The average geodesic path lengths between frontal, temporal, parietal, occipital, subcortical regions were computed using Dijkstra algorithm [3,4]. The regions were identified based on the IIT Desikan gray matter atlas [5]. The paths can be used to reason about the average efficiency of communication of electrical signals or propagation of pathology between brain lobes. Statistical analysis was performed to test the geodesic path length differences between the CU, MCI and the AD groups controlling for age and sex. The path lengths were normalized so that they were at unity for the CU group, and the differences were considered statistically significant when $p \leq 0.05$.

Results

Statistical analysis of differences in the relative geodesic path length (RGPL) between lobes are shown in Fig. 2. For all the different pairs of lobes, the mean length was consistently higher for the AD group compared to both the CU and MCI groups. For AD vs. CU all of the lobe-lobe path length differences were statistically significant, while for MCI vs. CU 6 of the 10 lobe-lobe lengths were.

Conclusions

The path lengths between all the major lobes are longer for the AD group compared to both the CU and MCI groups. These findings suggest that network efficiency is reduced in AD and may explain cognitive dysfunction observed in the Alzheimer's clinical syndrome. Future work entails studying the effects by separating disease groups by AD-biomarker status as well as investigating additional properties of the geodesic paths.

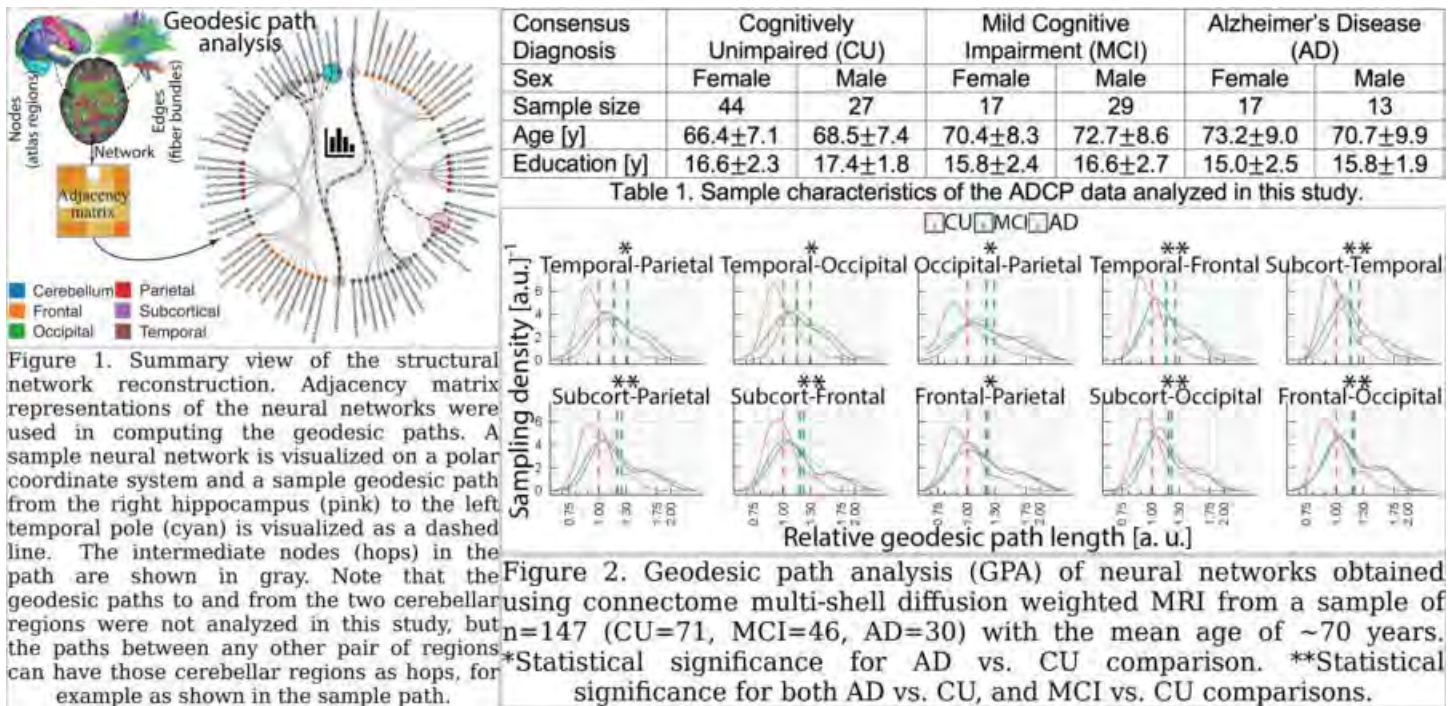


Figure 1. Summary view of the structural network reconstruction. Adjacency matrix representations of the neural networks were used in computing the geodesic paths. A sample neural network is visualized on a polar coordinate system and a sample geodesic path from the right hippocampus (pink) to the left temporal pole (cyan) is visualized as a dashed line. The intermediate nodes (hops) in the path are shown in gray. Note that the geodesic paths to and from the two cerebellar regions were not analyzed in this study, but the paths between any other pair of regions can have those cerebellar regions as hops, for example as shown in the sample path.

Figure 2. Geodesic path analysis (GPA) of neural networks obtained using connectome multi-shell diffusion weighted MRI from a sample of $n=147$ (CU=71, MCI=46, AD=30) with the mean age of ~70 years. *Statistical significance for AD vs. CU comparison. **Statistical significance for both AD vs. CU, and MCI vs. CU comparisons.

(Filename: TCT_1185_ASNR2021Graphic.jpg)

1273

Globe Displacement Ratio as a Novel Method for Improving Radiographic Accuracy in Determining Unilateral Proptosis in Orbital Computed Tomography Imaging

Z Igbino¹, T Nanda¹, P Jairam², M Maher³, J Sweigert⁴, A Famuyide¹, J Horowitz¹

¹Columbia University Irving Medical Center, New York, NY, ²Columbia University College of Physicians and Surgeons, New York, NY, ³Harvard Medical School-Massachusetts General Hospital, Boston, MA, ⁴University of California Los Angeles, Los Angeles, CA

Purpose

The presence of proptosis is a management-altering radiographic finding. The globe displacement ratio (GDR) may provide a more precise, quantitative method for determining proptosis. The goal of this study was to measure GDR in patients who received an orbital CT scan in order to evaluate its utility in determining proptosis.

Materials and Methods

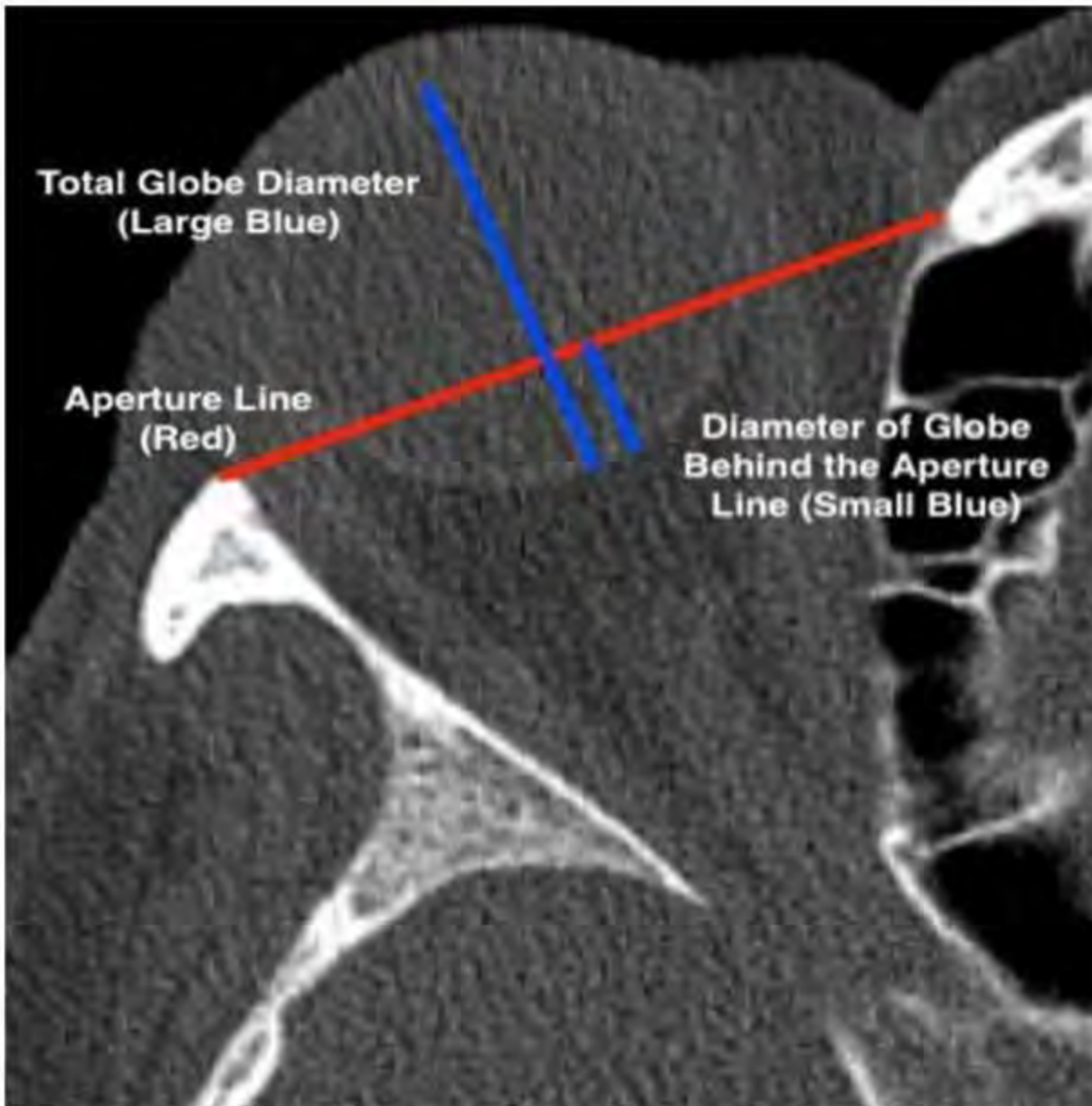
A retrospective review of orbital CT scans for "unilateral proptosis" from 2014-2019 was performed. GDR was defined as: Diameter of the Globe Posterior to the Bony Orbital Aperture / Total Globe Diameter (Figure 1) measured in the axial plane at the greatest globe diameter. The uninvolved eye in all cases served as a control group. Patients who clinically and radiographically had no report of proptosis, served as additional bilateral controls. Comparisons were made by two-sample t test (α of 0.05). Reproducibility was assessed by two-way random effects interclass correlation coefficient (ICC) with one expert and one novice rater.

Results

90 patients (180 orbits) met inclusion criteria for unilateral proptosis and 30 patients (60 orbits) served as bilateral controls (58% female; average age 48 (1-96)). Common indications included trauma (23.3%) and orbital/pre-septal cellulitis (27.8%). The average GDR difference between eyes amongst bilateral controls was 0.039 (median of 0.021, range: 0.00-0.10). Thus, we defined unilateral proptosis as a significant GDR difference between eyes (Δ) as $>|0.10|$. The average GDR amongst all normal orbits (150 orbits) was 0.46 +/- 0.14 (0.14-0.85). The average GDR amongst the proptosis cohort (90 orbits) was 0.29 +/- 0.14 (range: 0.0-0.67), $p<0.001$. In 3 cases proptosis was identified by GDR but not mentioned on the radiology report (Figure 1). In 19 cases, unilateral proptosis was erroneously reported when otherwise symmetric (avg. Δ 0.042). ICC was 0.93 for GDR, indicating excellent reproducibility (95% CI: 0.91-0.95, $p<0.001$).

Conclusions

In all reports included in this study, no objective quantitative measures were present to support the description of proptosis. With a high ICC, GDR is a quick and useful tool in patients with suspected unilateral pathology (in which inter-orbit comparison can serve as an individual control). 3 orbits had possible proptosis when none was reported, a potentially dangerous outcome. In the 19 cases in which proptosis was erroneously reported, the patients may undergo unnecessary treatment/work-up. In these cases, GDR appears helpful in tailoring descriptors, such as 'equivalent' or 'L>R'.



Case	Proptosis by Read	Right GDR / Left GDR	GDR Diff. b/w Eyes	Consensus Diagnosis using GDR
1	No	0.49 / 0.23	0.26	Carotid-Cavernous Fistula
2	No	0.41 / 0.59	0.18	Orbital Cellulitis
3	Yes (right eye)	0.13 / 0.23	0.09	Bilateral TED

(Filename: TCT_1273_Figure1.jpg)

Graph Based Functional Network Analysis in Focal Epilepsy Patients with Respect to Seizure Outcomes

M Alizadeh¹, A Manmatharayan¹, U Fatema¹, C Matias¹, F Mohamed¹, C Wu¹

¹Thomas Jefferson University, Philadelphia, PA

Purpose

NA

Materials and Methods

Recent advances in analytical neuroimaging increase our ability to create maps of neural networks in the brain called connectomes. Connectomic analyses are an invaluable platform for the characterization of aberrant structural and functional brain connectivity relative to clinical manifestations. This study seeks to investigate the relationship between functional connectome-based models of the epileptogenic networks and post-surgical seizure outcomes of patients with focal epilepsy who underwent laser interstitial thermal therapy (LiTT) using resting-state functional MRI (rsfMRI).

Results

This is a retrospective study of 27 patients age ranged 25-72 years with medically refractory unilateral mesial temporal lobe epilepsy (mTLE). They were scanned for rsfMRI with a 3.0T Achieva Philips scanner prior to the LiTT procedure. At 12 months after LiTT, 13 patients were classified as "seizure-free" (SF) and 14 were "not seizure-free" (NSF) using Engel's criteria [1]. Connectivity matrices were computed based on Pearson's correlation coefficients for the time course of all pairs of regions of interest (ROIs). Graph measures for each patient's connectivity matrix were calculated and compared between SF and NSF groups using two tailed t-test. The graph measures included (1) global efficiency; (2) local efficiency; (3) betweenness centrality; (4) clustering coefficient; and (5) degree

Conclusions

Results: At the whole brain level, the network topological substrate of SF and NSF patients differed beyond the hippocampus to interconnected network nodes including limbic and extra-limbic brain regions. Compared to SF subjects, NSF subjects had increased connections outside the temporal lobe. The ipsilateral parietal operculum cortex was more integrated in the NSF cohort. Conclusion: Our study demonstrates the potential for resting-state functional connectivity analysis to serve as a predictor of post-ablation seizure outcome, and highlights the significance of specific limbic and extra-limbic connectivity variations. Evidence involving extra-hippocampal pathology in mTLE suggests that a larger network of regions may be involved in the generation of seizures. We have shown that patients with diverging procedure outcomes have distinct preoperative network differences. This finding can potentially be used for outcome prediction and devising more targeted treatment protocols for improved seizure outcomes.

Analysis Measure	Region	MNI Coordinates (x,y,z)	beta-value	T-score	p-value
NODAL	Ipsilateral Parietal Operculum Cortex*	(-48,-32,20)	-0.10	-4.21	<0.001
GLOBAL	Contralateral Central Opercular Cortex	(49,-6,11)	-0.11	-2.73	0.01
EFFICIENCY	Contralateral Lingual Gyrus	(14,-63,-5)	0.06	2.89	0.009
LOCAL	Posterior Division of ipsilateral Temporal Fusiform Gyrus	(-36,-30,-25)	-0.35	-2.99	0.008
EFFICIENCY	Anterior Division of Middle Temporal Gyrus	(-57,-4,-22)	0.43	3.45	0.005
BETWEENNESS	Ipsilateral Parietal Operculum Cortex	(-48,-32,20)	-0.02	-3.03	0.007
CENTRALITY	Ipsilateral Caudate	(-13,9,10)	0.02	3.02	0.007
	Ipsilateral Supracalcarine Region	(-8,-73,15)	0.01	2.71	0.01
CLUSTERING	Posterior Division of ipsilateral Temporal Fusiform Cortex	(-36,-30,-25)	-0.31	-3.08	0.007
COEFFICIENT					
DEGREE	Ipsilateral Parietal Operculum Cortex*	(-48,-32,20)	-11.67	-4.46	<0.001
	Contralateral Central Opercular Cortex	(49,-6,11)	-11.16	-3.52	0.002
	Contralateral Cuneal Cortex	(9,-79,28)	7.39	2.99	0.009
	Contralateral Cerebellum Lobule 4 5	(16,-44,-19)	6.58	2.68	0.01
	Contralateral Lingual Gyrus	(14,-63,-5)	6.02	2.69	0.01
	Contralateral Temporal Occipital Fusiform	(35,-50,-17)	7.33	2.99	0.008

Table: Graph theory measures between SF (n=13) and NSF (n=14) patients at the significant level of $p \leq 0.01$; T-score < 0 indicates NSF>SF; *Significant after Bonferroni correction.

(Filename: TCT_1179_RS_image300.jpg)

1271

Group Analysis in Craniocervical Syndrome: Cerebrospinal Fluid Flow Alterations in Patient Subgroups

N Kulkarni¹, B Damadian¹, D Chu¹, R Caffrey², M Gianni¹, L Minkoff¹, R Wolf¹, R Damadian¹

¹FONAR Corporation, Melville, NY, ²Lehigh University, Bethlehem, PA

Purpose

The role of the craniocervical junction and cerebrospinal fluid (CSF) flow hydrodynamics in the development of neurologic symptoms has received increasing attention in recent years (1,2). Patients suffering craniocervical trauma or craniocervical instability due to another condition (ex: connective tissue disorder) often complain of non-focal neurologic symptoms. These symptoms include headache, tinnitus, visual disturbance, gait abnormality, and syncope, and have been characterized as craniocervical syndrome (CCS) (1). It has been reported that different patterns of CSF pressure changes are associated with varying symptoms (3). In this retrospective study, we investigate whether CCS patients with different combinations of symptoms have different CSF flow characteristics.

Materials and Methods

11 patients (5 F, mean age=35.2±14.9) with primary complaint of visual symptoms (ex: photophobia, tunnel vision) and 9 patients (6 F, mean age=48.6±17.6) with primary complaint of auditory or vestibular symptoms (ex: tinnitus, balance) were selected from the adult patients referred to our MRI center for clinically suspected CCS. 14 asymptomatic volunteers (6 F, mean age 25.5±5.1) served as controls. Patients with any major neurological disorder or spine surgery were excluded. Subjects underwent 0.6T MRI in a neutral sitting position. Phase contrast with peripheral gating was used to image and quantify CSF flow at the mid-C2 level. One-way ANOVA was used to compare CSF parameters between the three groups. Post hoc Tukey test was performed to further compare means between any two groups.

Results

CSF stroke volume per cardiac cycle was significantly different ($F_{2,31}=8.54$, $p=0.0011$) between the three groups (Fig. 1). Post hoc

Tukey test showed that CSF stroke volume in patients with auditory/vestibular symptoms (mean=0.14±0.06) was significantly lower than in patients with visual symptoms (mean=0.34±0.13) and controls (mean=0.25±0.11) (p=0.0007 and p=0.05, respectively). Peak-to-peak pressure gradient analysis was also significant (F2,31=9.67, p=0.0005) (Fig. 2). Post hoc Tukey test showed that peak-to-peak pressure gradient in patients with auditory symptoms (mean=0.014±0.003) was significantly lower than in the visual symptom group (mean=0.027±0.009) and controls (mean=0.026±0.008) (p=0.001 and p= 0.0019, respectively).

Conclusions

CSF flow parameters in CCS patients vary between symptom-based subgroups. Further studies are needed to understand the role played by CSF flow hydrodynamics in CCS subpopulations.

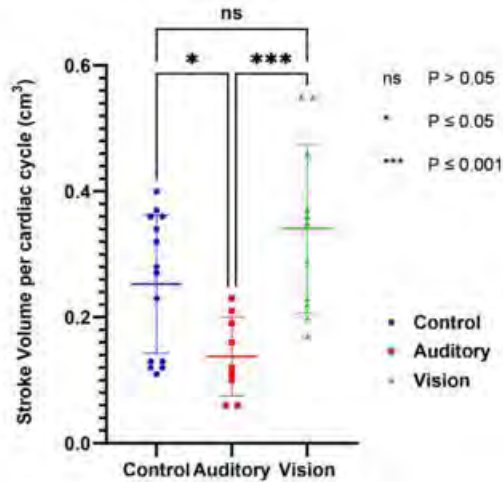


Figure 1. Stroke volume per cardiac cycle in CCS subgroups versus asymptomatic controls. (Error bars represent standard deviation)

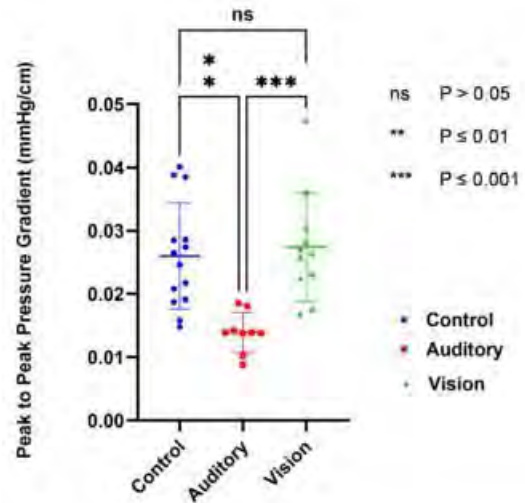


Figure 2. Peak to-peak pressure gradient in CCS subgroups versus asymptomatic controls. (Error bars represent standard deviation)

(Filename: TCT_1271_control-auditory-vision-graphics-combined.jpg)

710

Growth Trajectories, Sexual Dimorphism, and Lateral Asymmetries in the Brain of Typically Developing Fetuses

F Machado-Rivas¹, C Velasco-Annis¹, O Afacan¹, J Choi¹, S Warfield¹, A Gholipour¹, C Jaimes¹
¹Boston Children's Hospital, Boston, MA

Purpose

To characterize global and regional brain growth, sexual dimorphism, and lateral asymmetries with in vivo fetal brain MRI.

Materials and Methods

Prospective IRB approved study. Healthy pregnant volunteers in the 2nd and 3rd trimester were imaged at 3T. Multiplanar T2 HASTE scans were used to generate super resolution isotropic reconstructions with a slice-to-volume registration algorithm [1]. For segmentation, labels from a spatiotemporal atlas of fetal brain development were propagated to the individual subjects [2]. We analyzed 19 structures (some bilateral: L/R): cortical plate (CP), white matter (WM), hippocampus, amygdala, caudate, lentiform, thalamus, subthalamic nuclei (STN), internal capsule, lateral ventricles, and, cerebellar hemispheres; and some without laterality: hippocampal commissure (HC), corpus callosum, fornix, brainstem, and cerebrospinal fluid (CSF). Transient WM zones were separately analyzed for fetuses <31 weeks: proliferative zone (PZ), intermediate zone (IZ), and subplate (SP) (FigA). Linear regressions evaluated gestational age (GA) as predictors of volume with sex and laterality as covariates.

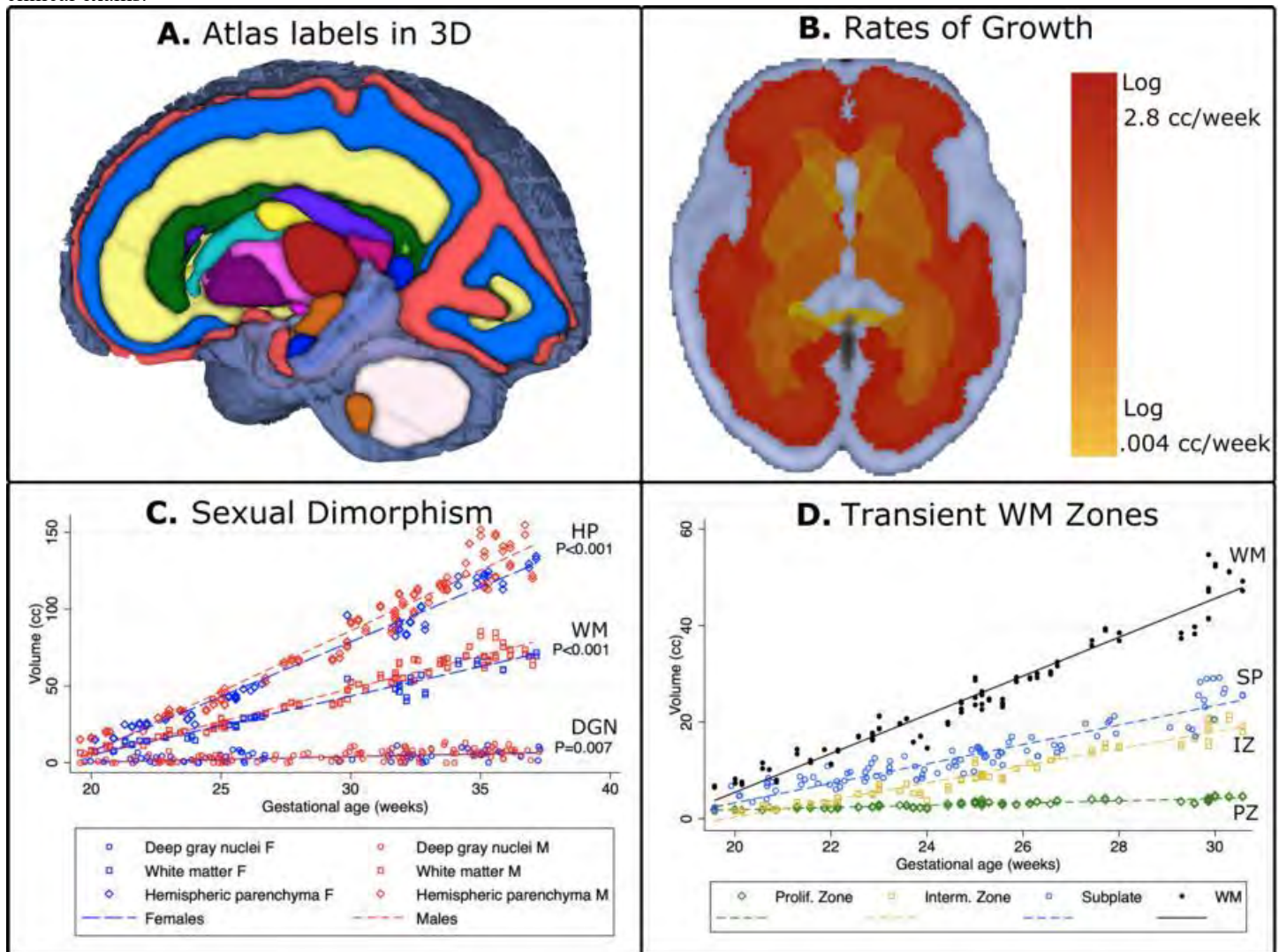
Results

92 typically developing fetuses (57 males) were analyzed; mean GA=29.08 weeks (SD±5.19). All regions significantly grew with GA (all P<0.001), with vast differences in rates of growth ranging from 0.004cc/week in subthalamic nuclei (95%CI 0.0038–0.0048, P<0.001) to 2.81cc/week in the CP (95%CI 2.68–2.93, P<0.001)(FigB). Whole-hemisphere parenchyma, deep gray nuclei (caudate, lentiform, thalamus and STN) and WM volume were larger in males (all P<0.007)(FigC). When analyzed individually, there was no difference between males and females in the caudate, STN, HC, fornix, CP, and SP (all P>0.136). There was leftward asymmetry of the caudate (P=0.001) and rightward asymmetry of the hippocampus (P<0.001). A trend towards a larger left lateral ventricle (P=0.056) was noted. The rest of the structures showed no lateral asymmetry (all P>0.066). WM change in fetuses <31 weeks was driven primarily by changes in the SP (2.0 cc/week, 95%CI 1.87-2.13, P<0.001) and the IZ (1.74 cc/week, 95%CI 1.65-1.83, P<0.001)(FigD).

Conclusions

The fetal brain exhibits complex growth trajectories that are influenced by individual region, sex, and laterality. These constitute

evidence of early functional specialization and possible vulnerability; also, they could help improve accuracy of interpretation of clinical exams.



(Filename: TCT_710_asnr_abstract_2021_final.jpg)

260

Hemodynamics differ in carotid atherosclerotic plaques compared to webs: A time-density curve study using DSA.

C Park¹, R El Sayed², D Haussen¹, B Risk³, J Oshinski², J Allen¹

¹Emory University, Atlanta, GA, ²Emory University and Georgia Institute of Technology, Atlanta, GA, ³Emory University Rollins School of Public Health, Atlanta, GA

Purpose

Carotid webs (CaW) are associated with cryptogenic ischemic strokes in younger patients without traditional risk factors who lack clinically significant stenosis. The aim of this study was to compare the hemodynamic parameters in the internal carotid artery (ICA) bulb segment in patients with CaW to patients with atherosclerotic stenosis using time-density curve (TDC) analysis of digital subtraction angiography (DSA) images.

Materials and Methods

We retrospectively analyzed DSA images of 47 carotid arteries in 41 adult patients who underwent ICA catheter angiography evaluation for ischemic stroke between December 2013 to August 2020. Hemodynamic parameters were estimated using TDC analyses of a region of interest (ROI) in the ICA bulb immediately distal to the web or atherosclerotic plaque, relative to a standardized ROI placed in the ipsilateral distal common carotid artery. Degree of atherosclerotic stenosis was defined as mild (<50%), moderate (51-69%), or severe (>70%) using NASCET criteria. Stenosis due to CaW were measured similarly using NASCET-like criteria. Data was analyzed using one-way analysis of variance (ANOVA) and post-hoc Tukey's tests.

Results

Mean age was 56.0 ± 13 years, and 53% were women 17 CaWs, 22 atherosclerotic plaques (36.4% of cases being mild, 31.8%

moderate, and 31.8% severe), and 8 normal carotid arteries were assessed. Mean stenosis of CaWs was $38.1 \pm 13.8\%$. ANOVA demonstrated significant differences in the relative mean transit time (rMTT) ($p=0.007$) and relative area under the curve (rAUC) ($p=0.003$) among patient group. Post Hoc Tukey's test showed prolonged rMTT in the CaW group compared to that of normal carotid (mean difference: 0.491, $p=0.037$) and mild atherosclerosis groups (mean difference: 0.490, $p=0.038$), but not moderate ($p=0.072$) and severe ($p=0.094$) atherosclerosis groups. CaW showed higher rAUC compared to those of the mild (mean difference: 0.704, $p=0.032$), moderate (mean difference: 0.710, $p=0.042$), and severe (mean difference: 0.800, $p=0.016$) groups, likely due to contrast pooling distal to the web.

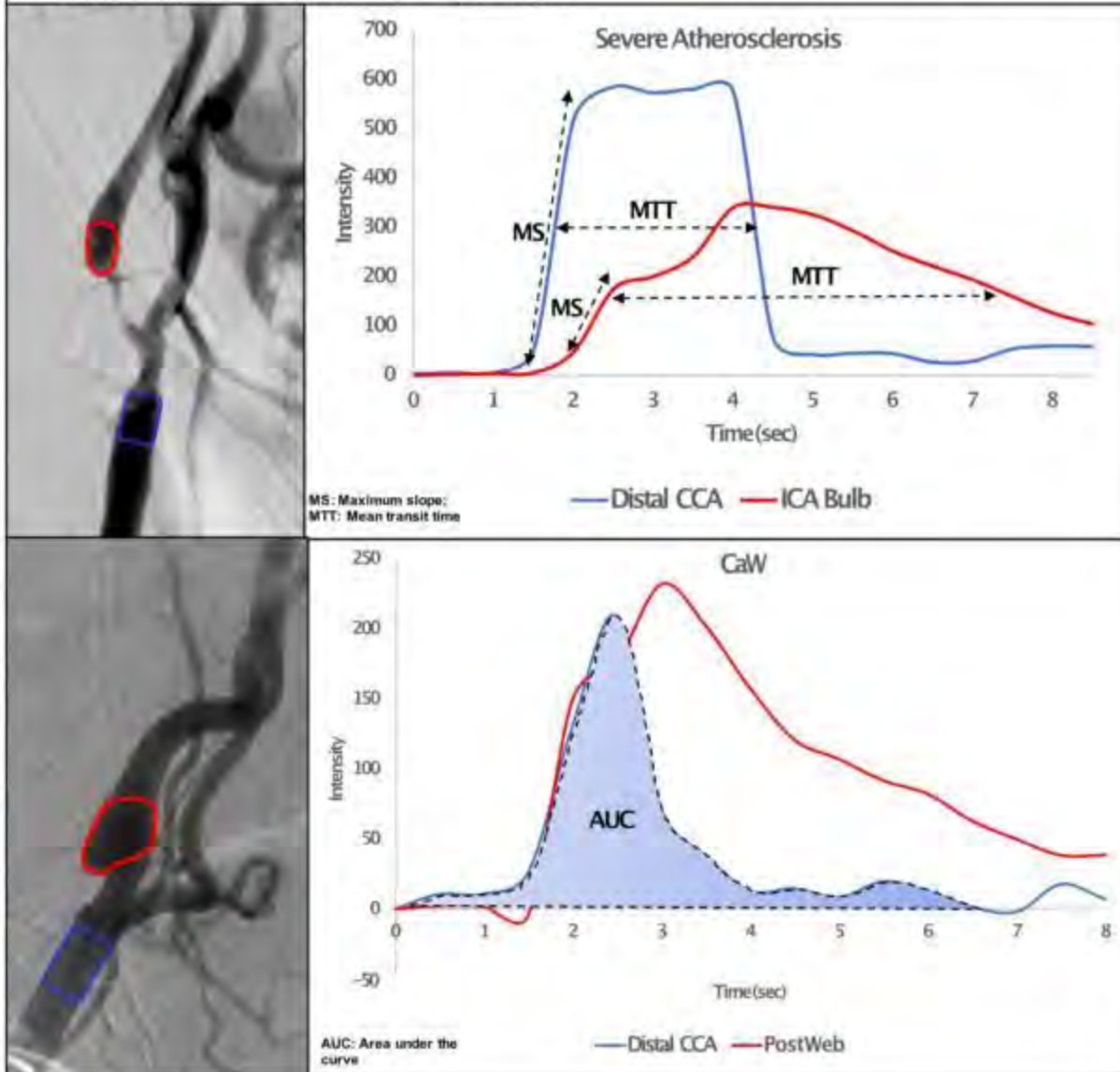
Conclusions

Despite having lesser degrees of stenosis, CaW results in large regional hemodynamic disruption comparable to those of moderate and severe atherosclerotic plaques. Future studies using advanced modalities to better assess the hemodynamic patterns and clarify the relationship between hemodynamic parameters and incidence of ischemic strokes may improve the risk stratification and clinical management of CaW.

Atherosclerotic ICA Stenosis

Parameter	Control	Mild	Moderate	Severe	CaW	F	p value
rAUC Total	1.15 ± 0.37	1.04 ± 0.22	1.03 ± 0.21	0.94 ± 0.34	1.74 ± 0.79	4.654	0.003
rAUC WI	1.09 ± 0.30	1.3 ± 1.05	1.31 ± 0.65	1.09 ± 0.53	2.37 ± 3.65	0.71	NS
rAUC WO	1.24 ± 0.52	1.22 ± 0.49	1.15 ± 0.69	0.94 ± 0.39	1.74 ± 0.77	2.657	0.046
rMTT	1.06 ± 0.15	1.06 ± 0.23	1.08 ± 0.27	1.10 ± 0.38	1.54 ± 0.52	4.124	0.007
rTTP	1.02 ± 0.14	1.04 ± 0.20	1.21 ± 0.50	1.29 ± 0.83	1.26 ± 0.56	0.535	NS
rMS	1.07 ± 0.32	0.87 ± 0.30	1.22 ± 0.26	0.68 ± 0.34	1.02 ± 0.28	3.447	0.016

r: relative (normalized to distal common carotid); AUC: area under the curve; WI: wash in; WO: wash out; MTT: mean transit time through a region of interest; TTP: time to peak; MS: maximum slope during wash in; NS: not significant



(Filename: TCT_260_ASNR2021DSACaWvsAtheroFigure.jpg)

High-Resolution Vessel Wall Magnetic Resonance Imaging Features in Moyamoya Disease: A Single Center Descriptive Analysis

A Larson¹, J Klaas², G Lanzino², W Brinjikji¹, L Savastano¹, V Lehman¹

¹Mayo Clinic, Rochester, MN, ²Mayo, Rochester, MN

Purpose

The pattern of high-resolution vessel wall imaging (HR-VWI) findings of the cerebral vasculature of patients with Moyamoya Disease (MMD) remains controversial. We sought to describe HR-VWI findings in a single-center cohort of MMD patients.

Materials and Methods

Consecutive patients who were evaluated at a Midwest American medical center with a HR-VWI exam were included. Fourteen anterior circulation arterial segments in each patient were analyzed: proximal and distal supraclinoid Internal Carotid Artery (ICA), proximal M1 segment of the Middle Cerebral Artery (MCA), mid-portion of the M1, distal M1, proximal A1 segment of the Anterior Cerebral Artery (ACA) and distal A1. Imaging variables that were collected from each segment included the presence of wall thickening (concentric vs eccentric), degree and pattern (concentric or eccentric) of contrast enhancement, and presence of positive or negative vessel remodeling. The total number and percentage of vessel segments demonstrating these characteristics were calculated. The number and percentage of patients with at least one segment demonstrating these characteristics were calculated. The laterality and location of each imaging feature present was determined for each patient.

Results

24 patients (17 females, 70.8%) with a diagnosis of idiopathic MMD were included. Overall, 161 of 336 segments (47.9%) demonstrated negative remodeling in 23 (95.8%) patients. Sixty-four segments (19.1%) demonstrated wall enhancement (44 concentric, 18 eccentric; 54 high grade, 10 low grade) in 21 (87.5%) patients. Fifty-eight segments (17.2%) demonstrated wall thickening (28 concentric, 28 eccentric, 2 mixed) in 21 (87.5%) patients. Unilateral wall enhancement was most-commonly visualized in the ICA (68.7%), MCA (61.5%) and ACA (77.8%). In contrast, bilateral remodeling was most-commonly visualized on all three vessels (63.2%, 52.2% and 64.7%, respectively). In regards to wall thickening, unilateral thickening was more-commonly observed in the ICA (76.9%) and MCA (69.2%), whereas bilateral thickening was most commonly seen in the ACA (62.5%).

Conclusions

Vessel wall enhancement, remodeling and thickening were present in a minority of arterial segments on HR-VWI. Concentric enhancement and negative remodeling were present in at least one arterial segment in a high percentage of patients with MMD. The location and laterality of each of these radiographic features was highly variable. The role for HR-VWI in recognizing idiopathic MMD requires further study.

Table 1. Enhancement patterns within arterial wall segments demonstrating at least some degree of enhancement

Location	Pattern of Wall Enhancement, no. (%)		
	Concentric	Eccentric	Mixed
Proximal ICA (N = 7)	4 (57.1)	3 (42.9)	0 (0.0)
Distal ICA (N = 16)	10 (62.5)	6 (37.5)	0 (0.0)
Proximal M1 (N = 16)	10 (62.5)	5 (31.3)	1 (6.3)
Mid-M1 (N = 9)	7 (77.8)	1 (11.1)	1 (11.1)
Distal M1 (N = 4)	2 (50.0)	2 (50.0)	0 (0.0)
Proximal A1 (N = 11)	10 (90.9)	1 (9.1)	0 (0.0)
Distal A1 (N = 1)	1 (100.0)	0 (0.0)	0 (0.0)
Overall (N = 64 overall)	44 (68.8)	18 (28.1)	2 (3.1)

Table 2. Patterns of arterial wall thickening

Location (N = 48 total per location)	Pattern of Wall Thickening, no. (%)			
	None	Concentric	Eccentric	Mixed
Proximal ICA, no. (%)	40 (83.3)	1 (2.1)	6 (12.5)	1 (2.1)
Distal ICA	36 (75.0)	2 (4.2)	9 (18.8)	1 (2.1)
Proximal M1	35 (72.9)	9 (18.8)	4 (8.3)	0 (0.0)
Mid-M1	40 (83.3)	5 (10.4)	3 (6.3)	0 (0.0)
Distal M1	43 (89.6)	2 (4.2)	3 (6.3)	0 (0.0)
Proximal A1	37 (77.1)	8 (16.7)	3 (6.3)	0 (0.0)
Distal A1	47 (97.9)	1 (2.1)	0 (0.0)	0 (0.0)
Overall (N = 336 overall)	278 (82.7)	28 (8.3)	28 (8.3)	2 (0.6)

Table 3. Patterns of arterial wall remodeling

Location (N = 48 total per location)	Pattern of Wall Remodeling, no. of segments (%)		
	None	Negative	Positive
Proximal ICA, no. (%)	41 (85.4)	7 (14.6)	0 (0.0)
Distal ICA	18 (37.5)	30 (62.5)	0 (0.0)
Proximal M1	16 (33.3)	32 (66.7)	0 (0.0)
Mid-M1	20 (41.7)	28 (58.3)	0 (0.0)
Distal M1	26 (54.2)	22 (45.8)	0 (0.0)
Proximal A1	22 (45.8)	26 (54.2)	0 (0.0)
Distal A1	32 (66.7)	16 (33.3)	0 (0.0)
Overall (N = 336 overall)	175 (52.1)	161 (47.9)	0 (0.0)

Table 4. Laterality of arterial wall abnormalities

	Laterality, no. of patients (%)	
	Bilateral	Unilateral
Contrast Enhancement (Any)		
ICA (N = 16)	5 (31.3)	11 (68.7)
MCA (N = 13)	5 (38.5)	8 (61.5)
ACA (N = 9)	2 (22.2)	7 (77.8)
Overall (N = 38)	12 (31.6)	26 (68.4)
Remodeling (Any)		
ICA (N = 19)	12 (63.2)	7 (36.8)
MCA (N = 23)	12 (52.2)	11 (47.8)
ACA (N = 17)	11 (64.7)	6 (35.3)
Overall (N = 59)	35 (59.3)	24 (40.7)
Thickening (Any)		
ICA (N = 13)	3 (23.1)	10 (76.9)
MCA (N = 13)	4 (30.8)	9 (69.2)
ACA (N = 8)	5 (62.5)	3 (37.5)
Overall (N = 34)	12 (35.3)	22 (64.7)

(Filename: TCT_618_Tables.gif)

1157

Iatrogenic Foreign Materials Associated with Retrieved Clot Tissue via Mechanical Thrombectomy

Purpose

Hydrophilic polymers and PTFE liners are commonly used in the construction of endovascular devices and they occasionally fragment and separate from devices procedures with subsequent embolization (1,2). We sought to determine frequency of such materials in thrombus specimens retrieved by mechanical thrombectomy (MT) in stroke patients

Materials and Methods

We retrospectively reviewed hematoxylin and eosin (H&E) stained thrombus sections for presence and types of foreign materials. We identified four types of foreign materials. Type I was light green with refraction and homogenous in texture. Type II was light gray or dark gray; it was thin, loose or dense in texture. Type III was light green with refraction, it was solitary in texture, irregular in shape, and was often associated with round or oval bubble-like particles and/or diffused black particles. Type IV was homogenous in texture and light pink or red in color. Polymer materials from different layers of used MT catheters were harvested, and compared to the foreign materials found in thrombus specimens.

Results

A total of 101 thrombi were evaluated. Foreign materials were found in 53 (52.5 %) of thrombus samples. The most common type was type I (90%), followed by type II (26%). Type III materials were found in 21% of samples (11/53) and were solitary in texture and irregular in shape. Type IV materials were found in 15% of cases (8/53) (Figure 1d). They were homogenous in texture and light pink/red in color, and presented as snake or worm-like in shape. They were either located at gaps between tissues or embedded within thrombus tissue. The size of foreign materials ranged from 5 μ m to 1340 μ m in length. The histopathological features of the polymer materials harvested from MT catheters were similar to the foreign materials found in thrombus specimens. The coating layer and Inner PTFE liners of catheters resembled Type II and Type I of the foreign materials respectively.

Conclusions

Foreign polymer materials are present in about half of retrieved thrombi, most commonly PTFE from catheter liners and less from hydrophilic coatings. Clinical significance of this phenomenon remains to be elucidated.

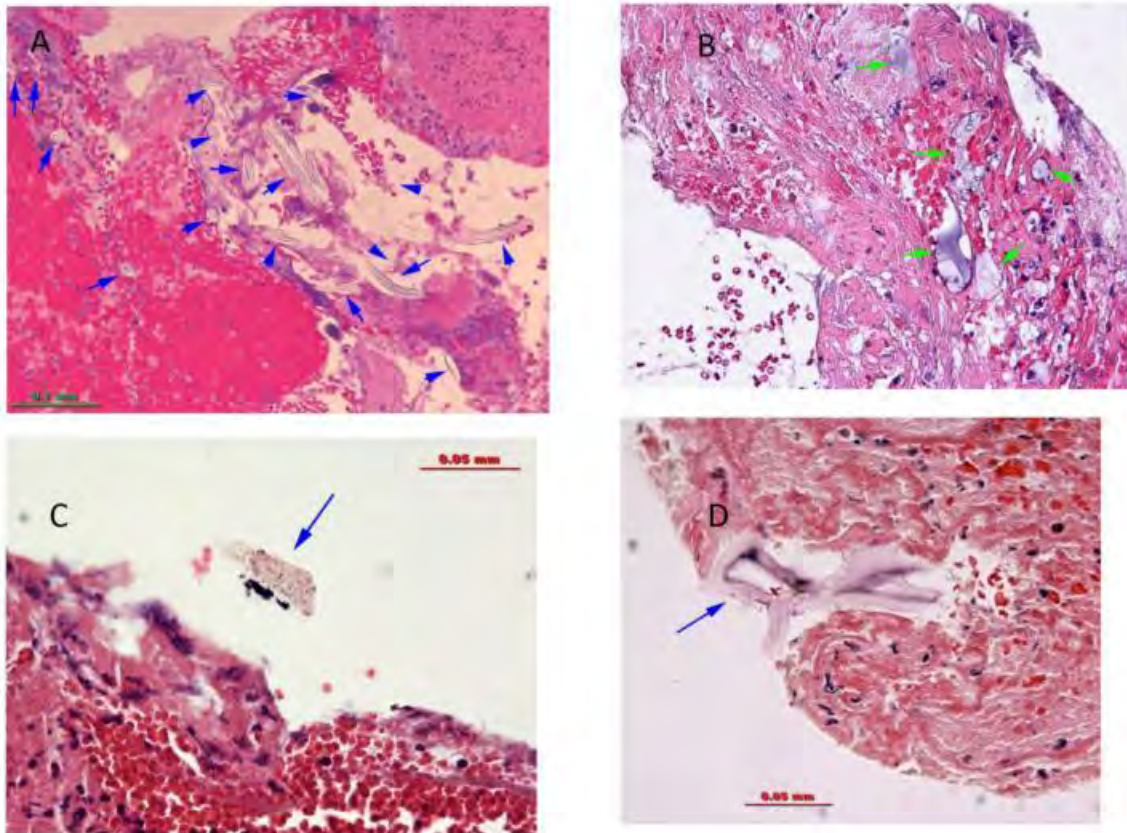


Figure 1, Microphotographs of different type of foreign material found in the retrieved thrombus tissue. A shows type I foreign material embedded within clot tissue. The material present as tubular, stripe and irregular piece in shape and light green in color (H&E, original magnification 200 x). B shows multiple, scattered pieces of type II foreign material (arrow) embedded within the clot tissue. The polymer presents as light /dark gray in color; they are thin or dense in texture. C shows one piece of irregular type III foreign material presents along the side of the clot tissue, it is associated with black pigment. D shows the worm-like homogenous Type IV foreign material found within the clot tissue, it is also covered with one layer of gray material that is similar as the seen in B (B-D, H&E, original magnification =400x)

Identification and Characterization of Leptomeningeal Metastases using SPINE, a web-based collaborative platform.

M Deol¹, M Palotai², A Morales-Pinzon², A Marciniak², G Bliault², A Jacobson², N Tran², X Li², A Thomas², J Guenette³, M Desalvo², C Guttman², R Huang²

¹Brigham and Women's Hospital, Brookline, MA, ²Brigham and Women's Hospital, Boston, MA, ³Brigham and Women's Hospital - Department of Radiology, Boston, MA

Purpose

Leptomeningeal metastases (LM) carry a poor prognosis. Existing scoring systems for LM tumor burden show variable reproducibility, limiting their utility for evaluation of treatment response. To improve reproducibility, we applied stringent operational criteria and procedures using SPINE, a novel web-based platform.

Materials and Methods

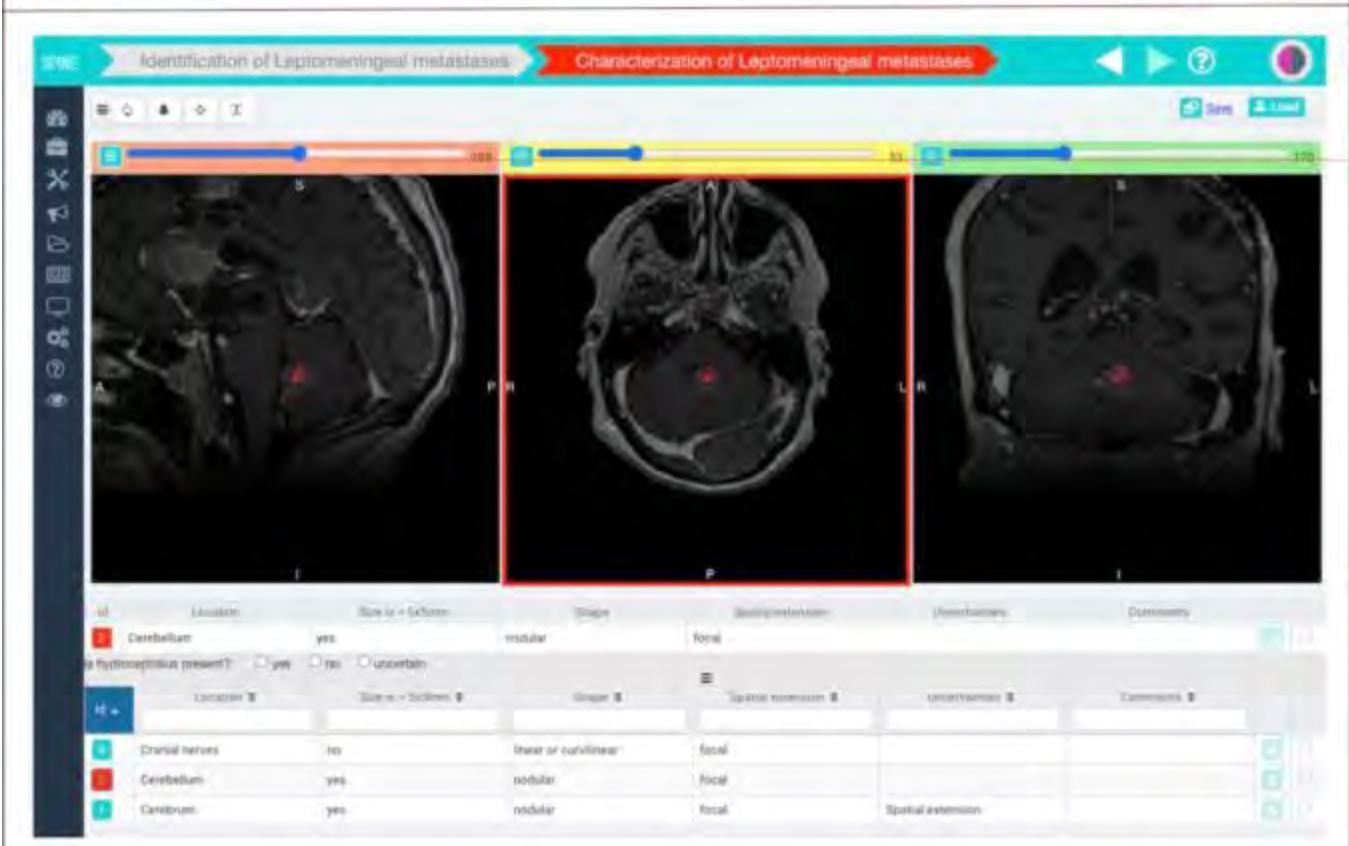
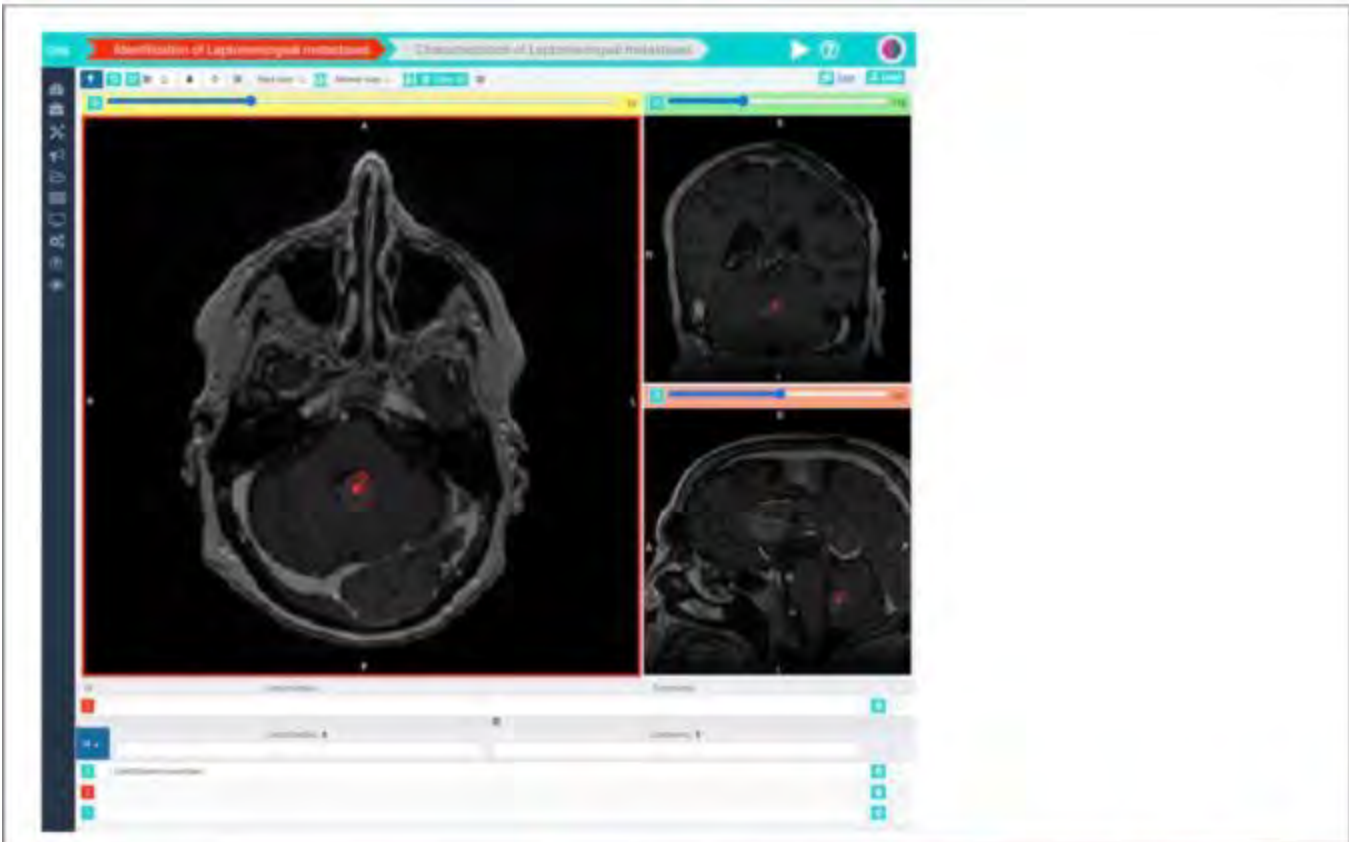
Stringent radiological definitions of LM and a customized interactive scoring system were implemented in SPINE (Structured Planning and Implementation of New Experiments). Five patients with brain LM and three patients with spine, but no brain, LM were selected. Prior to image analysis, test subjects completed a tutorial with definitions and pictorial examples of LM identification and characterization. Baseline post-contrast, T1-weighted, brain MRI for each patient was analyzed by three attending neuroradiologists, two neuroradiology fellows and two radiology residents. Raters were instructed to identify and characterize all LM based on: (1) location (cerebrum, cerebellum, brainstem, ventricle and/or cranial nerves); (2) shape (nodular and/or linear/curvilinear); (3) size (\geq or $<$ 5mm in two orthogonal diameters); (4) spatial extension (focal or diffuse). Inter-rater agreement and association of LM with patient survival were investigated.

Results

On average, 6.5 LM per case were detected. 49% of LM were cerebral and 41.2% were cerebellar. 86.6% of lesions were focal, 77.7% were nodular, and 66% were $<$ 5x5mm. Agreement on the total number of LM was higher between attendings (intra-class correlation (ICC)= 0.92) than fellows (ICC = 0.84) or residents (ICC = 0.73). Agreement on the number of LM with more prevalent characteristics (cerebral location, focal distribution, and size of $<$ 5x5 mm) was higher between attendings (ICC=0.85-0.94), than between fellows (ICC=0.36-0.8) or residents (ICC=0.21-0.53). Agreement on the number of nodular lesions was similar between attendings (ICC=0.8) and fellows (ICC=0.82). Agreement on ventricular, cranial nerve and nodular+linear LM was low even between attendings. The number of brainstem LM showed significant correlation with survival.

Conclusions

Structured education using SPINE may improve consistency in the reporting of LM and facilitate examination of treatment response. More extensive training through exemplification might further improve the performance of raters.



Identification (top) and Characterization (bottom) of Leptomeningeal Disease using SPINE, a web-based platform.

(Filename: TCT_125_ASNRfigure.JPG)

Identification of Critical Anatomic Variants of the Sphenoid Sinus Prior to Endoscopic Trans-sphenoidal Surgery

M Adin¹, E Schrickel², L Tu³, W Zucconi⁴

¹*Yale University, New Haven, CT*, ²*Yale University, new haven, CT*, ³*Yale School Of Medicine, New Haven, CT*, ⁴*Yale School of Medicine, New Haven, CT*

Purpose

To investigate the prevalence and key anatomical features of structures that have critical role in planning and performing transsphenoidal endoscopic skull base surgery.

Materials and Methods

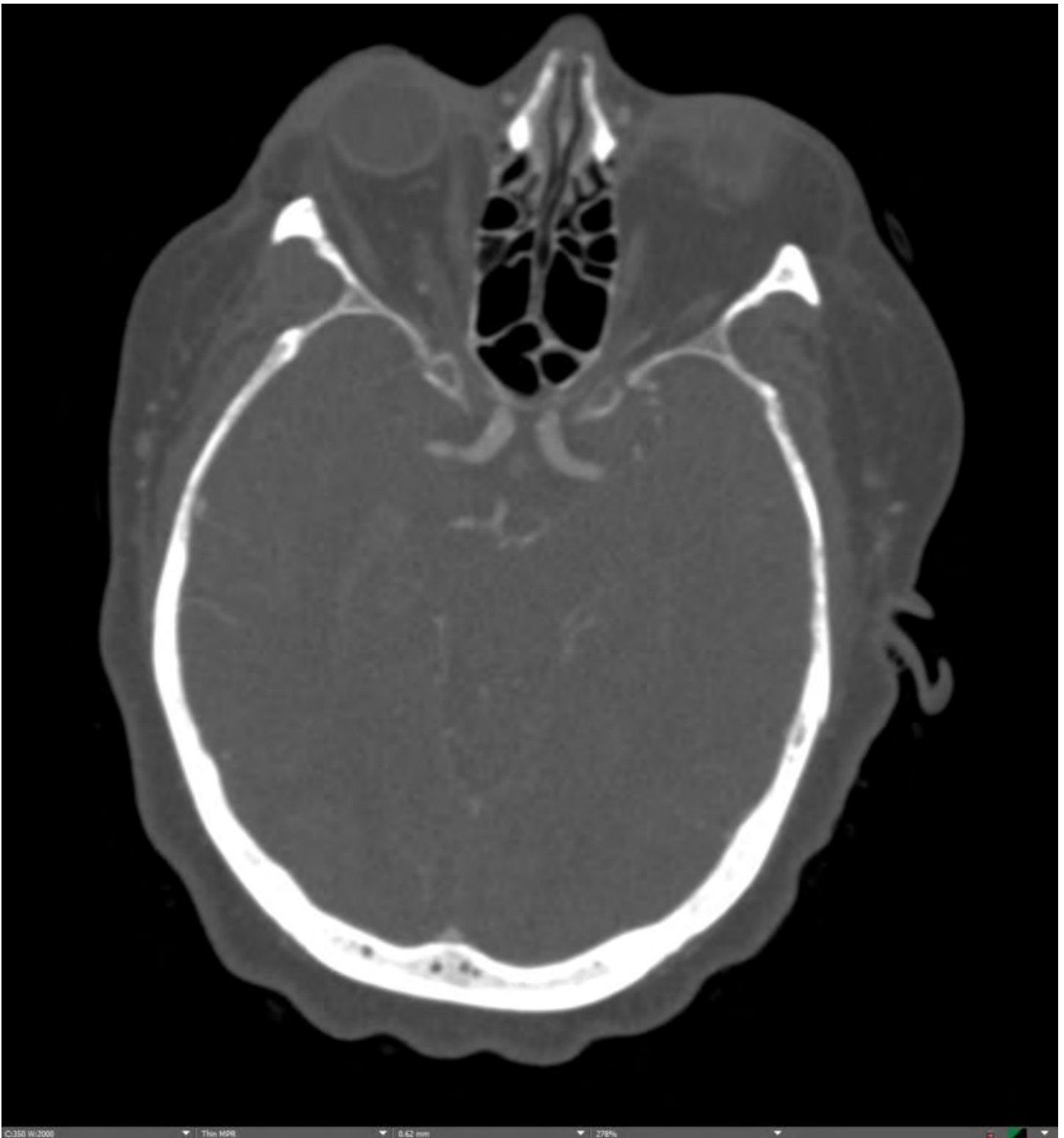
We reviewed CT images of 640 consecutive patients. Studies with artifactual degradations, space-occupying skull base lesions or prominent sinonasal pathologies, and those younger than 18-years- of age were excluded. 171 subjects included for further analysis of CT and CTA images.

Results

On CTA, average inter-carotid distance in surgical access room was 11 mm (range: 4-20). Sellar configuration was the most frequent pneumatization pattern of sphenoid sinus (58%), followed by postsellar (32%), presellar (9%) and conchal pneumatization (1%). 50% of sphenoid sinuses had single midline septum formation and showed lateral extension of pneumatization. 25% of subjects had Onodi cell and ACP pneumatization. Pneumatization of PCP was observed in 5% of subjects. Approximately 20% of ICAs were protruded into sphenoid sinus. In 3% of instances, there was no bony covering of ICA. 11% of optic nerves were protruded into sphenoid sinus. 5% of optic nerves had dehiscent bony covering. 4% had both protrusion and dehiscence.

Conclusions

Key anatomical features and relationship of skull base structures that have critical role in planning endoscopic transsphenoidal surgery were demonstrated. Intercarotid space is the main limiting factor of surgical access room and varies significantly, which makes presurgical vascular mapping critical.



(Filename: TCT_1556_intercarotid.jpg)

1390

Image Quality Analysis of Head CTs Obtained on a New Portable Scanner Compared to Stationary CT

M Kunst¹, J Small¹, M Smith¹, C Wald¹

¹Lahey Hospital and Medical Center, Burlington, MA

Purpose

The purpose of the study was to evaluate the image quality of a newly developed, recently FDA approved prototype portable CT scanner, compared to a fixed, standard of care (SOC) CT platform.

Materials and Methods

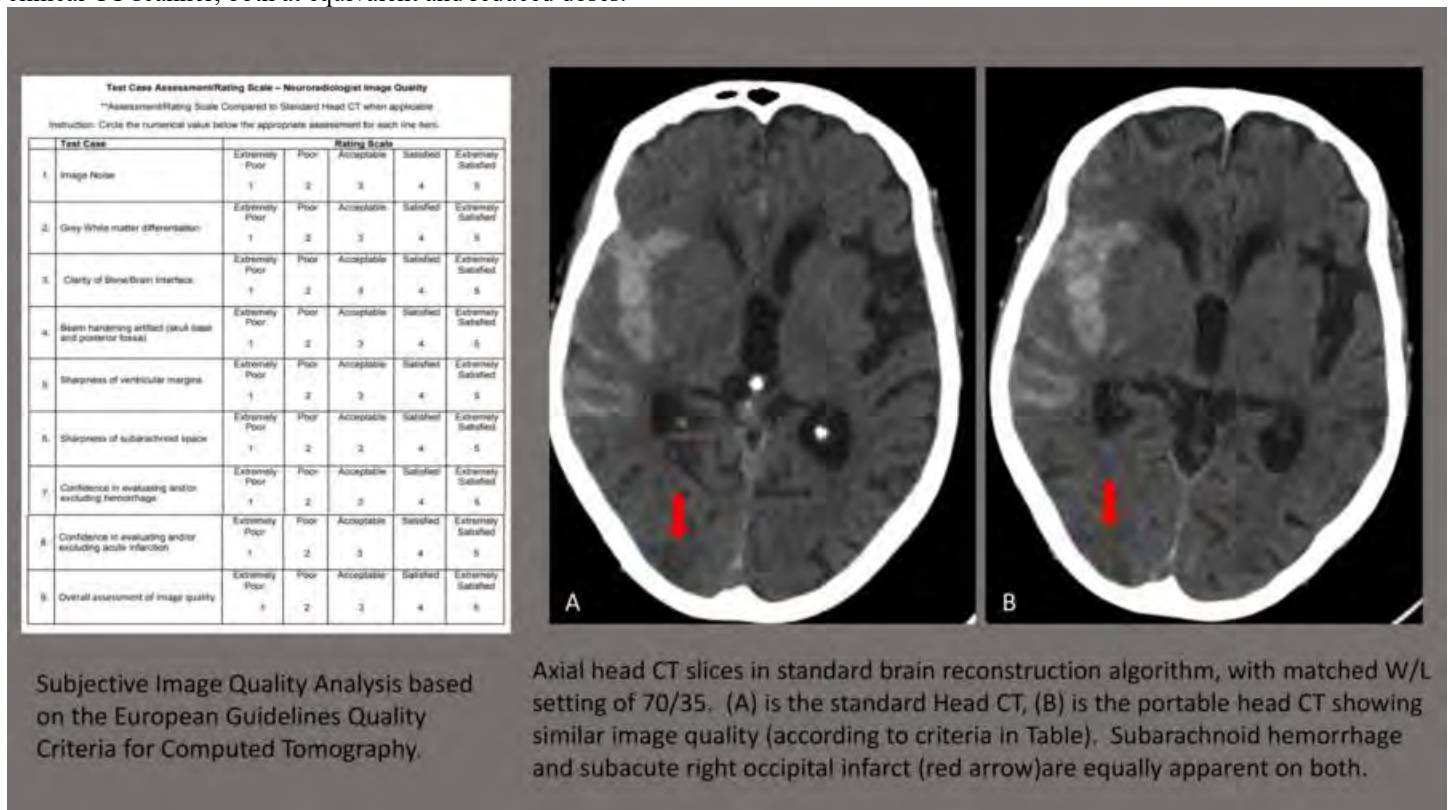
IRB approval was obtained. Inpatients (n=11), age > 60 requiring head CT evaluation were enrolled and consented to obtain an additional head CT on the portable CT, following their SOC exam on the stationary CT scanner. Following their SOC head CT on the stationary unit, the patient was transferred back to their bed or stretcher. The portable CT scanner was positioned at the head of the bed, and a second head CT was obtained. 10 patients provided written, informed consent, and 1 patient declining for concerns of additional radiation exposure. Overall 9 patients were able to complete the study. 1 patient felt ill following transfer back to her bed, and enrollment was terminated. 7 patients received 2 head CT exams with matched imaging technique, including kV 120, MA 327, CTDI 58.4 mGy. After there was sufficient confidence in portable head CT image quality, 2 patients received the portable head CT at a 20% reduced dose (CTDI 46.10 mGy). Spatial resolution was evaluated with the use of an ACR phantom. Subjective image quality analysis was performed independently by 3 CAQ certified Neuroradiologists evaluating 9 separate aspects of image quality, based on the European Guidelines quality Criteria for Computed Tomography (Table 1).

Results

Spatial resolution analysis demonstrated 7 lp/cm for the Standard head CT, and 8 lp/cm for the portable head CT. For the subjective image quality analysis, interreader agreement was high: on a Likert scale of 1-5, all assessment categories were rated 4 to 5 (satisfied to extremely satisfied), with an average score of 4.97 for overall assessment of image quality. Despite a slight increase in detectable image noise in the reduced dose exams, overall assessment of image quality remained high. For a maximum possible score of 45 per case, the average assessment score was 43, with a minimum score of 39 and a maximum score of 45. Individual reviewer comments identified difficulties with patient positioning of the portable CT scanner.

Conclusions

With proper patient positioning, the imaging quality of the newly developed portable scanner is comparable to that of a standard clinical CT scanner, both at equivalent and reduced doses.



(Filename: TCT_1390_ASNRAbstractFigure1.jpg)

709

Imaging and Survival Characteristics of Gliosarcoma Patients – the Largest Single-Institution Cohort Experience

A Amer¹, S Khose¹, H Alhasan¹, H Pokhylevych¹, G Fuller¹, N Chasen¹, J de Groot¹, J Johnson¹

¹The University of Texas MD Anderson Cancer Center, Houston, TX

Purpose

Gliosarcoma (GSM) is a variant of glioblastoma with sarcomatous features and lower 5-year survival rates. GSMs are divided into

primary (de novo) and secondary (arising from another glial neoplasm). In contrast to glioblastoma, there is limited literature regarding the relationship between GSM imaging characteristics and survival, so we sought to study this in the largest single-institution cohort in the literature.

Materials and Methods

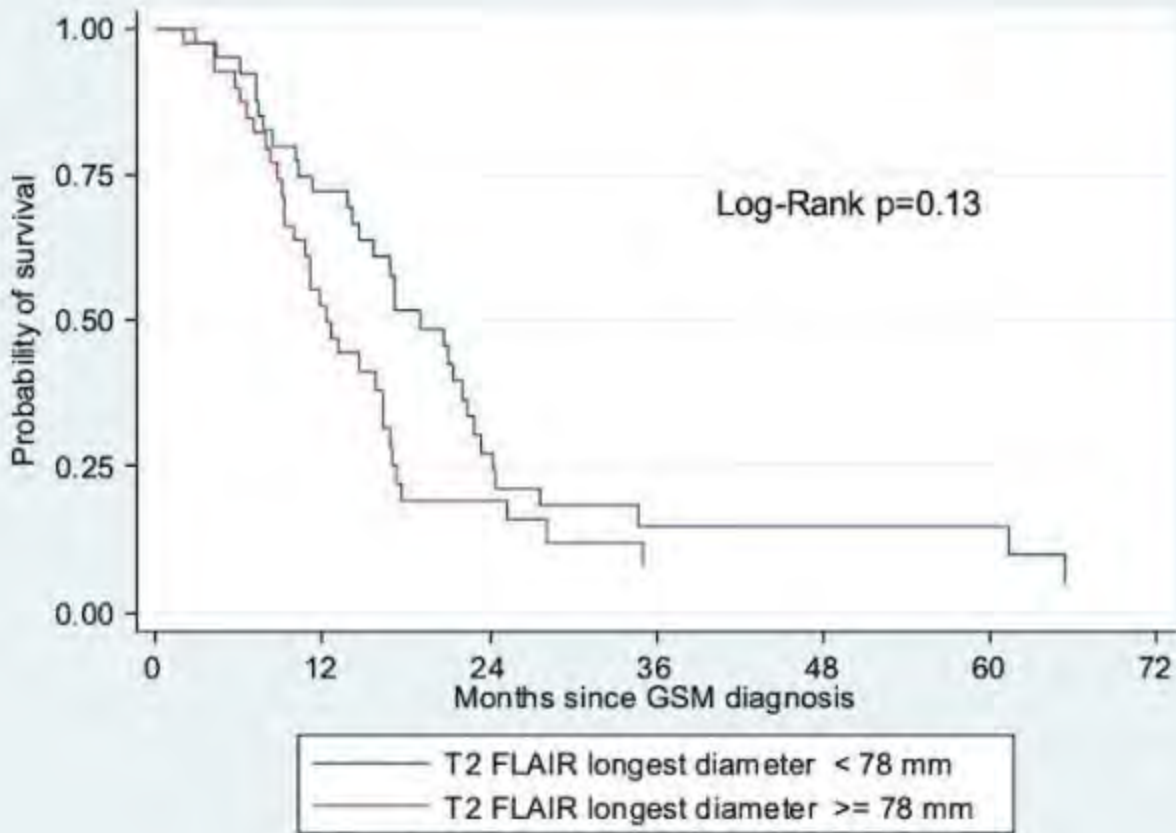
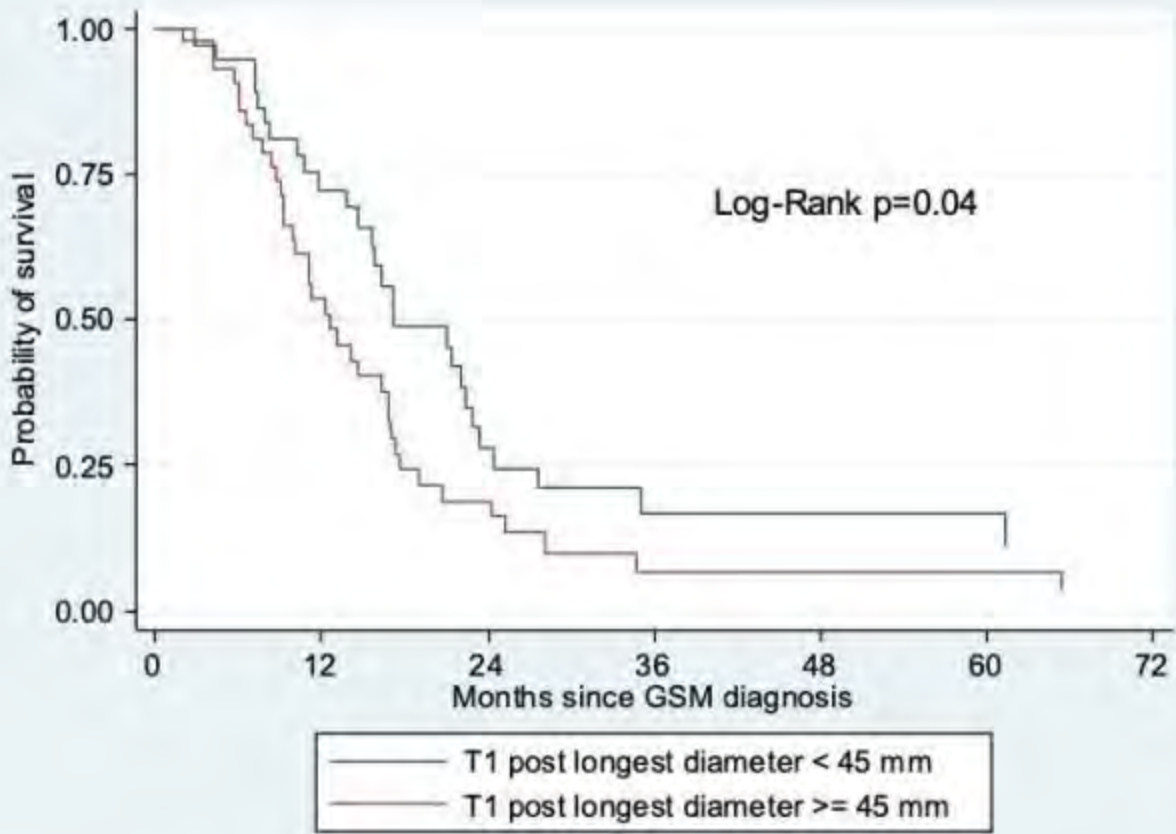
We identified patients presented at MD Anderson Cancer Center between 2004 and 2020 with a pathology-confirmed diagnosis of gliosarcoma, using retrospective review. Pre-treatment magnetic resonance imaging (MRI) characteristics, obtained from pre and post-contrast T1-weighted, axial T2-weighted, fluid-attenuated inversion recovery (FLAIR) and diffusion-weighted imaging (DWI), and their association with overall survival (OS) were studied using Kaplan-Meier survival estimates, log-rank tests and univariate Cox proportional hazards regression models. We defined OS from the date of pathological diagnosis of gliosarcoma. The size of the tumors, degree of enhancement, and the presence of restricted diffusivity were the primary study metrics.

Results

Of the 86 GSM patients, 60 (69.8%) were primary and 26 (30.2%) secondary GSM. The median age at initial diagnosis for all GSM patients was 58 years [IQR:50-65]. The majority of GSM tumors were located in the temporal lobe (43.0%), followed by the frontal (36.1%), parietal, and occipital lobes. The mean post-contrast longest T1 diameter was 44.9 ± 16.7 mm, while mean T2 FLAIR longest diameter was 41.6 ± 15.7 mm. On imaging 76.7% showed necrosis, 95.4% showed post-contrast enhancement and 34.9% showed restricted diffusion. The median overall survival (OS) from the pathological diagnosis of gliosarcoma for all patients was 15.7 months. Kaplan-Meier survival analysis showed significantly lower OS in those with larger enhancing volumes ≥ 45 mm (12.7 vs 17.2 months; log-rank $p=0.045$). Cox regression model also showed lower survival in those with larger enhancing volumes ≥ 45 mm [HR: 1.66 (1.01-2.73), $p=0.048$]. Those with higher total T2 FLAIR hyperintensity also experienced lower survival [HR: 1.02 (1.00- 1.03), $p=0.030$].

Conclusions

Our study is the largest single-institution evaluation of imaging characteristics of GSM and its relation with survival. Larger enhancing volumes and total T2 FLAIR hyperintensity are indicative of a poorer prognosis.



(Filename: TCT_709_ASNRGSMFigures.jpg)

Imaging Features of Spinal Cord Inflammatory Lesions in Children: Comparison between Anti-MOG Antibody Associated Disease, MS and Seronegative Monophasic Disease

C Alves¹, G Fadda², J Omahony³, D Castro⁴, E Yeh⁵, R Marrie⁶, D Arnold², A Bar-Or⁷, B Banwell⁸, A Vossough⁹

¹Children's Hospital of Philadelphia, Philadelphia, PA, ²Montreal Neurological Institute, McGill University, Montreal, QC, Canada, Montreal, CA, ³Children's Hospital of Philadelphia, Montreal, CA, ⁴Queen's University, Toronto, CA, ⁵University of Toronto, Toronto, CA, ⁶University of Manitoba, Winnipeg, MB, ⁷University of Pennsylvania, PHILADELPHIA, PA, ⁸The Children's Hospital of Philadelphia, PHILADELPHIA, PA, ⁹CHOP-UPENN, Philadelphia, PA

Purpose

To characterize the imaging features of spinal cord involvement in children with anti-MOG associated disease (MOGAD), multiple sclerosis (MS) and seronegative monophasic acquired demyelinating syndrome (monoADS), and assess their discriminative diagnostic utility.

Materials and Methods

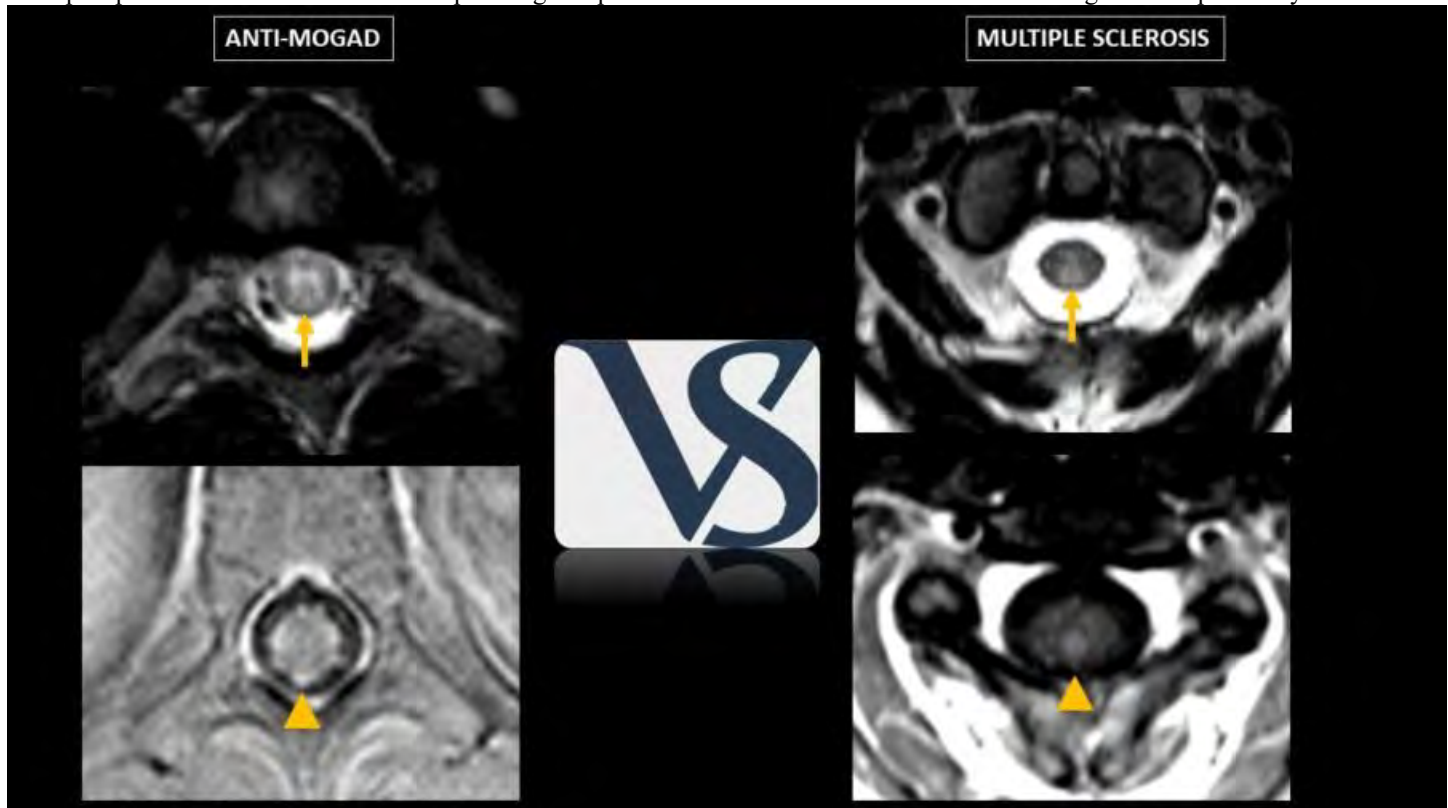
We analyzed spine MRI scans from 217 children and adolescents with ADS recruited in the prospective Canadian Pediatric Demyelinating Disease Study. Anti-MOG and anti-AQP4 antibody serology were assessed in archived serum samples obtained in proximity to clinical presentation. MRI scans were analyzed through a standardized scoring tool, blinded to brain MRI findings and clinical diagnosis. The imaging features were compared between MOGAD, MS and monoADS using descriptive statistics. AQP4-positive children were too few for meaningful inclusion.

Results

Spinal cord lesions were detected in 107/217 (49%) children (40/107 with MOGAD [37%], 21/107 MS [20%], and 46/107 with monoADS [43%]). The median age at first scan with lesions was 10.6 years (IQR 5.6-13.0). Lesions restricted to spinal cord white matter were found in 2/35 (6%) children with MOGAD, vs 13/19 (68%) with MS ($p < 0.0001$) and 6/43 (14%) with monoADS ($p = 0.28$). Axial gray matter T2-hyperintensity ("H-sign") was observed in 22/35 (63%) children with MOGAD, 14/43 (33%) with monoADS ($p = 0.015$), and in none of the participants with MS ($p < 0.0001$). Longitudinally extensive lesions (>3 segments) were common among children with MOGAD (30/40, 75%), rare in MS (1/21, 5%, $p < 0.0001$), and observed in 27/46 (59%) children with monoADS ($p = 0.096$). The presence of spinal leptomeningeal enhancement was highly suggestive for MOGAD (23/32 [75%], vs 0/15 MS and 7/38 [18%] monoADS, both $p < 0.0001$).

Conclusions

Multiple spinal cord MRI features can help distinguish pediatric MOGAD from MS and other seronegative idiopathic myelitis.



(Filename: TCT_867_ASNR_2021300.jpg)

Imaging of malignant brain tumors using hybrid 18F-Fluoro-Ethyl-Tyrosine PET MRI, integration into standard clinical care at a single US institution

W Scales¹, W Territo¹, J Sims¹, M Tann¹, V Aaron¹, A KAMER², M Green¹, G Hutchins¹, B Graner³, M Veronesi¹

¹Indiana University School of Medicine, Indianapolis, IN, ²INDIANA UNIVERSITY SCHOOL OF MEDICINE, INDIANAPOLIS, IN, ³Indiana University, Indianapolis, IN

Purpose

Preliminary results are presented from a single U.S. institution on the impact of integrating hybrid 18F-Fluoro-ethyl tyrosine (FET) PET/MR imaging into the clinical workflow for assessment of treated malignant brain tumors.

Materials and Methods

FET PET is clinically scarce in the U.S. despite evidence for its superiority and standardized international recommendations for its use (EANO/RANO). Perfusion MRI combined with FET PET has shown increased sensitivity and specificity for delineating progression of disease (POD) from treatment related change (TRC) for malignant brain tumors, with hybrid imaging further increasing specificity (1,2,3). This project provides a rationale for clinical use of hybrid FET PET/MRI in the U.S. to discern POD from TRC in malignant brain tumors, including high grade gliomas (HGG) and brain metastases (BM).

Results

27 lesions in 20 patients with HGG or BM underwent hybrid FET PET/MR + MR perfusion brain imaging on a Siemens 3T Biograph mMR PET/MRI unit. Quantitative assessment included rCBV, Ktrans, and Ve for MR perfusion, and static (TBRmax and TBRmean) and dynamic (time-to-peak (TTP) and slope) metrics for FET PET. Institutional DCE cutoffs were used for POD versus TRC, with literature based rCBV and FET cutoffs (1-4). A blinded 5-point Likert scale of TRC versus POD was employed by 3 neuroradiologists and 3 nuclear medicine physicians for interpretation. Seven lesions met all three FET cutoff values for POD (Table 1). FET and MR perfusion were most concordant in HGG (100% for TBRmax and rCBV). Susceptibility limited rCBV performance in BM, which also demonstrated poor Ktrans and FET concordance (46%). Likert ratings showed higher confidence for HGG compared to BM, with nuclear medicine physicians reporting increased diagnostic certainty overall. Pathologic, radiographic and/or clinical evidence consistent with POD was obtained in 5 HGG and 3 BM lesions during the three-month patient acquisition period. TBRmax and rCBV were 100% sensitive for POD (Table 2). The study population will be further monitored over the next five months to determine final specificity and accuracy based on receiver operator characteristics (ROC) analysis.

Conclusions

Reliable assessment of malignant brain tumor treatment response is limited with current imaging options in the US. This project outlines the hybrid FET PET/MR imaging protocol at our institution with preliminary data indicating improved sensitivity, specificity, and contribution to reader confidence over single modality imaging.

Table 1.

	HGG	MET	Total
Total Lesions	10	17	27
TBRmax > 2.5	6	5	11
TBRmean > 2.0	7	5	12
Slope (SUV/hr) < 0	6	3	9
All Three Criteria	5	2	7

Table 1: Five HGG and two MET lesions met all three FET progression criteria of TBRmax > 2.5, TBRmean > 2.0 and a negative dynamic slope over the last 20 minutes of acquisition.

Table 2.

	Sensitivity HGG	Sensitivity MET	Sensitivity Total
rCBV	100%	100%	100%
Ktrans	80%	100%	88%
TBRmax	100%	100%	100%
TBRmean	100%	67%	88%
FET Slope	80%	67%	75%

Table 2: Preliminary sensitivity data for 5 HGG and 3 MET lesions which demonstrated POD during the 3-month patient acquisition period.

(Filename: TCT_647_Tables.jpg)

323

Imaging of sinonasal malignant tumors : keys for diagnostic orientation.

E TALAB¹, S AMMARI², F Benoudiba³, A Moya-Plana⁴

¹GUSTAVE ROUSSY CANCER CAMPUS, Villejuif, France, ²GUSTAVE ROUSSY CANCER CAMPUS, villejuif, FRANCE, ³CHU de Bicêtre, Le Kremlin-Bicêtre, Val de Marne, ⁴GUSTAVE ROUSSY CANCER CAMPUS, Villejuif, Val de Marne

Purpose

I) Introduction II) Anatomy of sinonasal tract III) Frequent clinical presentations of malignant sinonasal tumors IV) Imaging role 1) Diagnosis 2) Extensions and therapeutic implications V) CT and MRI imaging features of the most common histological subtypes 1) Squamous cell carcinoma 2) Adenocarcinoma 3) Adenoid cystic carcinoma 4) Olfactory Neuroblastoma 5) Malignant Melanoma 6) Sarcomas 7) Lymphomas 8) Extramedullary Plasmocytoma VI) Conclusion

Materials and Methods

Sinonasal malignant tumors are rare (approximately 3% of head and neck tumours). They have a poor prognosis due to the advanced disease at diagnosis. Initial symptoms are similar to those found in sinonasal inflammatory pathologies, which represent the vast majority of sinus pathologies, both neglected by patients and doctors. When more alarming clinical signs lead to endoscopy and imaging, the tumor is often locally advanced. The complex anatomy of the sinonasal tract, and the rare occurrence of these neoplasms with several histology types, make these pathologies poorly known by the radiologist. Although only histopathologic examination can provide the correct diagnosis, these malignancies seem to have imaging features that can help predict the histological subtype. The rarity of these tumors makes it difficult to identify recurrent imaging features outside of specialized centers. Gustave Roussy Institute is a reference center for the treatment of these tumors, which has enabled us to analyze a number of clinical, anatomopathological and imaging data in order to identify imaging features that would help us to predict the histology of these tumors.

Results

We reviewed 360 files of patients treated in the Gustave Roussy Institute for sinonasal cancer from 1999 to 2020. Among these, we included 150 patients for whom histology was confirmed and initial pre-therapeutic imaging was available. We analyzed clinical data and characteristics of sinus lesions on CT and MRI scans.

Conclusions

The data collected allowed us to highlight certain MRI and CT imaging characteristics of the different sinonasal tumors. These results are intended to provide a didactic basis for the histological diagnosis orientation, through the analysis of a rare series of the main sinonasal tumors.

1352

Imaging Paraneoplastic /Autoimmune Neurological Syndromes: Lessons learnt from multidisciplinary case based whole body MRI PET at tertiary Neuropsychiatry center.

S Vankayalapati¹, S M², C Nagaraj³

¹National institute of Mental health and Neurosciences, Bengaluru, Karnataka, ²National Institute of Mental health and Neurosciences, Bengaluru, Karnataka, ³National Institute of Mental Health and Neurosciences, Bengaluru, Karnataka

Purpose

Autoimmune encephalitis (AIE) and Paraneoplastic neurological syndromes (PNS) are interchangeably used terms and are a heterogeneous collection of autoimmune central nervous system manifestations that may be or may not be associated with cancer. They may present in varied forms clinically eg :Classical type Encephalomyelitis, Limbic encephalitis, Subacute cerebellar degeneration or Nonclassical type include- Brainstem encephalitis, Acute sensorimotor neuropathy, Myasthenia gravis etc As many of these syndromes are seen before a tumour is clinically detected and is an early stage phenomenon an early detection makes this entity a potentially curable disease. During imaging for AIE the underlying tumour may be occult and hence a thorough study of multimodal multiparametric imaging is important and the whole body protocols are planned with knowledge of the commonly encountered paraneoplastic processes. Aims: Retrospective case based study of the usefulness of whole body MRI PET in workup of seropositive PNS in detecting the potential cause.

Materials and Methods

As per institute ethics retrospective study of clinical cases is approved. We present the retrospective review over 48 months with clinical indication and whole body imaging of MRI PET cases of neuropsychiatric patients with AIE/PNS, per consensus criteria, treated at a single tertiary center.

Results

112 suspected of having PNS underwent MRPET. Serum anti-neuronal antibodies were present in 38.2% of patients and plasma membrane protein antibody positivity in 67.8%. 35/112 (31.25%) were abnormal and suspicious of malignancy with abnormal PET. The prevalence of abnormal PET in patients presenting with classical PNS was 74.1% as opposed to 25.8% in patients with non-classical PNS. In most cases of paraneoplastic limbic encephalitis (55.3%), 18 F-FDG PET showed hypermetabolism in the temporal lobes. MRI PET demonstrated an abnormal uptake in 35 patients. The abnormal areas included the mediastinum (16 cases), lung (7 cases), breast (4 cases), gonads (2 cases), parotid gland (1 case), or the cervical, supraclavicular or axillary lymph nodes (5 cases).

Conclusions

Whole-body imaging with MR PET has an important role in workup of detecting occult malignancy in cases of suspected paraneoplastic neurological syndromes/AIE. Selection of the appropriate protocol for imaging is important in these cases, especially when history and physical examination are nonspecific.

1551

Impact of collateral flow status on cost-effectiveness of Endovascular Thrombectomy in patients with Acute large vessel occlusion

A Malhotra¹, M Khunte², X Wu³, S Payabvash²

Purpose

PURPOSE To determine the impact of collateral status on cost-effectiveness of endovascular thrombectomy (EVT) versus no-EVT in patients with acute large vessel occlusion stroke.

Materials and Methods

A decision-analytic study was performed with Markov modeling to estimate the lifetime quality-adjusted life years (QALY) and associated costs of EVT-treated patients compared to no-EVT in patients with good, moderate and poor collaterals. The study was performed over a lifetime horizon with a societal perspective in the United States setting. The Markov model incorporated the clinical course since the time of BAO, including acute hospitalization, long-term disability with possible rehabilitation, and recurrent stroke. Base case, one-way, two-way, and probabilistic sensitivity analyses were performed.

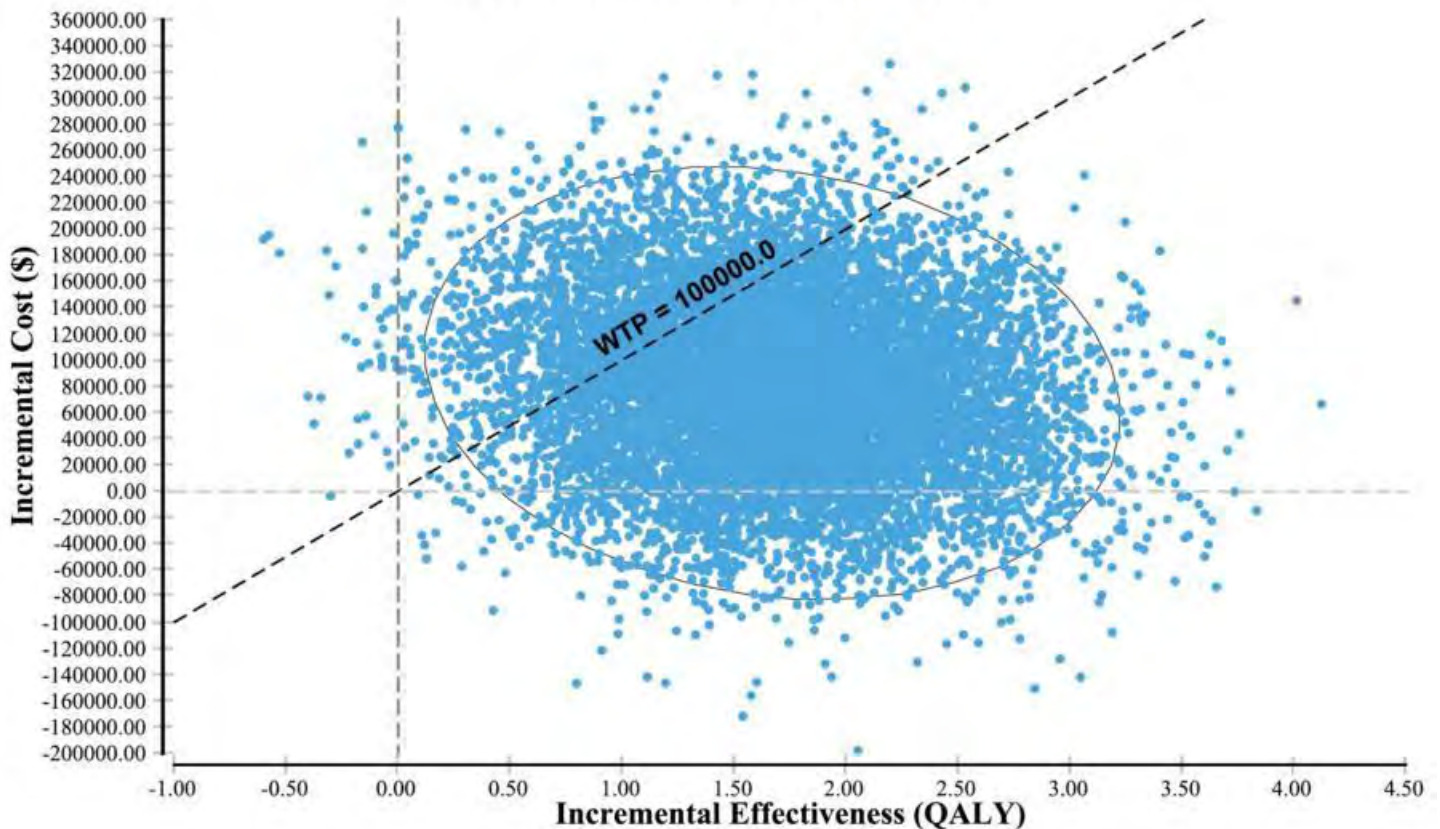
Results

EVT was the long-term cost-effective strategy in 81.03% of the iterations in the probabilistic sensitivity analysis. In patients with poor collaterals, EVT resulted in difference in health benefit of 1.68 QALYs in the 65-years age groups, equivalent to 613 days in perfect health. The ICER was \$49,217/QALY, which is below the \$100,000/QALY WTP threshold indicating that EVT is cost-effective. Varying outcomes after both strategies shows EVT to be more cost-effective when the probability of good outcome after EVT was only 4 to 6% higher relative to no-EVT in patients with poor collaterals. EVT remained cost-effective even when its cost exceeded \$100,000 (threshold was \$120,018). EVT was even more cost-effective for 55-year old compared to 65-year old patients.

Conclusions

Our study suggests EVT to be cost-effective for treatment of acute LVO irrespective of collateral status. Even in patients with poor collateral status, improved outcomes after thrombectomy lead to its cost-effectiveness over the long-term.

Probabilistic Sensitivity Analysis



(Filename: TCT_1551_PSA.jpg)

1306

Impact of Forcing Function Reporting on the Detection of Incidental Findings on Lumbar Spine MRIs.

E Obusez¹, A Wetzel², C Ilkanich¹, P RUGGIERI³, J Bullen¹, D Lockwood¹

¹Cleveland Clinic, Cleveland, OH, ²Cleveland Clinic, Cleveland, OH, ³CLEVELAND CLINIC FOUNDATION, Aurora, OH

Purpose

Extraspinal incidental findings (IFs) on magnetic resonance imaging (MRI) of the lumbar spine are common, with reportedly high non-detection rates. While majority are benign, there is significant prevalence and non-detection rate of potentially important clinical findings. The aim of this study was to determine if we could increase the detection rates of IFs in extraspinal soft tissues by using a forcing function pick list in our standardized structured lumbar MRI reporting template.

Materials and Methods

In this prospective, two-phase controlled study, we reviewed all lumbar MRI examinations reported by 12 neuroradiologists between February 2020 and April 2020. In the control group, all lumbar MRIs included in the study were first reported using our standardized structured reporting template. Subsequently, in the study group, a forcing function was introduced into extra-spinal findings pick list in the reporting template and then reported by the neuroradiologists. The IF detection rates were compared between both groups, including findings categorized by clinical impact. The Wilcoxon rank sum test and Fisher's exact test were used. A significance level of 0.05 was used for all tests.

Results

A total of 1014 MRIs of the lumbar spine were reported by the 12 neuroradiologists. Five-hundred and eighteen of 1014 (51%) reports contained at least one IF, accounting for a total of 707 IFs and an overall detection rate of 0.70 findings per study. The control group included a total of 629 lumbar MRIs and the study group included a total of 385 lumbar MRIs. The overall IF detection rate in the study group increased by 16.3% when compared to the control group, $p=0.019$. Additionally, the percentage of examinations detecting at least one IF increased from 48% to 56%, $p=0.012$. For high impact clinical findings, we observed an 89% increase in detection from 2.1% to 3.9% of examinations, ($p=0.113$).

Conclusions

Incorporating a forcing function into the pick list for extra-spinal findings within our structured reporting template increased the overall IF detection rates. Our results appear to show the use of a forcing function into structured reporting may improve detection of IFs in MRIs of the lumbar spine. The findings in this study may support the incorporation of a forcing function into structured reporting templates to improve the detection of IFs, which may ultimately contribute to improved patient care as a result of earlier detection of various pathologies. A larger prospective study may be warranted.

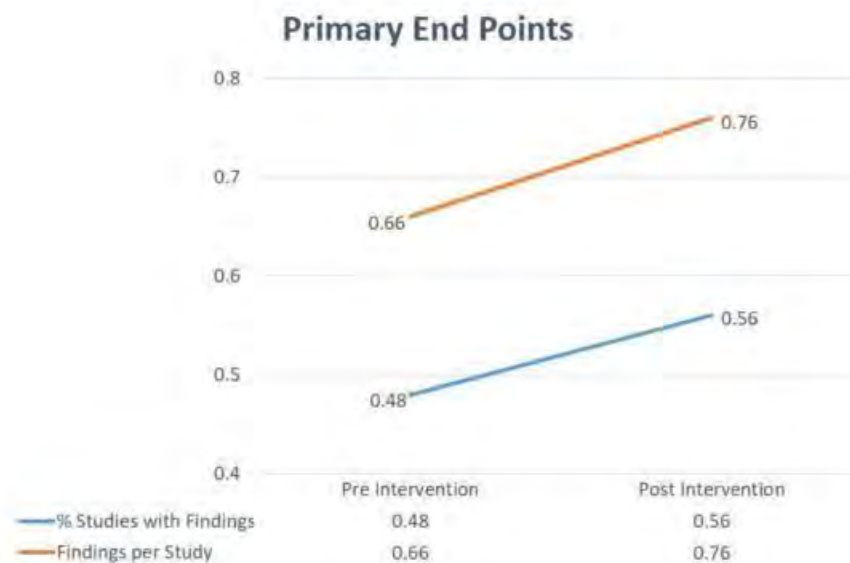


Figure: Shows increase in both the number of findings per study and percentage of studies with findings after incorporation of the forcing function.

(Filename: TCT_1306_ANSRFigurex.jpg)

1517

Impact of Gantry Angle on Metal Artifacts in Lumbar Spinal Fusion Hardware.

P Batchala¹, J Donahue¹, S Patel¹, J Patrie², S Mukherjee¹, T Eluvathingal Muttikkal¹

¹University of Virginia Health System, Charlottesville, VA, ²University of Virginia, Charlottesville, VA

Purpose

Artifact from the spinal fusion hardware on CT lumbar spine imaging impairs image quality and can obscure clinically important complications related to hardware malposition, fracture, and loosening. The aim of our study was to identify patient factors and modifiable technical factors affecting the degree of hardware-related artifact on CT lumbar spine imaging.

Materials and Methods

Twenty-five consecutive patients who had lumbar posterior spinal instrumented fusion with vertical rods and pedicle screws were included in the study. Hardware artifact was graded on a three-point scale (Table 1) at each pedicle screw level. Univariate and multivariate analyses determined the relationship between technical and patient factors such as Water-Equivalent Diameter (Dw), Effective Diameter (Deff), Body Mass Index (BMI), Effective tube current-time product (Eff.mAs), pedicle screw-gantry angle (SGA), location of pedicle screw, age, and gender with the severity of metal artifact.

Results

Twenty-five patients included 8 males and 17 females (age range 30 to 78y). SGA ($p<0.001$), Eff.mAs ($p=0.009$) and Dw ($p=0.001$) were significantly associated with metal artifact severity. Higher SGA was associated with lesser severity of pedicle screw metal artifact.

Conclusions

Pedicle screw-gantry angle is a novel modifiable technical factor that can be utilized to reduce metal artifact and improve the diagnostic yield of lumbar spine CT in the post-operative setting.

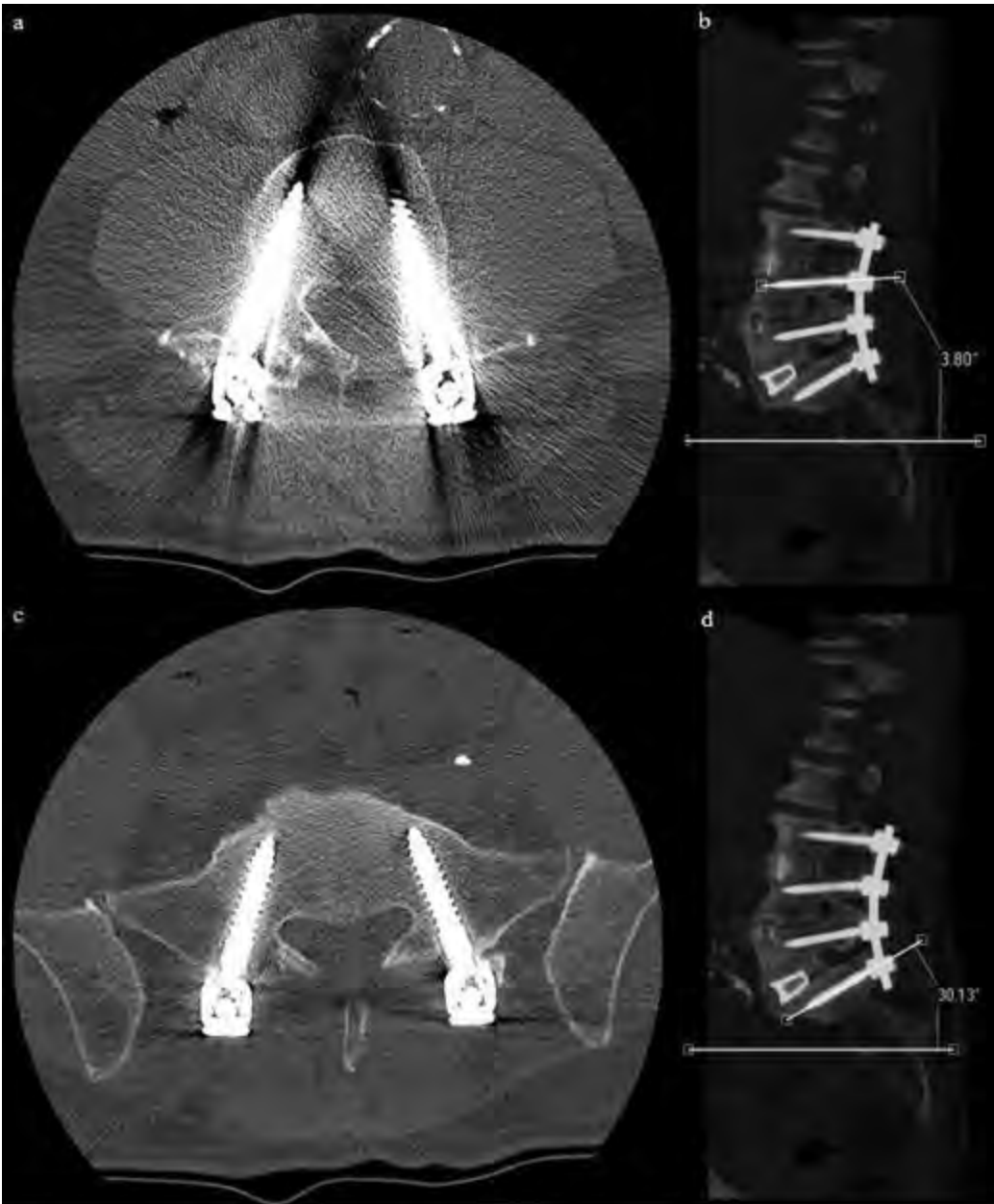


Fig 1. Lumbar CT of 58 year old male patient with posterior spinal instrumented fusion at L3-S1 level

- a) Axial image shows severe artifact from pedicle screws at L4 level obscuring medial bony margin of lateral recess on the left, and lateral bony margin of the pedicle on the right.
- b) Sagittal reformat shows narrow SGA between the pedicle screw and gantry at L4 level.
- c) Reformat through the plane of screws at S1 level with clear depiction of the individual threads of the screws due to decreased artifact from higher SGA.
- d) Sagittal reformat shows increased SGA between the pedicle screw and gantry at S1 level compared to L4 level.

Table 1: Grading of metal artifact severity.

MMK	Threads of the pedicle screw are visible individually.
Moderate	Artifact is present on the medial and/or the lateral edge of pedicle. The edges of the pedicle are visible through the artifact.
Severe	Artifact obscures the medial and/or the lateral edge of pedicle

(Filename: TCT_1517_Fig_1.jpg)

Implications of ADD/ADHD Diagnosis for fMRI-Driven Treatment of Patients with Chronic Post-Concussion Symptoms

J Loewen¹

¹*Cognitive FX, Provo, UT*

Purpose

Concussion, or mild traumatic brain injury (mTBI), can alter neurovascular coupling dynamics, which have been associated to the development to chronic post-concussion symptoms (PCS) in certain individuals¹. Many patients with PCS may also meet the criteria for attention or hyperactivity disorders, such as Attention Deficit (Hyperactivity) Disorder (ADD/ADHD)². ADD/ADHD can mimic PCS symptomology and can serve as a predictor of protracted recovery and/or a potential modifier of performance on neurocognitive testing^{2,3,4}. However, what implications the diagnosis of ADD/ADHD may have for the evaluation and treatment of individuals with PCS is under-researched. Our clinic has demonstrated the use of task-based functional MRI (fMRI) to detect dysfunction in neurovascular coupling (NVC) to successfully inform individualized treatment and observe objective within-subject treatment outcomes^{1,5}. Specifically, data from task-based fMRI is analyzed to provide a Severity Index Score (SIS) and five unique "biomarkers", which reveal overall and system-specific dysregulation of NVC pre- and post-fMRI-targeted treatment for PCS^{1,5}. Thus, we sought to investigate the neurophysiological implications of a diagnosis of ADD/ADHD for patients that completed fMRI-based rehabilitation for post-concussion symptoms.

Materials and Methods

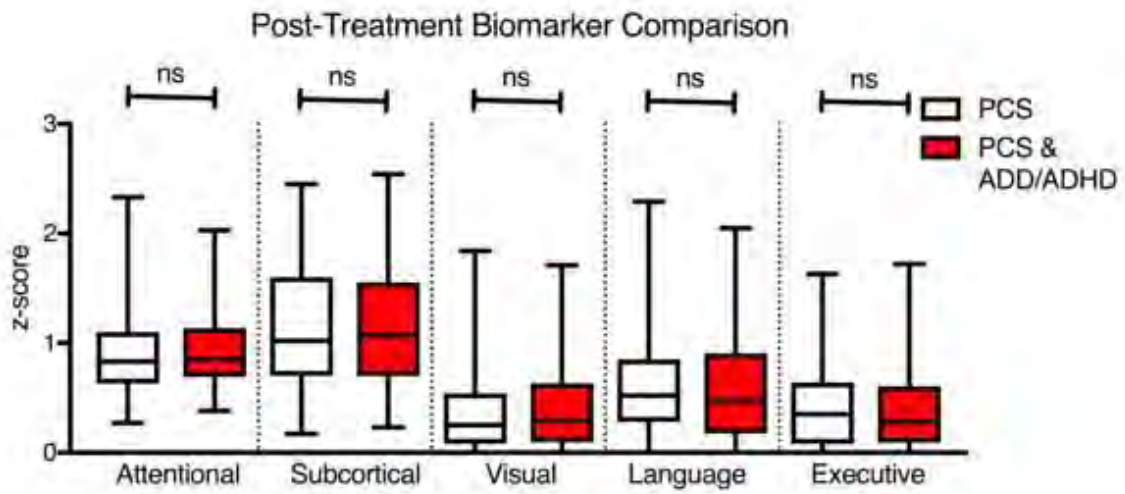
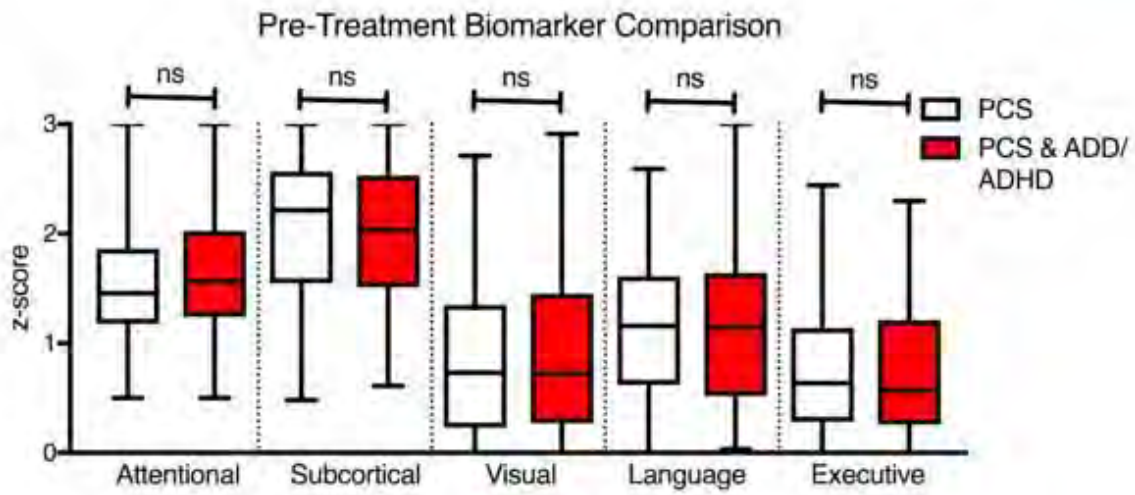
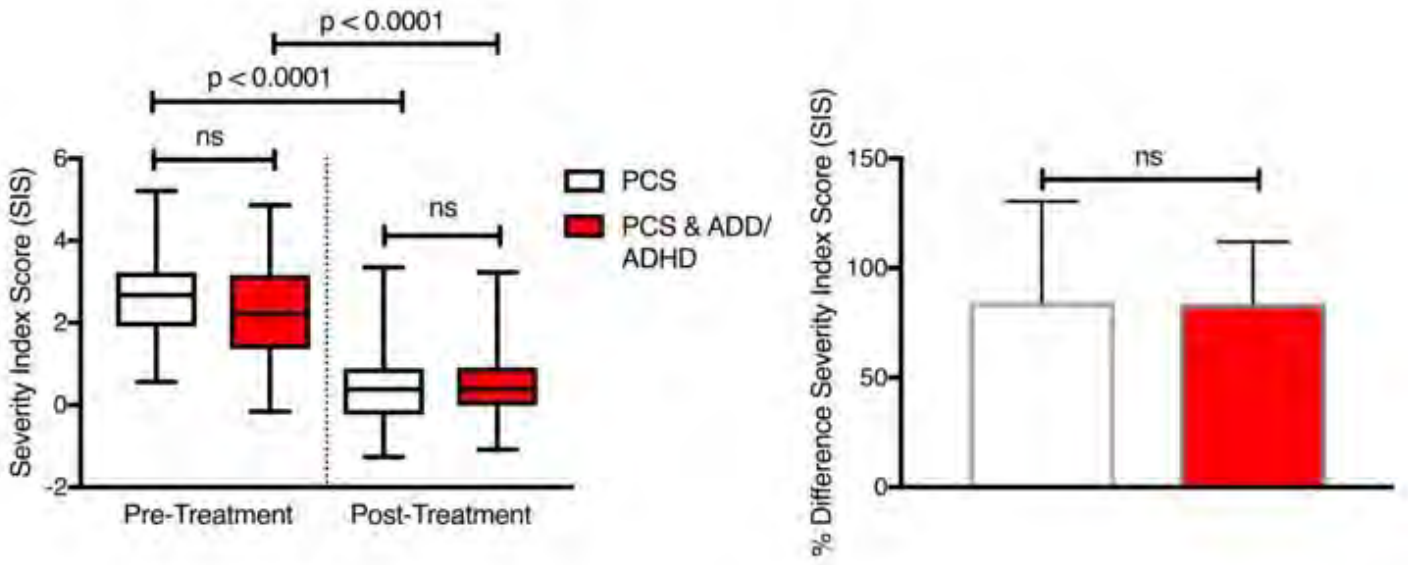
Utilizing methods as published in^{1,5}, we evaluated whether a diagnosis of ADD/ADHD in data collected from 345 male and female PCS patients correlated with 1) increased severity of neurovascular coupling dysfunction in attentional, subcortical, visual, language, and executive biomarkers, 2) increased overall NVC dysfunction and/or reduced treatment outcomes as measured by pre- and post-treatment SIS. Student's t tests were implemented to compare groups. $P < 0.05$ was considered significant.

Results

Our results show reported ADD/ADHD diagnosis was neither correlated with more severe NVC dysregulation nor reduced treatment outcomes. No effect was detected for gender, age, or number of concussions. The results of this study were subject to limitations, including dependence on self-reported ADD/ADHD or review of medical charts.

Conclusions

Additional research will be needed to determine the interaction of ADD/ADHD diagnosis pre- or post-mTBI and medication status. Nonetheless, these results provide promising indications that treatment for post-concussion symptoms in individuals with ADD/ADHD can be reliably and effectively based on task-based functional imaging.



(Filename: TCT_1079_addadhd.jpg)

Improved diagnostic performance from susceptibility-weighted imaging with compressed sensing and neuromelanin-sensitive magnetic resonance imaging for Parkinson disease

D Lee¹, C Suh², M Kim³, S Kim²

¹Asan Medical Center, Seoul, Korea, Republic of, ²Asan Medical Center, Seoul, Seoul, ³Asan Medical Center, Seoul, RI

Purpose

To verify the diagnostic performance of the loss of nigrosome 1 on the susceptibility-weighted imaging (SWI) with compressed sensing (CS) and the volume loss of neuromelanin on the neuromelanin-sensitive MRI (NM-MRI) on the diagnosis of Parkinson disease (PD).

Materials and Methods

One hundred forty-one patients who underwent the magnetic resonance (MR) imaging, including SWI with or without compressed sensing (CS) and NM-MRI between October 2019 and February 2020, were retrospectively reviewed. Two neuroradiologists visually assessed loss of nigrosome 1 on SWI and the volume loss of neuromelanin on the NM-MRI. All the MR imaging was obtained according to the standard axial plane. The result of F-18 FP-CIT positron emission tomography was set as the reference standard. The diagnostic performance of both imaging findings was evaluated by the area under the curve (AUC) of the receiver operating characteristic curve (ROC). Inter- and intra-reader agreement was assessed with κ statistics.

Results

The total study population was 141 patients (mean age \pm SD, 68.8 \pm 9.5 years; 68 females and 73 males). When CS was applied for the nigrosome 1 imaging on SWI, the nondiagnostic scan was significantly lowered from 18.2% (10 of 55) to 4.4% (3 of 68) ($P = 0.018$). Diagnosis of PD based on the loss of nigrosome 1 on the SWI turned out to be excellent (AUC 0.876, 95% CI=0.800-0.931) with the substantial inter-reader agreement ($\kappa = 0.824$). Diagnosis of PD based on the NM-MRI turned out to be excellent (AUC 0.941, 95% CI=0.883-0.976) with substantial inter-reader agreement ($\kappa = 0.656$). Similarly, the diagnosis of primary parkinsonism based on the loss of nigrosome 1 on the SWI showed good diagnostic value (AUC 0.879, 95% CI=0.808 -0.930) with perfect inter-reader agreement ($\kappa = 0.840$). Diagnosis of primary parkinsonism based on the NM-MRI turned out to be excellent (AUC 0.937, 95% CI=0.883-0.971) with substantial inter-reader agreement ($\kappa = 0.669$). Moreover, applying CS on SWI tends to improve the diagnostic performance of each readers.

Conclusions

CS may add the value of diagnostic capability of nigrosome 1 on SWI, to reduce the nondiagnostic scan. Furthermore, loss of nigrosome 1 on SWI or volume loss of neuromelanin on NM-MRI is useful for diagnosing PD.

Table 1. Interpretation of Parkinson disease compared to the essential tremor and normality

MR Sequence	Unreadable MR study	Analyzed MR study	Reader 1			Reader 2		
			Sensitivity (95% CI)	Specificity (95% CI)	AUC (95% CI)	Sensitivity (95% CI)	Specificity (95% CI)	AUC (95% CI)
SWI	13	110	95.3% (88.4-98.7)	80.0% (59.3-93.2)	0.876 (0.800-0.931)	92.9% (85.3-97.4)	76.0% (54.9-90.6)	0.845 (0.763-0.907)
With CS	3	65	92.2% (81.1-97.8)	85.7% (57.2-98.2)	0.889 (0.787-0.954)	90.2% (78.6-96.7)	92.9% (66.1-99.8)	0.915 (0.819-0.970)
Without CS	10	45	99.9% (89.7-99.9)	72.7% (39.0-94.0)	0.864 (0.728-0.948)	97.1% (84.7-99.9)	54.6% (23.4-83.3)	0.758 (0.607-0.873)
Neuromelanin	2	121	94.3% (87.2-98.1)	93.9% (79.8-99.3)	0.941 (0.883-0.976)	94.3% (87.2-98.1)	75.8% (57.7-88.9)	0.850 (0.774-0.909)

Abbreviation: area under curve=AUC; 95% confidence interval=95% CI

Table 2. Interpretation of Parkinson disease, MSA-P and MSA-mixed compared to the NPH, essential tremor and normality

MR Sequence	Unreadable MR study	Analyzed MR study	Reader 1			Reader 2		
			Sensitivity (95% CI)	Specificity (95% CI)	AUC (95% CI)	Sensitivity (95% CI)	Specificity (95% CI)	AUC (95% CI)
SWI	17	124	95.7% (89.5-98.8)	80.0% (61.4-92.3)	0.879 (0.808-0.930)	93.6% (86.6-97.6)	73.3% (54.1-87.7)	0.835 (0.757-0.895)
With CS	6	73	92.9% (82.7-98.0)	88.2% (63.6-98.5)	0.905 (0.814-0.961)	91.1% (80.4-97.0)	88.2% (63.6-98.5)	0.896 (0.803-0.956)
Without CS	11	51	99.9% (90.7-99.9)	69.2% (38.6-90.9)	0.846 (0.718-0.932)	97.4% (86.2-99.9)	53.9% (25.1-80.8)	0.756 (0.616-0.865)
Neuromelanin	2	139	95.0% (88.6-98.3)	92.5% (79.6-98.4)	0.937 (0.883-0.971)	93.9% (87.3-97.7)	75.0% (58.8-87.3)	0.845 (0.774-0.901)

Abbreviation: Parkinson disease=PD; multiple system atrophy-Parkinsonian type=MSA-P; multiple system atrophy-mixed type=MSA-mixed; normal pressure hydrocephalus=NPH; area under curve=AUC; 95% confidence interval=95% CI

Improving White Matter Hyperintensities Lesion Burden Assessment on ADNI 3D T2-FLAIRs Using StackGen-Net

G Guzman Perez-Carrillo¹, L Umapahty², B Winegar³, M Altbach², M Keerthivasan², A Bilgin²

¹Mallinckrodt Institute of Radiology, St. Louis, MO, ²University of Arizona, Tucson, AZ, ³University of Utah, Salt Lake City, Utah (UT)

Purpose

Accurate and reliable quantification of white matter hyperintensities (WMH) volume can provide better insight to assess neurological disease progression. In this work, we evaluate StackGen-Net, our deep learning-based stacked generalization ensemble of orthogonal 3D Convolutional Neural Networks (CNNs), on a subset of 3D T2-FLAIRs from the Alzheimer's Disease Neuroimaging Initiative (ADNI).

Materials and Methods

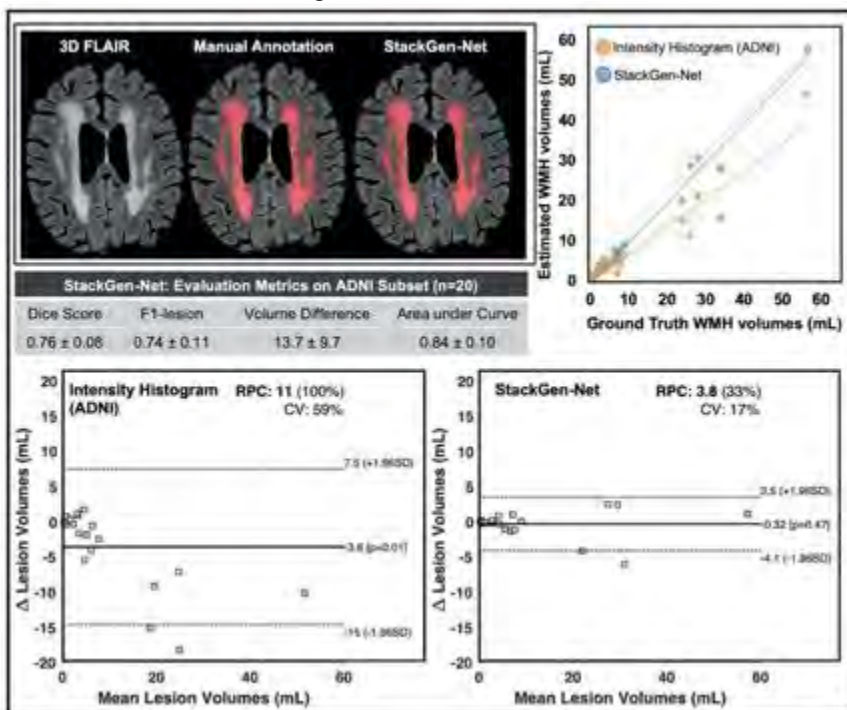
Our recently proposed CNN framework, StackGen-Net, has been shown to improve the WMH segmentation performance compared to some state-of-the-art CNN based segmentation techniques [1]. Here, we evaluate our technique on 20 non-demented participants selected randomly from phase 3 of publicly-available ADNI database (adni.loni.usc.edu). The corresponding WMH volumes assessed using intensity histograms algorithm [2] were also downloaded from ADNI for comparison. A neuro-radiologist manually annotated WMH in these images for ground truth. The agreement in WMH volumes (mL) between ground truth and the two techniques was evaluated using Bland Altman (BA) plots with R2, Coefficient of Variation (CV), repeatability coefficient (RPC) statistics.

Results

StackGen-Net achieved average Dice score, F1-lesion, absolute volume difference, and area under precision-recall curve of 0.76, 0.74, 13.7%, and 0.84, respectively. BA analysis showed excellent agreement with a tighter limit of agreement between ground-truth and StackGen-Net (R2=0.98, CV=17%, RPC=33%) with no significant difference in lesion volumes (P=0.47, n=20, two-sided paired t-test). In contrast, the intensity histograms showed a significant difference (P=.01) in lesion volumes (R2=0.91, CV=59%, RPC=100%) with ground truth.

Conclusions

The use of a stacked generalization of CNN models can provide more accurate quantitative evaluation of WMHs to study relationship between lesion burden and cognition.



(Filename: TCT_853_ASNR2021StackGenFig1.jpg)

1382

Incidence and Characterization of Metastatic Intracranial Lesions in Malignant and Metastatic Melanoma: A Single Institute Retrospective Analysis

M Sandhu¹, M Aboian¹, A Mahajan¹

Purpose

Brain metastases (BM) in melanoma are not uncommon. It has been the leading cause of morbidity and mortality in melanoma, with a historically reported median survival of fewer than 5 months. Recent studies on BM incidence in melanoma are predominantly cross-sectional studies and do not provide follow - up data. Through this study, we aim to update the literature about the recent incidence of BM during melanoma diagnosis and during follow-up period. We also aim to provide general characteristics of intracranial metastatic lesions along with genetic analysis.

Materials and Methods

Using our institution's tumor registry, we identified patients with initial diagnoses of stage III and stage IV from 2011 – 2017 and followed - up through December 2019. Brain imaging (MR, CT, or PET) of these patients were retrospectively analyzed for intracranial metastatic lesions by a trained neuroradiologist (AM). The number, location, and size of lesions were documented. Additionally, BRAF (V600E and V600K), c- KIT, and NRAS mutation status were also analyzed for stage IV patients.

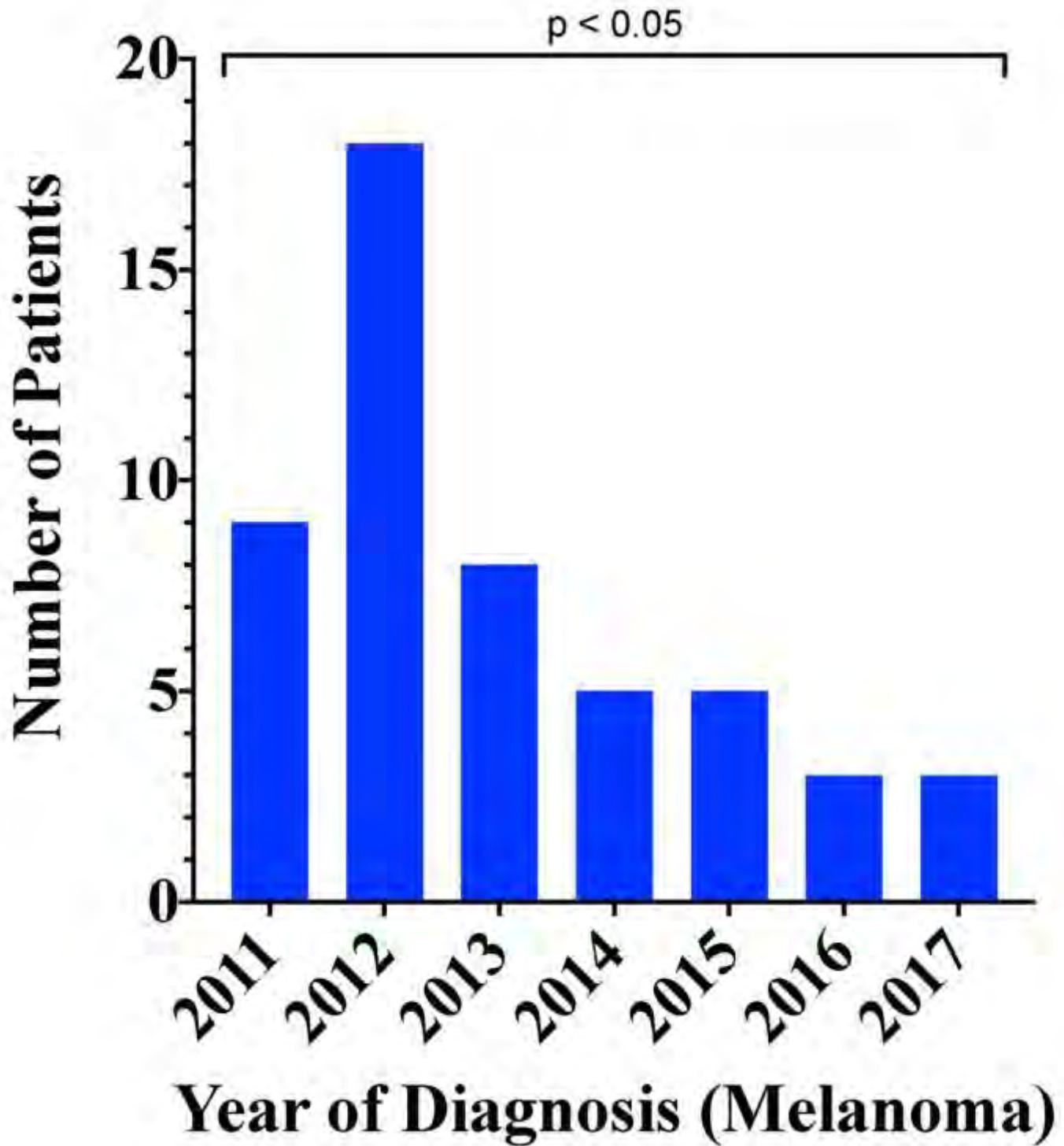
Results

Of 276 stage III and stage IV melanoma patients, 33% of patients were found to have BM, whereas 67% of patients did not develop BM. 37.7% patients had BM at the diagnosis of stage IV melanoma. During the follow-up period, BM incidence in stage III was 21%, similar to the incidence in stage IV patients (22%). A significant decreasing trend was observed in BM occurrence (follow - up) from 2011 to 2017 ($p < 0.05$; Figure 1). Time for BM occurrence in stage III was 24 months vs. 9 months in stage IV patients ($p < 0.05$). The mean diameter of the most extensive lesion was 15 mm (± 13). Furthermore, a higher number of BRAF mutations were found in patients with BM (69) vs. patients with no BM (31%; $p = 0.02$).

Conclusions

While the incidence of BM is still high, a decreasing trend in BM occurrence after melanoma diagnosis is encouraging. The extensive use of new immunomodulators could, in part, be responsible for this observed trend. Furthermore, our study shows that stage III and stage IV patients have a similar rate of BM occurrence during the follow - up period; therefore, highlighting the need for regular monitoring metastatic brain disease in patients with stage III. Lastly, our data suggest a higher rate of BRAF mutations in patients with BM, thus suggesting a role of BRAF in BM. Nevertheless, larger multi-institutional studies are required to confirm these findings.

Brain Metastases (Follow-up)



(Filename: TCT_1382_ASNR2020.jpg)

Incidence of Delayed Posttraumatic Intracranial Hemorrhage in Patients on Anticoagulation and Antiplatelet Agents Including Novel Anticoagulants: Two Year Experience in a Large Multi-hospital Integrated Delivery Network

W CHANG¹, D Yin¹, M Spearman¹, A Sohn¹, M Kulzer², T Tragon³, C LI¹, c wanamaker³, B Weston¹, L Eisenmenger⁴, M Goldberg¹
¹Allegheny Health Network, Pittsburgh, PA, ²Allegheny Health Network, PITTSBURGH, PA, ³N/A, N/A, ⁴University of Wisconsin - Madison, Middleton, WI

Purpose

The risk of delayed posttraumatic intracranial hemorrhage (DH) in patients on anticoagulant/antiplatelet medications, especially in patients taking novel anticoagulant medications (NOACs), is not well established. The prevalence of NOACs is increasing and in a recent study on anticoagulated patients was as high as 50%. Some groups found a low risk of posttraumatic DH in patients taking warfarin/clopidogrel, however, newer reports found >7% rate of DH and others found 1% mortality. We report our 2-year experience with DH including patients taking NOACs.

Materials and Methods

A template was created in our dictation system recommending repeat head CT for patients with trauma who are taking anticoagulant/antiplatelet medications. Patients were included in the study if their initial head CT was read as negative and a repeat exam was performed for evaluation of DH without further history of trauma. Average follow-up time was 21 hours and 99% were within 3 days. A total of 864 cases were included in the trial (Table 1a), almost evenly divided between NOAC and non-NOAC anticoagulant/antiplatelet agents. Cases were considered negative if both the initial and subsequent exam was interpreted as negative for ICH. Cases were considered positive if the initial exam was negative but ICH was detected on the follow-up examination. Each positive case was reviewed by 2 board-certified neuroradiologists. Cases where ICH was retrospectively seen on the initial scan by expert readers were not included. Cases where DH was considered artifactual or not seen were reclassified as negative. Cases where expert readers did not agree were adjudicated by an additional reader. Statistics were analyzed using Chi Squared and Fisher's Exact Probability analysis.

Results

Results are presented in Table 1b. The overall rate of DH in our study population was 1.9% with mortality from DH of 0.4%. All patients with DH on warfarin had INR > 2.0, and 5/9 had INR > 3.0. NOACs had significantly lower rate of DH than warfarin/clopidogrel (p <0.01, RR 4.6). Clopidogrel had the highest mortality, despite a similar rate of DH to warfarin.

Conclusions

Our study found nearly 2% rate of DH with 0.4% mortality, higher than some previously published reports. NOACs demonstrated significantly lower risk of hemorrhage than warfarin/clopidogrel. Given significant morbidity and mortality from DH, repeat CT in the setting of anticoagulant/antiplatelet medications should be considered, especially in patients on warfarin with elevated INR and clopidogrel.

Medication	Total Patients	Male	Female	Average age (years)
Apixiban (Eliquis)	280	119	161	78.9
Warfarin (Coumadin)	256	128	128	78.6
Rivaroxaban (Xarelto)	147	66	81	75.0
Clopidogrel (Plavix)	143	80	63	78.0
Other	49	27	22	76.0
Total	864	411	453	77.6

Medication	Total Patients	Negative Cases	Positive Cases	% Positive	Deaths	% Death
Apixiban (Eliquis)	280	280	0	0	0	0
Warfarin (Coumadin)	256	247	9	3.51%	1	0.4%
Rivaroxaban (Xarelto)	147	144	3	2.04%	0	0
Clopidogrel (Plavix)	143	139	4	2.80%	2	1.4%
Other	49	49	0	0	0	0
Total	864	848	16	1.90%	3	0.4%

Table 1: a) Demographics of the patients in the study. b) Positive/negative cases and mortality data.

1470

Infraoptic ACA or Carotid – ACA anastomosis: A very rare embryological variation. Radiological and surgical importance.

P Kochar¹, S Kanekar², A Megahed³

¹*Penn State Health Milton S Hershey Medical Center, Hershey, PA*, ²*Hershey Medical Center, Hershey, PA*, ³*Yale New Haven Health, Bridgeport Hospital, Bridgeport, CT*

Purpose

An infraoptic course of the ACA is a rare cerebrovascular variation that can be associated with anterior communicating artery aneurysm. The purpose of this study is: 1. Describe infraoptic ACA or Carotid-ACA anastomosis, a very rare vascular anatomic variation. 2. Discuss the embryology of this variant. 3. Demonstrate this rare embryological variation on CT and MR angiography. 4. Discuss its clinical significance. 5. Understand the anatomy for appropriate management of associated vascular pathology (Anterior communicating aneurysm).

Materials and Methods

Variations of the anterior cerebral artery–anterior communicating artery complex are common, however of little clinical significance. An infraoptic course of the ACA is a very rare variation. The magnetic resonance angiographic prevalence has been reported to be 0.086%. About 44% of patients with an infraoptic course of the ACA are associated with Anterior communicating artery aneurysm. This makes it a clinically important vascular variation for endovascular treatment planning. We describe the CT and MR angiographic findings of this rare vascular variation along with review of its embryology.

Results

Generally, ACA arises from the internal carotid artery (ICA) terminus and runs medially superior to the optic nerves (supraoptic course) and communicates with contralateral ACA through the anterior communicating artery. An infraoptic course of the A1 segment of the ACA is associated with a low ICA bifurcation. The bifurcation is usually located intradurally at or just above the level of the origin of the ophthalmic artery. Rarely, infraoptic origins of A1 are proximal or at the level of origin of the ophthalmic arteries and arise below the optic strut possibly extradurally. Abberant ACA course has been shown to be associated with aneurysms. This needs its prompt recognition, to allow optimum treatment planning (surgical / endovascular). Understanding and reporting of this variant is clinically important for management, either surgical or endovascular.

Conclusions

Abberant ACA course has been shown to be associated with aneurysms. This needs its prompt recognition, to allow optimum treatment planning (surgical / endovascular). Understanding and reporting of this variant is clinically important for management, either surgical or endovascular.

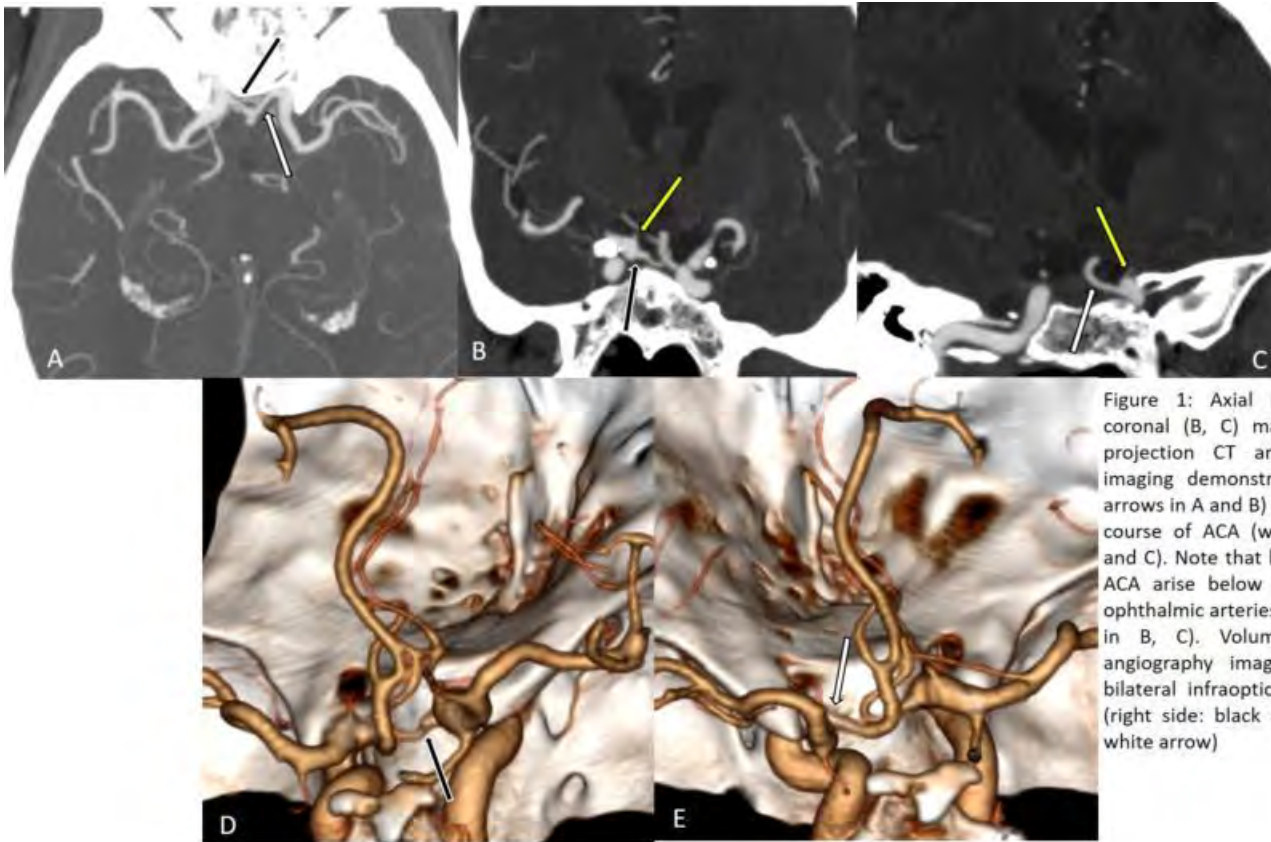


Figure 1: Axial (A) and oblique coronal (B, C) maximum intensity projection CT angiography (MIP) imaging demonstrates right (black arrows in A and B) and left infraoptic course of ACA (white arrows in A and C). Note that both the aberrant ACA arise below the level of the ophthalmic arteries (yellow arrows in B, C). Volume rendered CT angiography image (D, E) shows bilateral infraoptic course of ACA (right side: black arrow; left side: white arrow)

(Filename: TCT_1470_asnr.jpg)

1632

INITIAL EXPERIENCE WITH HYDROPHILIC POLYMER COATING FLOW-DIVERTERS FOR UNRUPTURED AND RUPTURED INTRACRANIAL ANEURYSMS

G Leone¹, F Giordano¹, M Muto¹, G Guarnieri¹, C Russo¹, D Romano², G Ambrosanio¹, M Muto¹

¹AORN Antonio Cardarelli, Napoli, Campania, ²AOU Ruggi, Salerno, Campania

Purpose

Flow diverter devices (FDD) completely changed endovascular treatment of intracranial aneurysms but concern remains about their use in the acute phase, due to the risks of using double antiplatelet therapy (DAPT). The p48-MW-HPC and p64-MW-HPC are a low-profile, intermediate-porosity flow diverter stents with hydrophilic polymer coating (pHPC); this coating has shown in vitro to reduce the thrombogenicity of nitinol device surfaces. The aim of the study was to evaluate initial experiences and technical innovations of new-generation FDDs (p48/64-MW-HPC, Phenox, Bochum, Germany) with hydrophilic polymer coating (HPC) for unruptured and rupture aneurysms treatment

Materials and Methods

Between July 2019 and September 2020, 16 intracranial aneurysms (12 F, 4 M; mean age 55.5 yrs) were treated with the p48/64-MW-HPC. A total of 18 stents were implanted. 11 aneurysms (69%) were saccular, 5 (31%) dissecting. 12/16 (75%) were located in the anterior and 4/16 (25%) in posterior circulation respectively. For unruptured aneurysms (11/16 or 69%) usual DAPT with Clopidogrel 75 mg/daily and Aspirin 100 mg/daily were administered; in the remaining ruptured cases (5/16 or 31%), single antiplatelet therapy (SAPT) in four cases with a loading dose of 1 g of salicylic acid iv, followed by 100 mg orally and regular DAPT in one, according to the Center practices. The occurrence of thromboembolic and hemorrhagic complications was recorded alongside the occlusion rates of the treated aneurysms

Results

Immediate post-treatment angiography showed reduced flow into all aneurysms. No hemorrhagic complications occurred. No ischemic complications occurred in those treated with DAPT. One intraprocedural thromboembolic complication occurred in the only one ruptured case treated with DAPT. One delayed thromboembolic complication occurred, (72 hours) with subsequent acute ischemic stroke occurred in ruptured case treated with SAPT. The follow-up with CTA and DSA showed complete occlusion in 12/16 aneurysm (75%). All the stents were patent at the last follow-up

Conclusions

Treatment of cerebral aneurysms with the p48/64-MW-HPC is a safe procedure with no technical complications. In our limited

experience the safety profile is similar to other FDD, particularly in the subgroup of patients with unruptured aneurysms treated by DAPT. In ruptured aneurysms thromboembolic complications rate are not negligible. Additional larger comparative studies are needed to confirm these results and optimize perioperative antiplatelet treatment.

265

Initial Results of the U-2 Pilot Longitudinal Brain MRI Screening Program

P Sherman¹, H Chapapas², B Cerqueira²

¹USAFSAM/59th Medical Wing, JBSA Lackland, TX, ²KBR Aerospace, JBSA Lackland, TX

Purpose

We previously reported increased subcortical and periventricular white matter (WM) injury and decreased white matter integrity associated with repetitive occupational exposure to non-hypoxic hypobaric conditions in high-altitude U-2 pilots. A longitudinal brain MRI screening program began in 2014 for high altitude pilots upon entry into the platform and every 3 years while flying. The cabin altitude restriction effort (CARE) decreased cabin altitude from 9,000 m (28,000-30,000 ft) while operating above 21,000 m to approximately 4,500 m (15,000 ft). We hypothesized that post CARE there would be no progression of WM injury.

Materials and Methods

Pilots underwent advanced MRI brain examinations at Wilford Hall Ambulatory Surgical Center [Siemens 3-T Verio magnet] in San Antonio, Texas and David Grant Medical Center [General Electric Discovery MR750 3-T magnet] in Fairfield, California, which included 3-D fluid attenuating inversion recovery (FLAIR) and 3-D T1, high resolution (0.8-mm isotropic) sequences. MRI exams were reviewed by two neuroradiologists. 3-D FLAIR imaging was quantitatively evaluated for white matter hyperintensity (WMH) volume.

Results

27 pilots completed two or more MRI brain examinations. All exams were available for review for 26 pilots. Of those 26 subjects, 22 subjects had complete imaging sequences that met quality standards for analysis. Of the 22 pilots, n= 17 had two MRIs; n= 4 had three MRIs, and n=1 had four MRIs; total of 50 MRI brain exams. Average change from baseline in total FLAIR volume was -0.025 cm³ (1.6% change from baseline). Average change from baseline in subcortical FLAIR volume 0.015 cm³ (1.2% change from baseline). Average change from baseline in periependymal FLAIR volume -0.040 cm³ (-0.4% change from baseline).

Conclusions

Since the CARE modification there has been a significant reduction in reported NDCS events. There was no significant interval change in white matter hyperintensity volume as measured by FLAIR MRI. There does not appear to be increased white matter injury as assessed by WMHs alone. Consideration should be made to include diffusion tensor imaging with fractional anisotropy assessment for the U-2 pilot MRI brain protocol.

1310

Integrating Whole-Brain Structural Deficits on MRI in Aging, Mild Cognitive Impairment, and Alzheimer's Disease using the Brain Atrophy and Lesion Index (BALI)

L Grajauskas¹, B Chinda², X Song³

¹Cumming School of Medicine, University of Calgary, Calgary, Alberta, ²Department of Biomedical Physiology and Kinesiology, Simon Fraser University, Burnaby, British Columbia, ³Health Sciences and Innovation, Fraser Health Authority, Surrey, British Columbia

Purpose

Neurodegeneration is a core element of Alzheimer's Disease (AD), and brain MRI is often indicated in the workup of a patient presenting with cognitive decline. However, existing tools such as the medial temporal atrophy score (MTAS) have inadequate sensitivity and specificity to be valuable in the diagnosis of AD (Westman et al., 2011). This is because in complex systems like the brain, single deficits generally do not lead to end stage failures such as AD on their own. Failure instead occurs when multiple deficits overlap and overwhelm cognitive reserve and capacity for self-repair (Grajauskas et al., 2019). Considering this, the Brain Atrophy and Lesion Index (BALI) was created to better reflect how neurodegeneration occurs in the entire brain, thus increasing predictive ability (Guo et al., 2017; Grajauskas et al., 2018). In the current work, the BALI was applied to imaging data from the multi-centre dataset created by the Australian Imaging, Biomarkers & Lifestyle (AIBL) Study of Ageing (Ellis et al., 2009) to examine the basic features of the BALI.

Materials and Methods

Clinical variables, laboratory values, and diagnostic data were obtained from the AIBL dataset in three diagnostic categories: Normal Cognition (NC), Mild Cognitive Impairment (MCI), and AD. MR images (3 Tesla, T1) were obtained for 492 participants (NC=354, MCI=78, AD=59). Images were assessed by trained raters, using the BALI evaluation method. The BALI includes 7 categories throughout the brain, such as white matter hyperintensities and small vessel changes (Fig 1). The relationships of the BALI scores

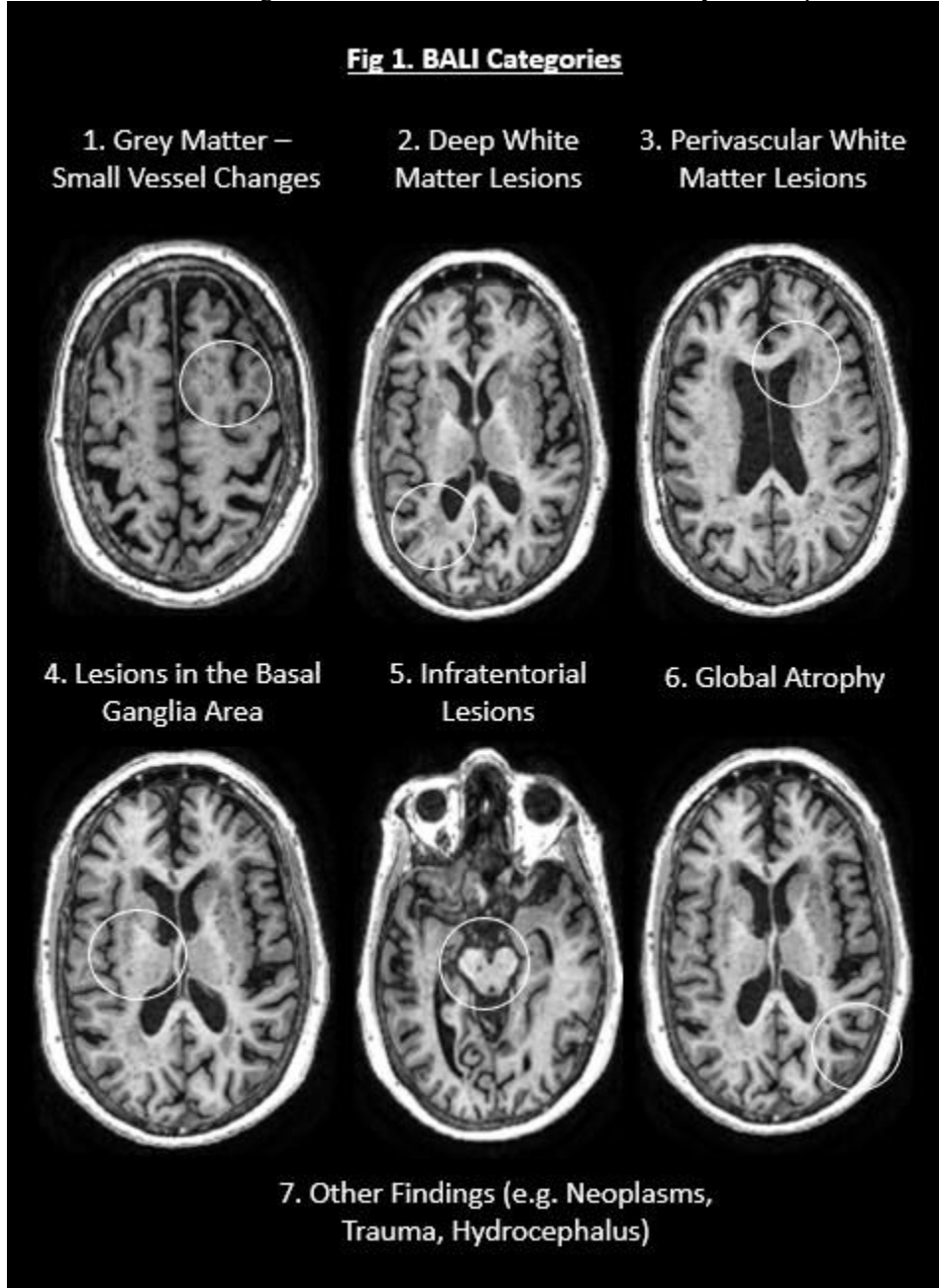
with age, cognitive scores, diagnosis, education, and physical activity were examined using correlation analysis and Wallis-Kruskal Chi2 test.

Results

The distribution of the BALI scores was slightly right skewed, varied significantly by diagnosis (AD>MCI>NC; p<0.05), and increased with age and correlated with cognition (p<0.05). Higher education level and physical activity were associated with lower BALI scores.

Conclusions

Application of the BALI to the AIBL dataset showed that the index behaves as expected when applied to new data, giving good diagnostic categorization and age association. Associations were also noted between education, physical activity, and BALI scores. Further work will examine the relationships between brain health and frailty, and test whether education and physical activity have direct effects on AD diagnosis, or if this association is mediated by their impacts on frailty and neurodegeneration.



(Filename: TCT_1310_ASNRFig1.jpg)

1127

Intensity Standardization and Contrast-to-Noise Ratios in Multicenter FLAIR MRI

J DiGregorio¹, G Arezza¹, P Jabehdar Maralani², H Khosravani², A Moody², A Khademi¹
¹Ryerson University, Toronto, Ontario, ²University of Toronto, Toronto, Ontario

Purpose

Differences in MRI hardware and acquisition parameters creates variation in image intensity, contrast, and noise which reduces reliability of automated analysis algorithms on multicenter data [1]. To reduce interscan variability, there are efforts to standardize acquisition protocols [2] and measure the effects of MRI platform upgrades [3]. To quantify the impact of standardized protocols and scanner upgrades, contrast-to-noise (CNR) ratios computed from T1/T2 MRI are commonly used [2]-[3]. In this work, we present the first fully automated method for computing CNR in multicenter FLAIR MRI. To verify reproducibility, CNR is computed across vendors in multicenter human phantom data. CNR is then computed on two clinical datasets (~250K images, 80 centers) to demonstrate utility of the proposed method for quantifying image quality and protocol/upgrade effects.

Materials and Methods

The human phantom data (SIMON) consisted of 62 volumes (7 GE/14 Philips/41 Siemens, CDIP protocol) [2]. Clinical data includes 871 volumes from CAIN [4] and 4102 volumes from ADNI [5]. An established intensity standardization method first aligns volume histograms [1] (Fig. 1) followed by brain extraction to remove non-intracranial structures. Standardization enables the same intensity thresholds to isolate tissues across datasets (Fig. 2). We adapt the CNR formula [2] to FLAIR tissue classes by using the cerebrospinal fluid (CSF) and brain. CNR is computed on original and standardized data and Kruskal-Wallis tests ($\alpha=0.05$) compare corresponding CNR values between vendors.

Results

Fig. 3 shows CNR computed on SIMON. Despite a uniform protocol, CNR varies across vendors in unstandardized data as significant differences exist across vendors for original data ($H=36.20$, $p=1.38E-9$) but not standardized data ($H=5.81$, $p=0.05$). Mean CNR is also higher in standardized volumes. Fig. 4 shows CNR computed on CAIN/ADNI. More variation exists due to the large number of subjects with different anatomy but CNR is again higher and more consistent across vendors on standardized data.

Conclusions

This work proposes a novel way to compute CNR for analyzing the impact of standardized acquisition protocols and scanner upgrades for multicenter FLAIR MRI. Standardization permits CNR computation, creates consistent CNR across vendors, and improves contrast properties of images. Future works will further apply this tool to new prospective FLAIR MRI data to quantify the effects of acquisition protocols and scanner upgrades.

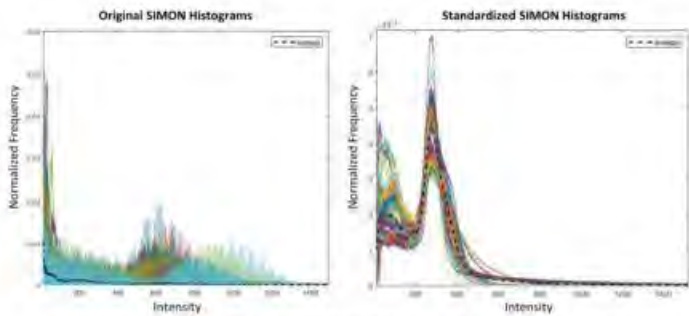


Figure 1: Intensity histograms for SIMON FLAIR MRI dataset, before and after standardization.

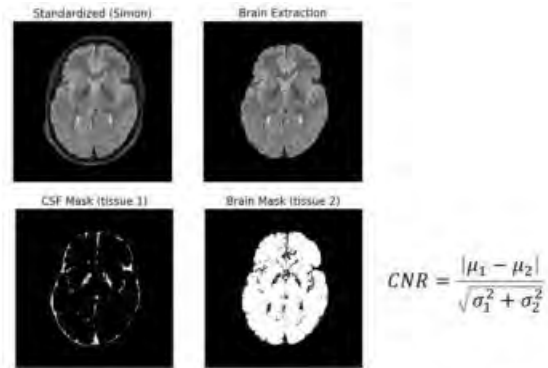


Figure 2: Standardized image slice, brain extraction result, and the extracted CSF and brain tissue masks computed from the human phantom data (SIMON). Equation for computing CNR using tissue regions from masks where μ_1 and σ_1 are the mean and standard deviation of the CSF, and μ_2 and σ_2 correspond to the brain tissue (gray matter + white matter in FLAIR MRI).

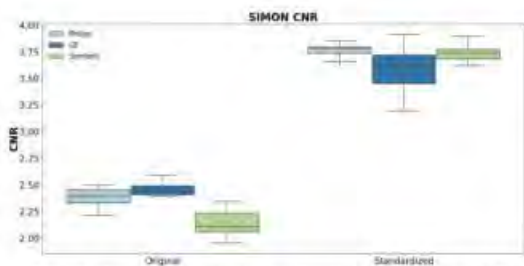


Figure 3: CNR measurements across the SIMON FLAIR MRI dataset, before and after standardization, grouped as a function of scanner vendor.

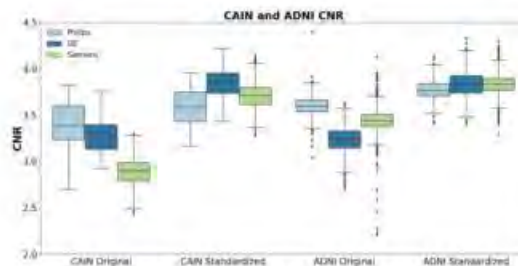


Figure 4: CNR measurements across the CAIN and ADNI FLAIR MRI datasets, before and after standardization, grouped as a function of scanner vendor.

(Filename: TCT_1127_ASNR2021Figures.jpg)

1301

Inter-institutional Variation in Brain Tumor MRI Reports: Does it Impact BT-RADS Text Classification by AI?

D Patel¹, P Smith¹, B Weinberg², L Lezotte¹, I Banerjee², M Hoch¹

¹University of Pennsylvania, Philadelphia, PA, ²Emory University, Atlanta, GA

Purpose

To evaluate the feasibility of a text machine-learning model (section-wise ensemble model) developed and trained at one academic institution (institution A) in the classification of Brain Tumor Reporting and Data System (BT-RADS) categories applied to unstructured reports from a different academic institution (institution B).

Materials and Methods

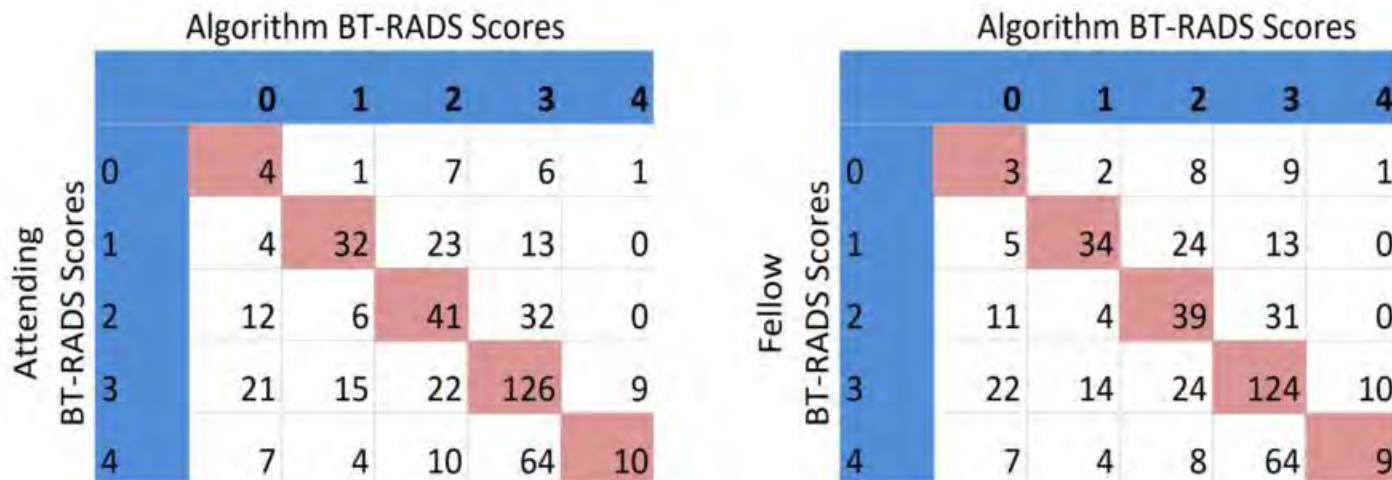
This retrospective study was approved by a multi-institutional IRB. Using the Montage search tool, brain MRI reports from 2013 to 2017 that contain keywords "Glioblastoma", "Glioblastoma multiforme", or "GBM" were identified, which generated 470 unique reports from institution B. The reports were extracted along with other data including age, gender, prior therapy, and genetic profile among other available information. BT-RADS scores were manually generated by a neuroradiologist and a neuroradiology fellow for these reports. The text machine-learning algorithm developed at institution A was previously validated on MRI reports to predict described BT-RADS categories at institution A (1,2). This model was then utilized to score unstructured reports from Institution B. The resulting BT-RADS assignments by the model, neuroradiologist, and neuroradiology fellow were compared. True agreement for BT-RADS categories and management based BT-RADS group (BT-RADS 2 or below = group 1/routine follow up group, BT-RADS 3 or above =group 3/change management group) was calculated.

Results

Overall distribution of BT-RADS category assignments for attending radiologist was 4%, 15%, 19%, 41%, and 20% for BT-RADS categories 0,1,2,3 and 4 respectively. Overall true agreement for exact BT-RADS categories as shown in Figure 1 was 45% between the attending and the algorithm and 44% between the fellow and the algorithm. The true agreement between the attending and the fellow was 93%. However, when BT-RADS categories were grouped by the management-based groups, the agreement rate increased to 72% between the attending and the algorithm, 72% between the fellow and the algorithm, and 97% between the attending and the fellow.

Conclusions

Applying a machine-learning algorithm developed at one institution to radiology reports at another institution is challenging, particularly when reports may follow a different structure or format. More work is needed to better understand the language variations and complexities in brain tumor reports across institutions, and retraining or model refinement will likely be needed when models are transferred to other settings.



(Filename: TCT_1301_Figure1.jpg)

958

Interpretable Neuroimage Classification in Dementia using Visual Attention and Reinforcement Learning

D Wood¹, T Booth², J Cole³

¹King's College London, London, UK, ²Kings College London, London, London, ³University College London, London, UK

Purpose

Deep learning has the potential to aid clinical decision-making in dementia, by automatically classifying brain images. However, several key limitations currently prohibit clinical adoption: 1) network design must be optimised for 3D neuroimaging; 2) analysis must be computationally feasible; 3) model decisions must be interpretable. Interpretability is particularly crucial, as clinicians need to understand how and why each automated decision is made.

Materials and Methods

We address these issues using a 3D recurrent visual attention model tailored for neuroimaging: NEURO-DRAM. The model comprises an agent which, trained by reinforcement learning, learns to navigate through volumetric images, selectively attending to the most informative regions for a given task. We trained and tested NEURO-DRAM using T1-weighted MRIs from the Alzheimer's

Disease Neuroimaging Initiative (ADNI) dataset. This entailed n=162 Alzheimer's Disease (AD) patients and n=160 healthy controls (HCs), split into training (90%) and testing (10%) data. Classification generalisability was evaluated using independent AD patients (n=130) and HCs (n=100) data from the Open Access Series of Imaging Studies (OASIS) dataset. Finally, we assessed the potential to transfer the classification task (i.e., no extra training needed) to discriminate between the baseline MRIs of people with stable or progressive mild cognitive impairment (MCI).

Results

NEURO-DRAM achieved 98.5% balanced accuracy when classifying AD patients from HCs from ADNI and 99.8% in OASIS, significantly out-performing a baseline convolutional neural network. When classifying stable versus progressive MCI, accuracy was 77.8%. For each test participant, an individualised trajectory was obtained, depicting the brain regions that were used to make the specific classification (Fig. 1). The regions 'visualised' by the model's trajectories included the hippocampus, parahippocampal gyrus and lateral ventricles. Computation time for training NEURO-DRAM was substantially faster than the baseline network (10 minutes versus 45 minutes).

Conclusions

Using a data-driven approach, near-perfect classification of AD patients from HCs can be achieved. To reach this high level of performance, our model learns to 'visually' attend to the areas of the brain radiologically associated with AD. Importantly, the neuroanatomical trajectory for each individual run through the analysis can be visualised, providing an intuitive way to interpret how NE

1099

Intravenous Thrombolysis Followed by Endovascular thrombectomy versus Direct Endovascular thrombectomy: a Randomized Controlled Trial

M Kappelhof¹, N LeCouffe¹, K Treurniet¹, L Rinkel¹, A Bruggeman¹, B Emmer¹, R van Oostenbrugge², W van Zwam², J Boiten³, G Lycklama³, K Keizer⁴, L Yo⁴, A van Es⁵, A van der Lugt⁶, D Dippel⁶, J Coutinho¹, Y Roos¹, C Majoie¹

¹Amsterdam UMC, University of Amsterdam, Amsterdam, Noord-Holland, ²Maastricht UMC+, Maastricht, Maastricht, ³Haaglanden MC, The Hague, Zuid-Holland, ⁴Catharina Hospital, Eindhoven, Noord-Brabant, ⁵Leiden University Medical Center, Leiden, Zuid-Holland, ⁶Erasmus Medical Center, Rotterdam, Zuid-Holland

Purpose

Guidelines recommend intravenous thrombolysis (IVT) to be administered in eligible patients with acute ischemic stroke and a proximal intracranial occlusion of the anterior circulation, prior to start of endovascular thrombectomy (EVT). However, based on data from observational studies and two recently completed randomized controlled trials, the added value of IVT in patients eligible for EVT remains unclear (1,2). The aim of the MR CLEAN NO-IV trial is to assess the efficacy and safety of direct EVT compared to IVT followed by EVT, in patients with acute ischemic stroke, caused by an occlusion of the anterior circulation.

Materials and Methods

MR CLEAN-NO IV is a randomized controlled, open label, blinded endpoint trial. Patients with acute ischemic stroke are eligible if they have a proximal occlusion of the intracranial carotid artery, M1, or proximal M2, a baseline NIHSS ≥ 2 , and present within 4.5 hours of symptom onset. Major exclusion criteria are significant pre-stroke disability and any contra-indication for IVT. Only patients who present directly to an EVT-capable hospital are included. Patients are randomly allocated (1:1) to direct EVT (intervention arm) or IVT with alteplase 0.9 mg/kg followed by EVT (control arm). The primary endpoint is the modified Rankin Scale score (mRS) at 90 days. Secondary endpoints include eTICI score and final infarct volume. Safety endpoints include symptomatic intracranial hemorrhage and embolization to new territory on angiography. Assessments of the primary outcome, imaging, and serious adverse events are performed by adjudication committees blinded to allocated treatment. We will perform subgroup analyses for occlusion location, collateral score and thrombus perviousness, among others. The study protocol and statistical analysis plan are accessible on <https://www.mrclean-noiv.nl/>.

Results

Between January 24, 2018 and October 28, 2020, we enrolled 540 patients in 20 centers in the Netherlands, Belgium, and France. Last follow-up is expected to be completed in January 2021 and we anticipate that the database will be closed in February 2021. Results will be presented at the conference.

Conclusions

The MR CLEAN-NO IV trial will provide robust data on whether IVT is beneficial to patients with acute ischemic stroke who are eligible for EVT and who present directly to a comprehensive stroke center.

1107

Introducing BrainSee: A Novel, MRI-Based Virtual Microscope Technology for Non-invasive Prognosis of Amnesic MCI in Clinics and Clinical Trials

K Vejdani¹

¹Darmiyan, Inc., San Francisco, CA

Purpose

Prediction of progression from amnesic mild cognitive impairment (aMCI) to Alzheimer's dementia (AD) is a critical need in the evaluation and management of cognitive impairments. Darmiyani Inc. has developed a novel virtual microscope technology, BrainSee, for accurate and reliable prediction of progression from aMCI to AD (Alzheimer's Dementia) based on standard clinical brain MRI and basic cognitive screening. The purpose of this study was to evaluate: 1. The performance accuracy of BrainSee for 5-year prognosis of aMCI 2. The robustness of BrainSee to standard routine clinical-grade data 3. Test-retest reliability of BrainSee 4. The clinical utility and usability of BrainSee's quantitative whole brain maps

Materials and Methods

Data for third party validation were provided by the Knight ADRC (Washington University), Huntington medical research institutes (HMRI), Baycrest Institute, University Health Network (UHN), and GERAS Hamilton Health Sciences (HHS). De-identified data including basic patient demographics (age, sex, education), MMSE, CDRSB, and brain MRI (T1, T2, DWI or DTI) were provided for analysis. BrainSee's algorithm was blind to the distribution and clinical outcomes of all patients. BrainSee generated a prognostic prediction of conversion to dementia within 5 years. Clinician's diagnosis at 5-year follow-up was considered the ground truth. Prognosis analysis sample: 95 subjects, 101 independent clinical time points, age range 51 to 95 years, male to female ratio 1.18. Test-retest reliability sample: 60 subjects, 78 scan sessions, age range 53 to 88 years, male to female ratio 1.21.

Results

Balanced accuracy of prognostic prediction = 91.0 % Sensitivity = 89.2 %, Specificity = 92.9 % PPV_{pc} = 92.6 %, NPV_{pc} = 89.6 % (prevalence corrected) Test-retest coefficient of variation = 4.6% BrainSee's report, grading system, and quantitative whole-brain maps were easy for clinicians to understand and interpret.

Conclusions

Darmiyani's novel virtual microscope technology (BrainSee) had a 91% prognostic performance accuracy on blind, clinical-grade brain MRI data from amnesic MCI patients and showed high test-retest reliability confirmed by third-party investigators. Darmiyani's BrainSee technology is therefore an accurate, non-invasive, and reliable tool to be used for prognostication of cognitive impairments in clinics and clinical trials.

716

Investigating Simultaneity for Deep Learning-enhanced Actual Ultra-low-dose Amyloid PET/MRI Imaging

K Chen¹, O Adeyeri², T Toueg¹, E Mormino¹, M Khalighi¹, G Zaharchuk¹

¹Stanford University, Stanford, CA, ²Salem State University, Salem, MA

Purpose

We have previously generated using deep learning diagnostic quality amyloid positron emission tomography (PET) images with actual ultra-low injected radiotracer dose and simultaneously acquired magnetic resonance imaging (MRI) inputs [1]. Here, we will investigate the value of simultaneity, where non-simultaneous inputs will allow for greater utility of ultra-low-dose imaging to include those acquired on standalone PET/computed tomography (CT) and MRI machines.

Materials and Methods

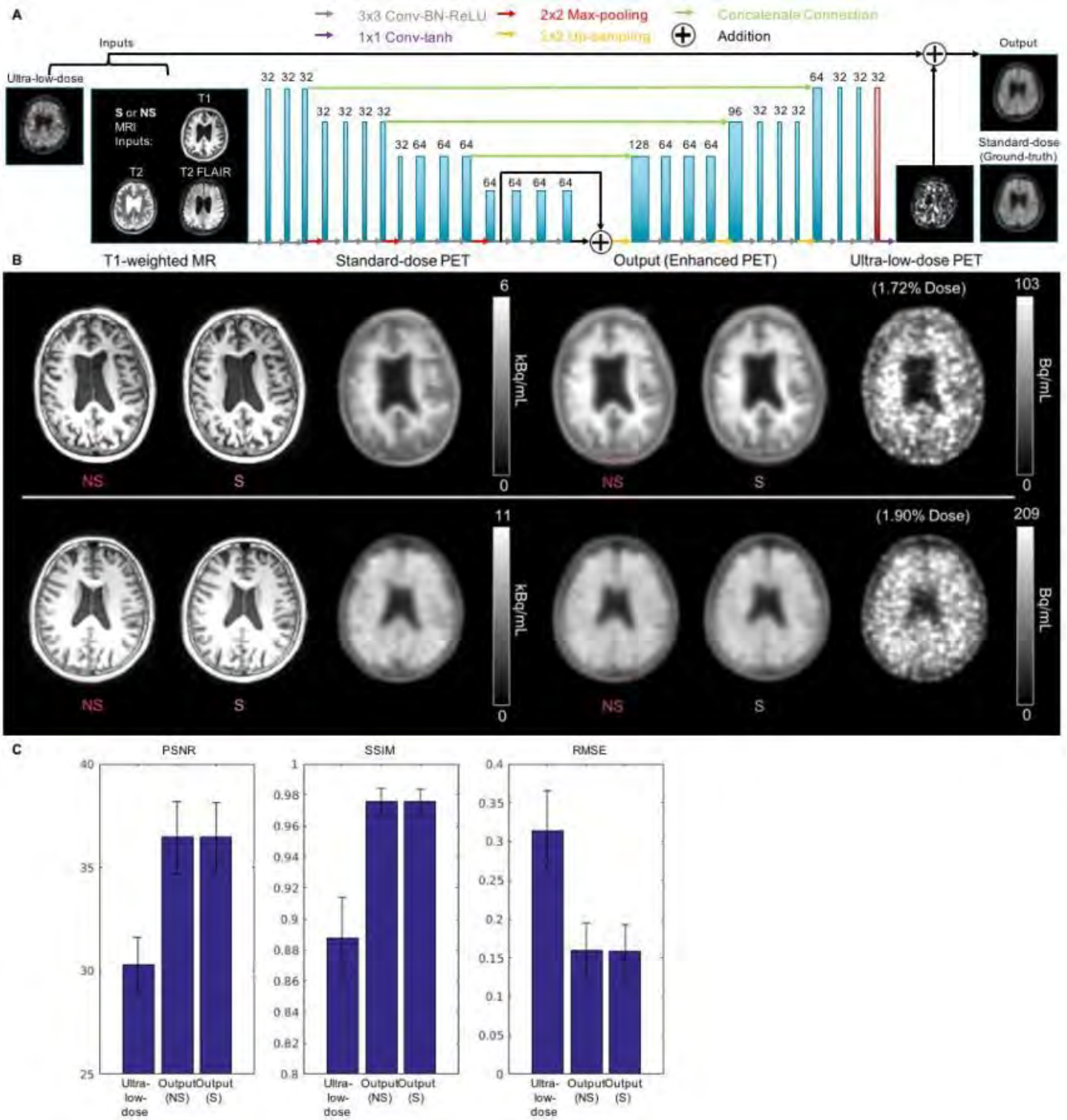
48 participants were recruited for the study. 32 (19 female, 68.2±7.1 years) were used for pre-training the network; 328±32 MBq of the amyloid radiotracer 18F-florbetaben were injected into the participants. 16 (6 female, 71.4±8.7 years) were scanned with the ultra-low-dose protocol. These participants were scanned in two PET/MRI sessions, with 6.49±3.76 and 300±14 MBq 18F-florbetaben injections respectively. In both sessions the T1-, T2-, and T2 FLAIR-weighted MR images were acquired simultaneously with PET (90-110 minutes after injection) on an integrated PET/MR scanner with time-of-flight capabilities. A pre-trained low-dose U-Net with multimodal PET/MRI inputs was derived from Chen et al. (Figure 1A) [2]. The last layer of the U-Net was fine-tuned using the actual low-dose datasets. 8-fold cross-validation to efficiently utilize all datasets (16 for training, 2 for testing per fold). The fine-tuning was carried out twice: once using PET/MRI inputs from the same scanning session (simultaneous: S) and once using PET and MRI from different sessions (non-simultaneous: NS). For each axial slice, the image quality of the enhanced and low-dose PET images within the brain were compared to the full-dose image using peak signal-to-noise ratio (PSNR), structural similarity (SSIM), and root mean square error (RMSE).

Results

Qualitatively, the enhanced images show marked improvement in noise reduction to the ultra-low-dose image and resemble the ground truth image (Figure 1B). All three metrics showed dramatic image quality improvement (Figure 1C) from the ultra-low-dose images to the enhanced images, and the metrics between the images enhanced from the S vs. NS inputs were not statistically significant with paired t-tests (PSNR: p=1.00, SSIM: p=0.79, RMSE: p=0.67).

Conclusions

This work has shown that amyloid PET images can be generated using trained U-Nets with both S and NS multimodal ultra-low-dose PET/MR images, broadening the utility of ultra-low-dose amyloid PET imaging.



(Filename: TCT_716_Figure1.jpg)

549

Iodinated Contrast Material Substitution Is More Effective Than Steroid Premedication at Preventing Repeat Acute Allergic-Like Reactions in Patients with a History of Allergic-Like Reaction to Contrast.

J MCDONALD¹, N Larson¹, J Schmitz¹, A Kolbe¹, C Hunt¹, R Hartman¹, D Maddox¹, D Kallmes¹, R MCDONALD¹
¹Mayo Clinic, ROCHESTER, MN

Purpose

To examine and compare prophylactic strategies for avoiding repeat acute allergic-like reactions to iodinated contrast material (ICM) in patients with a history of reaction.

Materials and Methods

All patients with a prior allergic-like reaction to an ICM that received intravenous ICM for a subsequent computed tomography (CT) exam at our institution from June, 2009 to May, 2017 were identified. Prior reaction details, including the specific ICM that caused the reaction, symptoms of the reaction, and severity of the reaction (American College of Radiology criteria of mild, moderate, and severe) were retrieved from the medical record. Prophylactic premedication administered prior to the subsequent CT exam and any allergic-like acute reactions that occurred at the time of the subsequent CT exam were retrieved. The effectiveness of various prophylactic strategies was compared by Pearson's Chi squared test.

Results

A total of 1973 patients were identified who received a total of 4360 subsequent CT exams. Patients were premedicated for approximately half of the exams (n=2397, 55%), most commonly with methylprednisolone at 12 and 2 hours prior to exam (n=1570, 36%), with smaller subsets of patients premedicated with methylprednisolone and diphenhydramine (n=250, 5.7%) or diphenhydramine alone within 2 hours prior to exam (n=488, 11%). A different ICM than the one that caused the prior reaction was used in approximately one third of scans (488/1656, 29%). A total of 280 subsequent allergic-like reactions (6.4% of exams) in 224 patients (11% of patients) occurred (242 mild, 37 moderate, 1 severe). Repeat reaction rates were observed with exams where: a different ICM was used and the patient was not premedicated (6/276 (2.2%)), a different ICM was used and the patient was premedicated (9/212 (4.3%)), the same ICM was used and the patient was not premedicated (84/589 (14%)) and the same ICM was used and the patient was premedicated (107/579 (18%)). Switching to a different ICM without premedication was associated with a significantly lower rate of repeat reactions than using the same ICM with or without premedication (p<.0001 for both). Similar results were observed when only patients treated with 12 and 2 hour methylprednisolone were included in the premedicated group.

Conclusions

In our cohort, a small percentage of patients with a history of acute allergic-like reaction to ICMs had a repeat reaction. Switching ICMs appears to be more effective at preventing repeat reactions than steroid premedication.

1393

Is it Really a Dermal Sinus or a Limited Dorsal Myeloschisis – More Beneath the Surface?

R Joshi¹, A Krishnan¹

¹William Beaumont Hospital, Royal Oak, MI

Purpose

Dermal sinuses are congenital epithelialized fistulous tracts extending from the skin to the spine. They can serve as a source for spinal infections and development of dermoids, and are associated with sacral dimples and other cutaneous markers. Limited Dorsal Myeloschisis (LDM) is a less commonly reported condition, first described in 2010, which shares similar features. In contrast to dermal sinuses, LDM is a closed neural tube defect characterized by a fibroneural stalk containing neuroglial tissue connecting the skin to the spinal cord, and is associated with skin abnormalities such as a sunken crater or "cigarette burn mark" lesion. We believe many cases described as dermal sinuses may in fact be LDMs.

Materials and Methods

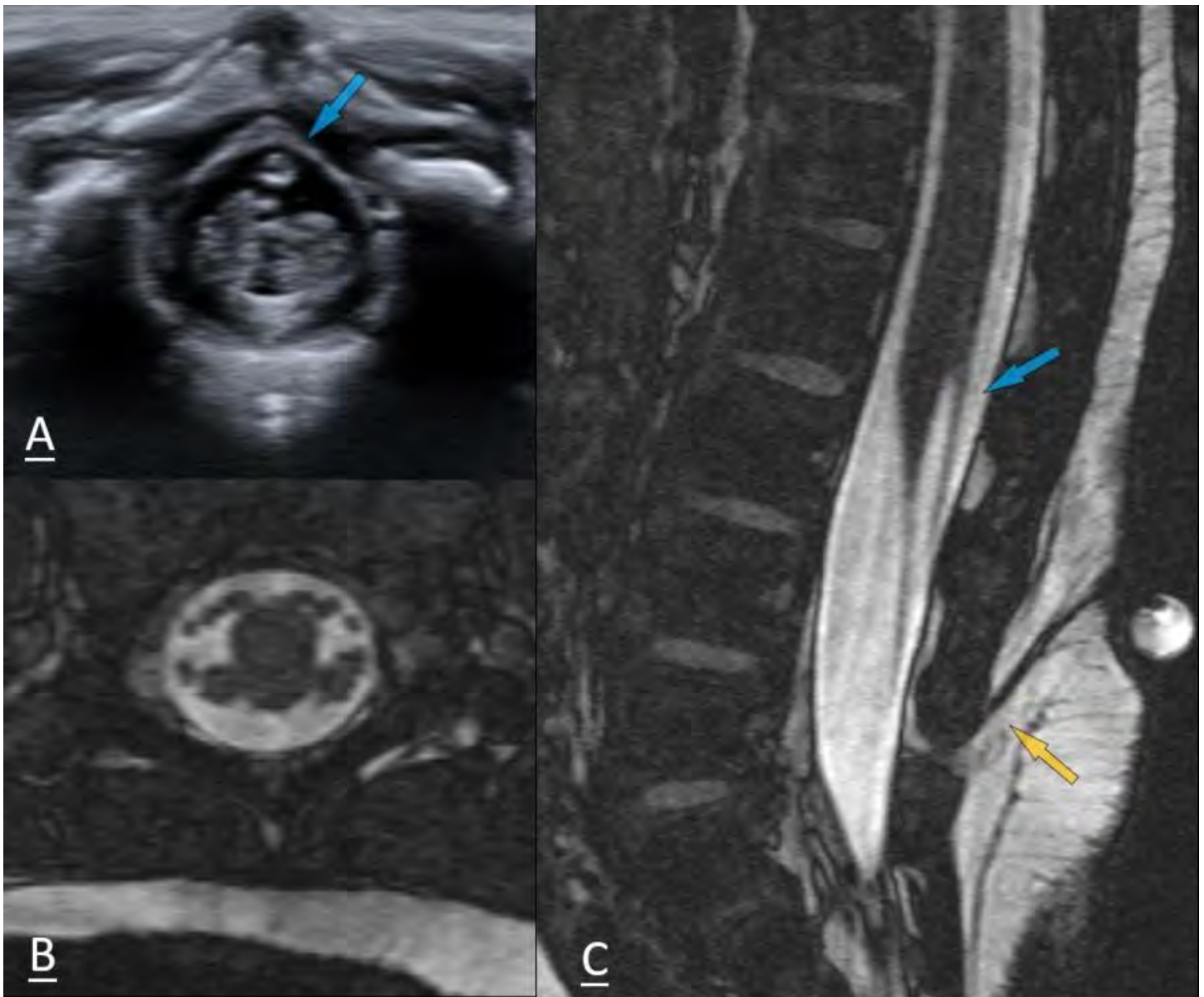
We retrospectively queried the imaging archive database in our institution for spine MRI reports mentioning dermal sinus tracts or synonymous terms. Being congenital conditions, we isolated our review to patients under the age of 18 with an MRI at the time of original diagnosis. We reviewed cases for features of LDMs such as an intradural tract extending to the skin and elongated anteroposterior dimension of the cord at the site of connection, as well as features of dermal sinuses such as presence of dermoids or infection. Chart review was performed to assess the clinical, surgical, and pathologic findings and available spinal ultrasounds were reviewed.

Results

Database query identified 25 cases describing a dermal sinus tract. 11 cases met our inclusion criteria and were further reviewed, 7 of which had an ultrasound preceding the MRI. On review, 5 of these 11 cases demonstrated features consistent with LDM, 2 of which had an associated intraspinal lipoma. In an additional case the initial MRI was suboptimal, but follow up ultrasound showed features of LDM on re-review. No definite dermal sinus or LDM was seen in 5 cases. Glial tissue was found on pathology in one case, and findings on two operative reports suggested presence of a potential intradural tract.

Conclusions

The vast majority of LDM cases are not described on imaging, surgical reports, or pathologic analysis, probably from a lack of knowledge of this condition, confirming that LDM remains underdiagnosed. Increasing awareness of this condition by neuroradiologists is necessary to guide the surgical and pathologic approach to facilitate identification of neuroglial elements in the fibroneural stalk and potentially improve care and outcomes for LDM patients.



A - Transverse ultrasound image of the spine demonstrating a fibroneural stalk separating dorsally from the cauda equina (blue arrow)

B - Axial CISS sequence image showing elongation of the spinal cord in the AP dimension

C - Sagittal CISS sequence image showing a fibroneural stalk distinctly separating from the distal spinal cord (blue arrow) and extending towards a closed skin defect (yellow arrow)

(Filename: TCT_1393_LDMImagesFinal.jpg)

361

K-space Based Deep Learning Reconstruction Empowers 50% Acceleration of MR Spine Imaging– A Prospective, Multicenter, Multireader Trial

L Tanenbaum¹, S Bash², M Thomas³, M Fung⁴, L Marc⁵

¹RadNet, New York, NY, ²RadNet, Woodland Hills, CA, ³GE, Hillsborough, NJ, ⁴GE Healthcare, Waukesha, NJ, ⁵N/A, N/A

Purpose

This prospective, multicenter, multireader study evaluates the impact on perceived image quality of 50% scan-time reduced spine MRI reconstructed with deep learning (DL).

Materials and Methods

With IRB approval and patient consent, 50 consecutive patients underwent standard-of-care (SOC) and accelerated (FAST) spine MRI exams acquired from a GE 3T Architect scanner. DL processing of the FAST scan data set (FAST-DL) was performed using an FDA-cleared CNN based, DL image enhancement product - Air Recon DLTM. The k-space based tool offers powerful denoising, sharpness enhancement and elimination of some artifacts such as truncation ringing. Two neuroradiologists were presented with the different image series as paired side-by-side datasets. Datasets were blinded and randomized in sequence and left-right display order. Image features were preference rated on a 5-point Likert scale.

Results

FAST-DL was qualitatively better than SOC for perceived signal-to-noise ratio (SNR), sharpness and artifacts. FAST-DL and SOC were better than FAST for all assessed features. No anatomic aberration or data loss was observed on the DL processed images.

Conclusions

DL enables 50% spine MRI scan time reduction as well as what radiologists perceive as enhanced image quality with benefits in SNR, image sharpness, and artifact reduction over SOC and FAST images without DL processing, providing gains in efficiency and portending practice utility for routine use.



FIG 1. Representative sagittal T2W lumbar spine images. [Left-to-right: SOC at 2:10 min; FAST-DL at 0:55 min; FAST at 0:55 min]

(Filename: TCT_361_GEFig.JPG)

1486

Key Value: A New Imaging Radiogenomic Marker Correlating IDH Mutation Status in Glioblastoma

E Alp¹, H Hatipoglu¹, S Guresci¹

¹University of Health Sciences Ankara Bilkent City Hospital, Ankara, Turkey

Purpose

To evaluate correlation of genetic and immunohistochemical biomarkers with MR perfusion parameters in glioblastoma.

Materials and Methods

In this retrospective study there were 47 patients with previously operated recurrent glioblastoma (M/F:28/19; mean age: 54.55 ± 15.39 years (age interval: 20-82 years)). IDH mutation was examined by immunohistochemical study with IDH1 antibody on paraffine embedded tissue blocks. Tumor tissue was assessed on FLAIR and contrast enhanced T1 images. DCE and DSC perfusion studies were evaluated by two radiologists. Highest values of DCE and DSC parameters were recorded. Kep value is the rate constant from extracellular extravascular space back into blood plasma. Cutoff Kep value was ascertained as 0.450 corresponding to the highest Youden index (0.776).

Results

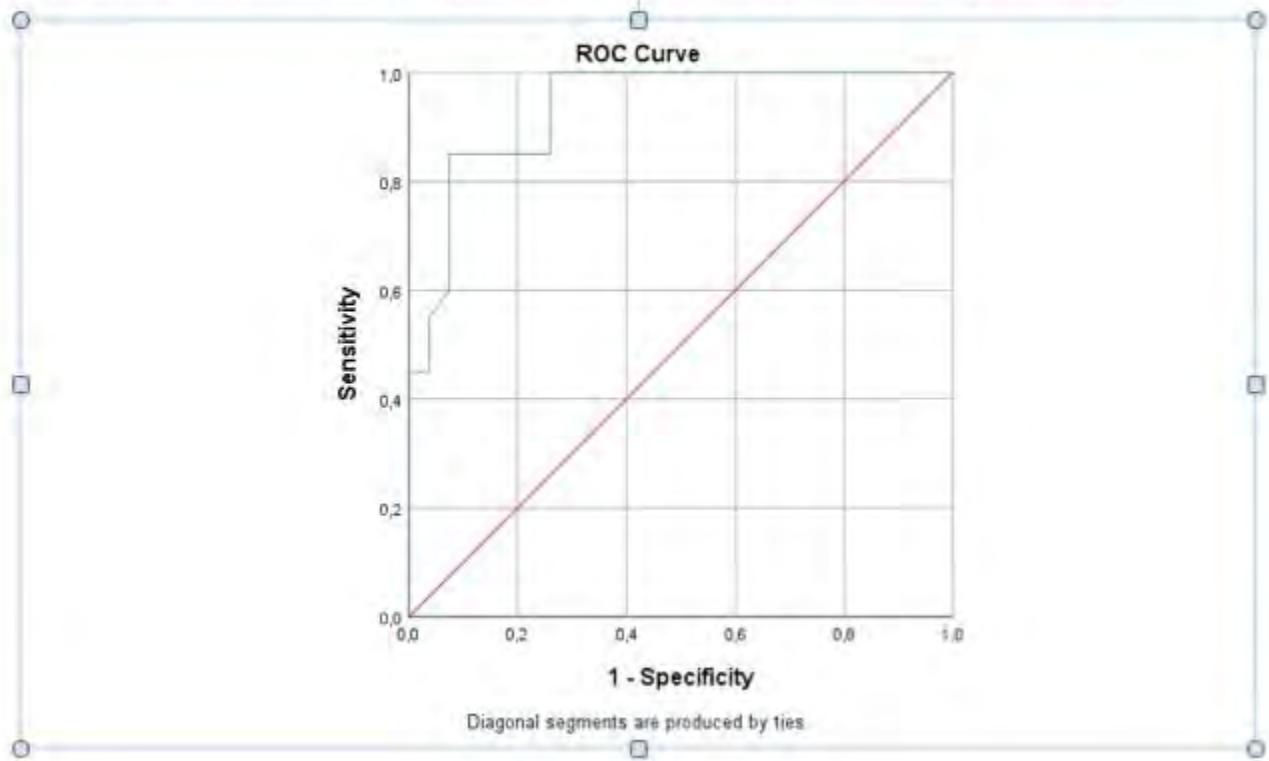
Twenty of the patients were IDH mutant and 26 were IDH wild type. Mean Kep was higher in the IDH-wild type compared to the

IDH-mutant type ($p < 0.001$). Area under the curve for ROC plotted for mean Kep value and IDH positivity was 93.6% ($p < 0.001$) (Table). Kep value of ≤ 0.450 allowed for prediction of IDH positivity with a 85.0% sensitivity and 92.6% specificity.

Conclusions

Kep value may be used to assess IDH mutation in glioblastoma as a radiogenomic biomarker.

Table. Area under the curve for ROC plotted for mean Kep value and IDH positivity



(Filename: TCT_1486_Table.jpg)

242

Large Vessel Occlusion Identification Using Machine Learning on Computed Tomography Angiography

S Lingam¹, L Remedios¹, B Landman², S Clark³, L Davis³

¹Vanderbilt University & Vanderbilt Institute for Surgery and Engineering, Nashville, TN, ²Vanderbilt University, Vanderbilt Inst. for Surgery & Engineering, Vanderbilt University Medical Ctr, Nashville, TN, ³Vanderbilt University Medical Center, Nashville, TN

Purpose

Patients with acute ischemic stroke due to large vessel occlusion (LVO) are at high risk for severe outcomes and benefit from early identification and reperfusion. Machine learning may aid this process, yet studies are limited on automated identification of LVO using computed tomography angiography (CTA). Our objective was to train a convolutional neural network (CNN) to identify LVO using CTA.

Materials and Methods

Stroke-alerted patients from a comprehensive stroke center during the period November 2017 – May 2019 were included. Exclusion criteria were missing or poor-quality images, intracranial hemorrhage or implant, or rare pathology including posterior circulation LVO. LVO labels were per chart review or neuroradiologist interpretation. Images were processed with registration, skull removal, intensity adjustment, and generation of 40mm axial maximum intensity projection images (MIP) to optimally depict anterior circulation. Figure 1 shows examples of processed images. Phi-Net [1], a deep CNN implemented using Keras and TensorFlow, was trained with 10-fold cross-validation for binary classification of LVO or no LVO. Dataset overall was balanced, though not necessarily in each fold, and 20% was held out for future test set use.

Results

Among 300 eligible patients, LVOs were 57% left-sided, 21% internal carotid artery, 55% M1, and 24% M2. See Table 1 for other clinical characteristics and demographics. Training included 240 patients. Mean metrics as 95% confidence intervals for test sets across 10 folds are precision-recall area under the curve (AUC) 0.868 ± 0.095 , F1 score 0.856 ± 0.04 , and receiver operating

characteristic (ROC) AUC 0.919 ± 0.048 . Figure 2 shows precision-recall and ROC curves. At threshold 0.5, accuracy $85\% \pm 4\%$, precision $82.8\% \pm 8.1\%$, recall $90.9\% \pm 5.3\%$, and specificity $81.4\% \pm 8.7\%$ were calculated.

Conclusions

We successfully classified LVO presence with high performance. With input of a single preprocessed CTA MIP, our ROC-AUC is 0.92 as compared to previously reported values of 0.89 using multi-phase CTA MIPs [2], and 0.88 [3] and 0.86 [4] using 3-dimensional CTA. Scope for future work includes enhancement of network robustness with data augmentation and parameter tuning, trial of other networks, and incorporation of 3-dimensional, clinical, and potentially multi-institutional data. With improved performance and full automation, future translation into clinical practice may accelerate stroke triage decisions.

Figure 1: Example processed images for a) LVO and b) no LVO

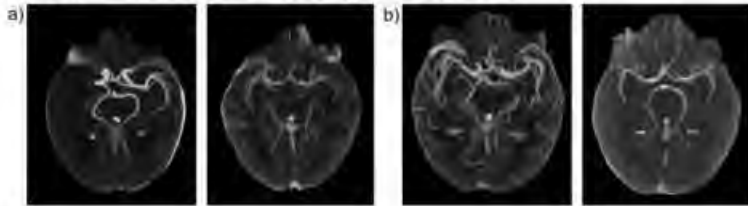


Figure 2: Curves for a) precision-recall and b) receiver operating characteristic

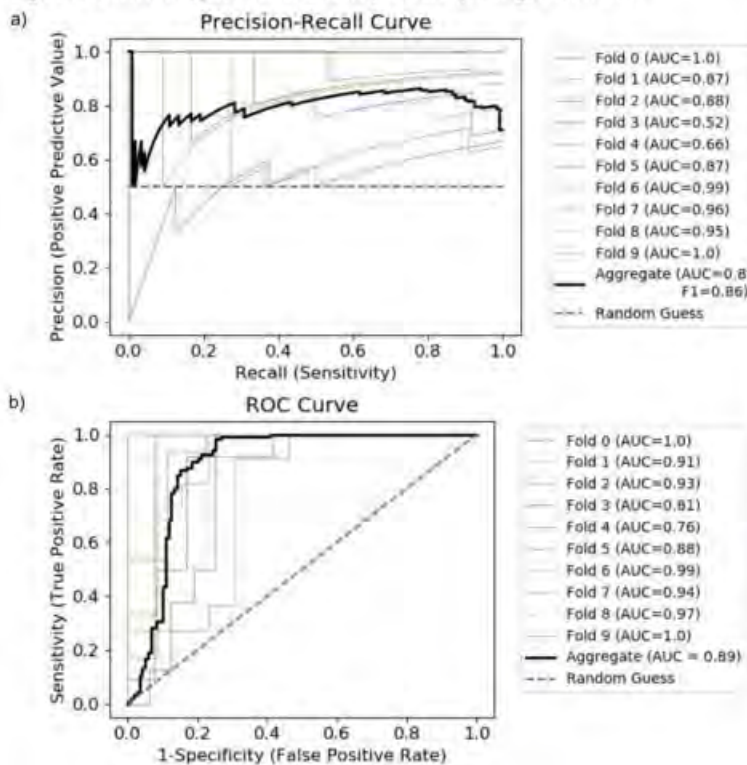


Table 1: Patient demographics and clinical characteristics

	No LVO (n=150)	LVO (n=150)
DEMOGRAPHICS		
Age, median (IQR) ^a	66 (54-76)	65 (55-76)
Female, %	53	44
Race, %		
Black	17	13
White	79	82
Other or Unknown	3	5
State of Residence, %		
Tennessee	83	75
Kentucky	13	12
Other	4	13
PAST MEDICAL HISTORY, %		
Hypertension	66	63
Diabetes	28	22
Hyperlipidemia	35	37
Smoking	31	35
Coronary Artery Disease	20	22
Congestive Heart Failure	10	14
Atrial Fibrillation	14	28
On Anticoagulation Medication	9	19
Prior Stroke or TIA ^b	21	19
STATUS ON ARRIVAL		
Transfer from Outside Hospital, %	38	67
NIHSS ^c on arrival, median (IQR)	4 (1-11)	14 (8-19)
SBP ^d , median (IQR)	156 (137-185)	155 (140-173)
INTERVENTION		
Received IV tPA ^c , %	25	39
Had Thrombectomy, %	N/A	55
Reperfusion with Thrombectomy, %	N/A	87
TIME INTERVALS (minutes), median (IQR)		
Last Known Well to VUMC Arrival	330 (128-645)	284 (151-571)
Arrival to Neurology Evaluation	13 (7-21)	7 (3-13)
Arrival to CT Imaging	13 (6-26)	8 (3-13)
CT to Radiology Interpretation	25 (17-56)	25 (15-70)
Last Known Well to tPA Initiation	157 (105-181)	136 (10-178)
Arrival to OR ^e for Thrombectomy	N/A	63 (53-79)
Last Known Well to Reperfusion	N/A	368 (247-708)
OUTCOMES		
Length of Stay (days), median (IQR)	3 (1-5)	5 (3-9)
Disposition, %		
Expired	3	13
Home	64	29
Rehab Facility	17	25
Skilled Nursing	12	23
Hospice	1	5
Other	3	6

(a) Interquartile range, (b) transient ischemic attack, (c) National Institutes of Health Stroke Scale, (d) systolic blood pressure, (e) intravenous tissue plasminogen activator, (f) operating room

(Filename: TCT_242_asnr_image_10302020.jpg)

305

Lateral Decubitus vs Supine Positioning for Transforaminal Lumbar Puncture: An Anatomical Study

E Nagarajan¹, C OZUTEMIZ¹, N Rubin¹, D Nascene¹

¹University of Minnesota, Minneapolis, MN

Purpose

The transforaminal lumbar puncture (TFLP) is an alternative to traditional lumbar puncture that has been used to deliver nusinersen effectively to patients with spinal muscular atrophy (SMA) who have extensive spinal fusions that preclude traditional access. When planning TFLP in SMA patients, organs such as colon or kidney may lie along ideal needle trajectories in supine position. We noted that abdominal organs frequently shift position when scoliotic patients move from supine to lateral decubitus positioning, allowing us to safely perform TFLP without injuring any organ. Here we quantify the change in organ distance from a theoretical needle path when patients are placed in lateral decubitus positioning for safer access in TFLP.

Materials and Methods

98 image-guided TFLPs for nusinersen injection in 13 patients with SMA were analyzed to assess the impact of lateral decubitus

positioning on kidney and colon position. Angle of patient rotation and the distance of the nearest abdominal organ to a theoretical needle path were compared between lateral decubitus scans and supine baseline scans for each patient for the vertebral levels L2-S1. A one-sample t-test was used to analyze significance of organ distance between lateral decubitus and supine scans. Mixed-effects linear regression modeling was used to analyze association between angle of rotation and organ movement.

Results

The distance of vulnerable organs from a theoretical needle path significantly increased from baseline to procedural scans at all measured vertebral levels with an overall mean increase in 14.6 mm of safe distance (all $p < 0.001$). The degree of patient rotation had a significant positive association with the distance of organ movement at the L2-3 level (L2: $p = 0.018$; L3: $p = 0.016$), but not at other levels.

Conclusions

This study quantitatively supports that lateral decubitus positioning for TFLP increases distance from abdominal organs from a theoretical needle path at all levels compared to supine position.

514

Lesion-deficit relationships defined using NIHSS sub-scores in acute ischemic stroke patients

D Rajashekar¹, M Wilms², M MacDonald³, S Schimert¹, M Hill⁴, M GOYAL³, A Demchuk², S Dukelow⁵, N Forkert⁵

¹University of Calgary, Calgary, Alberta, ²Cumming School of Medicine, University of Calgary, Calgary, Alberta, ³Cumming School of Medicine, University of Calgary, Calgary, Alberta, ⁴Cumming School of Medicine, University of Calgary, Calgary, Alberta, ⁵University of Calgary, Calgary, Alberta

Purpose

Lesion-symptom mapping (LSM) is a statistical technique to investigate the population-specific relationship between structural integrity post-stroke and clinical outcome scores [1]. The critical regions identified using LSM might prove useful to predict long-term clinical outcome of patients. These analyses are typically conducted using total assessment scores that encompass a variety of functional or neurological deficits induced by stroke, which might skew the LSM results towards overrepresented functions assessed, e.g. motor function in NIHSS. This motivates the use of sub-score information in the LSM framework to investigate category-specific structure-function relationships.

Materials and Methods

Using a multivariate technique, LSM analyses were conducted using 180 patients from the ESCAPE trial [2] with NIHSS assessment at 48-hours post-stroke. Therefore, the lesions from follow-up NCCT and FLAIR scans were manually segmented and registered non-linearly to a common NCCT-FLAIR elderly brain atlas [3] using ANTs. The NIHSS sub-scores were grouped into six categories (consciousness, language, motor, sensory, vision, and ataxia) and LSM was conducted independently for each category and the total NIHSS score. Brain regions were delineated using the AALCAT atlas [4,5], which includes grey and white matter regions. Critical regions and tracts were defined as those that are in the highest quartile (Q4) in either volume overlap or average LSM score.

Results

The results reveal that the sub-score maps not only identify most of the brain regions that are identified as critical by the total NIHSS score LSM analysis, but also reveal additional brain regions critical to each category of NIHSS assessment. For this MCA stroke sample, the consciousness LSM-map is predominantly right hemispheric while the language LSM map is left hemispheric. Bilateral critical association of the arcuate and corticospinal tract were found for the motor LSM-map, whereas critical regions are only in the right hemisphere in sensory LSM-map. Finally, the vision LSM-map shows bilateral critical regions, while the ataxia LSM-map shows right hemispheric dominance (see Tab 1).

Conclusions

The proposed framework to extend the use of LSMs using sub-score information leads to more detailed function-specific results, which might improve predictive modeling of stroke outcomes based on neuroimaging findings.

Region	Consciousness	Language	Motor	Sensory	Ataxia	Vision	Total
Left hemisphere							
Anterior segment	X	X	X	X	X	X	0.37 ± 0.21
Arcuate fasciculus	X	X	0.21 ± 0.09	0.19 ± 0.08	X	0.27 ± 0.14	0.0.3 ± 0.17
Corpus callosum	X	0.29 ± 0.09	X	X	X	X	X
Corticoponto cerebellum	X	X	0.23 ± 0.11	X	X	X	0.32 ± 0.16
Corticospinal tract	0.13 ± 0.03	0.2 ± 0.09	0.22 ± 0.09	X	0.22 ± 0.11	0.23 ± 0.13	X
Heschl's gyrus	X	0.35 ± 0.16	X	X	X	X	X
Long segment	X	X	X	X	X	X	0.32 ± 0.15
Postcentral gyrus	X	X	X	X	X	X	0.34 ± 0.18
Rolandic operculum	X	0.36 ± 0.19	X	X	X	X	X
Insula	X	0.32 ± 0.19	X	X	X	X	X
Right hemisphere							
Anterior segment	X	X	0.34 ± 0.04	X	X	X	0.19 ± 0.6
Anterior commissure	X	X	X	X	0.38 ± 0.22	X	X
Arcuate fasciculus	0.34 ± 0.21	X	0.23 ± 0.1	X	0.16 ± 0.05	X	X
Caudate	X	X	X	0.22 ± 0.1	X	X	X
Corticospinal tract	0.27 ± 0.16	X	0.33 ± 0.19	0.28 ± 0.18	X	X	0.18 ± 0.06
Corticoponto cerebellum	0.2 ± 0.07	X	0.33 ± 0.18	0.34 ± 0.21	X	X	X
Inferior longitudinal fasciculus	X	X	X	X	0.38 ± 0.23	X	X
Internal capsule	0.18 ± 0.06	X	X	0.32 ± 0.18	X	X	X
Long segment	0.43 ± 0.23	X	X	X	X	X	X
Pallidum	X	X	X	X	0.24 ± 0.12	X	X
Supramarginal gyrus	X	X	X	X	0.2 ± 0.08	X	X
Rolandic operculum	0.22 ± 0.09	X	X	X	X	0.36 ± 0.21	X
Temporal superior	X	X	X	X	X	0.38 ± 0.23	X

Table 1: Summary of critical regions across all six categories and the total score. The average score per region is calculated only using the non-zero voxels of the respective LSM maps.

(Filename: TCT_514_anstr-table-cropped.jpg)

391

Machine Learning based Differentiation of Glioblastoma from Brain Metastasis using MRI derived Radiomics Features

G Bathla¹, S Priya², C Ward³, Y Liu⁴, H Zhang⁵, N Le⁵, N Soni⁶, R Maheshwarappa¹, M Sonka⁷

¹University of Iowa Hospitals and Clinics, Iowa City, IA, ²University of Iowa hospitals and Clinics, IOWA CITY, IA, ³Univ of Iowa, Iowa City, IA, ⁴University of Iowa, Iowa City, IA, ⁵The Iowa Initiative for Artificial Intelligence, Iowa City, IA, ⁶UIHC, Iowa, IA, ⁷The University of Iowa, Iowa City, IA

Purpose

A few prior studies have addressed radiomics based differentiation of Glioblastoma (GBM) and intracranial metastatic disease (IMD). However, the effect of different tumor masks, comparison of single versus multiparametric MRI (mp-MRI) or ideal combination of sequences remains undefined. We cross-compared multiple radiomics based machine learning (ML) models across different tumor masks using mp-MRI to determine optimized configurations.

Materials and Methods

Our retrospective study included 50 GBM and 50 IMD (breast and lung primary) patients. Forty-five different combinations of ML models and feature selection strategies were assessed for features extracted from whole tumor and edema masks using mp-MRI [T1W, T2W, T1-contrast enhanced (T1CE), ADC, FLAIR], individual MRI sequences, and combined T1-CE and FLAIR sequences. Model performance was assessed using receiver operating characteristic curve.

Results

For mp-MRI, the highest performing model was LASSO fit using full feature set (AUC 0.953). FLAIR was the best individual sequence with highest performance (LASSO-full feature set, AUC 0.951). For combined T1-CE and FLAIR sequence, AdaBoost was the best model fit using full feature set (AUC 0.951). No significant difference was seen between the top performing models across all scenarios. Most of the important features were extracted from whole tumor mask and shape sphericity was the important feature.

Conclusions

Diagnostic performance of radiomics based machine learning models is comparable for single FLAIR sequence, mp-MRI and combined T1-CE and FLAIR sequence, suggesting that radiomics features derived from FLAIR alone could suffice for accurate distinction between GBM and IMD. Shape sphericity is an important discriminating feature.

Mean (SD) of performance metrics for two best performing models using all sequences, individual sequences, and T1-CE and FLAIR sequences

Performance Metric	Model					
	LASSO Full All Seqs	Elastic Net Full All Seqs	LASSO Full F	Elastic Net Full F	adaBoost Full CE + F	LASSO Full CE + F
Brier	0.088 (0.036)	0.088 (0.036)	0.083 (0.042)	0.088 (0.043)	0.086 (0.040)	0.102 (0.026)
Accuracy	0.892 (0.061)	0.892 (0.063)	0.897 (0.054)	0.885 (0.054)	0.888 (0.063)	0.887 (0.070)
ROC AUC	0.953 (0.041)	0.952 (0.038)	0.951 (0.049)	0.948 (0.049)	0.951 (0.040)	0.950 (0.042)
Sensitivity	0.887 (0.086)	0.893 (0.092)	0.917 (0.064)	0.903 (0.071)	0.900 (0.080)	0.907 (0.088)
Specificity	0.897 (0.073)	0.890 (0.079)	0.877 (0.094)	0.867 (0.102)	0.877 (0.111)	0.867 (0.115)

LASSO (least absolute shrinkage and selection operator; Enet, elastic net; ada: boosting of classification trees with adaBoost; F: FLAIR; CE: T1-CE

(Filename: TCT_391_GBMvsIMD.JPG)

612

Magnetic Resonance Fingerprinting (MRF) of Peritumoral White Matter in Glioblastomas

C Tippareddy¹, W Zhao², D Ma², A Sloan³, J Barnholtz-Sloan³, J Sunshine¹, M Griswold², C Badve⁴

¹N/A, N/A, ²Case Western Reserve University, Cleveland, OH, ³University Hospitals, Cleveland, OH, ⁴University Hospitals of Cleveland, Cleveland, OH

Purpose

Magnetic resonance fingerprinting (MRF) can differentiate between tumor types and grades (1, 2). Here, we assess peritumoral white matter in glioblastomas using radiomics analysis of magnetic resonance fingerprinting (MRF) maps to identify areas of tumor infiltration and retrospectively characterize areas of future tumor recurrence.

Materials and Methods

Whole brain 3D MRF imaging was performed in 22 untreated GB patients in an IRB approved study. The peritumoral white matter (PW) with T2/FLAIR hyperintensity surrounding the enhancing tumor (zone 1) was segmented. The PW region was divided into near (zone 2, within 1 cm of ST margin) and distant (zone 3, all signal abnormality beyond zone 2) regions and radiomic analysis was performed (Fig. 1A). In a subset of 5 patients with proven recurrence on subsequent MRI, the site of future recurrence (FRS) was analyzed on baseline MRF maps and compared with adjacent distant white matter with T2/FLAIR abnormality. Using GLCM and GLRLM, 38 different texture features were calculated for each region. Paired t-tests were used to compare zone 2 versus zone 3, as well as to compare FRS to distant white matter. A p value of less than 0.05 was considered significant.

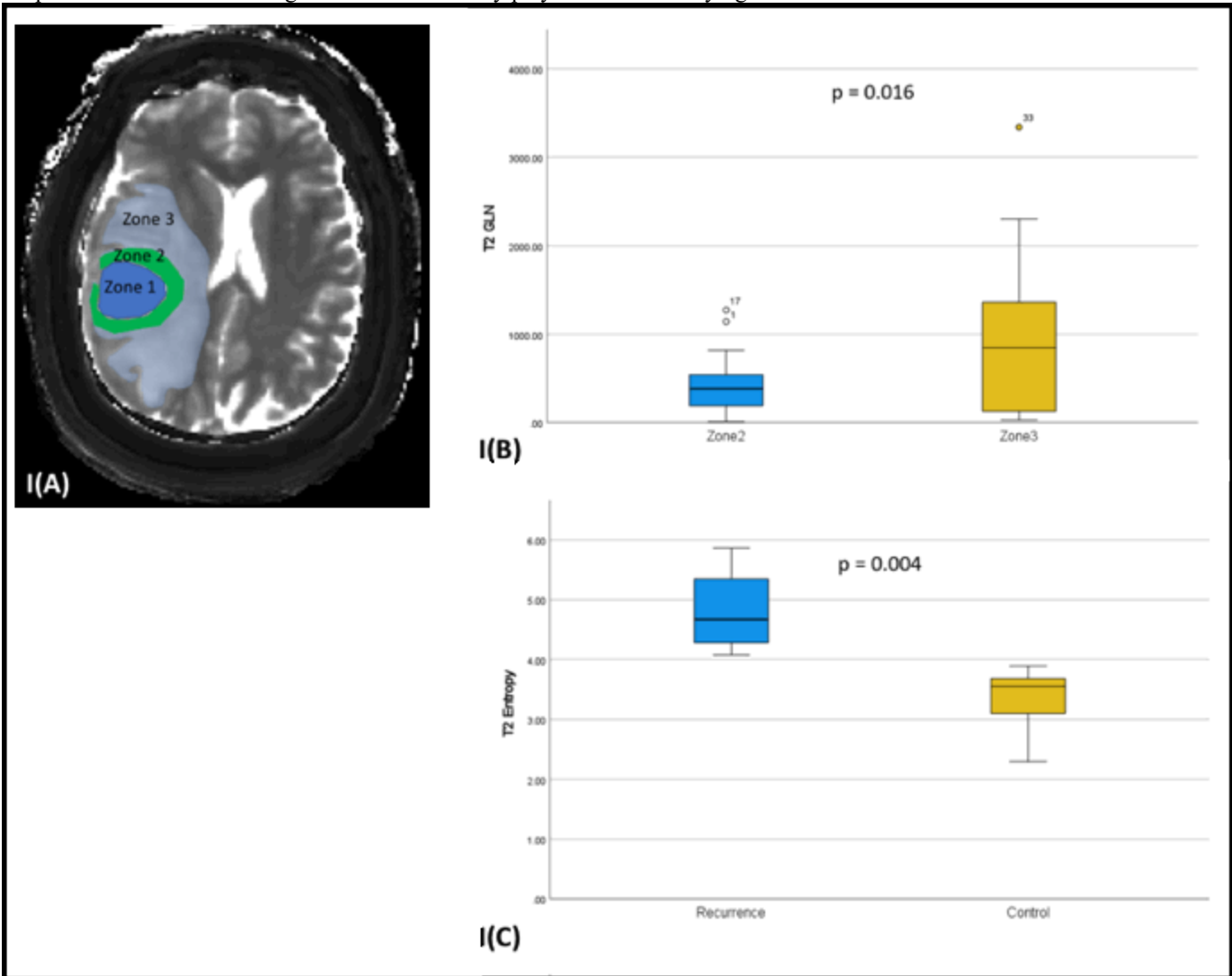
Results

Multiple texture features derived from MRF T1 and T2 maps demonstrated statistically significant difference between zone 2 and zone 3 as well as between FRS and adjacent white matter. Differences in T1 correlation, GLN and T2 Entropy, sum entropy were identified in both analyses and the differences were more pronounced in the subset analysis of future recurrence sites (Fig. 1B,C).

Conclusions

T2/FLAIR hyperintense peritumoral region in GBs consists of a combination of edema and tumor infiltration. Tumor infiltration is more frequently identified closer to the enhancing tumor and is a key cause of subsequent tumor recurrence which often occurs closer to the resection margins. Tumor infiltration cannot be identified based on current clinical imaging techniques. This study demonstrates

the capability of MRF based radiomics to quantitatively differentiate between near and far zones in the PW region. The subset analysis in GBs with proven recurrence further support these findings and suggest that MRF has the potential to offer a quantitative biomarker for peritumoral infiltration in glioblastomas and may play a role in identifying sites of future recurrence.



(Filename: TCT_612_Figure1.gif)

1405

Magnetic Resonance Imaging findings in children with first-time afebrile seizures.

C Tsetse¹, A Khanal¹, S Destian², J George¹

¹SUNY Upstate Medical University, Syracuse, NY, ²SUNY upstate, East Syracuse, NY

Purpose

The objective of this study is to determine the frequency of clinically significant lesions on magnetic resonance imaging (MRI) in children with first time afebrile seizures and to determine whether intravenous (IV) contrast contributes to an increase in neuroimaging yield.

Materials and Methods

We reviewed the medical records, EEG and MRI findings of pediatric patients, aged 1 to 12 years, admitted between November 1, 2019 and October 31, 2020 with a first unprovoked, afebrile seizure. Patients with known predisposing conditions for seizure were excluded. All patients had MRI using our departmental pediatric seizure protocol. MRI reports were categorized as normal and abnormal. The abnormal MRI findings are re-classified as follows: • Clinically significant MRI abnormality – Abnormal MRI finding correlated with both EEG finding and description of seizure type, or description of seizure type was nonspecific, but the abnormal MRI finding correlated with the EEG finding. • Indeterminate MRI abnormality- Abnormal MRI finding correlated with either EEG abnormality or description of seizure type but not both, or the description of seizure type was nonspecific, and EEG was normal, but MRI was abnormal. • Insignificant MRI abnormality – Abnormal MRI finding with no correlation to EEG finding or description of seizure type.

Results

Sixty-five children with a mean age of 5.9 ± 3.4 years met the inclusion criteria. Of the 65 subjects, 38 (58.0%) were males and 27 (42.0%) were females. MRI was positive in 29% (19/65) and negative in 48% cases (46/65). Of the positive MRI results, potential clinically significant lesions comprised 32% (6/19), indeterminate lesions 42% (8/19) and insignificant abnormalities comprised 26 % of the cases (5/19). Clinically significant MRI lesions included focal cortical dysplasia (n = 1), Agyria-pachygyria (n =1), Temporal lobe cystic mass (n =1), Hypoxic ischemic encephalopathy (n =1), Porencephalic cyst (n =1), and Lobar infarcts (n = 1). 58/65 patients had contrast MRI exams. Only 5 cases had a finding on the contrast portion of the exam (cystic right temporal lobe mass, right lateral ventricular cyst, hyperintense white matter lesions and DVA), although not necessarily the etiology of the seizures.

Conclusions

In children with first-time seizure, a clinically significant abnormality on MRI occurred with relatively low frequency. The use of intravenous contrast is not routinely necessary, but it is useful when neoplasm or inflammatory conditions are suspected.

Table 2: Clinically significant abnormalities on MRI

No.	Age	Gender	Seizure type	MRI abnormality	EEG findings
1.	3y	M	Focal	Porencephalic cyst with surrounding gliosis.	Abundant spike and wave located over right parietal region.
2.	7y	M	Focal	Focal cortical dysplasia in left temporo-parietal lobe.	Occasional spike and wave discharges over left occipital region.
3.	14m	F	Focal	Hypoxic Ischemic Encephalopathy with bilateral cerebral cortex involvement.	Normal.
4.	12y	M	Myoclonic	Agyria-pachygyria	Hypsarrhythmia.
5.	15m	F	Seizure-like activity	Left frontal lobe infarcts.	Focal high voltage slowing over the left frontotemporal region.
6.	2y	F	Seizure-like activity	Cystic mass lesion in right temporal lobe.	Frequent rhythmic delta slowing over right temporal region.

Table 3: Indeterminate abnormalities on MRI

No.	Age	Gender	Seizure type	MRI abnormality	EEG findings
1.	8y	F	Focal and generalized	Unmyelinated anterior medial temporal white matter.	Potential frontal epileptiform discharges.
2.	8y	M	Generalized	Mild right hippocampal volume loss.	Right temporal discharge with spread to left temporal and frontal region.
3.	10y	M	Focal with generalization	Small left middle cranial fossa arachnoid cyst.	Focal left temporal epileptiform discharge.
4.	7y	M	Generalized	Mild right hippocampal volume loss.	Frontal epileptiform discharges.
5.	7y	F	Seizure-like activity	Bilateral corona radiata white matter lesions.	Normal.
6.	12y	M	Seizure-like activity	Mild right hippocampal volume loss.	Normal.
7.	33m	M	Seizure-like activity	Right middle cranial fossa arachnoid cyst.	Normal.
8.	3y	F	Seizure-like activity	Right lateral ventriculomegaly with intraventricular cyst.	Normal.

(Filename: TCT_1405_Table2and3.GIF)

T NGUYEN¹, A Vaussy², C Habas³

¹C.H.N.O. QUINZE VINGTS PARIS, PARIS (12ÈME ARRONDISSEMENT), PARIS, ²SIEMENS HEALTHCARE, Saint Denis, France, ³C.H.N.O. QUINZE VINGTS PARIS, PARIS (12ème Arrondissement), France

Purpose

To assess the clinical performance of a 3D Fast Grey Acquisition T1 Inversion Recovery (FGATIR) sequence in MS patients for identification of brainstem tracts and nuclei damages.

Materials and Methods

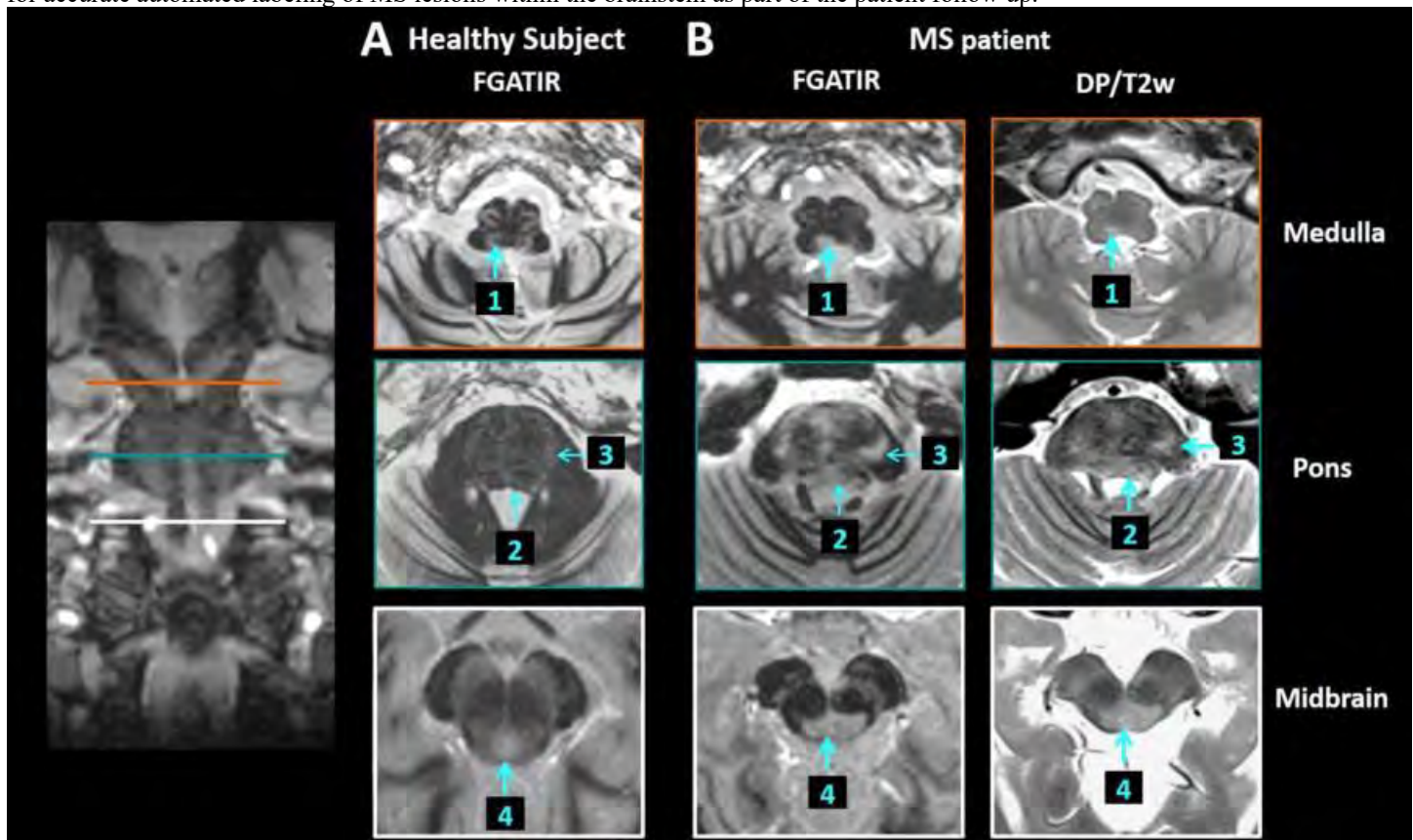
MRI was performed on a 3T system (MAGNETOM Skyra, Siemens Healthcare, Germany) using a 64-channel coil. From June 2019 to June 2020, 10 healthy volunteers and 100 patients (35% male, mean age 36) followed for MS in our neuro-imaging department were recruited. The study was approved by our Institutional Review Board and written informed consent was obtained from all participants. The 3D FGATIR (0.9x0.9x1.6 mm, scan time = 14 min 40) was first performed on healthy volunteers to classify tracts and nuclei macroscopically identifiable on the brainstem as described by Shepherd et al (1). Then, the 3D FGATIR was assessed in MS patients for lesion location within the brainstem in comparison to 2D DP/T2w (0.6x0.6x3mm, scan time = 3 min 30).

Results

In healthy volunteers, FGATIR allowed a precise visualization of tracts and nuclei within the brainstem according to their myelin density (Figure 1-A). Including the FGATIR sequence in the MR protocol enabled to identify elective structures affected by MS lesions (figure 1-B). Most damaged tracts were found on the pontocerebellar tract and cortico-spinal tract with a respective prevalence of 73 and 60 patients. Most frequently affected nuclei were the trigeminal group (51/100), the facial nerve (46/100), the vestibular nuclei (34/100), and the solitary tract (33/100). Of note, FGATIR helped delineate the medial longitudinal fascicle extending throughout the brainstem, and frequently responsible for internuclear ophthalmoplegia in MS patients (27/100).

Conclusions

We demonstrated that the 3D FGATIR provided a high signal discrimination allowing a macroscopic identification of internal brainstem structures. In this study, this sequence was applied to 100 MS patients and discriminated tracts and nuclei recurrently damaged within the brainstem. Data obtained with 3D FGATIR could be used to train an artificial neural network (machine learning) for accurate automated labeling of MS lesions within the brainstem as part of the patient follow up.



(Filename: TCT_630_FigureFGATIRArticle2.jpg)

Purpose

Medical malpractice claims in radiology ranked eighth highest among all subspecialties and medicolegal exposure continues to be a major concern for neuroradiologists.[1] Legal fees costs physicians in all specialties nationally upwards of \$10 billion annually.[2] The purpose of this study is to document the factors that contribute to verdicts and settlements resulting in indemnity payments in the field of neuroradiology.

Materials and Methods

Publicly available verdict reports from the Casetext national legal database were selected using the search terms "medical malpractice," "neuroradiology," and "neuroradiologist" with a date region from 1999 to 2019. These cases were analyzed for the alleged causes of malpractice, resulting injury, findings, and indemnity payment if applicable.

Results

The database search yielded 141 cases with 17% of cases (n = 24) involving neuroradiologists as defendants with the remaining cases involving neuroradiologists as expert witnesses in medical malpractice cases involving specialties outside of radiology. Of the cases involving neuroradiologists at defendants, 4 were dismissed, 1 was settled out of court, and the remaining 19 went to trial. Of those cases that went to trial, 58% saw defense verdicts (n= 11) and 42% saw plaintiff verdicts (n = 8). 23 cases (96%) claimed misdiagnosis and 1 (4%) claimed procedure complication. The majority of alleged misdiagnoses involved missed tumors (n=6), missed hemorrhage (n=5), or missed arterial occlusion or stroke (n=5). Overall, 62% of cases showed judgments in favor of the neuroradiologist.

Conclusions

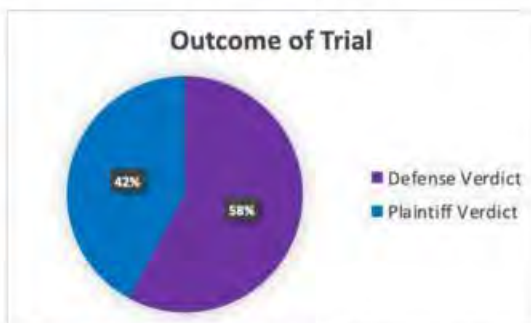
The main factor prompting a malpractice case in neuroradiology was misdiagnosis, with missed tumors, strokes, and hemorrhage making up the bulk of the cases. However, the majority of malpractice judgements favor the radiologist.



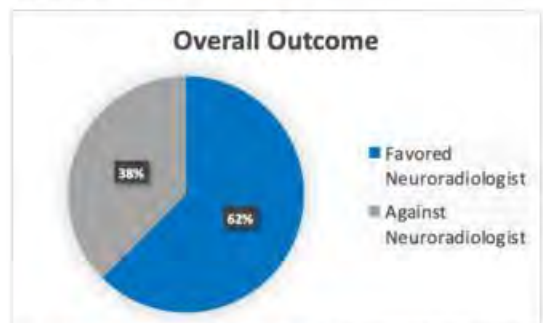
A. Role of Neuroradiologist cited in lawsuits.



B. Determination of lawsuit that cited neuroradiologists as defendants.



C. Outcome of trial of all cases that cited neuroradiologists as defendants.



D. Overall outcomes of all cases that cited neuroradiologists as defendants.

Mandibular Arteriovenous Malformation (AVM) Diagnosis and Curative Treatment

W Yakes¹

¹The Yakes Vascular Malformation Center, Englewood, CO

Purpose

To determine optimal management strategies for the treatment of intraosseous mandibular AVM.

Materials and Methods

12 patients (9 females, 3 males), age 9 -14; mean age 10, underwent endovascular therapy to treat their mandibular AVMs. 9 patients had distinct intraosseous AVMs. 3 had additional multiple facial and intra-maxillary AVMs requiring treatment. Outside institutions recommended massive hemi-facial resections in these patients. 4 patients had prior PVA and gel foam embolization, 1 patient had a lip graft, 1 had prior mandible surgery, all that had failed.

Results

All 12 patients have demonstrated MR and angiographic cure of their AVMs. 1 patient's therapy is not completed and is on-going. The patients mandibular AVMs cured, a third AVM in this patient in the infratemporal fossa is still undergoing treatment. The follow-up range is 11 months – 41 months, with a mean follow-up of 29 months. No complications were noted in treatment of mandibular AVMs. 1 patient required a minor gingival surgery after treatment of an additional intramaxillary AVM with inferior extension.

Conclusions

Endovascular approaches to manage mandibular AVM can be curative. The mandibular intraosseous variety is largely a fistula between artery and vein within the bone and the bulk are Yakes Type IIIa/IIIb AVMs. All respond and can be cured by endovascular ethanol therapy alone. Surgery was not required in any patient. Surprisingly no complications were encountered in this patient series. Long-term cures are noted in this patient series with endovascular approaches alone. No massive surgical resections in any patient, even in patients with multiple AVMs of the soft tissues, mandible and maxilla, was required to effect cure. In patients who suffered hemorrhages from floating teeth, bone formed and stabilized the teeth and no further hemorrhages occurred. Ethanol sclerotherapy proved curative in mandibular intraosseous AVMs in patients who had additional facial soft-tissue and intramaxillary AVMs that were cured as well at long-term follow-up.

591

Marshall, Rotterdam and Helsinki Prognostic CT Scoring Models in Traumatic Brain Injury Patients-A Comparative study

M Jayakumar¹, N BR², A Rangari³

¹AMD Imaging Systems and Solutions, Chennai, Tamilnadu, ²Bangalore Medical College, Bangalore, Karnataka, ³SCTIMST, Trivandrum, Trivandrum, Kerala

Purpose

Traumatic Brain Injury(TBI) is a major contributor to disability, mortality and socio-economic loss in developing countries. Marshall, Rotterdam and Helsinki CT scores were developed as prediction outcome scales by computing early CT abnormalities.

Prognostication and early outcome prediction can streamline clinical management and resource allocation .This study aims to evaluate the novel Helsinki CT score for predicting early outcome, in comparison with the Rotterdam CT score, Marshall CT classification and also assess which individual components of the CT scores best predict outcome.

Materials and Methods

This retrospective study included 280 consecutive TBI patients who underwent CT head scans at our centre from July 2017-June 2018. After calculating all three CT prognostic scores, a comparison across scale performances in predicting patients' early mortality and early outcome (by using GOS) was made. Area under the receiver operating characteristic curve (AUC) was used as the discriminatory power of each system. Independent CT scan outcome predictors were also identified after appropriate statistic analysis was carried out.

Results

The mean age of the patients in the study was 61.1 years, overall mortality was 18.6% and mean Glasgow coma score was 11. More deaths occurred among patients with higher scores (all P < 0.01). The areas under AUCs indicated that all scoring systems had high discriminative power in predicting early mortality. In comparison with Marshall and Rotterdam Scores, Helsinki score provided a better positive predictive value for mortality . Overall prognostic performance was more accurate for the Helsinki CT score. Midline shift, cistern obliteration, SAH, IVH and large mass lesions were found to be independent mortality predictors.

Conclusions

According to this study, Helsinki Scoring system is a better prognostic model for TBI with improved outcome prediction accuracy, although Marshall, Rotterdam systems also have good predictability and can guide clinical management. However large scale studies are needed for validation of the presented results.

Mastoid Effusion and Seventh and Eighth Nerve Enhancement in Patients with Lyme Disease

A Sahi¹, S Matharu¹, K Srinivasan¹, S Vellala¹, A Siddiqui², R Tu³, S Kathuria⁴, H Mangat⁵

¹University of Maryland-College Park, College Park, MD, ²Virginia Commonwealth University, Clarksburg, MD, ³MedStar Health, Baltimore, MD, ⁴Charter Radiology, Clarksville, MD, ⁵Howard University College of Medicine, Washington, DC

Purpose

Mastoid effusion is an accumulation of fluid in the mastoid cells in the mastoid process. When these cells pneumatize, the bone marrow develops honeycomb-shaped cavities where the fluid accumulates. The 7th and 8th nerves enter the petrous temporal bone at the internal auditory meatus and traverse the auditory canal; the 7th nerve continues into the mastoid process. Fluid aggregation within the outlying air cells is an indication of inflammation around the mastoid portion of the 7th nerve. Patients with Neuroborreliosis, the neurological form of Lyme Disease, have manifested mastoid effusion and enhanced 7th and 8th nerves [1]. On a 1.5-tesla MRI, the enhancement of these nerves are invisible [2,3]. However, on a 3-tesla MRI the abnormalities at the seventh and eighth nerves become apparent. This study demonstrates the significance of using a 3-tesla MRI to report findings of mastoid effusion, enhancement of the 7th nerve in the mastoid region, and enhancement of the 8th nerve in the IAC in patients with Neuroborreliosis.

Materials and Methods

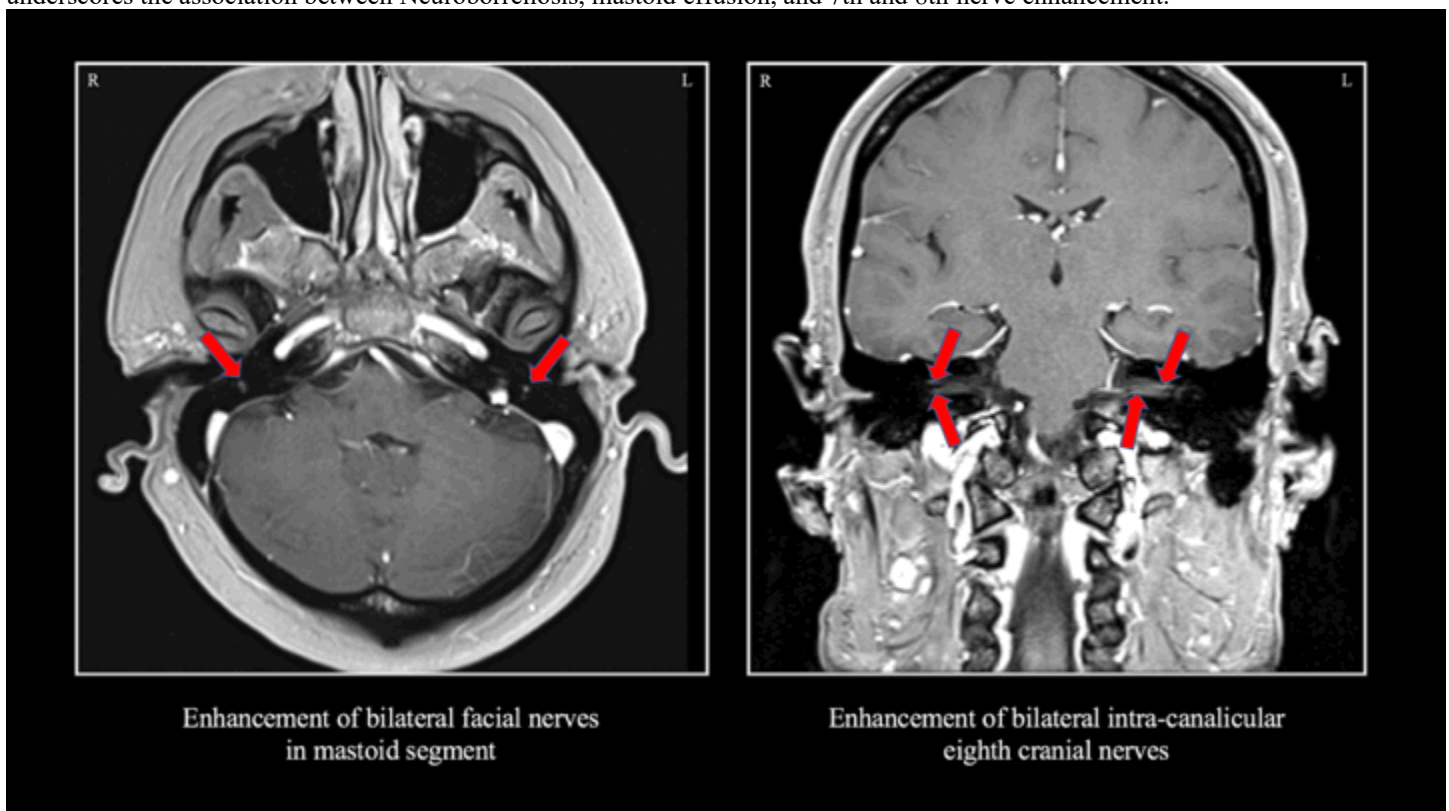
Retrospective studies were conducted on 53 patients with Neuroborreliosis from August 2017 until January 2020. Criteria for selection included a 3-tesla MRI of the internal auditory canal, lateral or orthogonal diplopia, and/or Argyll Robertson pupil. Patient data was taken from a Lyme endemic area of Maryland and analyzed by multiple neuroradiologists. P-values were obtained by comparing confirmed Neuroborreliosis with mastoid effusion, seventh and eighth (IAC) nerve enhancement, accounting for lateral and orthogonal diplopia, and Argyll Robertson pupil.

Results

Out of 53 patients, 46 had an MRI of the internal auditory canals taken with a 3-tesla unit. 39 of the MRI-confirmed patients had mastoid effusion, 43 had 7th nerve enhancement in the mastoid segment, and 15 exhibited 8th nerve enhancement in the IAC. All patients in this study had previously been diagnosed with Neuroborreliosis. After running t-tests for Neuroborreliosis against 7th and 8th nerve enhancement and mastoid effusion, a statistically significant correlation with a p-value<0.01 was obtained across all comparisons.

Conclusions

Patients with Neuroborreliosis were found to have a statistically significant correlation with mastoid effusion, and 7th and 8th nerve enhancement on a 3-tesla MRI. Although more data will be needed to corroborate these findings, the statistical significance underscores the association between Neuroborreliosis, mastoid effusion, and 7th and 8th nerve enhancement.



(Filename: TCT_1240_Nerves.gif)

MEG Language Lateralization Compared with Functional MRI in a Pediatric Population

S Teixeira¹, W Gaetz², A Vossough³, D Zarnow⁴, K Shekdar², T Roberts⁵, E Schwartz⁶

¹The Children's Hospital of Philadelphia, Philadelphia, PA, ²Children's Hospital of Philadelphia, Philadelphia, PA, ³CHOP-UPENN, Philadelphia, PA, ⁴N/A, N/A, ⁵The Children's Hosp. Of Philadelphia, Philadelphia, PA, ⁶Children's Hosp. Of Philadelphia, Philadelphia, PA

Purpose

Magnetoencephalography (MEG) is a potentially valuable, noninvasive method for identifying epileptogenic regions and performing high-spatial and temporal resolution functional mapping in children.¹ Functional magnetic resonance imaging (fMRI) reflects fluctuations in the oxygen levels through hemodynamic changes, with the drawback of low temporal, but high spatial, resolution.² MEG and fMRI may be complementary, however, confidence in a single functional imaging modality is more desirable. We sought to investigate the MEG and fMRI agreement in identifying the cerebral hemisphere supporting language processing, particularly in cases of "weak" evidence for lateralization by MEG.

Materials and Methods

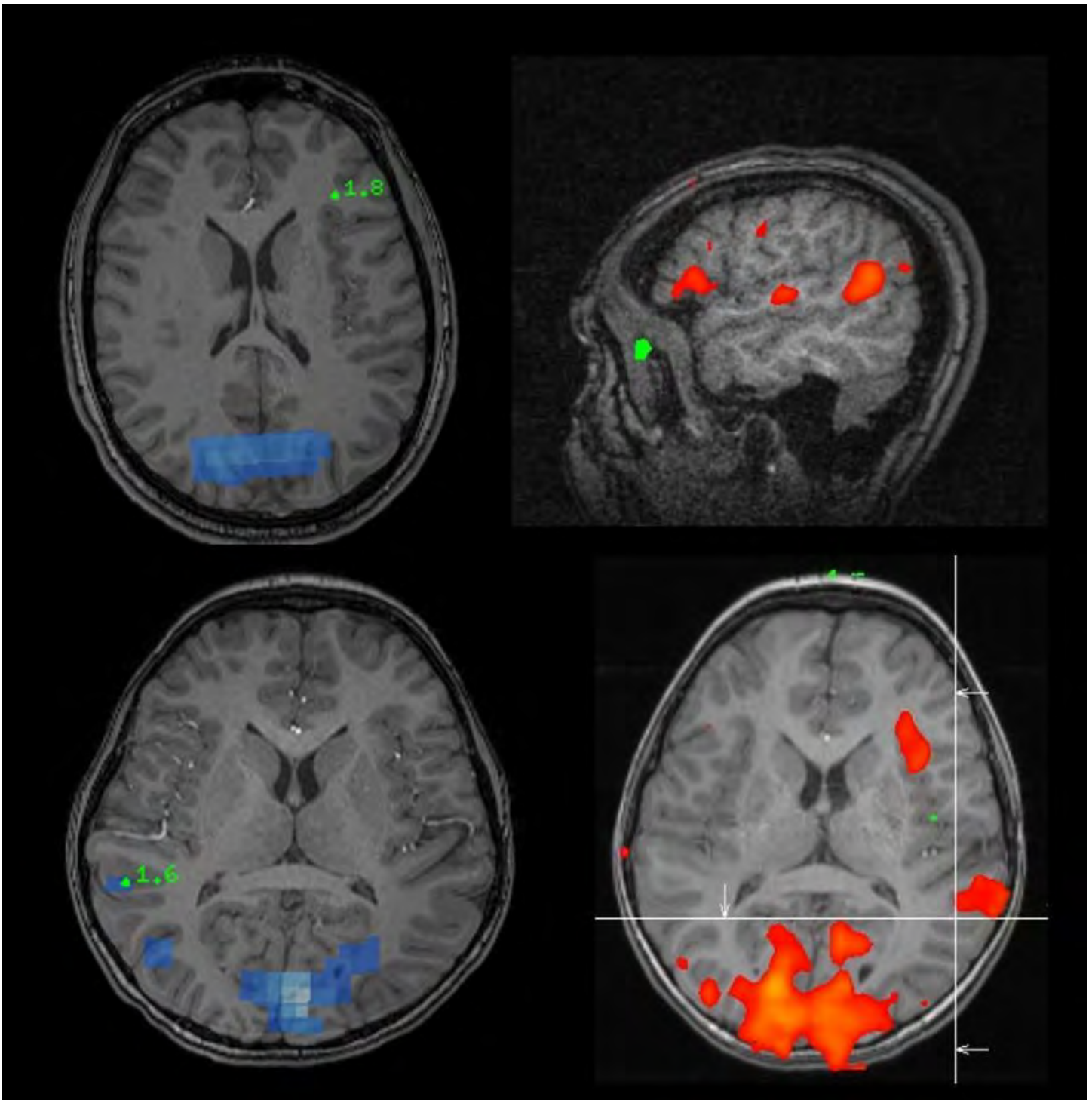
This is an institutional review board exempt, retrospective, cross sectional analysis of prospectively collected clinical data between 01/2007 and 07/2020. Inclusion criteria were: available reports for fMRI and MEG with language assessment performed in both imaging modalities. Language mapping with MEG was performed via assessment of hemispheric differences in areas of beta-band (15-30Hz) event-related desynchronization. fMRI was performed using gradient echo BOLD sequences. MEG support for language lateralization was considered "weakly" left sided when activity was identified bifrontally but only left posterior temporally.

Results

In total, 41 subjects were included; 15/41(36.6%) female. Median age was 13.6 years (IQR 10.2,16.6) at MEG and 14.4 years (IQR 10.9,16.8) at fMRI. Median of interval between MEG and fMRI was 77 days (IQR 9,226). MEG and fMRI language lateralization were concordant in 35/41(85.4%). In 16 cases of "weak" language activation on MEG, 14(87.5%) were concordant with fMRI results. The overall Cohen kappa coefficient was 0.59(95%CI[0.28,0.89]). In the 6 discordant cases, MEG identified activity in the right hemisphere (5/6 left hand dominant), while fMRI showed activation in the left hemisphere. In no case did MEG incorrectly indicate left hemisphere support for language.

Conclusions

We showed moderate to high agreement between MEG and fMRI in identifying the hemisphere supporting language processing, including those with weak activation on MEG, potentially obviating the need for subsequent fMRI in these children. Discordance was most commonly seen in left-handed patients with right hemisphere activity on MEG. While these data were collected in patients with epilepsy, one would expect MEG to perform even better when fMRI responses might be compromised by neurovascular uncoupling.



(Filename: TCT_1565_Picture2.jpg)

569

Meningeal Enhancement After Recent Lumbar Puncture

I Mark¹, W DILLON¹, J Villanueva-Meyer¹

¹UCSF, San Francisco, CA

Purpose

Meningeal enhancement on MRI has been reported after lumbar puncture (LP), attributable to loss of CSF volume or traumatic needle access that leads to blood in the subarachnoid space. The presence of meningeal enhancement after LP and its associations have previously been studied up to 30 days after LP. The purpose of our study was to examine the incidence of meningeal enhancement within 3 days after LP.

Materials and Methods

44 consecutive patients from January 1, 2019 to June 30, 2020 who underwent an MRI within 3 days of an image guided LP were included. MRI studies were evaluated for meningeal thickening and enhancement. LP procedural details were collected including needle size, opening pressure, quantity of CSF removed, and modality of image guidance. Additional data collected included patient age, alternative diagnoses associated with meningeal enhancement, and CSF analysis results including cell count and cultures.

Results

The mean age was 60.2 years. 17 (48.6%) patients were female. 11 (25%) patients had their MRI on the same day as their LP. 6/44 (13.6%) patients had meningeal enhancement, 5 of which were attributable to underlying pathologies including infection (2), sarcoidosis (1), metastatic disease (1), and preexisting CNS hypotension (1). Only one case (2.2%) of meningeal enhancement did not have an attributable cause. One patient underwent large volume lumbar puncture (32 ml), but did not have meningeal enhancement. Opening pressures were measured in 20 patients (range 7-40 cm H₂O).

Conclusions

Meningeal enhancement is a rare occurrence within 3 days after LP. Of the patients who underwent MRI within 3 days after LP, only 1 of 44 (2.2%) had unexplained meningeal enhancement. In the era of routine volumetric imaging, meningeal enhancement after LP may be rarer than previously thought, and likely indicative of underlying pathology.

1590

Metastatic Patterns of NF1 Molecular Subtype of Melanoma

J Sikder¹, A Mahajan², M Aboian³

¹Yale University School of Medicine, New Haven, CT, ²Yale University, New Haven, CT, ³Yale University, Woodbridge, CT

Purpose

Approximately 100,350 people are diagnosed and 6,850 people die every year from melanoma. NF1 molecular subtype melanoma has the highest mutational burden and increase risk of death with worse outcome survival than other mutations. Molecular subtyping of melanoma is gradually replacing more traditional methods of characterization in the current era of personalized medicine and targeted therapies. Metastatic patterns of melanoma are demonstrated to be driven by location of the sentinel lesion, therefore we propose that driver mutations within melanoma confer a unique identity and define metastatic patterns. Mutations are common in melanoma such as BRAF (50%), NRAS (13.25%), NF1 (12-18%), MEK1 (6%), KIT (2.6%), CTNNB1(2%–3%), GNA11 (2%), or GNAQ (1%). NF1 mutated subtype has a higher mutational burden with the strongest UV mutation signature illustrating differential biological and clinical characteristics. In our study, we describe the genomic and clinical characteristics of NF1 mutated melanoma that will help to direct image guidance, clinical follow up, and allow for the personalization of targeted therapies with a focus on published research.

Materials and Methods

Comprehensive analysis with review of published literature on NF1 mutated melanoma and its unique co-mutations and their clinical outcomes with applications to radiological significance were pursued. Images were reviewed using Visage Imaging Software with correlation to pathology, patient's oncologic history/treatments, and outcomes utilizing EPIC (Medical record system). Montage-Clinical Analytics for medical imaging was utilized to data mine.

Results

Comprehensive review of NF1 cases and their differential metastatic patterns were reviewed predominantly guided by tumor origin and molecular signature. Out of 2,746 patients with melanoma there were 11 found to have NF1 mutations. NF1 driver mutations were often associated with subjacent nodal metastases with lung often being the primary organ of metastases. About 27% (3/11) of the NF1 melanoma metastasized to the brain, however all of the brain metastases responded well to immunotherapy.

Conclusions

We present a comprehensive analysis of melanoma with NF1 driver mutations with focus on its metastatic patterns and imaging appearance of brain metastases. We demonstrate that brain metastases in this molecular subtype of melanoma occur late in the disease and respond well to immunotherapy.

Microgravity-induced Optic Disc Edema: Quantitative MRI Evaluation of Lower Body Negative Pressure as a Potential Countermeasure

L KRAMER¹, K Hasan¹, B Macias², K Marshall-Goebel³, S Laurie³, R Gabr⁴, A Kamali⁵, A Hargens⁶

¹UTSHC-Houston, Houston, TX, ²NASA, Houston, TX, ³KBR, Houston, TX, ⁴UTSHC-Houston, Houston, TX, ⁵UTSHC-Houston, N/A, ⁶UCSD, La Jolla, CA

Purpose

Optic disc edema develops in two-thirds of astronauts exposed to long duration spaceflight (1,2). Headward fluid shift and venous congestion, invariably present in microgravity, are hypothesized causes (3,4). Lower body negative pressure (LBNP) is a proposed countermeasure. In normal gravity, headward fluid shift and venous congestion occurs in the supine or head-down tilt positions compared to the upright position. Our goal was to determine if LBNP applied during supine positioning can approximate the physiology associated with upright positioning using quantitative MRI techniques.

Materials and Methods

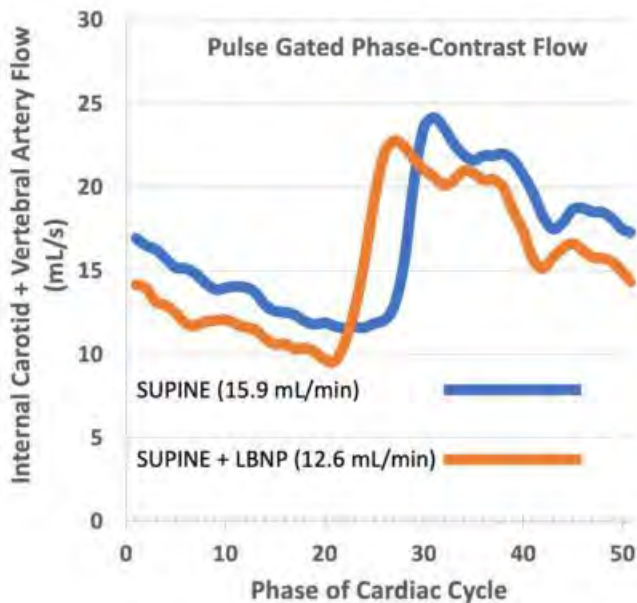
Nine healthy volunteers (5 women, 4 men, mean age = 39 ± 9 years) gave written consent to participate. At 3T the following sequences were obtained: 3D T1-weighted FSPGR for volumetry; pseudo-continuous arterial spin labelling (PCASL) to determine cerebral perfusion; and pulse-gated phase-contrast sequences to evaluate bulk cerebral arterial, internal jugular venous, and aqueductal CSF flow characteristics. Subjects were scanned in the supine position sequentially with and without the application of 25 mmHg LBNP in random order. Blood pressure (BP), heart rate, and oxygen saturation were monitored continuously.

Results

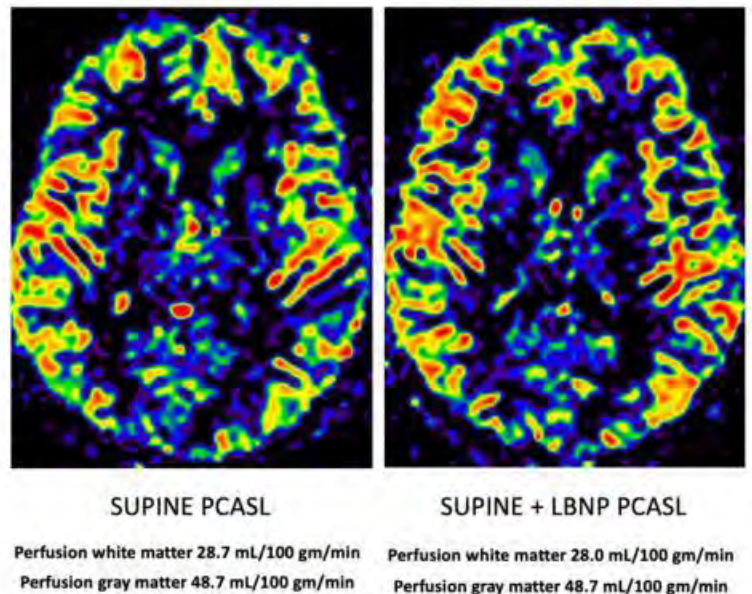
Oxygen saturation was 97 ± 2% during LBNP and 98 ± 2% without LBNP (P=.08). BP was 120/71 ± 12/7 mmHg during LBNP and 125/76 ± 15/11 mmHg without LBNP (P=.12). Heart rate was 71 ± 2 BPM during LBNP and 64 ± 9 BPM without LBNP (p=.0002). Cerebral arterial flow was 9.6 ± 1.8 mL/s during LBNP and to 12.2 ± 2.8 mL/s without LBNP (P=.007) (Fig A). Internal jugular vein cross-sectional area was 56 ± 31 mm² during LBNP and 112 ± 64 mm² without LBNP (P=.03). Internal jugular vein blood flow was 6.5 ± 3.1 mL/s during LBNP and 9.3 ± 3.5 mL/s without LBNP (P=.002). There was no significant change in brain, CSF and lateral ventricular volumes, cerebral perfusion (Fig B), carotid arterial resistive index or CSF flow velocity.

Conclusions

Application of LBNP in the supine position significantly reduces bulk cerebral blood flow and internal jugular cross-sectional area, but has no effect on cerebral perfusion, arterial vascular resistance, blood oxygenation, BP, brain volumetry or CSF aqueductal flow. These findings resemble the physiologic response associated with transitioning from the supine to upright posture in normal gravity (5). Our results suggest that LBNP could help reduce headward fluid shifts and venous congestion in microgravity without detriment to brain perfusion or oxygenation.



A



B

(Filename: TCT_276_AbtractImageASNR2021.jpg)

Microvascular Perfusion Alterations in Patients with Unilateral Critical Internal Carotid Artery Stenosis Following Stenting as Assessed by Intravoxel Incoherent Motion MRI

E Gumeler¹, S Balci², A Ullah³, S Parlak⁴, A Arat², E Arsava², M Topcuoglu², K Oguz¹

¹Hacettepe University Faculty of Medicine, Ankara, WY, ²Hacettepe University, Ankara, Eyalet/Yerleşke, ³National University of Science and Technology, Islamabad, Eyalet/Yerleşke, ⁴Hacettepe University, Ankara, altIndag

Purpose

Intravoxel incoherent motion (IVIM) is a diffusion weighted MRI technique that can measure microvascular perfusion by applying multiple b values. Here we aim to evaluate microvascular perfusion alterations in patients with critical internal carotid artery (ICA) stenosis following stenting.

Materials and Methods

We obtained IVIM MRI of the brain to the patients with unilateral critical ICA stenosis prior to and after stenting. Exclusion criteria included presence of acute infarct, bilateral critical ICA stenosis and hyperperfusion syndrome. Images were acquired within seven days prior to and 24 hours following the procedure. Four min 30 seconds MRI scan was performed in a 1.5T scanner (Aera, Siemens, Germany) with an axial echoplanar diffusion weighted imaging sequence with 9 b values (0, 10, 20, 40, 75, 100, 300, 500, 800 s/mm²). Other parameters were set as follows: TR/TE, 4800/58 ms, FOV=250mm, 24 slices with 5mm thickness and 0.5 mm gap. We processed IVIM data semiautomatically using syngo.via VB30A (Siemens Healthcare, Germany). D, D*, f, and fD* were collected from 7 region of interests (ROI) (200.7±33mm²) including six MCA cortical areas as defined by ASPECTS and the putamen from each cerebral hemispheres. Student t-test was used for comparison and p<0.05 was accepted significant.

Results

Nine patients (F/M=3/6, mean age=70±5.9 years) were included in the study. Mean D, D*, f and fD* values of all ROIs prior to stent were 0.78±0.06 (10-6 mm²/s), 5.69±1.68 (10-3 mm²/s), 1.39±0.47 (%) and 8.02±3.73 (10-6 mm²/s), after stent 0.8±0.08 (10-6 mm²/s), 7.18±3.39 (10-3 mm²/s), 1.69±0.72 (%) and 12.45±9.19 (10-6 mm²/s) on ipsilateral hemisphere. Mean D, D*, f and fD* values on contralateral hemisphere pre and post-stent were 0.77±0.06/0.79±0.06 (10-6 mm²/s), 5.67±2/7.23±4.38 (10-3 mm²/s), 1.43±0.38/1.78±0.83 (%), 8.24±3.8/13.14±10.75 (10-6 mm²/s), respectively. Mean D, D*, f and fD* did not differ between cerebral hemispheres on either pre- or post-stent imaging. However, mean D*, f and fD* changed significantly in both hemispheres following stenting (p<0.05).

Conclusions

As assessed by IVIM MRI, significant microvascular perfusion improvement occur in the MCA territory of both cerebral hemispheres in first 24 hours following amelioration of ICA stenosis by stenting. Use of IVIM MRI as a potential tool for hemodynamic assessment of patients with critical ICA stenosis warrants longitudinal follow-up studies with larger patient population.

233

MR surveillance imaging in neurofibromatosis type 2 with auditory brainstem or cochlear implant in situ

R Saqib¹, S Rutherford¹, E Stapleton², S Freeman¹, R Laitt¹, O Thomas¹

¹Salford Royal Hospital, Manchester, United Kingdom, ²Manchester University Hospitals Foundation Trust, Manchester, United Kingdom

Purpose

Hearing rehabilitation in neurofibromatosis type 2 (NF2) patients has been revolutionized by auditory brainstem (ABI) and cochlear implants (CI). However, these can result in potentially sizeable artefact in MR surveillance imaging. Our aim was to assess whether this significantly impairs diagnostic interpretation in our large cohort.

Materials and Methods

We retrospectively reviewed the 1.5T MR studies performed between 2007-17 for all patients with ABI/CIs under the care of the Manchester NF2 service (one of the four UK centres). Visualisation of the internal auditory meatus (IAMs) was assessed as either i) fully visible, ii) images partially distorted or iii) completely obscured by artefact on axial T2, axial T1 and coronal post contrast T1 sequences. Up to two MR studies were included for each patient. In patients with bilateral implants, each side was assessed individually. Additionally, an approximate maximum diameter of artefact was measured for each sequence.

Results

117 MR studies were included for 63 patients. 5/63 had bilateral implants. There were no reported adverse safety incidents. In all unilateral cases the contralateral IAMs were visible. Using axial T1, 73% (86/117) demonstrated fully visible IAMs, 26% (30/117) partial distortion and 1% (1/117) were fully obscured. For the axial T2 sequence, 68% (79/117) had fully visible IAMs, 29% (34/117) partial distortion and 1.5 % (2/117) were fully obscured. 1.5% (2/117) did not include an axial T2. 65% (76/117) of IAMs were fully visible on coronal T1 post contrast, 33% (39/117) partially distorted and none were fully obscured. 2% (2/117) did not include a post contrast coronal T1. Overall, in 85% of cases the ipsilateral IAM was fully visible on at least one sequence and 15% showed partial distortion but no studies demonstrated complete obscuration in all sequences. Average artefact dimension for axial T2, axial T1 and coronal T1 post contrast was 40.2, 50.8 and 50.9mm.

Conclusions

To our knowledge, this is the largest series of MR studies performed with ABI/CI and magnet in situ. MR imaging is safe using 1.5T and well tolerated in NF2 patients with implants. With appropriate MRI sequences, the image quality is not significantly impaired with 343/347 of the sequences of diagnostic quality, allowing disease surveillance.

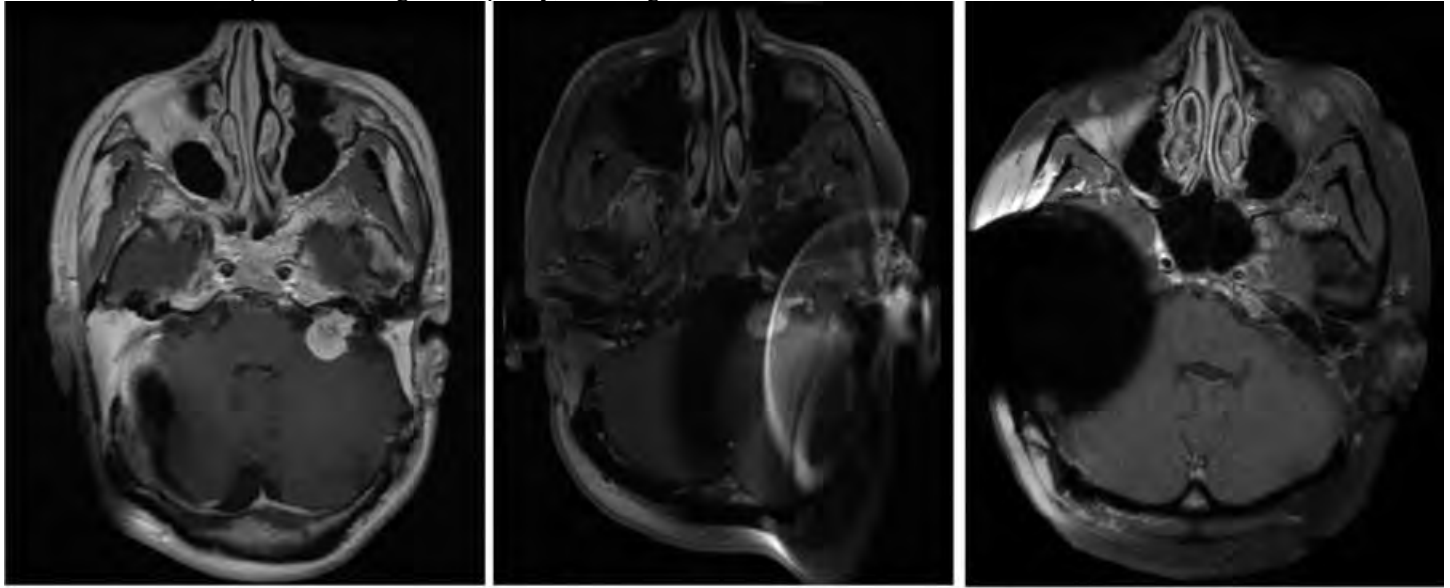


Figure 1: Axial T1 post contrast images. Left demonstrates a fully visible IAM (grade 0), middle partially distorted (grade 1) and right fully obscured (grade 2).

(Filename: TCT_233_Figure1-Gradeofobscuration.jpg)

940

MR Texture Analysis for Prediction of H3K27M Mutation in Diffuse Midline Gliomas

R Chauhan¹, N Kathrani¹, A Indoria¹, J Saini², V Santosh¹

¹National Institute of Mental Health and Neurosciences, Bangalore, Karnataka, ²NATIONAL INSTITUTE OF MENTAL HEALTH & NEURO SCIENCES, BANGALORE, India

Purpose

Diffuse midline glioma (DMG), H3K27M-mutant, has been described as a new entity in updated WHO classification assembling together diffuse intrinsic pontine gliomas (DIPGs) and infiltrating high grade gliomas of midline carrying similar canonical mutation at Lysine 27 residue of histone H3 N-terminal tail. The tumors with this mutation are high grade lesions, behave aggressively clinically and carry unfavorable prognosis compared with wild type (WT) DMGs. As H3K27M mutation has been shown to be an important prognostic factor, it is worthwhile to noninvasively predict this mutation with magnetic resonance imaging (MRI) prior to biopsy or surgery. MRI-based texture analysis (MRTA) is a novel imaging analytical technique that can comprehensively quantify the lesion phenotypes by extracting a large number of quantitative imaging features non-invasively. Therefore, our study aimed at analyzing textural MRI features of DMGs that might discriminate H3K27M-mutant DMGs from WT DMGs.

Materials and Methods

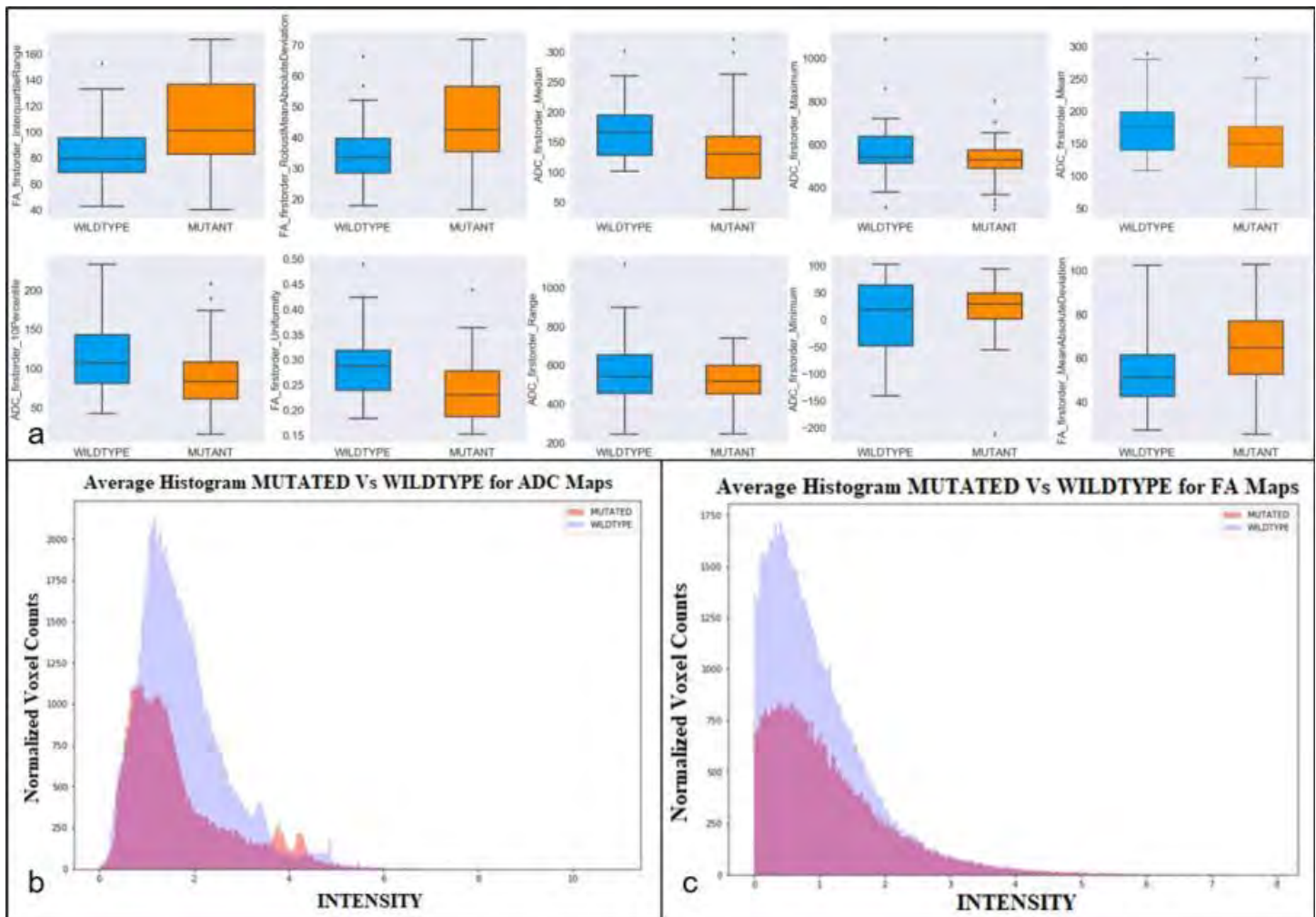
ROI was manually drawn on T2W images to delineate the tumor by segmentation wizard extension of 3D slicer version 4.10.2. Tumor segmentation was done and validated. The ADC and FA maps were registered to T2W images and z-score normalized for feature extraction. 36 first order statistical features were extracted by using PyRadiomics. Feature importance was calculated using gini-index based method. Boxplots were created to study the relation of selected features with mutation status. Dataset was split into training and testing data. A Fourfold cross validation was carried out on the training dataset to obtain the cross-validation score (ROC-AUC score). Ridge classifier was trained on reduced feature set after hyper parameter tuning. Classifier performance was assessed. Performance metrics used for comparison are ROC-AUC score, Accuracy, Sensitivity, Specificity and F1 score.

Results

Boxplots derived from our results indicate that the two groups (Mutant and WT) can be differentiated based on Radiomics features (Fig.1a). There was a significant difference in peak, center and height of the histograms that can be used to differentiate between the two groups (Fig.1b,c). 0.88 mean ROC AUC score was achieved after cross validation. The classifier also performed well on test dataset with accuracy, sensitivity, specificity, ROC-AUC score and F1 score of .916, .84, 1.0, .94 and .909 respectively.

Conclusions

We conclude that MRTA features derived from ADC/FA maps are useful for discriminating H3K27M mutants from WT DMGs.



(Filename: TCT_940_Fig1.jpg)

829

MRI Detection of Tumor-Associated Macrophages in Human Glioblastoma

S Guiry¹, A Nazem¹, M Pourfathi¹, J Ware¹, H Anderson¹, M Nasrallah¹, S Bagley¹, A Desai¹, D O'Rourke¹, S Brem¹, S Nabavizadeh¹
¹University of Pennsylvania, Philadelphia, PA

Purpose

Tumor associated macrophages (TAMS) are a major component of tumor microenvironment in glioblastoma (GBM) and are crucial players in tumor-host immune interaction and tumor progression. To sustain proliferation, cancer cells require iron, which they assimilate from their surroundings by modulating the expression of proteins involved in iron uptake. Pro-inflammatory M1 polarized macrophages within the GBM microenvironment sequester iron thereby limiting iron access of tumor cells. In contrast, M2 polarized macrophages support tumor growth by releasing iron into the tumor microenvironment. In this study, we assessed quantitative susceptibility mapping (QSM) as a method to quantify iron content, and by extension tumor associated macrophages in GBM.

Materials and Methods

In this prospective study, 21 adults with GBM were enrolled. Each participant underwent a 3 Tesla MRI. QSM maps were generated for 19 patients and were assessed for mean susceptibility in the enhancing region of the tumor segmented from structural imaging (Fig 1A). After surgical resection, the specimens were stained with CD 68 (Fig. 1B) and CD 206. Positive cell quantification was performed using a digital pathology method in tumor dense areas (OD >0.14) to quantify TAMS. For direct imaging-histology correlation, three of the formalin-fixed paraffin-embedded tissue specimens were imaged on a Bruker 9.4T 8.9 cm vertical bore MR. T2 TurboRARE and 3D multi-gradient echo scans were acquired at 60°C to ensure paraffin melt, and R2* maps were generated from multiecho GRE images. We used tissue segmentation on H&E as a guide for the placement of multiple ROIs on tumor dense areas. Following proper co-registration, these ROIs were then transferred to the corresponding IHC and R2* images to quantify CD68, CD206 positive cells and the corresponding R2* mean signal intensity (Fig. 1C).

Results

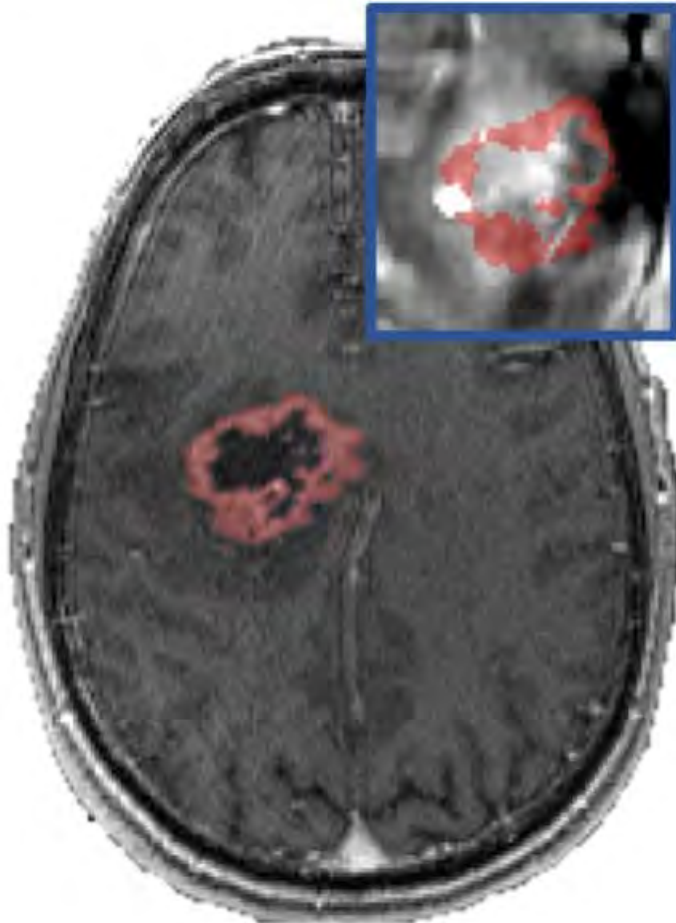
We found a significant correlation between CD 68 positivity% and mean R2* signal intensity among the ROIs used for direct ex vivo

imaging-histology correlation ($r=-0.61$, $p=0.019$). Similarly, there was a trend toward significance between in vivo susceptibility measurements from the tumor enhancing zone (0.004 ± 0.005) and CD68 positivity % ($r=0.43$, $p=0.072$). The correlation between QSM or $R2^*$ with CD206 was not significant in either of the analyses.

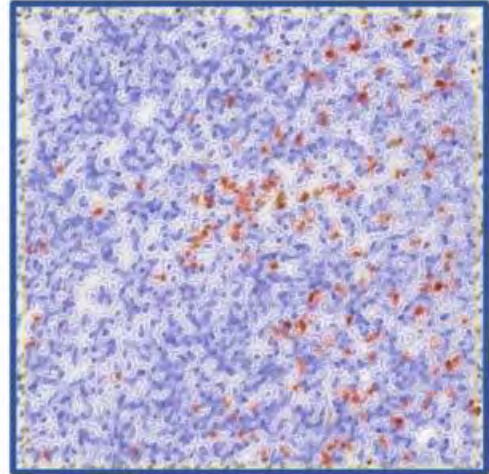
Conclusions

MRI measurements of susceptibility and $R2^*$ correlate with CD68 macrophages in GBM and potentially can be used as a quantitative imaging marker of TAMS.

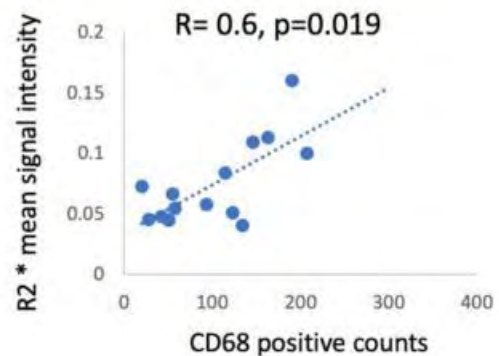
A.



B.



C.



(Filename: TCT_829_ASNR_abstract_figure_110120.jpg)

1087

MRI Morphometric Mapping of Trans-Third Ventricular Endoscopic Trajectories to the Pineal Gland around the Massa Intermedia

G Yamin¹, T Massoud²

¹Stanford University Medical Center, Stanford, CA, ²Stanford University School of Medicine, Stanford, CA

Purpose

Neuroendoscopic biopsies are routinely performed for ventricular tumors. The midline thalamic massa intermedia (MI) within the third ventricle (3V) varies in size and can be a physical obstacle during pineal gland (PG) tumor biopsy. To reach the posterior 3V, an endoscope is passed from foramen of Monro (FoM) usually in a standard infra-MI approach to reach the PG. However, this trajectory restricts views of the upper PG, thus limiting tumor biopsy specimens. Hence, a supra-MI approach is an alternative pathway to PG, but this may be more technically demanding when 3V is small or slit. Given the pros and cons of both endoscopic approaches, we hypothesized that geometric configurations within 3Vs would point to the supra-MI technique offering a more direct route from FoM to PG. However, no prior studies have addressed the neuroimaging dimensions of both pathways around MI. We investigated normative age-related MRI morphometrics of MIs and mapped supra-MI and infra-MI endoscopic trajectories in healthy subjects, prior to further studies in PG tumor and hydrocephalus patients.

Materials and Methods

We analyzed sagittal T1 MR images of 60 individuals having an MI and measured sagittal surface areas of MI (mm²) and 3V (mm²), height of 3V above and below MI (mm), composite length of paths (above and below MI) from FoM to mid anterior border of PG (mm), and angles formed by these two paths (180° being a straight trajectory). We measured Evans' index (EI) to account for global brain atrophy. We tested the effect of sex as an independent variable on measured dependent variables using ANOVA, and performed linear regression with age as the independent variable for dependent variables, with significance set at p<0.05.

Results

Study subjects were F:M=36:24 and mean age 46.6 years. All EIs were normal at <0.3. Mean results were: areas for MI and 3V = 23mm² and 563mm², respectively; 3V heights above and below MI = 7.6mm and 4.8mm, respectively; pathways to the PGs above and below MIs were 31mm and 32mm, respectively; angles formed by these trajectories were 155° and 137°, respectively. Mean height below MI was significantly larger in males (5.3mm) compared to females (4.4mm) (p=0.0007). Mean angle below MI was significantly larger in younger compared to older subjects (p=0.01).

Conclusions

The supra-MI approach may be useful in neuroendoscopic biopsy of PG tumors. We provide normative MRI dimensions of trajectories above and below the MI prior to future similar studies on patients with PG tumors and hydrocephalus.

211

MRI Needle Localization for Pediatric Spinal Surgery Planning

B Langdon¹, M Yazdani¹, D Patel², M Trevino³

¹Medical University of South Carolina, Charleston, SC, ²MUSC, Ladson, SC, ³MUSC, Charleston, SC

Purpose

Accurate spinal level identification is an essential step in the pre-operative planning for pediatric spine surgery patients. Accurate level identification is challenging in the pediatric population using conventional intraoperative fluoroscopy. Incomplete ossification of the pediatric spine leads to poor visualization of individual levels via fluoroscopy. Often, long fluoroscopic times and excessive ionizing radiation are required for adequate identification before surgical incision. Pre-operative MRI guided needle localization offers a unique method of overcoming these challenges with confident and accurate spinal level identification and lack of ionizing radiation.

Materials and Methods

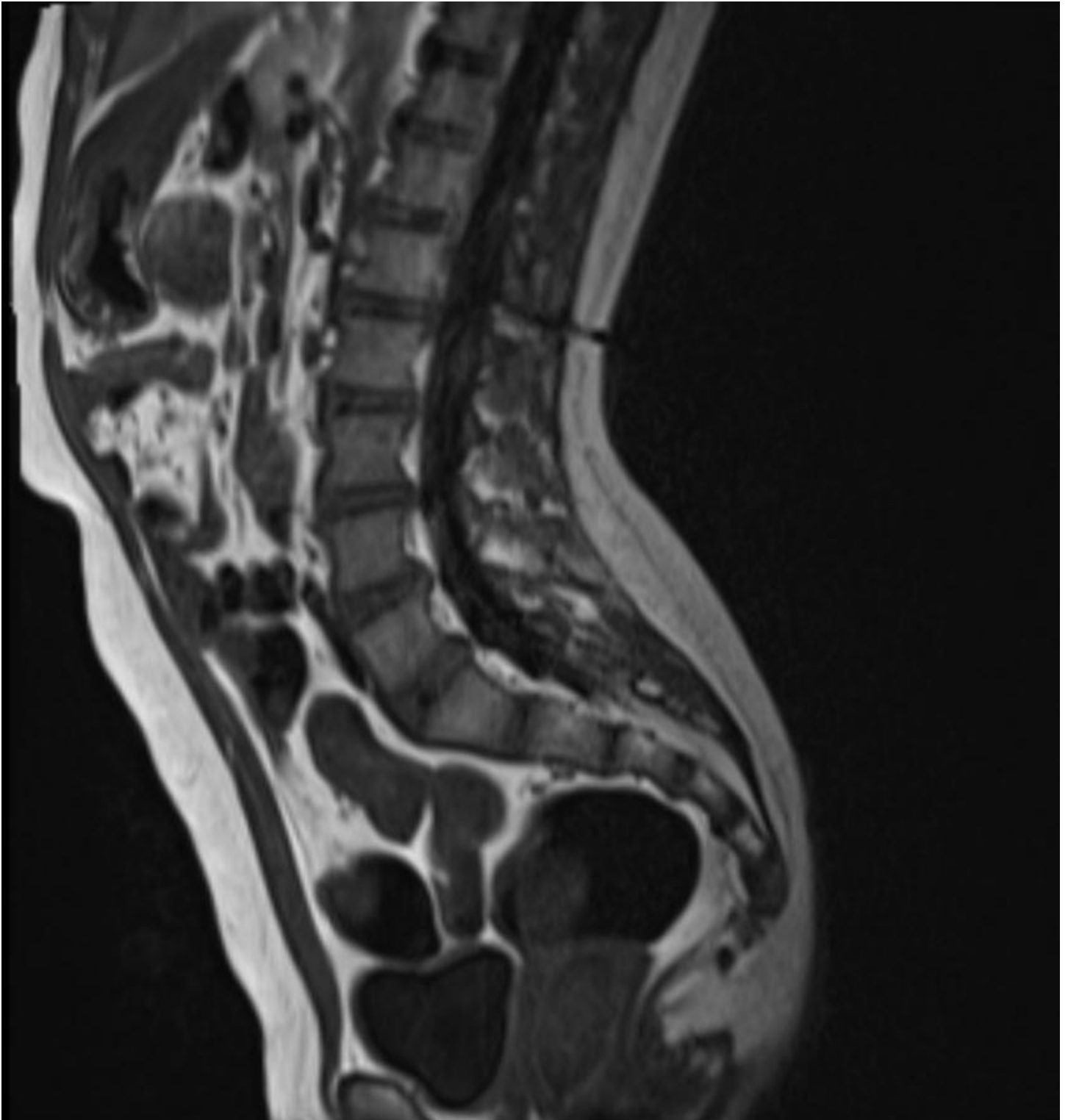
A patient undergoing spinal surgery is first placed under general anesthesia and brought to the MRI suite. The patient is placed in the prone position and a Vitamin E capsule is placed on the patient's posterior midline, approximating the desired vertebral level. In the case of a lumbar or thoracic level marking, a total spine T2 localizing sequence may be acquired to ensure accurate vertebral body numbering. Next, a sagittal T1 fast spin echo series is obtained of the appropriate spinal segment. The desired vertebral body level is identified in reference to the Vitamin E capsule. By palpating the spinous processes relative to the Vitamin E capsule, the desired vertebral body spinous process is identified. Next, an 18 gauge peripheral access needle is placed firmly into the desired vertebral body spinous process. The needle is removed, and gadolinium contrast is injected into the residual catheter. A final sagittal T1 fast spin echo series is obtained to confirm visualization of the needle at the appropriate spinous process level. The patient is then transferred directly to the operating room with the localizing needle/catheter in place.

Results

Our institution has so far performed 10 of these pre-operative MRI guided needle localizations with 100% successful and accurate vertebral body identification.

Conclusions

MRI guided pre-operative needle localization is a relatively quick and ionization-free way to accurately identify the spinous process of a desired vertebral body prior to surgery. The conventional method of intra-operative fluoroscopic guided vertebral level identification is difficult in the pediatric population due to several factors and also exposes this population to ionizing radiation. MRI guided needle localization is quick, accurate, technically straightforward, and requires no ionizing radiation.



(Filename: TCT_211_LumbarNeedleLoc.JPG)

1411

MRI Volumetry in Early Compared to Late Onset Alzheimer's Disease

C Raji¹, S Meysami², M Mendez²

¹Mallinckrodt Institute of Radiology Washington University in St. Louis, ST LOUIS, MO, ²David Geffen School of Medicine at UCLA, Los Angeles, CA

Purpose

Prior studies report greater parietal tau deposition and alternate frontoparietal network involvement in early onset Alzheimer's Disease (EOAD) with onset <65 years as compared with typical late onset AD (LOAD)[1,2]. We therefore evaluated whether clinical magnetic resonance imaging (MRI) brain volumes reflect these differences among patients with early onset Alzheimer's disease (EOAD) compared to persons with Late Onset Alzheimer Disease (LOAD).

Materials and Methods

This study investigated the clinical MRI scans of 45 persons with Clinically Probable AD with onset <65 years, and compared them to 32 with Clinically Probable AD with onset ≥65 years. Brain volumes on their T1 MRI scans were quantified with a volumetric program, which calculates percentage differences from normative scans, and regional volumes as fraction of total intracranial volume (TIV) were compared between both groups. Cohen's D effect sizes and receiver operating characteristic (ROC) analyses were performed.

Results

When adjusted for age, patients with EOAD had significantly smaller parietal lobes (volumetric percentiles) than those with LOAD. They also had decreased total white matter and right pallidum, whereas, LOAD had a smaller left putamen and hippocampus among other regions. ROC analysis showed an area under the curve (AUC) of 96.5% with brain region delineation of EOAD compared to LOAD.

Conclusions

When adjusted for age-related differences, the MRI scans of the EOAD patients were significantly different than those for the LOAD patients. In particular, the EOAD patients had distinctly smaller parietal lobes, out of proportion to any other differences and consistent with increased distribution of neuropathology, particularly cortical neurofibrillary tangles, in EOAD compared to LOAD. This study indicates the presence of parietal atrophy at less than 30% of normal on clinical MRI scans is suggestive of the diagnosis of EOAD.

1364

MRI with Gadolinium as a Measure of Blood-Labyrinth Barrier Integrity in Patients with Inner Ear Symptoms: A Scoping Review

C Song¹, J Pogson¹, N Andresen¹, B Ward¹

¹*Johns Hopkins University School of Medicine, Baltimore, MD*

Purpose

Increased permeability of the blood-labyrinth barrier (BLB), which separates the inner ear's blood supply from the perilymph and endolymph, has been hypothesized to cause disorders such as Meniere's disease and idiopathic sudden sensorineural hearing loss (ISSHL). There has been increased interest in using MRI with intravenous gadolinium (IV-Gd) to measure BLB permeability for diagnosis and research. The purpose of this systematic scoping review was to evaluate current evidence for contrast-enhanced MRI as an indicator of BLB permeability.

Materials and Methods

A systematic search of three databases (PubMed, EMBASE, CINAHL PLUS) was conducted to collect studies that assessed the BLB with IV-Gd MRI. Data was collected on the MRI protocols used and the inner ear enhancement patterns of diseased and healthy ears in humans and animals. Study quality was evaluated using the NIH Study Quality Assessment Tool.

Results

The systematic search yielded 59 human studies and 13 animal studies. In healthy human and animal ears, MRI with IV-Gd demonstrated a gradual rise in signal intensity over time that was limited to the perilymph. Signal intensity peaked at 80-100 minutes in rodents and at 4 hours in healthy humans. In humans, inner ear enhancement was best observed with 3D-FLAIR MRI sequences. Patients with ISSHL and otosclerosis had increased inner ear signal intensity compared to controls in MRI acquired both before contrast and shortly after IV-Gd. Patients with Meniere's disease and vestibular schwannoma had increased enhancement at 4 hours as compared to controls. Correlations between abnormal enhancement patterns and clinical characteristics were variable. All included studies lacked sample size justification and many lacked adequate control groups or did not specify if MRI assessors were blinded.

Conclusions

Included studies support that Gd crosses the BLB in both healthy and diseased ears. However, evidence was inconclusive on whether uptake is a marker for general permeability of the BLB in disease. Rigorous studies are needed with adequate controls, clear patient recruitment methods, and objective measures of enhancement patterns to determine the utility of contrast-enhanced MRI in assessing BLB integrity.

482

MRI-based Radiomics Signature Analyses for Improving Detection of Occult Tonsillar Cancer in Patients with Cervical Nodal Metastasis from an Unknown Primary Site at Presentation

E Ha¹

Purpose

To create a radiomics approach based on magnetic resonance imaging (MRI) features extracted from a volume of interest to detect occult palatine tonsil squamous cell carcinoma (SCC) in patients with cervical nodal metastasis from cancer of an unknown primary site.

Materials and Methods

Differences in the radiomics features of MRIs were assessed among occult palatine tonsil SCC (n= 29), overt palatine tonsil SCC (n= 49), and normal palatine tonsils (n= 94). An estimation of variable importance and variable selection was performed via modeling through Elastic Net regularization. The added value of radiomic feature analysis (RFA) over conventional MRI to detect occult palatine tonsil SCC was evaluated.

Results

Representative values of shape features and 3D fractal analyses were the two most significant factors among the three groups (all P < 0.001). The diagnostic performances of the model with radiomics features extracted from T1-weighted images (WI), T2WI, contrast-enhanced T1WI, and an apparent diffusion coefficient (ADC) map had area under the receiver operating characteristic (AUROC) curve values of 0.831, 0.840, 0.781, and 0.807, respectively, for differential diagnosis of occult palatine tonsil SCC from normal palatine tonsils. In terms of sensitivity, the best performing model with features from the ADC alone showed 90.0% sensitivity, while the model with features extracted from T1WI + T2WI + contrast-enhanced T1WI showed the highest AUROC of 0.853. The added sensitivity of the RFA were 34.6% over that of conventional MRI to detect occult palatine tonsil SCC.

Conclusions

Adding RFA to MRI can improve the detection sensitivity for occult palatine tonsil SCC in patients with a cervical nodal metastasis from cancer of an unknown primary site.

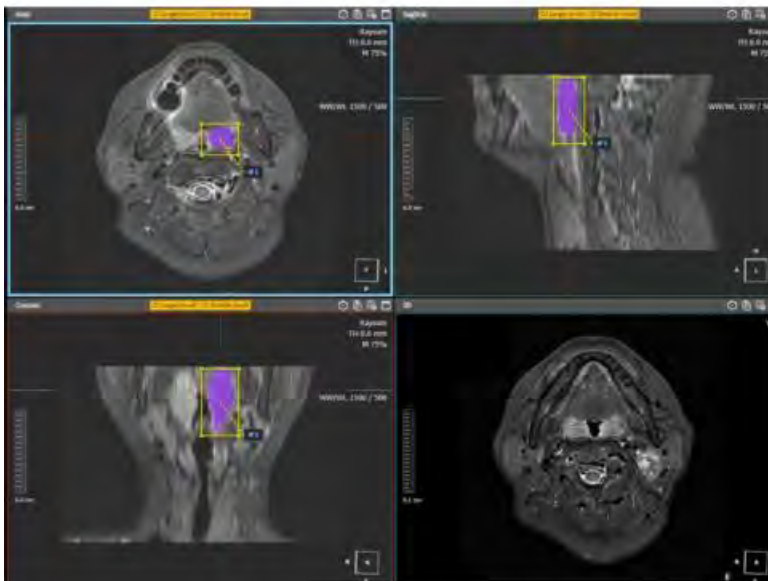
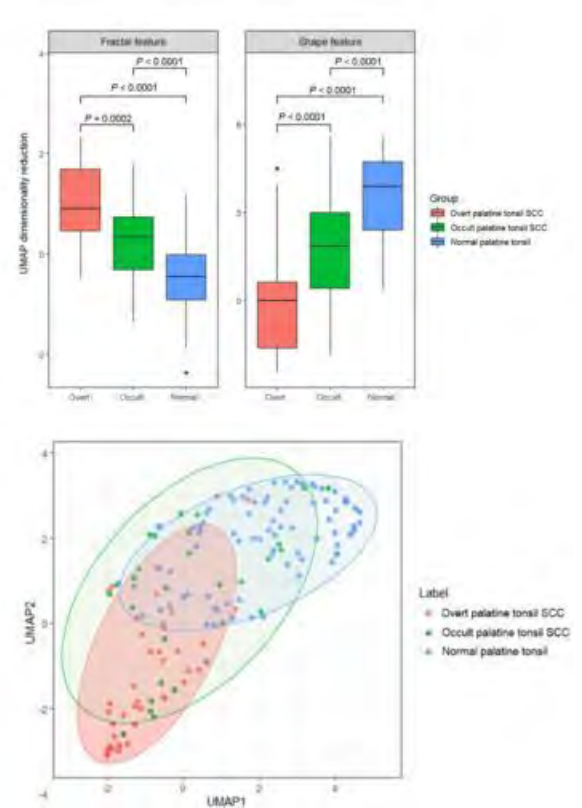


Figure 1. Workflow scheme of this study. Flow diagrams show the process from a VOI segmentation to model evaluation.

Figure 2. Box and whisker plots of the distribution of the representative values of shape features and fractal analyses in patients with overt palatine tonsil SCC, occult palatine tonsil SCC, and normal palatine tonsils on T2-weighted images.

Figure 3. Dimensionality reduction of shape features through the Uniform Manifold Approximation and Projection algorithm.



(Filename: TCT_482_AJNR.jpg)

785

Multidelay ASL: Added Value for Pediatric Neuroimaging

M Ho¹

¹Nationwide Children's Hospital, Dublin, OH

Purpose

To investigate the clinical utility and added value of multidelay arterial spin labeling (MDASL) for pediatric brain imaging.

Materials and Methods

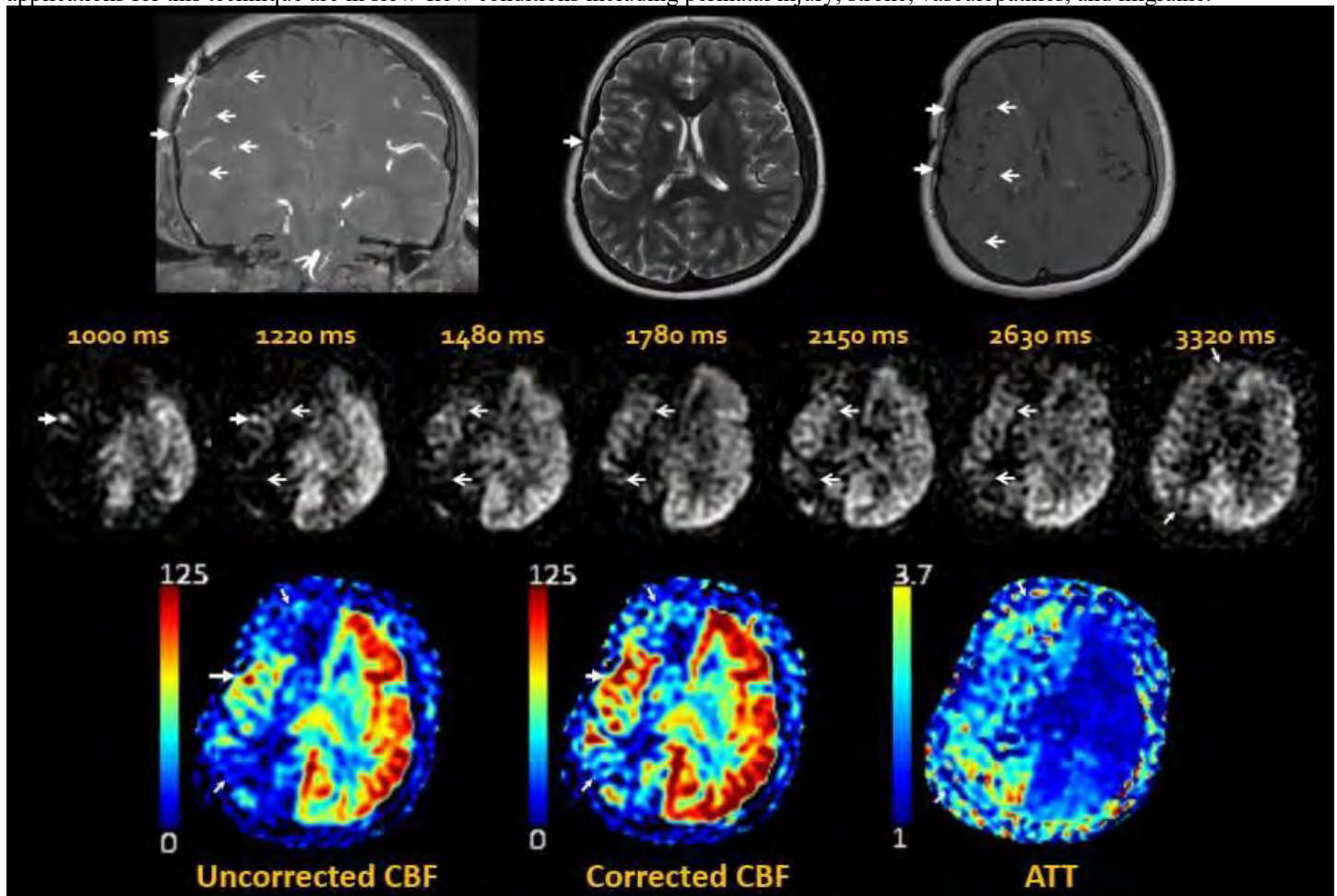
Pediatric patients were sequentially imaged on 3 Tesla MRI platforms with MDASL capability between 2018-2020. Technique involved 3D pseudocontinuous labeling with 7 postlabel delays (ranging from 1000-4000 ms) acquired over a 4-6 minute imaging period. Postprocessing included least-squares curve fitting with subsequent generation of weighted-delay cerebral blood flow, arterial transit time, and cerebral blood volume maps. Following clinical reporting of examinations, all MRI datasets were retrospectively reviewed by a board-certified pediatric neuroradiology attending with specific expertise in ASL. Perfusion and anatomic MRI findings were classified with respect to level of concordance. In cases of discordance, the initial imaging indications and final clinical impressions were also reviewed to determine the added value of MDASL for diagnosis.

Results

A total of 162 patients were imaged, with clinical indications for imaging as follows: 41 neonatal abstinence syndrome, 25 seizure, 19 stroke, 15 tumor, 14 vasculopathy, 14 perinatal injury, 8 trauma, 7 headache, 6 congenital heart disease, 6 congenital anomalies, 4 infection, and 3 developmental delay. Perfusion and anatomic MRI findings were concordant in 121/162 (74.7%) and discordant in 41/162 of cases. For the concordant cases, MRI findings were positive with perfusion data augmenting anatomic MRI in 79/121 cases (65.3%), while both perfusion and anatomic findings were negative in the remaining 42/121 cases. For cases in which perfusion and anatomic findings differed, MDASL yielded findings necessary for clinical diagnosis in 34/41 (82.9%) of cases, and was uninterpretable due to technical artifacts in the remaining 7/41 of cases. Using final clinical impression as the gold standard, the performance of MDASL was 98.7% sensitivity, 89.4% specificity, 96.9% positive predictive value, and 95.5% negative predictive value; while the performance of anatomic MRI was 78.1% sensitivity, 85.7% specificity, 94.5% positive predictive value, and 55.3% negative predictive value.

Conclusions

MDASL is a viable tool for pediatric neuroimaging that augments the diagnostic value of conventional MRI. The most promising applications for this technique are in slow-flow conditions including perinatal injury, stroke, vasculopathies, and migraine.



(Filename: TCT_785_MDASL.JPG)

786

Multidelay ASL: Added Value for Pediatric Neuroimaging

M Ho¹

Purpose

To investigate the clinical utility and added value of multidelay arterial spin labeling (MDASL) for pediatric brain imaging.

Materials and Methods

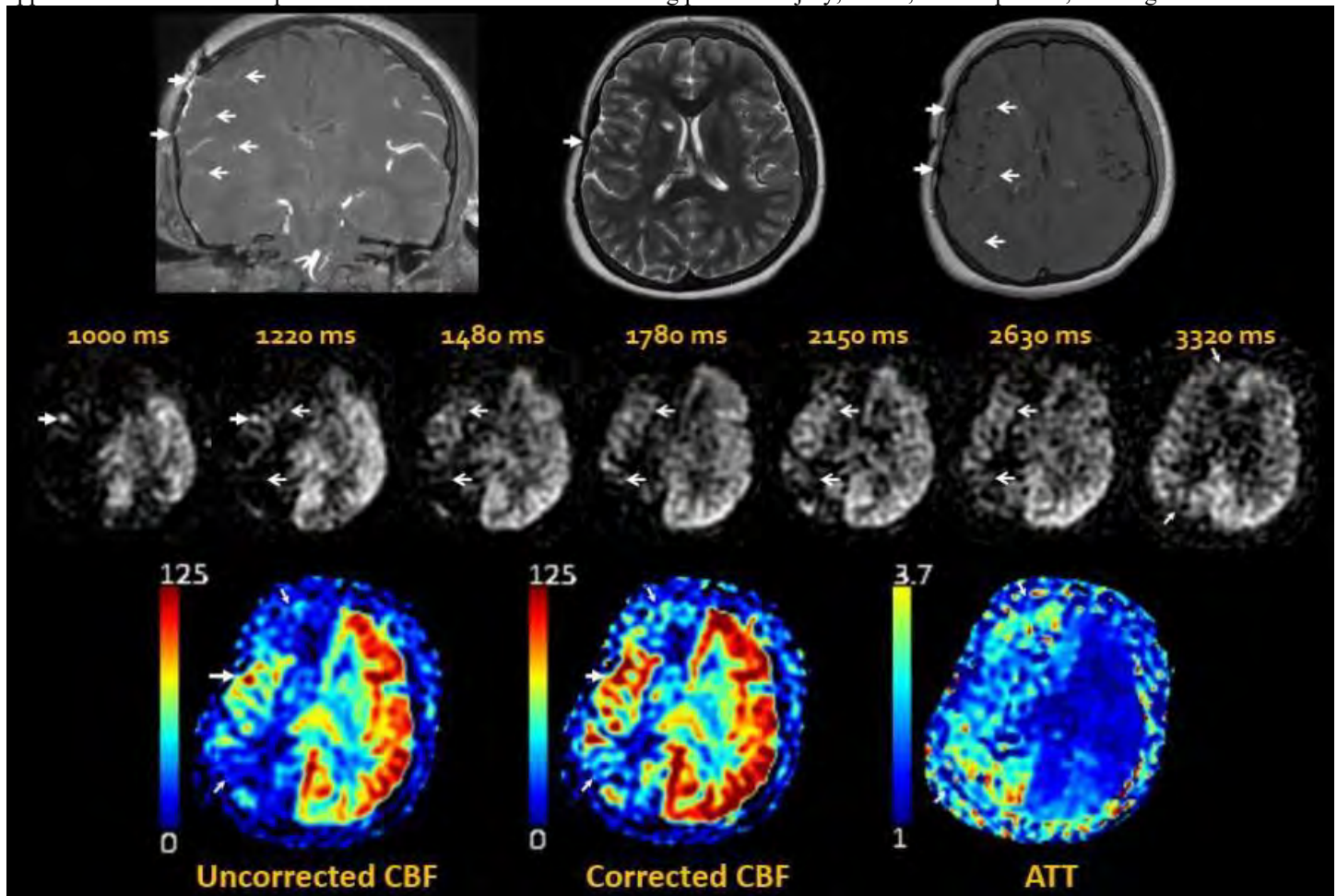
Pediatric patients were sequentially imaged on 3 Tesla MRI platforms with MDASL capability between 2018-2020. Technique involved 3D pseudocontinuous labeling with 7 postlabel delays (ranging from 1000-4000 ms) acquired over a 4-6 minute imaging period. Postprocessing included least-squares curve fitting with subsequent generation of weighted-delay cerebral blood flow, arterial transit time, and cerebral blood volume maps. Following clinical reporting of examinations, all MRI datasets were retrospectively reviewed by a board-certified pediatric neuroradiology attending with specific expertise in ASL. Perfusion and anatomic MRI findings were classified with respect to level of concordance. In cases of discordance, the initial imaging indications and final clinical impressions were also reviewed to determine the added value of MDASL for diagnosis.

Results

A total of 162 patients were imaged, with clinical indications for imaging as follows: 41 neonatal abstinence syndrome, 25 seizure, 19 stroke, 15 tumor, 14 vasculopathy, 14 perinatal injury, 8 trauma, 7 headache, 6 congenital heart disease, 6 congenital anomalies, 4 infection, and 3 developmental delay. Perfusion and anatomic MRI findings were concordant in 121/162 (74.7%) and discordant in 41/162 of cases. For the concordant cases, MRI findings were positive with perfusion data augmenting anatomic MRI in 79/121 cases (65.3%), while both perfusion and anatomic findings were negative in the remaining 42/121 cases. For cases in which perfusion and anatomic findings differed, MDASL yielded findings necessary for clinical diagnosis in 34/41 (82.9%) of cases, and was uninterpretable due to technical artifacts in the remaining 7/41 of cases. Using final clinical impression as the gold standard, the performance of MDASL was 98.7% sensitivity, 89.4% specificity, 96.9% positive predictive value, and 95.5% negative predictive value; while the performance of anatomic MRI was 78.1% sensitivity, 85.7% specificity, 94.5% positive predictive value, and 55.3% negative predictive value.

Conclusions

MDASL is a viable tool for pediatric neuroimaging that augments the diagnostic value of conventional MRI. The most promising applications for this technique are in slow-flow conditions including perinatal injury, stroke, vasculopathies, and migraine.



(Filename: TCT_786_MDASL.JPG)

Multimodal Deep Learning to Predict the Conversion of Mild Cognitive Impairment to Alzheimer's Disease

R Hussein¹, G Zaharchuk¹

¹Stanford University, Stanford, CA

Purpose

Alzheimer's disease (AD) is a progressive disorder that affects around 5.8 million people in the United States [1]. Mild cognitive impairment (MCI) is the stage between the cognitive decline of normal aging and AD. As current AD medications likely have a significant impact when provided at the early stages, identifying the MCI patients at high risk of conversion to AD is crucial for fighting against this disease [2]. This study aims to identify MCI patients at a high risk of conversion to Alzheimer's disease. We designed a multimodal deep learning architecture that integrates heterogeneous data modalities to predict whether an MCI in a particular patient will remain stable, reverts to normal cognition, or progress to Alzheimer's disease.

Materials and Methods

We have prepared a pilot dataset of 265 participants from the Alzheimer's Disease Neuroimaging Initiative (ADNI) database [3], which includes 75 subjects with normal cognition, 128 patients with MCI (58 MCI converter and 70 MCI non-converter), and 62 patients with AD. The 10-folds cross-validation was used for evaluating the proposed model performance. Our multimodal algorithm, shown in Figure 1, performs information fusion from different data modalities to further improve the MCI-to-AD conversion prediction. These data modalities include the patients' medical history, neurological and mental status assessments, blood tests, genetic information, and also PET and MRI exams. We took advantage of the recent advances in (i) convolutional neural networks (CNNs) to efficiently learn the distinguishable imaging biomarkers from MRI and PET scans simultaneously, and (ii) recurrent neural networks (RNNs) to capture the relevant temporal and textual features from the multi-dimensional clinical data of MCI patients.

Results

The results show that integrating multiple communicative medical data modalities can markedly improve the prediction of MCI-to-AD conversion and accurately measure the progression of MCI. We examined the performance of the proposed multimodal framework with the input of MRI images, PET scans, clinical and cognitive assessments, and also biological markers. An average prediction accuracy, sensitivity, and specificity of 74.68%, 76.56%, 72.99% were achieved, showing enhanced performance over competing imaging and non-imaging single modality methods.

Conclusions

This work demonstrates that multimodal deep learning architectures that integrate heterogeneous sources of medical data can better predict the likelihood of MCI conversion to AD.

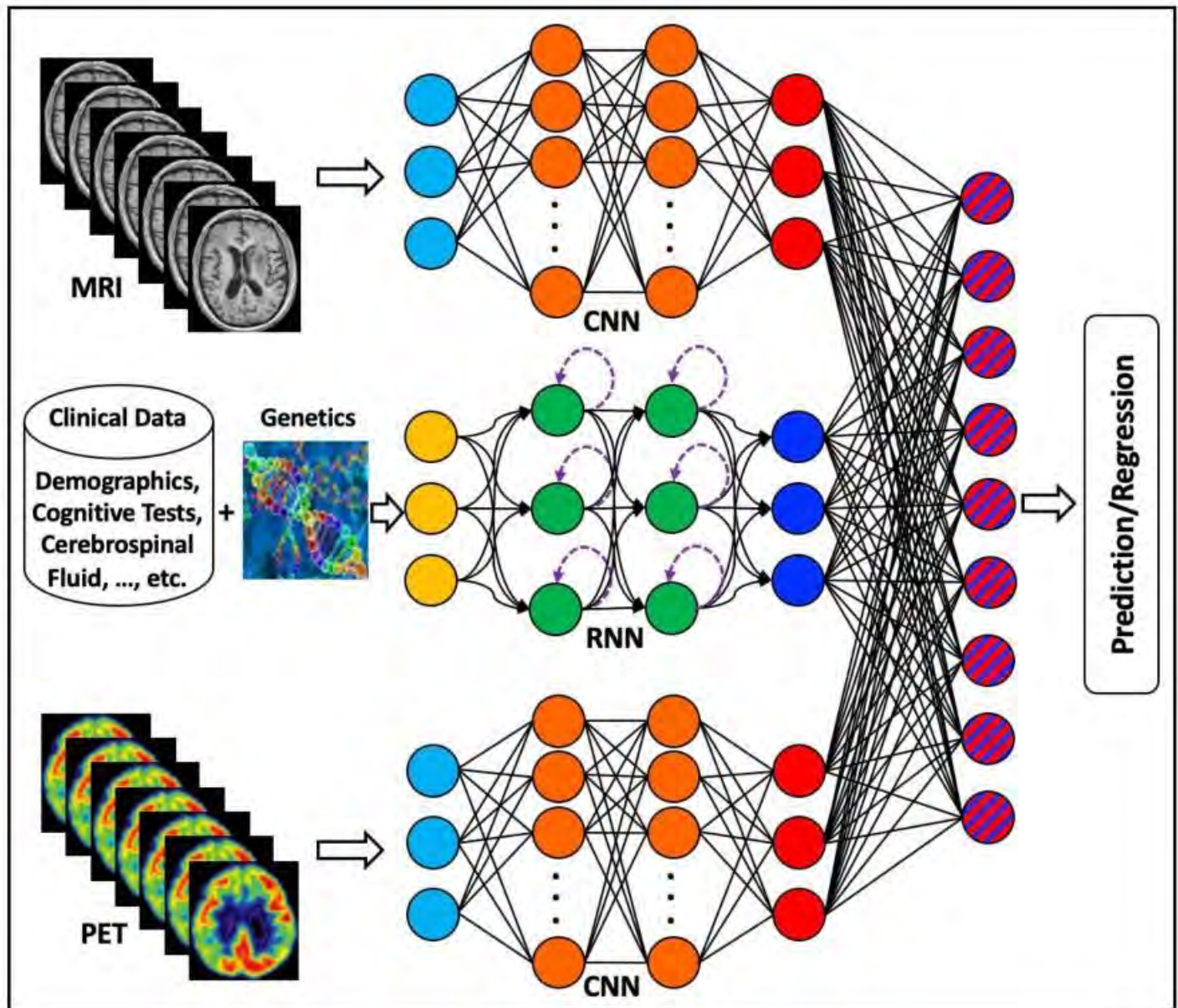


Figure 1. Our multimodal deep learning framework for MCI-to-AD conversion prediction

(Filename: TCT_1097_ASNRFigure1.jpg)

504

Multiparametric Perfusion MRI Differentiates between Progressive and Treated Tumor in Patients with Brain Metastases Following Treatment with Stereotactic Radiosurgery

F Kuo¹, S Soltys¹, G Li¹, M Iv¹
¹Stanford University, Stanford, CA

Purpose

Perfusion MRI can help to differentiate progressive tumor from treatment effect in malignant gliomas [1]. Data in treated brain metastases is more limited. The purpose of this study is to evaluate multiple perfusion parameters [CBF, rCBV, fractional tumor burden (FTB), and ktrans] in patients with brain metastases (BMs) previously treated with stereotactic radiosurgery (SRS).

Materials and Methods

This retrospective study included patients with BMs previously treated with SRS who had suspicious contrast-enhancing lesions on at least one follow-up perfusion MRI. Mean normalized and standardized rCBV and FTB (DSC-MRI), ktrans (DCE-MRI), and normalized CBF (ASL-MRI) and SUVmax (18F-FDG PET) were measured of the contrast-enhancing lesions at a single timepoint. Measurements were repeated on follow-up imaging, if available, to determine absolute change. Treatment effect (TE) vs progressive

tumor was defined by histopathology following resection, shrinking lesion following intervening SRS, or established imaging criteria (RANO-BM). Mann-Whitney test was used to compare mean perfusion values between progressive and treated tumors and absolute changes between two imaging timepoints. Performance was also assessed with area under the receiver (AUC) operating characteristic curve.

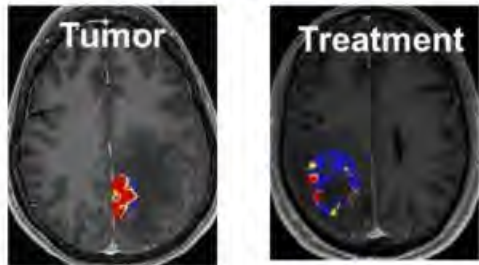
Results

30 patients (mean age 60.2 years; 18 females: 12 males) with previously treated BMs (37 lesions total) were included. Interval time from SRS to initial MRI was 26.4 months + 19.3. Mean normalized and standardized rCBV, FTB_{low}, and FTB_{high} were significantly different between the TE and tumor groups (P<0.002 for all), with tumor having greater FTB_{high} and rCBV. Mean k_{trans} was also significant for distinguishing tumor from TE (p=0.03). AUC for these parameters ranged from 0.73 to 0.85, with normalized FTB_{high} (0.82) and standardized rCBV (0.85) performing the best. Mean CBF-ASL and SUV_{max} were not significant in differentiating between the two groups (ASL p=0.42, AUC 0.63; PET p=0.32, AUC 0.66). Absolute change in MR perfusion parameters between initial and follow-up imaging (mean time interval: 4.3 months) was also not significantly discriminatory (p=0.39-0.96).

Conclusions

Of several MRI perfusion parameters investigated, FTB_{high} and rCBV best differentiated progressive from treated tumors in patients with previously treated BMs. The use of these biomarkers may be helpful to monitor therapeutic response to SRS.

Scan 1						Absolute change Between Scans 1 and 2			
	Treatment Effect (mean ± SD)	Tumor (mean ± SD)	P-Value (Mann Whitney)	AUC of ROC	95% CI		Treatment Effect	Tumor	P-Value (Mann Whitney)
FTB _{low} (norm)	50.6 ± 27.5	22.5 ± 15.5	0.002*	0.79	0.65-0.94	FTB _{low} (norm)	-2.3	0.7	0.64
FTB _{mid} (norm)	18.3 ± 10.5	15.5 ± 7.2	0.66	0.54	0.36-0.73	FTB _{mid} (norm)	2	-1	0.94
FTB _{high} (norm)	31.1 ± 23.7	62 ± 21.3	0.001*	0.82	0.69-0.96	FTB _{high} (norm)	2	0.3	0.72
rCBV (norm)	1.4 ± 0.7	3.0 ± 1.3	0.001*	0.81	0.67-0.95	rCBV (norm)	0.2	-0.1	0.96
FTB _{low} (std1.75)	66.1 ± 24.3	38.6 ± 20.4	<0.001*	0.83	0.70-0.95	FTB _{low} (std1.75)	1.2	-0.8	0.66
FTB _{mid} (std1.75)	19.9 ± 15.5	22.3 ± 7.6	0.22	0.62	0.44-0.80	FTB _{mid} (std1.75)	0.6	1.7	0.96
FTB _{high} (std1.75)	13.9 ± 11.3	39.1 ± 23.1	<0.001*	0.84	0.70-0.98	FTB _{high} (std 1.75)	-1.8	-0.9	0.7
rCBV (std)	0.9 ± 0.4	1.7 ± 0.7	<0.001*	0.85	0.73-0.98	rCBV (std)	0	0	0.83
k _{trans}	0.1 ± 0.1	0.4 ± 0.8	0.03*	0.73	0.56-0.9	k _{trans}	-0.007	-0.062	0.39
ASL-CBF	1.8 ± 0.7	2.3 ± 1.1	0.42	0.63	0.36-0.91				
SUV _{max} FDG-PET	1.8 ± 1.0	2.0 ± 0.5	0.32	0.66	0.37-0.94				



(Filename: TCT_504_Figure1.jpg)

1478

Multiparametric Radiogenomic Model to Predict 1p/19q Codeletion in Patients with Glioma: Added Value to T2-FLAIR Mismatch Sign

A Derakhshani¹, K Mahmoudi², A Bauer³, S KIHIRA², B Salehi⁴, N Pham¹, K Nael¹

¹UCLA, Los Angeles, CA, ²Icahn School of Medicine at Mount Sinai, New York, NY, ³Kaiser Permanente, Fontana, CA, ⁴UCLA, Encino, CA

Purpose

The "T2-FLAIR mismatch" sign has shown promising results in determination of IDH-mutant 1p/19q non-codeleted gliomas (1). We aimed to develop a multiparametric radiogenomic model using a combination of MRI texture features to predict 1p/19q codeletion status in patients with IDH-mutant glioma and to perform a comparative analysis with T2-FLAIR mismatch sign.

Materials and Methods

Inclusion criteria for this retrospective study were 1) diagnosis of IDH mutant glioma with known 1p/19q status and 2) availability of preoperative MRI (FLAIR). Two board certified neuroradiologists reviewed the images independently for T2-FLAIR mismatch sign. In each patient, tumor segmentation was performed to encompass the entire FLAIR hyperintense volume and a total of 92 texture features were extracted using Olea Sphere SP.22. From texture features, an imaging model was developed to predict 1p/19q codeletion

status using Least Absolute Shrinkage and Selection Operator (LASSO) regularization to reduce the risk of overfitting. This imaging model was then inserted into a backward stepwise logistic regression in conjunction with variables such as age, sex, tumor volume, tumor location and T2-FLAIR mismatch scores. Receiver-operating characteristic was performed to provide accuracy statistics.

Results

Thus far a total of 46 patients (age: 42.3 ± 11 , M 28) were included. 1p/19q status: intact (n=23) and codeleted (n=23). Interobserver agreement between two neuroradiologists in defining T2-FLAIR mismatch was modest ($k=0.46$). The overall diagnostic performance (sensitivity/specificity/accuracy) of T2-FLAIR mismatch sign in determining 1p/19q status was: 47.5% / 84% / 65.8%. Our imaging model generated from a combination of three texture features (first order uniformity, grey-level run length matrix run percentage, and neighborhood gray tone difference matrix strength) resulted in sensitivity/specificity/accuracy: 70% / 74% / 72%. In logistic regression analysis, this radiogenomic model remained as a significant ($p=0.022$) contributor to the final model in conjunction with T2-FLAIR mismatch ($p=0.008$). The overall accuracy of this final combined model was improved to 82.6% (balanced sensitivity and specificity 82.6% each).

Conclusions

Results show that application of multiparametric radiogenomic model provides added diagnostic value and in particular increases the sensitivity of the "T2-FLAIR mismatch" sign in determination of 1p/19q codeletion status in patients with glioma.

886

Multiparametric Radiogenomic Model to Predict Survival in Patients with Glioblastoma

K Mahmoudi¹, S KIHIRA¹, A Bauer², N Tsankova¹, F Khan¹, A Hormigo¹, A Lai³, T Cloughesy³, K Nael³

¹Icahn School of Medicine at Mount Sinai, New York, NY, ²Kaiser Permanente Fontana Medical Center, Los Angeles, CA, ³University of California, Los Angeles, Los Angeles, CA

Purpose

Several clinical, histopathological, and imaging variables have been associated with prognosis in patients with glioblastoma (GBM) [1]. We aimed to develop a multiparametric radiogenomic model using a combination of MRI texture features, demographic data, and glioma biomarker status to predict prognosis in patients with GBM.

Materials and Methods

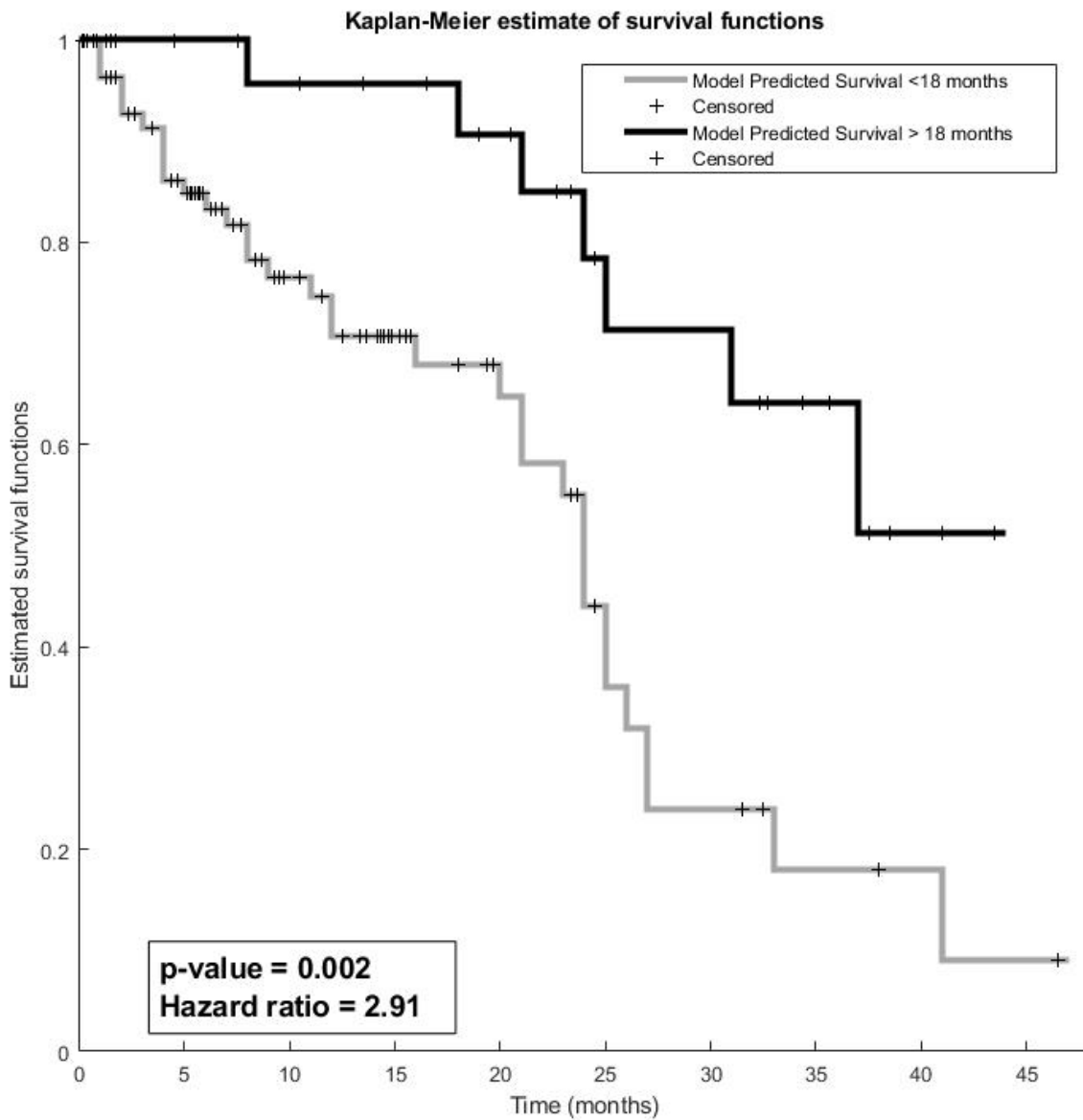
In this retrospective study, patients were included if they had 1) confirmed diagnosis of GBM, 2) pre- and post-operative MRI including T1c+, FLAIR, and diffusion sequences, and 3) glioma biomarker data (IDH-1, EGFR, MGMT, ATRX). Survival data was obtained from patients' charts and dichotomized (< 18 months, \geq 18 months). Tumor segmentation was performed using volume-of-interest analysis and a total of 92 texture features were obtained. From texture features, a predictive imaging model was developed using univariate analysis and Least Absolute Shrinkage and Selection Operator (LASSO) regularization to reduce the risk of overfitting. This imaging model was then inserted into a backward stepwise logistic regression model in conjunction with other variables including age, sex, initial tumor volume, resection volume (percentage), and 4 glioma biomarker (IDH-1, EGFR, MGMT, ATRX) status. Receiver-operating characteristic (ROC) and Kaplan-Meier curve analysis were performed.

Results

A total of 116 patients (age: 59.6 ± 13.9 , M/F 62/54) met our inclusion criteria. The median (IQR) survival was 12 (18) months. A total of 7 texture features were used in generating our imaging model in determination of > 18-months survival with AUC (SE/95%CI) of 0.72 (0.05/0.63-0.80) ($P=0.004$). In logistic regression analysis, our imaging model remained as a significant ($p<0.001$) contributor to the final multiparametric model in conjunction with age ($p=0.04$) and MGMT status ($p=0.02$). The overall accuracy of this final radiogenomic model was AUC (SE/95%CI) of 0.79 (0.04/0.70-0.86) ($p<0.001$). Using this final radiogenomic model to predict survival, Kaplan-Meier analysis showed a significantly ($p = 0.002$, HR= 2.91) longer overall survival (Figure).

Conclusions

Results show that our radiogenomic model generated from radiomic features at baseline (pre-operative) MRI in conjunction with age and MGMT status can predict survival > 18 months in patients with GBM.



(Filename: TCT_886_KMSurvival.jpg)

533

Multiple Post-labeling Delay Arterial Spin Labeling MRI Provides More Accurate Cerebrovascular Reactivity Measurements Using Oxygen-15 Water PET as the Reference

M Zhao¹, G Zaharchuk¹

¹Stanford University, Stanford, CA

Purpose

Cerebrovascular reactivity (CVR) reflects the change in cerebral blood flow (CBF) in response to a vasoactive stimulus. We compare the accuracy of CVR measurements of single and multiple post-labeling delay (PLD) arterial spin labeling (ASL) MRI using oxygen-15 water PET as a reference.

Materials and Methods

PET/MRI data were collected on a 3T PET/MRI scanner (GE SIGNA, Waukesha, WI, USA) from 19 healthy volunteers (25-66 years, 9 males). PET/MRI data were acquired simultaneously before and 15 minutes after the injection of acetazolamide at a dose of 15 mg/kg of body weight (maximum 1g). PET images were acquired using the technique in [1], and the mean amount of [15O]-Water injected was 862 MBq. Single-PLD ASL (PLD=2.025s) data were acquired using GE's product sequence, multi-PLD ASL (PLD=0.3,

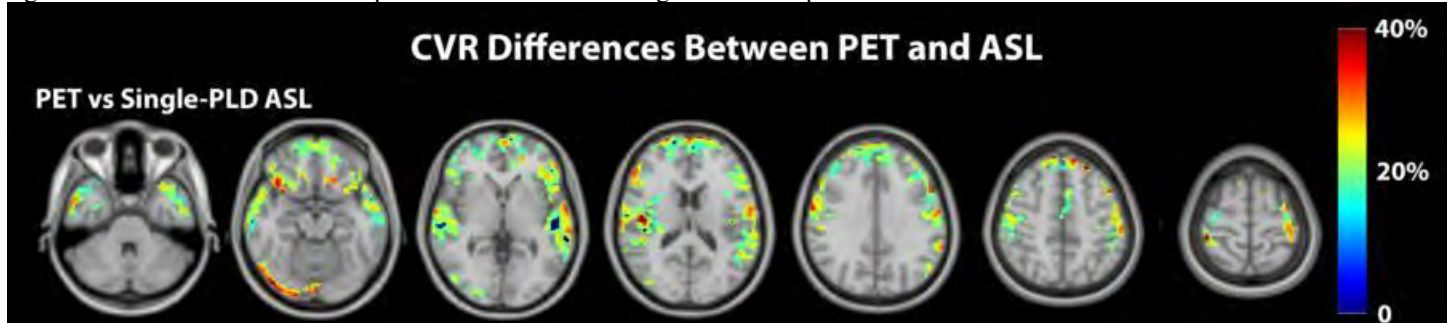
2, 3.7s) data were acquired using GE's eASL sequence [2]. PET CBF was estimated by fitting the pharmacokinetic model [3]; ASL CBF was quantified using the BASIL tool in FSL [4]. CVR was computed as the percentage of CBF change with respect to baseline CBF. Paired t-tests were conducted to compare the voxel-wise CVR difference between ASL and PET.

Results

Figure 1 shows the regions with significant CVR differences between single-PLD ASL and PET (corrected p-value < 0.05). No significant CVR differences were found between multi-PLD ASL and PET.

Conclusions

Multiple PLD ASL is the most accurate technique for CVR measurements using PET as the reference. Arterial transit time is a significant factor for the accurate quantification of CVR using ASL techniques.



(Filename: TCT_533_randomise_pet_vs_asl.jpg)

787

Multivariable Diagnostic Prediction Model Development Study to Detecting Hormone Secretion Profile from T2 Weighted MRI Radiomics with Artificial Neural Networks in Pituitary Adenomas

B Baysal¹, M Eser¹, M Dogan¹, M Kurşun¹

¹Istanbul Medeniyet University Goztepe Training and Research Hospital, Istanbul, Turkey

Purpose

This study aims to develop neural networks to detect hormone secretion profiles in the pituitary adenomas based on T2 weighted MRI radiomics.

Materials and Methods

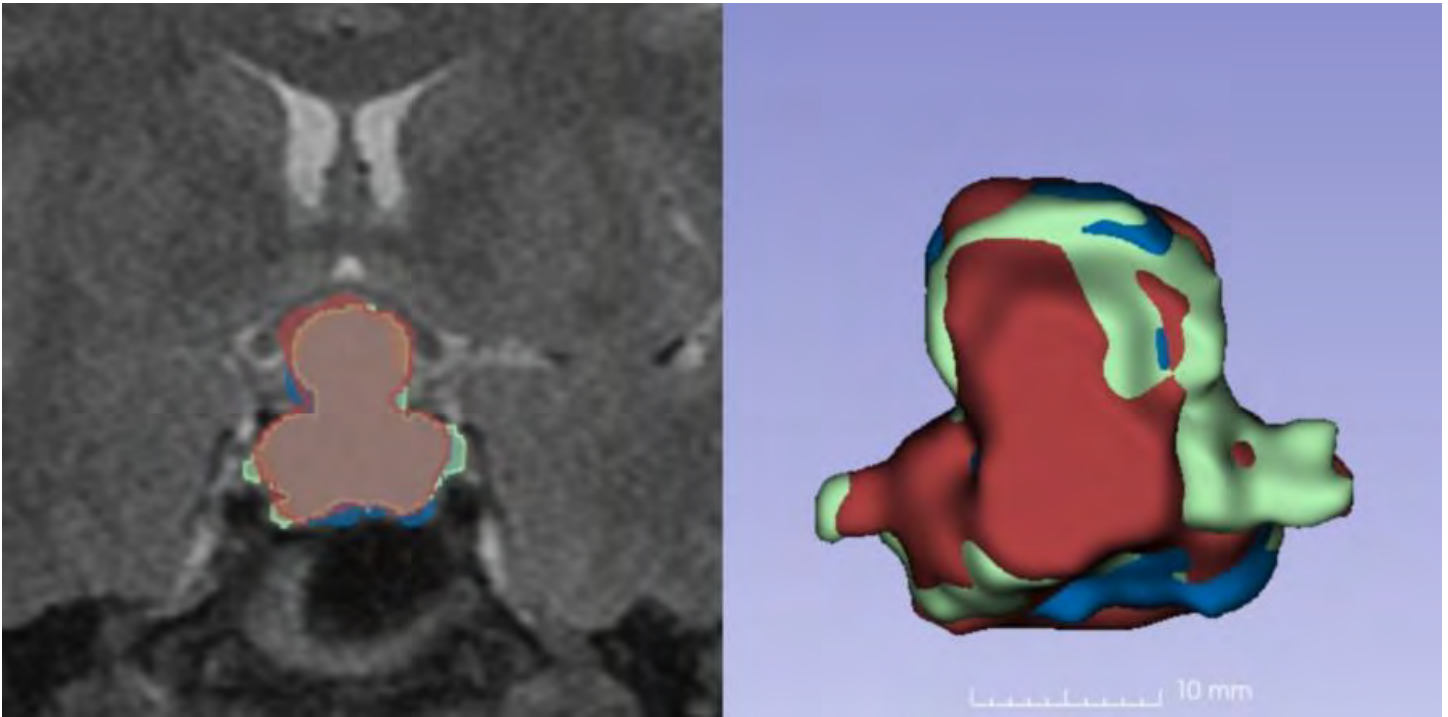
This retrospective model development study included a consecutive cohort of patients with pituitary adenomas from January 2015 to January 2020 in one tertiary university hospital. This study was included 130 cases of pituitary adenoma consecutively. The mean patient age was 46.49±13.69 years, and 76/130 (58.46%) were women. Three observers segmented lesions on coronal T2 weighted MRI, and an interrater agreement was evaluated using the Dice coefficient (Figure). Predictors were determined as radiomics features (n = 851). Feature selection was based on intraclass correlation coefficient (ICC), coefficient variance (CoV), variance inflation factor (VIF), and LASSO regression analysis. Outcomes were identified as seven hormone secretion profiles [Nonfunctional adenoma (NFA, n = 19), growth hormone-secreting adenomas (GHSA, n = 21), Prolactinomas (n = 64), adrenocorticotrophic hormone-secreting adenomas (ACTHSA, n = 6), Pluri-hormonal secreting adenomas (PLSA, n = 6), Follicle-stimulating hormone and Luteinizing hormone-secreting adenomas (FSA&LHSA, n = 8), and Thyroid-stimulating hormone adenomas (n = 6)]. A multivariable diagnostic prediction model was developed with artificial neural networks (ANN) for seven outcomes. Internal validation was performed using bootstrapping and cross-validation. ANN performance was presented as an area under the receiver operating characteristic curve (AUC) and accepted as successful if the AUC > 0.85 and p-value < 0.01.

Results

The 204 features were eliminated with ICC (<0.75). With CoV analysis (> 0.15), 552 features were eliminated. Finally, another 44 features were eliminated by VIF analysis due to collinearity. Most of the radiomics features were found to be unstable (n = 800, 94%). It was also found that stable features and outcomes are weakly correlated. LASSO was used for regularization due to the weak correlation between stable features and outcomes. ANN that distinguishing prolactinomas from other adenomas performance was excellent (AUC = 0.95, p < 0.001, sensitivity: 91%, specificity: 98%). PHSA AUC was 0.74 and p < 0.001. The AUC values for the other five ANN > 0.85, p < 0.001.

Conclusions

This study was successful in training neural networks that can differentiate pituitary adenomas. Neural networks distinguished prolactinomas from other types of adenomas accurately.



(Filename: TCT_787_fig_1.jpg)

1654

Myelin and axonal sensitive magnetic resonance imaging for the evaluation of pediatric demyelinating diseases

F F¹, T Kellermayer²

¹Physician, Dallas, TX, ²UT Southwestern, Houston, TX

Purpose

Pediatric demyelinating diseases impose significant challenges to those living with the disease and those attempting to characterize them. Current conventional MR imaging lacks specificity for the underlying pathophysiological changes which ultimately hinders our ability to correlate imaging with measures of clinical disability and relapse severity. Thus, in order to improve our ability to characterize disease burden in these conditions, and therefore improve outcomes for patients, we propose using advanced imaging methods such as neurite orientation dispersion and density imaging (NODDI) and macromolecular tissue volume (MTV) imaging to obtain estimates of axonal volume fraction (AVF), myelin volume fraction (MVF), and g-ratio.

Materials and Methods

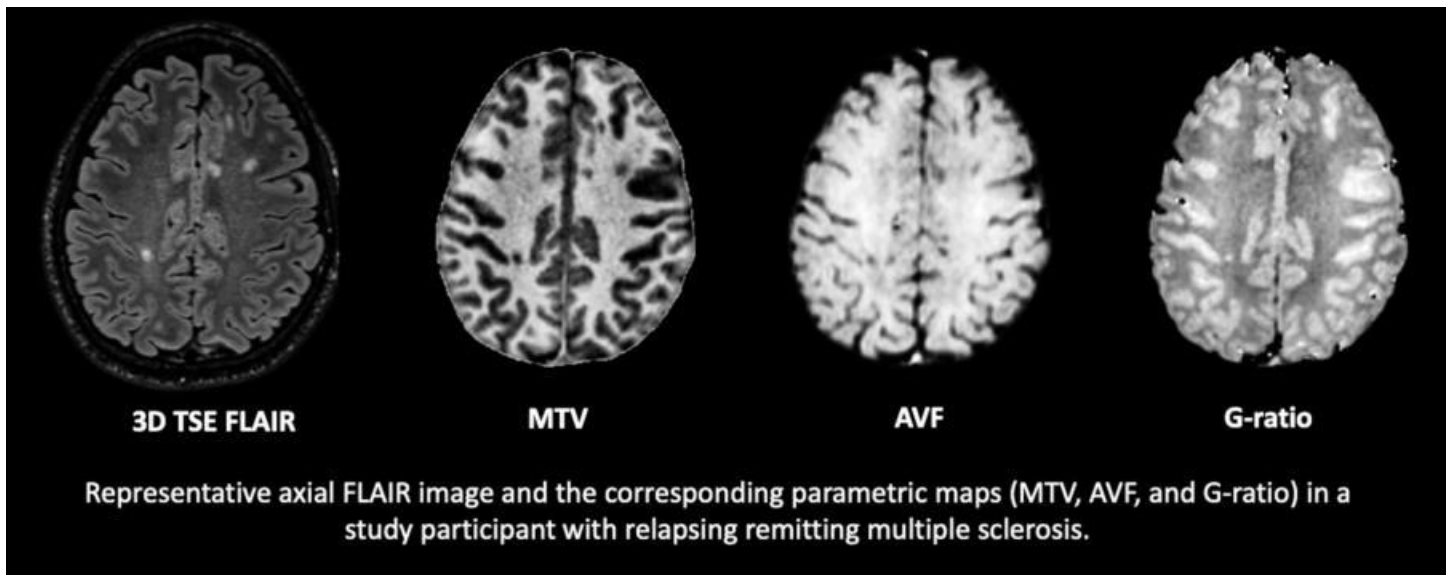
23 subjects with pediatric demyelinating disease (12 with relapsing-remitting multiple sclerosis [RRMS], 3 with anti-myelin oligodendrocyte glycoprotein-encephalomyelitis [MOG], 2 with neuromyelitis optica [NMO], 2 with neuromyelitis optica spectrum disease [NMOSD], and 4 healthy) were analyzed. MTV and NODDI were obtained on a 3T Siemens Prisma scanner to quantify the MVF and AVF, respectively (1,2). The g-ratio was calculated from the ratio of MVF and AVF (3). Between group comparisons were performed using Mann-Whitney U tests. Correlation between the imaging and clinical metrics was performed using Pearson correlation.

Results

The mean g-ratio (0.78 vs. 0.79) was not significantly different between lesions and normal-appearing WM (NAWM) for the demyelinating disease patients. The mean AVF was decreased significantly in lesions for RRMS (0.28 vs 0.37; $P < 0.01$) as well as NMOSD and MOG (0.28 vs 0.37; $P < 0.01$). Lesion MVF was significantly decreased in RRMS only (0.16 vs 0.22; $P < 0.01$).

Conclusions

Advanced MRI techniques such as AVF, MVF, and g-ratio could prove useful in the prognostication of children with demyelinating diseases. Furthermore, they present a unique opportunity to monitor treatment efficacy in clinical trials.



(Filename: TCT_1654_Figure1a.jpg)

1366

N-Acetylcysteine Administration Affects Cerebral Blood Flow as Measured by Arterial Spin Labeling MRI in Patients with Multiple Sclerosis

J Heholt¹, S Shahrampour¹, F Mohamed¹, M Alizadeh¹, N Wintering¹, A Newberg¹

¹Thomas Jefferson University, Philadelphia, PA

Purpose

A previous study exploring the effect of N-acetylcysteine (NAC) on glucose metabolism in patients with multiple sclerosis (MS) based on fluorodeoxyglucose (FDG)-positron emission tomography (PET) showed that NAC positively affected cerebral glucose metabolism. The purpose of this study is to explore if administration of NAC in patients with MS also results in altered cerebral blood flow (CBF) based on Arterial Spin Labeling (ASL) functional Magnetic Resonance Imaging (fMRI).

Materials and Methods

Twenty-three patients with mild to moderate MS, (17 relapsing remitting and 6 primary progressive) were randomized to either NAC plus standard of care (NAC group, N=11), or standard of care only (control group, N=12). The NAC group received NAC intravenously (50mg/kg) once per week and orally (500mg 2x/day) the other six days. Patients in both groups were evaluated initially and after 2 months with ASL fMRI, clinical symptom questionnaires were also completed at both time points. After data acquisition and preprocessing, CBF maps and the average whole brain CBF values were calculated for each patient at both time points. A 2x2 full factorial ANOVA design, was used to compare the NAC group to the control group in order to find the hemodynamic response to NAC administration. Regions that survived FDR correction for multiple comparisons with a P value <0.001 and cluster level > 10 voxels were identified.

Results

On average MS Patients who received NAC had an increase in whole brain CBF of 8.8 ± 1.5 ml/100g/min while the wait list control group had a decrease in whole brain CBF of 5.8 ± 13.5 ml/100g/min ($p=0.01$, Table 1). The global increase in CBF is visualized in an example patient from the NAC group (Figure 1). Significant differences were found in several brain regions including frontal and temporal gyri in the MS patients who received NAC, when compared to the control group ($p<0.001$, Table 2). Self-reported scores related to cognition and attention were also significantly improved in the NAC group as compared to the control group.

Conclusions

The results of this study suggest that NAC administration alters resting CBF in MS patients, and this is associated with qualitative improvements in cognition and attention. Given these findings, large scale efficacy studies will be of value to determine the potential clinical impact of NAC over the course of illness in patients with MS, as well as the most effective dosages and differential effects across subpopulations.

Subject	Intervention Group	Pre-Intervention Whole Brain Mean CBF ml/100g/min	Post-Intervention Whole Brain Mean CBF ml/100g/min	Difference in CBF ml/100g/min (Post - Pre intervention)
MS001	NAC	36.19	48.78	12.59
MS002	NAC	62.25	64.86	2.61
MS003	NAC	77.44	92.82	15.38
MS004	NAC	18.04	49.11	31.07
MS005	NAC	23.82	35.74	11.92
MS006	NAC	34.36	48.70	14.34
MS007	NAC	62.83	59.91	-2.72
MS008	NAC	46.54	52.72	6.18
MS009	NAC	33.53	47.03	13.50
MS010	NAC	76.31	82.48	6.17
MS011	NAC	56.06	42.16	-13.90
MS001	Control	59.04	37.09	-21.95
MS002	Control	75.81	55.60	-20.21
MS003	Control	38.18	30.21	-7.97
MS004	Control	25.12	48.65	23.53
MS005	Control	65.27	56.19	-9.08
MS006	Control	83.03	90.98	7.95
MS007	Control	59.96	55.86	-4.10
MS008	Control	85.69	73.89	-11.80
MS009	Control	51.08	52.51	1.43
MS010	Control	83.35	71.66	-11.69
MS011	Control	110.54	89.17	-21.37
MS012	Control	42.38	47.59	5.21

Table 1. Whole Brain CBF before and after intervention

Structure	Peak MNI Coordinate	Peak Intensity
Pons	0 -32 -30	3.67
Midbrain	14 -16 -12	3.82
L Superior Temporal Lobe	-36 0 16	4.24
L Hippocampus/Parahippocampus	-24 -38 -2	3.67
L Frontal Lobe	-38 -4 20	4.01
L Thalamus	-24 -22 8	4.53
R Middle Frontal Gyrus	42 56 8	-5.38
R Temporal/Hippocampus	36 -42 2	3.56

Table 2. List of significant brain regions with altered CBF (p<0.001, cluster level >10) found in the NAC Group compared to the Control group. A positive Peak Intensity indicates increased CBF and a negative indicates decreased CBF

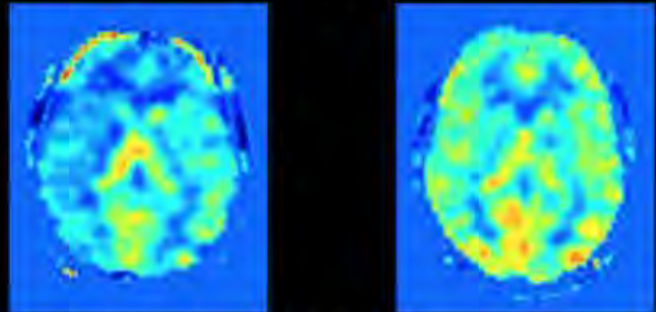


Figure 1. Comparison of the pre (left) and post (right) scan of an MS patient in the NAC group showing marked increase in global CBF after two months of receiving NAC.

(Filename: TCT_1366_AS_L_Abtract.jpg)

1650

Needle Free Perfusion MRI Using Endogenous Deoxyhemoglobin

D Mikulis¹, J Poubanc², O Sobczyk³, J Duffin⁴, K Uludag³, J Fisher³

¹Toronto Western Hospital, Toronto, ON, ²The Toronto Western Hospital, Toronto, Ontario, ³The University Health Network, Toronto, Ontario, ⁴University of Toronto, Toronto, Ontario

Purpose

To demonstrate the feasibility of "needle free" deoxyhemoglobin (dHb) bolus perfusion imaging.

Materials and Methods

A gas blender was used with a sequential gas delivery breathing circuit enabling prospective arterial blood gas targeting(1) to provide rapid isocapnic changes in pulmonary venous oxygen (PaO₂) during 3T BOLD MRI. This system enables configurable deoxyhemoglobin (dHb) boluses. A desat/resat/desat backbone was applied under 2 configurations: a baseline hypoxic stimulus was used in 3 controls, and a normoxic baseline in 1 patient with severe RMCA stenosis (fig.1). Linear regression of the BOLD signal (S) against best shifted arterial oxygen saturation (SaO₂) was used to calculate %BOLD, correlation, and time delay (TD) maps. SaO₂ was used for the arterial input function, and e^(-t/MTT) for the residue function. MTT was calculated as: S(t)=SaO₂ (t) ⊗ e^(-t/MTT). The residue function was set to 1 at t=0 and 1 at t=5 x MTT. MTT limits were 0-12s. Relative CBV (rCBV) was calculated using the area under the BOLD signal curve. Relative CBF was calculated as rCBF=rCBV/MTT. Perfusion maps are shown in figs.2 and 3. Average metric values were calculated for the right and left MCA gray matter territories (fig.4). For TD, MTT, rCBV and rCBF the ratio of left over right hemisphere was calculated (fig.4).

Results

All results are summarized in the table in fig.4. Both dHb bolus configurations yielded similar quality perfusion maps rivaling those obtained using contrast injections. Note the reduced CBF, increased CBV, and increased MTT in the right hemisphere well seen in the right MCA territory in the patient.

Conclusions

Non-invasive induction of abrupt configurable changes in [dHb] as a paramagnetic contrast agent shows potential to provide diagnostic quality perfusion imaging. Advantages include similar acquisition times as for Gd bolus perfusion imaging without risk of contrast reactions and potentially more accurate measures of perfusion especially for assessment of tumor perfusion as dHb does not leak into the tissues. Limited interrupted exposure to 75% SaO₂ provides safety.2

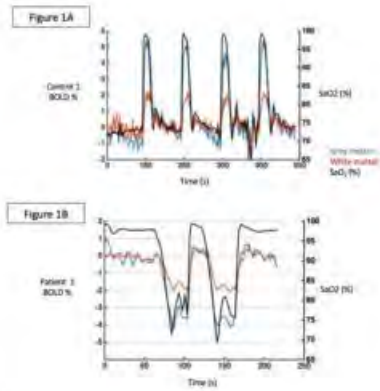


Figure 3

Patient with right MCA stenosis

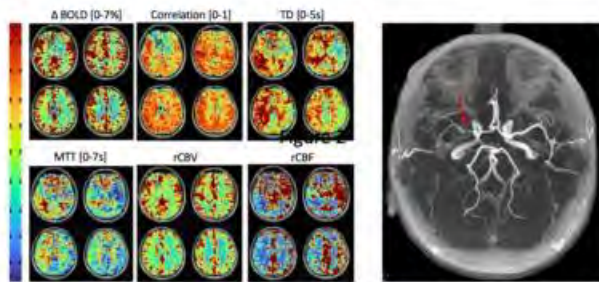


Figure 2

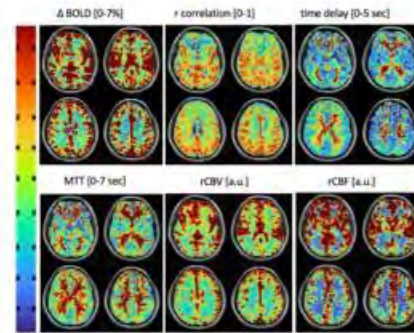


Figure 4

MCA grey matter region of interest

	side	% Δ BOLD	p value	r correlation	time delay (sec)	p value	MTT (sec)	p value	rCBV (L/R ratio)	rCBF (L/R ratio)
Patient	L	5.4±4.9	0.0001	0.7±0.2	0.9±1.3	0.0001	2.0±2.4	0.0001	1.07	0.54
	R	6.0±4.9		0.8±0.2	1.5±1.4		2.6±2.2			
Control #1	L	6.3±5.7	1	0.6±0.3	1.4±1.4	0.0018	3.2±2.7	0.012	0.99	0.90
	R	6.3±5.9		0.6±0.3	1.3±1.3		3.0±2.5			
Control #2	L	4.7±4.0	0.0061	0.7±0.3	3.1±1.3	0.0001	4.6±2.3	0.0001	0.90	0.86
	R	5.0±5.1		0.7±0.3	2.9±1.4		4.3±2.5			
Control #3	L	4.1±4.5	0.0502	0.4±0.3	2.5±1.7	1	5.1±3.6	1	0.93	0.90
	R	4.4±7.8		0.4±0.3	2.5±1.7		5.1±3.5			

(Filename: TCT_1650_Finalfigure.jpg)

146

Neuroimaging Based Prediction of Neurodevelopment Outcome for HIE Neonates

Y Youn¹, A Alber², Y Lin³, D Chow², P Chang²

¹Seoul St. Mary's Hospital - The Catholic University of Korea, South Korea, Seoul, Korea, ²UNIVERSITY OF CALIFORNIA IRVINE, IRVINE, CA, ³Taipei Medical University, Taipei, Taiwan

Purpose

This study examined the volumetric brain lesion count on MRI in addition to the location of injury patterns in association with neurodevelopmental (ND) outcomes at 18-24 months in HIE infants.

Materials and Methods

A total of 107 term or late preterm infants with HIE were identified between June 2012 and March 2016. All infants were treated with therapeutic hypothermia (TH) within the first 10 days of life. For each infant, DWI sequences from a 3T Siemens scanner were obtained for analysis. All imaging was performed after the infants were rewarmed and extubated from the ventilator. At 18-24 months, infants returned for follow-up evaluation, including cognitive, language, and motor composites of the Bayley Scales of Infant and Toddler Development III evaluated by certified examiners. DWI was analyzed both qualitatively and quantitatively for extent and pattern of brain injury. For qualitative assessment, all images were independently reviewed by two neuroradiologists who were blinded to the final outcome. Additionally, for quantitative assessment, both reviewers created manual 3D segmentation masks for all DWI lesions. Based on these annotations, quantitative metrics including lesion count, size and distribution were extracted.

Results

Of the 107 infants, 36 of the 107 infants (33.6%) had normal brain MR images, and 71 of the 107 infants (66.4%) had abnormal MRI findings. The number of clinical seizures was significantly higher in the abnormal MRI group ($p < 0.001$) than in the normal MRI group. At 18-24 months, 76 of the 107 infants (70.0%) showed normal ND stages, and 31 of the 107 infants (29.0%) exhibited abnormal ND stages. Overall, infants with ND demonstrated significantly greater total number (14.16 vs 5.29) and size (384 cm³ vs 91.2 cm³) of DWI lesions. Significant differences in lesion count and distribution were noted for small lesions (<0.67 cm³) and large lesions (>3.32 cm³), however not for intermediate sizes. Additionally, DWI lesion involvement of the basal ganglia (BG) and thalamus were statistically correlated with ND at 18-24 months. A summary of key findings are shown in Figure 1.

Conclusions

In addition to clinical seizure, a larger total lesion count, lesion size as well as lesion involvement of the basal ganglia and thalamus were significantly associated with abnormal neurodevelopment at 18-24 months.

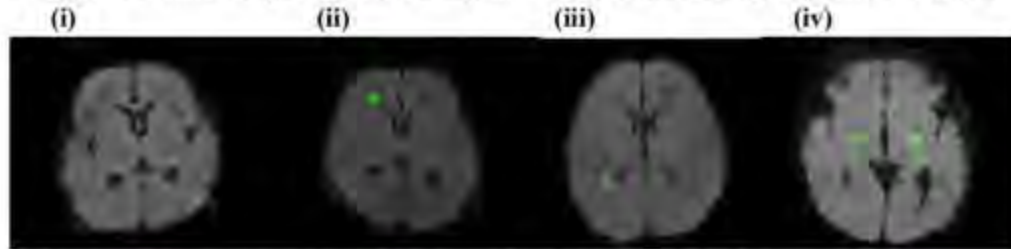
Fig1. Neonatal Hypoxic Ischemic Encephalopathy

A: Total lesion count and size in the brain MRI in association to neurodevelopmental (ND) outcomes at 18-24 months

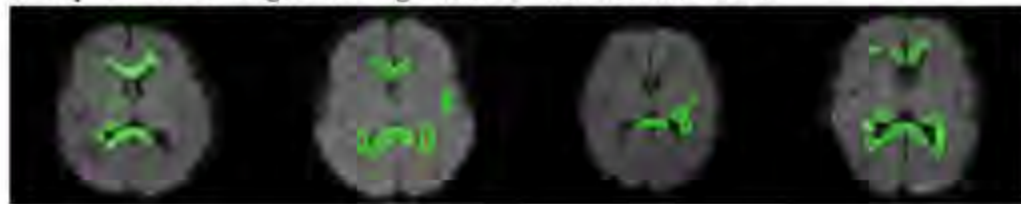
Brain MRI	Normal ND (n=71) ^a	Abnormal ND (n=36) ^a	p- value
Size, cm ³	91.25(179.63)	384.77(527.18)	<0.001
lesion size < 0.67	56(76.7)	12(38.7)	<0.001
lesion size 0.67-1.32	5(6.8)	3(9.7)	0.926
lesion size 1.32-3.32	8(11)	7(22.6)	0.216
lesion size >3.32	4(5.5)	9(29)	<0.001
Total lesion count	5.29(9.29)	14.16(12.49)	<0.001
counts <2	41(56.16)	9(29.03)	0.0113
count between 2-14	22(30.14)	4(12.90)	0.0634
count between 14-40	9(12)	16(51)	<0.001
count >40	1(1.37)	2(6.45)	0.1567
Total lesion count per volume, cm ⁻¹			
lesion size < 0.67	5.29(9.29)	14.16(12.49)	<0.001
lesion size 0.67-1.32	0.18 (0.54)	0.52(0.81)	0.014
lesion size 1.32-3.32	0.07 (0.38)	0.10 (0.40)	0.735
lesion size > 3.32	0.00 (0.00)	0.06 (0.25)	0.028

^aAll values reported as: mean (standard deviation)

B: Representative images from normal(i) and low lesion burden(ii-iv) neonatal MRIs



C: Representative images from high lesion burden neonatal MRIs



Neuroimaging Findings of Brain MRI and CT in Patients with COVID-19: A Systematic Review and Meta-analysis

Y CHOI¹

¹Seoul St. Mary's Hospital, Seoul, Korea, Republic of

Purpose

To comprehensively evaluate the incidences of abnormal neuroimaging findings in patients with COVID-19 via a systematic review and meta-analysis.

Materials and Methods

PubMed-MEDLINE and EMBASE were searched for original articles reporting imaging findings of the brain in adult patients with COVID-19 between January 1, 2020 and October 9, 2020. Abnormal neuroimaging findings were categorized as (1) cerebral microhemorrhages, (2) acute spontaneous intracranial hemorrhage (ICH), (3) acute to subacute infarcts, and (4) encephalitis or encephalopathy. Pooled incidences of neuroimaging findings were assessed using random-effects modeling. Between-study heterogeneity was explored by using the χ^2 statistic for pooled incidences and the inconsistency index I². The quality of the studies was evaluated using the Risk of Bias Assessment Tool for Nonrandomized Studies. Subgroup meta-regression analysis was performed to identify potential sources of heterogeneity.

Results

Twenty-one eligible papers, including 2125 patients, were identified. The pooled incidences of cerebral microhemorrhages, acute spontaneous ICH, acute/subacute infarcts, and encephalitis/encephalopathy were 6.9% (95% confidence interval [CI], 4.9%–8.9%), 5.4% (95% CI, 3.1%–7.6%), 24.0% (95% CI, 16.1%–31.8%), and 3.3% (95% CI, 1.9%–4.7%), respectively. Substantial heterogeneities were noted for all neuroimaging findings (I² = 87%–97%). Significant publication biases were present in the pooled incidences. In the subgroup meta-regression analysis, patients with mean or median ages over 65 years showed a significantly lower incidence of encephalitis/encephalopathy (P < 0.001). Furthermore, studies reported that patients in ICU had significantly higher incidences of cerebral microhemorrhages (P < 0.001) and encephalitis/encephalopathy (P < 0.001).

Conclusions

Considerable incidences of abnormal neuroimaging findings have been reported in patients with COVID-19. Acute to subacute cerebral infarction was the most prevalent neuroimaging finding.

932

Neuroimaging of Emergent Psychiatric Presentations: Toward Imaging Wisely

L Tu¹, A Venkatesh², A Malhotra³, K Sheth⁴, H Forman⁵

¹Yale School Of Medicine, New Haven, CT, ²Yale University, New Haven, CT, ³Yale University School of Medicine, New Canaan, CT, ⁴Yale, New Haven, CT, ⁵Yale University, new haven, CT

Purpose

Acutely psychotic, hallucinating, and delusional patients as well as those with suicidal or homicidal ideation are commonly imaged in the ED setting to exclude "medical" causes for behavioral disturbance. There is little summative guidance on the yield and value of these studies in the emergency setting. The purpose of this study is to describe the yield of emergent CT imaging in common acute psychiatric presentations.

Materials and Methods

Reports of CT head imaging for the period 3/1/2014-3/1/2020 at an academic medical center were searched for key terms including "hallucinations," "delusions," "psychosis," "suicidal," "homicidal," as well as related terms. Each report and the associated patient record were reviewed. Patients were classified based on whether they had an isolated psychiatric presentation or had other/additional indications for imaging. Reports were classified based on whether there were acute findings, non-acute but possibly explanatory findings, or had no contributory findings.

Results

Search of the imaging database revealed 270 patients who received CT head imaging for hallucinations, delusions, and/or other psychotic presentation. All patients with management changing findings (n=10) had another indication for head imaging or known underlying structural abnormality (n=61). These include neurologic defect, trauma, or brain metastatic disease. CT imaging had yield of 0% for patients with isolated hallucinations (0/133), isolated delusions (0/10), other psychotic presentation (0/48), and any combination of these (0/8). 98 patients were acutely suicidal and/or homicidal. All patients with management changing findings on CT (n=7) had suffered head trauma or had another indication for imaging (n=58). CT imaging had yield of 0% for all patients with isolated suicidal and/or homicidal ideation (n=40) without other indication for imaging. This includes patients (n=13) with an inhalational/ingestion event, as well as those with trauma to other parts of the body, e.g. wrists (n=2), which do not require head imaging. Review of the related literature similarly finds zero/near zero yield of potentially explanatory findings where patients are imaged for isolated psychiatric presentations.

Conclusions

We present updated evidence that CT head imaging in isolated, acute psychiatric presentations without other imaging indications has very low, perhaps even zero, diagnostic yield. A simple decision rule, expanding on what is found in the "Imaging Wisely" campaign is suggested.

681

Neuroimaging Signatures Across a Dimensionality-Reduced Spectrum of Post-Traumatic Psychopathology

S Pan¹, P Nédélec¹, M OLARU¹, A Rauschecker¹, L Sugrue¹

¹University of California, San Francisco, San Francisco, CA

Purpose

The spectrum of psychopathology in post-traumatic stress disorder (PTSD) is diverse, with distinct domains spanning symptoms of intrusion, avoidance, negative affect, and hyperarousal (1) (a). To interrogate the neurobiological basis of this diversity, we defined low-dimensional representations of post-traumatic stress symptoms (PTSS) within a large dataset of trauma-exposed adolescents and analyzed anatomical and functional neuroimaging signatures associated with those representations. The goal of the study is to identify putative neuroimaging biomarkers of PTSD endophenotypes to guide efforts for precision psychiatry therapies.

Materials and Methods

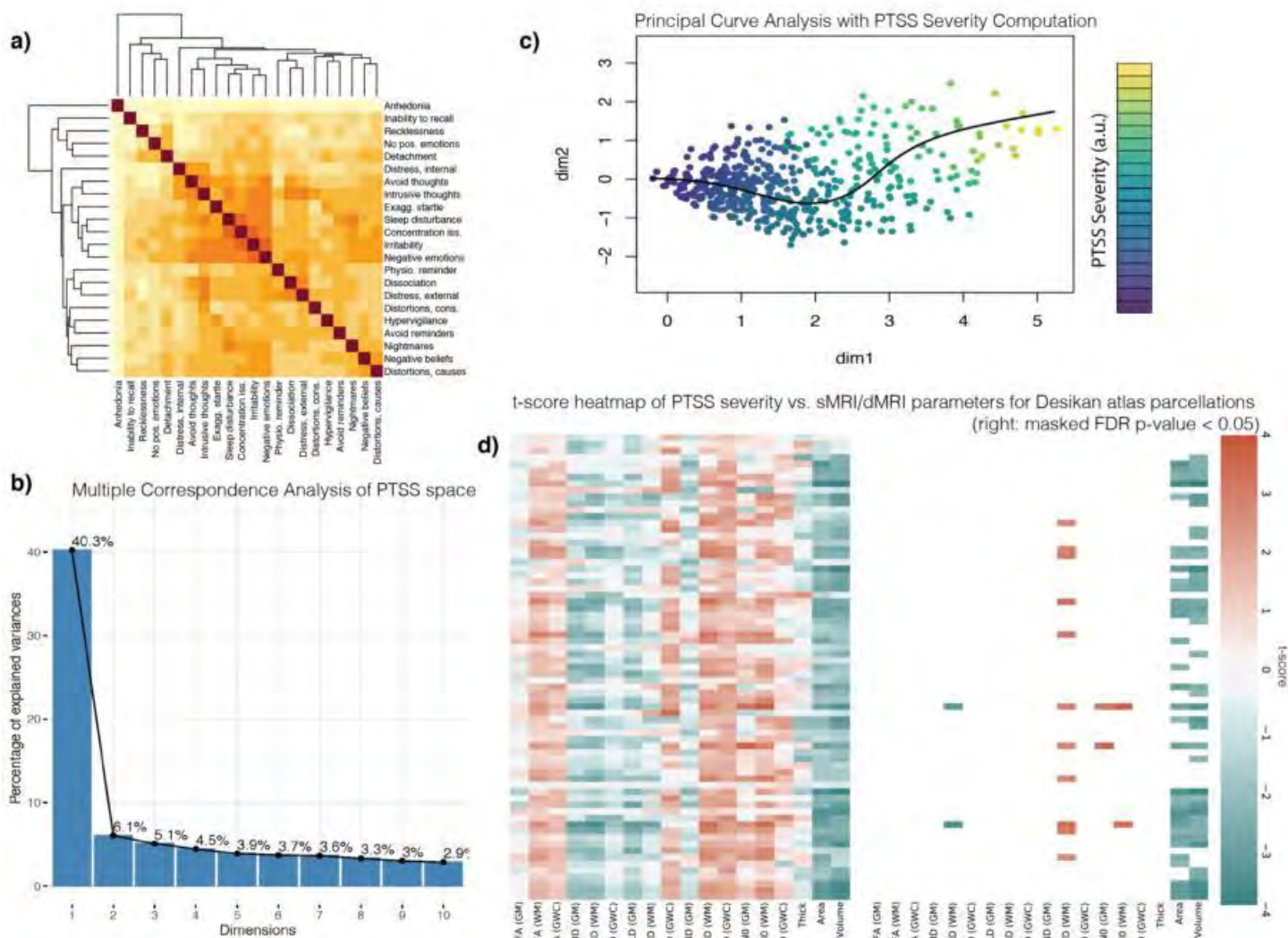
The Adolescent Brain Cognitive Development (ABCD) study is a nationwide study of over 11,000 developing adolescents who undergo yearly structural/functional MRI scans with psychosocial surveys (2,3). Multiple correspondence analysis (MCA) was performed on K-SADS questionnaire responses from subjects with a history of trauma exposure (b). Principal curve analysis was then applied to compute a general metric of PTSS severity (c). The first two principal dimensions and the PTSS severity were used as independent variables for mixed effects linear models for structural, diffusion, and functional MRI parameters across atlas parcellations of cortical and subcortical brain regions (d).

Results

MCA of PTSS K-SADS questionnaire responses yielded two dimensions explaining 46.4% of the variance in PTSS space. The first dimension (40.3% of variance) corresponded to symptoms of hyperarousal and physiological reactivity, while the second dimension (6.1% of variance) captured symptoms of negative affect such as detachment and anhedonia. Mixed effects linear modeling revealed global reductions in cortical and subcortical volume and area with increasing PTSS severity. Conversely, an increased neurite density signal was detected in multiple regions of cortical white matter as PTSS severity increased. Increased white matter neurite density but not decreased brain volume within trauma-exposed subjects was specifically associated with hyperarousal symptoms.

Conclusions

PTSS severity is associated with widespread reductions in brain volume and increased white matter neurite density in frontal and limbic circuits, possibly indicative of increased myelination. This putative increase in white matter myelination may be a specific biomarker for hyperarousal and irritability within trauma-exposed adolescents.



(Filename: TCT_681_2021_ASNR_ptsd.jpg)

198

Neuroradiologist Evaluation of the Partially Imaged Shoulder during MRI Brachial Plexus Exams: A Musculoskeletal Radiologist Peering over our Shoulders

I Ikuta¹, A Abou Karam², V ZHRABIAN³, A Malhotra⁴, A Wang⁵

¹Yale University School of Medicine, New Haven, CT, ²Yale Medicine, New Haven, CT, ³YALE SCHOOL OF MEDICINE, NEW HAVEN, CT, ⁴Yale University School of Medicine, New Canaan, CT, ⁵Yale New Haven Hospital, Guilford, CT

Purpose

At our institution, only neuroradiologists read MRI brachial plexus. However, it is not uncommon for a shoulder pathology to clinically mimic a brachial plexopathy. We asked a musculoskeletal (MSK) radiologist to evaluate our reporting of the partially visualized shoulder.

Materials and Methods

PACS was queried for MRI brachial plexus exams between 1/1/2019-8/30/2020 for patients older than 18 years. An academic, fellowship-trained MSK radiologist retrospectively reviewed the images & exam reports. The shoulder dictation was rated by the MSK radiologist as: 0=not reported; 1=disagree, addendum suggested; 2=disagree, no addendum suggested; 3=okay dictation; 4=excellent shoulder dictation. The MSK radiologist also rated report recommendations for MRI shoulder as: 0=no recommendation dictated; 1=disagree, addendum suggested; 2=agree, but would have changed arthrogram component; 3=agree, including any arthrogram recommendation. Percentages for each rating were calculated.

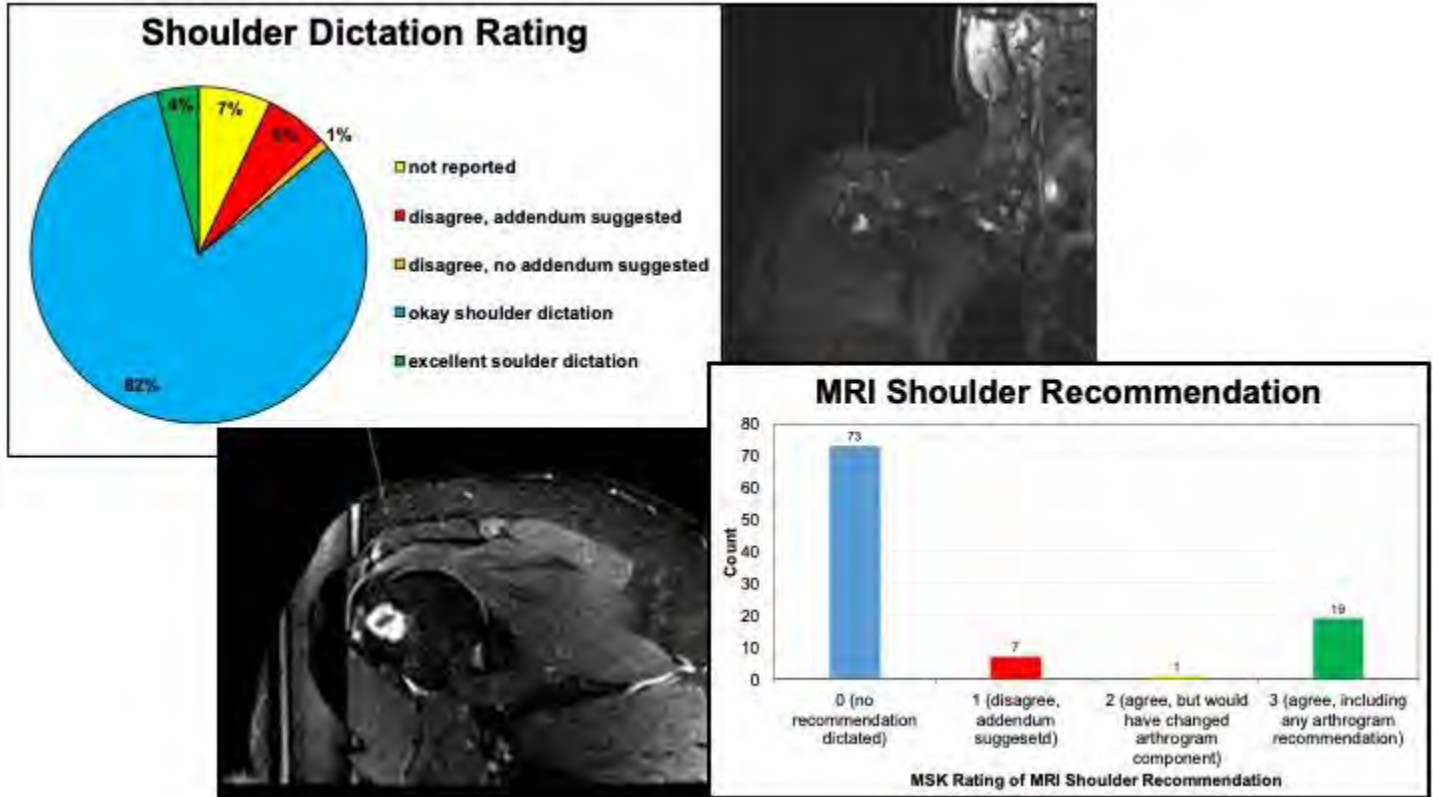
Results

100 MRI brachial plexus exam images and reports were reviewed by an MSK radiologist. For dictations of the partially imaged shoulder, 6% of cases were discordant with addendum suggested by the MSK radiologist. In 1% of cases the MSK radiologist

disagreed, but no addendum was necessary. 7% of cases had no report of the shoulder at all in the report. 86% of the reports were deemed okay or excellent by the MSK radiologist. With regards to reports recommending MRI shoulder exam, 7% had a disagreement with an addendum suggested. 1% study had an MRI shoulder recommended, but the MSK radiologist would have changed the arthrogram component. The MSK radiologist agreed with 19 MRI shoulder recommendations including arthrogram component. 73% of cases had no recommendation for MRI shoulder.

Conclusions

With 7% of neuroradiologist dictations discordant with MSK radiologist interpretations of the partial visualized shoulder on MRI brachial plexus, & 8% disagreement on dedicated MRI shoulder recommendations, there remains room for improvement. Perhaps our neuroradiologists could undergo some review & education on shoulder pathology on MRI. MRI brachial plexus is not a dedicated evaluation of the shoulder with special views, sequences, and arthrography, but that does not mean that it can be ignored. In fact, given the difficulty of interpreting a shoulder on suboptimal sequences, MRI brachial plexus might potentially benefit from separate MSK reads at academic institutions.



(Filename: TCT_198_Brachial_Shoulder_ASNR21.jpg)

657

Neuroradiologists’ Friend or Foe: Utility versus Futility of Contrast Enhanced MR Angiography in patients with previously treated dural AV Fistulas.

J Saucedo¹, R MATTAY², R Kurtz³, L Loevner⁴, S MOHAN⁵

¹Perelman School of Medicine, Philadelphia, PA, ²HOSPITAL OF THE UNIVERSITY OF PENNSYLVANIA, PHILADELPHIA, PA, ³University of Pennsylvania, Berwyn, PA, ⁴Hospital of the University of Pennsylvania, Philadelphia, PA, ⁵UNIVERSITY OF PENNSYLVANIA, PHILADELPHIA, PA

Purpose

In recent years, studies have explored the utility of contrast enhanced magnetic resonance angiography (CE MRA) as an accurate method to screen for and follow AVFs (1, 2, 3, 4). Despite the gaining popularity of this less invasive imaging modalities, it does carry with it certain risks and disadvantages, namely, gadolinium exposure, which has recently been linked to intracranial deposition in even healthy patients. As there is a lack of relevant literature systematically describing the utility of isolated unenhanced angiographic imaging in the follow-up of dAVF treated with embolization, we performed a retrospective review and comparison of CE and unenhanced 3D Time of Flight (TOF) MRA for the follow-up of post-embolized dAVF cases in order to document contrast necessity or lack thereof.

Materials and Methods

Two neuroradiologists, with 16 and 6 years of experience in neurovascular imaging, independently and prospectively reviewed retrospective TOF MRA and CE MRA imaging for evidence of residual dAVF among 20 patients who had been previously treated

with endovascular embolization. A ground truth of residual dAVF was ultimately confirmed by follow up DSA (n=10) or MRA (n=4) when available. For each patient, the radiologists initially analyzed the TOF images, recorded the presence or absence of dAVF and then analyzed the contrast enhanced images, again recording the presence or absence of residual dAVF.

Results

Of the 20 patients in our study (mean age: 51 y; 15 F), review by the two neuroradiologists showed that 12 had no evidence of residual dAVF, 7 had evidence of residual dAVF, and one had a false positive dAVF. AV shunting was detected on TOF MRA images of all 7 patients which had recurrence. In two cases, a residual dAVF as confirmed by follow up imaging was seen on only the TOF images and not seen on the CE MRA. In one case, both reviewers missed a subtle TOF abnormality, but found an abnormality on CE MRA (Figure). The presence of residual dAVF was absent on the subsequent DSA, suggesting a false positive finding. Among the 12 patients with no evidence of post-embolization dAVF, there was complete agreement between TOF and CE MRA for correctly identifying the absence of any lesion.

Conclusions

Patients who have undergone embolization for dAVF are often followed with CE MRA. Our study, however, highlights the viability of isolated unenhanced TOF MRA as an alternative for follow up imaging for this specific set of patients who are prone to more gadolinium exposure in their lifetime.

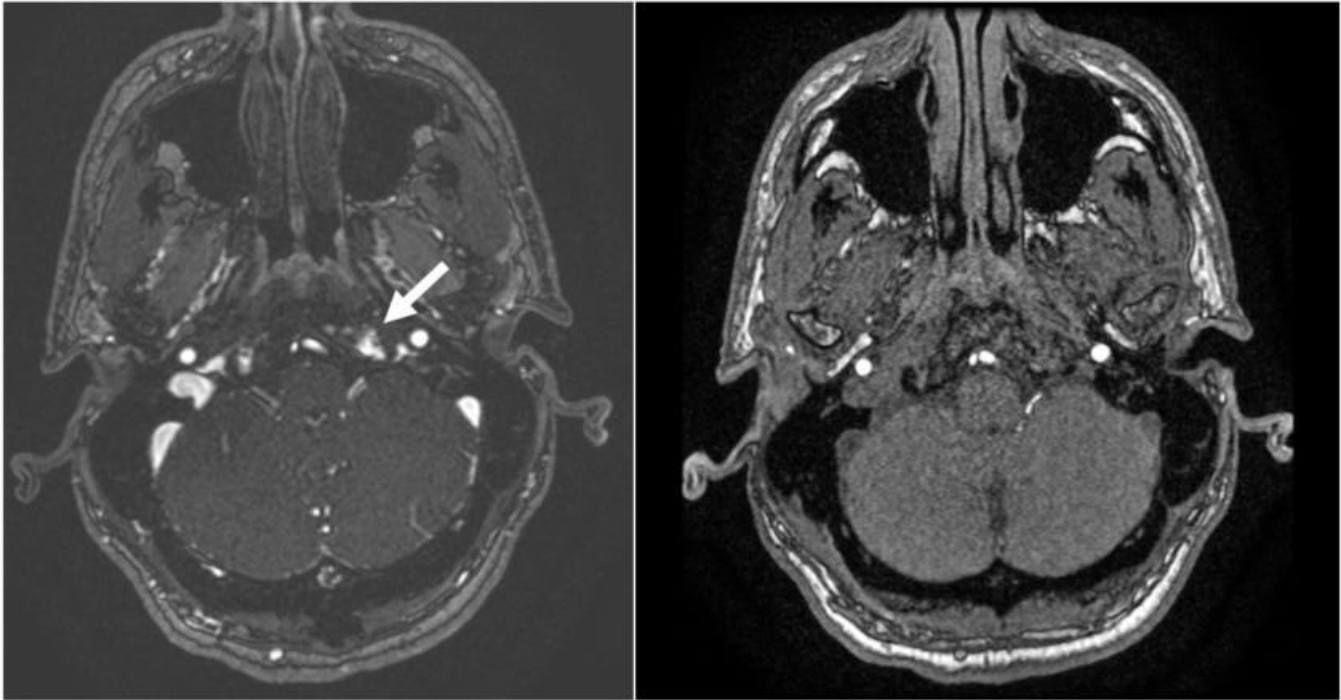


Figure 1: The CE MRA on the left displays abnormal enhancement at the left skull base (arrow). The TOF MRA on the right shows no evidence of arterialized flow shunting into this region of enhancement. As shown on follow-up DSA, there was no recurrence of dAVF, suggesting this is an example of a false positive recurrence on CE MRA. These findings were presumed to be from a small skull base osseous hemangioma.

(Filename: TCT_657_dAVFFigure1final____.jpg)

1053

Neuroradiology Peer Learning: Analysis of a Two-Year Experience at a Large Academic Institution

N Bates¹, T Massoud¹, S Hashmi²

¹Stanford University School of Medicine, Stanford, CA, ²Stanford College of Medicine, Palo Alto, CA

Purpose

Score-based peer review (PR) reflects an outdated quality assurance (QA) approach in Radiology. PR quantifies individual error rates for comparison to those of peers and national averages. Poor scores identify underperformers who can receive remediation, education, proctoring, counseling, but sometimes suspension or revocation of privileges. PR is often perceived as punitive; it thus undermines recognition of mistakes as learning opportunities, discourages openness and trust amongst peers, and fails at acknowledging successes.

Conversely, peer learning (PL) cultivates deep learning, fosters interpersonal professional relationships, and ultimately promotes high individual and organizational performances. In an anonymous fashion, PL focuses on lessons learned from mistakes rather than demonizing the responsible individuals. Hence PL is better aligned with the principles promoted by the Institute of Medicine's recommendations in reducing medical diagnostic errors. We critically appraised our PL program for its alignment with these principles and recommendations.

Materials and Methods

We routinely collect and review neuroradiology cases at PL conferences conducted on 6 occasions per year. Patient cases with diagnostic misses or "good pickups" are submitted by clinical staff to our quality improvement representative. We hold group discussions to identify types of errors that led to misses. We retrospectively analyzed our PL cases collected over 2 years and classified them according to the 12 Renfrew types of individual diagnostic errors.

Results

We observed individual and system errors in 120 PL cases over two years. Individual errors were perceptual (70%) and cognitive (30%). Our 12 error types were: "under-reading" (45%); "faulty reasoning" (22%); "poor communication" (9%); "location" based misses (6%); "satisfaction of search" (5%); and "complacency" where a finding was identified but attributed to incorrect cause, "lack of knowledge", "technique" and "history" errors due to incomplete clinical information at interpretation time (all <5%). We did not observe "satisfaction of report" related to over-reliance on prior reports, "prior examination" related to failure of reviewing prior imaging, and "complication" errors related to interventional procedures.

Conclusions

The Radiology academic community has steered away from a PR-based QA attitude and method towards PL. We share details of our PL program and quantify various types of errors we observed in a busy academic setting during a two-year period.

120

Neurovascular Complications in COVID-19 Infection

A FRANCESCHI¹, R Arora¹, R Wilson², O Ahmed³, L Giliberto¹, R Libman¹, M Castillo²

¹Northwell Health, Manhasset, NY, ²University of North Carolina, Chapel Hill, NC, ³SUNY Stony Brook, Stony Brook, NY

Purpose

COVID-19 is a predominantly acute respiratory disease caused by the severe acute respiratory syndrome coronavirus 2 (SARS-CoV-2). In addition to progressive atypical respiratory system distress, other organ systems including the central nervous system are affected in part due to the affinity of SARS-CoV-2 for the angiotensin-converting enzyme 2 (ACE2) receptors. A subgroup of patients with severe COVID-19 develop cytokine storm syndrome characterized by hyperinflammation due to rapid accumulation of T-cells and macrophages resulting in release of massive level of cytokines into the bloodstream aiming to destroy the offending pathogen leading to multi-organ system dysfunction. Furthermore, an important feature of COVID-19 infection is a thromboembolic diathesis, often resulting in devastating brain vascular events, and requiring anticoagulation/antiplatelets measures.

Materials and Methods

Available neuroimaging studies including CT head, CTA head and neck and MRI brain as well as medical records were reviewed for 12 hospitalized patients with COVID-19 confirmed by positive PCR for SARS-CoV-2 and with positive chest CT imaging demonstrating bilateral abnormalities, which were multi-lobar with subpleural, peripheral and posterior in distribution, and ranged from ground glass opacities to consolidation and cavitation.

Results

Twelve subjects included 5 females and 7 males, age range 37-73 years. Most of our patients (8 of 10) had significant comorbidities more commonly hypertension (6), morbid obesity (4), diabetes (3) and cancer (1). Nine patients required mechanical ventilation and 5 expired. Neurologic complications included 7 large vessel occlusion CVAs (five with petechial hemorrhages or hemorrhagic transformation), 2 microembolic-type infarctions, 2 cases of hemorrhagic posterior reversible encephalopathy syndrome (PRES) and 1 intra-axial cerebellar hemorrhage.

Conclusions

Although multifactorial, in many patients neurovascular diathesis in the setting of COVID-19 infection may be explained by a combination of cytokine release syndrome resulting in severe inflammation, leading to endothelial dysfunction, a hypercoagulable state, cardiopulmonary dysfunction with hypoxia and hemodynamic insufficiency accentuated by direct viral-mediated breakdown of the blood brain barrier. Although our study is a small observational series it demonstrates the wide range of severe brain findings in patients with COVID-19 and these should be kept in mind when imaging such patients.

674

Neurovascular Manifestations in pediatric patients with Hereditary Haemorrhagic Telangiectasia

R Azma¹, A Dmytriw¹, A Biswas¹, M Pollak¹, F Ratjen¹, A Amirabadi¹, H Branson¹, A Kulkarni¹, P Muthusami¹

¹The Hospital for Sick Children, University of Toronto, Toronto, Ontario

Purpose

Hereditary hemorrhagic telangiectasia (HHT) is a vascular dysplasia affecting various organs including lung, liver, brain, spine and mucocutaneous tissues (1). There are limited data in the literature regarding neurovascular manifestations and genotype-phenotype of HHT in children. The purpose of the study is to describe the neurovascular findings in a large cohort of children with HHT and to identify correlations between phenotype and genotype.

Materials and Methods

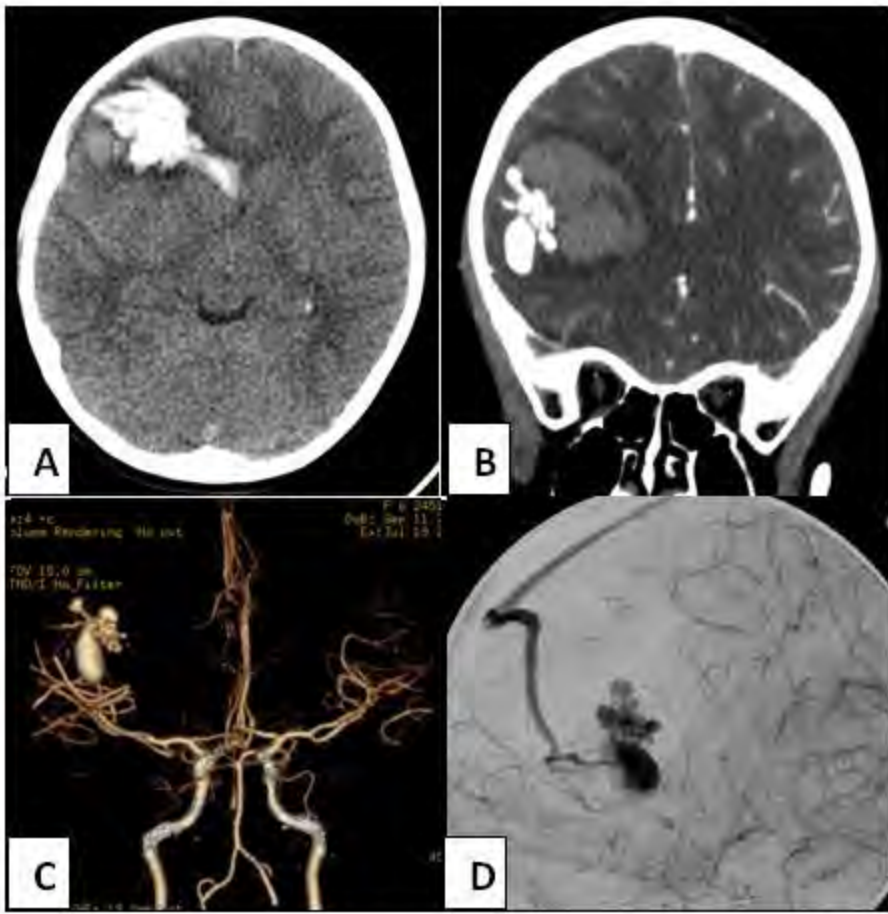
This retrospective study was conducted on 221 children (<18 years) with Curacao criteria-based and/or genetically proven HHT over a 19 year period. Demographic and clinical information, imaging findings and follow up information were gathered. Baseline and demographic characteristics were summarized using descriptive statistics as mean for continuous variables and fractions or percentages for categorical variables. Proportion of patients with bAVM was compared between different genotypes, using Chi-square or Fisher exact test. P value <0.05 (two-tailed) was considered statistically significant.

Results

221 children with HHT (70.6% genetically confirmed, and 99.1% positive family history) were included, with a mean age of 7.1 ± 4.6 years (range 0.3 to 17.0 years) and a 58.8% male predominance. Neurovascular lesions were found in 64/221 (28.9%) showing cerebral vascular malformations, with 3.1% prevalence of intracranial hemorrhage. The most commonly-observed vascular malformations were developmental venous anomalies (48.4%) and brain arteriovenous malformations (AVM, 29.7%), followed by capillary malformations (14.1%). Multiple arteriovenous malformations were seen in 10.0% of the cohort. We found no instances of de novo arteriovenous malformation (1281.8 patient-years). A significantly higher proportion of patients with endoglin (ENG) mutations [17/81 (30%)] were found to have bAVM, compared to activin A receptor type II-like 1 (ACVRL1) [2/61, (3.2%)] and SMAD4 [0/5, (0%)] mutations $p < 0.01$). More than half of the patients with bAVM [10/19 (52.6%)] had concomitant pulmonary AVM, all of whom were ENG positive.

Conclusions

We describe the neurovascular imaging findings from a large pediatric cohort of HHT allowing for clinical awareness, and guidance of management in pediatric HHT patients.



7 year-old girl presenting with depressed sensorium post seizure from ruptured pial arteriovenous fistula (AVF). A) Axial unenhanced CT section showing right frontal parenchymal hematoma dissecting through the white matter B) Coronal sections from CT angiography and C) 3D vascular reconstruction showing prominent arterial channels with a dilated venous pouch associated with the lateral aspect of the hematoma. D) Lateral projections from catheter angiography showing a single hole AVF fed from a prefrontal right middle cerebral artery branch, draining superficially to the superior sagittal sinus.

(Filename: TCT_674_FigurePialAVF.jpg)

1052

Non-Invasive Advanced Imaging Metrics Provide Potential Biomarkers For Glioblastoma Biological and Immunological Heterogeneity

C Kersch¹, R Barajas Jr.²

¹Oregon Health & Science University, Portland, OR, ²OHSU, Portland, OR

Purpose

Treatment of glioblastoma is complicated by extensive tumor heterogeneity, of which intra-tumoral variability is particularly challenging to thoroughly assess with direct tissue analysis methods. We hypothesize that transcriptomic analysis of brain tumor

regions with different magnetic resonance imaging (MRI) characteristics will define specific biological processes, providing a non-invasive method for tumor characterization and stratification.

Materials and Methods

Previously at the University of California San Francisco, treatment naïve glioblastoma tissue from gadolinium contrast enhancing lesion (CEL) and non-enhancing lesion (NCEL) regions were stereotactically sampled (Barajas et al 2010). Prior to resection, relative cerebral blood volume (rCBV) and apparent diffusion coefficient (ADC) were determined. The tissue samples were characterized by immunohistochemistry and assessed for gene expression by microarray analysis. We correlated gene expression patterns in the CEL, NCEL, and non-tumor gliotic brain samples with multimodal physiological imaging metrics phenotypes. Gene expression networks were probed using Gene Set Enrichment Analysis and deconvolution using CIBERSORT. Key immunologic genes were examined individually.

Results

Samples with differing MRI and histological phenotypes demonstrated transcriptomic variance reflecting distinct biological networks. We found significant differences in immune pathways, with immune gene signature prominent in CEL areas, moderate in NCEL and low in gliotic non-tumor brain. Within homogeneously enhancing areas of CEL and NCEL there was underlying heterogeneity detectable by variable rCBV, ADC and histological phenotypes, which correlate with differing gene expression profiles indicative of biological and immunological tumor microenvironments. Increasing rCBV was correlated with a more anti-inflammatory immune response in the CEL and pro-inflammatory immune response in the NCEL. Glioblastoma samples with the mesenchymal molecular subtype had the greatest immune response.

Conclusions

Multimodal MRI features identify regionally diverse transcriptomic-based biological and immunological phenotypes in glioblastoma. We propose that imaging genomics provides a technique for localizing biological processes and tumor immune microenvironments across space and time in glioblastoma.

472

Non-obstetrical Ping-Pong Fractures in Children

M RYAN¹, E Charleston², A Fingarson³

¹ANN & ROBERT H. LURIE CHILDREN'S HOSPITAL OF CHICAGO, CHICAGO, IL, ²ANN & ROBERT H. LURIE CHILDREN'S HOSPITAL OF CHICAGO, Chicago, IL, ³Ann and Robert H. Lurie Children's Hospital, Chicago, IL

Purpose

Skull fracture patterns in young children differ from adults due to a thinner, more malleable calvarium and incomplete ossification. One fracture type specific to young children is a depressed "ping pong" fracture characterized by deformation of the calvarium without discrete lucency (1). Ping pong fractures are most commonly described during birth, often as a consequence of obstetrical instrumentation (2,3). However, this type of fracture can also occur from other types of head trauma during the first few years of life (4). We retrospectively reviewed associated clinical and radiographic findings in children with non-obstetrical ping-pong type fractures

Materials and Methods

Patients were identified through a radiology report search engine (mPower) using "ping" and/or "pong" as keywords. Imaging was reviewed by a pediatric neuroradiologist and patient records and social work documents were reviewed by a child abuse pediatrician.

Results

We identified 12 children who demonstrated the classic morphology of this fracture. The mean age was 6.8 months (range 7 weeks to 11 months). All fractures were parietal (3 left and 9 right). Only 3 patients demonstrated scalp swelling, which was mild (2-6mm in depth); the remainder of the children showed no evidence of scalp swelling or hematoma. Intracranial injury, with ischemic changes and subdural hemorrhages, was present in only one child. A mechanism of fall was identified in 10 children. 2 patients were noted to have impacted a cornered surface; 2 patients impacted a flat surface without corner involvement and 6 patients impacted a known flat surface with an uncertain corner injury component. After evaluation by our hospital's multidisciplinary child abuse team, injuries were determined to be accidental in 9 patients, abusive in 2 patients and indeterminate in one child.

Conclusions

Ping-pong type fractures are a unique fracture morphology in young children. Although more often associated with accidental injury, this can also be seen with abusive head trauma. An identifiable corner impact may not always be present. Additionally, unlike more common linear parietal fractures, acute scalp swelling appears to be absent or relatively mild.

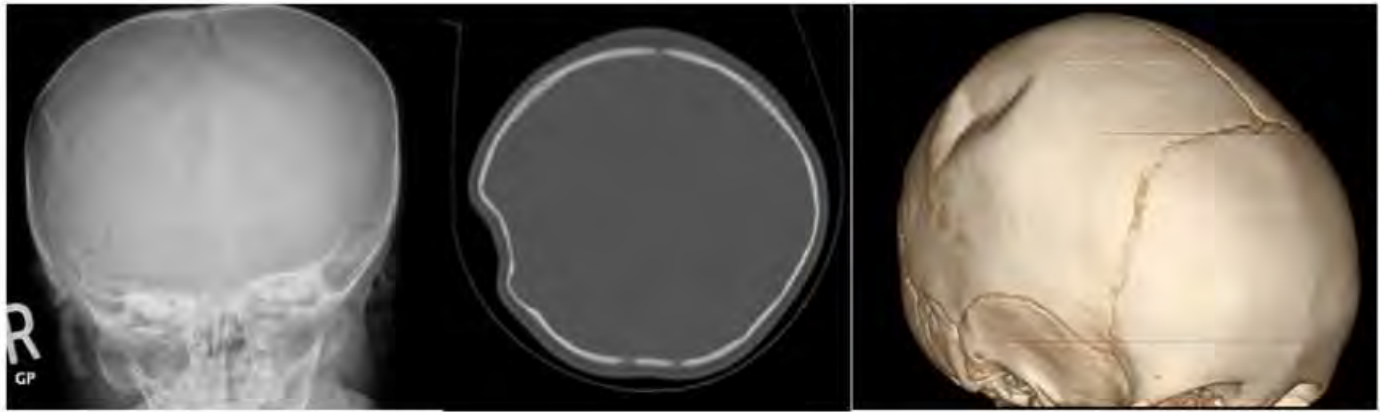


Figure: 7-month-old boy who fell 3 feet from a changing table. Ap skull films, axial and 3D reformatted CT images demonstrate a concave depression of the calvarium without a discrete lucent fracture line. Note the absence of associated scalp swelling.

(Filename: TCT_472_Fig1.JPG)

1539

Nondysraphic Intradural Spinal Lipoma: A Rare Case In A Child

A Lima Júnior¹, P Coimbra², N De Abreu³, J Rodrigues⁴, M Buratti Leal³, L Gomes⁵, A Sampaio Clarindo³, C Malveira³

¹Mount Sinai Hospital, New York, NY, ²Hospital Antônio Prudente, Fortaleza, Brazil, ³Hospital Antonio Prudente, Fortaleza, Ceará, ⁴Antonio Prudente Hospital, Ceará, Fortaleza, ⁵UniRV, Goianésia, Goiás

Purpose

Spinal cord lipomas represent a group of rare and benign tumors. It is equivalent to about 1% of all intramedullary tumors. These are injuries associated with spinal dysraphisms. The absence of association with dysraphism makes the lesion even more rare, representing about 1% of cases of spinal cord lipomas. The case to be discussed is that of a child diagnosed with intradural lipoma without associated dysraphism.

Materials and Methods

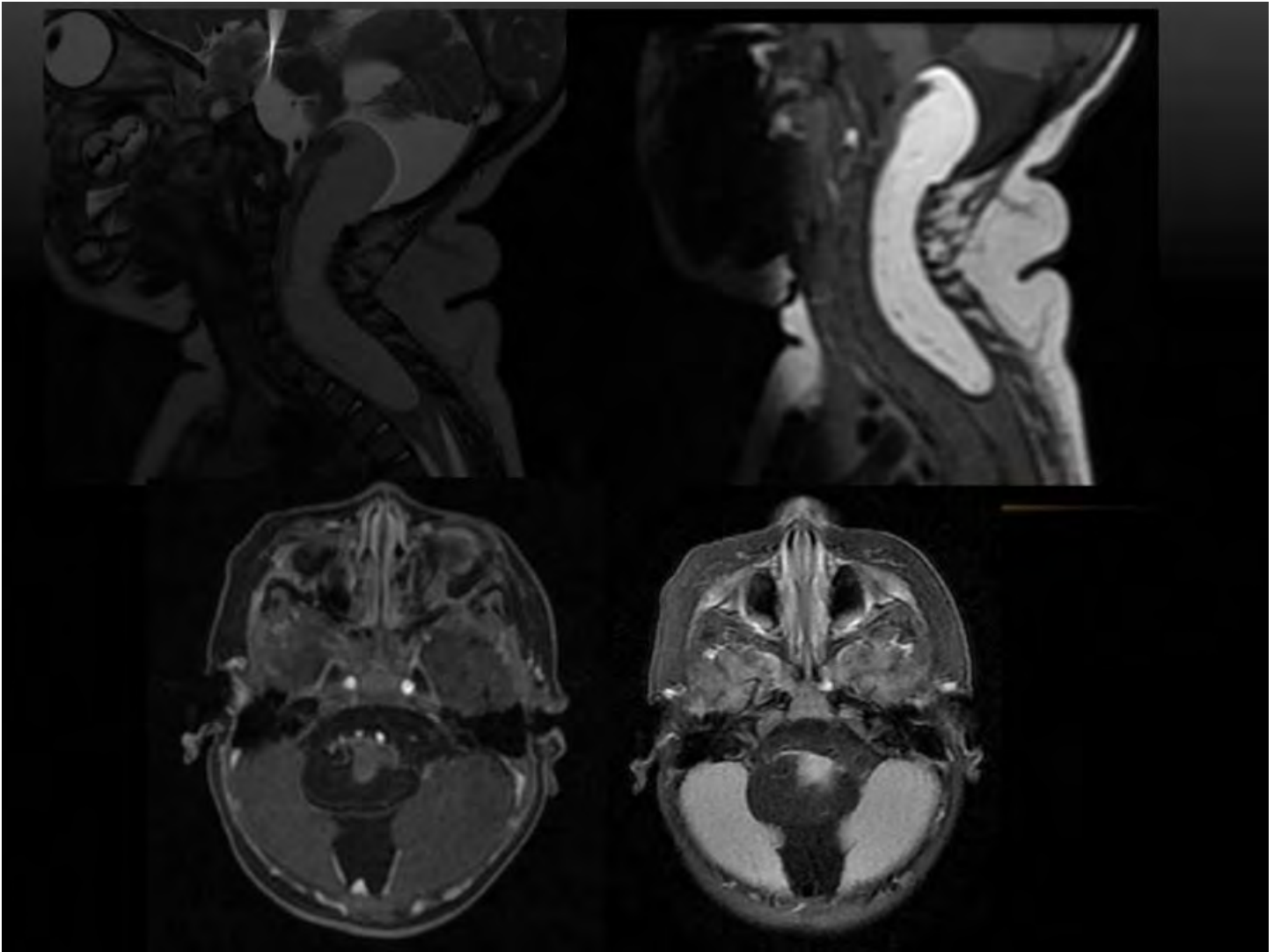
The case reported is that of an 8-month-old child who began to cry excessively, associated with a bent posture in the cervical and thoracic region at 3 months, progressively. Initially evaluated by an orthopedist who ruled out pathological processes. He presented delayed motor development, with difficulty in supporting his neck and trunk, without sitting at 7 months. Hospitalized at 8 months for gastrointestinal symptoms, where fontanelle bulging was observed, and a CT scan of the skull was requested, which showed an expansive lesion in the posterior fossa with an insinuation to the spinal canal. A skull MRI was performed, which showed an image compatible with spinal cord lipoma, with no signs of associated dysraphism. Undergoing a surgical procedure, where the tumor was partially resected due to the extent of the lesion. Is still hospitalized in ventricle shunt planning

Results

Expansive lobulated formation, well delimited and with regular contours, with a signal intensity similar to fat, is characterized in the medullary canal, extending from the cervical thoracic transition at the level of the D4 vertebral body to the posterior cranial fossa, at the level of the obex, suggestive of a lesion of lipomatous origin.

Conclusions

Intradural lipomas without association with dysraphism are rare conditions described in the literature, where the diagnosis is usually made clearly and objectively with MRI. Surgical treatment has as main objective the decompression of the spinal canal, with no need for complete excision of the lesion and contraindicated in asymptomatic patients.



(Filename: TCT_1539_Slide1-3.JPG)

1030

Noninvasive Assessment of Cerebral Hemodynamic Impairment in Intracranial Dural Arteriovenous Fistula Using Functional Near Infrared Spectroscopy- An Exploratory Study.

S SENTHILVELAN¹, S KANNATH², B Thomas², A KM³, C KESAVADAS³

¹*Sree Chitra Tirunal Institute For Medical Sciences and Technology, TRIVANDRUM, Kerala,* ²*SCTIMST, TRIVANDRUM, Kerala,* ³*SCTIMST, TRIVANDRUM, KERALA*

Purpose

Aggressive dural arteriovenous fistula could result in hemorrhage and nonhemorrhagic neurological deficits, like, cognitive impairment, aphasia etc (1). Structural imaging has not been found effective in assessing this latter complication (2). Thus, this study aims to test the feasibility of noninvasive assessment of cerebral hemodynamics using functional near infra-red spectroscopy (f-NIRS) in patients with intracranial dural arteriovenous fistula. The secondary objective is to assess the correlation between cognitive impairment in these patients with the change in the hemoglobin concentrations.

Materials and Methods

In this institutional ethics committee- approved study, after obtaining informed consent, 12 patients with intracranial dural arteriovenous fistula underwent task based functional near infrared spectroscopy before and 1 month after embolization procedure. fNIRS was also done in 12 healthy controls without any neurological disease. Additionally, neuropsychological testing was performed in all the patients and the controls. The mean change in the hemoglobin concentrations obtained from the prefrontal cortex was assessed for the oxy-, deoxy- hemoglobin and oxygen saturation (HbO, HbR and SO₂ respectively). The f-NIRS data obtained, were analysed using student t test. Neuropsychological scores were evaluated using Mann-Whitney U test and Wilcoxon signed rank test. Spearman correlation was used in assessing f-NIRS data and MMSE scores. $p < 0.05$ was considered significant.

Results

Changes in the oxy-hemoglobin was found to be consistent with a significant reduction in the oxy-hemoglobin in patients while it increased in controls ($-3.9E-05$ vs $1.8E-04$ mM, $p<0.001$). The reduced oxy-hemoglobin in the patients significantly improved after the embolization ($-3.9E-05$ vs $8.2E-05$; $p=0.003$). MMSE scores were significantly improved in controls (30 ± 1 vs 25 ± 18 in patients; $p<0.001$). MMSE scores also improved significantly in patients after embolization (25 ± 18 vs 30 ± 6 ; $p<0.001$). A moderate correlation was observed between MMSE scores and changes in the oxy-hemoglobin concentration with correlation coefficient (ρ) of about 0.5; $p=0.03$. Other hemodynamic f-NIRS parameters did not show any significant changes.

Conclusions

Task based f-NIRS with changes in the oxyhemoglobin concentration could be a useful noninvasive modality in the assessment of aggressive dural arteriovenous fistula (DAVF) with venous congestion and also assists in monitoring the treatment response in this patient sample.

DEMOGRAPHICS	PATIENT	CONTROLS	p-value
Age in years(Mean \pm S.D.)	48 \pm 13 (24-70)	45 \pm 17.8 (20-73)*	0.818
Gender (percentage)	11 males (91.7%), 1 female (8.3%).	8 males (69.6%), 4 females (30.4%).	0.557
Risk factors [#] (DM, HTN, CVT, Trauma, Hypercoagulable states)	8/12 (70%)	5/12 (41.7%)	0.192
MMSE scores [#] (Median \pm range)	25 \pm 18	30 \pm 1	<0.001

Table 1. Demographics of study participants.

DM: Diabetes mellitus, HTN: Hypertension, CVT: Cerebral venous thrombosis, MMSE: Mini-mental status examination

S.no.	Symptoms	Number of patients (n=12)
1.	Headache	7 (58.3%)
2.	Tinnitus	1 (8.3%)
3.	Ocular	4 (33.3%)
4.	Seizures	4 (33.3%)
5.	Cognitive and behavioural disturbances	5 (41.7%)
7.	Slurred speech	2 (16.7%)
8.	Tremors	1 (8.3%)

Table 2. Clinical features of the study participants

Novel Imaging Approach for Centromedian Thalamic Nucleus - Parafascicular Nucleus Visualization for Improved Deep Brain Stimulation Targeting and Outcome

L Okromelidze¹, C Lin¹, E Westerhold¹, P Vibhute¹, S Grewal¹, V Gupta², E Middlebrooks¹

¹Mayo Clinic, Jacksonville, FL, ²Mayo Clinic Florida, Jacksonville, FL

Purpose

Centromedian thalamic nucleus (CM) and parafascicular nucleus (Pf) are emerging targets for deep brain stimulation (DBS) for various neurological and psychiatric diseases, among which is drug-resistant epilepsy such as Lennox-Gastaut Syndrome. Several trials of CM-DBS reported mixed results, with positive outcomes associated with accurate positioning of the leads in CM. Unfortunately, direct visualization of CM and Pf is limited on current structural imaging techniques, and indirect targeting does not account for interpersonal variability in thalamic anatomy, leading to subprime DBS interventions as well as increased risk of surgical complications and side effects. The aim of our study was to develop the novel imaging approach for CM-Pf visualization for improved DBS targeting and outcome.

Materials and Methods

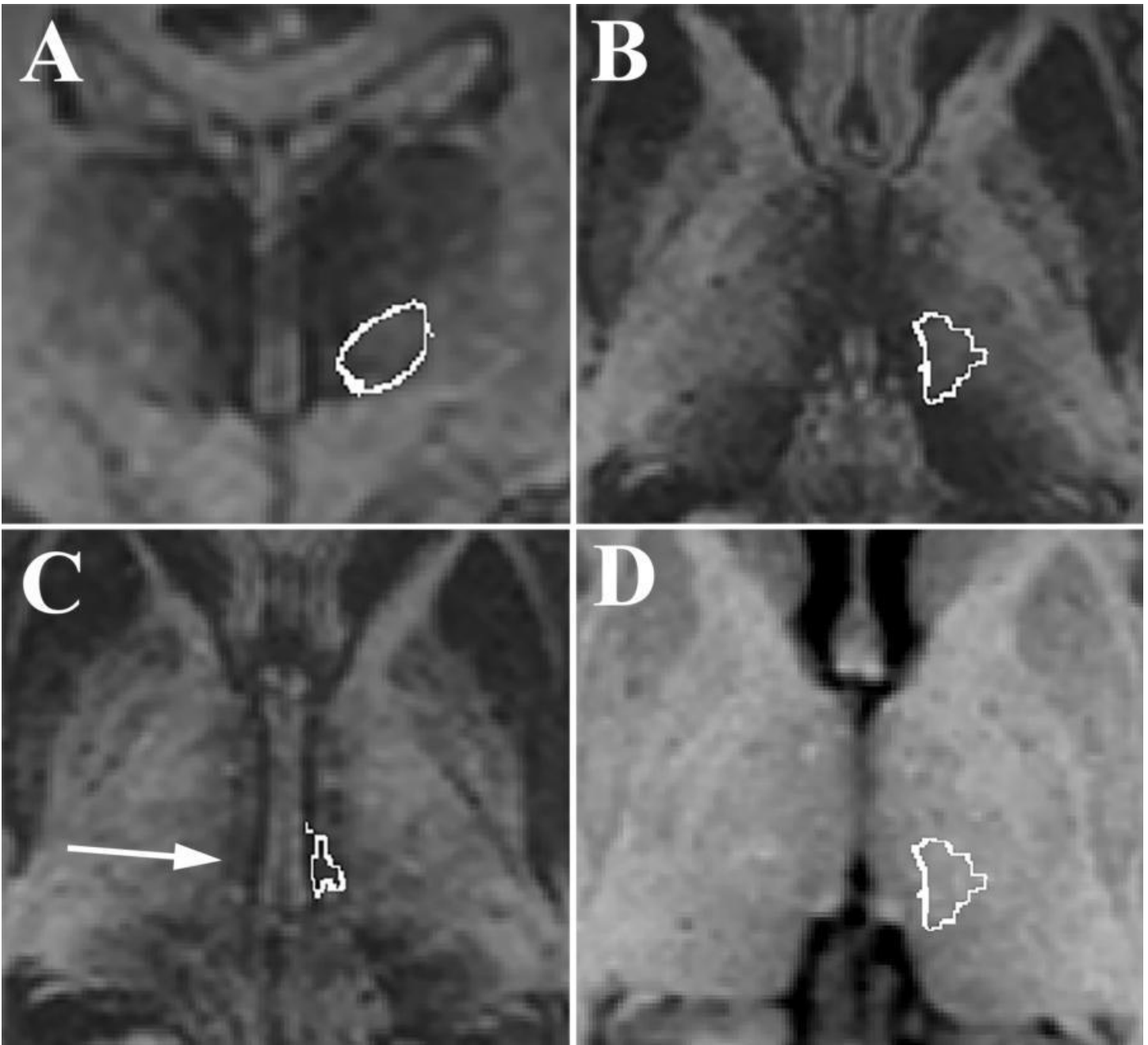
3D Edge-Enhancing Gradient Echo (3D-EDGE) is a novel MRI sequence that utilizes opposing phases of gray and white matter inversion that produces a variation in signal intensity due to variable concentration of myelinated and non-myelinated brain tissue. Multiple acquisitions were acquired on a 3T Siemens Prisma and subsequently co-registered and averaged using SPM v12 followed by resampling to 0.5 x 0.5 x 0.5 mm resolution. Resulting 3D-EDGE image was registered to the Schaltenbrand and Wahren atlas.

Results

On 3D-EDGE, both CM and Pf were readily identifiable and corresponded to the Schaltenbrand and Wahren atlas location (Figure: (A) Coronal and (B) axial 3D-EDGE image showing the corresponding location of the CM nucleus from the Schaltenbrand and Wahren atlas. The boundaries between the more hypointense medial thalamic nucleus (medially) and ventro-caudalis portae (posteriorly) are clearly visible. (C) Axial 3D-EDGE image showing the outline of the parafascicular nucleus from the Schaltenbrand and Wahren atlas and highlighted by the arrow on the opposite side. (D) High-resolution axial MP-RAGE image with overlay of the CM nucleus from the Schaltenbrand and Wahren atlas highlights the poor definition of the nucleus). On corresponding standard MP-RAGE MRI, the boundaries of neither structure were identifiable.

Conclusions

3D-EDGE produces a greater visualization of CM and Pf in comparison to other common MRI sequences. This novel imaging approach is a promising tool for improved DBS targeting and the treatment of drug-resistant epilepsy.



(Filename: TCT_719_asnr.jpg)

370

Novel machine learning method for clinically significant cortical lesion detection in multiple sclerosis

E Kazarian¹, J Port², M Aboian³

¹Yale University, New Haven, CT, ²Mayo Clinic, Rochester, MN, ³Yale University, Woodbridge, CT

Purpose

Multiple sclerosis (MS) is a CNS inflammatory demyelinating disease and is the most common cause of neurologic disability in young adults. While MS is considered a white matter disease, cortical gray matter lesions have been demonstrated to be the strongest predictor of MS disability. We propose a novel method for automatic detection of cortical lesions on advanced MR sequences.

Materials and Methods

Clinical and imaging records of 58 patients with multiple sclerosis evaluated between January, 2014 and April, 2016 were reviewed at Mayo Clinic. One-millimeter isotropic volumetric scans using MPRAGE, PSIR, GMDIR, and WMDIR imaging sequences were performed on each subject. Image volumes were processed using Freesurfer. The PSIR, GMDIR and WMDIR volumes were co-registered to the MPRAGE volume. Freesurfer calculated the pial and gray-white junction (GWJ) surfaces which were manually

cleaned up to improve accuracy. We interpolated surfaces parallel to the pial and GWJ surfaces at a distance of 1/3 and 2/3 the way between the pial and GWJ surfaces. We also interpolated a surface in the white matter approximately 1.3 mm deep to the GWJ surface, calling this the juxtacortical white matter. Average image intensity was calculated for each node in the surfaces for each sequence in the outer third, middle third, and inner third of the cortex as well as the juxtacortical white matter layer. The location of the intensity information was identified by the node location in the surface, and corresponding cortical thickness at that node was also estimated. Cortical lesion presence was identified by 4 different human raters; lesion detection differences were adjudicated amongst the readers to arrive at "the truth." An XGBoost machine learning model was applied for dichotomized classification of the presence of cortical lesions.

Results

XGBoost model was useful for detecting cortical lesions (AUC of 0.78 ± 0.02). Juxtacortical node intensities from the GMDIR, MPRAGE, and WMDIR sequences had highest predictive power for cortical lesion presence. Leukocortical lesions are the most common lesion type identified on MRI in clinical practice, which is consistent with our results that suggest that presence of juxtacortical signal abnormality indicates extension of abnormal signal into the adjacent inner cortex.

Conclusions

We demonstrate a novel machine learning model for prediction of cortical demyelinating lesions that are not easily visualized in clinical practice based on presence of visible subcortical lesions.

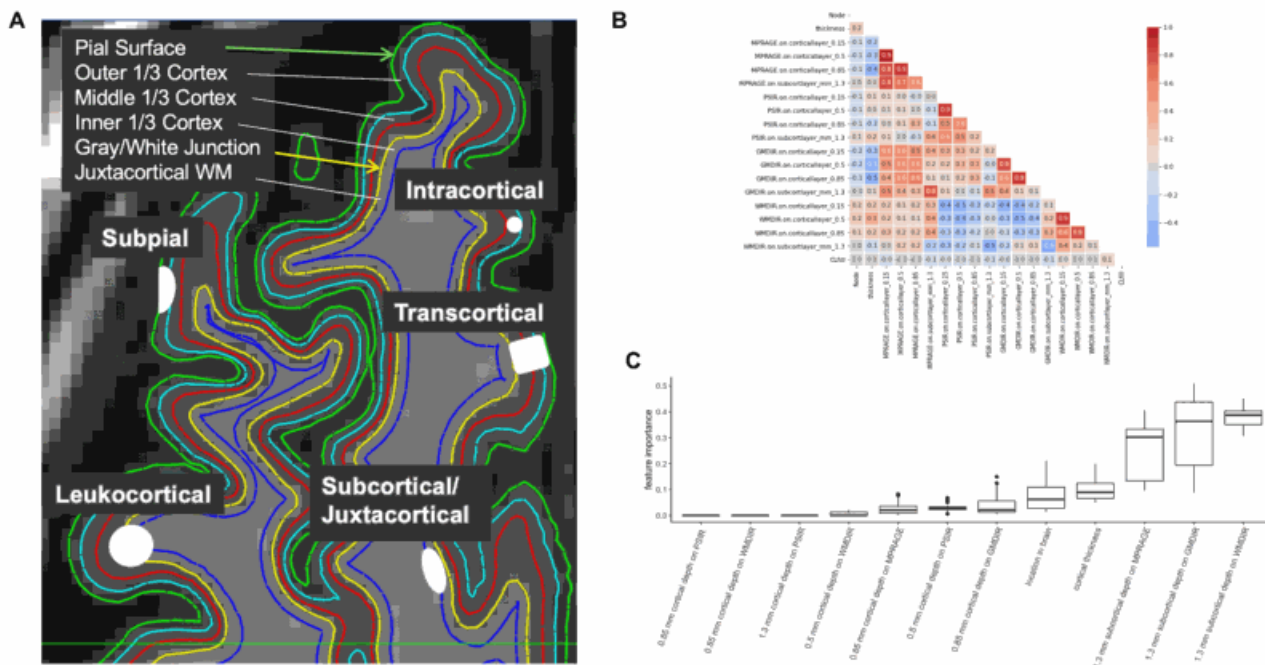


Figure 1: Subpial lesions are usually found in outer and middle cortical layers, transcortical lesions in all three cortical layers, intracortical in middle cortical layer, leukocortical in middle and outer cortical layers and juxtacortical white matter, and juxtacortical in the juxtacortical white matter(A). Correlation across features (B). Predictive power across features (C).

(Filename: TCT_370_ASNR_figures1.gif)

117

Number of Passes During Endovascular Treatment for Stroke Is Associated with Increased Risk of Symptomatic Intracranial Hemorrhage

A Ali¹, S Voleti¹, E Guerra¹, E Mistry², S Demel¹, C Prestigiacomo¹, A Grossman¹, S Peyman¹, B Zhang¹, P Khatri¹, A VAGAL¹
¹University of Cincinnati Medical Center, Cincinnati, OH, ²Vanderbilt University Medical Center, Nashville, TN

Purpose

While successful endovascular therapy (EVT) substantially improves outcomes of acute ischemic stroke, it is less clear if the number of device passes needed to achieve recanalization impacts outcome. We evaluated the effect of number of endovascular device passes on incidence of symptomatic intracranial hemorrhage (sICH) and functional outcome. We hypothesize that greater number of passes correlate with presence of sICH and poor outcomes.

Materials and Methods

We performed a retrospective review of our prospectively identified stroke registry at our Comprehensive Stroke Center. We included consecutive patients who underwent EVT between May 2016 to January 2019. We recorded demographics, clinical characteristics, EVT procedure details, modified treatment in cerebral ischemia (mTICI) score, modified Rankin Score (mRS) and presence of ICH on

post-procedural head CT. sICH was assigned according to the Heidelberg Bleeding Classification. We dichotomized groups receiving ≤ 3 vs >3 device passes during the EVT based on previously published safe thresholds (ref 1-2).

Results

Of the 424 patients who received EVT, 342 patients met our inclusion criteria. Patients who underwent mechanical revascularization by aspiration catheter or stent retriever for anterior circulation occlusion were included. Patients with posterior circulation stroke who underwent EVT and patients who only received intraarterial tPA only were excluded from this study. A total of 285 (83.3%) achieved successful recanalization (mTICI 2B–3), 117 (41.1%) after first device pass (contact aspiration or stent retriever). A total of 117 (32.7%) showed post EVT hemorrhage of which 42 (12.3%) patients had sICH. Patients receiving >3 passes required more procedure time (median 74.5 min vs 43 min, $P<0.01$) and were less likely to achieve successful recanalization (OR 0.229, 95% CI:0.119-0.443, $P=<0.001$). Patients receiving >3 passes of an endovascular device were significantly less likely to achieve favorable (mRS <2) functional outcomes (OR 0.189 95% CI:0.066-0.541, $P=<0.05$). There was no statistically significant difference in sICH between patients receiving ≤ 3 vs >3 passes. However, each successive pass was associated with increased risk of developing sICH (OR 1.30, 95%CI:1.02-1.66, $P=<0.05$).

Conclusions

Greater than three passes of an endovascular device is associated with lower rate of successful recanalization and worse functional outcome. Furthermore, each successive device pass is associated with increased risk of developing sICH.

Table 1. Comparison in outcomes according to number of passes of endovascular thrombectomy device

Outcome	Number of Passes		Adjusted Analysis	
	≤ 3 passes, n (%)	>3 passes n (%)	Odds Ratio (95% CI)	P-value
mTICI 2b or 3	252 (87.5)	33 (61.1)	0.229 (0.119-0.443)	<0.001
90 day mRS (0-2)	85 (30.1)	4 (7.5)	0.189 (0.066-0.541)	0.002
Any ICH	92 (32)	20 (37)	1.253 (0.684 – 2.296)	0.465
SICH	32 (11.1)	10 (18.5)	1.818 (0.834 – 3.961)	0.132

Table 2. Multivariate analysis of predictors of SICH for patients receiving EVT for stroke

Risk factor	Reference	Odds Ratio (95% CI)	P-value
Baseline SBP ≥ 145 mmHg	<145 mmHg	1.29 (0.65-2.58)	0.458
Baseline Glucose			
>200	70-200	2.82 (1.32-6.01)	0.007
Baseline NIHSS			
11-20	≤ 10	0.72 (0.29-1.76)	0.262
≥ 21	≤ 10	1.15 (0.46-2.85)	0.405
Treatment window time >360 min	≤ 360 min	0.42 (0.18-1.02)	0.056
Retriever passes >3	≤ 3	2.19 (0.94-5.10)	0.068
mTICI 0-2A	mTICI 2B or 3	1.85 (0.65-5.27)	0.249

Table 3. Risk factors for developing sICH after EVT

Risk factor	Odds Ratio (95% CI)*	P-value
Baseline Glucose	1.01 (1.00-1.01)	0.005
Baseline NIHSS	1.03 (0.97-1.09)	0.314
Retriever passes	1.30 (1.02-1.66)	0.037

* Reflects risk of developing sICH per point increase in risk factor

(Filename: TCT_117_ASNRDevicepassTables_Final.jpg)

1285

Objective Assessment of Thalamic Volumes in Preprocedural and Postprocedural MRI after HIFU Thalamotomy

F Siddiqui¹, E Obusez¹, S Jones¹, S Nagel¹, R Rammo¹, D Lockwood¹

¹Cleveland Clinic Foundation, Cleveland, OH

Purpose

MR-guided focused ultrasound (MRgFUS) thalamotomy is a relatively new FDA-approved technique for the treatment of essential tremor and tremor-dominant Parkinson's disease. The goal of the thalamic ablation is for maximum tremor relief, minimum side effects, and treatment durability. The lesion size typically expands immediately after treatment, and decreases in size with long term follow-up. Previous studies have characterized the typical appearance of the thalamotomy lesion and measurements of lesion size and location(1,2). However, qualitative lesion descriptions and human generated measurements can be subjective and laborious. In this study, we explored the use of automated thalamic volume measurements pre-treatment, one day post treatment, and with longer term follow up with the goal of automating measurement, removing human bias, and determining the long term effect on thalamic volume of MRgFUS.

Materials and Methods

Automated preprocedural volumetric thalamic measurements were calculated for 38 patients using NeuroQuant. MRgFUS thalamotomy was performed as has been previously described(3). All patients had tremor relief documented post procedure. Post-operative day one volumes were calculated for all patients. For 6 patients, longer term follow up volumetric images were obtained ranging from 1.5 to 7 months.

Results

Treated thalamic volumes were recorded with the untreated contralateral side as the control group. The volume of the treated thalamus increased on post procedure day one by $0.92 \pm 0.6 \text{ cm}^3$ ($p = <0.0001$). 6 patients returned for longer term follow-up imaging between 1.5 to 7 months. In these patients, the treated thalamus showed slight decrease in volume from pre-treatment volumes by $0.36 \pm 0.41 \text{ cm}^3$ ($p = 0.434$). 17 patients returned for appropriate clinical follow up and described significant tremor control.

Conclusions

Our study appears to show the feasibility of automated thalamic volume measurement as a clinical tool to evaluate the size MRgFUS thalamotomy lesions. With automated volumes, human bias is eliminated. The previously described immediate postprocedural changes were apparent on postprocedural imaging. Our study also shows long term, the treated thalamus decreases in size. A larger prospective study may be warranted to corroborate our findings and correlate long and short term thalamic volume change with lesion durability and clinical efficacy. Additional data is continuously being collected and will be presented.

1309

Olfactory bulb and tract abnormalities in children with Pierre Robin sequence (PRS)

S Subramanian¹, S Narayanan²

¹UPMC Children's Hospital of Pittsburgh, Pittsburgh, PA, ²Children's hospital of Pittsburgh of UPMC, Pittsburgh, PA

Purpose

Evaluate olfactory bulb and tract abnormalities in children with Pierre Robin sequence (PRS)

Materials and Methods

Retrospective review of MRI findings in children with diagnosis of PRS who underwent MRI brain for presence of olfactory system abnormalities and correlation with genetic information

Results

28 male and 17 female children with coronal T2 sequence and considered adequate for measurement were included. Genetic information was available in 62%. children with PRS had 47% incidence of olfactory system abnormalities. Olfactory system abnormalities were uncommon in children with PRS and skeletal dysplasia except in a child with campomelic dysplasia due to SOX9 mutation and another child with Nager syndrome. There was high incidence of olfactory system abnormalities in children PRS due to chromosomopathies (64%). Two children with Mobius syndrome (2/2-100%) (figure 1 a, b & c) and three children with Charge syndrome (3/3- 100%) had olfactory system abnormalities (3,4). 17q24.2q24.3 microdeletion resulting in Carney Complex was associated with olfactory bulb and tract agenesis.

Conclusions

Olfactory system abnormalities were uncommon in PRS due to skeletal dysplasia and more frequent in children with PRS with underlying chromosomopathies. Mobius syndrome, CHARGE, Carney and campomelic dysplasia are frequently associated with olfactory system abnormalities.

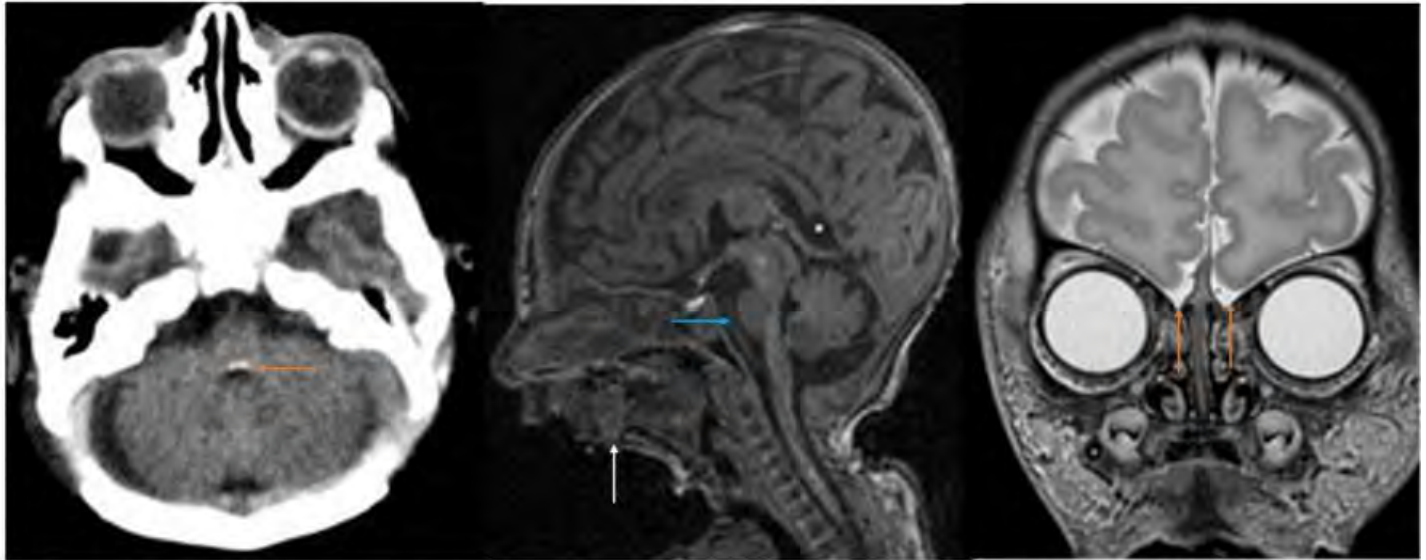


Fig. 1a: Axial Non contrast CT demonstrates dorsal Brainstem Calcification (brown arrow)

Fig. 1b: Sagittal T1W image demonstrates pontine hypoplasia (blue arrow) and mandibular hypoplasia (white arrow)

Fig. 1c: Coronal T2W image Bilateral olfactory bulb agenesis (brown arrows)

(Filename: TCT_1309_AnotatedJPEGfile.JPG)

172

Olfactory bulb MRI findings in persistent COVID-19 anosmia

S Kandemirli¹, A Altundag², D Yildirim³, D Tekcan Sanli⁴, O Saatci⁵

¹University of Iowa, Iowa city, IA, ²Biruni University, Medical Faculty; Acıbadem Taksim Hospital, Istanbul, NA, ³Mehmet Ali Aydınlar University, Acıbadem Taksim Hospital, Istanbul, NA, ⁴Acıbadem Kozyatağı Hospital, Istanbul, na, ⁵Sancaktepe Training and Research Hospital, Istanbul, NA

Purpose

There is limited literature consisting of case reports or series on olfactory bulb imaging in COVID-19 olfactory dysfunction. A systematic imaging study with objective clinical correlation is needed in COVID-19 anosmia in order to better understand underlying pathogenesis.

Materials and Methods

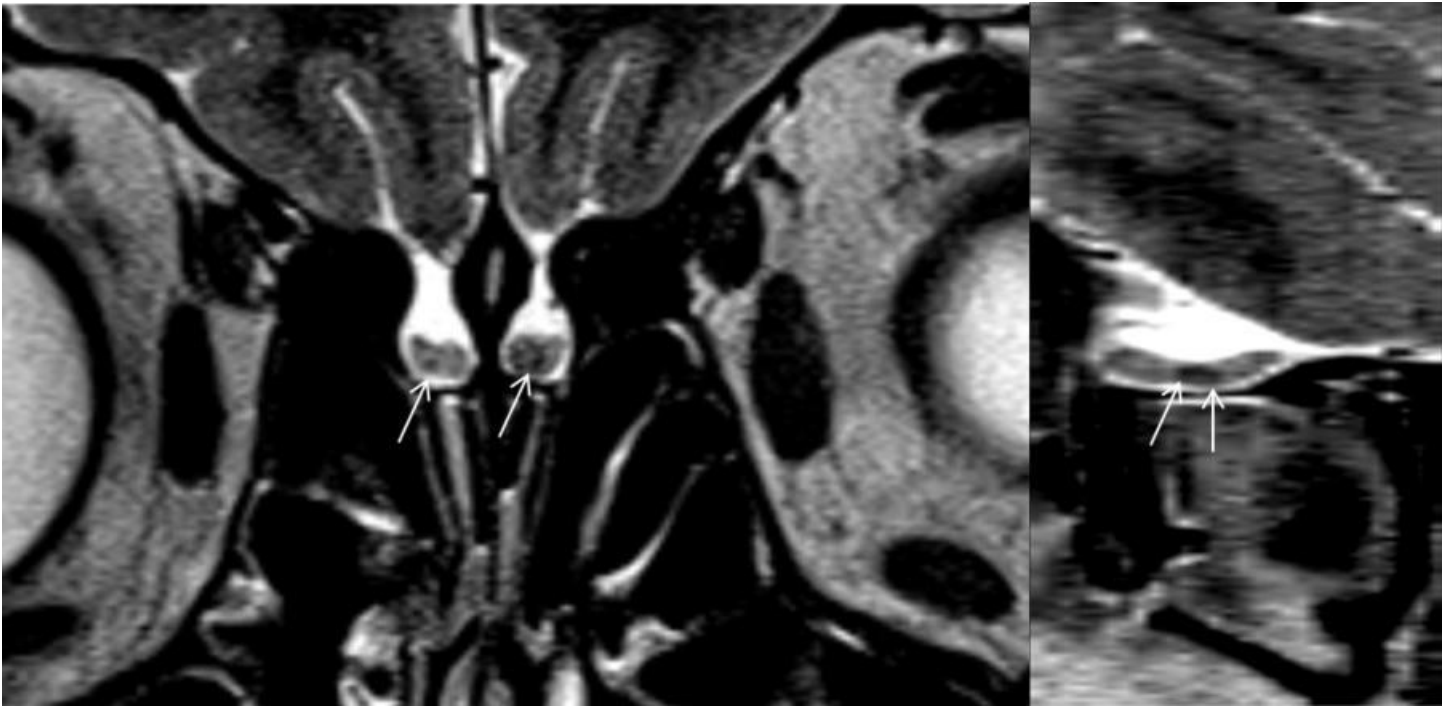
We evaluated 23 patients with persistent COVID-19 olfactory dysfunction. Patients included in this study had a minimum 1-month duration between onset of olfactory dysfunction and evaluation. Olfactory functions were evaluated with Sniffin' Sticks Test. Paranasal sinus CTs and MRI dedicated to olfactory nerves were acquired. On MRI, quantitative measurements of olfactory bulb volumes and olfactory sulcus depth and qualitative assessment of olfactory bulb morphology, signal intensity and olfactory nerve filia architecture were performed.

Results

All patients were anosmic at the time of imaging based on olfactory test results. Olfactory cleft opacification was seen in 73.9% of cases with a mid and posterior segment dominance. 43.5% of cases had below normal olfactory bulb volumes and 60.9% of cases had shallow olfactory sulci. 54.2% of cases had changes in normal inverted J shape of the bulb. 91.3% of cases had abnormality in olfactory bulb signal intensity in the forms of diffuse increased signal intensity, scattered hyperintense foci and microhemorrhages. Evident clumping of olfactory filia was seen in 34.8% of cases and thinning with scarcity of filia in 17.4%. Primary olfactory cortical signal abnormality was seen in 21.7% of cases.

Conclusions

Our findings support the observations of olfactory cleft inflammation in COVID-19 anosmia. Additionally, relatively high percentage of olfactory bulb degeneration suggests that direct/indirect injury to olfactory neuronal pathways may also take place.



(Filename: TCT_172_fig3.jpg)

452

Optic Nerve Sheath Dilation, the Most Sensitive and Specific Imaging Sign of Idiopathic Intracranial Hypertension

A Aein¹, S Mirbagheri², R Patel³, R Riascos³, L KRAMER⁴, R Gabr⁵, R Samant⁶, A Kamali⁷

¹University of Texas Health Science Center at Houston, Houston, TX, ²Johns Hopkins University, Baltimore, MD, ³The University of Texas Health Science Center at Houston, Houston, TX, ⁴UTSHC-Houston, Houston, TX, ⁵UTHSC-Houston, Houston, TX, ⁶UT Health, McGovern School of Medicine, Texas Medical Center, Houston, TX, ⁷University of Texas Health Science Center Houston, Houston, TX

Purpose

Clinical and imaging manifestations of idiopathic intracranial hypertension (IIH) should prompt early diagnosis and treatment to avoid permanent complications. Multiple diagnostic imaging criteria are reported to suspect diagnosis of IIH with questionable sensitivity and/or specificity. Increased intracranial pressure results in dilatation of the perineural cisternal spaces such as the optic nerve sheaths, papilledema and posterior globe flattening. We set up to investigate the sensitivity and specificity of multiple imaging signs of IIH in confirmed IIH patients versus healthy controls.

Materials and Methods

IRB was approved for this study. The MRI scans of 75 adult patients with confirmed diagnosis of IIH and 75 age and sex matched healthy controls were retrospectively studied. The empty/partial empty sella, optic nerve sheath dilation, posterior scleral flattening, papilledema and high grade stenosis of bilateral transverse venous sinuses were evaluated and recorded in both groups.

Results

The optic nerve sheath dilation (> 5.5 mm) showed 84% sensitivity and 84% specificity followed by empty/partial empty sella (92% sensitivity, 74% specificity), bilateral transverse venous sinus stenosis (73% sensitivity, 92% specificity), posterior scleral flattening (55% sensitivity, 100% specificity) and papilledema (45% sensitivity, 100% specificity).

Conclusions

Among the imaging signs of IIH, the optic nerve sheath dilation (> 5.5 mm) showed the highest combined sensitivity and specificity to differentiate the IIH patients from healthy controls.

Imaging signs	IH	Controls	Sensitivity	Specificity
Optic nerve sheath dilation	63 (84%)	12 (16%)	84	84
Empty/partially empty sella	69 (92%)	20 (26%)	92	74
Post scleral flattening	41 (55%)	0	55	100
Papilledema	34 (45%)	0	45	100
Bilateral TSS	55 (73%)	6 (8%)	73	92
Enlarged MC	56 (75%)	11 (14%)	75	86

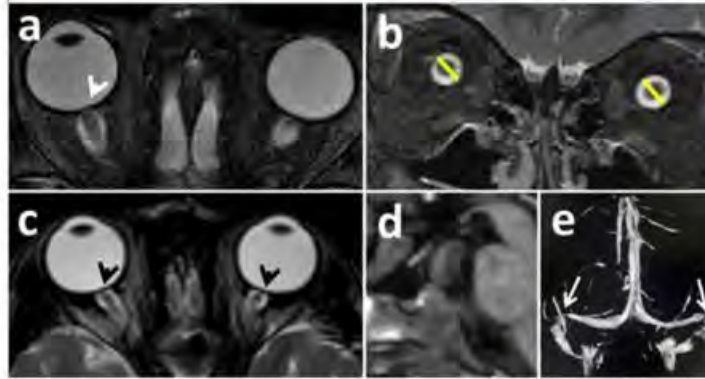


Figure 1: MRI and MRV images of patients with increased intracranial pressure: (a) Axial T2 weighted image shows papilledema on the right side (white arrow head); (b) Coronal T2W image shows bilateral optic nerve sheath distention (The yellow lines demonstrate the wall-to-wall measurements of the optic nerve sheaths diameters); (c) Axial T2 weighted image shows bilateral posterior globe flattening (black arrow heads); (d) Sagittal T1 weighted image in the midline shows partially empty sella; (e) Coronal MIP views of MRV shows bilateral distal transverse venous sinus stenosis at the junctions of the transverse and sigmoid venous sinuses (white arrows).

(Filename: TCT_452_FIGURE.jpg)

1156

Pathologic Correlation in 4DCT and Sestamibi Scanning for Parathyroid Adenoma

T Shestopalova¹, H Al-Jadiry², K RAGHURAM²
¹UT Medical Branch, Galveston, TX, ²N/A, N/A

Purpose

N/A

Materials and Methods

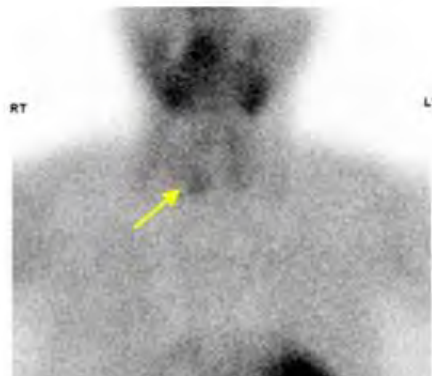
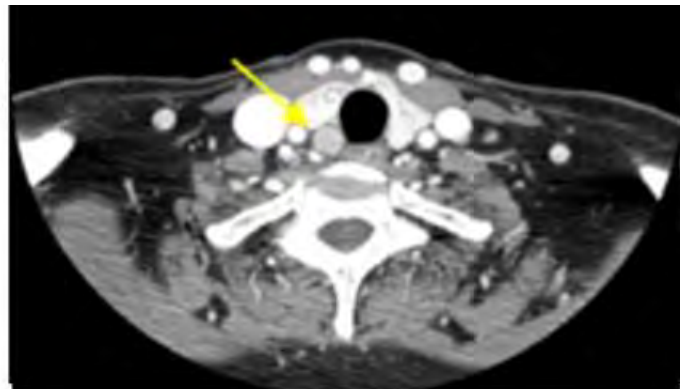
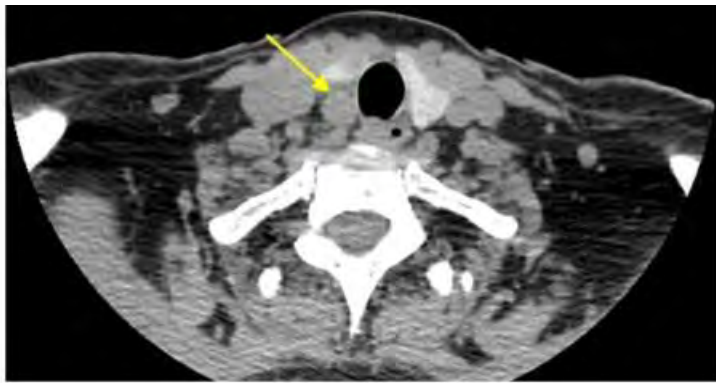
To evaluate the utility of 4DCT performed in conjunction with sestamibi scanning for the identification of parathyroid adenomas at our institution.

Results

7 patients who underwent 4DCT, sestamibi scan and subsequent surgery with definitive diagnosis or exclusion of parathyroid adenoma were collected between May of 2018 and October of 2019. 4DCT examinations were reviewed and enhancement pattern of the suspected lesions were deemed typical, atypical or semi-typical. Typical lesions were defined as those demonstrating hypoattenuation relative to normal thyroid on pre-contrast images, maximum enhancement on arterial phase and washout relative to normal thyroid on delayed phases. Cases were deemed semi-typical if either pre-contrast hypoattenuation or washout on delayed images (both relative to normal thyroid) was not demonstrated. Atypical lesions were those that demonstrated hypoenhancement relative to normal thyroid on post-contrast images. Correlation with pre-operative sestamibi scans and pathology results following surgical resection of suspected lesions was performed.

Conclusions

Out of the 7 cases of suspected parathyroid adenoma with pathologic correlation, 5 were positive for parathyroid adenoma on pathologic evaluation. Of these 5, 2 demonstrated a typical enhancement pattern, 2 were semi-typical and 1 was atypical. The 2 typical cases were positive on sestamibi while the semi-typical and atypical cases were sestamibi negative. The remaining 2 cases of CT identified lesions were negative on pathologic examination and demonstrated atypical and semi-typical enhancement characteristics. The atypical lesion was positive on sestamibi, though the patient remained hyperparathyroid by laboratory studies post-operatively and it is possible that the offending lesion was not resected. Overall, our experience suggests that 4DCT is most useful for the identification of parathyroid adenoma when the prototypical enhancement pattern is observed. Semi-typical and atypical enhancement patterns were seen in both path-proven cases as well as those with negative or equivocal pathologic findings. These non-prototypical enhancement patterns also appear more likely to be associated with a negative sestamibi scan.



(Filename: TCT_1156_4DCT.jpg)

1235

Patient Safety in C1-2 Puncture: Prevalence of High-Risk Vascular Variants

R Frederick¹, W Gibbs²

¹Mayo Clinic Arizona, Phoenix, AZ, ²Mayo Clinic, Scottsdale, AZ

Purpose

Lateral C1-2 puncture for collection of cerebrospinal fluid or injection of contrast or chemotherapy is perceived to be more dangerous and difficult to perform than lumbar puncture. CT guidance diminishes the risk of cord puncture, but injury to an anomalous origin or low-lying loop of the posterior inferior cerebellar artery (PICA) or a variant vertebral artery course overlying the posterior third of the spinal canal remains a concern. The purpose of this study is to investigate the prevalence of these variants on CT angiography in order to assess the risk of vascular injury in lateral C1-2 puncture.

Materials and Methods

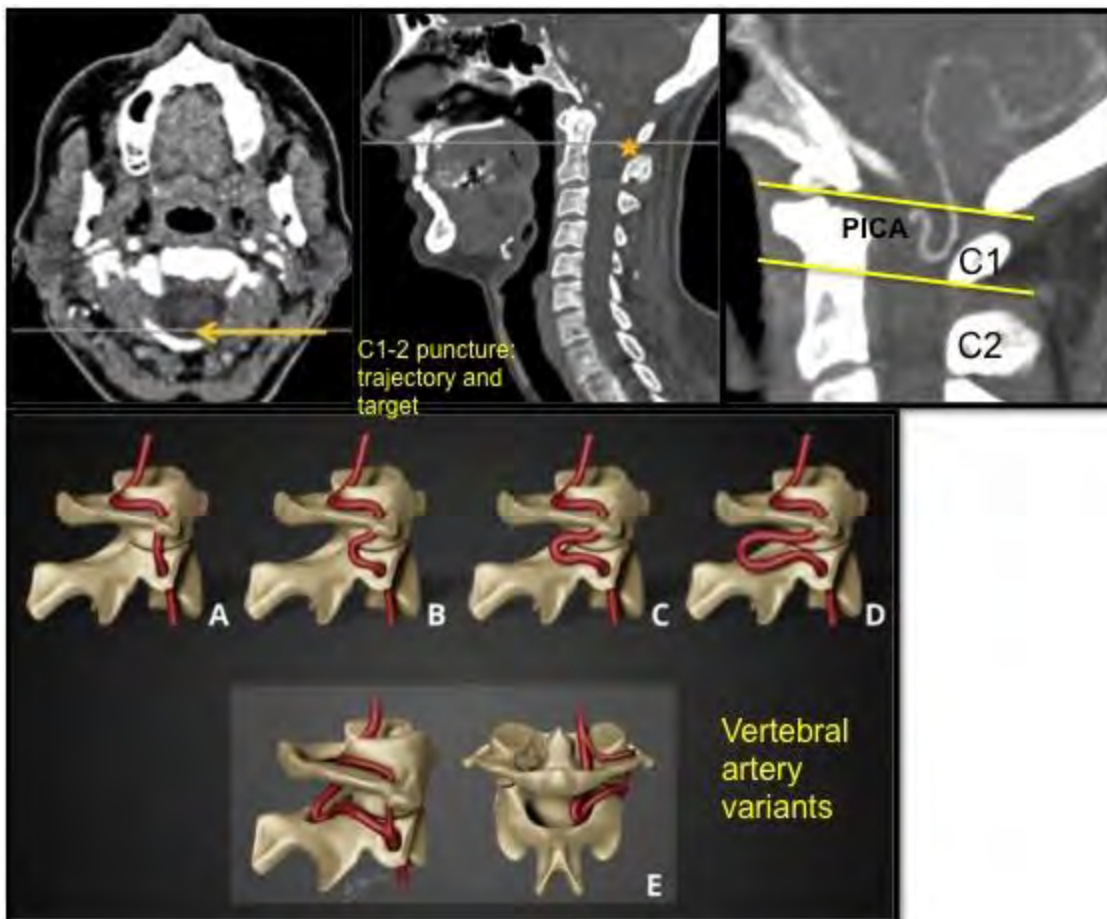
This is a retrospective study. 300 consecutive CT angiography studies will be evaluated by 2 radiologist investigators. Characteristics that would contraindicate C1-2 puncture (elevated intracranial pressure, Chiari malformation, craniocervical mass or stenosis) are exclusion criteria. In each subject the inferior extent of the PICAs (or AICA-PICA loop) and the PICA origins are characterized as intracranial, below the foramen magnum but above the inferior margin of C1, or below C1. The location of the vertebral artery at the C1-2 level is characterized as anterior to the canal, overlying the anterior 2/3 of the canal, or overlying the posterior 1/3 of the canal.

Results

At the time of abstract submission, 107 cases meeting criteria have been evaluated. The origin of the PICA was intracranial in 105/107 cases on the right, 103/107 cases on the left. Six total PICA loops originated below the foramen magnum but above the inferior margin of C1. PICA loops extended below the foramen magnum but above the inferior margin of C1 in 87/107 on the right, and 93/107 on the left. No origins or loops were seen below C1. The vertebral artery at the C1-2 level was anterior to the canal in 103/107 on the right, and 101/107 on the left. No vertebral arteries were in the posterior 1/3 of the canal.

Conclusions

No PICA origins or loops were found below the C1 level, and no vertebral arteries were over the posterior 1/3 of the canal, thus were not at risk in lateral C1-2 puncture. These results highlight the safety of this procedure, and increase confidence in its safe application even in urgent cases, when no vascular imaging has been performed.



(Filename: TCT_1235_ASNRC1-2.jpg)

734

Patterns of Hypoxic-Ischemic Brain Injury in Substance Use Related Cardiac Arrest

E Calabrese¹, S Gandhi¹, C Hemphill¹, D Randazzo¹, J Shih¹, J Talbott¹, J Vitt¹, E Amorim¹

¹University of California San Francisco, San Francisco, CA

Purpose

The purpose of this study is to evaluate patterns of hypoxic-ischemic brain injury in patients with substance use related cardiac arrest (SURCA) using quantitative diffusion MRI. In addition to aiding brain edema risk stratification and coma prognostication, quantitative approaches to brain imaging may advance our understanding about the neuroanatomical basis of coma recovery after acute brain injury in SURCA.

Materials and Methods

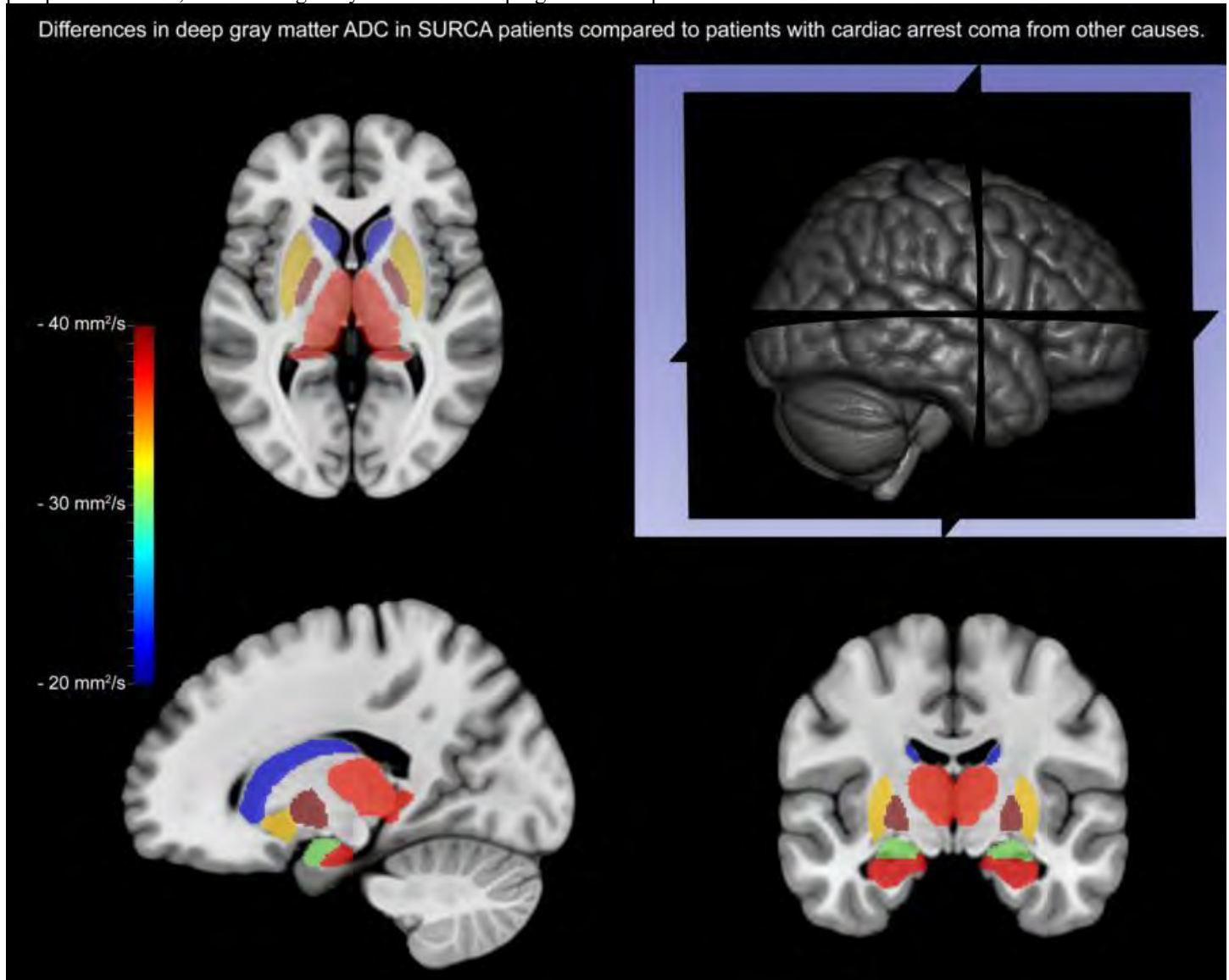
We retrospectively analyzed diffusion MR images from 60 comatose patients (Glasgow Coma Scale score <9) following cardiac arrest at a single academic medical center over a 4 year period. SURCA was defined as cardiac arrest in patients with a toxicology screen positive for stimulants, opioids, or benzodiazepines on presentation. The study group consisted of 31 SURCA and 29 non-SURCA subjects. Automated image processing steps included diffeomorphic registration of patient DWI/ADC volumes to the MNI atlas template, skull stripping, and cortical/subcortical anatomic parcellation with the Harvard Oxford atlas. A custom script (Python) was used to extract mean ADC values and thresholded volumes of brain tissue with $ADC < 650 \times 10^{-6} \text{ mm}^2/\text{s}$ for each brain region in individual subjects. ADC values were compared between SURCA and non-SURCA groups using t-tests with a false discovery rate corrected $p < 0.05$ considered significant.

Results

SURCA subjects were younger than non-SURCA subjects (49 ± 11 vs. 63 ± 16 yrs). There were no significant differences in sex (79% vs. 64% male), time to MRI (117 ± 41 vs. 131 ± 61 hours), or in hospital mortality (61% vs. 67%). ADC analysis revealed a global trend towards more severe brain injury in the SURCA group. Of the cortical and subcortical regions analyzed, five subcortical gray structures had lower (worse) ADC values in the SURCA group: the thalami, pallidi, hippocampi, amygdalae, and accumbens nuclei – with the largest differences in the pallidi ($44 \times 10^{-6} \text{ mm}^2/\text{s}$) and thalami ($37 \times 10^{-6} \text{ mm}^2/\text{s}$).

Conclusions

Our results suggest that SURCA is associated with more severe injury to deep gray structures than non-SURCA. If validated in larger prospective studies, these findings may facilitate coma prognostication post-cardiac arrest as well as brain edema risk stratification.



(Filename: TCT_734_fig1.jpg)

1015

Percutaneous CT-Guided Sacroiliac Joint Fixation With Unilateral Double Screw Approach in Sacro-iliac Instability

A De Vivo¹, R Martins², M Bellini³, S Marcia⁴, L Manfre⁵

¹I.O.M., Viagrande, Catania, Italy, ²Centro Hospitalar e Universitario do Porto, Porto, Portugal, ³Unit of Diagnostic and Functional Neuroimaging, Siena, Tuscany, ⁴SS TRINITA' HOSPITAL, CAGLIARI, SARDEGNA, ⁵Mediterranean Institute for Oncology, Viagrande, Catania

Purpose

In this study, we aimed to evaluate the effectiveness, in terms of pain and disability reduction, of a novel technique for SIJ fixation in treatment of patients with chronic LBP due to SIJ instability.

Materials and Methods

We performed percutaneous unilateral CT-guided SIJ fixation in 24 consecutive patients presenting with chronic LBP attributable to SIJ instability, with the insertion of two trans-articular screws. Pre- and post-procedure pain and disability levels were measured using the visual analogue scale (VAS) and Oswestry Disability Index (ODI).^[1]

Results

At 6 months follow up, SIJF resulted in significant reductions in both VAS and ODI scores. CT-guided procedures were tolerated well

by all patients under light sedation with a mean procedural time of 36 min, and there were no reported immediate or delayed procedural complications.^[1]

Conclusions

Percutaneous unilateral SIJ fixation with two screws seems to be a powerful technique for the treatment of patients with chronic LBP related to SIJ instability. CT-guided technique is fast, precise, and safe and can be performed in simple analgo-sedation.

730

Performance comparison for outcome-based feature selection between Statistically Equivalent Signature vs LASSO algorithms in high-dimensional texture data in Glioblastoma

B Behrouzi¹, S Daghighi¹, A Chan¹, A Sahgal¹, S Myrehaug¹, C Tseng¹, H Soliman¹, F Salehi¹, C Heyn¹, S SYMONS¹, P Tyrrell¹, P Jabehdar Maralani¹

¹University of Toronto, Toronto, Ontario

Purpose

Feature selection seeks to identify a small subset of features that is maximally predictive of the outcome of interest. It is particularly important for high-dimensional radiomics data where the number of features is orders of magnitude larger than the sample size. We compared two feature selection algorithms: the Statistically Equivalent Signature (SES) [1] and Least Absolute Shrinkage and Selection Operator (LASSO) [2]. SES is a constraint-based algorithm which identifies multiple predictive feature subsets with statistically equivalent performances while LASSO selects a single subset of features.

Materials and Methods

SES and LASSO were compared in terms of predictive performance, number of selected features, and computational efficiency on radiomics data (2870 features) from T1 and FLAIR images of the radiotherapy planning MRI of 50 patients with glioblastoma. Patients were stratified to "high-risk" if recurrence occurred before 6.9 months and "low-risk" if recurrence occurred after (binary outcome). Time to-event outcome was predicted based on progression-free survival (PFS) and overall survival (OS). Logistic and Cox regression procedures were used as predictive models while area under the curve (AUC) and concordance index (CI) were used as performance metrics for the binary and time-to-event outcome, respectively. 5-fold cross-validation procedure repeated 5 times was used for model selection and performance evaluation. For comparison, the first feature subset retrieved by SES was arbitrarily selected. The best hyperparameter configuration for SES was identified by 5-fold cross-validation selection procedure (cv.ses) with maximum conditioning variables size "k" and significance level "a" varying between [3, 4, 5] and [0.05, 0.01, 0.001], repeated 5 times and the median selected. Shrinkage parameter "λ" for the LASSO algorithm was calculated as the mean of 5 repeats of 5-fold cross-validation model (cv.glmnet) giving the minimum cross-validated error.

Results

Our results, summarized in table 1, shows that SES is on par or outperforms LASSO in terms of predictive accuracy in both binary and survival tasks and selects fewer number of variables. Regarding computational time, LASSO is more efficient but SES provides multiple, equally predictive signatures.

Conclusions

SES performs comparably well to LASSO and provides multiple solutions which facilitates getting insight to high dimensional domain of study and selecting a clinically relevant subset of features.

	Classification task (low vs high risk)			Survival task (OS)			Survival task (PFS)		
	AUC (cv)	#vars (cv)	Time (cv)	CI (cv)	#vars (cv)	Time (cv)	CI (cv)	#vars (cv)	Time (cv)
SES	0.912 (16.2%)	1.96 (10.2%)	32.035 (4.1%)	0.702 (18.6%)	1.72 (31.5%)	94.275 (1.5%)	0.629 (15.6%)	2.08 (13.3%)	95.332 (1.7%)
LASSO	0.827 (18.3%)	5.00 (38.7%)	0.741 (6.8%)	0.728 (12.3%)	6.60 (21%)	1.318 (5.4%)	0.639 (16%)	4.6 (28.8%)	1.616 (3.5%)
P value	0.002	<0.001	<0.001	0.288	<0.001	<0.001	0.712	<0.001	<0.001

Table 1: Comparison between SES and LASSO in terms of predictive performance, number of selected features (#vars), and computational time (over 5 folds, in seconds). Both the average and coefficient of variation (cv) values are reported for the test dataset performance over 5 folds and 5 repeats, compared by paired t-test between SES and LASSO. Performance metrics are area under the curve (AUC) for classification task and concordance index (CI) for survival task.

(Filename: TCT_730_Table.jpg)

Performance of a Deep Learning Algorithm for the Detection of Cervical Spine Fractures

A Voter¹, M Larson¹, J Garrett², J Yu¹

¹University of Wisconsin-Madison, Madison, WI, ²UW Madison -Department of Radiology, Madison, WI

Purpose

Artificial intelligence (AI) decision support systems (DSS) are a rapidly growing tool to support radiologists manage an ever-increasing volume of imaging. Several DSSs have been developed to aid the detection of cervical spine fractures, but to the best of our knowledge, their performance has not been rigorously evaluated. Because these deep learning systems have known weaknesses and poorly performing support systems can hinder radiologists, we aimed to assess the diagnostic performance of Aidoc, a common AI DSS as implemented at our institution.

Materials and Methods

This prospective study included 1916 adult, emergent non-contrast cervical spine CT scans (61 ± 22 years, 50.4% men). The presence of a cervical spine fracture was determined from the Aidoc and attending neuroradiologist interpretations and, if required, adjudicated by a second radiologist. Algorithm performance was assessed by calculation of the diagnostic accuracy and subsequent failure mode analysis.

Results

Overall, there was a 91.1% concordance between Aidoc and the attending radiologist. Aidoc correctly identified 66 of the 121 fractures (54.5%) with 107 false positives. Diagnostic performance was determined: sensitivity, 54.5%; specificity, 94.0%; positive predictive value (PPV), 38.2%; and negative predictive value (NPV), 96.8. Impaired performance was observed in the detection of chronic fractures and in patients with significant osseous degenerative changes.

Conclusions

We report the unanticipated limited diagnostic accuracy of AI DSS for the detection of cervical spine fractures. Many similar algorithms have also received little or no external validation and this study raises concerns about their generalizability and rapid pace of deployment. Further rigorous evaluations are needed to understand the weakness of these tools before widespread implementation.

195

Performance of Latest Generation PET/CT Scanner for detection of Metastatic Lymph Nodes in Head and Neck Cancer

F Butt¹, N Tocci², J Paydarfar¹, D Pastel¹

¹Dartmouth-Hitchcock Medical Center, Lebanon, NH, ²Dartmouth Geisel School of Medicine, Hanover, NH

Purpose

Cervical lymph node metastasis is one of the most important prognostic factors in staging of head and neck cancers. In May 2019 our department installed the newest generation PET/CT scanner (Siemens Healthineers Biograph Vision digital PET/CT system) with improved spatial resolution and photon detectors. Much of the existing literature on the accuracy of PET/CT in detecting cervical nodal metastases in head and neck cancer patients reports data from older generation scanners. The purpose of this study is to report the sensitivity, specificity and accuracy of the newest generation PET/CT scanner in detecting metastatic lymph nodes in head and neck cancer patients.

Materials and Methods

55 consecutive head and neck cancer patients who underwent surgical neck dissection after installation of the new PET/CT scanner were included in the study. The location and number of reported PET/CT positive metastatic lymph nodes and of metastatic lymph nodes on surgical pathology following neck dissection was recorded.

Results

21/55 of the provided head and neck cancer patients underwent a PET/CT scan on our newest generation scanner followed by surgical neck nodal dissection. Surgical pathology was used as the gold standard. FDG-avid cervical lymph nodes reported as nodal metastasis on PET/CT were identified in 14/21 (66%) patients. In these 14 patients, metastatic lymph nodes were identified in 24 cervical nodal stations. 1/24 nodal stations reported as having lymph node metastasis on PET/CT was negative for malignancy on pathology. A single 9 mm metastatic lymph node identified on surgical pathology was not identified on the pre-operative PET/CT. These results yield an overall sensitivity of 93%, specificity of 86%, positive likelihood ratio (+LR) of 6.50 and negative likelihood ratio (-LR) of 0.08 for the 21 patients evaluated. For the total number of cervical nodal stations evaluated in these patients (n=210) the sensitivity of PET/CT is 96% and specificity is 99%.

Conclusions

Our newest generation PET/CT scanner demonstrates both high sensitivity and specificity in detecting cervical lymph node metastasis in head and neck cancer patients and is at least comparable to previous studies. (Kyvas et al. and Goel et al.)

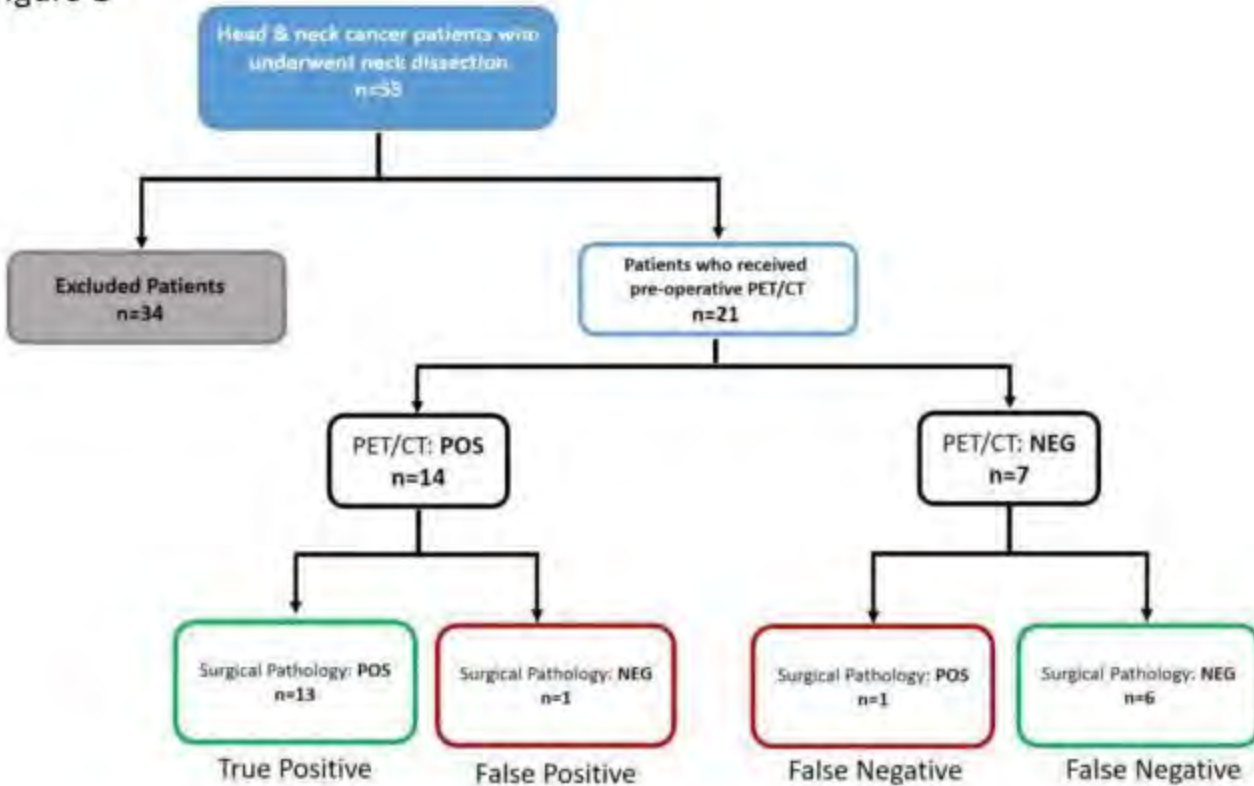
TABLE 1: CERVICAL NODAL STATIONS EVALUATED FOR METASTASIS (n = 210)

		Surgical Pathology	
		Positive	Negative
PET/CT	Positive	23	1
	Negative	1	184

TABLE 2: HEAD AND NECK CANCER PATIENTS EVALUATED FOR CERVICAL METASTASIS (n=21)

		Surgical Pathology	
		Positive	Negative
PET/CT	Positive	13	1
	Negative	1	6

Figure 1



(Filename: TCT_195_TABLE1_TABLE2_FIGURE1_V2_FINAL.jpg)

Performance of MRI sequences for diagnosis of radiation necrosis and true progression in brain tumors: comparison of expert review to Radiomics signature

S AMMARI¹, I dercle², I antonios³, S Jovina⁴, E Chouzenoux⁵, N LASSAU⁶, C Balleyguier⁷

¹GUSTAVE ROUSSY CANCER CAMPUS, villejuif, FRANCE, ²Columbia University Irving Medical Center New York, United States, NEW YORK, NY, ³Gustave roussy campus cancer, villejuif, villejuif, ⁴Center for Visual Computing, CentraleSupélec, Inria Saclay, Université Paris-Saclay, Gif-sur-Yvette,, Gif-sur-Yvette, gif sur Yvette, ⁵Center for Visual Computing, CentraleSupélec, Inria Saclay, Université Paris-Saclay, Gif-sur-Yvette,, Gif-sur-Yvette, FM, ⁶MD PHD, paris, FRANCE, ⁷Gustave ROUSSY, paris, FRANCE

Purpose

To compare the performance of quantitative imaging biomarkers alone or in combination (signature) for the diagnosis of radiation necrosis and residual/recurrent tumor to determine if the effectiveness of radiation therapy.

Materials and Methods

184 patients with solitary metastatic brains treated with radiation therapy were enrolled in a monocentric retrospective study from June 2012 to May 2017. Patient were randomized in training set (n=144) and testing set (n=40). The reference standard for the diagnosis of radiation necrosis (training set: n=113/184) and tumor (n=71/184). Brain tumor were segmented on MRI sequences after radiation therapy on the same 3 Tesla MRI. We recorded variables including 3 clinical variables (age, primary tumor type and systemic immunotherapy treatment) and 9 imaging biomarkers extracted from 4 MRI sequences: (i) first-pass perfusion: relative cerebral blood volume (rCBV), relative amplitude of the peak (rHP) and the percentage signal recovery (PSR); (ii) diffusion; (iii) delayed-contrast MRI (TRAM); (iv) three-dimensional T1-weighted post-gadolinium (T1w+) acquisitions (n=100 Radiomics features). In the training set, the machine-learning classifier reaching the highest performance or the prediction of the diagnosis was selected as the radiomics signature. Performance was evaluated using nested 100 fold cross validation and area under the receiver operating characteristic curve (AUC). Our primary endpoint was to compare the performance of the signature to expert radiologist in the testing set.

Results

the expert reached a significantly higher AUC of 78.7 (72.3-85.1) with all sequences including TRAM than without TRAM sequence (AUC 57.4 (50.7-64.1)). Of note, the performance of using a quantitative measurement on TRAM sequence only was comparable to expert radiologist: AUC 76.8% (70.3%-83.3%) The signature AUC was 0.92 [0.87; 0.97] in the training set and 0.85 in the validation set. expert, hence was not statistically different from expert performance. The signature selected imaging biomarkers characterizing the texture and spatial heterogeneity of the lesion on T1w+ sequence that were not correlated with other known imaging biomarkers such as TRAM, ADC, CBV (entropy: AUC 72.1% (64.5-79.7); rHP AUC 67.7 (59.3-76.1)).

Conclusions

Delayed-contrast MRI (TRAM) sequence is the best sequence for the diagnosis of radiation necrosis and residual/recurrent tumor

586

Perfusion Collateral Index vs. Hypoperfusion Intensity Ratio in Assessment of Angiographic Collateral Scores in Patients with Acute Ischemic Stroke

B Tsui¹, I Chen¹, J Qiao¹, K Khatibi¹, L Sharma¹, S Tateshima¹, M Bahr-Hosseini¹, G Colby¹, K Miller¹, J Saver¹, R Jahan¹, g duckwiler¹, D Liebeskind¹, K Nael¹

¹UCLA, Los Angeles, CA

Purpose

In acute ischemic stroke (AIS), perfusion imaging, while not directly visualizing collateral vessels, can provide important insight into collateral robustness, indexed by perfusion lesion volume and by perfusion lesion heterogeneity. Two proposed perfusion lesion heterogeneity measures indexing collateral status are the Perfusion Collateral Index (PCI) and Hypoperfusion Intensity Ratio (HIR), but their accuracy compared with direct collateral assessment on DSA has been incompletely characterized.

Materials and Methods

Consecutive AIS patients with anterior circulation large vessel occlusion who underwent pre-endovascular thrombectomy MRI perfusion imaging were included. MRI measures analyzed were: 1) Perfusion Collateral Index (PCI) - the volume of moderately hypoperfused tissue (arterial tissue delay time between 2 and 6 seconds: ATD 2-6sec) multiplied by its corresponding relative cerebral blood volume using Olea software; 2) Hypoperfusion Intensity Ratio (HIR) - ratio of moderate TMax >6 s lesion volume versus severe Tmax >10 s lesion volume with the RAPID software program. DSA collateral scores were evaluated by ASITN grading and dichotomized to inadequate (ASTIN score less than 2) vs. adequate (ASTIN score 3 or greater).

Results

Among 48 patients meeting entry criteria, age (mean \pm SD) was 70 (\pm 15.2), 54% female, and NIHSS (median, IQR) was 15 (10-19). For HIR, there was no significant difference in score values in patients with adequate vs inadequate collaterals: 0.35 ± 0.20 vs 0.39 ± 0.25 , $p=0.68$. ROC analysis using previously described cut-off of 0.4 resulted in an AUC of 0.52 and sensitivity/specificity of 71% /

33%. For PCI, score values were significantly higher in patients with adequate vs inadequate collaterals, 117 ± 61 vs. 57 ± 41 , $p=0.002$. ROC analysis using previously described cut-off of 62 resulted in an AUC of 0.8 and sensitivity/specificity of 84% / 78%.

Conclusions

Collateral status can be accurately assessed on perfusion MRI with the Perfusion Collateral Index, which outperformed the Hypoperfusion Intensity Ratio. MRI-PCI is an informative imaging biomarker of collateral status in patients with AIS.

1501

Perfusion metrics in meningeal tumors: are they correlated with tumor grades?

S Manupipatpong¹, D Lin²

¹Johns Hopkins University School of Medicine, Baltimore, MD, ²Doris Lin, Baltimore, MD

Purpose

Perfusion imaging with relative cerebral blood volume (CBV) measurements has been correlated with histologic tumor grade and overall survival, particularly in primary glial tumors. Its utility in distinguishing benign meningioma from higher-grade meningeal tumors is, however, not well-established. We explored perfusion characteristics in grade I (G1) meningiomas and higher-grade meningeal tumors (grade II-III (G2-3) meningioma, hemangiopericytoma).

Materials and Methods

Patients with a histopathological diagnosis of meningioma or hemangiopericytoma and presurgical MRI that included dynamic susceptibility contrast (DSC) perfusion imaging from August 2013 to 2019 were included in this retrospective review. Perfusion imaging was post-processed using Olea Sphere 3.0.20 (Olea Medical, La Ciotat, France) to generate leakage-corrected relative blood volume (rBV), relative blood flow (rBF), time-to-maximum (Tmax), and leakage coefficient (K2). The enhancing tumor was contoured (Fig. 1) on one slice and perfusion parameters were measured, then normalized against contralateral normal-appearing white matter (frontoparietal centrum semiovale). A comparison of G1 meningiomas (group 1) and higher-grade meningeal tumors (group 2) was then performed (Mann-Whitney U test, $\alpha < 0.05$).

Results

40 patients with G1 meningioma (82.5% F, age 57.9 ± 12.3) and 19 patients with higher grade meningeal tumors (42.1% F, age 68.3 ± 11.3 ; 12 G2 and 4 G3 meningioma, 3 hemangiopericytoma) were included in our analysis. Tumor to normal tissue ratios for leakage-corrected rBV, rBF, and K2 in group 1 were: 4.37 ± 1.96 , 3.99 ± 1.91 , and -0.26 ± 18.47 . For group 2, they were: 5.14 ± 2.52 , 4.77 ± 2.70 , and -3.32 ± 13.83 . Difference in Tmax compared to normal tissue was 2.33 ± 10.76 for group 1 and 3.83 ± 7.31 for group 2. None of the differences in perfusion metrics between the 2 groups were statistically significant (Fig. 2).

Conclusions

We found no significant differences in the perfusion metrics between G1 meningioma and higher-grade meningeal tumors. While consistent with a few prior studies, this study is limited due to unbalanced samples, with a small sample size and greater heterogeneity in group 2, as other previously published studies suggested CBV could be used to characterize meningeal tumors. The wide Tmax range suggests that a nuanced exploration of perfusion in these characteristically hypervascular tumors may be warranted. Further, K2 as a surrogate for vascular permeability may provide insight to tumor grade and type in a future, larger, study.

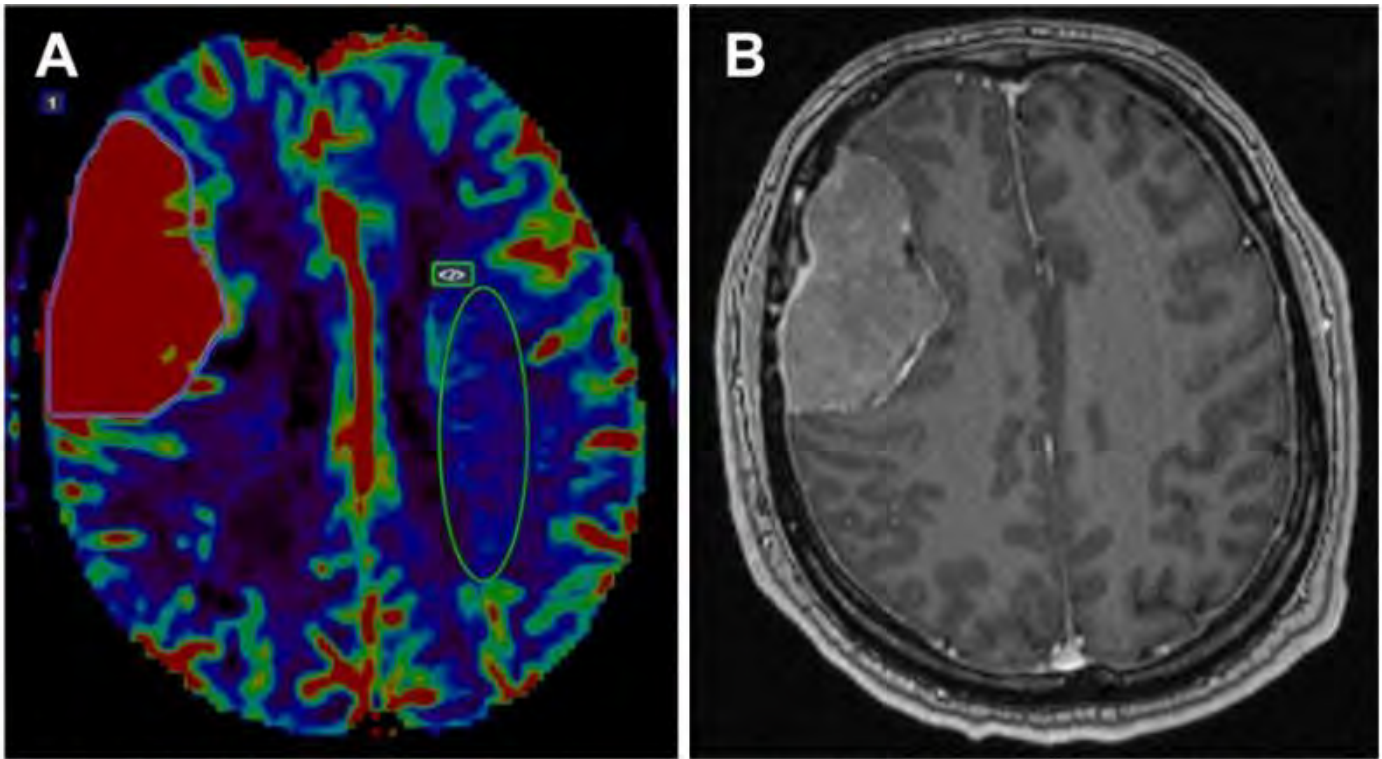


Figure 1: Olea Sphere contouring for tumor and white matter reference area. A) Olea Sphere region of interest for a sample patient, with <1> indicating the tumor and <2> indicating the white matter reference. **B)** Corresponding T1 post-contrast imaging.

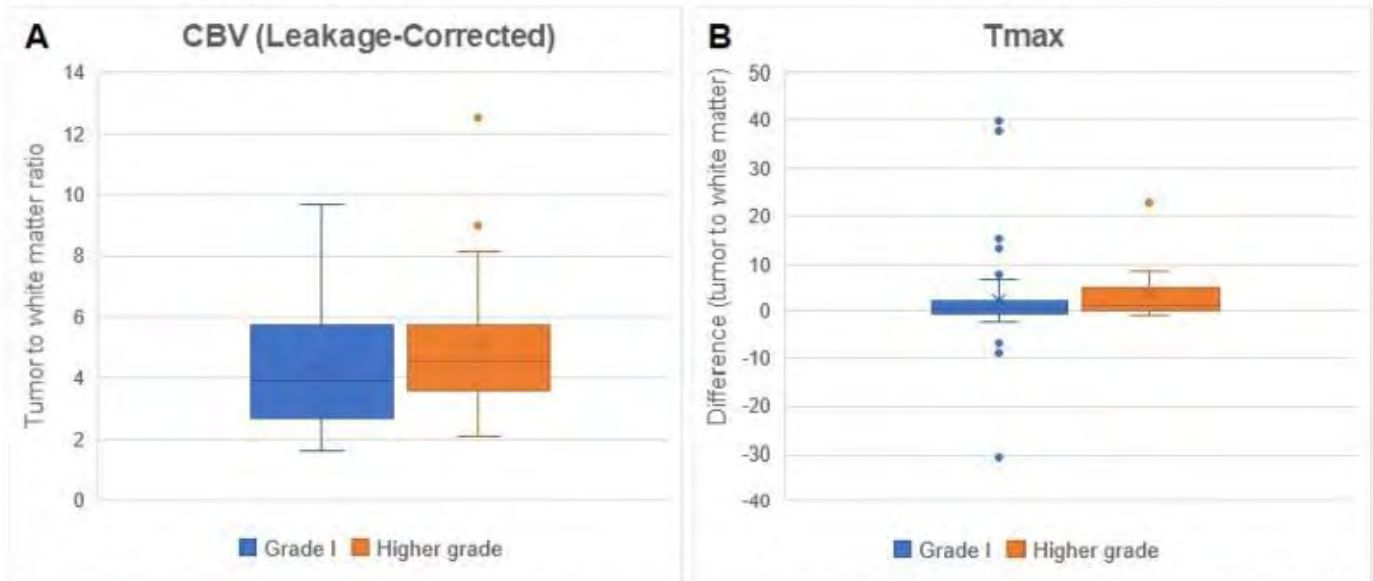


Figure 2: Box-and-whisker plots comparing grade I meningiomas and higher-grade meningiomas. A) Contrast leakage-corrected cerebral blood flow, **B)** time-to-maximum.

(Filename: TCT_1501_Figure1and2.jpg)

219

Positive Predictive Value of Automated Vessel Density (RAPID-CTA) For Detection of Large Vessel Occlusion: One Year Experience

J Adhya¹, C LI¹, M Goldberg¹, L Eisenmenger², W CHANG¹

¹Allegheny Health Network, Pittsburgh, PA, ²University of Wisconsin - Madison, Middleton, WI

Purpose

With several large trials validating the efficacy of mechanical thrombectomy in the treatment of large vessel occlusion (LVO), prompt identification of patients with LVO has high clinical utility. Several new techniques have emerged for detecting anterior circulation LVO by quantifying relative vessel density in the MCA territory (compared to the contralateral side), including RAPID-CTA (iSchemaView, Menlo Park, CA). In this study we present our one year experience on the positive predictive value (PPV) of RAPID-CTA for the detection of LVO in patients presenting with stroke symptoms.

Materials and Methods

We included all patients presenting for CTA that had RAPID-CTA performed for the evaluation of stroke or neurologic deficit demonstrating relative vessel density <60% corresponding to red (<45% vessel density) or yellow (45-60% vessel density) on the RAPID-CTA examinations. 310 patients were included in the study (average age 72.2y, 145 male, 165 female). Examinations were considered positive if there was evidence of LVO or high grade (at least moderate) large vessel stenosis.

Results

Of the 310 patients in the study, 114 had occlusions of the ICA, carotid terminus, or M1 segment. 101 of these patients had <45% relative vessel density and 13 had 45-60% density. 47 patients had M2/branch occlusions, 28 patients had <45% relative vessel density and 19 had 45-60% density. 129/161 LVO were detected at a threshold of <45% vessel density (80% sensitivity in this cohort). In patients demonstrating <45% vessel density, 163/172 were positive (95% PPV), with 129 having large vessel occlusion (75% PPV). In patients demonstrating 45-60% vessel density, 107/138 were positive (78% PPV) with 32 having large vessel occlusion (23% PPV). Most positive cases in the 45-60% category demonstrated moderate to high grade stenosis or relative narrowing in the setting of prior infarct. Overall, 270/310 were positive (87% PPV) with 52% PPV for LVO. The cases which were negative were often limited by metallic artifact, demonstrated tumors or intracranial hemorrhage which affected vessel density, or were limited by motion or other technical factors such as poor bolus timing.

Conclusions

Rapid CTA using automated relative vessel density of <45% had high PPV for LVO and could be used to prioritize potentially positive CTA exams. Increasing the threshold to <60% vessel density would increase the sensitivity for LVO detection but would have a higher rate of false positives and detect more intracranial stenoses.

Color	Patients	Age	Gender	M1 occlusion	M2 occlusion	LVO	Stenosis	Positive	Negative
Red (<45%)	172	71.1y	81M 91F	101	28	129 (75% PPV)	34	163 (95% PPV)	9
Yellow (45-60%)	138	68.7y	64M 74F	13	19	32 (23% PPV)	75	107 (78% PPV)	31
Total	310	72.2y	145M 165F	114	47	161 (52% PPV)	109	270 (87% PPV)	40

(Filename: TCT_219_tableb.jpg)

407

Potential value of artificial intelligence applications in detection of intracranial hemorrhage

A Nada¹, A Khan¹, H Hassanein¹, A Alt¹, A Anokhin¹, R Ngnitewe Massa a¹, A Gaballah²

¹University of Missouri Healthcare, Columbia, MO, ²University of Missouri Healthcare, Columbia, MO

Purpose

Our aim was to compare results of AI analysis of Computed Tomography (CT) brain imaging against interpretation by experienced and board-certified neuroradiologists, determining the presence versus absence of intracranial brain hemorrhage findings and calculate accuracy of the software in detection of intracranial hemorrhage.

Materials and Methods

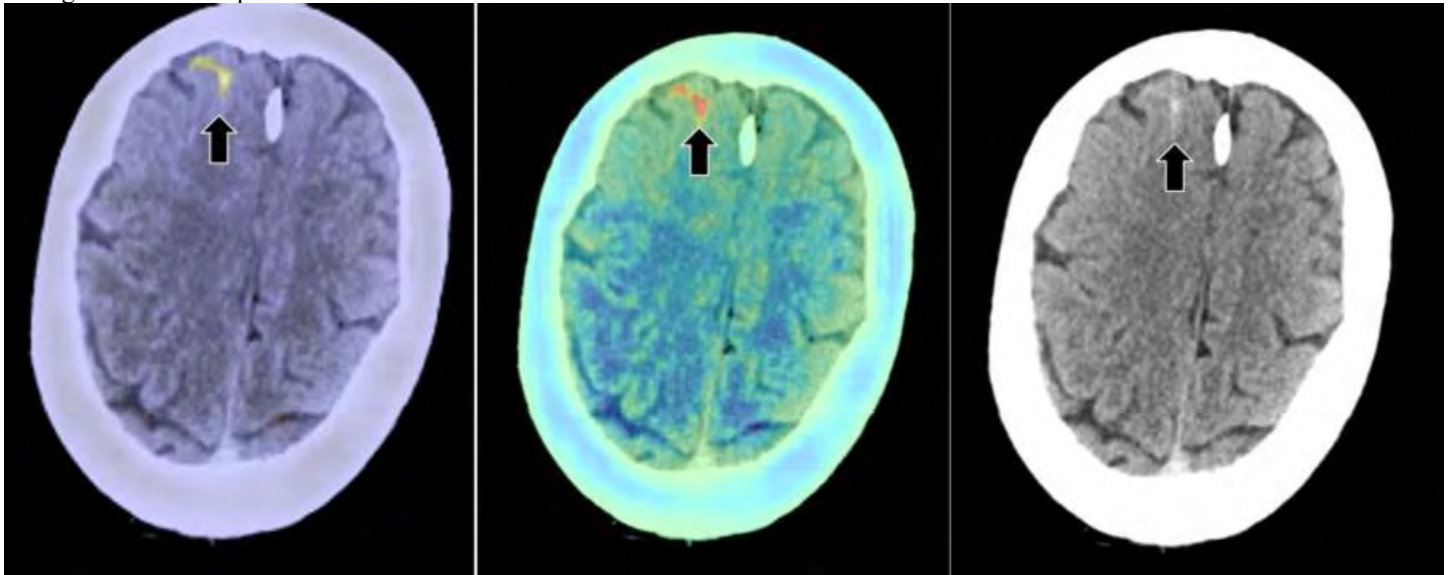
An IRB approved prospective study was performed to investigate the accuracy of an AI software (AiDoc) for detection of intracranial hemorrhage. Our cohort included 1200 patients for whom CT head was performed from July 28, 2020 through September 5, 2020. No subject exclusions were made based on patient age, sex, past medical history, or reason for scan. The AiDoc software was subsequently used for detection of intracranial hemorrhage. The CT scans were reviewed by two independent neuroradiologists with 20, and 10 year-experience. The performance of the software was compared to the results of neuroradiologists. The sensitivity, specificity and accuracy of the software-based detection have been calculated.

Results

Of the 1200 patients who had CT head performed from July 28 through September 5, 2020, a total of 417 patients were found to have an intracranial hemorrhage. Of these 417 patients, AiDoc software correctly identified 403 (true positive, TP), while misidentifying 14 (false negative, FN). Of the remaining 783 hemorrhage-negative patients, the software correctly identified 774 negative findings (true negative, TN), while misidentifying 9 as false positives (FP). The sensitivity of software hemorrhage identification was found to be 96.64% with a negative predictive value of 98.22%. Specificity of software identification was 98.85% with a positive predictive value of 97.82%. Overall accuracy of software reports was found to be 98.08%. The positive likelihood ratio was calculated to be 84.08 with a negative likelihood ratio of 0.03.

Conclusions

AI software is both sensitive and specific in detecting intracranial hemorrhage and thus is a promising tool in aiding accurate detection of brain hemorrhage, especially in acute-care settings. The software also helps to reprioritize the inpatient and outpatient CT scans with positive findings. This aids in accurate prompt detection of positive cases with intracranial hemorrhage and allows for urgent management of these patients.



(Filename: TCT_407_Fig.jpg)

508

Pre-Examinations improve automated Metastases Detection on cranial MRI

K Deike-Hofmann¹, D Dancs¹, D Paech¹, B Philipp¹, A Radbruch², M Götz¹

¹German Cancer Research Center, Heidelberg, Baden-Württemberg, ²Universityclinic Bonn, Bonn, Nordrhein-Westfalen

Purpose

To assess the diagnostic value of inclusion of pre-diagnosis MRI and different MRI sequences for automated detection of metastases from malignant melanoma (MM) on an annotated real-life cranial MRI dataset. In contrast to the majority of previous studies, diagnostic performance was challenged by extracerebral-intracranial MM and by inclusion of MRI with heterogeneous sequence parameters [1, 2].

Materials and Methods

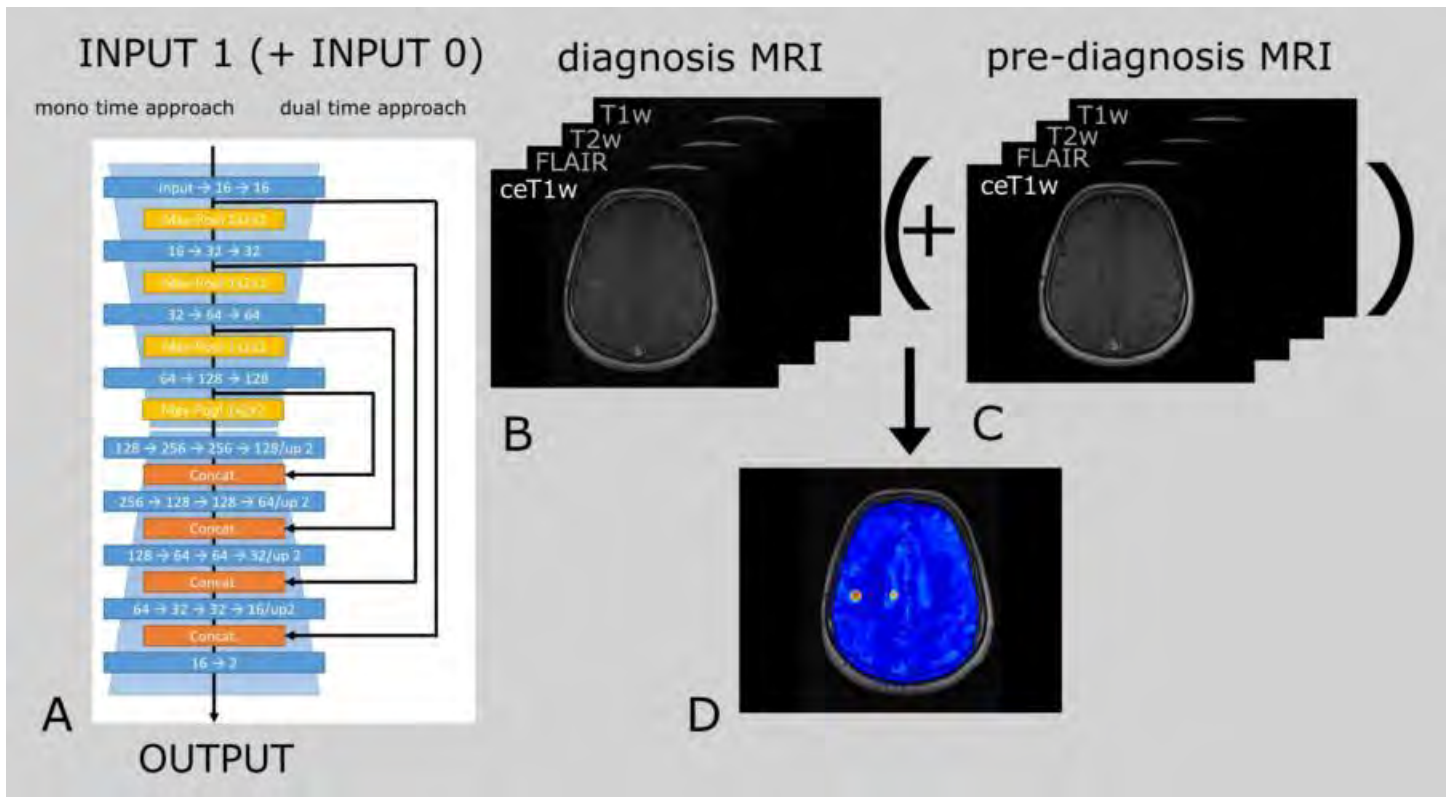
Our local ethics committee approved this retrospective monocenter study. A fully convolutional neural network was trained in automated metastases detection [3, 4]. Firstly, a dual time approach was assessed, for which the CNN was provided sequences of the MRI that firstly depicted new MM (diagnosis MRI) as well as of a pre-diagnosis MRI: Inclusion of only contrast-enhanced T1-weightings (CNNdual_ce) was compared to inclusion of also the native T1-weightings, T2-weightings and FLAIR sequences of both time points (CNNdual_all). Secondly, results were compared to the corresponding single time approaches, in which the CNN was provided exclusively the respective sequences of the diagnosis MRI. Case-wise diagnostic performance parameters were calculated from five-fold cross validation.

Results

In total, 94 cases with 494 MM were included. Overall, the highest diagnostic performance was achieved by inclusion of only the contrast-enhanced T1-weightings of the diagnosis and of a pre-diagnosis MRI (CNNdual_ce, sensitivity = 73 %, PPV = 25 %, F1-score = 36 %). Using exclusively contrast-enhanced T1-weightings as input resulted in significantly less false positives (FPs) compared to inclusion of further sequences beyond contrast-enhanced T1-weightings (FPs = 5 / 7 for CNNdual_ce / CNNdual_all, $p < 1e-5$). Comparison of contrast-enhanced dual and mono time approaches revealed that exclusion of pre-diagnosis MRI significantly increased FPs (FPs = 5 / 10 for CNNdual_ce / CNNce, $p < 1e-9$). Approaches with only native sequences were clearly inferior to CNNs that were provided contrast-enhanced sequences.

Conclusions

Automated MM detection performed with high sensitivity when including contrast-enhanced T1-weightings, which concurs well with results from human readings [5]. Frequent FPs due to artifacts and vessels were significantly reduced by additional inclusion of pre-diagnosis MRI, but not by inclusion of further sequences beyond contrast-enhanced T1w. Future studies might investigate different change detection architectures for computer-aided detection.



(Filename: TCT_508_bild.jpg)

637

Pre-treatment Normal WM MTR Predicts Risk for Radiation Necrosis in Children with Medulloblastoma

J Harreld¹, P Zou¹, A Edwards¹, N Sabin¹, Y Han¹, Y Li¹, O Bieri², A Gajjar¹, G Robinson¹, T Merchant¹
¹St. Jude Children's Research Hospital, Memphis, TN, ²University Hospital Basel, Basel, n/a

Purpose

Radiation necrosis, for which abnormal white matter (WM) enhancement is a hallmark, is an uncommon complication of craniospinal irradiation (CSI) in children with medulloblastoma (MB).[1] Magnetization transfer ratio (MTR) measures macromolecular content, dominated by myelin in WM.[2] We investigated whether pre-treatment supratentorial (non-surgical) WM MTR could predict children at risk for radiation necrosis after CSI for MB.

Materials and Methods

114 children with medulloblastoma (37% female, 10.8±5.3 years old) had baseline bSSFP-based MT MRI [2] (3T Siemens; flip angle=30°, TR/TE/RF 3.09/1.55/200ms (MMT) and 4.39/2.2/1500ms (M0)) before proton or photon CSI. Associations between baseline supratentorial (ST) MTR, post-CSI enhancing radiation changes (ERC=spontaneously resolving/improving parenchymal enhancement in the radiation field)[3], age and presence of visible brain metastases were explored by logistic regression and parametric/nonparametric techniques as appropriate (SAS 9.4).

Results

24/114 (21%) children (46% female, 10.6±6.6 years) developed ERC after CSI (22 PF, 1 ST, 1 both). Pre-treatment ST WM MTR was significantly lower in these children (43.16 vs. 43.52, p=0.0073) and negatively associated with development of ERC after CSI (p=0.04, odds ratio=0.48). There was no association between ST WM MTR and age or presence of visible brain metastases.

Conclusions

Lower baseline supratentorial WM MTR may indicate underlying structural WM susceptibility to radiation damage and identify children at risk for developing radiation necrosis after CSI for medulloblastoma.

621

Prediction of BRAFV600E-Mutation Status Using Preoperative MR Imaging Phenotypes in Glioblastoma

M Bledsoe¹, S Khanpara¹, O Arevalo², C Yalniz¹, R Samant¹, X Zhang¹, C Soto³, A Dono¹, L Ballester¹, Y Esquenazi¹, J Zhu¹, R Riascos¹

Purpose

Glioblastomas (GBM) are divided into two different subgroups: isocitrate dehydrogenase (IDH)-wildtype and IDH-mutant. Different molecular subtypes have been reported to have different degrees of treatment response and prognosis. Some clinical trials have reported promising treatment response rates to targeted therapies in patients with an uncommon subtype of GBM IDHwt harboring the BRAF mutation. We sought to evaluate the predictive value of imaging phenotypes assessed with the Visually AcceSAbLe Rembrandt Images lexicon to discriminate two molecular subtypes of GBM- BRAF-mutated and BRAF-wildtype.

Materials and Methods

MR imaging scans of 253 patients with GBM IDHwt with known BRAF status were included (242 BRAFwt, 11 BRAFmut). MR imaging features were reviewed by using VASARI, and semiautomatic segmentation was performed (volumetric measurement of the enhancement, FLAIR hyperintensity, and necrosis). Association between genotype and the MR features was evaluated by Fisher's exact test for categorical variables and the Wilcoxon rank-sum test for continuous variables.

Results

Only two of the twenty-five imaging features of the VASARI set was significantly different according to BRAF mutation. A lower frequency of deep white matter structures (DWMS) invasion was seen in tumors harboring the BRAF mutation ($p = 0.009$). BRAF wildtype tumors had more well-defined margins of the non-enhancing tumor ($p = 0.01$). There was no significant difference in the volumes or ratios of the different tumor compartments after analysis of the segmentation data. The absence of cortical involvement ($P = 0.05$) is a potential predictor of BRAF mutation according to Fisher's exact test.

Conclusions

New diagnostic challenges arise with the newer genotypic classifications and identifying imaging biomarkers for the early recognition of specific genotypes becomes crucial as new highly-effective targeted, effective therapies become more available. Frequency of DWMS invasion, characteristic of the non-enhancing margin and the presence of cortical involvement showed a tendency for potential imaging biomarkers. It is hypothesized that further multicenter studies with a larger sample size could find discriminative imaging features.

Table 1: Association between imaging features and BRAF mutation status in patients with GBM IDH wild type (N=153)

Features	BRAF mutant – Yes (N=31)	BRAF mutant – No (N=122)	P value
FLAIR cm3, median (IQR)	95 (67, 129)	105 (54, 150)	0.87
Enhancement cm3, median (IQR)	11.4 (7.9, 16.0)	17.0 (7.7, 33.5)	0.40
Necrosis cm3, median (IQR)	4.2 (2.1, 12.4)	5.2 (1.0, 11.5)	0.85
Tum volume FLAIR+Enh+Nec, median (IQR)	125 (82, 154)	136 (71, 195)	0.70
F1 - Tumor location			0.61
Frontal	3 (27%)	79 (35%)	
Temporal	6 (54%)	81 (36%)	
Insular	0 (0%)	6 (3%)	
Parietal	1 (9%)	44 (20%)	
Occipital	1 (9%)	8 (4%)	
Corpus callosum	0 (0%)	6 (3%)	
F2 - Side			0.16
Right	4 (16%)	121 (54%)	
Center	0 (0%)	9 (4%)	
Left	7 (64%)	94 (42%)	
F3 - Eloquent brain (Yes)	7 (64%)	109 (49%)	0.37
F4-Enhancement quality			0.16
Marked/avid	10 (91%)	190 (85%)	
Minimal/mild	0 (0%)	27 (12%)	
None	1 (9%)	7 (3%)	
F5 - Proportion enhancing, median (IQR)	12.16 (9.16, 13.54)	15.37 (9.05, 21.26)	0.15
F6 - Proportion nCET, median (IQR)	82.1 (70.0, 89.8)	77.5 (69.9, 88.6)	0.29
F7 - Proportion of Necrosis, median (IQR)	3.91 (1.69, 8.88)	4.33 (1.54, 8.11)	0.81
F8 - Cysts (Yes)	1 (9%)	31 (14%)	1.00
F9 - Multifocal/Multicentric (Yes)	2 (18%)	34 (15%)	0.68
F10 - T1/FLAIR ratio			0.23
Expansive	5 (45%)	138 (62%)	
Mixed	1 (9%)	34 (15%)	
Infiltrative	5 (45%)	52 (23%)	
F11 - Thickness of enhancing margin			0.37
Solid	1 (9%)	17 (8%)	
Thick	7 (64%)	167 (74%)	
Thin	2 (18%)	32 (14%)	
None	1 (9%)	8 (4%)	
F12 - Definition of enhancing margin			0.31
Well defined	7 (64%)	158 (71%)	
Poorly defined	3 (27%)	61 (27%)	
None	1 (9%)	5 (2%)	
F13 - Definition of the non-enhancing margin			0.018
Well defined	11 (100%)	145 (65%)	
Poorly defined	0 (0%)	79 (35%)	
F14 - Proportion of edema			0.97
None	2 (18%)	31 (24%)	
<5%	3 (27%)	58 (26%)	
6-33%	4 (36%)	78 (35%)	
34-67%	2 (18%)	57 (25%)	
F15 - Hemorrhage (Yes)	7 (64%)	126 (56%)	0.76
F17 - Diffusion characteristics			0.42
Facilitated	3 (46%)	65 (29%)	
Restricted	4 (36%)	86 (38%)	
Mixed	2 (18%)	73 (33%)	
F18 - Pial invasion (Yes)	3 (27%)	102 (46%)	0.35
F19 - Ependymal extension (Yes)	4 (36%)	50 (22%)	0.28
F20 - Cortical involvement (Yes)	7 (64%)	195 (87%)	0.05
F21 - Deep WM invasion			0.009
Brainstem	3 (18%)	4 (2%)	
Corpus callosum	0 (0%)	62 (28%)	
Internal capsule	2 (18%)	35 (18%)	
No	7 (64%)	123 (55%)	
F22 - nCET crosses midline (Yes)	1 (9%)	45 (20)	0.70
F23 - CET crosses midline (Yes)	1 (9%)	20 (9%)	1.00
F24 - Satellites (Yes)	4 (36%)	72 (32%)	0.75
F25 - Calvarial remodeling (Yes)	0 (0%)	4 (2%)	1.00

Table 2: AUC for continuous variables in differentiating BRAF mutant from BRAF wildtype

Features	AUC	95% CI
FLAIR cm3	0.515	0.373 – 0.657
Enhancement cm3	0.576	0.412 – 0.739
Necrosis cm3	0.517	0.335 – 0.699
Tum volume FLAIR+Enh+Nec	0.534	0.368 – 0.681
F5 - Proportion enhancing	0.627	0.482 – 0.773
F6 - Proportion nCET	0.595	0.421 – 0.770
F7 - Proportion of Necrosis	0.519	0.335 – 0.703

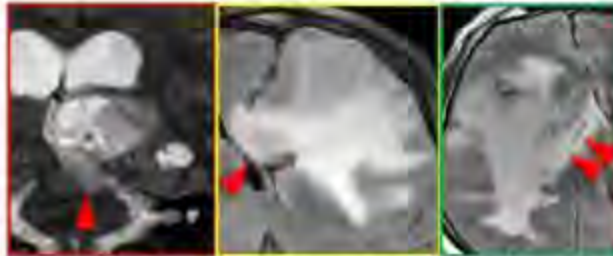


Fig: Deep white matter structures invasion. Images of different patients with glioblastoma IDH wildtype, without BRAF^{V600} mutation. On the left panel, the heterogeneous T2/FLAIR signal abnormality extends to the left cerebral peduncle. The middle image shows involvement of the genu of the corpus callosum by the mass-like T2/FLAIR hyperintensity. On the right frame, the extensive T2/FLAIR changes surround and splay the corticospinal tract fibers within the posterior limb of the internal capsule.

Prediction of IDH1/2-Mutation Status in Preoperative MR Imaging Phenotypes in Glioblastoma using the VASARI feature set

S Khanpara¹, O Arevalo², C Yalniz¹, R Samant¹, A Aein¹, X Zhang¹, C Soto³, A Dono¹, L Ballester¹, J Zhu¹, R Riascos¹

¹University of Texas Health Science Center at Houston, Houston, TX, ²MD Anderson Cancer Center, Houston, TX, ³National University of Colombia, Bogota, TX

Purpose

Glioblastomas (GBM) are classified by the presence of a mutation in the isocitrate dehydrogenase genes in wildtype (IDH1/2-WT) and mutant (IDH1/2-Mut), which have prominent differences in prognosis. We aimed to evaluate the predictive value of imaging phenotypes to discriminate these subtypes by the assessment of the Visually AcceSAbLe Rembrandt Images lexicon (VASARI).

Materials and Methods

MR imaging scans of 248 patients with pathological diagnosis of GBM with known IDH1/2 statuses were included (231 IDH1/2-WT, 17 IDH1/2-Mut). MR imaging features were reviewed using VASARI, moreover semiautomatic segmentation was performed (volumetric measurement of the enhancement, FLAIR hyperintensity, and necrosis). The association between genotype and MR features was evaluated by Fisher's exact test for categorical variables. For continuous variables, the Wilcoxon rank-sum test and AUC were used.

Results

9 out of 25 imaging features of the VASARI set were significantly different according to IDH1/2-mutation. IDH1/2-WT GBMs showed higher enhancement and necrosis volumes ($p < 0.001$), enhancement/FLAIR ($p < 0.001$), and necrosis/enhancement ($p < 0.001$) volume ratios. The IDH1/2-Mut GBMs demonstrated a predilection for the frontal and parietal lobes ($p = 0.03$), a higher prevalence of cysts ($p = 0.018$), and higher rates for ill-defined enhancing margin ($p < 0.001$). The AUC on the ROC curve was significant for the volume of enhancement (0.791) and necrosis (0.808), and the different ratios between enhancing, non-enhancing, and necrotic tumor (0.791-0.827).

Conclusions

Imaging features predict IDH1/2 mutations in GBM on standard-of-care (SOC) MR scans. Our results are in concordance and validate other published studies on isolated imaging biomarkers. A combination of the discriminating depicted features on SOC MR scans, including volumetric measurements, demonstrated value in distinguishing between GBMs harboring IDH1/2-mutation from their wildtype counterpart.

Table 1: Association between imaging features and IDH1 mutation status in patients with GBM (N=167)

Feature	IDH1 mutant (N=17)	IDH1 wildtype (N=231)	P value
FLAIR cm3, median (IQR)	112 (52.2, 124)	105 (55.3, 150)	0.92
Enhancement cm3, median (IQR)	2.96 (0.58, 6.48)	17.5 (8.4, 34.2)	<0.001
Necrosis cm3, median (IQR)	0.1 (0, 1.9)	5.8 (1.3, 12.4)	<0.001
Tum volume FLAIR+Enh+Nec, median (IQR)	116 (52, 125)	137 (74, 194)	0.38
F1 - Tumor location			0.035
Frontal	13 (76%)	74 (32%)	
Temporal	2 (12%)	88 (38%)	
Insular	0 (0%)	6 (3%)	
Parietal	2 (12%)	48 (21%)	
Occipital	0 (0%)	9 (4%)	
Corpus callosum	0 (0%)	6 (3%)	
F2 - Side			0.72
Right	8 (47%)	125 (54%)	
Center	0 (0%)	9 (4%)	
Left	9 (53%)	97 (42%)	
F3 - Eloquent brain (Yes)	6 (35%)	115 (50%)	0.32
F4-Enhancement quality			<0.001
Marked/avid	5 (29%)	206 (89%)	
Minimal/mild	9 (53%)	20 (9%)	
None	3 (18%)	5 (2%)	
F5 - Proportion enhancing, median (IQR)	2.69 (0.50, 5.47)	15.75 (9.95, 21.01)	<0.001
F6 - Proportion nCET, median (IQR)	97.1 (91.2, 99.4)	77.4 (69.7, 85.5)	<0.001
F7 - Proportion of Necrosis, median (IQR)	0.16 (0, 1.24)	4.69 (1.94, 8.76)	<0.001
F8 - Cysts (Yes)	6 (35%)	28 (12%)	0.018
F9 - Multifocal/Multicentric (Yes)	2 (12%)	40 (17%)	0.75
F10 - T1/FLAIR ratio			0.39
Expansive	10 (59%)	142 (61%)	
Mixed	1 (6%)	36 (16%)	
Infiltrative	6 (35%)	53 (23%)	
F11 - Thickness of enhancing margin			<0.001
Solid	6 (35%)	178 (77%)	
Thick	2 (12%)	35 (15%)	
Thin	3 (18%)	6 (3%)	
None			
F12 - Definition of enhancing margin			<0.001
Well defined	2 (12%)	174 (75%)	
Poorly defined	12 (71%)	54 (23%)	
None	3 (18%)	3 (1%)	
F13 - Definition of the non-enhancing margin			0.61
Well defined	5 (29%)	86 (37%)	
Poorly defined	12 (71%)	145 (63%)	
F14 - Proportion of edema			0.006
None	7 (41%)	27 (12%)	
<5%	5 (29%)	58 (25%)	
6-33%	4 (24%)	81 (35%)	
34-67%	1 (6%)	65 (28%)	
F16 - Hemorrhage (Yes)	6 (35%)	133 (58%)	0.08
F17 - Diffusion characteristics			0.26
Facilitated	8 (47%)	64 (28%)	
Restricted	4 (24%)	90 (39%)	
Mixed	5 (29%)	77 (33%)	
F18 - Pial invasion (Yes)	4 (24%)	105 (45%)	0.13
F19 - Ependymal extension (Yes)	1 (6%)	54 (23%)	0.13
F20 - Cortical involvement (Yes)	17 (100%)	197 (85%)	0.14
F21 - Deep WM invasion			0.24
Brainstem	0 (0%)	6 (3%)	
Corpus callosum	8 (47%)	56 (24%)	
Internal capsule	1 (6%)	36 (16%)	
No	8 (47%)	133 (58%)	
F22 - nCET crosses midline (Yes)	6 (35%)	41 (18%)	0.10
F23 - CET crosses midline (Yes)	2 (12%)	19 (8%)	0.64
F24 - Satellites (Yes)	2 (12%)	80 (35%)	0.06
F25 - Calvarial remodeling (Yes)	0 (0%)	5 (2%)	1.00

Table 2: AUC for continuous variables in differentiating IDH1 mutant from IDH1 wildtype

Features	AUC	95% CI
FLAIR cm3	0.508	0.353 – 0.662
Enhancement cm3	0.791	0.658 – 0.924
Necrosis cm3	0.808	0.706 – 0.911
Tum volume FLAIR+Enh+Nec	0.565	0.412 – 0.717
F5 - Proportion enhancing	0.791	0.636 – 0.947
F6 - Proportion nCET	0.818	0.678 – 0.958
F7 - Proportion of Necrosis	0.827	0.720 – 0.934

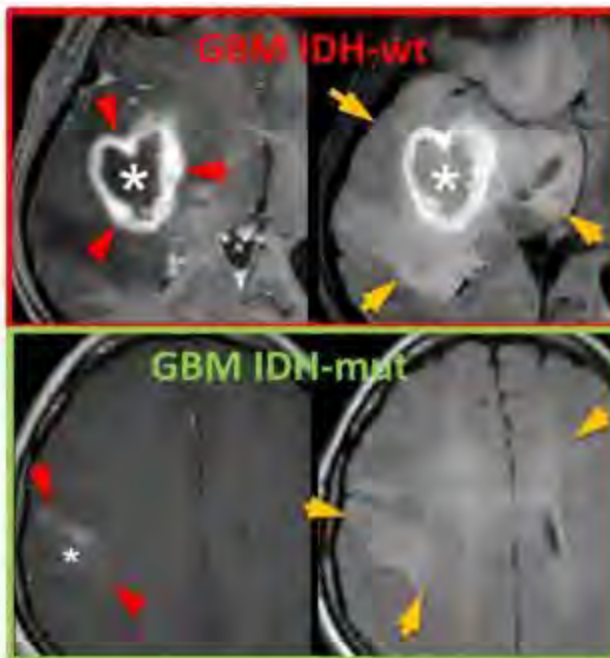


Fig: Note the different proportions among the three main tumor compartments:

- Necrosis (*)
- Enhancement (→)
- FLAIR signal abnormality (↔)

Prediction of pTERT-Mutation Status Using Preoperative MR Imaging Phenotypes in Glioblastoma

S Khanpara¹, O Arevalo², C Yalniz¹, R Samant¹, X Zhang¹, L De Alba³, C Soto⁴, A Dono¹, L Ballester¹, Y Esquenazi¹, J Zhu¹, R Riascos⁵

¹University of Texas Health Science Center at Houston, Houston, TX, ²MD Anderson Cancer Center, Houston, TX, ³N/A, N/A, ⁴National University of Colombia, Bogota, TX, ⁵The University of Texas Health Science Center at Houston, Houston, TX

Purpose

Glioblastomas (GBM) are divided into two subgroups: isocitrate dehydrogenase (IDH)-wildtype and IDH-mutant. Different molecular subtypes have varied response to treatment and prognosis. The combination of pTERT mutation and wild-type isocitrate dehydrogenase 1 (IDH1) is the most common genotype, occurring in more than 80% of GBM, and is associated with a worse prognosis. Noninvasive preoperative identification of a TERT mutation can help customize treatment with telomerase targeted therapies and predict prognosis. Our purpose is to evaluate if imaging features in preoperative MR can help distinguish between pTERT-mutated and pTERT-wildtype GBM.

Materials and Methods

Preoperative MR imaging scans of 167 patients with GBM with known pTERT status were retrospectively included (93 pTERTmut, 74 pTERTwt). MR imaging features were evaluated by using Visually AcceSable Rembrandt Images (VASARI), and semiautomatic segmentation was performed (volumetric measurement of the enhancement, FLAIR hyperintensity, and necrosis). Association between pTERT status and MR features was evaluated by Fisher's exact test for categorical variables. The Wilcoxon rank-sum test and AUC were used for continuous variables. For AUC, a value higher than 0.75 was considered significant.

Results

None of the volumetric or VASARI features reached statistical significance for distinguishing pTERTmut from pTERTwt. None of the volumetric/VASARI features showed any tendency towards statistical significance. AUC curves derived for the continuous variables also failed to show any statistical significance in differentiating pTERTmut from pTERTwt. We had done a similar analysis last year exclusively with IDH wildtype Glioblastoma pTERT mutants and wildtypes with similar results.

Conclusions

Preoperative MR imaging features were not found to be capable of discrimination between pTERTmut and pTERTwt GBM's when used as single variables.

Table 1. Association between imaging factors and pTERT mutation status in glioblastoma cases (N=167)

Features	pTERT mutant (N=93)	pTERT wild-type (N=74)	P value
FLAIR cm3, median (IQR)	103 (58, 134)	117 (61, 167)	0.12
Enhancement cm3, median (IQR)	17.5 (10.9, 31.0)	22.4 (7.6, 35.2)	0.66
Necrosis cm3, median (IQR)	5.6 (2.1, 12.3)	6.2 (1.2, 10.5)	0.61
Tum volume FLAIR+Enh+Nec, median (IQR)	135 (74, 181)	140 (92, 218)	0.16
F1 - Tumor location			0.08
Frontal	24 (26%)	33 (45%)	
Temporal	44 (47%)	24 (32%)	
Insular	2 (2%)	2 (3%)	
Parietal	18 (19%)	10 (13%)	
Occipital	4 (4%)	2 (3%)	
Corpus callosum	1 (1%)	3 (4%)	
F2 - Side			0.30
Right	55 (59%)	35 (47%)	
Center	2 (2%)	3 (4%)	
Left	36 (39%)	36 (49%)	
F3 - Eloquent brain (Yes)	44 (47%)	38 (51%)	0.64
F4-Enhancement quality			0.49
Marked/avid	83 (89%)	63 (85%)	
Minimal/mild	9 (10%)	8 (11%)	
None	1 (1%)	3 (4%)	
F5 - Proportion enhancing, median (IQR)	15.89 (10.76, 21.18)	15.0 (8.30, 21.99)	0.76
F6 - Proportion nCET, median (IQR)	77.4 (68.4, 85.2)	77.9 (70.1, 86.0)	0.56
F7 - Proportion of Necrosis, median (IQR)	4.29 (2.32, 8.76)	4.16 (1.24, 6.93)	0.23
F8 - Cysts (Yes)	10 (11%)	16 (22%)	0.08
F9 - Multifocal/Multicentric (Yes)	9 (10%)	8 (11%)	0.80
F10 - T1/FLAIR ratio			0.12
Expansive	53 (57%)	44 (59%)	
Mixed	8 (9%)	13 (18%)	
Infiltrative	32 (34%)	17 (23%)	
F11 - Thickness of enhancing margin			0.09
Solid	5 (5%)	9 (12%)	
Thick	68 (73%)	52 (70%)	
Thin	19 (20%)	9 (12%)	
None	1 (1%)	4 (5%)	
F12 - Definition of enhancing margin			0.08
Well defined	70 (75%)	45 (61%)	
Poorly defined	22 (24%)	28 (38%)	
None	1 (1%)	1 (1%)	
F13 - Definition of the non-enhancing margin			1.00
Well defined	18 (19%)	15 (20%)	
Poorly defined	75 (81%)	59 (80%)	
F14 - Proportion of edema			0.10
None	12 (13%)	7 (9%)	
<5%	28 (30%)	17 (23%)	
6-33%	38 (41%)	26 (35%)	
34-67%	15 (16%)	24 (32%)	
F16 - Hemorrhage (Yes)	59 (63%)	41 (55%)	0.34
F17 - Diffusion characteristics			0.17
Facilitated	32 (34%)	22 (30%)	
Restricted	45 (48%)	30 (40%)	
Mixed	16 (17%)	22 (30%)	
F18 - Pial invasion (Yes)	46 (49%)	36 (49%)	1.00
F19 - Ependymal extension (Yes)	27 (29%)	16 (22%)	0.29
F20 - Cortical involvement (Yes)	77 (83%)	65 (88%)	0.39
F21 - Deep WM invasion			0.15
Brainstem	3 (3%)	1 (1%)	
Corpus callosum	18 (19%)	22 (30%)	
Internal capsule	16 (17%)	18 (24%)	
No	56 (60%)	33 (45%)	
F22 - nCET crosses midline (Yes)	14 (15%)	15 (20%)	0.42
F23 - CET crosses midline (Yes)	4 (4%)	5 (7%)	0.51
F24 - Satellites (Yes)	36 (39%)	19 (26%)	0.10
F25 - Calvarial remodeling (Yes)	1 (1%)	3 (4%)	0.32

Table 2. AUC for continuous variables in differentiating pTERT mutant from pTERT wildtype

Features	AUC	95% CI
FLAIR cm3	0.570	0.480 – 0.660
Enhancement cm3	0.520	0.428 – 0.612
Necrosis cm3	0.477	0.388 – 0.566
Tum volume FLAIR+Enh+Nec	0.563	0.473 – 0.653
F5 - Proportion enhancing	0.514	0.423 – 0.605
F6 - Proportion nCET	0.526	0.437 – 0.616
F7 - Proportion of Necrosis	0.554	0.465 – 0.643

(Filename: TCT_625_TERT.jpg)

Predictive Model of Pial Collaterals using MR DSC Perfusion in Ischemic Stroke

Y Jeong¹, G Christoforidis¹, N Saadat¹, M Niekrasz¹, T Carroll¹, S Roth²

¹University of Chicago, Chicago, IL, ²University of Illinois College of Medicine, Chicago, IL

Purpose

In the event of an ischemic stroke, blood flow may be restored to the affected territory via pial collaterals. Depending on the collaterals, care management may vary, and invasive treatment plans may not be necessary. However, determining the degree of pial collateralization currently requires the use of invasive imaging techniques. In this study, we examine the potential of MR perfusion as a predictor of pial collaterals by applying delay and dispersion corrections to accurately capture delayed blood flow through the collaterals.

Materials and Methods

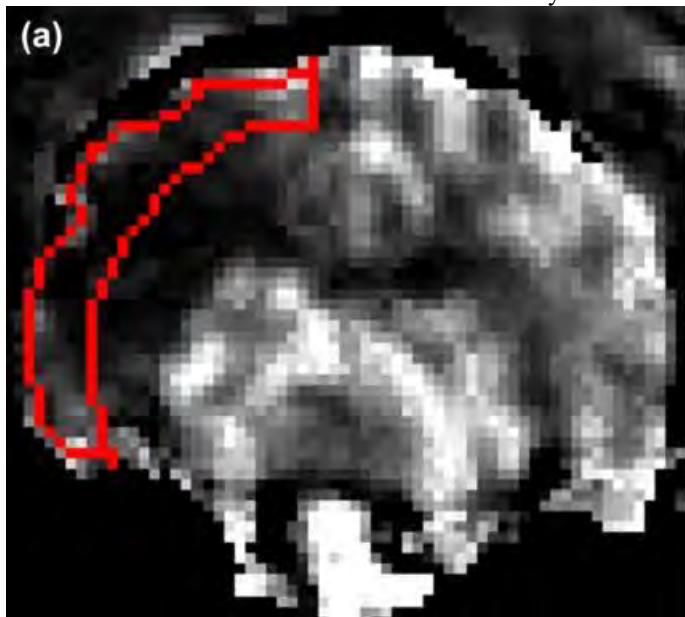
This study was approved by the University of Chicago Institutional Animal Care and Use Committee. Seven mongrel canines underwent permanent endovascular occlusion of the M1 segment of the middle cerebral artery. Anesthesia was maintained using isoflurane, propofol and rocuronium. Arteriography images were taken 15 minutes after occlusion for scoring of pial collaterals based on a previously published 11-point scoring system. Then 2 hours after occlusion, MR DSC and T1 Look-Locker EPI scans were acquired based on the Bookend method for measuring CBF. To measure CBF more accurately in the presence of delayed arrival, delay and dispersion corrections were applied based on a previously published method. Briefly, the arterial input function was convolved by a dispersion model as a function of delayed arrival time and shifted by the delay time before deconvolution. For each case, cortical ROIs were drawn on the infarct side (Figure 1a), and average CBF before and after correction were calculated for analysis. The 7 cases were used to train an ordinal logistic regression model using leave-one-out cross-validation.

Results

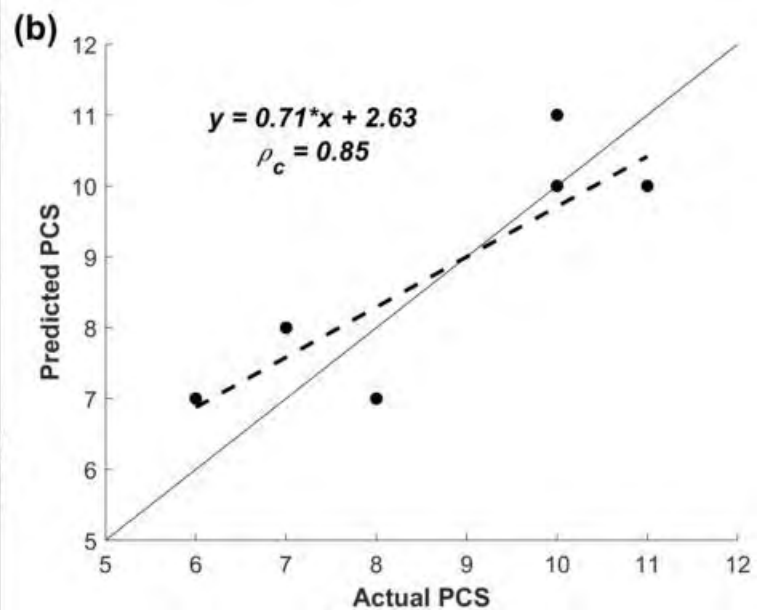
CBF with and without correction, and the percent difference in CBF were used as predictors of pial collateral score (PCS). The best model from cross-validation resulted in the percent difference in CBF being the most significant predictor as assessed by Lin's concordance correlation coefficient between predicted scores and actual scores measured by a neuroradiologist. The concordance correlation coefficient was 0.85, Pearson correlation coefficient (precision) was 0.87, and bias (accuracy) was 0.98 (Figure 1b). Adding the other predictors to the model resulted in a lower correlation coefficient.

Conclusions

Although the sample size was small, the change in CBF due to correction was used to predict pial collaterals with good agreement. Further research with more data would be necessary for a better performance measure of the predictive model.



(Filename: TCT_1367_figure1.jpg)



359

Prenatal Evaluation of Intracranial Hemorrhage on Fetal MRI

K Epstein¹, U Nagaraj², M Habli³, C Venkatesan³, B Kline-Fath¹

¹Cincinnati Children's Hospital Medical Center, Cincinnati, OH, ²Cincinnati Children's Hospital Medical Center, Cincinnati, OH, ³Cincinnati Children's Hospital Medical Center, Cincinnati, OH

Purpose

The evaluation and characterization of germinal matrix hemorrhages (GMHs) has been predominantly described and classified on postnatal head ultrasound in premature neonates. However GMH that are seen in premature neonates can be also seen in fetuses of the same post-conceptual age, and is now more frequently encountered in the era of fetal MRI. Our aim is to examine and describe the MR imaging findings of fetuses with intracranial hemorrhage.

Materials and Methods

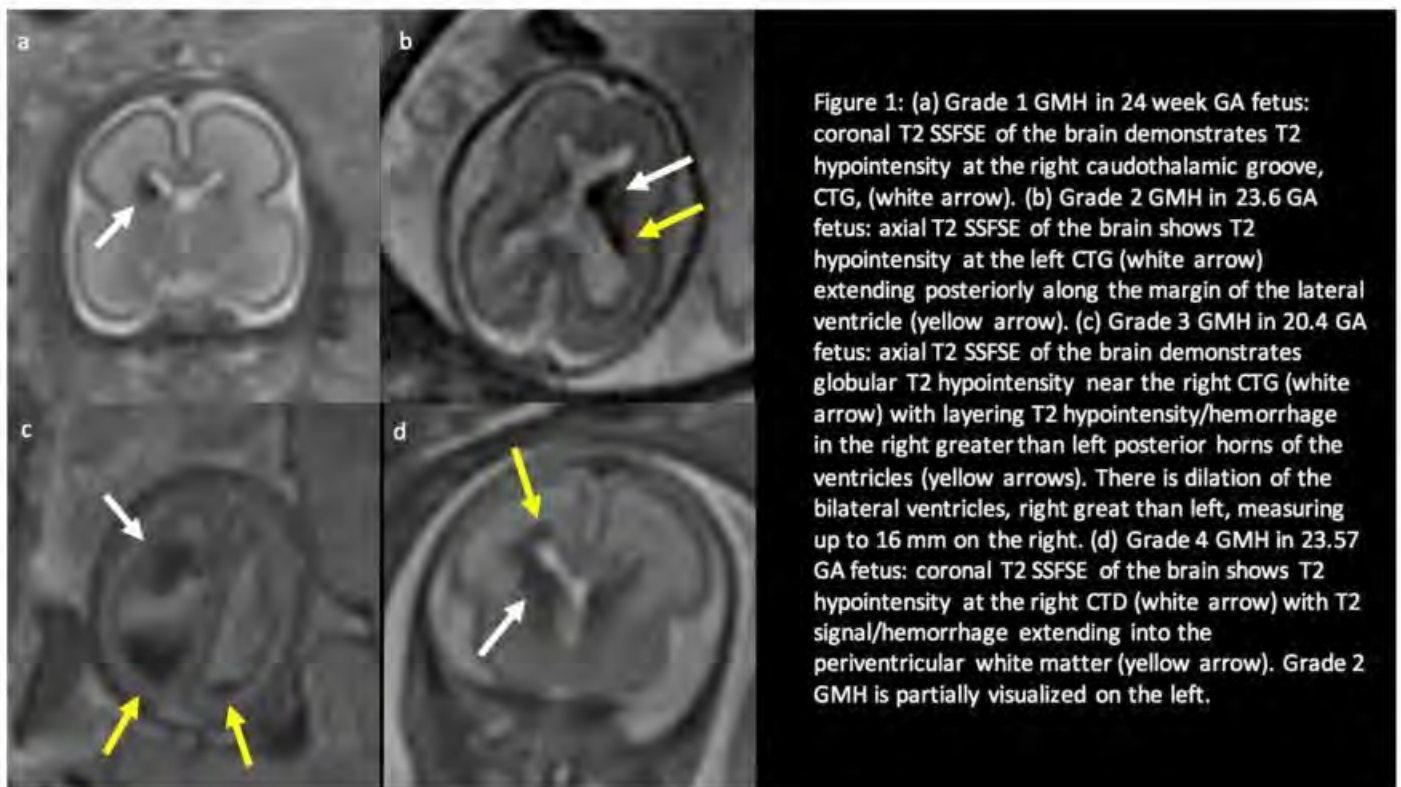
An IRB-approved retrospective review of fetal MRIs with intracranial hemorrhage from January 2004 to May 2020 was performed. Relevant clinical notes, US reports and postnatal imaging was reviewed. Fetuses with diagnostic quality MR studies with intracranial hemorrhage were included. T1, T2 SSFSE, DWI, and EPI imaging characteristics of the fetal intracranial hemorrhages were documented. Hemorrhages were classified as GMH vs non-GMH, and GMHs were subsequently graded by the Burstein and Papile Modified Grading System. "Grade 0" was added to include the patients with imaging sequelae of prior grade 1 GMH. Multiple additional clinical and imaging parameters were also examined and recorded.

Results

177 fetuses with mean gestational age of 25.73 ± 5.01 weeks met criteria and were included. GMH was identified in 59.9% (106/177) of patients (grade 0=12, grade 1=31, grade 2=30, grade 3=7, grade 4=26) and non-GMH in 40.1.9% (71/177) of patients. 23.9% (17/71) of non-GMH were cerebellar hemorrhages. 65.1% (69/106) GMHs were singleton pregnancies, and 34.9% (37/106) were multiple gestation pregnancies. The mean ventricular size was 12.76 ± 7.54 mm, with 59.3% (105/177) fetuses with ventriculomegaly (>10 mm). 79.1% (140/177) fetuses had other imaging abnormalities (i.e. aqueductal stenosis, Chiari II malformation, twin-twin transfusion, and extra-cranial congenital anomalies, etc.). T2 and EPI were positive for hemorrhage in 84.7% and 96.3% of all positive cases, respectively. However T1 and DWI demonstrated 46% and 57.8% positivity, respectively.

Conclusions

MRI has become a key tool in diagnosis and characterization of intracranial hemorrhage in the fetus. T2 and EPI sequences are the most important sequences for identification. GMH that occur in the fetus are more commonly limited to the germinal matrix +/- ventricular extension, without ventricular dilation (<15 mm). Appropriate characterization is important for optimizing work-up, therapeutic approach and prenatal counseling.



527

Prevalence of Cervical Arterial Abnormalities in Patients with Spontaneous Coronary Artery Dissection

J Benson¹, V Lehman¹, J VERDOORN², D Shlapak¹, S Hayes¹, M Tweet¹

¹Mayo Clinic, Rochester, MN, ²N/A, N/A

Purpose

Little is known about the association between spontaneous coronary artery dissection (SCAD) and abnormalities of the cervical arterial vasculature. This study sought to assess the association between SCAD and cervical arterial anomalies.

Materials and Methods

A retrospective analysis was completed of consecutive patients who underwent CTA imaging of the neck as part of routine vascular assessment following the diagnosis of SCAD. Arteries were evaluated for the presence of fibromuscular dysplasia (FMD), dissection and/or pseudoaneurysm, ectasia and/or aneurysmal dilatation, atherosclerosis, and webs. Carotid tortuosity was categorized into kinks, loops, coils, and retrojugular and/or retropharyngeal carotid courses; vertebral tortuosity was classified by subjective analysis of severity. All findings were compared to a cohort of age-matched control patients without a diagnosis of SCAD.

Results

214 patients were included in the final cohort, of which 206 (95.8%) were female; average age was 54.4 years. Of the 94 control subjects, average age was 52.3 years. FMD was the most frequently observed abnormality, in 83 patients (38.8%), and was significantly more common than in controls ($p < 0.0001$). Arterial ectasia and/or aneurysmal dilatation and carotid webs were also more common in SCAD patients than controls ($p = 0.0004$ and $p = 0.04$, respectively). 28/214 (13.1%) of SCAD patients had a dissection and/or pseudoaneurysm, though this was not significantly higher than controls (0.71). No difference was noted between SCAD patients and controls in either the prevalence of carotid tortuosity markers or severity of vertebral artery tortuosity ($p = 0.80$ and $p = 0.97$, respectively).

Conclusions

Both cervical arterial FMD and carotid webs are more common in SCAD patients than controls, offering a possible explanation for the proclivity of such patients to undergo spontaneous dissection.

1596

Prevalence of Complications of Internal Carotid Artery Stenting without Filter Device

A Zandifar¹, L Tierradentro-García¹, J Kim¹, M Saadatnia²

¹Children's Hospital of Philadelphia, Philadelphia, PA, ²Isfahan University of Medical Sciences, Isfahan, PA

Purpose

Filter device is an added-cost for neurovascular procedures and may not be present in all environments. Although it might decrease procedural embolic events after carotid stenting, there is little evidence that objectively supports its use in the clinical setting as a standardized procedure for preventing complications. This study aimed to evaluate outcomes in adult patients undergoing internal carotid artery (ICA) stenting without filter device.

Materials and Methods

This study was conducted in two tertiary referral hospitals from March/2016 to June/2018. We included sixty-one patients diagnosed with stroke who had undergone ICA stenting/angioplasty without filter device protection. All patients were followed-up for two weeks as per the institutional standardized interventional protocol for stroke and early complications were recorded. Vascular-related complications were documented up to three months after the procedure.

Results

Age mean \pm SD was 71.9 ± 8.3 . Male/female ratio was 5:1. Based on the clinical history, 89.1% of patients had at least one risk factor including diabetes, hypertension, ischemic heart disease, or smoking history. Left ICA stenting was performed in 48.6% of patients. Two of them (3.3%) had minor complications (watershed infarct and transient ischemic attack) and only one (1.6%) had a major complication (intracranial hemorrhage). None of these patients presented with new embolic events related to long-term disabilities.

Conclusions

We found that ICA stenting without filter protection results in very low procedural complications and imposes less financial burden. Further research with a larger sample size is recommended to better assess the relative advantages and disadvantages of filter device placement when performing carotid stenting.

1259

Qualitative Assessment of Fractional Anisotropy Maps in Prediction of Meningioma Subtypes

Purpose

Surgical management of meningioma depend on their histopathological subtype, certain subtypes having higher recurrence rates (1). Fractional anisotropy (FA), a component of Diffusion Tensor Imaging (DTI), represents the directional asymmetry of diffusion and is affected by microstructural changes (2). In this study we explore the role of FA maps in predicting the histopathological subtypes of meningioma.

Materials and Methods

Retrospective analysis of pre-operative MRI of 98 cases of histopathologically proven subtypes of meningothelial, chordoid, transitional, fibroblastic, microcystic, angiomatous and atypical meningioma was done. FA maps were evaluated by two blinded observers. An ordinal scale of 1 to 4 was used to grade the degree of fractional anisotropy in each lesion. Grade 1 was assigned to those tumors which were nearly dark and grade 4 to those which were nearly bright. Values of 2 and 3 were assigned to tumors which were predominantly dark with patchy bright areas and predominantly bright with scattered dark areas respectively.

Results

Out of the 98 histopathologically proven cases of meningioma, 9 were meningothelial, 15 were transitional, 14 were chordoid, 8 were angiomatous, 15 were microcystic, 17 were fibroblastic and 20 were atypical meningiomas. Interobserver reliability was excellent with an intraclass correlation coefficient of 0.92. Using the Kruskal-Wallis test with Bonferroni correction for intergroup comparison revealed a significant difference (p value .000-.026) in the FA grade between microcystic meningioma and meningothelial, chordoid, fibroblastic and atypical meningioma subtypes with low FA of microcystic meningiomas. Fibroblastic subtype showed higher FA grade with a significant difference between fibroblastic and microcystic, transitional and angiomatous meningioma subtypes. However, there was an significant overlap with the remaining subtypes and no statistically significant difference was seen.

Conclusions

Qualitative grading of FA maps may be useful in predicting the meningioma subtype with microcystic meningiomas showing consistently low FA along with transitional and angiomatous variants. The low FA may be attributed to a myxoid matrix with abundant extracellular space in microcystic meningioma thus reducing directional constraints on diffusion of protons. This is unlike fibroblastic meningioma which is composed of sheet like structure of spindle cells with thick fibres of collagen leading to anisotropic diffusion and high FA grades.

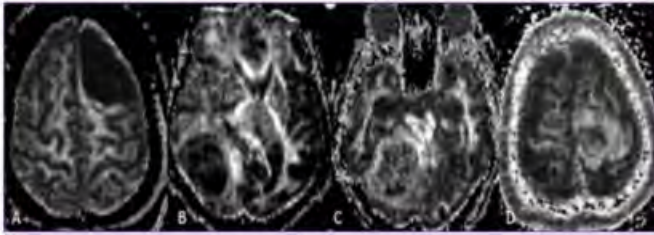


FIG-1 Figure showing the representative images of the four different FA grades of meningioma subtypes. Image (A) shows the lesion in the left frontal convexity to be almost completely dark, representative of FA grade 1. Image (B) shows few bright areas (<50%) within the right parietal convexity tumor, depicting FA grade of 2. Image (C) shows >50% bright areas within the lesion in right cerebellopontine angle corresponding to FA grade of 3. Image (D) shows the lesion in left frontal convexity to be almost bright representing FA grade 4 lesion.

Table 1: Table showing the FA grade of different meningioma subtypes

MENINGIOMA SUBTYPE	GRADE 1	GRADE 2	GRADE 3	GRADE 4
Meningothelial	1	2	6	0
Transitional	1	8	6	0
Chordoid	2	4	8	0
Angiomatous	4	3	1	0
Microcystic	9	6	0	0
Fibroblastic	0	1	11	5
Atypical	0	6	12	2

Table 3: Table showing pair wise comparison of FA grade amongst different subtypes of meningioma

SUBTYPE	Adjusted p value						
	Meningothelial	Transitional	Microcystic	Chordoid	Angiomatous	Fibroblastic	Atypical
Meningothelial	-	1.000	.027	1.000	.504	1.000	1.000
Transitional	1.000	-	.103	1.000	1.000	.042	1.000
Microcystic	.027	.103	-	.026	1.000	.000	.000
Chordoid	1.000	1.000	.026	-	.727	.223	1.000
Angiomatous	.504	1.000	1.000	.727	-	.000	.029
Fibroblastic	1.000	.042	.000	.223	.000	-	1.000
Atypical	1.000	1.000	.000	1.000	.029	1.000	-

Table 2: Table showing the intraclass correlation co-efficient (ICC) between two observers

	Intraclass Correlation *	95% Confidence Interval		F Test with True Value 0			
		Lower bound	Upper bound	Value	df1	df2	Sig
Single Measures	.850*	.796	.903	13.139	97	97	.000
Average measures	.924*	.886	.948	13.139	97	97	.000

(Filename: TCT_1259_fameningioma300.jpg)

M Liu¹, Y Jeong², G Christoforidis³, N Saadat³, M Niekrasz², T Carroll²

¹The University of Chicago, Chicago, IL, ²University of Chicago, Chicago, IL, ³N/A, N/A

Purpose

The purpose of this work is to validate a fully quantitative non-contrast Intra-Voxel Incoherent Motion (IVIM) scan over a range of physiologic conditions related to neurovascular disease.

Materials and Methods

IVIM perfusion values and diffusion volumes were compared directly with neutron-captured microsphere deposition and ADC calculated infarct volume at baseline, under carbogen respiration, and after middle cerebral artery occlusion. Mongrel canines (20-30 kg) were instrumented under x-ray guidance after which Dynamic Susceptibility Contrast (DSC) and IVIM scans were acquired under normal breathing, hypercapnia, and occlusion of the middle cerebral artery (MCAO). Diffusion weighted images (DWI) for IVIM were collected at 10 b-values from 0 to 1000 and 3 directions with 50 slices to cover the entire head (2D single shot EPI, TR/TE= 3056/91 ms, slices/thickness= 2mm, SENSE Factor=2, spatial resolution = 1.25 mm x 1.25 mm x 2.0 mm). Scan time for the IVIM sequence was 5:38. Quantitative DSC CBF images were acquired within 5 minutes of the IVIM scans. Multi-phase, single shot EPI, FOV/matrix = 160/128, 5 2.0 mm thick slices, 50 measurements, with a 3 ml iv Gd with fast T1 maps were acquired before and after the contrast scan. Neutron captured microsphere quantitative CBF was acquired with 4mL of stable-isotope labeled 15 μ m microspheres (STERIspheres, BioPal Inc, Medford, MA) within 15 minutes of the MRI scans. Brains were then analyzed through neutron activation (perfusion) along with standardized level-set threshold diffusion volumes. IVIM images, normalized to b0-value, were fit to $S(b)/S(b=0) = fe^{(D^* \times b)} + (1-f) e^{-(D \times b)}$ to yield 2D parametric images of fD* which was quantified to qCBF [mL/100g/min] at all physiologic states by a quantification factor. Infarct volume for IVIM images were defined as within the parenchyma with a threshold ($D < 5.15e^{-4}$). Regions of interest were compared using standard scatterplots which were pooled over physiologic conditions.

Results

We found that a strong linear correlation existed between IVIM and microsphere qCBF over a wide range of values (0 – 250 ml/100g/min) shown in Figure A, with DSC qCBF comparison in Figure C. There is a similarly strong linear correlation between IVIM D and standard ADC infarct volume shown in Figures B and D.

Conclusions

We found that a single 5:00 minute IVIM perfusion can provide quantitative perfusion [ml/100g/min] and diffusion volumes (cm³) without the need of contrast administration.

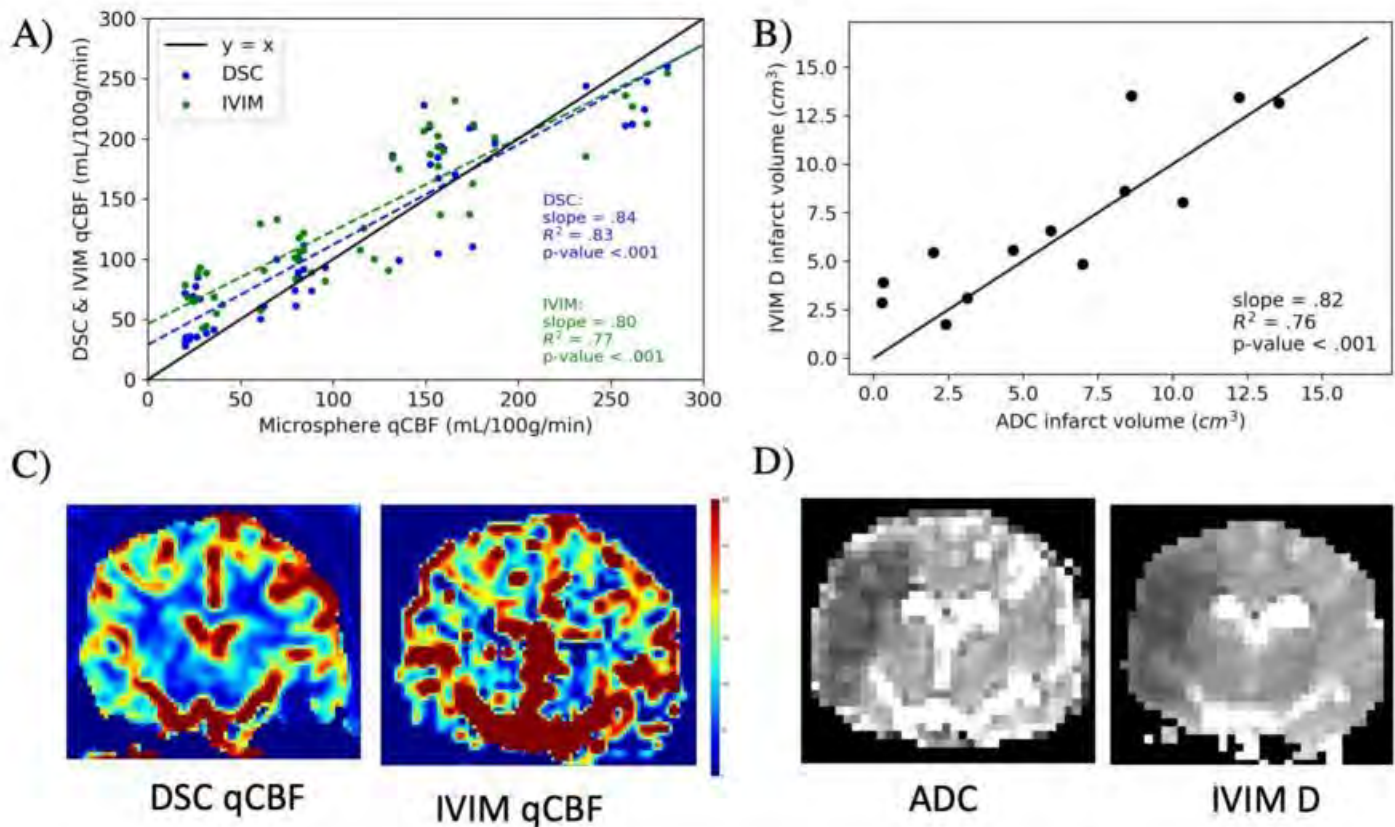


Figure 1 (A,B) hemispheric correlation between both DSC and IVIM perfusion values and reference standard values are strong. Figure 1 (C,D) are representative images of CBF and ADC respectively. Note the artifactual enhancement from cortical branches of the MCA in the DSC images, whereas the IVIM reflects the flow in CSF at the cortical surface.

(Filename: TCT_1358_ASNRFig.jpg)

1319

Quantitative Susceptibility Maps of Iron Deposition predicts rate of Whole Brain Atrophy Rates and Cognition in Transient Ischemic Attack Patients

B McDougall¹, C McDougall¹, C d'Esterre¹, P Barber¹
¹University of Calgary, Calgary, Alberta

Purpose

Patients with Transient Ischemic Attack (TIA) have an increased risk of dementia. Magnetic Resonance Imaging (MRI) modality Quantitative Susceptibility Maps (QSMs) measure iron deposition which has been shown to be associated with neurodegeneration, and therefore might be a useful tool for predicting cognitive decline in TIA patients without dementia.

Materials and Methods

One hundred and one (N=101) TIA patients and sixty-five (N=65) age-, sex- and education-matched healthy controls were recruited from the PREVENT study. Neuropsychological assessments and MRI scans were performed within 10 days of incident event and were repeated at 1 year. Susceptibility values were extracted from subcortical regions on the QSM, and T1-weighted images were used to determine whole brain atrophy rate (mL per annum). Two-way two-sample t-tests and Wilcoxon Rank-Sum tests were used to compare TIA and control groups and linear regression was used to analyze the relationship between the predictor values – QSM iron susceptibility – and the outcome values – cognition and whole brain atrophy.

Results

TIA patients were 66.8 ± 7.8 years old and had 14.4 ± 2.6 years of education whereas control participants were 65.7 ± 7.2 years old and

had 14.5 ± 2.2 years of education. There was no significant difference between the two groups for age ($p=0.318$), sex ($p=0.072$) or education ($p=0.667$). TIA patients had a median MMSE score of 30.0 (28.0-30.0), whereas control participants had a median score of 30.0 (29.0-30.0) ($p=0.011$). TIA patients scored lower on WAIS-IV Digit Symbol Coding ($p<0.001$), and Trail Making Tests A ($p=0.003$) and B ($p=0.014$). BVMT ($p=0.188$) and RAVLT ($p=0.068$) between groups were similar. TIA patients had a susceptibility value of 0.117ppm within the caudate, whereas healthy controls had a value of 0.109ppm ($p=0.022$). Other subcortical regions did not significantly differ between the groups. TIA patients had a mean atrophy rate of -11.99mL/year, whereas control participants had a rate of -4.77mL/year ($p<0.001$). Iron susceptibility values linearly correlated with whole brain atrophy within caudate ($p<0.01$) and putamen ($p<0.001$) regions. There was no correlation between susceptibility and cognition at baseline.

Conclusions

QSM iron susceptibility values within the caudate and putamen are promising biomarkers to utilize when predicting increased whole brain atrophy rates in a TIA patient. The PREVENT study will further explore the relationship with QSM, brain atrophy and cognition over a longer period of follow-up.

615

Quantitative "SyMRI"-based Mapping of the Fetal Brain

V Schmidbauer¹, G Dovjak², M Yildirim³, B Ulm³, D Prayer⁴, G Kasprian⁵

¹Medical University of Vienna, Vienna, Vienna, ²Medical University of Vienna, Vienna, Austria, ³Medical University of Vienna, Vienna, Vienna, ⁴Medical University Vienna, Vienna, Vienna, ⁵MEDICAL UNIVERSITY OF VIENNA, VIENNA, Austria

Purpose

Based on a single multi-dynamic multi-echo (MDME) sequence acquisition, the MRI data post-processing software "SyMRI" generates a variety of MR contrasts characterizing tissue-specific properties. The aim of this study is to assess the feasibility of "SyMRI" in the early prenatal characterization of brain maturation.

Materials and Methods

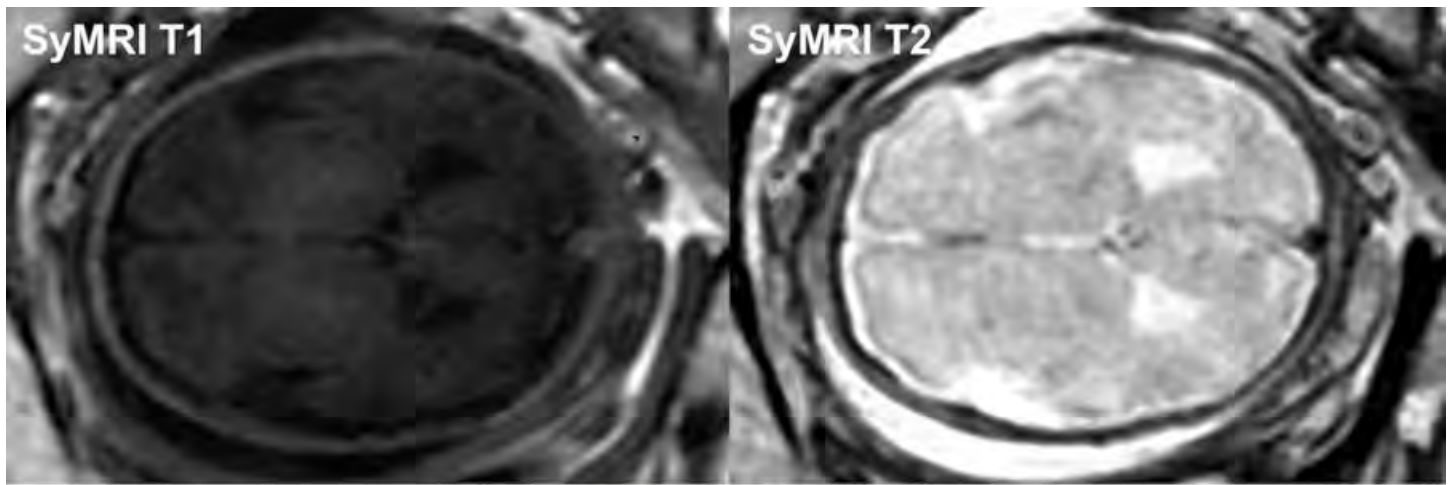
47 fetuses were examined using a standardized fetal MRI protocol (1.5 Tesla). MDME sequence (acquisition time: 3 min. 20 sec.)-based post-processing was performed using "SyMRI" (Synthetic MR AB, Linköping, Sweden; Version 11.1.5). T1-relaxation time (T1R), T2-relaxation time (T2R) (ms), and proton density (PD) (%) of the germinal matrix were determined.

Results

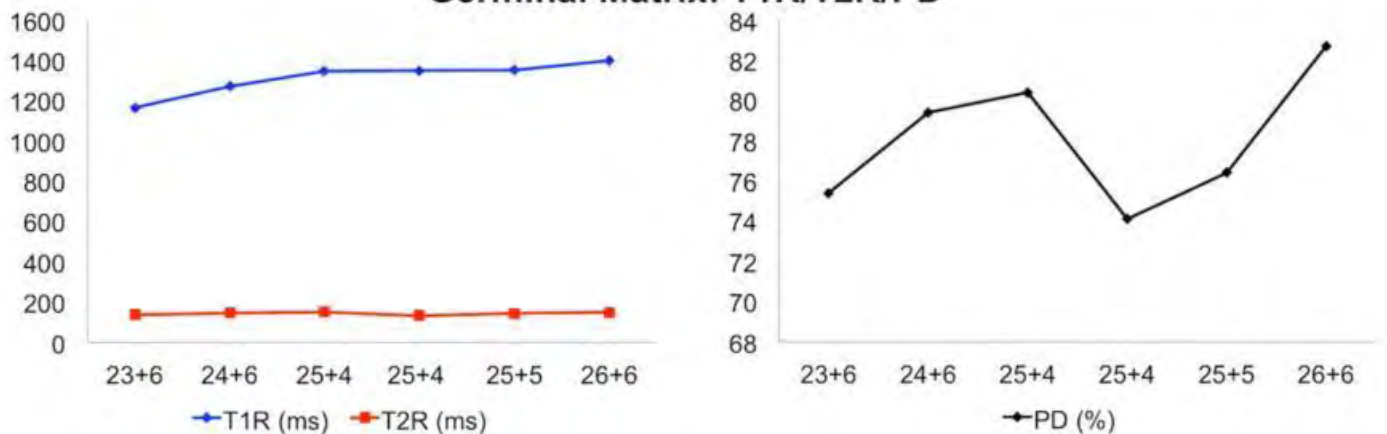
Fetal motion limited the use of "SyMRI" in 39/47 (82.98%) and provided non-motion degraded images of diagnostic quality in 8/47 (17.02%) [gestational age (GA): 23+6; 24+6; 25+4; 25+4; 25+5; 26+6; 32+4; 34+0]. T1R, T2R, and PD of the germinal matrix were determined in six fetuses and revealed maturation-related differences [range GA: 23+6 – 26+6 (T1R: 1195 – 1399; T2: 137 – 150; PD: 75.4 – 82.7)].

Conclusions

Although limited by fetal motion, "SyMRI" for MDME-based MR post-processing is feasible to provide MR contrasts of diagnostic image quality. Moreover, maturational changes of transient brain structures such as the ganglionic eminence can be initially quantified in utero and in vivo. In a small sample of non-motion distorted MDME acquisitions, higher T1-relaxation parameters of the germinal matrix were consistently associated with higher GA.



Germinal Matrix: T1R/T2R/PD



(Filename: TCT_615_Figure.jpg)

1457

Radiation dose distribution and lesion characteristics of glioblastoma at first recurrence

S Shidoh¹, H Ullman¹, R Savjani², C Raymond³, N Salamon⁴, B Ellingson³

¹David Geffen School of Medicine, University of California Los Angeles, Los Angeles, CA, ²UCLA, Santa Clara, CA, ³University of California, Los Angeles, Los Angeles, CA, ⁴University of California Los Angeles, Los Angeles, CA

Purpose

Despite multiple new treatments, glioblastoma (GBM) remains the most aggressive and fatal form of primary brain tumor with a near total relapse rate. Standard care consists of maximum safe surgical resection followed by postoperative radiation therapy and concurrent temozolomide chemotherapy. Previous studies have suggested that most recurrences occur within the original 60Gy dose regions, while dose escalation studies beyond 60Gy have failed to show a significant survival benefit. The purpose of the current study was to confirm the relationship between original radiation dose distribution and location of tumor recurrence, evaluating how radiation dose may influence radiographic characteristics lesions at the time of recurrence.

Materials and Methods

Fiftyone glioblastoma patients underwent postoperative IMRT with concurrent temozolomide between 2011 and 2019. All the patients are evaluated with MRI before and after treatment initiation until the time of radiographic recurrence defined via RANO criteria. All the MRI and radiation dose maps were registered to the pre-treatment time. The original radiation dose and lesion characteristics at the pre-treatment and recurrent time points were evaluated.

Results

All the total tumor volume at recurrence was originally part of the 60Gy field. 49 patients had recurrence and 34 patients progressed before 3months after radiation completed. 42 patients had recurrence within 15mm from the centroid of the pre-radiation tumor. The average distance of the centroid between pre-radiation and recurrent tumor was 12.8mm. The mean solidity of the pre-radiation tumors was significantly lower than the recurrent tumors ($p < 0.05$). The increased solidity between the baseline and recurrent tumor significantly correlated with progression within 3months after finishing radiation therapy ($p < 0.05$). Higher solidity of the recurrent tumors showed a tendency for lower overall survival ($p = 0.09$).

Conclusions

Results confirm that recurrence occurs in areas of therapeutic radiation dose (~60 Gy) in all patients. Recurrent tumors showed significantly higher solidity on MRI. There is a possibility that the solidity shows the treatment-induced changes in recurrent tumor and considering that mostly the pseudoprogression(PsP) occurs within the first 3months after radiation, difference of the solidity from baseline to recurrence could have relationship with PsP. Tumor solidity measured by MRI may be interesting as a prognostic biomarker for survival in GBM, which warrants further investigation.

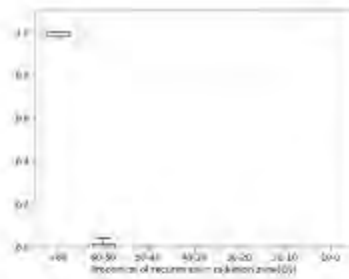


Fig1. Proportion of recurrence separated by dose for the recurrent tumors.

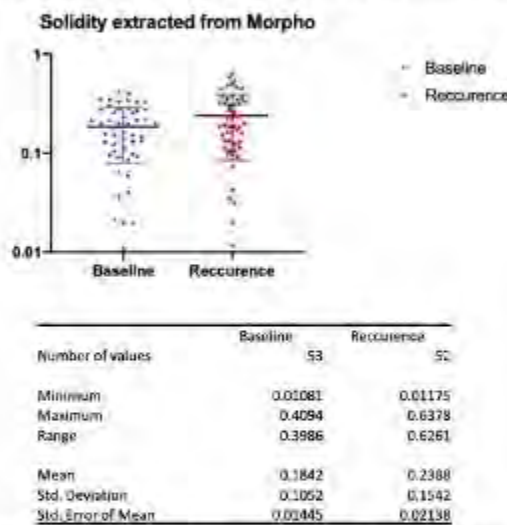


Fig2. Solidity difference of the tumor in pre-radiation and recurrent time point. Recurrent tumor showed significantly higher solidity ($p < 0.05$).

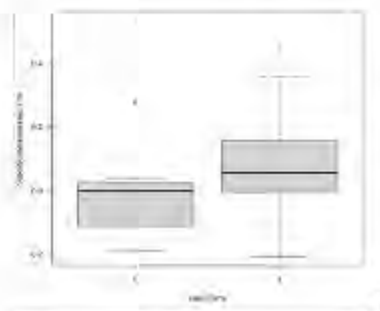


Fig3. Difference in solidity between recurrent tumor and baseline tumor on the x axis. Groups are separated based on early (< 3months) and late (>3months) recurrence ($p < 0.05$).

(Filename: TCT_1457_ASNRfig.jpg)

Radiologic Extrinsic Tongue Muscle Invasion as a Negative Prognostic Marker in Oral Cavity Squamous Cell Carcinoma

L Chien¹, K BAUGNON¹, J Junn², J Beitler¹, Y Zhang³, M Patel¹, A Aiken¹

Purpose

Extrinsic tongue muscle invasion (ETMI) was removed as a T4a feature in oral cavity squamous cell carcinoma (OCC) in the most recent American Joint Committee on Cancer 8th edition (AJCC 8) staging criterion. Junn et al showed that confirming pathologic ETMI was difficult and there is sparse data on its prognostic significance. Depth of invasion (DOI) has replaced ETMI as a measure for endophytic growth in AJCC 8. The impact of this change on treatment is unknown. Previously, Junn et al showed mass-like enhancement indistinguishable from extrinsic tongue muscle on CT to be the most specific and predictive of surgical and pathologic ETMI. We aim to determine whether radiologic ETMI, defined as mass-like enhancement, in and of itself has prognostic significance as measured by treatment failure.

Materials and Methods

In this IRB-approved retrospective study, 66 patients with a new diagnosis of OCC of tongue and floor of mouth were included. Patients were primarily from previously published cohort from Junn et al, and were followed for at least 12 months to evaluate for longitudinal treatment failure. Two head and neck radiologists jointly reviewed images for presence of mass-like enhancement of genioglossus and hyoglossus. The largest tumor dimension and presence of pathologic cervical nodes on CT were documented. Tumor sizes were grouped into ≤ 2 cm, >2 cm and ≤ 4 cm, and >4 cm according to T categories in AJCC 8. DOI was approximated by measuring perpendicularly from the mucosal surface to the deepest edge of tumor on axial images. The outcome measured was presence of locoregional recurrence and distant metastases.

Results

There were a total of 7 tumors <2 cm, 44 tumors 2-4cm, and 15 tumors >4 cm in size. On multivariate analysis of the 44 tumors 2-4cm in size, while controlling for radiologic nodal involvement, mass-like enhancement was significantly associated with outcome. Patients with mass-like enhancement were 8.77 times more likely to have locoregional recurrence and/or metastases, than those without ($p=0.005$). Within the group of 2-4cm tumors with mass-like enhancement, there were 4 T2 tumors with DOI ≤ 10 mm based on AJCC 8. These tumors would have been upstaged to T4a in prior AJCC 7. 3 of these 4 patients developed locoregional failure and/or metastases.

Conclusions

Radiologic ETMI is a negative prognostic factor in OCC, independent of radiologic nodal stage and pathologic confirmation. As a marker for high-risk disease, radiologic ETMI alone could be considered for treatment planning.

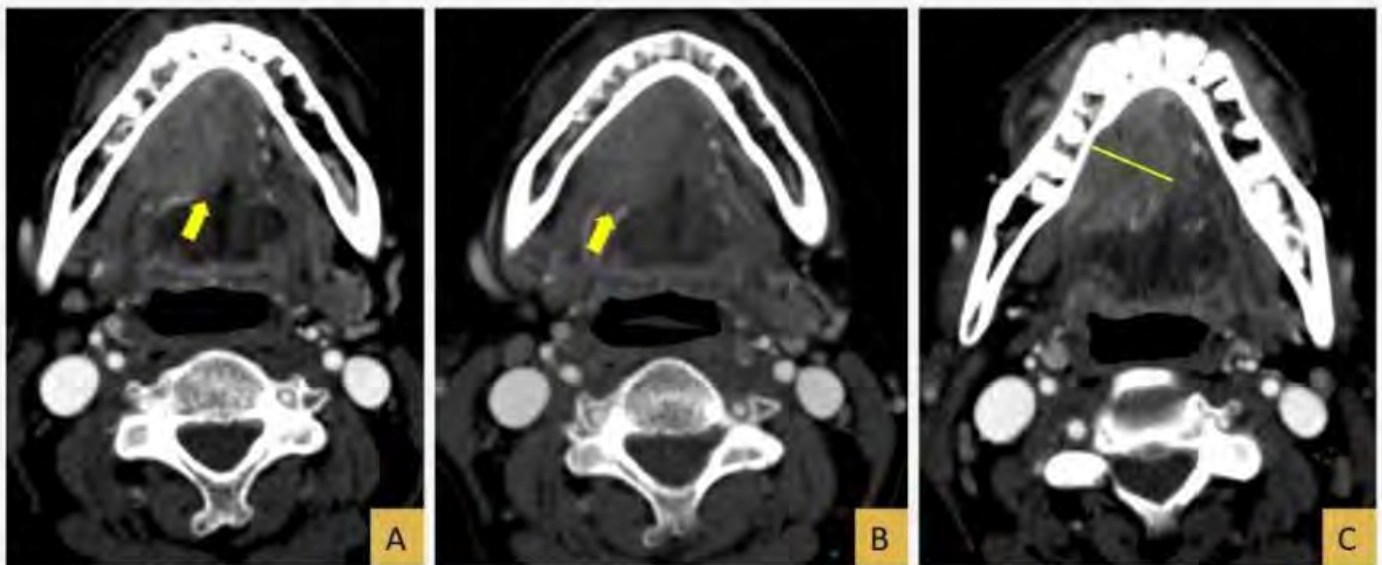


Figure 1. CT neck with contrast: Squamous cell carcinoma of the right floor of mouth. A) Arrow points to mass-like enhancement involving the right genioglossus muscle. B) Arrow points to mass-like enhancement involving the right hyoglossus muscle. C) Depth of invasion is approximated by measuring perpendicularly from the mucosal surface to the deepest edge of tumor on axial images.

(Filename: TCT_884_Figure1withcaption.JPG)

G Bathla¹, S Priya², Y Liu³, C Ward⁴, H Zhang⁵, N Le⁵, N Soni⁶, R Maheshwarappa¹, V Monga², M Sonka⁷

¹University of Iowa Hospitals and Clinics, Iowa City, IA, ²University of Iowa hospitals and Clinics, IOWA CITY, IA, ³University of Iowa, Iowa City, IA, ⁴Univ of Iowa, Iowa City, IA, ⁵The Iowa Initiative for Artificial Intelligence, Iowa City, IA, ⁶UIHC, Iowa, IA, ⁷The University of Iowa, Iowa City, IA

Purpose

Several radiomic-based studies in neuro-oncology have previously shown excellent diagnostic performance in differentiating tumor types but have predominantly focused on a two-class problem which limits generalizability. The performance of radiomic-based models in differentiating three most common malignant brain tumors (glioblastoma (GBM), primary central nervous system lymphoma (PCNSL) and metastatic disease), factors affecting model performance and usefulness of single sequence versus multiparametric MRI (MP-MRI) remain largely unaddressed.

Materials and Methods

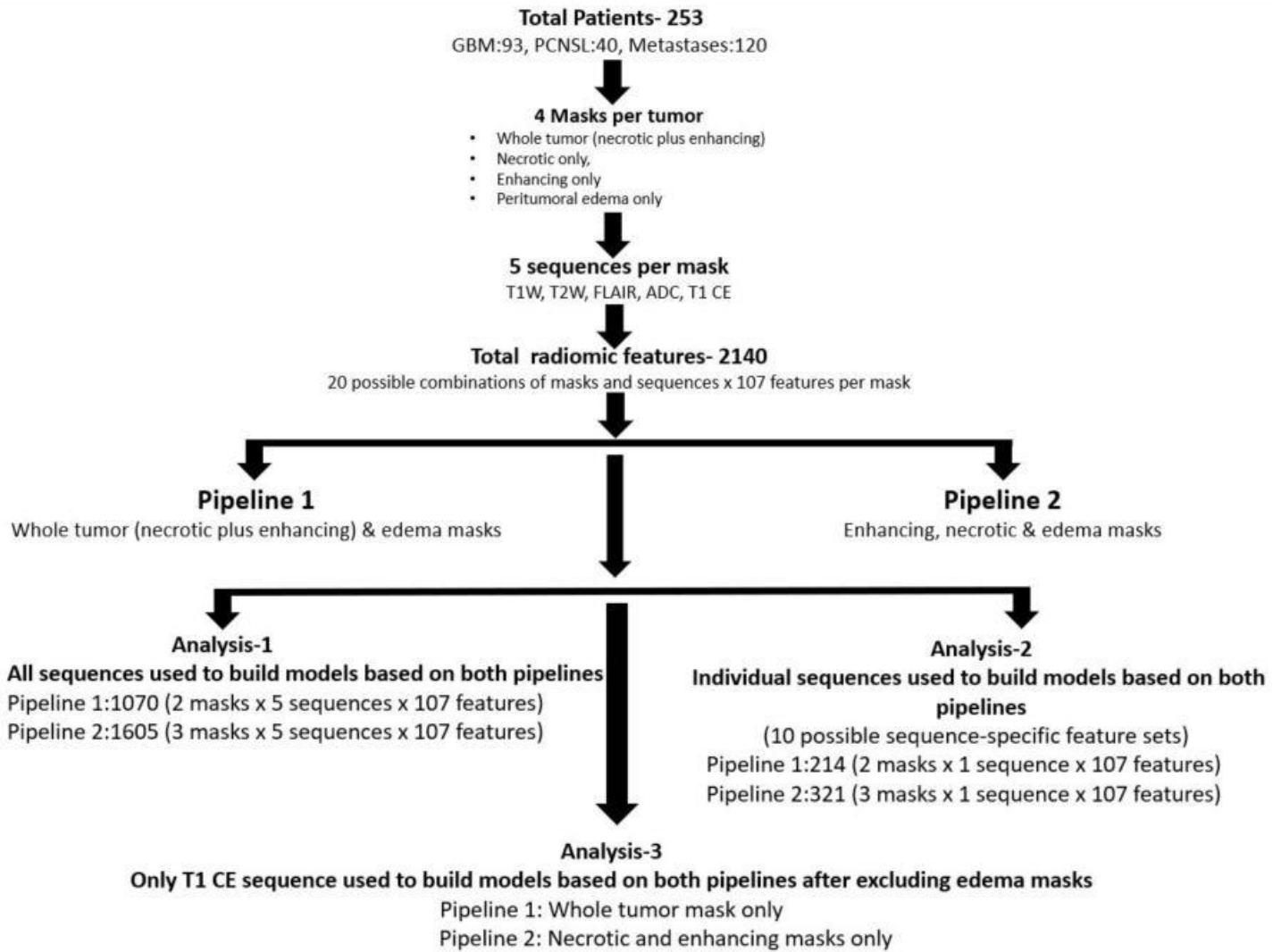
Our retrospective study included 253 patients (120 metastatic, 40 PCNSL and 93 GBM). Radiomic features were extracted for whole tumor mask (enhancing plus necrotic component) and edema mask (first pipeline), and for separate enhancing, necrotic and edema masks (second pipeline). Model performance was evaluated for models using MP-MRI, individual sequences and also T1-CE sequence without edema mask] across 45 possible model and feature selection combinations.

Results

Second pipeline showed significantly high performance across all sequence combinations (Brier score 0.298- 0.302). Elastic net model with full feature set selection technique was the best overall model for both multiparametric imaging and individual T1 CE sequence. Majority of top performing models were built using full feature set and in-built feature selection. No significant difference was seen between top performing models from multiparametric MRI (AUC 0.910) and T1 CE sequence with (AUC 0.914) and without edema mask (AUC 0.906). Most important features were derived from the enhancing and necrotic masks for second pipeline.

Conclusions

Radiomics based differentiation between three malignant brain tumors with high diagnostic performance is feasible. T1 CE is the single best sequence with comparable performance to multiparametric imaging. The model performance varies considerably based on tumor subregion, and combination of model and feature selection methods.



(Filename: TCT_368_Fig1.JPG)

366

Radiomics Based Differentiation Between Glioblastoma and Primary Central Nervous System Lymphoma: A Comparison of Diagnostic Performance Across Different Sequences and Machine Learning Techniques

G Bathla¹, S Priya², Y Liu³, C Ward⁴, N Le⁵, N Soni⁶, R Maheshwarappa¹, V Monga², H Zhang⁵, M Sonka⁵

¹University of Iowa Hospitals and Clinics, Iowa City, IA, ²University of Iowa hospitals and Clinics, IOWA CITY, IA, ³University of Iowa, Iowa City, IA, ⁴Univ of Iowa, Iowa City, IA, ⁵The Iowa Initiative for Artificial Intelligence, Iowa City, IA, ⁶N/A, N/A

Purpose

Multiple studies have reported robust diagnostic performance for differentiating between glioblastoma (GBM) and primary central nervous lymphoma (PCNSL) using MRI based radiomic features. However, the best sequence or a combination of sequences and model performance across various machine learning pipelines remain undefined. In this study, we compared diagnostic performance of a radiomic based model to differentiate GBM from PCNSL across various sequences and machine learning techniques.

Materials and Methods

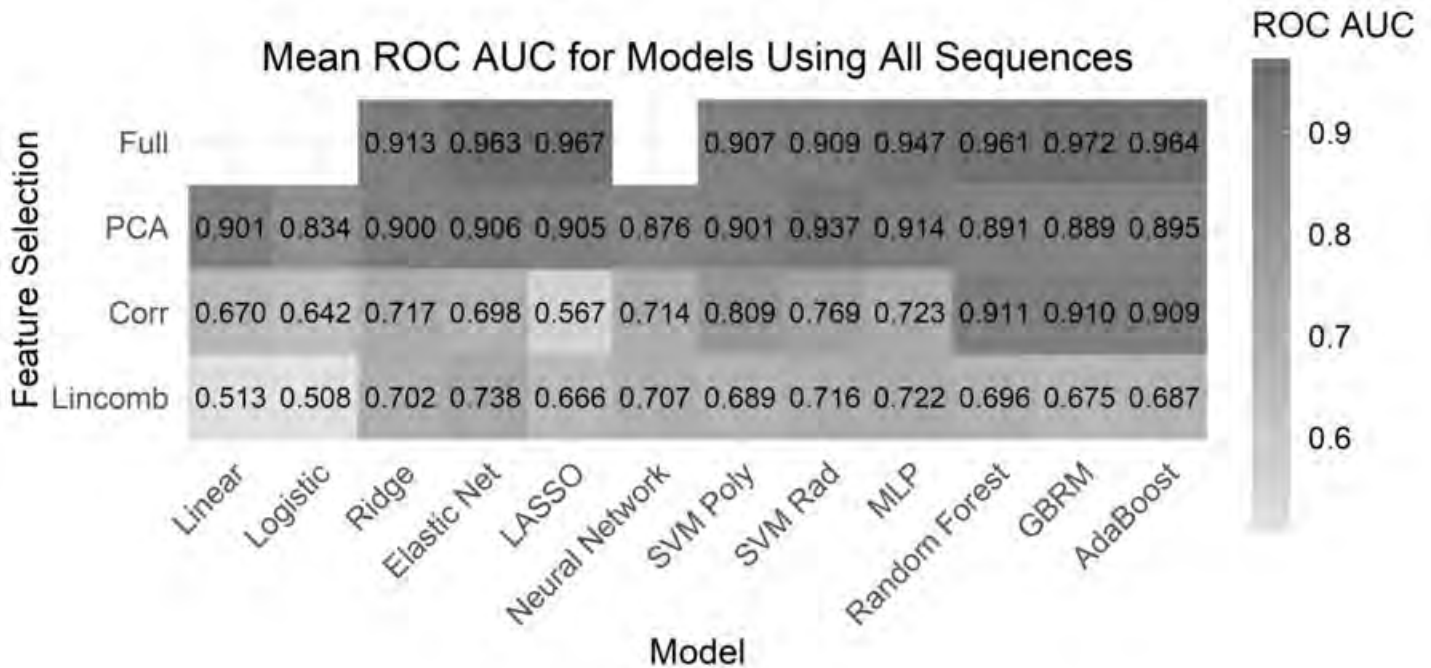
Our retrospective study included 94 patients (34 with PCNSL and 60 with GBM). Model performance was assessed using various MRI sequences across 45 possible model and feature selection combinations.

Results

When using all features, the cross-validated model performance, both using individual and a combination of sequences was fairly robust across multiple top performing models (AUC: 0.961-0.977) but did show considerable variation between the best and worst performing models. The top performing individual sequences had comparable performance to multiparametric models. The best prediction model in our study used a combination ADC, FLAIR and T1-CE achieving the highest AUC of 0.977, while the second ranked model used T1-CE and ADC, achieving a cross-validated AUC of 0.975.

Conclusions

Even though GBM and PCNSL can be robustly differentiated using a radiomic based approach, the diagnostic performance can be impacted considerably, based on the model and feature selection methods as well as the combination of sequences used. Also, models derived from limited sequences show performance comparable to those derived from all five sequences.



(Filename: TCT_366_Fig-1.jpg)

907

Radiomics Based Prognostication of Overall Survival in Glioblastoma: Chasing a Mirage?

G Bathla¹, S Priya², J Rytlewski³, Y Liu³, C Ward⁴, N Le⁵, H Zhang⁵, V Monga², M Sonka⁶

¹University of Iowa Hospitals and Clinics, Iowa City, IA, ²University of Iowa hospitals and Clinics, IOWA CITY, IA, ³University of Iowa, Iowa City, IA, ⁴Univ of Iowa, Iowa City, IA, ⁵The Iowa Initiative for Artificial Intelligence, Iowa City, IA, ⁶The University of Iowa, Iowa City, IA

Purpose

Despite multiple studies showing robust performance of radiomics based machine learning models (RBMLM) in diagnostic performance neuro-oncological problems, radiomics based prediction of overall survival in glioblastoma (GBM) remains a challenge. We explored the potential utility of RBMLM in prediction of overall survival in GBM.

Materials and Methods

Single center retrospective IRB approved study, including 93 patients with available multiparametric pre-operative MRI study. Post image pre-processing, combined enhancing and necrotic as well as non-enhancing FLAIR components were segmented using an in-house 3D-segmentation tool. Radiomic features were extracted using Pyradiomics. Clinical features were also measured for each subject, including gender, age, KPS at diagnosis, ECOG at diagnosis, tumor therapy, and treatment indicators for radiation and chemotherapy. Separate prediction models were built using clinical and radiomics features alone and then in combination. A total of 16 model and feature selection combinations were tested for RBMLM. Root mean square error (RMSE) was used to measure predictive performance.

Results

The median survival time was 14.5 months (0.25-94.5 months). Ridge regression model based on clinical features alone had the overall highest diagnostic performance (RMSE = 16.92). For RBMLM, Random Forest was the best model built using ADC sequence (RMSE = 17.94). SVM with radial kernel fit was the best model for combined clinical and radiomics features (RMSE = 17.53). The performance of models with clinical features only was statistically superior to the models with radiomics features only (p = 0.0354).

No significant difference was seen between models with combined radiomics and clinical features compared to model with clinical features alone ($p=0.1440$).

Conclusions

Survival prediction models built using clinical features alone perform significantly better than RBMLM. No additional advantage of combining radiomics with clinical features in GBM prognostication.

386

Radiomics of pediatric low grade gliomas: toward a pre-therapeutic differentiation of BRAF-mutated and BRAF-fused tumors

M WAGNER¹, N Hainc¹, F Khalvati¹, K Namdar¹, L Figueiredo¹, M Sheng¹, S Laughlin¹, M Shroff², E Bouffet¹, U Tabori¹, K Yeom², B Ertl-Wagner³

¹The Hospital for Sick Children, Toronto, Ontario, ²N/A, N/A, ³The Hospital for Sick Children, University of Toronto, Toronto, Ontario

Purpose

BRAF status has important implications for prognosis and therapy of pediatric low grade gliomas. Currently, BRAF status classification relies on biopsy. Our aim was to train and validate a radiomics approach to predict BRAF fusion and BRAF V600E mutation.

Materials and Methods

In this bi-institutional retrospective study, FLAIR MRI datasets of 115 pediatric patients with low grade glioma (pLGG) from 2 children's hospitals acquired between January 2009 and January 2016 were included and analyzed. Radiomics features were extracted from tumor segmentations and the predictive model was tested using independent training and testing datasets, with all available tumor types. The model was selected based on a grid search on number of trees opting for the best split for a random forest. We used the area under the receiver operating characteristic curve to evaluate model performance.

Results

The training cohort consisted of 94 pLGGs (mean age: 9.4 years, 45 male) and the external validation cohort comprised 21 pLGGs (mean age: 8.37 years, 12 male). A 4-fold cross-validation scheme predicted BRAF status with AUC of 0.75 ± 0.12 , 95% confidence interval: [0.62 – 0.89] on the internal validation cohort. Using the optimal hyperparameters determined by 4-fold cross validation, the AUC for the external validation was 0.85. Age and tumor location were significant predictors for BRAF status (p -values: 0.04 and <0.001 , respectively). Sex was not a significant predictor (p -value = 0.96).

Conclusions

Radiomics-based prediction of BRAF status in pediatric low grade gliomas appears feasible in this bi-institutional exploratory study.

1145

Random Neural Network Features in Patients with Multiple Sclerosis

M Hamwi¹, G Melkus¹, S Thebault¹, L Walker¹, S Chakraborty¹, C Torres¹, M Freedman¹, R Aviv¹

¹Ottawa Hospital Research Institute, Ottawa, Ontario

Purpose

We used graph theory to examine longitudinal correlation between cortical health & function and cortical covariance network parameters in multiple sclerosis patients receiving autologous stem cell transplant, building on previous work in this field¹.

Materials and Methods

We use voxel-based structural similarity determined from T1-weighted MRI scans of 23 patients followed over 3 years to compute cortical covariance network parameters using graph theory. We examined the strength and significance of associations between network measures of cortical integration (i.e. path length, lambda) or segregation (i.e. clustering) and biochemical/clinical measures of cortical health (i.e. NAA/Cr ratio, neurofilament (nfl), brain atrophy) or function (i.e. 2-second PASAT) using Spearman correlation coefficients. $P < 0.05$ was considered significant.

Results

Path length increase was associated with markers of greater inflammation ($\rho = 0.56$, $P < .046$) at baseline and reduced Naa/Cr ratio ($P < .041$) at 12 months. Reduced lambda was associated with markers of greater grey matter atrophy ($\rho = 0.55$, $P < .019$) after 12 months and lower cognition ($\rho = 0.56$, $P < .008$) at 12 months. Reduced clustering was associated with higher nfl ($\rho = -0.68$, $P < .010$) at baseline, greater white matter atrophy ($\rho = 0.62$, $P < .006$) after 12 months, lower PASAT performance ($\rho = 0.56$, $P < .011$) at baseline, and reduced Naa/Cr ratio ($P < .001$) at 12 months.

Conclusions

Reduced cortical integration and segregation (i.e. random network features) co-occur with unfavourable markers of cortical health and function in patients with multiple sclerosis receiving autologous stem cell transplant. Network features show promise as important longitudinal markers of both patient status and progression.

Reducing Bias in Medical School Admissions Using Artificial Intelligence

G Keir¹, W Hu², C Filippi³, L Ellenbogen⁴, C Fazio⁴, L Miller⁴, R Woldenberg⁵

¹Northwell, Mineola, NY, ²Lenox Hill Hospital, New York, NY, ³Tufts University Medical Center, Boston, MA, ⁴Zucker School of Medicine at Hofstra Northwell, Hempstead, NY, ⁵Northwell Health, Manhasset, NY

Purpose

Determining which applicants will have the privilege of becoming future physicians is a critical mission for medical schools. Despite measures to standardize the evaluation process, inter-observer variability in which conscious or unconscious bias may factor are a concern for under-represented groups. Artificial intelligence may present a unique opportunity to systematically apply a fairer standard to all applicants and yet maintain sensitivity to nuances that may have otherwise be missed by current hard cutoffs and screening metrics.

Materials and Methods

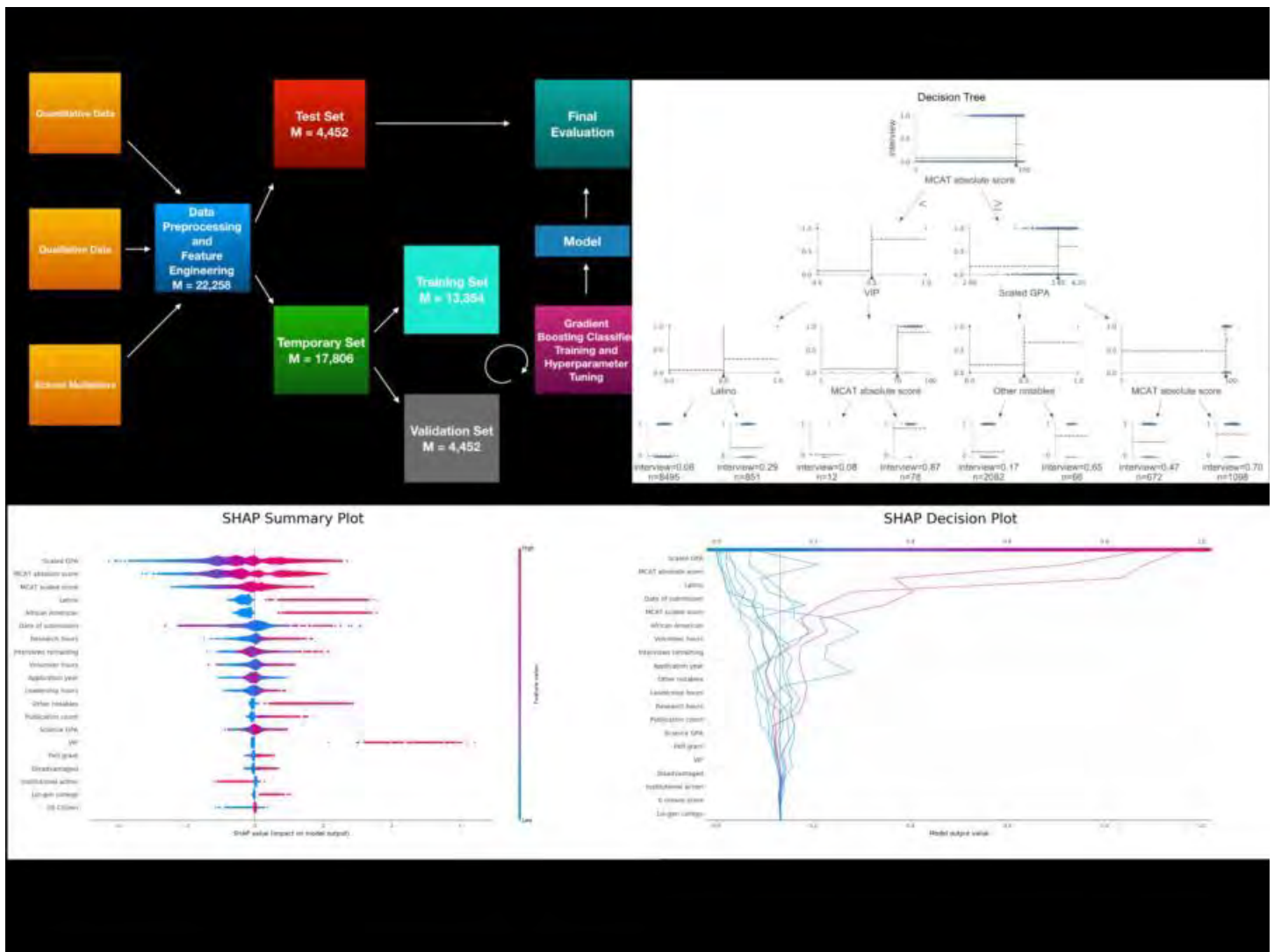
Data from 5 years of medical school applications was retrospectively accrued and analyzed. The applicants (m = 22,258 applicants) were split 60%-20%-20% into a training set (m = 13,354), validation set (m = 4,452), and test set (m = 4,452). An AI model was trained on the training set, parameters were tuned according to the validation set, and performance was evaluated on the independent holdout test set. Ground truth was whether a given applicant was invited for an interview. The code was written in Python 3.7 and predictive modeling was performed using XGBoost, an ensemble tree-based learner with gradient boosting. Hyperparameter tuning was optimized on the validation set using binary cross-entropy and F1 scores. After the model was trained and optimized, SHAP values were obtained to determine the impact of individual features on the model's final prediction.

Results

The algorithm had an accuracy of 95% on the training set, 88% on the validation set, and 88% on the test set. The precision score and recall respectively were 0.80 and 0.92 on the training set, 0.63 and 0.76 on the validation set, and 0.63 and 0.74 on the test set. The F1 Score was 0.86 on the training set, 0.69 on the validation set, and 0.68 on the test set. The Area Under the Curve of the test set was 0.93. The SHAP values demonstrated that the model utilizes features in a concordant manner with current admissions rubrics.

Conclusions

These results show the feasibility of an AI approach applied to medical school admissions screening decisions. By providing the algorithm with only predefined information necessary for decision making, this may minimize the opportunity for the algorithm to learn biases, while reducing variability in the process. The SHAP values provide explainability for the model, allowing us to ensure that the model is making decisions as intended. Future directions include improving and validating the model and applying it to radiology residency programs.



(Filename: TCT_270_Figures.jpg)

575

Reductions in Global and Regional Cerebellar Volumes in Individuals with 22q11.2 Deletion Syndrome Using MAGeT Segmentation

J DeBevis¹, J Schmitt², S Zakharenko³, D Roalf¹, D McDonald-McGinn¹, R Gur¹

¹University of Pennsylvania, Philadelphia, PA, ²Hospital of the University of Pennsylvania, Philadelphia, PA, ³St. Jude's Medical Center, Memphis, TN

Purpose

1. 22q11DS is a chromosomal condition with an increased risk of several psychotic disorders, and is a predictive risk factor for the development of psychosis. 2. Compared with typically-developing controls and non-deleted subjects with psychotic symptoms, 22q11DS subjects have significantly lower cerebellar volumes. 3. Our findings suggest structural changes of the cerebellum may play a role in the behavioral manifestations of these subjects.

Materials and Methods

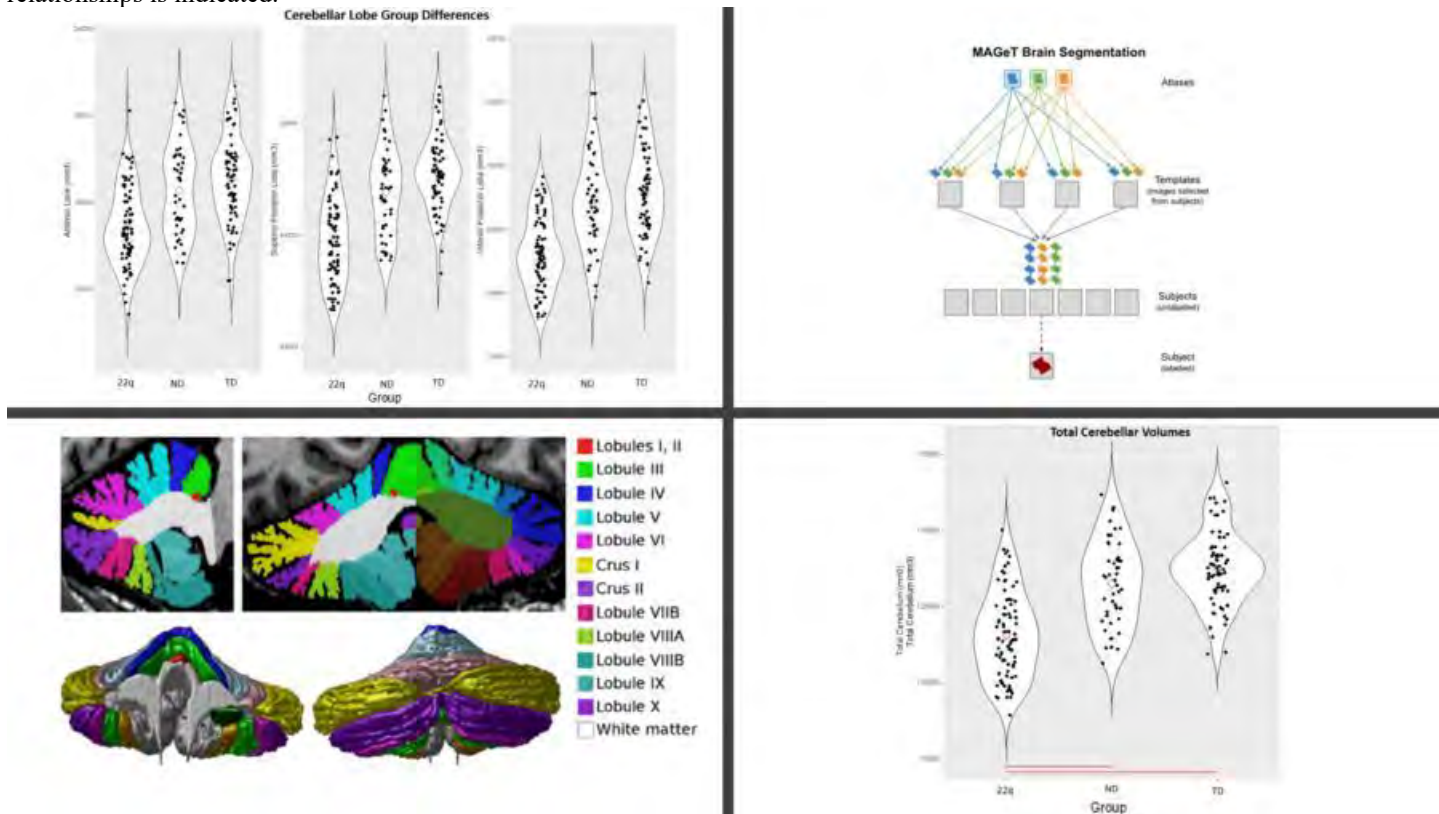
The 22q11.2 deletion syndrome (22q11DS) is an uncommon condition with an increased risk of several psychiatric disorders. A 22q11DS deletion represents one of the most predictive risk factors for the development of psychosis. The cerebellum is an understudied brain region that has emerged as a potential biomarker for several psychiatric diseases, including schizophrenia. Our goal was to further characterize cerebellar anatomy in 22q11DS.

Results

83 subjects with 22q11DS, 47 non-deleted subjects with psychotic symptoms (ND), and 71 typically-developing (TD) controls were scanned at 3T via high-resolution T1 MP-RAGE. Utilizing the Multiple Automatically Generated Template (MAGeT) segmentation algorithm, total, lobar, and lobular cerebellar volumes were calculated. Group differences were assessed via ANOVA.

Conclusions

Individuals with 22q11DS had significantly lower cerebellar volumes compared to both TD and ND groups [$F(2,190) = 57.65$; $p < 0.0001$], with 16% decrease relative to TD and 13% relative to ND. Similarly, cerebellar lobes ($p < 0.0001$) and lobules ($p < 0.0001$) were substantially lower in 22q11DS. Regional cerebellar volumes were highly correlated, and regional group differences were attenuated after covarying for total cerebellar volume. In summary, cerebellar volumes are substantially reduced in 22q11DS relative to non-deleted individuals, potentially contributing to its neuropsychiatric profile. Further investigation of potential brain-behavioral relationships is indicated.



(Filename: TCT_575_ASNRfig.jpg)

224

Regional Diffusion Changes Associated with Biomechanical Strain Measures in Non-concussed Youth Football Players

J Holcomb¹, R Fiscaro¹, L Miller², E Davenport¹, B Wagner³, C Whitlow⁴, J Maldjian³

¹UT SOUTHWESTERN MEDICAL CENTER, Dallas, TX, ²Wake Forest School of Medicine, Winston-Salem, NC, ³University of Texas Southwestern Medical Center, Dallas, TX, ⁴N/A, N/A

Purpose

The purpose of this study is to identify white matter regions which demonstrate fractional anisotropy (FA) changes associated with the cumulative maximal principal strain 1 and strain rate (CMPS1xSR) experienced by non-concussed youth football players.

Materials and Methods

Preseason and postseason diffusion tensor imaging (DTI), including FA estimations, were acquired on 102 youth football player seasons and 16 non-collision control athletes. FA images were normalized to the IXI template using the Statistical Parametric Mapping 8 toolbox (SPM8). Percent change FA (% Δ FA) images were generated in MATLAB. Using data from the head impact telemetry system, CMPS1xSR, a measure of the cumulative tensile brain strain and strain rate for one season, was generated for each subject. Linear regression analyses were performed in SPM8 to identify significant relationships between CMPS1xSR and % Δ FA within the international consortium brain mapping white matter mask. Age, BMI, days between pre and postseason imaging, prior brain injury, attention disorder diagnosis, and imaging protocol were included as covariates. FDR correction was used with alphas of 0.025 and voxel thresholds of zero. The mean % Δ FA from each subject and control was extracted from the significant SPM voxels (% Δ FASPM). Football subject seasons were stratified into high and low strain groups. Pairwise Wilcoxon rank sum tests with Benjamini-Hochberg correction were used to compare % Δ FASPM between the high-strain football (n=16), low-strain football (n=16), and control athlete (n=16) groups. Group analysis was performed in R 3.6.0 with alphas of 0.05.

Results

Controlling for all covariates, a significant, positive linear relationship between % Δ FA and CMPS1xSR was identified in the white matter of the cingulum, fornix, internal capsules, corpus callosum, corona radiata, corticospinal tract, cerebral and cerebellar

peduncles, superior longitudinal fasciculus, and inferior fronto-occipital fasciculus. No inverse relationship between CMPS1xSR and % Δ FA was identified. The high strain football group demonstrated significantly greater increases in % Δ FASPM when compared to both controls and low strain groups (p-values of 2.4×10^{-4} and 2.1×10^{-4} , respectively). No significant difference in % Δ FASPM between the low strain and control groups was observed (p-value = 0.70).

Conclusions

In the absence of clinically diagnosed concussion, youth football players experience regional white matter increases in FA that are significantly associated with CMPS1xSR.

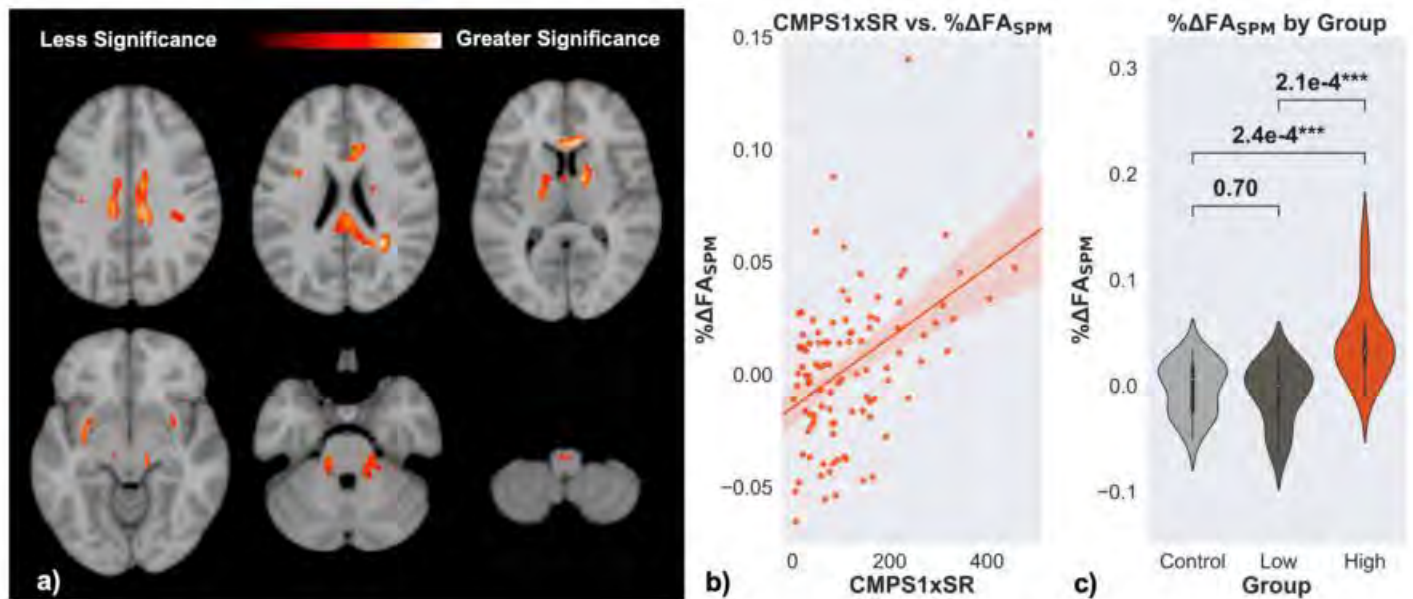


Figure 1a. Colored white matter regions indicate locations with significant positive linear relationships between % Δ FA and CMPS1xSR. **Figure 1b.** Linear relationship between CMPS1xSR and % Δ FA_{SPM}. **Figure 1c.** Distribution of % Δ FA_{SPM} by high strain, low strain, and control athlete groups.

(Filename: TCT_224_ASNR_2021_final3.jpg)

1357

Regional Gender Discrepancies in Academic Neuroradiology with Respect to Academic Rank and Years of Practice

A Vashi¹, A Goswami², A Khaja², B Majdalany³

¹Carle Illinois College of Medicine, Champaign, IL, ²Emory University School of Medicine, Atlanta, GA, ³Emory University Department of Radiology, Atlanta, GA

Purpose

To determine whether gender differences exist in United States academic neuroradiology departments with respect to years of experience, academic rank, and geographic location.

Materials and Methods

All fellowship trained neuroradiologists on faculty as of January 2019 at 98 academic centers were cataloged using official institution websites, including all neuroradiology fellowship programs. Gender, academic rank (Instructor, Assistant Professor, Associate Professor, and Professor), and years of practice data were obtained from a combination of institutional websites and Doximity, an online physician database. Institutions were organized into geographic groups based on region as defined by the United States Census Bureau (NE, MW, S, W). Years of practice were categorized into 3 groups (0-15, 16-30, 31+). Analysis of gender representation among all groups was performed using Chi square.

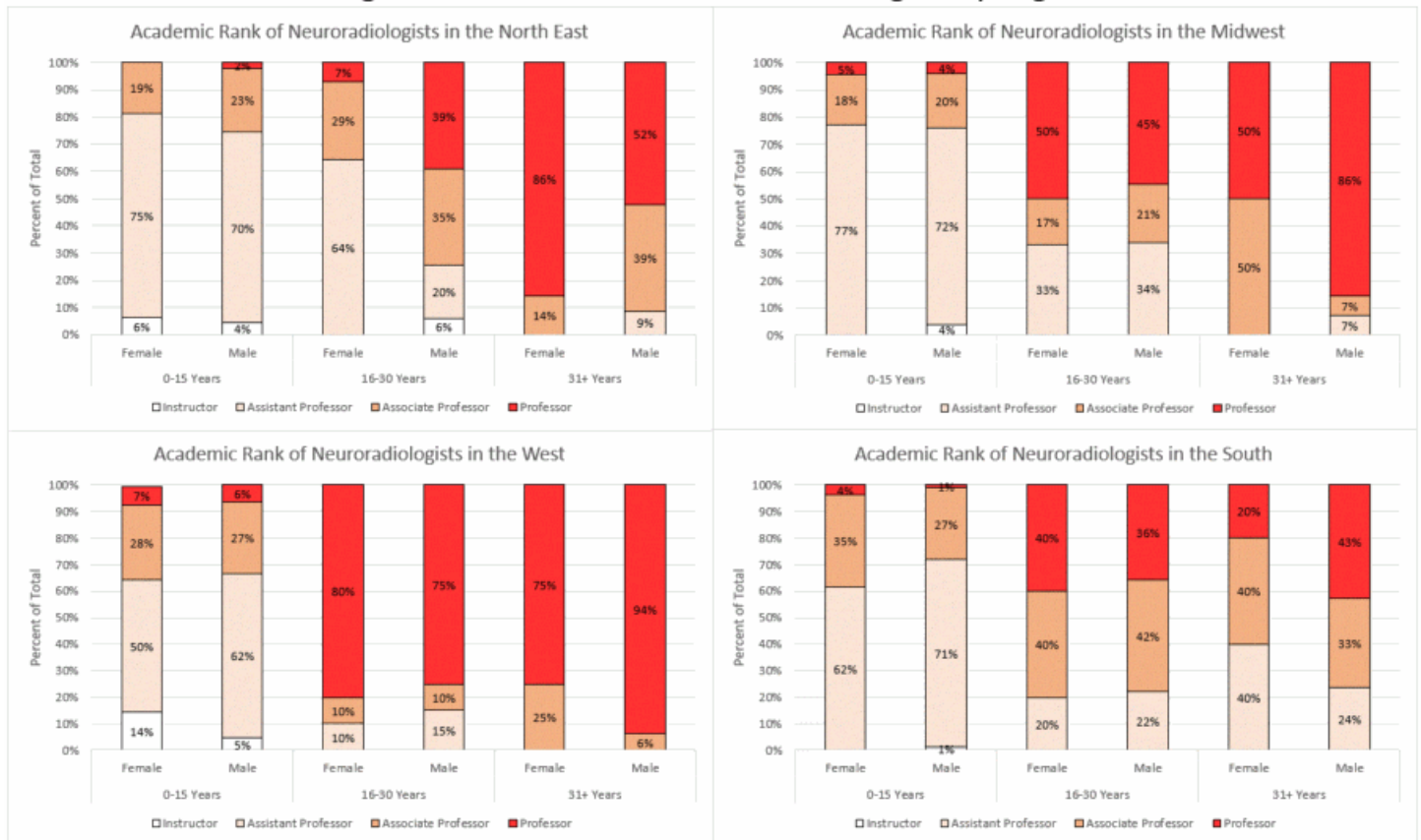
Results

A total of 948 academic neuroradiologists (77.2% M, 22.8% F) were identified. Verifiable academic rank was obtained for 824 neuroradiologists (76.9% M, 23.1% F). Nationally, there were no significant gender representation differences between geographic regions (P = 0.74), among increasing academic rank (P = 0.83), or across progressive years of practice (P = 0.58). Subgroup analysis of geographic regions found no significant gender differences in the MW, S, and W. However, when stratifying the NE by years of practice, female professors with 16-30 years of practice were significantly underrepresented when compared to their male counterparts in the NE (P = 0.004) and to their female counterparts nationwide (P = 0.006). Among NE academic neuroradiologists with 16-30 years of practice, 39% of men were full professors while only 7% of women were full professors. Nationally, 34% of women with 16-30 years of practice were full professors. Complete data is shown in Figure 1.

Conclusions

Women appear to progress up academic ranks slower than men in the NE. While overall rates of professorship are similar between genders, stratifying by years of practice revealed that women achieved professorship later in their careers when compared to men, especially in the NE. More work is needed to determine causes for this discrepancy.

Figure 1: Academic Rank of Neuroradiologists by Region



(Filename: TCT_1357_Capture2.GIF)

1514

Reinforcement learning using Deep Q Networks and Q learning accurately localizes brain tumors on MRI with very small training sets.

J Stember¹, H Shalu²

¹Memorial Sloan Kettering Cancer Center, New York, NY, ²Indian Institute of Technology Madras, Madras, Madras

Purpose

Supervised deep learning in radiology suffers from notorious inherent limitations: 1) It requires large, hand-annotated data sets, 2) It is non-generalizable, and 3) It lacks explainability and intuition. We have recently proposed Reinforcement Learning to address all three shortcomings. However, we applied it to images with radiologist eye tracking points, which limits the state-action space. Here we generalize the Deep-Q Learning approach to a gridworld-based environment, so that only the images and image masks are required.

Materials and Methods

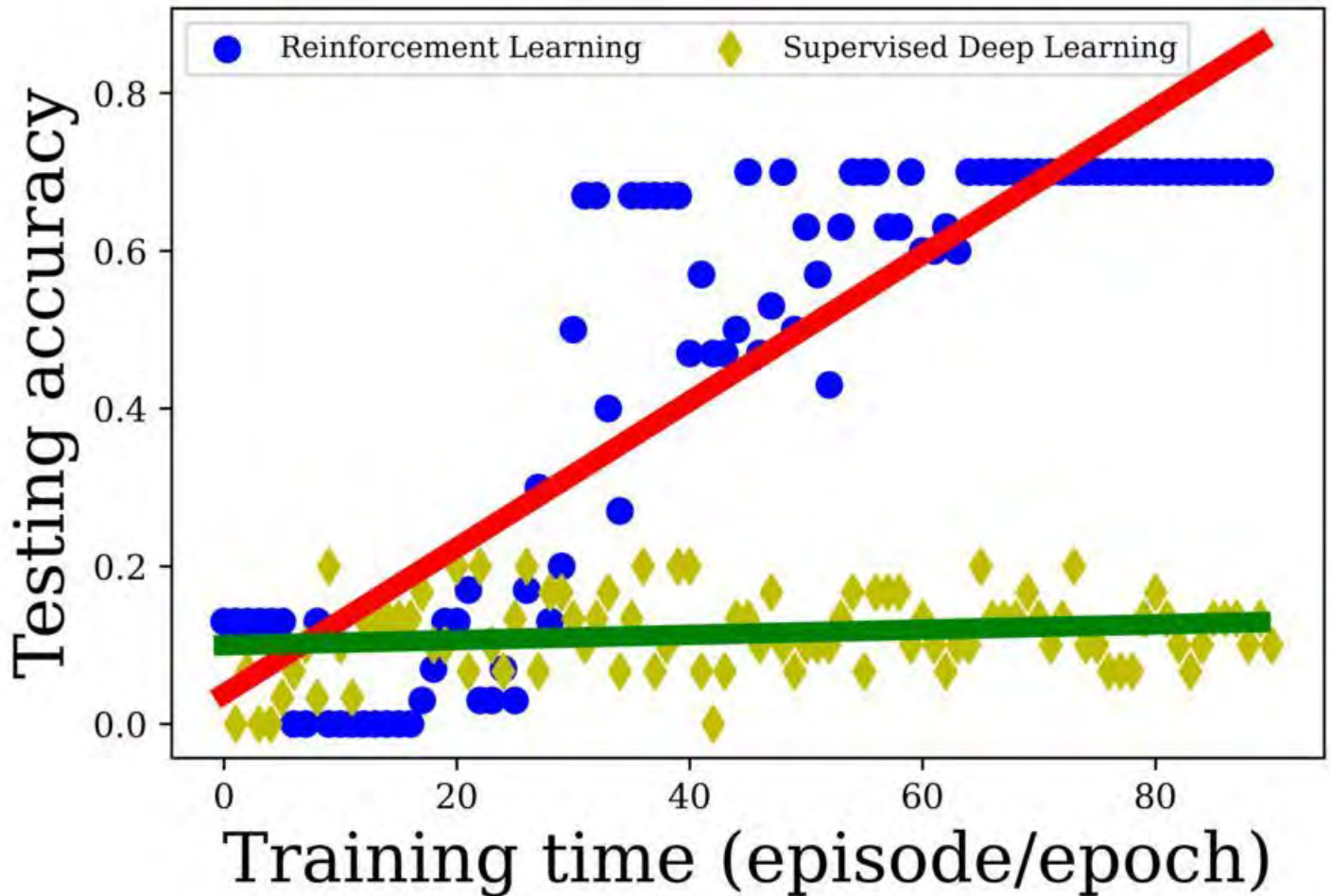
We trained a Deep Q network on 30 two-dimensional image slices from the BraTS brain tumor database. Each image contained one lesion. We then tested the trained Deep Q network on a separate set of 30 testing set images. For comparison, we also trained and tested a keypoint detection supervised deep learning network for the same set of training / testing images.

Results

As expected, the supervised approach quickly overfit the training data, and performed poorly on the testing set, with 11% accuracy. In contrast, the Deep-Q learning approach showed progressively improved generalizability to the testing set during training (Figure 1), reaching 70% accuracy.

Conclusions

We have shown a proof-of-principle application of reinforcement learning to radiological images, here using 2D contrast-enhanced MRI brain images with the goal of localizing brain tumors. This represents a generalization of recent work to a gridworld setting, naturally suitable for analyzing medical images.



(Filename: TCT_1514_DQN_vs_keypointCNN_gridworld_testing_acc.jpg)

1295

Relative Incidence of Variable Imaging Characteristics of Rathke Cleft Cysts on MRI

D Groskreutz¹, B Omay², K Seifert³, A Mahajan²

¹Frank H Netter School of Medicine, North Haven, CT, ²Yale University, New Haven, CT, ³Stanford University School of Medicine, Stanford, CA

Purpose

Rathke cleft cysts are benign, congenital, epithelium lined cysts that derive from the embryonic remains of the pituitary Rathke pouch. Distinguishing Rathke cleft cysts from various other cystic sellar/suprasellar masses such as craniopharyngioma, cystic pituitary adenomas, and arachnoid cysts through the use of imaging has remained challenging.¹ This study therefore attempts to describe the Magnetic Resonance Imaging (MRI) characteristics of 98 Rathke cleft cysts to facilitate the differentiation of sellar/suprasellar cystic lesions.

Materials and Methods

MRI studies of Rathke cleft cysts were obtained from 98 patients at Yale New Haven Hospital. Patients were 67 Female vs. 31 Male with an average age of 39.6 (range: 0.67-81 years). Average follow up was 2.8 years (range: 4 months–10 years). Each case was analyzed for characteristics of anatomical location (sellar vs suprasellar) and signal intensity (hyper vs iso vs hypointense relative to brain parenchyma) on both T1 and T2-weighted images.

Results

95/98 (96.9%) of Rathke cleft cysts were anatomically localized to the sella, while the remaining 3/98 (3.1%) were suprasellar. For T1-weighted images, 57/98 (58.2%) of cystic lesions appeared hypointense, while 26/98 (26.5%) revealed hyperintensity and the remaining 15/98 (15.3%) revealed an intensity similar to the brain parenchyma. For T2-weighted images, 24/93 (25.8%) appeared hypointense, 59/93 (63.4%) revealed hyperintensity, and 6/93 (6.5%) demonstrated an intensity similar to the surrounding brain parenchyma. All lesions demonstrated lack of enhancement on postcontrast images.

Conclusions

Signal Intensity of Rathke's cleft cyst are variable, depending on the contents of the cyst. While the majority demonstrate T1-weighted

hypointensity and T2-weighted hyperintensity, at least 26% of these are hyperintense on T1-weighted images, which may reflect a higher protein content within these lesions.

539

Repeat MRI in Epilepsy: Rate of Occurrence and Associated Costs

E Albach¹, K Nelson¹, A Thaker¹, V Timpone¹

¹University of Colorado Anschutz Medical Campus, Aurora, CO

Purpose

The initial evaluation of epilepsy patients requires high resolution MR imaging at 3T or greater to optimize detection of surgically treatable epileptogenic lesions. Since MR imaging at lower resolution and field strength may miss subtle epileptogenic foci, repeat brain MR imaging at 3T is generally indicated. The purpose of this study is to evaluate the rate of repeat MR imaging and associated costs in a population of epilepsy patients referred to a tertiary care center.

Materials and Methods

Imaging and clinical data were reviewed for 230 consecutive patients admitted for phase 1 seizure monitoring. "Necessary repeat MRI" was defined if outside imaging was performed at 1.5 T or less, lacked high resolution volumetric T2-FLAIR and T1 imaging, or had artifact degradation. Scans excluded from "necessary repeat MRI" were those older than 12 months from repeat scan, scans performed due to change in symptoms, scans for surgical navigation, tumor follow-ups, or those performed in an emergent setting. An "unnecessary repeat MRI" was identified as a repeat scan when outside imaging was performed at 3.0 T, contained volumetric T2-FLAIR and T1 imaging, was diagnostic quality free of artifact, performed in past 12 months, and no interval change in patient symptoms. Extraneous MRI was defined as "necessary repeat MRI" + "unnecessary repeat MRI".

Results

26 of 230 (11.3%) patients had extraneous MRI performed. 11 of 230 were "necessary repeat MRI" and 15 of 230 were "unnecessary repeat MRI." The 11 "necessary repeat MRI" had one or more of the following imaging characteristics prompting re-imaging: Scan performed at 1.5 T (5/11); lack of high resolution volumetric T2-FLAIR and T1 imaging (4/11); and artifact degradation (5/11). The national average Medicare fee schedule for combined technical and professional component charges for an MR brain without contrast is identified as \$417.96 per scan. At the extraneous MR imaging rate of 11.3% observed, estimated cost per 1,000 patients imaged would be \$47,229 USD.

Conclusions

Regional MR overutilization is observed in our epilepsy population. We identify opportunities to mitigate extraneous imaging and associated costs by always prescribing a high resolution 3.0 T MR brain on eligible epilepsy patients, recalling patients that are nondiagnostic due to artifact, and preventing unnecessary repeat imaging in patients that have already received a diagnostic scan.

1392

Resting-State fMRI Brain Connectivity Correlates of Anxiety, Depression and PTSD Measures in Patients with Blast-Related Post-Concussion Vestibular Dysfunction

A Trofimova¹, J Smith¹, V Ahluwalia², S Akhnoukh³, R Gore⁴, J Allen¹

¹Emory University, Atlanta, GA, ²Georgia Institute of Technology, ATLANTA, GA, ³Emory University School of Medicine, Palm Harbor, FL, ⁴Shepherd Center, Atlanta, GA

Purpose

To correlate resting-state fMRI (rs-fMRI) connectivity and clinical measures of anxiety, depression and post-traumatic stress disorder (PTSD) in blast-related post-concussion vestibular dysfunction (b_PCVD).

Materials and Methods

IRB approved study. 10 subjects with b_PCVD and 13 healthy subjects (HC) underwent rs-fMRI, clinical vestibular testing and self-reported measures of depression (Beck Depression Index, BDI), anxiety (Beck Anxiety Index, BAI), and PTSD (PTSD Checklist for DSM-5, PCL-5). rs-fMRI acquired on 3.0T magnet, 32-channel head coil (2.5mm isovoxel, TR/TE=750/32ms, flip angle=52°). CONN Toolbox used for preprocessing and analysis. Multivoxel pattern analysis (MVPA) was conducted to localize voxel clusters which differed in whole-brain connectivity as a function of BDI, BAI, and PCL-5 scores. ROI-ROI connectome analysis (general linear model) was conducted to estimate differences in connectivity among suprathreshold ROIs as a function of group, BDI, BAI, and PCL5 scores. All statistics were corrected for multiple comparisons using family-wise error correction (p<0.05).

Results

Statistically significant differences were found in BAI, BDI and PCL-5 scores between HC and b-PCVD groups. b_PCVD group exhibited decreased connectivity in the subgenual, middle, and posterior cingulate, middle and inferotemporal, orbitofrontal, and superior parietal cortices, but increased connectivity in occipitopolar, supramarginal, lateral postcentral, and lateral prefrontal cortices and the anterior cingulate. Higher PTSD and anxiety scores were associated with an increase in connectivity between the inferior parietal gyrus and frontal, prefrontal, orbitofrontal, and temporal cortex, but decreased connectivity among caudate, vestibular,

precentral, and supramarginal areas. Higher depression scores were associated with decreased connectivity between temporal and caudate areas, visual cortex, and posterior hippocampus.

Conclusions

Significant correlations between rs-fMRI increased connectivity and measures of PTSD and anxiety suggest pathologic over-weighting of executive and sensory processing with selectively decreased weighting of vestibular, motor and somatosensory integration in subjects with b_PCVD at rest. Additionally, decreased weighting of sensory, visual and memory input with increase in depression scores is suggested in this patient population.

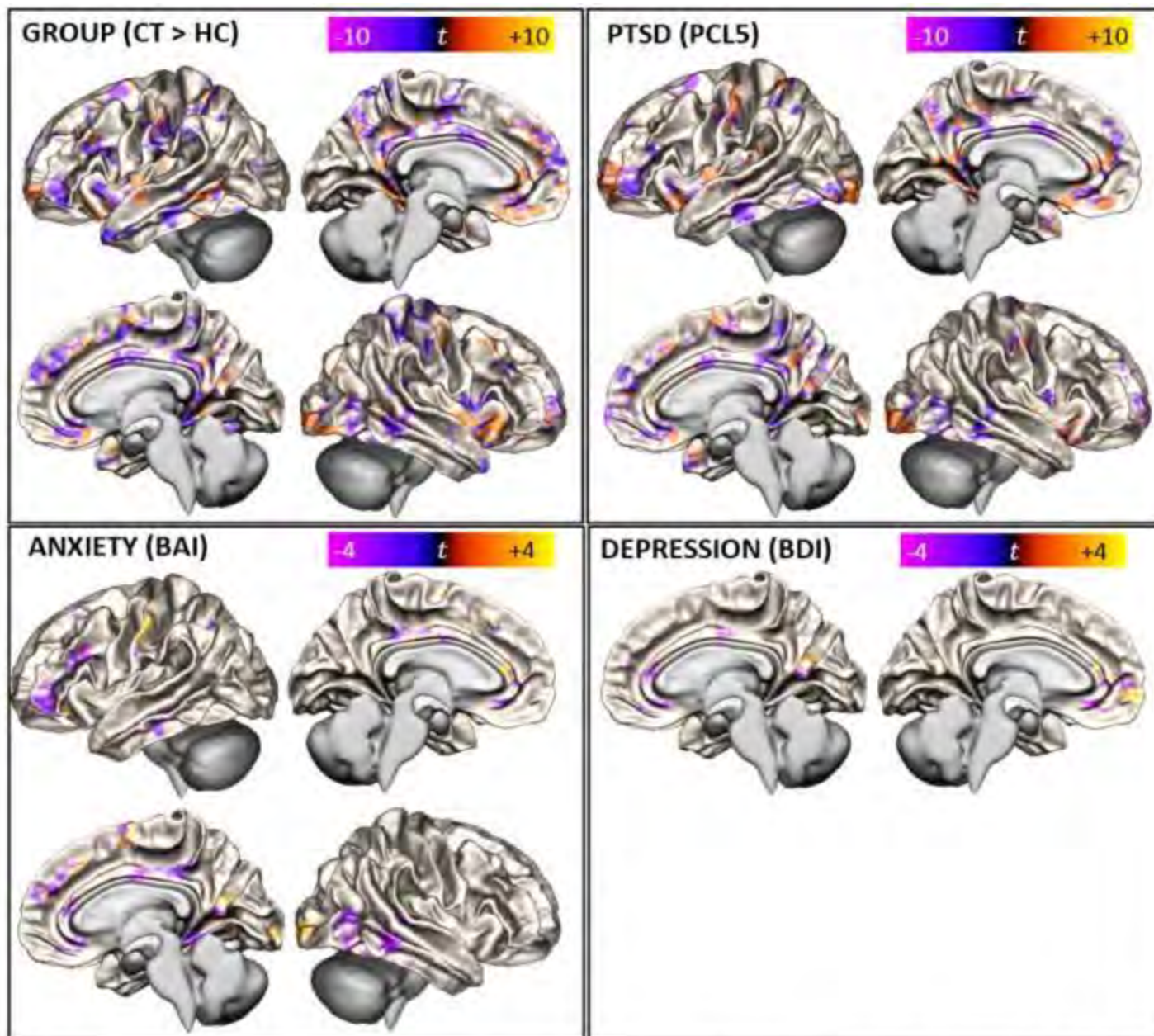


Figure 1: rs-fMRI connectivity, multivoxel pattern analysis (MVPA). Left upper panel: MVPA group difference, b_PCVD (CT) and healthy controls (HC). Cool colors represent decreased connectivity, and warm colors increased connectivity in the b_PCVD group (CT). MVPA correlations with BAI scores (left lower panel), PCL5 scores (right upper panel) and BDI scores (right lower panel): cool colors represent decreased connectivity with higher score, and warm colors increased connectivity with higher score, across both HC and b_PCVD groups.

(Filename: TCT_1392_PictureforAbstractCT.jpg)

Resting-state fMRI functional connectivity in patients treated with post-operative electrical stimulation during the hospitalization for coronary artery bypass graft (CABG)

G Sparacia¹, M Shahriari², V Lo Re¹, G Parla¹, G Mamone³, A Iaia², G Iannolo¹, M Bulati⁴, G Russell¹, E Lo Gerfo¹, R Miraglia³, M Pilato¹, F Ambrosio⁵

¹IRCCS-ISMETT, Palermo, Italy, ²Christiana Care Health System, Newark, DE, ³IRCCS-ISMETT, Palermo, Sicily, ⁴IRCCS-ISMETT, Palermo, ITALY, ⁵University of Pittsburgh, Pittsburgh, PA

Purpose

Cognitive decline in the absence of focal neurologic signs is still a common long-term neurologic complication following coronary artery bypass graft (CABG), affecting 43% of patients acutely, this resolved to 19% at 4–6 months and then increased to 25% of patients between 6-months to 1-year post-operatively. Clinically assessment of cognitive changes after CABG surgery is problematic because of the absence of a means to obtain reproducible, objective, and quantitative measures of the neural disturbances that cause altered brain function. The aim of this single-center pilot clinical trial was to test the hypothesis that the initiation of an early rehabilitation protocol, through neuromuscular electrical stimulation (NMES)+usual care, will preserve skeletal muscle mass in CABG patients promoting the expression of circulating factors important for the preservation of cognitive functions that would be assessed by means of resting-state functional magnetic resonance imaging (rest-fMRI) as a biomarker of cognitive outcome.

Materials and Methods

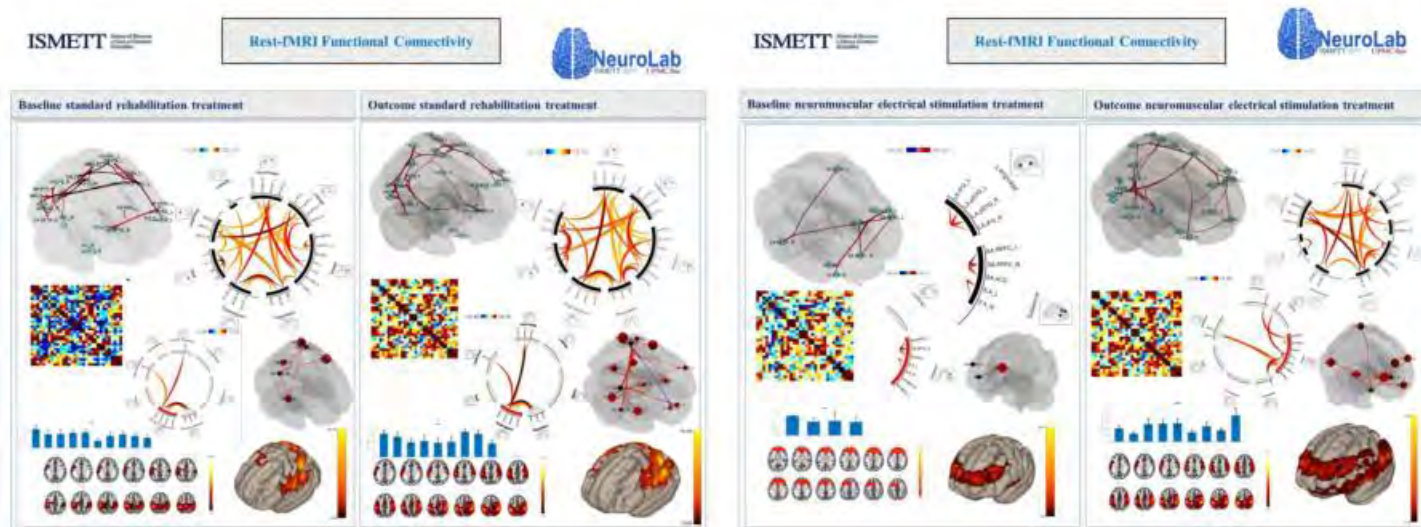
This was a randomized controlled trial performed at a single center between February 1th 2019 and July 31th2020. This study was approved by the Institutional Research Review Board (IRRB). Adult patients affected by critical coronary artery disease (CAD) scheduled for elective or urgent CABG surgery, were enrolled in the study as soon as possible after CABG surgery and randomly assigned to the intervention (NMES + standard rehab) or control group (standard rehab). The analysis included only patients who completed the entire protocol (38 patients; NMES group: 16; control group: 22). Imaging and clinical biomarkers were collected at the baseline, at the end of the treatment (up to 15 days), and at 3 months after the hospital discharge. The baseline brain rest-fMRIs were performed with a 3T unit as soon as possible during the surgical hospitalization and 3 months after the hospital stay. Cognitive assessments was performed at 3 month after the hospital discharge.

Results

Functional connectivity significantly ($<.05$) improved in patients treated with NMES compared to patients treated with standard rehabilitation while cognitive improvement assessed with tests was unremarkable.

Conclusions

Functional connectivity assessed by rest-fMRI could aid in the development of targeted and specific rehabilitation interventions designed to minimize cognitive disability and, ultimately, enhance the quality of life for individuals following an hospital stay for cardiac surgery



(Filename: TCT_1256_ASNR_2021_FIG.jpg)

351

Retrospective Review of the Relationship Among Spontaneous Intracerebral Hemorrhage Associated Perihematomal Edema and Clinical Outcomes

D Shin¹, D Musatova², J Shulman², M Abdalkader¹, B Bayliss¹, G Haider², D Greer², A Mian³, C Takahashi²

Purpose

Perihematomal edema (PHE) is a radiological manifestation of secondary injury that can be seen with intracerebral hemorrhage (ICH)[1-3]. Our aim is to evaluate how PHE is related to clinical outcomes such as mortality, hospital length of stay, and the need for medical or surgical interventions.

Materials and Methods

Patients with ICH who had a non-contrast head computed tomography upon admission and within 24 hours post-admission were identified retrospectively in this single center study. Baseline clinical characteristics and clinical outcomes data were obtained via chart review. ICH and PHE volumes were calculated from the imaging studies. Different PHE measures were investigated to aid in comparison with prior studies, including total baseline PHE volume, PHE to ICH volume ratio at baseline, and PHE growth rate at follow up imaging study. Multiple logistic regression was employed to evaluate the relationship between the PHE measures and clinical outcomes. Cox proportional hazard model was used to assess the relation between PHE measures and hospital length of stay.

Results

A total of 87 patients were included in the analysis. Baseline volume of PHE was associated with in-hospital mortality independent of the baseline ICH volume with every 10 ml increase in the PHE volume associated with 80% increase in the odds of death ($p = 0.047$). PHE growth rate only showed significant association with hospital length of stay with every 1 ml/hour increase in the PHE growth rate associated with a hazard ratio of 1.23 for being discharged from hospital ($p = 0.011$). PHE to ICH ratio did not demonstrate any significant association with clinical outcome variables. As expected, NIHSS on admission demonstrated a significant relationship with odds of death with odds ratio of 1.19 to 1.55 for every unit increase in the NIHSS. Patients with Medicaid were more likely to have longer hospital length of stay when compared to those with private insurance with a hazard ratio of being discharged of 0.12 to 0.24.

Conclusions

PHE volume at baseline is associated with mortality independent of the baseline ICH volume. With every 10 ml increase in the PHE volume at baseline, there is 80% increased odds of death during the hospital stay. The PHE to ICH ratio and PHE growth rate were not significantly associated with meaningful clinical outcomes.

1066

Reversible Lesion Hypodensity in Stroke CT After Thrombectomy - Challenging the Imaging Paradigms of Brain Infarct

G BROOCKS¹, R McDonough¹, L Meyer¹, J Fiehler², A Kemmling³

¹University Hamburg, Hamburg, NA, ²University Hospital Hamburg-Eppendorf, Hamburg, Hamburg, ³University Lübeck, Lübeck, NA

Purpose

In acute stroke, early ischemic lesion hypodensity in computed tomography (CT) is considered the imaging hallmark of brain infarction, representing a state of irreversible tissue damage with a continual increase in net water uptake. This dogma is however challenged by rare cases of apparently reversed early lesion hypodensity following complete reperfusion. The purpose of this study was to investigate the occurrence of reversible ischemic edema after endovascular treatment.

Materials and Methods

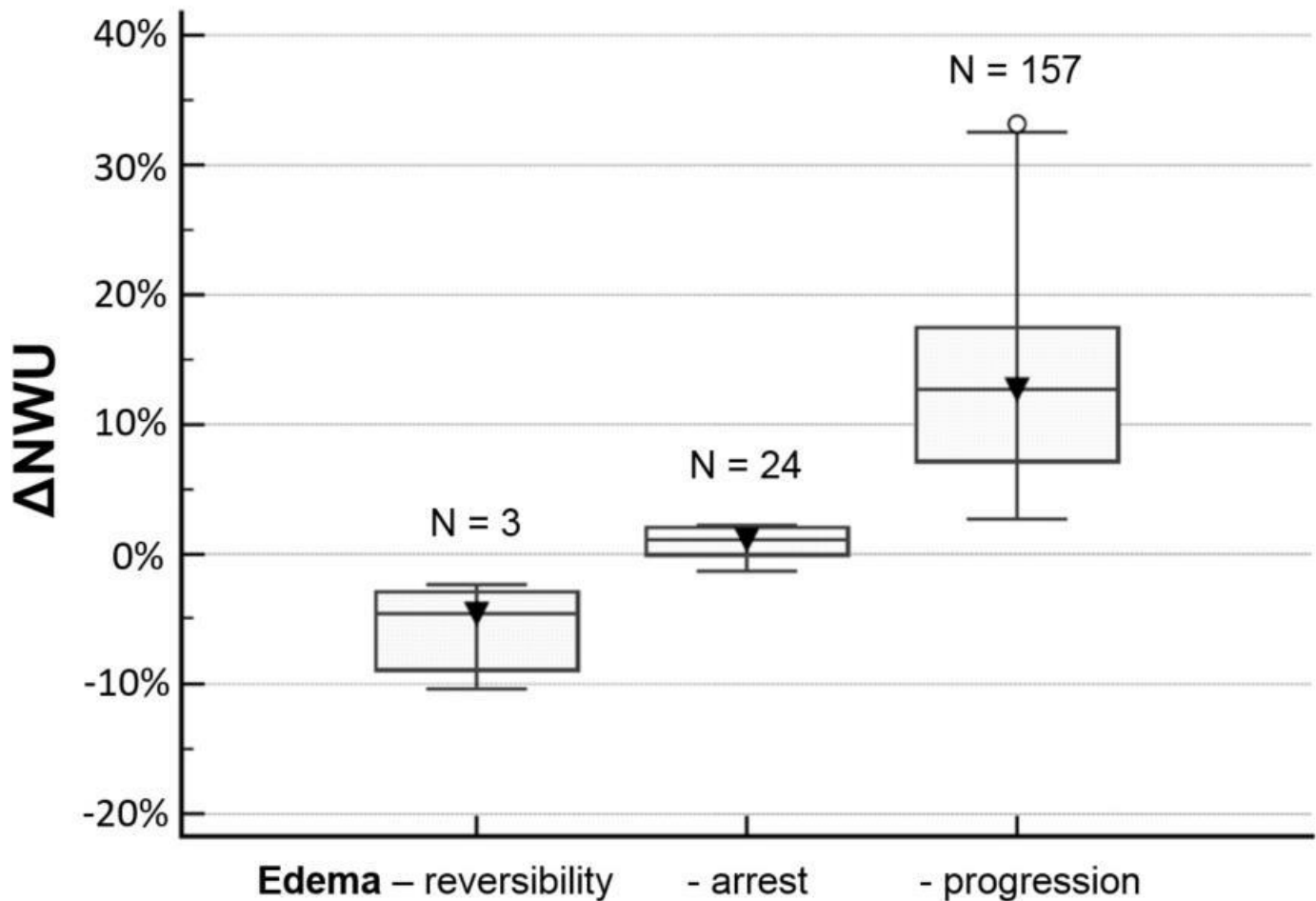
184 acute ischemic anterior circulation stroke patients were included after consecutive screening. Ischemic brain edema was determined using quantitative lesion net water uptake (NWU) in admission-CT and follow-up CT based on CT-densitometry and Δ NWU was calculated as the difference. The association of edema progression to imaging and clinical parameters was investigated. Clinical outcome was assessed using modified Ranking Scale (mRS) scores at day 90.

Results

27/184 patients (14.7%) showed edema arrest and 3 patients (1.6%) exhibited significant edema reversibility. Higher degree of recanalization (odds ratio (OR): 2.96, 95%CI: 1.46-6.01, $p < 0.01$) and shorter time from imaging to recanalization (OR/hour: 0.32, 95%CI: 0.18-0.54, $p < 0.0001$) were significantly associated with edema arrest or reversibility. Clinical outcome was significantly better in patients without edema progression (median mRS 2 versus mRS 5, $p = 0.004$).

Conclusions

Albeit rare, lesion hypodensity considered to be representative of early infarct in acute stroke CT may be reversible following complete recanalization. Arrest of edema progression of acute brain infarct lesions may occur after successful rapid vessel recanalization, resulting in improved functional outcome. Future research is needed to investigate conditions where early revascularization may halt or even reverse vasogenic edema of ischemic tissue.



(Filename: TCT_1066_fig2.jpg)

1293

ROI-based Analysis of T1-weighted Images to Predict Complete Response in Patients with Spinal Metastases Treated with SBRT: Initial Experience

B Moazen¹, M Mojtahed Zadeh¹, A Chan¹, A Sahgal¹, S Myrehaug¹, J Detsky¹, H Soliman¹, Z Husain¹, C Tseng¹, P Jabejdar Maralani¹

¹University of Toronto, Toronto, ON

Purpose

To investigate whether radiologically-derived measurements using T1-weighted images can be used as a prognostic biomarker for progression after patients demonstrate complete response (CR) for their spinal metastases after treatment with stereotactic body radiation therapy (SBRT).

Materials and Methods

Patients that had their spinal metastases treated at our institution with SBRT had all routine follow-up MRIs evaluated retrospectively. In treated spinal segments that demonstrated CR—where the tumor was indiscernible—on T1-weighted imaging, a region of interest (ROI) was drawn over the metastatic sector [1] where there was tumor previously, and the signal intensity was measured. The signal intensity was normalized by dividing its value by the value obtained by a separate ROI, drawn over the midline of the Oblique Capitis Inferioris muscle on the same MRI scan. Tumors from a different sector, but within the same vertebrae [1] were considered independently. Outcomes of progression vs non-progression were determined by the last follow up scan available, with progression defined as any tumor reappearance after CR within the sector of interest. The mean ROI ratios (\pm standard deviation) were calculated for each sector that demonstrated CR and those that did not, and were compared.

Results

40 sectors from 23 patients which demonstrated CR were evaluated for a median follow up time of 12.5 months (interquartile range=27). Of these, 38 sectors had CR and no further progression. Two lesions progressed after CR. The mean ROI ratio for CR and progressed sectors were 1.72 (\pm 0.464) and 1.39 (\pm 0.006), respectively ($p < 0.05$).

Conclusions

ROI ratio of the metastatic lesion to Oblique Capitis Inferioris muscle can be used as a prognostic biomarker of sector-specific complete response in T1-weighted images from patients with spinal metastases undergoing SBRT.

1344

Role of CT in Conductive Hearing Loss with Normal Tympanic Membrane

R HASSAN KARUVATH¹, A NAGADI², H chadaga²

¹COLUMBIA ASIA, MALAPPURAM, KERALA, ²COLUMBIA ASIA, BANGALORE, KARNATAKA

Purpose

1. Determine the prevalence of aetiologies leading to conductive hearing loss with normal tympanic membrane. 2. Determine the sensitivity, specificity, PPV and NPV of HRCT in diagnosing pathologies of temporal bone 4. To correlate the radiological abnormalities with audiological findings. 5. To develop a systematic checklist for HRCT evaluation in the assessment of these patients

Materials and Methods

A prospective study, done with a sample size of 80 patients (160 ears) who were referred to our department with history of conductive hearing loss and had normal tympanic membrane on otoscopic examination. All the patients included in the study were subjected to full clinical examination and had also undergone full audiological assessment at the time of diagnosis including pure tone audiometry, tympanometry and stapedia reflex analysis. HRCT was done using a Philips Ingenuity 128 slice CT machine with dual localisers. The imaging findings were correlated with audiometry and surgical findings and the data was analysed using standard statistical methods.

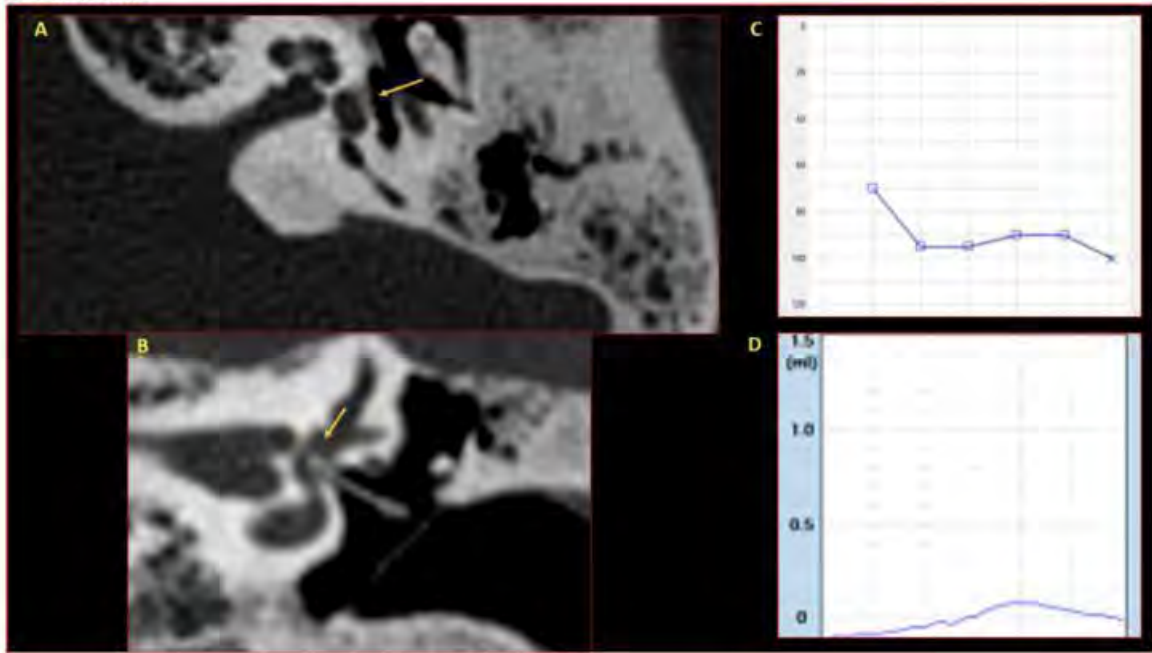
Results

The most common pathology was found to be otosclerosis (58.75%). HRCT had a sensitivity of 94.23 %, specificity, PPV of 100 %, NPV of 95% and accuracy of 94.23 % in diagnosing temporal bone pathologies. The extension and severity of the otosclerotic lesions have a good correlation with the degree of hearing loss assessed by preoperative pure tone audiometry (ANOVA, $p < 0.001$). HRCT diagnosis was in concordance with impedance audiometry in 85.63% of ears and discordant in 14.37% of ears. We observed the most common site of distribution of otospongiotic plaques in our study was in the fissula ante fenestrum ($n=44;67.69%$). There was a significant correlation (Mann Whitney Rank Sum Test, $p < 0.001$) between the increasing site of involvement of otospongiotic plaques with worsening pure tone audiometry findings. For each additional site affected, the average ABG increased by 5.522 dB (95% confidence interval [CI], 3.656 to 7.388 dB; $p = < 0.001$). We also observed that assessment of HRCT temporal bone in a systematic fashion using a check list and appropriate reconstructions can improve the ability to diagnose pathologies.

Conclusions

There's a good statistically significant correlation between audiometry and surgical findings with imaging findings as diagnosed in HRCT temporal bone. Using a checklist for systematic review and analysis and using appropriate image reconstructions can positively aid in the evaluation of pathologies in HRCT temporal bone.

FENESTRAL OTOSCLEROSIS



Case of fenestral otosclerosis with intra vestibular protrusion of stapes prosthesis:

- A- Axial HRCT left temporal bone demonstrates otospongiotic plaque is seen at the fissula ante fenestrum.
- B- Double-oblique coronal short-axis view HRCT left temporal bone demonstrates intra vestibular protrusion of the stapes prosthesis.
- C- Pure tone audiogram of the left ear demonstrates profound hearing loss
- D- Left tympanogram demonstrates As type of curve

(Filename: TCT_1344_asnr.jpg)

949

Safety and efficacy of a new percutaneous interspinous spacer: A multi-center retrospective study

s marcia¹, L Manfrè², M Bellini³, E Piras⁴, A De Vivo⁵, C Zini⁶

¹SS TRINITA' HOSPITAL, CAGLIARI, SARDEGNA, ²Mediterranean Institute for Oncology, Viagrande, Catania, ³Unit of Diagnostic and Functional Neuroimaging, Siena, Tuscany, ⁴P.O. Santissima Trinità, 09121, Italy, ⁵I.O.M., Catania, ITALY, ⁶Uniti of Radiology, Hospital Santa maria annunziata,USL Centro, Firenze, FI

Purpose

To evaluate safety and efficacy of a new percutaneous interspinous process device (IPD) Lobster® (Techlamed, Firenze, Italy) in 147 patients with degenerative lumbar spinal stenosis(DLSS) from 3 different centers.

Materials and Methods

From November 2016 and March 2020, 147 patients(67 male, age 72 ± 9.7 years old, range 45-91) with neurogenic intermittent claudication because of DLSS related to mono/bi-segmental lumbar central canal and/or foraminal stenosis were enrolled in the present study. Clinical outcomes were evaluated using Visual Analog Scale(VAS) and Zurich Claudication Questionnaire (ZCQ) before and after the procedure. Technical success was defined as correct placement of the IPD demonstrated with computer tomography (CT), performed immediately after treatment; spinoplasty was accomplished in patients with BMD T-score < - 2.5.

Results

In 178 levels (L2-L3=7; L3-L4=61; L4-L5=102; L5-S1=8) a total of 177 IPDs (8mm= 60;10 mm=90;12 mm=26;14 mm=1) were implanted; in 22 patients more than 1 level have been treated in the same session; spinoplasty was accomplished in 66 patients. We registered 99,4% of technical success: in 1 case, because of spinous process rupture during spinoplasty, the device was not implanted. In 2 cases we observed displacement of the IPD subsequently removed under fluoroscopy and replaced. No major complications were registered. 5 point of VAS reduction was registered after the procedure(mean VAS pre-procedure= 7.74 ± 0.69 ;mean VAS post-procedure= 3.36 ± 1.3)($p < 0.001$); mean pre-procedural ZCQ was 50.6 ± 10.67 and post-procedural ZCQ was 30 ± 1.3 ($p < 0.001$).

Conclusions

The Lobster®IPD is safe and effective totally percutaneous minimally-invasive decompression procedure in DLSS.

733

Safety and Efficacy of Vascular Closure Devices in Interventional Radiological Procedures

E Kim¹, A Lee¹, S Ande², B Goncalves Sebastiao¹, J Shankar¹

¹University of Manitoba, Winnipeg, Manitoba, ²University of Manitoba, Winnipeg, MB

Purpose

Vascular closure devices (VCD) are routinely used in both neurovascular and vascular interventional procedures. At our center, a VCD is routinely used for diagnostic procedures as well, which is unique compared to other centers around the world. The purpose of our study was to assess the safety and efficacy of the VCDs for diagnostic and interventional neurovascular and vascular interventional procedures.

Materials and Methods

The study was approved by our research ethics board. A retrospective review was conducted of the interventional radiology database between January 2017 and December 2019. All patients underwent a diagnostic or interventional procedure through a common femoral arterial access and a VCD was used to close the access site. The data was collected from the Picture Archiving and Communication System (PACS) and collected in an excel spreadsheet. The data points included the date of study, operator, type of VCD, the type of procedure and any immediate or late complication from the VCD. Patient demographics and clinical information included age, sex, BMI, past medical history, smoking history, anticoagulation/antiplatelet medications, lab values (creatinine, eGFR, INR, platelets, hemoglobin), and stroke data (t-PA if given, any clinical deficits). Three separate data collectors gathered information. Descriptive statistics and chi-squared tests were performed using STATA 13 software. A $p < 0.05$ was considered significant.

Results

VCD was used in a total of 1151 patients. VCDs were successfully deployed in 94% with 6% failure. Immediate perioperative complications were seen in 6.2% of patients. These included oozing or bleeding from the puncture site (28%), small hematoma (28%), large hematoma (6%), pain (1.4%), hematuria (1.4%), emesis (1.4%) and loss of vascular access (1.4%). The complication rates were significantly ($p=0.025$) associated with the type of procedures with diagnostic and interventional neuroradiology, vascular diagnostic and interventional procedures having 3.2% and 6.4%, 8.6% and 4.3 % respectively. Complications were seen significantly ($p=0.044$) higher in outpatients (7.7%) compared to 4% in the inpatients and those from emergency room.

Conclusions

VCDs were successfully deployed in 94% of the patients with 6% perioperative complications. Most of the complications were minor and were more commonly associated with outpatient and diagnostic vascular procedures.

1428

Search for the Missing: Visualization of Nucleus Pulposus and Inner Annulus Fibrosus on Routine Lumbar Spine MR Imaging

G Venkataraman¹, R Eldaya², M Parsons³, A Sharma³

¹Mallinckrodt Institute of Radiology, St Louis, MO, ²Washington University, St Louis, MO, ³Mallinckrodt Institute of Radiology, St. Louis, MO

Purpose

Central hyperintense region on T2-weighted MR images of normal lumbar intervertebral discs (IVDs) represents a combination of inner annulus fibrosus (IAF) and nucleus pulposus (NP) [ref. 1]. Ability to identify NP as distinct from IAF can help improve our understanding of normal intervertebral disc morphology in-vivo while allowing for optimization of quantitative techniques such as T2-relaxometry that rely upon accurate segmentation of individual disc components. We hypothesized that while the interface between IAF and NP is visually occult, there are underlying intensity differences between these two structures on T2-weighted images. We further hypothesized that IAF and NP could be rendered visible on routine T2-weighted images using image post-processing techniques that could accentuate differences in their inherent signal intensity.

Materials and Methods

Sagittal T2-weighted TSE MR images of 150 lumbar IVDs from 25 patients were analyzed. MR images were processed using a custom algorithm that markedly increased the signal intensity of structures with inherent signal intensity within two defined intensity thresholds [ref. 2]. Signal intensity and contrast-to-noise ratio (CNR) between outer annulus fibrosus, IAF, and NP were assessed at baseline and after processing (fig. 1). To assess consistency of underlying T2 differences, similar analysis was done on 108 discs from 18 patients in whom additional sagittal T2-weighted STIR images were available. Success of image processing in revealing NP was compared for normal and abnormal discs categorized as such on the basis of IVDs grading on Pfirman's scale.

Results

Following image processing, apparent IAF and NP were rendered visible in 86% and 84.3% IVDs on T2-weighted TSE and STIR images respectively. While signal intensity of these two regions was inherently different ($p < 0.001$) before processing on TSE and STIR images, their visualization was facilitated by a significant increase ($P < 0.001$) in CNR after processing (fig. 2 and fig. 3). Non-visualization of NP was associated with disc degeneration ($p < 0.001$).

Conclusions

Inherent differences exist in signal intensities of normal NP and IAF on T2-weighted MR images. Accentuating these differences using image post-processing techniques can render these two structures visible. Degeneration of IVDs is likely to be associated with loss of underlying contrast between NP and IAF.



Figure 1: Sagittal T2-weighted image through the lower lumbar spine in a 15-years-old male with spondylolytic anterolysthesis at L4-5 level, before (a) and after (b) image processing done to facilitate distinction between inner annulus fibrosus and nucleus pulposus. Note that on post-processed image, the margins of nucleus pulposus (I), inner annulus fibrosus (II), and outer annulus fibrosus (III) become distinct in discs without overt signs of degeneration.

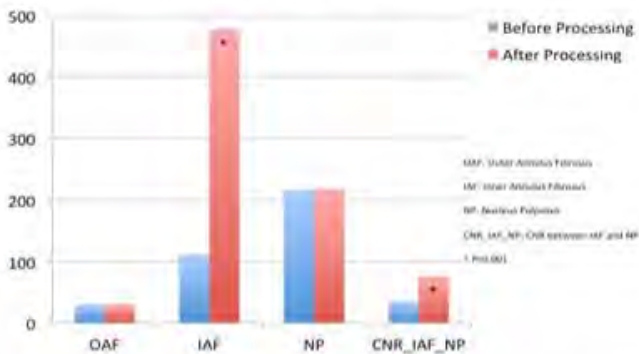


Figure 2: Effect of Image Processing on Signal Intensity and CNR of Individual Disc Components on T2-Weighted TSE MR Images (Filename: TCT_1428_figs.jpg)

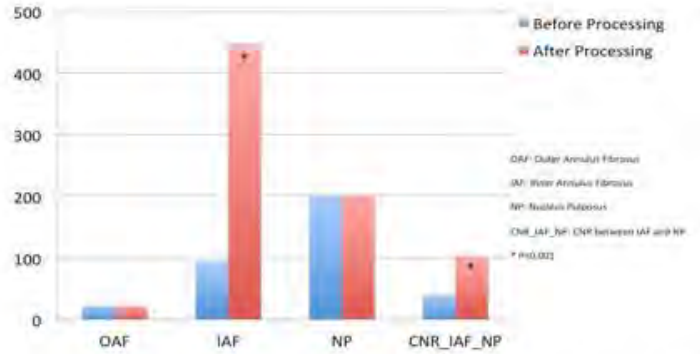


Figure 3: Effect of Image Processing on Signal Intensity and CNR of Individual Disc Components on T2-Weighted STIR MR Images

590

Segmentation is all you need: few-shot classification of cervical spinal stenosis with clinically interpretable deep learning

U Bharadwaj¹, V Padoia¹, S Majumdar¹, C Chin²

¹University of California, San Francisco, San Francisco, CA, ²UCSF, San Francisco, CA

Purpose

To evaluate few-shot learning for cervical central canal stenosis: deep learning segmentation models trained on related anatomical structures (lumbar spine) are adapted to cervical spine with minimal fine-tuning.

Materials and Methods

In a retrospective cross-sectional study, cervical spine MRIs acquired over three months were evaluated after excluding cases with transitional anatomy, fractures, post-operative changes, and extensive hardware. The study included 44 patients (23 Female, 21 Male) with mean age 60 [30, 88] years and BMI 26.6 [11.0, 43.0] kg/m² presenting with acute-to-chronic spectrum of neck pain,

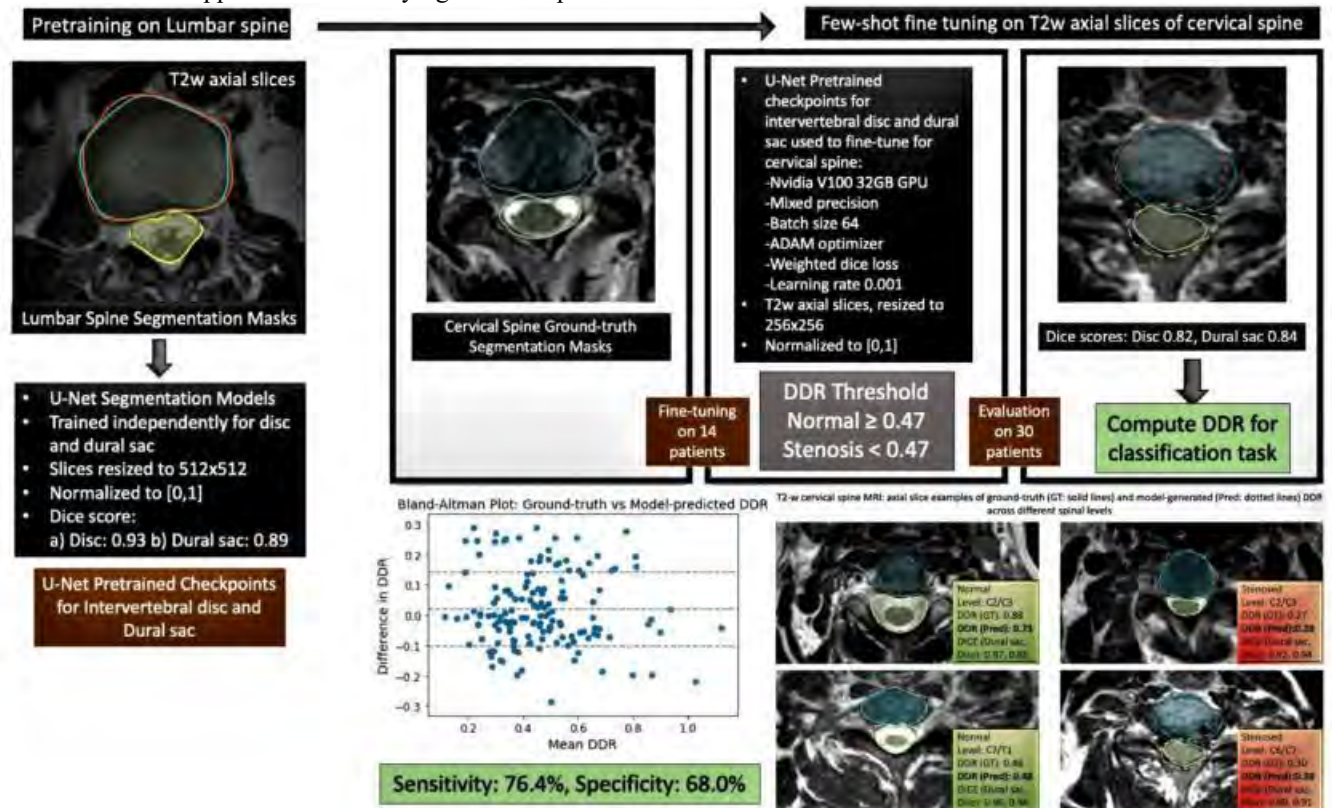
radiculopathy, and myelopathy. A neuro-radiologist qualitatively graded the central canal at each level as normal (n=148 levels) vs stenosed (n=146 levels). The patient cohort (n=44) was partitioned into two randomized splits: few-shot fine tuning data (n=14) and held-out evaluation data (n=30). U-Net models for segmenting the intervertebral disc and dural sac on T2-weighted axial slices were pretrained on lumbar spine MRIs (n=53) and subsequently fine-tuned on cervical spine data. Segmentation performance on the evaluation data was characterized using the dice coefficient. A normalized quantitative metric – Dural sac-to-Disc Ratio (DDR) – the ratio between cross-sectional areas of the dural sac and disc was implemented. Threshold for classifying stenosis was determined on fine-tuning data, selecting DDR at equal error rate. Classification performance of ground-truth as well as model-generated DDR was characterized using sensitivity and specificity along with their confidence intervals.

Results

U-Net segmentation models after few-shot transfer learning achieved dice coefficient value of 0.84 for dural sac segmentation and 0.82 for disc segmentation on cervical spine evaluation data. A threshold of 0.47 was selected for ground-truth DDR. At this threshold, stenosis classification based on ground-truth DDR achieved sensitivity of 73.9% [72.4%, 75.4%] and specificity of 83.3% [81.8%, 84.9%]; classification based on model-generated DDR at the same threshold achieved sensitivity of 76.4% [75.0%, 77.8%] and specificity of 68.0% [66.9%, 69.4%].

Conclusions

Several quantitative metrics have been proposed to standardize definitions for spinal stenosis; the basis of our proposed DDR metric is that the canal is most stenotic at disc levels. Model segmentations generalize well to new anatomical structures with little fine-tuning, and can be an economical approach for classifying cervical spinal stenosis.



(Filename: TCT_590_ASNR_UUB.jpg)

474

Semiautomated Carotid Artery Plaque Composition: Are Intraplaque CT Imaging Features Associated with Cardiovascular Risk Factors?

J Benson¹, G Lanzino², V Nardi¹, L Savastano¹, A Lerman¹, W Brinjikji¹

¹Mayo Clinic, Rochester, MN, ²Mayo, Rochester, MN

Purpose

Little remains known about the connection between cardiovascular (CV) risk factors and carotid plaque morphologies. This study set out to assess for any such associations.

Materials and Methods

A retrospective review was completed of consecutive patients that had CTA neck imaging prior to CEA. Body mass index (BMI), tobacco and/or alcohol use, and history of diabetes and/or hypertension were collected from patients' medical records. Lab values were dichotomized based on values: total cholesterol <200 or ≥200; low-density lipoprotein (LDL) <130 or ≥130, high-density lipoprotein

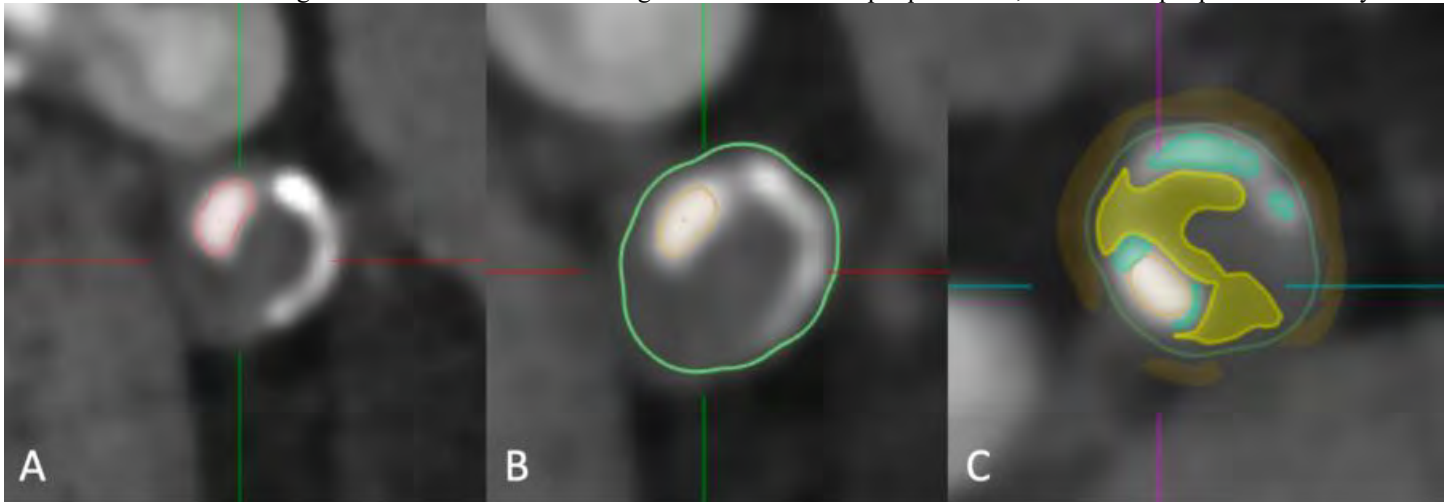
<35 or ≥35, and triglycerides <200 or ≥200. A semiautomated analysis of CTA images computed maximum stenosis, intraplaque volumes of intraplaque hemorrhage, lipid-rich necrotic core (LRNC), and matrix, and intraplaque volume and proportional plaque makeup of calcifications of each carotid plaque.

Results

Of 87 included patients, 54 (62.1%) were male. Mean age was 70.1 years old. Both diabetes and hypertension were associated with greater intraplaque calcification volume ($p=0.0009$ and $p=0.01$, respectively), and greater proportion of calcification within a plaque ($p=0.004$ and $p=0.01$, respectively). Higher BMI was associated with greater intraplaque volume of LRNC ($p=0.02$) and matrix ($p=0.0007$). Elevated total cholesterol was associated with both larger intraplaque calcification volume ($p=0.04$) and greater proportion of calcification within a plaque ($p=0.01$); elevated LDL was associated with greater intraplaque calcification volume ($p=0.005$).

Conclusions

Multiple CV risk factors are associated with morphological differences in carotid artery plaques. Dysregulation of both total cholesterol and LDL and higher BMI are associated with higher volumes of intraplaque LRNC, a marker of plaque vulnerability.



(Filename: TCT_474_Figure1.jpg.jpg)

458

Sexual Dimorphism in the Association of White Matter Connectome with Cognition in Healthy Adults

F Rahmani¹, N McKay¹, A Dincer¹, S Keefe¹, C Raji², T Benzinger¹

¹Washington University in St. Louis, Saint Louis, MO, ²N/A, N/A

Purpose

We aim to investigate the association between white matter connectivity and cognition in a group of non-demented older adults

Materials and Methods

We enrolled 460 individuals (male:231, mean age:69.8±8 and education:16±2.6 years) from the Knight Alzheimer Disease Research Center (ADRC) at Washington University School of Medicine in St. Louis from Jan 2010 to Jan 2019. Subjects were included if they had a neuropsychological assessment within 12 months of a diffusion MRI (DMRI) scan and excluded if they had a clinical dementia rating (CDR) score greater than 0.5. Twenty-three participants had a CDR: 0.5 and the remaining 437 had CDR:0. Four tasks measuring memory, verbal fluency, and processing speed were adopted from the standard Knight ADRC battery. These included the Trail Making Test (part B), the Animal Naming Test, the Delayed Recall of Logical Memory subtask of the Wechsler Memory Scale (WMS), and the Information subtest of the Wechsler Adult Intelligence Scale (WAIS). A composite cognitive score was calculated by averaging the z-scores of these tests for each participant². DMRI data were acquired on a SIEMENS TrioTim scanner using a 2D EPI diffusion sequence and connectometry analyses were performed using the DSI Studio (<http://dsi-studio.labsolver.org>). Data was then reconstructed in the MNI space using q-space diffeomorphic reconstruction (QSDR)³. The quantitative anisotropy was extracted as the local connectome fingerprint⁴. A semi-automated atlas-based deterministic tracking algorithm was used to obtain correlation tractography in a linear regression model⁵. Age and sex were used as covariates in all tests.

Results

We identified fibers in which connectivity was positively and independently associated with cognitive composite score: the frontoparietal part of right cingulum, superior longitudinal fasciculus, inferior frontooccipital fasciculus (IFOF), corticospinal tract, and anterior thalamic radiation (ATR) all in the right hemisphere, as well as the left IFOF (FDR: 0.000734)(Fig.1). Bilateral cerebellar white matter connectivity had an inverse relationship with cognitive composite score (FDR: 0.0196). Connectivity in right ATR and cerebellar white matter were positively associated with WMS and WAIS (FDR: 0.00022 and 0.00076).

Conclusions

We provide evidence of the independent relationships between episodic memory, verbal fluency, and processing speed tasks and connectivity of long-range white matter tracts in healthy older adults.

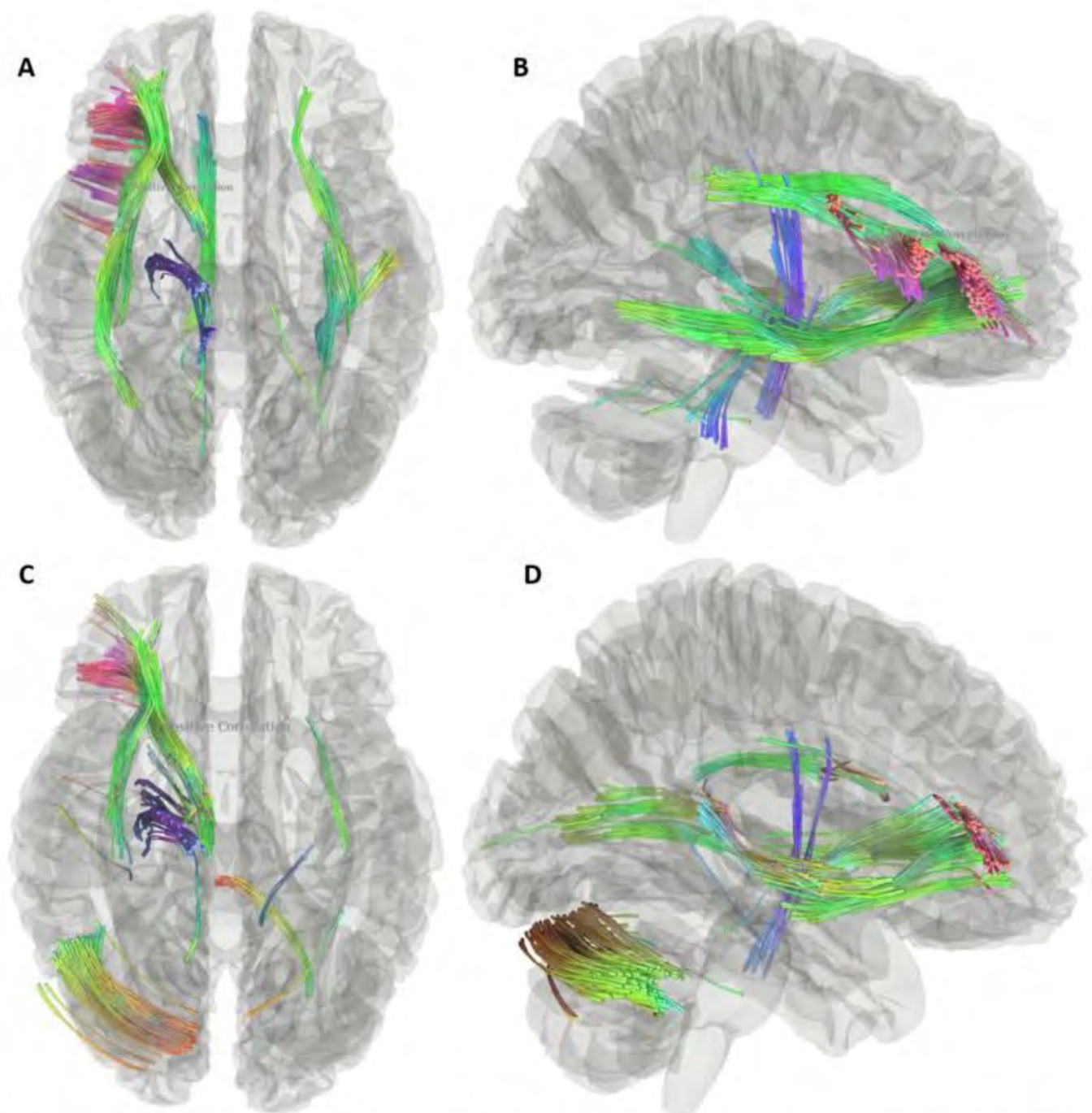


Fig 1. Tracks where QA positively correlated with composite cognitive score (A and B), and Delayed Recall of Logical Memory subtask of the Wechsler Memory Scale (C), and the Information subtest of the Wechsler Adult Intelligence Scale (D).

(Filename: TCT_458_Fig1.jpg)

715

Simulation Based Curriculum for Lumbar Puncture in a Medical Student Cohort

P Rana¹, J Shafa², A Levitt³, A Ortiz⁴

¹Jacobi Medical Center - Albert Einstein College of Medicine, New York, NY, ²Albert Einstein College of Medicine - Jacobi Medical Center, Bronx, NY, ³N/A, N/A, ⁴Jacobi Medical Center, Bronx, NY

Purpose

Image-guided lumbar punctures (LPs) are increasingly being performed by radiologists. It is important for doctors in training to practice these technical skills early in their careers to develop the competence and confidence necessary to perform procedures independently. According to a recent questionnaire only 36% percent of graduating medical students report that they are proficient in LP procedure (1).

Materials and Methods

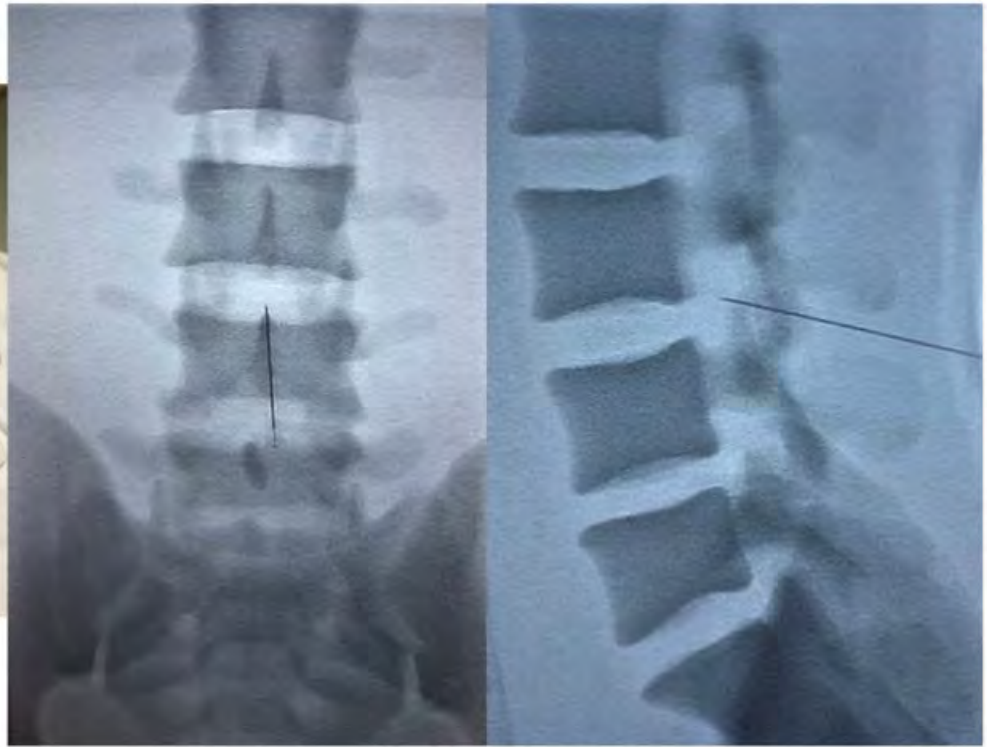
The purpose of this study was to assess the impact on medical student comfort and knowledge of LPs following a single day didactic and simulation-based training session in fluoroscopy guided LP using a lumbar spine phantom.

Results

A 45-minute didactic course and 2-hour hands-on simulation training session with a lumbar spine phantom was designed for a small group of medical students on clinical clerkships in radiology. Fifteen senior medical students (MS4) completed the course. A pre-test and post-test were designed to evaluate student's knowledge of lumbar spine anatomy, radiation safety, LP indications and contraindications, and LP technique. Additional questionnaire assessed student's confidence with lumbar spine anatomy, equipment used, and procedure technique on an incremental 5-point Likert scale. Analysis was preformed using paired T test.

Conclusions

Results from the 15 MS4s who participated in the LP course demonstrates a statistically significant increase (greater than 1.4 points on a 5-point scale across all three categories) upon survey of student's level of confidence on a number scale with regards to lumbar spine anatomy, equipment involved, and LP technique after taking the course. A statistically significant improvement ($P < 0.001$) in the average post-course test score was observed (90% average, standard deviation 15.2%) as compared to the pre-course test (50% average, standard deviation 9.7%). These findings are consistent with a similar study that utilized LP simulation training with radiology residents (2). Our simulation-based LP course resulted in improved operator confidence and knowledge amongst the medical students who participated. Our preliminary results demonstrate this single-day lumbar puncture simulation training session appears to have a promising favorable impact on medical student education. Education-enhanced simulation training has a favorable impact on medical student learning and should be considered when teaching invasive procedures.



	Confidence Anatomy	Confidence Equipment	Confidence Procedure	Overall Knowledge
Pre-test Averages	2.3	2.1	1.9	5.1
Post-test Averages	3.7	3.9	3.6	9.0

(Filename: TCT_715_Figures.jpg)

926

Single-energy Metal Reduction Artifact (SEMAR) Reduces CT Dental Artifact in Super-high Resolution CT Imaging of the Neck and Improves Visualization of Masses in the Oral Cavity and Oropharynx

N Pham¹, O Raslan²

¹UCLA, Los Angeles, CA, ²UC Davis, Sacramento, CA

Purpose

Although super-high spatial resolution CT imaging can be clinically advantageous for detecting head and neck pathology compared to conventional CT, it is also accompanied by a decrease in signal-to-noise (SNR), which can exacerbate CT artifact from dental amalgam and prostheses. The objective of this study is to demonstrate the clinical utility of a single-energy metal artifact reduction (SEMAR) algorithm that can be performed with super-high resolution CT of the neck to reduce CT dental artifact and improve the detection of oral cavity and oropharyngeal neoplasms.

Materials and Methods

13 patients were retrospectively identified from the radiology data base from September 2019 to March 2020 who underwent imaging on the super-high resolution CT scanner (1792 channels per detector row, 0.25 mm × 160 rows; matrix size, 1024). For each patient, two sets of axial images with 2-mm slices were reconstructed: non SEMAR images and SEMAR images. Two board-certified radiologists who were blinded to the reconstruction algorithms independently rated the image quality on the non-SEMAR and SEMAR images. The severity of CT artifact was scored on a 4-point scale: 4=severe (unacceptable); 3=moderate (acceptable only

under limited conditions); 2=mild (mostly acceptable); and 1=minimal/absent. The visibility of the oral cavity or oropharyngeal tumor was scored on a 4-point scale: 4=no visualization; 3=poor (only partially visible); 2=moderate (mostly visible); and 1=good (completely visible). The metal artifact index was calculated for SEMAR and non-SEMAR images.

Results

SEMAR images demonstrated significantly less metal artifact ($P < 0.001$) and improved visibility of oral cavity and oropharyngeal tumors compared with non-SEMAR images ($P < 0.001$). Interobserver agreement was excellent ($k = 0.88$) for all evaluation criteria. The mean Hounsfield unit (HU), standard deviation (SD), and metal artifact index for the oral cavity SEMAR images were significantly lower than those for non-SEMAR images ($P < 0.001$).

Conclusions

The use of SEMAR, a raw-data metal artifact reconstruction algorithm, can significantly reduce dental artifact on super-high resolution CT imaging of the neck and allow for improved visualization of masses in the oral cavity and oropharynx.

Table 1. Qualitative analysis of non-SEMAR and SEMAR images. SEMAR images demonstrated significantly less metal artifact ($P < 0.001$) and improved visibility of oral cavity and oropharyngeal tumors compared with non-SEMAR images ($P < 0.001$). Interobserver agreement was excellent ($k = 0.88$) for all evaluation criteria.

Qualitative Image Analysis	Mean (SD)		P-values	k-Value
	Non-SEMAR	SEMAR		
Severity of metallic artifacts in the oral cavity and oropharynx	3.50 (0.58)	1.54 (0.65)	<0.001*	0.87
Visibility of oral cavity and oropharyngeal tumor	1.69 (0.74)	3.46 (0.65)	<0.001*	0.88

Figure 1



Table 2. Quantitative analysis of non-SEMAR and SEMAR images. The mean Hounsfield unit (HU), standard deviation (SD), and metal artifact index for the oral cavity SEMAR images were significantly lower than those for non-SEMAR images ($P < 0.001$). For the paraspinal musculature at the level of the hyoid not affected by metal artifacts, no significant differences in mean HU and SD were observed between both images.

Anatomic Structures	NON-SEMAR	SEMAR	P-Values SEMAR vs NON-SEMAR
CT Hounsfield Unit (HU)			
Oral Cavity	363.15 (154.25)	101.05 (55.59)	<0.001*
Paraspinal Musculature	56.79 (14.06)	57.26 (13.98)	0.927
Standard Deviation (SD)			
Oral Cavity	145.58 (47.06)	50.69 (27.05)	<0.001*
Paraspinal Musculature	13.45 (4.58)	13.29 (3.29)	0.709
Metal Artifact Index			
Oral Cavity	144.72 (47.62)	48.05 (28.50)	<0.001*

Figure 1A-B

90y year old female with a history of a T2N0M0 right oral cavity squamous cell carcinoma s/p right floor of mouth resection and submental flap reconstruction. Recent clinical examination revealed a new left floor of mouth lesion which was biopsied and proven to be squamous cell carcinoma. Left floor of mouth necrotic tumor (1A) non SEMAR image and (1B) SEMAR image; evidence for prior right floor of mouth surgical resection is present on both images, however only the SEMAR image demonstrates clearly new enhancing left floor of mouth carcinoma (1B, arrow).

(Filename: TCT_926_SEMAR.jpg)

357

Sinonasal and Orbital NUT Carcinoma

A Kanwar¹, K Traylor¹
¹UPMC, Pittsburgh, PA

Purpose

NUT (nuclear protein in testis) carcinoma, formerly NUT midline carcinoma, is a rare and highly aggressive malignancy, recently defined in the WHO Classification of Head and Neck Tumors, Fourth Edition. Only a few cases have been reported. Patients initially may present with epistaxis, epiphora, nasal congestion, and cranial neuropathies. Orbital involvement at presentation causes eye pain and proptosis. This entity is genetically defined and requires identification of NUTM1 gene rearrangement, most commonly a t(15;19) translocation resulting in production of a NUTM1-BRD4 fusion oncogene. We present an aggressive case of NUT carcinoma confirmed with genetic analysis.

Materials and Methods

A young male with no relevant history presented with facial pain and proptosis. Imaging showed a locally aggressive, FDG-avid mass centered within the right paranasal sinuses and orbit extending to the orbital apex. Pathology showed sinonasal undifferentiated carcinoma. The patient underwent neoadjuvant chemotherapy. However, the disease progressed despite treatment. Given marked rate of disease progression despite multiple treatment attempts, the patient was referred for palliative resection.

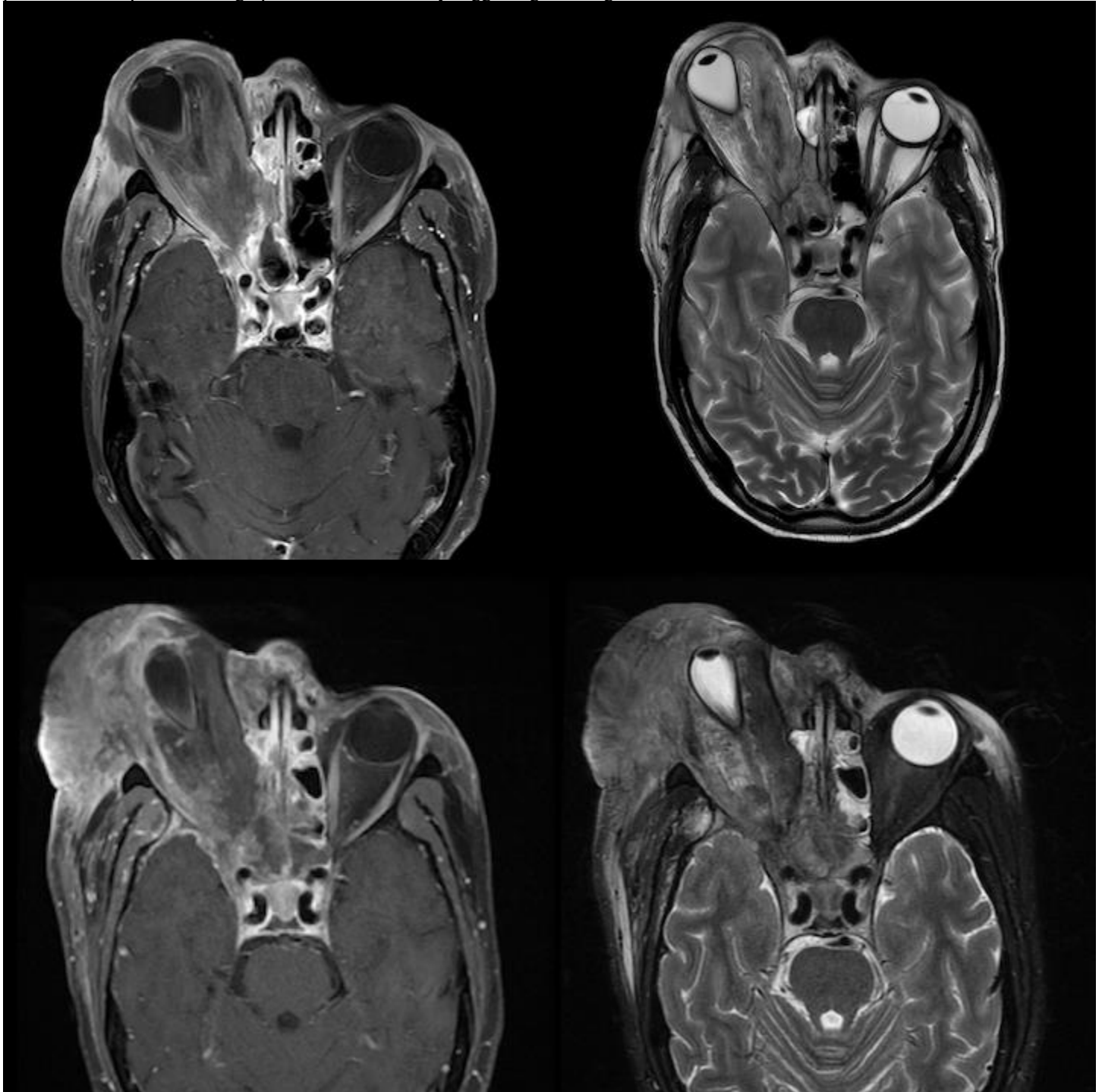
Results

One month after initial workup, contrast-enhanced CT and MR were repeated for pre-operative evaluation. CECT demonstrated a large mass centered in the right orbit displacing the orbital contents with invasion of the globe, anterior cranial base/fossa,

nasopharynx, and paranasal sinuses. The mass also extended into the right facial soft tissues and cavernous sinus. Skull base MRI showed enhancing tumor centered in the right orbit and multifocal extension similar to CT as well as extensive perineural tumor spread along several cranial nerves. Surgical pathology with molecular and genetic analyses were positive for the presence of BRD4-NUTM1 fusion oncogene, thus confirming the diagnosis of NUT carcinoma.

Conclusions

NUT carcinoma is a rare and highly aggressive tumor found in the head and neck. The imaging appearance of NUT carcinoma overlaps with that of other locally aggressive tumors and should be considered in the differential diagnosis of destructive, rapidly progressive head and neck mass. In such cases, molecular and genetic testing can detect the presence of NUTM1 gene rearrangement. As it may be a potentially underdiagnosed malignancy, neuroradiologists can serve an important role in further elucidating the true prevalence and patient demographics of this disease by suggesting this diagnosis.



(Filename: TCT_357_Composite.jpg)

Sinonasal Fungal Infections: The Good, the Bad and the Ugly

V Wu¹, V Lee¹, B Ozgen Mocan¹

¹*University of Illinois at Chicago, Chicago, IL*

Purpose

Fungal colonization of the nasal cavity and sinuses is a common condition, as fungal spores are present throughout the environment and are constantly inhaled. The deposited fungi can cause a wide spectrum of sinonasal disease, depending on the immune status of the patients, that varies from asymptomatic/mild symptomatic cases to severely ill patients with high morbidity and mortality. This exhibit will review the important imaging features and specific differentiating features of noninvasive and invasive fungal infections of the sinonasal cavity with illustrative cases.

Materials and Methods

Fungal colonization of the nasal cavity and sinuses is a common condition, as fungal spores are present throughout the environment and are constantly inhaled. The deposited fungi can cause a wide spectrum of sinonasal disease, depending on the immune status of the patients, that varies from asymptomatic/mild symptomatic cases to severely ill patients with high morbidity and mortality. This exhibit will review the important imaging features and specific differentiating features of noninvasive and invasive fungal infections of the sinonasal cavity with illustrative cases.

Results

N/A

Conclusions

Fungal infections of the nasal cavity and paranasal sinuses can be classified into the non-invasive and invasive forms. In the non-invasive forms, the fungal elements are limited to the involved sinus where they can become trapped in dense sinus sections and form fungus balls (mycetoma) or they may result in a hypersensitivity response to result in allergic fungal rhinosinusitis (AFRS). In invasive disease, there is extension of fungi into the blood vessels and surrounding bone with possible intra-orbital and intracranial extension. These invasive fungal infections are categorized into acute, chronic or chronic granulomatous entities. Although the diagnosis is dependent upon histopathologic demonstration of fungal invasion by biopsy of involved areas, imaging plays a crucial role in early diagnosis of these cases that might present with nonspecific symptoms. More importantly imaging is critical in delineating the extent of the disease for appropriate management and also to assess residual disease after surgery with possible use of diffusion imaging in that context. The invasive and non-invasive forms of fungal rhinosinusitis have characteristic imaging features that can help establish the diagnosis and can guide the treatment especially in the setting of invasive disease.

748

Spinal Phosphaturic Mesenchymal Tumor

G Sistani¹, W Ng¹, B Davis¹, M Sharma¹

¹*London Health Science Center, LONDON, ON*

Purpose

Phosphaturic mesenchymal tumor (PMT) is a rare mesenchymal tumor that its diagnosis is often delayed due to being relatively unknown (1). The purpose of this study is to increase familiarity with this disease, its clinical and imaging features, and diagnosis.

Materials and Methods

The case report is regarding a 70-year-old female patient with a history of unsteady and shuffling gait and generalized body pain who was referred to the neurology clinic for assessment of possible parkinsonism.

Results

Her history and physical examination were atypical for Parkinson's disease. As a result, the patient underwent MR head and spine for further evaluation. MR spine showed an intradural avidly enhancing mass involving filum terminale in the sacral spinal canal (Figure 1). The patient underwent a CT guided biopsy of the intradural sacral lesion, and pathology showed: "fibro-osseous lesion of neural axis with no evidence of malignancy." Meanwhile, the patient developed progressive urinary incontinence and bilateral heels, ribs, and left hip pain. Further work-up with bone and CT scan showed multiple fractures involving bilateral ribs, left femoral neck and bilateral calcaneus. As a result, the decision was made to proceed with surgery to establish a definitive diagnosis and also to decompress the sacral nerve roots to determine whether that would improve her bladder function. The surgical pathology revealed a PMT unexpectedly. She showed a drastic improvement with almost complete resolution of multifocal skeletal pain and gait improvement.

Conclusions

PMT can involve soft tissue or bone in any part of the body (2). The bone lesions are typically osteolytic, with a narrow zone of transition on the CT scan (3). The soft tissue type of PMTs are typically isointense on T1-weighted sequence, hyperintense on T2-weighted sequence and demonstrate avid enhancement (3). PMT causes diffuse muscle pain and weakness and tumor-induced osteomalacia (TIO) secondary to hypophosphatemia (4). Early diagnosis of disease and tumor excision leads to near-complete resolution of symptoms and biochemical abnormalities (5).

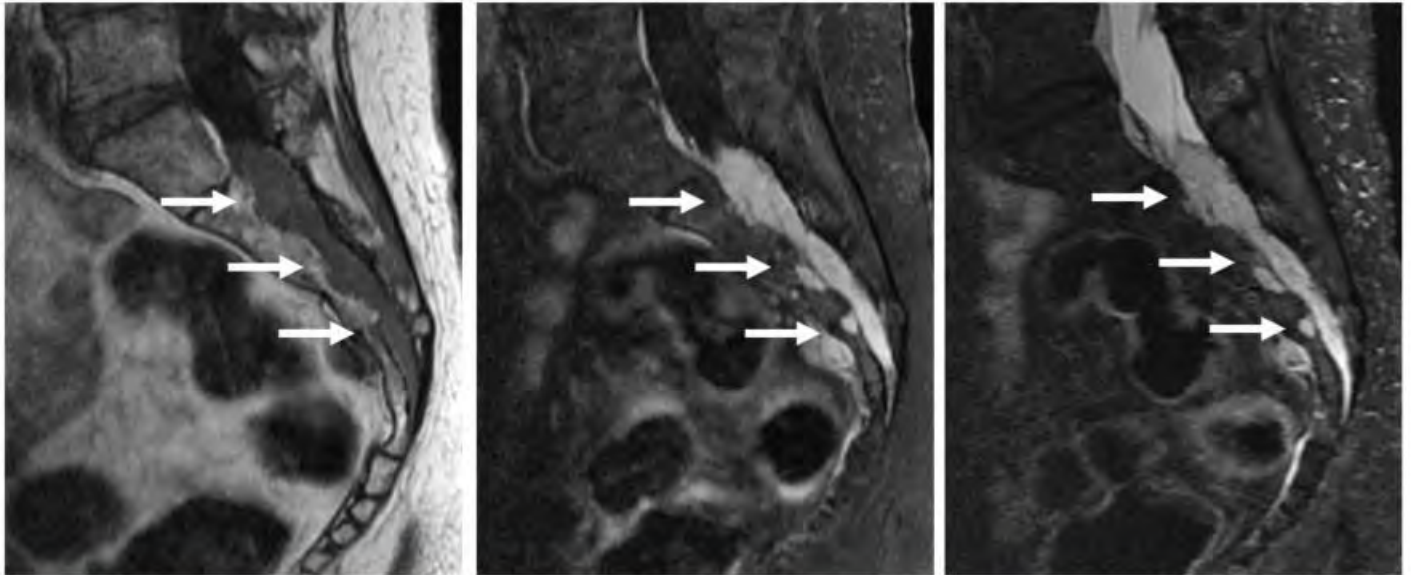


Figure 1. Selected T1-weighted, T1-weighted with fat saturation and contrast, and FIR images. There is a lobulated intradural avidly enhancing mass filling the sacral spinal canal and extending through the anterior sacral foramina.

(Filename: TCT_748_PMT.jpg)

1343

Staging in Head and Neck cancer, value of dual-energy CT

A Postma¹, B Faes¹, E Roele¹

¹MUMC+, Maastricht, The Netherlands

Purpose

Dual-energy CT (DECT) is increasingly used in the clinical situation, especially outside the head and neck region. Quality is as good as conventional CT and dose is considered equal. Early publications discussed the additional value of DECT in the staging of laryngeal cancer. We investigated whether the additional use of DECT derived virtual monochromatic and iodine fusion images changes the staging in head and neck carcinoma

Materials and Methods

Between January 2016 and October 2020 patients with a suspected primary head-neck carcinoma from a tertiary referral center underwent tumor staging with dual-energy CT. Contrast enhanced DECT was performed with a dual-source, dual energy scanner (Siemens Healthcare) with either 80-140 kVp (Siemens Flash) or 80-150 kVp (Siemens Force). Images were reconstructed with a weighted average to simulate SECT-like images, reconstructed with a soft tissue kernel. Using DECT kernels optimal virtual monoenergetic images were reconstructed for 40 keV (optimal CNR from previous study) as well as iodine fusion images with iodine overlay (IO). Radiological Tumor staging was noted as T-stage at SECT-like images alone, with additional 40 keV VMI and iodine fusion images. Assessment was done by an experienced head and neck radiologist.

Results

163 patients were included, 131 males and 47 females, mean age was 68 yr (+/-10). Tumor locations were as follows: oropharynx (8), oral cavity (36), hypopharynx (13), supraglottis (29), glottis (83), and other (9). T stage changed in 16/163 patients after additional use of VMI and in 25/163 in IO. This was at hypopharynx (5), supraglottis (1) and glottis (14) location. This could either be an up- or downstage.

Conclusions

Additional evaluation of DECT derived optimal VMI and iodine fusion images can increase confidence in tumor delineation, however in experienced hands addition of DECT postprocessing only changed tumor staging in a small amount of patients. Determination of absence or presence of cartilage invasion can be easier seen with DECT postprocessing.

747

Standardized Therapy Monitoring in Patients with Spontaneous Intracranial Hypotension based on the Brain SIH Score

T Dobrocky¹, E Piechowiak²

¹Inselspital, Bern, Switzerland, ²Inselspital, Bern, Bern

Purpose

To assess suitability of the brain magnetic resonance imaging (MRI)-based, SIH score (bSIH) for quantitative monitoring of SIH patients with a proven spinal cerebrospinal fluid (CSF) leak after microsurgical closure of the underlying dural breach, and correlation of the score with the clinical presentation.

Materials and Methods

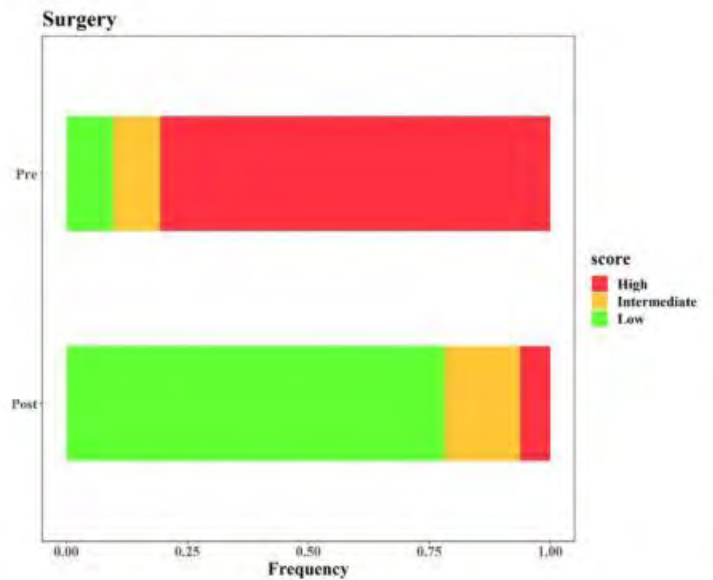
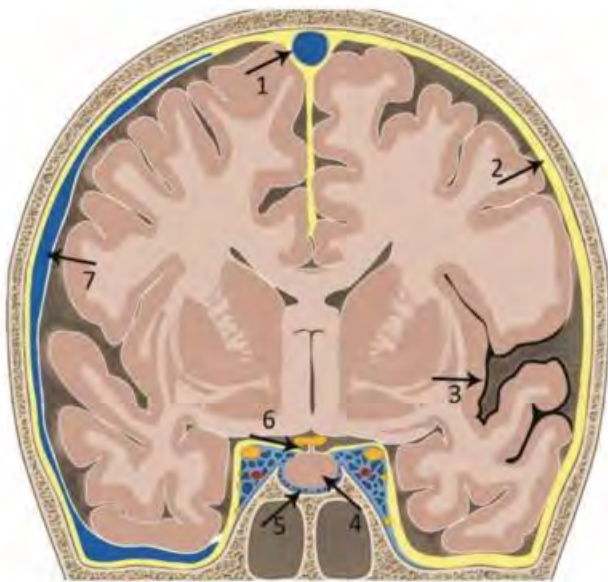
This retrospective cohort study included consecutive SIH patients with a proven spinal CSF leak, investigated at our department from January 2012 to March 2020. Patients with missing brain MRI before or after therapy, and patients with post-puncture headache were excluded. The bSIH score integrates 6 imaging findings; 3 major (2 points each) and 3 minor (1 point each), and ranges from 0 to 9, with 0 indicating very low and 9 very high probability of spinal CSF loss. The score was calculated before and after surgical treatment of the underlying CSF leak. In addition, headache intensity was registered on a numeric rating scale (NRS) (range: 0–10).

Results

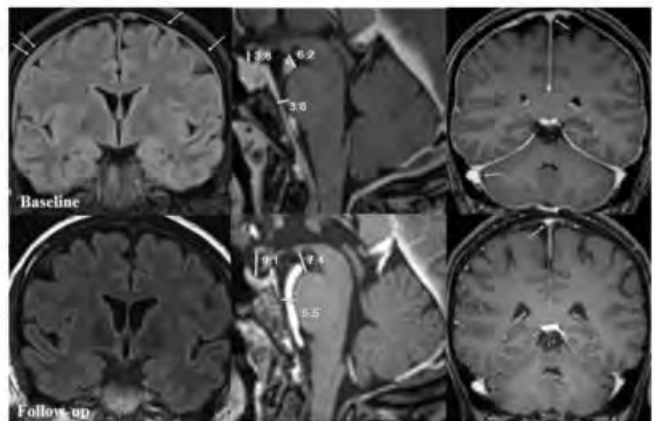
Fifty-two SIH patients (35 [67%] female; mean age, 45.3 years) with a proven spinal CSF leak were included. The mean bSIH score decreased significantly from baseline to after surgical closure of the underlying dural breach (6.9 vs 1.3, $P < .001$). This was paralleled by a decrease in the NRS score (8.6 vs 1.2, $P < .001$).

Conclusions

The bSIH score is a simple and objective tool for therapy monitoring of patients with spinal CSF loss syndrome and a valuable indicator of recovery. Its rapid decrease after surgical closure of the underlying spinal dural breach indicates restoration of an equilibrium within the CSF compartment and correlates well with the clinical presentation.



	Score	
Major	Engorgement venous sinus	2
	Pachymeningeal enhancement	2
	Suprasellar cistern (≤ 4 mm)	2
Minor	Subdural fluid collection	1
	Prepontine cistern (≤ 5 mm)	1
	Mamillopontine distance (≤ 6.5 mm)	1



(Filename: TCT_747_ASNR.jpg)

682

Structural and Functional Neuroimaging Correlates of Reading and Screentime Habits in Developing Adolescents

S Pan¹, A Rauschecker¹, M OLARU¹, P Nédélec¹, R Nillo¹, L Sugrue¹
¹University of California, San Francisco, San Francisco, CA

Purpose

Screen time and digital media have become an integral component of daily life, and their influence on neurodevelopmental outcomes in developing adolescents is a significant public health concern (1). Similarly, reading is perceived as a beneficial habit but the extent and mechanisms through which reading positively influences brain development are not fully understood (2). In this study, we build on our previous findings linking these habits to changes in cortical thickness and cognition to further interrogate their effects on diffusion and functional MRI parameters.

Materials and Methods

The Adolescent Brain Cognitive Development (ABCD) study is a nationwide, longitudinal study following over 11,000 developing adolescents from ages 9 – 10 years old who undergo yearly structural and functional MRI scans and psychosocial surveys (3,4). Daily hours television watching, daily hours of reading, and history of reading in years were used as independent variables to generate mixed effects linear models examining their relationships with structural/diffusion/functional MRI parameters and performance on the NIH toolbox cognition battery while controlling for demographic and socioeconomic factors.

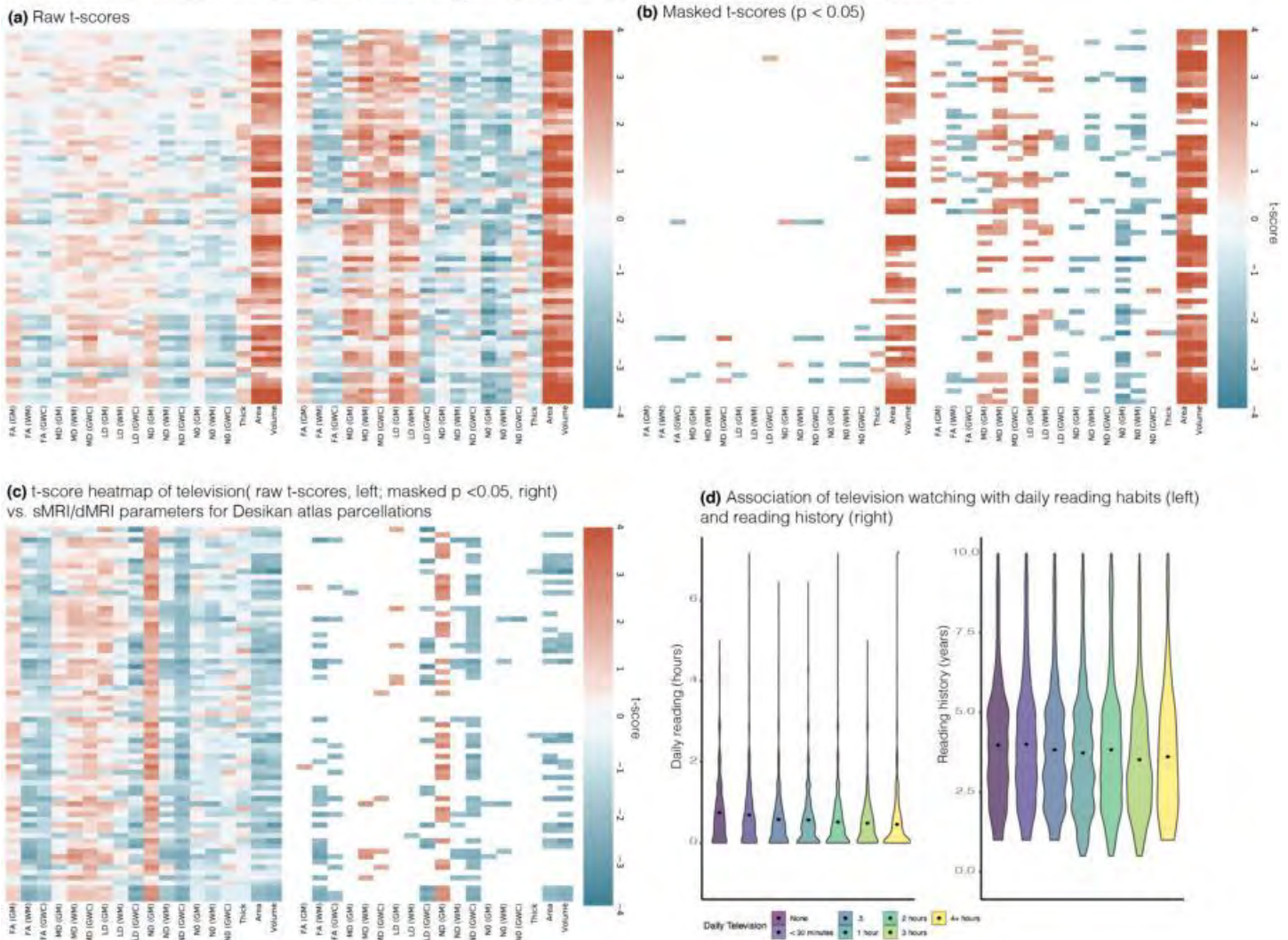
Results

Increased daily reading and reading history are associated with increases in brain volume and fiber tract volume (a,b). Conversely, increased daily television watching is associated with reductions in brain volume, fiber tract volume, white matter integrity, and resting state connectivity (c). Performance on NIH cognition toolbox tests is negatively associated with television watching and positively associated with reading habits and reading history. Television watching is inversely related to daily reading and reading history, but the relationships of television or reading with structural MRI parameters and cognitive performance remain when modeling the opposing variable as a random effect (d).

Conclusions

We expand our previous findings by evaluating the effects of reading and television watching on diffusion MRI parameters and resting state functional connectivity. Furthermore, within-subject analysis reveals that increased television watching is associated with decreased reading. However, television, daily reading, and reading history all exert independent effects on neuroimaging parameters and cognition. These findings collectively advocate for initiatives to limit screen time and encourage pleasurable reading amongst developing children.

t-score heatmap of reading (daily hours, left; years, right) vs. sMRI/dMRI parameters for Desikan atlas parcellations



(Filename: TCT_682_2021_ASNR_reading.jpg)

619

Structural MRI analysis of adaptor protein complex 4 – associated hereditary spastic paraplegia

E Yang¹, G Geisel², M Sahin², D Ebrahimi-Fakhari²

¹Boston Children's Hospital, Jamaica Plain, MA, ²Boston Children's Hospital, Boston, MA

Purpose

The hereditary spastic paraplegias (HSPs) include 80 monogenic disorders which collectively represent the most common cause of inherited spasticity. Bi-allelic loss of function mutations in subunits of the adaptor protein complex 4, involved in membrane protein trafficking through the trans-Golgi network, represent a recently described cause of HSP (SPG47, SPG50, SPG51, and SPG52) featuring early-onset progressive spasticity, developmental delay, postnatal microcephaly, and increased risk of epilepsy. We sought to describe brain imaging features of AP-4 associated hereditary spastic paraplegia (AP-4-HSP) in the largest cohort so far assembled.

Materials and Methods

Subjects were recruited through the AP-4-HSP International Registry yielding 65 subjects with brain MRIs suitable for review. Myelination status, biometry of critical structures (periatrinal white matter, callosum, brainstem), and congenital structural abnormalities were assessed for each subject with reference to age-matched normative data. To additionally assess the specificity of anterior commissure anomalies for AP-4-HSP, 16 consecutive premature infants identified in our local database were reviewed.

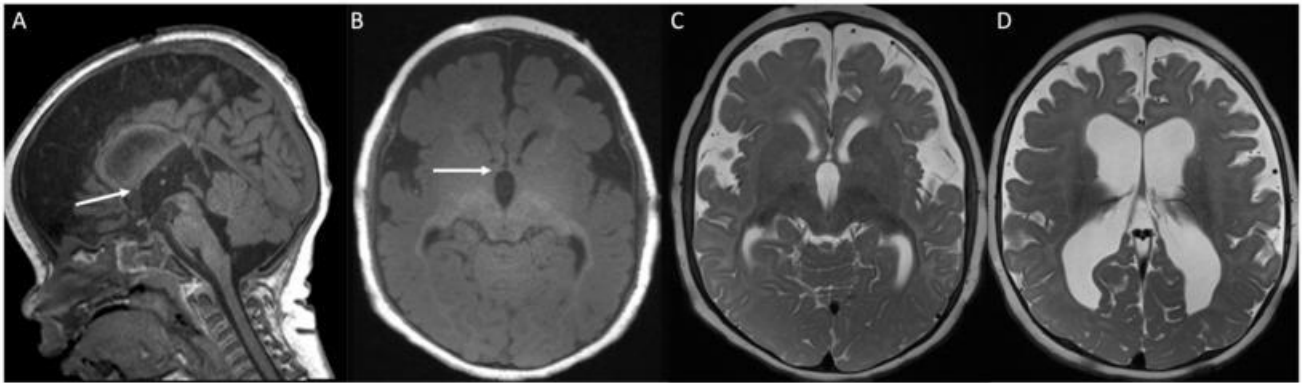
Results

Myelination was delayed in 17 and normal in 48 subjects at the time of most recent imaging. Where serial imaging was available, 3 of 6 delayed subjects demonstrated myelination progress, and 4 of 13 normal subjects demonstrated myelination delay on an earlier study. Dysmyelination or gliosis was present in the periventricular white matter of 33 subjects and in a wider anatomic distribution for 17 subjects. Callosal abnormalities were common: genu thickness, splenium thickness, and AP dimension were less than the 3rd

percentile for age in 42%, 91%, and 53% of subjects. The callosal thinning corresponded to depressed periaxial white matter thickness ($3.7 \pm 1.4 \text{ mm}$) and mild ventriculomegaly (frontal occipital horn ratio of 0.42 ± 0.04). Congenital structural abnormalities in our dataset included polymicrogyria/dysgyria in 25% of subjects, gray matter heterotopia in 1 case, and an undiscernible anterior commissure in 77% of subjects. In premature control subjects, the anterior commissure anomaly was not found in any subject ($p < 0.0001$).

Conclusions

In AP-4-HSP, callosal anomalies, depressed periaxial white matter volume, myelination delays, abnormal gyration, and an undetectable anterior commissure were common findings. The thin anterior commissure may implicate this structure in the pathogenesis of this form of HSP.



Typical AP-4-HSP patient at 8 months (subject 097). Sagittal T1 MPRAGE (A) and axial reformat (B) demonstrate AP foreshortening and posterior-predominant thinning of the corpus callosum as well as a thin anterior commissure (arrow) and delayed myelination for age. Axial T2 images at two levels (C,D) demonstrate depressed white matter volume (posterior > anterior) and perisylvian polymicrogyria.

(Filename: TCT_619_AP-4-HSP-examplecopy.jpg)

545

Subacute Combined Degeneration Imaging Pattern as seen in Metabolic & Toxic Myelopathies, and its Mimics

G Mittl¹, R Kurtz²

¹University of Pennsylvania, Philadelphia, PA, ²N/A, N/A

Purpose

Educational Objectives: 1. To describe the classic B12 dysmetabolic pathways associated with subacute combined degeneration (SCD), their clinical manifestations and imaging findings. 2. To present additional dysmetabolic pathways, resulting from Vitamin E and copper deficiencies, that also produce a SCD imaging pattern. 3. To increase understanding of the prevalence and causes of these disorders and their clinical management. 4. To review the radiologist's role in confirming the clinical diagnosis of SCD and expediting management. Summary: Subacute combined degeneration (SCD) is the most common metabolic disorder affecting the spinal cord and is the result of a vacuolar myelopathy. Vitamin B12 deficiency is recognized as the most common cause of SCD and has characteristic findings on magnetic resonance imaging, notably T2 hyperintensity of the posterior columns ("inverted 'V' sign"). The same metabolic

pathway affected by Vitamin B12 deficiency may also be affected by Vitamin B9 (folate) deficiency or in nitrous oxide toxicity (Image A), resulting in identical MR imaging findings. An SCD imaging pattern is also seen in copper and Vitamin E deficiencies, as well as zinc excess, although the molecular pathways are distinct. We review the metabolic pathways associated with the SCD imaging pattern, the overlapping MR findings of the different entities, and describe SCD mimics that merit consideration in a patient presenting the characteristic clinical syndrome. A sample of cases that we present are: • A 70-year-old female with pernicious anemia who developed rare permanent neuroimaging sequelae of SCD (Image B) • A 55-year-old female who presented with worsening lower extremity paresthesias and a SCD imaging pattern and was subsequently found to have copper deficiency (Image C) • A 67-year-old male with myelomalacia of the cord as a result of severe cervical stenosis that mimics the posterior and lateral column involvement of SCD (Image D) Additionally, we discuss the radiologist's role in confirming a metabolic or toxic cause of the patient's clinical presentation and our role in the expeditious management of a largely reversible cause of myelopathy.

Materials and Methods

N/A

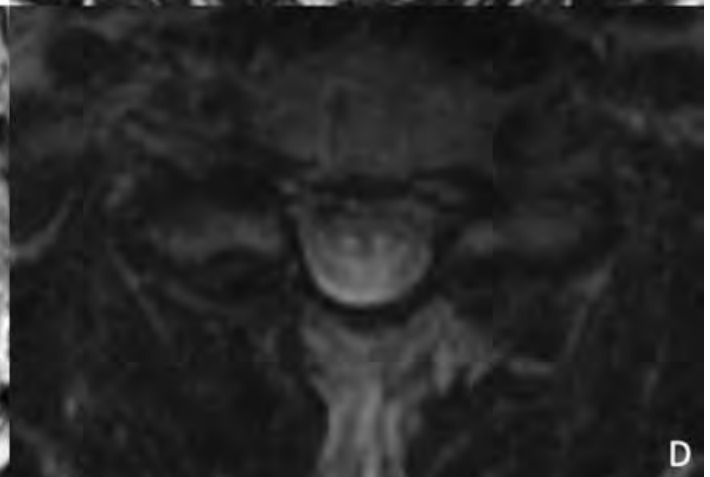
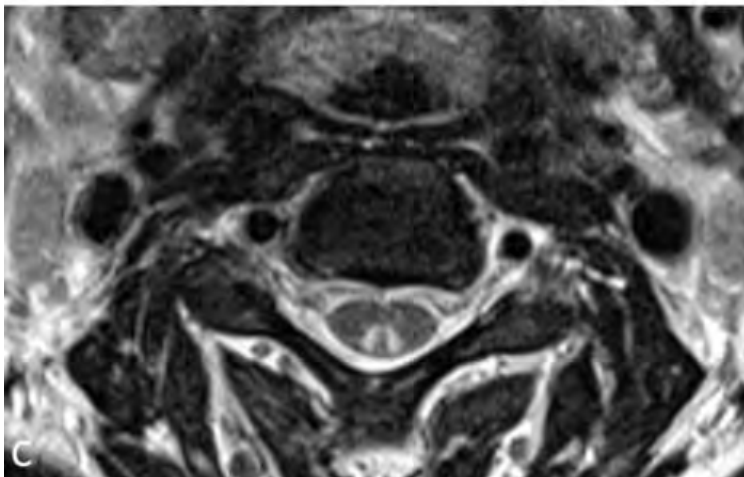
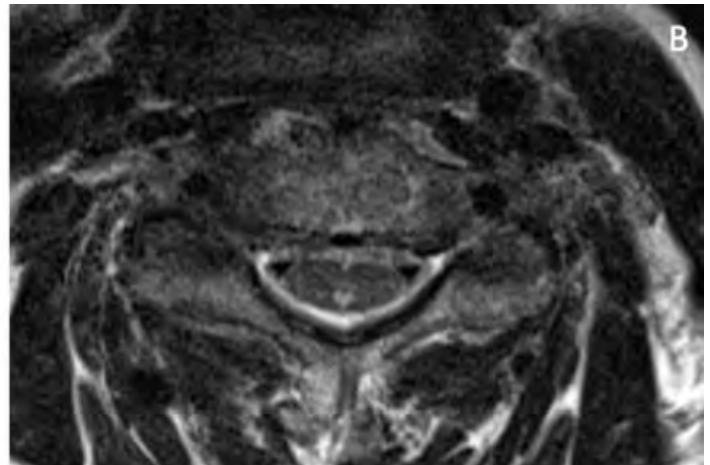
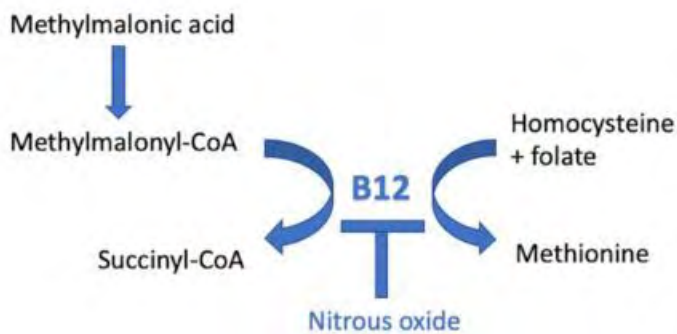
Results

N/A

Conclusions

N/A

A



(Filename: TCT_545_ASNRAbstractFigure102920.jpg)

848

Successful use of percutaneous interspinous spacers and adjunctive spinoplasty in a 9 year cohort of patients

I Gil¹, A De Vivo², L Manfre³, H Alqatami⁴, J Hirsch³

¹Centro Hospitalar Lisboa Ocidental - CHLO, Lisboa, Portugal, ²I.O.M., Catania, ITALY, ³N/A, N/A, ⁴Institute of Hamad Medical Corporation, doha, qatar

Purpose

Lumbar spinal canal stenosis and lumbar spinal foraminal stenosis are common, degenerative pathologies which can result in neurogenic claudication trophy. and have a negative impact on function and quality of life. Percutaneous interspinous devices are a recently-developed, minimally-invasive, alternative treatment option. This study details a 9 year single-centre experience with

percutaneous interspinous devices and examines the complementary use of spinous process augmentation (spinoplasty) to reduce failure rates.

Materials and Methods

A retrospective cohort assessment of 800 consecutive patients who presented to a specialized spine hospital was performed with 688 receiving treatment. Inclusion was based on high-grade stenosis, failure of conservative management and electromyography. 256 had percutaneous interspinous devices alone while 432 had concurrent polymethyl methacrylate augmentation of the adjacent spinous processes. The patients were followed up at 3 and 12 months using the Zurich claudication Questionnaire and Oswestry Disability index.

Results

Both groups showed marked improvement in the patients' Zurich claudication Questionnaire scores (3.2 to 1.3) and Oswestry Disability index scores (32 to 21), with strong satisfaction results (1.7). The symptom recurrence rate from complications for the group which received concurrent spinous process augmentation was reduced when compared with the percutaneous interspinous devices alone cohort (<1% vs 11.3%).

Conclusions

This study demonstrates the efficacy of percutaneous interspinous devices in treating lumbar spinal stenosis. It also provides evidence that concurrent spinous process augmentation reduces the rate of symptom recurrence.

294

Supradental Fat Pad Effacement on Cervical Spine CT in Adults Trauma Patients: A Sign of Tectorial Membrane Ligamentous Injury

P Fiester¹, D Rao², M Jenson², E Soule²

¹N/A, N/A, ²University of Florida College of Medicine Jacksonville, Jacksonville, FL

Purpose

The supradental recess is a small, predominantly fat-filled recess superior to the atlanto-axial joint and inferior to the basion of the clivus that contains a small venous plexus. The posterior boundary of the supradental recess is formed by the tectorial membrane, a stabilizing ligament of the craniovertebral junction. The purpose of our study was to examine the imaging appearance of the supradental recess on cervical CT in patients with tectorial membrane injury.

Materials and Methods

Adult patients with tectorial membrane injury were identified utilizing keyword searches of radiology reports using Nuance mPower software between January 2012 and July 2020. Two neuroradiologists evaluated the cervical CT exams of these patients for supradental fat pad effacement and obtained Hounsfield Unit measurements within the supradental recess. The integrity of the osteoligamentous structures of the craniovertebral junction was recorded along with demographic information, clinical history, surgical management, and global outcome.

Results

Sixteen adults were diagnosed with tectorial membrane injury on cervical MRI. All patients with a visible supradental recess demonstrated fat pad effacement and hyperdense attenuation consistent with hematoma formation (median Hounsfield Units of 69). Concomitant osteoligamentous injuries of the craniocervical junction were common. Half the patients required occipital cervical fusion for craniocervical junction instability. Clinical outcomes were variable with two deceased patients, one quadriplegic patient, and four patients experiencing chronic neurologic deficits.

Conclusions

The 'supradental recess sign,' defined as hematoma formation in the supradental recess with effacement of the supradental fat pad is a reliable indicator of tectorial membrane injury in adult trauma patients. This may indicate major craniocervical junction injury and instability requiring occipital cervical fusion.



Sagittal CT reconstruction (A) of the craniocervical junction demonstrating effacement of the fat pad and increased attenuation within the supradental recess (white arrow). Sagittal T1 weighted MRI (B) demonstrating effacement of the supradental fat pad (white arrow). Sagittal T2 and STIR weighted MRI (C, D) demonstrating edema and blood products within the supradental recess with a type 2 subclival tectorial membrane tear at the level of the dens (white arrows). Additional tears in anterior longitudinal ligament at C2 (white dashed arrow) with a large prevertebral effusion (red star) and mid cervical interspinous ligaments are also noted.

(Filename: TCT_294_supradental_ASNR.jpg)

1202

SWI as Prognostic Factor in Stroke-like Migraine Attacks After Radiation Therapy (SMART) syndrome

Y Ota¹, R Kurokawa¹, A Baba¹, T Moritani¹, G Bathla², A Capizzano¹

¹University of Michigan, Ann Arbor, MI, ²University of Iowa Hospitals and Clinics, Iowa City, IA

Purpose

To assess the correlation between the clinical outcomes of SMART syndrome and imaging findings.

Materials and Methods

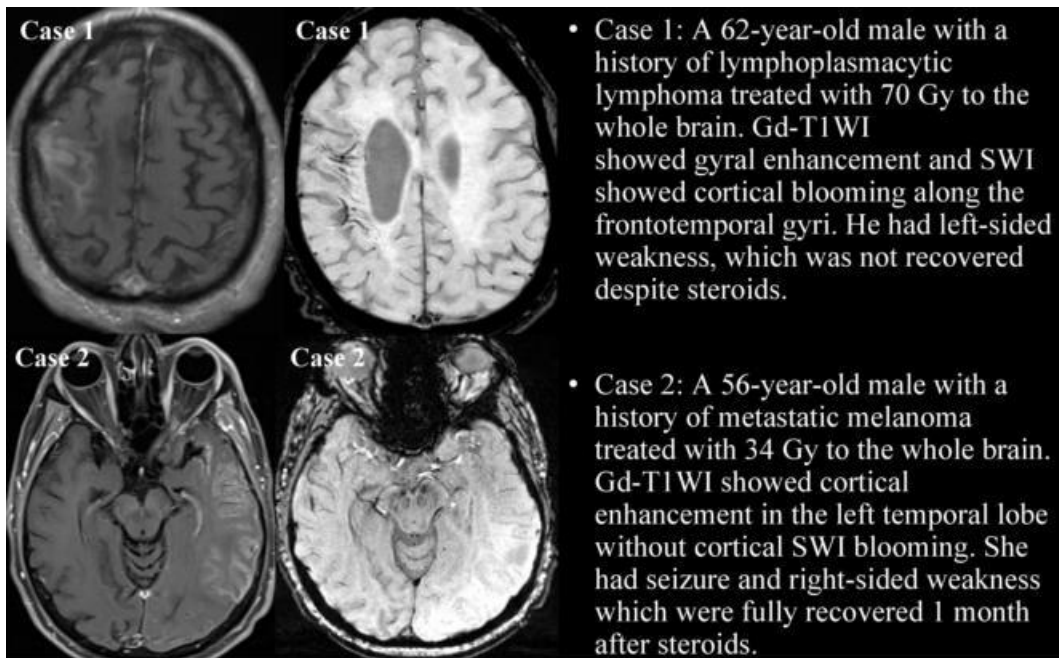
We retrospectively reviewed the clinical manifestations and imaging findings of 17 patients with stroke-like migraine attack after radiation therapy (SMART) syndrome from 2014 to 2020. Patients were diagnosed with SMART syndrome by: 1. Past history of radiation therapy to the brain, 2. New onset of neurologic symptoms, typically seizures or focal neurologic deficit in conjunction or not with migraine starting years after brain irradiation, 3. MR imaging findings characteristic of SMART syndrome, 4. Exclusion of other diagnoses on clinical and imaging follow-up, particularly tumor recurrence and stroke, and 5. At least partial reversibility on follow up. Patients' demographics, original pathologic diagnoses, radiation therapy (RT) dose, and its distribution, concurrent chemotherapy, time since radiation, clinical and MRI features of SMART attacks, were reviewed. MRI features of SMART syndrome included gyral enhancement, cortical or white matter edematous change, restricted diffusion, and cortical SWI signal blooming in the acute lesions. Patients were scanned in 1.5T or 3.0T MRI scanners with the following clinical MRI sequences: T1WI, T2WI, FLAIR, DWI, Gd-T1WI, SWI, and in selected cases DSC-or DCE-MR perfusion, and MR spectroscopy. The patient sample was divided into a fully clinically recovered group (FR) and a not fully clinically recovered group (NR). Age, total RT dose, and time since RT were compared by Mann-Whitney U test, while categorical variables such as sex and MRI features were compared by Fisher's exact test.

Results

FR (n=9; age range; 35-56 years, 2 females) received RT for metastatic melanoma (2 cases), anaplastic oligodendroglioma, teratoma, pineoblastoma, DLBCL, oligodendroglioma, and anaplastic astrocytoma, and medulloblastoma. NR (n=8; age range; 29-69 years, 4 females) received RT for glioblastoma (2 cases), medulloblastoma, meningioma, pineal teratoma, lymphoplasmacytic lymphoma, DLBCL, and nasal cavity squamous cell carcinoma. There was a significant difference between the 2 groups in the presence of cortical SWI signal blooming in NR vs FR (FR:2/9 positive vs NR: 8/8 positive; P=0.003). There was no significant difference in age, sex, RT dose, time since RT and other MRI features between 2 groups.

Conclusions

Cortical SWI blooming, likely reflecting parenchymal hemorrhage, may represent a negative prognostic factor in SMART syndrome.



(Filename: TCT_1202_SMRTsyndrome.jpg)

989

Systematic Review of Radiological Cervical Foraminal Grading Systems

J Meacock¹, M Schramm², S Selvanathan², S Currie³, D Stocken⁴, D Jayne⁵, S Thomson²

¹Leeds Teaching Hospital Trust, Leeds, United Kingdom, ²Leeds Teaching Hospital Trust, Leeds, West Yorkshire, ³Leeds Teaching Hospitals, Leeds, West Yorkshire, ⁴University of Leeds, Leeds, West Yorkshire, ⁵Leeds Teaching Hospitals NHS Trust, Leeds, West Yorkshire

Purpose

To evaluate the existing radiological grading systems that are used to assess cervical foraminal stenosis. The importance of imaging the cervical spine using CT or MRI in evaluating cervical foraminal stenosis is widely accepted however there is no consensus for standardised methodology to assess the compression of the cervical nerve roots.

Materials and Methods

A systematic search of Ovid Medline databases, Embase 1947 to present, Cinahl, Web of Science, Cochrane Library, ISRCTN and WHO international clinical trials was performed for reports of cervical foraminal stenosis published before 01.02.2020. In collaboration with the University of Leeds a search strategy was developed.

Results

6952 articles were identified with 59 included. Reports involved multiple imaging modalities, standard axial and sagittal MR imaging is used the most. The most mature grading for cervical foraminal stenosis is described by Kim et al. 2015 and Park et al. 2013.

Conclusions

Imaging of the cervical nerve root canals is mostly performed using MRI and is reported using subjective terminology. The Park, Kim and Modified Kim systems for classifying the degree of stenosis of the nerve root canal have been described. Clinical application of these scoring systems is limited by their reliance on non-standard imaging (Park), limited validation against clinical symptoms and surgical outcome data. Oblique fine cut images derived from three dimensional MRI datasets may yield more consistency, better clinical correlation, enhanced surgical decision making and outcomes.

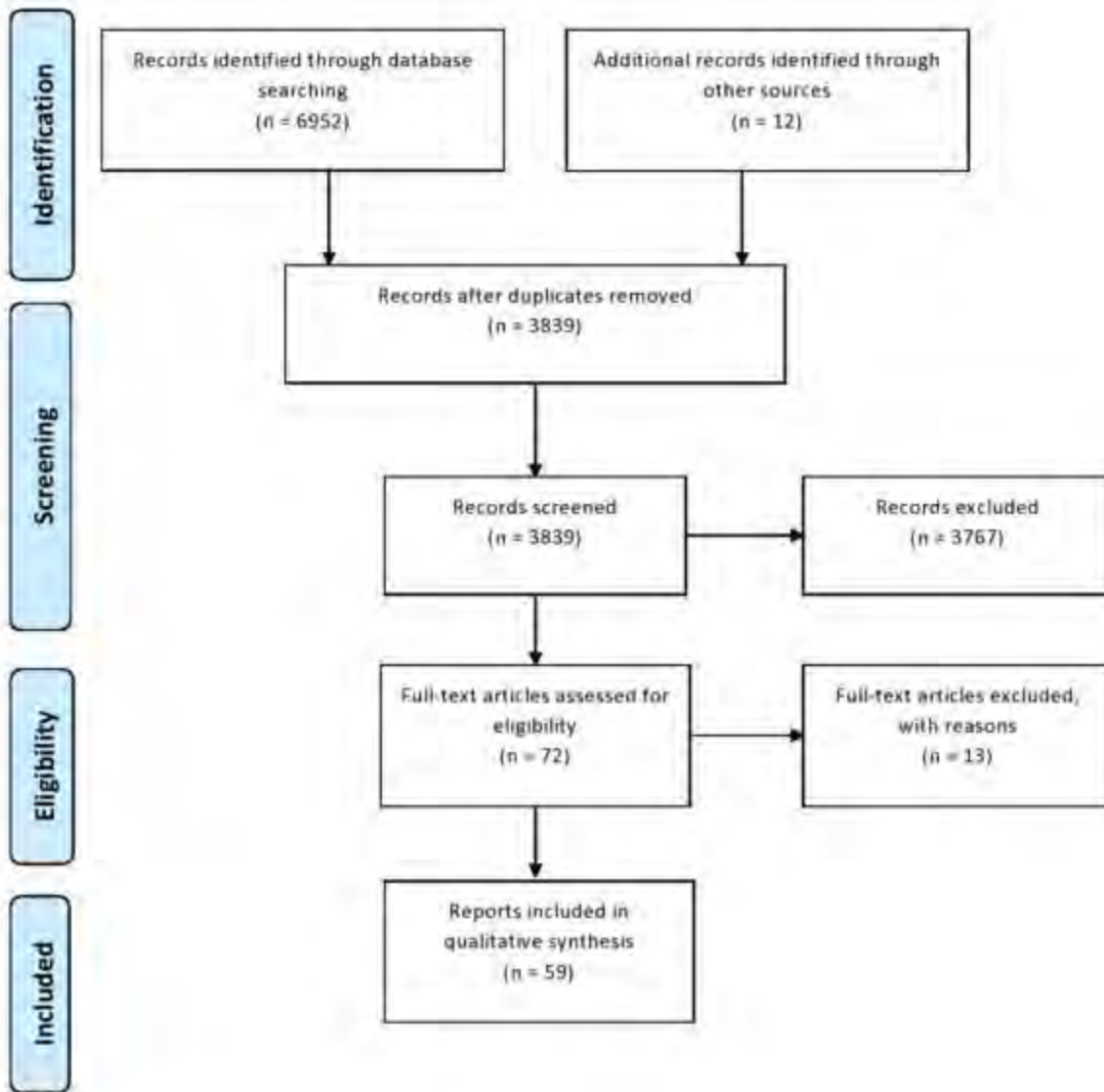


Figure 1. Prisma diagram depicting the flow of information through the different phases of the systematic review

Systematic Review of Radiological reference standards used for evaluating treatment response biomarkers in Gliomas

A Mirchandani¹, A Al Busaidi², T Booth³

¹Cambridge University Hospitals NHS Foundation Trust, Cambridge, Cambridgeshire, ²Kings College Hospital, London, United Kingdom, ³Kings College London, London, London

Purpose

The aim of this systematic review was to assess whether appropriate radiological reference standards have been used for the evaluation of monitoring (treatment response) biomarkers.

Materials and Methods

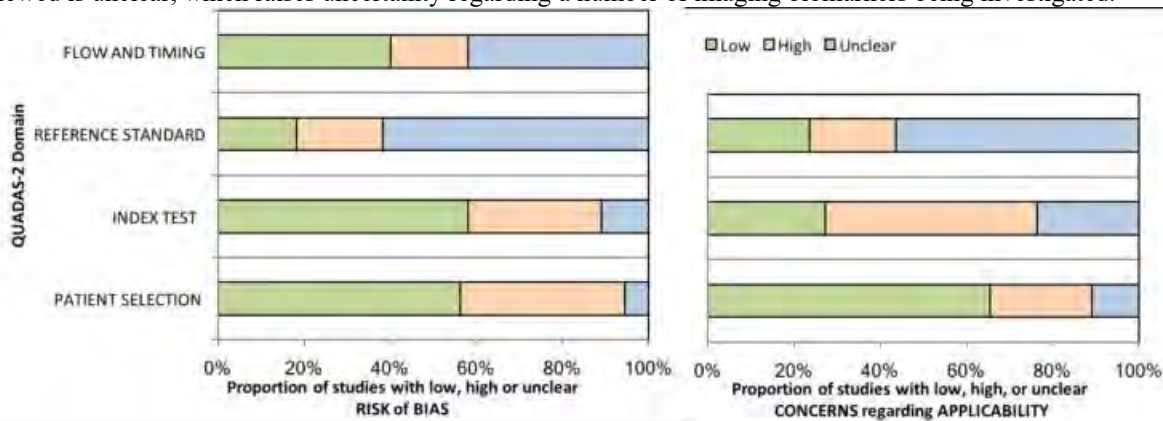
PRISMA-DTA methodology was followed. The definition of an appropriate reference standard was based on the 2010 Response-Assessment in Neuro-oncology (RANO) criteria, incorporating more recent evidence such as pseudo progression occurring within 6 months rather than 12 weeks. The index test (ie. monitoring biomarkers under evaluation) included CEST measurements, perfusion based markers, and diffusion weighted markers. Articles published between 01/2016- 05/2020 were searched using OVID Embase, OVID MEDLINE (includes PUBMED) and the Cochrane Register. Case studies and review studies were excluded. Search criteria was refined by authors to widen the number of eligible studies by using a combination of MESH terms and subject headings. Included studies used radiological response in human subjects to assess response to gliomas/glioblastomas. Given the aim of this systematic review was to evaluate imaging reference standards, all studies with histopathological reference standards alone were excluded. Two hundred and seventy-two abstracts were screened by two independent authors at different time points to assess for review eligibility. Data was extracted from fifty-five studies using predefined data fields. Data was appraised using a tailored QUADAS-2.

Results

Notable ambiguity in methodology used to assess radiological response is noted amongst studies. In particular, studies were unclear about defining measurable disease (62%), and the quantitative percentage changes (56%) used in the definition of progression/partial response. Nearly half of the studies analysed do not account for drug-related or surgery-related confounding factors when assessing radiological response. 19% of the literature did not follow up patients for long enough to differentiate between pseudo progression and progression. In 42% of studies, it is unclear how long patients diagnosed with progression/pseudoprogression were followed up for.

Conclusions

Despite the challenges raised with qualitatively assessing diagnostic validity, the RANO guidelines provide key domains that should be addressed to reduce false positives. The methodology to validate radiological progression in gliomas in 40-60% of the literature reviewed is unclear, which raises uncertainty regarding a number of imaging biomarkers being investigated.



(Filename: TCT_1325_diagram1.jpg)

Targeting the VIM/DRT for Essential Tremor using MR Susceptibility Imaging with Short Echo Time (MR-SISET): Pilot Study

S Chung¹, T Shepherd¹, P Storey¹, A Mogilner², Y Lui¹

¹NYU Grossman School of Medicine, New York, NY, ²NYU Lagone Health, New York, NY

Purpose

Essential tremor (ET) is the most common movement disorder, affecting ~10 million Americans. For medically refractory ET, neurosurgical treatment may be an option. Surgical interventions generally target the ventral intermediate nucleus (VIM) of thalamus and/or the dentato-rubro-thalamic tract (DRT) [1]. Our previous work has demonstrated the ability of MR susceptibility imaging with short echo time (MR-SISET) to directly visualize intra-thalamic structure [2]. Here we validate the position of the potential VIM/DRT target region on MR-SISET map using DTI tractography.

Materials and Methods

We studied 4 healthy individuals (age, 23-41 years). MR-SISET imaging was performed using a 3D multiple-GRE imaging on 3T MR scanners (Skyra/Prisma, Siemens) (FOV=220x170x75mm³, 1.25mm-isotropic resolution, FA=22, TR=92ms, 20 TEs=1.90:2.32:45.98ms). MR-SISET maps were generated by using the MEDI toolbox [3]. For validation, DTI was performed with b=2.5ms/ μm^2 with 60 diffusion directions using multiband (factor=2) echo-planar imaging (FOV=220x220mm², 2.5mm-isotropic resolution, TR/TE=4.9s/95ms, GRAPPA=2). The position of the intended target was selected on MR-SISET map where the two (red/blue) lines crossed (Fig.1). To validate the position, its cortical projections to the motor cortex were generated using MRtrix3 [4].

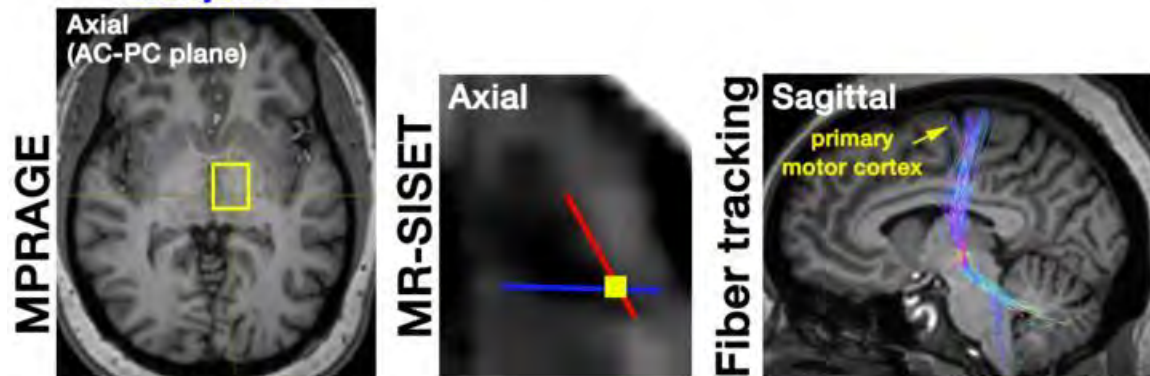
Results

In all 4 subjects, the VIM/DRT region is clearly visualized as relatively low negative susceptibility signal (i.e., diamagnetic susceptibility) on MR-SISET map (dark region in Fig.1). Fiber tracking further confirms tracts from the identified target region (yellow voxel) extend to the primary motor cortex.

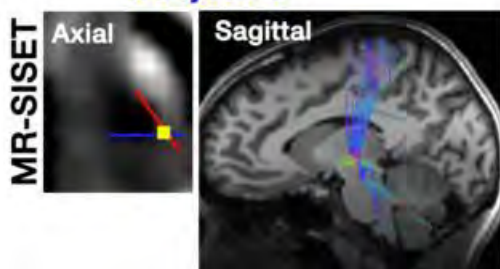
Conclusions

MR-SISET imaging provides direct visualization of the VIM/DRT in healthy controls. We validate the position of this neurosurgical target used commonly in the treatment of essential tremor by DTI tractography. The susceptibility contrast seen between VIM/DRT tract and its neighbors is believed to arise from differences in myelin content and fiber orientation.

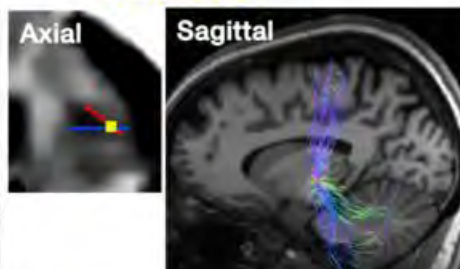
Subject 1



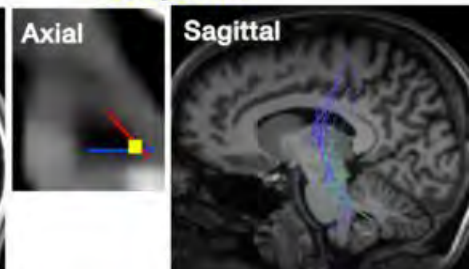
Subject 2



Subject 3



Subject 4



(Filename: TCT_895_figure1_new.jpg)

551

Testing the 2018 NIA-AA Framework in a Cohort of Individuals with Mild Cognitive Impairment: Associations with Mesial Temporal Atrophy

M Spampinato¹, B Langdon², H Fayyaz², J Ulber², H Collins²

¹MUSC, Charleston, SC, ²Medical University of South Carolina, Charleston, SC

Purpose

The 2018 NIA-AA research framework is a classification scheme for the characterization of Alzheimer's disease (AD) in living persons. Our aim was to apply the framework to a cohort of individuals with mild cognitive impairment (MCI). We hypothesized that neuroimaging characteristics differ among groups classified using cerebrospinal fluid-based biomarkers of A β plaques (A), fibrillar tau (T), and neurodegeneration (N).

Materials and Methods

We identified 344 subjects from the Alzheimer's Disease Neuroimaging Initiative 2 cohort with a baseline diagnosis of MCI. Using the AT(N) biomarker classification, patients were divided into 3 biomarker profiles: normal AD biomarkers (n = 61), non-AD pathologic change (n = 70), AD pathologic change (n = 213). We recorded hippocampal (HV) and entorhinal cortex (ERCv) volumes, normalized to the intracranial volume (ICV), from brain MRIs obtained during the first and second year of study participation. We evaluated differences among groups using one-way ANOVA, univariate ANOVA, and general linear model repeated measures. Results were considered significant when p < 0.05.

Results

We found significant differences in age among groups ($p = 0.006$). Subjects with AD pathologic change (mean age \pm SD = 72.5 years \pm 7) were older than the other two groups. Year 1 HV differed between the three groups when accounting for differences in age ($p = 0.003$). Post-hoc tests showed that year 1 HV was lower in the AD-pathologic change than in the non-AD pathologic change group ($p = 0.003$). Year 1 ERCV did not differ between the three groups when accounting for differences in age. Analyses of longitudinal imaging data demonstrated different trajectories of ERCV loss among groups when accounting for differences in age ($p = 0.001$). Differences in the trajectory of HV loss were not significantly different after correction for multiple comparisons.

Conclusions

The severity of mesial temporal atrophy differ among MCI subjects classified using the AT(N) biomarker profiles. The AT(N) classification could identify MCI individuals more likely to progress to dementia, for inclusion in future therapeutic trials.

631

The Association of Extracranial Carotid Plaque and Cognitive Dysfunction: a Systematic Review and Meta-analysis

H Baradaran¹, K Dahlstrom¹

¹University of Utah, Salt Lake City, UT

Purpose

Dementia is an epidemic affecting over 35 million people worldwide, costing over \$600 billion annually without available prevention or treatment. Extracranial carotid atherosclerosis has been variably associated with cognitive dysfunction and dementia. Prior studies have focused on the association of carotid intima media thickness or degree of carotid stenosis, however, there is evidence that the actual carotid plaque may play a role in the development of dementia via microembolic phenomena. We sought to evaluate the role of carotid plaque in contributing to vascular cognitive impairment and dementia. To accomplish this, we performed a systematic review and meta-analysis to summarize the association between the presence of carotid plaque and cognitive dysfunction and dementia.

Materials and Methods

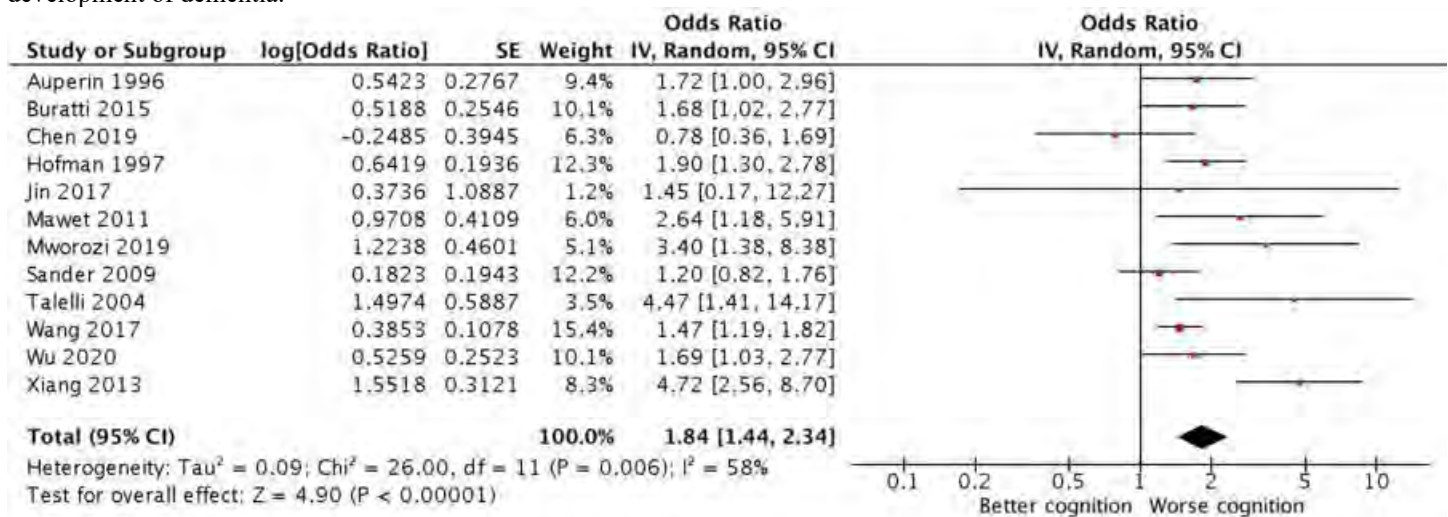
We performed a comprehensive literature search evaluating the association of carotid plaque to cognitive dysfunction and dementia. We included studies that measured carotid plaque on either ultrasound, CT, or MR and also evaluated cognitive function through neuropsychological testing, such as mini-mental state examinations. We performed subset analyses based on plaque measurement method and type of neuropsychological testing. A meta-analysis with assessment of study heterogeneity and publication bias was performed. Results were presented in a forest plot and summarized using a random-effects model.

Results

After screening 1018 studies, we included 12 studies with a total of 12,537 patients in the meta-analysis. We found a significant positive relationship between presence of carotid plaque and cognitive dysfunction with a pooled random-effects odds ratio (OR) of 1.84 (95% CI, 1.44, 2.34) (Figure, OR on logarithmic scale). There was no statistically significant difference in the OR in the subset analyses divided by plaque measurement method and type of neuropsychological testing. Measures of heterogeneity showed moderate heterogeneity between studies (I-squared statistic = 58%).

Conclusions

The presence of carotid plaque is significantly associated with cognitive dysfunction and dementia. After further confirmation of high risk plaque features being associated with dementia, our results support carotid plaque being a potentially modifiable risk factor in the development of dementia.



(Filename: TCT_631_AbstractCPMAFigure.jpg)

The Brain Metabolic Signature in Superagers Using Non-invasive in Vivo Proton Magnetic Resonance Spectroscopy

L de Godoy¹, A Studart-Neto², M Wilezinska-Arridge¹, M Tsunemi³, N Moraes², M Yassuda², A Coutinho², C Buchpiguel², R Nitirini², S Bisdas¹, C Leite⁴

¹University College London, London, United Kingdom, ²University of Sao Paulo, Sao Paulo, Sao Paulo, ³Paulista State University, Botucatu, Sao Paulo, ⁴University of São Paulo, São Paulo, São Paulo

Purpose

Youthful memory performance in older adults may reflect an underlying resilience to the conventional pathways of aging. Subjects displaying this unusual characteristic are recently termed as superagers. This study aims to explore a non-invasive imaging biomarker through a proton magnetic resonance spectroscopy (1H-MRS) to characterize and monitor the memory performance in superagers.

Materials and Methods

From 55 elderly over 80 years old evaluated through a standardized neuropsychological protocol, 25 participants, being 12 superagers and 13 age-matched controls, were statistically analyzed. We applied a reliable method using a 3 Tesla 1H-MRS to quantify 18 neurochemicals in both groups' posterior cingulate cortex. All spectroscopic data were analyzed using LCModel. Results were further processed using two strategies to support variable accuracy: 1) statistical analysis and comparison of metabolites concentrations estimated only with standard deviation < 30%; 2) calculation and comparison of weighted means of all metabolite concentrations.

Results

The main finding observed was a higher total N- acetyl aspartate (N- acetyl aspartate+N-acetylaspartyl glutamate) concentration in superagers than in age-matched controls in both strategies, reflecting a positive association of total N- acetyl aspartate with higher cognitive performance. This metabolite is considered a marker of neuronal health and mitochondrial function, which may support memory preservation in late-life.

Conclusions

In conclusion, the present 1H-MRS study provides direct in vivo evidence that superior memory performance in late-life is positively associated with total NAA in the posterior cingulate cortex of superagers when compared to age-matched controls. These findings point to the direction that higher total NAA can contribute to the resilience process of the conventional pathways of aging present in superagers. As a matter of fact, 1H-MRS quantification of neurochemical biomarkers in the aging population can provide diagnostic and prognostic biomarkers, and monitor future interventional therapies to preserve or enhance cognition in later life.

ASNR 59th Annual Meeting



Fig 1. Voxel placement for 1H-MRS on the posterior cingulate cortex. CSF (yellow) and gray and white matter (red).

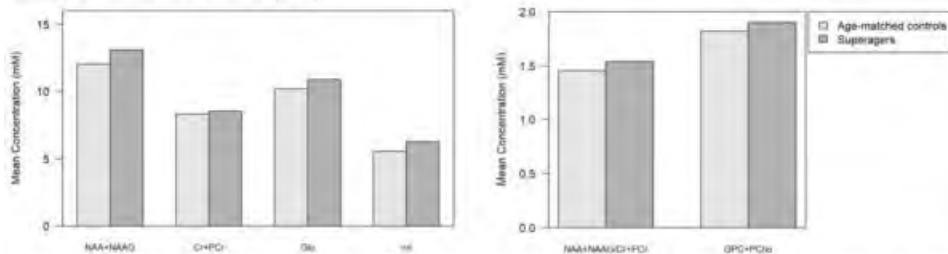


Fig 2. NAA+NAAG was elevated in the posterior cingulate cortex of superagers compared with age-matched controls ($P = 0.02$) and ml demonstrated a trend to be higher in superagers ($P = 0.05$). Cr+PCr, Glu, GPC+PCh, and NAA+NAAG/Cr+PCr were not significantly different across groups.

(Filename: TCT_1169_ASNRFIGURES.jpg)

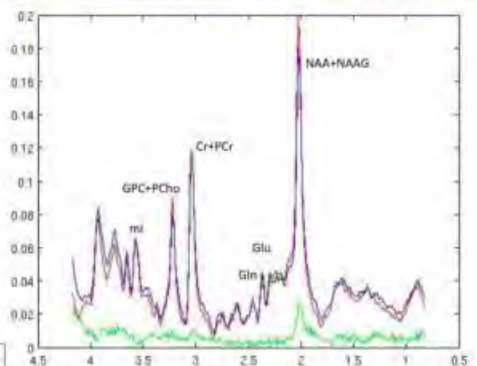


Fig 3. Averaged spectra for superagers (red), age-matched controls (blue), and the difference between groups (green). The most prominent difference is for NAA and NAA+NAAG metabolites (2.02 ppm), a small difference for Cr (3.03ppm), and ml (~3.56 ppm).

N Haine¹, N Alsafwani², A Gao², P O'Halloran¹, E Gutierrez³, D Shultz³, T Krings⁴, P Alcaide Leon⁴

¹Toronto Western Hospital, Toronto, Ontario, ²University Health Network, Toronto, Ontario, ³Princess Margaret Cancer Centre, Toronto, Ontario, ⁴University of Toronto, Toronto, Ontario

Purpose

Both radiation necrosis and tumor progression can present as size-increasing, ring-enhancing lesions after stereotactic radiosurgery (SRS) of brain metastases, and differentiation of the two entities is challenging. Here, we assess the performance of the centrally restricted diffusion sign for differentiation.

Materials and Methods

IRB approval was obtained. One hundred forty one patients with brain metastases treated with SRS who underwent a consecutive intervention (biopsy/resection) between February 2008 to February 2020 were retrospectively reviewed. Inclusion criteria were: a size-increasing, ring-enhancing lesion at the site of SRS, preoperative MRI exams with pre- and post-contrast T1, DWI, SWI, and histopathologic correlation. Excluded were lesions containing increased susceptibility limiting assessment of DWI and lesions without central necrosis. Two neuroradiologists classified the location of the diffusion restriction with respect to the post-contrast T1 images as centrally within the ring-enhancement (the centrally restricted diffusion sign), peripherally correlating to the rim of contrast enhancement, both locations, or none. Measures of diagnostic accuracy and 95% CI were calculated for the centrally restricted diffusion sign. The two-sided Fisher's exact test was performed to assess for significance and Cohen's kappa was calculated to identify the interobserver agreement.

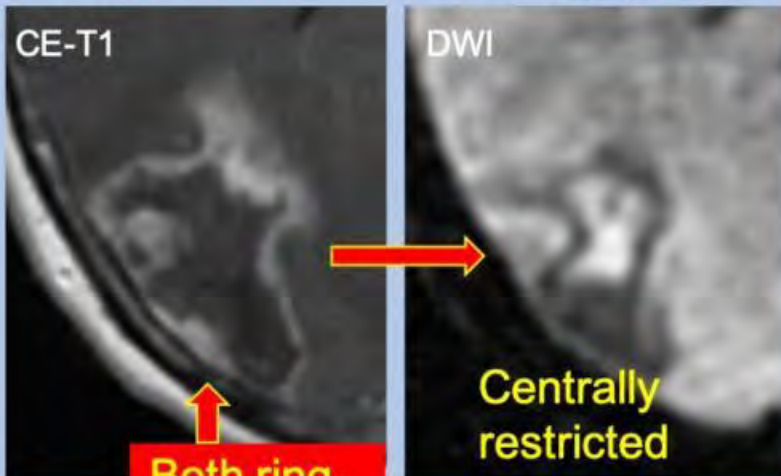
Results

Fifty-nine patients (36 female; mean age 59, range 40 to 80) were included, 36 with tumor progression and 23 with radiation necrosis based on histopathology. Primary tumors included 34 lung, 12 breast, 5 melanoma, 3 colorectal, 2 esophagus, 1 head and neck, 1 endometrium, and 1 thyroid. Mean time period from SRS to surgery was 410 days (range 71 to 1001 days). Mean SRS dose was 18 Gy (range 10 to 27 Gy). The centrally restricted diffusion sign was seen in 19/23 radiation necrosis cases (sensitivity 83% (95% CI=63 to 93%), specificity 64% (95% CI=48 to 78%), PPV 59% (95% CI=42 to 74%), NPV 85% (95% CI=68 to 94%)) and 13/36 tumor progression cases (difference $p < 0.001$). Interobserver agreement among the four DWI options was substantial ($K=0.61$).

Conclusions

Radiation necrosis was highly unlikely in the absence of the centrally restricted diffusion sign.

Centrally restricted diffusion pattern in a patient with **biopsy proven radiation necrosis** after stereotactic radiosurgery for brain metastasis

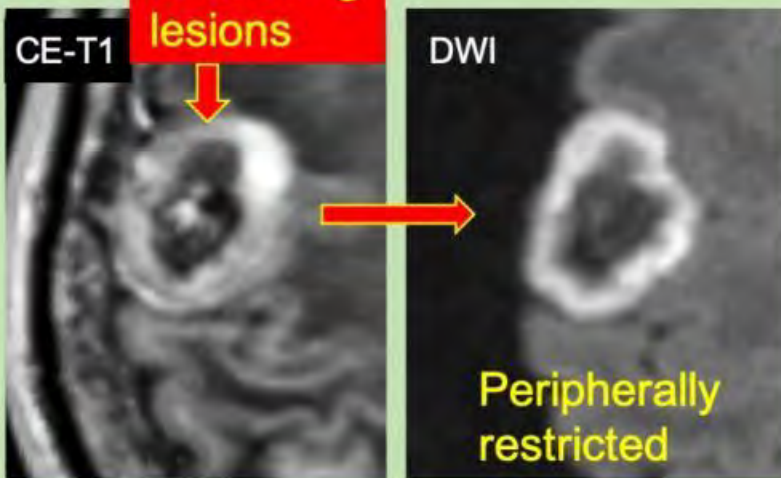


Both ring-enhancing lesions

AFTER STEREOTACTIC RADIOSURGERY FOR BRAIN METASTASES:

The centrally restricted diffusion sign:

- present in 83% (19/23) of cases with radiation necrosis (95% CI=63 to 93%)
- absence had an 85% negative predictive value for radiation necrosis (95% CI= 68 to 94%)



Exclusively peripheral or absent restricted diffusion:

- present in 64% (23/36) of cases with tumor progression (95% CI= 48 to 78%)

Peripherally restricted diffusion pattern in a patient with **biopsy proven tumor progression** after stereotactic radiosurgery for brain metastasis

(Filename: TCT_695_Fig1.jpg)

1298

The Combined Effect of Age and Baseline Alberta Stroke Program Early CT Score on Post-Thrombectomy Clinical Outcomes in the MR CLEAN Registry

J Ospel¹, M Kappelhof², N LeCouffe², J Coutinho², A Yoo³, L Yo⁴, L Beenen², W van Zwam⁵, A van der Lugt⁶, A Postma⁷, Y Roos⁸, M GOYAL⁹, C Majoie¹⁰

¹University Hospital Basel, Basel, Basel, ²Amsterdam UMC, University of Amsterdam, Amsterdam, Noord-Holland, ³Texas Stroke Institute, Plano, TX, ⁴Catharina Hospital, Eindhoven, Noord-Brabant, ⁵Maastricht UMC+, Maastricht, Maastricht, ⁶Erasmus Medical Center, Rotterdam, Zuid-Holland, ⁷MUMC+, Maastricht, Netherlands Antilles, ⁸Amsterdam University Medical Center, Amsterdam, Noord Holland, ⁹University of Calgary, CALGARY, ALBERTA, ¹⁰Amsterdam University Medical Centers, Amsterdam, Noord-Holland

Purpose

High patient age and low baseline Alberta Stroke Program Early CT score (ASPECTS) are independently associated with outcome following endovascular therapy (EVT)(1,2). Ischemic brain tissue damage may be more impactful in older than in younger patients, though this has not been studied. We aimed to investigate whether there is an interaction effect between combined age and ASPECTS on functional outcome in acute ischemic stroke patients undergoing EVT.

Materials and Methods

We included patients with anterior circulation stroke from the Dutch MR CLEAN Registry. Multivariable ordinal logistic regression was performed to obtain effect size estimates (adjusted common odds ratio [acOR]) on functional outcome (modified Rankin Scale score [mRS]) for continuous age and granular ASPECTS, with a two-way multiplicative interaction term (age*ASPECTS). In addition, we assessed outcomes in four patient subgroups based on age (< vs. ≥ median of 71.8 years) and baseline ASPECTS (6-10 vs. 0-5). Benefit of successful reperfusion was assessed for each age-ASPECTS subgroup on mRS using multivariable logistic regression. Subgroup analyses were exploratory in case of non-significant three-way interaction (dichotomized age*dichotomized ASPECTS*successful reperfusion).

Results

3279 patients were included. We did not find a significant interaction between age and ASPECTS on mRS (p=0.925). The highest proportion of mRS 5-6 was observed in patients >71.8y with baseline ASPECTS 0-5 (68/107, 63.6%). There was benefit of reperfusion in all age-ASPECTS subgroups (Figure 1). Although the acOR was lower in patients >71.8y with ASPECTS 0-5 (acOR 1.60 [95%CI 0.66 – 3.88], n=110), there was no significant difference from the main effect (p=0.299).

Conclusions

We did not find a significant interaction effect between age and ASPECTS on functional outcome. Although the proportion of poor outcome following EVT was highest in older patients with low ASPECTS, outcomes did not significantly differ from the main effect. This study's results do not support withholding EVT based on combined age and ASPECTS.

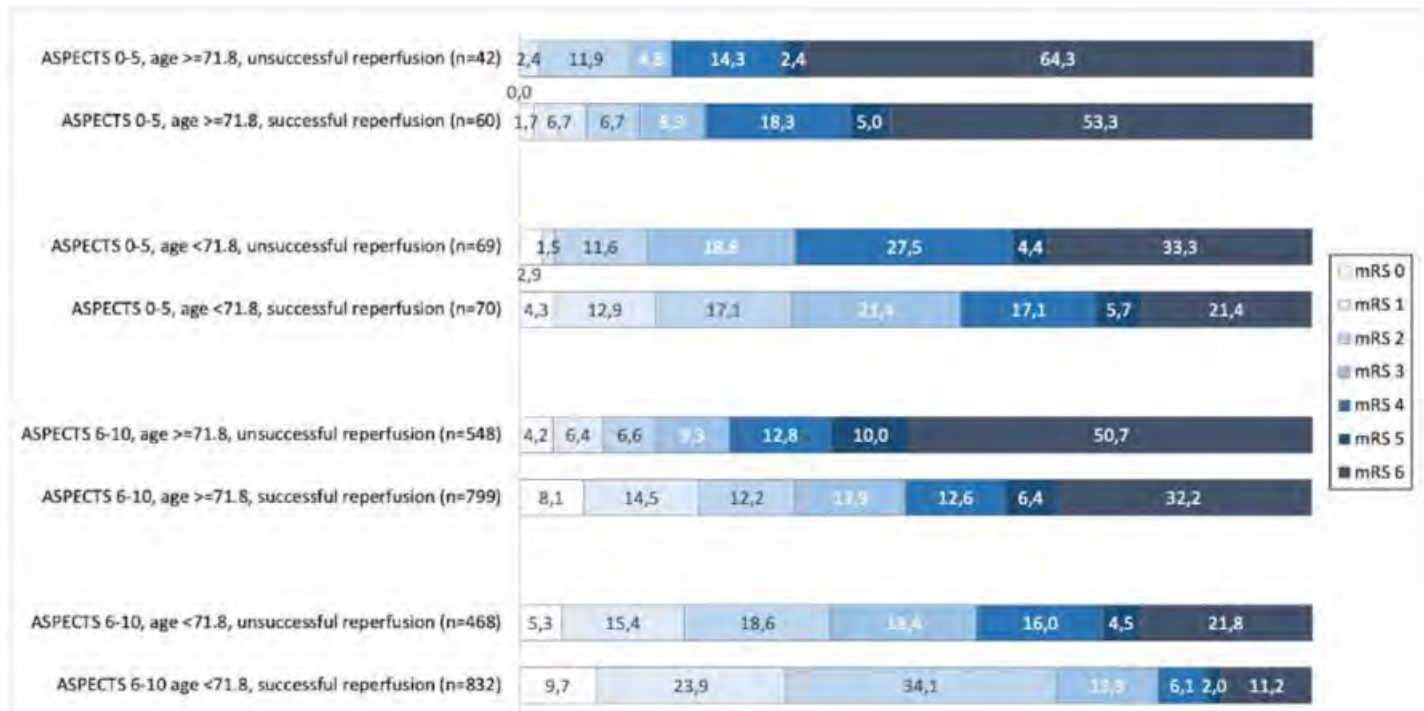


Figure 1. Modified Rankin Scale score at 90 days for age and ASPECTS subgroups, by reperfusion status. Numbers in bars are percentages of total subgroup. Successful reperfusion was defined as expanded thrombolysis in cerebral infarction (eTICI) score 2B-3. ASPECTS, Alberta Stroke Program Early CT Score; y, years.

(Filename: TCT_1298_ASNR_ageASPECTS_MRCLEAN_Fig1.jpg)

935

The Development of Clinical Decision Rules for Imaging Dizziness and Vertigo: Feature Selection and Decision Tree Models

L Tu¹, A Malhotra², A Venkatesh³, R Yaesoubi³, H Forman⁴

¹Yale School Of Medicine, New Haven, CT, ²Yale University School of Medicine, New Canaan, CT, ³Yale University, New Haven, CT, ⁴Yale University, new haven, CT

Purpose

Dizziness and vertigo are high priority areas for the development of clinical decision rules. The rate of positive or explanatory findings on imaging is reported to be low, with significant practice variation in the emergency setting. The purpose of this work is to develop a clinical decision rule through which patients at very low risk of acute pathology can be identified as safe to manage without the use of advanced imaging. To this end, we apply modern data science methods to large coded patient datasets.

Materials and Methods

The emergency department (ED) records of adult patients with encounters between 1/1/2014 and 1/1/2018 are obtained at an academic medical center with three emergency departments. Queried data include patient identifiers, demographics, ED chief complaint, medical history, physical exam findings, and numerous other clinical variables. Each data element was discretized into structured/categorical formats. Patients presenting with dizziness/vertigo and subsequently receiving CT/CTA head imaging are extracted from the larger data set. In the preliminary model, ED disposition (i.e. discharge) is used as the target variable, as a proxy for the absence of acute finding on clinical and imaging evaluation. A decision tree model is trained on these data and predictive features are reported.

Results

Among a total of 15683 ED visits with chief complaint dizziness/vertigo, 2732 received CT Head (17%) and 1461 received CTA Head and Neck (9%) Of those patients receiving CT head exams, a decision tree model produces a subset (51/949 discharges), where all discharged patients share a set of clinical variables. The eight features are: age < 47.5, no syncope, no vomiting, temperature > 96.85, respirations < 21/min, no acute distress on exam, no focal weakness on exam, and normal reflexes. A similar (though not identical) set of characteristics predicts discharge of patients (38/503) receiving CTA head and neck exams. Model metrics and details of coding are will be presented in the full presentation.

Conclusions

Decision tree models built via recursive partitioning of patient records on a target variable of patient ED disposition suggests features which can predict the presence of underlying acute pathology. Similar sets of clinical features will be used in further development of a decision rule to exclude acute pathology on imaging for patients presenting with vertigo/dizziness.

1327

The Effect of Age and Baseline Alberta Stroke Program Early CT Score on Endovascular Treatment Effect and Outcomes in Acute Ischemic Stroke: Results from the HERMES Collaboration.

J.Ospel¹, M Kappelhof², N Kashani³, B Menon⁴, B Campbell⁵, A Demchuk⁶, D Dippel⁷, J Saver⁸, T Jovin⁹, K Muir¹⁰, F Guillemin¹¹, C Majoie¹², M Hill¹³, S Brown¹⁴, M GOYAL¹⁵

¹University Hospital Basel, Basel, Basel, ²Amsterdam UMC, University of Amsterdam, Amsterdam, Noord-Holland, ³Foothills Medical Centre, University of Calgary, Calgary, Alberta, ⁴University of Calgary, Calgary, Alberta, ⁵Royal Melbourne Hospital, University of Melbourne, Melbourne, Melbourne, ⁶Cumming School of Medicine, University of Calgary, Calgary, Alberta, ⁷Erasmus Medical Center, Rotterdam, Zuid-Holland, ⁸UCLA, Los Angeles, CA, ⁹University of Pittsburgh, Pittsburgh, PA, ¹⁰University of Glasgow, Glasgow, na, ¹¹Université de Lorraine, Vandoeuvre-les-nancy, France, ¹²Amsterdam University Medical Centers, Amsterdam, Noord-Holland, ¹³Cumming School of Medicine, University of Calgary, Calgary, Alberta, ¹⁴Altair Biostatistics, St Louis Park, MN, ¹⁵University of Calgary, CALGARY, ALBERTA

Purpose

Patient age and baseline Alberta Stroke Program Early CT score (ASPECTS) are both independent predictors of outcome in acute ischemic stroke patients treated with endovascular therapy (EVT)(1,2), but little is known about the combined prognostic effect of both variables. We aimed to identify a possible multiplicative interaction between the two on clinical outcome in acute ischemic stroke patients with LVO with and without EVT and performed an exploratory analysis to determine the treatment effect of EVT in different age/ASPECTS subgroups.

Materials and Methods

The HERMES collaboration pooled patient data of seven randomized controlled trials that investigated safety and efficacy of EVT in patients with acute ischemic stroke. Adjusted ordinal and binary logistic regression with a two-way multiplicative interaction term (age*ASPECTS) was performed to test for interaction of age and ASPECTS with the primary outcome (ordinal mRS) and secondary outcomes (good outcome [mRS 0-2], excellent outcome [mRS 0-1], and moderate outcome [mRS 0-3]). In an exploratory analysis, patients were then dichotomized by age (<75 years vs. ≥75 years) and trichotomized by ASPECTS (0 - 5 vs. 6 - 7 vs. 8 - 10), and adjusted effect size estimates for the association of EVT with primary and secondary outcomes were derived from logistic regression models for the six age/ASPECTS subgroups.

Results

1735 patients were included in the analysis. There was no significant interaction of age and ASPECTS on clinical outcomes. In the exploratory subgroup analysis, we found a nominally negative point estimate for the association of EVT with clinical outcome in the ASPECTS 0-5/age ≥75, subgroup with wide confidence intervals (aOR 0.36, 95%CI 0.07-1.89), but the point estimate for moderate outcome was positive (aOR 1.24, 95%CI 0.16-9.84). In all other age and ASPECTS groups, effect size estimates were consistently in favor of EVT (Figure 1).

Conclusions

There was no evidence of an interaction effect of age and ASPECTS in this study. Outcomes in patients ≥ 75 years with ASPECTS 0-5 were generally poor. Further investigation to define the role of EVT and range of acceptable outcome in this subgroup is warranted.

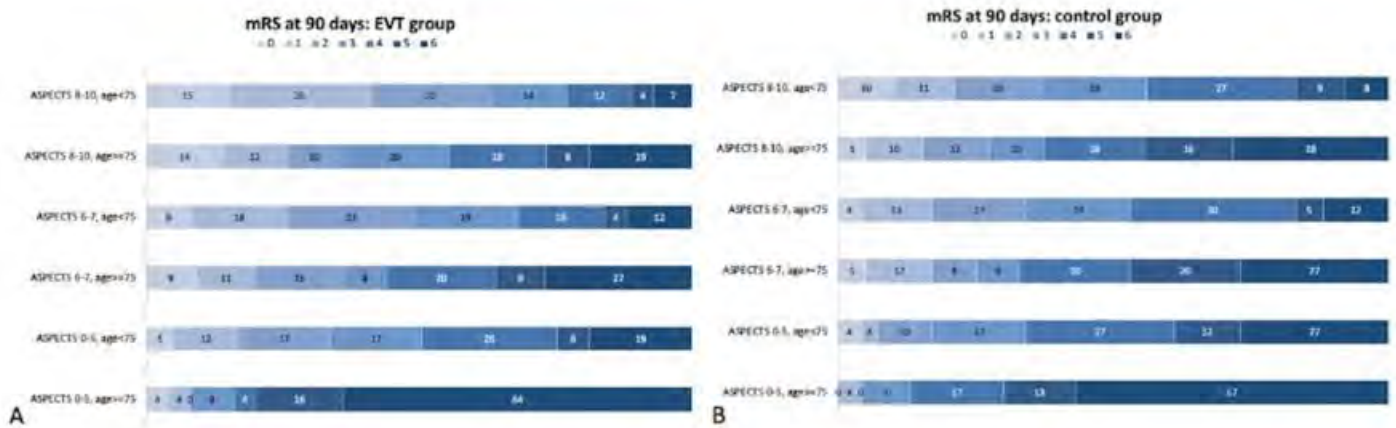


Figure 1: 90-day clinical outcomes by age and ASPECTS subgroups in the EVT arm (A) and the control arm (B). Numbers in bars are percentages of total subgroup. Note: ASPECTS = Alberta Stroke Program Early CT Score.

(Filename: TCT_1327_ASNR_ageASPECTS_HERMES_Fig1.jpg)

874

The Evolution of Endovascular Treatment of Wide Necked Bifurcation Aneurysms: A Single Center Experience

A Copelan¹, J Delgado¹, Y Kayan¹, J Schmitt²

¹Abbott Northwestern Hospital, Minneapolis, MN, ²Hospital of the University of Pennsylvania, Philadelphia, PA

Purpose

To present our single center experience utilizing balloon-assisted coiling (BAC), stent-assisted coiling (SAC) and WEB embolization for the treatment of both ruptured and unruptured wide necked bifurcation aneurysms (WNBAs) with a focus on the safety and efficacy profiles of each technique.

Materials and Methods

In this retrospective analysis of a prospectively collected aneurysm database, we assessed all patients who underwent endovascular treatment of WNBAs at our institution between January 1998 and 2020 with BAC, SAC, and WEB embolization. Required aneurysm characteristics were in line with the pivotal WEB Intracranial Therapy (WEB-IT) study and included: ruptured or unruptured status; size of dome between 3mm and 10mm; wide-neck defined by neck size ≥ 4 mm or dome-to-neck ratio < 2 ; and location limited to the basilar tip (BTA), internal carotid artery terminus (ICA), anterior communicating artery complex (ACOM), and MCA bifurcation. We collected and analyzed patient demographic variables, aneurysm characteristics, intraprocedural technical difficulties, perioperative complications, and aneurysm occlusion rates. Group differences were assessed and logistic regression models were utilized to analyze more complex relationships to adjust for potential confounding effects.

Results

WNBAs meeting the inclusion criteria included 422 in the BAC group, 127 in the SAC group, and 79 in the WEB group. The average patient age was 57.6 years (± 11.8 years), 67% of patients were female, and 25% of aneurysms were ruptured. The average aneurysm size was 6.3mm (± 1.8 mm), average neck 3.4mm (± 1.3 mm), and dome-to-neck ratio was 1.5 (± 0.5). There was a 9% incidence of intraprocedural technical difficulties in the WEB cohort, significantly less than the 32% incidence in SAC ($p < 0.005$) and less than the 17% incidence with BAC ($p = 0.066$). Resulting new persistent neurological deficits occurred in 7% of SACs, significantly higher than the 2% incidence in the BAC cohort ($p = 0.019$) and the WEB cohort in which there were none ($p = 0.021$). There was no difference in adequate aneurysm occlusion rates amongst the three treatment arms with rates of 89% in the BAC group, 90% in the SAC group, and 85% in the WEB group ($p = 0.5669$).

Conclusions

The WEB device is a valuable addition to the neurointerventionalist's armamentarium, permitting adequate embolization of challenging WNBAs often not suitable for BAC and with a drastically improved safety profile relative to SAC.

1051

The Innominate Substance: A Neuroimaging Morphometric Analysis Relevant to the Dementias and DBS Treatment

A Chiu¹, B Dang¹, T Massoud¹

¹Stanford University School of Medicine, Stanford, CA

Purpose

The innominate substance (IS) is a flat band of mostly gray matter below the lentiform nucleus. It is part of the basal forebrain containing cholinergic regions Ch1-Ch4. The basal nucleus of Meynert (BNM, region Ch4) is embedded in IS, providing major cholinergic innervation to neocortex, and is essential for cognitive function. BNM neurons are vulnerable to neurodegeneration and early loss of Ch4 is a key event in Alzheimer's disease (AD) pathogenesis. MRI studies reveals that IS thickness is significantly decreased in Lewy body dementia > AD > mild cognitive impairment > vascular dementia > control patients, reflecting neuronal loss and shrinkage in BNM. Patients with mild IS atrophy may benefit from deep brain stimulation (DBS) of BNM. Low-frequency DBS may exert excitatory effects on the remaining cholinergic system, leading to increased cholinergic transmission, analogous to effects of pharmacotherapies in AD. However, previous MRI studies, especially in elderly controls, have not factored for underlying age-related brain atrophy when assessing IS thickness. We hypothesized that this important variable may considerably affect the normative IS dimensions relative to which diagnostic and treatment decisions are made. We established normative age-related MRI IS morphometrics in healthy middle-aged subjects, prior to future studies in elderly controls and AD patients.

Materials and Methods

We retrospectively analyzed coronal CUBE FLAIR images of 39 subjects for bilateral thickness of each IS (mm) and right-left symmetry. We also measured Evans' index (EI) to account for global brain atrophy. We tested the effect of sex on measured right and left IS thickness using ANOVA, and performed linear regressions with age as the independent variable for IS thickness as the dependent variable, and significance set at $p < 0.05$.

Results

Study subjects were F:M=21:18 and mean age 44.3 years. All EI's were normal at < 0.3 . The mean IS thickness = 2.72mm (right = 2.44mm and 2.83mm in males and females, respectively; and Left = 2.58mm and 2.96 mm in males and females, respectively). 13 ISs displayed bilateral symmetry. Females had thicker right ISs ($p=0.038$), but sex did not correlate with left IS thickness ($p=0.068$). Older age significantly correlated with thinner right and left ISs ($p=0.009$ and $p=0.026$, respectively).

Conclusions

We established normative MRI morphometrics of IS in non-atrophic brains to better guide future diagnostic-accuracy testing of IS thickness as a biomarker for dementias and a target for DBS.

1213

The Middle Meningeal Sign in Cranial Dural Arteriovenous Fistulas

S Foo¹, T Krings¹

¹University of Toronto, Toronto, Ontario

Purpose

The diagnosis of cranial dural arteriovenous fistula (cDAVF) on cross-sectional imaging can be challenging and depend on multiple factors including cortical venous reflux, location of the fistula and impact on the underlying brain (such as presence of venous congestion). A common feature for most dural AVF is the presence of dilated meningeal feeding vessels, we sought to evaluate in a consecutive series of dAVF seen in our institution how often a dilated middle meningeal artery (dMMA) was present in cases of confirmed dAVF.

Materials and Methods

A retrospective analysis of a single-center database of cDAVFs proven by DSA in our institution between January 2006 to July 2020 was undertaken. We only include cases of cDAVFs with a high-quality pre-treatment MR intracranial angiogram. The presence and side of a dilated MMA, defined as enlargement and asymmetry of the middle meningeal artery compared to the contralateral side, was recorded. Information on cDAVF characteristics and patient presentations have been previously recorded.

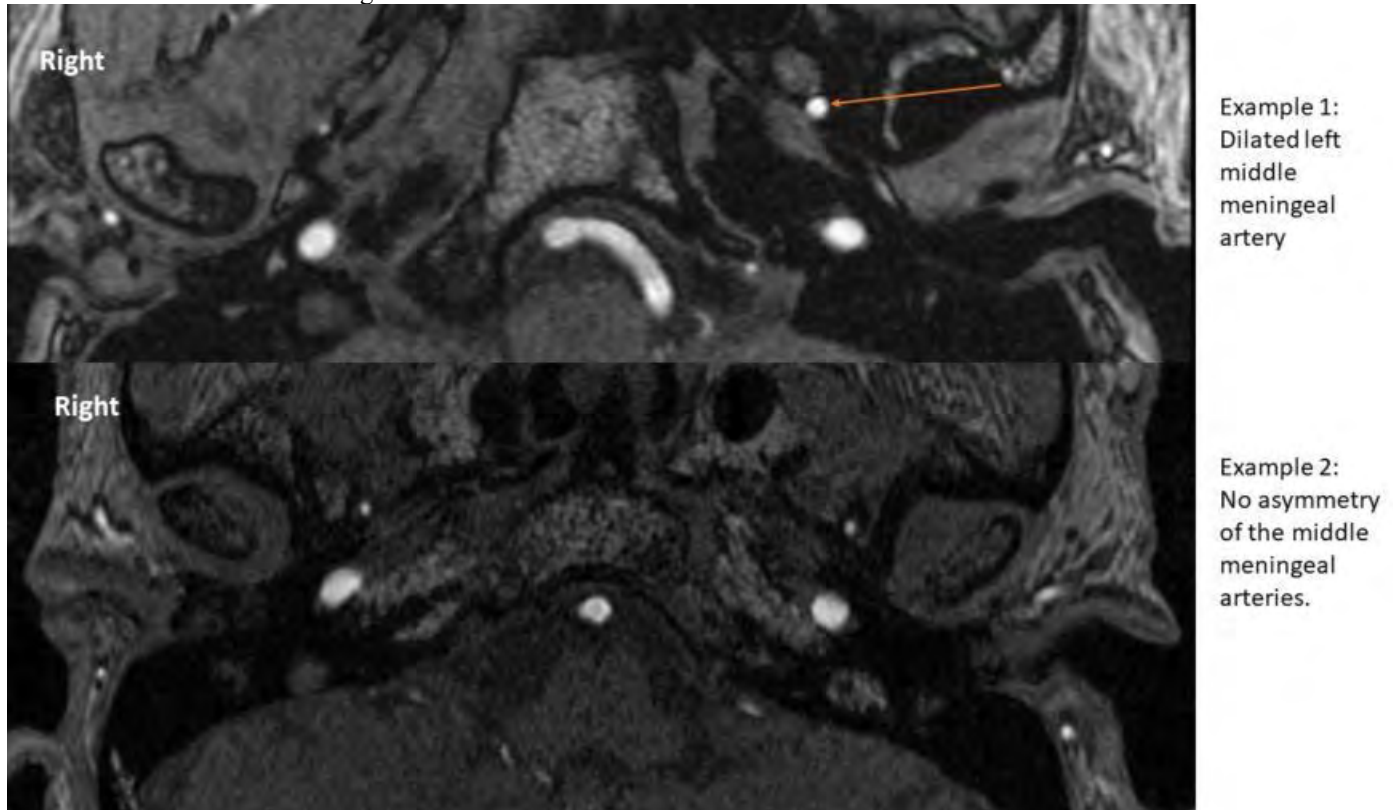
Results

Of 335 patients managed in this time frame in our institution, 51 had a pre-treatment intracranial MRA available for review. These are included in the present study. There were 23 women and 28 men with a mean age of 57.4 (range 29-84 years). Asymmetry of the MMA due to a dilated MMA was detected in 38/51 (72.5%). MMA was identified as one of the main three arterial feeders on DSA in 26 of the 38 cases. Location of dAVF was transverse-sigmoid sinus in 16, petrous in 7, convexities in 2 and lateral tentorial region in 1. The side of lesion was correctly identified in 22/26 (84.6%) cases. A dilated MMA was demonstrated in the remainder 12 cases on MRA even though DSA did not identify it as a main arterial feeder. The location of dAVF was transverse-sigmoid sinus (6), foramen magnum (2), cavernous (1), superior sagittal sinus (SSS) (1) and medial tentorial region (2). MRA misidentified the side of 2/12 lesions (transverse-sigmoid and foramen magnum), lateralized the midline SSS lesion and failed to identify the concurrent contralateral MMA feeder in a bilateral transverse-sigmoid lesion. MRA correctly identified dMMA in a case with bilateral meningeal feeders.

Conclusions

The dilated MMA is useful in predicting the side and main feeder of a cDAVF, particularly at the transverse-sigmoid region. Presence

of a dMMA even when not mainly supplied by the MMA suggests that it could be used as a screening tool to raise suspicion of this vascular lesion for further investigation.



(Filename: TCT_1213_dMMAFigure.jpg)

1456

The reliability of automated measurements of the hippocampus and inferior lateral ventricles volumes at age-sex specific normative thresholds

D Sima¹, T Phan², S Vercruyssen², E Ghumare³

¹icomatrix NV, Leuven, Vlaams-Brabant, ²icomatrix NV, Leuven, Vlaams-Brabant, Belgium, ³icomatrix NV, Leuven, Belgium

Purpose

The assessment of hippocampal atrophy to predict neurodegenerative disease progression from mild cognitive impairment (MCI) to Alzheimer's disease (AD) is critical in clinical practice. The neurodegeneration of the hippocampus (HC) typically co-occurs with an enlargement of the inferior lateral ventricle (ILV). This enlargement differentiates individuals with congenitally small hippocampi from those due to neurodegeneration [1]. Some studies indicated the clinical efficacy of combining information of both HC and ILV, such as the Hippocampal Occupancy (HOC: the ratio of HC volume to the sum of HC and ILV volumes) [2]. However, a small variability in measurement due to segmentation errors could lead to misinterpretation of the normative percentiles based on age- and sex-matched healthy population. In this study, we aim to determine the impact of measurement variability on the normative percentile computation of HV, ILV, and ILV/HC ratio indicated on the icobrain dm+ report and HOC.

Materials and Methods

The automatic icobrain software computes the volume of the HC and ILV [3]. icobrain was applied to MR images from 637 subjects (260 males and 377 females) with normal findings, aged 60 to 85. The resulting HC and ILV volumes were used to determine the ratio of ILV/HC, HOC, and age- and sex-matched normal range defined by 1st-99th percentiles. icobrain's measures were considered abnormal if they were below a threshold of 1st percentile for HC and HOC and above 99th percentile for ILV and the ILV/HC ratio. The measurement errors were obtained from independent test-retest datasets of 36 subjects [4]. We calculated corresponding errors in percentile at 1st and 99th percentiles across the group for males and females.

Results

Figure 1 illustrates the percentile errors at thresholds of 1st percentile for HC and HOC and 99th percentiles for ILV and ILV/HC ratio for females and males aged 60-85. The results revealed smaller errors for measures considering the ILV, with the ILV/HC ratio showing the smallest error. The median error in females was 1.44 and 2.01 for ILV/HC ratio and HOC, respectively. Whereas in males, median error for ILV/HC ratio was 1.92 and 2.87 for HOC. The difference was more pronounced in the higher age range.

Conclusions

Considering both HC and ILV, especially the ILV/HC ratio, is an added-value as it leads to smaller error in percentiles based on age-

and sex-matched healthy population. This is important for detecting abnormalities during the radiological interpretation of MCI and AD.

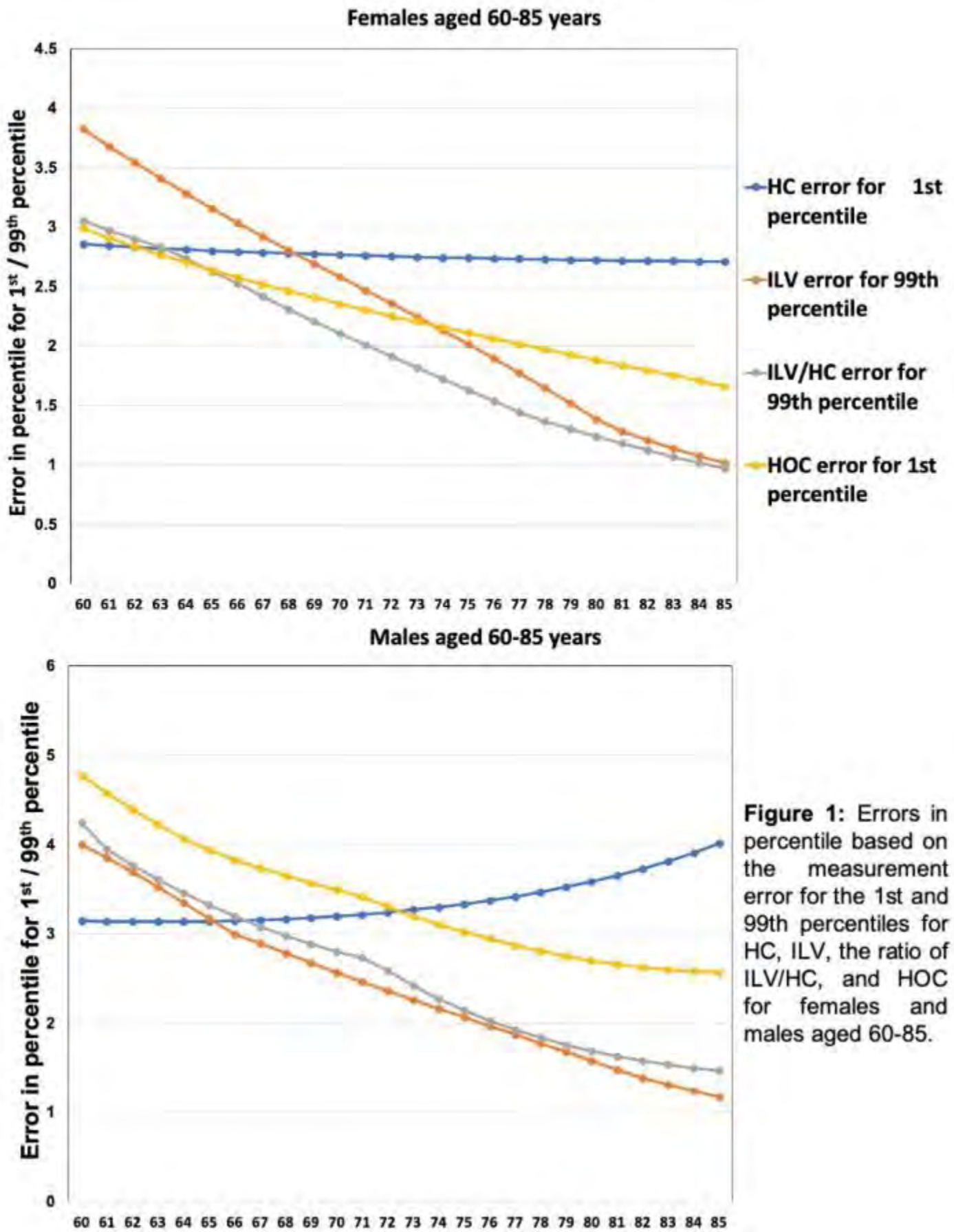


Figure 1: Errors in percentile based on the measurement error for the 1st and 99th percentiles for HC, ILV, the ratio of ILV/HC, and HOC for females and males aged 60-85.

The Role of Brain Tumor Reporting and Data System in the Management of Low-Grade Glioma Patients

A Goswami¹, A Somasundaram², L Peng³, M Hoch⁴, B Weinberg⁵

¹Emory University School of Medicine, Atlanta, GA, ²Emory, Atlanta, GA, ³University of Pittsburgh, Pittsburgh, PA, ⁴University of Pennsylvania School of Medicine, Philadelphia, PA, ⁵Emory University, Atlanta, GA

Purpose

Low-grade gliomas are a diverse group of neoplasms with variable treatments and outcomes. Patients may remain stable or require treatment with surgical resection, radiation, and chemotherapy, but follow-up decisions are guided by longitudinal MRI performed at routine intervals. The Brain Tumor Reporting and Data System (BT-RADS) is a proposed structured system for reporting post-treatment brain MRIs. The purpose of this study is to establish a relationship between BT-RADS scores and clinical outcomes in patients diagnosed with low-grade gliomas.

Materials and Methods

Chart review of grade 2 and 3 astrocytoma and oligodendroglioma patients who had an MRI at a single institution from November 2017 to November 2019 was performed. Patients' longitudinal BT-RADS scores, mortality, and tumor characteristics were recorded. Mean follow-up interval was determined according to BT-RADS scores using a linear mixed model. Outcome analysis was performed using a time-dependent Cox model. Significance level of 0.05 was used.

Results

The study identified 157 patients with low-grade gliomas (n=84 for astrocytoma; n=73 for oligodendroglioma) who had a total of 923 BT-RADS MRI reports. Individual BT-RADS score frequencies are detailed in Figure A. Mean age of patients was 48 years old. Mean progression-free survival (PFS) from date of pathological diagnosis was 6.0 years while mean overall survival (OS) from date of pathological diagnosis was 8.2 years. Mean PFS from date of each MRI scan for each BT-RADS score ranged from 6.0-10.8 months while OS ranged from 8.0-13.6 months (Figure B). There was a trend towards decreasing PFS and OS with increasing BT-RADS score. BT-RADS scores of 1a and 2 were most likely to remain the same or improve on subsequent scan (71.7% and 86.7% respectively) while scores of 1b, 3a, 3b, 3c, and 4 were likely to worsen on subsequent scan (72.7%, 54.5%, 53.4%, 46.2%, and 57.1% respectively), with $p < 0.005$ using Chi square.

Conclusions

BT-RADS scores for post-treatment brain MRIs can be used to anticipate whether low-grade glioma patients' subsequent MRI will be improved, stable, or worsened. The scoring system can also be used to predict clinical outcomes and prognosis. Further work is needed to investigate how this information can be used to guide clinical decision making.

Figure A: BT-RADS Score Frequency

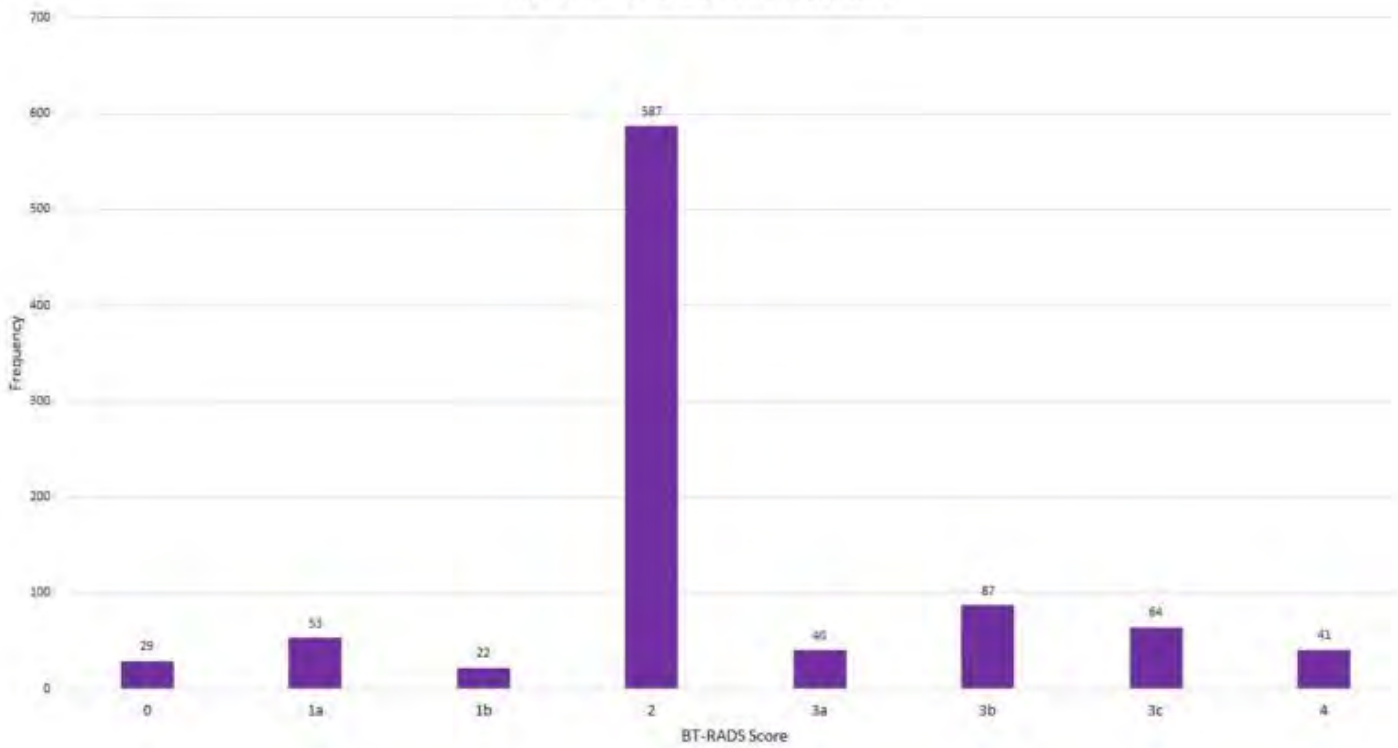
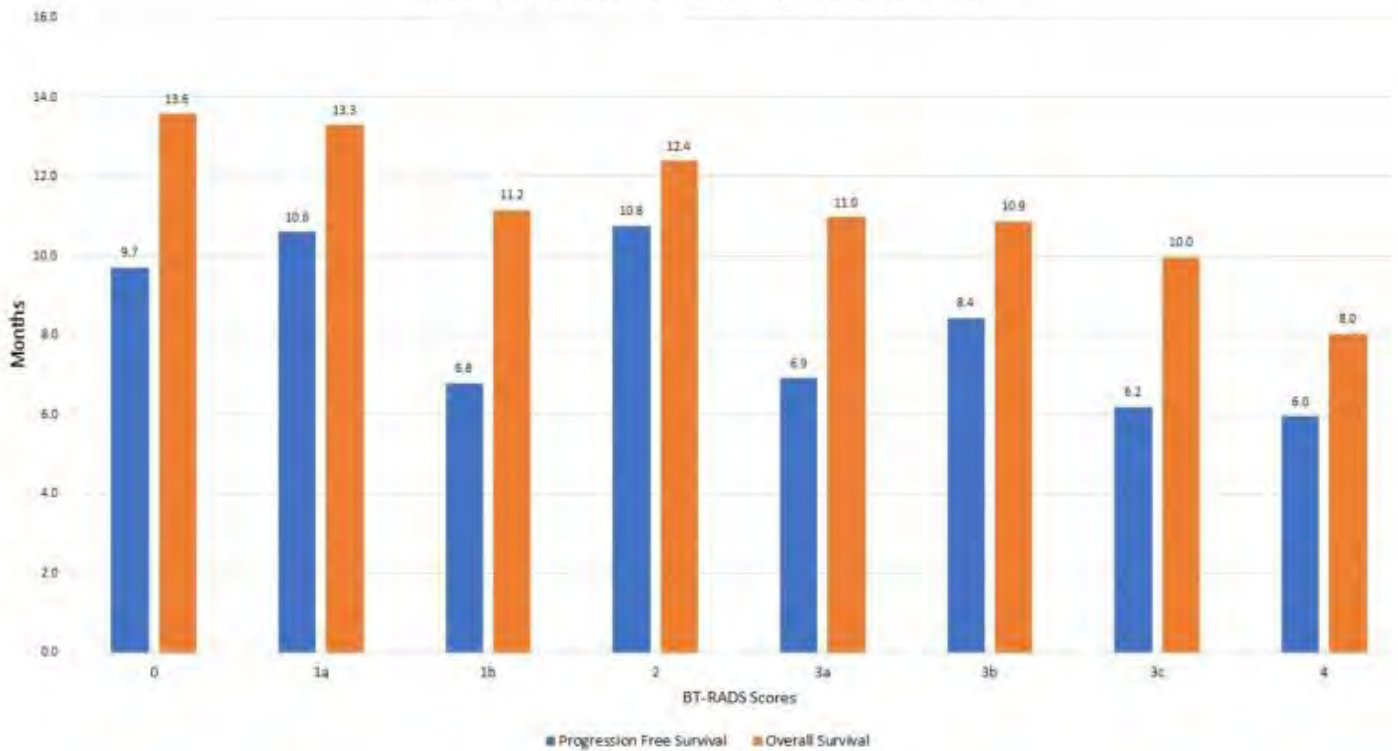


Figure B: Mean Survival after BT-RADS scan in months



(Filename: TCT_834_ASNRFigV2.jpg)

987

The Role of Radiomics in Grading of the Glioma: A systematic Review.

M Tabatabaei¹, Z Saadatpour², A Rezaei², A Sarrami³, A Singhal², H Sotoudeh⁴

Purpose

In this systematic review, we evaluate the role of Radiomics in grading of the glioma.

Materials and Methods

Three main datasets (Pubmed, Embase, Scopus) were searched for 7 different search strings. The papers were reviewed by 4 radiologists and the papers related to our research project were selected. The same radiologists performed the second round of study by studying the full-text of the selected papers. After the implementation of inclusion criteria, the remaining papers were selected for the final evaluation. Inclusion criteria: 1. Study done after 2015 2. Study has full text available 3. Full text is in English 4. Study is about glioma in human 5. The study has a gold standard for diagnosis (histopathology) 6. Study is in adults 7. The number of each grade (grade 1-4) is clearly mentioned in the study 8. Detailed information about the machine learning models and model performance (Sensitivity, Specificity, Accuracy, ROC) is provided in the study. 9. Study is about grade prediction in glioma.

Results

Using the first search, 1177 papers were selected. After evaluation of the title and abstract, 371 papers were selected. After evaluation of the full-text and implementation of inclusion criteria, 31 papers regarding the grading in glioma were used for the final review. On average, 3894 features were used in each study. The most common sequence was T1 followed by FLAIR, T2, T1+C, DWI and MR-perfusion. The most commonly used software was Matlab, followed by ITK-SNAP and PyRadiomics. In total, 4971 patients were used with an average of 165 patients per study. The most common AI model was logistic regression, followed by SVM, LASSO, Random forest, K means, KNN, CNN and Decision tree. The average sensitivity, specificity, accuracy, and area under the curve (AUC) by ROC analysis were 91.7%, 85.1%, 91.6%, and 0.92, respectively.

Conclusions

Radiomics is a robust technique to predict the tumor grade in glioma with an accuracy of 91.6% and ROC analysis of AUC of 0.92. Old AI models (Logistic regression) are the most promising models in this prediction task.

1379

The Simple Perfusion Reconstruction Algorithm (SPIRAL): Equivalency with Cine CT perfusion

C McDougall¹, L Chan¹, N Reaume¹, J Guo¹, C d'Esterre¹, P Barber¹

¹University of Calgary, Calgary, Alberta

Purpose

SPIRAL provides CT perfusion infarct core images with high accuracy from a single multi-phase helical CT acquisition, as shown in the literature (ref. 1). The current study aims to compare SPIRAL with penumbra outputs from the General Electric (GE) Advantage Workstation (AW) perfusion system.

Materials and Methods

225 stroke patients with occlusion visible on baseline CTA were acutely imaged with three-phase CTA. Multi-phase CTA (mCTA) (ref. 2) and cine CTP were acquired at admission for SPIRAL map and GE functional map processing. The patient sample was split into training (N=122), testing (N=40) and validation (N=40) sets. The mCTA data was analyzed to produce filtered perfusion-base maps (FPBMs), which each represent a perfusion or statistical measurement (for example, measuring the slope of the three phases) on a voxel-by-voxel basis through the 3 phases of the CTA acquisition. Multiple FPBMs were generated and used as variables within a logistic regression model (see Fig. 1a), which is trained to detect the penumbra/normal tissue threshold. Additionally, models were trained within large regions identified by a vascular atlas registered to the CTA phases (ACA, PCA, MCA, Basal Ganglia and Cerebellum), which were later amalgamated into a global SPIRAL map. The training binary endpoint was defined from the GE-CTP TMAX map as TMAX = 9.9 (penumbra/normal) (ref. 3). The training set was used to train the FPBM coefficients for the logistic regression models in each vascular region (ACA, PCA, MCA, Basal ganglia, and Cerebellum). The testing set was used to determine the ideal global threshold of the SPIRAL map for discerning penumbra and normal tissue. The validation set was used to prospectively evaluate the sensitivity and specificity of the final model/thresholds when compared to the GE-CTP outputs as the gold standard.

Results

The SPIRAL map generated an ROC curve with a global Area-Under-Curve (AUC) of 0.87 (regional results: ACA = 0.84, PCA = 0.83, MCA = 0.92, Basal Ganglia = 0.92, Cerebellum = 0.82) with global validation sensitivity and specificity of 0.76 and 0.82, respectively, for the penumbra/normal model.

Conclusions

The SPIRAL map generated from mCTA performed similarly to CTP perfusion maps to identify the penumbra region. Immediate future work will include discerning core from penumbra by training a logistic regression model on CTP maps thresholded at a higher TMAX value. From this analysis, a clinical mismatch ratio can be calculated and compared to GE-CTP outputs.

Fig 1a. FPBM intermediate maps and SPIRAL final map compared to GE-CTP output

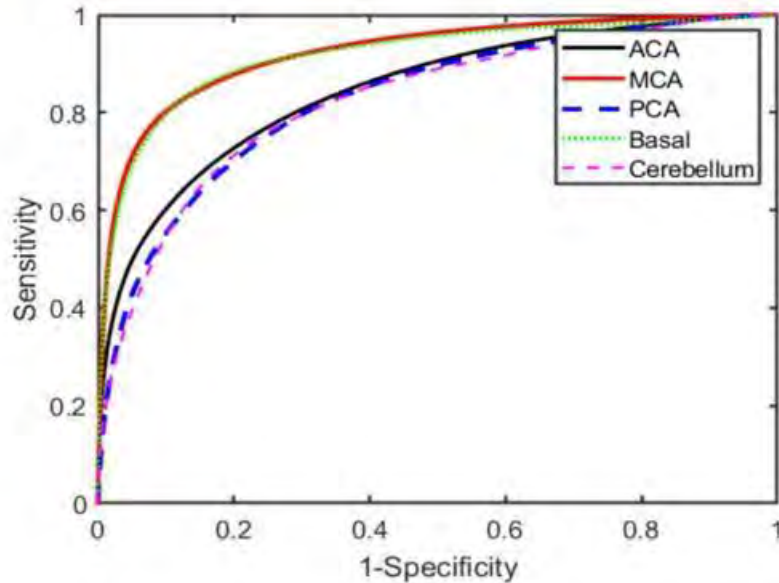
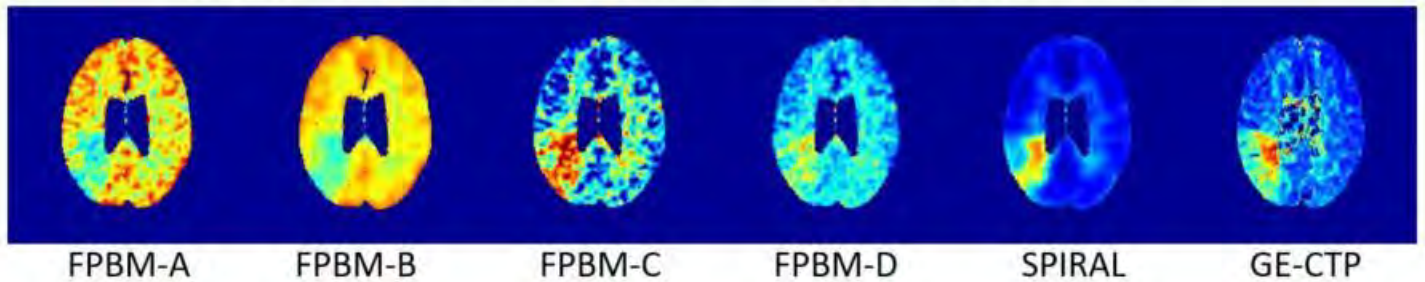


Fig 1b. ROC analysis of penumbra vs. healthy tissue (TMAX threshold of 9.9) for each vascular territory

(Filename: TCT_1379_Fig1400.JPG)

813

Three-dimensional Spinal Angiography Techniques in Pediatric Patients: Safety and indication in 33 consecutive patients

M Martinez¹, M Motaghi², M PEARL³, P Gailloud²

¹Indiana University School of Medicine, Indianapolis, IN, ²Johns Hopkins Hospital, Baltimore, MD, ³JOHNS HOPKINS HOSPITAL, BALTIMORE, MD

Purpose

To investigate the role and safety of spinal three-dimensional digital subtraction angiography (3D-DSA) and flat panel catheter angiography (FPCA) in the pediatric population.

Materials and Methods

This study reviews all 3D-DSA and FPCA studies performed by the authors in patients up to 21 years of age at a single institution during a 10-year period.

Results

Whole cohort 35 studies were performed in 33 patients, including 14 girls and 19 boys with an average age of 24 (median=16, range 0.2 to 21). The procedures included 11 3D-DSA and 24 FPCA obtained at the cervical (11), thoracic (20), or lumbar (4) levels. Indications were spinal vascular malformations (24, 73%), hematomyelia (3, 9%), spinal stroke (4, 12%), or spine/spinal cord tumor (2, 6%). Critical vessels were injected in 30 cases (18 anterior radiculomedullary arteries (RMA), 5 posterior RMAs, 7 vertebral arteries (VA)). There was no neurological complication, no contrast-related complication, and no access site complication requiring additional management or delaying discharge. The average air kerma was 214.9 mGy (median=202.0, range 13.4 to 428) and the average dose area product (DAP) was 5321.3 μGym^2 (median=4225.2, range 358.6 to 11711.0). Cervical studies The 11 cervical studies included 2 3D-DSAs and 9 FPCAs. Critical vessels were injected in all cases (4 anterior RMAs, 7 VAs). Thoracolumbar studies The 24 thoracolumbar studies included 9 3D-DSA and 15 FPCAs. Critical vessels were injected in 19 cases (14 anterior RMAs, 5 posterior RMAs). 3D-DSA The dose associated with 3D-DSA (n=11) (Figure 1) was as follows: average air kerma=89.1 mGy (median=88.6, range 13.4 to 171.9), DAP=2015.6 μGym^2 (median=1588.1, range 358.6 to 4571.7). FPCA The dose associated

with FPCA (n=24) (Figure 2) was as follows: average air kerma=275.1 mGy (median=273, range 91.8 to 428), DAP=6902.3 μGym^2 (median=7038.9, range 1633.8 to 11711.0).

Conclusions

Spinal three-dimensional techniques are safe in the pediatric population even when they require relatively long injections (up to 20 seconds) involving critical vessels such as an RMA or VA. FPCA currently generates about 3 and a half times the radiation dose of 3D-DSA; it must therefore be used with care, notably in young patients. In general, 3D-DSA was in our practice preferred high-flow vascular malformations and FPCA for low-flow lesions or anomalies without arteriovenous shunt.



Figure 1. 3D-DSA in a 7-year-old girl with a spinal cord arteriovenous malformation (left T12 injection)

Figure 2. FPCA in a 10-year-old girl with a low-flow spinal epidural arteriovenous fistula (left T6 injection)

(Filename: TCT_813_Fig.jpg)

340

Time is of the essence: Longitudinal Imaging Characteristics of High-grade Gliomas Before and After Immunotherapy

F Najmi Varzaneh¹, J Cui², J Ivanidze³, M Aboian¹

¹Yale New Haven Hospital, NewHaven, CT, ²Brain Tumor Research Group, Yale University, New Haven, CT, ³Weill Cornell Medicine Radiology, New York, NY

Purpose

Approximately 74,274 people are diagnosed with high-grade glioma (HGG) annually. HGG carry poor prognosis and standard of care has not significantly changed in over 10 years. Immunotherapy is a new treatment that has been shown results in multiple malignancies and is increasingly incorporated into HGG clinical trials. However, evaluation of treatment response after immunotherapy in HGG is a common diagnostic challenge. The purpose of this study is to describe conventional and DSC MRI features of HGG in the post-immunotherapy setting in patients treated with Nivolumab and Pembrolizumab.

Materials and Methods

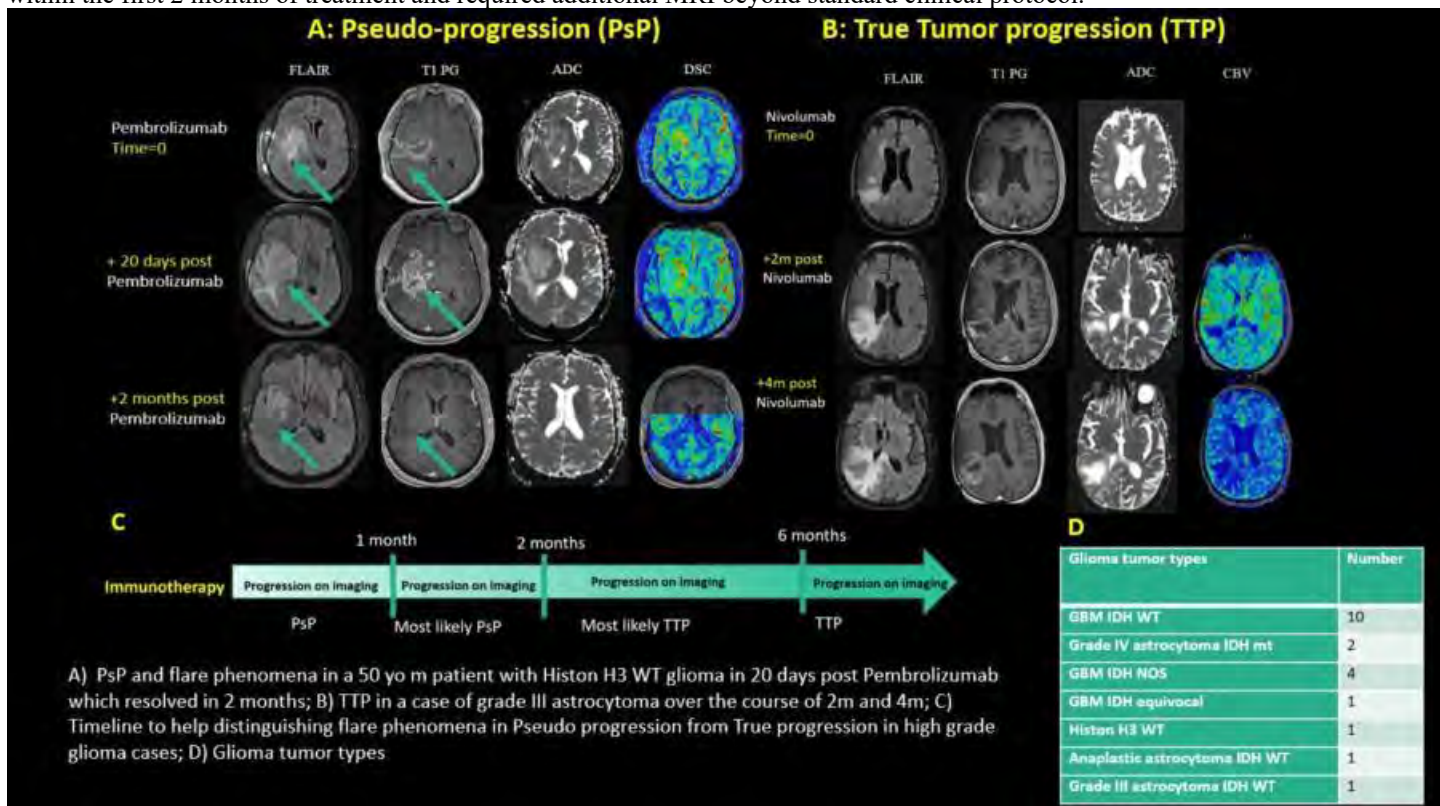
In this IRB-approved retrospective study, we identified 20 patients with pathologically proven HGG. 16 patients received Nivolumab and 4 patients received Pembrolizumab. Qualitative MRI characteristics and DSC parametric maps were assessed by neuroradiology attending utilizing Visage Imaging software (Pro Medicus Limited, Visage 7). Patients were followed for 6 months post immunotherapy. In our study, pseudoprogression (PsP) is defined as transient increase in tumor enhancement and mass-like T2-FLAIR hyperintensity, which resolved on follow-up imaging. True Tumor Progression (TTP) is defined per iRANO criteria.

Results

In the Pembrolizumab group, PsP was seen in 2/4 cases; stable disease in 1/4 case and no imaging was available in early post treatment for 1/4 case. Of the two PsP cases, imaging changes occurred at 1 week or 3 weeks post therapy and resolved with steroid/Bevacizumab on follow up imaging. There was no disease recurrence in 6 months post therapy. In the Nivolumab group, there was one case of PsP which occurred in 1 month after therapy and there was no disease recurrence at 6 months; however TTP was seen in 8/16 cases with interval progressive increase in tumor size at the 2 months, 4 months and 6 months timeline. Timing of appearance of imaging abnormalities represented the key differentiating factor in distinguishing PsP from TTP. In addition, our study demonstrated specific post immunotherapy changes in the subependymal region with avid reduced diffusion and peripheral lace-like enhancement.

Conclusions

Our comprehensive retrospective longitudinal study demonstrated specific timeline in interpretation of treatment response after starting immunotherapy for HGG. Our cohort showed 15% PsP in cases of high-grade glioma post immunotherapy, which occurred within the first 2 months of treatment and required additional MRI beyond standard clinical protocol.



(Filename: TCT_340_Capture2.JPG)

307

Topographical expression patterns of genes implicated as driver mutations in pediatric high-grade gliomas

E Kazarian¹, A Marks², J Cui¹, A Darbinyan¹, E Tong³, C Kline⁴, S Cha⁵, M Aboian¹

¹Yale University, New Haven, CT, ²Yale New Haven Hospital, New Haven, CT, ³Stanford University, Stanford, CA, ⁴Children's Hospital of Philadelphia, Philadelphia, PA, ⁵University of California San Francisco, San Francisco, CA

Purpose

Diffuse midline gliomas, H3 K27M mutation are aggressive tumors commonly found in children with similar imaging characteristics to diffuse midline gliomas, H3 K27M-wildtype, while high-grade gliomas within the cerebral hemispheres have different imaging features. Driver mutations that are critical for tumorigenesis are different between diffuse midline gliomas and hemispheric high-grade gliomas. The purpose of our study was to evaluate the topographic distribution of normal expression patterns of genes that serve as driver mutations in diffuse midline gliomas and hemispheric high-grade gliomas.

Materials and Methods

We identified 18 patients (<21 years old) with diffuse midline glioma or high-grade glioma with preoperative MRI imaging from tumor board review and that had either 500 or 50 gene panel mutation testing at two academic institutions. Imaging features of these tumors were characterized and gene expression patterns in normal brain were analyzed using Allen Brain Atlas.

Results

11 of the patients had diffuse midline gliomas and 7 had hemispheric high-grade gliomas. 10 of the diffuse midline gliomas had the K27M mutation in the tail of histone H3 protein. All of the patients undergoing 50 and 500 gene panel testing were found to have additional mutations in a variety of genes, with most common being ACVR1, PPM1D, and p53. On contrast-enhanced MR imaging, diffuse midline gliomas lacked prominent enhancement while hemispheric high-grade gliomas with multiple mutations showed prominent enhancement. Gene expression analysis in normal brains based on Allen Brain Atlas demonstrated that genes mutated in diffuse midline gliomas had higher expression along the midline brain structures with low expression within the cerebral hemispheres. On the other hand, genes mutated in hemispheric high-grade gliomas had normal high expression levels along the hemispheres.

Conclusions

Our study suggests that normal topographical expression patterns of genes that have been shown to be mutated in midline gliomas and hemispheric gliomas is different. This suggests that gene expression environment within different locations of the brain defines the driver mutations found in tumors that arise from those locations.

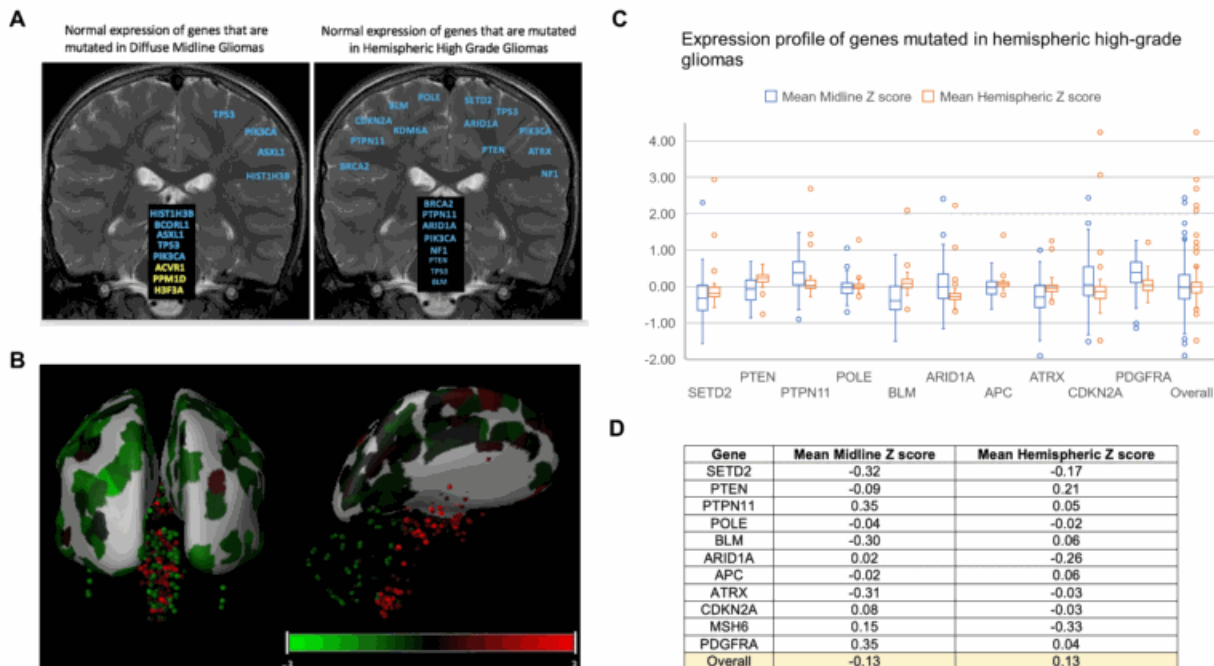


Figure 1: Normal expression of genes in hemispheric and midline structures (A). TP53 expression patterns by z-score (B). Genes mutated in hemispheric high-grade gliomas have demonstrably higher gene expression in hemispheric structures (C, D).

(Filename: TCT_307_Slide1.GIF)

381

Towards Standardisation of Probabilistic Tractography of the Arcuate Fasciculus: A Pilot Study

J Ansell¹, E De Vita¹, J Jarosz², M Borri²

¹King's College London, London, UK, ²King's College Hospital, Denmark Hill, London

Purpose

Pre-surgical functional mapping can be used to protect eloquent brain function and optimise the neurosurgical plan; this is particularly relevant when language structures are involved, as they are highly individual specific and can reorganise [1]. In this area, fMRI and multi-fibre probabilistic tractography are established tools [2], but there are no widely accepted protocols for clinically feasible and

robust acquisition and processing. In this pilot study we investigate the standardisation of arcuate fasciculus (AF) tractography, focussing on definition of seed and end regions using both brain atlases and fMRI data.

Materials and Methods

Multi-fibre probabilistic AF tractography was performed in MRTrax3 [3] from 64-direction DTI data (SE-EPI, TE/TR=86/9500ms, voxel=(2.5mm)³, b=1500s/mm²) acquired on 5 healthy right-handed volunteers at 1.5T. 5 potential methods for defining seed and end regions were implemented (Table 1). Tractography was run on the dominant left hemisphere from seed to end region and vice-versa, and only the overlapping tracts were preserved. For quantitative evaluation, the final track density images from each method were compared to an AF atlas probability map (MegaTrack DTI [4], registered to subject space) and sensitivity and specificity calculated from the overlap of the two maps (Figure 1).

Results

Overall, all methods overlap with the reference AF atlas (Figures 2, 3), with tracts matching expected anatomical paths. In general, the atlas based methods have higher sensitivity (43-79%, vs 28-51% for fMRI), while fMRI based methods select more specific paths (Figures 1-3). Within the atlas based approaches, methods with full seed and end regions show the highest sensitivity. In fMRI based approaches, peak activation for all tasks were found to be spatially close, and therefore tracts generated using a single vs all tasks method are very similar.

Conclusions

Initial results suggest that both atlas and fMRI based methods have potential for a standardised approach. Within this pilot cohort, the atlas based methods have high sensitivity and specificity. However, for patients with large lesions or abnormalities, where atlas registration might be compromised, fMRI methods may be more robust. This work is being expanded to a larger volunteer cohort before being applied retrospectively and prospectively to patient data. For validation, intra-operative data will replace the atlas AF, which has limitations as a clinical reference tract.

	Basis for regions	Method	Definition of the region
Atlas	Wernicke and Broca probabilistic atlas: Julich Histological Atlas and Harvard-Oxford Cortical Structural Atlas, registered to subject space.	M1: Full to Full	Full Wernicke and Broca region from the atlases.
		M2: 50% to 50%	Core of Wernicke and Broca regions (50% probability threshold).
		M3: 50% to Full	Seed region = core (50% probability threshold), end region = full Wernicke and Broca, and vice versa.
fMRI	fMRI data from 3 language tasks: Verb Generation, Picture Naming, and Word Fluency.	M4: Verb Generation	7 mm radius sphere around peak fMRI activation (within language areas) from Verb Generation task.
		M5: All Language Tasks	7 mm radius sphere around centre of mass (COM) of fMRI activation peaks from all language tasks.

Table 1: Methods to define seed and end regions to guide AF tractography. Sphere around peak fMRI as proposed by [5].

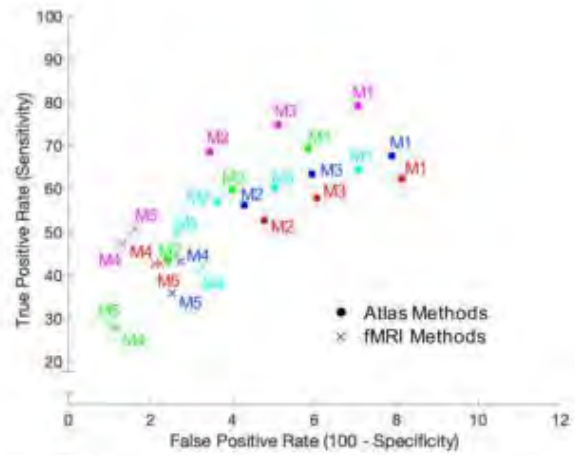


Figure 1: Sensitivity and specificity of alternative methods to define seed and end regions. Colours represent different volunteer data. Methods labelled as in Table 1. Specificity = true negatives/(true negative + false positives); calculated over the whole left hemisphere. Sensitivity = true positives/(true positives + false negatives); true positives = overlap tractography AF and atlas AF.

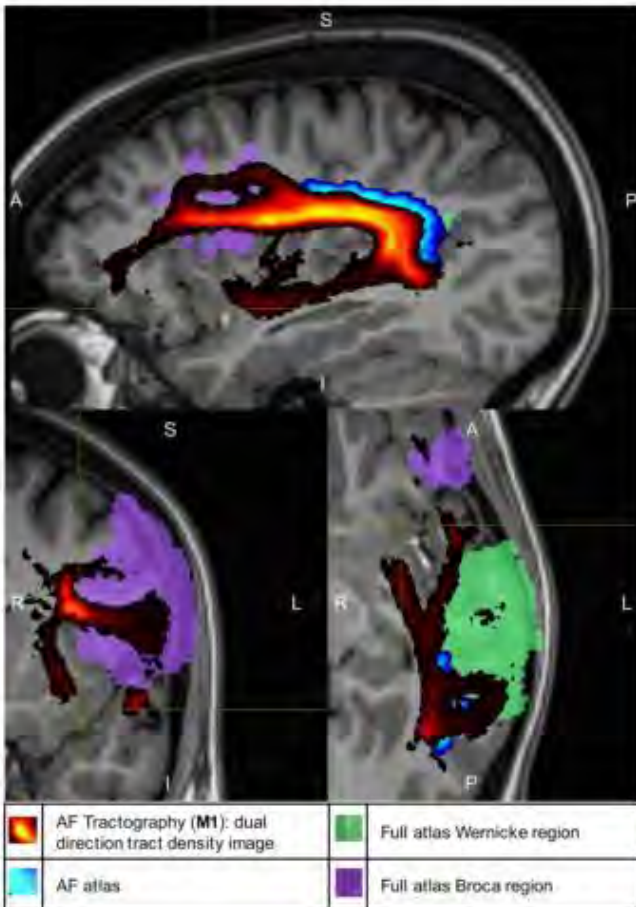


Figure 2: Tractography of the AF using Method 1.

(Filename: TCT_381_Abstract_Figures_FINAL.jpg)

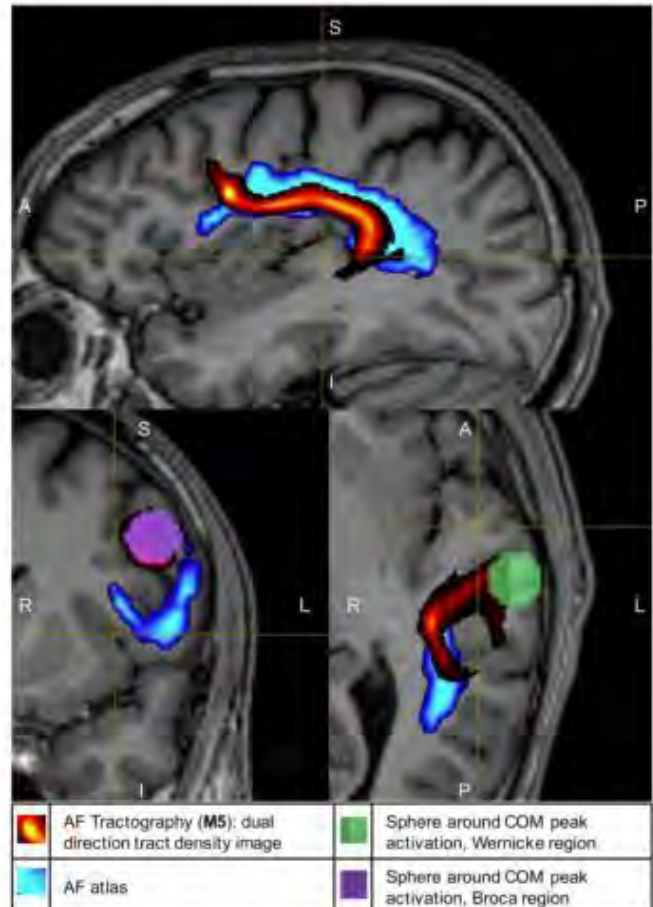


Figure 3: Tractography of the AF using Method 5.

Training of advanced neurointerventional cases using live-streaming technology: Experience from the pan-European ESMINT – EYMINT e-Fellowship program

M BECHSTEIN¹, J Fiehler¹, J Kaesmacher², G Boulouis³, U HANNING¹

¹University Medical Center Hamburg-Eppendorf, Hamburg, Germany, ²University Hospital Bern, Bern, Switzerland, ³Centre Hospitalier Universitaire de Tours; Interventional and Diagnostic Neuroradiology Department, Tours, France

Purpose

Training of advanced neurointerventional procedures requires hands-on-training with mentoring from experienced peers. This has traditionally been achieved by fellowships of trainee interventionalists in neurovascular centers with high case volumes. With governmental and institutional travel restrictions in place, e.g. in face of the current COVID-19 pandemic, this mode of training has been largely impaired. We present a pan-European initiative, the ESMINT–EYMINT e-Fellowship program, which uses dedicated live-streaming technology to foster remote neuroendovascular training of "e-fellows".

Materials and Methods

Organized by the European Society of Minimally Invasive Neurological Therapy (ESMINT) and its affiliated organization for young neurointerventionalists (EYMINT), a multinational teleproctoring infrastructure was established with a total of seven Tegus camera rigs across high volume neurovascular centers in Europe. Highly experienced neurointerventionalists at the respective institutions invited qualifying e-fellows (minimum requirement of a fulfilled 12 months residency in interventional neuroradiology/endovascular neurosurgery) to join endovascular procedures through a web-based platform, accessible on-demand from a personal computer. The technology enables low-latency high-resolution streaming with emphasis on stable image transmission and minimal resource requirements (Tegus Medical, Hamburg, Germany) (1).

Results

During a four months period, e-fellows were on standby to monitor complex neurointerventional procedures in real time by accessing the telestream platform from a conventional computer at their place of residence or workplace. Personal mentoring was achieved through a 1:1 allocation of fellow and mentor with direct two-way communication. A high level of situational awareness was reported by the fellows, mainly attributable to the ability to move the field of view of the camera inside the angiography suite at their own discretion on any spot of the procedure, e.g. the arterial access site or the angiography monitor without disturbing the interventionalists. Each session was concluded with a debriefing and standardized questionnaire for the proctor and fellow.

Conclusions

Streaming technology facilitates geographically independent training of complex neurointerventional procedures and may supplement hands-on-training. Further studies will examine the impact of teleproctoring on the learning curves of interventionalists and ultimately patient safety in daily clinical practice.

1262

Transient Global Amnesia, Diagnostic Approach and MRI Findings

S Rodriguez¹, A Fernández de Castro², C Trillos³

¹Clinica de Marly, Bogotá, Cundinamarca, ²Hospital Universitario Mayor - Méderi, Bogotá, Cundinamarca, ³Universidad del Rosario, Bogotá, Cundinamarca

Purpose

Describe the characteristics of patients with clinical suspicion of TGA, its diagnostic approach (highlighting the shortcomings of clinical criteria), the differential diagnosis, the technical factors that influenced positive findings on MRI images, and the inter-reader agreement of these findings (1-5).

Materials and Methods

Medical records of 130 patients with suspected TGA between 2014 and 2018 were reviewed. All MRIs were conducted using a 1.5T magnet Siemens Essenza. In the years 2014 and 2015 the following parameters were used: FOV 240, matrix 160x160, voxel size: 1.5 x 1.5 x 5 mm, gap thickness 5-7 mm, TR 3700ms, and TE 105 ms. In 2016 the protocol was updated with the following parameters: FOV 240, matrix 192x192, voxel size: 1.25 x 1.25 x 3mm, gap thickness 3mm, TR 8500, and TE 130. Three radiologists independently defined the presence or absence of hippocampal peripheral focal lesions in MRI, and the concordance kappa coefficient was calculated. In the 69 patients with a final diagnosis of TGA with magnetic resonance imaging (MRI), a bivariate analysis was performed, dividing them into two groups based on the presence or absence of hippocampal lesions.

Results

Eighty-two% of patients had a confirmatory diagnosis of TGA. Among these the median age was 65 years (IQR 58-71), and 76% were women. 45% did not meet Hodges and Warlow clinical criteria. The episode had a median duration of 4 hours (IQR 2-7). The median length of in-hospital stay was 49 hours (IQR 64). MRI was performed in 69 patients. Cohen's kappa coefficient was 0.88; IC95%, 0,79-0,97. Forty-seven MRIs (68%) were positive for hippocampal findings. When exploring the operative parameters of positive and negative MRIs in patients with a definitive diagnosis of TGA, significant differences were observed concerning the following variables: (i) the time from the onset of the event and execution of the MRI, when dividing it by the studies carried out

between 24-84 hours and the studies carried out before and after this interval, (ii) the use of a 3mm slice thickness, (iii) a 3-4mm slice interval and (iv) a matrix of 192 x 192 voxels (Table 1.)

Conclusions

For the detection of peripheral punctate hippocampal lesions on DWI, Cohen's kappa concordance coefficient was very good. For improving the detection of characteristic hippocampal findings on DWI, the study should be performed between 24 and 84 hours after the event, voxel and gap thickness should be at least 3 mm, and the matrix size should be 192 x 192 or larger.

	Positive MRI n=47			Negative MRI n=22					p value
	Median	p 25	p 75	Median	p 25	p 75			
Time (in hours) elapsed between the beginning of the event and the MRI	35	28	47	24	18	44			0,044
		No.	%		No.	%	OR	IC 95%	
Voxel thickness of 3 mm		28	59,6		7	31,8	3,16	1,08-9,2	0,032
Voxel thickness of 5mm		19	40,4		15	68,2			
Gap thickness 3 - 4 mm		30	63,8		8	36,4	3,09	1,08-8,9	0,033
Gap thickness 5,6 or 7 mm		17	36,2		14	63,6			
Matrix 192 x 192		31	66		8	36,4	3,39	1,18-9,8	0,02
Matrix 160 x 160		16	34		14	63,6			
MRI performed between 24 and 84 hours (percentile 13-95)		40	85,1		10	45,5	6,8	2,15-21,9	0,001

(Filename: TCT_1262_Table11.jpg)

254

Transmantle Pressure Computed from MR Measurements of Aqueduct Flow and Dimensions

S Sincomb¹, W Coenen², E Criado-Hidalgo³, K Wei⁴, K King⁵, M Borzage⁶, V Haughton⁷, A Sanchez³, J Lasheras¹
¹University of California - San Diego, San Diego, CA, ²Universidad Carlos III de Madrid, Leganes, Madrid, ³University of California-San Diego, San Diego, CA, ⁴Huntington Medical Research Institutes, Pasadena, CA, ⁵Barrow Neurological Institute, Phoenix, AZ, ⁶University of Southern California, Los Angeles, CA, ⁷University of Wisconsin, Madison, WI

Purpose

Measuring transmantle pressure, the instantaneous pressure difference between the lateral ventricles and the cranial subarachnoid space, by intracranial pressure sensors has limitations. The aim of this study was to compute transmantle pressure non-invasively with a novel non-dimensional fluid mechanics model in volunteers and to identify differences related to age and aqueduct dimensions.

Materials and Methods

Brain MR images including cardiac-gated 2D PC-MRI and FSPGR were obtained in 77 volunteers ranging in age from 25-92 years. Transmantle pressure was computed over the cardiac cycle with a fluid mechanics model from the measured aqueduct flow rate, stroke volume, aqueduct length and cross-sectional area, and heart rate. Peak pressures during caudal and rostral aqueduct flow were tabulated. The computed transmantle pressure, aqueduct dimensions and stroke volume were estimated, and the differences due to sex and age calculated and tested for significance.

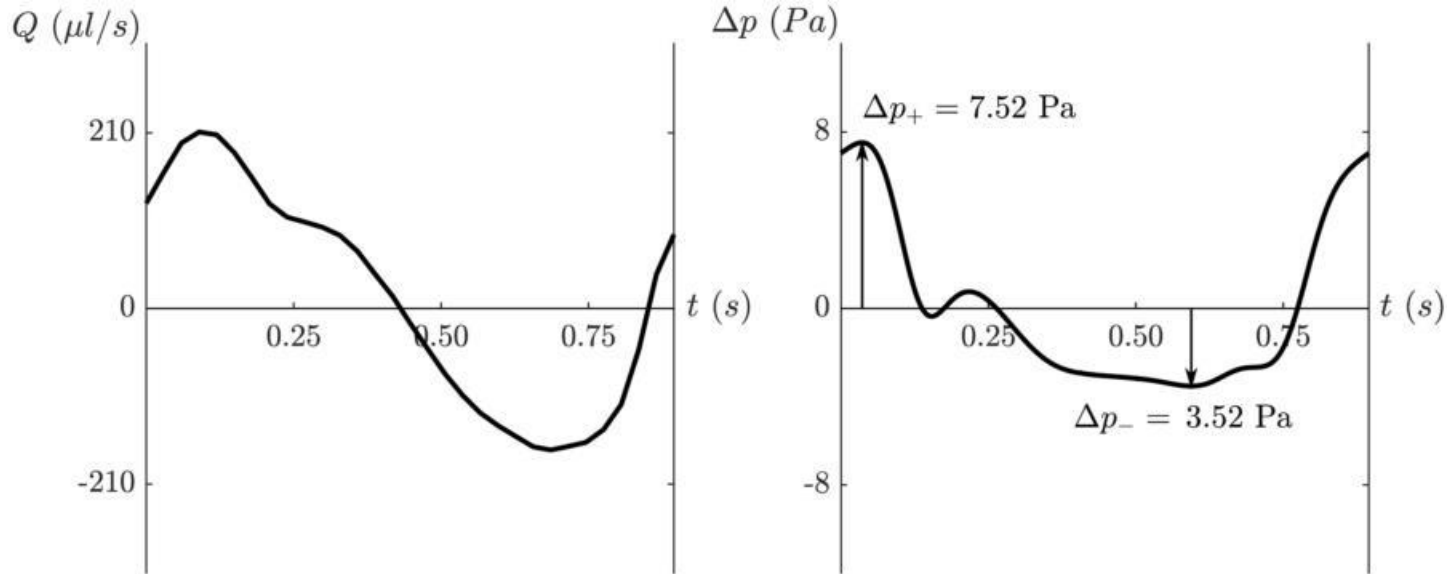
Results

Peak transmantle pressure was calculated with the non-dimensional model averaged 14.4 +/- 6.5 Pascals during caudal flow and 6.9 +/- 2.8 Pascals during rostral flow. It did not differ significantly between male and female or correlate significantly with heart rate. Peak transmantle pressure increased with age and correlated with aqueduct dimensions and stroke volume.

Conclusions

Our study shows that the computational fluid mechanics method based on a non-dimensional formulation has sufficient precision to detect differences in transmantle pressure due to age or aqueduct dimensions, two important issues that have not sufficiently been evaluated to date. The computation can be performed with a readily available straightforward computer program in a few minutes and may be easily applied in the clinical setting. Computation of transmantle pressure may be preferable to measurement of aqueduct

velocity or stroke volume as an index of abnormal CSF dynamics. Computational studies of transmantle pressures are warranted in NPH, communicating hydrocephalus and in other conditions with altered CSF dynamics.



(Filename: TCT_254_Figure3.jpg)

322

Tumor Habitat Analysis by Magnetic Resonance Imaging Distinguishes Tumor Progression from Radiation Necrosis in Brain Metastases after Stereotactic Radiosurgery

D Lee¹, J Park¹, H Kim²

¹Asan Medical Center, Seoul, Korea, Republic of, ²Asan medical center, seoul, seoul

Purpose

To determine whether the tumor habitats obtained by anatomic and physiologic MRI could distinguish tumor progression from radiation necrosis of brain metastases after SRS.

Materials and Methods

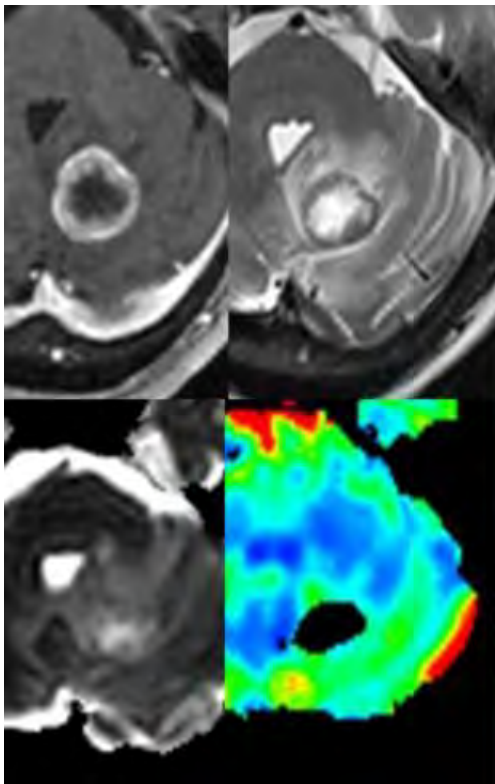
Sixty-nine metastases from 52 patients who underwent SRS between September 2014 and February 2020 and had enlarged contrast-enhancing lesion (CEL) on follow-up MRI were enrolled. The reference standard was clinicroadiologic follow-up or surgery. CEL was divided into spatial habitats by voxel-wise clustering between contrast-enhancing-T1-weighted and T2-weighted values (anatomic habitats) and between apparent diffusion coefficient (ADC) and cerebral blood volume (CBV) (physiologic habitats). Predictors of the voxel fraction of each habitat were selected by logistic regression. Performance was determined using the area under the receiver-operating-characteristics curve (AUC) to distinguish tumor progression.

Results

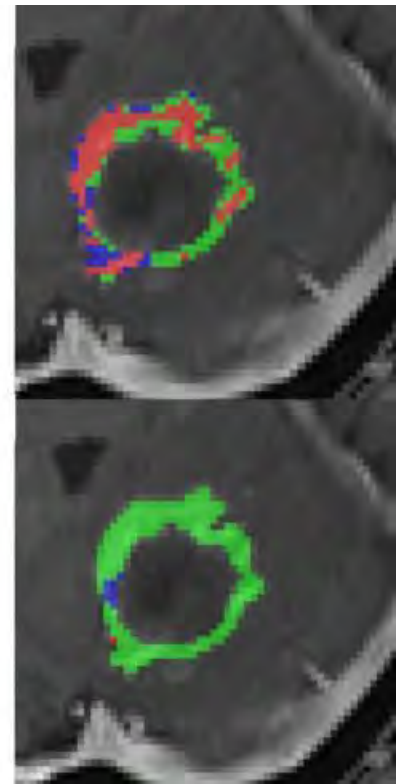
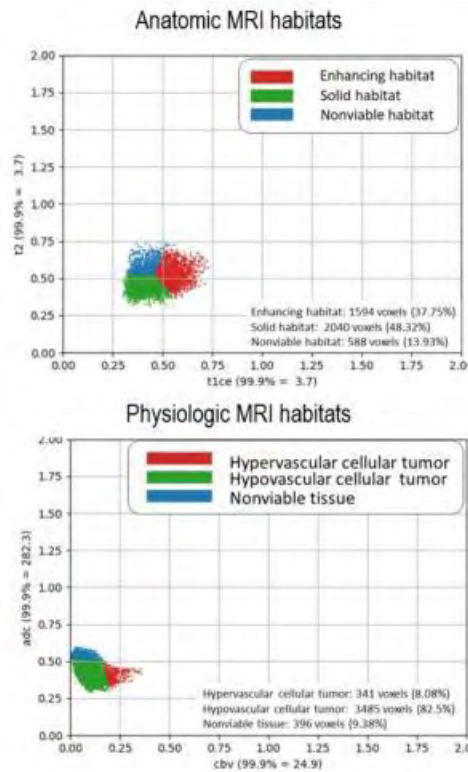
High voxel fraction of anatomic solid tumor habitat (low T2 values and lower CE-T1 values) was predictive of tumor progression (odds ratio [OR], 1.74, $P < 0.001$), whereas a high voxel fraction of anatomic nonviable tissue habitat (low CE-T1 and high T2 values) was predictive of radiation necrosis (OR, 0.55, $P < 0.001$). Combined anatomic solid and nonviable tissue habitat showed good discriminatory ability (AUC 0.85, 95% confidence interval [95% CI] = 0.77-0.94) and outweighed the ADC (AUC 0.64) and CBV (AUC 0.58) values.

Conclusions

Voxel fractions of solid tumor and nonviable tissue habitats determined by anatomic MRI may help to diagnose the tumor progression and radiation necrosis in patients with brain metastases after SRS.



(Filename: TCT_322_Figure2.jpg)



1329 Tumor-Tract Relationships Detected by Novel Clinical Research Application with Tractography for Neurosurgical Planning

D Krahulec¹, A Radwan², J Kirschke³, S Sunaert², K van de Ven¹, M Versluis¹, M Breeuwer¹
¹Philips Healthcare, MR R&D Clinical Science, Best, Netherlands, ²KU Leuven, Dept. of Imaging & Pathology, Translational MRI, Leuven, Belgium, ³Dept. of Neuroradiology, School of Medicine, Technical University of Munich, Munich, Germany

Purpose

One of the primary aims in surgical neuro-oncology is to maximize the extent of resection while minimizing irreversible harm to healthy tissue. Before surgery, oncological neurosurgeons estimate perioperative risks, potential functional deficits, and recovery. Therefore, the ability to preoperatively recognize relationships between pathology and surrounding white-matter fiber bundles is key to selecting adequate neurosurgical approaches. In this work, we demonstrate the feasibility of identifying fiber infiltration or displacement in routine clinical data using a new, workflow enhancing clinical research application with advanced diffusion MRI-based tractography.

Materials and Methods

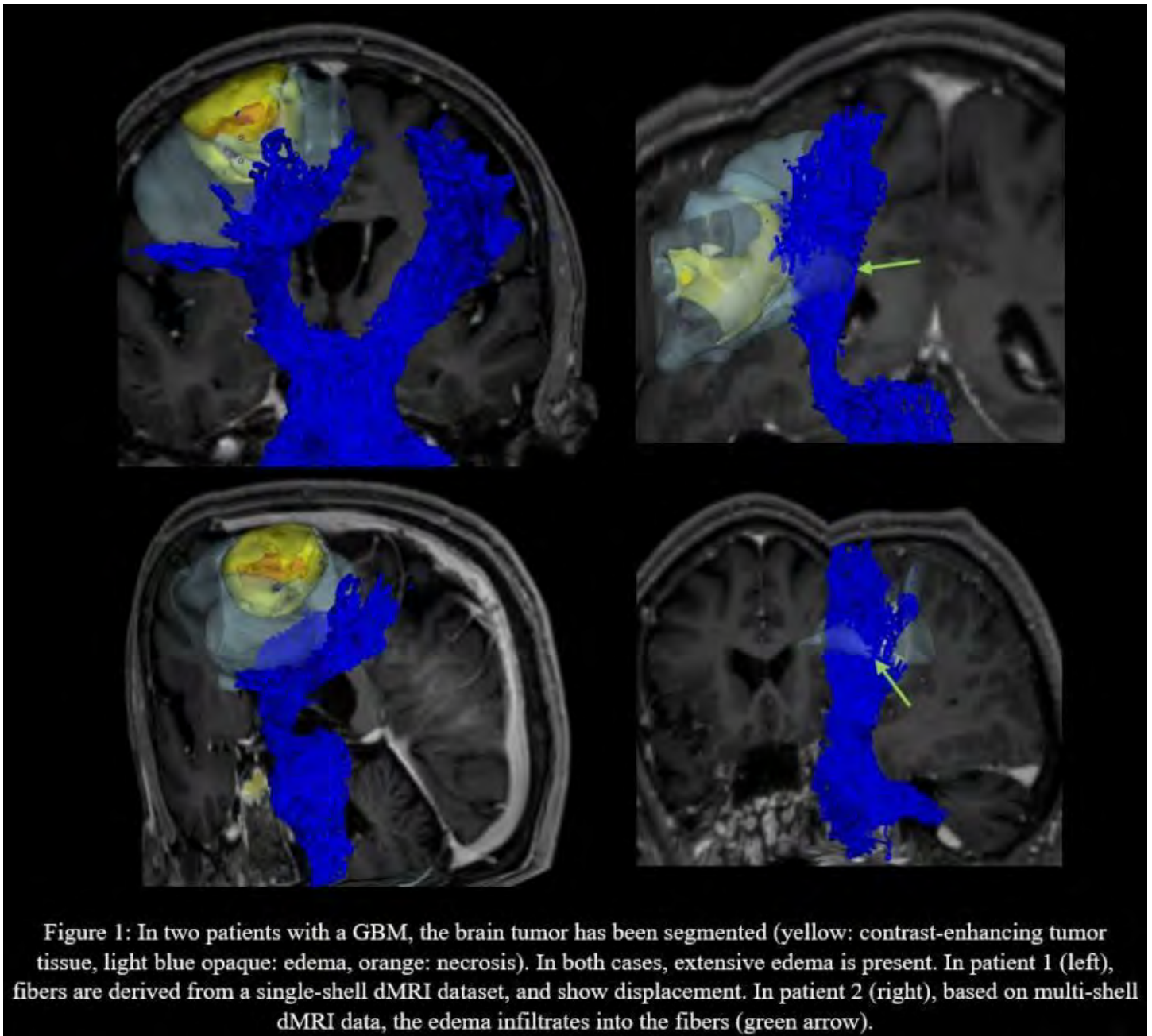
A clinical research software application has been developed to facilitate fast, accurate and fully automated data processing [1]. Brain tumor patient data have been collected from two clinical sites: Klinikum rechts der Isar, Munich – single-shell EPI-dMRI (33 vol., voxel size: 2 mm iso, b=0/1000 s/mm², TE/TR = 78/5000 ms), T1 (voxel size: 0.75 mm iso); UZ Leuven – multi-shell EPI-dMRI (258 vol., voxel size: 1.96 x 1.96 x 2.04 mm, b=0/1200/2500 s/mm², TE/TR = 58/4500 ms), T1 (voxel size: 0.9 mm iso). Both datasets also contain a T2, contrast-enhanced T1 and FLAIR images. Diffusion volumes were initially corrected for motion, EPI distortion, and registered to T1 space. Further processing consisted of voxel-wise fiber orientation estimation using the constrained spherical deconvolution algorithm (CSD) [2]. Probabilistic tractography of the corticospinal tract (CST) was performed using cortical labels acquired from volumetric brain and tumor segmentation [3, 4]. Spurious fibers were suppressed by a recently introduced filtering method [5].

Results

Both patient cases (Fig. 1) present with a glioblastoma (GBM) and extensive edema. In the first patient, the left CST shows signs of displacement induced by accumulated edema of a GBM in the left frontal precentral gyrus. Conversely, in the second patient, results indicate edematous infiltration of the CST related to a GBM in the right-sided operculum. Peripheral fiber infiltration was confirmed by neurosurgery.

Conclusions

Our proposed clinical research application helps reveal qualitative information about peritumoral white matter fibers that may be essential in neurosurgical decision-making. Evidence also suggests that using multi-shell diffusion MRI data with higher angular resolution and more diffusion directions is beneficial for fiber identification in edematous zones.



(Filename: TCT_1329_results.jpg)

738

Ultra-high and Super-high Resolution CT Imaging of the Temporal Bones

N Pham¹, O Raslan²

¹UCLA, Los Angeles, ²UC Davis, Sacramento, CA

Purpose

Temporal bone imaging is challenging due to the complex spatial orientation, interrelationships, and compartmentalization of the small osseous structures comprising the auditory and vestibular pathways. Super-high and ultra-high spatial resolution CT imaging can be advantageous for detecting temporal bone pathology and guiding treatment strategies.

Materials and Methods

6 temporal bone cadaveric specimens were used to compare and evaluate the temporal bone microanatomic structures, utilizing the following CT reconstruction modes: normal resolution (NR, 0.5 mm slice thickness, 512² matrix), high-resolution (HR, 0.5 mm slice thickness, 1024² matrix), super-high resolution (SHR, 0.25 mm slice thickness, 1024² matrix), and ultra-high resolution (UHR, 0.25 mm slice thickness, 2048² matrix). Noise and signal-to-noise ratio (SNR) for bone and air were measured at each reconstruction mode. Two observers assessed the ability to visualize 7 small anatomic structures using a 4-point scale at each reconstruction mode.

Results

Noise was significantly higher and SNR significantly lower with increases in spatial resolution (NR, HR, and SHR). However, there was no statistical difference between the SHR and UHR modes with regards to noise and SNR. There was significantly improved visibility of all temporal bone osseous structures of interest with the SHR and UHR modes relative to NR mode ($p < 0.001$) and most of the temporal bone osseous structures relative to the HR mode. However, there was no statistical difference in the subjective image quality between SHR and UHR CT imaging of the temporal bone ($p \geq 0.085$).

Conclusions

Super-high resolution and ultra-high resolution CT imaging results in significant improvement in image quality compared to normal resolution and high resolution CT imaging of the temporal bone. This study also suggests equivalency between super-high and ultra-high spatial resolution temporal bone CT imaging protocols for clinical use.

Figure 1 and 2. Axial and coronal images of the ossicles acquired at (A) ultra-high resolution (B) super-high resolution (C) high-resolution and (D) normal resolution. Super and ultra-high resolution CT imaging demonstrates improve visualization of the stapes crura. Air is seen within the petrous carotid canal and intracranially secondary to the use of cadaveric specimens.

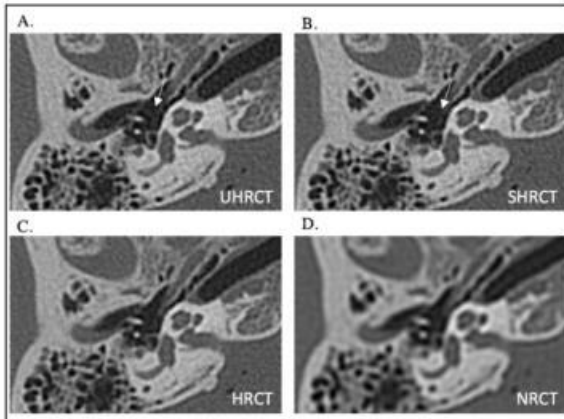


Figure 1

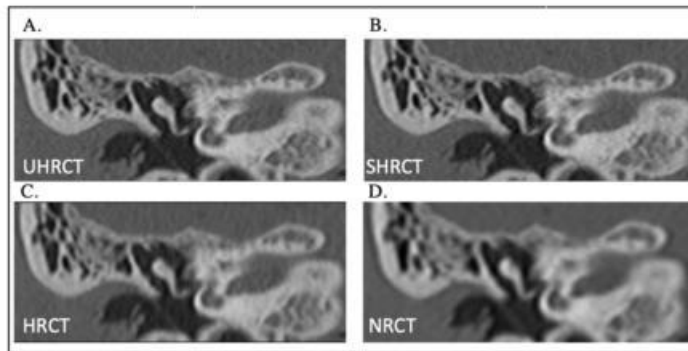


Figure 2

Table 1. Qualitative analysis scores of UHR, SHR, HR, and NR CT images. Image quality was scored using a semi-quantitative 4-point scale: 4, excellent delineation of structure; 3, good delineation of structure; 2, fair delineation of structure; and 1, poor delineation of structure [mean (SD)]. P-values were obtained from tests based on ordinal logistic mixed effects models. Bonferroni correction was used to adjust for multiple comparisons with a $p < 0.0083 (=0.05/6)$ considered as significant.

Structures	Reconstruction Modes				P-values (*not significant)			
	UHR	SHR	HR	NR	UHR vs SHR	UHR vs HR	UHR vs NR	SHR vs HR
Anterior Crus Stapes	3.33 (0.78)	3.00 (0.60)	2.50 (0.67)	1.17 (0.39)	0.085*	<0.001	<0.001	0.022*
Posterior Crus Stapes	3.33 (0.78)	3.08 (0.67)	2.50 (0.67)	1.17 (0.39)	0.191*	<0.001	<0.001	0.007
Incudomalleolar Articulation	3.92 (0.29)	3.67 (0.49)	3.17 (0.58)	1.67 (0.65)	0.131*	0.001	<0.001	0.017*
Incudostapedial Articulation	3.67 (0.49)	3.50 (0.52)	2.92 (0.29)	1.33 (0.49)	0.368*	0.001	<0.001	0.006
Spiral osseous lamina of the cochlea	3.75 (0.45)	3.83 (0.39)	3.08 (0.51)	1.08 (0.29)	0.599*	0.002	<0.001	0.001
Vestibular aqueduct	3.75 (0.45)	3.92 (0.29)	3.08 (0.29)	1.92 (0.29)	0.273*	0.002	<0.001	0.001
Cochlear Aqueduct	3.58 (0.51)	3.67 (0.49)	3.33 (0.78)	1.92 (0.29)	0.653*	0.287*	<0.001	0.14*

(Filename: TCT_738_TemporalBone.jpg)

1114

Unique Pseudoprogression Imaging Changes After Proton Versus Photon Radiation in Gliomas

J Graber¹, R Ritterbusch²

¹University of Washington, Seattle, WA, ²University of Washington School of Medicine, Laramie, WY

Purpose

Radiologic Assessment in Neuro-Oncology (RANO) criteria define pseudoprogression (Ps) after photon radiation for gliomas, as occurring less than twelve weeks from radiation, adjacent to or within the high dose radiation field. We observed lesions after Proton radiation therapy that appeared subjectively different from photon Ps based on timing and location, which would be designated as tumor progression by RANO criteria. We wanted to compare post treatment changes after proton versus photon radiation to describe their appearance, timing and location.

Materials and Methods

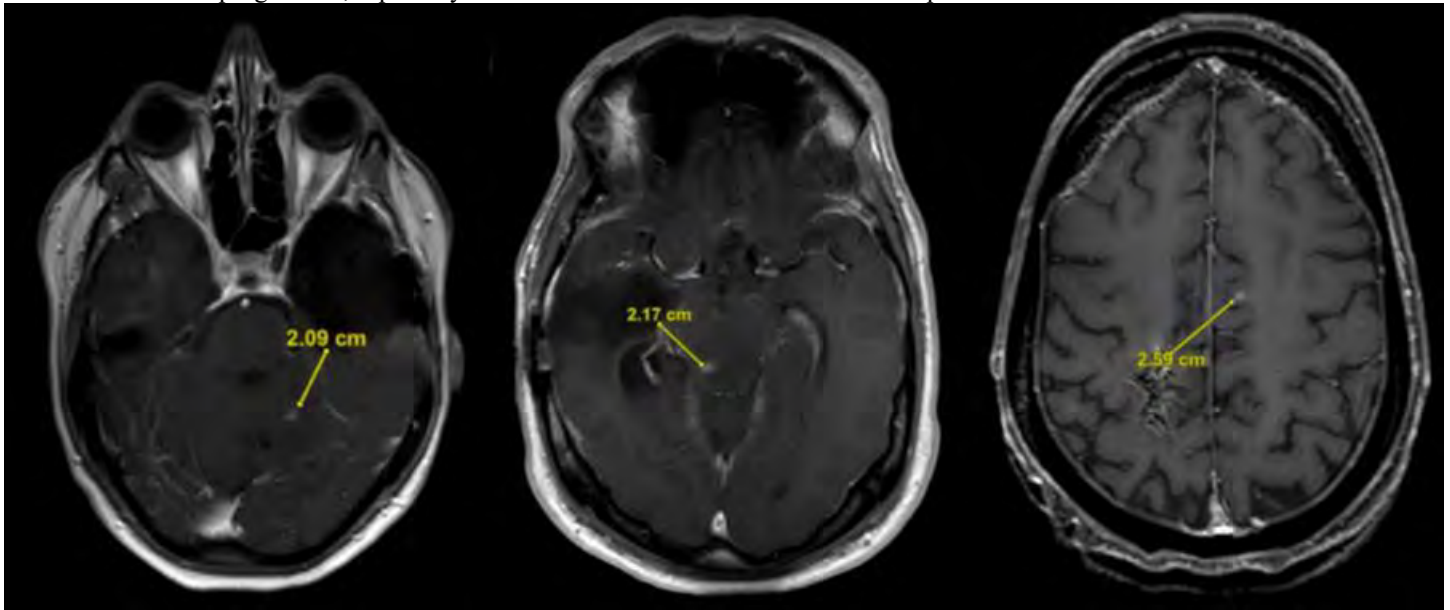
MRIs of patients with gliomas after proton or photon radiation were reviewed, along with clinical data. 77 proton patients and 64 photon patients were reviewed for imaging changes. Data collected included the location, timing, and morphology of the lesions, tumor type, chemotherapy, and clinical symptoms.

Results

16 (21%) of the patients who received protons had imaging changes unique to protons, at a mean of 14.6 months after radiation, which we called "Proton Pseudoprogression" or "ProPs". We established the following criteria to characterize ProPs: not immediately in or adjacent to the resection cavity; ~ 2cm opposite from target beam entry; can resolve without treatment; subjectively were often multifocal, patchy, and small (<1cm). None of the photon patients had lesions that met our criteria for ProPs ($p < 0.001$).

Conclusions

Patients who receive protons can have a spatially and temporally unique subtype of pseudoprogression (Ps), which we refer to as proton pseudoprogression (or ProPs). These lesions could be mistaken for tumor progression, but occur in a predictable time and location, and typically resolve spontaneously. ProPs can possibly be explained by the increased relative biological effectiveness of protons and beam angle selection which may deposit at ~2cm deep to the target, opposite the angle of proton entry. Interpretation of these changes requires awareness of the radiation modality and treatment plan. Recognizing these lesions can prevent unnecessary treatment for tumor progression, especially in the context of clinical trials that include proton.



(Filename: TCT_1114_PropsPic.jpg)

1121

Usefulness of 3D Fast Spin-Echo T1 Black-Blood Imaging in the Diagnosis of Facial Neuritis: Comparison with contrast-enhanced 3D spoiled GRE T1CE

S Jo¹, S Lee¹, S Chang¹

¹Dongtan Sacred Heart Hospital, Hallym University Medical Center, Hwaseong-si, South Korea

Purpose

Contrast-enhanced 3D fast spin-echo T1 black-blood imaging (CE-T1BB) selectively suppresses the signal of blood flow and could provide a higher contrast-to-noise ratio compared with contrast-enhanced 3D T1-SPACE. Our aim was to evaluate the usefulness of CE-T1BB with fat suppression sequences compared with 3D T1-SPACE with fat suppression (CE-T1FS) sequences in patients with facial neuritis.

Materials and Methods

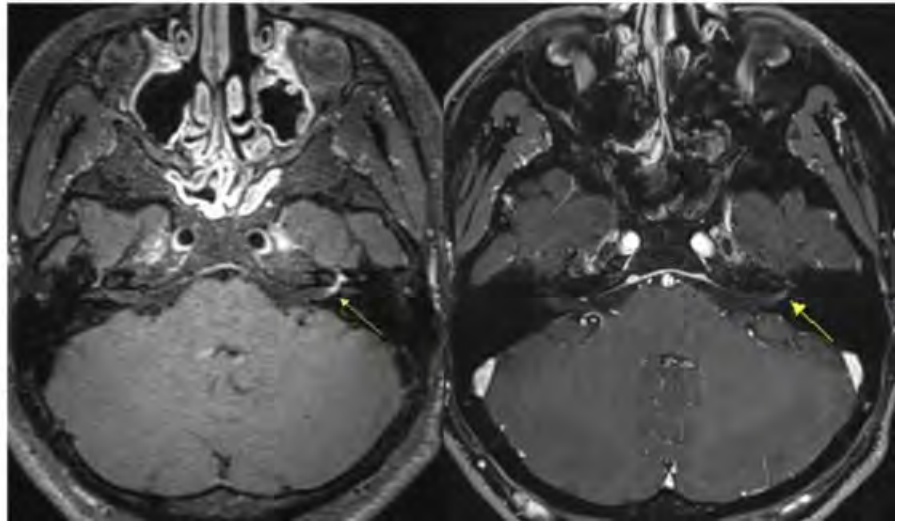
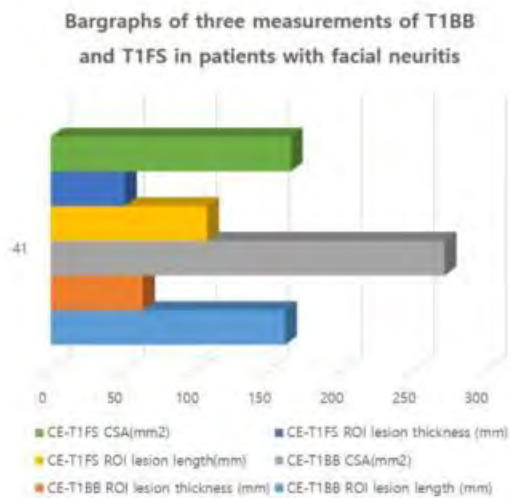
Institutional review board approved this retrospective study. 40 patients with facial neuritis who had undergone brain MR imaging were consecutively included. Brain MR imaging, including CE-T1BB and CE-T1FS, was performed in all patients using a 3T MRI scanner. The order of the MRI sequence was CE-T1FS, followed by CE-T1BB. Contrast-enhanced lesion length, thickness, and square areas were measured at canalicular segment of the facial nerves by using a measuring tool on the PACS. We compared the three quantitative measurements of the two MR sequences with Mann-Whitney test.

Results

All three measurements on CE-T1BB (length; 3.2 mm [IQR : 2.3-4.3 mm], thickness; 1.38 mm [IQR: 1.2-1.7 mm], square area; 4.82 mm² [IQR : 2.81-6.87 mm²]) were significantly greater than those on CE-T1FS. (length; 1.5 mm [IQR : 1.0-2.0 mm], thickness; 1.5 mm [IQR: 1.0-2.0 mm], square area; 1.5 mm² [IQR : 1.0-2.0 mm²])

Conclusions

We found that CE T1-BB was superior to CE-T1FS, in terms of lesion visualization of the facial neuritis.

CE-T1BB**CE-T1FS**

(Filename: TCT_1121_ASNR2020T1BBvsT1FSIable300DPI.jpg)

140

Using Deep Multi-Task Learning to Classify Brain MR Images by Sequence and Orientation

M Lee¹, N Kasmanoff², M Parente¹, N Razavian², Y Lui¹

¹NYU Grossman School of Medicine, New York, NY, ²NYU Center for Data Science, New York, NY

Purpose

Increasing complexity of MRI studies and variable series naming conventions reveal limitations of rule-based image routing, particularly relevant in health systems with multiple scanners/sites. An accurate method to identify series based on image content would aid in tasks like post-processing and PACS viewing. Recent efforts using deep learning (DL) show proof-of-concept identification of 8 basic brain series [1,2,3]. Here, we present a 2D convolutional neural network (CNN) with multi-task learning (MTL) to differentiate 23 series and image orientation.

Materials and Methods

Training data include 20,904 studies (86,089 series; 235,674 images). Test data include 2,589 studies (19,590 series; 1,237,521 images). Series are separated into 23 classes: T1, T1 IAC, MPRAGE, VIBE/GRASP (pre & post); T2, T2 HASTE, T2 SPACE, CISS, T2 FLAIR, 3D FLAIR; diffusion, ADC; SWI, SWI magnitude, phase, MIP; perfusion, scout, other. Series orientation (axial, coronal, sagittal, other) was also labeled. Out-of-domain external test data of 1,252 studies (2,150 series; 234,944 images) were also used for final evaluation. The CNN was built in PyTorch (Fig 1). Images were resized (256x256), normalized by pixel intensity, and data were augmented (rotation, scaling/cropping, translation). MTL was used to separately predict sequence & orientation. Majority-rules vote over all slices in a volume was used for final prediction. F1 score (harmonic mean of precision and recall) was used to evaluate performance.

Results

Confusion matrix shows high concordance between predictions and ground truth (Fig 2). Holdout test set accuracy was 97% with 100% F1 score for diffusion, ADC, SWI MIP, SWI phase, & scout. F1 was lowest for MPRAGE post (0%; 1 series), VIBE post (75%; 20 series), & T1 IAC post (85%; 136 series). Orientation accuracy was >99%. External test set accuracy was 97% with 99% F1 score for MPRAGE pre and other. Analysis of discrepancies found instances where ground truth labels were incorrect due to ambiguous/incorrect descriptions while the CNN correctly classified.

Conclusions

The model accurately classifies 23 brain MR series and identifies orientation, performing well on holdout test and external data. MTL is advantageous: it increases focus on relevant features, allows classifiers to share features, and reduces overfitting. This work shows that a DL approach for series identification accommodates the complexity of MRI studies present in state-of-the-art clinical practice. The model is transferable to other anatomy.

Figure 1. Convolutional neural network architecture. After 10 layers of convolution, batch normalization, and ReLU activation, the output is split into two heads for parallel multi-task learning of sequence and orientation.

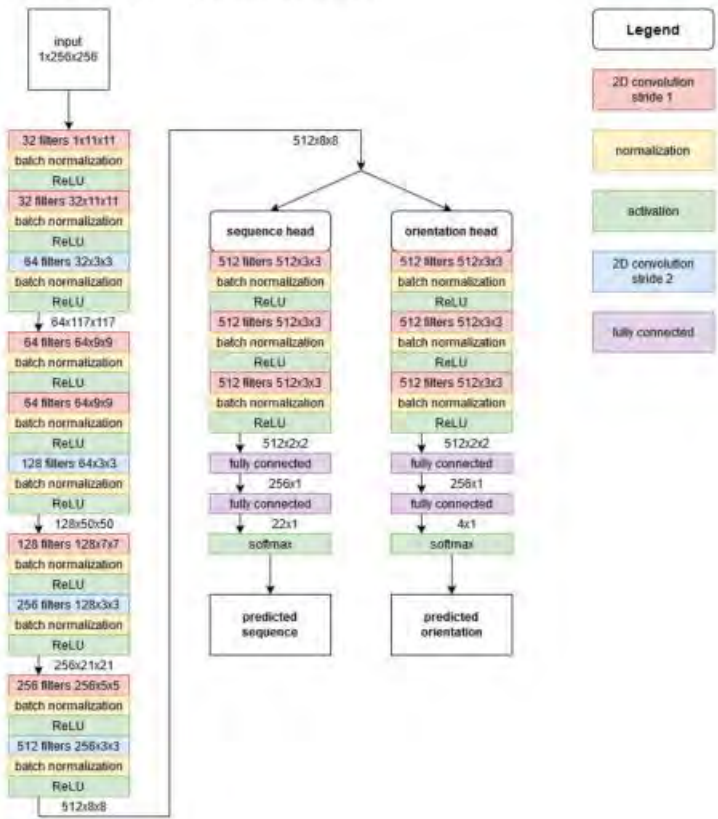
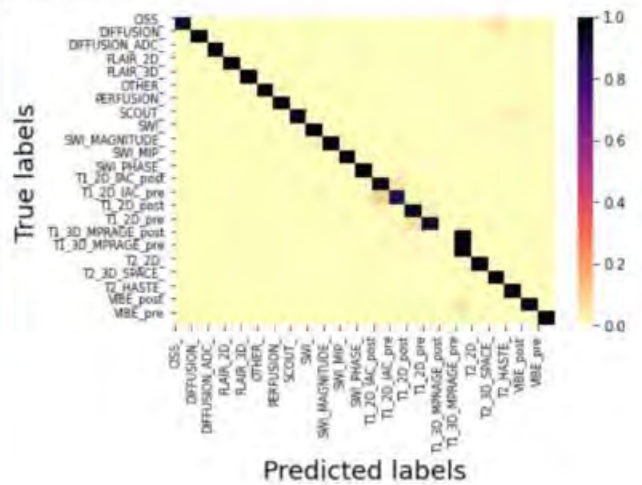


Figure 2. Confusion matrix of CNN classification performance on holdout test set. The color of each square corresponds to the proportion of sequence labels predicted for each ground-truth label.



(Filename: TCT_140_MRseriesCNN.jpg)

1636

Using high resolution functional imaging to investigate column-scale encoding of personal space in human parietal cortex

Z Nasirivanaki¹, B Babadi¹, S Nasr¹, D Greve¹, J Polimeni², D Holt¹, R Tootell¹

¹Massachusetts General Hospital, Boston, MA, ²Harvard Medical School, Massachusetts General Hospital, Charlestown, MA

Purpose

The regulation of preferred physical distance from another individual ('personal space') is altered in several neuropsychiatric conditions, including autism and schizophrenia. Prior studies have described regions in inferior parietal cortex that respond selectively to visual stimuli (including faces) that intrude into near (personal) space. To better understand that functional organization, we conducted high-resolution functional imaging (7T, 1.1 mm isotropic), extensively signal-averaged in within-subject analyses. High B0 magnetic field strength allows functional imaging with high contrast-to-noise ratios and improved spatial resolution, compared to clinical field strengths.

Materials and Methods

Seven healthy subjects were scanned in three experiments. In the main experiment, subjects viewed human face images that appeared to approach or withdraw from the subjects. In a second (control) experiment, we tested responses to stationary (rather than moving) face stimuli. In a third (control) experiment, we presented random dot stereograms, which formed a stereoscopic (3D) percept of a cuboid at different distances from a subject.

Results

The first experiment (approaching vs. withdrawing faces) activated discrete patches in inferior parietal cortex. All patches were radially elongated, i.e. cortical 'columns' in 3D. Approach-biased patches dominated the withdrawal-biased patches, in size and number. The columns based on personal space were systematically interdigitated with the columns based on visually defined (stereoscopic) distance. The third experiment revealed that the approach-biased patches showed a BOLD amplitude x distance response that was similar to that found earlier in behavioral tests: i.e. highest to the nearest faces, decreasing to increasingly further faces as a power function, reaching baseline near and beyond the behaviorally-defined personal space boundary in each subject.

Conclusions

High resolution images acquired at 7T reliably demonstrate specific radially-elongated patches ('columns') located in inferior parietal cortex, which are activated by faces that intrude into personal space. To our knowledge, this is the first demonstration of such columns

in human cortex which respond to complex, body-centered features, rather than single stimulus dimensions, e.g. lower level visual stimuli.

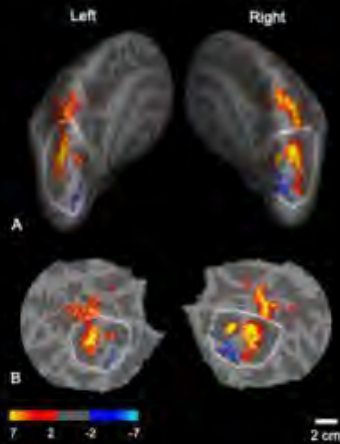


Figure 1. Group average of 7T activity (n=7) in response to approaching vs. withdrawing stimuli

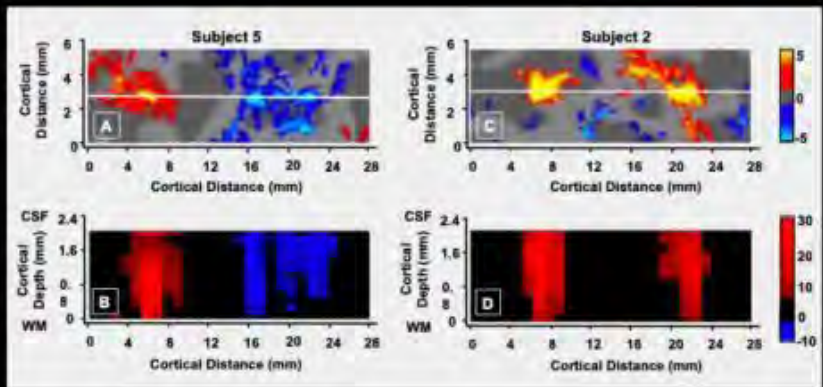


Figure 2. BOLD patches evoked by approaching- and withdrawing face stimuli are radially elongated ('columnar') in inferior parietal cortex.

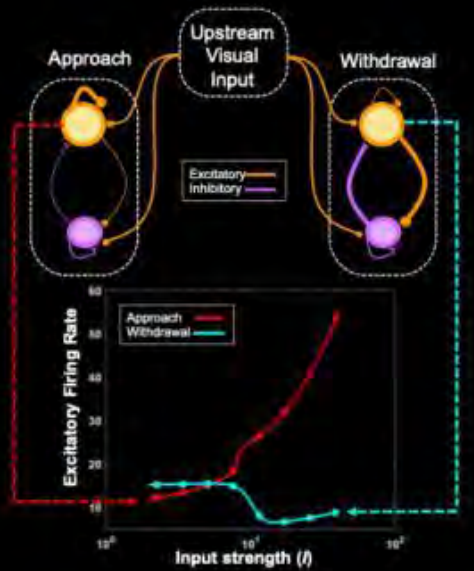


Figure 3. Computational model that explains the response profiles of the approach and withdrawal patches by the interplay of the excitatory and inhibitory components of their underlying cortical circuits.

(Filename: TCT_1636_Figures.jpg)

1620

Using Multimodal Deep Learning to Predict Infant Brain Age From Normal Myelination Patterns

G Chaudhari¹, J Chen¹, A Rauschecker², Y LI²

Purpose

Myelination in the first two years of life follows an orderly, predictable pattern, with changes in signal intensity on T1- and T2-weighted imaging based on corrected gestational ages (CGA). Deviation from these norms are used by neuroradiologists to evaluate for delayed myelination. This determination can be visually difficult, allowing for improved standardization with artificial intelligence. We demonstrate that a multimodal convolutional neural network (CNN) uses myelination patterns to predict the CGA of infants from T1- and T2-weighted MRI sequences.

Materials and Methods

Brain MRIs from 1995-2020 of infants 0 days to 25 months of age with reported normal myelination based on radiology reports were collected from our institutional database (n= 5838). The reports were manually screened for normal myelination without global white matter or structural abnormalities and sampled to balance the distribution of ages (Figure 1). The CGA at the time of imaging was manually calculated. T1 and T2 weighted sequences of the remaining scans (n= 389) were preprocessed with skull-stripping, linear registration to MNI305, z-scoring to normalize voxel intensities, and downsampling by 2x2x2. The neural network used was a 3-dimensional regression CNN (Figure 2) and was trained with linear weighting and data augmentation. The training was repeated for 10 iterations with random data splits. To calculate attention maps on trained networks, Layer-wise Relevance Propagation was used.

Results

The mean absolute error (MAE) of CGA prediction over 10 runs was 6.67 ± 0.77 weeks (Figure 3), with the multimodal network more accurate for younger infants (<70 weeks MAE = 5.35) than for older infants (>70 weeks MAE = 11.19). Attention map analysis of trained networks (Figure 4) demonstrates that the network is more attentive to cerebellum, posterior white matter and basal ganglia signal in younger infants and anterior white matter signal in older infants, which corresponds to known radiologic progression of myelination.

Conclusions

A 3D CNN is able to reliably predict the CGA of infants in the preterm to 25 month age range, based on brain myelination patterns on T1 and T2 weighted images. Such a deep learning approach has potential to augment radiologists' determination of appropriateness of infant myelination by MRI.

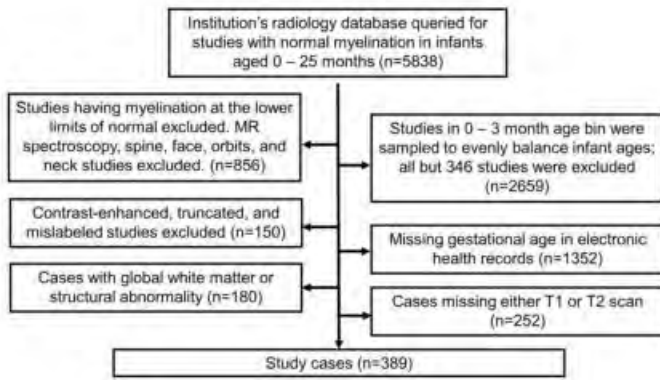


Figure 1: Flowchart of MRI study selection for CNN

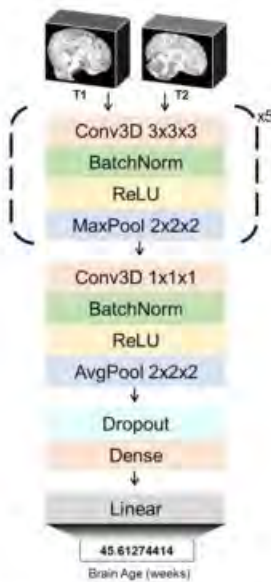


Figure 2: Multimodal 3D Convolutional Neural Network Architecture.

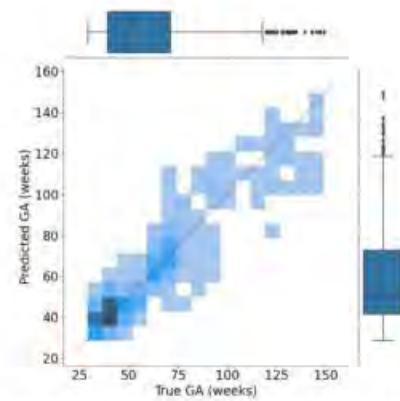


Figure 3: Scatter plot of true corrected gestational age vs. predicted corrected gestational age from the best performing multimodal network over 10 runs. Abbreviations: GA (corrected gestational age)

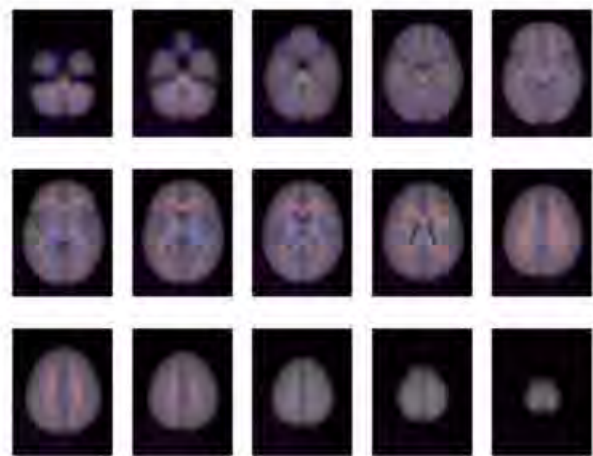


Figure 4: Overlay of average attention maps of older infants (>120 weeks, red) and younger infants (<40 weeks, blue), with overlap subtracted. Attention maps demonstrate that the network is more attentive to the cerebellum, deep gray nuclei and posterior cerebrum in the younger age group and the anterior supratentorial white matter in the older age group, which corresponds with the known progression in myelination.

(Filename: TCT_1620_ASNRAbstractFigures.jpg)

1297

Using T1-Weighted Images to Predict Vertebral Compression Fracture in Patients who Underwent SBRT for Metastases: Initial Experience

M Mojtahed Zadeh¹, B Moazen¹, A Chan¹, A Sahgal¹, S Myrehaug¹, J Detsky¹, H Soliman¹, Z Husain¹, C Tseng¹, P Jabejdar Maralani¹

¹University of Toronto, Toronto, Ontario

Purpose

Stereotactic body radiation therapy (SBRT) was recently demonstrated to be superior to conventional radiation therapy for the treatment of spinal metastases [1]. Rates of vertebral compression fraction (VCF) have been previously reported [2], but not in patients that demonstrated complete response (CR) on MR imaging. This study aimed to determine the incidence of non-progression-related VCF in patients that achieved CR post-SBRT on MRI, against those that did not.

Materials and Methods

This was a retrospective, single-centre study. Consecutive patients with spinal metastases were treated with SBRT. Spinal metastases were stratified by ISRC sectors [3], and those in the vertebral body sector were investigated. All available follow-up MRIs were assessed. Vertebral bodies that initially had VCF, previous vertebroplasty or stabilizing surgery were excluded, resulting in a total of

95 sectors in the final dataset. We stratified this cohort into two groups: the lesions that had CR (N=15), defined as the point where the tumor appears indiscernible on MRI, and the group who did not (N=80). Incidence of VCF was compared using Fisher's exact test.

Results

Among sectors with CR on MRI (N=15), four (26.7%) subsequently developed VCF over the course of their follow up. In the other group (N=80), VCF was observed in 5 vertebral bodies (6.25%). There was a significantly higher rate of VCF in the group that had CR on MRI (p=0.03).

Conclusions

Our study showed that rates of VCF appear higher in the vertebral body sectors that demonstrate CR on MRI. This may be due to the higher radiation dose per fraction, which successfully eradicates metastatic lesions but also destroys the bony scaffold and is subsequently replaced by fatty infiltration.

881

Utility of CT Angiography of Both the Head and Neck as A Screening Tool in a Level One Trauma Center

S Belchuk¹, C Sitton¹, R Riascos¹, M Bledsoe¹, C Yalniz¹, M VIRARKAR¹, S Khanpara²

¹The University of Texas Health Science Center at Houston, Houston, TX, ²University of Texas Health Science Center at Houston, Houston, TX

Purpose

Recently there has been a shift toward obtaining CTAs of both the head and neck in patients being evaluated in our ED. The trend applies to patients assessed by both the trauma and neurology service. There were 1165 such exams performed in the ED setting between October 2019 and October 2020. The cost of adding a head CTA for a trauma patient or neck CTA for a stroke patient approaches 0.15 FTE per year. The purpose of our investigation was to see what value these additional studies add to patient care.

Materials and Methods

Reports of 300 consecutive CTAs of the head and neck performed in the ED were reviewed by a staff neuroradiologist and neuroradiology fellow. The examinations were categorized under either Trauma or Neuro, depending on the provided history. The impression was examined for acute vascular findings. The report from the preceding NCCT was also examined for acute findings to determine whether the CTAs added any new information. Incidental findings likely to require medical follow-up were also recorded. CTAs which also included CT perfusion for evaluation of large vessel occlusion were excluded from this analysis, as were CTAs of only the neck.

Results

Of the 162 head CTAs performed for trauma, 26 (16%) contained significant intracranial findings, including active extravasation (5.6%), BCVI (2.5%), venous thrombosis or injury (2.5%), and brain death (1.9%); see Table 1. Of the 138 neck CTAs performed for acute neurologic findings, 12 (8.7%) contained significant findings, including complete vessel occlusion (3.6%), dissection (1.4%), and ulcerative plaque (1.4%); see Table 2.

Conclusions

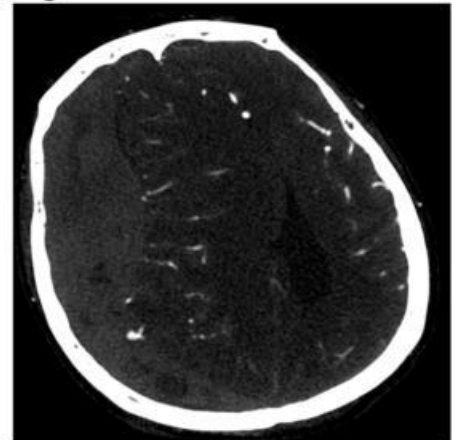
To our surprise, brain CTAs for trauma patients yielded more actionable findings than anticipated. Incidence of BCVI such as pseudoaneurysm formation could warrant previously unanticipated invasive angiography. Detection of active extravasation may lead to alteration in triage, but would need further investigation and discussion with our neurosurgery colleagues. Additionally, multiple studies demonstrated active extravasation or BCVI in a distal vessel which would have been outside the coverage included within our standard CTA neck protocol. Finally, more timely diagnosis of brain death could potentially alter decision making regarding organ donation. CTAs of the neck yielded little actionable information in the work-up of acute neurologic symptoms.

Table 1 - CTA Head for Trauma

Active extravasation	9 (5.6%)
Atherosclerotic stenosis	5 (3.1%)
BCVI	4 (2.5%)
Vasospasm	4 (2.5%)
Venous thrombosis or injury	4 (2.5%)
Aneurysm (incidental)	3 (1.9%)
Mass or vascular malformation	3 (1.9%)
Brain death	3 (1.9%)
Arterial vascular compression from mass effect	1 (0.6%)
Chronic dissection	1 (0.6%)
Global anoxic injury	1 (0.6%)

Figure 1

Active extravasation within subdural hematoma

Figure 2

Pseudoaneurysm at margin of SDH

Table 2 - CTA Neck for Neurologic Symptoms

Atherosclerotic stenosis (50-69%)*	4 (2.8%)
Atherosclerotic stenosis (>70% without occlusion)	2 (1.4%)
Atherosclerotic stenosis (complete occlusion)	5 (3.6%)
Ulcerative plaque	2 (1.4%)
Dissection	2 (1.4%)
Fibromuscular dysplasia (FMD)	2 (1.4%)
Extrinsic compression	1 (0.7%)
Aneurysm (extra-cranial)	1 (0.7%)

*Quantitative stenosis grading was not always available and is likely underestimated

(Filename: TCT_881_ASNRCTAgraphics.jpg)

524

Utility of MR-Contrast for Initial Work-up of Adult Onset Seizure

K Nelson¹, E Albach¹, A Thaker¹, V Timpone¹

¹University of Colorado Anschutz Medical Campus, Aurora, CO

Purpose

The diagnostic utility of contrast MR imaging in adult onset seizures without known or suspected neoplasia or infection is not well defined in the literature. Current imaging guidelines consider both contrast and noncontrast MR imaging examinations appropriate in this clinical scenario. The purpose of this study was to evaluate the utility of adding contrast MR sequences in the initial evaluation of seizure in patients without suspicion for neoplasia and infection.

Materials and Methods

Imaging and clinical data were reviewed for 336 consecutive patients admitted for phase 1 seizure monitoring, of which 103 met the following inclusion criteria: 1) Seizure protocol MRI brain performed with and without contrast; 2) No clinical suspicion for CNS infection; 3) No prior history of CNS neoplasia or suspected metastatic disease. Two board certified neuroradiologists reviewed MR studies and by consensus determined whether cases were lesional or non-lesional. For cases that were lesional, the finding was designated as either visualized on noncontrast sequence only, contrast sequence only, or visualized on both.

Results

29 of 103 (28%) patients had potentially epileptogenic lesions identified, 75 of 103 (72%) were non-lesional studies. The lesional cases were identified as: mesial temporal sclerosis (7), encephalomalacia (7), cortical dysplasia (5), grey matter heterotopia (4), dysembryoplastic neuroepithelial tumor (2), astrocytoma (1), cavernous malformation (1), and tuberous sclerosis complex (1). All lesional abnormalities were detected on noncontrast sequences. 23 of 29 (79.3%) lesional cases were visualized on both noncontrast and noncontrast sequences while 3 of 29 (10.3%) were visualized only on noncontrast sequences. No lesional cases were detected exclusively on post contrast sequences. Using national average Medicare fee schedule for combined technical and professional component charges, the difference in cost between an MR brain without contrast and an MR brain with and without contrast was \$144 USD. With an observed non-lesional extraneous contrast MR imaging rate of 72%, estimated excess cost of contrast MR imaging per 1,000 patients would be \$103,680 USD.

Conclusions

Contrast MR imaging has limited diagnostic utility in initial screening of seizure patients without known or suspected neoplasia or infection. More judicious use of contrast MR imaging in this patient population would reduce unnecessary exposure to gadolinium and associated healthcare costs.

864

Utilization Trends of Advanced Imaging in the Emergency Room Setting: An Alarming Trend

Purpose

This study aimed to assess historical trends in the utilization of spine imaging in the emergency room setting (ED).

Materials and Methods

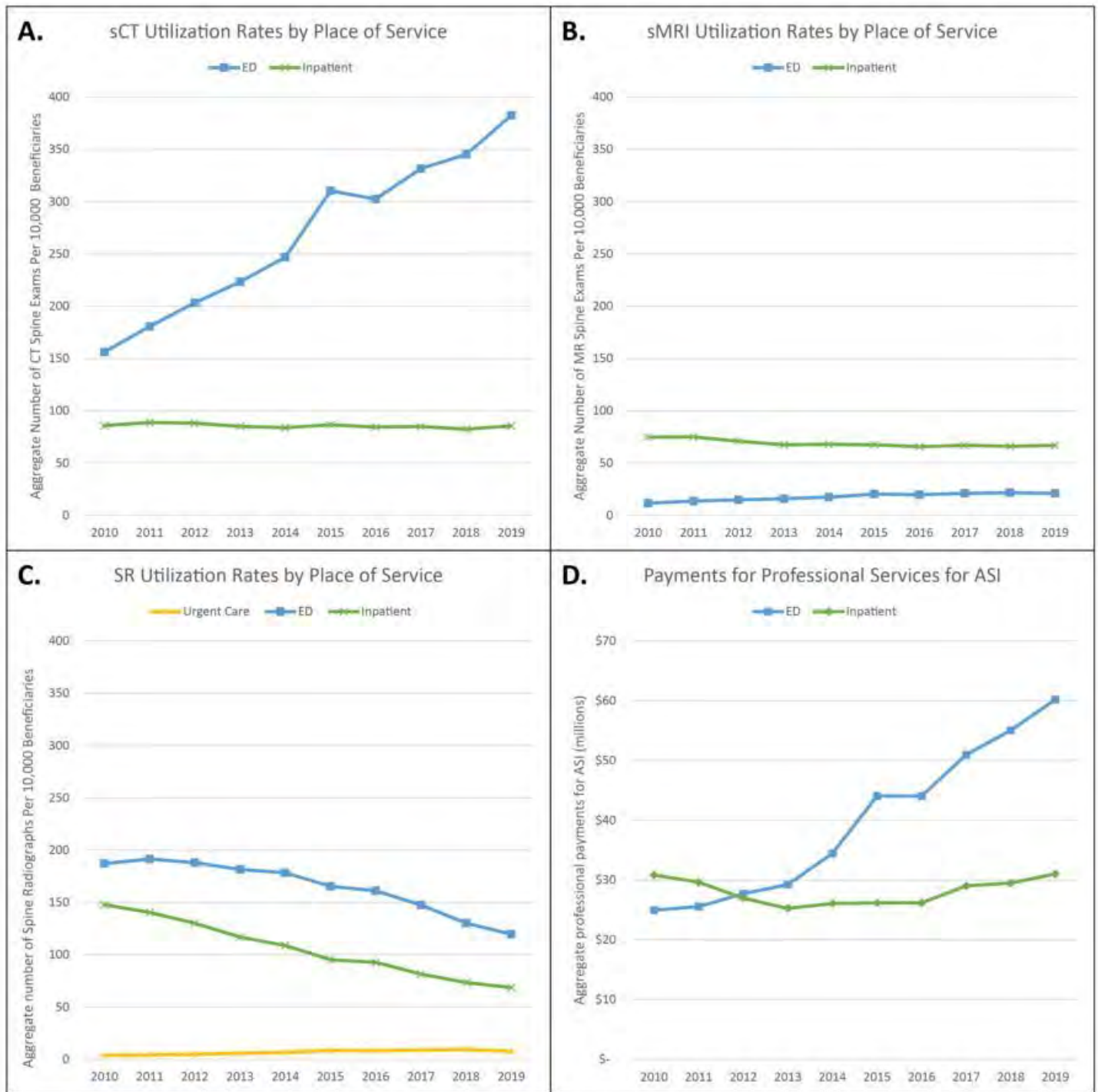
The national 2010-2019 physician supplier procedure summary files were used to determine spine imaging utilization in Medicare beneficiaries. Healthcare common procedure codes were used to extract all advanced spine imaging (ASI) exams, specifically all spinal computed tomography (sCT) and spinal magnetic resonance (sMR) studies. Claims for the technical component of imaging alone were excluded to prevent double counting. The procedure counts and charge amounts were aggregated based on location, as well as by ED and inpatient (INPT) settings. Results were converted into rates per 10,000 beneficiaries to correct for yearly population changes. Using a similar approach, we collected spine radiograph (SR) volumes to assess for any shift from radiography to ASI; for this analysis, we included the urgent care (UC) setting since they compete for SR.

Results

From 2010 to 2019, the rate of sCT performed in the ED per 10,000 beneficiaries increased from 156 to 382 (+245%). However, over the same timeframe, the sCT rate in the INPT setting remained unchanged (86 to 86). Over this period, the rate of sMR in the ED also increased rapidly from 12 to 21 (+175%), but sMR in the INPT setting fell from 75 to 67 (-11%). The utilization of SR in the ED decreased from 187 to 120 (-36%) and in the INPT setting from 148 to 69 (-53%). SR grew in the UC setting from 4 to 8 (+200%), but volumes in the UC setting remain low compared to the ED (15-fold difference in 2019). In 2012, the total professional payments for ASI in the ED setting overtook INPT. In 2019, ASI's total professional payments totaled \$60 million for the ED and \$31 million for inpatients (1.9-fold difference).

Conclusions

Despite the development of clinical criteria and appropriate use guidelines, there has been dramatic growth in ED utilization of sCT and sMR with a continued shift away from SR. The decreasing use of SR only partially explains the near doubling of ASI rates and suggests that most of this growth is inappropriate utilization. Increasing availability and liberal use of ASI in the ED has increased costs with often unclear benefits. These trends are likely exacerbated by patients increasingly seeking primary care services in the ED setting and the low threshold for performing ASI in the ED.



(Filename: TCT_864_EDSpineImagingFigures.jpg)

781

Utilizing an E-learning Platform in the Development of a Curriculum to Teach Neuroradiology Skills to Radiology Residents in the Midst of a Pandemic

E Bonfante-Mejia¹, J McCarty², c sitton³, E Friedman⁴, R Riascos⁵
¹UTHealth Houston, HOUSTON, TX, ²UTHealth Houston, Houston, TX, ³UT Health, Houston, TX, ⁴University of Texas HSC Houston, Houston, TX, ⁵The University of Texas Health Science Center at Houston, Houston, TX

Purpose

The 2020 Pandemic has imposed multiple challenges in the interaction of faculty and trainees. In addition, the goals and objectives of our curriculum were not clearly delineated. The delivery of content at the workstation, the emphasis on different components of the

curriculum, and the opportunities for application of knowledge skills were inconsistent amongst residents. To achieve a more consistent learning outcome we: • Delineated clear goals and objectives by creating a rubric with tiered skill levels for identification of baseline knowledge and a progression roadmap for acquisition of new skills. • Used an e-learning platform to deliver a self-directed course with video lectures, to ensure that the transmission of content from faculty to residents is consistent and focused on the objectives of the rotation. • Supplement the application of knowledge skills providing a repository of practice cases tagged with skill objectives and difficulty level.

Materials and Methods

1. Creation of a rubric with the goals and objectives using Qualtrics survey, with a tiered skill progression roadmap. 2. Use of the Canvas e-learning platform to deliver 13 video lectures. 3. Evaluation tools for individual modules, progression of each resident, and longitudinal evaluation of the curriculum is performed at multiple time-points. 4. Additional resources: We will create a repository of deidentified CT examinations in a DICOM viewer for targeted skill practice.

Results

As of October 2020, we have delivered the curriculum to 6 residents, collected feedback from residents and faculty, and identified areas of improvement. We are collecting data to compare the performance of the current first year class with the previous class, which did not utilize the curriculum.

Conclusions

We present our experience in the development of a structured curriculum for teaching neuroradiology skills and evaluating residents, using and e-learning platform. This curriculum addresses some of the limitations of our previous curriculum, uses tools that are attractive to young learners, frees time for application of skills at the workstations in the daily workflow, facilitates teaching in the setting of social distancing, and has evaluation tools that allow us to ascertain its impact and make adjustments to improve it.

1494

Utilizing Perfusion MRI, fMRI, and DTI to Plan Surgical Resection of Metastatic Melanoma to the Thalamus

A Mao¹, B Martin²

¹University of South Alabama College of Medicine, Mobile, AL, ²USA Health University Hospital, Mobile, AL

Purpose

In this educational exhibit, we discuss case presentation, multimodal imaging characteristics, and management of a patient with metastatic melanoma to the thalamus.

Materials and Methods

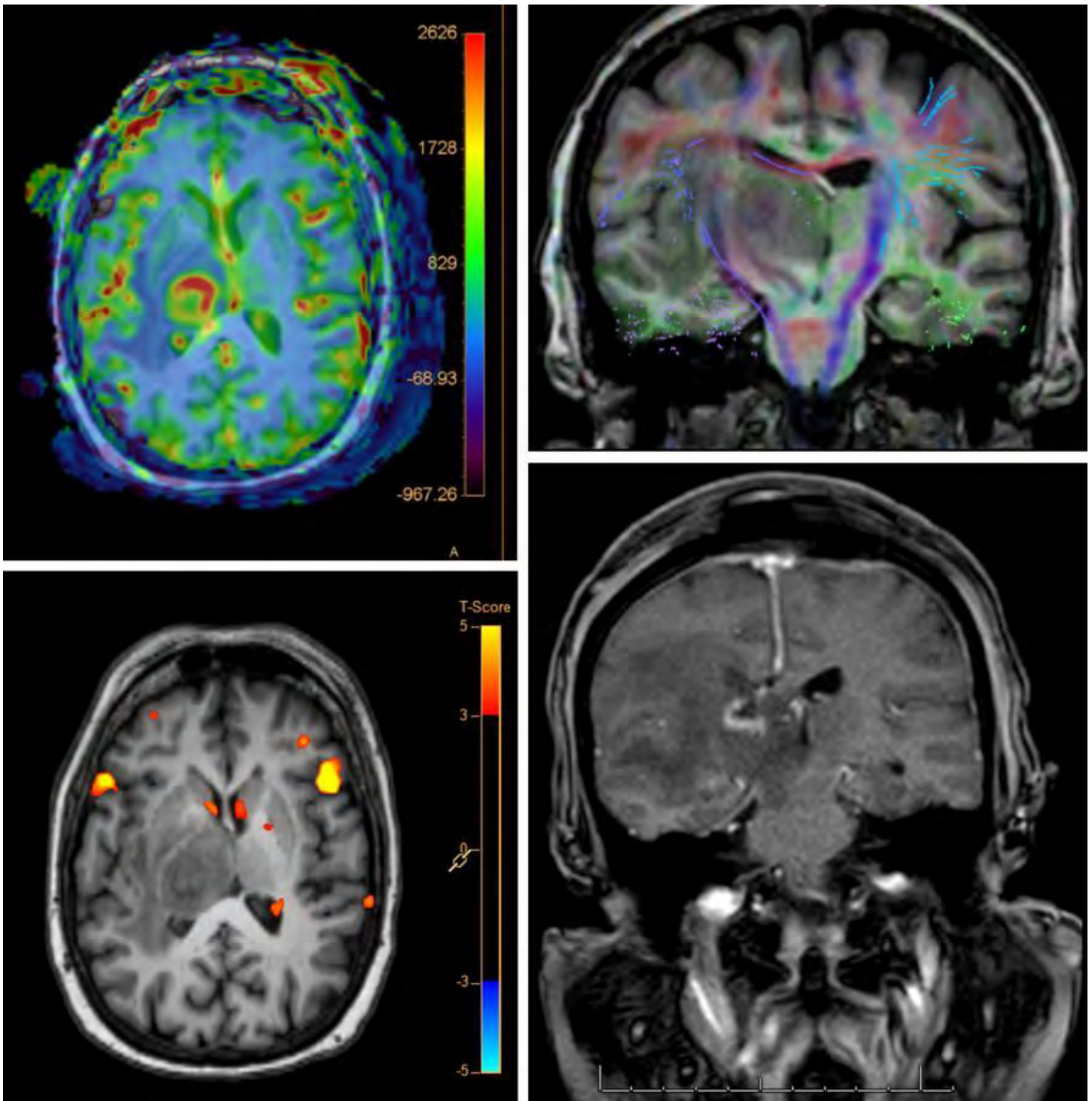
71-year-old female with history of pT4b melanoma and Breslow depth of 5.8 mm, status-post wide local excision of right parietal scalp, presents to the neurosurgery clinic for new-onset dizziness, ataxia, and left-sided weakness. Initial MRI showed a 2 x 2 x 2 cm contrast-enhancing tumor in the right thalamus with significant peritumoral edema causing mass-effect, likely metastatic melanoma given the patient's history of scalp melanoma. We aimed to emphasize the imaging characteristics of the lesion, which assisted in perioperative planning for successful surgical resection of the tumor.

Results

Repeat MRI brain with perfusion showed an increased 2.3 x 2.2 x 2.3 cm mass in the right thalamus demonstrating T2 hyperintensity and T1 iso-hypointense signal with avid postcontrast enhancement. The tumor demonstrates markedly increased cerebral blood flow and blood volume. The area of highest CBV is a crescentic region along the anterior and medial aspect of the right thalamic mass. Further presurgical characterization with functional MRI (fMRI) localized increased cortical activity in the left hemisphere with respect to word generation. Diffusion tensor imaging (DTI) demonstrated lateral displacement of the right corticospinal tract. Management of the tumor was anatomically challenging given its thalamic location. In addition, metastatic brain melanoma is typically considered radioresistant. Neurosurgery decided the safest option would be a left-sided craniotomy for contralateral interhemispheric transfalciine, transcalsal, transventricular approach with resection of right thalamic tumor. Postoperative coronal T1 post-contrast showed successful resection of the thalamic mass. One week after surgery, she is stable and monitored in the ICU for improvement of cerebral edema with Decadron taper.

Conclusions

Brain metastases are a frequent complication in patients with regional metastatic melanoma and cause morbidity and mortality. Prognosis has been substantially improved by major advances in neuroimaging and enhanced neurosurgical and radiotherapeutic treatment of brain metastases. We highlight a remarkable case of a patient with metastatic melanoma to the right thalamus. A combination of perfusion MRI, fMRI, and DTI helped with perioperative planning and the patient underwent successful surgical resection of the tumor.



(Filename: TCT_1494_PerfusionMRIfMRIDTIandCoronalT1-PostContrast.jpg)

969

Vacuolar Tauopathy: Imaging Findings of a Novel Autosomal Dominant Tauopathy

I Nasrallah¹, J Papatriantafyllou², N Darwich¹, J Phan¹, B Kim¹, E Suh¹, S Papageorgiou³, M Grossman¹, L Massimo¹, D Irwin¹, C Toro⁴, G Aguirre¹, V Van Deerlin¹, E Lee¹, C McMillan¹

¹University of Pennsylvania, Philadelphia, PA, ²Medical Center of Athens, Athens, MH, ³Medical School, National and Kapodistrian University of Athens, 1st Department of Neurology, Athens, Greece, ⁴NIH, Bethesda, MD

Purpose

Tauopathies are a group of neurodegenerative diseases characterized by accumulation of pathologic tau aggregates, usually regionally localized where they are associated with brain atrophy. Alzheimer Disease is the most common tauopathy, characterized by paired

helical filaments which aggregate in intracellular neurofibrillary tangles. Several syndromes are characterized as Frontotemporal Lobar Degeneration (FTLD), some of which are associated with specific genetic mutations. For example, mutations in the microtubule-associated protein tau gene (MAPT) are known to result in familial FTLD. Two kindred were identified with autosomal frontotemporal dementia lacking previously known causative mutations; the proband initially presented with personality changes and language dysfunction. Radiologic, neuropathologic, and genetic analyses were performed to characterize this syndrome.

Materials and Methods

Clinical structural MRI was performed on affected individuals, including FLAIR and diffusion imaging. Tau PET was performed using 10.4 mCi ¹⁸F-flortaucipir, with imaging 75-105 minutes after injection (6 x 5 minute frames). Autopsy of the proband included hematoxylin and eosin staining, and immunohistochemistry for PHF1 and GT-38 antibodies.

Results

Longitudinal MRI showed progressive frontal atrophy (Fig 1A). Diffusion imaging revealed prominent cortical diffusion restriction in the posterior cerebrum (Fig 1B), particularly occipital and parietal lobes. This feature is reminiscent of imaging findings of Creutzfeldt-Jacob disease related to vacuolization, but notably in a region without significant atrophy. Tau PET identified cortical tracer binding (Fig 1C). Genetic sequencing identified a hypomorph mutation in Valosin-containing protein (VCP) shared by affected individuals. Neuropathologic studies indicated that neurodegeneration was associated with neurofibrillary tangles and neuronal vacuolization. Tau aggregates were morphologically and biochemically similar to AD neurofibrillary tangles: immunoreactive with antibodies specific to phosphorylated tau (PHF1) and the tau conformation specific to AD (GT-38). Consistent with neuroimaging, neuronal vacuolization and neurofibrillary degeneration were inversely related.

Conclusions

Radiologic, neuropathologic, and genetic analyses identified a novel tauopathy that features rostral tau deposition and neurodegeneration and caudal cortical vacuolization, with characteristic imaging findings on MRI and tau PET. We have named this disease vacuolar tauopathy.

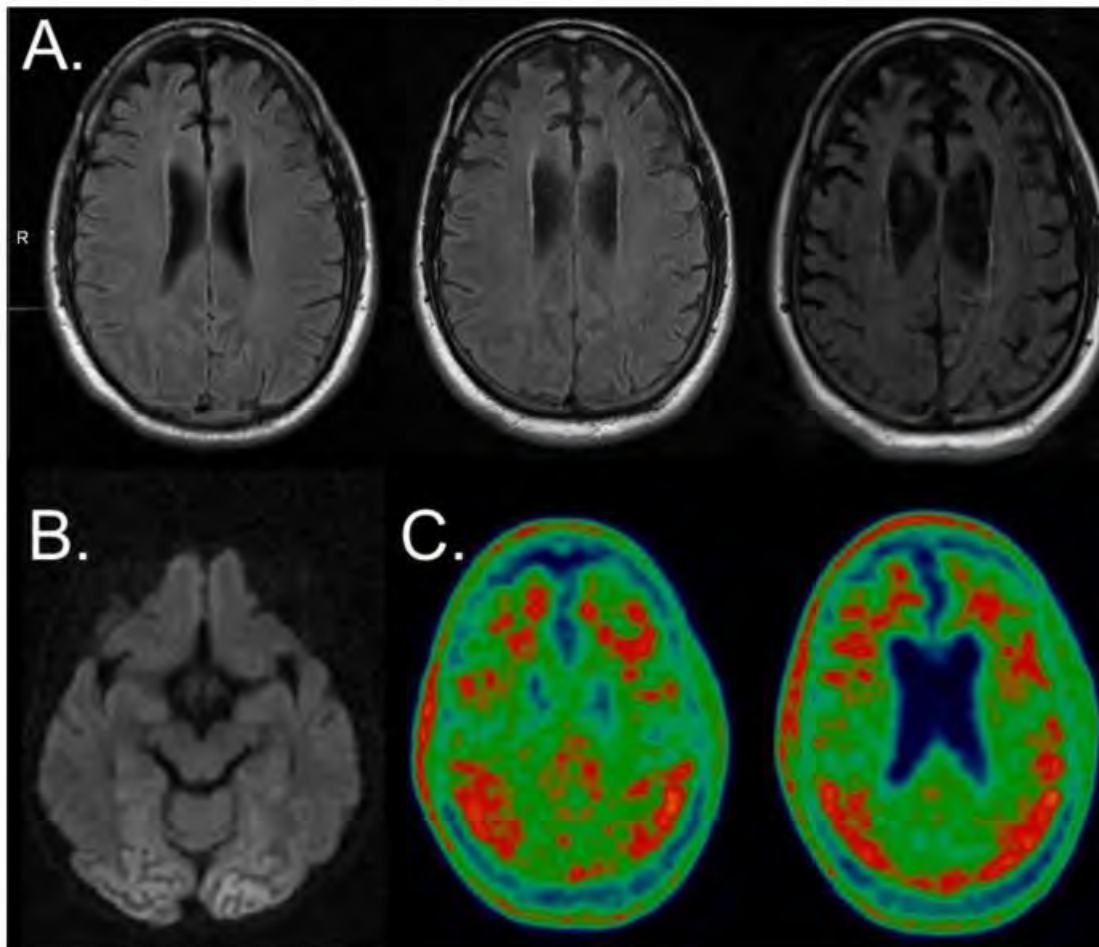


Figure 1. Neuroimaging findings in vacuolar tauopathy. A. FLAIR images from three studies, each 2 years apart (earliest on the left) showing progressive frontal atrophy. B. Diffusion-weighted imaging shows posterior cortical diffusion restriction. C. ¹⁸F-flortaucipir PET shows tracer binding.

(Filename: TCT_969_1.jpg)

579

Validation of a Deep Learning Tool in the Detection of Intracerebral Hemorrhage and Large Vessel Occlusion

J McLouth¹, S Elstrott¹, S Quenet², Y CHAIBI³, P Chang¹, D Chow¹, J Soun¹

¹University of California, Irvine, Orange, CA, ²Avicenna.AI, La Ciotat, France, ³Olea Medical, La Ciotat, France

Purpose

Recently developed machine-learning algorithms have demonstrated strong performance in the detection of intracerebral hemorrhage (ICH) and large vessel occlusion (LVO). However, their generalizability is limited given geographic bias of studies. The aim of this study was to validate a commercially available deep learning-based tool in the detection of both ICH and LVO across multiple hospital sites and vendors throughout the U.S.

Materials and Methods

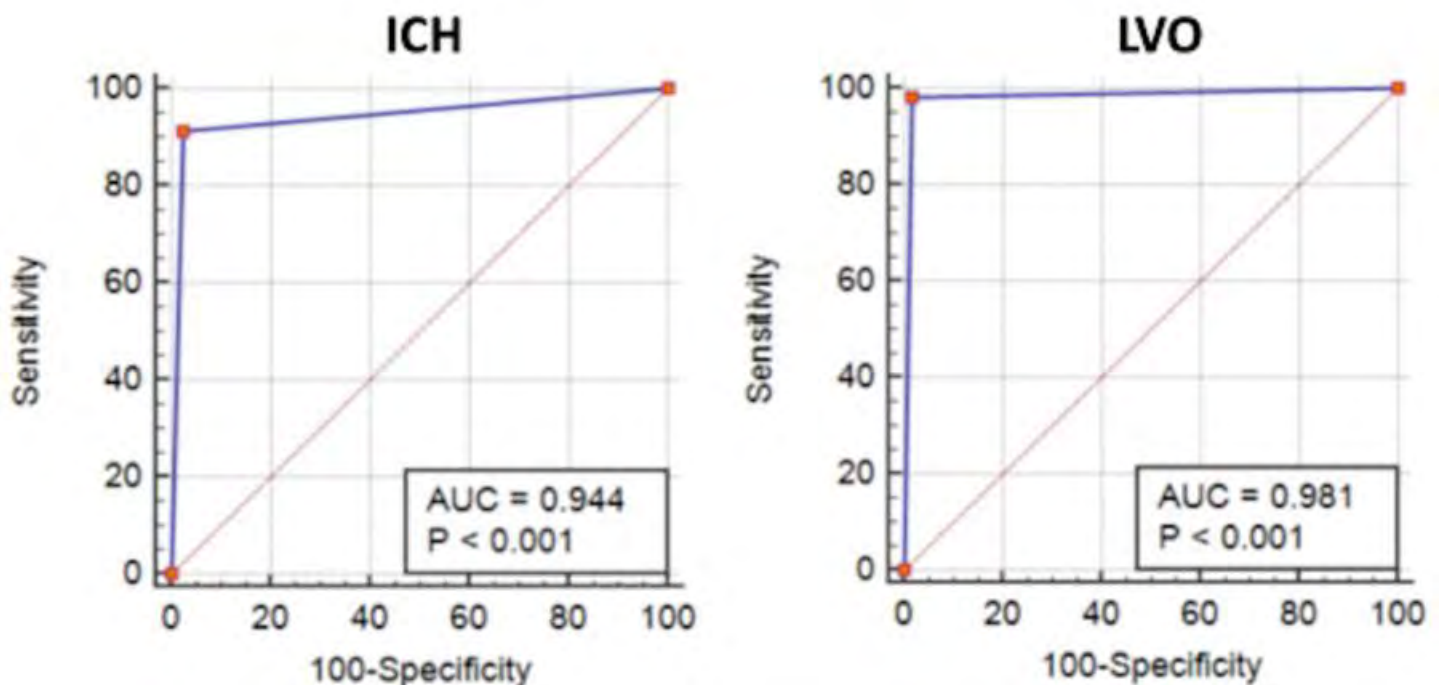
This was a retrospective study using anonymized data from two institutions. 814 non-contrast CT cases and 378 CT angiography cases were analyzed in regards to ICH and LVO, respectively. The tool's ability to detect and quantify ICH, LVO and their various subtypes was assessed amongst multiple CT vendors and hospitals across the United States. Ground truth was based off imaging interpretations from two board-certified neuroradiologists.

Results

There were 255 positive and 559 negative ICH cases. Accuracy was 95.6%, sensitivity was 91.4% and specificity was 97.5%. AUC ($p < 0.001$) was 0.94. ICH was further stratified into the following subtypes: intraparenchymal, intraventricular, epidural/subdural and subarachnoid with true positive rates of 92.9%, 100%, 94.3% and 89.9%, respectively. ICH subtypes were further divided into small (<5 mL), medium (5-25 mL) and large (>25 mL) volumes, with true positive rates of 71.8%, 100% and 100%, respectively. There were 156 positive and 222 negative LVO cases. Accuracy was 98.1%, sensitivity was 98.1% and specificity was 98.2%. AUC ($p < 0.001$) was 0.98. A subset of 55 randomly selected cases were also assessed for LVO detection at various sites, including the distal internal carotid artery, middle cerebral artery M1 segment, proximal middle cerebral artery M2 segment and distal middle cerebral artery M2 segment with an accuracy of 97.0%, sensitivity of 94.3% and specificity of 97.4%.

Conclusions

Deep learning tools can be effective in the detection of both ICH and LVO across a wide-variety of hospital systems. While some limitations were identified, specifically in the detection of small ICH and distal M2 occlusion, this study highlights a deep learning tool that can assist radiologists in the detection of emergent findings in a variety of practice settings.



(Filename: TCT_579_Abstractfigure1.jpg)

1073

Validation of Deep Learning Based Critical hypoperfusion and Ischemic Core Prediction in a Multicenter External Randomized Controlled Trial

Y Yu¹, Y Xie¹, S Christensen², E Gong³, G Albers⁴, G Zaharchuk¹

¹Stanford University, Stanford, CA, ²GrayNumber Analytics, Lomma, Sweden, ³Subtle Medical Inc., Menlo Park, CA, ⁴Stanford University Medical Center, Palo Alto, CA

Purpose

We previously developed two separate deep learning (DL) models to segment the ischemic core and critically hypoperfused tissue on

baseline imaging of acute ischemic stroke patients. We aimed to validate the models in an external, multi-center randomized clinical trial (DEFUSE3) and compare with the current clinical standard.

Materials and Methods

The DL models were previously trained in a separate dataset in which follow-up MRI, obtained at 3-7 days, was used as the reference for critically hypoperfused tissue in patients who did not reperfuse and as the reference for the ischemic core in patients who did reperfuse. For validation, we included DEFUSE3 patients with adequate quality baseline MR perfusion and a 24-hour follow-up DWI scan. The 24-hour DWI lesion served as the reference for ischemic core in patients in the thrombectomy arm and for critically hypoperfused tissue for patients in the medical arm. RAPID was used to generate perfusion maps (Tmax, cerebral blood flow, cerebral blood volume, and mean transient time). The accuracy of segmenting the ischemic core and critically hypoperfused tissue on baseline imaging was compared between the DL approach and the traditional thresholding approach implemented in RAPID.

Results

In the 46 patients included for analysis, 24 were in the medical arm and 22 in the thrombectomy arm. Compared to a traditional thresholding method, the DL model segmented the ischemic core more accurately (AUC of 0.92 vs 0.72, $p=0.0001$ and volume difference of -8ml vs -21ml, $p=0.001$). Similarly, the DL model segmented critically hypoperfused tissue more accurately (AUC of 0.93 vs 0.80, $p<0.0001$; volume difference 14ml vs. 55ml, $p=0.0005$). However, great heterogeneity in final infarct was noticed in medical arm. See tables and figures.

Conclusions

The DL-based critical hypoperfusion and ischemic core prediction provides more accurate prediction on final infarct than a commonly used thresholding method in this external validation.

Table 1. accuracy of DL model and RAPID segmentation in patients with thrombectomy and medical treatment only.

<i>Thrombectomy (n=22)</i>	<i>AUC</i>	<i>dice</i>	<i>volume difference, ml</i>	<i>absolute volume difference, ml</i>
DL Model	0.92 (0.85-0.94)	0.54 (0.45-0.68)	-8 (-27, 1)	10 (6, 27)
RAPID	0.72 (0.64-0.79)	0.51 (0.38-0.59)	-21 (-41, -4)	21 (4, 41)
<i>p-value</i>	0.0001	0.019	0.001	0.02
<i>Medical treatment (n=24)</i>	<i>AUC</i>	<i>dice</i>	<i>volume difference, ml</i>	<i>absolute volume difference, ml</i>
DL Model	0.93 (0.91-0.96)	0.55 (0.38-0.65)	14 (-6, 63)	23 (10, 77)
RAPID	0.80 (0.76-0.83)	0.36 (0.26-0.53)	55 (21, 104)	60 (24, 104)
<i>p-value</i>	<0.0001	0.0001	0.0005	0.009

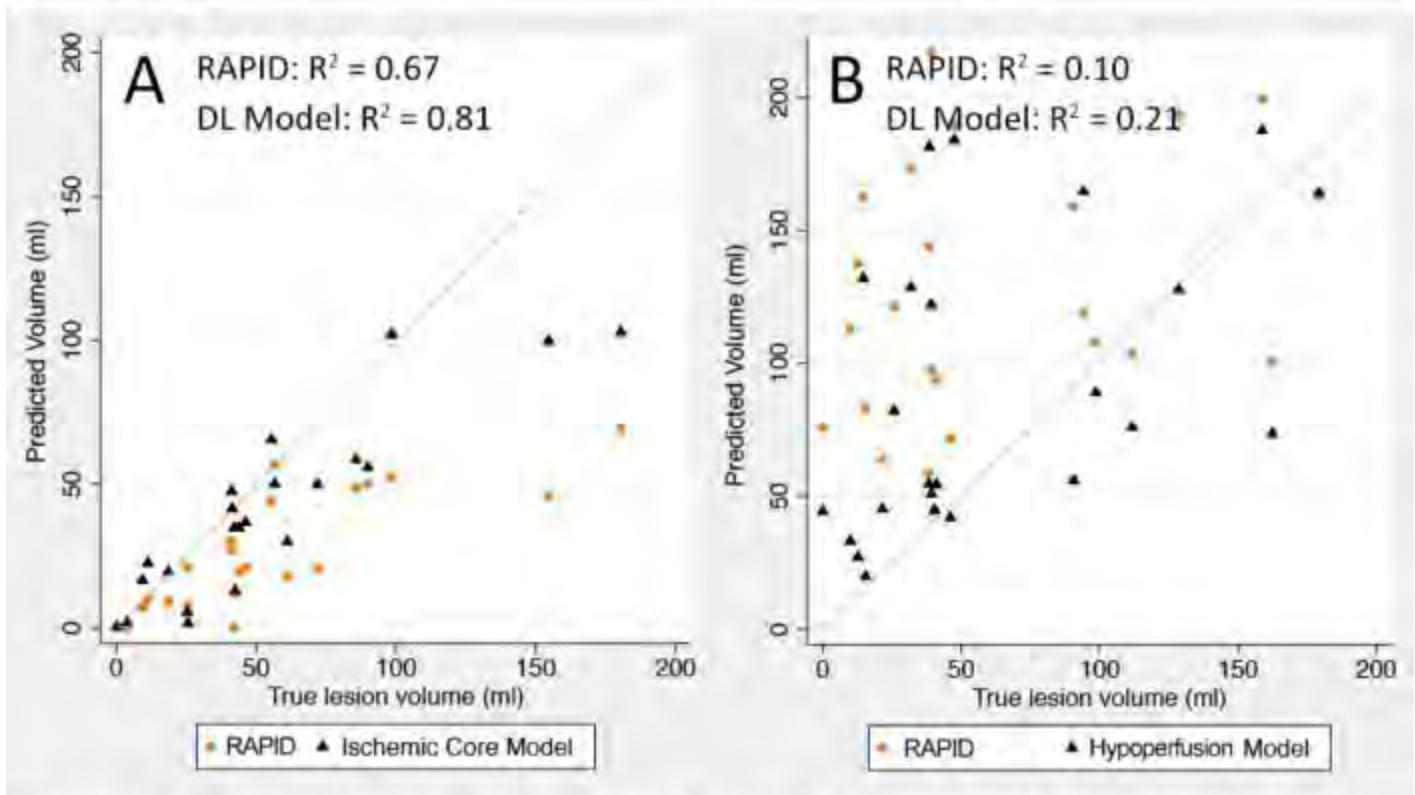


Figure. Volume correlation between deep learning model and true infarct volume, and between thresholding method and true infarct volume. A) Patients with thrombectomy. DL model is compared with ADC < 620 segmentation from RAPID. B) Patients with medical treatment only. DL model is compared with the union of Tmax>6s and ADC<620 segmentation from RAPID. The dotted grey line represent perfect correlation.

(Filename: TCT_1073_D3validation-new.jpg)

Validation of Newly Developed CT Perfusion Software Compared to RAPID iSchemaView in 143 Patients with Acute Ischemic Stroke

J Derakhshan¹, A Abedini¹, R Dhar¹, M Goyal¹, R McKinstry¹, J Lee²

¹Washington University in St. Louis, St. Louis, MO, ²Washington University in St. Louis, St. Louis, MO

Purpose

To compare perfusion defect volumes as well as hypoperfusion intensity ratio (HIR)[1] obtained with newly developed CT perfusion deconvolution software operating at the native resolution compared to FDA-approved Rapid iSchemaView (which downsamples the data spatial resolution by 2x in all directions) in acute ischemic stroke patients.

Materials and Methods

CT perfusion scans in 125 consecutive patients with large vessel occlusion (LVO) over a 1-year time interval (10/20/2018-11/17/2019) were studied. The raw CTP data was analyzed using CT perfusion software written in MATLAB and previously used to compare different tissue-based metrics of collateral blood flow to vascular metrics[2] and also previously compared to RAPID in a smaller cohort of 43 patients[3]. There were 143 unique patients between these groups. Clinical data was available in the GENESIS cohort and included age=68.4±13, baseline NIH Stroke Scale (NIHSS)=14±6.4, 24-hour NIHSS=11.2±9, mRS at 90 days=4±1.8. Ischemic core was determined as volume of brain with CBF < 0.3*normal brain (Tmax<4s), ischemic penumbra (Tmax>6s). HIR=Vol(Tmax>10s)/Vol(Tmax>6s). Outliers were identified using Bland-Altman analysis (>2 standard deviations from the mean difference) and reviewed.

Results

Mean difference (-2.5mL) and standard deviation of difference (30.3mL) of core volume compared favorably to prior studies that have compared different commercial software in the same patient (mean core size differences=1.8-55mL, standard deviations=15-50ml)[4]. The small number of outliers for core and penumbra (<3.5% of cases) were predominantly related to bone stripping in our algorithm. There was one patient that the software did not identify a large core and penumbra defect identified by RAPID. The fits showed core and penumbra volumes are 25% smaller than RAPID with small positive offsets in intercept. Prior studies have shown that RAPID sensitivity for detecting infarct is only 40.5%[5].

Conclusions

The software performed reliably in a large cohort of LVO patients with small number of outliers compared to RAPID, small mean differences in core and penumbra volume and similar or better variations in individual patients compared to RAPID than prior comparisons with SyngoVia and Olea. This software can be used to assess different perfusion parameters for research purposes. Further study is warranted to investigate both the offsets in slope and intercepts of the fit as well as differences between the techniques in individual patients.

Table 1. Summary of the difference in core and penumbra volumes as well as HIR compared to RAPID iSchemaView as well as the linear regression results between the two methods.

	RAPID - US Difference (mean ± std)	Number of outliers	Fit (y = our data x = RAPID data)	R ²
Core volume	-2.7 ± 30.3 mL	5	y = 0.74x + 11.5	0.74**
Penumbra volume	8.6 ± 53.3 mL	4	y = 0.76x + 18.0	0.66**
HIR	0 ± 0.2	11	y = 0.95x + 0.05	0.81**

** p < 0.001

(Filename: TCT_1090_CTPtoRAPIDcomparison.jpg)

531

Validation of T1 REtrospective Quantification Using Internal REferences (T1-REQUIRE) Algorithm

A Hasse¹, Y Jeong², S Foxley¹, A Javed¹, T Carroll¹

¹University of Chicago, Chicago, IL, ²N/A, N/A

Purpose

MR Relaxometry has been shown to be a useful tool for analysis of a variety of pathology. Now, with increased usage of machine learning on large datasets, relaxometry has the ability to harmonize the data, resulting in a better and more accurate prediction algorithm. However, relaxometry sequences are not often acquired due to time, expense, and limited clinical use. Therefore, the ability

to retrospectively generate quantitative MR maps from weighted MR sequences is desired. In this study, we present the validation of a T1 REtrospective Quantification Using Internal REferences (T1-REQUIRE) algorithm using T1-weighted spin-echo MR images.

Materials and Methods

8 healthy volunteers (31 ± 8.98 years, 6 males, 2 females) underwent an IRB-approved study at the University of Chicago. A 3T Philips Ingenia scanner was used to acquire both T1-weighted spin-echo images (TE = 10 ms, TR = 525 ms, 240x196x65 mm³ FOV) and a Look-Locker (TE = 4.6 ms, TR = 8 ms, TI = 150-3500 ms, 240x196x65 mm³ FOV) T1 mapping sequence of the brain. Using healthy tissues segmented using Statistical Parameter Mapping v12 on the T1-weighted MRI, the T1 relaxation times of fat, gray matter, and cerebrospinal fluid (CSF) as internal references were used to generate a T1 relaxation time versus signal intensity plot for each slice (Figure 1). This then was applied to the entire slice to generate an estimated T1 map. The results were compared to the T1 map generated by the corrected Look-Locker mapping sequence.

Results

Figure 2 shows the correlation between the average T1 relaxation times of four tissue types (gray matter, white matter, CSF, and fat) generated by the two methods. T1-REQUIRE shows good agreement with the reference standard Look-Locker, with a slope of $m = 1.02$ and Pearson's correlation coefficient of $R = 0.955$. The Bland-Altman plot shows a minimal bias of 13 ms, although there does seem to be a large variation as shown by the large 95% confidence interval (Figure 3).

Conclusions

A high correlation coefficient and correlation slope of one shows that T1-REQUIRE may be an efficient way to estimate T1. The T1-REQUIRE algorithm took 90 seconds to complete, whereas the Look-Locker took 90 minutes to complete the same resolution on the same computer. However, we did find an increased variation, most likely resulting from filters put on the T1-weighted spin-echo image changing signal intensity. More work needs to be done to understand the increased variability, along with expanding the REQUIRE algorithm to other sequences.

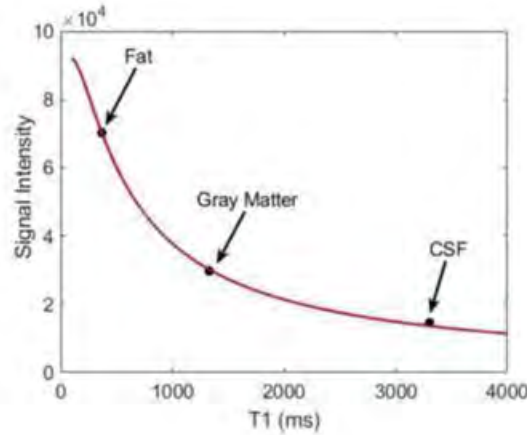


Figure 1

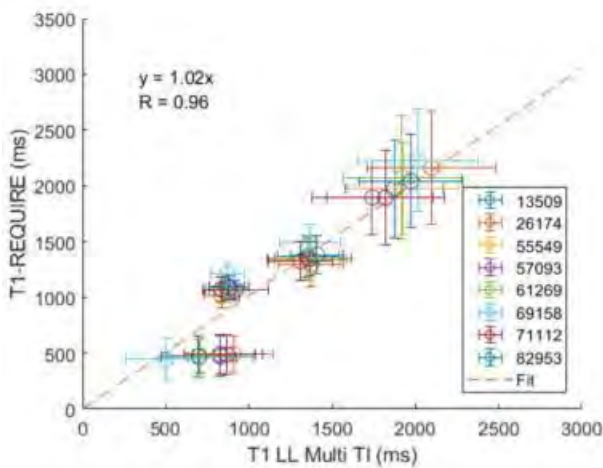


Figure 2

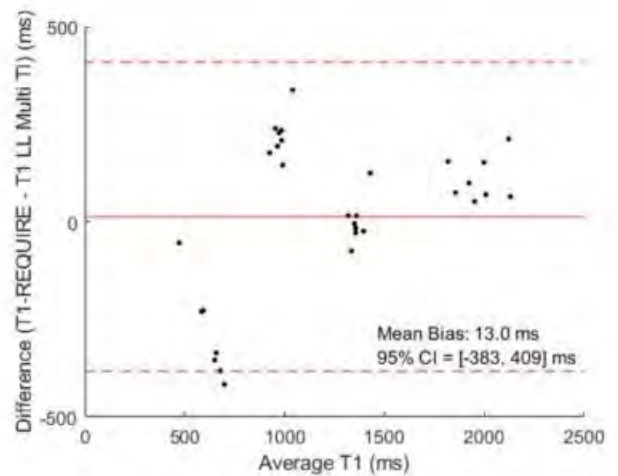


Figure 3

(Filename: TCT_531_t1_require_fig_combined.jpg)

Value of DWI and T2 SI in MRI post-treatment surveillance for head and neck squamous cell carcinoma: A proposed NI-RADS MRI lexicon

M Ashour¹, E Darwish², R Fahiem², T Abdelaziz²

¹Ain Shams University, Cairo, Egypt, ²Ain Shams University, Cairo, other

Purpose

The aim of this work was to recommend a new NI-RADS lexicon for MRI surveillance using DWI and T2 signals and to evaluate the diagnostic performance of integrating this lexicon into the existing NI-RADS algorithm.

Materials and Methods

This retrospective study included 69 head and neck squamous cell carcinoma patients who underwent post-treatment CEMRI imaging surveillance using a 1.5-T scanner. Scans were interpreted by two neuroradiologists with 5 and 15 years of experience, blinded to the clinical or pathological outcome. Image analysis included assessment of the primary tumor site by the current ACR NI-RADS for CEPT +/- PET, T2 SI, and DWIs. NI-RADS re-scoring was performed based on our proposed lexicon using T2 signal and diffusion features. The gold standard was a defined set of criteria, including clinical and imaging follow-up and/or pathological assessment. The average ADCmean value was estimated for all targets. The scale for T2 SI evaluation in non-fat saturated T2WIs was as follows: (1) no abnormality, (2) low T2 SI, (3) intermediate T2 SI; similar to the initial tumor signal, and (4) high T2 SI. T2 SI and DWI as modifying rules for NI-RADS categories: The presence of both diffusion restriction and intermediate T2 SI would upgrade the NI-RADS categories by one grade. The absence of both would downgrade NI-RADS categories by one grade. The presence of only one feature without the other feature would not alter the original NI-RADS category. Statistical analysis The collected data were coded, and tabulated using SPSS 20. ROC curve analysis of ADCmean values was performed.

Results

The study population consisted of 41 male and 28 female, and mean age was 50.55 ± 16.82 . LTR occurred in 26/69 (37.7%) patients. The diagnostic performance of T2 SI, DWI, NI-RADS and NI-RADS re-scoring; for the detection of LTR for the primary targets are enlisted in Table 1 Incorporation of T2 SI and diffusion features into NI-RADS as modifying rules showed higher diagnostic performance compared to the current ACR NI-RADS template. For diffusion criteria, there was no statistically significant difference between the qualitative and quantitative assessment of DWI. ROC curve analysis showed an AUC of 0.945 (0.875-0.990 CI), with cutoff $ADC_{mean} \leq 1.3 \times 10^{-3} \text{ mm}^2/\text{s}$.

Conclusions

Incorporation of diffusion criteria and T2 SI into the current NI-RADS lexicon for primary tumor site assessment as modifying rules enhanced diagnostic validity and accuracy of the ACR NI-RADS template.

Table 1: Diagnostic performance of T2 SI, DWI (qualitative and quantitative), NI-RADS and NI-RADS re-scoring; for the detection of LTR for the primary targets.

	T2 SI	DWI with ADC=<1.3	NI-RADS	NI-RADS-DWI-T2 SI
TP (n)	24	24	22	23
TN (n)	38	39	35	40
FP (n)	5	4	8	3
FN (n)	2	2	4	3
Sensitivity (%)	92.31	92.3	84.62%	88.46
(95% CI)	74.87% to 99.05%	74.87% to 99.05%	65.13% to 95.64%	69.85% to 97.55%
Specificity (%)	88.37	90.7	81.4	93.02
(95% CI)	74.92% to 96.11%	77.86% to 97.41%	66.60% to 91.61%	80.94% to 98.54%
PPV (%)	82.76	85.71	73.33	88.46
(95% CI)	67.64% to 91.68%	70.10% to 93.89%	59.03% to 84.00%	71.84% to 95.84%
NPV (%)	95.00	95.12	89.74%	93.02%
(95% CI)	83.32% to 98.64%	83.69% to 98.67%	77.84% to 95.61%	82.10% to 97.49%
Accuracy (%)	89.86%	91.30	82.61	91.30%
(95% CI)	80.21% to 95.82%	82.03% to 96.74%	71.59% to 90.68%	82.03% to 96.74%

**TP: true positive, TN: true negative, FP: false positive, FN: false negative
NPV: negative predictive value, PPV: positive predictive value, CI: confidence interval**

(Filename: TCT_1436_Diagnosticperformance.jpg)

643

Value of MRI in grading of upper cervical spine injuries based on the new AO spine classification

S Khanpara¹, N Doyle¹, J McCarty¹, A Acin¹, Y Cai¹, R Patel¹, J Stark¹, R Riascos¹

¹University of Texas Health Science Center at Houston, Houston, TX

Purpose

The recent AO spine classification for upper cervical spine injuries now includes ligamentous injuries in addition to the fractures and translational/distracton injuries. All trauma patients are initially evaluated on a CT done in the ED and are prone to under/overestimation of soft tissue injury. In this study, we evaluate the role of MRI in comparison to CT in grading these injuries according to the AO spine classification.

Materials and Methods

Retrospective analysis of 124 patients (>18 years) with upper cervical spine injury was performed at a level I trauma center presenting during a course of one year. All of the patients were randomly selected from a list generated from the institutional database for trauma for the year 2019-2020 and had CT and MRI performed at the time of admission. 74 patients with: no upper cervical spine injury, no acute injuries (presence of chronic fractures), lack of CT/MRI, missing sequence and motion artifact limiting evaluation were

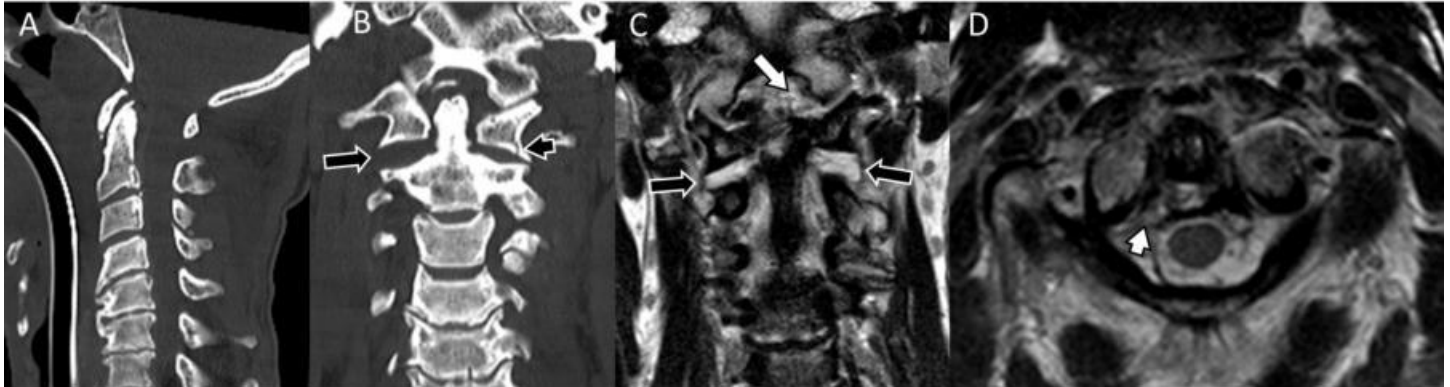
excluded with inclusion of 50 patients. The level, type of injury and imaging modifiers (M3-stiff spine, M4-blunt cerebrovascular injury) were noted down on CT by a neuroradiology fellow. Similar review was later carried out on MRI. Any discrepancy in the reading was then analyzed at a later stage.

Results

Mean age of the study population was 50 years with a male to female ratio of 1.78:1. 74 injury levels were identified in a total of 50 patients on CT. The most common injured level was C1 (37.8%) and the least injured level was the occipital bone (28.4%). Type A injuries (48 levels) were the most common followed by type C (15 levels) and type B (10 levels) injuries. After analyzing the MRI, a total of 12 discrepancies were identified which were significantly different compared to the CT analysis ($p < 0.001$, Fischer exact test). A change in level was observed in 3 patients with added level in 2 patients and subtracted level in one patient. Change in the injury type was seen in 6 patients (all involving type B and C) with upgraded injury in 4 and downgraded in 2 patients. Change in the modifier was identified in 4 patients with upgraded injury in one and downgraded in 3 patients.

Conclusions

MRI provides significant improvement in accurately grading upper cervical spine injuries based on the new AO spine classification and should be incorporated in routine imaging with even the slightest clinical suspicion of type B and C injuries.



59-year-old male presenting to the ED after motor vehicle accident. Initial CT (A, B) shows widening of the C1-C2 joint space on the right side consistent with a C1:C injury (black arrow) with C1:A injury (black arrowhead). MR of the craniocervical junction (C, D) done later the same day corroborated the C1:C injury (black arrows), which now looks more prominent on the left side compared to the CT. In addition, complete rupture of the left alar ligament (white arrow) and the right attachment of transverse atlantal ligament (white arrowhead) were also identified resulting in addition of a new level C0:B and upgrade of the injury at C1 to type B, relative to the CT.

(Filename: TCT_643_CTvsMRI.jpg)

364

Variability of Loes Scores and Gadolinium Enhancement Status in MRI Assessment of Cerebral Adrenoleukodystrophy Following Gene Therapy or Allogeneic Hematopoietic Stem Cell Transplantation

D Lin¹, D Nascene², F Eichler³, U Löbel⁴, K Buch³, O Rapalino³, R Walovitch⁵, E Shamir⁶, J Xu⁶, A Dietz⁶, P Orchard⁷, D Williams⁸, D McNeil⁶, D Loes²

¹Russell H. Morgan Department of Radiology and Radiological Science, Johns Hopkins University School, Baltimore, MD, ²University of Minnesota, Minneapolis, MN, ³Massachusetts General Hospital and Harvard Medical School, Boston, MA, ⁴Great Ormond Street Hospital for Children, London, UK, ⁵WorldCare Clinical, Boston, MA, ⁶bluebird bio, Inc., Cambridge, MA, ⁷University of Minnesota Children's Hospital, Minneapolis, MN, ⁸Dana-Farber/Boston Children's Cancer and Blood Disorders Center, Harvard Medical School, Boston, MA

Purpose

Cerebral adrenoleukodystrophy (CALD) is a genetic disease of inflammatory demyelination and neurodegeneration that mainly affects young boys. 1 MRI findings such as Loes score and gadolinium enhancement (GdE) status are used to quantify CALD severity, and monitor CALD post-therapy. This study evaluated the inter- and intra-rater variability of Loes scores and GdE assignment in two clinical trials for CALD.

Materials and Methods

MRIs were obtained over time from boys with CALD treated with allogeneic hematopoietic stem cell transplantation (ALD-103 trial) and with elivaldogene autotemcel (eli-cel; Lenti-D) gene therapy in the ALD-102/LTF-304 trial. In both trials, Loes score (range 0 to 34) and GdE status (present/absent) were assigned by a central site neuroradiologist (RS). In the current study, MRIs were evaluated in random order by 2 pairs of neuroradiologists/raters (R1/R2 [N=125] and R3/R4 [N=126]) and compared with RS and pairwise. Also, 134 MRIs from ALD-102/LTF-304 were assessed in sequential order by R1, R2 and RS. Intra-rater variability was evaluated on a subset of MRIs (Random, n=14; Sequential, n=77). Loes scores were transformed into categories (1: 0, 2: ≥ 0.5 to ≤ 9 , and 3: 10-34),

with <3-point difference in agreement proportion shown here (exploratory analysis). Agreement is also shown as weighted Kappa (K) scores (Loes) and K scores (GdE).

Results

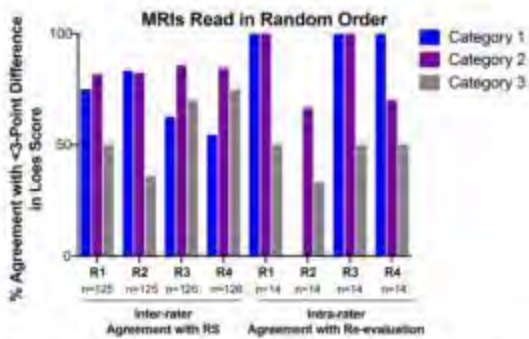
Inter- and intra-rater Loes score agreements were 36%–86% and 33%–100%, respectively (random reads; Figure 1A). Disagreement was most apparent in the parieto-occipital region, auditory and visual pathways, and frontopontine and corticospinal fibers (data not shown). Inter-rater agreement was generally excellent for Loes scores (weighted K score range 0.55–0.85), but moderate for GdE (0.42–0.75; Figure 1Bi); similar pattern was observed with 3/4 intra-rater agreements. Sequential reads generally did not improve the proportion of Loes score agreements (Figure 1C) or K scores (Figure 1Bii).

Conclusions

Inter- and intra-rater agreement for Loes scores showed acceptable degree of homogeneity and were higher than for GdE status. Optimizing and standardizing imaging protocols and focusing future training on neuroanatomical locations with greatest disagreement among raters, may help further decrease any variability in MRI reading for patients with CALD.

Figure 1. (A) Proportion of Inter-rater and Intra-rater Agreement Based on Loes Score Categories With <3-Point Difference for MRIs Read in Random Order; (B) Inter-rater and Intra-rater Agreement Among Loes Scores and GdE for MRIs Read in Random and Sequential Order; (C) Proportion of Inter-rater and Intra-rater Agreement Based on Loes Score Categories With <3-Point Difference for MRIs Read in Sequential Order

A.



Category 1, Loes score = 0; Category 2, Loes score ≥0.5 to ≤0; Category 3, Loes score ≥0.
 For inter-rater agreement, MRI scan distribution per category was as follows: R1 - Category 1 (n=8), Category 2 (n=100), and Category 3 (n=12); R2 - Category 1 (n=8), Category 2 (n=81), and Category 3 (n=25); R3 - Category 1 (n=16), Category 2 (n=78), and Category 3 (n=30); R4 - Category 1 (n=22), Category 2 (n=75), and Category 3 (n=24).
 For intra-rater agreement, MRI scan distribution per category was as follows: R1 - Category 1 (n=1), Category 2 (n=10), and Category 3 (n=2); R2 - Category 1 (n=1), Category 2 (n=9), and Category 3 (n=3); R3 - Category 1 (n=2), Category 2 (n=10), and Category 3 (n=2); R4 - Category 1 (n=2), Category 2 (n=10), and Category 3 (n=2).
 For R2, missing were n = 3 and n = 1 MRIs in inter- and intra-rater sites, respectively.
 Two MRI scans were removed from the RS group since they were outside contrast window.
 R1 = Reviewer 1, R2 = Reviewer 2, R3 = Reviewer 3, R4 = Reviewer 4, RS = Reference Standard.

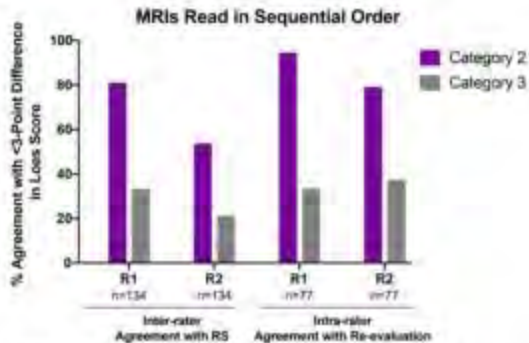
B.

	1. Reads read in random order		2. Reads read in sequential order	
	Loes Weighted K (90% CI)	GdE K (90% CI)	Loes Weighted K (90% CI)	GdE K (90% CI)
R1 vs RS	0.63 (0.49, 0.77)	0.43 (0.28, 0.57)	0.56 (0.40, 0.73)	0.47 (0.35, 0.56)
R2 vs RS	0.65 (0.77, 0.94)	0.75 (0.64, 0.85)	0.68 (0.57, 0.80)	0.48 (0.37, 0.60)
R3 vs RS	0.75 (0.66, 0.83)	0.42 (0.35, 0.55)		
R4 vs RS	0.73 (0.64, 0.82)	0.54 (0.50, 0.68)		
R1 vs R2	0.55 (0.41, 0.70)	0.43 (0.29, 0.56)		
R3 vs R4	0.76 (0.67, 0.85)	0.48 (0.44, 0.61)		
R1 vs R1	0.96 (1.00, 1.00)	0.73 (0.68, 0.78)	0.74 (0.48, 1.00)	0.43 (0.27, 0.60)
R2 vs R2	0.47 (0.16, 0.76)	0.78 (0.45, 1.00)	0.64 (0.48, 0.81)	0.76 (0.63, 0.88)
R3 vs R3	1.0 (1.00, 1.00)	1.0 (1.00, 1.00)		
R4 vs R4	0.75 (0.50, 1.00)	0.60 (0.08, 1.00)		
RS vs RS			0.65 (0.75, 0.96)	0.59 (0.42, 0.80)



CI = Confidence Interval, GdE = Gadolinium enhancement, K = Kappa score, R1 = Reviewer 1, R2 = Reviewer 2, R3 = Reviewer 3, R4 = Reviewer 4, RS = Reference Standard.

C.



Category 1, Loes score = 0; Category 2, Loes score ≥0.5 to ≤0; Category 3, Loes score ≥0.
 For inter-rater agreement with RS, MRI scan distribution per category was as follows: R1 - Category 2 (n=122) and Category 3 (n=12); R2 - Category 2 (n=82) and Category 3 (n=52).
 For intra-rater agreement, MRI scan distribution per category was as follows: R1 - Category 2 (n=14) and Category 3 (n=2); R2 - Category 2 (n=13) and Category 3 (n=24).
 No Category 1 MRI scans were included for this part of the study in which MRIs were assessed in sequential order.
 R1 = Reviewer 1, R2 = Reviewer 2, R3 = Reviewer 3, R4 = Reviewer 4, RS = Reference Standard.

(Filename: TCT_364_ASNRAbstractFigure_11-2-20Final.jpg)

Vascular Manifestations In Neurosarcoidosis: Early Experiences From A Vessel Wall Imaging Study

G Bathla¹, L Abdel Wahed², S Gupta², A Agarwal³, S Priya², K Jones², T Cho²

¹University of Iowa Hospitals and Clinics, Iowa City, IA, ²University of Iowa hospitals and Clinics, IOWA CITY, IA, ³UT Southwestern, Dallas, TX

Purpose

Cerebrovascular manifestations in Neurosarcoidosis (NS) were previously considered rare but are being increasingly recognized. We report our preliminary experience in patients with NS who underwent high-resolution vessel wall imaging (VWI) study.

Materials and Methods

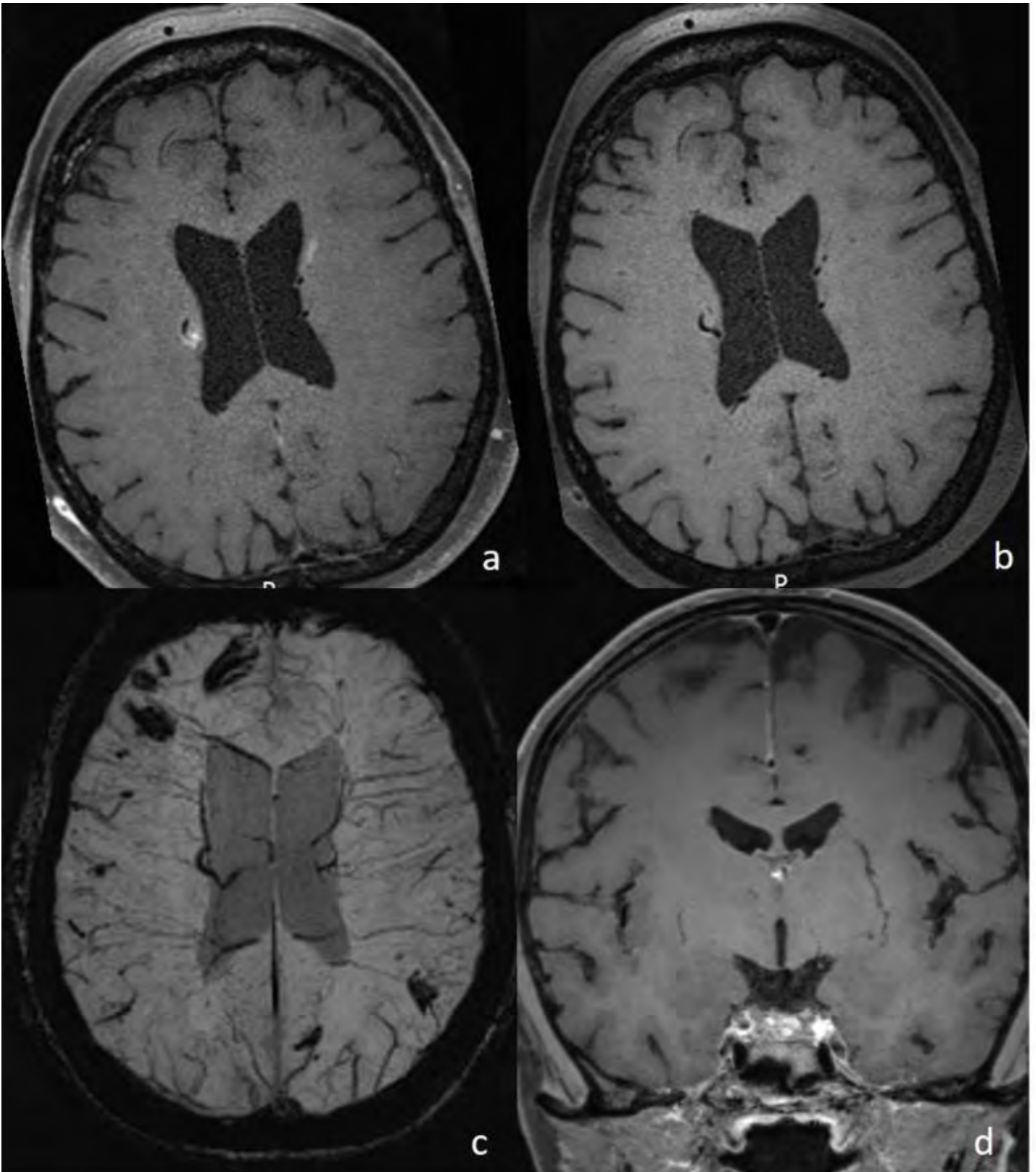
A total of 13 NS patients underwent VWI study. Images were analyzed by two neuroradiologists in consensus. The assessment included segment-wise evaluation of larger and medium sized vessels (ICA, M1-M3 MCA; A1-A3 ACA; V4 segments of vertebral arteries; Basilar artery and P1-P3 PCA), lenticulostriate perforator vessels, medullary and deep cerebral veins. Cortical veins were not assessed due to high proportion of flow-related artifacts. Brain biopsy findings were available in six cases and were also reviewed.

Results

Mean patient age was 55 years (33-71 yrs) with M:F of 8:5. Mean duration between initial diagnosis and VWI study was 18 months. Overall, 9/13 (69%) patients had some vascular findings. Circumferential large vessel enhancement was seen in 4/13 (31%) patients, while perforator vessel involvement was seen in 6/13 (46%) patients. Medullary and deep vein involvement was also seen in 6/13 patients. Additionally, 7/13 (54%) patients had microhemorrhages in SWI and 4/13 (31%) had chronic infarcts. On biopsy, 5/6 cases showed perivascular granulomas with vessel wall involvement in 4/6 cases.

Conclusions

Our preliminary findings suggest that involvement of intracranial vascular structures may be a common finding in NS patients and should be routinely looked for as they may provide clues to correct diagnosis. These findings appear concordant with previously reported autopsy literature and need to be validated on a larger scale.



(Filename: TCT_661_NSabstractimage.jpg)

247

Vendor Agnostic DICOM-Based Deep Learning Reconstruction Enables 40% Faster Spine MR Scans which Match or Exceed Quality of Standard of Care- A Prospective, Multicenter, Multireader Trial

S Bash¹, B Johnson², W Gibbs³, G Zaharchuk⁴, E Gong⁵, P Gulaka⁶, H Gandhi⁶, T Zhang⁷, A Shankaranarayanan⁸, L Tanenbaum⁹
¹RadNet, Los Angeles, CA, ²Center for Diagnostic Imaging, Minneapolis, MN, ³Mayo Clinic, Scottsdale, AZ, ⁴Stanford University, Palo Alto, CA, ⁵Subtle Medical Inc., Menlo Park, CA, ⁶Subtle Medical, Menlo park, CA, ⁷Subtle Medical, Menlo Park, CA, ⁸Subtle Medical Inc, Menlo Park, CA, ⁹RadNet, New York, NY

Purpose

This prospective, multicenter, multireader study was designed to evaluate the performance of 40% scan-time reduced spine MRI reconstructed with vendor agnostic DICOM-based deep learning (DL).

Materials and Methods

With IRB approval and patient consent, 61 consecutive patients underwent standard-of-care (SOC) and accelerated (FAST) spine MRI (14 cervical, 9 thoracic and 88 lumbar) acquired from 5 scanners at 5 imaging centers. DL processing of the FAST scan data set (FAST-DL) was performed offline using an FDA-cleared vendor agnostic DICOM-based CNN DL image enhancement product, SubtleMR™. Three experienced neuroradiologists (>17 years) were presented with 666 different image series as 333 paired side-by-side datasets (SOC vs. FAST, SOC vs. FAST-DL, FAST-DL vs. FAST) randomized in sequential and left-right display order. Image features were preference rated on a 5 point Likert scale. Structural similarity index (SSIM) was assessed for the image sets pre and post DL-enhancement as a quantitative assessment of image integrity impact.

Results

FAST-DL was statistically better than SOC for perceived SNR and imaging artifacts (p-values <0.05), and equivalent for perceived spatial resolution, cord delineation, cord/CSF contrast, disk related pathology, bone lesions, and facet/ligamentous pathology. Wilcoxon Rank Sum Test results for Likert scale analysis are collectively summarized for all 3 readers in Table 1. Qualitative assessment of image integrity was equivalent across the 3 datasets for all 3 blinded readers, indicating that there was no perceived loss or aberration of anatomy or pathology (Figure 1). Spearman rank-order correlation coefficient analysis demonstrated moderately strong inter-rater agreement between the 3 blinded neuroradiologists. Quantitative assessment of image similarity using the SSIM was 0.981 ± 0.011 for SOC vs. SOC-DL and 0.984 ± 0.009 for FAST vs. FAST-DL. This supports the absence of substantial anatomic aberration by DL-processing of the source series.

Conclusions

DL matches or exceeds the perceived image quality and diagnostic qualitative performance of standard of care spine MRI exams, enabling a 40% scan time reduction. DL qualitatively outperformed standard of care in reduction of image artifacts and perceived signal-to-noise ratio. Quantitative structural similarity index metrics (SSIM) attest to image integrity preservation after DL-processing. This study suggests the potential for routine utility of DL reconstructed MRI in clinical practice.

Feature	SOC vs FAST		FAST-DL vs SOC		FAST-DL vs FAST	
	Mean ± Std	P value	Mean ± Std	P value	Mean ± Std	P value
SNR	3.7 ± 0.5	<0.05	3.4 ± 0.6	<0.05	3.9 ± 0.4	<0.05
Resolution	3.0 ± 0.3	<0.05	3.0 ± 0.3	0.41	3.0 ± 0.2	0.25
Artifacts	3.3 ± 0.6	<0.05	3.1 ± 0.5	<0.05	3.1 ± 0.3	<0.05
Cord Delineation	3.1 ± 0.2	<0.05	3.0 ± 0.2	0.25	3.0 ± 0.1	0.16
Cord/CSF Contrast	3.1 ± 0.3	<0.05	3.0 ± 0.3	0.56	3.0 ± 0.1	1
Disk Pathology	3.1 ± 0.2	<0.05	3.0 ± 0.2	0.64	3.0 ± 0.1	0.1
Bone Lesions	3.1 ± 0.3	<0.05	3.0 ± 0.3	0.3	3.0 ± 0.1	0.41
Facet/Ligamentous Pathology	3.1 ± 0.2	<0.05	3.0 ± 0.1	0.26	3.0 ± 0.1	<0.05

TABLE 1. Wilcoxon Rank Sum Test Results. All readers combined. P-value <0.05 (bold) suggests statistical significance for features in one dataset with respect to its comparison. SOC is better than FAST for all criteria. FAST-DL (SubtleMR™) is better than SOC for SNR and artifacts and equal for other criteria. FAST-DL is better than FAST for SNR, artifacts, and facet/ligamentous pathology and equal for other criteria.

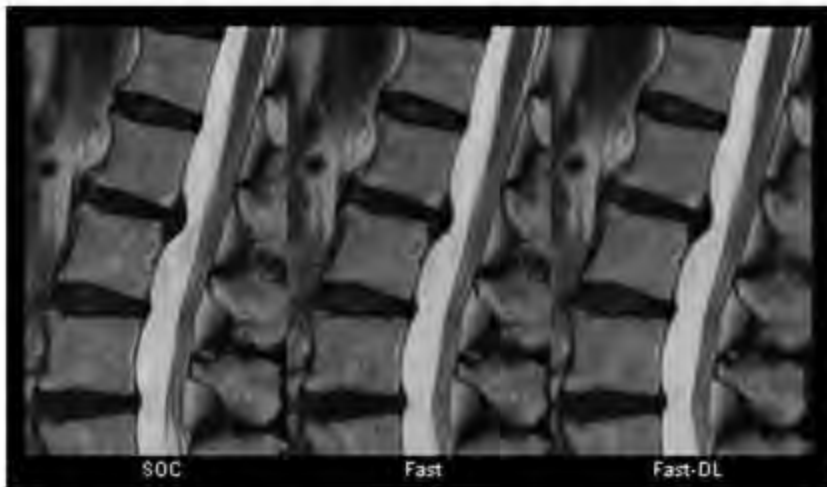


Fig 1. Consistency Across Datasets. Magnified sagittal T2 (left-to-right): SOC, FAST, FAST-DL. Blinded Readers found no variations in image integrity (morphology/signal) across the datasets.

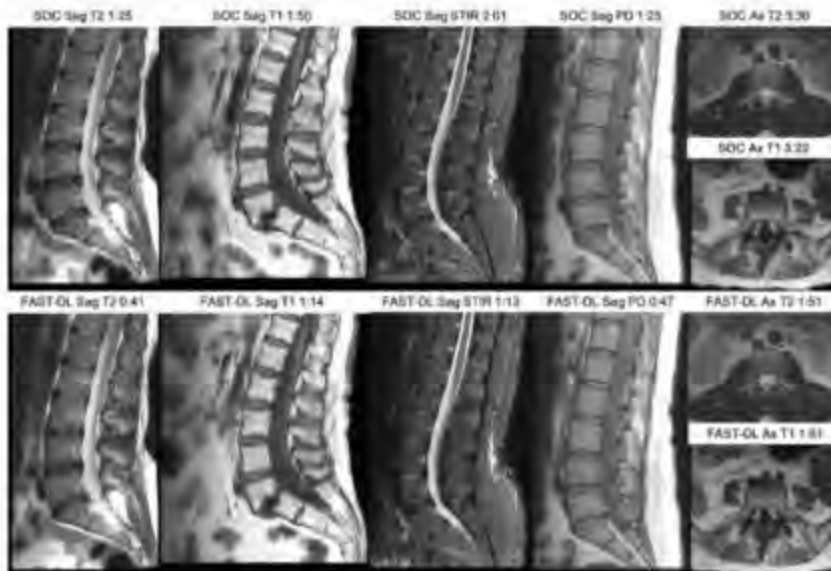


FIG 2. Multisequence Imaging. SOC (upper) and FAST-DL (lower) with representative acquisition times. |

(Filename: TCT_247_ASNR2021SpineAbstract.JPG)

Viable Disc Tissue Allograft Supplementation in the Treatment of Degenerated Intervertebral Discs the One Year Results of a Randomized Control Trial.

D Beall¹

¹*Summit Medical Center, Edmond, OK*

Purpose

A viable disc tissue allograft has been developed to augment the loss of tissue associated with degenerative lumbar disc disease and the development of chronic lower back pain (CLBP). This viable disc allograft was injected into painful degenerated discs to evaluate safety and to determine whether it can improve pain and function in patients with CLBP.

Materials and Methods

A prospective, multicentered, blinded randomized, clinical trial (RCT) for subjects with one or two-level degenerative lumbar disc disease was conducted. 218 patients with CLBP secondary to degenerative disc disease were enrolled in the study. Subjects were blinded and randomized to receive intradiscal injections of either viable disc allograft or saline or to continue with non-surgical management (NSM). Standardized clinical outcome instruments were used, including Oswestry Disability Index (ODI) and Visual Analogue Scale of Pain Intensity (VASPI). Plain radiographs and MRI scans were used to assess disc space height and spinal alignment, and to determine the degree of disc degeneration. The NSM group could cross over to the allograft group after 3 months. Patients were assessed at 6 and 12 months. Patient adverse events were continuously assessed.

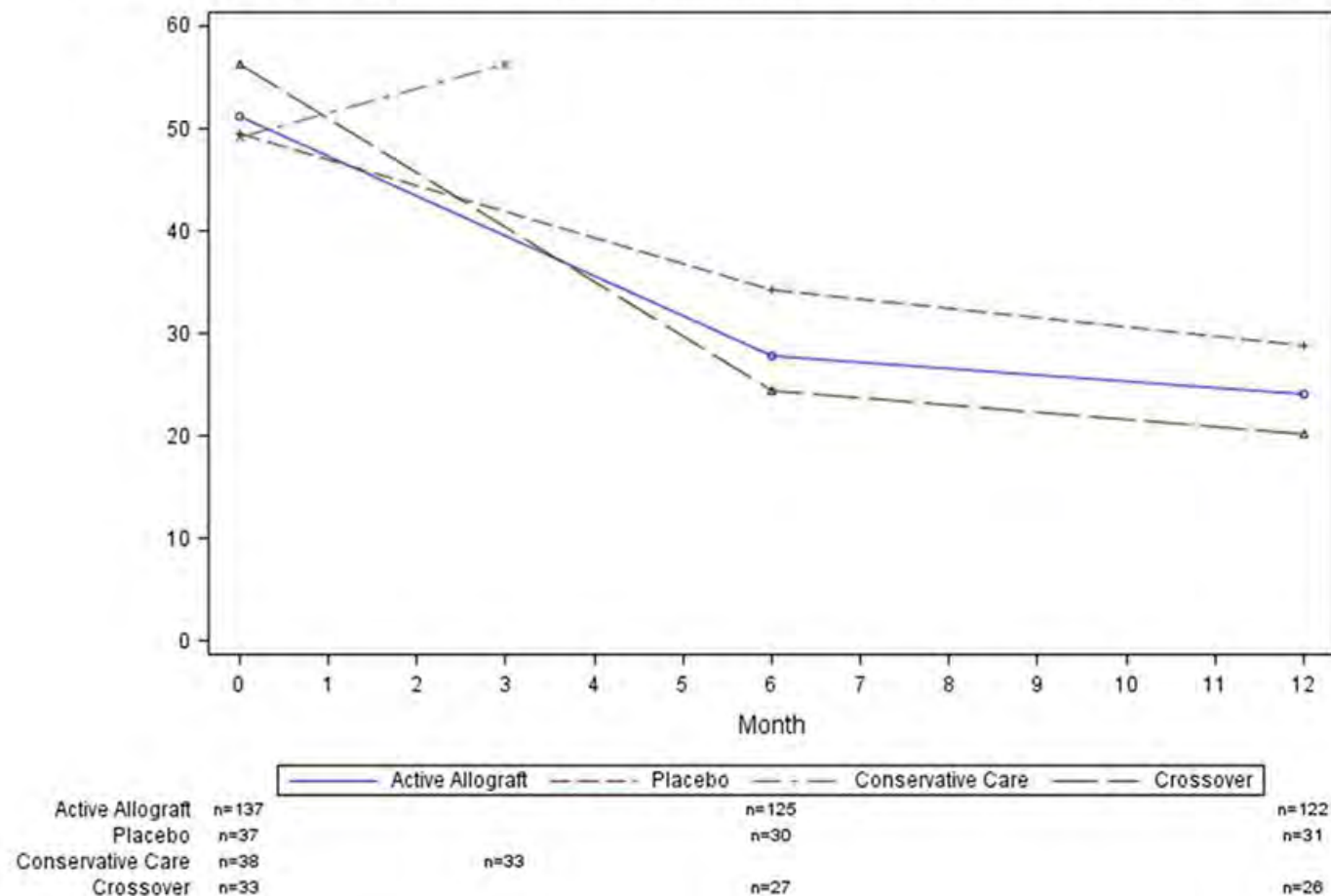
Results

At 12 months, clinically meaningful improvements in mean VASPI and ODI scores were achieved with statistically significant improvements in ODI in group treated with allograft as compared to placebo ($p = 0.029$). In the group of patients randomized to allograft, 76.5% were responders ($p = 0.03$) as compared to 56.7% in the saline group. The VAS decreased in all groups with patients in the subgroup of ≥ 20 -point reduction in pain reaching statistical significance ($p = 0.028$). At one year in the investigational allograft group, pain improved 54% and was accompanied by a 53% improvement in ODI. NSM subjects following crossover attained a 65% improvement in pain at 12 months combined with a 64% improvement in ODI. Patients with two-level treatment with allograft did better than those receiving one-level treatment with allograft while those with two-level treatment with placebo had lesser response. In the allograft group, 11 safety adverse events occurred in 141 subjects (3.5%) and there were no persistently symptomatic AEs or SAEs.

Conclusions

This large prospective blinded RCT demonstrates that cellular allograft supplementation of the lumbar intervertebral discs is a safe and effective treatment that significantly improved pain and function at 12 months.

Co-Primary Endpoint ODI: 12-Month, 179 subject Oswestry Disability



(Filename: TCT_982_VASTFigure1.jpg)

680

Volume versus area: Comparison of different measurement methods for treatment response evaluation in children with plexiform neurofibromas or low-grade gliomas

M Oztek¹, A Sato², N Millard², N Vitanza², S Leary², F Perez²

¹University of Washington, Seattle, WA, ²Seattle Children's Hospital, Seattle, WA

Purpose

A major difficulty in clinical trials for pediatric tumors is assessing imaging treatment response. While comparing volumes of tumors over time is ideal, this requires special software or time-consuming manual contouring of the entire tumor for every study. Alternative approaches such as using only the largest cross-sectional areas or dimensions can be very practical; however, the best method and

thresholds to define progressive disease (PD) or partial response (PR) are not clear. The purpose of this study is to evaluate alternative methods to assess treatment response and compare them to standard criteria using tumor volume or RANO.

Materials and Methods

29 pediatric patients who started trametinib treatment for plexiform neurofibromas (pNF) or low-grade gliomas (LGG) and had at least one baseline and 2 follow-up MRI studies were included (n=138 MRI studies). For each timepoint, volume (V), largest axial area (AX), largest coronal area (COR) and sum of AX and COR (SUM) were retrospectively measured by manual contouring of images that showed the tumor best. The product of largest two diameters (RANO) was also calculated. Gold standard for pNF was tumor V, with >20% increase being PD, >20% decrease being PR and any other disease being stable disease (SD)^{1,2}. For LGG, RANO criteria was the gold standard with >50% decrease in bi-dimensional product being PR and >25% increase being PD³. ROC analysis was performed to optimize thresholds for PD and PR between measurement approaches compared to the gold standards, and kappa values for agreement of tumor response classification were then calculated.

Results

Optimized response thresholds and Kappa values for agreement in tumor response assessment categories using various tumor measurement approaches are summarized in Table 1. In the pNF group, AX had the greatest agreement, compared to COR in the LGG group. In the LGG group, COR and SUM both misclassified 1 case with PD as PR.

Conclusions

Based on our preliminary data, depending on the type of tumor, AX or COR can be practical ways of evaluating for tumor response, demonstrating substantial to almost-perfect agreement with gold standard measurements. However, thresholds cannot be transferred between different measurement methods and need to be calculated and validated for each method. Studies in larger patient groups are required to confirm our findings and refine the thresholds.

	THRESHOLDS ¹				KAPPA	
	pNF (V)		LGG (RANO)		pNF (V)	LGG (RANO)
	PD	PR	PD	PR		
V	N/A ²	-20% ³	10%	-64%	1.0 ³	0.60
COR	N/A ²	-11%	27%	-49%	0.33	0.76
AX	N/A ²	-12%	11%	-43%	0.71	0.60
SUM	N/A ²	-13%	15%	-46%	0.66	0.74
RANO	N/A ²	-10%	25% ³	-50% ³	0.56	1.0 ³

Table 1: Optimized thresholds of percent change in size compared to baseline for different measurement methods and Kappa values for agreement in response assessment using various measurement approaches across all patients and broken down by tumor type.

¹ Negative values indicate decrease in size compared to baseline.

² In our series, there were no pNF cases with PD by volume criteria reported in the literature.

³ Note that since V categorization uses V and RANO uses bi-dimensional products with well-established thresholds, proposed thresholds in those situations are not needed. Because of this, Kappa values for V in the pNF group and PROD in the LGG group are 1.

AX: Largest axial cross-dimensional area, COR: Largest coronal cross-dimensional area, LGG: Low-grade glioma, PD: Progressive disease, pNF: Plexiform neurofibroma, PR: Partial response, RANO: Response Assessment in Neuro-Oncology, SUM: Sum of axial and coronal largest cross-sectional area, V: Target lesion volume.

Volumetric Response Assessment in Low-Grade Glioma: Towards a Fully Automated and Clinically Deployable Workflow

T Gleason¹, P Damasceno¹, T Luks¹, J Villanueva-Meyer¹

¹University of California San Francisco (UCSF), San Francisco, CA

Purpose

Tumor volume calculations can decrease time to detection of progression in low grade glioma. However, volume calculations have not been routinely adopted into glioma response assessment due to lengthy times for manual segmentation and unreliable measurements provided by automated algorithms. Novel artificial intelligence approaches have significantly improved lesion segmentation with performance accuracies >90%. However, their adoption into routine practice remains limited due to poor generalizability and high failure rates when incorporated into clinical workflow. The goal of this study was to demonstrate how simple modifications to a robust network coupled with an integrated workflow can provide reliable measures of tumor volume for real-time use in the reading room.

Materials and Methods

Leveraging NVIDIA's Clara-Train software and a dataset of 195 labeled post-operative low-grade glioma cases, we modified a top-performing ensembled 2D-U-Net to require a single image-volume input (FLAIR). Input and segmentation masks were pre-processed to have uniform resolution of 1 mm³, normalized, and randomly cropped. The cases were divided into training (80%) and validation (20%) sets. DICE scores between manual and automatic segmentation were used as loss function and also for performance evaluation. Training was performed on 4 GPUs (NVIDIA Tesla V100, 32GB) using Automatic Mixed Precision (AMP) and multi-GPU communication via Horovod. The algorithm was then applied to 104 patients with serial imaging exams (304 cases total).

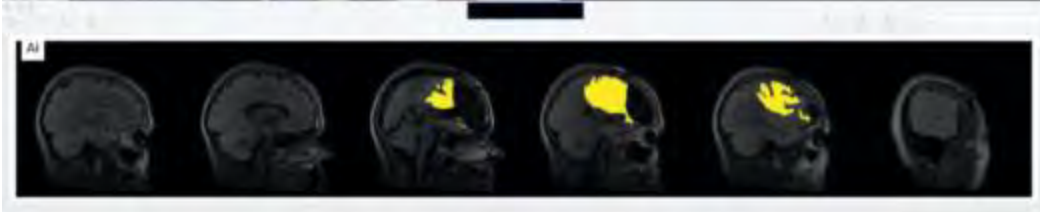
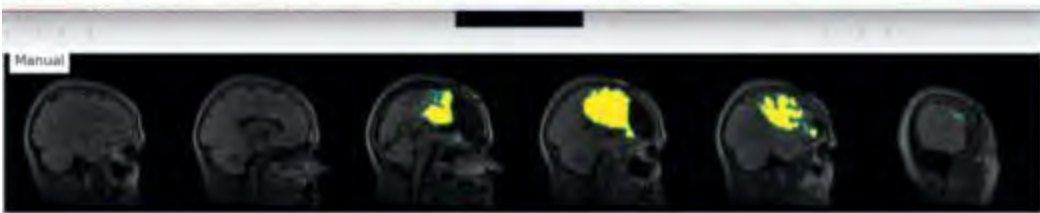
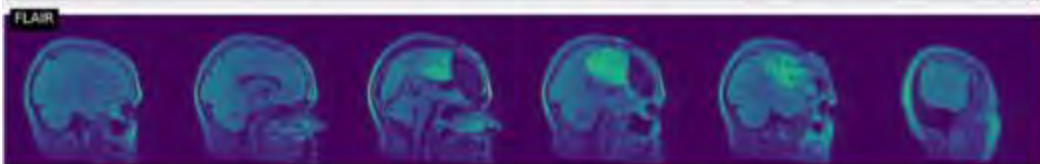
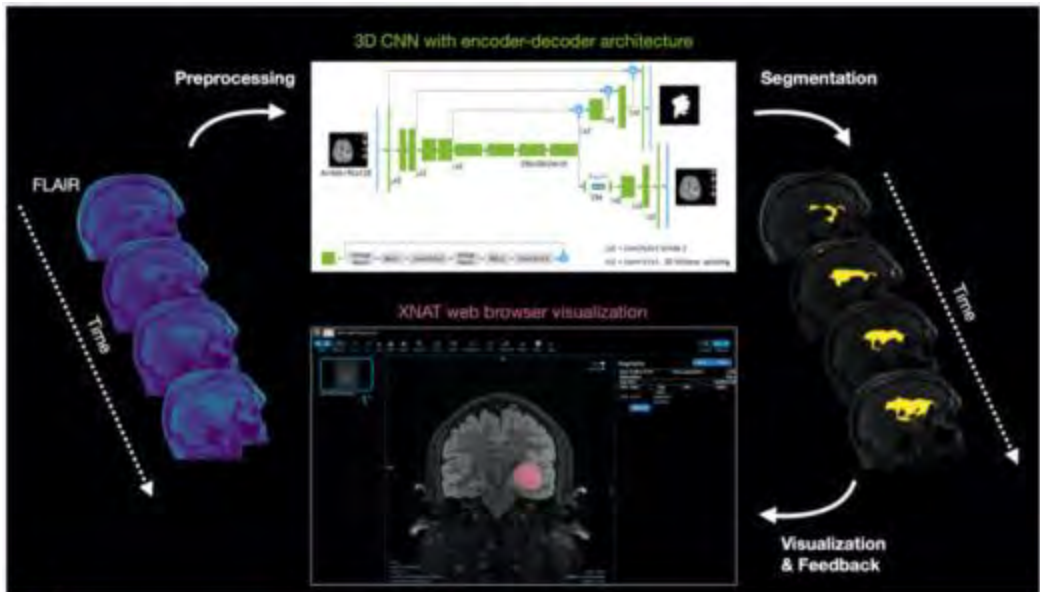
Results

Training on 156 labeled cases, we achieved Dice scores of 91% for the training set and 83% for our validation set (39 cases).

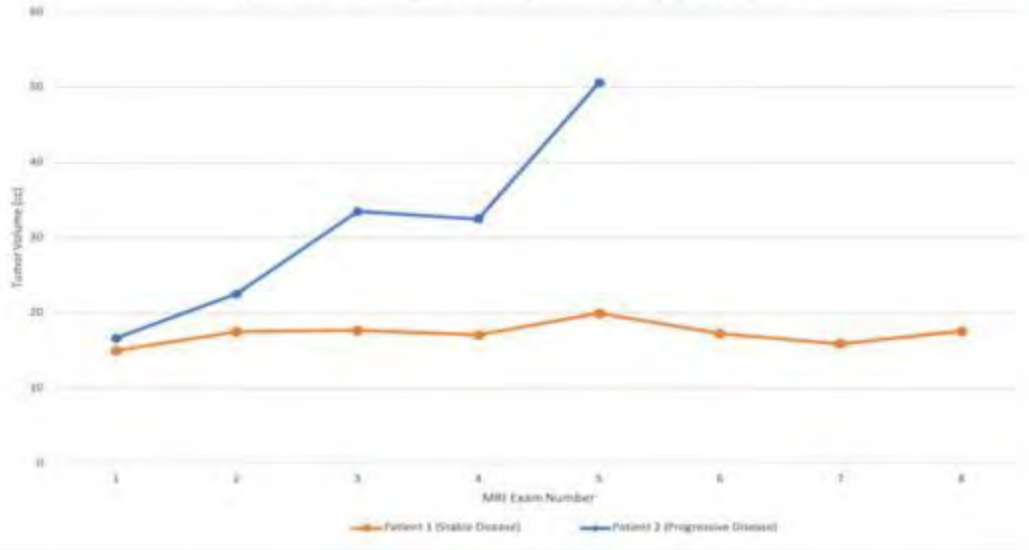
Preliminary data on 104 patients with serial imaging exams demonstrated several patients where a small increase in tumor volume on one exam preceded a much larger increase on a subsequent exam raising the possibility that we could detect tumor progression earlier in these cases.

Conclusions

DICE scores were similar to a prior segmentation model that required four separate inputs (T2, FLAIR, and T1 pre and post contrast; internal data) and also compare favorably with reported DICE scores for segmentations done by multiple human readers. Once deployed, radiologists will be able to view segmentations directly from PACS as contours or overlays and provide qualitative feedback for model refinement as well as edit these segmentations for quantitative assessment. The proposed workflow can be easily shared for deployment on any clinical PACS.



Automated Segmentation of Tumor Volumes on Serial MRI Exams



(Filename: TCT_566_FiguresFinal.jpg)

Which Acute Ischemic Stroke Patients are “Fast Progressors”? Results from the ESCAPE Trial Control Arm.

J Ospel¹, M Hill², M Kappelhof³, A Demchuk⁴, B Menon⁵, A Mayank⁵, D Dowlatshahi⁶, D Frei⁷, J Rempel⁸, M GOYAL⁹

¹University Hospital Basel, Basel, Basel, ²Cumming School of Medicine, University of Calgary, Calgary, Alberta, ³Amsterdam UMC, University of Amsterdam, Amsterdam, Noord-Holland, ⁴Cumming School of Medicine, University of Calgary, Calgary, Alberta, ⁵University of Calgary, Calgary, Alberta, ⁶The Ottawa Hospital, Ottawa, ON, ⁷Radiology Imaging Associates/RIA Neurovascular, Englewood, CO, ⁸University of Alberta, Edmonton, Alberta, ⁹University of Calgary, CALGARY, ALBERTA

Purpose

Fast infarct progression in acute ischemic stroke (AIS) has a severe impact on patient prognosis and benefit of endovascular thrombectomy (EVT). In this post hoc analysis of the ESCAPE trial, we identified AIS patients with rapid infarct growth and investigated their baseline clinical and imaging characteristics.

Materials and Methods

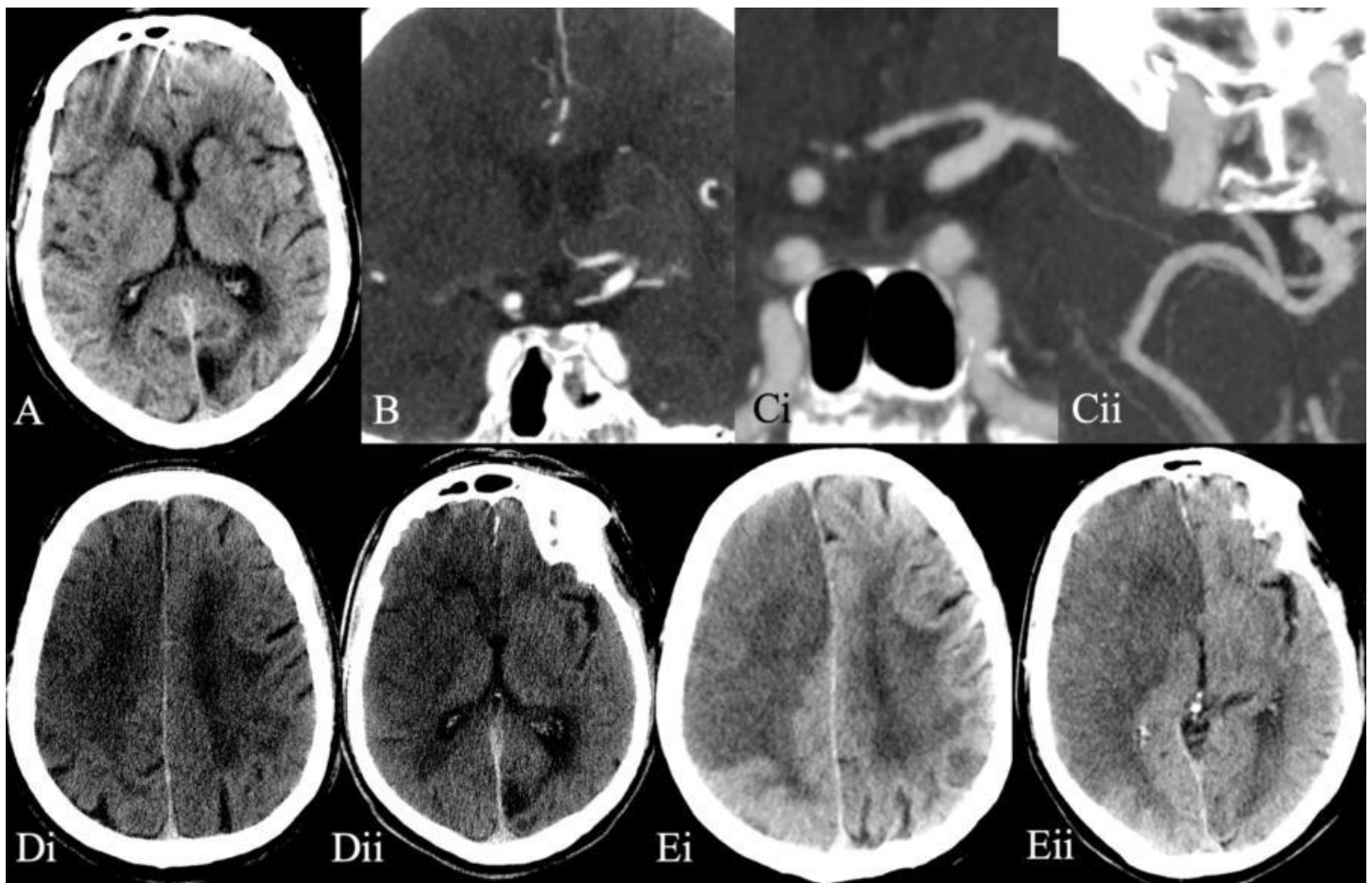
Control arm patients were included if they had follow-up imaging at 2-8 hours without substantial recanalization, and if their baseline Alberta Stroke Program Early CT Score (ASPECTS) was >9. "Fast infarct progression" was defined as ASPECTS decay ≥ 3 points from baseline to 2-8-hour follow-up imaging. Clinical and imaging baseline characteristics were compared between fast progressors and other patients, and occlusion site and collateral flow patterns were assessed in detail.

Results

Fast infarct progression occurred in 15 of 43 included patients (34.9%). The figure shows an exemplary case of a patient with fast infarct progression. Alberta Stroke Program Early CT Score (ASPECTS) at baseline was 10 (A). Baseline mCTA showed an occlusion of the terminal internal carotid artery, M1 and A1 segments ("ICA-T occlusion", shown in B). The patient had no anterior communicating artery (Ci), while the ipsilateral P1 segment and posterior communicating artery were of moderate to large caliber (Cii). Collateral flow via the posterior cerebral artery was therefore possible while collateral flow via the anterior cerebral artery was impaired. Early follow-up imaging was performed at 3 hours and showed an ASPECTS of 3 and infarction of the anterior but not the posterior cerebral artery territory (Di, Dii). (Ei) and (Eii) show 24-hour non-contrast head CT on which infarcts were more clearly demarcated. Fast progressors had worse collaterals (poor in 3/15 [20%] vs. 0/28 patients, $p=.021$), and more carotid-T or -L occlusions (8/15 [53.4%] vs. 3/28[10.7%], $p=.021$). In 8/15 (53.3%), occlusion site and circle of Willis configuration prevented collateral flow via the anterior and/or posterior cerebral artery.

Conclusions

Most patients with fast infarct progression had terminal carotid occlusions and impaired collateral flow via the anterior and/or posterior cerebral artery, indicating that occlusion location and intracranial vascular anatomy are relevant for infarct progression.



(Filename: TCT_1253_figure_fastprogressors.jpg)

911

White Matter Changes Detected Using Multi-shell Diffusion MRI in Asymptomatic Mild Traumatic Brain Injury

S Chung¹, P Amorapanth¹, E Fieremans¹, J Rath¹, D Novikov¹, S Flanagan¹, Y Lui¹

¹NYU Grossman School of Medicine, New York, NY

Purpose

Mild traumatic brain injury (MTBI) is a significant worldwide public health problem. Some MTBI patients recover quickly from a symptomatic perspective, however, it is believed that complete biologic recovery occurs in a delayed fashion after symptom recovery [1,2]. Here we study white matter (WM) microstructure in MTBI subjects with low symptom burden (SCAT3 score of 0 or 1), comparing them both against controls as well as a group of highly symptomatic MTBI patients (SCAT3 score of 3 or higher) using WM tract integrity (WMTI) [3] metrics of multi-shell diffusion MRI in addition to DTI and DKI.

Materials and Methods

We studied 24 MTBI patients (38.5±12.8yrs) within a month of injury and 14 age/gender matched normal controls (NC) (39±12.4yrs). Two MTBI subgroups were identified based on symptom score using the Sport Concussion Assessment Tool (SCAT3): symptomatic MTBI (SCAT3 score of 3 or higher; 5 patients) and asymptomatic MTBI (SCAT3 score of 0 or 1; 9 patients). MR imaging was performed on a 3T scanner (Skyra, Siemens). Diffusion imaging was done using 5 b-values (0.25,1,1.5,2,2.5ms/μm²) with a total of 137 diffusion-encoding-directions using multiband=2, echo-planar imaging (FOV=220×220mm², 2.5mm-isotropic resolution, TR/TE=4.9s/95ms, GRAPPA=2). We calculated maps of WMTI metrics (axonal water fraction [AWF], intra-axonal diffusivity [D_{axon}], extra-axonal axial/radial diffusivity [D_{e,||}/D_{e,⊥}]), as well as DTI (fractional anisotropy [FA], mean/axial/radial diffusivity [MD/AD/RD]) and DKI metrics (mean/axial/radial kurtosis [MK/AK/RK]). The four study groups were compared using region-of-interest (ROI) analysis of 29 regions with age/gender as covariates. A statistically significant level of 0.05 was used.

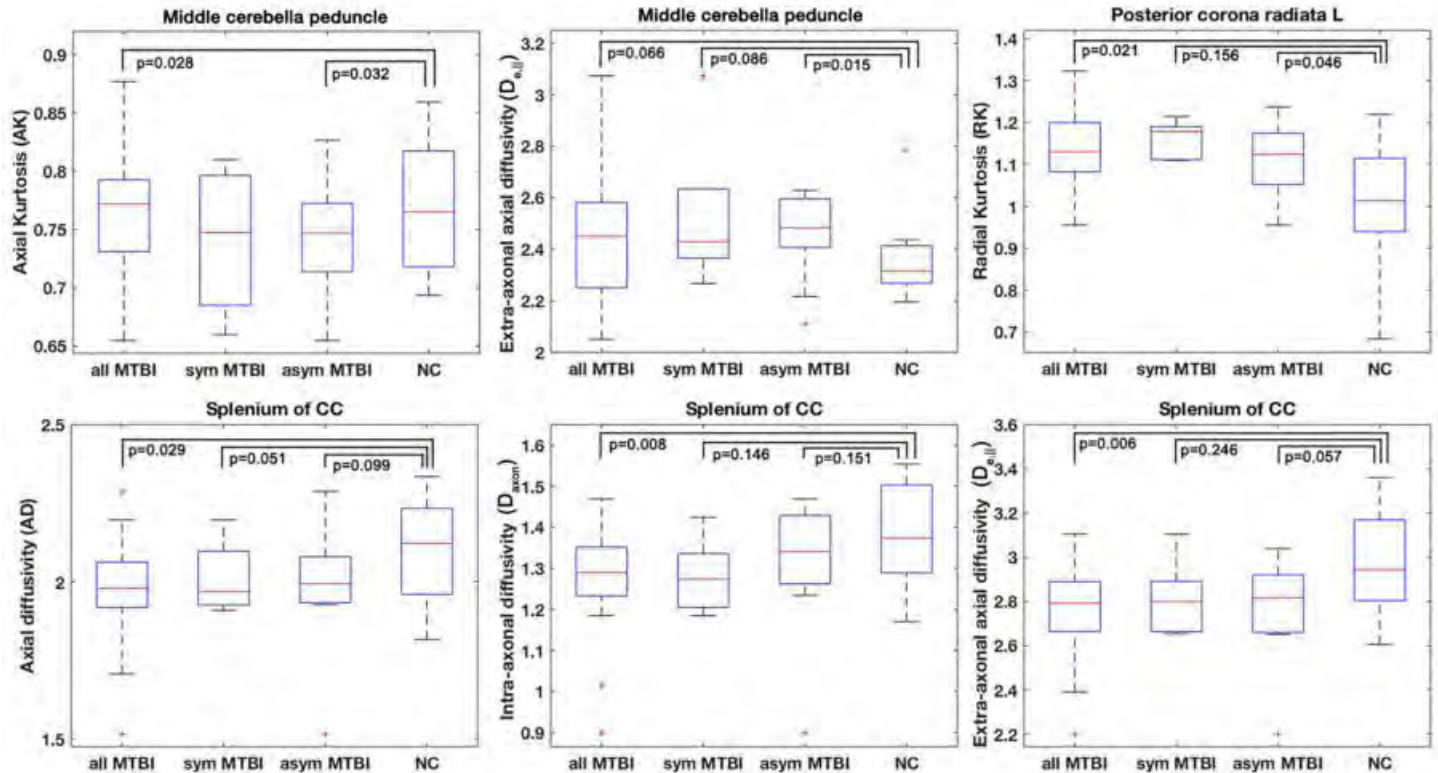
Results

There are significant differences between MTBI groups and controls in several regions (Figure): In MTBI, lower AK and higher D_{e,||} were present in the middle cerebellar peduncle, and higher RK in the posterior corona radiata. In the splenium, a trend towards lower AD, D_{axon} and D_{e,||} was present in MTBI.

Conclusions

Preliminary results show localized WM microstructure differences in several regions of particular vulnerability to injury between

controls and MTBI, specifically including those with low symptom burden. In fact, there are similar differences between low symptom burden MTBI and controls as there are between high symptom burden MTBI and controls. Our results support the idea that biologic recovery lags behind symptom recovery after MTBI.



(Filename: TCT_911_boxplot_all.jpg)

768

Whole - brain intracellular pH imaging in glioma patients using 31P MRSI at 7 Tesla

D Paech¹, N Weckesser², J Breitling², S Goerke², K Deike-Hofmann³, A Unterberg⁴, M Ladd², A Korzowski²

¹German Cancer Research Center, Heidelberg, Baden-Württemberg, ²German Cancer Research Center, Heidelberg, BW, ³Deutsches Krebsforschungszentrum, Heidelberg, Baden-Württemberg, ⁴University Hospital Heidelberg, Heidelberg, BW

Purpose

To obtain whole-brain quantitative intracellular pH maps (pHi) in brain tumors of newly diagnosed patients with glioma employing 31P magnetic resonance spectroscopic imaging (MRSI) at 7.0 T.

Materials and Methods

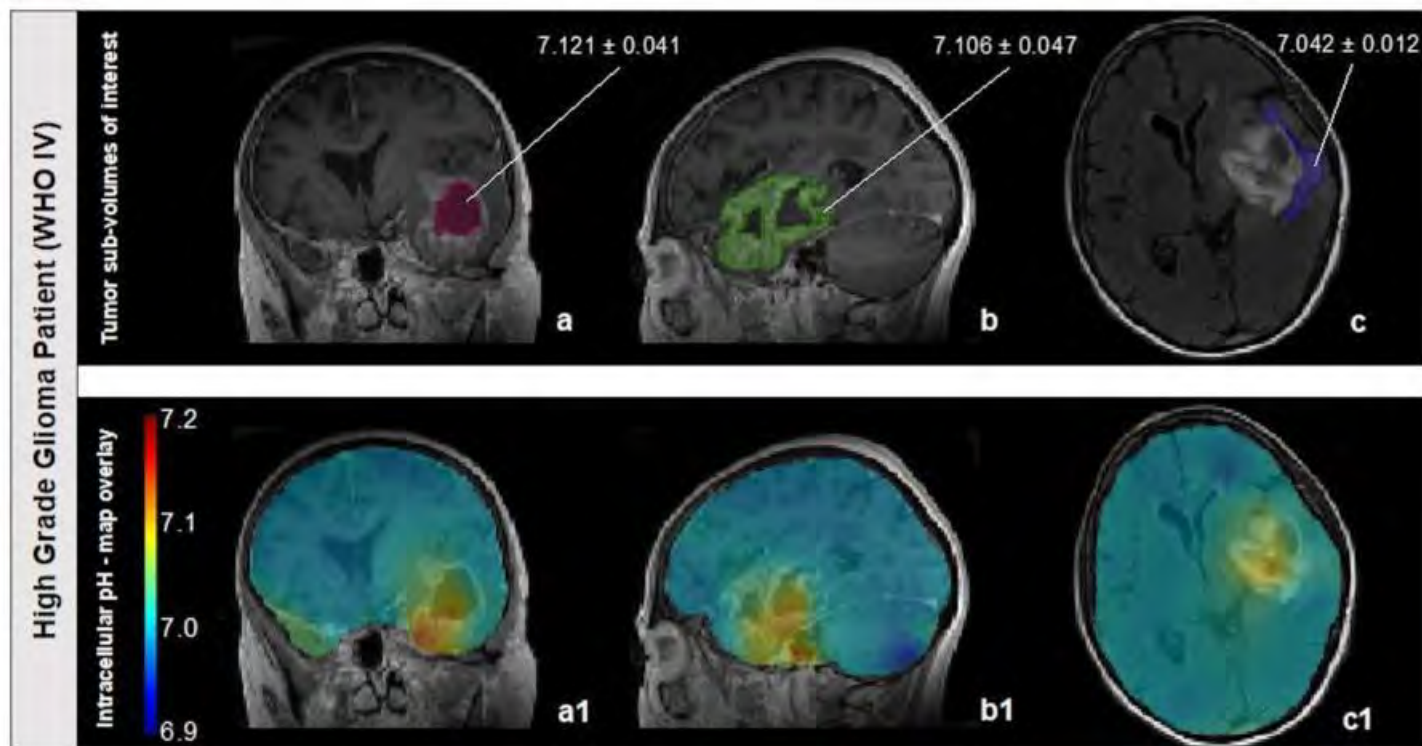
Individuals with newly diagnosed, previously untreated glioma (World Health Organization grade II – IV) were included in this prospective IRB-approved study from September 2018 to November 2019. Highly resolution 31P spectra (voxel volumes with 5.7ml, matrix size = 20x24x16, nominal isotropic resolution = (1.25cm)³, TR = 250ms, $\alpha = 20^\circ$; AT = 51 Min, 18 averages) were acquired at 7.0 T whole-body MRI using a 31P/1H phased array head coil together with a 3D 31P CSI sequence. pHi was quantified in gliomas using 3D volumetric segmentations of the whole tumor volume (WTV) as well as tumor sub-regions (necrosis, gadolinium contrast enhancement, peritumoral edema, and normal-appearing white matter volumes of interest (VOIs)). Segmentations were pHi values in WTV and normal-appearing white matter were compared by using the Wilcoxon rank sum tests. For patients with high-grade glioma, the tumor sub-regions have additionally been compared by using the non-parametric Friedman tests followed by pair-wise Holm-Sidak post hoc tests.

Results

Thirteen participants (58 ± 17 years [mean age ± standard deviation]; eight men) with histopathologically proven glioma were included. Mean pHi values were higher in the WTV (7.050 ± 0.025) compared to normal-appearing white matter (7.007 ± 0.012) over all patients (P < .001) (Fig. 1). In the tumor sub-regions, pHi was increased (necrosis: 7.068 ± 0.031, gadolinium contrast enhancement: 7.066 ± 0.027, edema: 7.039 ± 0.014) compared to normal-appearing white matter (7.005 ± 0.013) for all high-grade glioma patients (P < .001).

Conclusions

Non-invasive whole-brain mapping of pHi is feasible employing high-resolution 31P MRSI at 7.0 T. The presented approach may provide new insights into the pathophysiologically altered tumor microenvironment and glioma metabolism.



(Filename: TCT_768_Fig_1.jpg)

939

Zero-dose PET Reconstruction with Missing Input by U-Net with Attention Modules

J Ouyang¹, K Chen², G Zaharchuk¹

¹Stanford University, Stanford, CA, ²STANFORD UNIVERSITY, STANFORD, CA

Purpose

To synthesize realistic and clinically-meaningful FDG-PET images by multi-contrast MRI using U-Net model with attention modules.

Materials and Methods

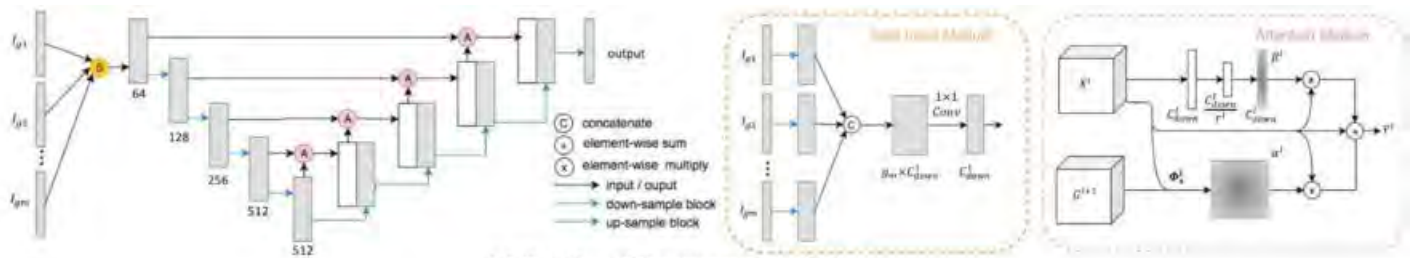
Data Acquisition and Preprocessing: 38 patients with glioblastoma with paired FDG PET and MRI (T1 with contrast [T1c], T2-FLAIR, and ASL) exams were acquired. MRI images were co-registered to PET and further normalized to a standard template. The volumes were normalized by the mean of the non-zero regions. Flipping along the X axis was used for data augmentation. Case-wise 5-fold validation was adopted. **Model:** A 2.5D U-Net worked as the backbone, on which spatial-wise and channel-wise attention modules were added to the short-cuts between layers. The symmetry-aware spatial-wise attention module (SSA) took features with a larger perceptive field from the lower upstream layer as the "guide" signal for learning attention for the detailed features from the downstream layer. Moreover, we flipped the guide signal to take advantage of asymmetry to find abnormalities. The channel-wise attention module (CA) factored out the spatial dependency by global average pooling to learn a channel-specific value that can be used to re-weight the feature maps and emphasize the useful contrasts. We designed a split input module (SI) that first split each channel, and then combined them with CA module before feeding into the U-Net. To handle missing contrasts in the input, we introduced a random dropout training strategy.

Results

Quantitatively, the proposed method improved 10.00% in PSNR, 8.63% in SSIM, and 25.41% in RMSE comparing to the baseline U-Net. Improved performance in the ablation study suggested the effectiveness of all proposed modules. Qualitatively, all three methods performed similarly on the normal regions of the brain. However, the proposed method generated images with more accurate pathological features on the tumor region, which demonstrates the benefits of the precise highlighting in the attention map. For results from the proposed model with random input dropout, it achieved acceptable results except for ASL only as input, as ASL had weak signal and did not provide fine-grained structural information.

Conclusions

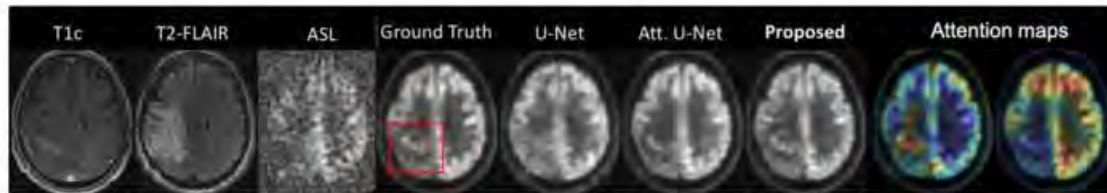
Multi-contrast MRI can be used to synthesize FDG-PET images for GBM cases by the proposed U-Net based model with attention modules.



(a) Overview of the proposed method.

	U-Net (U)	Attention U-Net	(U+SSA)	Proposed (U+SSA+CA)	(U+SSA+CA+SI)
PSNR	26.979±9.500	28.773±12.312	29.246±13.138	29.491±12.562	29.677±12.907
SSIM	0.799±0.007	0.850±0.006	0.861±0.006	0.860±0.006	0.868±0.005
RMSE	0.303±0.007	0.254±0.010	0.243±0.008	0.240±0.006	0.226±0.005

(b) Qualitative Results.



(c) Qualitative results. Left to right: multi-contrast MR inputs, ground-truth FDG PET, results from U-Net, attention U-Net, proposed method, attention maps (3rd and 4th layer) from proposed method.



(d) Results with missing contrast. For outputs from model with random input dropout, missing: No, ASL, T2-FLAIR, T1c, T2-FLAIR+ASL, T1c+ASL, T1c+T2-FLAIR.

(Filename: TCT_939_figure-all.jpg)

624

”Hyperdense Crescent Sign” on Non-contrast Head CT as a Predictor of Craniocervical Junction Injury in Pediatric Trauma

A Cho¹, A Achiriloaic¹, P Kim¹, S Harder¹

¹Department of Radiology, Loma Linda University Medical Center, Loma Linda, CA

Purpose

Pediatric traumatic cervical spine injury occurs at an incidence of up to 1.3%, resulting in significant morbidity (i.e. 60% with permanent neurologic damage) and up to 50% mortality rate, predominantly due to motor vehicle accidents and falls. For patients with suspected head trauma, the initial non-contrast head computed tomography (CT) provides an opportunity to screen for craniocervical junction injuries. Prior studies have found high associations between stripping of the tectorial membrane, atlantoaxial ligament injuries, and the presence of retroclival hematoma in patients younger than 15 years old. Under soft-tissue windows, the detection of retroclival hematoma with lifting of the tectorial membrane at the level of C2 is a critical clue for atlantoaxial ligament injuries and atlantooccipital dissociation (AOD), so-called "hyperdense crescent sign." The aim of the current study is to determine the sensitivity and specificity of this sign on axial non-contrast head CT among trauma pediatric population with AOD.

Materials and Methods

From a single level one trauma tertiary medical center between January of 2004 and July of 2016, a retrospective search resulted in 26 pediatric patients diagnosed with AOD. Sixteen subjects revealed injuries confirmed on cervical spine magnetic resonance imaging, and without significant CT artifact at the craniocervical junction (median age 50, range 2 – 109 months). This trauma group was randomized with a control group of 16 subjects with normal non-contrast CT head studies (median age 57, range 2 – 132 months). These two groups were matched for age and gender. Two board-certified neuroradiologists were blinded from the study subjects, and independently interpreted on the absence or presence of hyperdense retroclival tissue.

Results

Between the trauma and control groups, there were no significant differences for age (mean 50.3 vs 53.3 months; $p = 0.82$) and gender (females 8 vs 10; $p = 0.5$). A Cohen's Kappa analysis for inter-rater reliability demonstrated substantial interobserver agreement

($k=0.65$, 95% confidence interval [0.46,0.85]). Consensus interpretation among the radiologists resulted in a sensitivity of 68.8% and specificity of 100% with negative and positive predictive values of 76.2% and 100%, respectively.

Conclusions

In conclusion, identification of the "hyperdense crescent sign" for retroclival hematoma on axial non-contrast head CT should prompt dedicated imaging to evaluate for craniocervical injury.

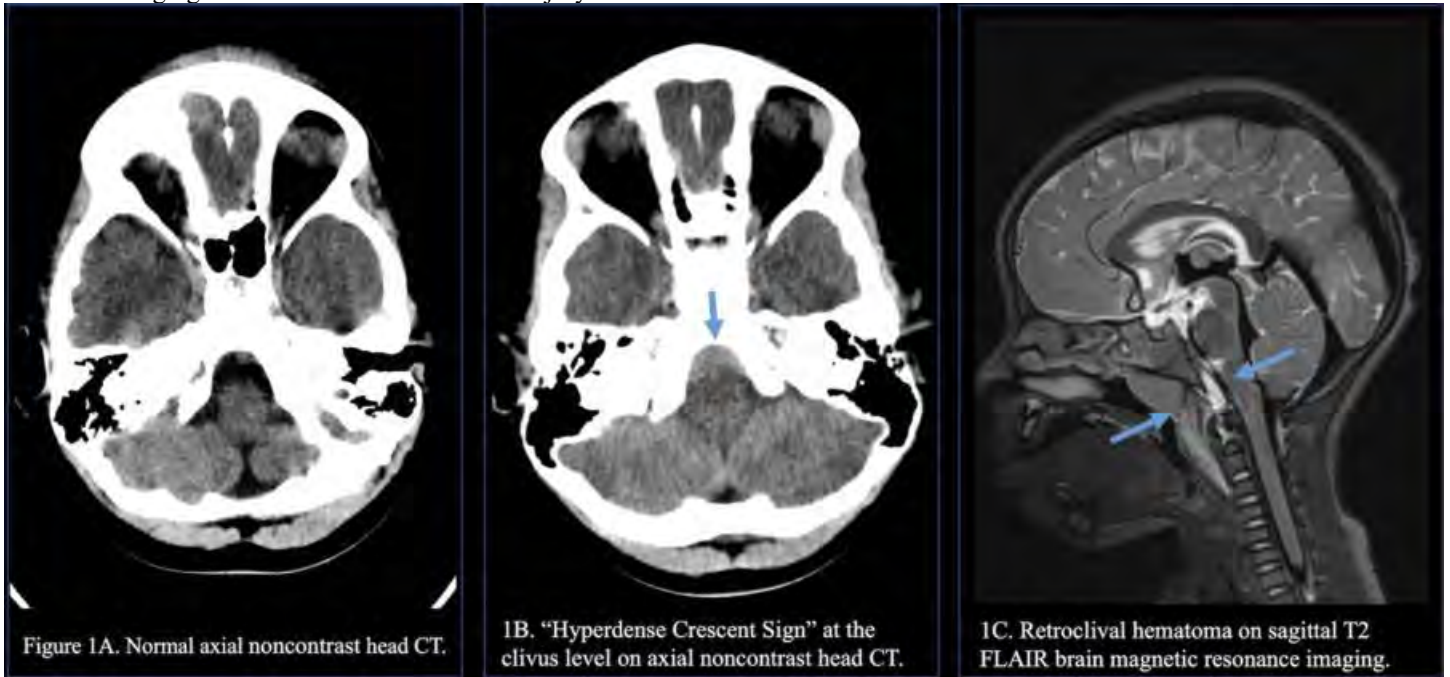


Figure 1A. Normal axial noncontrast head CT.

1B. "Hyperdense Crescent Sign" at the clivus level on axial noncontrast head CT.

1C. Retroclival hematoma on sagittal T2 FLAIR brain magnetic resonance imaging.

(Filename: TCT_624_Figure1.jpg)